DEVELOPMENT OF A GENERAL METHODOLOGY FOR EVALUATION OF CARBON SEQUESTRATION ACTIVITIES

K. Thomas Klasson and Brian H. Davison

Life Sciences Division
Oak Ridge National Laboratory
Oak Ridge, Tennessee 37831-6226

Introduction

The United States may soon be focusing national attention on processes and activities that mitigate the release of CO_2 to the atmosphere and, in some cases, may remove CO_2 from the atmosphere. As we invest national resources to these ends, it is important to evaluate options and invest wisely. How can we apply consistent standards to evaluate and compare various CO_2 sequestration technologies? A standard methodology that considers all the carbon impacts is needed. This would be useful for policy makers to understand the range of options and for technology developers and investors to guide investment decisions. It would also serve as a source of information for calculations or estimations of carbon credits in a future credit trading system.

The performance objective for a sequestration technology is not necessarily zero emission of CO_2 but rather a reduction compared with the baseline of current practice. To make sure that all carbon aspects are considered, care must be taken to ensure that there are no hidden emissions when making an alteration from the baseline. The fundamental question underlying an analysis of merit of a process or alteration of a process is as follows:

How much CO_2 is generated as a result of the sequestration process, and what is the sequestered carbon's ultimate fate?

Both inputs and outputs must be considered to obtain a total picture. When we speak of carbon sequestration in this manuscript, we refer to all greenhouse gas sequestration measured in carbon dioxide or carbon equivalence (CE). The carbon dioxide equivalence is also called the Global Warming Potential (GWP). A complete list of GWP values has been prepared by IPCC.[1]

To address our objective, we have developed and elaborated on the following concepts:

- All resources used in a sequestration activity should be reviewed by estimating the amount of greenhouse gas emissions for which they historically are responsible. We have done this by introducing a quantifier we term *Full-Cycle Carbon Emissions* (FCCE), which is tied to the resource or product.[2]
- The future fate of sequestered carbon should be included in technology evaluations. We have addressed this by introducing a variable called *Time-Adjusted Value of Carbon Sequestration* (TVCS) to weigh potential future releases of carbon, escaping the sequestered form.
- The *Figure of Merit* of a sequestration technology should address the entire life cycle of an activity. The figures of merit we have developed relate the investment made (carbon release during the construction phase) to the lifetime sequestration capacity of the activity.[2] To account for carbon flows that occur during different times of an activity, we incorporate the *Time Value of Carbon Flows*.

In this short preprint we limit ourselves to discussing the development of TVCS and how it relates to FCCE.

Results

Future carbon emissions occurring from sequestered carbon should be considered when evaluating different sequestration approaches. To determine the FCCEs for streams that will cause carbon emissions in the future, we introduce the Time-Adjusted Value of Carbon Sequestration (TVCS). One way to estimate this value is to employ our global climate models to predict changes in atmospheric CO_2 levels as a result of sequestration and future release from sequestered carbon. This would be a labor-intensive task. Moreover, if an individual sequestration effort is moderate, it will be considered merely as noise in existing global models. We propose another approach—to start by defining a sequestration duration goal that will serve as a metric for future reference. For example, we may chose to use 200 years as our goal for sequestration. In this scenario, if we sequester 2 megatons of carbon (2 MtC = 7.4 Mt of CO_2) today and are able to keep it sequestered for at least 200 years, we should receive full value (100%) for the activity. If we have partial or full release in less than 200 years, we are not doing as well and the value is less. The question is this: how do we evaluate different carbon release profiles and determine their proper values?

Consider the graphs in Figure 1a–1d, in which several value curves have been constructed based on the instantaneous release of 2 Mt of sequestered carbon sometime in the future. We will later consider partial release over time. Figure 1a shows a scenario that does not give any value (or credit) to a sequestration of less than 200 years. Figure 1b takes a more gradual approach by applying a straight-line model. Here, if we instantaneously release all the carbon at any time before 200 years (e.g., 150 years), we would get fractional credit (e.g., 150/200×2=1.5 MtC). To give proportionally more credit to longer sequestration periods, we can construct a curve as in Figure 1c. Here we emphasize that there is increasingly more value in focusing on technologies that will keep the carbon sequestered longer, thus discouraging activities with potential quick release. It is clear that this third approach is very sensitive to prior knowledge about the future release, especially for the years close to year 200. To counter this, we may choose to use a fourth approach (Figure 1d) which suggests that we should consider short-term solutions favorably while recognizing that future predictions are hard to make. In all the cases, we have chosen to give full credit, or value, to sequestration past 200 years (or whatever metric we select as a goal).

It should be pointed out that all the curves drawn in Figure 1 were constructed using the same basic equation, namely (for $y \le Y$)

$$Value = \left(Amount\ of\ Carbon\ Released\right) \times \left[\frac{(1+i)^y - 1}{(1+i)^Y - 1}\right] , \qquad (1)$$

where i is the penalty interest rate, y is the number of years sequestered, and Y is the sequestration goal (expressed in years). This equation is of the same type as interest rate functions but has been normalized by the expression in the denominator so that the function takes a value of 1 (one) when $y = Y$. The different curve shapes constructed in Figure 1 were obtained by changing the penalty interest rate from 500% to 0.01% to 3% to –3% for Figure 1a, 1b, 1c, and 1d, respectively. We propose the following abbreviated expression for the modifier:

$$V = R \times TVCS(i, y, Y) \ , \qquad (2)$$

where V is the value of carbon sequestration and R is the amount of carbon released.

The preceding example showed how to penalize (or discount) the maximum sequestration value for discrete releases of the sequestered carbon; however, it is more likely that future carbon release from an activity is predicted via a mathematical expression (e.g., a half-life constant). In this case, Equation 2 is modified to yield the time-integrated value,

$$V = S_C - \int_0^Y R(y) \times \left(1 - TVCS(i, y, Y)\right) dy \ , \qquad (3)$$

where S_C is the net amount of carbon initially sequestered and $R(y)$ is the release profile. The carbon release profile could, for example, be from the use of slowly decomposing ammonium carbonate fertilizer.

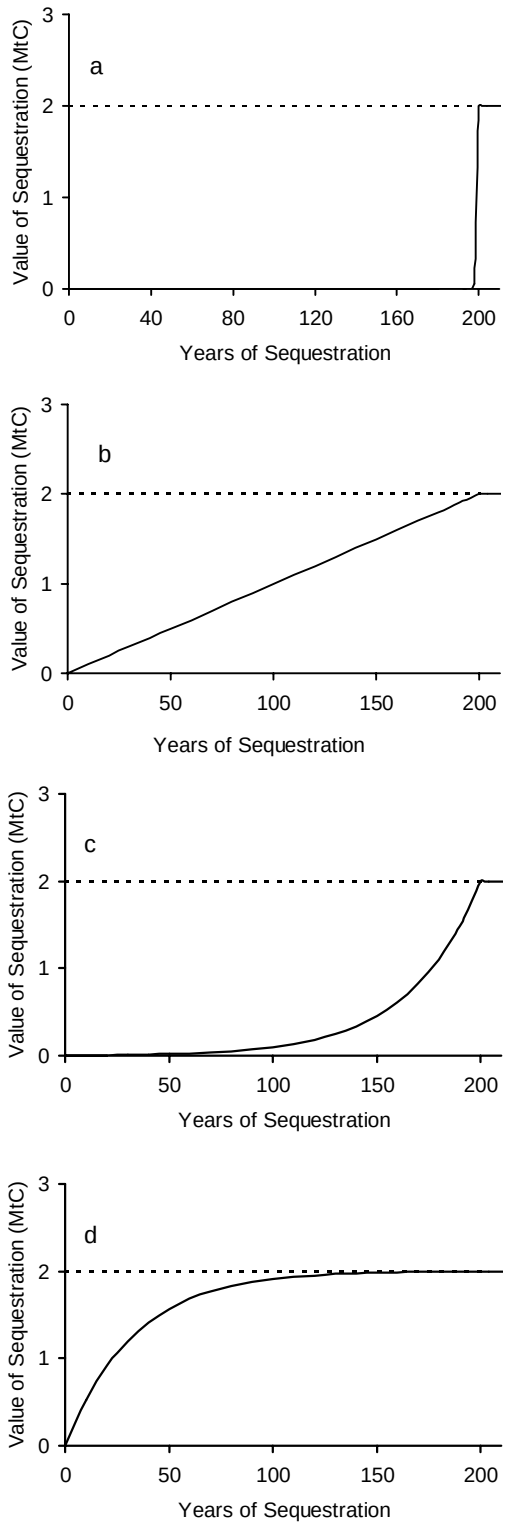

Figure 1. Several potential profiles for calculation of the time value of carbon sequestration.

We have discussed the future release of carbon from a sequestration activity. We should also consider that energy and materials might be needed in the future for "maintenance" to retain the carbon in its sequestered form. Intuitively, we can say that the use of energy and materials in the future should be limited. Because we expect that their use generate CO_2, we need to incorporate this knowledge in the value of sequestration. To keep with the approach that we have taken concerning TVCS, we would value delayed use of energy more than early use. The easiest way to visualize this it to realize that any maintenance in the future will generate CO_2, and this amount must be added to that potentially released from the sequestered carbon. Thus, R in Equations 2 and 3 represent the total CO_2 (or CE) released in the future, whether from captured CO_2 itself or from any CO_2-generating activity associated with the captured carbon. Incorporating maintenance activities into the projected scenario creates a situation that would cause some sequestration technologies to have a negative value, indicating a poor carbon management strategy.

The FCCE of the sequestered carbon stream is the amount of carbon equivalents of future emissions related to this stream. In introducing the TVCS, we have acknowledged that emissions may occur in the future from the sequestered carbon and we have also incorporated a projected value to address future releases. Thus, the time-adjusted FCCE is the right-hand part of the expression in Equation 3,

$$FCCE = \int_0^Y R(y) \times \left(1 - TVCS(i, y_j, Y)\right) dy \,. \qquad (4)$$

Conclusions

Our objective was to develop a general methodology for evaluation of carbon sequestration technologies. We wanted to provide a method that was quantitative but also structured to give robust qualitative comparisons despite changes in detailed method parameters—that is, it does not matter what "grade" a sequestration technology gets, but a "better" technology should always achieve a higher score. We think that the methodology we have begun to develop provides this capability.

- This is a methodology that will assist in evaluation and comparison of well-defined sequestration activities.
- This is a methodology that should be used to address long-term merit prior to engaging in an activity.
- This is a methodology that treats a sequestration activity as an engineering process of which we have knowledge and control.
- This is a methodology that addresses carbon sequestration in life-cycle terms.

Acknowledgement. This work was supported by the U.S. Department of Energy's Office of Fossil Energy Advanced Research Program.

References

(1) *Climate Change 1995—The Science of Climate Change*, Houton, J. T.; Meira Filho, L. G.; Callander, B. A.; Harris, N.; Kattenberg, A.; Maskell, K., Eds.; Cambridge University Press: Cambridge, MA, 1996; pp. 21–22.

(2) Klasson, K. T.; Davison, B. H. *A General Methodology for Evaluation of Carbon Dioxide Sequestration Activities*. Presented at the First National Conference on Carbon Sequestration, May 14–17, 2001, Washington, DC.

A PROTOCOL FOR DETECTION OF SURFACE LEAKAGE FROM A CO_2 INJECTION PROJECT

Ronald W. Klusman

Dept. of Chemistry and Geochemistry
Colorado School of Mines
Golden, CO 80401

Introduction

The success of CO_2 sequestration by deep injection in geologic formations is dependent on the seals and aquitards being able to confine the large amount of fluid injected under overpressured conditions. The possibility for relatively rapid vertical transport of a buoyant phase increases with overpressuring of a reservoir during the injection process. The Rangely, Colorado field has been undergoing large-scale CO_2 injection since 1986 for purposes of enhanced oil recovery (EOR). Cumulative CO_2 injection has been 27.4 billion cubic meters (BCM), of which 11.3 BCM is new, the remainder being recycled gas from production wells.

This report is on methods to detect diffuse surface leakage of gases at the surface. A protocol for the detection of a deep source of gases in the presence of a large amount of surface and near-surface biological production of gases requires a thorough understanding of the noise being generated in the shallow parts of the system and processes influencing soil gas exchange with the atmosphere.

Experimental

Measurements of CO_2, CH_4 and light alkanes at 30-, 60-, and 100 cm in soil gas, and as fluxes into the atmosphere were made in the winter of 2000-01 and summer of 2001, and will continue in the winter of 2001-02. The measurements were at 67 locations over the Rangely field, a background area, and a major fault adjacent to the field. The measurements of CO_2 concentrations for flux calculations were made at each location by field infrared spectroscopy on circulating air from under three closed 1.00 m^2 flux chambers set 10 m apart. Methane from under the flux chambers and soil gas CH_4, CO_2, and light alkanes were analyzed by laboratory gas chromatography. Stable carbon isotope ratios were measured in CO_2 from soil gas and flux chamber samples by isotope ratio mass spectrometry.

Additional measurements were made of soil moisture and temperature, air temperature and barometric pressure, gas permeability of soils and subsoils, stable carbon isotope ratios of various solid and gaseous samples. Five "deep" holes were augered for nested sampling of gases at depths of 1-, 2-, 3-, 5-, and total depth, which ranged from seven to nine meters.

Results and Discussion

The summer fluxes of CO_2 from the soil to the atmosphere had a median of 3.8 g CO_2 m^{-2} day^{-1} and CH_4 fluxes had a median of 0.46 mg m^{-2} day^{-1}, with soil microbiological production/consumption dominating as indicated by stable isotopes. The preliminary winter measurements in 2000/2001 averaged 0.2 g CO_2 m^{-2} day^{-1} and 0.1 mg CH_4 m^{-2} day^{-1}, respectively. These data are summarized in Table 1 where means are shown, and also medians for highly skewed data.

Seasonal variation in both CO_2 and CH_4 fluxes, and in shallow soil gas samples was the largest source of variation. Summer CO_2 fluxes were at least a factor of ten greater than winter fluxes at Rangely, due to rise and fall of root respiration and soil microbiological activity. Methane fluxes were largely influenced by rise and fall of methanotrophic activity, which can consume CH_4 from a subsurface source, and/or from the atmosphere, which then results in negative (downward) fluxes.

Soil gas CO_2 concentrations vary by about a factor of three from summer to winter. Soil gas CH_4 showed little variation from atmospheric concentration, except in a few locations. The stable carbon isotopic data exhibited slight negative values during the winter, suggesting a small, but dominating biological influence on soil CO_2. The atmospheric influence was reduced in the winter of 2000/01 because the soils had some snow cover, and were frozen to at least 30 cm depth. The summer stable carbon isotope data were very close to atmospheric ratios, suggesting an effective exchange with the atmosphere through dry, porous soils.

Two of three "deep" holes over the Rangely field had high CH_4 and alkane concentrations suggesting a deep source of these gases. One of the holes over the field, the single hole over background and the single hole over the Mellen Hill Fault indicated methanotrophic activity consuming atmospheric CH_4.

Short-term noise related to precipitation events, time-of-day measurements, and barometric variation also occurred. In a dry climate, a precipitation event will cause a burst in soil microbiological activity, increasing flux, and shifting stable carbon and oxygen isotopic ratios to more negative values. Barometric gradients exert a significant influence on flux magnitude, resulting in an increased upward flux with falling pressure.

Table 2 illustrates parameters where significant differences were found among the on-field, background, and fault locations for the summer of 2001.

Conclusions

Some evidence of a small magnitude deep source was indicated at Rangely by stable isotopes, and supported by the presence of light alkanes in shallow soil gas over the field, and their absence in a background area of similar surface geology, soils, and climate. Detection of a low intensity, deep diffuse signal requires special care in selection of the parameters to be measured. Faults may serve as conduits for leakage and should also be monitored. The best time for making flux and soil gas measurements will be under winter conditions, when soil respiration and microbiological activity is at a minimum, possibly allowing a deep-source signal to be detected.

Acknowledgement. Financial support provided by Department of Energy, under the "Climate Change Technology Initiative," Grant DE-FG03-00ER15090 to the Colorado School of Mines.

Table 1. Summary of Seasonal Variations in Key Parameters.

	Winter 2000/01 Mean (Median)	Summer 2001 Mean (Median)
CO_2 Flux (g $m^{-2}day^{-1}$)	0.23 (0.19)	3.80 (3.02)
CH_4 Flux (mg $m^{-2}day^{-1}$)	0.10 (-0.18)	3.59 (0.46)
30 cm CO_2 (ppmv)	518.	1091.
60 cm CO_2 (ppmv)	621.	2043.
100 cm CO_2 (ppmv)	836.	2751.
30 cm CH_4 (ppmv)	1.98	32.1(2.39)
60 cm CH_4 (ppmv)	2.03	404.(2.49)
100 cm CH_4 (ppmv)	2.29.	1925.(2.61)
Chamber $\delta^{13}C_{CO2}$-Atm. $\delta^{13}C_{CO2}$(‰)	-0.67	-0.03
30 cm $\delta^{13}C_{CO2}$-Atm. $\delta^{13}C_{CO2}$(‰)	-1.92	+0.02
60 cm $\delta^{13}C_{CO2}$-Atm. $\delta^{13}C_{CO2}$(‰)	-1.58	+0.26
100 cm $\delta^{13}C_{CO2}$-Atm. $\delta^{13}C_{CO2}$(‰)	-1.78	+0.23

Table 2. Non-Parametric Two Group Median Test.

	Background Area	Mellen Hill Fault
CO_2 Flux	-	NA
CH_4 Flux	-	NA
30 cm CO_2	*	*
60 cm CO_2	-	-
100 cm CO_2	-	-
30 cm $\delta^{13}C_{CO2}$	-	* Fault
60 cm $\delta^{13}C_{CO2}$	-	** More
100 cm $\delta^{13}C_{CO2}$	*	* Negative
30 cm CH_4	** On-Field	-
60 cm CH_4	** Highest	-
100 cm CH_4	*	-

NA - Only two flux measurements on Mellen Hill Fault
- Not significant
* Significant at α=0.05
** Significant at α=0.01

Terrestrial Carbon Sequestration Potential

F. Blaine Metting[1], Gary K. Jacobs[2], Jeffrey S. Amthor[2] and Roger Dahlman[3]

Pacific Northwest National Laboratory[1], Oak Ridge National Laboratory[2], U.S. Department of Energy[3]

Introduction

Fossil fuel and land use change have increased the atmospheric content of CO_2 and other greenhouse gases that may be impacting climatic change. Enhanced terrestrial uptake of CO_2 during this century has been suggested as a way to reclaim the 150 or more gigatons of carbon (Gt C) lost to the atmosphere from vegetation and soil as a consequence of land use change, thus effectively "buying time" for development and implementation of long term technical solutions, such as C-free fuels (1). However, the true potential for C sequestration is unknown because of inadequate understanding of biogeochemical, microbial and plant processes responsible for ecosystem storage, particularly as they influence storage in soils, which account for two-thirds of global terrestrial organic C stocks. Technical issues associated with measurement, leakage and longevity need resolution. This presentation considers current understanding of ecosystem potential and innovative technology and addresses key scientific issues related to enhancing C sequestration potential through ecosystem management.

Ecosystem Sequestration Potential

Land use options for enhanced C sequestration at the landscape and regional scales include protection and selective management of native ecosystems, and use of appropriate and advanced management practices in manipulated ecosystems. Table 1 includes estimates of sequestration potential for major ecosystems. Sustained, long-term annual sequestration of more than 5 Gt C is speculative, of course, given that terrestrial systems today sequester only about half this amount, with the exact amount being uncertain (1).

Ecosystem	Primary Method to Increase CS*	Potential CS (GtC/y)
Agricultural lands	Management (H)	0.85 – 0.90
Biomass crop lands	Manipulation (H)	0.5 - 0.8
Grasslands	Management (M)	0.5
Rangelands	Management (M)	1.2
Forests	Management (M)	1 - 2
Wetlands	Restoration and maintenance (M)	0.1 – 0.2
Urban forest and grass lands	Creation and maintenance (M)	< 0.1
Deserts & Degraded lands	Manipulation (H)	0.8 – 1.3
Sediments and aquatic systems	Protection (L)	0.6 – 1.5
Tundra and taiga	Protection (L)	0.1 – 0.3
TOTAL		**~ 5.5 – 8.7**

Table I. Sustained Terrestrial C Sequestration Potential.
*The primary C sequestration method is rated with High (H), Medium (M), and Low (L) levels of sustained management intensity required over the long term. Global potential C sequestration (CS) rates were estimated that might be sustained over a period of up to 50 years (2).

Sequestration Potential In Managed Ecosystems

Enhancing terrestrial C sequestration with proven management practices includes converting marginal land to productive grassland or forest, increasing productivity on crop and forest land with residue management, reduced C loss with modified tillage practices, the efficient use of fertilizer, pesticide, and water, and other technologies. It is difficult to estimate global C sequestration enhancement potential because of inadequate baseline inventories. However, an analysis of the U.S. potential for soil C sequestration can be made (Table 2). Based on such information, conclusions regarding C sequestration potential of managed systems should be applicable wherever in the world local land use and economic conditions are known.

Table 2. Annual U.S. potential for C sequestration from managed forests, arable lands and pastures (2).

	Average C sequestration	
	Low estimate	High estimate
	--- Pg C / year ----	
Forestry		
Converting marginal crop/pasture to forest	0.033	0.119
Increasing timber growth on timber land	0.138	0.190
Growing short-rotation woody crops for energy	0.091	0.180
Increasing tree numbers/canopy cover in urban areas	0.011	0.034
Planting trees in shelter belts	0.003	0.006
Subtotal	0.276	0.529
Arable land		
Cropland conversion to CRP (excluding agroforestry)	0.006	0.014
Soil restoration (eroded land, mine land, salt affected soil)	0.011	0.025
Conservation tillage/residue management	0.035	0.107
Better cropping systems (fertilizer, cover crops, manure)	0.024	0.063
Subtotal	0.075	0.208
Total managed forests, arable land, pastures	0.351	0.737

Enhanced C sequestration in managed lands aims to increase the productivity of crop and forestland. In agriculture, adoption of conservation tillage practices is a viable mechanism that also reduces erosion, increases soil aggregation, and lessens loss of SOM to microbial oxidation (3). The C sequestration potential of the combined practices of no-till, mulch, and ridge tillage was estimated to be 14.1 x 10^6 MT (0.014 Gt) C/yr, with associated savings in fossil fuel equivalent to 1.6 x 10^6 MT C/yr. In addition, managing crop residues from these systems may sequester another 22.5 x 10^6 MT C/yr. As of 1997, 37% of all U.S. cropland was under some form of conservation tillage (3).

The U.S. Forest Service has estimated that 85 Mha of forested land has the potential to increase production through regeneration and stocking control. For an economic constraint of 4% annual return on investment, much of this area could sequester 0.138 Gt C/yr under appropriate management. If all timberlands were managed for C sequestration, the potential might increase to 0.19 Gt C/yr. Another strategy for sequestrating C is the conversion or reallocation of agricultural land to woody crops. Wright et al. (4) estimated that between 14-and-28 Mha of cropland are suitable for woody biomass species with a sequestration potential of between 0.09 to 0.18 Gt C/yr.

Worldwide, temperate grasslands may also be significant. To enhance production and sequestration, it is necessary to manage these lands more closely, with one option being N fertilization. However, grasslands have an inherent capacity to emit N_2O, a strong greenhouse gas. Thus, a comprehensive accounting that includes all greenhouse gas emissions and the C cost of fertilizer production and application is needed to evaluate net sequestration benefits.

Degraded lands also represent some potential for C sequestration. Worldwide, there are approximately 1965 x 10^6 ha of degraded soils;

4% from physical degradation, 56% from water erosion, 28% from wind erosion, and 12% from chemical degradation. With proper management this represents a potential to sequester between 0.81 and 1.03 Gt C/yr. (5).

New Technology for Terrestrial Carbon Sequestration

Science and technology that might drive enhanced terrestrial C sequestration includes (a) technology for soil, crop and forest management, (b) exploitation of underutilized land resources and existing biodiversity, (c) plant biotechnology, (d) microbial biotechnology, and (e) innovative chemical technology. Included is precision agriculture applied to food crops and forestry; i.e., sensor technology, aerial and satellite imaging "just in time" irrigation, fertilization, and other, yet-to-be identified innovations.

Science Needs

There are many fundamental knowledge gaps in our understanding of terrestrial C sequestration needed to identify, develop and implement new sequestration technology. Research efforts to improve basic understanding can be addressed in the context of a primary set of overarching questions in need of resolution:

- How can we best reduce the large uncertainties in global terrestrial C inventories?
- Are native ecosystem C sequestration capacities equivalent to their maximum carrying capacities?
- Is historic storage capacity of terrestrial systems equivalent to maximum inherent capacity?
- What will be the effects of climate change?
- How can ancillary benefits and risks of enhanced C sequestration be adequately quantified?
- What is the potential for plant and microbial biology in the post-genome era to impact C sequestration?

Summary

Storage of C in soils and plants has the potential to offset CO_2 emissions to the atmosphere in the coming decades while new "clean" energy production and CO_2 sequestration technologies are developed and deployed. Because they are economically important, have a rich history of directed research and can be most easily managed, forests and croplands are best suited for application of existing and new technology to enhance terrestrial C sequestration in the near term. Nonetheless, estimates of the potential for enhanced C storage, even in the United States, vary more than two-fold. In addition to proven management approaches, new management, chemical, and biological technology have the potential to impact C storage. What is needed is basic research to improve our fundamental understanding of natural phenomena controlling soil C sequestration and basic and applied research and development to bring new management and technology to the challenge.

Acknowledgement. This contribution is supported by the U.S. Department of Energy, Office of Biological and Environmental Research, provided to the DOE Consortium for Research on Enhanced Carbon Sequestration in Terrestrial Ecosystems (CSiTE).

(1) Intergovernmental Panel on Climate Change; *Climate Change 1995, Impacts, Adaptations and Mitigation of Climate Change: Scientific-Technical Analyses*; Cambridge University Press: Cambridge, **1996**.
(2) Metting, F.B.; Smith, J.L.; Amthor, J.S.; Izaurralde, R.C. *Climatic Change* **2001**, *51*, 11.
(3) Lal, R.; Kimble, J.M.; Follett, R.F.; Cole, C.V. *The Potential of U.S. Cropland to Sequester Carbon and Mitigate the Greenhouse Effect*; Ann Arbor Press: Chelsea MI, **1998**.
(4) Wright, L.L.; Graham, R.L.; Turhollow, A.F.; English, B.C. In *Forests and Global Change: Vol. 1, Opportunities for Increasing Forest Cover*; Sampson, R.N.; Hair, D.Eds.; American Forests Ass., Washington, D.C., **1992**, pp. 123-156.
(5) Lal, R.; *Climatic Change* **2001**, *51*, 35.

Characterization of Soil Organic Matter with Rapid Pyrolysis Molecular Beam Mass Spectrometry (py-MBMS)

K. A. Magrini, C. M. Hoover, R. J. Evans, M. Looker, and M. F. Davis

Chemistry for Bioenergy Systems Center
National Renewable Energy Laboratory
1617 Cole Blvd.
Golden, CO 80401

Introduction

Soil carbon is one of the most poorly understood global carbon pools. This is partly due to the difficulty and expense of current techniques available to measure soil organic matter (SOM) components and changes and partly due to spatial variability and the difficulty of obtaining representative samples. As a result, the uncertainty in SOM knowledge is so great that opposition exists to giving credit for soil carbon sequestration in international greenhouse gas negotiations. The perception is that it will be difficult, if not impossible, to verify claims that carbon is actually being absorbed and retained in soils, a problem that is compounded by the fact that the dynamics and chemistry of SOM are not well understood. The work described here begins to address the need to develop and demonstrate analytical techniques that can rapidly provide information on soil carbon concentration and chemistry, information that is crucial to verifying carbon uptake and storage in the largest terrestrial pool – soil.[1]

A primary component of soil organic matter comes from the decomposition of biomass-derived materials. The resulting humic substances vary greatly in their decomposition rates, and when accurately measured, provide a foundation for estimating the uptake of carbon in soils. Separating and measuring these components with classical techniques is both difficult and complex. Most soil analyses require mechanical preparation, extraction and one or more chemical analyses; processes which are time consuming and labor intensive. Moreover, some analyses may not be representative of the original material due to the harsh chemical separations used.

We have developed the py-MBMS technique for analyzing a wide range of large and complex biomolecules that include lignins, cellulosic materials, plastics, and polymers. Schulten[2] details the application of pyrolysis field ionization mass spectroscopy to identify SOM components. This work applies MBMS analyses to whole soils. The method consists of rapidly heating soil samples (0.1 g) in an inert, helium atmosphere at 500°C for pyrolysis analysis and to 800°C in a helium/oxygen mixture for combustion analysis. Both processes take place at ambient pressure in a quartz reactor, which is connected to the inlet of the MBMS. The generated pyrolysis or combustion products are sampled directly in real time by expanding through a sampling orifice with subsequent formation of the molecular beam, which provides rapid sample quenching and inhibits sample condensation.[3,4,5,6] The molecular beam method of sample generation is rapid (1-5 minutes) and provides sample throughputs of 100-200 samples per day depending on analytical conditions.

To demonstrate the feasibility of these techniques for SOM and total carbon and nitrogen analysis, we analyzed forest soil samples taken from three experimental sites in the Northeast and North Central regions of the country, and agricultural soils managed for switchgrass production (South Central) and hybrid poplar production (Northwest).

At each of the sites, only mineral soil was sampled and 5-cm cores were taken as a function of depth. Samples were dried and sieved through a 2-mm screen prior to MBMS analysis. Soil samples (~0.1 g) were weighed in quartz boats in triplicates and pyrolyzed or combusted in a reactor consisting of a 2.5 cm quartz tube with helium flowing through at 5 L/min (at STP). The reactor tube was oriented so that the sampling orifice of the molecular-beam mass spectrometer (Figure 1) was inside the end of the quartz reactor. We used a molecular beam system comprised of an ExtrelTM Model TQMS C50 mass spectrometer for both pyrolysis and combustion vapor analysis. The reactor was electrically heated and its temperature maintained at 500°C or 800°C. Total pyrolysis time was 5 minutes and combustion time 2 minutes. The residence time of the vapors in the reactor pyrolysis zone was estimated to be ~75 ms. This residence time is short enough that secondary cracking reactions in the quartz reactor are minimal. We used a soil reference material (Carlo Erba, Milan, Italy, PN 33840026) containing 3.55 wt% C and 0.37 wt% N to calibrate the m/z 44 (CO_2) and the m/z 30 (NO) mass spectral peaks.

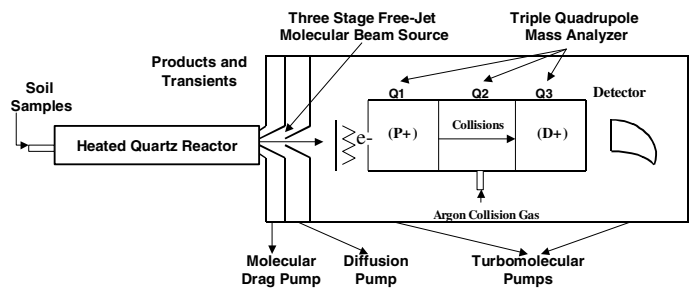

Figure 1. Schematic representation of the molecular beam sampling mass spectrometer (py-MBMS) system. The soil samples were introduced into the heated quartz reactor for pyrolysis and combustion analysis.

Mass spectral data from 15-350 amu were acquired on a Teknivent Vector 2™ data acquisition system using 22eV electron impact ionization. Data acquisition was continuous, through digitization of electron-multiplier signals from the arrival of positive ions and programmed storage in an IBM PC computer. Repetitive scans (typically one 300 amu scan/s) were recorded during the evolution of a pyrolysis or combustion wave from each soil sample. The stored spectra could be manipulated to give average spectra, subtracted spectra, or time evolution of different masses. Using this system, both light gases and heavy molecules are sampled simultaneously and in real time. We used multivariate data analysis (pattern recognition) to handle mass spectral data sets and identify trends to discover the underlying chemical changes that may not be obvious by comparison of such complex mass spectra.[7-8]

Results and Discussion

Figure 2 shows the weight percentages (wt%) of total carbon and nitrogen obtained from combustion-MBMS data from agricultural soils managed for hybrid poplar production. Hybrid poplars, which

grow rapidly, are biomass energy crops. Three sites were sampled in depth increments of 0-5, 5-10, and 10-20 cm. Total carbon (C) and nitrogen (N) contents are the average of two separate samples per site. Site 1 is fallow after one rotation of hybrid poplar, site 2 is currently in a second rotation of hybrid poplar, and site 3 is adjacent unmanaged sagebrush. All samples exhibited decreasing C and N contents with increasing depth. The fallow soil contained the least total carbon and nitrogen likely because of soil disturbance from harvesting the rotation. The soil in the second rotation of poplars contained about twice as much C and N as the fallow site and the amounts were approximately equal in the deeper increments. The unmanaged sagebrush contained the most C and N in the 0-5 cm increment and C and N contents in the 5-10 and 10-20 cm increments were about equal to those of the second rotation. The high C and N content in the 0-5 cm sagebrush increment may be attributed to the presence of dense fine roots from the sagebrush. These preliminary results show the utility of combustion-MBMS method for rapidly determining total C and N contents.

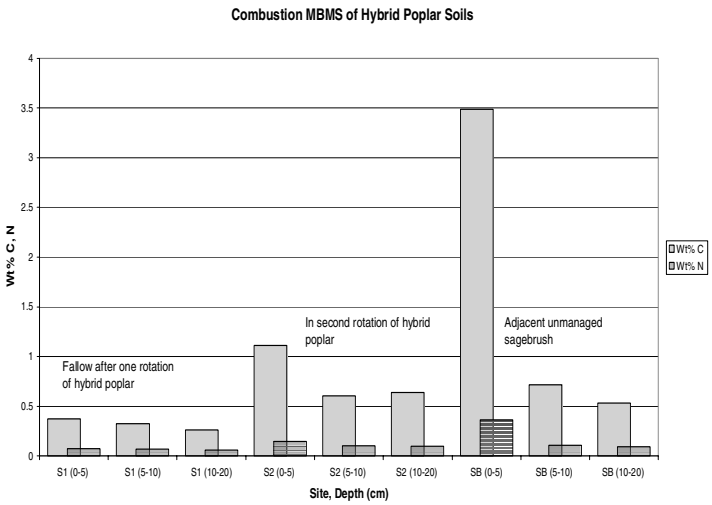

Figure 2. Total carbon and nitrogen contents of soils from a hybrid poplar plantation. Soil cores were taken in depth increments of 0-5, 5-10, and 10-20 cm. The first site (left 3 samples) was fallow after one rotation of poplar had been harvested, the middle 3 samples come from a site in a second rotation of poplar, and the 3 samples on the right are from adjacent unmanaged sagebrush.

Figure 3 shows mass spectra from the pyrolysis of soil samples taken from the Tionesta Scenic and Research Area in northwestern New York. These forest soils, which come from a site vegetated with 600-year old virgin beech hemlock, were chosen for maximum SOM carbon content. Figure 3a shows the pyrolysis mass spectrum for the 0-5 cm depth increment and Figure 3b the spectrum from the 15-30 cm increment. Comparison of the spectra shows that the shallow increment contains pyrolysis products characteristic of more recent biomass decomposition (carbohydrates, lignin) and the deep increment contains more degraded forms of biomass (phenolics, nitrogen-containing compounds).

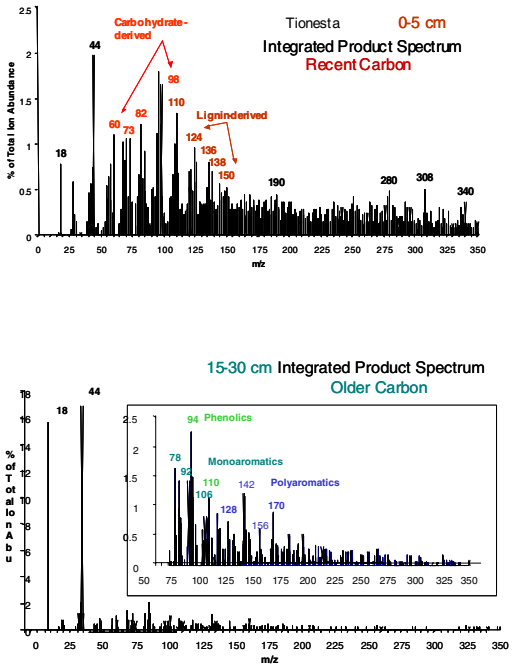

Figure 3: Integrated spectra for 0-5-cm (a) and 15-30-cm (b) samples from the py-MBMS analysis of the Tionesta forest soil. The mass spectra that occur over the pyrolysis wave for each sample are averaged. Higher mass ranges are shown in the inset of (b).

These preliminary results show that py-MBMS can distinguish the chemical changes that occur with depth. Recent biomass is characteristic of shallow samples and more aromatic species, representative of more degraded biomass, are found in the deeper samples. This technique can also distinguish among samples of different ecological sites. With continued development, this rapid analytical technique offers the opportunity to greatly increase our understanding of the role of SOM in carbon sequestration and carbon cycling, and to assess how forest and agricultural management practices can enhance that role.

References

(1) Rosenberg, N. J.; Izaurralde, R. C.; and Malone, E. L. (Eds.), *Carbon Sequestration in Soils: Science, Monitoring, and Beyond;* Battelle Memorial Press, Columbus, Ohio, **1998**; pp. 1-199.

(2) Schulten, H. R., In *Mass Spectrometry of Soils*; Boutton, T. W., Yamasaki, S.-H. Eds., Marcel Dekker, Inc., New York, **1996**, pp. 373-436.

(3) Evans, R. J. and Milne, T. A., *Energy and Fuels,* **1987,** *1*, 123-137.

(4) Evans, R. J.; Milne, T. A.; Soltys, M. N., *J. Anal. Appl. Pyrolysis*, 1986, *9*, 207-236.

(5) Evans, R. J.; Milne, T. A.; Soltys, M. N.; Schulten, H. R., *J. Anal. Appl. Pyrolysis*, **1984,** *6*, 273-283.

(6) Milne, T. A. and Soltys, M. N., *J. Anal. Appl. Pyrolysis*, **1983,** *5*, 93-131
(7) Windig, W.; McClennen, W.H.; Muezelaar, H.L.C., Che*mometrics & Intelligent Lab. Systems,* **1987,** *1*, 151-165.
(8) Agblevor, F. A.; Evans, R.J.; and Johnson, L.D., *J. Anal. Appl. Pyrol.,* **1994,** *30*, 125-144.

ADSORPTION CAPACITY OF CARBON DIOXIDE ON ARGONNE PREMIUM COALS

Karl Schroeder[1], Ekrem Ozdemir[1,2], and Badie I. Morsi[2]

[1] U.S. Department of Energy (DOE) - National Energy Technology Laboratory (NETL), P.O.Box 10940, Pittsburgh, PA 15236
[2] Chemical and Petroleum Engineering Department, University of Pittsburgh, 1249 Benedum Hall, Pittsburgh, PA 15261

Introduction

The sequestration of carbon dioxide (CO_2) in coal seams is one of the geologic strategies being considered to mitigate increasing atmospheric concentrations of CO_2. Historically, the adsorption of CO_2 on coals has been studied to estimate the coal surface area.[1] Usually, these measurements have been conducted at low pressures and low temperatures.[2] Although information obtained from measurements such as these is important to current sequestration efforts, low-pressure adsorption isotherm data may not represent high-pressure in-seam conditions. On the other hand, CO_2 adsorption data obtained at high pressure has been reported to poorly fit the conventional adsorption equations such as the Langmuir (monolayer), BET (multiplayer), and Dubinin (pore filling) equations.[3,4]

The inconsistency between the experimental data and the isotherm equations is proposed to be due to coal swelling.[5] We have derived an expression, which incorporates the effect of swelling and shrinkage of the coal on the CO_2 adsorption isotherm. Its generalized form is given in Equation 1,

$$n_{\exp} = n_{ads} + k\left(\frac{P}{z}\right) \qquad (1)$$

where n_{exp} is the amount of adsorbed gas calculated from the ΔP determined experimentally when the void volume of the sample chamber (V_o) is considered constant at the value estimated by the He-expansion method, n_{ads} is the amount of gas actually adsorbed on the coal sample, and k is a constant, which includes the effect of the volume change in the sample cell. The constant, k, explicitly accounts for the change in volume:

$$k = \frac{(\Delta V/w)}{RT} = \frac{(\Delta V/V_0)}{\rho_0 RT} \qquad (2)$$

where $DV/$w is the change in accessible volume per gram of sample, DV/V_o is the ratio of the change in accessible volume of the sample to the initial sample volume, as estimated by He-expansion, and ρ_o is the helium-density of the sample.

According to Eq.1, the measured adsorption isotherm has two contributing parts: (1) the physical adsorption of CO_2 on the coal sample, n_{ads}, and (2) an artifact of coal swelling caused by the change in accessible pore volume which is closed to helium but accessible to CO_2, $k(P/z)$. A number of equations, including the Langmuir and Dubinin, can be substituted for the physical adsorption term, n_{ads}, to give good correlations. Herein, we use the Langmuir equation. The increased volume available for gas compression we attribute to an opening of the restricted pores by CO_2 which increases the void volume of the sample cell beyond that measurable by helium.

In this study, we report on the adsorption capacity of CO_2 on some of the Argonne Premium coals employing the newly derived adsorption equation.

Experimental

Coal Samples. The proximate and ultimate analyses for the Argonne premium coal samples are shown in **Table 1**.[6] Minus 100 mesh samples were used in all experiments. Sample handling was performed in a helium-flushed glove bag under a positive pressure of helium. Each sample was dried *in-situ* at 80 °C under vacuum for 36 hours before measurements were performed.

Table 1. Proximate and Ultimate Analyses of the Argonne Premium Coal Samples

Coal Sample	Rank	Proximate Analysis (wt%) Moisture	Ash[a]	VM[b]	Ultimate Analysis (wt%, daf) C	H	O	S	N
Pocahontas No.3	Lvb.	0.65	4.74	18.48	91.0	4.4	2.0	0.7	1.27
Upper Freeport	Mvb.	1.13	13.2	27.45	85.5	4.7	7.5	0.74	1.55
Illinois No. 6	Hvb.	7.97	15.5	40.05	77.7	5.0	13.5	2.38	1.37
Wyodak	Subbit.	28.09	6.31	32.17	75.0	5.4	18.0	0.6	1.20
Beulah-Zap	Lignite	32.24	6.59	30.45	73.0	4.8	20.0	0.8	1.04

[a] dry basis
[b] volatile matter, dry basis

Gas adsorption apparatus. Gaseous carbon dioxide adsorption isotherms were obtained using a manometric gas adsorption apparatus described elsewhere.[7] Briefly, the manometric apparatus consists of a reference cell of approximately 13 ml and a sample cell of about 6 ml; both contained within a temperature-controlled bath (±0.1 °C). The cell volumes were estimated by the He-expansion method. The pressure within each of the cells was monitored using a pressure transducer (Omega PX300-5KGV), accurate to ± 0.25% full scale. An ISCO syringe pump was used to deliver pressurized CO_2.

Measurement Methods. Adsorption isotherms of CO_2 on the Argonne Premium coals were measured at 22, 30, 40, and 55 °C. The reference cell was pressurized to the desired level as indicated on a pressure transducer. Thermocouples within the cells showed that thermal equilibrium was established within 3 min. A portion of the gas was then transferred from the reference cell to the sample cell. It was found that 20-30 min was sufficient for the adsorption to reach equilibrium as evidenced by stable temperature and pressure readings. From the calculated volumes of the reference and sample cells, and the constant temperature, the amount of gas that was transferred from the reference cell to the sample cell was calculated using the real gas law, which accounts for the gas compressibility.[8] The difference between the moles transferred from the reference cell and the moles in the gas phase in the sample cell was accounted to the adsorption of CO_2 on the coal. The pressure in the reference cell was then increased and the process was repeated. Adsorption isotherms were plotted as the total amount of adsorbed gas at each equilibrium pressure.

Results and Discussion

The adsorption and desorption isotherms of CO_2 on the Argonne Premium coals were measured at 22, 30, 40, and 55 °C and at pressures up to 4 MPa. **Figure 1** shows the adsorption (open symbols) and desorption (closed symbols) isotherms for CO_2 on these coals at 22 °C. The lines were calculated by substituting the Langmuir expression for n_{ads} in Equation 1 and fitting the resultant equation to the entire range of adsorption data. In general, both adsorption and desorption data fall on the same line. Similar isotherm shapes but with a lower extent of adsorption were seen at the higher temperatures. A small amount of hysteresis was observed only for the Illinois No. 6 sample. The fact that the data for all 5 coals could be fit well using Equation 1 argues favorably for its general form although we recognize that the fit alone does not prove the underlying assumptions of the derivation.

Eq.1 can be employed to differentiate between the adsorbed CO_2 and the effect of coal swelling. This partitioning of the adsorbed amount is shown in **Figure 2** where the measured adsorption isotherm for the Pocahontas coal is divided into the two contributing parts. The portion of the missing gas apportioned to the physical adsorption of the CO_2 is shown as the solid-line Langmuir portion of Equation 1 and the effect of the change in accessible pore volume is displayed as the dashed line. Due to CO_2-induced swelling of the coal during adsorption, the accessible volume available for gas compression increases so that more volume becomes available to the CO_2 than the volume initially estimated by helium expansion. At low-pressures, the effect of swelling on the adsorption isotherm is small when compared with the amount of CO_2 actually adsorbed. At high pressures, however, the amount of gas in the additional void volume is considerably higher due to the compressibility of CO_2.

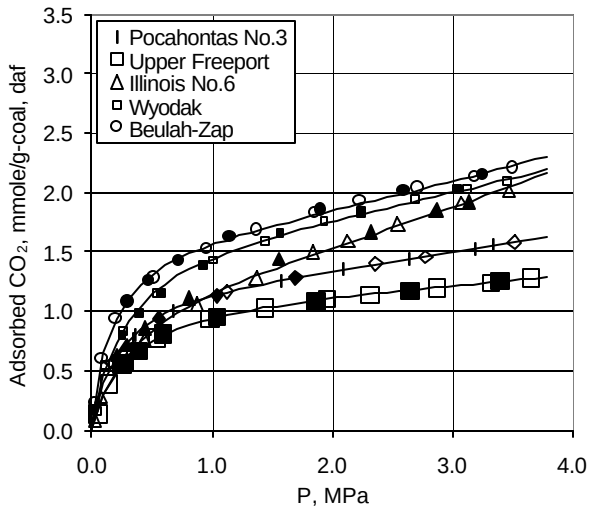

Figure 1. CO_2 adsorption (open symbols) and desorption (closed symbols) isotherms of several of the Argonne Premium.

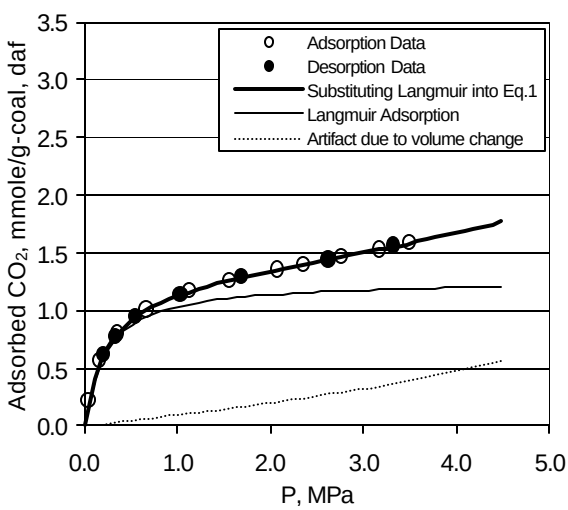

Figure 2. Best fit of Eq.1 (heavy solid line) to the adsorption (open symbols) and desorption (closed symbols) isotherms of the Argonne Premium Pocahontas No.3 coal showing the relative contributions of Langmuir adsorption (solid line) and swelling effects (dashed line).

By substituting the Langmuir or Dubinin-Astakhov equations for n_{ads} in Equation 1, the adsorption capacities were calculated. The heats of adsorption for CO_2 were calculated directly from the Dubinin-Astakhov equation and by using the Clausius-Clapeyron equation and the temperature dependence of the adsorption isotherms in the case of the Langmuir best-fits. These are shown as a function of maf carbon in **Figure 3**. Both decrease with maturation of the coal up to 80-86% C, and then increase with increasing maturation consistent with the U-shaped dependence typical of surface areas, densities, and porosities of coals of different rank.[9] However, the variations in the adsorption capacity and the characteristic heat of adsorption are not large. The adsorption capacities and characteristic heats of adsorption are 0.9-1.7 mmole/g-coal, daf-basis and –26 to –30 kJ/mole, regardless of coal rank.

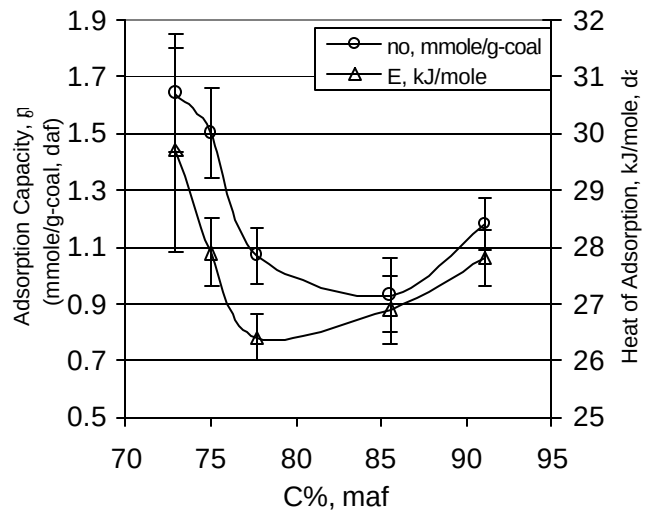

Figure 3. Adsorption capacity and heat of adsorption of CO_2 on several of the Argonne Premium coals.

References

[1] Ettinger, I.; Chaplinsky, A.; Lamba, E. and Adamov, V. *Fuel*, **1965**, 351-356.

[2] Walker, P.L. and Kini, K.A. *Fuel*, **1965**, 44, 453.

[3] Clarkson, C.R.; Bustin, R.M.; and Levy, J.H. *Carbon*, **1997**, 35 (12), 1689-1705.

[4] Duda, J.M.; Duda, J.; Nodzenski, A. and Lakatos, J. *Langmuir*, **2000**, 16, 5458-5466.

[5] Ozdemir, E.; Schroeder, K.; and Morsi, B.I. **2001**, in preparation.

[6] Vorres, K., *Energy Fuels,* **1990**, 4, 420-426.

[7] Ozdemir, E.; Schroeder, K. and Morsi, B.I. Prepr. Pap. - *Am. Chem. Soc., Div. Fuel Chem.*, **2001**, 46 (1), xxx.

[8] Span, R. and Wagner, W. *J. Phys. Chem. Ref. Data*, **1996**, 25(6), 1509-1596.

[9] Jones, A.H.; Bell, G.J. and Schraufnagel, R.A. In: Coalbed Methane, SPE Preprint Series, No.35, SPE, Richardson, TX, 1992.

EFFECT OF SWELLING ON THE ADSORPTION ISOTHERM OF CARBON DIOXIDE ON COAL

Ekrem Ozdemir[1,2], Karl Schroeder[2], and Badie I. Morsi[1]

[1] Chemical and Petroleum Engineering Department, University of Pittsburgh, 1249 Benedum Hall, Pittsburgh, PA 15261
[2] U.S. Department of Energy (DOE) - National Energy Technology Laboratory (NETL), P.O.Box 10940, Pittsburgh, PA 15236

Introduction

Although the study of the adsorption of carbon dioxide (CO_2) on coals has a long history, most of these measurements have been conducted at low pressures (below atmospheric) and low temperatures (-78 °C to 25 °C)[1] in order to estimate coal surface areas.[2] Isotherms obtained at high pressures have been reported to poorly fit the conventional adsorption models including monolayer (Langmuir), multi-layer (BET), and pore filling (Dubinin-Radushkevich (DR) and Dubinin-Astakhov (DA)) models.[3,4]

The purpose of this study was to determine the effect that swelling might have on the equations used to develop the adsorption/desorption isotherms of CO_2 on coal and to apply the newly derived equation to the interpretation of the isotherm data, particularly at pressures greater than one atmosphere.

Experimental

Adsorption apparatus. Gaseous CO_2 adsorption isotherms were obtained using the manometric gas adsorption apparatus as shown schematically in **Figure 1**. The manometric apparatus consists of a reference cell of approximately 13 ml and a sample cell of about 6 ml; both contained within a temperature-controlled bath (±0.1 °C). The cell volumes were estimated by the helium expansion method. The pressure within each of the cells was monitored using a pressure transducer (Omega PX300-5KGV), accurate to ± 0.25% full scale

Measurement Methods. Because the volume of each cell can be calculated, the temperature of the system is constant, and the pressure within each cell is measured, the number of gas-phase moles of any adsorbate in each cell can be calculated from Eq 1 where *z*, the compressibility factor, corrects for real gases.

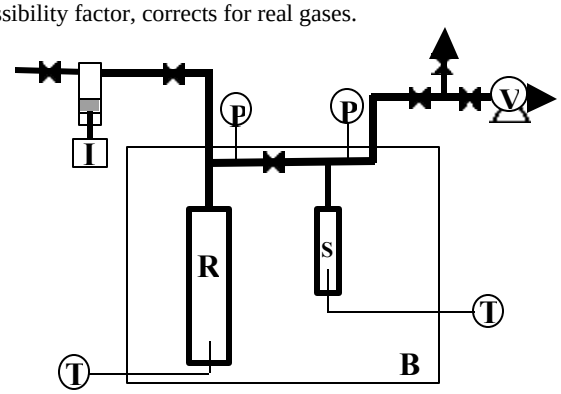

Figure 1. Manometric gas adsorption apparatus: **R**: reference cell, **S**: sample cell, **P**: pressure transducer, **I**: ISCO syringe pump, **V**: vacuum pump **T**: thermocouples **B**: constant temperature bath.

$$n = \frac{PV}{zRT} \qquad (1)$$

The following procedure was used to estimate the amount of CO_2 adsorbed on a coal. (1) Initially, the reference and sample cells contained n_{R1} moles of gas at a pressure of P_{R1} and n_{S1} moles of gas at a pressure of P_{S1}, respectively. (2) The reference cell was charged with n moles of CO_2. At this point, the moles of gas in the reference cell became $(n_{R1}+n)$ at a pressure of P_{R2}. (3) A portion of the gas, Δn_{R1} moles, was transferred from the reference to the sample cell and both cells were allowed to equilibrate. During this period both temperature and pressure were monitored to ensure both thermal and adsorptive equilibrium. At equilibrium, the reference and the sample cells contained $(n_{R1}+n-\Delta n_{R1})$ moles of gas at a pressure of P_{R3} and $(n_{S1}+\Delta n_{S1})$ moles of gas in the gas phase at the pressure of P_{S3}, respectively. If no adsorption were to occur Δn_{S1} would equal Δn_{R1}. Normally, however, the gas phase moles transferred from the reference cell did not equal the gas phase moles found in the sample cell and the missing gas was accounted to CO_2 adsorption on the coal.

The amount of adsorbed CO_2 was calculated from the mass balance in the form of measurable quantities according to

$$\Delta n_{ads} = \frac{1}{w}\left[\left(\frac{P_{R_2}}{z_{R_2}} - \frac{P_{R_3}}{z_{R_3}}\right)\frac{V_R}{RT} - \left(\frac{P_{S_3}}{z_{S_3}} - \frac{P_{S_1}}{z_{S_1}}\right)\frac{V_0}{RT}\right] \qquad (2)$$

where w is the weight of the sample, V_R is the reference volume, and V_0 is the void volume of the sample cell, which is not occupied by the adsorbent (coal) and which was estimated by the helium expansion method prior to the original introduction of CO_2 into the sample cell.

The above procedure was repeated for incrementally increasing pressures of CO_2. Finally, the estimate of the total amount of gas adsorbed, n_{ads}, at the end of the ith step was determined from

$$n_{ads} = \Delta n_{ads_1} + \Delta n_{ads_2} + \Delta n_{ads_3} + ... + \Delta n_{ads_i} \qquad (3)$$

The procedure to this point is typical for the measurement of adsorption isotherms and is applicable to rigid solids. However, we believe it to be inadequate for the description of porous materials that swell in the presence of the adsorbate.

Results and Discussion

Eq 2 is valid only when the void volume in the sample cell (V_0) is constant. However, for coals, it is likely that changes in the available volume in the sample cell occur due to the swelling of the coal, which results from the sorption of CO_2. For example, some micropores are closed to helium and may be accessed by CO_2[5] as shown schematically in **Figure 2**. It can be argued that the void volume measured by helium is not the same as the void volume when these adsorbing gases and vapors are presented to the sample. Thus, an extra accessible volume within the sample cell would be created and should be taken into consideration.

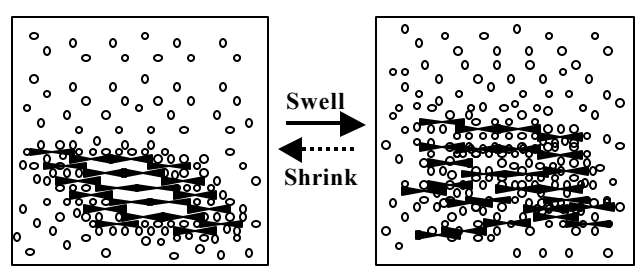

Figure 2. Depiction of the change in the void volume in the sample cell due to pore opening upon the sorption of swelling gases.

In the presence of a volume change, Eq 2 can be written as

$$\Delta n_{ads} = \left(\frac{P_{R_2}}{z_{R_2}} - \frac{P_{R_3}}{z_{R_3}}\right)\frac{V_R}{wRT} - \left(\frac{P_{S_3}}{z_{S_3}}\frac{V_1}{wRT} - \frac{P_{S_1}}{z_{S_1}}\frac{V_0}{wRT}\right) \qquad (4)$$

where V_1 is the void volume accessible for gas compression after the

introduction of CO_2 has swollen the coal and V_0 is the void volume of sample cell as initially measured by the traditional helium expansion method. In this interpretation, the volume inaccessible to the helium and represented by the hollow areas, or bubbles, on the left side of **Figure 2** becomes available for the gas phase compression of CO_2 in the swollen coal. This can be generalized by defining the change in the accessible volume as

$$\chi_i = \frac{V_i - V_{i-1}}{V_{i-1}} \qquad (5)$$

where χ_i is the pore opening coefficient which is dependent on the change in volume at each step (shown as indices i) compared to the previous volume during the adsorption/desorption process. The actual amount adsorbed can be calculated from Eqs 4 and 5 to give Eq 6.

$$\Delta n_{ads} = \underbrace{\left(\frac{P_{R_2}}{z_{R_2}} - \frac{P_{R_3}}{z_{R_3}}\right)\frac{V_R}{wRT} - \left(\frac{P_{S_3}}{z_{S_3}} - \frac{P_{S_1}}{z_{S_1}}\right)\frac{V_0}{wRT}}_{PART\,II} - \underbrace{\frac{P_{S_3}}{z_{S_3}}\frac{\chi_1 V_0}{wRT}}_{PART\,III} \qquad (6)$$

As shown in Eq.6, the adsorbed amount has two parts. The first part (PART I) is the experimentally determined amount of adsorbed gas (n_{exp}), in which there is no change in the volume in the sample cell and it remains constant at the value estimated by helium expansion. The second part (PART II) is the amount of gas occupied by the nascent cell volume, which was created as a result of the change in the accessible pore volume that occurred when the adsorbent became swollen or shrunken upon the adsorption or desorption of the gas, respectively. A general form of the adsorption equation can be obtained by combining Eqs 3, 5, and 6 to give:

$$n_{\exp} = n_{ads} + k\left(\frac{P}{z}\right) \qquad (7)$$

where n_{exp} is the same as n_{ads} in Eq 3, above, and represents the experimentally calculated total amount of adsorbed gas when the void volume of the sample cell (V_o) is constant, n_{ads} is the actual amount of adsorbed gas on the coal sample, and k is a constant expressed as

$$k = \frac{(\Delta V/w)}{RT} = \frac{(\Delta V/V_0)}{\rho_0 RT} \qquad (8)$$

where DV/w is the change in the accessible pore volume per gram of sample, DV/V_o is the ratio of the change in accessible pore volume of sample per the initial volume, and ρ_o is the helium-density of the sample.

In Eq.7, the only unknowns are the n_{ads} and k. Several equations can be used for the gas adsorption term (n_{ads}) including the Langmuir, DR, and DA equations. When a particular adsorption model is used to fit the experimental adsorption isotherm data, information about coal-CO_2 interactions, such as the monolayer adsorption capacity, the micropore volume, the equilibrium (Langmuir) constant, and/or the characteristic heat of adsorption, can be estimated along with the change in the accessible pore volume in the coal.

The adsorption isotherms of CO_2 at 22°C on the Argonne Pocahontas No.3 and Beulah-Zap coals are shown in **Figure 3**. The lines represent the best-fit values over the entire range of adsorption data. The Langmuir and DA are shown as examples of models that may be used. In practice, we found no significant difference among the three adsorption models investigated once the effect of the swelling was taken into account. As shown in **Figure 3**, the measured adsorption isotherms can be divided into two contributing parts. One is the actual, physical adsorption of CO_2 (Langmuir or DA in the Figure), and the other is the effect of swelling on the accessible pore volume. At low-pressures, the effect of the swelling on the adsorption isotherm is small when compared with the amount actually adsorbed. At high pressures, however, the amount of gas in the additional void volume is considerably higher due to the compressibility of CO_2. Thus, the derived equation is especially important at higher pressures when coal swelling cannot be ignored.

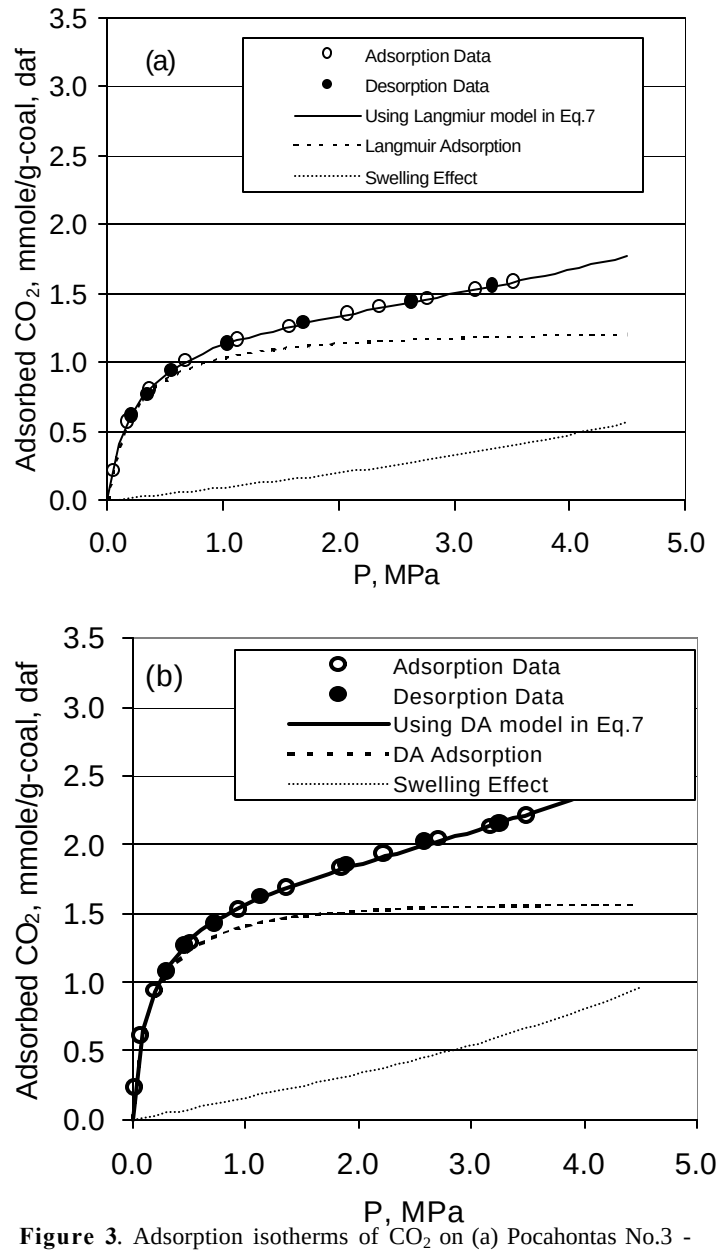

Figure 3. Adsorption isotherms of CO_2 on (a) Pocahontas No.3 - modified Langmuir Eq. (b) Beulah-Zap - modified DA Eq.

References

[1] Walker, Jr., P.L. and Kini, K.A. *Fuel*, **1965**, 44, 453.
[2] Ettinger, I.; Chaplinsky, A.; Lamba, E.; and Adamov, V. *Fuel*, **1965**, 351-356
[3] Clarkson, C.R.; Bustin, R.M.; and Levy, J.H. *Carbon*, **1997**, 35 (12), 1689-1705
[4] Duda, J.M.; Duda, J.; Nodzenski, A.; and Lakatos, J. *Langmuir*, **2000**, 16, 5458-5466
[5] Toda, Y. *Fuel*, **1972**, 44, 108

Molecular Basis for Carbon Dioxide Sequestration in Coal

Thomas J. Dick, Orlando Acevedo, Pranav Dalal, Jeffry D. Madura, Jeffrey D. Evanseck, and Jonathan P. Mathews[#]

Center of Computational Sciences, and Department of Chemistry and Biochemistry, Duquesne University, 600 Forbes Avenue, Pittsburgh, PA 15226;
The Energy Institute & Department of Energy & Go-Environmental Engineering, 151 Hosler Building, The Pennsylvania State University, University Park, PA 16802

Introduction

Sequestration of CO_2 within coal seams that are either too deep, thin, or uneconomic has been suggested to mitigate climate change. Additionally, if there is methane present within the coal it can be replaced with the carbon dioxide, apparently at a 2:1 ratio (1) thus releasing CH_4 to help offset the sequestration cost. We have utilized computational molecular modeling to investigate the forces involved between bituminous coal structure (or idealized pores) and the molecular species CH_4 and CO_2. The molecular computations and simulations provide useful information on accessible pore volumes, energy of interactions between host and guest molecules, self-diffusion coefficients, identification of likely sorption sites, impact of carbon dioxide sorption/methane exchange upon the coal matrix (expansion/contraction), and competitive adsorption isotherms.

Experimental

Density functional theory, second-order Moller-Plesset theory, and classical molecular dynamics were utilized to investigate three chemical models of coal. In order of increasing model sophistication, small molecules (CH_4, CO_2, and N_2) were complexed with (a) anthracene, (b) nanotube(s), and (c) model of bituminous coal structure. Our goal is to uncover the fundamental physical interactions between small molecules and simple aromatic structures, and use the computed information to enhance the sequestration of CO_2 in more complex coal structures.

Anthracene Model. All density functional theory calculations were carried out with the Gaussian 98 program (2), using a 16-node SP IBM RS/6000 super computer. The Becke three parameter exchange functional and the nonlocal correlation functional of Lee, Yang, and Parr (B3LYP) with 6-31G(d) basis set was employed. All energy optimizations and frequency analyses were performed using the B3LYP/6-31G(d) level of theory, which has been shown to produce realistic structures and energies for weak nonbonding interactions between aromatics and small organic molecules. Vibrational frequency calculations at the same level of theory were used to confirm all stationary points as either minima or transition structures, and provide thermodynamic and zero-point energy corrections. The energy profile for CH_4, CO_2, and N_2 traversing across anthracene, see Figure 1, are investigated to determine the structure and energy of interaction as the small molecules passes over the aromatic structure.

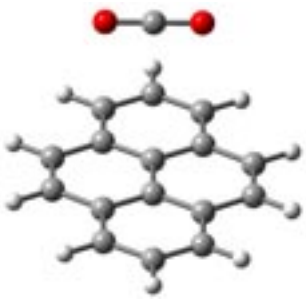

Figure 1. Oblique View of CO_2 Interacting with Anthracene.

Nanotube Model. Insight II was used to plot the energy profile of the gases within idealized pores, here treated as buckeytubes and buckyballs. In our first case, a nanotube was constructed, as shown in Figure 2. Dummy atoms set along the centerline of the "pore" was used to define a pathway for the molecules. A strong harmonic "pushed" the guest molecule along the defined pathway and the structure allowed to minimize. To save computational expense the "pore" was rigid and did not relax or strain with the passage of the molecule. Step size along the centerline was 0.2 Å. The dummy atoms were placed several rings within the tube to reduce "end effects". The energy of interaction between the host and guess molecule were followed. Similar techniques have been used in Zeolite simulations (3) and are well discussed there.

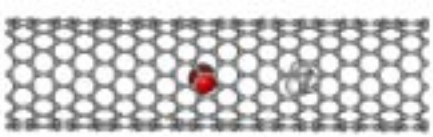

Figure 2. 3D Representation of a nanotube with CH_4 and CO_2 inserted in its cavity.

Classical molecular dynamics calculations were performed to compute the potential of mean force of each solute through the nanotube model. Self-diffusion coefficients were also computed using molecular dynamics simulations.

Bituminous Coal Model. Recent experimental and computational advances have the potential to produce a first-time reasonable constitutional model (chemical and physical structure) and enable its use. First, structural diversity may be incorporated through the combination of high-resolution transmission electron microscopy (HRTEM) and laser desorption mass spectroscopy, which has not been previously included into a three-dimensional structural model of coal (4). Secondly, methodological advances in molecular simulations that have been successfully applied to biomolecular systems and new engineering materials coupled with available high capacity and high speed parallel super computers make the modeling of CO_2 sequestration by coal realistic and practical. A relatively simplistic three-dimensional model of bituminous coal structure (5) is given in Figure 3.

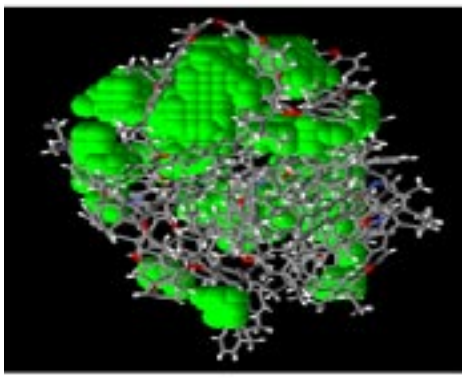

Figure 3. Porosity (green spheres) of a Bituminous Vitrinite Coal Model

The CHARMM (6,7) force-field was used in our simulation work (many more will be evaluated). Constant pressure molecular dynamics have been carried out using periodic boundary conditions. Physical aspects such as porosity will be compared to experimental values to ensure a reasonable representation of our proposed large-scale coal model simulation (> 50,000 atoms). The time-scale used will be consistent with the diffusion times of the slowest diffusion rates.

Results & Discussion

Figure 4 shows the relative size and shape of the three gasses: nitrogen, methane, and carbon dioxide. The sizes appear similar to the naked eye although significant differences in size are present (when in appropriately sized pores), although methane is bulkier. The quadrupole and octapole from the higher-level quantum mechanical computations are also used to better understand the sorption of the small molecules to aromatic surfaces.

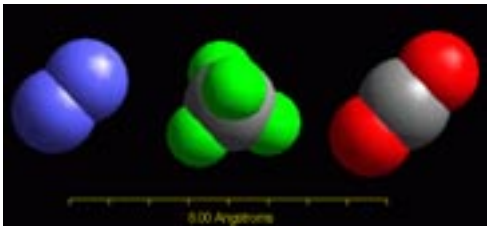

Figure 4. Relative Size and Shape of N_2, CH_4 and CO_2

To test the molecular interactions, a low level of molecular modeling was first utilized. The results of this basic simulation are shown in Figure 5. Nitrogen as expected had the "easiest" transition through the "pore". The shape of the molecule permitted the long axis to lie perpendicular to the "pore" axis and low energetic strain indicated only slight conformational changes where required. Methane being a bulkier molecule has to undergo conformational changes to "squeeze" through the pore. An oblique view of both CO_2 and CH_4 inside of the nanotube is given in Figure 6. Greater peaks and valleys in the plot (Figure 5) indicate conformational changes to accommodate the passage. These conformational changes can be treated as an apparent activation energy. This low apparent activation energy indicates the molecule will pass though the pore with little retention. Carbon dioxide however has a very different profile and a much higher apparent activation energy to the passage within the pore. Several local energy minima and global energy minima are present. These are sites where the interaction energy between the host and guest molecule would require significant conformational rearrangement to proceed through the pore, possibly becoming "trapped" within the pore.

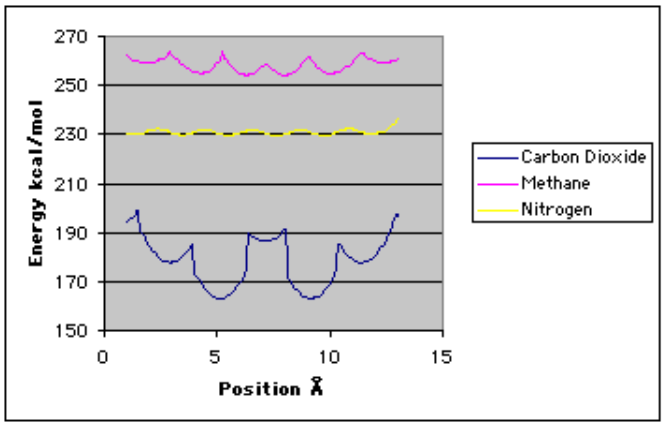

Figure 5. Energy Profile of CO_2, CH_4 and N_2 within a Nanotube

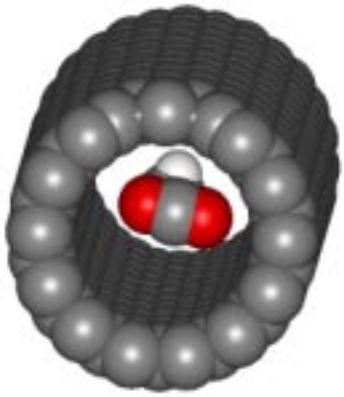

Figure 6. CPK representation of CO_2 (front) and CH_4 (back) inside the nanotube.

Conclusions

We aim to use accurately computed atomic-level structural and dynamical information to aid in the creation of technology for optimal geological sequestration of CO_2. Our strategy is to generate a realistic and testable three-dimensional state-of-the-art molecular model of Pocahontas No. 3 coal by incorporating new structural diversity information based upon HRTEM and laser desorption data (rather than average values), while maintaining traditional analytical information (i.e., H/C aromaticity) and physical parameters (i.e., density and pore volume). Large-scale molecular dynamics simulations (> 50,000 atoms) will be carried out on this model to follow its structural changes during addition of CO_2 and removal of CH_4. The simulation work will also be used to determine the differences in sorption characteristics and diffusion rates between CO_2, H_2O, N_2 and CH_4. This significance of the proposal is that new opportunities in the optimization and gaseous management necessary for low-cost forms of CO_2 sequestration will result from this novel procedure.

Acknowledgement. The authors thank support from the University Coal Research Program at American Universities for funding for this research.

References

1. Gentzis, T., *International Journal of Coal Geology*, 2000, **43**, (1-4), 287.
2. Frisch MJ, Trucks GW, Schlegel HB, Scuseria GE, Robb MA, Cheeseman JR, Zakrzewski VG, Montgomery JA Jr., Stratmann RE, Burant JC, Dapprich S, Millam JM, Daniels AD, Kudin KN, Strain MC, Farkas O, Tomasi J, Barone V, Cossi M, Cammi R, Mennucci B, Pomelli C, Adamo C, Clifford S, Ochterski J, Petersson GA, Ayala PY, Cui Q, Morokuma K, Malick DK, Rabuck AD, Raghavachari K, Foresman JB, Cioslowski J, Ortiz JV, Stefanov BB, Liu G, Liashenko A, Piskorz P, Komaromi I, Gomperts R, Martin RL, Fox DJ, Keith T, Al-Laham MA, Peng CY, Nanayakkara A, Gonzalez C, Challacombe M, Gill PMW, Johnson B, Chen W, Wong MW, Andres JL, Gonzalez C, Head-Gordon M, Replogle ES, Pople JA. Gaussian, Inc., Pittsburgh PA, 1998; *Gaussian 98*, Revision A.5.
3. Horsley, J. A., Fellmann, J. D., Derouane, E. G. and Freeman, C. M., *J. of Catalysis*, 1994, **147**, 231.
4. Mathews, J. P., Jones, A. D., Pappano, P. J., Hurt, R. and Schobert, H. H., New insights into coal structure from the combination of HRTEM and laser desorption ionization mass spectrometry, 11th Int. Conf. on Coal Science, 2001, San Fransico, CA
5. Mathews, J. P., Hatcher, P. G. and Scaroni, A. W., Proposed Model Structures for Upper Freeport and Lewiston-Stockton Vitrinites, Energy & Fuels, 2001, 15, (4).
6. MacKerell, A. D Jr.; Bashford, D.; Bellott, M.; Dunbrack, R. L.; Evanseck, J. D.; Field, M. J.; Gao, J.; Guo, H.; Ha, S.; Joseph, D.; Kuchnir, L.; Kuczera, K.; Lau, F. T. K.; Mattos, C.; Michnick, S.; Ngo, T.; Nguyen, D. T.; Prodhom, B.; Reiher, W. E.; Roux, B.; Schlenkrich, M.; Smith, J.; Stote, R.; Straub, J.; Watanabe, M.; Wiorkiewicz–Kuczera, J.; Yin, D.; Karplus, M. *J. Phys. Chem. B* **1998**, *102*, 3586.
7. B. R. Brooks, R. E. Bruccoleri, B. D. Olafson, D. J. States, S. Swaminathan and M. Karplus, *J. Comput. Chem.*, 1983, **4**, 187-217.

Thermodynamics of the Sequestration of Carbon Dioxide in Methane Hydrates in Porous Media

Joseph W. Wilder, Kal Seshadri, Duane H. Smith

U.S. Department of Energy, National Energy Technology Laboratory, Morgantown, WV 26507-0880, dsmith@netl.doe.gov, Phone:(304) 285-4069

Concerns about potential effects of rising carbon dioxide levels in the atmosphere have stimulated interest in a number of carbon dioxide sequestration studies. One suggestion is the sequestration of carbon dioxide as clathrate hydrates by injection of carbon dioxide into methane hydrates. Energy-supply research estimates indicate that natural gas hydrates in arctic and sub-seafloor formations contain more energy than all other fossil fuel deposits combined. The simultaneous sequestration of carbon dioxide into deposits of natural gas hydrates, if possible, represents a potentially efficient and cost effective option for the sequestration of carbon dioxide.

Data in the literature show that the conversion of bulk methane hydrate into carbon dioxide hydrate is thermodynamically favored. These results are not directly applicable to naturally occurring hydrates, because the hydrates in these locations are embedded in sediments. In addition, naturally occurring hydrates are normally made up of mixtures of natural gases, often predominately methane. The thermodynamics of any potential conversion of hydrates involving methane to carbon dioxide hydrate would therefore be affected by the size of the pores in which the conversion would take place, as well as the composition of the gas. We have developed a model that can be used to interpret or predict hydrate formation in porous media for any pore size distribution, allowing for the calculation of the heats of formation of these hydrates in porous media as a function of pore size and temperature. These results are applied to mixtures of methane and carbon dioxide. This allows for a preliminary assessment of the thermodynamic feasibility of converting hydrates formed from methane to carbon dioxide hydrate in porous media involving various size pores.

Introduction

The build up of carbon dioxide in the atmosphere has become of great interest due to the potential of this gas to play an important role in greenhouse effects, and its reported potential to induce global warming on the order of 2 – 5 K over the next century[1]. As a result of these concerns, researchers have suggested various methods to sequester carbon dioxide in order to remove it from the atmosphere. One sequestration scheme[2] is the injection of carbon dioxide into methane hydrate deposits, which it is suggested could result in the simultaneous sequestration of the carbon dioxide and the liberation of methane (which could then be collected and used as a clean fuel). Gas hydrates are crystalline structures that involve a lattice made up of hydrogen-bonded water molecules. This lattice includes cavities that can be occupied by gas molecules. Gas hydrates (such as methane hydrate) form under low temperature – high pressure conditions, both above and below the freezing point of water. Due to the large size of naturally occurring methane hydrate deposits, this represents a vast potential supply of methane. The simultaneous sequestration of carbon dioxide and liberation of methane represents a potentially cost-effective sequestration scheme for carbon dioxide. Since much of the worlds naturally occurring methane hydrates are in sediments below the ocean floors or in permafrost regions, it is necessary to consider the effects of porous media on the formation of gas hydrates.

Studies by Makogon[3] in sandstones suggested that the pressure required for hydrate formation increased as the pore size was decreased. Differences in chemical potentials and interfacial forces between the bulk and pore water affect hydrate formation in pores. Handa and Stupin[4] studied methane and propane hydrates in silica gel of 7.5 nm nominal pore radius, and Uchida et al.[5] investigated the properties of methane hydrate in three porous Vycor glass samples with pore radii of 25 nm, 15 nm, and 5 nm. In a recent work[6] the authors presented measurements for propane hydrate formation in silica gels of nominal pore radii of 7.5 nm, 5.0 nm, 3.0 nm, and 2.0 nm. Injection of carbon dioxide into methane hydrate deposits with the subsequent sequestration of the carbon dioxide and liberation of the methane would result in hydrates in equilibrium with a mixture of free carbon dioxide and methane. No results for hydrates in porous media formed from gas mixtures have been reported in the literature. In this work we consider the prediction of the equilibrium pressure for mixtures of methane and carbon dioxide in porous media based on a statistical thermodynamic model. The model is then used to estimate enthalpies of dissociation of hydrates formed from mixtures of carbon dioxide and methane in porous media.

Model Description

Munck et al.[7] presented a single equation involving T_f and P_f (the temperature and pressure under which the hydrate forms) that can be used to predict hydrate formation conditions under bulk conditions. This equation can be written as

$$\frac{\Delta m_W^0}{RT_0} - \int_{T_0}^{T_f} \frac{\Delta H_w}{RT^2} dT + \int_0^{P_f} \frac{\Delta V_w}{R\bar{T}} dP - \ln\left(g_w X_w\right) + \sum_i h_i \ln\left(1 - \sum_k Y_{ki}\right) = 0 \tag{1}$$

In eq (1), $\bar{T} = (T_0 + T)/2$, T_0 is the temperature of the standard reference state (T = 273.15 K, P = 0), Δm_W^0 is the chemical potential difference between the empty hydrate lattice and pure water in the reference state, h_i is the ratio of the number of cavities of type *i* to the number of water molecules in the hydrate lattice, and Y_i denotes the probability of a cavity of type *i* being occupied by the guest molecule. The probability Y_i is given in terms of the fugacity of the hydrate guest in the gaseous state (f_i) and the Langmuir adsorption constant (C_i) by $Y_{ki} = C_{ki} f_k / (1 + \sum_j C_{ji} f_j)$. Additionally, $\Delta H_W = \Delta H_W^0 + \Delta C_p^0(T')(T - T_0)$, where ΔH_W^0 is a reference enthalpy difference between the empty hydrate lattice and the pure water phase at the reference temperature, ΔC_p^0 is the reference heat capacity difference, and ΔV_W is the volume difference between the empty hydrate and pure water (at T_0), and is assumed constant. Also note that the values used for ΔC_p^0, ΔH_W^0, and ΔV_W depend on whether the equilibrium involves liquid or solid water. In this work, the temperature dependence of the Langmuir constants will be accounted for by using the form presented by Munck et al.[7] This form is given by $C_{ki} = (A_{ki}/T)\exp\left(B_{ki}/T\right)$, where A_i and B_i are experimentally fit parameters, and are dependent on which guest molecule is present, as well as which of the hydrate structures is formed. To consider hydrate formation in porous media, eq. (1) must be modified to include the effect of the relevant interface on the activity of the water. After

making the necessary modifications in the region where the equilibria involve liquid water, eq. (1) becomes[8]

$$\frac{\Delta m_W^0}{RT_0} - \int_{T_0}^{T_f} \frac{\Delta H_w}{RT^2} dT + \int_0^{P_f} \frac{\Delta V_w}{R\overline{T}} dP - \ln(g_w X_w) + \sum_i h_i \ln\left(1 - \sum_k Y_{ki}\right) + V_L \frac{2\cos(q) s_{hw}}{RT_f r} = 0 \qquad (2)$$

In eq. (2), V_L is the molar volume of water in the pure water state, è is the contact angle between the aqueous phase and the hydrate, s_{hw} is the surface tension between the aqueous and hydrate phases (taken as 0.0267 J/m^2 as given by Clennell et al[9]), and r is the radius of the pores in the porous medium. Eq. (2) can be used for all temperatures above the ice point of water in the corresponding pore of radius r. Below the ice point one recovers eq. (1) since the current model assumes there are no surface effects between ice and hydrate.

Results and Discussion

Figure 1a shows the results of using eq. (1) to predict the hydrate equilibrium pressure for bulk mixtures of methane and carbon dioxide. Also shown in the Figure are the experimental data given in Sloan.[10] We note that all of the experimental data are in the liquid water region, and involve Structure I hydrates. We also note that for temperatures slightly above those depicted in Fig 1a as part of the calculated surface, the mixture involves liquid carbon dioxide, and the predictions become less accurate.

Surfaces similar to Fig. 1a can be constructed using eq. (2) for hydrate formation in porous media. For example, Figure 1b shows the results for pore radii of 3, 6, and 9 nm. The upper right hand corner of Fig. 1b shows a dramatic change in slope in the logarithm of the equilibrium pressure, due to the effects of the magnitude of the pressure on the state of the carbon dioxide involved in the equilibria. Also note the non-linearity of the surface in Fig. 1b for larger temperatures (and therefore pressures), which indicates the changing character of the carbon dioxide involved in the equilibria.

The equilibrium pressure of mixtures in porous media is a function of 3 variables (temperature, mole fraction, and pore radius). As a result, one can examine cross-sections of the 3 dimensional surface (which lies in a 4 dimensional space) other than the one shown in Fig. 1b. For example, in Figure 2 the logarithm of the equilibrium pressure is shown as a function of 1/T and 1/r for five values (0.0, 0.25, 0.5, 0.75, and 1.0) of the mole fraction of carbon dioxide in the mixtures. Due to the higher hydrate equilibrium pressure in porous media, changes in the state of the carbon dioxide in the mixture take place at lower temperatures than they do in the bulk. This can lead to different types of equilibria taking place at the same temperature in different size pores in the porous media. Fig. 2a shows the surfaces for pressures where both components (CO_2 and CH_4) remain in gaseous form. We note that as the mole fraction of CO_2 increases, the equilibrium pressure decreases due to the lower equilibrium pressure for hydrates formed from pure gaseous CO_2, as compared to that of those formed from pure gaseous CH_4. Higher temperatures and/or smaller pore sizes result in higher equilibrium pressures. At some of these higher pressures CO_2 liquefies. Due to the larger equilibrium pressure for hydrates formed from liquid CO_2 as compared to those for hydrates formed from either gaseous CH_4 or gaseous carbon dioxide, equilibria involving liquid CO2 have significantly higher equilibrium pressures. Under conditions where either the temperature is high enough or the pore size is small enough, mixtures with larger mole fractions of CO_2 have higher equilibrium pressures than pure methane hydrates (as seen in Fig. 2b), suggesting the presence of liquid carbon dioxide. In addition to the limitations of calculations involving liquefied components, the form of the Langmuir constants employed here may not be as accurate as more complicated forms. This potential source of inaccuracy will be investigated in future work.

As is made clear from these preliminary results, the evaluation of the potential sequestration of carbon dioxide by injection into sediment deposits containing methane hydrates may require accurate methods of predicting hydrate equilibrium pressures when the mixtures involve liquid carbon dioxide and gaseous methane. Since the determination of liquid phase densities and fugacities can

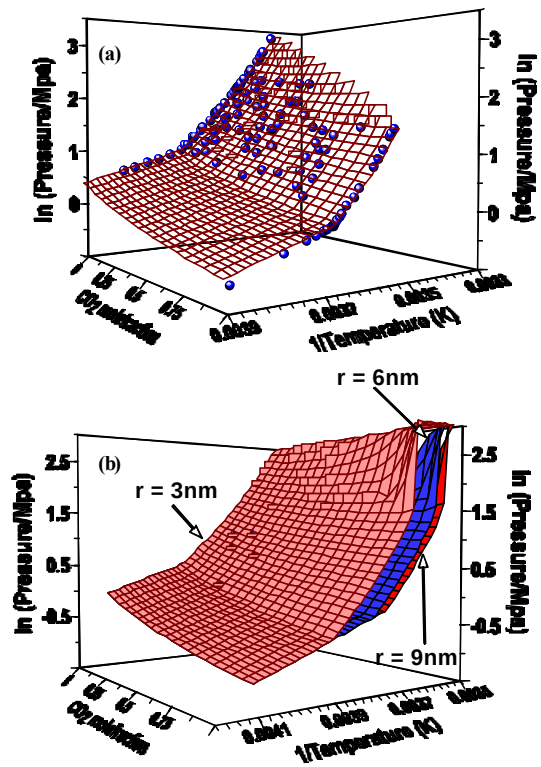

Figure 1. **(a)** Surface showing predicted equilibrium pressures for CO_2/CH_4 mixtures and experimental data for bulk hydrate formation. **(b)** Calculated surfaces for equilibrium pressures for CO_2/CH_4 mixtures in porous media with pore radii of 3, 6, or 9 nm.

involve larger errors than those for the gaseous phase,[10] great care must be taken in developing such predictions.

In addition to calculating the equilibrium pressure, eq. (2) can be used along with the Clausius-Clapeyron equation $d(\ln(P))/d(1/T) = -\Delta H/zR$ to estimate the enthalpy of formation of mixtures of carbon dioxide and methane in porous media. In the above equation, z is the gas compressibility, and is calculated using

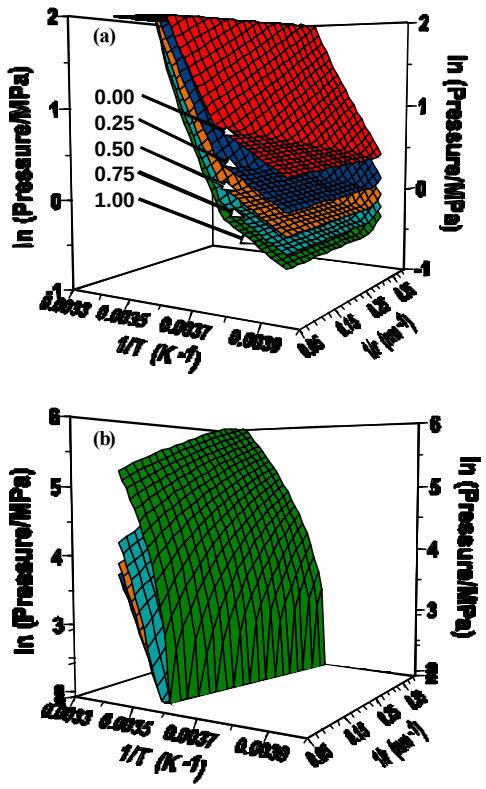

Figure 2. Calculated surfaces for equilibrium pressures for CO_2/CH_4 mixtures having CO_2 mole fractions of 0.0, 0.25, 0.5, 0.75, and 1.0 in porous media.

the Soave-Redlich-Kwong equation of state. Figure 3a shows the results of calculation of the enthalpy of dissociation for mixtures of

carbon dioxide and methane in a porous medium containing pores with 5 nm radii. Results from Figure 3a for a temperature of 273.2 K are shown in Fig. 3b, along with the results for pores having a 3 nm radius and for bulk calculations (dotted trace). We note that the very rapid changes evident in Figs 2 and 3 for pure CO_2 (a mole fraction of 1.0) are due to its liquefaction (due to the larger equilibrium pressures necessary in porous media). The calculations presented here for hydrate formation involving liquefied states may have more limitations than do those only involving gases, and as such these preliminary results will only be examined from a qualitative standpoint at this time. The difference between the enthalpy of dissociation in porous media and that in the bulk for a mixture with a mole fraction of 0.2 or greater seems to increase as the pore size decreases. For mole fractions below this there seems to be a more complicated behavior. This suggests that CO_2 sequestration in porous media via conversion of methane hydrate into CO_2 hydrate may be even more favored, thermodynamically, than it is in the bulk. While intriguing, quantitative interpretation of these results will require further investigation.

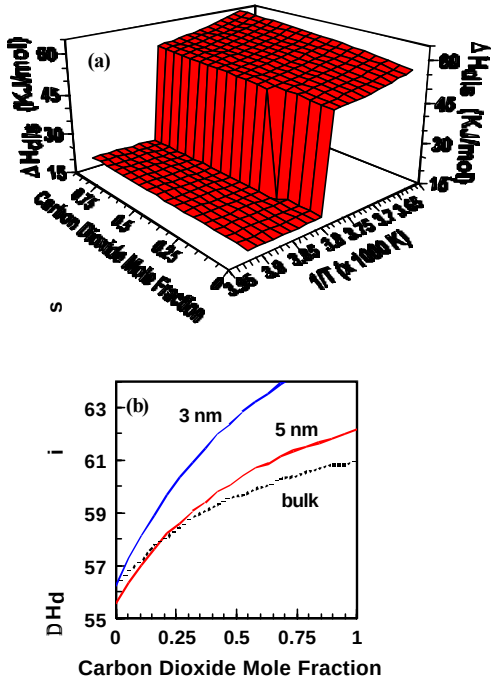

Figure 3. (a) Calculated surface showing the enthalpy of dissociation for CO_2/CH_4 mixtures in a porous medium having pore radii of 5.0 nm. **(b)** The enthalpy of dissociation at 273.2 K as a function of the mole fraction of carbon dioxide for the bulk (dotted trace) as well as in porous media with 3 and 5 nm pores.

References

1. Ravkin, A.; *Global Warming: understanding the forecast*. New York: Abbeville Press, 1992.
2. Komai, T.; Yamamoto, Y.; and Ikegami, S.; *Preprints, Am. Chem. Soc. Div. Fuel. Chem.* **1997**, *42* (2), 568.
3. Makogon, Y.F. *Hydrates of Natural Gas*, PennWell: Tulsa, 1981.
4. Handa, Y.P.; Stupin, D. *J. Phys. Chem.* **1992**, *96*, 8599.
5. Uchida, T.; Ebinuma, T.; Ishizaki, T. *Phys. Chem.* **1999**, *103*, 3659.
6. Seshadri, K.; Wilder, J.W.; Smith, D.H., *J. Phys. Chem.* B, **2001**; *105* (13); 2627.
7. Munck, J.; Skjoid-Jorgensen, S.; Rasmussen, P. *Chem. Eng. Sci.* **1988,** *43*, 2661.
8. Henry, P.; Thomas, M.; Clennell, M.B. *J. Geophys. Res.* **1999**, *104*, 23005.
9. Clennell, M.B.; Hovland, M.; Booth, J.S.; Henry, P.; Winters, W.J., *J. Geophys. Res.*, **1999**; *104*; 22985.
10. Sloan, E.D. *Clathrate Hydrates of Natural Gases,* 2nd ed.; Marcel Dekker: New York, 1997.

EFFECT OF $CaCO_3$ PARTICLES ON THE FORMATION PROCESS OF CO_2 HYDRATE AND DISPOSAL PROCESS IN THE OCEAN

*Satoko Takano, Minoru Fujii, Yukio Yanagisawa, and Akihiro Yamasaki**

School of Frontier Sciences, The University fo Tokyo
7-3-1 Hongo, Bunkyo-ku, Tokyo, JAPAN

*Institute of Environmental Management
National Institute of Advance Industrial Science and Technology
16-1 Onogawa, Tsukuba, JAPAN

Introduction

Ocean disposal scenario of anthropogenic CO_2 in the form of clathrate hydrate have been proposed for mitigation of global warming[1]. The disposal process of CO_2 hydrate has advantages over direct discharge of gaseous or liquid CO_2 from the environmental impact. Since the density of CO_2 hydrate is larger than that of seawater, the disposed hydrate particles has negative buoyancy in the seawater and descend to the ocean bottom. On the other hand, the density of liquid or gaseous CO_2 is smaller than that of seawater at the dept shallower than 3000 m, the discharged CO_2 would ascend to the ocean surface, and some part might be release to the atmosphere when the dissolution is not completed. The hydrate particles disposed in the ocean have a dissociation fate because they are unstable when the ambient seawater is unsaturated with CO_2. The dissociation of CO_2 hydrate would release CO_2, and cause an impact on the marine environment. However, the impact would depend on the rates of descending and dissociation of CO_2 hydrate particles in the ocean. Since these rates depend primarily on the particle size, the environmental impact could be controllable through a proper design of the formation process of the hydrate particle.

The hydrate particle growth process should depend on various factors. In this study, effect of calcium carbonate particles was studied from the following viewpoints.

- The addition of calcium carbonate would increase the CO_2 solubility in water, which is favorable for the hydrate formation. In addition, the $CaCO_3$ particles would provide a crystallization center for the CO_2 hydrate. Consequently, the hydrate formation could be promoted by $CaCO_3$ addition.
- After formation of the CO_2 hydrate, the remained $CaCO_3$ could be disposed of with the hydrate particles in the form of slurry. Since the $CaCO_3$ has a buffering effect for the pH change caused by the dissolution of CO_2 released from the hydrate particles, the disposal process could be more environmentally benign.

Effect of $CaCO_3$ addition on the CO_2 hydrate formation process has been investigated experimentally in a laboratory scale setup. Also numerical simulations of the buffering effect of $CaCO_3$ on the pH change caused by a disposal process of CO_2 hydrate have been conducted.

Experimental Apparatus and Procedure

Figure 1 shows a schematic drawing for the experimental system for the hydrate formation. The batch-type high-pressure reactor was composed of a transparent polycarbonate tube that can bear pressure up to 200 bar. A Pyrex glass tube (inner volume was about 740 cm^3) was inserted in the polycarbonate tube to avoid the direct contact of liquid CO_2 with polycarbonate tube, which could cause a severe damage to the material. The absolute pressure in the Pyrex tube was controlled by a piston-type pressure controller in the range of 1 to 100 bar with an accuracy of 0.1 bar. Pressure between the Pyrex glass tube and the polycarbonate tube was equilibrated by a pressure equilibrator to avoid the excess pressure difference on the Pyrex tube (maximum bearing pressure 20 bar). The reaction contents could be stirred by a 3-wing propeller type agitator with the speed range of 0 to 750 rpm. The temperature was controlled by immersing the reactor in a constant-temperature bath of which the temperature was controlled with an accuracy of 0.1 K through a constant-temperature cooling unit.

A known amount of ion-exchanged water was first introduced to the reactor with or without a given amount of $CaCO_3$ particle at the atmospheric pressure. Then liquid CO_2 was supplied to the system through a high-pressure pump after pre-cooling. After reaching the experimental pressure, the supply of CO_2 was stopped, and the agitation was started. Formation process of hydrate was directly observed and recorded by a digital video camera through the reactor.

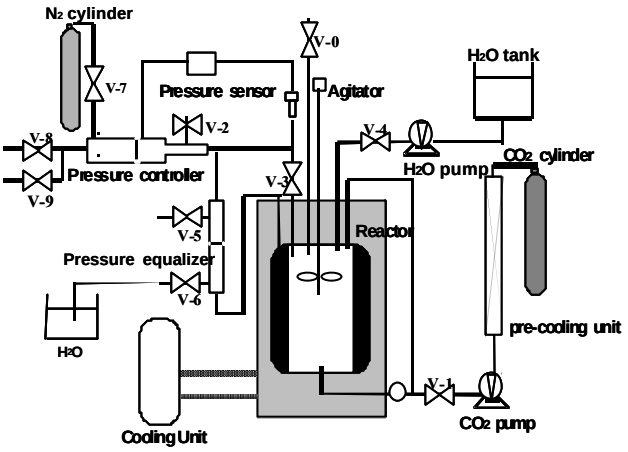

Figure 1. Schematic drawing for the experimental apparatus

Results and Discussion

Observation of hydrate formation process

Without agitation or with agitation at low speed (< 200 rpm), the liquid CO_2 phase and the water phase was separated with a thin hydrate film at the interface. With an increasing in the agitation rate, the hydrate film collapsed at 200 rpm, and liquid CO_2 drops and hydrate particles (about several mm diameter) were dispersed into water phase. When the agitation stopped, the hydrate particles coagulated to form a cluster, but the cluster was easily broken into smaller hydrate particles by a slight agitation (Figure 2) for the cases without $CaCO_3$. For the cases with $CaCO_3$, on the other hand, a large lump of CO_2 hydrate (about 7~10 cm diameter) formation was observed after agitation at 750 rpm as shown in Figure 3. The effect of $CaCO_3$ found to depend on various conditions such as the agitation rate, temperature, and $CaCO_3$ content. No clear effect of the $CaCO_3$ addition on the hydrate formation rate was noticed because the

hydrate formation took place immediately after the agitation even without $CaCO_3$. Thus, the addition of $CaCO_3$ may help the formation of large CO_2 hydrate particle.

Simulation of pH change caused by the CO_2 hydrate particle disposed in the ocean

Numerical simulation of pH change in the seawater by the ocean disposal process of CO_2 was conducted based on the following assumption. In the process, CO_2 was captured and separated from the flue gas of an LNG-fired thermal power plant of 3000 MW. The emission rate of CO_2 is 370 kg/s; this amount of CO_2 will be converted into hydrate particles with $CaCO_3$ addition in a submerged hydrate reactor at 500 m depth. Then hydrate particles will be disposed of in the ocean with an excess amount of $CaCO_3$ slurry. The hydrate particles disposed will descend in the ocean with $CaCO_3$ slurry, and will be dissociated to release CO_2 into the ambient sweater during the descending process. In the meantime, the hydrate particles will be transported horizontally by the eddy diffusion and the ocean current. The following assumption was made for the calculation of pH change caused by the dissolution of CO_2 in the seawater. The following ionic equilibrium relations are always established in the ambient seawater.

$$[H_2CO_3] / P_{CO2} = 10^{-1.5} \quad (1)$$

$$[H^+]\,[HCO^{3-}] / [H_2CO_3] = 10^{-6.3} \quad (2)$$

$$[H^+]\,[CO_3^{2-}] / [HCO^{3-}] = 10^{-10.3} \quad (3)$$

$$[H^+]\,[OH^-] = 10^{-14} \quad (4)$$

$$[Ca^{2+}]\,[CO_3^{2-}] = 10^{-8.4} \quad (5)$$

- The charge is conserved.

$$[H^+]+2[Ca^{2+}] = [OH^-]+[HCO^{3-}]+2[CO_3^{2-}], \text{ with } CaCO_3 \quad (6)$$

$$[H^+] = [OH^-]+[HCO^{3-}]+2[CO_3^{2-}], \text{ without } CaCO_3 \quad (7)$$

- Emission rate of CO_2 by the dissociation of CO_2 hydrate particles was given by the following mass transfer equation.

$$-C_h^* \frac{d}{dt}\left(\frac{4pr^3}{3}\right) = 4pr^2 k(C_L - C_W) \quad (8)$$

where C_h* is the concentration of CO_2 in the hydrate, C_L is the solubility of CO_2 in the seawater, and C_w is the CO_2 concentration in the ambient seawater. r is the radius of CO_2 hydrate, and k is the overall mass transfer coefficient. The value of mass transfer coefficient is constant at 10^{-7} m/s.

- The descending rate of hydrate particles in the sweater is the terminal velocity in seawater; the drag coefficient, C_D, was given by the following equations depending on the diameter-based Reynolds number (Re).

$$C_D = \begin{cases} 24 / \mathrm{Re} & (\mathrm{Re} < 2) \\ 24/\mathrm{Re}^{1/2} & (2 < \mathrm{Re} < 500) \\ 0.44 & (\mathrm{Re} > 500) \end{cases} \quad (9)$$

where

$$\mathrm{Re} = r\,v\,d / m \quad (10)$$

r and m are the density and the viscosity of the seawater, respectively, and v and d are the terminal velocity and the diameter of the hydrate particle, respectively. All the properties used for the calculation were those for the seawater at 283 K, and temperature or pressure dependency was neglected.

- The horizontal eddy diffusion coefficient in the ocean is 30 m^2/s (y-direction), and that for vertical direction was negligible. The average ocean current was 0.1 m/s (x-direction) horizontally. The vertical mass transfer of CO_2 takes place mainly by the descending (z-direction) process of hydrate particle in the seawater.

Based on the above assumptions, the pH change caused by the continuous disposal of CO_2 hydrate particles were simulated numerically. Figure 4 shows a steady state pH profile of the seawater at the depth of z = 1300 m as a function of the (y-direction) horizontal distance at x = 1000 m. The initial diameter of CO_2 hydrate particles was also shown in the figure. The pH change was significantly reduced by the addition of $CaCO_3$; the minimum pH in this point was larger than 6 when 0.1 m hydrate particle was disposed at 500 m. With an increase in the hydrate particle size, the low pH region was spread horizontally at this depth. This is so because the larger the initial size, the deeper the hydrate particles could reach.

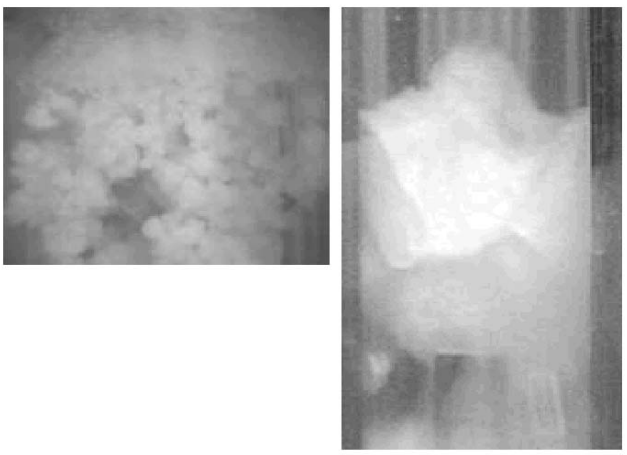

Figure 2. Formation of CO_2 hydrate; (a) hydrate particles cluster formed without $CaCO_3$, (b) hydrate lump formed with $CaCO_3$

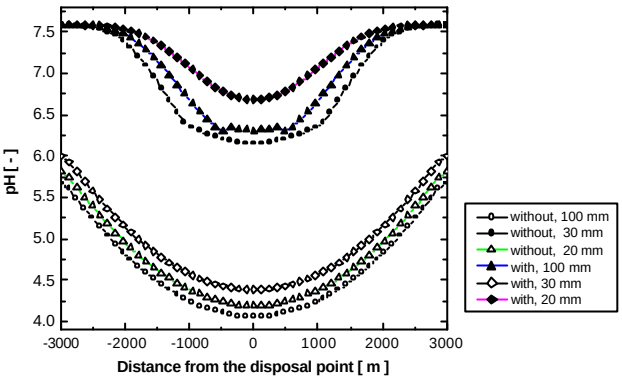

Figure 3. pH change simulation result at the depth of 1300 m and 1000 m away from the disposal point for various initial diameter of the CO_2 hydrate particles. The disposal depth was 500 m.

Conclusions

$CaCO_3$ addition was effective both for the size control of the hydrate particle size in the formation process and for the buffering of pH change by the dissociation of CO_2 hydrate in the ocean.

References

(1) Yamasaki, A.; Wakatsuki, M.; Teng, H.; Yanagisawa, Y.; and Yamada, K. *Energy*, **2000**, 25, 85.

Recent advances in deep-sea CO_2 sequestration experiments.

Edward T. Peltzer, Peter G. Brewer, Rachel M. Dunk, Jon Erickson, Gregor Rehder and Peter Walz.

Monterey Bay Aquarium Research Institute
7700 Sandholdt Road,
Moss Landing, CA 95039-9644.

Introduction

Over the last five years, we have developed and refined techniques for the precise and controlled release of small quantities (0.5-7L) of liquid CO_2 in the deep ocean using MBARI's advanced remotely operated vehicle (ROV) technology. We have used this technology to pursue fundamental chemical, physical, and biological studies associated with ocean CO_2 sequestration. This technology was designed to allow us to conduct experiments mimicking some of the many ocean CO_2 sequestration processes which have been proposed, such as those summarized by Hanisch[1]. Notably, we wanted to observe and test ideas concerning CO_2 behavior during releases in the mid-water (400m to 2000m), to mimic plumes of CO_2 that might arise from CO_2 released from shallow pipelines or pipes towed from tankers, and in the deep-sea (>3000m), where liquid CO_2 is denser than the surrounding seawater and the experiments are gravitationally stable. We report here the development of a 56L accumulator system, capable of delivering 42-46L of liquid CO_2 at 3600m depth, constructed of carbon fiber composite, for meso-scale studies. This represents the size and weight limit possible with current MBARI ROV technology.

Subsequently, we have completed a series of experiments in Monterey Bay using this technology. We have used this system for new observations of the fate of liquid CO_2 on the sea floor at depths >3000m. We have used a time lapse camera to image the fate of ~16L of liquid CO_2 in a 50cm diameter corral at 3600m depth; where dissolution was complete in 14 days. We have observed *in situ* the pH of a pocket formed in the liquid CO_2 surface film, and migration of CO_2 saturated water into the sediments with massive hydrate formation following.

Experimental

Technology Development. Our initial device consisted of two hydraulic cylinders mechanically connected in tandem. One cylinder was controlled using the hydraulic system on the ROV. When this device was activated, its ram would move the piston in the other cylinder and expel the liquid CO_2 contained therein. Although the capacity was small (0.5L), use of this device did allow us to conduct our earliest experiments and to gather needed experience with handling, transferring and deploying liquid CO_2 in the ocean from an ROV[2]. However, the small capacity of this system quickly proved to be limiting on both the size and duration of the experiments we could undertake, so we developed a larger CO_2 delivery system that employed a steel, 9L piston accumulator as the liquid CO_2 reservoir. A tandem cylinder pump was used to force seawater into one side of the piston accumulator. This pumping action served to drive the internal piston and expel liquid CO_2 from the other end. The use of these pumps freed us from the volume restrictions imposed by the size of the ROV hydraulic system reservoir and also served to provide us with a precise volume measurement of the amount of liquid CO_2 dispensed. This device served us well for both our first benthic CO_2 release study[3], and subsequent droplet experiments at mid-water depths[4].

The desire to conduct experiments with volumes several times larger than the 9L capacity of our steel accumulator system, yet wanting to avoid wasting valuable ROV dive-time ferrying liquid CO_2 to the sea-floor, led us to develop a larger system limited only by the ROV payload capacity in terms of weight and size. This system consists of a carbon-fiber composite piston accumulator of 56L internal capacity constructed by Hydratech, Fresno, CA. At 23 cm outside diameter and 194 cm length, it is close to the largest object the ROV can contain within the tool-sled. Yet the use of a carbon-fiber reinforced fiberglass composite for construction of the accumulator barrel provided sufficient strength (3000 psig rating) at a fraction of the weight of a steel cylinder of comparable size.

Tandem cylinder pumps were used to actuate the 56L CO_2 accumulator as was done previously. In order to have both fine control of small volumes of liquid CO_2 dispensed, and the capacity to deliver larger volumes relatively quickly, we choose to use two tandem cylinder pumps: one of 128mL capacity and a second of 970mL capacity. The two pumps also provide a level of redundancy to successfully complete a CO_2 deployment should either of the tandem cylinder pumps fail to function during a dive.

Deep-sea Releases. We have now completed several release experiments using the 56L piston accumulator at depths of 3000m and deeper. Our initial attempt using this system was at a site 153km west of Moss Landing, CA, at a water depth of 3604m. We made several deployments of 10-20L aliquots of liquid CO_2 into plastic "corrals" made of 50cm, pipe cut to 12cm lengths (Figure 1). One of these corrals occupied the field of view of our deep-sea time-lapsed video camera so "continuous" observations could be made for several weeks. In addition, we repeated the beaker experiment[3] at this site. All told six delivery dives were made successfully.

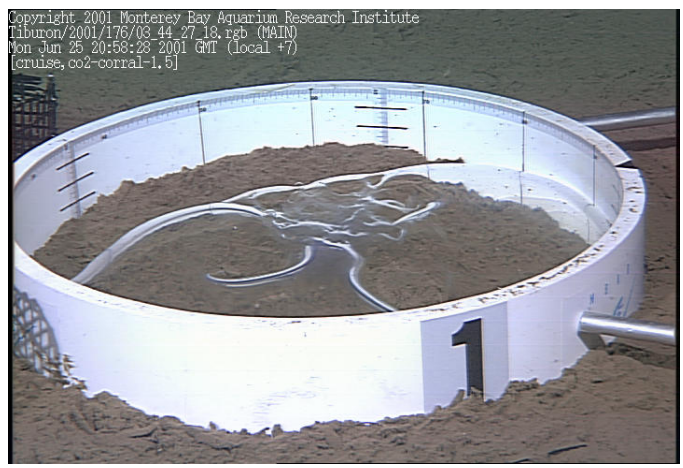

Figure 1. A "corral" filled with liquid CO_2 at 3604m water depth and 1.55ºC. Notice that the strong surface tension precludes the liquid CO_2 from completely covering the bottom of the corral.

Our second series of CO_2 releases using the 56L accumulator system occurred at a site 100km southwest of Moss Landing, CA, with a water depth of 3322m. This time, 30cm deep corrals were used and the time-lapse video camera was deployed to make long-term observations. Additionally, an attempt to measure the surface strength of the hydrate skin was made. Only two delivery dives were made at this site. Both were successful and on the last we delivered the maximum theoretical volume of liquid CO_2 that could be contained within the CO_2 piston accumulator.

In all of these experiments, pH measurements were made near the liquid CO_2 seawater interface both inside the CO_2 containers (beakers and corrals) as well as outside the containers in ambient

seawater using a Sea-Bird SBE-18 pH probe (Figure 2). These pH measurements were made inside the containers by moving the pH probe with the ROV manipulator arm as well as several meters up-stream or down-stream of the corrals by relocating the ROV.

Figure 2. Sea-Bird pH probe (SBE-18) measuring ambient pH within a few cm of a pool of liquid CO_2 at 3604m depth.

Results

Unlike the smaller steel cylinder reservoirs which were easily filled with liquid CO_2, the carbon fiber composite cylinder required a different protocol to completely fill it with liquid CO_2. The steel cylinders can be easily cooled, either with flowing water or packed in ice, to facilitate the transfer of heat from the cylinder and condensation of liquid CO_2 inside. However, the carbon fiber composite does not allow this easy removal of heat, so the CO_2 has to be transferred as a cooled liquid and kept under pressure at all times. This required a delicate balancing of the CO_2 delivery into one side of the piston accumulator along with the venting of water from the other side. If the piston was allowed to move too quickly, or if the internal pressure of the system dropped below the vapor pressure of the liquid CO_2, then a gas pocket formed inside the accumulator and incomplete filling resulted.

Because of the compressibility of liquid CO_2, the volume of CO_2 delivered at-depth is dependent upon both the ambient PT conditions at-depth and the temperature and pressure of the liquid CO_2 at the time the accumulator is filled. The colder the liquid CO_2 is during the filling operation, the greater volume that will be available for release at depth. Theoretical delivery volumes for the 56L accumulator at two release depths are given in Table 1.

Table 1. Theoretical Delivery Volumes (L) for 56L Cylinder

Fill T (ºC) at 900 psig	3200m, 1.60ºC	3600m, 1.55ºC
12	46.7	46.1
16	45.0	44.4
20	42.8	42.2

Behavior of the liquid CO_2 released at depth varied from experiment to experiment and even between different corrals during the same experiment. The spontaneous over-flow of liquid CO_2 from a 4L beaker due to the rapid formation of CO_2-hydrate observed in our initial CO_2 deployment[3] during 1998 was not observed. However, other dramatic behavior was observed. At the 3604m site, CO_2 hydrate formed overnight within the sediment at one of the corrals creating a massive "frost-heave" (Figure 3), yet a similar corral nearby, showed no such behavior. The reason(s) for this stochastic behavior elude us, however it does suggest that minor changes in the conditions of deployment leads to different outcomes.

Figure 3. CO_2-hydrate frost heave that formed overnight.

The dissolution rate of the liquid CO_2 was measured in two separate experiments. In one, we observed the slow decrease in the level of the liquid CO_2 pool inside a corral using the time-lapse video camera system. From this change in volume across a fixed surface area a crude approximation of the CO_2 dissolution rate of 0.2 $\mu mol/cm^2/sec$ was made. In the second experiment, a pH probe was inserted about 10 cm into a pool of liquid CO_2. Because of the strong tensile strength of the CO_2 hydrate skin, the liquid CO_2 did not flood the trapped volume, but instead a well containing ambient seawater was formed. From the observed change in pH as a function of time a dissolution rate of 1.8 $\mu mol/cm^2/sec$ was calculated. There are obvious uncertainties in both of these determinations, but as first-approximations they may prove useful to guide future work on deep ocean CO_2 sequestration.

Conclusions

It is now possible to deploy up to 46L of liquid CO_2 from a single ROV dive to depths of 3000-4000m. From initial dissolution rate measurements, we can expect that small pools (50cm dia., 10-20cm depth) of liquid CO_2 will have lifetimes on the order of a few weeks. This lifetime is sufficient to meet the needs of various benthic biology and geochemistry experiments.

Acknowledgement. This work was supported by a grant to MBARI from the David and Lucille Packard foundation and a grant from the Department of Energy, DE-FC26-00NT40929.

References

(1) Hanisch, C. *Environ. Sci. Tech.*, **1998**, *32* (1), 20A-24A.
(2) Brewer, P. G., Orr, F. M., Friederich, G., Kvenvolden, K. A., Orange, D. A. *Energy Fuels*, **1998**, *12*, 183-188.
(3) Brewer, P. G., Friederich, G., Peltzer, E. T., Orr, F. M. *Science*, **1999**, *284*, 943-945.
(4) Peltzer, E. T., Brewer, P. G., Friederich, G., Rehder, G. Prepr. Pap. - *Am. Chem. Soc., Div. Fuel Chem.*, **2000**, *45* (4), 794-798.

HIGH-PRESSURE WATER TUNNEL FACILITY FOR OCEAN CO_2 STORAGE EXPERIMENTATION

Robert P. Warzinski and Ronald J. Lynn
U.S. Department of Energy, National Energy Technology Center
P.O. Box 10940, Pittsburgh, PA 15236-0940

Anne M. Robertson and Igor V. Haljasmaa
University of Pittsburgh, Department of Mechanical Engineering
648 Benedum Hall, Pittsburgh, PA 15260

Introduction

In recent years, considerable effort has been devoted to investigating non-atmospheric storage of anthropogenic CO_2 emissions [1,2]. Deep ocean disposal (>500 m depth) is being considered as one option for long-term storage of large quantities of CO_2. The capacity of the Earth's oceans for CO_2 sequestration has the potential to exceed that of all other alternatives [2].

Such a serious action as large-scale CO_2 sequestration requires extensive and thorough investigation of all aspects of the process, including CO_2 fluid particle behavior after injection. Predicting the behavior of liquid CO_2 injected into the ocean at depths greater than 500 m is complicated by formation of crystalline CO_2 clathrate hydrate. Hydrate can form as discrete particles or as shells on CO_2 drops and significantly affects mechanical and chemical particle behavior (buoyancy, dissolution rates, etc.) [3]. Experiments in the ocean are very expensive and difficult to perform. It would be preferable to use laboratory facilities designed to simulate the deep ocean.

A previous publication [3] described the initial efforts of the National Energy Technology Laboratory (NETL) of the U.S. Department of Energy to develop experimental units intended to model direct ocean sequestration. We discussed some aspects of the development of a High-Pressure Water Tunnel Facility (HWTF) and outlined steps for design optimization. Assembly of the HWTF is now complete, and experiments with CO_2 droplets will soon be initiated. This paper describes recent design optimization efforts.

The HWTF

The water tunnel associated with the HWTF is depicted in Figure 1. It consists of a test section integrated into a closed flow loop with a centrifugal variable-speed pump and control valves for precise water circulation control; a syringe pump to generate and control high pressure in the system; and a chiller for cooling the system to deep-ocean temperatures. The pressurized components are located in a securely-isolated and structurally-reinforced room. Observations and control of all the system components are performed from a control room computer by means of programs developed using Labview software from National Instruments.

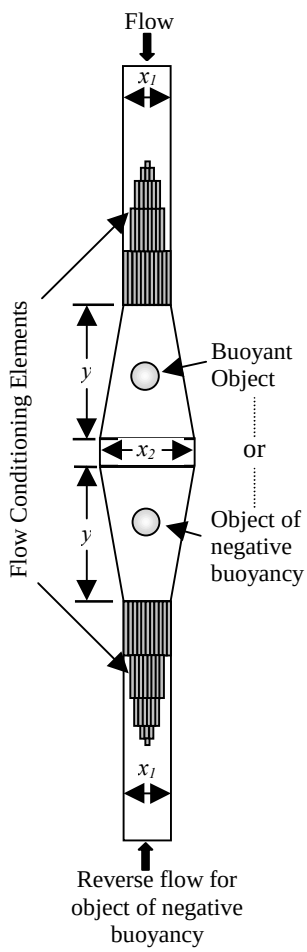

Figure 1. Water tunnel schematic.

Two conical test sections allow stabilization of either a rising or sinking fluid particle by countercurrent flow. Several ports on different levels of the test section serve for fluid/gas injection into the system. For direct observation of fluid particle behavior, as well as for automatic control of the particle motion, both conical sections have two pairs of windows. The HWTF can operate under pressures up to 350 bars and temperatures down to the freezing point of the circulating fluid.

Experiments in the HWTF will be more cost effective than direct experiments in the ocean; however, there are legitimate concerns about being able to adequately simulate fluid particle behavior in such an experimental facility. Therefore, it is important that the design and operation of the unit minimizes any unnatural chemical or physical behavior.

The parameters most easily set to real ocean conditions include water salinity and alkalinity, pressure and temperature. For salinity and alkalinity, natural or artificially constituted ocean water can be used. The pressure and temperature in the system can be varied during the experiment to simulate that experienced by a particle rising or sinking in the ocean. It is more challenging to simulate the level of dissolved CO_2. Finally, the most significant concern is the dynamic behavior of a particle in a relatively small pipe (ID=51-75mm); that can be strikingly different from its free ocean counterpart. This last issue is discussed below.

Discussion

Reference 3 describes a Low-Pressure Water Tunnel Facility (LWTF) designed and operated at NETL. The LWTF serves as a benchmark system to test fluid particle behavior for various test section designs and flow conditions. It is also used to develop and evaluate theoretical models of the system. The section below describes some experimental results on the LWTF unit and their applicability to the HWTF.

Flow conditioning elements are used to provide a desired velocity profile for lateral stabilization of a fluid particle in the test section. They are composed of a bundle of small (from 1/9 to 1/15 of pipe ID) straws of different length located in the straight pipe above and below the test section. The central part of the conditioner typically has longer straws, causing a local velocity minimum in the center of the pipe (for more details see Reference 3). An automated traversing Pitot tube system was used to determine the velocity profiles in the test section.

Figure 2 displays the development of a representative velocity profile downstream of the flow conditioner. The length of the region adjacent to the conditioner outlet where the influence of individual jets from the straws is pronounced depends on the flow rate and straw diameter. This zone of active mixing and high shear rates should be avoided by the fluid particles. For example, in the experiment depicted in Figure 2, a particle should be kept at a distance of at least 2 pipe ID's (D = x_1) from the conditioner. However, a problem will also arise if the particle is too far away from the conditioner outlet and the desired profile is lost. Fortunately, the development length for a single straw (order of centimeters) is much less than the development length for the whole pipe (order of a meter). Therefore, these data show that the desired velocity profile can be achieved and the high-shear region avoided.

In the process of this research, concepts on the shape of the optimal velocity profile underwent significant evolution. Early flow conditioners were designed to stabilize an air bubble. The properties

of air (negligible density compared to water) required a design with a deep, narrow well in the velocity profile at the center of the pipe. Though these conditioners managed to keep the bubble relatively stable near the pipe axis, they did not provide a good simulation of particle behavior in the oceanic environment. The narrow velocity well restricts natural lateral motion of a particle, which often occurs as a particle rises in water in geometries with negligible wall effects [4]. In addition, the high velocity gradients of the narrow velocity well, can alter flow patterns around the particle compared with flow in the open ocean. These altered flow patterns can cause unrealistic heat and mass transfer and material shaving from the particle. They may also affect hydrate formation and dissolution kinetics.

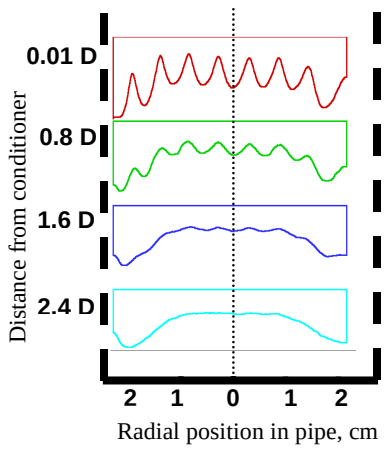

Figure 2. Velocity profile development in the LWTF.

The purpose of more recent flow conditioners was to provide a wide velocity well with relatively low-velocity gradients near the center. Such a profile would keep a particle away from the wall and at the same time allow some freedom of lateral motion. The maximum velocity gradient in the profile should also be kept as small as possible to minimize deviation from natural heat and mass transfer. Figure 3 depicts velocity profiles for 3 similar conditioner designs. They were obtained by progressive shortening (from conditioner 1 to 3) of the central section of straws. In light of the above factors, conditioner 3, with the flattest central part and lowest velocity gradient, would be the most preferable.

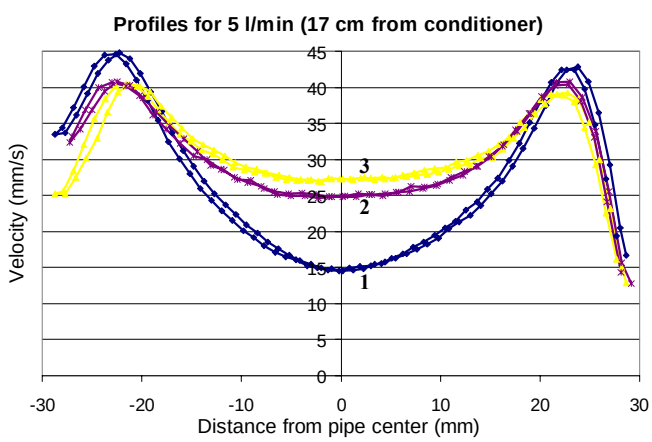

Figure 3. Effect of conditioner size on velocity profiles.

These conditioners were used to stabilize a particle of vegetable oil (Specific Gravity ≈ 0.91). Oil particles with an equivalent diameter in the range of 0.3 cm to 1 cm were successfully kept in the test section for several hours (equivalent diameter of a non-spherical particle is defined as the diameter of a spherical particle with the same volume).

Under certain assumptions, the behavior of a liquid particle in a fluid flow may be uniquely defined by two dimensionless parameters, the Eotvos and Morton numbers [3]:

$$Eo = \Delta\rho g D_e^2 / \gamma \text{ and } Mo = \Delta\rho g \mu^4 / (\rho \gamma^3),$$

where ρ and μ – fluid density and viscosity, $\Delta\rho$ – particle-fluid density difference, γ – interfacial surface tension on particle liquid boundary, D_e – equivalent particle diameter. These two parameters for an oil particle in LWTF are relatively close to the values for a CO_2 particle at the depth of approximately 1000 m. For example, for a particle with an equivalent diameter of 4 mm, the dimensionless numbers for both cases fall into the range: $Eo \approx 0.6 - 0.75$ and $Mo \approx 0.5 - 1.5 \times 10^{-10}$. The full range of these parameters for physical systems is $Eo \approx 0.01 - 1000$ and $Mo \approx 10^{-12} - 10^{5}$, and rising velocity dependence from these parameters is rather monotonic. Hence, we expect that behavior of both particles will be very similar. Therefore, model experiments with vegetable oil in the LWTF are used to mimic the behavior of CO_2 drop in the HWTF.

For proper simulation, the size of a fluid particle must not only be significantly smaller than the pipe diameter, but also the width of the 'velocity well'. In particular:

$$D_e << D_{pipe}, \qquad (\partial u / \partial y) D_e << u_{av},$$

where u and $\partial u / \partial y$ are the axial velocity and its gradient at the position of the particle. This will help to minimize the wall effects, as well as lateral particle migration caused by velocity profile gradients. Since the lift force is proportional to some powers of particle size and velocity gradient, even low gradients can cause significant lift on relatively large particles. Based on the profile shapes from Figure 3 and noting that the pipe diameter in the stabilization area is about 6 cm, we expect that a suitable size for the particle would be about 0.5 cm (particle cross section area / pipe cross section area < 1%).

In the LWTF with the velocity profiles shown in Figure 3, we also noticed differences in the behavior of solid and liquid particles of the same volume. An oil particle with an effective diameter of about 1-1.5 cm successfully remained in the central part of the pipe, close to the location of the local velocity minimum. Solid particles of the same diameter tended to stabilize away from the pipe center.

Unfortunately, there have been no systematic experimental studies devoted to buoyant solid or liquid particle behavior in vertical pipe or channel flows. Thus, systematization of such a behavior and attempts to reveal its mechanisms are interesting and challenging theoretical and experimental studies. An additional complication is possible if a thin hydrate shell forms on a CO_2 particle. Such an encased particle is intermediate between a solid or liquid particle and its behavior will likely differ from both.

References

1. Carbon Sequestration Research and Development, U.S. Department of Energy Report, DOE/SC/FE-1, 1999, available NTIS.
2. Herzog, H.; Eliasson, B.; Kaarstad, O. *Scientific American*, Feb., 2000, 72-79.
3. Warzinski, R.P.; Lynn, R.J.; Robertson, A.M.; Haljasmaa, I.V.; *Prepr. Pap., Amer. Chem. Soc., Div. Fuel Chem.,* 2000, **45**(4), 809-813.
4. Ellingsen K.; Risso, F., *J. Fluid Mech.,* 2001, **440**, 235-268.

PROPOSAL OF SLURRY TYPE CO_2 SENDING SYSTEM TO THE OCEAN FLOOR, NEW COSMOS

Izuo Aya[1], Kenji Yamane[1], Koki Shiozaki[2], Peter G. Brewer[3], and Edward Peltzer[3]

1) Osaka Branch, National Maritime Research Inst. (NMRI)
3-5-10 Amanogahara, Katano, Osaka 576-0034, Japan
2) Power and Energy Div, NMRI
3) Monterey Bay Aquarium Research Inst. (MBARI)

Introduction

The idea to store CO_2, recovered from power plants, in the deep ocean[1] has been a promising measure to mitigate the global warming especially after the Third Conference of the Parties (COP 3) held in Kyoto, December 1997, because the achievement of Kyoto Protocol was thought difficult only by conventional measures such as the energy saving and the forestation. This CO_2 ocean sequestration can be divided into two categories, that is, the dissolution (or dilution) method and the storage method.

In the former method, CO_2 droplets are released in mid depth of 1000 to 2000 meters where CO_2 is lighter than seawater, and they completely dissolve before reaching phase change boundary of about 400 meters depth. The sequestration term is expected to be the order of hundred years, which depends on the release point and the depth.[2]

On the other hand, in the latter method, CO_2 is stored in a depression on the ocean floor deeper than 3500 meters where liquid CO_2 is heavier than CO_2 saturated seawater. Its sequestration term is expected to be longer than a few thousand years equivalent to the vertical circulation term of the ocean.[3] It is a shortcoming of this method, however, to send CO_2 deeper than the former method.

The Maritime Research Institute (NMRI, the former name of the Ship Research Institute) had investigated the various aspects of the latter method in the last decade.[4-15] And in 1998, the authors proposed a system to overcome the above mentioned shortcoming of the storage method.[16,17] This system called as COSMOS, CO_2 Sending Method for Ocean Storage, is characterized as cold release of large CO_2 droplets with about 1 meter diameter into rather shallow waters such as 500 meters depth, where CO_2 colder than -30 Celsius is heavier than the ambient seawater and sinks to the ocean floor although being warmed up by the heat transfer from seawater.

In order to get the basic data prior to the development of the real COSMOS, an international joint research with University of Bergen supported by the NEDO (New Energy and Industrial Technology Development Organization) was started in 1999.[18] And parallel with this research, two *in situ* experiments with the Monterey Bay Aquarium Research Institute (MBARI) were also conducted in 1999 and 2000 to confirm the performance of manufactured trial cold CO_2 release nozzle.[19] Through the process of the joint research with University of Bergen, it was found that Taylor type instability[20] on the interface were too strong for a large cold CO_2 droplet to keep its shape, although ice and hydrate layers covering cold CO_2 droplet had been expected to support its shape.[21] From the latest *in situ* experiment with the MBARI, CO_2 slurry, that is, mixture of solid CO_2 (dry ice) and cold CO_2 of -55 Celsius, showed its capability to prevent from breaking up during sinking process.

Then the authors proposed a new COSMOS[22] modified from the original one, in which CO_2 is released as slurry balls into much shallower depth such as 200 meters. The New COSMOS, which is much easier to be realized because the limit droplet size is about 40 % of the original COSMOS, has another advantage that it can be applied to the dissolution type as well as the storage type. Moreover, the cost is also expected to be drastically reduced due to shallower release depth that requires a shorter pipeline equivalent to the length of CO_2 carrier, which means no troublesome connecting works on the ocean.

Concept of COSMOS

CO_2 carriers are required when we apply the storage method because the potential sites deeper than 3500 meters are too far for a pipeline to be laid down from the land. And liquid CO_2 transported by a carrier should be cooled down to -55 Celsius to reduce the tank pressure as much as possible (The triple point of CO_2 is -56.6 Celsius). Such cold CO_2 is heavier than the seawater even in rather shallow sea. If a CO_2 droplet released into 500 meters depth is lager than a certain diameter, which depend on the temperature of CO_2, it sinks to the storage site beyond 2700 meters depth where the density of CO_2 in thermally equilibrium (the same temperature) is the same as that of the seawater. Paying attention to this nature of cold CO_2, the NMRI proposed an innovative CO_2 sending method, COSMOS, and got a Japanese patent in March 1999. **Figure 1** shows the conceptual drawing of COSMOS, which was expected to solve the above-mentioned shortcoming of the storage method.

The temperature of liquid CO_2 released into the shallow sea is -45 to -30 Celsius that depends on the thermal insulation of riser tube from the CO_2 carrier. When such cold CO_2 is released into the seawater, a CO_2 droplet will soon be covered with ice layer and CO_2 hydrate membrane. These were expected to prevent the break up of a large droplet into small droplets but they will make difficult to release smoothly and steadily large CO_2 droplets from the nozzle. Therefore, the technical breakthrough to realize the COSMOS was thought as the development of CO_2 release nozzle.

Then in 1999, the NMRI started an international joint research with the University of Bergen to get the basic data to develop the release nozzle for cold CO_2, under the auspice of the New Energy and Industrial Technology Development Organization (NEDO).[18]

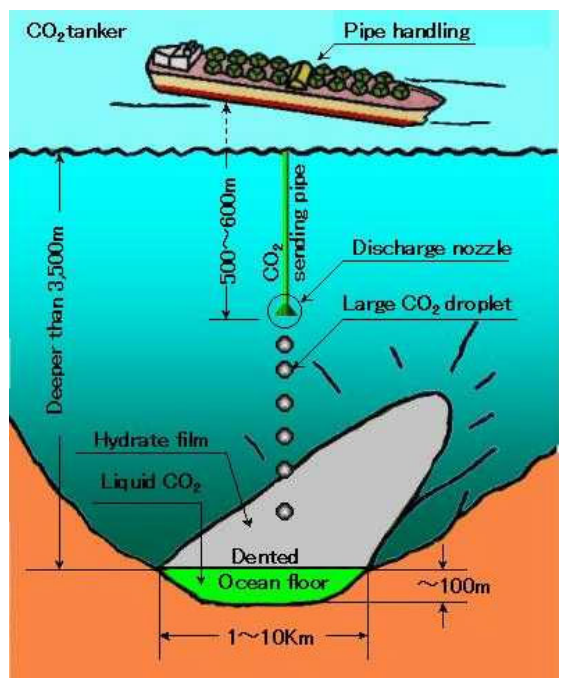

Figure 1. Concept of COSMOS proposed in 1998.

Figure 2. Original trial CO_2 release nozzle.

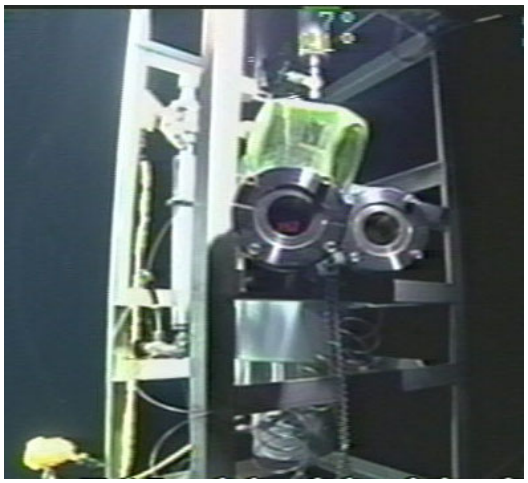

Figure 3. Temperature and pressure monitors mounted on the second trial nozzle.

In 1999 and 2000, the NMRI and the MBARI also conducted two joint *in situ* experiments to confirm the function of trial CO_2 release system.

Land Experiments

To ensure the success of *in situ* experiments with the MBARI, some land-based experiments with a mock liquid and cold CO_2 were conducted for original and second trial nozzles.

Trial CO_2 release nozzles. **Figure 2** shows the original trial CO_2 release nozzle used for the performance test at the *in situ* experiment in 1999. And **Figure 3** shows the second trial nozzle used to release CO_2 slurry ball at the *in situ* experiment in the fall of

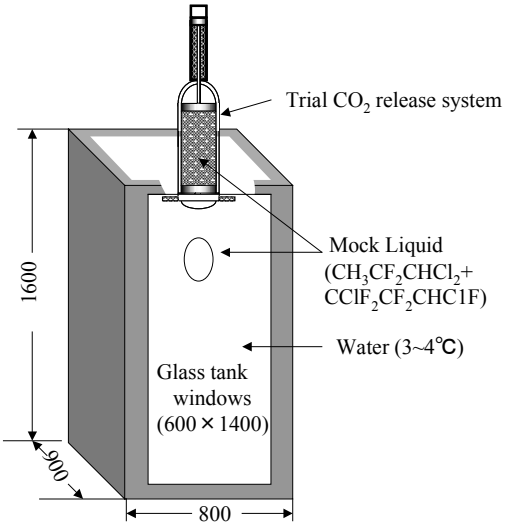

Figure 4. Layout of atmospheric simulation experiment.

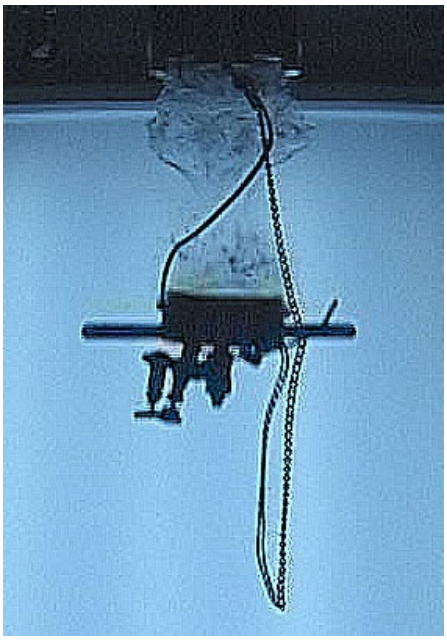

Figure 5. Cold mock liquid just flowed out from the chamber.

2000. The original nozzle was designed to release CO_2 in 500 meters depth through simple two actions that the ROV pilot can easily manipulate through the robot arm. The volume and the diameter of chamber to hold CO_2 or mock liquid were 2.16 liters and 10 cm, respectively. The total weight including frames was about 60 kg, which was smaller than the weight limit of the ROV, 113 kg (= 250 lbs).

The second nozzle, of which specifications were almost the same as the original one, was not only improved in its thermal insulation to keep CO_2 cool enough until its release but also the temperature and pressure monitoring devices were installed.

Mock liquid experiment. Because the saturation pressure of CO_2 at room temperature (≒20 Celsius) is 5.8 MPa, an appropriate mock liquid was required to check the performance of the manufactured CO_2 release nozzle at atmospheric pressure. Then

Figure 6. Large test tank for trial CO_2 release nozzles.

considering the properties of density, specific heat, boiling and solidification points, surface tension and noxiousness, *Asahi-Kurin AK-225* (mixture of $CH_3CF_2CHCl_2$ and $CClF_2CF_2CHClF$) was selected as the mock liquid for simulation experiment (specific density: 1.55, specific heat: 1.00 J/(gr·K), boiling point: 54 Celsius, solidification point: -131 Celsius, surface tension: 16.2 mN/m, weak noxious). **Figure 4** shows the layout of atmospheric simulation experiment. And **Figure 5** shows the scene that the cold mock liquid just flowed down from the opening of the chamber. As shown in this figure, the mock liquid was pushed out as one mass following the sinking lid of the chamber but not covered with ice layer although it was initially cooled down to about -60 Celsius. And the liquid mass broke up into small droplets in a several seconds. Its small specific heat (about a half of CO_2, about a quarter of water) was thought to be not enough to form thick ice layer so fast that the shape of large droplet was kept one mass.

Tank experiment with CO_2. A large tank made of stainless steel, of which main specifications are 5 MPa, 1.0 meter diameter and 3.0 meters height, was manufactured to confirm the perform-ance of CO_2 release nozzles, prior to shipping it to the MBARI. **Figure 6** shows the large tank fixed at the pit. The tank and the foothold for the experiment were enclosed with thermal-insulated room of which temperature was controlled from 5 to 20 Celsius by an air-conditioning system.

Figure 7 shows the scene that the cold CO_2 melted from dry ice was pushed down from the original release nozzle. It was seen that some liquid CO_2 was drown by the falling lid and other CO_2 followed it. Comparing Figs 5 and 7, the ratio of drown liquid in case of CO_2 seems larger than the case of mock liquid. **Figure 8** shows a lot of ascending small CO_2 droplets that might have been broken up from heated CO_2 mass once fell down to the bottom of tank. Figure 8 also shows an ice horn (hollowed icicle) appearing after almost CO_2 was discharged, which implies that cold CO_2 has enough cold heat capacity to make hard ice layer around CO_2 mass.

The results of simulation tests with the mock liquid and CO_2 suggested that the heat transfer rate to form ice layer on the cold CO_2 might not be fast enough to form strong ice layer to keep the shape of a large CO_2 mass against Taylor type interface instability, although the heat capacity of cold CO_2 is enough to form thick ice.

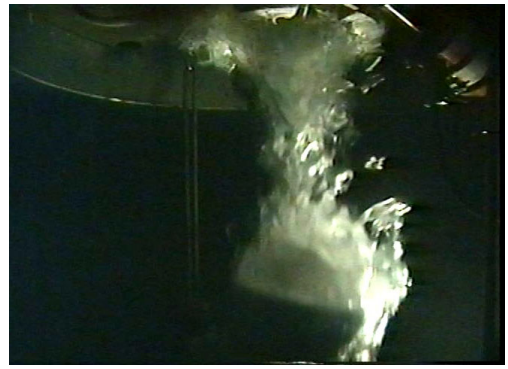

Figure 7. Cold CO_2 pushed down from the release nozzle.

Figure 8. Ascending small CO_2 droplets broken up from heated CO_2 mass and hollowed icicle.

***In Situ* Experiments**

Experiment with original release nozzle. On October 12, 1999, using the original release nozzle shown by Fig. 2, an *in situ* CO_2 release test was conducted in Monterey Bay as the 2nd joint experiment with the MBARI.[23] **Figure 9** shows the original CO_2 release nozzle mounted on the ROV, Ventana. It took about one hour to charge CO_2 into the chamber and to bring it down to the release point by the ROV. The thermal insulation of the release nozzle, which was tested before shipping the nozzle to the MBARI, was not enough for cold CO_2 release. So the temperature of CO_2 in the chamber increased to the same level of the ambient seawater when reached the release depth of 450 meters.

Figure 10 shows that CO_2 was released as one mass from the nozzle, but as shown in **Figure 11**, CO_2 mass was broken up in a few seconds to a lot of small CO_2 droplets which might be covered with hydrate membrane and ascended around CO_2 release nozzle.

The basic performances required to a cold CO_2 release nozzle, that is, two simple actions for the initiation of CO_2 release, were well demonstrated at the *in situ* experiment with the original release nozzle, but the capability to release cold CO_2 mass, which was expected to be covered with thick ice layer, was not achieved.

Experiment with improved release nozzle. The second CO_2 release nozzle was manufactured, considering the defects found in

Figure 9. CO_2 release nozzle mounted on the ROV, Ventana.

Figure 10. CO_2 mass just released from the nozzle.

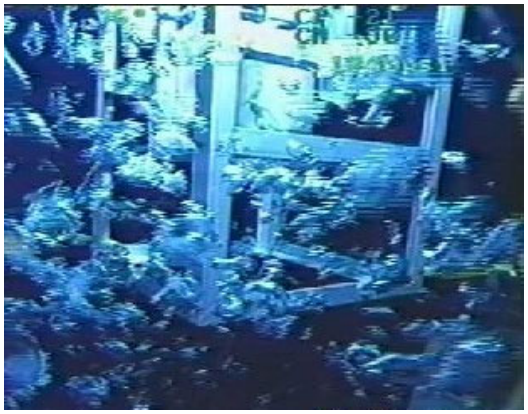

Figure 11. Ascending CO_2 droplets covered with hydrate.

the above-mentioned *in situ* experiment. That is, the thermal insulation was improved by covering it thick with air-containing cast plastic and monitoring devices for the temperature and pressure in the chamber were attached.

On October 5 and 6, 2000, two cold CO_2 release trials were conducted at the same water as before. **Figure 12** shows the improved release nozzle mounted on the ROV. After checking carefully the valves and devices of the nozzle with 2 kg of dry ice,

Figure 12. Improved release nozzle mounted on the ROV.

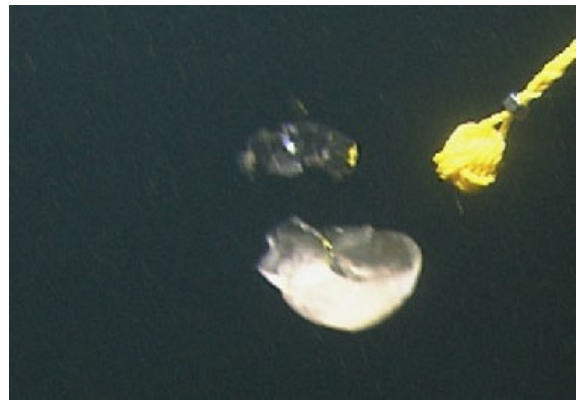

Figure 13. A CO_2 slurry mass（8 cm）sinking at 0.3 m/s.

the ROV sank to 500 meters depth in about 15 minutes, which was almost two times faster than the usual sinking rate. This time, the thermal insulation was improved so much that almost CO_2 was kept as dry ice when arriving at the release point of 500 meters depth.

At the first trial on October 5, being thought worth to observe the behavior of released dry ice mass, cold CO_2 almost consisting of dry ice was released by the simple two actions of robot arm explained above. The dry ice ball with about 10 cm diameter sank so fast that the ROV could not catch up with it. Only the release and very first sinking scene was recorded.

At the second trial on the next day, after two-hours wait at the releasing depth for warming up of CO_2, 2 kg of cold CO_2 including some dry ice was released as the same manner as before. And melted and warmed CO_2, which occupied in the upper space of the chamber, followed the cold CO_2 and broke up into small droplets ascending in the ocean. The content of dry ice in the cold CO_2 mass was estimated about 50 % from the sinking rate that the ROV could catch up with. **Figure 13** shows the scene that a CO_2 slurry mass with 8 cm diameter sank in around 530 meters depth at the rate of 0.3 meters per second. As shown in Fig. 13, CO_2 slurry was coated with thick ice layer. From the video image during sinking process of this slurry mass for about four minutes while the ROV could follow, it was confirmed that this ice layer had enough strength to prevent from breaking up to small slurries. Thin hydrate layer should also form between CO_2 slurry and ice layer, but it was not observed due to its thinness and transparency. It was observed that some part of melt CO_2 due to heating up by ambient seawater leaked upward

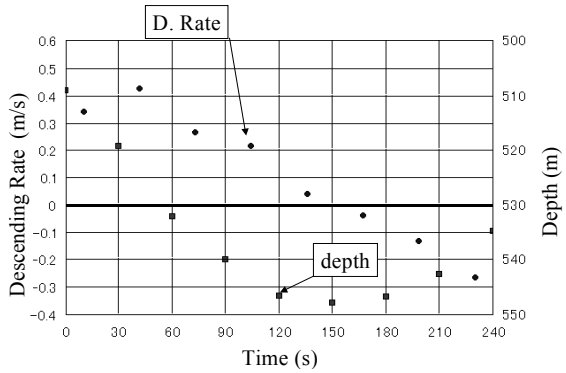

Figure 14. Depth and velocity of a sinking slurry ball.

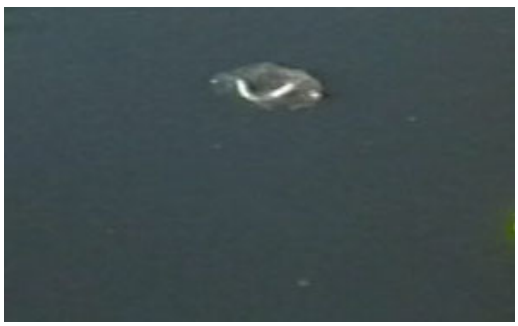

(a) Just before breaking

(a) Just after breaking

Figure15. Deformed and breaking CO_2 mass covered with hydrate film.

from the slurry. This volume increase came from the fact that the density of dry ice is about 1.4 times larger than cold liquid CO_2.

Figure 14 shows how the depth and velocity of the slurry mass observed in the second trial change with lapse of time. It was shown that the slurry once reached 548 meters depth at 150 seconds but it began to ascend, which means the slurry mass was heated up during 150 seconds descent and lost its negative buoyancy. During ascent, the ice layer continued to shrink and at 240 seconds it broke up to small CO_2 droplets covered with hydrate membrane. Just before breaking up, curious movement of CO_2 mass due to changes of surface tension was seen. **Figure 15** shows its deformed shape during such unique movement. The size of broken up droplets is 2 to 3 cm, which can dissolves in the ascent less than 1000 meters.

Proposal of New COSMOS

Results of land-based and *in situ* experiments. Through several land-based experiments and two *in situ* experiments the following results were obtained:

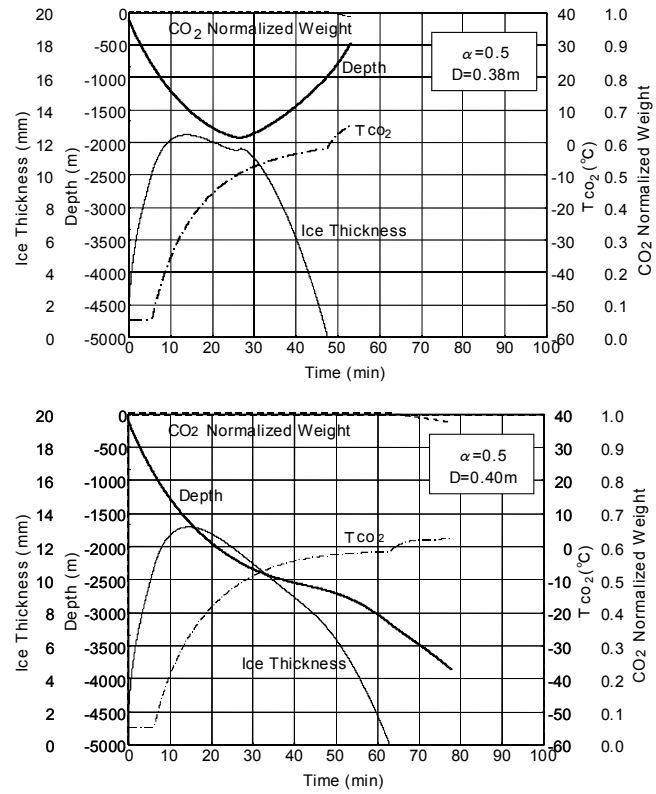

Figure16. Behavior of a CO_2 slurry ball released into 100 meters depth

(1) The basic skill to release small amount of cold CO_2 (2kg) to 500 meters depth was established.
(2) Simulation of cold CO_2 release using a mock liquid was difficult because no liquid having the same properties as those of CO_2.
(3) The heat capacity of cold CO_2 is enough to form thick ice layer to protect a cold CO_2 droplet.
(4) But the surface instability of a cold CO_2 (Taylor type instability) was so large that thick ice layer was difficult to form before released CO_2 mass broke up.
(5) Only CO_2 slurry (mixture of dry ice and cold CO_2) can sink in the ocean without breaking up.
(6) It might be possible to realize the original COSMOS proposed in 1998, but it should be much easier to release CO_2 as slurry balls.

Motion of CO_2 slurry ball in the ocean. Considering above results, the authors would like to propose another CO_2 Sending Method for Ocean Storage, new COSMOS, in which CO_2 will be released as slurry balls instead of cold CO_2 droplets. In case of slurry release, the required depth is 100 to 200 meters, much shallower than 500 meters the original COSMOS requires, because cold heat capacity of a slurry ball is larger than a cold CO_2 droplet and melt CO_2 is expected not to be heated up before reaching the phase change boundary, about 400 meters depth.

Figure 16 is an example of numerical simulation to show how a CO_2 slurry ball released into 100 meters depth behaves.[22] The dry ice ratio, α, was chosen as 0.5 in this simulation. In case of 0.38 meter, the slurry ball reaches 1950 meters then ascends, but in case of 0.4 meter, it sinks to the ocean floor through 2700 meters of density equilibrium depth. In both cases, the temperature of slurry ball is kept -55 Celsius, melting point of CO_2, until it reaches 800 to 900 meters

depth, far deeper than the phase change boundary, which means the cold heat capacity of a slurry ball is enough. At this depth, a slurry ball becomes a cold CO_2 droplet covered with thick ice layer. Then a CO_2 droplet is gradually heated up as shown in Fig. 16. When the temperature becomes -1.9 Celsius, the ice layer completely melts and the dissolution of CO_2 starts (the normalized weight starts to decrease). Heating up rate increases when ice layer disappears. The maximum thickness of ice layer reaches 12.5 and 13 cm for D = 0.38 meter and 0.40 meter, respectively.

Figure 17 shows the simulation result as the relation of the depth and temperature of a slurry ball (α = 0.5, release depth = 100 meters). From this figure, the limit size that can sink to the ocean floor is between 0.38 meter and 0.40 meter as mentioned above. This size is less than 40 % of original COSMOS (cold liquid CO_2 release). The similar results like Figs. 16 and 17 were obtained by B. Kvamme, a member of the international joint research team.[24]

Advantages of New COSMOS. Figure 18 shows the concept of new COSMOS to be applied for a Japanese patent. The only additional component required by new COSMOS is a refrigerator to change cold CO_2 of -55 Celsius to CO_2 slurry. When the main engine of 200 thousand tons CO_2 carrier is used for the compressor of the refrigerator, it will take two days to make all CO_2 slurry. This treating rate is almost equivalent to the amount of CO_2 released from five power plants of 1000 MW. Since the volume of dry ice is 1.4 times smaller than cold CO_2, the choking of pipe while making slurry might be avoided.

The new COSMOS has the following advantages:

(1) Easy to realize. The basic techniques to release a CO_2 slurry mass into the ocean have accumulated through *in situ* experiments with the MBARI. And it was confirmed that a CO_2 slurry ball does not break up until the ice layer covering it almost completely melts. Therefore it can be said that the most important phenomenological aspects of new COSMOS has been elucidated.

On the other hand, it may not be so easy to keep a large CO_2 droplet as one mass, the most important requirement of original COSMOS, because the Taylor type interface instability is so strong for ice layer to cover the droplet before breaking, although the heat capacity of cold CO_2 droplet is large enough.

(2) Low initial cost. As shown in Fig. 17, the CO_2 slurry size to be sent to the ocean floor is around 0.4 meter, although it depends on dry ice ratio, α. This size is 0.4 times smaller than the original COSMOS. And the required pipe length is also 0.4 times (200/500 = 0.4). Such smaller sizes will result in drastic cost reduction.

(3) Low running cost. The theoretically required pipe length is less than 100 meter, but 200 meters pipe is recommended in the new COSMOS for the safety. This 200 meters pipe can be put on the deck of 200 thousand tons of CO_2 carrier. Therefore, troublesome works to connect a lot of pipes on the deck, which original COSMOS and other CO_2 ocean sequestration methods require, can be avoided.

(4) Applicable to the dissolution method. Considering the facts that a CO_2 droplet breaks up to small ones just before complete melting of the ice layer which covers the droplet and broken up droplets are so small that they can dissolve before reaching the phase boundary depth of about 400 meters, the new COSMOS can be applied to the dissolution method as well as the storage method. That is, if the dry ice content, α, and the slurry size are well controlled, we can optionally choose the depth that the CO_2 slurry released in 200 meters depth turns back. Moreover, if we set the turn-back depth to a little bit shallower and deeper than the neutral depth of around 2700 meter, the full depth from the ocean floor to the phase boundary can be used for the CO_2 dissolution field, which makes the maximum CO_2 concentration the lowest. Figure 17 also suggests that the application to the dissolution method is not difficult.

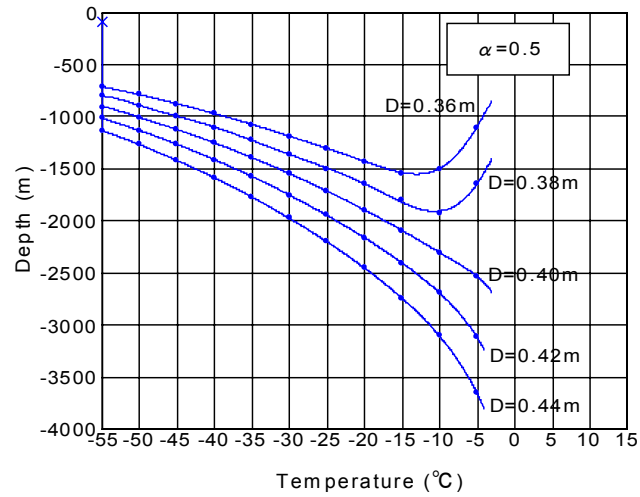

Figure17. Relation of the depth and temperature of a slurry ball (α = 0.5, release depth = 100 m).

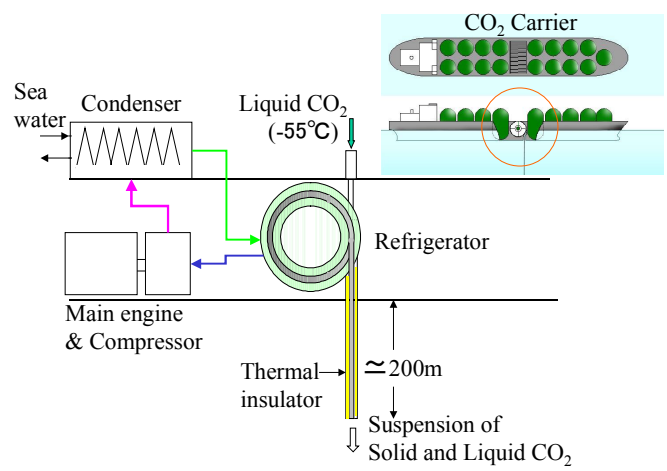

Figure18. Concept of new COSMOS, in which CO_2 is released as slurry balls.

Conclusions

Through various types of land-based and *in situ* experiments with the MBARI, it was found that the development of a cold CO_2 release nozzle, which was thought to be a breakthrough technology to realize the COSMOS proposed in 1998, was not necessarily easy. Moreover, the last *in situ* experiment and the numerical simulation for a CO_2 slurry mass release suggest that the release of CO_2 as slurry mass was much easier than cold liquid CO_2 release. Then the authors proposed a new COSMOS in which CO_2 transported by a CO_2 carrier is released as slurry masses into 200 meters depth.

The new COSMOS has several advantages compared to the original COSMOS and other CO_2 ocean sequestration methods proposed so far. That is, the new COSMOS is easy to realize and requires low initial and running costs. And when applying the new COSMOS to the dissolution method, the full depth from the ocean floor to the phase change boundary can be utilized for the dissolution field, which results in the lowest CO_2 concentration.

Acknowledgement

This work was done as a part of COSMOS Project supported by an International Research Grant from the NEDO (New Energy and Industrial Technology Development Organization). The authors wish

to express their sincere gratitude to Drs. P. G. Brewer and E. T. Peltzer of the MBARI for the successful joint *in situ* experiments and three COSMOS project members, Profs. B. Kvamme, T. Johannessen and P. M. Haugan of University of Bergen for their useful comments on the design of new CO_2 release nozzle.

References

1. Machetti, C., *Climate Change*, 1977, p.59-68.
2. NEDO Report, NEDO-GET-9407 (in Japanese), 1995, p.200.
3. Ohsumi, T., *Institute of Applied Energy*, **19- 4**, 1997, p.45-54.
4. Aya, I.; Yamane, K., 17th Mtg. of UJNR/MFP, 1991, p.273-279.
5. Aya, I.; Yamane, K.; Yamada, N., 1st Int. Conf. on Offshore and Polar Engineering (ISOPE-91), 1991, p.427-432.
6. Aya, I.; Yamane, K.; Yamada, N., ASME 1992 Winter Annual Mtg., HTD-Vol.215, Fundamentals of Phase Change: Freezing, Melting and Sublimation, 1992, p.17-22.
7. Aya, I., 2nd Int. Workshop on Interaction between CO_2 and Ocean, 1993, p.233-238.
8. Aya, I.; Yamane, K.; Yamada, N., Int. Symposium on CO_2 Fixation and Efficient Utilization of Energy, 1993, p.351-360.
9. Aya, I.; Yamane, K.; Yamada, N., *Energy Convers. Mgmt.* **36**, 6-9, 1995, p.485-488.
10. Aya, I.; Yamane, K.; Nariai, H., *Energy-Int. Journal*, 22, 2/3, 1997, p.263-271.
11. Yamane, K.; Aya, I.; Nariai, H., 2nd ISOPE Mining Symposium, 1997, p.154-158.
12. Yamane, K.; Aya, I.; Namie, S.; Nariai, H., Greenhouse Gas Control Tech., Pergamon, Proc. of GHGT-4, 1998, p.1069-1071.
13. Yamane, K.; Aya, I.; Namie, S.; Nariai, H., *Annals of New York Academy of Science*, 2000, p.254-260.
14. Aya, I.; Yamane, K.; Kojima, R, Greenhouse Gas Control Tech., GHGT-5, CISRO, 2001, p.423-428.
15. Aya, I.; Yamane, K.; Kojima, R.; Nariai, H., *ditto*, p.492-498.
16. Aya, I.; Yamane, K.; Shiozaki, K., Greenhouse Gas Control Tech., Pergamon, Proc. of GHGT-4, 1998, p.269-274.
17. Aya, I.; Yamane, K.; Shiozaki, K., 22nd Mtg. of UJNR /MFP, 1998, p.152-157.
18. Kvamme, B.; Aya, I.; Johannessen, T.; Haugan, P. M., NEDO Int. Joint Res. Grant, Ind. Tech. Dep., NEDO, 2000, p.119-120.
19. Aya, I.; Yamane, K.; Kojima, R.; Brewer, P. G.; Peltzer, E. T., 23rd UJNR/MFP, 2, 2000.
20. Schlichting, H., Boundary Layer Theory, McGraw Hill, 1955, p.439.
21. Kvamme, B., Greenhouse Gas Control Tech., GHGT-5, CISRO 2001, p.435-439.
22. Yamane, K.; Aya, I.; Kojima, R.; K. Shiozaki, K., 1st Mtg. of Maritime Res. Inst., 39, 2001, p.177-180.
23. Aya, I.; Yamane, K., *Techno Marine*, **846** (in Japanese), 1999, p.890-894.
24. Kvamme, B., Proc. of 11th Int. Offshore and Polar Eng. Conf. (ISOPE-2001), 1, 2001, p.498-505.

Producing Negatively Buoyant CO_2 Streams at Intermediate Ocean Depths

Olivia R. West, Costas Tsouris, Liyuan Liang, Sangyong Lee

Oak Ridge National Laboratory
Oak Ridge, TN 37831

Introduction

Direct injection of CO_2 into the ocean has been proposed as a means for carbon sequestration because the ocean has a large storage capacity for carbon (Herzog, 1998; Audus, 1997, Brewer et al., 1999). A fraction of the CO_2 injected into the ocean will eventually repartition back into the atmosphere. However, depending on the depth of injection as well as the subsequent interaction of CO_2 with seawater, CO_2 residence time in the ocean can be on the order of several hundred years leading to significantly reduced peak levels of atmospheric CO2 (Herzog et al., 1997).

One of the proposed methods for direct ocean injection is to release liquid CO_2 at intermediate ocean depths between 800 and 1500 m, forming a rising plume of CO_2 droplets. To prolong the residence time of the injected CO_2, the injection depth for the droplet plume must be sufficiently great to allow for complete dissolution of the CO_2 into the surrounding seawater before the droplets reach depths of ~0.5km where pressures are low enough for the CO_2 to gasify and more rapidly partition back into the atmosphere. Another approach is to perform injections at depths greater than 3000 m where CO_2 is denser than seawater. CO_2 released at these depths will sink through the water column resulting in increased residence time and improvement in the overall efficiency of ocean carbon sequestration by direct CO_2 injections. However, this improved efficiency comes with implementation costs and energy requirements that increase significantly with injection depth.

The objective of the research described here is to develop a new technique for direct ocean CO_2 injection in which CO_2 can be disposed at ocean depths of 1000 to 1300 m in the form of a water/ CO_2/hydrate composite stream. Produced by intense in-line mixing of CO_2 and water, this composite stream can be negatively buoyant, prolonging the residence of injected CO_2 in the ocean and improving the overall efficiency of ocean carbon sequestration by direct CO_2 injection.

Experimental Methods

Experiments were conducted to test the concept of promoting CO_2 hydrate formation by mixing water with CO_2 in a discharge pipeline. A co-flow injector was designed and set up in the ORNL Seafloor Process Simulator (SPS), a 70-L, temperature controlled, high-pressure vessel designed for simulating conditions at intermediate ocean depths (Fig. 1; Phelps et al., 2001). The injector (Fig. 2) consists of an internal capillary tube located at the center of an outer tube, where the inner and outer tubes are for water and CO_2, respectively. The mixing zone, as shown in Fig. 2, is the space between the ends of the inner and outer tubes. In a typical experiment, the SPS was filled with water, pressurized up to a predetermined level (10 to 13 MPa, corresponding to ~1 to 1.3 km depth) then cooled in a temperature-controlled room down to the experimental temperature. (4-7ºC). Liquid CO_2 and water were then delivered through the injector using syringe pumps at predetermined flow rates ranging from 15-25 mL/min and 4-20 mL/min, respectively. Vessel pressure increased slightly (less than 0.5 MPa) during the injection experiments, or was kept constant using a backpressure regulator. The stream issuing from the injector was then observed and recorded by a video camera through one of the 5-cm diameter sapphire windows on the SPS.

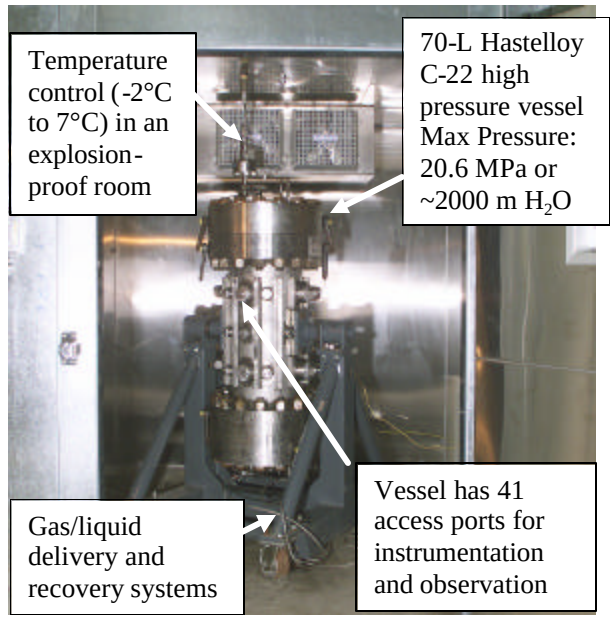

Figure 1. The ORNL Seafloor Process Simulator (SPS).

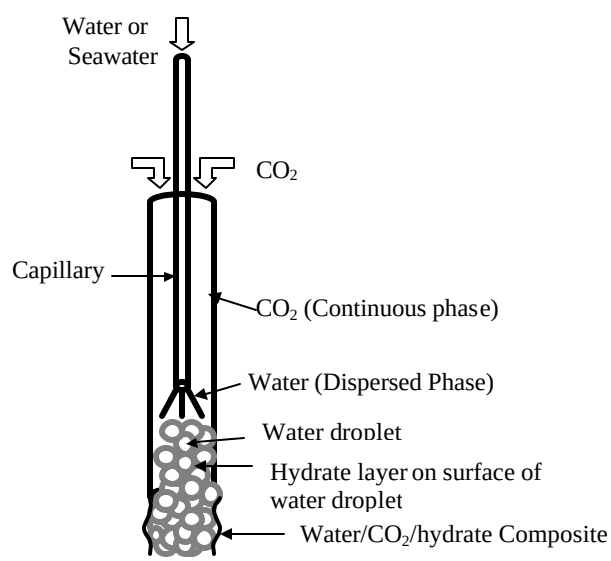

Figure 2. Schematic of the co-flow injector for producing a water/CO2/hydrate composite stream.

Results and Discussion

Using the co-flow injector at varying flow-rate ratios of water and CO_2, we obtained a paste-like stream (Fig. 3) under conditions typical of intermediate ocean depths (1-1.3 km). The produced stream maintained its cylindrical shape and remained fairly intact when released from the injector, occasionally breaking up into cylindrical sections. For a given ambient pressure, the stream was negatively buoyant at certain flow rate ratios between water and CO_2. To eliminate the effects of jet flow that may be pushing the stream down in a vertically oriented injector, experiments were also conducted with the injector mounted horizontally in the SPS. Negative buoyancy in this case was indicated by a stream that bent downward as it was released from the injector (Fig. 4). Experiments using both distilled and seawater showed that a negatively buoyant stream can be produced at pressures as low as 10.3 MPa, corresponding to an ocean depth of ~1 km.

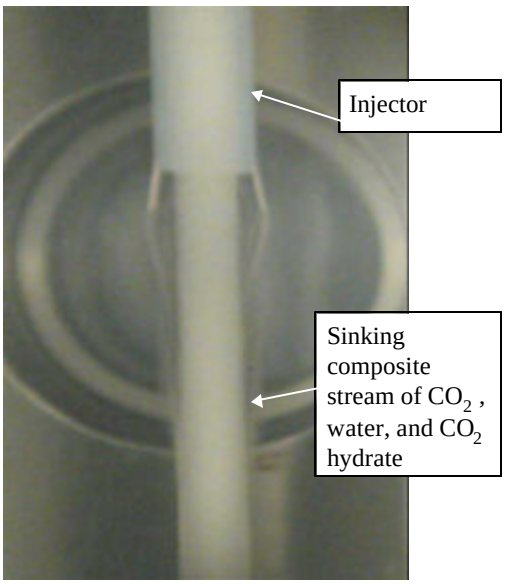

Figure 3. Negatively buoyant stream produced by CO_2 injector oriented vertically in the SPS.

The stream produced by our injector probably consists of a composite of liquid CO_2, water, and CO_2 hydrate where the solid hydrate serves as a cementing phase for the other stream components. Presence of water in the stream was inferred from the flow rate ratios between water and CO_2 used to produce the stream, which exceeded what was required for complete conversion of CO_2 to CO_2 hydrate. It was also observed that some streams that were initially positively buoyant would sink some time after being released from the injector, or when vessel pressure was increased. These observations indicate the presence of liquid CO_2 trapped in the produced stream, where it either continues to convert to CO_2 hydrate with time or becomes denser with increasing pressure.

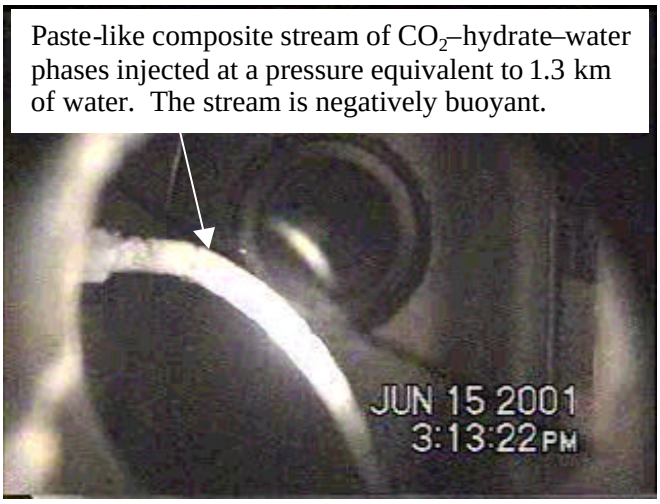

Figure 4. Negatively buoyant stream produced by CO_2 injector oriented horizontally in the SPS.

Conclusions

A negatively buoyant composite stream containing CO_2 hydrate, liquid CO_2, and water at conditions simulating intermediate ocean depths (~1-1.3 km) was produced using a novel concept of premixing seawater into a CO_2 stream before injection. Such a development is significant because it generates a sinking stream at depths <1.5 km, which will prolong the residence of CO_2 injected into the ocean and improve the overall efficiency of direct CO_2 injections for ocean carbon sequestration. Because implementation costs increase significantly with injection depth, this approach allows CO_2 injections to be performed not only with a lower risk of leakage to the atmosphere, but also without significant increase in operating cost when compared with other proposed injection methods. Additionally, because of its low surface-to-volume ratio, the produced composite stream is expected to have a slower dissolution rate than that of a similar volume of liquid CO_2 in the form of a droplet plume. The deeper the CO_2 hydrate stream sinks after injection, the more stable it becomes internally, the deeper it is dissolved, and the more dispersed is the resulting CO_2 plume. This slower rate will reduce the potential for low-pH conditions surrounding the injector, thereby minimizing the negative impact of direct CO2 injections on the ocean environment.

Acknowledgment. This research was funded by the Ocean Carbon Sequestration Program, Biological and Environmental Research (BER), U.S. Department of Energy (Grant #KP120203), and by the Oak Ridge National Laboratory's Seed Money Program. We would also like to thank Scott McCallum and David Riestenberg for their assistance with the laboratory experiments. Oak Ridge National Laboratory is managed by UT-Battelle, LLC, for the U.S. Department of Energy under Contract No. DE-AC05-00OR22725.

References

(1) Herzog, H. J. Ocean Sequestration of CO2—An Overview. in *Fourth International Conference on Greenhouse Gas Control Technologies,* **1998** (Interlaken, Switzerland).

(2) Audus, H. *Energy*, **1997**, *22*, 217.
(3) Brewer, P. G.; Friederich, G.; Peltzer, E. T.; Orr, F. *Science*, **1999**, *284*, 943.
(4) Herzog, H.; Drake, E.; Adams, E. *CO2 Capture, Reuse and Storage Technologies for Mitigating Global Climate Change*. **1997**, MIT Energy Laboratory, Cambridge, MA.

CARBON SEQUESTRATION UTILIZING INDUSTRIAL SOLID RESIDUES

Daniel J. Fauth, Yee Soong, and Curt M. White

U.S. Department of Energy, National Energy Technology Laboratory
P.O. Box 10940, Pittsburgh, PA 15236-01940

Introduction

Increasing public concern related to the possible effects that anthropogenic emissions of CO_2 may have on global climate has led the Department of Energy (DOE) to embark on development of a number of carbon sequestration processes for mitigating carbon dioxide. Anthropogenic emissions of CO_2 generated by the combustion of fossil fuels are estimated at 6 GtC/year[1]. The intent of the Carbon Sequestration program is to significantly decrease emissions of greenhouse gases and stabilize atmospheric CO_2 concentrations at 550 ppm, by 2025. Complementary to traditional areas of energy research, such as improving energy efficiency or shifting to renewable or nuclear energy sources, carbon sequestration will allow continued use of fossil energy, buying decades of time needed for transitioning into less carbon-intensive and more energy-efficient methods for generating energy in the future.

Mineral carbonation, the reaction of CO_2 with non-carbonated minerals to form stable, benign, mineral carbonates, has been identified as a possible safe, long-term, and unmonitored option for storing carbon dioxide[2-7]. In this chemical approach, CO_2 reacts with alkaline earth containing silicate minerals, such as serpentine $Mg_3Si_2O_5(OH)_4$, forming magnesite, $MgCO_3$. Moreover, Goff and Lackner have shown the economics of using magnesium silicates for carbonation and their abundance are well matched concerning the scale of CO_2 storage[8]. Current studies using serpentine, a Mg-rich lamellar hydroxide based mineral, however, requires prior pulverization to the mineral, removal of iron oxide, magnetite, prior to carbonation, and thermal activation at high temperatures (630°C) to successfully achieve rapid and high rates of conversion to magnesite. Thus, alternative chemical and mechanical methods focusing on surface activation of serpentine to accelerate the carbonation reaction efficiency have been under investigation[9,10].

The objective of our study was to use industrial solid residues (FBC ash and FGD spray dryer ash) rather than natural minerals, for investigating their potential in permanently sequestering CO_2 as mineral carbonates. Although not available in sufficient quantities to make an impact on worldwide CO_2 emissions, these materials are readily available at low cost, easily gathered at or near energy and industrial sites, and readily accessible in fine particle sizes. Use of these alternative feeds were envisioned to provide a faster reaction pathway optimizing energy management along with providing an immediate incentive toward the development of a high-pressure direct carbonation method for processing these commercial by-products.

Experimental

Mineral Carbonation Experiments Initial proof-of-concept tests were conducted using samples obtained from Freeman United Coal Mining Company, Farmersville, Illinois, USA and Consol Energy, Library, PA, USA, respectively. Carbonation reactions were carried out in a 1-liter Hastelloy C-2000 continuous-stirred-tank-reactor (CSTR). In a representative experiment, a determined amount of solid reactant was mixed with an aqueous bicarbonate solution (0.5 M Na_2CO_3/0.5 M $NaHCO_3$; 1.0 M NaCl) and charged into the CSTR. The CSTR was sealed, and purged with gaseous carbon dioxide. A pre-determined amount of liquid CO_2 was then carefully injected through the side port of the CSTR. The solid reactant/bicarbonate solution/liquid CO_2 mixture was sufficiently agitated during both heat up and testing to prevent any settling of solid reactant. The carbonation studies were conducted at temperatures (155 &185°C) and CO_2 pressures (75 & 115 atm) for 1 hour at an agitation speed of 1000 rpm. At the conclusion of the test, the remaining CO_2 was vented, and the carbonated slurry was flushed from the CSTR and filtered to separate solids from the aqueous bicarbonate solution. The washed carbonated solid product was dried at 105°C in air overnight. A digital pH meter was used to determine the pH values of pre-and post-product solutions.

X-ray powder diffraction (XRD) XRD measurements of untreated and supercritical CO_2–treated solids were carried out using a Rigaku DAD-IIA powder diffractometer with a Cu-Kα X-ray source at 40kV and 25 mA. The powder sample was mounted on a glass sample holder. The XRD patterns were recorded over a 2θ range of 2° to 90° and compared with the JCPDS mineral powder diffraction file.

Scanning Electron Microscopy (SEM) SEM analyses were performed using an Aspex Personal SEM™ equipped with a Noran energy dispersive detector enabling x-ray detection of elements with atomic number 6 (carbon) and greater. Sample preparation involved mounting a portion of a representative sample in epoxy and polishing to obtain a cross section of the particles. Polished cross sections of supercritical CO_2-treated solid products were analyzed at an accelerating voltage of 20 KeV and working distance of 16-19 mm. Prior to analyses, samples were coated with a thin layer of carbon to provide an electrically conductive surface. The samples were examined in backscattered electron imaging (BSI) mode coupled with energy dispersive spectroscopy (EDS).

Results and Discussion

The chemical analyses of the major components were determined by ICP-AES, with a preliminary preparation of acid digestion. The chemical composition of FBC and FGD solid residues and their corresponding carbonation products are summarized in Table 1. The crystalline phases of the FBC solid residue was analyzed by XRD. Anhydrite ($CaSO_4$), quartz (SiO_2), periclase

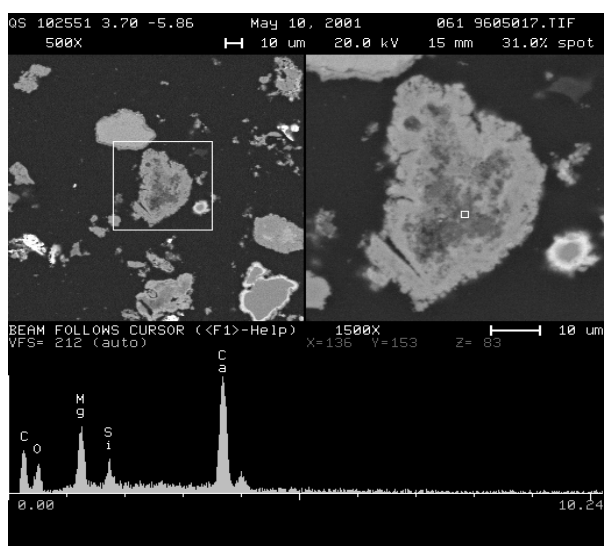

Figure 1. SEM image with EDS spectra of supercritical CO_2-treated FBC ash (Freeman United Coal Mining Co.)

(MgO), lime (CaO) and hematite (Fe_2O_3) were identified as minor phases for the FBC ash (Freeman United Coal Co.) feed sample. XRD confirmed a trace constituent; calcite ($CaCO_3$) was also present. Dolomite, $CaMg(CO_3)_2$ and calcite were determined as being the primary constituents in the supercritical CO_2-treated FBC solid product. Free CaO was identified as the primary constituent for the FGD spray dryer ash material obtained from Consol Energy. XRD analysis coupled with a relatively high CO_2 concentration of in FGD reaction product, confirmed $CaCO_3$ as the major element in the Consol Energy FGD carbonation product.

Table 1. Chemical composition of FBC and FGD solid residues

Oxide	FBC Residue	FBC Product	FGD Residue	FGD Product
Al_2O_3	5.9	6.1	15.9	12.7
CaO	27.1	22.7	31.9	23.1
FeO, Fe_2O_3	6.3	5.9	3.9	3.2
MgO	9.6	8.0	1.4	1.2
SiO_2	24.4	25.0	35.0	26.8
Na_2O	0.6	0.7	0.3	0.3
TiO_2	0.3	0.3	0.8	0.8
P_2O_5	0.1	0.1	0.1	0.1

Figure 1 shows a SEM photomicrograph with EDS spectra obtained for a supercritical CO_2-treated FBC ash (Freeman United Coal Co.). Although the EDS spectra are elemental, it is assumed that they are representative of the oxide species, unless otherwise noted. SEM with EDS spectra identified a number of large grains within the representative sample to contain relatively high concentrations of Ca, Mg, C, and O with trace amounts of silica. These particles dispersed throughout the mount were identified as dolomite by SEM-EDS. SEM-EDS analysis also showed the majority of the grains to contain high concentrations of silica. These particles could represent unreactive quartz (SiO_2).

Results obtained from tests investigating the mineral carbonation efficiency of FBC residues (Freeman United Coal Mining Co.) and FGD residues (Consol Energy) in an aqueous bicarbonate/NaCl solution are shown in Table 2. Extent of reaction achieved in tests conducted for one hour using the FBC solid residue was 50 and 51% stoichiometric, respectively. The main components of the FBC solid residue from coal combustion in fluidized beds, using limestone as a sorbent of SO_2 formed during the combustion process, are those arising from the reaction ($CaSO_4$), and by-products of reaction (CaO, $CaCO_3$). These reactants, including $CaSO_4$ react with the dissolved CO_2 to form the resulting mineral carbonate. Tests conducted with the latter feed (FGD residue) resulted in higher stiochiometric conversion to calcite. The concentration of free lime (CaO) was obvious much higher for the FGD residue than for the corresponding FBC solid residue.

The annual production rate of the FBC solid residue was estimated at approximately 400,000 t/year. Based on our preliminary results and the composition of the FBC solid residue, the order of magnitude of CO_2 sequestration is 15.8 wt % of the FBC residue. Therefore, 63,200 t CO_2/year or about 17,236 t C/year could be sequestered at the Farmerville, Illinois complex.

Conclusions

Preliminary results at NETL indicate direct aqueous mineral carbonation to be a viable technique for converting both FBC ashes and FGD materials into mineral carbonates. Although the sequestration potential of these materials are small, the ability to effectively process such a stream could lead to industrial interest in the development of a cost effective direct aqueous carbonation technology.

References

1. Freund, P.; Ormerod, W.G., *Energy Conversion Management*; No. 8:S199; 1997.
2. Seifritz, W. *Nature* 345, 486, 1990
3. Lackner, K.; Wendt, C.; Butt, D; Joyce Jr. E.; Sharp, D., *Energy* **20**, 1153-70, 1995
4. Walters, R.P.; Chen, Z.Y.; Goldberg, P.M.; Lackner, K.S.; McKelvy, M.J.; Ziock, H., *Mineral Carbonation: A Viable Method for CO_2 Sequestration*; Program Plan and Approach, National Energy Technology Laboratory, http://www.fetc.doe.gov/products/ggc, 1999
5. Dahlin, D.C.; O'Connor, W.K.; Nilsen, D.N.; Rush, G.E.; Walters, R.P.; Turner, P.C., *A Method for Permanent CO_2 Sequestration: Supercritical CO_2 Mineral Carbonation;* 17th Annual International Pittsburgh Coal Conference, Sept.2000
6. O'Connor, W.K.; Dahlin, D.C.; Nilsen, D.N.; Walters, R.P.; Turner, P.C., Proceedings of the 25th International Technical Conference on Coal Utilization & Fuel Systems, Clearwater, Florida, 153-64, Edited by B.A. Sakkestad, Coal Technology Association, Rockville, Md., 2000
7. Fauth, D.J.; Baltrus, J.P.; Knoer, J.P.; Soong, Y.; Howard, B.H.; Graham, W.J.; Maroto-Valer, M. M.; Andrésen, J.M.;; Prepr.Symp. *Am. Chem. Soc., Div. Fuel Chem.*, **2001**, 46 (1), 278.
8. Goff, F.; and Lackner, K.S.; *Environmental Geosciences*; **5**, 88-101
9. Maroto-Valer, M.M., Fauth, D.J.; Kuchta, M.E.; Zhang, Y.; Andrésen, J.M.; Soong, Y.; *Study of Magnesium Rich Minerals as Carbonation Feedstock Materials for CO_2 Sequestration;* 18th Annual International Pittsburgh Coal Conference, New South Wales, Australia, December, 2001
10. O'Connor, W.K.; Dahlin, D.C.; Nilsen, D.N.; Gerdemann, S.J.; Rush, G.E.; Walters, R.P.; Turner, P.C.; *Research Status on the Sequestration of Carbon Dioxide by Direct Aqueous Mineral Carbonation*; 18th Annual International Pittsburgh Coal Conference, New South Wales, Australia, December, 2001

Table 2. Summary of FBC and FGD Carbonation Experiments

Feed sample	Temp., °C	P_{CO2} , atm.	Time, hrs.	Carbonation solution	Pct. Stoich. Conv.
FBC - Freeman	185	75	1	0.5 M Na_2CO_3/0.5 M NaHCO3, 1 M NaCl	50
FBC - Freeman	155	75	1	0.5 M Na_2CO_3/0.5 M NaHCO3, 1 M NaCl	51
FGD - Consol	185	115	1	0.5 M Na_2CO_3/0.5 M NaHCO3, 1 M NaCl	72
FGD - Consol	155	115	1	0.5 M Na_2CO_3/0.5 M NaHCO3, 1 M NaCl	69

ENZYMATICALLY CATALYZED CO_2 SEQUESTRATION

[1]*Gillian M. Bond,* [2]*Brian McPherson,* [3]*John Stringer,* [2]*Tristan Wellman,* [2]*Aaron Abel, and* [1]*Margaret-Gail Medina*

[1] Dept Materials & Met. Eng, New Mexico Tech, Socorro, NM 87801; [2] Dept Earth & Environmental Science, New Mexico Tech, Socorro, NM 87801; [3] EPRI, Palo Alto, CA 94304

Introduction

Long-term sequestration of anthropogenic CO_2 is one suggested approach to the reduction of greenhouse gases in response to concerns over global warming. The most easily addressable source of CO_2 is that from the generation of electric power, and particularly that from the coal-burning stations, since they comprise a relatively small number of very large stationary sources. Coal-fired power plants currently account for a little more than half the total electricity generation. It is unlikely that there will be a dramatic change in this situation in the next twenty years, not least because there is a considerable quantity of coal-burning electricity-generating plant in place that is still operational, and its retirement and replacement would present a considerable economic penalty. In each of the last three years, the coal consumed by the electric utilities in the U.S. has been close to 900,000,000 tonnes. It is therefore essential that CO_2 sequestration is part of any carbon management strategy.

Geologic sequestration of CO_2 is the subject of many ongoing research studies, the majority of which are aimed at injection of supercritical CO_2 into underground formations, particularly deep saline aquifers. It should be noted that CO_2 represents about 18% by weight of the exhaust gas, or 15% by volume, and hence is relatively dilute. There are significant cost penalties associated with the concentration of CO_2 from the flue gas, compression to supercritical form, and subsequent transportation. Several environmental issues associated with the sequestration of supercritical CO_2 also cause concern. These include the risks associated with leaks in the transport lines (since, unlike natural gas, released CO_2 will concentrate in low-lying regions adjacent to the leak, and is not easy to detect), and the possibility of seeps of CO_2 from the subsurface, potentially causing air quality (suffocation) hazards within the vicinity of the seep. Characterization of the "cap rock" or upper confining units of the host formation must be completed to avoid areas in the basin where seeps may form. The possibility of unintended displacement of brines as a result of continued injection of supercritical CO_2 must also be considered.

Conversion of CO_2 to solid carbonates offers the possibility of a safe, stable product for long-term carbon sequestration. Naturally occurring carbonate minerals already comprise a massive carbon reservoir that has existed for millions of years. Large quantities of these carbonate minerals are of biogenic origin. Calcium carbonate can be precipitated from aqueous solution, given a suitable supersaturation of calcium and carbonate ions, and so the issue becomes one of how to produce carbonate ions rapidly from CO_2 and H_2O (1), a process which first requires the formation of bicarbonate ions. One important parameter to be considered is pH, because of its strong effect on the proportions of the carbonic species present (2), and because, at low pH, carbonates will tend to dissolve rather than precipitate. Although carbonate could be formed rapidly at high pH, this would pose both economic and environmental concerns, and hence a process that operates at very mildly basic pH values would be desirable. The rate-controlling step in the fixation of gaseous CO_2 into carbonate ions (Table 1) is the hydration of CO_2 (except at high pH). Thus, if a viable means to accelerate this reaction can be found, it should be feasible to fix large quantities of CO_2 into calcium carbonate at moderate pH. The solution to this problem in fact already exists in biological systems, in the form of a biological catalyst, the enzyme carbonic anhydrase. We have, in fact, demonstrated proof of principle for a novel biomimetic approach to carbon sequestration, which uses carbonic anhydrase to accelerate the formation of bicarbonate ions in aqueous solution (4). In the presence of suitable cations, this can then be precipitated out in carbonate form.

Table 1. Basic carbonate aqueous chemistry reactions.
Equilibrium constants from Langmuir (3).

(1) $CO_2\,(g) = CO_2\,(aqueous)$
(2) $CO_2\,(aqueous) + H_2O = H_2CO_3$
(3) $CO_2\,(g) + H_2O = H_2CO_3 \quad K = K_{CO2} = 10^{-1.47}$
(4) $H_2CO_3 = H^+ + HCO_3^- \quad K_1 = 10^{-6.35}$
(5) $HCO_3^- = H^+ + CO_3^{2-} \quad K_2 = 10^{-10.33}$

Cation Sources: Brines

One of the issues we are now addressing is the selection of suitable sources of cations. Along with seawater, and waste brines from desalination operations, brines from deep saline aquifers offer an attractive possibility. In this context, it is important to understand the effects of brine flow on geologic media, both during brine extraction and during possible reinjection of bicarbonate-enriched brines. A preliminary numerical analysis of a sedimentary basin, the Powder River Basin of Wyoming, has been performed. The numerical model includes multiphase flow of CO_2, groundwater and brine, allowing evaluation of residence times in possible aquifer storage sites, and migration patterns and rates away from such sites in the Powder River Basin of Wyoming. The model has also been used to simulate CO_2 flow through fractures, to evaluate partitioning of CO_2 between the fracture network and rock matrix. These simulations provide insight regarding the ultimate propensity of permeability reduction versus permeability enhancement in the fracture zone associated with carbonate reactions.

A two-dimensional finite-volume model of the Powder River Basin cross-section SW-NE was used for all the simulation analyses. The model domain is 230 km horizontal by 5 km vertical, consisting of 5000 grid-blocks (100 horizontal by 50 vertical), each 2300 m by 100 m. The TOUGH2 code (5), which couples flow of heat, groundwater, and brine, was used for these simulations.

Results (Figure 1) suggest that sustained injection of CO_2 may incur wide-scale brine displacement out of adjacent sealing layers, depending on the injection history, initial brine composition, and hydrologic properties of both aquifers and seals. While the results presented here are unique to the simplified model of the Powder River Basin used in this analysis, they may have more general implications for other basins of interest for CO_2 sequestration.

We are also using numerical simulations to evaluate and compare the effects of supercritical CO_2 flow to the effects of bicarbonate solution flow on geologic media. Specifically, we are examining diagenetic changes and time-scales of these changes associated with flow of the two different fluids. For these simulations we are using a reactive transport model that includes coupled groundwater flow, heat flow, and relevant geochemical reactions. The model simulates mass and energy flow and subsequent chemical reactions induced by carbon dioxide and bicarbonate solution injection in the subsurface. Chemical reactions and solute transport are evaluated by TRANS, a simulator developed by Peter Lichtner at Los Alamos National Laboratory (6). Fluid and heat flow are evaluated

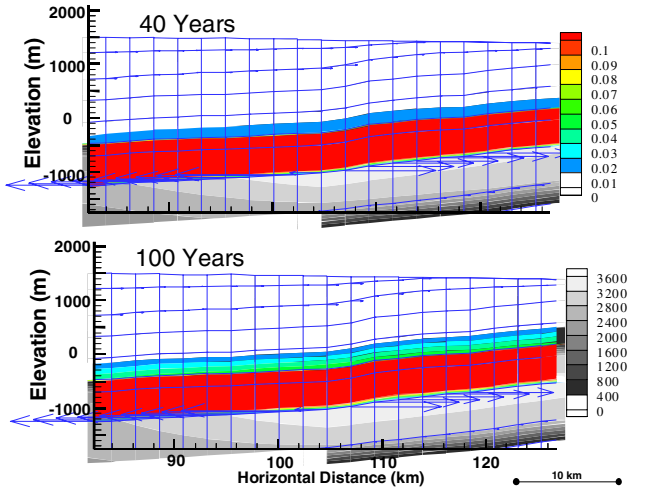

Figure 1. Simulation results illustrating displacement of brine out of a shale sealing layer as a consequence of CO_2 injection in aquifer below. Color contours are brine saturation in the sealing layer and aquifer above, grayscale contours are equivalent hydraulic head in the aquifer below. Arrows are flow vectors illustrating flow away from the injection well.

using TOUGH2, a geothermal simulator developed by Pruess at the Lawrence Berkeley National Laboratory (5). A driver program for coupling the two codes was recently completed by co-author Wellman, for this study. These simulations are being conducted for laboratory-scale models, with the intention that these results will be used for calibration of and upscaling to larger-scale hydrogeologic models.

Catalyst Response in Presence of Toxic Metal Ions

The concentration ranges of various monovalent and divalent ions in seawater, brackish water and saline reservoir waters vary widely. The levels of toxic metal ions that are emitted in flue gases are very carefully limited, and are extremely low (7). Nevertheless, they will not be zero. In a system based on a biological catalyst, it is important that the catalyst still function in the presence of representative levels of these ions. Satisfactory performance in solutions both representing, and more concentrated than, seawater has already been demonstrated (4).

Recent data provide information relating to the performance of solutions containing either purified bovine carbonic anhydrase (BCA) or live cells (modified bacteria, E. coli, expressing human carbonic anhydrase II (HCA II)), in the presence of a range of concentrations of these ions. It is found that the amounts of arsenic, mercury or lead that inhibit enzyme activity are considerably higher than the amounts (10 or 15 µg/ton (7, 8)) that may be present in volumes of air. Thus it appears that neither the live-cell nor the purified-enzyme activities would be significantly affected by the small traces of arsenic, mercury and lead that might be present in flue gases. For both the live cells and the purified enzyme, activity can be seen to decrease strongly, however, at concentrations of these cations in the mg/ton (parts per billion) range. Figure 2, for example, illustrates the activity of both enzyme sources when exposed to increasing concentrations of arsenic ions. Arsenic may attack cell function, leading to large-scale loss of enzyme activity from whole cells at 29 mg/ton, whereas the purified enzyme shows loss of activity at 290 mg/ton.

The purified enzyme performs better than the live-cell enzyme in all experimental conditions. The cost of pure enzyme may prove prohibitive, however, for industrial application, and the difference in activity may not seem so stark when the low cost of live cell production is taken into account. Purified bovine carbonic anhydrase is available commercially for about US$300/gram, whereas E. coli cells expressing HCAII may be produced for about US$0.001/gram (9).

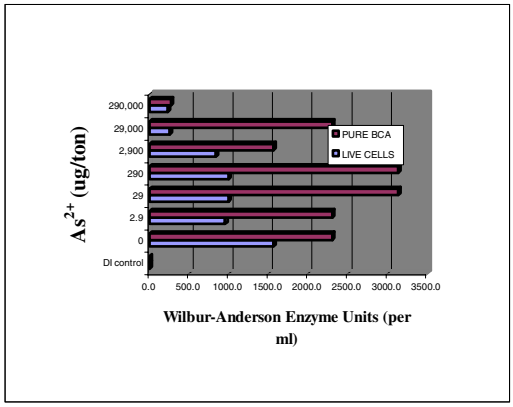

Figure 2. Activity of live E. coli cells versus purified BCA in the presence of arsenic ions.

Acknowledgement. Support for this research from EPRI (WO9000-26) is gratefully acknowledged.

References

(1) Wilbur, K.M. and Simkiss K., *Comparative Biochemistry* **1968,** *26A,* 229.
(2) Loewenthal, R.E. and Marais, G.v.R. *Carbonate Chemistry of Aquatic Systems: Theory and Application, volume 1,* chapter 3, Ann Arbor Science: Ann Arbor (second printing, 1978).
(3) Langmuir, D., *Aqueous Environmental Geochemistry,* Prentice-Hall: New Jersey, 1997.
(4) Bond, G.M., Stringer, J., Brandvold, D.K., Simsek, F.A., Medina, M-G., and Egeland, G. *Energy & Fuels,* **2001,** *15,* 309.
(5) Pruess, K., TOUGH2: A general-purpose numerical simulator for multiphase fluid and heat flow, *Rep. LBL - 29400*, Lawrence Berkeley Lab., September 1991.
(6) Lichtner, P. C., FLOTRAN User's Manual, Los Alamos Laboratory Report, **2000**.
(7) Johnson, J., *Chemical & Engineering News* **2001,** 79(1), 18.
(8) www.atsdr.cdc.gov/tfacts13.html
(9) Belfort, G. *Biotechnology and Bioengineering,* **1989,** *33,* 1047.

FUNDAMENTAL ELEMENTS OF GEOLOGIC CO_2 SEQUESTRATION IN SALINE AQUIFERS

James W. Johnson, John J. Nitao, and Carl I. Steefel

Geosciences and Environmental Technologies Division
Lawrence Livermore National Laboratory
Livermore, CA 94550

Introduction

Geologic sequestration represents a promising strategy for isolating CO_2 waste streams from the atmosphere. Successful implementation of this approach hinges on our ability to predict the relative effectiveness of subsurface CO_2 migration and sequestration as a function of key target-formation and cap-rock properties, which will enable us to identify optimal sites and evaluate their long-term isolation performance. Quantifying this functional relationship requires a modeling capability that explicitly couples multiphase flow and kinetically controlled geochemical processes.

We have developed a unique computational package that meets these criteria, and used it to model CO_2 injection at Statoil's North-Sea Sleipner facility, the world's first saline-aquifer storage site. The package integrates a state-of-the-art reactive transport simulator (NUFT[1]) with supporting geochemical software and databases (SUPCRT92[2]). In our Sleipner study[3], we have quantified—for the first time—the influence of intra-aquifer shales and aquifer/cap-rock composition on migration/sequestration balance, sequestration partitioning among hydrodynamic, solubility, and mineral trapping mechanisms, and the isolation performance of shale cap rocks.

Here, we review the fundamental elements of geologic CO_2 sequestration in saline aquifers as revealed from model XSH of our Sleipner study[3]; this model, unlike CSH[3] and DSH[3], does not address the complicating (yet advantageous) presence of intra-aquifer shales.

Reactive Transport Modeling of CO_2 Injection at Sleipner

In the Sleipner field, CO_2-rich natural gas is produced from 3500 m below the seabed. Excess CO_2 is removed from the production stream by amine absorption on the platform, then stripped from the amine and injected—at the rate of one million tons per year since 1996—into a saline aquifer (the Utsira) 2500 m above the hydrocarbon reservoir.[4] The 200-m-thick Utsira is a highly permeable, fluid-saturated sandstone, which is capped by the Nordland Shale. Hydrologic and compositional properties of the Utsira are relatively well constrained, while those of the Nordland Shale are virtually unknown, and must therefore be estimated.[3]

Our reactive transport simulations of CO_2 injection at Sleipner focus on the near-field sequestration environment. The adopted spatial domain extends 600 m horizontally and 250 m vertically; it contains a 200-m-thick saline aquifer (35% porosity, 3-darcy permeability), 25-m-thick shale cap rock (5% porosity, 3-microdarcy permeability), and an overlying 25-m-thick saline aquifer.[3] Pure CO_2 is injected at the rate of 10,000 tons/yr into the basal center of this domain (37°C, 111 bars), which corresponds to a 1-m-thick cross-section though the actual 100-m screen length at Sleipner.[3,4]

Compositionally, the saline aquifers are represented as impure quartz sand (80% quartz, 10% K-feldspar, 5% plag-ab_{80}, 3% muscovite, 2% phlogopite), while the shale cap rock is represented as 60% clay minerals (50% muscovite, 10% Mg-chlorite), 35% quartz, and 5% K-feldspar.[3] Mg end-member components (phlogopite, Mg-chlorite) are used to represent Fe/Mg solid solutions because *in situ* oxidation states are unknown.[3] The saline aquifers and shale are all saturated with an aqueous phase of near-seawater composition.[3,4]

The simulations are carried out for 20 years, with equal-duration prograde (active-injection) and retrograde (post-injection) phases.

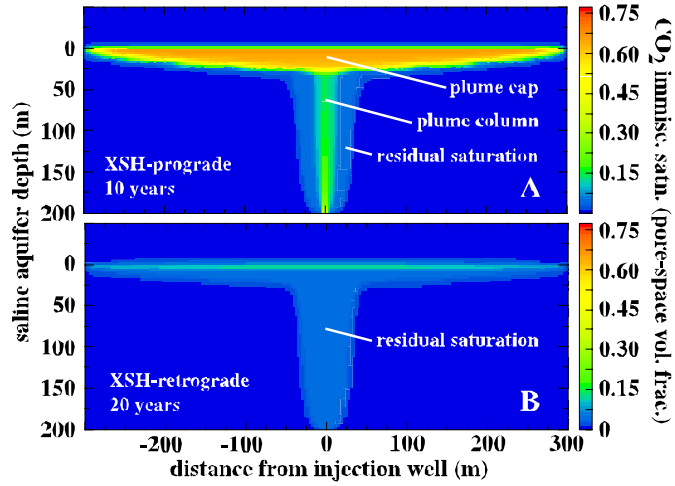

Figure 1. Steady-state configuration of the immiscible CO_2 plume during (A) the prograde phase after 10 years of continuous injection, and (B) the retrograde phase 10 years after injection has ceased.

Modeling Results and Discussion

CO_2 migration/sequestration balance is most conveniently evaluated in terms of contributions from three interdependent yet conceptually distinct processes: CO_2 migration as an immiscible fluid phase, direct interaction of the immiscible plume with formation waters, and indirect plume interaction with formation minerals through the aqueous wetting phase. The first process is directly linked to hydrodynamic trapping, the second to solubility trapping and pH evolution, and the third to mineral trapping.

CO_2 immiscible migration and hydrodynamic trapping. Steady-state configuration of the immiscible CO_2 plume during the prograde phase is realized within one year. In the narrow, sharply delineated plume cap zone, CO_2 immiscible saturation increases from 0.55 at this time to 0.65 at 10 years (Figure 1A). The plume column represents the main conduit of immiscible CO_2 migration, while the residual saturation zone (where immiscible CO_2 is no longer a contiguous migrating phase) marks the wake of initial plume ascent.

In the near-field environment, roughly 85% of injected CO_2 remains and migrates as an immiscible fluid phase ultimately subject to hydrodynamic trapping beneath the cap rock—a very effective seal in this model (Figure 1). The immiscible plume establishes and defines the spatial framework of prograde solubility and mineral trapping. During the retrograde phase, residual CO_2 immiscible saturation (Figure 1B) effectively maintains the prograde extent of solubility trapping and continually enhances that of mineral trapping.

Solubility trapping and pH evolution. As the immiscible plume interacts and equilibrates with saline formation waters, intra-plume aqueous CO_2 concentration (primarily as CO_2(aq) and HCO3-) rapidly achieves the solubility limit, while pH decreases:

$$CO_2(f) + H_2O \leftrightarrow CO_2(aq) + H_2O \leftrightarrow HCO_3^- + H^+ \ .$$

For the present chemical system and P-T conditions, equilibrium aqueous CO_2 solubility is 1.1-1.2 molal (Figure 2A), accounting for about 15% of injected CO_2. Owing to residual saturation of immiscible CO_2 (Figure 1B), this degree of solubility trapping is virtually constant throughout the prograde and retrograde phases.

The initial pH drop caused by prograde solubility trapping—from 7.1 to 4.5—catalyzes silicate dissolution, which after 20 years has increased pH from 4.5 to 5.3 (Figure 2B). This dissolution hydrolyzes potential carbonate-forming cations (here, primarily Na,

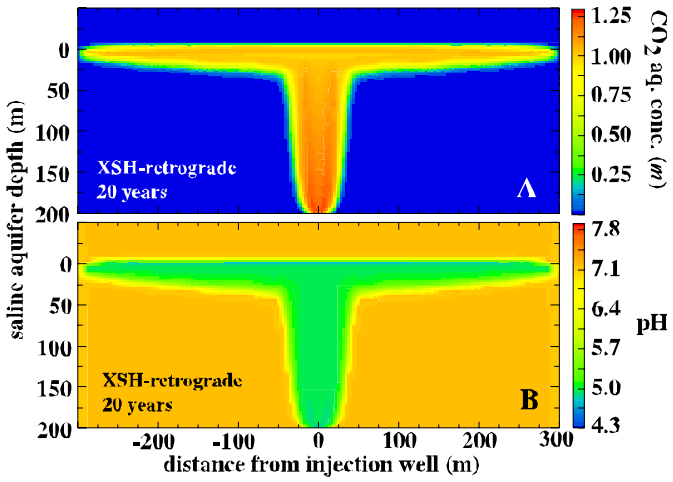

Figure 2. (A) Solubility trapping and (B) pH after 20 years.

Al, and Mg) within the immiscible-plume source region, and thus represents the critical forerunner of all mineral trapping mechanisms.

Mineral trapping. There are four distinct mechanisms whereby CO_2 precipitates as carbonate minerals.

Intra-plume dawsonite cementation (Figure 3A) is catalyzed by high ambient Na^+ concentration, plume-induced CO_2 aqueous solubility, and acid-induced K-feldspar dissolution:

$$\underset{\text{K-feldspar}}{\underline{KAlSi_3O_8}} + Na^+ + CO_2(aq) + H_2O \leftrightarrow \underset{\text{dawsonite}}{\underline{NaAlCO_3(OH)_2}} + \underset{\text{qtz+chal+crist}}{3\ \underline{SiO_2}} + K^+$$

This kinetic reaction proceeds to the right with an increase in solid-phase volume of 17%; hence, it leads to a slight (0.02%) decrease in intra-plume aquifer porosity over 20 years.[3] Pervasive dawsonite cementation will likely be characteristic of saline aquifer storage in any feldspathic sandstone. In fact, there is a natural analog for this process: widespread dawsonite cement in the Bowen-Gunnedah-Sydney basin of Eastern Australia, which has been interpreted to reflect magmatic CO_2 seepage on a continental scale.[5]

Magnesite rind forms along lateral and upper plume boundaries; genetically distinct, these two processes can be described by:

$$\underline{MgCO_3}\ (\text{magnesite}) + 2\ H^+ \leftrightarrow Mg^{+2} + CO_2(aq) + H_2O\ .$$

As intra-plume formation waters, progressively enriched in Mg^{+2} from phlogopite dissolution, migrate outward across lateral plume boundaries, they traverse steep gradients in CO_2(aq) and pH; the net effect strongly promotes magnesite precipitation (Figure 3B). In the plume cap zone, CO_2(aq) concentration and pH are nearly constant, but aqueous Mg^{+2} concentration increases most rapidly here because formation-water saturation is minimized; this leads to magnesite cementation from the cap-rock interface downward (Figure 3B).

However, magnesite precipitation is most extensive from this interface *upwards* (cf. Figures 3B-C), owing to the relatively high concentration of Mg in clay-rich shales. The coupled reaction is:

$$\underset{\text{K-feldspar}}{\underline{KAlSi_3O_8}} + 2.5\ \underset{\text{Mg-chlorite}}{\underline{Mg_5Al_2Si_3O_{10}(OH)_8}} + 12.5\ CO_2(aq)$$
$$\leftrightarrow$$
$$\underset{\text{muscovite}}{\underline{KAl_3Si_3O_{10}(OH)_2}} + 1.5\ \underset{\text{kaolinite}}{\underline{Al_2Si_2O_5(OH)_4}} + 12.5\ \underset{\text{magnesite}}{\underline{MgCO_3}} + \underset{\text{qtz+chal}}{4.5\ \underline{SiO_2}} + 6\ H_2O.$$

This kinetic reaction proceeds to the right with an increase in solid-phase volume of 18.5% (magnesite accounting for 47 vol.% of the product assemblage), which after 20 years has reduced porosity and permeability of the 5-m-thick cap-rock base by 8% and 22%.[3]

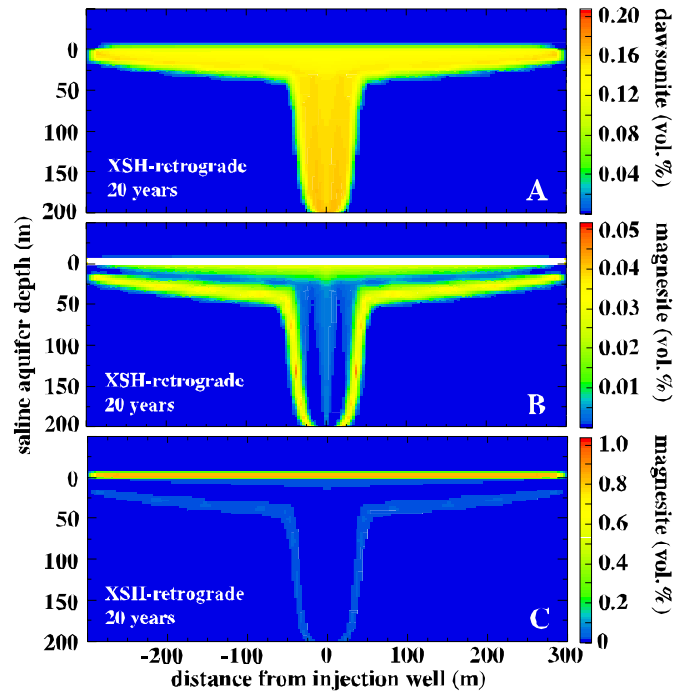

Figure 3. Mineral trapping mechanisms: (A) intra-plume dawsonite cementation, (B) magnesite precipitation—lateral and upper plume boundaries, and (C) magnesite precipitation—shale cap rock.

Conclusions

Geologic CO_2 sequestration in saline aquifers can be subdivided into three fundamental elements: prograde migration of the immiscible plume, direct interaction of the plume with formation waters, and its indirect interaction with formation/cap-rock minerals through the aqueous wetting phase. In the near-field environment of Sleipner-like settings, relative effectiveness of the associated trapping mechanisms on a mass basis is hydrodynamic (85%) >> solubility (15%) >> mineral (<1%).[3]

Although seemingly negligible, mineral trapping has enormous strategic significance: it improves cap-rock integrity and thereby improves containment of the voluminous immiscible plume. Moreover, the prograde extent of mineral trapping is continuously enhanced during the retrograde phase—which spans geologic time scales—by the presence of residual CO_2 immiscible saturation in the aquifer and hydrodynamically-trapped CO_2 beneath the cap rock.[3]

Intra-aquifer shales, solid solutions, and other refinements do not modify the set of fundamental elements reviewed above; they do impose key variations on the style and interaction of these elements.[3]

References

(1) Nitao, J.J., 1998, UCRL-MA-130651, LLNL, 55 p.

(2) Johnson, J.W., Oelkers, E.H., and Helgeson, H.C., 1992: *Comp. Geosci.*, 18(7), 899-947.

(3) Johnson, J.W., Nitao, J.J., Steefel, C.I., and Knauss, K.G., *Proceedings, First Natl. Conf. Carbon Sequestration*, 2001, 60 p., www.netl.doe.gov/publications/proceedings/01/carbon_seq/P28.pdf

(4) Final Technical Report "SACS"—Saline Aquifer CO_2 Storage, 34 p., and other documents available at www.ieagreen.org.uk/sacshome.htm

(5) Baker, J.C., Bai, G.P., Hamilton, P.J., Golding, S.D., and Keene, J.B., *J. Sed. Res., Sec. A – Sed. Petrol. Processes*, 1995, 65(3): p. 522-530.

CO_2 SEQUESTRATION USING BRINES

Y. Soong, J. R. Jones, S. W. Hedges, D. K. Harrison, J. P. Knoer, J. P. Baltrus and R. L. Thompson*[1]

*U.S. Department of Energy, National Energy Technology Laboratory, P.O. Box 10940, Pittsburgh, PA 15236
[1]Parsons Project Services, Inc. P.O. Box 618, South Park, PA 15129

Introduction

Among various proposed sequestration options, injection of CO_2 into confined geologic formations-in particular, saline aquifers-is one of the most promising alternatives. In general, CO_2 can be stored by hydrodynamic trapping, which traps the CO_2 into flow systems for geological periods of time. The most important concern of hydrodynamic trapping is the potential for CO_2 leakage through imperfect confinement. In addition, mineral trapping, which involves a series of interactions between the formation mineralogy and CO_2-enriched formation waters, can convert CO_2 to an immobile and harmless carbonate mineral form that can be stored for millions of years.[1-2]

Various carbonates such as calcite, magnesite, dolomite, and siderite can be formed in the brine aquifer by mineral trapping. Conversion of CO_2 to stable carbonate minerals is expected to be slow. A computer simulation of the mineral trapping process (kinetic water-rock reaction model) was conducted under reservoir conditions by the Alberta Research Council, Canada.[2] These authors calculated times for precipitation of the various carbonates are on the order of hundreds of years. The extended long time required for mineral trapping is the major drawback of this process.

Several researchers[3-4] have conducted mineral trapping studies. Sass et al., [3] studied CO_2 and brine reactions over rocks for 7 days at a pressure of 800 psi and 110 °C. They found increased levels of calcium, magnesium, and carbonate in solution, which they interpreted as the dissolution of dolomite. They interpreted decreased brine concentration of calcium and sulfate as evidence for anhydrite precipitation. However, no extensive studies of the interaction between CO_2 and brine have been reported. The objective of this paper is to examine the feasibility of conducting mineral trapping of carbon dioxide with brine solution reactions in an autoclave reactor.

Experimental

Three different brine samples were used in this study. One was from a brine treatment facility located in Creekside, PA, which was a composite sample. A second sample was collected from the Oriskany formation in Indiana county, PA. In addition, brine obtained from Oklahoma was also used.

Brine carbonation experiments were carried out in a ½ liter autoclave (Hastelloy C-276) manufactured by Progressive Equipment Corp. In a representative experiment, 180 ml of brine was charged into the reactor. The reactor was sealed, and purged/evacuated with carbon dioxide three times. Finally, a predetermined amount of CO_2 was charged into the reactor to the desired testing pressure (450 or 650 psi). The brine/CO_2 mixture was agitated at 400 rpm during both heating to the desired temperature (155 °C) and testing to prevent any settling of precipitate. At the completion of each test, the remaining CO_2 was vented, and the slurry was removed from the reactor and filtered to separate solids from the aqueous solution. A digital pH meter was used to determine the pH values of pre- and post-product solutions. The brine was used either as received or its pH was adjusted before the reaction by adding KOH. The starting brines and brine products were prepared for analysis by filtration through a 0.45 µm membrane using a water aspirator. The collected solids were rinsed with deionized water on the membrane and dried in a nitrogen-purged oven at 110 °C. Metal concentrations were determined using inductively coupled plasma - atomic emission spectroscopy (ICP-AES) on a Perkin Elmer Optima 3000 ICP spectrometer.

Results and Discussion

Table 1. Carbonation Results for Brine Obtained from Creekside, PA

	units	Raw	Rxn 1	Rxn 2
Reaction Condition			155 °C, 950 psi CO_2, 400 rpm, 3 hrs	KOH was added to adjust the pH to 9. 155 °C, 690 psi CO_2, 400 rpm, 1 hr
Liquid	pH	3.2	-	3.8
Ba	mg/liter	663	556	534
Ca	mg/liter	16120	19120	15700
Mg	mg/liter	2098	2540	2210
K	mg/liter	177	212	7040
Na	mg/liter	53800	58240	53200
Fe	mg/liter	117	65	15800
Solid	g	none	0.38	0.0293
Ba	µg/g	N/A	117	57
Ca	µg/g	N/A	40000	2400
Mg	µg/g	N/A	13500	19500
K	µg/g	N/A	3790	1090
Na	µg/g	N/A	109000	N/A
Fe	µg/g	N/A	230000	331000

The scoping experiments on brine carbonation were conducted in two different ways. The reaction was conducted either with brine as received and CO_2 (Rxn 1) or after the pH of the brine was adjusted before reaction with CO_2 (Rxn 2). Results of the solids and solution analyses before and after reaction are shown in Tables 1, 2 and 3 for Creekside, PA; Indiana county, PA; and Oklahoma brines, respectively. The initial brine compositions are also shown for comparison with various reacted mixtures. In general, the changes of compositions in solution before and after the reaction were small. However, the amount of solid precipitated and the composition of solids varied with the reaction conditions utilized.

For the case of Creekside brine, the raw brine was very acidic with a pH value of 3.2 (Table 1). The reaction between the brine and CO_2 under the reaction conditions of Rxn 1 resulted in the precipitation of 0.38 gram of solids. Adjusting the pH of brine to 9 (Rxn 2) before reacting with CO_2 resulted in a lesser amount of solid precipitate (0.0293 g). The composition of the solids also varied with the reaction conditions. Under the conditions of Rxn 1, the precipitates were high in Na, Fe and Ca. However, under the reaction conditions of Rxn 2, the precipitation of Ca was significantly reduced by a factor of 10. Furthermore, the concentration of Fe in the precipitate increased from 230,000 to 331,000 µg/g in going from Rxn 1 to Rxn 2.

The results for brines collected from Indiana county, PA and the Oklahoma showed similar trends (Tables 2 and 3). More solids were precipitated when the pH of the brines was modified before reaction. The major elements present in the solids under reaction conditions Rxn 1 were Ca, Na, and Fe. However, after the pH was adjusted prior to reaction Rxn 2, the concentrations of Na and Fe in the precipitated solids were reduced by a factor of 100. Moreover, the concentration of Ca in the precipitated solid increased by a factor of 10.

About 53,300 µg/g of Barium were observed in the precipitated solid under the reaction conditions of Rxn 1 for the brine obtained from Indiana county, PA. The exact form of Ba is still under investigation. However, under the reaction conditions of Rxn 2, the concentration of Ba in the precipitate was significantly reduced from 53,300 to 1390 µg/g.

In general, the net increase in total solid precipitation could be attributed to the precipitation of mineral matter (primarily calcium, but may include carbonates, sodium and other minerals) during the reaction. It is important to note that values of alkalinity and pH in Tables 1, 2, and 3 might not be representative of actual conditions while the experiments were in progress.

Table 2 Carbonation Results for Brine Obtained from Indiana County, PA

	units	Raw	Rxn 1	Rxn 2
Reaction Condition			155 °C, 900 psi CO_2, 400 rpm, 1 hr	KOH added to adjust pH to 11, 155 °C, 670 psi CO_2, 400 rpm, 1 hr
Liquid	pH	3.9	3.6	3.9
Ba	mg/liter	1070	1060	1030
Ca	mg/liter	35000	34900	29500
Mg	mg/liter	2250	2250	2040
K	mg/liter	2600	2620	13800
Na	mg/liter	70400	70200	69100
Fe	mg/liter	234	188	1
Solid	g	0.02	0.048	2.069
Ba	µg/g	1570	53300	1390
Ca	µg/g	34900	49100	341000
Mg	µg/g	2010	3000	2710
K	µg/g	3250	2020	63
Na	µg/g	59900	47200	552
Fe	µg/g	311000	119000	16700

Significant amounts of sodium along with some aluminum (not shown in Tables) were found for all brine tested under the reaction conditions of Rxn 1. However, the concentration of sodium precipitated under the conditions of Rxn 2 was reduced by a factor of 1000 for all brine tested. It was speculated that the sodium precipitated might be related to the formation of dawsonite ($NaAlCO_3(OH)_2$).[5] In general, calcium, precipitated under the reaction conditions of Rxn 1 was probably in the form of calcium carbonate. The same general behavior was observed for brines obtained from Indiana county, PA and Oklahoma. The observation that significantly less calcium precipitated under the reaction conditions of Rxn 1 could be attributed to the pH of the brine solution remaining too low to stabilize a carbonate mineral. In subsequent experiments, a pH buffer (KOH) was added to control the pH. As a result of the pH increase, about 10 fold more calcium precipitated under the conditions of Rxn 2 than that of Rxn 1. However, an opposite behavior in Ca concentration was observed for the brine collected from Creekside, PA. Magnesium, precipitated during the reaction is probably in the form of magnesium carbonate. Its precipitation is not affected by the variation of pH. Siderite ($FeCO_3$) was observed in the precipitated solids. Significant siderite was found under the reaction conditions of Rxn 1 for the Oklahoma brine and brine obtained from Indiana county, PA. As the pH increased, siderite precipitation was drastically reduced. The opposite trend was found for the Creekside, PA brine. The pH of brine has a significant effect on the carbonation reaction. For the mineral trapping processes to occur, the following reactions have to proceed:

CO_2 (gas) -> CO_2 (aq); CO_2 (aq) + H_2O -> H_2CO_3;
H_2CO_3 -> H^+ + HCO_3^-; HCO_3- -> H+ + CO_3^{2-}
Ca^{++} + CO_3^{2-} --> ($CaCO_3$); Ca^{++} + Mg^{++} + CO_3^{2-} --->$CaMg(CO_3)_2$
Fe^{++} + CO_3^{2-} ---> $FeCO_3$; Mg^{++} + CO_3^{2-} --> $MgCO_3$

Table 3. Carbonation Results for Brine Obtained from OK

	units	Raw	Rxn 1	Rxn 2
Reaction Condition			155 °C, 900 psi CO_2, 400 rpm, 1 hr	KOH was added to adjust the pH to 9.2, 155 °C, 670 psi CO_2, 400 rpm, 1 hr
Liquid	pH	5.5	4.5	5
Ba	mg/liter	323	338	321
Ca	mg/liter	10700	11200	9525
Mg	mg/liter	1965	2050	1975
K	mg/liter	525	559	3475
Na	mg/liter	52400	54700	53100
Fe	mg/liter	3	3	1.5
Solid	g	0.0586	0.046	0.4846
Ba	µg/g	1410	1215	1630
Ca	µg/g	23300	33900	326000
Mg	µg/g	4150	6720	4690
K	µg/g	1165	1750	45
Na	µg/g	51000	150000	1440
Fe	µg/g	56200	677000	6130

The pH along with other factors have an impact on these reactions. At low pH, H_2CO_3 (carbonic acid) dominates; at mid pH, HCO_3- (bicarbonate) dominates; and at high pH. CO_3^{2-} (carbonate) dominates. Temperature and pressure also play an important role in determining the solubility of CO_2 in solution. Aqueous-phase equilibration with CO_2 (g) promotes carbonate precipitation, while acidic conditions favor carbonate dissolution. Therefore, increased pH favors carbonate precipitation. The actual effectiveness of brine carbonation probably depends on the initial concentration of carbonate forming cations within the brine and the pH of the brine.

Conclusions

A study of mineral trapping (under temperature and pressure) in an autoclave reactor with the brine solution has been initiated by NETL. Three different brines were tested in a 1/2-liter autoclave under various conditions. Preliminary results indicated that the mineral species and amounts of solid precipitated depend on the source and the pH of the brine.

References

1. DOE report, DOE/SC/FE-1, Carbon Sequestration Research and Development, December 1999.
2. Hitchon, B., Gunter, W. D., Gentzis, T and Bailey, R. T., *Ener. Conv. & Man.* 40 (1999) 825-843.
3. Sass, B. N., Gupta, J., Ickes, J., Eagelhard, M., Bergman, P., and Byaer, C., " Interaction of Rock Minerals with CO_2 and Brine: a hydrothermal Investigation", Conference CD, 1st National Conference on Carbon Sequestration, Washington, D.C., May 15-17,2001.
4. Lebro'n, I and Suarez, D. L., Geochim. Cosmochim. Acta 62 (1998) 405-416.
5. Johnson, J. W., Nitao, J. J., Steefel, C. I., and Knauss, K. G.., "Reactive transport modeling of geologic CO_2 sequestration in saline aquifers ":Conference CD, 1st National Carbon Sequestration meeting, May 12-15, 2001, Washington, DC.

NETWORK MODELING OF BRINEFIELD CO_2 SEQUESTRATION: DISPLACEMENT EFFICIENCIES AND FUNDAMENTAL LIMITATIONS ON CO_2 STORAGE VOLUMES

M. Ferer, Grant S. Bromhal, Duane H. Smith

National Energy Technology Laboratory, 3610 Collins Ferry Rd., Morgantown, WV 26505-0880, duane.smith@netl.doe.gov, W: 304-285-4069, F: 304-285-4403

The sequestration of liquid carbon dioxide in deep brine-saturated formations has been cited as an important potential component in an overall carbon dioxide sequestration strategy. Brinefield sequestration of CO_2 is a commercially-proven technology; however, the effective saturation of carbon dioxide in brine-saturated formations is very low, on the order of a percent of available void space. It is known that fluid viscosity, fluid density, and interfacial tension are significant factors in determining the efficiency of displacement in two-phase fluid flow.

We have developed a pore-level numerical model of the immiscible injection of one fluid (CO_2) into a porous medium saturated with another fluid (brine). The model incorporates a distribution of throat radii, fluid viscosities, and fluid densities to mechanistically represent the flow. This model has previously been used to study the relationship between saturation and important dimensionless numbers, such as the Bond number (ratio of gravitational to capillary forces) and the capillary number (ratio of viscous to capillary forces). The model is now being used to calculate the displacement efficiency for a variety of capillary and Bond numbers.

I. Introduction

Flow in porous media is a subject of scientific and engineering interest for a number of reasons. Flow in porous media has long been modeled as a compact (i.e., Euclidean) process whereby the interface advances linearly with the total amount of the fluid as predicted by a Darcy's law treatment using saturation-dependent relative permeability.[1]-[5] In the last fifteen years, it has been appreciated that flow in porous media is fractal in certain well-defined limits.[6]-[9] The flow is known to be described by self-similar diffusion-limited-aggregation (DLA) fractals in the limit of zero viscosity ratio, $M = \mu_I / \mu_D = 0$. [6]-[8],[10]-[12] The flow is known to be described by self-similar invasion percolation (IP) fractals in the limit of zero capillary number (see Eq. 6a), where viscous drag forces (viscosity of the displaced fluid times average fluid velocity) are zero, while the capillary forces (proportional to interfacial tension, times cosine of the contact angle) are finite.

Recently, we have shown that our model produces results which agree with both DLA (large viscosity ratio limit) and with IP with trapping (IPwt) (small capillary number limit).[13] Having demonstrated the validity of our model in these two very different limits, with the physicality of the model and the excellent consistency with fluid conservation, we are confident in extending our study to the physically relevant intermediate regime, where the limiting models (DLA and IPwt) are not valid.

II. Description of the Model

The pore-level model is intended to realistically incorporate both the capillary pressure that tends to block the invasion of narrow throats and the viscous pressure drop in a flowing fluid. The two-dimensional model porous medium is a diamond lattice, which consists of pore bodies of volume ℓ^3 at the lattice sites and throats connecting the pore bodies, which are of length ℓ and have a randomly chosen cylindrical cross-sectional area between 0 and ℓ^2. Compared to several models reported in the recent literature, we believe that our model should be both more general and more flexible, in part because both the throats and the pore bodies have finite volume in comparison first with refs. [6] and [14], where the throats contain zero volume of fluid, and secondly with refs. [15]-[17], where the pore bodies have zero volume. Furthermore, in our model, the volumes of both the pore bodies and throats can be set as desired. In this sense the work of Periera is closer to our model but focuses on three-phase flows at constant pressure.[18] Of course all of these models include the essential features of random capillary pressures blocking the narrowest throats and a random conductivity depending on a given viscosity ratio.

Capillary pressure determines the pressure drop needed to move a meniscus through a throat. The radius of curvature, R, of the meniscus is fixed by contact angle, 2, and the radius of the pore throat, r, so that the pressure drop across the meniscus is fixed at the capillary pressure,

$$P_{cap} = \frac{2\sigma \cos\theta}{r}, \qquad (1)$$

where F is the interfacial tension. Following refs. [15]-[17], we modify Eq. (1) to remedy problems arising from blockages at throat entries, giving

$$P_{cap} = \frac{2\sigma \cos\theta}{r} \sin(\pi x), \qquad (2)$$

where $x\ell$ is the distance along the throat from 0 to ℓ. This sine dependence solves problems encountered in adjusting throat blockages and in maintaining a constant velocity condition and can be assumed to result from variations in contact angle.

The pressure difference due to buoyancy across a throat and its connecting pores also is calculated for each throat. The invading fluid is assumed to be a ball in the center of the spherical pore, while the defending (wetting) fluid surrounds it and stays next to the pore wall, so the pressure gradient along the pore is

$$P_G = \rho_{nw} g \left(\frac{3a}{4\pi}\right)^{1/3} \sin\psi + \rho_w g \left[\left(\frac{3}{4\pi}\right)^{1/3} - \left(\frac{3a}{4\pi}\right)^{1/3}\right] \sin\psi, \qquad (3)$$

where D_{nw} and D_w are the non-wetting and wetting fluid densities, respectively, g is the acceleration due to gravity, R is the angle that the throat makes with respect to the horizontal, and a is the volume fraction of invading fluid in the pore. Thus (see Fig. 1) the flow velocity is given by the throat conductance times the total pressure drop across the throat:

$$q = g_{throat}\left(P_{nw} - P_w - P_{cap} + P_G\right), \qquad (4a)$$

where g_{throat} is the conductance of a throat from Poiseuille's law, and P_{nw} and P_w are the pressures of the non-wetting and wetting fluids in their respective pores. In the model, the transmissibility (conductance) of the throat is given by

$$g_{throat} = g * \frac{\left(A_{throat}^2 / \ell^4\right)}{\ell\left[x + (1-x)M\right]}, \qquad (4b)$$

where A_{throat} is the throat cross-sectional area, x is the fraction of the throat of length ℓ which is filled with defending fluid, and M is the ratio of the non-wetting, invading fluid's viscosity to that of the wetting, defending fluid, $M = \mu_{nw}/\mu_w$.

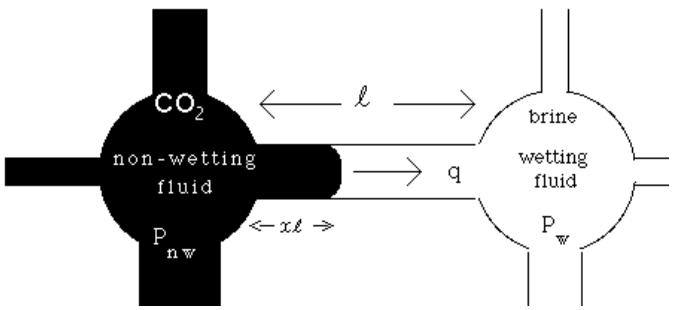

Figure 1 shows the CO_2 displacing the brine with volume flow velocity $q_{throat} = g_{throat}\,(P_{nw} - P_w - P_{cap})$. Of course, if $P_{nw} - P_w < P_{cap}$, the CO_2 retreats and the brine re-occupies the throat.

The quantity, g^*, carries all the dimensionality of g_{throat}, $g^* = \ell^3/(8B\,\mu w)$. From Eq. (4a), the non-wetting fluid advances if the pressure difference between the pore filled with CO_2 (non-wetting fluid) and the pore filled with brine exceeds the capillary pressure. Otherwise the CO_2 will retreat.

The pressures in the pore bodies cane be determined from the volume conservation of the incompressible fluid, dictates that the net volume flow q out of any pore body must be zero. Let us consider use of the above rules for the situation in Fig 2. In Fig. 2, the flow velocities, as directed out of the (i,j) pore body through the throats are

$$\begin{aligned} q_{i-2,j-1} &= g_{i-2,j-1}\left(P_{i,j} - P_{i-2,j-2}\right) \\ q_{i,j+1} &= g_{i,j+1}\left(P_{i,j} - P_{i+2,j+2} - P_{cap,i,j+1}\right) \\ q_{i-1,j} &= g_{i-1,j}\left(P_{i,j} - P_{i-2,j} - P_{cap,i-1,j}\right) \\ q_{i+1,j} &= g_{i+1,j}\left(P_{i,j} - P_{i+2,j} - P_{cap,i+1,j}\right). \end{aligned} \qquad (5)$$

Once the location of the interface is known, the numerical value of the capillary pressure in each throat is determined. Then the program iterates (Eq. 5), determining the pressure field until pressure balance is achieved. In one of the typical sets of five runs presented in this paper, after an average of 77,000 time steps there was an average difference of less than 1% between the total volume of fluid injected into the medium and the total volume of fluid expelled from the medium.

To maintain a constant volume flow q_o, the flow velocity was determined for two estimates of the inlet pressure. The linear relationship between flow velocity and inlet pressure (Eq. 4) predicts an inlet pressure, P_o, producing the desired volume flow, q_o.[17] With a good choice of initial estimates, this procedure is very accurate, with error less than of 0.007%.

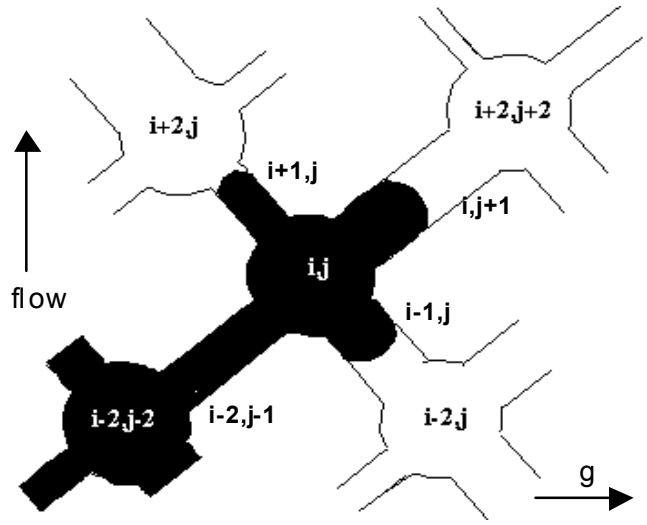

Figure 2 shows a possible occupation of adjacent pore-bodies. For this occupation, the flow velocities are given by Eq. (4) and the pressure in the (i,j) pore body can be calculated from Eq. (5).

Once the pressure field has been determined, the flow rules determine the interface advance through a time interval Δt. A throat is on the interface, if the pore body at one end contains some wetting fluid (it may be filled with wetting fluid) and if the pore body at the other end is fully invaded by non-wetting fluid (or was fully invaded and is not yet fully re-invaded by wetting fluid due to backflow). As discussed earlier, a time interval, Δt, needs to be chosen which is small enough that spurious local oscillations in the flow are avoided but not so small that the program run-time is unnecessarily long. For the cases discussed here, with large surface tension, the following prescription seems adequate. For all interfacial throats where the non-wetting fluid has yet to reach the midpoint of that throat, so that the capillary pressure is still increasing, the time interval is chosen so that the non-wetting fluid advances no more than 3.5% into any such throat. For all throats where the non-wetting fluid has advanced past the midpoint, so that the capillary pressure is decreasing, the time step allows the interface to advance no further than 33% into any such throat.

Flow increases the amount of CO_2 within the pore throat (Fig. 3a) or through the pore throat into the pore body (Fig. 3b). Similarly, backflow causes the interface to retreat within the pore throat or through the pore throat into the pore body. If either type of fluid over-fills a pore body, the outflow throats share the excess.

We have attempted to make the flow-rules as non-restrictive and physical as possible: i) all parts of the porous medium have a volume which can be occupied by either type of fluid; ii) locally, back-flow and forward flow are allowed if ordained by the local pressure drops; iii) complications, such as over-filled pore bodies, are treated as physically as possible; iv) unphysical aspects, such as isolated 'blobs' of wetting fluids residing in pore-bodies, are tracked and have been found to be insignificant; and v) most importantly, the flow rules accurately account for all of the non-wetting fluid injected into the porous medium.

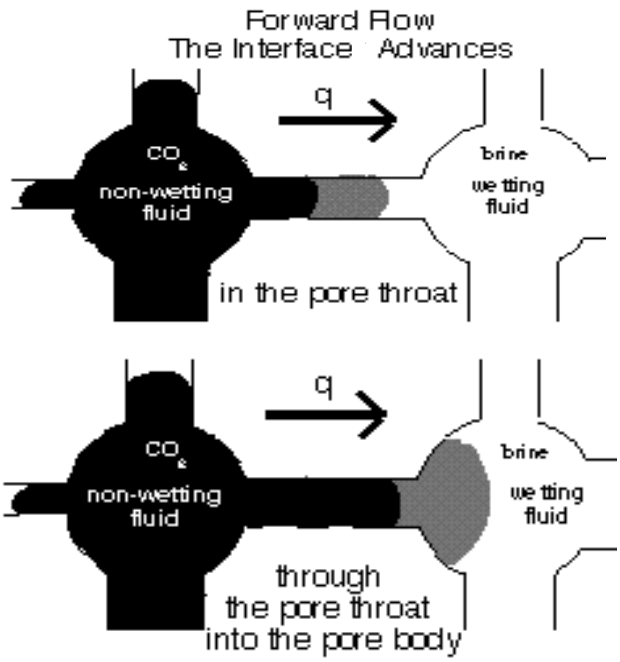

Figure 3. The CO_2 can advance in a throat (upper fig., 3a) or through a throat into the pore body (lower fig., 3b).

III. Simulations and Results

The model was run for 16 simulations of sizes 60x30 pore networks for a range of capillary and Bond numbers:

$$Ca = \frac{v\mu_w}{\sigma\cos\theta}, \qquad (6a)$$

$$B = \frac{\Delta\rho g d L}{\sigma}, \qquad (6b)$$

where v is the average velocity of the total fluid system, σ is the interfacial tension between the two fluids, $)D=D_{nw}-D_w$, L is number of pores in the direction of flow, and d is the average throat diameter. The capillary number, Ca, is a ratio of viscous to capillary forces, and the Bond number, B, is the ratio of buoyancy to capillary forces. These dimensionless numbers have been shown to be related to residual saturation.[20],[21] All simulations use a viscosity ratio, M, of 0.05 to correspond to carbon dioxide infiltrating brine.

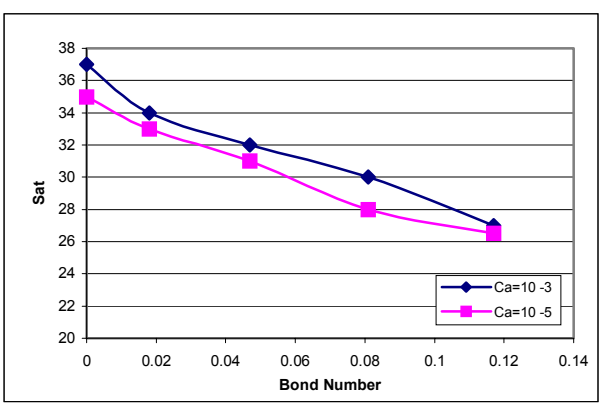

Figure 4. Plot of breakthrough saturation vs. Bond number on a 60x30 network at M=0.05.

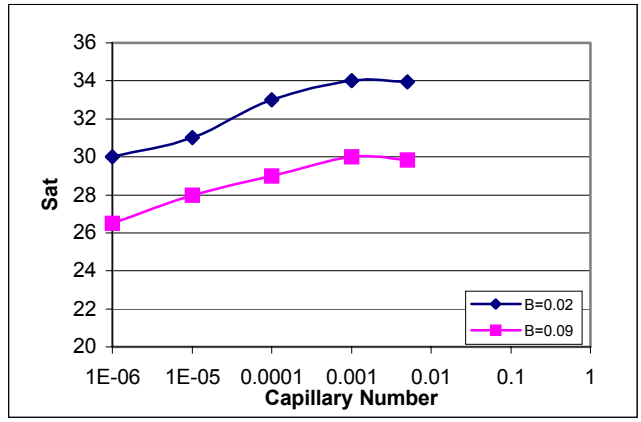

Figure 5. Breakthrough saturation vs. capillary number on a 60x30 network at M=0.05.

The results from these simulations are presented in Figures 4 and 5. These initial results show relationships between saturation and Bond number and capillary number similar to what others have found.[20],[21] They show that saturation decreases with decreasing capillary number, though this dependence is not as strong as seen in water flooding experiments, most likely because of the low viscosity ratio between CO_2 and brine. Saturation also decreases with increasing Bond number, and at a more rapid rate than with capillary number.

IV. Discussion

The results presented here are preliminary, both in the size of the networks and in the number of simulations. However, they do support what is already known about the relationships between the capillary and Bond numbers and the saturation of the invading fluid. The results also suggest that there is a fundamental limitation on the storage capacity of a homogeneous aquifer (perhaps different for heterogeneous aquifers [22]) for CO_2, and it is less than 50% of the available void space.

Acknowledgement. This work was performed while Grant Bromhal held a National Research Council Research Associateship.

References

1. Blackwell, R. J., J. R. Rayne and W. M. Terry, Trans. AIME, **216**, 1-8, (1959).
2. Collins, R. E., "Flow of Fluids through Porous Materials," 1961 Reinhold Publishing Corporation, New York.
3. Bear, J., "Hydraulics of Ground Water," 1979 McGraw-Hill Publ. Co., New York.
4. Dullien, F.A.L. "Porous Media: Fluid Transport and Pore Structure," 2nd ed., Academic Press, New York, (1992).
5. Rhee, H.-K., R. Aris and N. R. Amundson, "1st-Order Partial Differential Equations: Vol. I (Theory and Applications of Single Equations," 1986 Prentice Hall, Englewood Cliffs, New Jersey.
6. Lenormand, R., E. Touboul and C. Zarcone, J. Fluid Mech., **189**, 165-187, (1988).
7. Feder, J., "Fractals," 1988 Plenum Press, New York.
8. Vicsek, T., "Fractal Growth Phenomena," 1989 World Scientific, Singapore.
9. Meakin, P., "Fractals, scaling, and growth far from equilibrium," 1998 Cambridge University Press, Cambridge.

10. Chen, J.-D. and D. Wilkinson, Phys. Rev. Lett., **55**, 1892-1895, (1985).
11. Nittmann, J., G. Daccord and H. E. Stanley, Nature, **314**, 141-144, (1985).
12. Daccord, G., J. Nittmann and H. E. Stanley, Phys. Rev. Lett., **56**, 336, (1986).
13. Ferer, M., G. S. Bromhal and D. H. Smith, Groundwater, to be sumbitted, (2001).
14. van der Marck, S. C., T. Matsuura and J. Glas, Phys. Rev. E, **56**, 5675-5687, (1997).
15. Aker, E. et al, Transport in Porous Media, **32**, 163-186, (1998).
16. Aker, E., K. Jorgen-Maloy and A. Hansen, Phys. Rev. E, **58**, 2217-2226, (1998).
17. Aker, E., K. Jorgen-Maloy and A. Hansen, Phys. Rev. E, **61**, 2936-2946, (2000).
18. Pereira, G., Phys. Rev. E, **59**, 4229-4242, (1999).
19. Akers, E., A Simulation for Two-Phase Flow in Porous Media, Thesis, Univ. of Oslo, (1996).
20. Morrow, N.R. and B.Songkren, "Surface Phenomenon in EOR," ed. D.O. Shah, 1981 Plenum Press, New York.
21. Pennell, K.D., G.A. Pope, and L.M. Abriola. ES&T, **30**, 4, 1328-1335, (1996).
21. Benson, Sally Proceedings of the First National Conference on Carbon Sequestration, May 14-17, (2001).

CO_2 ABSORPTION PERFORMANCE OF AQUEOUS ALKANOLAMINES IN PACKED COLUMNS

Amornvadee Veawab, Adisorn Aroonwilas, and Paitoon Tontiwachwuthikul

Faculty of Engineering, University of Regina
Regina, Saskatchewan, Canada S4S 0A2

Introduction

It is now scientifically evident that human activities have caused concentrations of greenhouse gases to rise significantly over the last two hundred years.[1] This causes a change in the atmosphere composition and the problem of global warming. The desire to alleviate the global warming problem has resulted in a serious environmental concern and a need to either reduce greenhouse gas emissions from industrial sources or put them into long term storage. Carbon dioxide (CO_2) is the largest contributor to the global warming problem, and is thus the major target for the reduction. Among the capture techniques, the flue gas scrubbing using absorption solvents is the most mature and readily applied technology for the reduction of CO_2 emissions from the stationary power plants.[2]

Aqueous solutions of alkanolamines are the chemical solvents that have been used extensively for the CO_2 capture.[3] Common alkanolamines are monoethanolamine (MEA), diglycolamine (DGA), diethanolamine (DEA), diisopropanolamine (DIPA) and methyldiethanolamine (MDEA). At present, formulated solutions containing a variety of alkanolamines are gaining popularity in the gas separation industry. These solutions often provide a greater absorption performance or meet unique needs when compared to the aqueous solutions of single alkanolamines.[4] The most common formulations consist of blends of MDEA and other alkanolamines to form MDEA-based solvents. The MDEA-based solvents can provide excellent absorption capacity, great energy efficiency and low corrosivity in comparison with the single alkanolamines.[5]

Research objective

The choice of the absorption solvents can be determined by a number of factors, such as absorption efficiency, energy consumption, corrosion, and solvent degradation. The absorption efficiency is an important factor since it measures the mass-transfer rate of acid gas into the absorption solvent that is required to achieve a removal target. In most cases, the efficiency is theoretically evaluated by using classical laboratory reactors, such as stirred cell and laminar jet absorber where the interfacial area for the mass-transfer is known and fixed. These reactors do not take into account the hydrodynamic features of the contacting devices, which may vary with type of absorption solvents during the plant operation. Therefore, it is necessary to use a column (packed or tray) as a gas-liquid contacting device for evaluating the absorption efficiency of any solvent of interest. This work evaluated and compared the CO_2 absorption efficiency of the aqueous solutions of single and blended alkanolamines in a packed column fitted with structured packing. Effects of two important operating conditions, including CO_2 loading of solution and liquid load (flow rate per cross sectional area), on the absorption efficiency were also examined. The test alkanolamines were MEA, DEA, DIPA, MDEA, and MEA-MDEA.

Experiments

The experiments were carried out in a bench-scale absorption unit of which the main component was the acrylic absorption column with an internal diameter of 20-mm and height of 2.0-m. The column was packed with stainless steel structured packing (Sulzer DX). A series of gas sampling points were installed for measuring the gas-phase CO_2 concentrations along the column. An IR gas analyzer (model 301D, Nova Analytical System Inc.) was used for measuring the CO_2 concentration with an accuracy of ±0.4%. The liquid samples taken from the bottom of the column were analyzed for their compositions using titration methods. The experimental results were presented as gas-phase CO_2 concentration profiles along the height of the absorption column. The CO_2 absorption or removal efficiency (η) was determined using the following equation:

$$\eta = \left[1 - \left(\frac{y_{out}}{1-y_{out}}\right) \times \left(\frac{1-y_{in}}{y_{in}}\right)\right] \times 100 \qquad (1)$$

where y_{in} and y_{out} denote mole fractions of CO_2 in gas-phase at the bottom and the top of the absorption column, respectively.

Results and discussion

CO_2 absorption performance of single alkanolamines. MEA and DEA were found to have a superior CO_2 absorption performance over DIPA and MDEA. As shown in Figure 1, 10% CO_2 in the feed gas was completely absorbed by the fresh (nil CO_2 loading) aqueous solutions of MEA and DEA within 2.0-m column height, while certain amounts of CO_2 in the treated gas (at the column top) were detected in cases of DIPA and MDEA.

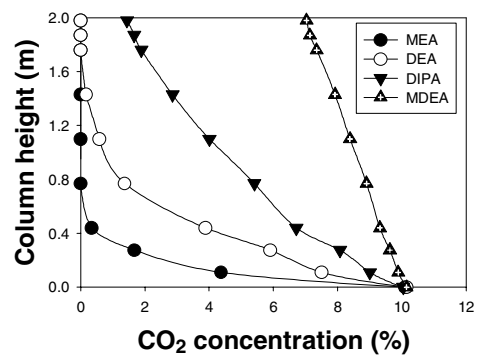

Figure 1. Gas-phase CO_2 concentration profile along the column for single alkanolamine solutions (3 kmol/m^3 solution concentration; 0.00 mol/mol CO_2 loading; 10.0 m^3/m^2-h liquid load).

Although both MEA and DEA were able to provide a complete removal of CO_2, their absorption performance can be distinguished by considering the column height required for the absorption. The CO_2 absorption into the MEA solution took place within only 0.8-m from the column bottom while the DEA required as high as 1.8-m to complete the same task. This illustrated the superior performance of MEA over the DEA solution. Consequently, the absorption performance of the test solutions was in the following order: MEA > DEA > DIPA > MDEA.

The absorption experiments were further conducted under different CO_2 loadings of the solution and different liquid loads in order to broaden the performance comparison. The CO_2 loading and the liquid load were found to have no impact on the order of the absorption efficiency (Figures 2 and 3). The order remained as it was under the fresh solution condition, i.e. MEA > DEA > DIPA > MDEA. However, the performance of the CO_2 absorption had an inverse relationship with the CO_2 loading of the feed solution, i.e. it decreases with the increasing CO_2 loading of the solution. The deterioration of the absorption efficiency was caused by a reduction of the available reactive alkanolamine concentration that provided a driving force during the mass transfer. The result also shows that increasing the liquid load caused a reduction in the CO_2 concentration

of gas phase, indicating a greater absorption efficiency. This was a result of two basic phenomena that take place in parallel. First, an increase in the liquid load led to a greater degree of the wetted packing surface (hydrodynamics) participating in the mass transfer process. Second, the liquid solution at a higher flow rate experienced a smaller change in its concentration, thus retaining the bulk of its absorption capacity throughout the column and maintaining the mass transfer driving force.

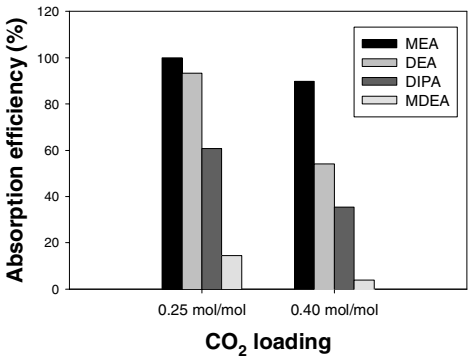

Figure 2. CO_2 absorption efficiency of single alkanolamine solutions (3 kmol/m^3 solution concentration; 10.0 m^3/m^2-h liquid load).

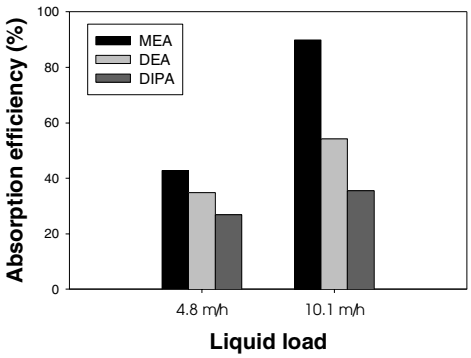

Figure 3. CO_2 absorption efficiency for single alkanolamine solutions (3 kmol/m^3; 0.00 CO_2 loading).

CO_2 absorption performance of blended alkanolamines. The CO_2 concentration profiles of the MEA-MDEA lie between those of the pure components (Figure 4), indicating a hybrid absorption behavior. The absorption also appeared to be influenced by the variations in CO_2 loading. As the CO_2 loading increased, the CO_2 concentration profile of the MEA-MDEA shifted upwards, resulting in a lower CO_2 absorption efficiency. It was noticed that the CO_2 concentration profile or absorption efficiency of the MEA-MDEA was close to that of the MEA in case of no or very small CO_2 loading. However, once the CO_2 loading was increased, the profile (efficiency) of MEA-MDEA moved towards in a direction of the MDEA profile. This behavior manifests a kinetic competition of the two components (MEA and MDEA) in the blended solution. It is likely that, under low CO_2 loading conditions, the MEA plays a dominant role in the CO_2 absorption since its reaction rate with CO_2 is much faster than the MDEA's. However, once the CO_2 loading increases to a certain value, the MEA will loose its competitive characteristic in absorbing the CO_2 due to the depleting active MEA. As a result, the MDEA will gain its role in absorption at high CO_2 loading. This behavior suggests that, the transfer of CO_2 from gas phase at the top portion of the column takes place primarily due to the pure solution with a faster reaction rate with CO_2 (MEA) while that at the bottom portion of the column takes place primarily due to the solution with a lower reaction (MDEA).

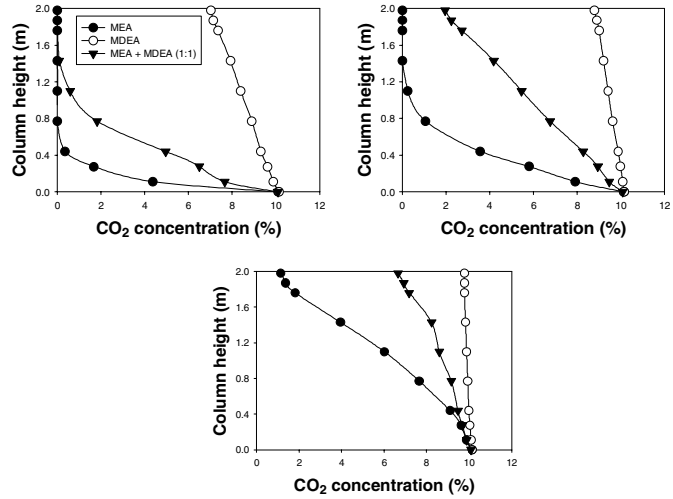

Figure 4. Gas-phase CO_2 concentration profile along the column for 3 kmol/m^3 MEA-MDEA (1:1) solution (0.00-top-left, 0.25-top-right and 0.40-bottom mol/mol CO_2 loading; 10.0 m^3/m^2-h liquid load).

Conclusions

The absorption efficiency of various alkanolamines was evaluated in a packed column where the hydrodynamic feature was taken into account. The absorption efficiency increased in the order of MEA > DEA > DIPA > MDEA. The absorption efficiency of MEA-MDEA solution was a combination of those of the pure components. A kinetic competition behavior was exhibited. At low CO_2 loading, the component with a faster CO_2 absorption rate was primarily attributable to the CO_2 removal whereas the component with a slower rate played a dominant role at high CO_2 loading.

Acknowledgment

Authors gratefully acknowledge the financial support received from the Natural Science and Engineering Research Council of Canada (NSERC) and the structured packing supplied by the Sulzer Chemtech, Switzerland.

References

1. Wilkinson, C. Negotiating the Climate: Canada and the International Politics of Global Warming- A Report on Key Issues at the Sixth Conference of the Parties (COP6) to the United Nations Framewaork Convention on Climate Change (UNFCCC), commissioned by The David Suzuki Foundation, BC, Canada, November 2000.
2. Wolsky, A. M.; Daniels, E. J.; Jody, B. J. *Environmental Progress* 1994, *13(3)*, 214-219.
3. Maddox, R. N. *Gas Conditioning and Processing, Vol.4: Gas and Liquid Sweetening*, 3rd ed.; Campbell Petroleum Series: Oklahoma, 1984.
4. White, L.; Street, D. E. Corrosion Control in Amine Treating Units. *Proceedings of Corrosion in the Oil Refining Industry Conference*, Phoenix, Sep. 17-18, 1998.
5. Ball, T.; Veldman, R. Improve Gas Treating. *Chemical Engineering Progress* 1991, *87(1)*, 67-72.

RIGOROUS DESIGN MODEL FOR CO_2 ABSORBER FITTED WITH STRUCTURED PACKING

Adisorn Aroonwilas[1] , Amornvadee Veawab[1], Amit Chakma[2], and Paitoon Tontiwachwuthikul[1]

[1]Faculty of Engineering, University of Regina
Regina, Saskatchewan, Canada S4S 0A2

[2]Department of Chemical Engineering, University of Waterloo
Waterloo, Ontario, Canada N2L 3G1

Introduction

The need to alleviate the problem of global warming has resulted in environmental concern over a reduction of greenhouse gas emissions from industrial sources. Carbon dioxide (CO_2), the largest contributor to the problem, is the major target for reduction. Under these circumstances, the removal of CO_2 from industrial waste gases, which would otherwise be vented to the atmosphere, becomes important. The CO_2 removal can be achieved by a number of separation techniques, of which the most suitable process approach for removing CO_2 from high-volume waste gas streams is an absorption into the liquid solvent.

The industrial use of structured packings for CO_2 absorption has not yet been reported in the open literature. However, the potential use of the packings has been investigated.[1,2] These studies confirmed that a column fitted with structured packings yields superior performance when compared to a column using random packings. With this excellent performance, taken together with the intense environmental concern over CO_2 reduction, future use of structured packings for CO_2 absorption is anticipated

Fundamental information on the mass-transfer characteristics of the packings is required to design a CO_2 absorption column packed with structured packings. A number of research studies have been focused on determining characteristics such as mass-transfer coefficient and effective mass-transfer area for various types of structured packings. However, these have been based primarily on fitting experimental data to empirical expressions. Use of such information is therefore limited to only that particular structured packing and application.

An understanding of fluid dynamics inside the packing elements is essentially required to fundamentally describe the mass-transfer performance of structured packings. Only a few mass-transfer models have been developed so far with regard to column dynamic information. This basically indicates that the models still lack full understanding of the fluid dynamics inside the packings. The present study therefore proposes a mechanistic concept that presents the fluid dynamic and mass-transfer behavior inside the structured packings used for CO_2 absorption.

Model development

The mechanistic concept was developed on the basis of liquid irrigation features through the packing elements, which can be determined from the details of the packing geometry. The concept was also based on an integration of a number of theoretical models, that aim to determine the distribution pattern of the flowing liquid inside the packing element, effective interfacial area, mass-transfer coefficients (based on penetration theory) and other information such as thermodynamic contributions (based on electrolyte NRTL model). A Fortran-90 computer program was written for the mechanistic concept in order to simulate the CO_2 absorption performance of columns packed with structured packings. The simulation was based on the theoretical packed column design procedure for adiabatic gas absorption with chemical reaction, which was first described by Pandya (1983). The procedure accounted for heats of absorption, solvent evaporation and condensation, chemical reactions in the liquid phase, and heat-and mass-transfer resistance in both gas and liquid phases. To execute the simulation, the developed computer program required a set of input information, including feed conditions of the gas and the liquid phases (i.e. compositions, temperature and flow rates), pattern of liquid irrigation from the distributor, number and arrangement of structured packing elements in the absorption column, and geometry of the packings.

Model simulation

Simulation results. The model simulation can generate the essential required information for the absorption system design including the concentrations of CO_2 in the gas phase, concentrations of reactants in the liquid phase, mass-transfer coefficients, and the effective interfacial area at different axial positions along the packed column. The patterns of the liquid irrigation inside the structured packing elements can also be provided as shown in Figure 1.

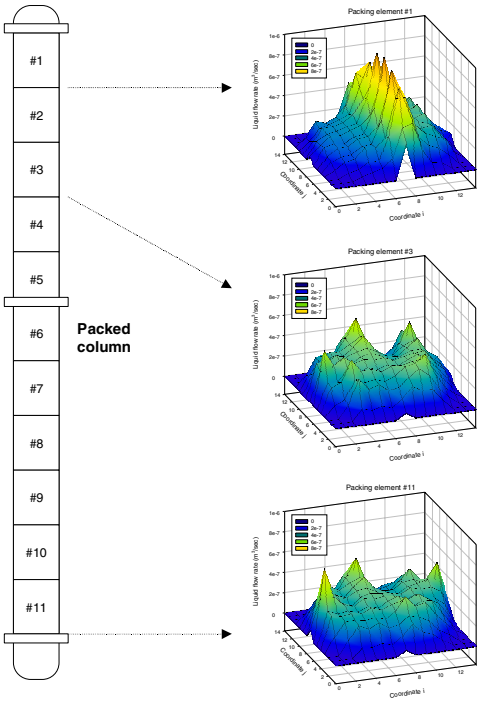

Figure 1. Examples of simulated liquid distribution plots.

Model verification. The verification of the developed concept was based on the prediction of mass-transfer performance in the CO_2-MEA absorption system. The simulation results were generally presented in terms of the gas-phase CO_2 concentration profiles along the absorption column, which were plotted against the experimental data for comparison purposes. The comparisons were made over the wide ranges of operating conditions where the thermodynamics contribution was significant in controlling the mass-transfer phenomena in the absorption system. Good agreement between the experimental and simulation results was found for all packings tested. An example of the result comparison is given in Figure 2.

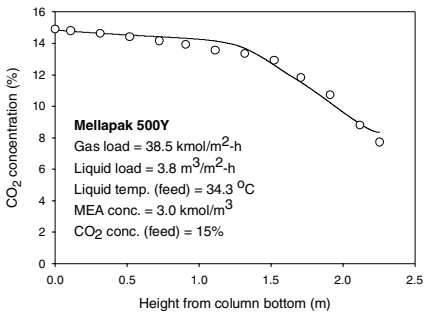

Figure 2. Comparison between the experimental (open circles) and simulated (solid lines) CO_2 concentration profiles.

Mass-transfer with different liquid loads. The liquid load was found from the simulation results that it has a significant effect on the performance of packed column. Higher liquid load enhances the CO_2 absorption efficiency due to an increasing interfacial area as evidenced by the simulation results in Figure 3.

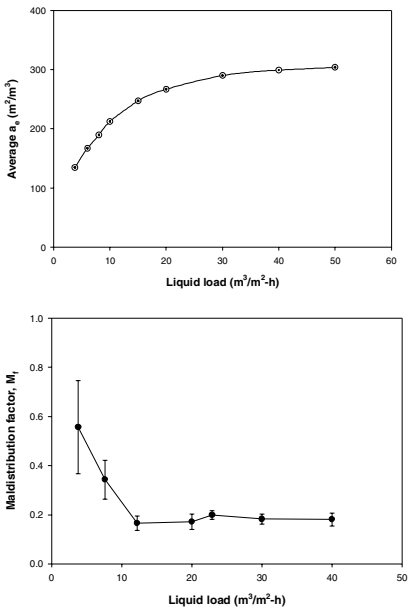

Figure 3. Simulated effective interfacial area plots of GemPak 4A structured packing (Top) and simulated maldistribution factor of Mellapak 500 Y (Bottom).

The increasing interfacial area with the liquid load is also evidenced by the quality of the liquid distribution illustrated in Figure 3. The higher maldistribution factor at the low liquid load indicates poor quality of the distribution, reflecting the lower degree of packing surface that takes part in facilitating the liquid to contact with the gas-phase. As the liquid load increases, the distribution quality is improved and the maldistribution decreases considerably. The lower maldistribution factor basically indicates a nearly uniform distribution, providing the greatest interfacial area for mass-transfer process.

Mass-transfer with different initial liquid distribution patterns. The quality of the initial liquid distribution from distributor is another important factor that has an effect on the mass-transfer performance of the packed column. Poor initial liquid distribution promotes the maldistribution phenomena, which can deteriorate the column efficiency. Figure 4 shows the simulated and experimental gas-phase CO_2 concentration profiles of the columns, operated with the two different initial liquid distribution patterns. It is apparent that the liquid distribution model well established the influence of the initial distribution on the mass-transfer performance of the column containing structured packing, i.e. the noticeable divergence between the two concentration profiles at the top packing element (element height of 0.245 m for Gempak 4A). The full-distribution pattern with the greater drip-point density generally gave higher CO_2 absorption performance than the 4H-distribution type. The lower effective interfacial area (a_e) is the primary cause of the lower absorption performance in the column with 4H-distribution.

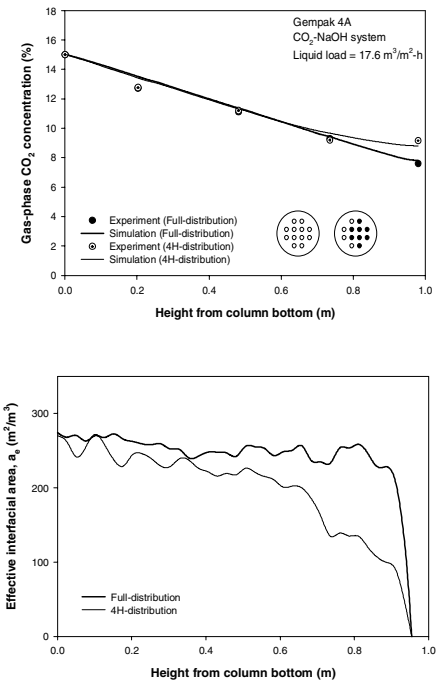

Figure 4. Gas-phase CO_2 concentration profiles based on two different initial liquid distribution patterns (Top) and their simulated effective areas.

Conclusion

The concept was developed on the basis of liquid irrigation features through the packing elements, which can be determined from the details of the packing geometry. The results of this research lead to a better understanding of the fluid dynamics within the columns fitted with structured packings. This can be used to design and simulate the CO_2 absorption process or even to optimize and customize the geometric features of new structured packings as they are developed to fit particular separation tasks.

References

1. Aroonwilas, A. (1996) High Efficiency Structured Packing for CO_2 Absorption Using 2-Amino-2-Methyl-1-Propanol (AMP): *M.A.Sc. Thesis*, University of Regina, regina, Saskatchewan, Canada.
2. Aroonwilas, A.; Veawab, A. and Tontiwachwuthikul, P. (1999) Behavior of Mass Transfer Coefficient of Structured Packings in CO_2 Absorbers with Chemical Reactions. *Industrial & Engineering Chemistry Research*. 38(5), 2044-2050.

CARBON DIOXIDE CAPTURE BY AMINES: INCREASING THE EFFICIENCY BY AMINE STRUCTURE MODIFICATION

Angela Dibenedetto, Michele Aresta and Marcella Narracci*

University of Bari and METEA Research Center
Department of Chemistry, Campus Universitario, 70126 - Bari, Italy,
fax +39 080 544 2083, e-mail: a.dibenedetto@chimica.uniba.it

Introduction

Carbon dioxide is the largest contributor to the greenhouse effect, being produced in the combustion of fossil fuels as oil, natural gas or coal, for energy production or heating, and in industrial processes.

Carbon dioxide can be recovered by using several technologies such as the absorption into an appropriate solution[1] or the membrane separation.[2] The former is used in several industrial applications such as CO_2 separation from power plants flue gases, natural gas treatment and landfill gas upgrading. The capacity of the amine to uptake/bind CO_2 is of fundamental importance for sizing the separation tower.

In this paper we consider the advantage of using new amines for capturing carbon dioxide from gas mixtures. The kinetics of CO_2 uptake using four new different amines is compared with that of absorption by MEA.

Experimental

All data were recorded under the same conditions: 1 atm of CO_2 and 298 K. The kinetics was followed in tetrahydrofuran (THF) as solvent. 8 mL of THF were saturated with CO_2 in the absorption flask, then the amine (0.90 mmol) was added. The uptake of CO_2 was followed using a gas burette.
Neat amines have been also used.

Results and Discussion

Aliphatic amines are known to react promptly with CO_2 [Eq 1] to afford an ammonium carbamate.[3]

$$2\ RNH_2 + CO_2 \longrightarrow RNH_3^{+-}O_2CNHR \quad (1)$$

We have investigated the behaviour of mono- (A, B, C) and di-amines (D, E)[4] towards CO_2 at various temperatures. Mono-amines A, B and MEA (C) react rapidly with CO_2 at 298 K in THF. Figure 1a-b-c show that the reaction is almost complete in 15 minutes and the amount of CO_2 taken up by the amine (*ca.* 0.55 mol/mol amine) says that one mol of CO_2 reacts with two moles of amine, as required by the stoichiometry of reaction 1, to afford ammonium carbamates.

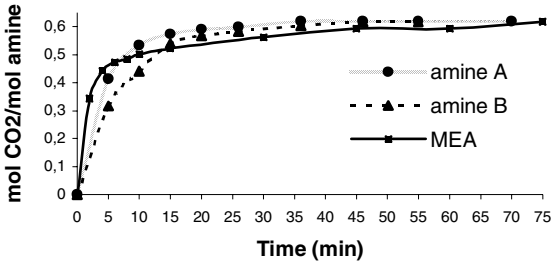

Figure 1. Kinetics of reactions of mono-amines with carbon dioxide

Amines A and B are as performing as MEA. In all cases, the solution at the end of the reaction is cloudy due to a fine suspension of a white solid. Interestingly, if the reaction is carried out at 273 K, the amount of CO_2 fixed by amines A and B, after a fast initial uptake, of ca. 0.50 mol/mol, increases slowly to 1 mol/mol within three hours. This feature can be explained assuming that at low temperature any of the ammonium carbamates $RNHCOO^{-+}H_3NR$ slowly converts into the dimeric form of the relevant carbamic $(RNHCOOH)_2$ acid. We have already shown that, in the same conditions, the carbamate/carbamic acid conversion takes place with benzylamine[5] and other N-compounds. (Eq.2) In the case of R=benzyl, the dimeric carbamic acid has been isolated and characterized by X-ray[5a].

$$RNHCOO^{-+}H_3NR + CO_2 \rightarrow (RNHCOOH)_2 \qquad R = \text{Benzyl} \qquad (2)$$

Carbamates of amines (A and B) do not release CO_2 easily upon heating. Therefore, they are not good candidates for the separation of carbon dioxide from other gases (e.g., from flue gases) as they can not advantageously operate in a cyclic system implying the uptake and release of carbon dioxide.
When diamine D or E is used, the CO_2 uptake curve (Fig. 2) at 298 K has a different shape with respect to that characteristic of monoamines.

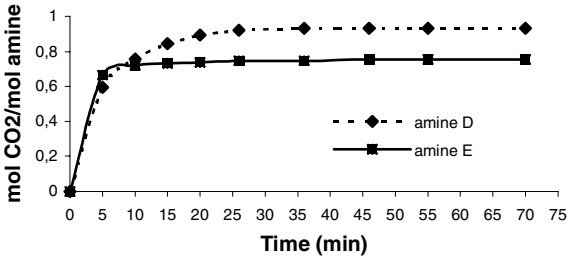

Figure 2. Kinetics of reactions of di-amines with carbon dioxide

Diamines D, E take up CO_2 with a 0.8-1 molar ratio, to afford a glassy material that occludes solvent. The reaction quickly takes place also in absence of solvent. The resulting carbamates have been isolated and characterised. Diamines are thus by far more efficient than monoamines for CO_2-capturing. This aspect is quite important as by using diamines it would be possible to reduce to half the amount of amine necessary for the separation of a given amount of CO_2, and thus the volume of the absorption tower. Interestingly, the carbamates of diamines easily release carbon dioxide at moderate temperatures, making such systems quite interesting candidates for CO_2 separation.

We are now working at some improvement of the amine molecular structure in order to further increase the separation efficiency.

Acknowledgement. This work was supported by MURST, Project no. 9803026360 and MM03027791

References

(1) Rangwala H.A. *J. Memb. Science* **1986**, 112, 229.
(2) RUCADI Project, BRRT-CT98-5089.
(3) a) Aresta, M. and Quaranta, E. *Tetrahedron*, **1991**, 47, 9489; b) Aresta, M. and Quaranta, E. *Ital. Pat.* 1237207, **1993.**

(4) The structure of the amines A, B, C, D will be discussed at the symposium.
(5) a) Aresta, M.; Ballivet-Tkatchenko, D.; Belli Dell'Amico, D.; Bonnet, M. C.; Boschi, D.; Calderazzo, F.; Faure, R.; Labella, L. and Marchetti, F. *Chem. Commun.* **2000**, 1099**;** b) Aresta, M.; Ballivet-Tkatchenko, D.; Bonnet, M. C.; Faure, R.; and Loiseleur, H. *J. Am. Chem. Soc.* **1985**, 107, 2994

DEGRADATION OF MONOETHANOLAMINE USED IN CO_2 CAPTURE FROM FLUE GAS OF A COAL-FIRED ELECTRIC POWER GENERATING STATION

Brian R. Strazisar, Richard R. Anderson, and Curt M. White

U. S. Department of Energy, National Energy Technology Laboratory
P. O. Box 10940, Pittsburgh, PA 15236

Introduction

Increasing awareness of the possible influence of greenhouse gases on global climate change has led to recent efforts to develop strategies for the reduction of carbon dioxide (CO_2) emissions.[1,2] One such strategy that has received a great deal of attention involves the capture of CO_2 from large point sources (such as fossil fuel-fired power plants) and the long-term storage underground or in the ocean. The CO_2 capture step is expected to make up the majority (up to 75%) of the expense for a carbon sequestration process.[2]

Although there are several different methods that have been proposed for the capture and separation of CO_2, the only method that has been proven to work on an industrial scale is chemical absorption using monoethanolamine (MEA) as a solvent.[2] In this method, MEA absorbs CO_2 through chemical reaction in an absorber column. Since the reaction is reversible, the CO_2 can be driven off by heating the CO_2 rich amine in a separate stripper column. The MEA may be recycled through the process. For the low CO_2 partial pressure present in flue gas, alternative methods of CO_2 removal are less efficient and more expensive than chemical absorption.[2]

A major problem associated with chemical absorption using MEA is the degradation of the solvent through irreversible side reactions with CO_2 and other flue gas components.[3,4,5] This leads to numerous problems with the process. First, degradation of MEA results in solvent loss, requiring the replacement of up to 8 pounds of MEA per ton of CO_2 captured.[6] It is also known to lead to foaming, fouling, and increased viscosity of the amine. In existing CO_2 capture facilities, the degradation products are separated in an evaporative reclaimer and disposed of as hazardous chemical waste.

In the case of carbon sequestration, the most significant problem presented by MEA degradation is associated with increased corrosion caused by the degradation.[3] In order to keep machinery corrosion rates at an acceptable level, the concentration of MEA must be kept low (typically under 20% for coal boilers and ~30% for natural gas-derived flue gas and then only if corrosion inhibitors are employed). Low MEA concentration reduces the effectiveness of the solvent, necessitating large equipment sizes and faster circulation rates. In addition, more energy is required in the stripping column in order to regenerate the amine.[7] This increased "parasitic load" is of particular concern for carbon sequestration. In addition to being an additional cost, producing this extra energy leads to increased CO_2 emissions, which decreases the overall benefit of sequestration.[2] A sensitivity analysis indicates that increasing the concentration of MEA to 70% will cut the parasitic load on a power plant by more than half.[7]

The current study is aimed at developing an increased chemical understanding of MEA degradation processes. Increased insight into the mechanisms and chemical pathways associated with MEA degradation may result in decreasing or eliminating its negative effects. There have been several previous studies on reactions of alkanolamines with O_2,[5] CO_2,[3] COS,[8] or CS_2.[9] Most of these studies were aimed at understanding natural gas sweetening processes, and all were conducted under laboratory conditions. However, in flue gas from a fossil fuel-fired boiler, the process becomes much more complicated due to the presence of a mixture of CO_2, O_2, CO, SO_x, NO_x, fly ash, and other constituents. The degradation process in this case remains poorly understood, particularly under conditions that are common to power plants.[10]

Experimental

The IMC Chemicals Facility in Trona, California is a plant that has been performing CO_2 capture from flue gas since 1978. CO_2 is separated from flue gas of a coal-fired boiler, which is used to produce electricity. In this case, the captured CO_2 is used for carbonation of brine from Searles Lake, California for the commercial production of sodium carbonate. For the current study, MEA samples were obtained from this plant in order to identify the degradation products from the CO_2 separation process. Three samples were obtained: (1)virgin concentrated MEA, (2)"lean" MEA, taken before the CO_2 absorption step, and (3)reclaimer bottoms, which represents the still bottoms that remain after the amine is distilled to remove the degradation products.

In order to identify the volatile organic compounds in the samples, each mixture was separated and analyzed using combined gas chromatography-mass spectrometry (GC-MS) and combined gas chromatography-Fourier transform infrared absorption spectrophotometry (GC-FTIR). Two separate gas chromatographic columns were used for separation. The first was a 60 m × 0.32 mm i. d. fused silica column coated with a 0.25-µm film of 14%-(cyanopropyl-phenyl)-methylpolysiloxane (DB-1701 from J&W Scientific). This column was temperature programmed from 35 to 280°C at 1 C°/min. The second column, a 60 m × 0.25 mm i. d. column coated with 0.25-µm modified polyethylene glycol (Nukol™ from Supelco), was temperature programmed from 50 to 200°C at 5 C°/min. Helium carrier gas was used with initial linear velocities of 40 and 36 cm/s, respectively. In both cases, samples were introduced via a split injector held at 250°C. GC-MS experiments were performed using an HP 5973 mass selective detector (MSD) and GC-FTIR experiments employed an HP 5965A infrared detector (IRD).

In addition, precise molecular masses of the organic compounds were obtained using low voltage high-resolution mass spectrometry (LVHRMS). Mass spectra were acquired on a Kratos MS-50 high-resolution mass spectrometer. In this experiment, the samples were introduced to the ion source directly without prior separation.

Inorganic ionic species were identified using ion chromatography (IC) as well as combined inductively coupled plasma-atomic emission spectroscopy (ICP-AES). IC experiments were performed for anions using a Dionex DX-100 Ion Chromatograph equipped with a conductivity detector. The analytical column used was an IonPac CS14 (4 mm), and the guard column was an IonPac AG14 (4 mm). The eluent was 3.5 mM sodium carbonate/1 mM sodium bicarbonate, at a flow rate of 1.2 ml/min. A self-regenerating ASRS-Ultra (4 mm) suppressor was used. ICP-AES experiments were performed using a Perkin Elmer Optima 3000 to measure trace metal concentrations.

Also, analyses were performed to determine the total nitrosamine concentration in each sample by a technique described elsewhere.[11]

Results and Discussion

Since the focus of this study was on the MEA degradation products, the reclaimer bottoms sample, where these products were concentrated as a result of distillation provided the most important information. Organic compounds that were identified are listed in Table 1 along with the methods of identification. An "x" in the GC-MS or GC-FTIR column indicates a positive match from an electronic search of either MS or FTIR libraries. MS library searches were performed using the NIST/NIH/EPA Mass Spectral Library. FTIR searches were performed using the FTIRsearch.com service.

The LVHRMS column indicates whether a match within 0.003 amu of the mass of the indicated molecule was present in the mass spectrum of the entire sample. Also included in Table 1 is an indication of the column used for the experiment in which each compound was detected. The % of total area refers to the integrated peak area from the total ion chromatogram as a percentage of the total signal intensity for each chromatogram. Other than the MEA, none of the peaks identified in Table 1 were present in identical experiments performed on the virgin MEA.

Table 1. Identified organic compounds from MEA reclaimer bottoms

		method of identification			GC column		%of total area	
peak	compound	GC-MS	GC-FTIR	LVHRMS	DB-1701	Nukol	DB-1701	Nukol
1	N-acetylethanolamine ($C_4H_9NO_2$)	x		x	x	x	8.86	6.28
2	N-glycylglycine ($C_4H_8N_2O_3$)	x		x	x		<0.01	
3	N-(hydroxyethyl)-succinimide ($C_6H_9NO_3$)	x		x	x	x	0.16	*
4	N-(2-hydroxyethyl)-lactamide ($C_5H_{11}NO_3$)	x	x	x	x		0.07	
5	1-(2-hydroxyethyl)-2-imidazolidinone ($C_5H_{10}N_2O_2$)	x	x		x		0.24	
6	N,N-diacetylethanolamine ($C_6H_{11}NO_3$)		x	x	x		21.83	
7	ammonia (NH_3)	x				x		0.10
8	acetic acid ($C_2H_4O_2$)	x		x		x		2.02
9	propionic acid ($C_3H_6O_2$)	x				x		0.30
10	*n*-butyric acid ($C_4H_8O_2$)	x		x		x		0.01
11	monoethanolamine (C_2H_7NO)	x	x	x	x	x	*	35.18
12	2,6-dimethyl-4-pyridinamine ($C_7H_{10}N_2$)	x		x		x		0.05
13	2-imidazolecarboxaldehyde ($C_4H_4N_2O$)	x		x		x		0.05
14	1-methyl-2-imidazolecarboxaldehyde ($C_5H_6N_2O$)	x		x		x		0.17
15	2-oxazolidone ($C_3H_5NO_2$)	x		x		x		0.80

* Area percentage not calculated due to overlap with other peaks

Peaks 5 and 15 are known degradation products of MEA resulting from reaction with CO_2,[3] but are relatively minor components. Carboxylic acids (peaks 8,9, and 10) have been previously identified as products of oxygen induced MEA degradation.[5] The acetylated MEA components (peaks 1 and 6) are the most abundant degradation products, and are believed to be the result of reaction between acetic acid and MEA.

The results of the ICP-AES and IC analyses are shown in Table 2. ICP-AES measurements were made for 23 different metal cations. Shown are seven metals that were present at no less than 0.2 ppm concentration in either of the two samples. Most prominent is the sodium concentration, mostly due to the sodium carbonate added to the reclaimer in order to regenerate MEA that has been converted to its protonated (acidic) form. Other metals are believed to originate in large part from the coal. In addition, mercury was found to be present in the reclaimer bottoms at 1.0 ppb and was not detectable in the lean MEA (<0.02 ppb).

Anion concentrations are all relatively higher, with chloride being the most significant at 4.9% (wt.). The halogens present in the samples are thought to be present as a result of simple acid/base chemistry between mineral acids (HX where X is any halogen) present in the flue gas with MEA to form "heat stable salts". HX is the combustion product of halogens present in the feed coal. Also, note that, with one exception, the concentration of various anions is greater in the reclaimer bottoms than in the lean MEA. This is what would be expected, since the purpose of the reclaimer is to remove contaminants from MEA and concentrate them in the bottoms. The exception is the sulfate, which is an order of magnitude more concentrated in the lean MEA than in the reclaimer bottoms. It is thought that the concentration of sulfate in the reclaimer bottoms is limited by solubility factors.

Nitrosamines are known carcinogens that are formed by a reaction between an amine with a nitrogen oxide. Nitrosamines were found to be present at a concentration of 580 ppm in the lean MEA. This is believed to be due to reaction between MEA and nitrogen oxides from the flue gas. There was not a detectable amount of Nitrosamines in the reclaimer bottoms, likely due to their low boiling point.

Table 2. Ion Concentrations in ppm

	Lean MEA	Reclaimer Bottoms
Cations		
Sodium	80	821
Potassium	2.2	18
Calcium	1.1	1.3
Iron	1.4	1.1
Copper	0.2	0.1
Zinc	0.3	0.2
Aluminum	not detectable	0.4
Selenium	not detectable	17.4
Arsenic	not detectable	1.7
Anions		
Fluoride	300	1500
Chloride	1600	49000
Bromide	0.9	80
Sulfate	2200	250
Nitrate	290	3100
Nitrite	130	**
Phosphate	7.8	230

** not quantified due to overlap with chloride peak

Acknowledgements

Some work was performed while B.R.S. held a National Research Council Research Associateship Award at the National Energy Technology Laboratory. GC-IR spectra were obtained at the Mass Spectrometry Facility, Department of Chemistry and Chemical Biology, Cornell University. Nitrosamine measurements were performed by Delbert Eatough of Brigham Young University. The authors wish to thank Leroy Williams of IMC Chemicals Inc. for providing the samples and information about the process.

References

1. *Carbon Sequestration Research and Development*, U. S. Dept. of Energy Report, (December 1999).
2. Herzog, H., "An Introduction to CO_2 Separation and Capture Technologies," Energy Laboratory Working Paper, Massachusetts Institute of Technology (August 1999).
3. Polderman, L. D.; Dillon, C. P.; Steele, A. B. *Oil & Gas Journal* **1955**, *54(2)*, 180-183.
4. Chi, S. and Rochelle, G. T., "Oxidative Degradation of Monoethanolamine", Presented at the First National Conference on Carbon Sequestration, Washington, D. C. **2001**.
5. Rooney, P. C.; DuPart, M. S.; Bacon, T. R. *Hydrocarbon Processing*, July **1998**, 109-113.
6. Arnold, D. S.; Barret, D. A.; Isom, R. H. *Oil and Gas Journal* 1982, *80**(47)***, 130-136.
7. Leci, C. L. *Energy Convers. Mgmt*. **1997**, **38**, S45-S50.
8. Dawodu, O. F; Meisen, A. *Ind. Eng. Chem. Res*. **1994,** *33*, 480-487.
9. Dawodu, O. F.; Meisen, A. *Gas. Sep. Purif*. **1996**, *10*, 1-11.
10. Meisen, A.; Shuai, X. *Energy Convers. Mgmt*. **1997**, *38*, S37-S42.
11. Ding, Y.; Lee, M. L.; Eatough, D. J. *Int. J. Envir. Anal. Chem.* **1998**, *69*, 243-255.

RECOVERY AND RECYCLING OF CO_2 IN AN ENZYMATIC REACTOR

Anne Tremblay and Frédéric Dutil

CO_2 Solution inc.
1091 Pie-XI blvd.
Val-Bélair, Quebec, Canada G3K 1J9

Introduction

The carbon dioxide greenhouse question has led many researchers involved in a variety of fields to study the phenomenon. Kyoto Protocol, which will be ratified by most of developed country this year, is a mechanism that will reduce global GHG emissions by 5.2 % in 2012 compared to 1990 level.

In response to that issue, CO_2 Solution has developed a system that involved the use of a biological process for the transformation of CO_2 into harmless compound, bicarbonate. This transformation of CO_2, also called ionisation, is catalyzed in presence of an enzyme.

The challenges associated with the bioreactor operation were to optimize gas to liquid flow ratio, packing height, concentration of gas at inlet, and pH of the liquid phase. Those operational parameters were set for the highest enzyme activity. Furthermore, one of our main objectives was to determine the best way to recycle bicarbonate ions. Studies were oriented toward precipitation in the form of metal carbonate such as calcite, magnesite, etc.

Over the past several years, the concept of employing an enzyme-based reactor to reduce CO_2 levels in many environments was successfully demonstrated. Results on CO_2 removal and beneficial reuse are presented in this document.

Experimental

Bioreactor system. The bioreactor is a packed column with enzyme immobilized onto the packing material. A packed column design was adopted since it enables an optimal contact area between gas, liquid and solid (the packing material with immobilized enzymes) phases. In this bioreactor, a gas containing CO_2 will enter the bioreactor and contact the liquid phase that will absorb the CO_2 stream. Immobilized enzyme will transform aqueous CO_2 into H^+ and HCO_3^-. A schematic representation of the bioreactor is presented in **Figure 1**.

Experimental conditions. Different operating conditions were tested with the bioreactor. When the notation "with enzyme" is used, the packing used has active enzyme bonded and immobilized to its surface. A packing "without enzyme" is one with all of the treatment for immobilisation but no enzyme on its surface.

All tests were conducted with an inlet gas concentration of approximately 5000 ppm CO_2, a Tris solution adjusted to a pH of 8.3 with H_2SO_4, a packing height of 15 cm and a gas flow of 0.064 kg/h. The effect of the variation of some of these parameters on the reaction rate of ionisation were studied: liquid/gas flow ratio, packing height and concentration of gas at inlet.

Precipitation of bicarbonate. Ions produced in the chemical reactions were concentrated with an anionic resin. Bicarbonate ions were then precipitated by the addition of dissolved cations. pH was varied by adding NaOH 2N. Solids were recovered by centrifugation or filtration through 0.4 µm filters and dried at 90°C. Solutions of 0.1 M $CaCl_2$ and $BaCl_2$ and dissolved synthetic sea salt (38 g/l) were used to precipitate bicarbonate ions. Glassware were used to limit solids adsorption. Essays were done in batch with 0.1 M $NaHCO_3$ to simulate bicarbonate concentration coming from an anion resin regenerating phase (after the bioreactor).

Analysis. Mineral identification was performed on few samples by electronic microscopy, X-rays diffraction and fluorescence. Metal concentration analysis were obtained by atomic absorption.

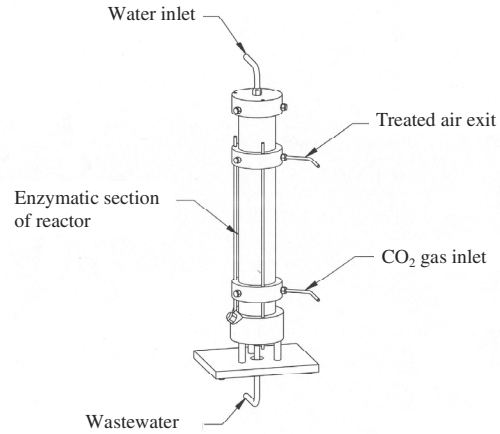

Figure 1. Schematic representation of the laboratory scale bioreactor.

Results and Discussion

Bioreactor optimization. Optimization of inherent parameters of the bioreactor allowed the determination of optimal operational conditions.

CO_2 ionisation rate in relation to packing (with or without enzyme) and liquid loading rate is presented in **Figure 2.** It shows that transformation rate rises when liquid to gas flow ratio (L/V) is increased. The major drawback of amplifying L/V is a higher liquid consumption and, thus, energy need. When calculating the improvement, in percentage, of the transformation rate when using enzyme compared to no enzyme, a lower L/V is better. For example, at a liquid loading rate of 6,500 kg/h.m^2 the improvement is 51 % compared to 39 % at 26,000 kg/h.m^2. A low L/V presents, hence, the best flow condition for a optimized operation.

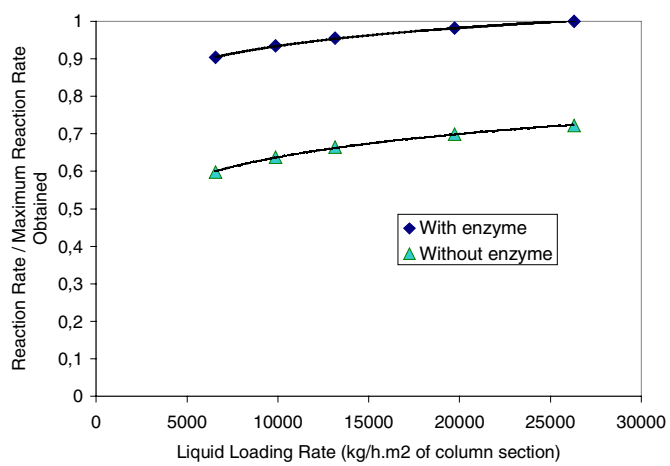

Figure 2. CO_2 ionisation rate in relation to packing (with or without enzyme) and liquid loading rate.

An increase in packing height shows a proportional rise in CO_2 transformation rate, the packing with enzyme being higher. Increasing CO_2 gas concentrations inlet from 1,000 ppm to 10,000 ppm has little influence on the reactor efficiency.

Finally, varying pH of the liquid media increased the CO_2 transformation in bicarbonate and subsequently in carbonate ions. A

few essays have demonstrated that fact (pH 6.5 to 10 increased slightly the global CO_2 removal efficiency). A numerical model predicted that pH over 11 will maximize CO_2 removal. But, to maintain a so high pH you must add chemicals and you may lose enzyme efficiency.

Globally, in the conditions tested, packing efficiency is 52 % more efficient than a packing without enzyme.

Precipitation of bicarbonate. Our first essays to precipitate calcite have demonstrated that mixing a source of carbonate and calcium ions ($CaCl_2$ + $NaHCO_3$ + NaOH) results in the formation of orthorhombic calcite crystals (diameter of about 5 µm; **Figure 3**).

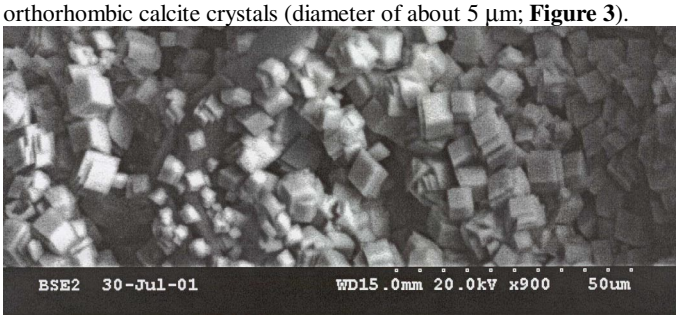

Figure 3. Electronic microscopy picture of calcite crystals.

Other essays have being done to study pH variation effect. **Figure 4** shows that the maximum weight that can precipitate is achieved at a pH as low as 8.

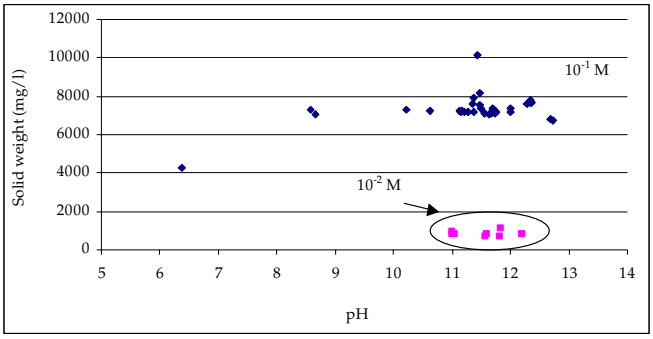

Figure 4. Relationship with calcite precipitation and pH (10^{-1} M and 10^{-2} M).

A chemical equilibrium model also predicted that calcite formation is optimal at pH 7 to 8 at operating conditions (**Figure 5**).

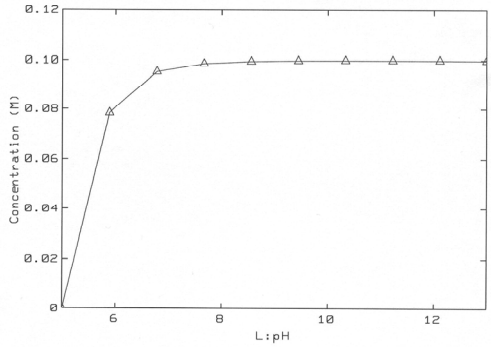

Figure 5. Relationship between calcite precipitation and pH.

However, a difference between theory (9.2 g/l of calcite attended) and experimental results (7.7 g/l ± 0.09) of 16 % is still remaining. One hypothesis to this difference is that a constant equilibrium is happening between the sample surface and atmosphere. Each time we shake the bottle to homogenize the sample, effervescence occurred, so CO_2 must be stripping in air. A mass balance study could confirm this hypothesis and will be realized on other essays.

A few experiments were done to precipitate witherite ($BaCO_3$), presented in **Figure 6**. Solid weight was about 18 g/l, either at pH 8 and 12, at an initial concentration of 0.1 M of both Ba and carbonate. There was no such significant difference with theory (19 g/l). Witherite is probably more stable than calcite (solubility product of 2.58E-9 and 3.36E-9 respectively).

Precipitation of bicarbonate ions with diluted synthetic sea salt was experimented in laboratory. For one sample, an electronic microscopy analysis has detected no crystals except an amorphous matrix. For another sample, in which we add $CaCl_2$ and sea salt to promote calcite precipitation, aragonite, a lesser stable form of calcium carbonate, and halite were detected.

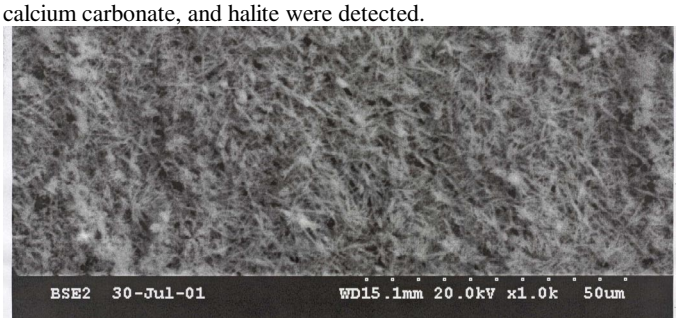

Figure 6. Electronic microscopy picture of whiterite crystals

Different pH (from 8 to 11) were tested for the precipitation of bicarbonate ions with sea salt. The results showed that at pH lower than 9.5 nothing really precipitate, and global solid weight increased with pH up to 11. The model predicted that calcite should mainly precipitate at pH higher than 11. Below that, dolomite ($CaMgCO_3$), $CaSO_{4(aq)}$ and Ca^{2+} are dominating species. More experiments will be done at pH 12 to verify this assumption.

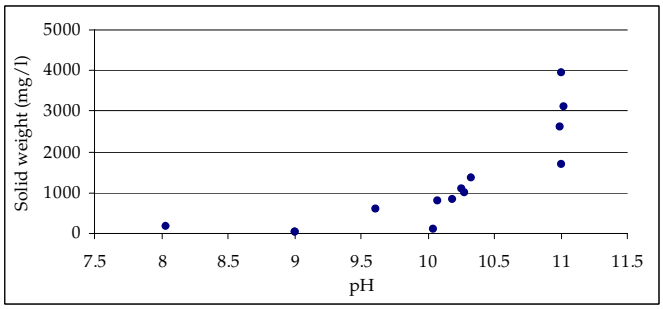

Figure 7. Relationship between precipitate weight and pH (sea salt).

Conclusions

CO_2 gas transformation in bicarbonate was realized in an enzymatic bioreactor. Bicarbonate ions are concentrated on an anionic resin, and subsequently precipitated with Ca - calcite, Ba – witherite and sea salt. Experiments have shown that precipitate weights are optimal at pH 8 for calcite and witherite minerals. On the opposite, solid weight of precipitates obtained with diluted sea salt is increasing with pH.

References

1. Khalifah, R.G. The Carbon Dioxide Hydration Activity of Carbonic Anhydrase. *J. Biol. Chem*. **1971** *(246)* 2561.
2. Steiner, H., B.-H. Jonsson and S. Lindskog. The Catalytic Mechanism of Carbonic Anhydrase. *Eur. J. Biochem*. **1975** (*59)* 253.

HIGH EFFICIENCY CAPTURE OF CO_2 FROM MIXED GAS STREAMS

Jijun Ge, Yinjie Qin, Robert M. Cowan, and Michael C. Trachtenberg

Sapient's Institute, 20 Ag Extension Way, Cook College/Rutgers University, New Brunswick, NJ 08901, and Carbozyme, Inc., 1200 Florence-Columbus Rd., Bordentown, NJ 08505

Introduction

The economic capture of CO_2 from mixed gas streams for purification and/or use in CO_2 sequestration remains a substantial hurdle to the widespread application of greenhouse gas remediation. We have developed technologies to help address this need. Our technology development program devised reactors for the efficient removal of CO_2 from Human Space Flight crew environments (e.g. space shuttle, space station, and spacesuit). More recently it has involved the study of CO_2 removal from natural gas, and as described here the CO_2 capture from a wide variety of sources. We have generated an enzyme based contained liquid membrane (EBCLM) reactor as the technological basis for a family of CO_2 removal and capture devices.

The EBCLM works as follows: CO_2 in a mixed gas stream diffuses across a microporous hydrophobic membrane to contact an aqueous buffered enzyme solution. The enzyme, carbonic anhydrase (CA – EC 4.2.1.1), greatly increases solvation via catalytic hydration of CO_2 resulting in the formation of bicarbonate. Bicarbonate diffuses across the liquid membrane. At the permeate side gas-liquid interface CA catalyzes the dehydration reaction and CO_2 is released to the sweep gas stream having diffused through a second microporous hydrophobic polymer membrane.

Experimental

Materials and methods

Bovine carbonic anhydrase (BCA2 - Sigma Chemical Co.) was used as the enzyme catalyst. The buffer was made from monobasic anhydrous potassium phosphate (99.0% purity - Sigma) and dibasic anhydrous sodium phosphate (99.5% purity - Fisher Scientific). Microporous polypropylene (Celgard PP-2400 - Celanese) was used to contain the enzyme/buffer solution. The Celgard PP-2400 membrane is 25.4 µm thick, with a porosity of 35%, a nominal pore size of 41 nm x 120 nm with a tortuosity value of 5 [1]. The thickness of the liquid membrane was controlled by the use of polyester mesh (Small Parts Inc., CMY-200) spacers cut in the form of flattened O-rings. Gases, purchased from Matheson, included ultra-zero air, ultra high purity argon and high purity CO_2. Air and argon were purged of residual CO_2 by a purification column (OMI-4, Supelco) before being used.

Bioreactor configuration and test stand setup

The membrane reactor is constructed by sandwiching a CA containing phosphate buffered solution between two polypropylene membranes. Perforated metal screens (Millipore) retain the polymer membranes. The total liquid membrane area is 380.1 mm^2. The thickness of the aqueous phase was 330 µm. The liquid membrane volume was maintained by means of a fluid reservoir. The feed gas stream delivered via an Environics mass flow controller (Environics, Series 2020 – NIST-traceable calibration). The composition of gas was measured by mass spectrometer (Questor IV, ABB Extrel) The separation performance includes selectivity ($\alpha = Q_i/Q_j$) and permeance ($Q = J/\Delta P$) where J is the flux through the membrane and ΔP is the partial pressure difference across the membrane. The unit of Q is mol m^{-2} Pa^{-1} s^{-1}, i, and j are permeance for species i and j, respectively.

Results and Discussion

Table 1 contains examples of selectivity and permeance values that have been obtained using the EBCLM. Along with these values Table 1 provides information regarding the feed stream CO_2 concentration, the concentration of CA and buffer in the liquid membrane, and the sweep stream condition (pressure and composition). Figure 1 provides a different view of these results in a plot of selectivity versus permeance. This plot also contains information obtained from the literature detailing the performance of competing membrane technologies.

Table 1. Examples of Selectivity and Permeance for CO_2 Separation from Air, Oxygen, and Methane

Sweep pressure	$[CO_2]$ in feed	[CA]	[Buffer]	Selectivity	Permeance	Other Gas(es)
kPa	(%)	(mg/ml)	(mM)		(mol/m^2-Pa-s)	
101.3	0.23%	5.0	75	1401	1.44E-7	N_2 & O_2
-70.0	0.50	5.0	75	269.0	8.0E-09	O_2
-70.0	0.50	20.0	800	335.7	8.3E-09	O_2
101.3	2.44	5.0	75	187.4	7.4E-09	CH_4

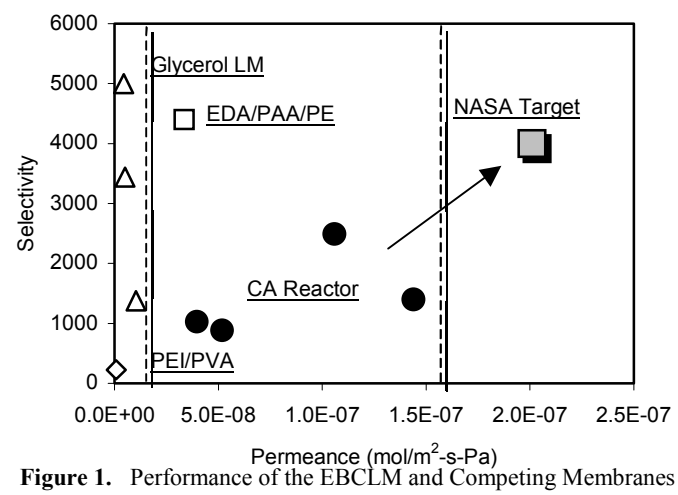

Figure 1. Performance of the EBCLM and Competing Membranes - CO_2 Removal from Air and Other Low Concentration Sources

As seen from Figure 1 the use of traditional nonporous polymer membranes (*e.g.*, PEI/PVA) for CO_2 separation from air provides very low permeance and selectivity [2]. With the use of the glycerol LMs reported by Sirkar and colleagues [1] and the EDA/PAA/PE gel filled membranes of Matsuyama et al. [2] it is possible to obtain high selectivity versus N_2, but the permeance values are at best moderate. While these high selectivity membranes can provide good CO_2 enrichment, the low permeance means large membrane area is needed. This will increase the volume, weight and cost of the membrane device. The data given in Figure 1 for our CLM (closed circles) shows the evolution of its performance [3-8] and the NASA target. Our EBCLM both high permeance and high selectivity are possible, making this CA based EBCLM desirable for use in the capture of CO_2 from very low concentration sources.

Understanding EBCLM Performance

Because the configuration of EBCLM is complicated space and time restrictions prevent full coverage of the topic. The focus here is on a few select influences on EBCLM performance. These include CA chemistry and the influence of environmental factors on CA activity; physical and chemical configuration of the EBCLM (e.g., LM thickness, buffer composition and buffer concentration), and operational factors which influence optimization of the EBCLM design for use in a particular application (e.g., effects of feed and sweep gas composition and pressure).

CA Chemistry

CA is a naturally occurring enzyme that increases the rates of hydration of CO_2 to form H_2CO_3, and the dehydration of H_2CO_3 to form CO_2. As expected from the importance of CO_2 to living organisms CA is present in all animals, most plants, and many fungi, archaea, and bacteria. CA provides a means of making a set of reactions that occur quickly at extremes of pH occur quickly at more neutral pH. Figure 2 illustrates, as a function of pH, the rates of CO_2 hydration and dehydration for both the uncatalyzed and the CA (HCA II) catalyzed conditions. From Figure 2 it is clear that without CA low values of pH favor the dehydration of H_2CO_3; high pH favors hydration of CO_2; and over the range of pH shown (5 to 10) both rates are quite slow. When CA is present there is an approximately 100 to 1000 times increase in the rate of the hydration and dehydration reactions over this entire pH range.

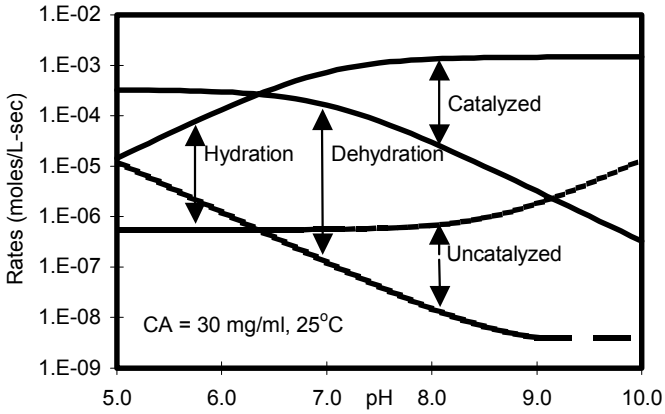

Figure 2. Effect of pH on the Rates of CO_2 Hydration and H_2CO_3 Dehydration

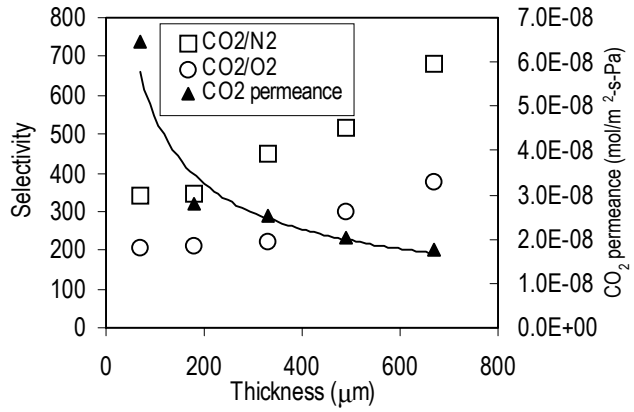

Figure 3. Effect of Thickness on separation performance

Other influences on CA activity include temperature, ionic strength, the concentrations of carbonate and bicarbonate, and the concentration of specific inhibitors of the enzyme such as halides. The particulars of these influences depend on which CA isozyme is in use

EBCLM Configuration – Liquid Membrane Thickness

Figure 3 illustrates the way in which liquid membrane thickness influences the selectivity and permeance of the EBCLM. The results show that as thickness increase, selectivity increases but permeance decreases.

Conclusions

The creation of a CA-based EBCLM accomplishes the following: the generation of a highly selective, high permeance CO_2 capture membrane capable of removing CO_2 from a variety of gas mixtures over a range of temperatures and pressures. The CO_2 can be removed when very dilute (<0.1%) to moderate concentrations (~20%). In current form this system is capable of operating to at least 45°C but may be modified to temperatures possibly as high as 75°C. The system operates independent of relative humidity in the feed or sweep streams and can use a wide variety of gases in the sweep. The design relies on CA to convert a solution-limited process to a diffusion-limited process. Finally, the various parameters controlling the design can be identified, analyzed, modeled and independently manipulated. The performance characteristics, if maintained on scaling and with long-term stability support the idea of a dramatic improvement in CO_2 capture efficiency and consequent decrease in cost, a key to industrial and environmental application.

Acknowledgement.
This work was supported by NASA grants NAG 9-1021, NAG 9-1923, NAG 9–1383 and DOE grant DE-FG02-01ER86129. Additional support was provided by Cook College and the NJ EcoComplex both of Rutgers University, and by M. Toro and M.E. Opper.

References

1. Chen H., Kovvali A.S., Majumdar S. and Sirkar K.K., *Ind. Eng. Chem. Res.*, 38(9) (1999) 3489-3498; Chen, H.; Obuskovic, G.; Majumdar, S.; Sirkar, K. K., *J. Membr. Sci.* 183 (2001) 75-88.
2. Matsuyama H., Terada A., Nakagawara T., Hitamura Y., Teramoto M., *J. Membr. Sci*., 163 (1999) 221-227; Matsuyama H., Teramoto M., Iwai K., *J. Membr. Sci.* 93 (1994) 237-244.
3. J.-J. Ge, R. M. Cowan, C.-K. Tu, M. L. McGregor, M. C. Trachtenberg, Life Support & Biosphere Science, submitted.;
4. Ge J.-J., Trachtenberg M. C., McGregor M. L., Cowan R. M., 31st International Conference on Environmental Systems (ICES), Orlando, Florida, July, 9-12, 2001;
5. Trachtenberg M. C., Tu C.K., Landers R. A., Willson R. C., McGregor M. L., Laipis P.J., Kennedy J. F., Paterson M., Silverman D.N., Thomas D., Smith R.L., and Rudolph F.B., Life Support & Biosphere Science, 6 (1999) 293-302;
6. Trachtenberg M.C., Ge J.-J., Cowan, R. M., McGregor M.L., NAMS, May 15-20, 2001, Lexington, Kentucky;
7. Trachtenberg M.C., Cowan R .M., Ge, J. J., and McGregor M. L., International Conference of Life Support & Biosphere Science, LSBS'2000, Aug.6-9, 2000;
8. Trachtenberg M.C., Ge J. J., Cowan R .M., and McGregor M. L., Bioastronautics Investigators' Workshop, January 17-19, 2001, Galveston, TX, 218-219.

OPTIMAL CHOICE OF IMMOBILIZED, SUPPORTED AMINES FOR CO_2 REMOVAL

Thomas Filburn
University of Hartford
West Hartford, CT 06117

R. A. Weiss, Joseph Helble, Samuel Huang
University of Connecticut
Storrs, CT 06296

William Papale
Hamilton Sundstrand Space Systems International
Windsor Locks, CT 06096

Introduction

Aqueous solutions of amines have long been used by industry as absorbents for acid gas (CO_2, H_2S) removal, and in fact provide a large percentage of the natural gas sweetening operations[1]. While these chemical solutions have found a dominant position in the natural gas and refinery gas treatment, they have several shortcomings that can be greatly mitigated by immobilizing them into a solid polymeric support, an approach that has been used by NASA to provide regenerative CO_2 removal on long-term space shuttle orbiter missions[1].

Recent research in our group has produced a new solid amine CO_2 sorbent that has displayed approximately a twofold increase in cyclic CO_2 removal capacity over the material presently operated on board the space shuttle. This boost in capacity has been achieved through the application of a stable secondary amine onto a solid non-ionic polymeric support. This new sorbent may have applicability in the global search for methods to reduce greenhouse gas emissions. When combining these solid amine sorbents with a sequestration mechanism, long term, lower energy CO_2 sequestration systems may be achieved.

The first and foremost shortcoming presented by aqueous liquid amine systems comes from their corrosive effects on the metal piping systems used to contain them. The combination of acid gases and high pH sorbents can greatly accelerate the corrosive action on many mild steel components (valves, piping and pipe fittings). Numerous additives are frequently added to the aqueous liquid amine systems to minimize foaming, prevent corrosion, and promote the acid gas/ amine reaction. Our solid amine system greatly diminishes the corrosion concern and eliminates the need for many additives like foam depressants.

When applied as a fixed sorbent bed the solid amine system has the potential to simplify the present scrubbing system. Incorporating a solid amine system has the potential for eliminating several of the phase separation steps, as well as requiring a smaller absorbing and desorbing column. The smaller columns come from the higher amine/gas contact efficiency and increased amine density possible with the solid support pellets versus the packed trays typically used in the liquid systems. Finally, eliminating the aqueous carrier liquid offers the potential of lower regeneration energy. The liquid amine systems consistently keep amine concentrations below 30%, chiefly for corrosion concerns, however this reduced concentration raises both the fluid circulation rate and the regeneration energy costs.

Experimental

Amine Types.

Figure 1 shows the three amine types for the ethanolamine molecules investigated, monoethanolamine (MEA, primary), diethanolamine (DEA, secondary), and triethanolamine (TEA, tertiary).

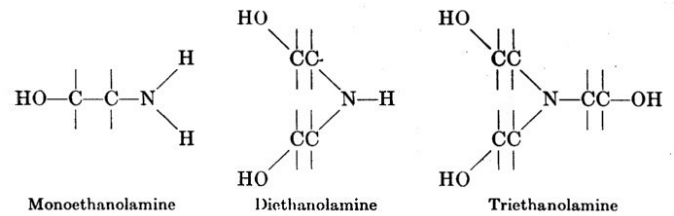

Figure 1. Amine Types MEA, DEA, TEA.

These amine types were immobilized into the pores of HP2MG, a poly(methylmethacrylate) support manufactured by Mitsubishi Chemical. This non-ionic polymeric support provided a high surface area (475 m^2/gm), large pore volume (1.2 ml/gm) to retain the amine and produced a pseudo-solid acid gas removal bead.

TEPAN a reaction product of TEPA (tetraethylenepentamine) and acrylonitrile, Figure 2, was also investigated for its CO_2 removal capacity while loaded onto the same PMMA support. Unlike the MEA, DEA and TEA, this amine, TEPAN, is not an alkanolamine.

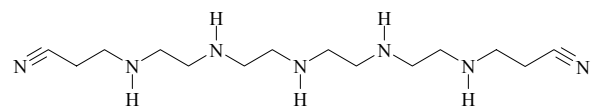

Figure 2. Schematic of TEPAN Molecule

Sorbent Manufacture.

Solvent evaporation with a rotary evaporator was used to immobilize the amine within the pores of the support. In this process we mixed the amine to be impregnated with an equal volume of methanol. The alcohol allowed the amine mixture to diffuse into the bead pore volume much more rapidly. The alcohol also allowed the support to become easily wetted by the amine/alcohol solution, as well as reduced the viscosity of the mixture. We heated the solution and porous beads to 100 °C while under a slight vacuum (~4-8 psia). This step allowed us to evaporate the alcohol from the support while leaving the amine within the pores. After the bulk of the alcohol had been removed as vapor we removed the beads from the flask and tested their capacity for CO_2 removal.

Capacity Measurements

We used a 110 cc aluminum reactor to retain the solid amine beads while testing their capacity for CO_2 removal. This reactor used a fine mesh screen at the inlet and outlet face to hold the beads within the reactor volume. An open cell aluminum foam (10% density) was also brazed into the reactor cavity. This foam coupled with the aluminum of the reactor housing provided an essentially isothermal test for both the absorb and desorb cycles. The testing used a fixed inlet concentration of 1 kPa of CO_2 with the balance being N_2 and water vapor at a total pressure of 1 atmosphere. An IR CO_2 analyzer monitored the outlet CO_2 concentration during the fixed absorption time period (25 minutes). After the absorb period an equal time (25 minutes) of vacuum desorption allowed the sorbent beads to partially regenerate. The data reported represents the steady state working capacity of the various sorbents. The amines can remove CO_2 more effectively with moisture, so the inlet gas stream was maintained at a 7 °C Dew point for all the tests.

Results and Discussion

Figure 3 shows the comparison between the three amine types. A nearly 50% increase in the amine cyclic utilization was achieved for the secondary amine (DEA) compared with the primary amine (MEA). The slight variation in amine loading was (0.22M vs. 0.26M) removed by normalizing the capacity data based on the total amount of amine present. The low capacity shown by the tertiary amine is not surprising at these low CO_2 concentrations. The weak bond formed between the tertiary amine and the CO_2 molecule does not provide a ready means for removing the acid CO_2 molecule from our gas stream.

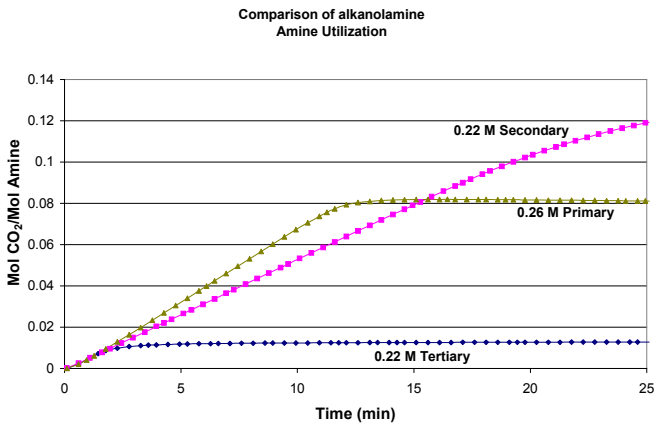

Figure 3. Normalized CO_2 Removal capacity for Primary (MEA), Secondary (DEA) and Tertiary (TEA) amine.

Figure 4 below shows the effect of amine loading within the support on its utilization in removing the CO_2 gas. The 4X (0.114 M – 0.515 M) range in amine loading within the support did not appreciably change the utilization of the amine on the support. This indicates that any surface interaction between the support and the amine did not diminish the activity of the amine for CO_2 removal. If interaction between the amine and the support had occurred, we would expect a difference in the amine utilization curves especially at the lower loadings. The shallower slope and lower utilization limit shown by the higher amine loadings in Figure 4 simply are an artifact of the fixed cycle time used. If the cycle had been extended for the higher loading case a similar utilization limit, as shown by the lower loadings, would have been reached.

Table 1 below shows a comparison of the physical/chemical properties of the 4 amines reported in this preprint. All four of the amines show a similar range of pH values. The large range in viscosity values do not provide any indication in the CO_2 removal capacity. TEPAN had the highest viscosity and the largest CO_2 removal capacity, TEA had the 2nd highest viscosity and showed no capacity for CO_2 removal.

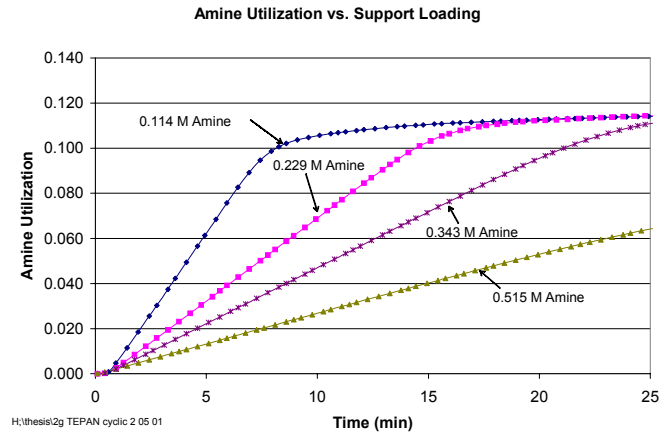

Figure 4. Normalized CO_2 Removal Capacity for variable loading of TEPAN amine within HP2MG support.

Amine	pH	Viscosity cp	BP °C	MW
MEA	11.66	18.9	171	61
DEA	11.32	352	269	105
TEA	10.55	614	340	149
TEPAN	10.98	750		311

Table 1. Physical/Chemical Property Data of amine types

Conclusions

The results of the alkanolamine CO_2 removal testing clearly show the higher working capacity displayed by secondary amines. The primary amines also show some effective affinity, but are clearly eclipsed by the secondary amines. The tertiary amines display a very weak capacity for CO_2 at the low levels (1 kPa) tested here.

All of the TEPAN amine results shown in Figure 4 display a similar asymptotic limit in CO_2 capacity, normalized for the amount of amine present on support. These curves show that the amine and support do not interact, at least in a manner that renders the functional site on the amine molecule unavailable for CO_2 removal. The lower amine loadings did not display any reduction in amine utilization as would be expected if surface/amine interaction affected the amine functional group.

Acknowledgment

Tom Filburn and Bill Papale are grateful for the support of Hamilton Sundstrand Space Systems International.

References

1. Ouellette, F., Winkler, E., Smith, G.," The Extended Duration Orbiter Regenerable CO_2 Removal System", SAE 901292, presented at 20th ICES, July 1990
2. Kohl, A., Nielsen, "**Gas Purification**", 5th Ed. Gulf Publishing, Houston TX,1997

Solid Amine CO_2 Capture Sorbents

M. L. Gray[1], Y. Soong[1], K. J. Champagne[1], R.W. Stevens, Jr.[2], P.Toochinda[2], and S. S. C. Chuang[2].

[1]US Department of Energy, National Energy Technology Laboratory, P.O. Box 10940, Pittsburgh, PA, 15236. Gray@NETL.DOE.GOV. (412) 386-4826, Fax (412) 386-4826.
[2]Chemical Engineering Department, University of Akron, Akron, OH, 44325-3906.

ABSTRACT
The capture of CO_2 from gas streams has been achieved by the utilization of amine- enriched, solid-sorbent systems. The initial solid sorbents were generated by the chemical treatment of carbon-enriched fly ash concentrates with various amine compounds. It was determined that these amine-enriched fly ash carbon concentrates performed at a 18 % CO_2 capture capacity based on commercially available sorbents. Alternative oxygen rich solids, such as, silica gel, activated carbon, and molecular sieves were examined as potential sorbents for the capture of CO_2 from gas streams. The chemical sorption performance of these solid amine sorbents will be described within this paper.

Keywords: carbon dioxide, capture, and amine sorbent

INTRODUCTION
The concentration of CO_2 in our atmosphere is promoted by the combustion of fossil fuels for the generation of electricity. Capturing CO_2 from flue-gas streams is an essential parameter for the carbon management for sequestrating of CO_2 from our environment. Current technologies[1] being considered for CO_2 sequestration include: disposal of CO_2 in deep oceans; depleted oil and gas fields; deep saline formations (aquifers); and recovery of enhanced oil, gas, and coal-bed methane. However, the current cost for the utilization of these types of technologies has proven to be too expensive. Consequently, reducing the cost for the capture of CO_2 will be a critical step in the overall carbon management program.

The physical and chemical adsorption of CO_2 can be achieved by using solvents, cryogenic techniques, membranes, and solid sorbents. The large-scale operation of these technologies is energy intensive when applied to capturing CO_2 in dilute stream, such as flue gas, which consist of 15% CO_2 by volume for most coal combustion systems. Amine-based, solvent-capture systems are the most energy efficient option, but are energy intensive due to the large amount of water needed in these system. Excessive water is required because of the corrosion and air flow problems created by the use of monoethanolamine (MEA), diethanolamine (DEA), or methyldiethanolamine (MDEA) in these aqueous-based, CO_2-capture systems. The proposed reaction sequences for using primary, secondary, and tertiary alkanolamines reacting with dissolve CO_2 are shown below.

Formation of the zwitterion ion:

$$(1)\ R_1R_2NH + CO_2 \longleftrightarrow R_1R_2NH^+CO2^-$$

Formation of amine carbamate:

$$(2)\ R_1R_2NH + R_1R_2NH{+}CO_2 \longleftrightarrow R_1R_2NH^+ + R_1R_2NCO_2^-$$

Protonation of amine:

$$(3)\ R_1R_2R_3N + H_2O + CO_2\ (aq) \longleftrightarrow R_1R_2R_3NH{+}\ HCO_3^-$$

Solid-amine CO_2 sorbents should have similar reactions with airborne CO_2, water vapor, and the amine functional group on its surface. Consequently, these types of sorbents are being used in aircraft, submarine, and spacecraft technologies[2-4]. However, the cost of these sorbents is too expensive for large-scale applications in the utility industry. Consequently, the development of economical amine-enriched sorbents based on carbon fly ash and other oxygen rich sorbents will be discussed within this paper.

EXPERIMENTAL PROCEDURES
Samples--A fly ash containing 9.5% of unburned carbon was collected from the bag house of the 500-lbs/hr-combustion unit at the National Energy Technology Laboratory (NETL). The fly-ash sample examined in this study resulted from the combustion of a Pittsburgh-seam coal from the Black Creek mine. A column agglomeration process[5-6] developed at NETL was use for the collection of the unburned carbon samples.

The three alternative oxygen rich solid substrates that were examined as CO_2 capture sorbents were a silica gel (grade 3, 8 mesh) from Aldrich Chemical Company, a coal based activated carbon from Calgon Inc. and a 13X molecular sieve from Sud Chemie.

Amine Treatment Process--The actual conditions for incorporating the amine group into the structure of the unburned carbon samples will not be discussed in this paper due to pending patent applications.

CO_2 Capture Capacity--The chemical CO_2 capture capacities were determined by the combination of Diffuse Reflectance Infrared Transform Spectroscopy (DRIFTS) Temperature Programmed Desorption (TPD) and Mass Spectroscopy (MS) analyses. The physical adsorption of CO_2 was not analyzed due to the limitations of the experimental reactor systems. The detailed operating conditions for this procedure were previously described in the literature[7].

RESULTS AND DISCUSSION
Initially, the original fly-ash concentrates (95) were generated from the feed fly ash (59) by using the column agglomeration process. The amine treated carbon concentrates (95A, 95B, and 95C) were then examined as CO_2 capture sorbents. These samples were place in a $H_2O/CO_2/He$ stream and DRIFTS, TPD, and MS analyses determined the CO_2 capture capacity. The adsorption/desorption of CO_2 for these samples were determined over the temperature range of 25 –120 ^oC. Typical DRIFTS and TPD/MS spectra are shown in figures 1 and 2. According to the DRIFTS spectra, the formation of the corresponding carbamate-amine product was indicated by the presence of the two peaks at 1087 and 1148. The other major peaks at approximately 2380 are the physically adsorbed CO_2. The desorption of the CO_2 was observed as the temperature was increased to 120 ^oC. At this elevated temperature, the TPD/MS spectra indicates the mass numbers (m/e) for the desorption of CO_2 (m/e 44), H20 (m/e 18), O_2 (m/e 32) and CO or N_2 (m/e 28). The m/e value of 28 may be the decomposition of the surface amine compound or the breakdown of the carbamate amine product. If this is the decomposition of the surface amine compound, it will have a direct effect on the regenerable properties of these sorbents. The overall CO_2 capture capacities are summarized in Table 1.

Table 1: TPD CO_2 Desorption Data of Amine Treated Sorbents

Sample #	Treatment	μmol/g CO_2 Captured
59 Feed Fly Ash	None	24.4
95 Carbon	None	72.9
95 A Carbon	A	81.1
95 B Carbon	B	117.9
95 C Carbon	C	174.6
95C Carbon (rengenerated)	C	140.6

As shown in Table 1., the physical absorbed CO_2 in samples 59 and 95 increased with the amine chemical treatment. The best sample was 95C, which had the CO_2 capture capacity of 174.5 µmol/g, and was regenerable for an additional test (140.6 µmol/g). In comparison to commercially available sorbents with surface areas of 1000-1700 m^2/g and CO_2 capture capacities of 800-1000 µmol/g, the 95C was only able to achieve 18 % of the CO_2 capture capacity. However, the surface area of the 95C amine- enriched sorbent was only 27 m^2/g, which may account for its low CO_2 capture capacity.

Alternative oxygen-rich solid substrates tested as amine-enriched sorbents for the capture of CO_2 are summarized in Table2.

Amine Treated Samples	µmol/g CO_2 Captured	% CO_2 Capacity[1]
NETL Fly Ash	24.4	
Treated NETL Fly Ash	174.6	**615.5**
Silica Gel	4.9	
Treated Silica Gel	31.5	**531.2**
Calgon Activated Carbon	8.0	
Treated Calgon Activated Carbon	28.7	**258.7**
Sud Chemie Molecular Sieve 13X	13.6	
Treated Sud Chemie Molecular Sieve 13X	15.8	**16.1**

[1] the percentage sorbent capacity is the change of the treated support compared to the baseline support.

According to Table 2, this amine treatment can be successfully applied on a variety of oxygen rich solid substrates, such as, silica gels, activated carbons, and molecular sieves. The CO_2 capture capacities were improved for all of the solid substrates tested, however, their performance were lower then the initial NETL fly ash sample examined under these reaction conditions. It is also important to point out that our current CO_2 capture experimental procedures are based only on the chemical absorbed species; physical absorbed CO_2 is purged from the surface prior to the desorption stage. Consequently, additional work is required to refine the experimental procedures (include the physical absorbed CO_2) and to increase capture capacities to the range of 800-1000 µmol/g, which will make them competitive with existing technology. Presently, additional materials with higher surface areas are being treated with this amine process and will be reported in future publications.

CONCLUSION

The amine treatment process was successful in improving the CO_2 capture capacities of these fly-ash carbon concentrates and oxygen rich solid substrates. However, the performance of the regenerable sorbents was only able to reach 18 % of the required CO_2 capture capacity to make them competitive with the existing CO_2 sorbents. Alternative low-cost, high surface oxygen-rich solid substrates and CO_2 capture procedures are being examined and will be reported in future publications.

REFERENCES

1. DOE Report Doe/ER-30194, "Research Needs Assessment for the Capture, Utilization and Disposal of Carbon Dioxide from Fossil Fuel-Fired Power Plants," 1993.
2. US Patent 4,810,266, Zinnen, H. A., Oroskar, A. R., and Chang, C. H."CO_2 Removal using Aminated Carbon Molecular Sieves," 1989.
3. US Patent 5,492,683, Bibara P.J., Naletta T. A. "Regenerable Support Amine Polyol Sorbent," 1996.
4. US Patent 5,876,488, Bibara P. J. Filburn T. P., Nalette T. A. "regenerable Solid Amine Sorbent," 1999.
5. US Patent 6,126,014, Gray, M. L., Champagne, K. J., and Finseth, D. H. "Continuous Air Agglomeration for High Carbon Fly Ash Benefication," 2000.
6. Gray, M. L., Champagne, K. J., Soong, Y., and Finseth, D. H. "Parametric Study of the Column Agglomeration of Fly Ash," Fuel, Vol. 80, pp. 867-871, 2001.
7. Soong, Y., Gray, M. L., Siriwardane, R. V., Champagne, K. J., Stevens, Jr., R. W., Toochinda, P., and Chuang, S. S. C. "Novel Amine Enriched Solid Sorbents for Carbon Dioxide Capture," Fuel preprint, 46 (1), pp. 285, 2001.

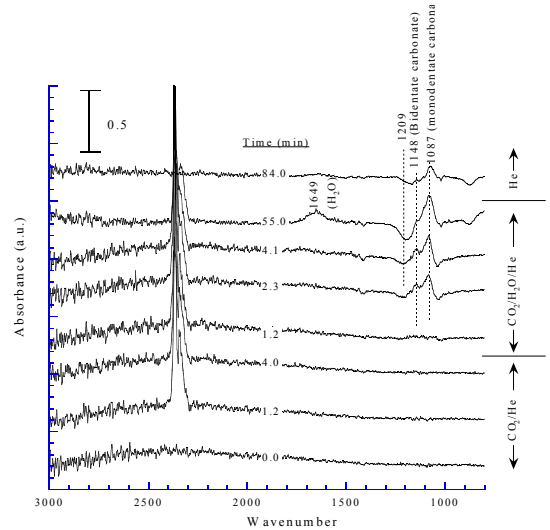

Figure 1: Typical DRIFTS CO2 absorption spectra for 95C

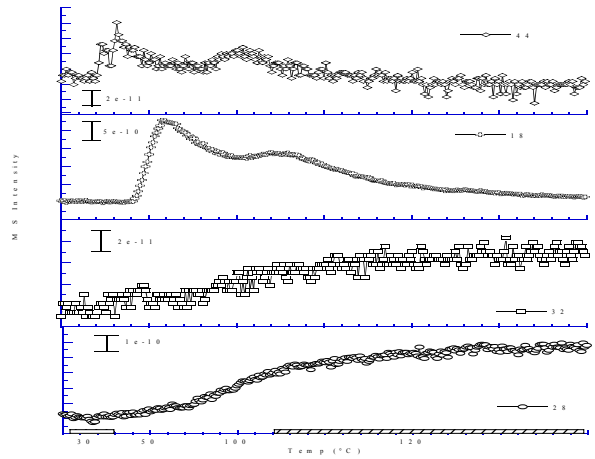

Figure 2: Typical TPD/MS spectra for 95C

Hybrid Mesoporous Materials for Carbon Dioxide Separation

Seamus W Delaney, Gregory P Knowles, Alan L Chaffee

School of Chemistry, PO Box 23, Monash University, Victoria 3800, Australia

Introduction

Gas separation processes are becoming increasingly important in a world changing the way it looks at energy production and its emissions. Increased energy demand has led to an increase of fossil fuel burning, releasing large amounts of gases such as CO_2 into the atmosphere. This is the major cause of several environmental phenomena, including the 'greenhouse effect'[1].

Methods for long-term sequestration of CO_2 have been proposed. Long term storage in used oil wells and deep ocean waters is being considered as an alternative to releasing CO_2 into the atmosphere.[2] There are also proposals to re-use CO_2 produced from one process in another process such as dry reforming of natural gas.[3] However, such applications would require CO_2 to be 'captured' in concentrated form.

One common method for CO_2 separation from mixed gas streams is by absorption in aqueous solutions of alkanolamines[4], for example monoethanolamine (MEA) or diethanolamine (DEA). It is widely accepted that CO_2 becomes absorbed via the formation of both carbamates and bicarbonates.

However, some of the problems associated with this absorption approach include: (a) the corrosive nature of the scrubbing solutions leading to the build up of corrosion by products; (b) vapourisation losses due to relatively high volatility of alkanolamines; and (c) energy intensive regeneration of the absorbent solutions, due to high heats of dissolution[4].

A recent report by Leal et al[5,6] indicated that CO_2 reversibly adsorbs on silica gel (Davidson grade 62) modified by the addition of 3-aminopropyl groups bonded to the surface. In this solid phase analogue of the liquid phase process the amine functional groups behave as active sites for CO_2 chemisorption. Adsorption capacities of approximately 10 STP cm3 dry CO_2 per gram of adsorbent (or 1.8% by weight) were achieved at room temperature and the CO_2 could be desorbed at temperatures below 100ºC. The mechanism of adsorption appears to involve the formation of surface bound carbamates (see Figure 1). In dry CO_2, this limits the adsorption capacity to 1 mole of CO_2 for every 2 moles of surface bound amino groups. In the presence of water, however, the capacity for CO_2 adsorption doubles since the possibility for proton transfer allows the carbon dioxide adsorption capacity to be doubled by the transformation of surface bound carbamate into bicarbonate.

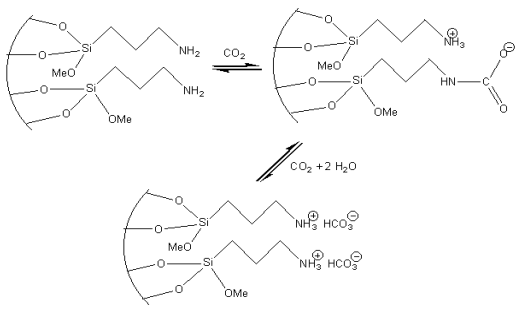

Figure 1. Scheme of the surface reaction of carbon dioxide with modified HMS materials

The silica gel used by Leal et al has a substantial surface area (380 m^2/g), but we reasoned that much improved CO_2 adsorption capacities could be achieved with (a) the use of higher surface area support materials and/or (b) the use of surface modifying groups that contain more amine functional groups.

In this study, solid phase hexagonal mesoporous silicas (HMS) of known porosity (pore diameter) were modified using aminopropyl-trimethoxysilane and related compounds to provide very high surface area materials with varied concentrations of surface bound amine and hydroxyl functional groups (see Figures 2 and 3).

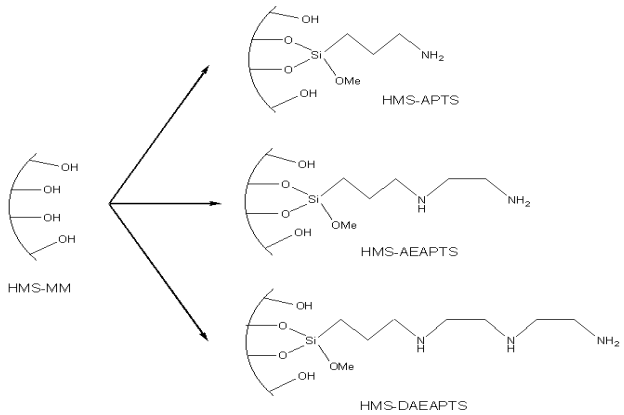

Figure 2. Modified HMS materials with increasing amine content employed in the present study.

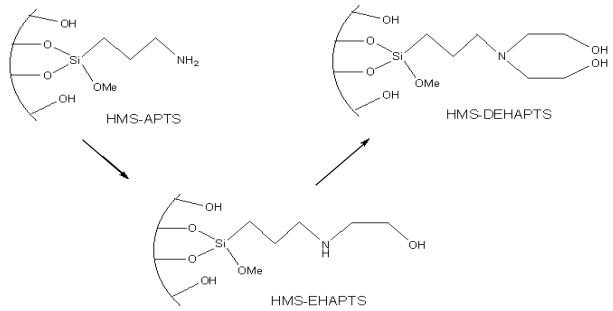

Figure 3. Modified HMS materials with increasing hydroxyl group content employed in the present study.

Experimental

Preparation of HMS. HMS materials were prepared by the neutral template method[7] using dodecylamine (DDA). The reaction involved the addition of tetraethyl-orthosilicate to the amine template in a water and ethanol solution, which was left to age at ambient temperature for 24 hours. The solvent was then removed from the crude "template filled" silica formed via evaporation under gentle air-flow at ambient temperature. The template was subsequently extracted from the crude silica into hot ethanol. The remaining solids were then collected over filter, washed with hot EtOH and finally dried under vacuum at 150ºC to form an HMS product with a total pore volume of 0.53 mL/g.

Preparation of Hybrid HMS. Five modified HMS materials were prepared as illustrated by Figures 2 and 3. Aminopropyl-trimethoxysilane (APTS), aminoethyl-aminopropyl-trimethoxysilane (AEAPTS) and N-[3-(Trimethoxysilyl)propyl)diethylenetriamine (DAEAPTS) modified HMS were prepared in toluene solution (room temperature, 2h) using a published alkylsilylation procedure[8].

Ethylhydroxyl-aminopropyl-trimethoxysilane (EHAPTS) and diethylhydroxyl-aminopropyl-trimethoxysilane (DEHAPTS) modified HMS were prepared by N-alkylation of the APTS HMS using bromoethanol in ethanol solution (room temperature, 2h). The modified silica was then filtered and dried under vacuum at 150ºC.

Characterization of Materials. N_2 adsorption/desorption experiments were conducted at –196°C using a Micromeritics ASAP 2010 instrument. BET surface areas (SA) were determined from the adsorption isotherms over the partial pressure range 0.05 - 0.22. BJH pore size distributions were determined from the desorption isotherms. Mass % elemental N compositions were determined by CMAS P/L, Belmont Vic.

Carbon Dioxide Adsorption. CO_2 adsorption and desorption experiments were conducted on a Setaram Thermogravimetric analyzer (TGA). In a typical experiment, the adsorbent sample was heated to 150ºC (held 40 min) under flowing Ar (60 mL/min) to remove residual water. The sample was cooled to 20ºC before the gas flow was switched to CO_2. CO_2 adsorption capacities were determined from the weight increase observed after 75 minutes CO_2 exposure. After 75 minutes, the gas flow was reverted to Ar so as to monitor the CO_2 desorption. Approximately 90% of the adsorbed CO_2 was desorbed immediately. The remaining CO_2 was removed by heating the adsorbent to 65ºC. High purity CO_2 (99.95%) was used with a manufacturer specified moisture content of <100 ppm. In some experiments, a molecular sieve trap was placed on the feed gas line to ensure the complete exclusion of water from the gas feed stream.

Results and Discussion

Table 1 reports the properties determined from nitrogen isotherm characterization of the HMS materials prepared in this study. It can be seen that the unmodified HMS material has an average pore diameter and surface area of 24.1Å and 1425m^2/g, respectively. Both these figures are substantially higher than the corresponding figures (14.0Å and 340m^2/g, respectively) reported for silica gel described in references 5 and 6. In addition, it can also be seen that the pore diameters and surface areas are both reduced as the length of the modifier used or the extent of substitution at the N atom increases.

Table 1. N_2 Isotherm Results for Modified HMS Materials

Sample	BET SA (± 10m^2/g)	BJH Av. Pore Dia. (± 0.2Å)
HMS	1425	24.1
HMS-APTS	1268	20.1
HMS-AEAPTS	1047	19.6
HMS-DAEAPTS	869	18.6
HMS-EHAPTS	1186	19.3
HMS-DEHAPTS	1108	19.0

Table 2 reports the carbon dioxide adsorption capacities that were observed for these materials. The unmodified HMS material itself has the capacity to adsorb 2.0% CO_2 by mass. This is already higher than the 1.8% reported for APTS modified silica gel. However, the CO_2 adsorption capacity is substantially further improved through modification with N-containing tethers. HMS-APTS adsorbs 3.8% CO_2 by weight and the incorporation of more N atoms and/or hydroxyl groups into the tether increased CO_2 adsorption still further. In all cases the, adsorbed CO_2 was completely desorbed at temperatures below 100ºC.

It is interesting to note that for HMS-APTS, HMS-AEAPTS and HMS-DEAPTS the ratio of carbon dioxide molecules adsorbed per available N atom is approximately 0.5. This is consistent with the carbamate formation mechanism postulated for silica gel (Figure 1).

Table 2. CO_2 Adsorption Results for Modified HMS Materials

Sample	Weight % N incorporated in sample (± 0.1)	CO_2 adsorption capacity Weight % (±0.1)	mole CO_2 adsorbed / mole N incorporated
HMS	0	2.0	-
HMS-APTS	2.3	3.8	0.54
HMS-AEAPTS	5.1	7.5	0.46
HMS-DAEAPTS	6.4	8.2	0.41
HMS-EHAPTS	2.1	5.0	0.74
HMS-DEHAPTS	1.5	5.1	0.98

With HMS-DEHAPTS the ratio is approximately 1. Tertiary amines cannot form stable carbamates so that another mechanism must be invoked to explain the substantial enhancement of adsorption capacity (and changed stoichiometry) that is observed in the presence of hydroxyl groups. Currently it is thought that the hydroxyl groups may serve to stabilise carbamate type zwitterions in a manner depicted by Figure 3. The CO_2 adsorption behaviour of HMS-EHAPTS can then be understood as a mixture of the two mechanisms (some carbamate formation and some zwitterion stabilization).

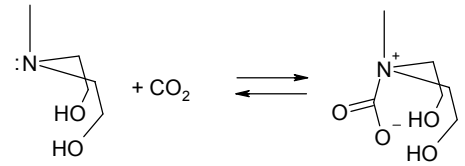

Figure 3. Proposed scheme of the surface reaction of carbon dioxide with HMS-DEHAPTS.

Conclusions

Modified HMS materials have been shown to reversibly adsorb substantially more CO_2 than previously observed for modified silica gel. There is substantial scope to further tailor the surface of HMS materials to achieve higher adsorption capacities and more selective adsorption behaviour. On a stoichiometric basis the same adsorption capacities are observed as for the liquid phase absorption process. Thus the development of a solid phase adsorption analogue of the current liquid phase absorption process may offer technical benefits.

Acknowledgement. The authors acknowledge support from the Monash University Research Fund.

References

(1) Socolow, R. (Ed.). R & D paper, C*arbon Sequestration: State of the Science;* US DoE - Office of Science (Fossil Energy): Washington, DC, 1999; pp. 21-28.
(2) Adams, E.; Golomb, D.; Zhang, X.; Herzog, H. *Direct ocean disposal of carbon dioxide*; Washington, DC, 1995; pp. 153-164.
(3) Herzog, H.; Drake, E.; Tester, J.; Rosenthal, R. A*ssessment for the capture, utilisation and disposal of carbon dioxide*; US DoE - Office of Science (Fossil Energy): Washington, DC, 1993; 13.
(4) Kohl, A.; Nielsen, R. *Gas Purification*, Gulf Publishing Company: Houston, Texas, 1997; pp.41-52.
(5) Leal, O.; et al. *Inorganica Chimica Acta.***1995**, *240*, pp. 183-189.
(6) Leal, O.; et al. US Patent, **1991**, no. 5,087,597.
(7) Beck, J. S.; et al. *J. Am. Chem. Soc.* **1992**, *114*, pp. 10834-10843.
(8) Vrancken, K.; et al. *J. Coll. Interfac. Sci* **1995**, *170*, pp. 71-77.

PREPARATION OF NOVEL CO_2 "MOLECULAR BASKET" OF POLYMER MODIFIED MCM-41

Xiaochun Xu, John M. Andresen, Chunshan Song, Bruce G. Miller, and Alan W. Scaroni*

Clean Fuels and Catalysis Program, The Energy Institute, and Department of Energy & Geo-Environmental Engineering, The Pennsylvania State University, 209 Academic Projects Building, University Park, PA 16802, USA

* Corresponding author. E-mail: csong@psu.edu; Tel: 814-863-4466; Fax: 814-865-3248

Introduction

Fossil fuels will remain the mainstay of energy production well into the 21st century. The availability of these fuels to provide clean, affordable energy is essential for prosperity and security in the world. However, an increase in the concentration of CO_2 in the atmosphere due to carbon emissions is expected to occur unless energy systems incorporate carbon emission reduction concepts. Carbon sequestration, along with reduced carbon content of fuels and improved efficiency of energy production and use are considered to be viable ways to stabilize and ultimately reduce the concentration of this greenhouse gas.[1] For carbon sequestration, the costs of separation and capture are generally estimated to make up about three quarters of the total costs of ocean or geologic sequestration.[2] Novel technologies to decrease the cost of CO_2 separation have great social and commercial value.

Adsorption is one of the promising methods that could be applicable for separating CO_2 from gas mixtures. Generally, molecular sieves and activated carbons yield relatively high adsorption capacity.[3-4] However, these adsorption capacities rapidly decline with incremental increase in temperature and separation factors are low. For practical use, many of the separations require operation at relatively high temperature, e.g., ~150 ^oC for flue gas. Developing an adsorbent with high CO_2 selectivity and high CO_2 adsorption capacity, which can also be operated at relatively high temperature, is critical for the success of this method.

Recently, we developed a new kind of high-capacity, highly selective CO_2 adsorbent, which is a CO_2 "molecular basket".[5] By loading the sterically branched polymer polyethylenimine (PEI), which has branched chains with numerous CO_2-capturing sites such as amino groups, into the large pore volume of MCM-41, its adsorption capacity was significantly increased. In this paper, the preparation approaches to further improve the CO_2 adsorption performance of the novel "molecular basket" are reported. The synergetic effect of the MCM-41 on the adsorption of CO_2 by the PEI is discussed.

Experimental

Mesoporous molecular sieve of MCM-41 with different Si/Al ratios was synthesized as reported in a previous publication.[6] The PEI modified MCM-41 (MCM-41-PEI) was prepared by the wet impregnation method. In a typical preparation, the desired amount of PEI was dissolved in 20 g methanol under stirring for about 15 min, after which 5 g of calcined MCM-41 was added to the mixture solution. The resultant slurry was continuously stirred for about 30 min and dried at 70 ^oC for 16 h under vacuum. The preparation conditions, such as PEI loadings, preparation methods, Si/Al ratio of the MCM-41, and third component of PEG were investigated.

The mesoporous molecular sieves of MCM-41 before and after modification were characterized by X-ray diffraction (XRD, Rigaku Geigerflex), N_2 adsorption/desorption (Quantachrome Autosorb 1) and thermalgravimetric analysis (TGA, PE-TGA 7).

The adsorption and desorption performances of the adsorbents were measured in a flow system under pure CO_2 atomosphere at 75 ^oC. A PE-TGA 7 thermalgravimeter was used to track the weight change of the adsorbent in the experiments. Adsorption capacity in mg of adsorbate/g of adsorbent and desorption capacity in percentage were used to evaluate the adsorbent and were calculated from the weight change of the sample in the adsorption/desorption process. The desorption capacity in percentage was defined as the ratio of the amount of the gas desorbed to the amount of gas adsorbed.

Results and Discussions

1 Preparation and characterization of MCM-41-PEI

The MCM-41-PEI with different PEI loadings was prepared and characterized by XRD, N_2 adsorption/desorption and TGA. After loading the PEI, the structure of the MCM-41 was preserved. However, the intensity of the diffraction patterns of the MCM-41 decreased. Meanwhile, the Bragg diffraction angle of the 100 plane of MCM-41 slightly shifted to a higher degree, which indicated that the PEI was loaded into the channels of the MCM-41.[6] N_2 adsorption/desorption showed that the pore size, surface area and pore volume decreased after loading the PEI, which confirmed that the PEI was loaded into the channels of the MCM-41. When the PEI loading was 50 wt%, the mesopores were completely filled with PEI.

TGA results showed that there was no weight loss for MCM-41 until 600 ^oC. The PEI lost 3.8% of its original mass at 100 ^oC, and began to decompose above 150 ^oC. A sharp weight loss happened at 205 ^oC. At 600 ^oC, the PEI was completely decomposed and removed as volatiles. After the PEI was loaded into the channels of the MCM-41, a sharp weight loss takes place at a lower temperature, e.g., 125 ^oC for MCM-41-PEI with PEI loading of 50 wt%, which indicated that the decomposition temperature of PEI had decreased. The weight loss also took place in a narrower temperature range than that of the pure PEI. These phenomena can be ascribed to the uniform dispersion of the PEI throughout the nanopores, since the melt or decomposition temperature will decrease when the particle size of the substance decreases.[7]

2 Adsorption performance of MCM-41-PEI

2.1 The influence of preparation method

Two methods, i.e., wet impregnation and mechanical mixing, were employed for the preparation of the MCM-41-PEI adsorbent. The PEI loading was 50 wt%. The adsorption capacity was 99 mg/g adsorbent for the adsorbent prepared by the mechanical mixing method and 112 mg/g for the adsorbent prepared by the wet impregnation method. The high adsorption capacity of the wet impregnation method can be ascribed to the uniform dispersion of the PEI into the channels of the MCM-41. For the mechanical mixing method, only part of the PEI was loaded into the channels of the MCM-41. The remaining PEI may coat the outer surfaces of the particles as a thick layer, which may block CO_2 adsorption sites and impede CO_2 from accessing the channels of the molecular sieve.

2.2 The influence of PEI loading

The influence of PEI loading on the CO_2 adsorption performance of MCM-41-PEI was investigated and the results are shown in Figure 1. Before the PEI was loaded, the bare MCM-41 showed a CO_2 adsorption capacity of 8.6 mg/g adsorbent. After loading the PEI, the adsorption capacity increased. The adsorption capacities were 112 mg/g adsorbent and 133 mg/g adsorbent for PEI loadings of 50 wt% and 75 wt%, respectively, both of which are higher than that of the pure PEI of 109 mg/g adsorbent. The MCM-41

showed synergism for the adsorption of CO_2 by PEI. The desorption was complete for all the MCM-41-PEI adsorbents as well as the MCM-41 support. However, desorption for the pure PEI was slow and was not complete for the same desoption time. The fast desorption of CO_2 from MCM-41-PEI can be explained by the high dispersion of PEI into the MCM-41 channels, which was indicated by the N_2 adsorption/desorption and the TGA data.

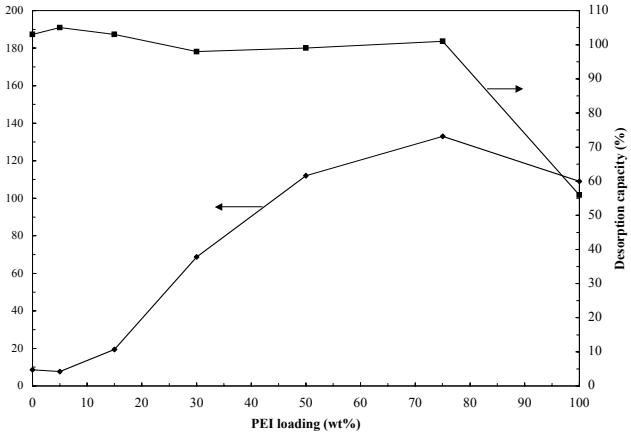

Figure 1 The influence of PEI loading on the adsorption and desorption performance of MCM-41-PEI

2.3 The influence of the Si/Al ratio of the MCM-41

A change in the Si/Al ratio of the MCM-41 will not only change the physical properties of the support (e.g., pore size, pore volume and surface area), but also change the interaction between the support and PEI. Figure 2 shows the adsorption capacity of MCM-41 and MCM-41-PEI with different Si/Al ratios. The adsorption capacity was nearly identical for the MCM-41 support with different Si/Al ratios. However, the Si/Al ratio of the MCM-41 influenced the adsorption capacity of MCM-41-PEI. The higher the Si/Al ratio, the higher the adsorption capacity. The adsorption capacity of MCM-41-PEI with a Si/Al ratio of 100 was 12 % higher than that of MCM-41-PEI with pure silica.

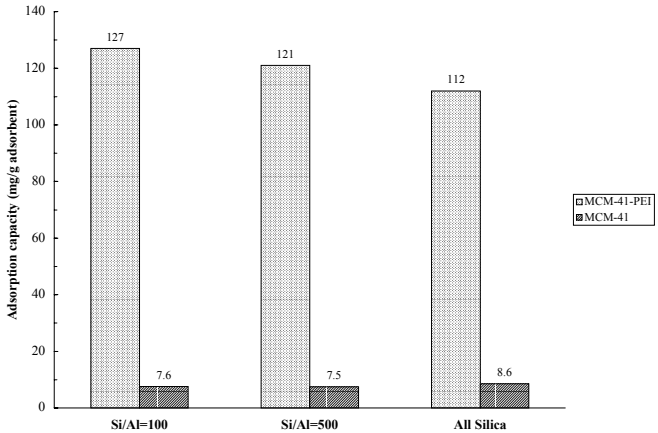

Figure 2 The influence of Si/Al ratio on the adsorption performance of the MCM-41-PEI (PEI loading: 50wt%)

2.4 The influence of third component of PEG

The influence of the third component of PEG on the adsorption/desorption performance of the MCM-41-PEI was investigated. Figure 3 compares the adsorption and desorption performance of the adsorbent with and without the addition of PEG. The adsorption and desorption rates of the MCM-41-PEI-PEG were faster than those of the MCM-41-PEI. In addition, the adsorption capacity of the MCM-41-PEI-PEG was higher than that of MCM-41-PEI.

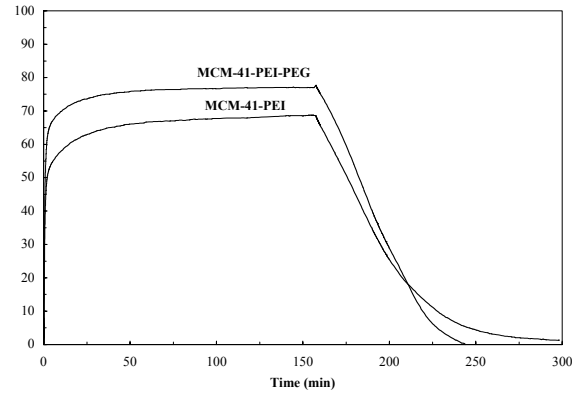

Figure 3 The effect of PEG on the CO_2 adsorption/desorption performance of MCM-41-PEI. (PEI loading: 30 wt%, PEG loading: 20 wt%)

Conclusion

A novel CO_2 "molecular basket" based on PEI modified mesoporous molecular sieve of MCM-41 (MCM-41-PEI) has been successfully developed. The MCM-41 had a synergetic effect on the adsorption of CO_2 by PEI. By loading substances with affinities for different gases to the mesoporous molecular sieve, this concept can be used to develop different types of highly selective, high adsorption capacity "molecular baskets".

Acknowledgments

Funding for the work was provided by the U.S. Department of Defense (via an interagency agreement with the U.S. Department of Energy) and the Commonwealth of Pennsylvania under Cooperative Agreement No. DE-FC22-92PC92162.

Reference

1. DOE Fossil Energy-Carbon Sequestration, **2001**, http://fossil.energy.gov/coal_power/sequestration/index.shtml
2. DOE, Carbon sequestration research and development, Chapter 2-Separation and capture of carbon dioxide. **1999**
3. Ishibashi, M.; Ota, H.; Akutsu, N.; Umeda, S.; Tajika, M.; Izumi, J.; Yasutake, A.; Kabata, T.; Kageyama, Y. *Energy Conv. Manag.*, **1996**, *37*, 929-933.
4. Foeth, F.; Bosch, H.; Sjostrand, A.; Aly, G.; Reith, T. *Sep. Sci. Tech.*, **1996**, *31*, 21-38.
5. Xu, X.C.; Andresen, J.M., Song, C.S., Miller, B.G., Scaroni, A.W. *Energy & Fuels*, in preparation
6. Reddy, K.M.; Song, C. *Catal. Lett.*, **1996**, *36*, 103-109.
7. Zeng, P., Zajac, S., Clapp, P.C., Rifkin, J.A. *Mat. Sci. Eng. A-Struct.,* **1998**, *252*, 301-306.

CO_2 ELECTROCHEMICAL SEPARATION BY MOLTEN CARBONATE TECHNOLOGY

Hidekazu Kasai

Energy System Technology Department
Ishikawajima-Harima Heavy Industries, Co., Ltd.,
2-16,Toyosu 3-Chome, Koto-ku,
Tokyo, JAPAN

Introduction

Molten carbonate ($MxCO_3$) recognizes high activity and high electrical conductivity under high temperature. Then its have been used as electrolyte of MCFC•(molten carbonate fuel cell). In this cell CO_2 and O_2 translate between as carbonate ions. This method is expected to be applicable to CO_2 and O_2 recovery and production processes.

The concentration of CO_2 has been studied by Weaver[1] using MCFC. However, separation is also possible in other process using molten carbonate as the electrolyte. In this case, electrical energy is required for electrolysis. This system is shown schematically in Fig.1. Electrode reactions are as follows,

Cathode : $CO_2 + 1/2O_2 + 2e^- \rightarrow CO_3^{2-}$ (1)

Anode : $CO_3^{2-} \rightarrow CO_2 + 1/2O_2 + 2e^-$ (2)

This electrochemical process can apply CO_2 separation & concentration systems. We have investigated this mechanism and confirmed the CO_2 separation[2]. This system has high efficiency and can separate very low-level CO_2 gas. (Less than 0.5%). farther this system is very simple than other CO_2 separation system because its not needs mechanical pumping or pressurized system.

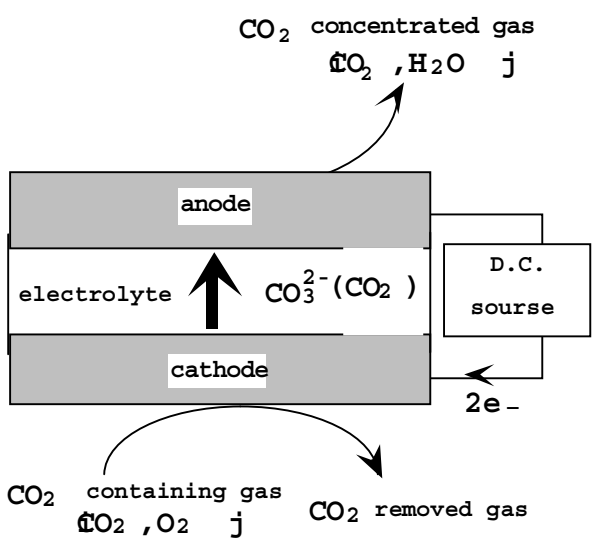

Fig.1 Schematic drawing of CO_2 separation using molten carbonate electrolytic cell.

The reaction (2) is the reverse of (1). Raw gas is introduced into the cathode and carbonate ions are formed. Carbonate ions move from the cathode to the anode. CO_2 and O_2 are produced by the decomposition of carbonate ions at the anode with a ratio of 2:1. Therefore the concentration of CO_2 at the outlet is 67 %. And 33 % O_2 is obtained theoretically, that means the concentration of O_2 is also increased in this process. The theoretical potential difference Ur for reactions (1) and (2) is expressed as follows,

$$Ur = (RT/2F)\ln(Pco_{2(a)}Po_{2(a)}^{0.5}/Pco_{2(c)}Po_{2(c)}^{0.5}) \quad (3)$$

Where (a) and (c) indicate the anode and cathode, respectively. When oxygen pressure is the same at the cathode and anode at 923 K. Only 0.09 V is required for 10 times concentration of CO_2. In this process, the over potential arising from electrode kinetics and resistance of the electrolytic cell are key factors for the practical application. Then we attempted to confirm the concentration of CO_2 in this study.

Experimental

Cell components of the electrolytic cell are shown in Fig. 2. SUS310S was used for housing material and the current collector was SUS316L. The electrolytic matrix was $LiAlO_2$ and the electrolyte is carbonate mixture.

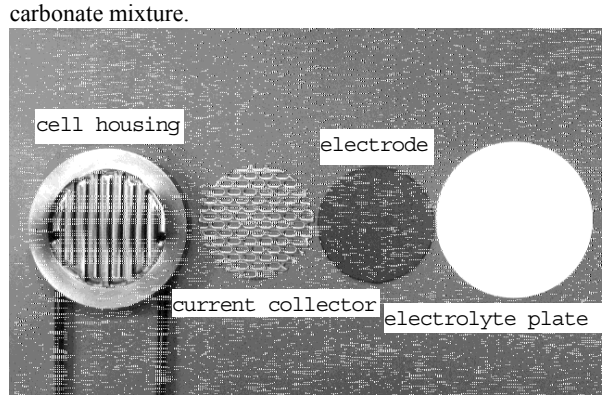

Fig.2 The example of small Cell Components.

The electrolyte plates and electrodes were formed by tapecasting. Both electrodes consist of porous NiO that oxidized and lithiated with carbonate. These components specifications are described in Table 1. We can make over $1m^2$ size of these parts. Cell operating conditions are indicated in Table 2.

Parts	Material
Cathode	NiO(porous)
Anode	NiO(porous)
Electrolyte plate	Li_2CO_3/K_2CO_3=70/30(electrolyte) LiAlO2(Matrix)

Table 1. Cell component specifications.

Result and Discussion

During electrolysis, the example of gas composition of anode outlet is shown in Table 3. The concentration of CO_2 in Cathode inlet is closed to the value of the exhaust gas from electric power station. Anode outlet gas was always maintained at CO_2 66.7 %, O_2 33.3 %. CO_2 concentration in the anode outlet gas was 130 times higher than that of cathode inlet gas in our cell test.

This composition is equal to the theoretical value determined based on the stoichiometric ratio of carbonate ion decomposition at the anode. Further more in this case, increase of O_2 concentration is also possible. The flow rate of anode outlet gas agreed with the theoretical flow rate calculated from the cell current. Therefore it was found that the current efficiency for CO_2 separation was almost 100 %. At 150 mA/cm^2 of current density, approximately 1 cm^3 CO_2 separates per 1cm^2 electrode area from the cathode to the anode.

Temperature	923 K
Pressure	0.1Mpa
Cathode gas flow rate (inlet)	300 cm^3/min
Anode gas flow rate (inlet)	0 cm^3/min
Current density	0～150 mA/cm^2

Table 2. Condition of cell test

Sampling position	O2(%)	N2(%)	CO2(%)
Cathode inlet	20.9	70.6	0.5
Anode outlet	33.3	0	66.7

Table 3. the example of gas composition of cell

The cell voltage, which actually decided the efficiency, significantly depended on current density during electrolysis. This relation is shown in Fig. 4 .

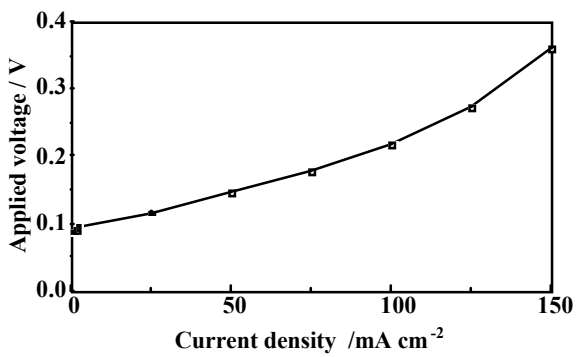

Fig.4 I-V curve of CO2 separation at 923K. The gas composition of Cathode is O2/N2/CO2=19/71/10

The cell voltage includes potential difference of both electrodes gases, over potential of the electrodes reactions and internal resistance of the cell (IR loss). IR loss of the cell was obtained by internal resistance and current. Therefore over voltage (Up) of reactions may be determined by subtracting potential difference (Ur) for CO_2 concentration from equation (3) and IR loss (U_{IR}) from total cell voltage (U) by the equation (4):

$$U_p = U - U_r - U_{IR} \qquad (4)$$

From equation (4), the sum of over voltage due to cathode and anode reactions was 200 mV. These result shown in Fig.5.

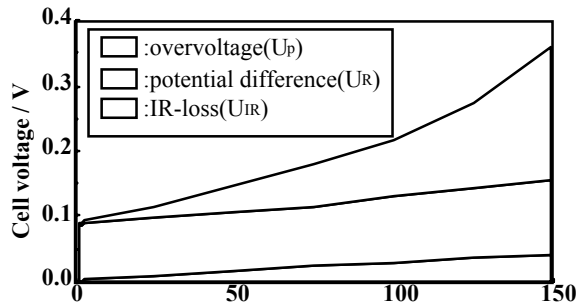

Fig. 5 Constitution of cell voltage for electrolytic CO2 separation at 923K. The gas composition of Cathode is O2/N2/CO2=19/71/10

Conclusion

CO_2 separation and concentration were confirmed to occur in a high temperature electrolysis cell using molten carbonate and NiO electrodes. Current efficiency was almost 100 % and stoichiometric gas composition at the anode outlet was obtained.

References

1. J.L.Weaver and J.Winnick, *J.Electrochem.Soc.*,**1983**, 130, 20.
2. H.Kasai, T.Matsuo, M,Hosaka, N.Motohira, N.Kamiya,K.Ota, DENKKI KAGAKU,**1998**,66,635-640

ELECTROCHEMICAL REDUCTION OF CO_2 TO METHANE IN METHANOL AT LOW TEMPERATURE

S. Kaneco,[1] M. Yabuuchi,[1] H. Katsumata,[1] T. Suzuki,[2] and K. Ohta[1]

[1]Department of Chemistry for Materials,
Faculty of Engineering,
Mie University, Tsu, Mie 514-8507, Japan
kaneco@chem.mie-u.ac.jp

[2]Environmental Preservation Center,
Mie University, Tsu, Mie 514-8507, Japan

Introduction

In the past 60 years, the amount of anthropogenic carbon dioxide (CO_2) emitted to the atmosphere, primarily because of expanding use of fossil fuels for energy, has risen from preindustrial levels of 280 parts per million (ppm) to present levels of over 365 ppm. Consequently, the dire warning of severe weather perturbations and globally rising temperatures have been given. Although scientists, engineers, policy makers, and others are looking for ways to reduce the growing threat of climate change, there is no single answer. Therefore, the development of carbon capture and sequestration technologies, which has accelerated greatly in the last decade, may play a significant role in addressing this issue. Carbon sequestration can be defined as the capture and secure storage of carbon that would otherwise be emitted to or remain in the atmosphere. In order that CO_2 can be economically transported and sequestered, carbon capture prefers a relatively pure stream of the gas. Pathways for carbon capture come from potential sources such as several industrial processes which produce highly concentrated streams of CO_2 as a byproduct, power plants which emit more than one-third of CO_2 emissions worldwide and the production method of hydrogen fuels from carbon-rich feedstocks. CO_2 can be removed from the gas streams by physical and chemical absorption. Recently, the chemical absorption using amines represents the most widely deployed commercial technology for capture. However, in other commercial applications, the typical solvents for physically absorbing CO_2 include glycol-based compounds and cold methanol.

Methanol is a better solvent of CO_2 than water, particular at low temperature, because the solubility of CO_2 in methanol is approximately five times that in water at ambient temperature and eight to fifteen times that in water at temperatures below 273 K.[1] Therefore, methanol has been industrially used as the physical absorbent of CO_2 in Rectisol method at low temperature.[1] Currently, over 70 large-scale plants apply the Rectisol process.

On the other hand, for the CO_2 sequestration technologies, the chemical conversion of CO_2 by radiochemical, chemical, thermochemical, photochemical, electrochemical and biochemical procedures has been of significant interest from the practical viewpoints. The electrochemical method appears to be a very suitable method for the conversion and reduction of CO_2. Since the present conversion efficiencies of single crystal, polycrystalline and amorphous silicon solar cells attainable in laboratory experiments are at the respective levels of about 20 %, 15 % and 12%, respectively, one possible system to industrially convert CO_2 to useful products may be a hybrid method of the solar cell and the CO_2 electrochemical reduction cell. Therefore, a combination technology of the Rectisol CO_2 absorption process and the electrochemical CO_2 conversion method will be able to apply the large scale plant.

Recently, many investigators have actively studied the electrochemical reduction of CO_2 using various metal electrodes in organic solvents, because organic aprotic solvents dissolve much more CO_2 than water.[2-4] It has been described that low reduced products containing carbon monoxide, oxalic acid and formic acid were produced by the electroreduction of CO_2 in dimethly sulfoxide, *N,N*-dimethyl formamide, propylene carbonate and acetonitrile. However, even at a cupper electrode, few hydrocarbons have been obtained in these organic solvents. Therefore, we tried to the electrochemical reduction of CO_2 at Cu electrode in methanol-based electrolyte.[5-7] In the electrochemical CO_2 reduction system using methanol, hydrocarbons were formed with relatively high Faradaic efficiencies and their Faradaic efficiencies increased with decreasing temperature.

Since the electrochemical reduction of CO_2 in organic solvents except for methanol was investigated only at ambient temperature,[2-4] there is little information on the effect of low temperature on the electrochemical CO_2 reduction in organic solvents. Therefore, in the present paper, the electrochemical reduction of CO_2 on copper electrode at 273 K are studied in a variety of organic solvents containing dimethly sulfoxide, *N,N*-dimethyl formamide, propylene carbonate, acetonitrile, ethanol, and methanol. The product distribution in the electrochemical reduction of CO_2 on copper electrode in methanol at 273 K is compared with those obtained in the residual organic solvents.

Experimental

The apparatus and experimental conditions for the electrochemical reduction of CO_2 are shown in **Table 1**. The electrochemical reduction of CO_2 was performed in a home-made, divided H-type cell. An Aldrich Nafion 117-type ion exchange membrane (0.18 mm thickness) was used as the diaphragm. The cathode potential was measured with respect to a silver rod quasi-reference electrode (QRE).

Dimethly sulfoxide, *N,N*-dimethyl formamide, propylene carbonate, acetonitrile, ethanol, and methanol was used as the catholyte. 300 mmol-dm^{-3} lithium perchlorate (Nacalai Tesque, Inc.) was used as the ionophore in the catholyte. Mechanical processing of the Cu and Pt electrodes required polishing each surface with successively finer grades of alumina powder (Baikalox emulsion, manufactured by Baikowski International Co.) down to 0.05 . m, followed by the removal of grease with acetone. Both electrodes were activated electrochemically at 500 mA, for 100 s, in 14.7 mol-dm^{-3} phosphoric acid. Following the above treatment, the electrodes were rinsed with both water and ethanol.

A discontinuous electroreduction procedure was used: first, CO_2 gas was bubbled into the catholyte for 1 h at a rate of 30 ml-min^{-1},

Table 1. Apparatus and experimental conditions

Electrochemical reduction	
Cell	H-type cell
Potentiostat/ galvanostat	Hokuto HA-105
Coulometer	Integrator 1109 (Fusou Seisakujyo, Inc., Japan)
Potential sweep	Hokuto HB-111 function generator
XY recorder	Graphtec WX1100
Thermostat	EYELA, Tokyo Rikakikai CO., LTD., CA-1500
Working electrode	Cu foil (30 mm × 20 mm, 0.1 mm thickness, 99.98 % purity)
Counter electrode	Pt foil (30 mm × 20 mm, 0.1 mm thickness, 99.98 % purity)
Reference electrode	Silver rod quasi-reference electrode
Electrolyte	
Catholyte	300 mmol-dm^{-3} $LiClO_4$ in dimethly sulfoxide, N,N-dimethyl formamide, propylene carbonate, acetonitrile, ethanol, and methanol
Anolyte	300 mmol-dm^{-3} KOH in methanol
Carbon dioxide	99.9999 % purity
Potential	-2.0 to -5.5 V vs. Ag/AgCl sat. KCl
Temperature	273 ± 0.5 K
Product analysis	
Gas products	Gas-chromatography
	TCD (GL Science GC-320, Molecular Sieve 5A; 13X-S, Ar and He carrier gas)
	FID (Shimadzu GC-14B, Porapak Q, N_2 and H_2 carrier gas)
Liquid products	HPLC with UV detector (Hitachi L4000)
	TCD and FID gas-chromatography

then the CO_2-saturated solution was reduced electrolytically at cathodic polarizations in the range from -2.0 to -5.5 V vs. Ag QRE. The electrolysis was performed at 273 K. The catholyte was stirred magnetically. The Faradaic efficiency of the main products was calculated assuming that a total of 50 coulombs of charge passed through the cell. Gaseous products obtained during electroreduction were collected in a gas collector and were analyzed by GC. Products soluble in the catholyte were analyzed by using HPLC and GC.

Results and Discussion

Hori et al. found that copper was an excellent electrode for the formation of hydrocarbons.[8] Therefore, copper was used as a cathode in this study. A suitable supporting salt was explored in order to compare the product distributions in the electrochemical reduction of CO_2 on Cu in various organic solvents. Since lithium perchlorate rapidly dissolved in all organic solvents tested, it was selected as the ionophore in the present work.

Product Faradaic efficiency

In the electrochemical reduction of CO_2 at Cu electrode in dimethly sulfoxide, when the temperature decreased to 273 K, the current density at –3.0 V was very low. Therefore, in order to obtain the current density enough to evaluate the product Faradaic efficiency, the electrolysis was performed at –5.0 V. In the electrolysis, dimethly sulfoxide was not stable and decomposed. Because the current efficiency of this decomposition could not be negligible, the electrochemical reduction of CO_2 on Cu electrode in dimethly sulfoxide at low temperature seems to be not an effective technology.

In the CO_2 electrochemical reduction on Cu in *N,N*-dimethyl formamide and propylene carbonate at low temperature, the current densities even at relatively negative potential were extremely low. Therefore, the CO_2 electrochemical reduction method using *N,N*-dimethyl formamide and propylene carbonate at 273 K appears to be able to apply the practical system.

The results dealing with the effect of the potential on the current efficiencies for the products by electrochemical reduction of CO_2 on Cu in $LiClO_4$/ethanol at 273 K are illustrated in **Figure 1**. Methane was detected as reduction product from CO_2. However, the formation efficiency was less than 2 %. The current efficiency for hydrogen was approximately 100 %. Hence, the applied energy was wasted on hydrogen evolution instead of being used for the reduction of CO_2. Although the electrochemical reduction of CO_2 was studied at relatively positive potential, the current density was < 1 mA-cm^{-2} and the product formation efficiency with low current density could not be evaluated in the view point of practical value. The product distribution obtained in the electrochemical reduction of CO_2 with

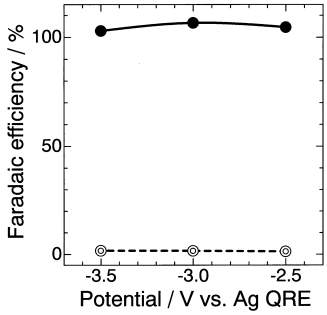

Figure 1. Effect of potential on Faradaic efficiencies for the products by electrochemical reduction of CO_2 at Cu electrode in ethanol at 273 K. CH_4 ; double circle, H_2 ; solid circle.

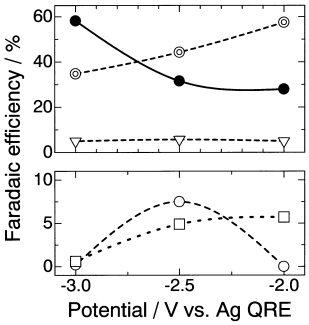

Figure 2. Effect of potential on Faradaic efficiencies for the products by electrochemical reduction of CO_2 at Cu electrode in methanol at 273 K. CH_4 ; double circle, C_2H_4 ; open triangle, CO ; open circle, HCOOH ; open square, H_2 ; solid circle.

copper electrode in acetonitrile was similar to those in ethanol. In the acetonitrile-based electrolyte, the reduction product from CO_2 was only methane and its Faradaic efficiency was < 2 %. On the contrary, the Faradaic efficiency of hydrogen was very large (about 100%).

Figure 2 shows the effect of potential on current efficiencies for the products by electrochemical reduction of CO_2 with Cu electrode in methanol at 273 K. The main products from CO_2 were methane, ethylene, carbon monoxide, and formic acid. The Faradaic efficiency for methane increased to 58 % with decreasing potential. In contrast, hydrogen formation at 273 K decreased to 28 %. A GC-MS study with deuterated methanol catholyte demonstrated that no reduction product was produced from methanol.[5] When the electrolysis was conducted under nitrogen atmosphere, electrolysis yielded exclusively hydrogen. Consequently, the targeted products were produced by the electrochemical reduction of CO_2.

Conclusions

The electrochemical reduction of CO_2 on copper electrode at 273 K was investigated in various organic solvents containing dimethly sulfoxide, *N,N*-dimethyl formamide, propylene carbonate, acetonitrile, ethanol, and methanol. Only in the methanol-based electrolyte, high formation efficiency of methane was observed at low temperature.

Acknowledgement. The present research was partly supported by a Grant-in-Aid for Scientific Research No.12750729 from the Ministry of Education, Science, Sports and Culture of Japan, as well as Industrial Technology Research Grant Program in '00 (No. 00B66010c) from the New Energy and Industrial Technology Development Organization (NEDO).

References

(1) Hochgesand, G. *Ind. Eng. Chem.*, **1970**, 62, 37.
(2) Ito, K.; Ikeda, S.; Iida, T.; Nomura, A. *Denki Kagaku*, **1982**, 50, 463.
(3) Ito, K.; Ikeda, S.; Yamauti, N.; Iida, T.; Takagi, T. *Bull. Chem. Soc. Jpn.*, **1985**, 58, 3027.
(4) Ikeda, S.; Takagi, T.; Ito, K. *Bull. Chem. Soc. Jpn.*, **1985**, 60, 2517.
(5) Naitoh, A.; Ohta, K.; Mizuno, T.; Yoshida, H.; Sakai, M.; Noda, H. *Electrochim. Acta*, **1993**, 38, 2177.
(6) Kaneco, S.; Iiba, K.; Ohta, K.; Mizuno, T. *Int. J. Energy Envion. Econ.*, **1998**, 7, 153
(7) Kaneco, S.; Iiba, K.; Suzuki, S.; Ohta, K.; Mizuno, T. *J. Phys. Chem. B*, **1999**, 103, 7456.
(8) Hori, Y.; Kikuchi, K.; Suzuki, S. *Chem. Lett.*, **1985**, 1695.

A STUDY ON FACILITATED TRANSPORT MEMBRANES FOR REMOVAL OF CO_2 FROM CH_4

Ying Zhang, Zhi Wang, and Shichang Wang*

Chemical Engineering Research Center, School of Chemical Engineering and Technology, Tianjin University, Tianjin 300072, China

Introduction

The membrane separation for removal of carbon dioxide from natural gas has advantages over the conventional separation methods because of low capital, high-energy efficiency and the environmental friends. Usually, the commercially available polymeric membranes have either high permeability or high selectivity, but not both[1]. However, facilitated transport membranes (including supported liquid membranes (SLMs), ion-exchange membranes and fixed carrier membranes) selectively permeate CO_2 by means of the reversible reaction between CO_2 and the carriers in the membranes, so that they possess high permeability as well as high selectivity. The fixed carrier membranes are generally favorable compared with SLMs and ion-exchange membranes for their superior durability.

In recent years, the fixed carrier membranes, especially the CO_2 separation membranes with facilitated transport groups, amine moiety, have been investigated extensively[2-4].

We think it is more beneficial for the facilitated transport of CO_2 to introduce more kinds of carriers than one in a membrane. On the basis of this idea, we developed two kinds of membrane materials with second amine and carboxyl groups, the latter also acts as a carrier of CO_2, by the hydrolysis of polylvinylpyrrolidone(PVP) and vinyl pyrrolidone-acrylamide copolymer respectively. Then, the fixed carrier composite membranes with the materials for CO_2 separation were prepared.

Experimental

Materials. The PVP was synthesized through radical polymerization in 20% N-vinyl pyrrolidone aqueous solution by using azobisisobutyronitrile(AIBN) (it was twice recrystallized from ethanol) as the initiator at 60 °C in the inert atmosphere of nitrogen gas[5]. The PVP was hydrolyzed in an alkali solution at boiling temperature (scheme 1). The resulting polymer was precipitated by using acetone, then the polymer was dissolved in water. This aqueous solution was purified with ion-exchange resin to remove low-molecular-weight impurities and the purified polymer solution was used for membrane-casting.

The copolymer of N-Vinyl pyrrolidone and acrylamide(AAM) was prepared as the same method, but the reaction temperature is 50°C. The hydrolysis and treatment are as above (scheme 2).

Analysis. The content of active carriers (second amine and carboxyl groups) was measured by titration. The molecular weight of resulting polymer was roughly obtained from the intrinsic viscosity.

Membrane preparation and evaluation. The purified polymer solution was cast on a polysulfone(PS) support membrane by an applicator to form composite membrane. The gas permeation experiments were carried out by using a set of test cell. The effective area of the composite membrane used in the test cell is 19.26 cm^2. Prior to contacting the membrane, both the feed and the sweep (H_2) gases were passed through gas bubblers containing water. The outlet sweep gas composition was analyzed by a gas chromatography equipped with a thermal conductivity detector (HP4890, Porapak N). The fluxes of CO_2 and CH_4 were calculated from the sweep gas flow rate and its composition. The permeance is defined as the flux divided by the partial pressure difference between the upstream and downstream sides of the membrane, $R_i = N_i / \Delta P_i$, and the selectivity α was defined as the ratio of the CO_2 permeance to the CH_4 permeance. The downstream pressure in our apparatus is one atmosphere pressure.

Results and Discussion

Figures 1 and 2 show the effects of feed gas pressure on the performances of the membrane (membrane material was prepared by scheme 1). Both permeance of CO_2 and selectivity of CO_2/CH_4 decrease with the raising of feed pressure. This is the characteristic of the facilitated transport mechanism[6]. The facilitated transport mechanism with the carriers of second amine and carboxyl groups is as follow [6,7]:

$$RNH(CH_2)_3COO^- + 2H_2O + 2CO_2 \rightleftharpoons 2HCO_3^- + RNH_2^+(CH_2)_3COOH$$

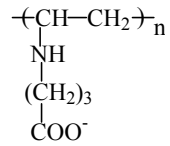

Scheme 1

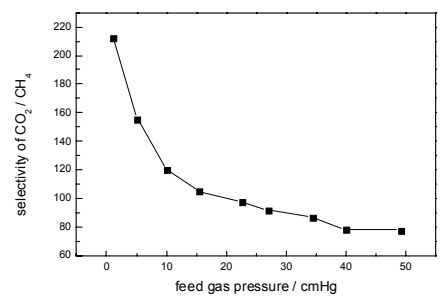

Figure 1. Effect of feed pressure on selectivity of CO_2 over CH_4 by using pure gases respectively.
Membrane material: scheme 1.Testing temperature: 27°C.

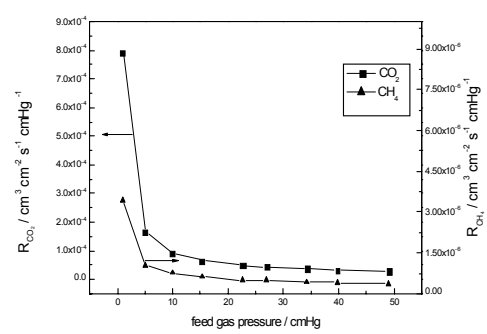

Figure 2. Effect of feed pressure on permeance by using pure gases respectively.
Membrane material: scheme 1.Testing temperature: 27°C.

CO_2 is transformed into small and easy moving ion HCO_3^-, therefore, the transport of CO_2 is enhanced by the carriers. From the standpoint of the membrane structure, the high polarity in the membrane diminishes the solubility of non-polarity component (CH_4),

this is helpful to increase the CO_2 permeation and the selectivity of CO_2 over CH_4. Furthermore, the membrane is swollen by water and forms gel. So that the diffusion coefficient is enhanced due to the decrement of movement resistance. As a result, the membrane possesses high CO_2 permeance and CO_2/CH_4 selectivity which are comparable with that of other fixed membranes in literatures[3,4].

Permeation of CH_4 is a simple solution-diffusion process. The permeance of CH_4 decreases with increasing pressure, in accordance with the "dual-mode" sorption model of gas permeation through glassy polymers [8].

The composite membrane performances were also investigated by using mixed gases (50/50 vol% CO_2/CH_4 mixture), as shown in **Figure 3** and **Figure 4**. From the Figures, it can be seen that the selectivity of CO_2 over CH_4 and permeance of CO_2 are not as good as in Figures 1 and 2. The reason may be the coupling effects between CO_2 and CH_4.

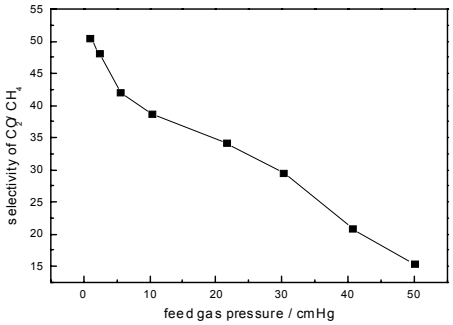

Figure 3. Effect of feed pressure on selectivity by using mixed gas. Membrane material: scheme 1.Testing temperature: 27°C. Feed gas: 50 vol% CO_2+50 vol% CH_4.

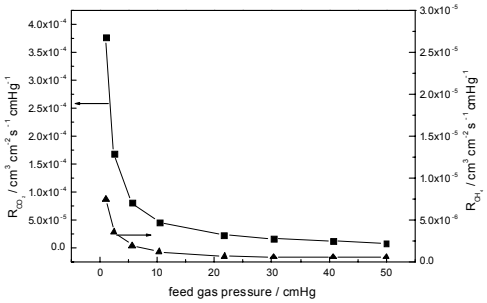

Figure 4. Effect of feed pressure on permeance by using mixed gas. Membrane material: scheme 1.Testing temperature: 27°C. Feed gas: 50 vol% CO_2+50 vol% CH_4.

The performances of the composite membrane which was prepared by scheme 2 were also investigated with mixed gas (50/50 vol% CO_2/CH_4 mixture), as shown in **Figure 5** and **Figure 6**. From the results, it can be seen that the membrane possesses better permselectiviy and it is accordance with the facilitated transport mechanism.

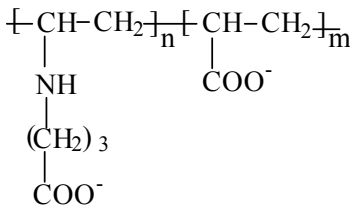

Scheme 2

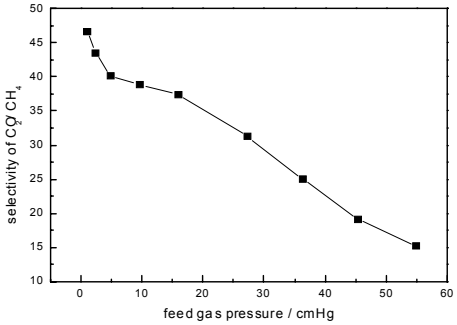

Figure 5. Effect of feed pressure on selectivity by using mixed gas. Membrane material: scheme 2. NVP: AAM =70:30(mass). Testing temperature: 20°C. Feed gas: 50 vol% CO_2+50 vol% CH_4

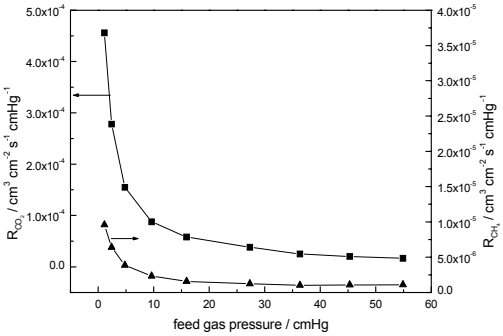

Figure 6. Effect of feed pressure on permeance by using mixed gas. Membrane material: scheme 2. NVP: AAM =70:30(mass). Testing temperature: 20°C. Feed gas: 50 vol% CO_2+50 vol% CH_4

Acknowledgement

This research is supported by the Natural Science Foundation of China (No.29976031, No.29876027), the Natural Science Foundation of Tianjin and the Foundation of Outstanding Teacher at University.

References

1. Robeson, L. M. *J. Membr. Sci*., **1991**, 62,165-185.
2. Wang, Z.; Zhen, H. F.; Li, B. A.; Ren, Y.; Wang, S. C. *J. Chem. Ind. & Eng (ch)*., **2000**, 51(6), 823-825.
3. Yoshikawa, M.; Fujimoto. K.; Kinugawa, H.; Kitao, T.; Ogata, N. *Chem. lett*., **1994,** 243-246.
4. Matsuyama, H.; Terada, A.; Nakagawara, T.; Kitamura, Y.; Teramoto, M. *J. Membr. Sci.,* **1999**, 163, 221-227.
5. Mathakiya, I.; Rakshit, A. K. *J. Appl. Polym. Sci*., **1998**, 68, 91-102.
6. Quinn, R.; Appleby, J. B.; Pez, G. P. *J. Membr. Sci.,* **1995,** 104, 139-146.
7. Matsuyama, H.; Teramoto, M.; Sakakura, H. *J. Membr. Sci.,* **1996**, 114, 193-200.
8. Houde, A. Y.; Krishnakumar, B.; Charati, S. G.; Stern, S. A. *J. Appl. Polym. Sci.,* **1996,** 62, 2181-2192.

CO_2 CAPTURE UTILIZING SOLID SORBENTS

Ranjani Siriwardane, Ming Shen, Edward Fisher, and James Poston

U.S. Department of Energy
National Energy Technology Laboratory
3610 Collins Ferry Road, P.O. Box 880
Morgantown, WV 26507-0880
(rsiriw@netl.doe.gov; 304-285-4513, Fax: 304-285-4403)

Introduction

Fossil fuels supply more than 98 percent of the world's energy needs. However, the combustion of fossil fuels is one of the major sources of the greenhouse gas, CO_2. It is necessary to develop technologies that will allow us to utilize the fossil fuels while reducing the emissions of greenhouse gases. Commercial CO_2 capture technology that exists today is very expensive and energy intensive. Improved technologies for CO_2 capture are necessary to achieve low energy penalties. Pressure swing adsorption (PSA) is one of the potential techniques that could be applicable for removal of CO_2 from high-pressure gas streams, such as those encountered in integrated gasification combined-cycle (IGCC) systems.

PSA processes[1-4] are based on preferential adsorption of the desired gas (e.g., CO_2) on porous materials at a high pressure. When the pressure is decreased, the gas is desorbed from the porous sorbent and the sorbent can be reused for subsequent adsorption. PSA technology has gained interest due to low energy requirements and low capital investment costs. Development of regenerable sorbents that have high selectivity for CO_2 and high adsorption capacity for CO_2 is critical for the success of the PSA process.

The objective of this work is to understand the adsorption properties of CO_2 on both synthetic and natural molecular sieves[5] that can be utilized in PSA processes. In this work adsorption and desorption of CO_2 was studied on both synthetic and natural zeolites. Volumetric adsorption and desorption studies of CO_2, N_2, O_2, or H_2 with the sorbents were conducted at 25 °C up to a pressure of 300 psi (~2 x 10^6 Pa). Competitive gas adsorption studies were also conducted with CO_2-containing gas mixtures in the presence of water vapor.

Experimental

Adsorption and desorption isotherms at 25 °C of pure CO_2, N_2, O_2, and H_2 on molecular sieves Z10-08 and Z10-10 (proprietary zeolites from Sud Chemie) and three natural zeolites were measured up to an equilibrium pressure of about 300 psi (~2 x 10^6 Pa) utilizing a volumetric adsorption apparatus. Approximately 10 ml of the sorbent materials were placed in the sample chamber, which was evacuated to ~5 x 10^{-5} Torr (~6.75 x 10^{-3} Pa). The amount of CO_2 adsorbed was calculated utilizing the pressure measurements before and after the exposure of the sample chamber to CO_2. Desorption studies were conducted by gradually decreasing the pressure from 300 psi after the adsorption cycle. After each cycle the sorbent was evacuated overnight. Competitive gas adsorption studies were conducted in a lab-scale, fixed-bed reactor at 14.7 psi (~1.01 x 10^5 Pa) using a gas mixture with a composition of 15 percent CO_2, 82 percent N_2, 3 percent O_2 in the presence of water vapor at ambient temperature. The samples were heated at 100 °C for 1 hour and cooled down to ambient temperature before the introduction of the gas mixture.

Results and Discussion

Volumetric adsorption/desorption isotherms of CO_2, N_2, O_2, and H_2 on molecular sieve Z10-08 at 25 °C are shown in **Figure 1**. The CO_2 adsorption increased rapidly when the pressure was increased up to 50 psi but the CO_2 adsorption after 50 psi appeared to be gradual. At all pressures, adsorption isotherms of nitrogen were lower than those of CO_2, and adsorption isotherms of hydrogen were significantly lower than those of CO_2. Preferential adsorption of CO_2 indicates that this material can be used for separation of CO_2 from some gas mixtures. The adsorption and desorption isotherms were very similar indicating that the adsorption of CO_2 on Z10-08 is reversible. Thus, the adsorbed CO_2 can be recovered by lowering the pressure.

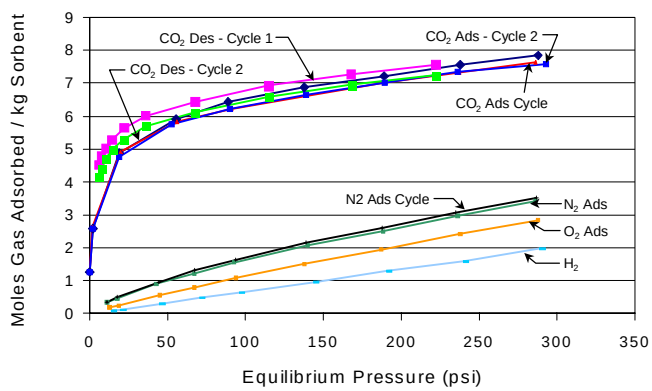

Figure 1. Adsorption and desorption isotherms of Z10-08.

The results of the competitive gas adsorption studies conducted utilizing a gas mixture of 15 percent CO_2, 82 percent N_2, 3 percent O_2, and water vapor on molecular sieve Z10-08 in the atmospheric micro reactor are shown in **Figure 2**. The gas mixture was introduced to 1 g of molecular sieve at a flow rate of 15 cc/min and at 25 °C. After the introduction of the gas mixture to the molecular sieve Z10-08, the CO_2 concentration decreased to almost zero until the breakthrough. This indicates that an excellent separation of CO_2 can be obtained from a gas

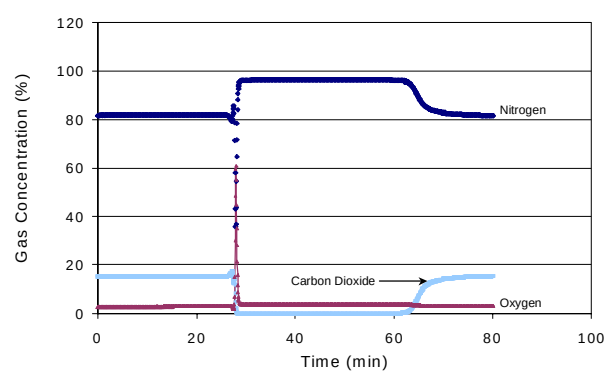

Figure 2. Competitive adsorption of CO_2, N_2, and O_2 on Z10-08 *(15% CO_2, 3% O_2, 82% N_2, and saturated with water vapor at 25 °C, 15 cc/min).*

mixture of N_2, O_2, H_2O, and CO_2 with molecular sieve Z10-08. The total amount of CO_2 adsorbed at the breakthrough or saturation as calculated from the data was about 2.5-3 moles/kg of the sorbent. This value is very similar to the amount of CO_2 adsorbed at 1 atm from volumetric equilibrium adsorption studies, as shown in **Figure 1**. This indicates that the full capacity of the molecular sieve Z10-08 was utilized for CO_2 adsorption during competitive gas adsorption from a CO_2, N_2, O_2, and water vapor mixture. It is apparent that the water vapor does not affect the adsorption of CO_2 on molecular sieve Z10-08.

The results of both volumetric gas adsorption isotherm studies and competitive gas adsorption studies in the micro reactor of molecular sieve Z10-10 were very similar to that of Z10-08. However, the CO_2 adsorption capacity at high pressure (2×10^6 Pa) of Z10-08 was better than that of Z10-10.

The properties of three natural zeolites are shown in **Table 1**. The gas adsorption isotherms on the three natural zeolites indicated that there is preferential adsorption of CO_2 with all three zeolites. The adsorption capacities of both synthetic and natural zeolites are shown in **Table 2**. The natural zeolite with the highest sodium content and the highest surface area showed the highest CO_2 adsorption capacity at both low and high pressures.

Table 1. Natural Zeolites

Natural Zeolite	Chemical Composition (wt% Ratios)	Average Pore Diameter (A^0)	Surface Area (m^2/g)
Natural Herschelite-Sodium Chabazite	Sodium alumino silicate 1 Na_2O/K_2O - 7.4 SiO_2/Al_2O_3 = 3.7	4.3	520
Clinoptilolite	Sodium alumino silicate 2 Na_2O/K_2O - 1.1 SiO_2/Al_2O_3 = 6.3	4.3	40
Clinoptilolite	Potassium calcium sodium alumino silicate Na_2O/K_2O - 0.3 SiO_2/Al_2O_3 = 5.1 CaO/K_2O = 1	4.3	40

Table 2. Comparison of CO_2 Capture Capacities of Different Sorbents

Sorbents	Moles of CO_2/kg at 1 atm	Moles of CO_2/kg at 20 atm
Sythetic Zeolites		
Z10-08	2.5 - 3	7 - 8
Z10-10	2.5 - 3	6 - 8
Natural Zeolites		
Sodium Alumino Silicate 1	1 - 1.5	4 - 5
Sodium Alumino Silicate 2	0.5 - 1	2 - 2.5
Calcium Potassium Alumino Silicate	0.1 - 0.2	1 - 1.5

Conclusions

All molecular sieves showed preferential adsorption of CO_2 over nitrogen, oxygen, and hydrogen at all pressures up to 250 psi. The molecular sieve Z10-08 showed better CO_2 uptake than the other zeolites. Water vapor and oxygen did not affect the adsorption of CO_2 on synthetic molecular sieves during competitive gas adsorption studies.

References

(1) Skarstrom, C. W. U.S. Patent 2,944,627, **1960**.
(2) Guerrin de Montgareuil, P.; Domine, D. U.S. Patent 3,155,468, **1964**.
(3) Cheu, K.; Jong-Nam, K.; Yun-Jong, Y.; Soon-Haeng, C. Fundamentals of Adsorption, Proc. Int. Conf., D. LeVan (ed), Kluwer Academi Publishers, Boston, Massachusetts, 1996; pp. 203-210.
(4) Dong, F.; Lou, H.; Goto, M.; Hirose, T. Separation & Purification Technology, **1990**, *15*, 31-40.
(5) Siriwardane, R. V.; Shen, M.; Fisher, E.; Poston, J. Energy and Fuels, **2001**, *15*, 279-284.

COST ESTIMATION OF CO_2 RECOVERY TECHNOLOGY USING HYDRATES

Fumio Kiyono, Akihiro Yamazaki, and Keiichi Ogasawara

Institute for Environmental Management Technology
National Institute of Advanced Industrial Science and Technology
16-1, Onogawa, Tsukuba, Ibaraki, 305-8569, Japan

Introduction

Although the global warming problems may be one of the most crucial matters that will threat the future existence of human beings, the steps for solving are late. Main reason for the delay is said to lie in economical problems. For instance, if we recovered CO2 from a thermal electric power station and sequestrated it in an isolated place we would lose 40% of the total energy produced. Among many cost factors the separation cost accounts for main part. So far several methods, like the amine absorption method or the zeolite adsorption method, have been presented but in those methods we must use expensive chemicals.

Recently the separation technology using hydrates is attracting many concerns, where necessary chemicals for separation are mere water which exists everywhere and is obtained effortlessly. So the hydrate separation technology has a potential as an alternative method since its cost could be low if an appropriate process was developed. In this paper the results of cost estimation is presented when applying the hydrate separation technology to the case of CO2 separation at the thermal electric power station.

Separation mechanisms by hydrates

The basic phenomenon that explains the reason why hydrates can separate the specified constituent from mixed gases is demonstrated in **Figure 1**. The constituent is separated as the solid solutions.

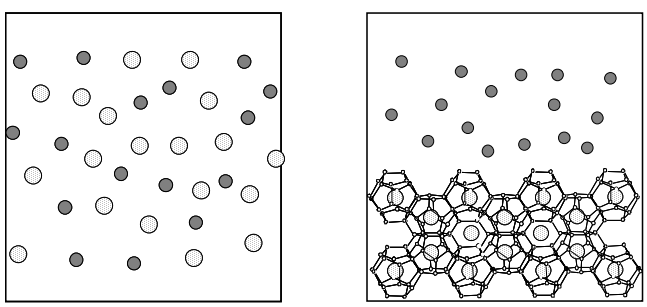

Figure 1. The separation mechanism of the specified constituent from mixed gases by hydrates.

If the mixed gases were compounded of the components that formed hydrates and the components that could not make hydrates, the former components would be captured in hydrates' cages and the latter components should be left in the mixed gases.

In addition intermolecular force between the gas molecule in the cage and water molecules that surrounding the gas molecule is different among gas components, so the specified constituent exists excessively in the hydrate phase.

The mole fraction of each component in hydrate phase depends basically upon the fugacity of each component in the gas phase and the intermolecular potential between the gas molecule and water molecules when they take the hydrate structure. The flue gases from the thermal electric power station contained mainly CO_2, N_2, O_2, and H_2O. Although these components all can make hydrates, but the intermolecular potential is different each other, that enables us to separate CO_2 from other components. The comparison of the intermolecular potential is indicated in **Figure 2**. The potential well depth of CO_2 is deeper than that of other components and it means that CO_2 makes hydrates in more moderate condition than others.

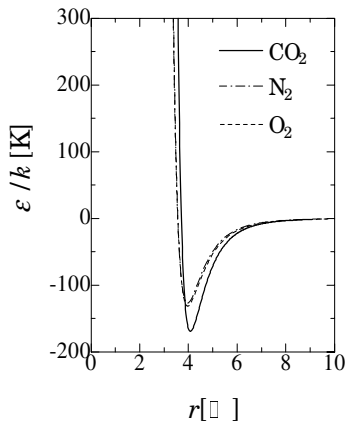

Figure 2. The intermolecular potentials of CO_2, N_2, and O_2.

Hydrate separation process

A simple outline of the hydrates separation process is demonstrated in **Figure 3**. Hydrates are generally formed in high pressure and low temperature conditions. At first the pressure of flue gases is increased up to 20 atm by the compressor. At the same time, the temperature rises up to almost 560°C owing to the work given. This extra heat is recovered at the heat exchanger and utilized to rotate turbine blades in the gas turbine. At the next stage, flue gases are cooled down to 4°C, and then conveyed to the hydrate formation chamber where flue gases make hydrates in contact with sprayed water. The formation heat of hydrates must be removed from the chamber. Then hydrates are carried to the separator and decomposed to water and gases again. The heat of decomposition is supplied from sea water.

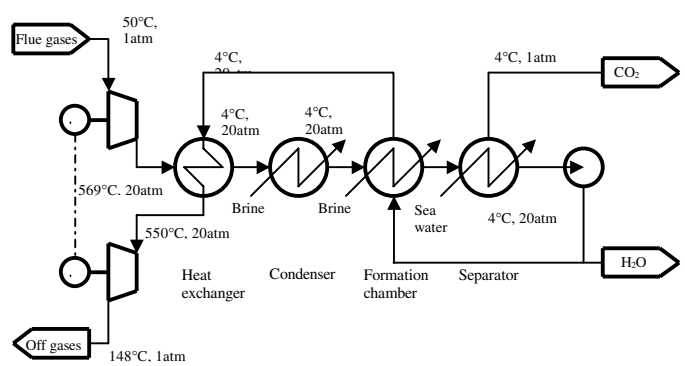

Figure 3. The outline of hydrates separation process.

Composition of flue gases. Main constituents of flue gases are CO_2, N_2, O_2, and water after eliminating NO_X and SO_X. The mole fraction of CO_2 differs according to the type of the electric power station. In case of a coal fired power station the mole fraction of CO_2 is almost 0.15. While in a natural gas fired power station this figure is relatively low. In this estimation the mole fraction of CO2 in flue gases is assumed to be 0.1. The composition of flue gases is

summarized in **Table 1**. The temperature of flue gases is set at 50. and pressure 1 atm. The flow rate of flue gases is guessed at 1 M Nm^3/h.

Table 1. The Composition of Flue Gases

	Mole Fraction	Molar Weight	Feed Rate		
			kmol/h	Nm^3/h	t/h
$CO_2(g)$	0.10	44.010	4,464	100,000	196
$N_2(g)$	0.79	28.010	35,268	790,000	988
$O_2(g)$	0.04	32.000	1,786	40,000	57
$H_2O(g)$	0.07	18.020	3,125	70,000	56
Flue Gases	1.00	29.070	44,643	1,000,000	1298

Compression of flue gases. The flue gases must be compressed to achieve the pressure sufficient to make hydrates. This pressure differs according to the temperature, the composition of flue gases, and whether hydrate promoters exist or not. In this estimation necessary pressure is assumed to be 20 atm.

The temperature of flue gases increases with compression. For simplicity adiabatic compression is adopted. The temperature of flue gases alters from 50°C to 569 °C.

The energy that needs to compress the flue gases can be calculated by the enthalpy difference after and before compression. Mole heat capacities of each component and the mean value of the flue gases are indicated in **Table 2** and results of enthalpy calculation are summarized in **Table 3**. Necessary energy for the compression is 681,637MJ/h.

Table 2. The Mole Heat Capacity of CO_2, N_2, O_2, H_2O, and Flue Gases

	Mole Fraction	Cp J/(K mol)		
		a	10^3b	10^6c
$CO_2(g)$	0.10	26.748	42.258	-14.247
$N_2(g)$	0.79	27.016	5.812	-0.289
$O_2(g)$	0.04	25.594	13.251	-4.205
$H_2O(g)$	0.07	30.204	9.933	1.117
Flue Gases	1.00	27.155	10.043	-1.743

Table 3. The Enthalpy Change of Flue Gases at the Compressor

		a	10^3b	10^6c	
		27.155	10.043	-1.743	
T_1 (K)	T_2 (K)	$a.\Delta T$	$b/2.\Delta T^2$	$c/3.\Delta T^3$	q . J/mol. h)
323	842	14,094	1,353	-81	15,365

Cooling of flue gases. The high temperature of flue gases due to compression must be decreased to the sufficient low temperature to make hydrates. Flue gases are cooled by two steps.

In the first stage the temperature is decreased to 40°C at the heat exchanger by utilizing the off gases (4°C, 20 atm) from the hydrate chamber. This recovered energy is utilized to rotate the gas turbine of the compressor. In the second stage the temperature of 40°C falls down to 4°C. Here brine is used as the coolant. The recovered energy at the heat exchanger is calculated as the difference of enthalpy of gases before cooling and after cooling. Necessary data for the enthalpy calculation and results are indicated in **Table 4**. The recovered energy is 575,000MJ/h.

The removed energy at the condenser is also estimated as the enthalpy difference of flue gases. Data used in the calculation and results are shown in **Table 5**. In this process the heat of condensation of water must be also considered. The enthalpy change due to condensation is 134400MJ/h and that due to cooling is 43400MJ/h, so total enthalpy change at the condenser is 177800MJ/h.

Table 4. The Enthalpy Change of Flue Gases at the Heat Exchanger

		a	10^3b	10^6c	
		27.155	10.043	-1.743	
T_1 (K)	T_2 (K)	$a.\Delta T$	$b/2.\Delta T^2$	$c/3.\Delta T^3$	q . J/mol. h)
842	313	-14,365	1,405	86	-12,874

Table 5. The Enthalpy Change of Flue Gases at the Condenser

		a	10^3b	10^6c	
		27.155	10.043	-1.743	
T_1 (K)	T_2 (K)	$a.\Delta T$	$b/2.\Delta T^2$	$c/3.\Delta T^3$	q . J/mol. h)
313	277	-978	7	0	-971

Formation of CO_2 hydrates. After compression and cooling, flue gases are transported to the hydrates formation chamber where flue gases contact with water and make hydrates. The mole fraction of CO_2 in the hydrate phase is higher than that in flue gases. The recovery rate of CO2 is assumed to be 3844kmole/h.

To continuously make hydrates the heat of formation must be removed from the hydrate chamber. For this purpose brine is utilized. If the heat of formation of hydrates is assumed to be 63kJ/mol, total heat that should be removed from the chamber is 242,200MJ/h.

Dissociation of CO_2 hydrates. After CO_2 is separated from flue gases as hydrates at the hydrate formation chamber, CO_2 hydrates are transported to the separator, where CO_2 hydrates are dissociated to water and gaseous CO_2 again. It is also possible to send CO_2 hydrates to the deep sea bottom without dissociation. The heat is 242,200MJ/h that needs to decompose hydrates.

Cost estimation

Results of the thermodynamic analysis of the process enable us to estimate capacities, sizes, abilities, and so on of necessary equipments like the compressor, the heat exchanger, the hydrate formation chamber, and so on. According to these specifications the cost of facilities can be decided. Also energy cost can be calculated. Final results of the cost estimation are summarized in **Table 6**. In this table the cost of the amine absorption method is also shown for comparison. It is concluded that the hydrates separation method has enough cost competitive position.

Table 6. Results of Cost Estimation

	Hydrates yen/kg-CO_2	Amine absorption yen/kg-CO_2
Depreciation cost	1.02	0.65
Repair & Supplies	0.27	0.17
Labor cost	0.09	0.09
Energy cost	4.18	5.03
Total cost	5.56	5.94

REDUCTION OF CO_2 TO C_1 PRODUCTS AND FUEL

Theodore Mill
SRI
Menlo Park, CA 94025

David Ross
U.S Geological Survey
Menlo Park, Ca 94025

Introduction

The combustion-based production of CO_2 has led to a major international environmental challenge to deal with global climate warming produced by atmospheric CO_2[1]. Global warming is projected to lead to disastrous consequences for most of the low-lying areas of the world[2]. The 1997 Kyoto Treaty to curtail CO_2 emissions includes collection and storage of a significant fraction of the 24 billion tons of CO_2 produced worldwide each year using depleted oil/gas reservoirs, deep saline aquifers, coal beds, and the deep ocean[3].

Sequestering CO_2 is a rational solution to reducing emissions , but a potentially more rewarding route to CO_2 reduction is to use chemical energy available from sunlight-driven semiconductors or from thermally promoted reduction with Fe(II) minerals to convert CO_2 back to C_1 products and fuel; in both cases, water serves as the hydrogen source.

Photoreduction of CO_2

Reduction of CO_2 to a variety of C_1 products using ZnO and $TiO_2$was reported in the early 1980s, but efficiencies generally were low (<5%)[4]. Reduction of CO_2 is effected by a photo-promoted electron with concomitant oxidation of water (Reactions [1] and [2]) by the valence band hole[5]. Generally, reduction efficiencies using bulk semiconductor particles are low. However, Q-ZnS nanoparticles in isopropyl alcohol, gave reduction efficiencies of over 20%[6].

$$CO_2 + 2e^- + 2H \longrightarrow HCO_2H \text{ (conduct band)} \quad (1)$$

$$2H_2O \longrightarrow 4H^+ + O_2 + 2\,e^- \text{ (hole)} \quad (2)$$

Reduction of CO_2 by several other materials, including GaP, WO_3, CdS, $LiNbO_3$, and several doped TiO_2 semiconductors has also been reported[7-12]. The band gap of TiO_2 of ~3.7 eV means that onset of UV absorption is near 360 nm, thus excluding the major fraction of energetic solar photons.

Hematite (Fe_2O_3) has a band gap of about 2.2 eV, thus extending the spectral range of sunlight that can be captured to about 550 nm[13]. The oxidation/reduction potentials are sufficient for Reactions (1) and (2), but electron hole recombination is fast and the reported efficiency of hematite for oxidation of water is low[14]. Nanometer particle films of hematite gave improved efficiency[15].

Ohta and coworkers[16] effected reduction of CO_2 to formate by solar irradiation of rocks containing hematite. Reduction of CO_2 using $CaFe_2O_4$ to methanol and formaldehyde is reported[17].

A variety of C_1 and C_2 products form on reduction of CO_2 depending on the semiconductor, wavelength, solvent polarity, and perhaps other factors[4]. In one case, the product changes from CO in water to formate in dichloromethane with isopropyl alcohol as the reducing agent. In propylene carbonate solvent, CO_2 reduction gave mostly methanol[18].

Thermal Reduction of CO_2

McCollom and coworkers[19-20] found that reaction of dissolved CO_2 with olivine in hydrothermal media, immediately gave formate at 300°C and 350 bar. Some experiments were conducted with no headspace possibly inhibiting further reduction to alkanes, a thermodynamically favored process.

When reduction was conducted with headspace, aqueous formate gave a broad array of Fischer-Tropsch-like products in the alkanes, alkenes, and oxygenated products, at 175°C. When headspace is available, further reduction of formate takes place in the gas phase through the molecular acid, probably on the reactor surfaces. Although no elemental balances were provided in the report, it is likely that the conversions proceeded through a series of highly exoergic formic acid disproportionations, like that in Reaction (3) for the formation of alkanes:

$$(3n+1)HCO_2H \longrightarrow (2n+1)CO_2 + C_nH_{2n+2} + 2n\,H_2O$$

Summary

Photochemical semiconductor processes readily reduce CO_2 to a broad range of C_1 products. However the intrinsic and solar efficiencies for the processes are low. Improved quantum efficiencies can be achieved using quantum-sized particles, but at the expense of using less of the visible solar spectrum. Conversely, semiconductors with small bandgaps utilize more of the visible solar spectrum at the expense of quantum efficiency.

Thermal reduction of CO_2 with Fe(II) is thermodynamically favored for forming many kinds of organic compounds and occurs readily with olivine and other Fe(II) minerals above 200° C to form higher alkanes and alkenes. No added hydrogen is required.

References

1. Stevens, W. K.. Seas and Soils Emerge as Keys to Climate, New York Times, May 16, 2000.
2. Revkin, A. Warming effects to be widespread. New York Times, June 12, 2000.
3. Noserale, D. News release, U.S. Geological Survey, October 22, 1999.
4. Yoneyama, H. Cat. Today **1997**, 39:169.
5. Hagfeldt, A. and Gratzel, M, Chem. Res. **1995**, 95**:**49.
6. Inoue, H., Torimoto, T. Sakata, T. Mori, H. and Yoneyama, H. Chem. Lett. **199**,1483.
7. Inoue, T., Fujishima, A. Konishi, S. and Honda. K. Nature **1979**, 277:637.
8. Aliwi, S. M., Al-Daghasteni. I. J. Solar Energy Res. **1989**, 7:49.
9. Ulman, M., Aurian-Bajeni, B. and Halmann, M. Isr. J. Chem. **1982**, 22:177.
10. Solymasi, F.,. Tombacy, I. Catal. Lett. **1994**, 27:61.

11. Goren, Z., Willner, I.. Nelson, A. J and. Frank, A. J J. Phys. Chem. **1990,** 94:3784.

12. Hoffman, M., Martin, S. T. Choi, W. and. Bahnemann, D. W Chem. Res. **1995**, 95:69.

13. Dare-Edwards, M. P., Goodenough, J. B. Hamnett, A. and Trevelick, P. R. J. Chem. Soc. Faraday Trans. 1 **1983**, 79:2027.

14. Kennedy, J. H., Frese, Jr., K. W. J. Electrochemical Soc. **1978**, 125:109.

15. Bjorksten, V., Moser, J. Gratzel, Chem. Mater. **1994,** 6:858.

16. Ohta, K., Ogawa, H. and Mizuno, T. Applied Geochemistry **2000,** 15:91.

17.Matsumoto, Y., Ohta, M. and Hombo, J. J. Phys. Chem. **1994**, 98:2950.

18. Liu, B.-J., Torimoto, T.. Matsumoto, H and Yoneyama, Y. Photochem. Photobiol. A **1997**,108:187.

19. McCollom, T. M. Presentation at First Astrobiology Science Conference, Ames Research Center, Mountain View, California, April 2-5, 2000.

20. McCollom, T. M., Ritter, G. and. Simoneit, B.R.T . Origins of Life and Evol. of the Biosphere **1999**, 29:153.

EXTRACTION OF CARBON DIOXIDE FROM THE ATMOSPHERE THROUGH ENGINEERED CHEMICAL SINKAGE

M. K. Dubey, H. Ziock, G. Rueff, S. Elliott and W. S. Smith

Earth and Environmental Sciences Division
MS D462, Los Alamos National Laboratory, Los Alamos, NM 87545

K. S. Lackner
H. Krumb School of Mines
Columbia University, New York, NY 10027-4711

N. A. Johnston
Division of Natural Sciences
Lewis-Clark State College, Lewiston, Idaho 83501

Introduction

The 2001 Third Annual Report of the Intergovernmental Panel on Climate Change projects that atmospheric carbon dioxide (CO_2) can approach 1000 ppm in 2100.[1] In addition it concludes that the observed warming over the last 50 years is likely to have been due to the increase in greenhouse gas concentrations, particularly the 30% rise in atmospheric CO_2 caused by man. Fossil fuel use will be limited by our ability to mitigate their environmental effects since they are abundant and cost effective. Future concerns are underscored by the long lifetime of CO_2 in the atmosphere, the accelerating rate of fossil-fuel consumption, and our non-linear climate system that can migrate to a different state in response radiative forcing on decadal time-scales. Consequently technologies for reduction of the world's CO_2 emissions are being explored aggressively. Current emphasis is on fixing CO_2 at large sources such as centralized power plants by emission free conversion of fossil fuels to electricity and hydrogen.[2] However, more than half of the total emissions is from the transportation sector and small distributed sources such as home heating and small industry. Most solutions for dealing with these sources explicitly or implicitly imply a complete overhaul of the existing infrastructure. To surmount this problem Los Alamos National Laboratory has conceived a novel concept of extracting CO_2 directly from the atmosphere by engineering a chemical sink.[3,4]

Direct CO_2 extraction converts the dilute CO_2 (370 ppm) in the atmosphere (from all sources) to a pure CO_2 stream ideal for permanent sequestration. For dealing with the world's total fossil fuel related CO_2 emission rate, extracting CO_2 from the air involves processing of on the order of up to 1% of the earth's atmosphere (containing ~750 Gt CO_2) each year. The fast time scales of atmospheric mixing make this approach feasible. It is a massive undertaking with offsetting advantages:

- Preserves our existing energy use and fuel distribution network that represents a huge investment,
- Captures CO_2 from a myriad of small, distributed, and mobile sources that otherwise are not accessible to sequestration,
- Allows atmospheric CO_2 levels to be restored to their pre-industrial age value,
- Provides free transport of CO_2 to suitable sequestration sites by using the natural atmospheric circulation, and
- Is relatively compact and therefore inexpensive approach when compared to renewable concepts.

This method compensates for all CO_2 sources, can be scaled to yield a net zero or negative emissions, and harnesses the atmosphere as a free CO_2 transportation network.

Our CO_2 extraction from air concept is summarized here and developed it in more detail later. By equating an amount of CO_2 with the energy released in a combustion process, one can associate an energy density with CO_2 in air. By this measure, the energy associated with atmospheric CO_2 is a factor of approximately 100 times more concentrated than wind energy, which is harnessed routinely. Building on this premise our concept harnesses atmospheric circulation to extract CO_2 from air (where it is present at 370 ppm) and binds it to an adsorbent. The saturated absorbent is subsequently heated to release the bound CO_2 thereby generating a pure CO_2 stream for disposal and adsorbent ready for reuse. Low cost chemical extraction reagents such as calcium hydroxide (a prime ingredient in mortar) readily extract CO_2 and demonstrate the feasibility. The reagents would be continuously recycled with the captured CO_2 being recovered and sent to a permanent disposal process such as the mineral carbonation of serpentine deposits that permanently sequester the CO_2 as solid, harmless, and inert mineral carbonates,[5] or direct injection in underground reservoirs or in the deep ocean.

Case for CO_2 Extraction from Air

Concept. To determine the viability of CO_2 extraction from air we compare it to renewable energy options, examining the relative size and therefore likely cost and environmental impact. We also examine the energy requirements of one specific approach to CO_2 capture, which although far from ideal demonstrates feasibility. Our estimates are meant to establish orders of magnitude rather than precise values. The yardstick we employ is the primary energy per unit area and unit time available. We start by examining wind power, which is routinely harvested, albeit on a modest scale. The power per unit area is given by $1/2\ \rho v^3$, where ρ is the density of air and v is its wind velocity. At 10 m/s the wind power contained in the airflow is 0.6 kW/m^2. The time averaged power flux from sunlight on the ground is less, amounting to 0.2 kW/m^2 in the US. The equivalent power collected by biomass represents no more than 0.003 kW/m^2 of heat of combustion amounting to 50t of dry mass hectare^{-1} year^{-1}.

For the extraction of CO_2 from the atmosphere, we consider the same airflow as for wind power. The 10 m^3 of air that flows through the 1 m^2 aperture in one second contain 0.15 moles of CO_2. There is of course no energy in this CO_2. However, if we were to remove all CO_2 from the 10 m^3 of air, we would then be able to burn a certain amount of carbon based fuel without increasing the net CO_2 content of the air. For gasoline we would generate 100 kJ of heat energy per second, less for coal and more for natural gas. Thus in the above example, a combined CO_2 extraction unit/gasoline motor would be able to produce 100 kW/m^2 of primary energy without any impact on the atmospheric level of CO_2. In contrast, a windmill of the same area would only draw on 0.6 kW/m^2 of raw power, a factor of over 100 less. Comparison with other renewable resources is even more dramatic.

Process Description. The low CO_2 concentration in air limits the choice of collection methods. Chemical or physical absorption from an essentially free flow atmospheric air stream appears to be the only viable option. For absorption, the primary energy demand lies in absorbent recycling. The free energy of mixing sets a lower bound on energy expenditure. It is given by $RT \log(P/P_0)$. P_0 is the ambient CO_2 partial pressure, P the desired output pressure, R is the gas constant, and T, the absolute temperature. Separating CO_2 from air at ambient conditions and delivering the output at 1 bar requires 20 kJ/mole. This is only 3% of the energy released in the combustion of gasoline. However, practical implementations will require more energy for rapid CO_2 absorption and concentration.

As air moves over an absorber surface, CO_2 is stripped out. The rate of extraction depends on the efficiency of the absorber, but even the best absorber is limited by the transport of CO_2 through air. The molecular diffusion coefficient of CO_2 in air at ambient temperature is $D = 1.39 \times 10^{-5}$ m^2/s. The mass flux to an absorbing surface is given by $\mathbf{N} = D\ \mathbf{grad}\ \rho_{CO_2}$, ρ_{CO_2} being the local density of CO_2 in the air. For a good absorber, the partial pressure of CO_2 at the absorption surface nearly vanishes, and the mass flux, N_0, to a boundary is given approximately by $N_0 = D\ \rho_{CO_2}/\ L$. Here, L is the transport distance; *i.e.* the typical distance to the nearest surface or for an open system the thickness of a boundary layer. As a specific example, consider air flowing at 10 m/s through a set of parallel tubes, 2.5 mm in diameter. Empirical formulae suggest an effective $L = R/1.8$, where R is the radius of the tube. Comparing the CO_2 flux to the wall with the CO_2 flux through the tubes suggests that most of the CO_2 will be removed after ~ 30 cm. The distance over which the CO_2 is absorbed is proportional to the flow velocity. With a typical velocity of 3 m/s the length of the tube is reduced to less than 10 cm.

In passing over an absorber that removes a portion of the CO_2 from the air-stream, a similar fraction of the air's momentum will be removed, as these two molecular diffusion processes operate similarly. Thus, for a system designed to extract most of the CO_2, the pressure drop is roughly the kinetic energy density in the gas or about 0.06 kPa at 10 m/s. Thus, maintaining the airflow requires an energy input of 0.06 kJ/m^3, which is less than 1% of the energy released in producing that CO_2. Quite likely, a practical implementation would utilize natural convection or wind for this task.

CO_2 Adsorption Collection. Can CO_2 be collected? The common reagent $Ca(OH)_2$ provides a proof of principle. An aqueous solution of $Ca(OH)_2$ is very efficient in collecting CO_2 from air. Simply bubbling air through a few centimeters of $Ca(OH)_2$ solution removes the bulk of the CO_2. The overall resistance to mass transfer is not substantially larger than the transfer resistance in the gas phase. The high degree of extraction that is achieved with $Ca(OH)_2$ is obtained at the price of a substantial binding energy. The reaction can be summarized as follows: $Ca(OH)_2 + CO_2 \rightarrow CaCO_3 + H_2O +$ 114 kJ of energy release. The return calcination reaction $CaCO_3 \rightarrow CaO + CO_2$ requires 179 kJ/mole, which is the energy penalty for recovering CO_2. While this is a non-negligible fraction of the energy from burning gasoline (~650 kJ/mole CO_2), it is still a manageable amount.

System Design. Based on these observations, an idealized process plant would have a number of units, presumably wind or convection driven, that form $CaCO_3$ from an aqueous $Ca(OH)_2$ solution. The $CaCO_3$ precipitate is dried and calcined, which requires energy. The energy for drying could be provided by the heat of hydration when CaO is transformed back into $Ca(OH)_2$. However, calcination would require additional energy, which can come from a number of sources. To be specific, we assume that it is provided by the combustion of coal. The amount of CO_2 generated in the combustion is about 40% of what is stored on the sorbent. Since the process operates on a large scale and is obviously located at a disposal site, the CO_2 from the coal would be directly captured and disposed of.

Cost and Economics. To estimate costs we assume that the cost per unit area of airflow is the same for a windmill and a CO_2 absorption unit. This assumption is justified, since lightweight structures covered with a film of calcium hydroxide solution would be sufficient. Windmills cost about \$700/m^2 of swept area. A CO_2 collection unit of 1 m^2 sweep area, with an extraction efficiency of 50%, and seeing an average wind velocity of 3 m/s would collect 3.6 kg of CO_2 per hour. Assuming a total annual cost for capital investment, operation, and maintenance of 30% of the cost of the machine, the collection cost is \$6.70 per tonne of CO_2. At this point, the collected CO_2 is in the form of $CaCO_3$. Freeing the CO_2 again requires energy. Without accounting for inefficiencies, one would need ~0.15 t coal/t of CO_2. At a price of \$20/t, the cost of this coal would add \$3.00 to the tonne of CO_2. A rough estimate of the annual cost of the calcination plant is determined by multiplying the fuel cost by a factor of four. This is approximately the situation for a power plant. With these assumptions, the calcination process would add \$12/t of CO_2 to the cost of the capture process. This cost would be tolerable compared to the cost of today's energy as well as compared to other sequestration efforts. For example, the cost of pipelining CO_2 a distance of 1,000 km has been estimated at ~\$10/t of CO_2. For a coal-fired power plant at 33% conversion efficiency, \$10/t of CO_2 translates into a little less than 1¢/kWh of electricity. Based on the relative carbon contents of coal and gasoline, the calcination required to collect the CO_2 from one liter of gasoline consumes about 0.7¢ worth of coal. Using the calculations performed above, the price of the complete process should be less than 5¢ per liter of gasoline, well within the range of recent price changes.

Land Requirements. Finally the size of the facilities to collect CO_2 or the required land area is considered. Imagine small collection units of some extent normal to the airflow, but of a height that is negligible on the horizontal scale of the system. On the large scale, one may consider the surface of the horizontal area to be a good CO_2 absorber reducing the CO_2 density from an ambient value of ρ_{CO_2} to $(1 - \varepsilon)\rho_{CO_2}$, where ε is the CO_2 removal efficiency. CO_2 is transported horizontally over the area by a wind velocity v, and it is transported vertically through eddy diffusion. The collection units near the surface remove CO_2 providing a gradient for vertical eddy diffusion transport. The observed eddy diffusion coefficient of the lower atmosphere is 10 m^2/s. The vertical rate of mass transport is roughly $\varepsilon\rho_{CO_2}\ (D_e v/L)^{1/2}$, where L is the dimension of the collection area in the wind direction. Thus for an area of size L×W, the total rate of CO_2 removal is given by $\varepsilon\rho_{CO_2} W(D_e L v)^{1/2}$. Assuming that L=W, ε=0.5 and v=3 m/s, the land area required for collecting all CO_2 from a residential vehicle fleet of a city of 2 million is about 2.8 km on the side. A square, 530 km on the side, is sufficient to collect the CO_2 from all current anthropogenic sources. Since the rate of collection is proportional to $L^{1/2}$ rather than L, collection from several separate smaller areas would be more efficient than a single large area. If combined into a single area, these units will interfere with each other, with downwind units extracting CO_2 from already depleted air. *If one were to limit the size of a collection unit to a square of 100 m on the side, then the world output of CO_2 would require 380,000 units, which is 1.4% of the area of a single collection system*. Each of the hectare units could consist of five vertical units, each 19 m tall by 19 m wide. Intuitive estimates indicate that the individual collection areas need to be spread over a total area as calculated above. Further spreading is not effective.

Results and Discussion

We are performing global and high resolution atmospheric modeling and laboratory uptake experiments to further examine, quantify and develop CO_2 extraction from air as an advanced greenhouse gas separation and capture technology.

Global Scale Modeling. We have conducted large scale global simulations and sensitivity studies at 4° x 5° latitude/longitude resolution where a single grid-point land-based flat CO_2 sink is placed at various locations and with various deposition velocities (ν)

in the UC Irvine Chemical Transport Model (CTM).[6] The CTM contains nine vertical layers centered at 975, 909, 800, 645, 478, 328, 206, 112 and 40 mbar. The vertical resolution of the bottom layer is of order 1 km. This off-line code accepts wind fields from general circulation models and advects chemically interacting tracers and has been validated for many tropospheric applications. It allows us to assess the efficacy of global scale CO_2 extraction and identify locations that minimize impacts on downwind ecosystems that will experience reduced CO_2 levels and enhanced alkaline aerosols.

Figure-1 below shows the CTM's sensitivity of the calculated amount of CO_2 extracted from the entire atmosphere as a function of time for a range of deposition velocities (ν) at a single grid point surface sink centered in Nevada, USA. Observed deposition velocities for gases that react rapidly at terrestrial surfaces like SO_2 and HNO_3 are 1 and 4 cm/sec respectively.[7] Our simulations indicate that extraction of the order of 10 Gtonnes-C/year is possible, even with a simple flat sink. These simulations also reveal the magnitude and extent of CO_2 depletion downwind of the sink that will be valuable to identify locations that minimize impact on terrestrial ecosystems. Saturation effects at high deposition velocities are caused by inability of mixing to replenish the sink box with more CO_2 from the rest of the atmosphere in this coarse CTM model.

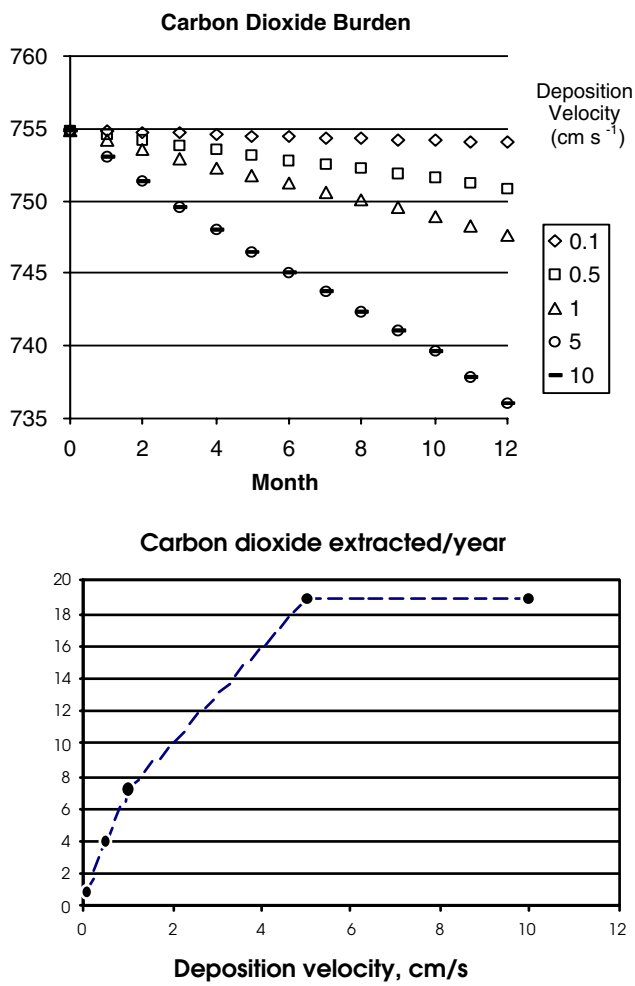

Figure 1 Top panel: total atmospheric CO_2 burden (Gton C) as a function of time for 4° x 5° sink centered in Nevada box for various deposition velocities. Bottom panel: The amount of CO_2 extracted from air in a year as a function of deposition velocity.

High Resolution Modeling. The coarse global scale CTM modeling results presented above provide a lower limit to the CO_2 uptake flux per unit land area, as we illustrated earlier using scaling arguments in our land requirements section. Clearly we can improve our collection efficiency per unit of active land area by orders of magnitude by using smaller units with optimal spacing and designing structures that enhance turbulent mixing. We are using LANL's *high resolution and strong gradient* (HIGRAD) code to quantitatively examine the detailed effects of mixing and turbulence on CO_2 collection.[8,9] The code operates on a grid-point, finite-difference, compressible, and non-hydrostatic platform in terrain following coordinates with adaptive mesh capabilities. It uses a forward-in-time integration scheme that preserves local extremes and signs of transported properties. The parallel architecture allows it to harness our high-performance supercomputing platforms.

We are performing high-resolution simulations of air extraction of CO_2 using HIGRAD. The 2-Dimensional computations presented here have a horizontal resolution of 200 m and 63 vertical boxes with vertical grid being stretched gradually from 23 m at the surface to ~200 m at the top layer at 1.2 km. The velocity was set to 4 m/sec, and temperature of 300 K in an atmosphere with neutral buoyancy. The simulation used a steady stream of air with 370 ppm of CO_2 as its initial condition. The CO_2 concentrations were set to zero at the surface boundary to mimic an ideal flat sink that covers the entire horizontal domain. A parametric relation between the aerodynamic roughness and the friction velocity over water and similarity theory were used to treat the sub-grid fluxes and the vertical logarithmic wind profile above the surface.[10]

The results shown below in Figure 2, clearly reveal that CO_2 loss is observed hundreds of meters above the surface layer. Vertical mixing by turbulence is an effective source for CO_2 to the surface layer in a neutral atmosphere. Because we start with a uniform velocity profile, the turbulent velocity takes some time to get established as evident below. After this is achieved the real turbulent eddy structures become apparent for the conditions of our simulation.

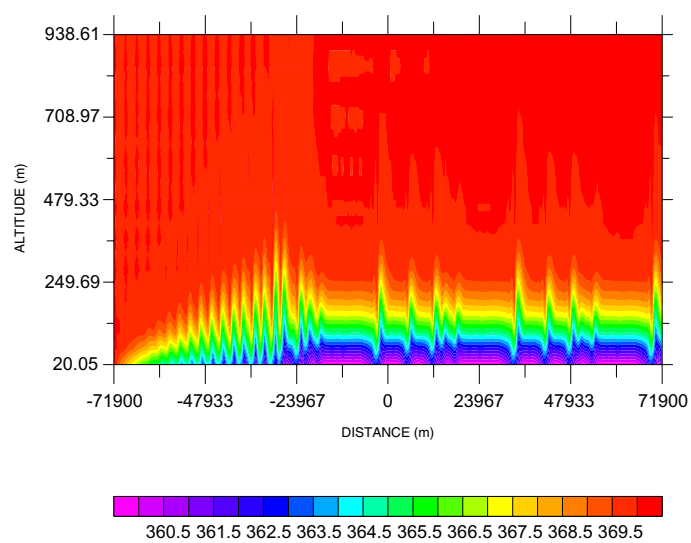

Figure-2: Carbon dioxide concentration in ppm over a perfect aqueous sink simulated using HIGRAD. The distances are in meters above the surface and horizontally about a center of the domain.

Laboratory Experiments. We are performing controlled experiments of CO_2 uptake by saturated $Ca(OH)_2$ solutions in the laboratory. Ambient air is bubbled through a saturated $Ca(OH)_2$

solution with excess solid in an impinger. Care is taken to avoid evaporation by humidifying the input air stream. A metering pump is used to maintain stable slow flow that generates individual bubbles of a few mm in size that rise and remain intact in the solution. The amount of $CaCO_3$ formed at the end of a run (ranging from 15 minutes to 8 hours) is measured by titrating the mixture with acid and monitoring the pH. The inflection points of the pH curve yield the hydroxide, carbonate and bicarbonate fractions. The titration is done slowly and with rapid-stirring to ensure prompt dissolution of the fine $Ca(OH)_2$ particles. A LICOR CO_2 sensor is also being used to provide a continuous measure of the CO_2 extracted from the air by bubbling.

The results from several CO_2 uptake experiments are summarized in Figure 3. There is close to a linear increase in $CaCO_3$ formed and CO_2 uptake with the volume of air processed. The contact time of the bubbles with the solution was varied by changing the height of the solution column. From the slopes of the above $CaCO_3$ formation data for 11 experiments we derive a the mean CO_2 collection efficiency of 53 ± 5% from air by a saturated $Ca(OH)_2$ solution. The collection efficiency could be limited by kinetic factors such as CO_2 diffusion in the bubble and local in-homogeneity in the $Ca(OH)_2$ concentrations and pH of the solution in the vicinity of the bubble which will strongly influence the CO_2 uptake.[11] However, an efficiency of this size should be sufficient to effectively extract CO_2 from air.

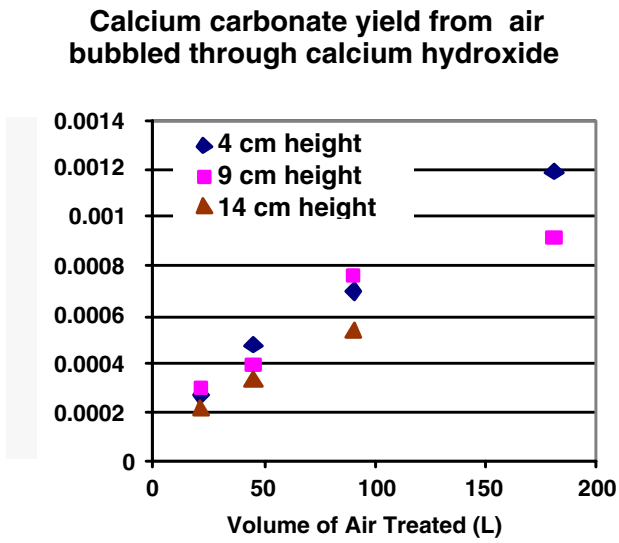

Figure 3. Measurements of $CaCO_3$ formed as a function of the volume of ambient air (~370 ppm CO_2) bubbled through a saturated $Ca(OH)_2$ solution under controlled laboratory conditions.

Conclusions and Directions

Our economics and scaling arguments, atmospheric simulations, and laboratory experiments make a strong case to explore carbon-dioxide extraction from air as an advanced CO_2 capture and sequestration technology. By all measures we applied, this process compares very favorably against renewable sources such as solar, wind, or biomass. This scheme is attractive because; it allows CO_2 sequestration without a costly change in the existing infrastructure; it collects the CO_2 from the transportation and other distributed power sources; it retains carbon-based energy, which continues to be highly cost-effective, and it has the potential of restoring atmospheric CO_2 to pre-industrial levels providing us insurance against any large and rapid climate change events in the future. We are aggressively pursuing research on active and passive collection schemes, feasibility of CO_2 adsorbents like zeolites, silicates, amines, and $Mg(OH)_2$ with lower binding energy than $CaCO_3$, and identify locations that maximize collection, facilitate disposal, and minimize environmental impact. Our goal is to optimize the scale of the processes in order to design, construct, and develop a small prototype CO_2 extraction plant for field studies.

Acknowledgment

This work is supported by the Laboratory Directed Research and Development (LDRD) Program at Los Alamos National Laboratory, Los Alamos NM 87545.

References

1. http://www.ipcc.ch for *Climate Change 2000* and *Climate Change 1995,* Cambridge University Press, 1996.
2. http://www.zeca.org, Zero Emissions Coal Alliance.
3. Lackner, K. S.; Grimes, P.; Ziock, H., *Proceedings of the 24th Annual Technical Conference on Coal Utilization And Fuel Systems,* March 8–11**, 1999**. Clearwater, Florida. Available as Los Alamos National Laboratory Report LA-UR-99-583.
4. Elliott, S.; Lackner, K.; Ziock, H.; Dubey, M. K.; Hanson, H. P.; Barr, S.; Ciszkowski, N. A.; Blake, D. R., *Geophys. Res. Lett.*, **2001,** *28,* 1235-1238.
5. Lackner, K. S.; Butt, D. P.; Wendt, C. H., *Energy Convers. and Mgmt.*, **1997**, 38, Suppl, S259-S264, Elsevier Science Ltd.
6. Johnston, N. A. C.; Blake, D. R.; Rowland, F. S.; Elliott, S.; Lackner, K.; Ziock, H. J.; Dubey, M. K.; Hanson, H. P.; Barr, S., Submitted to *Energy Convers. and Mgmt.,* **2001.**
7. Sienfeld, J. H.; Pandis, S.N., Atmospheric Chemistry and Physics: From air Pollution to Climate Change, John Wiley and Sons: New York, 1998.
8. Smith, W. S.; Reisner, J. M.; Kao, C.Y.J., Atmos. Env., **2001**, *35*, 3811-3821.
9. Reisner, J.; Wynne, S.; Margolin, L.; Linn, R., *Monthly Weather Rev.,* **2000**, *128*, 3683-3691.
10. Pielke, R. A., Mesoscale Meteorological Modeling, Academic Press: London, 1984.
11. Boniface, J.; Shi, Q.; Li, Q.; Cheung, J.L.; Rattigan, O.V.; Davidovits, P.; Worsnop, D. R.; Jayne, J. T., Kolb, C. E., *J. Phys. Chem. A,* **2000,** *104*, 7502-7510.

HIGH EFFICIENCY DIRECT CARBON FUEL CELL FOR CO_2 EMISSION AND SEQUESTRATION

Meyer Steinberg

Energy Resources Division
Brookhaven National Laboratory
Upton, NY 11973-5000

John F. Cooper

Lawrence Livermore National Laboratory
Livermore, CA 94551

Introduction

Hydrogen fuel cells have been under advanced development for a number of years and are now nearing commercial applications. Direct carbon fuel cells have, heretofore, not reached practical development because of difficulties in fuel and electrolyte configuration. The carbon/air fuel cell has the advantage of near zero entropy change allowing 100% theoretical thermodynamic efficiency at temperatures to 1000°C. The activities of the C fuel and CO2 product are invariant allowing constant EMF and full utilization of fuel in a single pass mode of operation. The hydrogen fuel cell has a theoretical thermodynamic efficiency of only 70% at 1000°C and the activity of the H_2 fuel and H_2O product limit utilization to 80% in a single pass (Table 1). A direct carbon fuel cell is currently being developed which utilizes clean reactive carbon particulate in a molten carbonate salt slurry. Concentrated CO_2 is evolved at the anode and oxygen from air is utilized at the cathode (Fig. 1).[1,2] At temperatures of 750°C to 850°C, a voltage efficiency of 80% has been achieved at a power density of 1Kw/sqM (Fig. 2).[1,2] The clean carbon and hydrogen fuel is produced from (1) natural gas, by thermal decomposition (Fig. 3), (2) petroleum, by pyrolysis coking (Fig. 4), (3) coal, by sequential hydrogasification and thermal pyrolysis (Fig. 5), and (4) biomass, by sequential hydro- and thermal-pyrolysis (Fig. 6), and are integrated with C and H_2, fuel cells for power cycle estimates.[3] Thermal to electric efficiencies indicate 80% (HHV), 85% (LHV) for petroleum, 75.5% (HHV), 83.4% (LHV) for natural gas and 68.3% (HHV), 70.8% (LHV) for lignite coal (Table 2). The benefits of integrated combined carbon and hydrogen fuel cell power generation cycles include, (1) more than twice the efficiency of conventional fossil fuel steam plants, (2) reduced power generation cost, especially for increasing fossil fuel cost, (3) reduced CO_2 emission by over a factor of 2 or more, and (4) capability for direct sequestration or utilization of the concentrated CO_2 from the carbon fuel cell effluent.

References

References should use ACS style. References may be inserted and numbered manually, or automatically by using the endnote/footnote function of the word processor. For manual insertion, format the references as follows:

(1) Cooper, J. F..; Cherepy, N.; Upadhye, R.; Pasternak, A.; and Steinberg, M. Direct Carbon Conversion, Report No. UCRL ID 141818. Lawrence Livermore National Laboratory, Livermore, CA, **2000**.

(2) (2) Turning Carbon Directly into Electricity, *Science and Technology Review*, **2001**, pp. 4-12, Lawrence Livermore National Laboratory, Livermore, CA.

(3) Steinberg, M; Technologies and Economics for Production of Electrochemical Fuels from Fossil Fuel Resources for use in High Efficiency Integrated Fuel Cell Combined Cycle Power Generation Plants, Consultant Report to Lawrence Livermore National Laboratory, Livermore, CA, 2001.

Table 1. Comparison of Efficiencies of Fuel Cells Using Synthetic or Refined Fuels Operating Temp. 750°C - 850°C

Fuels	Thermal Efficiency 100%ΔG/ΔH %	Fuel Utilization Factor	Voltage Efficiency	Net Efficiency
C	100.3	1.0	0.8 - 0.9	0.80 - 0.90
H_2	70.0	0.75 - 0.85	0.8	0.42 - 0.48
CH_4*	89.0	0.75 - 0.85	0.8	0.53 - 0.60

*Assumes efficient internal steam reforming reaction. Direct electrochemical reaction of methane at a catalyst surface does not occur at practical rates.

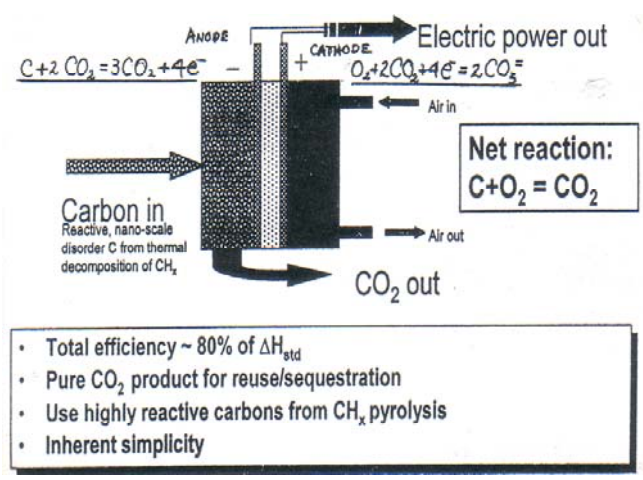

Figure 1. Direct Carbon Conversion (DCC): electric power from electrochemical reaction of C and O_2.

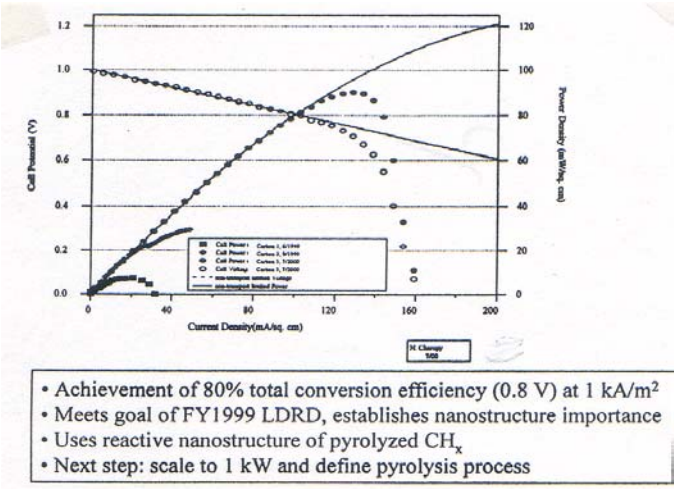

Figure 2. Carbon/air cells operate at sufficiently high power density for base-load power applications.

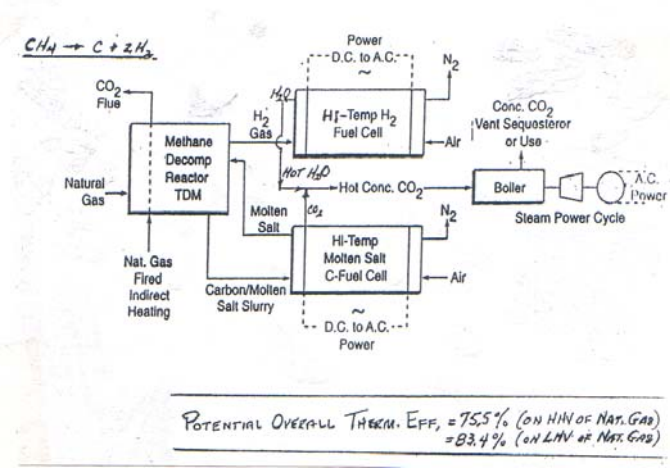

Figure 4. Crude oil fired integrated combined fuel cell power cycle hi-efficiency.

Figure 3. Natural gas combined fuel cell power cycle hi-efficiency.

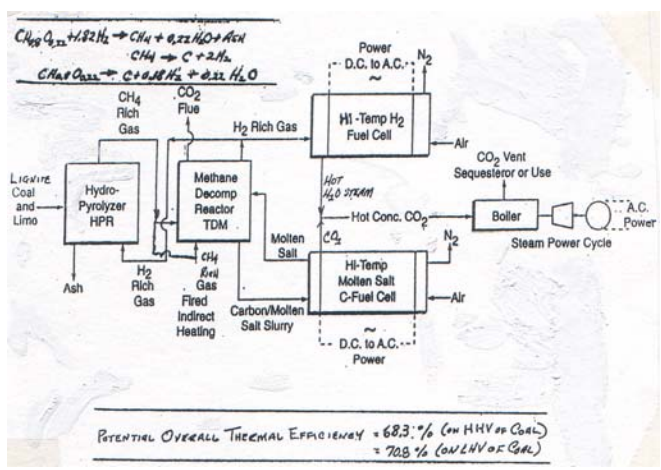

Figure 5. Coal fueled reversible hydrocarb combined fuel cell power cycle.

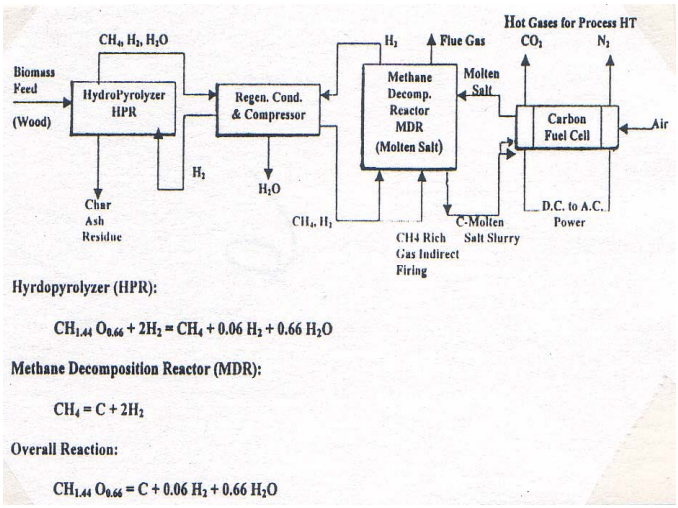

Figure 6. Biomass fueled carbon fuel cell power plant.

EFFECT OF THE AMOUNT OF BASE SITE ON CATALYTIC BEHAVIOR OF CAO FOR SYNTHESIS OF DIMETHYL CARBONATE FROM PROPYLENE CARBONATE AND METHANOL

Tong Wei Wei Wei Mouhua Wang Yuhan Sun*
Bing Zhong

State Key Laboratory of Coal Conversion Institute of Coal Chemistry Chinese Academic of Sciences, Taiyuan, 030001

Introduction

Dimethyl carbonate (DMC) is a unique molecule having versatile chemical property and has been used mainly as methylating and methoxycarbonylating agent substituting for toxic phosgene, dimethyl sulfate, or methyl iodide [1-3]. It can be synthesized by transesterification method, in which CO_2 reacts with propylene oxide to yield propylene carbonate (PC), which continually reacts with methanol (MeOH) to yield DMC[4,5]. The reaction of PC with MeOH can be catalyzed by solid base with high conversion and selectivity [6]. On the basis of the discussion in the other paper submitted to this meeting, the effect of the amount of base site on catalytic behavior of CaO for synthesis of DMC from PC and MeOH was investigated in detail.

Experimental

CaO was prepared from $CaCO_3$ calcined at1073K or 1173K in N_2 atmosphere. The reaction was carried out in a 250mL flask equipped with reflux condenser, water bath and magnetic stirring. Catalyst was added into the flask accompanied with violent magnetic stirring after the temperature reached to the expected one. Reaction product was analyzed by Gas Chromatograph after centrifugal separation of solid catalyst from liquid.

Results and discussion

It was reported that CaO calcined from $CaCO_3$ was super base. Thus in present paper, CaO was prepared from $CaCO_3$ calcined at 1073K and 1173K respectively. BET surface area of CaO was listed in Tab. 1; XRD and CO_2TPD results of CaO were illustrated in Fig.1, 2. It can be seen from Fig.1 that $CaCO_3$ was totally dissociated when calcined at 1073K for 1hr and yields cubic CaO. Both the extendedness of calcinations time and the increase of temperature result in surface area increase as shown in Tab.1. From Fig.2 we can see that there is four kinds of base site with CO_2 desorption temperature being 430K, 470K, 640K and 890K respectively. With the extendedness of time and the increase of temperature, the amount of base site increases greatly with the sequence being 1173K/2hr> 1073K/2hr> 1073K/1hr.

Tab.1 BET Surface area of CaO obtained from $CaCO_3$ calcined under different condition(m^2/g)

Calcinition temperature/K	Calcinition time /hr	BET Surface Area /m^2. g^{-1}
1073	1	3.848
1073	2	12.706
1173	1	12.166

* To whom corresponding should be addressed. Fax: +86 351 4041153
E-Mail: yhsun@sxicc.ac.cn or weiwei@sxicc.ac.cn

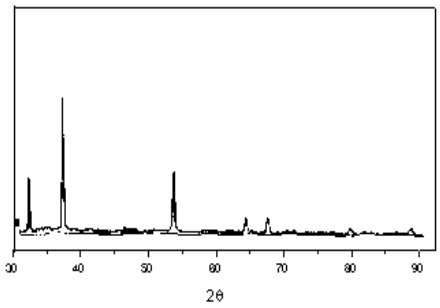

Fig.1 XRD of CaO calcined from $CaCO_3$ at 1073K for 1hr

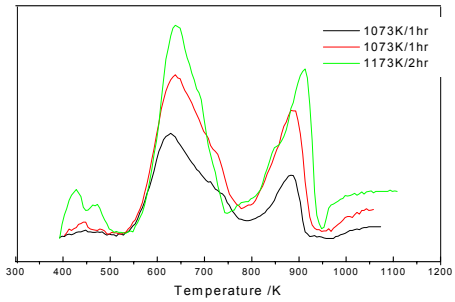

Fig. 2 CO_2 TPD of CaO calcined from $CaCO_3$

Since this reaction usually catalyzed by strong base, the effective base site may be that with CO_2 desorption temperature being 640K and 890K respectively. The effect of the amount of base site on DMC yield, DMC selectivity and reaction rate was shown in Fig. 3-5. It can be seen that with the increase of the amount of base site, the time need to reach equilibrium was shortened while equilibrium DMC yield was unchanged , which means the increase of the amount of base site can result in the increase of reaction rate but not change the equilibrium. On the other hand, the DMC selectivity decreases gradually with the increase of the amount of base site. The base site can catalyze both the subject reaction and the polymerization of PC, therefore the increase of bas site will also promote the side reaction and consequently make the DMC selectivity decrease. Fig. 5 shows the effect of the amount of base site on the reaction rate, with the increase of the amount of base site, the maximum rate increase and the induction time was shortened. As side in the other paper, the induction time comes from the activation of MeOH, the increase of base site amount can not only promote the activation of MeOH, but also make the surface concentration of activated MeOH increase and consequently promote the surface reaction of PC with activated MeOH.

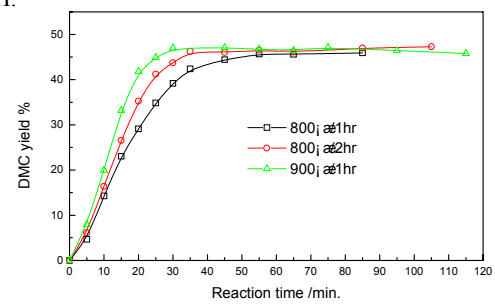

Fig. 3 Effect of basicity on DMC yield

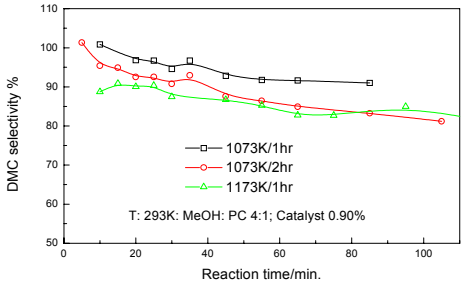

Fig.4 Effect of basicity on DMC selectivity

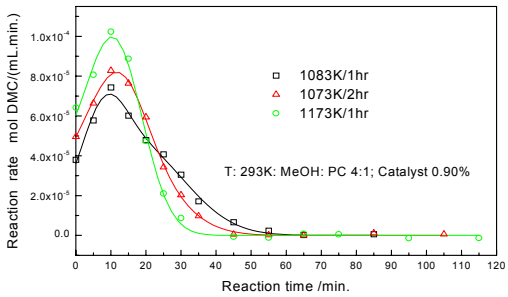

Fig. 5 Effect of basicity on reaction rate

Conclusion

1. $CaCO_3$ calcined at 1073K and 1173K can yield cubic CaO, which shows excellent catalytic activity for synthesis of DMC from PC and MeOH.
2. Both the surface area and the amount of base site of CaO increase with the increase of calcinatio temperature and the extendedness of calcination time for $CaCO_3$.
3. The increase of the amount of base site can promote both subject reaction and side reaction, therefore although the reaction rate increases, the DMC selectivity decreases with the increase of the amount of base site.

Reference

(1) Watanabe, Y.; Tatsumi, T. Microporous and mesoporous materials 1998, 22,399~407

(2) Pacheco, M. A.; Marshall, C. L. *Energy & Fuels* 1991, 11, 2~29

(3) Shaikh, A.G. *Chem. Rev.* 1996, 96, 951~976

(4) Ono, Y. Appl. Cata. A: General 1997, 155, 133~166

(5) Knifton, J.F., Duranleau, R.G. *Journal of molecular Catalysis*, 1991, 67, 389~399

(6) Zhao, T. *Dr Dissertation,* Shanxi Institute of Coal Chemistry, Chinese Academy of Sciences, 1999

DEHYDRO-OLIGOMERIZATION OF METHANE TO BENZENE AND NAPHTHALENE WITHOUT ADDING OXYGEN: PROMOTIONAL EFFECT OF IN OVER MO/HZSM-5 CATALYST

Jinfeng Zhao, Xiaodong Wang, Tao Zhang, Lin Li, Ning Li, Mingyuan Zheng, Liwu Lin*

* State Key Laboratory of Catalysis,
Dalian Institute of Chemical Physics,
Chinese Academy of Sciences,
P.O.Box 110, Dalian 116023, China

Introduction

Methane dehydro-oligomerization and aromatization without adding oxygen over Mo/HZSM-5 catalyst have been widely studied.[1-8] However, the existing problem in this route is the low yield of aromatics, due to the high stability of methane. Recently, introduction of second metal species has been believed to be a promising route to improve methane non-oxidative transformation on the Mo/HZSM-5 catalyst.[9-13] Our previous work reported on the studies of the structures of Mo/HZSM-5 catalysts and the enhancing stability of Mo/HZSM-5 with incorporation of platinum in the process of dehydro-oligomerization of methane to benzene and ethylene.[9, 14] In the meanwhile, we found that indium took great effect on the activation of methane in the reaction of selective catalytic reduction of NO by methane over In/HZSM-5.[15,16] Therefore, in this paper, indium was used to be expected to promote the catalytic performance of Mo/HZSM-5 for methane non-oxidative reaction. Indeed, it was found that Mo-In/HZSM-5 exhibited much higher conversion of methane and production of benzene and naphthalene than Mo/HZSM-5.

Experimental

Catalysts preparation. Mo/HZSM-5, Mo-In/HZSM-5, In/Mo/HZSM-5 and Mo/In/HZSM-5 catalysts were prepared by impregnation, co-impregnation and successive impregnation methods, respectively. The component of catalysts were denoted by the weight ratio.

Catalytic tests. Methane conversion test was carried out in the fixed-bed continuous-flow micro-reactor system, with a 6.4mm i.d. quartz tubular reactor containing 0.2g catalyst (24-32 mesh). The catalysts were first heated to 973K under Ar stream (30ml/min) and held for 30 min. Then, the stream was switched to the feed gas mixture of 90% CH_4 (99.999%) with 10% N_2 as internal standard. The reaction was conducted at 973K under a total pressure of 1 atm. The hydrocarbon products were analyzed by on-line HP 6890 gas chromatograph.

An internal standard analyzing method similar to that reported by Liu et al. was used to calculate CH_4 conversion and selectivity toward hydrocarbon products according to mass balance for carbon. The selectivity of coke, including undetected heavy aromatics, would be obtained.[11]

Results and discussion

Table1 shows that the addition of 0.3-2% In to 6% Mo/HZSM-5 catalyst induces a significant effect on the catalytic performance. It is clear to see that the selectivity of aromatics increase remarkably after the introduction of small amount of In to Mo/HZSM-5. When In content reaches 0.7% in Mo-In/HZSM-5, the catalyst exhibits the best catalytic activity, leading to an increase in methane conversion from 11.13 to 13.14% and yield of aromatics from 7.25 to 9.42 as compared with Mo/HZSM-5. Meanwhile, it is observed that the selectivity of coke decreased considerably from 27.10 to 21.98%. This indicates that the improvement of catalyst activity and selectivity by In additives to Mo/HZSM-5 most probably originates from the alleviation of coke deposition. It is interesting to note that catalytic behavior of Mo-In/HZSM-5 catalyst is sensitive to the additive amount of In. Further increase in In content up to 2% causes methane conversion to slightly decrease, however, the yield of aromatics is higher and the selectivity of coke is less than Mo/HZSM-5. These results show that a proper amount of In introduced into Mo/HZSM-5 can evidently improve its catalytic activity for methane dehydro-oligomerization.

Fig.1 shows a comparison of the catalytic performances of both Mo/HZSM-5 and In-promoted Mo/HZSM-5 on time on stream. It can be seen that the methane conversion and the yield of aromatics on Mo-0.7In/HZSM-5 are always significantly higher than those on Mo/HZSM-5 in the range of time on stream. It is demonstrated that the addition of In is favorable for the dehydrogenation of methane

Table 1 Catalytic performances of Mo-In/HZSM-5 catalysts.

Catalysts	CH_4 Conv. (%)	Selectivity (%)					Yield of aromatics (%)
		C2	Benz.	C7-C8	Nap.	Coke	
6Mo/HZ	11.13	3.71	50.66	2.92	11.54	27.10	7.25
6Mo-0.3In/HZ	11.60	3.24	54.15	3.03	12.62	23.55	8.10
6Mo-0.7In/HZ	13.14	3.64	54.32	2.73	14.66	21.98	9.42
6Mo-1.0In/HZ	12.14	3.45	56.05	3.04	13.08	20.73	8.76
6Mo-1.5In/HZ	11.45	3.64	53.18	3.12	12.28	24.05	7.85
6Mo-2.0In/HZ	11.00	2.89	52.89	3.03	14.36	23.15	7.73

T=973K, P=1atm, t=60min, space velocity=1500mlg^{-1}h^{-1},HZSM-5=HZ.

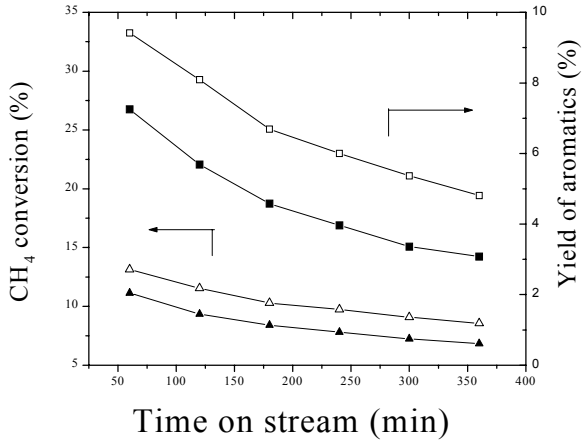

Fig.1 CH_4 conversion (triangle) and yield of aromatics (square) on Mo-0.7In/HZSM-5 (open) and Mo/HZSM-5 (solid) versus time on stream.

and the formation of aromatic hydrocarbons.

The impregnation sequence of Mo and In species during the catalyst preparation is also important for good catalytic performance. The result is summarized in **Table 2**. It is easy to find that the Mo-In/HZSM-5 catalyst prepared by co-impregnation method exhibits the best catalytic activity among the three different catalysts. The possible reason is that the catalyst prepared by co-impregnation method allows the two metal components to interact with the zeolite support simultaneously and evenly, thus inhibiting the formation of coke and resulting in higher activity and selectivity. However, for the successive impregnating method, the interaction between one metal and zeolite can be weakened when another metal component has united with HZSM-5 firmly.

Table 2 The effect of impregnation sequence on the catalytic performance of In promoted Mo/HZSM-5.

Catalysts	CH_4 Conv. (%)	Selectivity (%)					Yield of aromatics (%)
		C2	Benz.	C7-C8	Nap.	Coke	
6Mo/HZ	11.13	3.71	50.66	2.92	11.54	27.10	7.25
Mo/In/HZ	9.08	4.26	42.14	2.74	6.88	39.82	4.70
In/Mo/HZ	10.85	3.90	54.42	3.13	14.82	20.31	7.85
Mo-In/HZ	13.14	3.64	54.32	2.73	14.66	21.98	9.42

T=973K, P=1atm, t=60min, space velocity=1500mlg^{-1}h^{-1}, HZSM-5=HZ, Mo:In:HZ=6:0.7:93.3.

4. Conclusions

Introduction of a proper amount of In into Mo/HZSM-5 greatly enhances the catalyst activity and the selectivity of aromatics in methane non-oxidative reaction. In addition, the improvement of In over Mo/HZSM-5 is also due to the catalyst preparation method.

References

1 L. Wang, J. Hang, L. Tao, M. Xie and G. Xu, Catal. Lett., 1993,21,35.

2 Y. Xu, S. Liu, L. Wang, M. Xie and X. Guo, Catal. Lett., 1995,30,135.

3 F. Solymosi, A.Erdohelyi and A. Szoke, Catal. Lett., 1995,32,43.

4 L. Chen, L. Lin, Z. Xu, X. Li and T Zhang, J. Catal., 1995,157,190.

5 D. Wang, J.H. Lunsford and M.P. Rosynek, J. Catal., 1997,169,347.

6 R. Ohnishi, S. Liu, Q. Dong, L .Wang and M. Ichikawa, J. Catal.,1999,182,92.

7 L. Wang , Y. Xu, M. Xie, S. Liu and L.Tao, Stud. Surf. Sci. Catal.,1995,94,495.

8 S. T. Wong, Y. Xu, L. Wang and M. Xie, Catal. Lett., 1996,38,39.

9 L. Chen, L. Lin, Z. Xu, T. Zhang and X. Li, Catal. Lett., 1996,39,169.

10 Y. Shu, Y. Xu, S. Wong, L. Wang and X. Guo, J. Catal.,1997,170,11.

11 S. Liu, Q. Dong, R. Ohnishi and M. Ichikawa, Chem. Commun., 1997,1455.

12 R. Meriaudeau and C. Naccache, J. Catal., 1995,157,283.

13 B. Liu, Y. Yang and A. Sayari, Appl. Catal. A: General, 2001,214,95.

14 L. Chen, L. Lin, Z. Xu, X. Li and T, Zhang, J. Catal. 1995,157,190.

15 X. Zhou, T. Zhang, and L.Lin, Catal. Lett., 1996,40,35.

16 X. Zhou, Z, Xu, T. Zhang, and L.Lin, J. Mol. Catal. A, 1997,122,125

CH_4 DECOMPOSITION ON Co/SiO_2: INFLUENCE OF METAL PARTICLE SIZE AND GAS PHASE COMPOSITION ON DECOMPOSITION RATE

Yi Zhang and Kevin J. Smith

Department of Chemical & Biological Engineering
University of British Columbia, Vancouver, B.C.
Canada, V6T 1Z4

Introduction

Methane decomposition is important in a number of reactions that aim to convert natural gas to more valuable products using supported metal catalysts. These include methane steam reforming for synthesis gas production and methane decomposition for hydrogen production[1-4]. Also, initial CH_4 decomposition kinetics on Co catalysts have been reported at relatively mild conditions (450°C and 101kPa) relevant to CH_4 homologation: a two-step process in which CH_4 decomposition ($CH_4 \rightarrow CH_x \bullet S + H \bullet S$) at 350-450°C is followed by lower temperature hydrogenation ($CH_x \bullet S + H_2 \rightarrow S + C_2H_6$, C_3H_8). At these conditions[3], the initial high rate of CH_4 decomposition decreases rapidly but continues despite the nominal coverage of surface Co being greater than 1. A semi-empirical model that was developed to describe this observation assumed decomposition of CH_4 on a Co site with migration of the resulting CH_3 surface species from the metal to the support, thereby regenerating the metal site. This migration step was considered essential to explain the observed kinetics[3]. However, despite the low temperature, it is possible that filamentous carbon is formed during the reaction, in which case active metal sites would be regenerated as surface carbon is absorbed by the metal before diffusing through the metal particle.

The mechanism of catalyst deactivation during CH_4 decomposition is complex[4]. The deactivation rate depends on the rate of carbon build up on the surface of the catalyst, which in turn is a consequence of a number of interacting effects, including the effect of metal particle size on carbon diffusion rate, carbon gasification rate due to the presence of H_2 (whose evolution parallels CH_4 decomposition on the metal catalyst), and carbon morphology. The present work is aimed at clarifying some aspects of the deactivation during the decomposition of methane at moderate temperatures on low loaded Co/SiO_2 catalysts.

Experimental

Catalyst Preparation. Co catalysts were prepared by incipient wetness impregnation of the support using an aqueous solution of $Co(NO_3)_2 \bullet 6H_2O$ (+98% Aldrich) [3]. The catalysts were dried, calcined and reduced by temperature-programmed reduction (TPR) in a 100ml/min flow of 40% H_2/60%Ar to the reduction temperature. Co content was varied from 5-12wt%, and the degree of reduction of these catalysts was >83% in all cases, the reduction degree increasing to 96% for the 10 and 12wt%Co/SiO_2 catalysts.

Catalyst Characterization. The Co dispersion was determined by CO chemisorption using a thermogravimetric analyzer (Shimadzu TGA-50). The metal dispersion was calculated from the CO uptake and reported as a percent of reduced Co. The Co particle size was estimated from the equation d (nm)=0.962/Φ, where Φ is the percent metal dispersion. Carbon filament formation was confirmed by TEM using a Hitachi H-800 electron microscope, operated at 100-150 kV.

Methane Decomposition. Kinetic experiments were performed in a fixed-bed reactor system, details of which have been given elsewhere.[3] The reactor was operated in a differential mode (<10% CH_4 conversion), free of external and internal diffusional effects as confirmed by the methods of Froment and Bischoff [5].

Results and Discussion

The rate of methane decomposition over the 12% Co/SiO_2 catalyst at 500°C and 101 kPa shows a steady decrease in the period 0-60 minutes time-on-stream, as shown in Figure 1. The deactivation profile can be described by a 1st-order deactivation rate equation. Two parameters, the initial rate of reaction r_0 and the rate of the decay k_d, describe the deactivation rate according to the equations: $dr/dt = -k_d r$, such that $r = -k_d r_0 \exp(-k_d t)$. The solid line of Figure 1 shows the fit of this empirical equation to the measured data. Note that the equation does not include the migration of carbon from the catalyst surface as proposed previously[3], since here the deactivation is being considered over a longer time period. The migration step is relevant only at the initial stage of reaction[3] as evidenced by the data of Figure 2. CO is produced by reaction between CH_x (that has migrated from the metal to the support) and oxygen of the support. Within about 3 minutes of the start of the reaction, the CO has declined to a minimal amount, suggesting that the rate of CH_x migration has also decreased significantly.

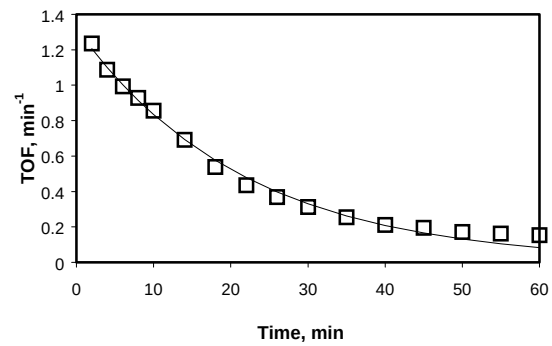

Figure 1. CH_4 TOF as a function of time at 500°C on 12wt% Co/SiO_2 with 5.16%CH_4 in Ar

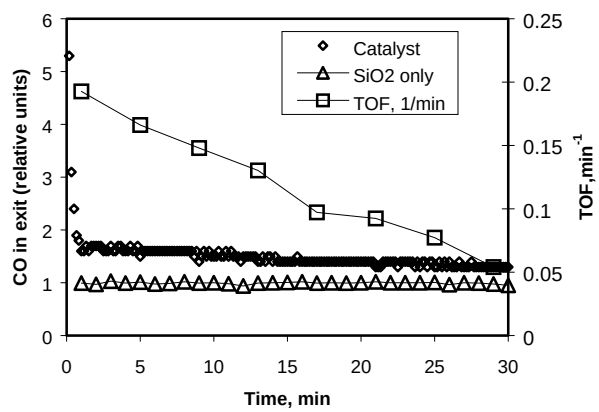

Figure 2. CO production during CH_4 decomposition at 450°C on 12%Co/SiO_2 catalyst (Feed 5.16% CH_4 in Ar).

Metal particle size effects. The influence of metal particle size on the CH_4 decomposition rate at 450ºC over Co/SiO_2 catalysts was investigated using catalysts with nominal metal loading of 5-12wt%. The Co particle size increased with metal loading in the range d = 5.8 – 11.4 nm. The dependency of initial TOF (r_o) and decay rate (k_d) on metal particle size were obtained by curve fitting the CH_4 decomposition rate versus time data to the empirical deactivation equation presented above. Data in Fig. 3 show that Co/SiO_2 catalyst exhibited structure sensitivity, where the initial TOF increased with

increasing Co particle size. Data in Fig. 4 show that an increase in Co particle size resulted in a minor decrease in deactivation rate.

Filamentous carbon formation on the 12wt% Co/SiO_2 (d=11.4 nm) catalyst, exposed to 5.16%CH_4/Ar for a reaction time of 120 minutes was confirmed by TEM of the used catalyst. Filament formation corresponds to a low value of k_d as reported in Fig. 4. The TEM micrograph showed that the filamentous carbon diameter was approximately 10 nm, in agreement with the particle size of 11.4 nm measured by CO chemisorption on the fresh catalyst.

Hence, both migration of carbon species and filamentous carbon formation occurred during CH_4 decomposition on 12wt%Co/SiO_2 catalyst. Fig 2 showed that the migration rate decreased to a very low level within a few minutes of the start of the reaction. Over longer reaction times (>10min) the absorption and diffusion of surface carbon into the metal particle must therefore be the main mechanism for sustained catalyst activity (and hence $k_d \rightarrow 0$).

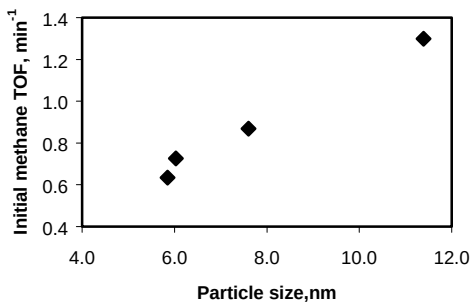

Figure 3. Effect of metal particle size on initial decomposition activity (TOF). (Feed gas 5.16 %CH_4/Ar at 450ºC.)

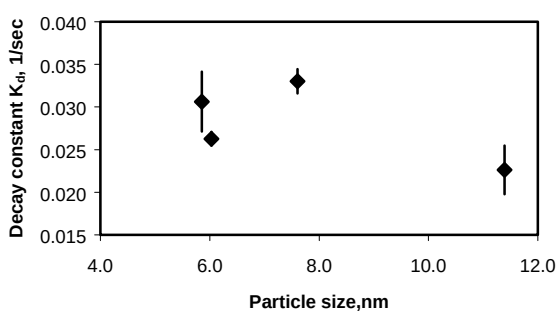

Figure 4. Effect of metal particle size on decay constant (k_d). (Feed gas 5.16 %CH_4/Ar at 450ºC.)

The above data can be interpreted using a simplified model for catalyst deactivation. Accordingly, the deactivation rate (r_d=dr/dt) for CH_4 decomposition is assumed dependent on the difference in the net rate of carbon formation ($r_{f,n}$, the rate of carbon formation minus the rate of gasification of carbon/coke precursor) and the net rate of carbon removal ($r_{r,n}$, mainly due to filamentous carbon formation) i.e. $r_d=r_{f,n}-r_{r,n}$. The rate of catalyst deactivation will depend on the difference between $r_{f,n}$ and $r_{r,n}$. From Fig. 3 we can conclude that $r_{f,n}$ must increase with metal particle size, and since k_d decreases marginally with particle size, we can also conclude that the net rate of carbon removal $r_{r,n}$ must increase with particle size. Considering size effects on the carbon diffusion mechanism, a similar conclusion can be reached.

Gas composition effects. The composition of the gas phase also affects the rate of catalyst deactivation and the formation of filamentous carbon. The presence of H_2 (1.2%) in the feed gas (5.16%CH_4/Ar) reduced the initial TOF and the deactivation rate of the catalyst (Fig.5). The difference between $r_{f,n}$ and $r_{r,n}$ (i.e. the deactivation rate) decreases because H_2 increases the hydrogenation of surface carbon and therefore, $r_{f,n}$ decreases. In the case of CO (0.36% in 5.16%CH_4/Ar), however, the initial TOF is not reduced significantly, whereas the deactivation rate remains low (Fig. 5). CO adsorption must therefore increase $r_{r,n}$, either by enhanced carbon diffusion due to CO surface modification[6], or displacement of surface H from the catalyst surface.

Conclusions

CH_4 decomposition kinetics on supported Co catalysts are strongly influenced by the metal particle size and gas phase composition. These effects have been explained in terms of the relative magnitudes of the net rate of carbon formation and the net rate of carbon removal from the catalyst surface. Filamentous carbon formation occurs when both rates are approximately equal, resulting in a low apparent deactivation rate.

Acknowledgement. Funding from the Natural Sciences and Engineering Research Council of Canada is gratefully acknowledged.

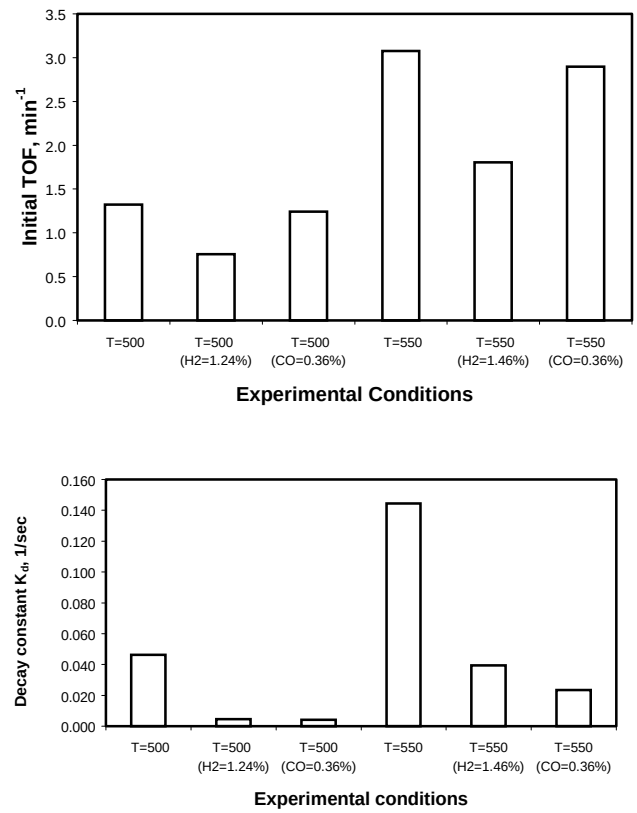

Figure 5. Effect of H_2 and CO on the initial activity and deactivation rate. (12wt% Co/SiO_2 catalysts with Co particle size 9.5 nm, exposed to 5.16%CH_4/Ar at temperature indicated).

References

(1) Amariglio, H.; Saint-Just, J.; Amariglio, A., *Fuel Processing Technology*, **1995,** *42,* 291.
(2) Guczi L.; Van Santen , R.A. and Sarma, K.V., *Catal. Rev.-Sci.*, **1996**, *38 (2)* 249.
(3) Zadeh, J.S.M. and Smith, K.J., *J. Catal.*, **1998,** *176,* 115.
(4) Snoek, J.W., Froment, G.F. and Fowles, M., *J. Catal.,* **1997**, *169*, 240 and *J. Catal.*, **1997**, *169*, 250.
(5) Froment, G.F. and Bischoff, K. B., "Chemical Reactor Analysis and Design" Wiley, New York, **1990**.
(6) Rodriguez ,N.M.; Kim M.S. and Baker R.T.K., J. Catal., **1993,** *144* , 93.

CO_2 Reforming and Partial Oxidation of Methane on Pt/Al_2O_3, Pt/ZrO_2 and $Pt/Ce\text{-}ZrO_2$ Catalysts

L.V. Mattos[1], E. R. de Oliveira[2], D. E. Resasco[3], F.B. Passos[2] and F.B. Noronha[1]

[1] Laboratório de Catálise, Instituto Nacional de Tecnologia, Rio de Janeiro, Brazil
[2] Departamento de Engenharia Química, Universidade Federal Fluminense, Niterói, Brazil
[3] School of Chemical engineering and Materials Science, University of Oklahoma, Norman, USA.

Introduction

Increasing concern about world dependence on petroleum oil has generated interest in the use of natural gas. However, the majority of these reserves are unmarketable since they are located in remote regions. The conversion of natural gas into transportation fuels such as gasoline and diesel is an alternative to the prohibitive transportation costs. The so-called gas-to-liquids technology (GTL) is based on the conversion of natural gas to a synthesis gas prior to the liquid production through the Fischer-Tropsch Synthesis (1).

Today, autothermal reforming (ATR) and catalytic partial oxidation (CPO) represent the technologies that fulfill the requirements to a gas with $H_2/CO = 2$, the ratio necessary to GTL plant. The ATR technology requires the addition of CO_2 or CO_2-rich gas in order to adjust the syngas composition to the desired H_2/CO ratio of the FT- synthesis (2).

The major obstacle associated with the CO_2 reforming reaction is the deactivation of the catalysts due to carbon deposition. Several studies have shown that Pt/ZrO_2 catalysts are very stable for the CO_2 reforming of methane (3,4). A mechanism involving two independent paths has been proposed to explain the CO_2 reforming of methane on Pt/ZrO_2 catalysts. In this mechanism, the support participates in the dissociative adsorption of CO_2 near the metal particles, transfering oxygen to the metal surface and accelerating the removal of carbon from the metal. More recently, we have reported that the use of promoters such as cerium oxide improves the activity and stability of Pt/ZrO_2 catalysts under severely deactivating reaction conditions (5,6). These results were attributed to the increase of the reducibility and oxygen transfer ability of the support by the addition of cerium oxide.

The aim of this work is to compare the performance of the $Pt/Ce\text{-}ZrO_2$ catalyst on the CO_2 reforming of methane and the partial oxidation of methane. The effect of the support reducibility on the catalytic activity of both reactions is evaluated.

Experimental

The ZrO_2 support was prepared by calcination of zirconium hydroxide (MEL) at 1073 K for 1h in flowing air. The alumina (Engelhard) was calcined at 1073K. The $Ce_{0.75}Zr_{0.25}O_2$ supports was synthesized following the method published by Hori et al. (7). The catalysts were prepared by incipient wetness impregnation of the supports with an aqueous solution of $H_2PtCl_6.6H_2O$ (Aldrich). Pt/ZrO_2 and $Pt/Ce_{0.75}Zr_{0.25}O_2$ samples were dried at 393K and calcined at 673K for 2h. Pt/Al_2O_3 sample was dried at 393K and calcined at 973K for 2h. The samples contained 1.5 wt.% of Pt.

Oxygen storage capacity (OSC) measurements were carried out in a micro-reactor coupled to a quadrupole mass spectrometer (Balzers, Omnistar). The samples were reduced under H_2 at 773K for 1h and then heated to 1073K in flowing He. Then, the samples were cooled to 723K and a $5\%O_2/He$ mixture was passed through the catalyst until the oxygen uptake was finished. Then, the reactor was purged with He and the dead volume was obtained by switching the gas to the $5\%O_2/He$ mixture. Finally, N_2 pulses were injected in order to calculate the amount of oxygen consumed on the catalysts taking into account a previous calibration of the mass spectrometer.

The dispersion was calculated from CO chemisorption by using pulses of a mixture containing 10%CO / He at room temperature. This experiment was performed on the same apparatus described to the OSC measurements and the same pretreatment was used.

Reactions were performed in a quartz reactor at atmospheric pressure. Prior to reaction, the sample was reduced under H_2 at 773K for 1h and then heated to 1073K in He. CO_2 reforming of methane was performed at 1073K with a $CH_4:CO_2$ ratio of 2:1 and a flow rate of 150 cm^3/min. The partial oxidation of methane was carried out at 1073K and a reactant mixture containing $CH_4:O_2$ ratio of 2:1 at a flow rate of 100 cm^3/min.

Results and Discussion

Table 1 presents the oxygen uptakes measured for the catalysts. The oxygen storage capacity of the $Pt/Ce_{0.75}Zr_{0.25}O_2$ catalyst is much higher than the one of the Pt/Al_2O_3 and Pt/ZrO_2 catalysts. The incorporation of ZrO_2 into CeO_2 lattice strongly increase the oxygen vacancies of the support due to the high oxygen mobility (8). The dispersion of the catalysts is also listed in Table 1. Pt/Al_2O_3 and $Pt/Ce_{0.75}Zr_{0.25}O_2$ catalysts exhibit approximately the same dispersion whereas the Pt/ZrO_2 catalysts had a higher dispersion.

Table 1. O_2 uptakes measured at 723K and dispersion calculated from the CO chemisorption at 298K.

Catalyst	O_2 uptake ($\mu mol/g_{catal}$)	Dispersion (%)
Pt/Al_2O_3	0.0	10
Pt/ZrO_2	8.5	24
$Pt/Ce_{0.75}Zr_{0.25}O_2$	625.6	8

The conversions of methane on the CO_2-reforming reaction at 1073K are shown in Figure 1. The Pt/Al_2O_3 catalyst had a low initial activity and rapidly deactivated due to coke deposition. The Pt catalysts supported on unpromoted zirconia and ceria-doped zirconia exhibited much higher activity and stability than the Pt/Al_2O_3 catalysts. The enhancement of the activity and the stability on the CO_2-reforming reaction could be assigned to the higher amount of oxygen vacancies in the proximity of metal particles as revealed by the OSC measurements (Table 1). According to the two-path mechanism proposed for the CO_2 reforming of methane (6), the addition of ceria to zirconia support greatly increases the rate of oxygen transfer and consequently the carbon removal.

Figure 1 shows the methane conversion on the partial oxidation of methane at 1073K. A strong deactivation is observed on the Pt/Al_2O_3 catalyst and less pronounced on the Pt/ZrO_2 catalyst. The $Pt/Ce_{0.75}Zr_{0.25}O_2$ catalyst practically did not loose their activity after 24 h time on stream (TOS).

Furthermore, a significant change in the selectivity towards CO and CO_2 was observed on the Pt/Al_2O_3 and Pt/ZrO_2 catalyst during the reaction (Figure 2). The production of CO_2 increased and the selectivity to CO decreased as the CH_4 conversion decreased. This effect is much less significant on the $Pt/Ce_{0.75}Zr_{0.25}O_2$ catalyst.

These results could be explained through the two step mechanism proposed for the partial oxidation of methane. According to this mechanism, in the first stage, combustion of methane occurs producing CO_2 and H_2. In the second one, synthesis gas is produced via carbon dioxide and steam-reforming reaction of the unreacted methane (9). Since the production of carbon and CO_2 increased on the Pt/Al_2O_3 and Pt/ZrO_2 catalyst during the reaction (Figure 2), the

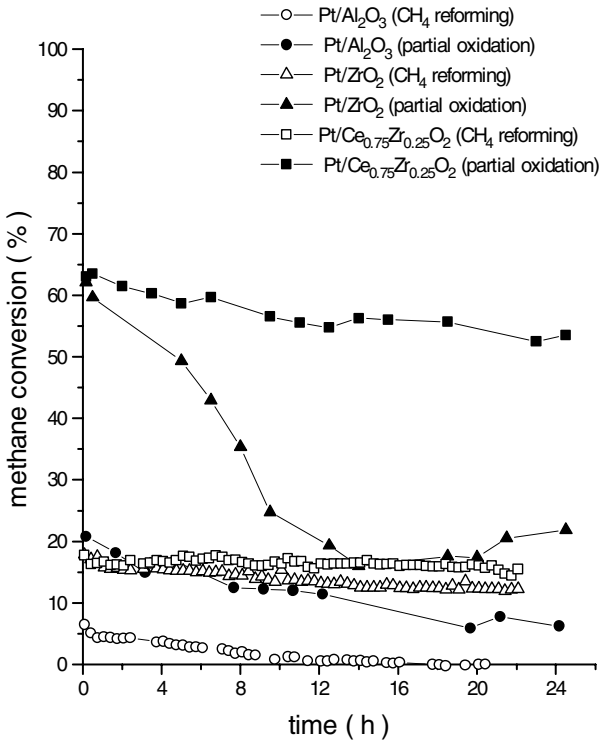

Figure 1. Catalytic activity on both CO_2-reforming of methane (open symbols) and partial oxidation of methane (solid symbols) versus time on stream for Pt/Al_2O_3, Pt/ZrO_2 and $Pt/Ce_{0.75}Zr_{0.25}O_2$ catalyst. Reaction conditions: T= 1073K; CH_4:CO_2 ratio = 2:1; CH_4:O_2 ratio = 2:1.

second step of the mechanism should be inhibited. From Figure 1, it is clear that the increase of carbon deposits around or near the particle metal affects the CO_2 dissociation and inhibits the CO_2 reforming of methane mainly on the Pt/Al_2O_3 catalyst and on less extent on the Pt/ZrO_2 catalyst. On the $Pt/Ce_{0.75}Zr_{0.25}O_2$ catalyst, the selectivity towards CO practically did not change during reaction due to the redox mechanism of carbon removal promoted by the support.

Conclusions

The results of catalytic activity on both the CO_2 reforming and the partial oxidation of methane revealed the important role of the support on the mechanism of these reactions. A strong deactivation was observed on the Pt/Al_2O_3 catalyst on both reactions. The addition of ceria to zirconia greatly promoted the stability of the catalyst due to higher oxygen exchange capacity of the support. The higher rate of oxygen transfer keep the metal surface free of carbon. This promotional effect on the CO_2 reforming of methane affects the partial oxidation of methane, which comprehends two steps: combustion of methane and CO_2 and steam reforming of unreacted methane.

Acknowledgement. The authors wish to acknowledge the financial support of the CNPq/CTPETRO (462530/00-0) and FNDCT/CTPETRO (65.00.0395.00) program. We also thanks MEL Chemicals for providing the zirconium hydroxide.

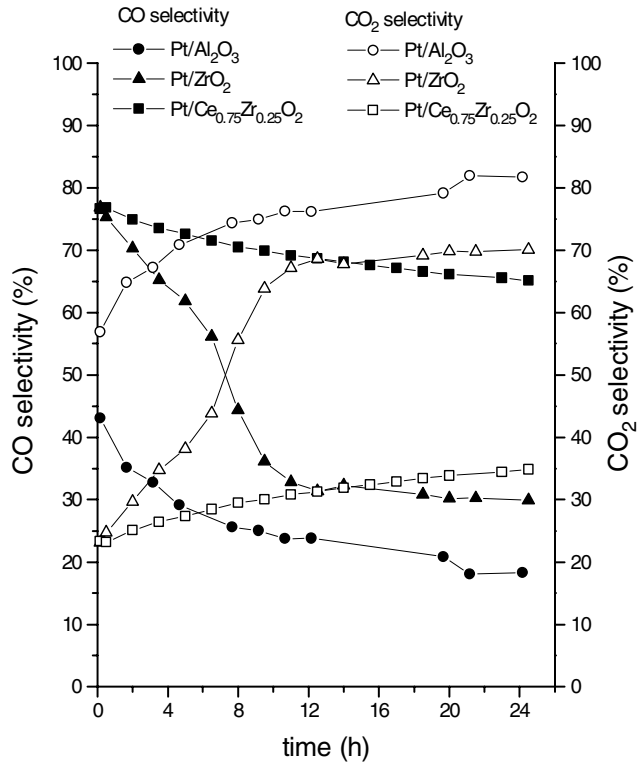

Figure 2. CO and CO_2 selectivity on partial oxidation of methane versus time on stream for: Pt/Al_2O_3, Pt/ZrO_2 and $Pt/Ce_{0.75}Zr_{0.25}O_2$ catalyst. Reaction conditions: T= 1073K; CH_4:O_2 ratio = 2:1.

References

(1) Venkataraman, V.K., Guthrie, H.D., Avellanet, R.A . and Driscoll, D.J., *Stud.Surf.Sci.Catal*. **1998**, *119*, 913.
(2) Dybkjaer, I. and Christensen, T.S., *Stud.Surf.Sci.Catal*. **2001**, *136*, 435.
(3) Van Keulen, A.N.J., Hegarty, M.E.S., Ross, J.R.H. e van den Oosterkamp, P.F., *Stud.Surf.Sci.Catal*. **1997**, *107*, 537.
(4) Stagg, S.M., Romeo, E., Padro, C., Resasco, D.E., *J.Catal.* **1998**, *178*, 139.
(5) Stagg-Willians, S.M., Noronha, F.B., Fendley, G. e Resasco, D.E., *J.Catal*. **2000**, *194*, 240.
(6) Noronha, F.B., Fendley, E.G., Soares, R.R., Alvarez, W.E. e Resasco, D.E., *Chem.Eng.Journal* **2001**, 82, 21.
(7) Hori, C.E., Permana, H., Simon Ng, K.Y., Brenner, A., More, K., Rahmoeller, K.M., Belton, D., *Appl. Catal. Envir. B* **1998**, 16, 105.
(8) Vlaic, G., Fornasiero, P., Geremia, S., Kaspar, J., Graziani, M., *J.Catal*. **1997**, *168*, 386.
(9) O'Connor, A ., M. and Ross, J.R.H., *Catal.Today* **1998**, 46, 203

Recent Developments in Autothermal Reforming and Prereforming for Synthesis Gas Production in GTL Applications

Kim Aasberg-Petersen, Thomas S. Christensen, Charlotte Stub Nielsen, Ib Dybkjær*

Haldor Topsøe A/S, Nymøllevej 55, DK-2800 Lyngby, Denmark

Introduction

Processes for conversion of natural gas into liquid fuels ("Gas-to-Liquids" or GTL) such as gasoline or diesel produced by Fischer-Tropsch (FT) synthesis are attracting increased attention. A GTL-plant for production of FT-products can be divided into three sections. In the first section, the natural gas is converted into synthesis gas – a mixture of hydrogen and carbon oxides. In the second part, the actual FT synthesis takes place and in the final section, product upgrading and separation occurs.

The most capital-intensive part of the GTL-plant is the preparation of synthesis gas, which may account for 50-75% of the capital cost [1]. Hence, there is a considerable incentive to optimise technologies for reducing the cost. Autothermal Reforming (ATR) has been identified as the preferred option for large-scale safe and economic synthesis gas production. This paper will focus on recent developments in the prereforming and ATR technology for synthesis gas production.

Process Concepts and Synthesis Gas Composition

A typical process concept for production of synthesis gas based on ATR is shown in Figure 1. The key steps in the process scheme are desulphurisation, adiabatic prereforming, autothermal reforming, and heat recovery.

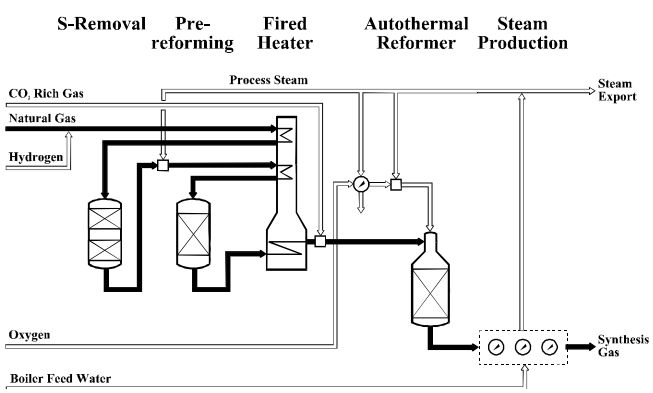

Figure 1. Process Concept for Synthesis Gas Production by Adiabatic Prereforming and Autothermal Reforming

The desired exit gas composition for most FT-applications is an H_2/CO-ratio of about 2. This ratio is achieved by recirculating CO_2. Reducing the amount of steam added to the hydrocarbon feedstock decreases the H_2/CO-ratio and the required recirculation of carbon dioxide. Operation at low steam-to-carbon (H_2O/C) ratio improves process economics, as illustrated in Table 1 [1]. Operation at H_2O/C-ratios of 0.6 has been proven industrially [3] and large-scale GTL projects for production of FT-fuels based on ATR have been publicized [4].

Table 1. Process Economics with Various H_2O/C-Ratios [1]

H_2O/C	0.2	0.6	1.0
Relative Energy Consumption	0.97	1.00	1.03
Relative Investment	0.9	1.0	1.1

The Air Separation Unit (ASU) for production of pure oxygen accounts for a large part of the investment of the production of synthesis gas. The use of a prereformer in the process scheme in Figure 1 upstream the ATR reactor reduces the oxygen consumption per unit of product produced.

Prereforming and ATR at Low H_2O/C-ratios

In the prereformer, all higher hydrocarbons (C_{2+}) are converted into a mixture of methane, hydrogen, and carbon oxides according to the following reactions:

$$C_nH_m + nH_2O \Rightarrow nCO + (n + m/2)H_2 \quad (1)$$
$$3\,H_2 + CO \Leftrightarrow CH_4 + H_2O \quad (2)$$
$$CO + H_2O \Leftrightarrow H_2 + CO_2 \quad (3)$$

The prereformer is an adiabatic fixed-bed reactor with highly active nickel catalysts.

The ATR reactor consists of a burner, a combustion chamber, and a fixed bed catalyst section contained in a refractory lined pressure shell [2]. The key elements in the ATR reactor is the burner and the catalyst bed [2]. The burner provides mixing of the feed streams and the natural gas is converted in a turbulent diffusion flame often simplified by the following reaction:

$$CH_4 + 3/2\,O_2 \Rightarrow CO + 2H_2O \quad (4)$$

The catalyst bed equilibrates the methane steam reforming (reverse of (2)) and the shift (3) reactions.

As shown in Table 1, there is a considerable economic incentive to reduce the H_2O/C-ratio in a GTL plant. However, operation with low H_2O/C-ratios involves the risk of soot formation in the ATR reactor and whisker carbon formation in the prereformer. In order to overcome this challenge, both fundamental studies and extensive pilot plant operation have been carried out to understand and push the limits towards lower H_2O/C-ratios.

In a prereformer, whisker carbon can be formed either from methane or higher hydrocarbons. The lower limit of the H_2O/C-ratio depends on a number of factors including the feed gas composition, the operating temperature and the choice of catalyst. In a prereformer operating at low H_2O/C-ratio, the risk of carbon formation [5] from methane is most pronounced in the reaction zone where the temperature is highest. Carbon formation from higher hydrocarbons can only take place in the first part of the reactor with the highest concentrations of C_{2+} compounds. In Figure 2, a measured temperature profile from a prereformer pilot plant run operating at an H_2O/C-ratio of 0.4 is presented. Post-test analysis of the catalyst showed that no carbon formation had occurred.

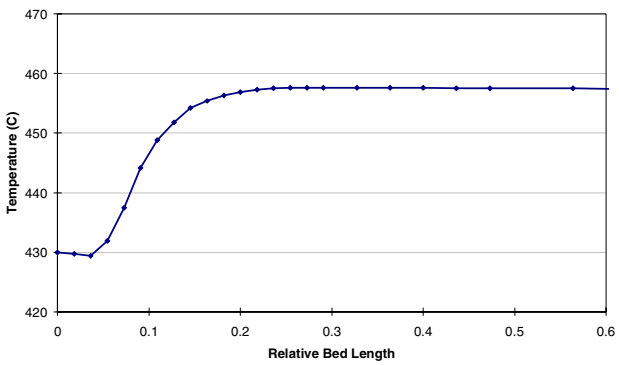

Figure 2. Temperature profile in Adiabatic Prereformer during pilot plant operation. $H_2O/C = 0.4$.

The risk of soot formation in an ATR reactor depends on a number of parameters including feed gas composition, temperature, pressure, and especially burner design. Soot precursors may be formed in the combustion chamber during operation. It is essential that the design of burner, catalyst and reactor is such that the precursors are destroyed by the catalyst bed to avoid soot formation. In Table 2, examples of operating conditions without soot formation in a pilot plant are given [2].

Table 2: Autothermal Reforming - Pilot Plant Demonstration Runs at Low H_2O/C-Ratios [2]

Test	A	B
Feed Ratios [1)](mole/mole)		
H_2O/C	0.60	0.36
O_2/C [2)]	0.58	0.57
Product Gas		
Temperature, (˚C)	1020	1022
Pressure, (bar)	28.5	28.5
H_2/CO, (mole/mole)	2.30	2.15
Total run hours	2235	920

Notes: 1) Mole per mole of hydrocarbon C-atoms
2) The O_2/C-ratio is approximately 5% higher than truly adiabatic reactors with same exit temperature.

Conclusion

The combination of adiabatic prereforming and autothermal reforming at low H_2O/C-ratios is a preferred layout for production of synthesis gas for large GTL-plants. Extensive testing and demonstration in pilot plants have proven that the technologies are ready for application in large industrial scale.

References

[1] Dybkjær, I. and Christensen, T.S., *Stud. Surf. Sci. Catal.*, 136 (**2001**) 435.

[2] Christensen, T.S.; Østberg, M.; and Bak Hansen, J.-H., "Process Demonstration of Autothermal Reforming at Low Steam-to-Carbon Ratios for Production of Synthesis Gas", *AIChE Annual Meeting*, Reno, USA, Nov. 4-9, **2001**

[3] Ernst, W.S.; Venables, S.C.; Christensen, P.S.; and Berthelsen, A.C., *Hydrocarbon Proc.*, 79(3) (**2000**), 100-C

[4] Rostrup-Nielsen, J.R.; Dybkjær, I.; and Coulthard, G.R.G., "Synthesis Gas for Large-Scale GTL-Plants", *AIChE Spring Annual Meeting*, Houston, USA, April 22-26, 2001

[5] Rostrup-Nielsen, J.R. and Sehested, J., *Stud. Surf. Sci. Catal.,* 139 (**2001**) 1.

DEVELOPMENT OF A PRESSURE DEPENDENT REACTION MODEL FOR METHANE/METHANOL MIXTURES UNDER PYROLYTIC AND OXIDATIVE CONDITIONS AND COMPARISON WITH EXPERIMENT

Chad Sheng, Joseph W. Bozzelli and Wen-chiun Ing

Dept of Cheml Engrg, Chem and Envir Sci
New Jersey Institute of Technology, Newark, NJ 07102

ABSTRACT

Methanol experimental data are obtained under pyrolysis, fuel lean ($\phi = 0.75$) and stoichiometric mixtures with methane in a flow reactor. Methanol pyrolysis experiments are performed under isothermal conditions of 1073K over a pressure range from 1 to 10 atm. Oxidation environments are performed over a temperature range from 873 - 1073K and a pressure range from 1 - 5 atm. Oxidation experiments consisting of methane/methanol mixtures are performed under stoichiometric conditions, with varying ratios of the two fuels. A pressure dependent mechanism for methane/methanol oxidation and pyrolysis reaction system is developed and compared with experimental data. Pathways for formation of higher molecular weight species, such as methyl-ethers, are also incorporated in this mechanism. The mechanism consists of about 150 species and 450 elementary reaction steps, with over 200 elementary reactions being pressure dependent. Pressure and temperature dependent rate constants are determined by utilizing quantum RRK (QRRK) analysis on bimolecular (chemical activation) association, addition and insertion reactions and in unimolecular dissociation and isomerization reaction systems, combined with "modified strong collision" treatment for fall-off. Pressure and temperature dependent rate constants are determined by the QRRK code and expressed in the form of an 7 x 3 Chebyshev polynomial formalism over the pressure range of 0.001 to 100 atm and a temperature range of 250 to 2500K. Methane oxidation increased significantly with addition of methanol.

INTRODUCTION

Oxygenated hydrocarbons play an important role in both industrial and environmental chemistry. Alcohols, such as methanol and ethanol, are in use as alternative motor fuels and as additives to conventional transportation fuels to improve performance. Ethers, such as methyl tert-butyl ether (MTBE), are in use as oxygen additives as anti-knock components in gasoline and other ethers are being considered as additives for diesel fuels. The oxidation and pyrolysis of gas phase methanol has been reported in a number of studies over the past half century by different experimental methods, which range from laser induced fluorescence, diffusion flame, shock-tube and static or flow reactors. Both De Avillez Pereira *et. al* and Held and Dryer present recent experimental data on this system, as well as a thorough compilation of previous works done on this system.[5,10]

Three different wide ranges of experimental conditions are performed: methanol pyrolysis, methanol oxidation and methanol/methane oxidation. A reaction mechanism model is also developed, which includes about 200 pressure dependent reaction steps. Pressure and temperature dependent rate constants are represented in Chebyshev polynomial form over a pressure range from 0.001 - 100 atm and a temperature range of 250 – 2500K. Included in the mechanism are pressure effects on important unimolecular and bimolecular reactions plus negative temperature dependence and pressure effects on hydrocarbon (HC) and oxy-hydrocarbon (OHC) species reactions. Pathways for formation and oxidation of higher molecular weight products, such as C2 hydrocarbons and methyl-ethers, which we observe in this study, are also included.

EXPERIMENTAL SETUP:

The reactor used in the experiment is a 6mm ID (12mm OD) quartz tube, housed in a 75 cm three-zone clamshell 3 cm ID electric tube furnace equipped with three independent digital temperature controllers. A 200 psi back pressure regulator is used to maintain the desired pressure within the reactor. (Refer to Figure 1 for experimental setup).

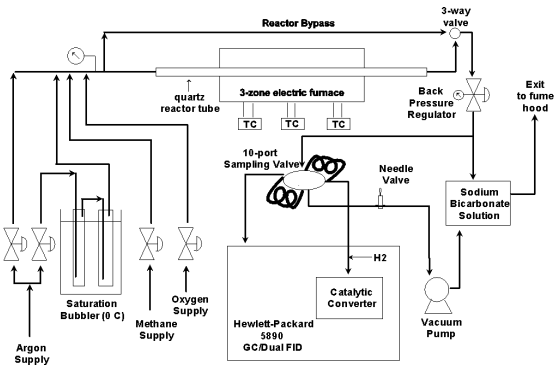

Figure 1. Schematic of experimental flow reactor and analytical system.

The feed mixtures are preheated to about 373ºK to prevent condensation and improve reactor temperature control. Gas samples are drawn through by a mechanical vacuum pump. An HP-5890 Series II gas chromatograph (GC) with two flame ionization detectors (FID) is used on-line for analysis. A packed column is used for the separation of CO, CO_2 and light HC's and a capillary column is used for heavier HC's and OHC's separation. A catalytic converter is used to improve quantitative analysis of CO and CO_2 by converting the mixture to methane, which can be detected by the FID. Batch samples of reactor gas drawn from the reactor are collected into evacuated 25 cm^3 stainless steel sample cylinders for verification of products using a GC/MS.

Methanol pyrolysis experiments are all performed under isothermal condition at 1073ºK, with varying concentrations of CH_3OH over a pressure range from 1 to 10 atm. Experimental data on the decomposition of methanol in presence of oxygen and argon were obtained for both fuel lean ($\phi = 0.75$) and stoichiometric ($\phi = 1.0$) conditions over a temperature range from 873 to 1073ºK and a pressure range of 1 to 5 atm. All methanol/methane oxidation experiments are carried out under overall stoichiometric conditions. Experimental data for methanol/methane oxidation experiments at two different temperatures and pressure combination conditions are collected: either 873ºK and 5 atm or 1073 and 1 atm. Various methanol/methane concentration ratios, ranging from 0:2 to 2:0, were studied for each of the two temperature/pressure conditions.

COMPUTATIONAL METHODS

Thermodynamic properties. Thermodynamic properties of species are from literature, theoretical and estimation techniques, such

as group additivity[2], hydrogen bond increment (HBI)[12] and *ab initio* or density function calculations. The molecular properties for the explicit CH_3OH dissociation system, including methanol, transition states (TS) and products, are determined by the high level composite CBS-APNO *ab initio* calculations. The *ab initio* calculations are performed using Gaussian94.[6] The CBS-APNO calculations are performed in accordance to the method outlined by Montgomery *et al*[15]. Vibrational frequencies, ZPVE and thermal correction contributions are calculated at the HF/6-311G(d,p) level of theory, with scaling factors consistent with the recommended values by Scott and Radom.[18] The optimized geometry is calculated at the QCISD/6-311G(d,p) level of theory. Figure 2 illustrates the potential energy diagram of the CH_3OH subsystem. The enthalpies of the two biradicals in the system are determined by use of isodesmic working reactions[9] with group balance.

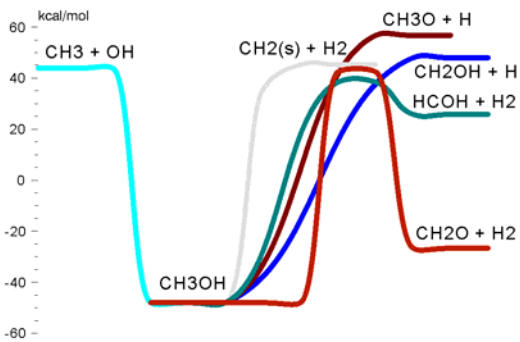

Figure 2. Potential energy diagram of the methanol subsystem calculated at CBS-APNO level of theory.

Conventional statistical mechanics analysis was employed to determine the vibrational, external rotational and translational contributions to entropy and $C_p(T)$. Unpaired electrons are also included in the S^{298} and $C_p(T)$ calculations accordingly. Contributions of internal rotation to S^{298} and $C_p(T)$ are incorporated based on the Pitzer-Gwinn formalism.[17]

Calculation of High-Pressure Rate Constants. Abstraction reaction rate constants are not pressure dependent and are usually taken from evaluated literature when available. Evans-Polanyi analysis is used on the reaction in the exothermic direction to estimate the energy of activation (E_a) for rate constant.

The high-pressure forward rate constants in the CH_3OH subsystem are determined by application of macrocanonical transition state theory (CTST) for temperatures from 300 – 2500 K. Forward rate constants from 300 – 2500 K are calculated and fitted by a nonlinear least squares method to the form of a modified Arrhenius rate expression. The rate constants for the three combination and dissociation reaction in the CH_3OH system are calculated by variational transistion state theory (VTST), with thermochemical properties determine at the CBS-Q//B3LYP/6-31G(d,p) level of theory.[16,1,13] The combination reaction rate constant is determined by satisfying the microscopic reversibility criteria.

Kinetic Analysis. Pressure and temperature dependent rate constants are determined by a modified quantum RRK (QRRK) formalism for *k(E)*. Two methods to analyze the collisional deactivation of the energized adduct are used: master equation analysis and the modified strong collision model. Chang *et al* described a modified QRRK analysis that is used in this paper.[4] Master equation analysis is used for fall-off in this analysis as described by Sheng *et al*[19] and follows Gilbert and Smith[7].

Pressure Dependent CHEMKIN Mechanism.: Both the modified strong collision and master equation codes incorporate a temperature and pressure dependent output formalism for the rate constants, in the form of an N x M Chebyshev polynomial expression. The temperature-pressure dependent rate coefficients in Chebyshev format for the current system of interest are derived from application of the methodology described by Venkatesh *et al*[21,20]. The CHEMKIN interpreter is modified to accept the N x M Chebyshev polynomial formalism of rate constant.[11]

RESULTS AND DISCUSSION

Enthalpies of CH3OH Subsystem. The sum of enthalpies for the respective product sets are compared with data from the study of Walch[22] and Harding *et al*[8]. Harding *et al*'s data are calculated at the RMP4/6-31G(d,p) level of theory and Walch's data are derived using complete-active-space self-consistent-field (CASSCF) / internally contracted configuration-interaction (CCI), *ab initio* calculations.

Table 1. Comparison of Product Enthalpies in the Methanol System with Literature Data.

	CBS-APNO	Walch[22]	Harding *et al*.[8]
CH_3OH	0	0.0	0.0
$CH_3O + H$	104.1		
$CH_2OH + H$	95.1		
$^1CH_2 + H_2O$	91.8	88.8	94.9
$^3CH_2 - {}^1CH_2$	-8.99	-9.0	
$CH_3 + OH$	90.5		
$^1HCOH + H_2$	72.8	71.1	71.1
$CH_2O + H_2$	20.1	18.1	16.4
$[H_2CO\cdots H_2]^{\ddagger}$	90.7	91.9	96.5
$[HCOH\cdots H_2]^{\ddagger}$	86.5	85.0	91.0
$[^1CH_2\cdots H_2O]^{\ddagger}$	83.6	82.3	84.6

The enthalpy for the transition state of $^1CH_2 + H_2O$ channel, as reported also by Walch and Harding *et al*, is lower than the enthalpy of $^1CH_2 + H_2O$. The CH_3OH dissociation barrier, through the $^1CH_2 + H_2O$ channel is calculated form canonical transition state theory, based on an excited state of TS that has the same enthalpy as the enthalpy of $^1CH_2 + H_2O$ with a corresponding entropy at the same energy level as the "excited" TS. The high-pressure limit rate constants are shown in Table 2.

Table 2. High-Pressure Limit Rate Coefficient for the CH_3OH System.

Reaction	A	n	Ea (kcal/mol)	
$CH_3 + OH \rightarrow CH_3OH$	3.3133E6	2.0765	-1.7551	a
$CH_3OH \rightarrow CH_3 + OH$	3.2591E10	2.05451	90.347	b
$CH_3OH \rightarrow CH_2OH + H$	1.6369E7	2.54513	91.951	b
$CH_3OH \rightarrow CH_3O + H$	1.1908E7	2.38792	99.614	b
$CH_3OH \rightarrow CH_2O + H_2$	1.1004E9	1.28149	90.233	c
$CH_3OH \rightarrow {}^1HCOH + H_2$	2.0299E10	1.22342	86.411	c
$CH_3OH \rightarrow {}^1CH_2 + H_2O$	2.8735E11	1.60030	92.538	d

(a) Microscopic reversibility (b) Variational transition state theory calculation, based on CBS-Q//B3LYP/6-31G(d,p) (c) Canonical transition state theory calculation, based on CBS-APNO (d) Adjusted canonical

transition state theory calculation – thermochemical properties of the transition state taken at the corresponding energy level of the sum of the products.

After methanol decomposition occurs (refer to Figure 1), CH_3OH + OH is the critical reaction responsible for methanol decay. The formation of CH_2O + HO_2 adduct is the dominant channel for pressures < 1 atm and temperature < 2000ºK. Formaldehyde then decays mostly by the reaction of CH_2O + OH $\rightarrow$ HCO + H_2O. The decomposition reaction of HCO + M $\rightarrow$ CO + H + M is found to be the dominant channel to form carbon monoxide and CO + O + M $\rightarrow$ CO_2 + M to form final product of carbon dioxide.

The comparison of methane and methanol oxidation can be described in three stages: initiation, propagation and oxidation. During initiation, formation of key radicals is determined by the most favorable thermochemical kinetic of the respective elementary reaction. Several channels of CH_3OH unimolecular decomposition are much lower in energy than CH_4 and, therefore, faster than CH_4 decomposition. Therefore, propagation reactions in CH_3OH oxidation occur more rapidly than CH_4 oxidation.

CH_3 is the initial radical intermediate in CH_4 oxidation. The major reaction of CH_3 at low CH_3 concentration is reaction with O_2. CH_3 reaction with O_2 to form the $[CH_3OO]^*$ complex which can isomerize to $[CH_2OOH]^*$ and then form the products CH_2O + OH.

Formation of C2 Species. The current mechanism also includes the kinetics of several C2 species. The formation of C2 species is from the combination of two methyl radicals to form ethane. Abstraction of hydrogen from ethane by radicals from the radical pool forms ethyl radicals, which can undergo addition reaction to form ethylperoxy radical. The dominant products is C_2H_4 + HO_2.

Vinyl radicals are formed from the loss of hydrogen in the ethylene molecule, via abstraction reaction with radicals. The vinyl oxidation system used is from Chang *et al*.[4] This vinyl oxidation subsystem includes 5 possible stabilized adducts with multiple exit channels, including the formation of the 3-member ring dioxiranyl radical, which has recently been recognized to be an important channel.[3] The lowest energy process is peroxy radical attack on the ipso carbon, forming a di-oxirane methylene radical, which then isomerizes through an epoxide and cleaves the weak peroxy O—O bond. A further beta scission opens this epoxide ring to form the H_2C•-O-CHO isomer. This isomer beta scissions to form CH_2O + HCO before stabilization can occur. The peroxy radical can also undergo a concerted elimination to form acetylene + HO_2, isomerize via a hydrogen shift to form the vinyl hydroperoxide radical or isomerize to form a 4-member ring. The 4-member ring can ring open to form product pairs such as HCO + H_2CO or H + glyoxal, or redissociate to reactants.

CH_3C●O + O_2 and ●CH_2CHO + O_2 subsystems are obtained from Lee and Bozzelli[14] where thermochemical and kinetic properties are calculated at CBS-Q level of theory. Both reaction systems initiate by the addition of oxygen onto the radical site forming a peroxy radical. One product set resulting from both systems is the formation of ●CH_2CO + HO_2. In both oxidation systems, the ●CH_2CO + HO_2 products can be formed through two channels; direct molecular elimination or β-scission of the hydroperoxy radical formed from isomerization. The other channel that can occur with the hydroperoxy radical is ring closure to form a carbonyl-oxirane specie plus OH. In the ●CH_2CHO + O_2 subsystem, the hydroperoxy ethyl-aldehyde radical can also undergo a fast reaction, albeit complex, to form the product set consisting of OH + CO + H_2CO.

Comparisons with Experimental Results. Methanol pyrolysis comparisons between the model with experimental results at 1 atm is illustrated in Figure 3. Comparisons of the methanol oxidation model and the experimental results at 5 atm at an equivalence ratio of $\phi = 1$ is shown in Figures 4. These show reasonable agreement for reactant decay and main product formation.

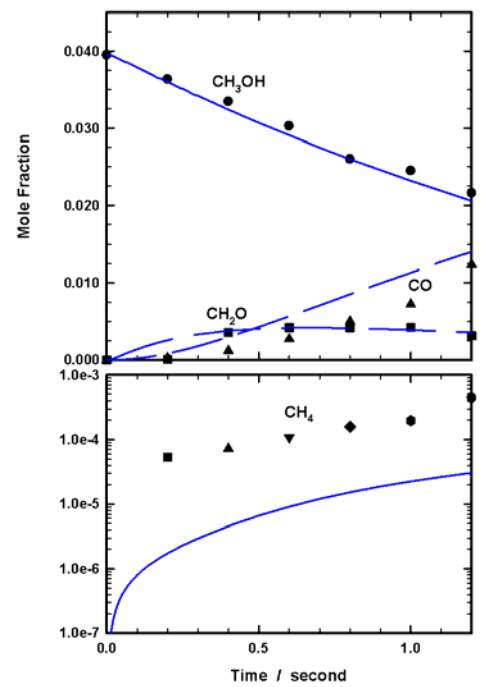

Figure 3. Comparison of experimental data with model for CH_3OH pyrolysis at 1073 K, 1 atm, X_0 = 3.95 %

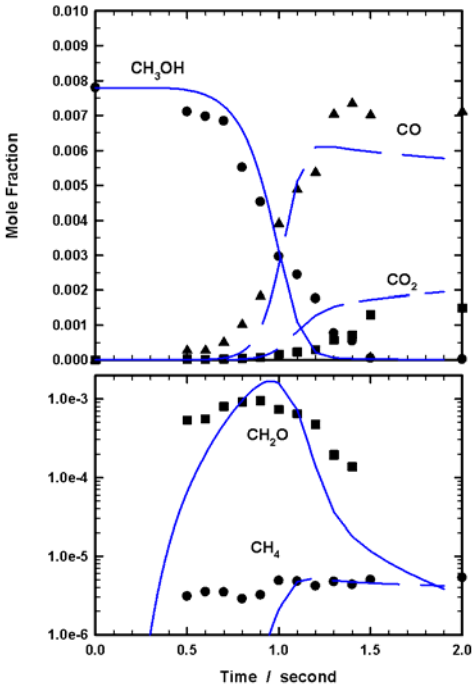

Figure 4. Comparison of experimental data with model for CH_3OH oxidation at 873 K, 5 atm, X_0 = 0.78 %

Figures 5 and 6 shows comparison of methane/methanol mixture experiment at 873ºK, 5 atm and equal initial concentration of methane/methanol, with a fuel equivalence ratio of unity. The initial methane concentration in Figure 5 is 0.78% and in Figure 6 it is 0.39%. Agreements between model and experimental data on methane and methanol predictions are relatively well matched. The model predicts methanol reacts slightly faster than experimental data. The model under predicts CO at both conditions, while CO_2 is over predicted. Formaldehyde formation between the model and experimental data has very good agreement. The model is able to predict a maximum inflection point in the concentration profile, which is observed in the experimental data as well. Trace product concentrations of ethane and ethylene, as predicted by the model, are higher than expected compared to experimental data.

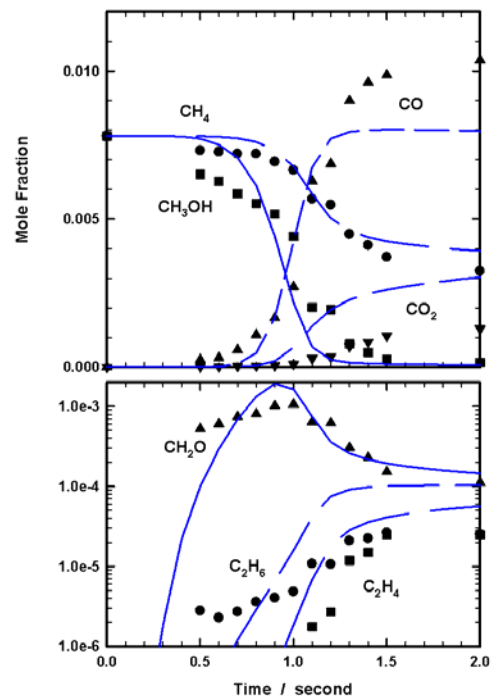

Figure 5. Comparison of experimental data with model for CH_3OH/CH_4 oxidation at 873 K, 5 atm, $X_{CH3OH,0}$ = 0.78%, X_{CH40} = 0.78%

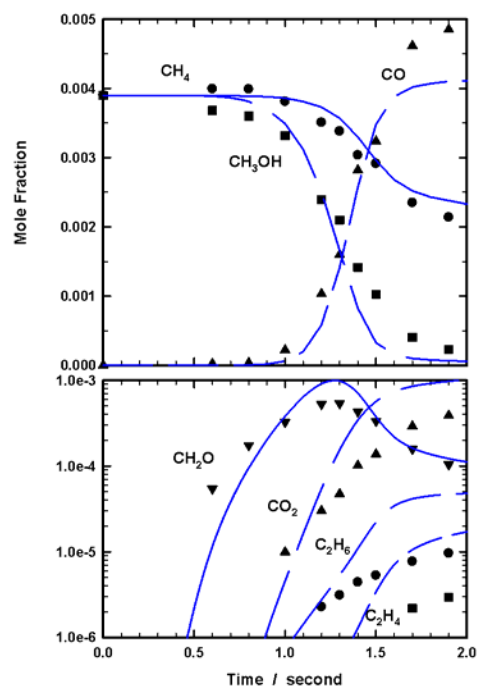

Figure 6. Comparison of experimental data with model for CH_3OH/CH_4 oxidation at 873 K, 5 atm, $X_{CH3OH,0}$ = 0.39%, X_{CH40} = 0.39%

CONCLUSION:

Experimental data and a kinetic model has been developed and tested for various types of reaction system (i.e. pyrolysis, fuel lean, stoichiometric and fuel additive) at different system conditions (temperature, pressure and initial fuel concentration). Comparison between experimental and the kinetic model shows relatively good agreement. This mechanism can serve as a basis for future studies on other higher molecular weight hydrocarbon and oxy-hydrocarbon system, especially since data on addition of oxy-hydrocarbon to hydrocarbon specie significantly accelerates the decay of the hydrocarbon specie.

REFERENCES

(1) Becke, A. D. *J. Chem. Phys.* **1993**, *98*.

(2) Benson, S. W. *Thermochemical Kinetics*, 2nd ed.; Wiley-Interscience: New York, 1976.

(3) Carpenter, B. K. *J. Phys. Chem.* **1995**, *99*, 9801.

(4) Chang, A. Y.; Bozzelli, J. W.; Dean, A. M. *Zeit. Phys. Ch.* **2000**, 1533-1568.

(5) De Avillez Pereira, R.; Baulch, D. L.; Pilling, M. J.; Robertson, S. H.; Zeng, G. *J. Phys. Chem. A* **1997**, *101*, 9681-9693.

(6) Frisch, M. J.; Trucks, G. W.; Head-Gordon, M.; Gill, P. M. W.; Wong, M. W.; Foresman, J. B.; Johnson, B. G.; Schlegel, H. B.; Robb, M. A.; Replogle, E. S.; Gromperts, R.; Andres, J. L.; Raghavachari, K.; Binkley, J. S.; Gonzalez, C.; Martin, R. L.; Fox, D. J.; Defrees, D. J.; Baker, J.; Stewart, J. J. P.; Pople, J. A.; Eds. *Gaussian 94 computer program, Revision C.2*; Gaussian Inc.: Pittsburgh, 1995.

(7) Gilbert, R. G.; Smith, S. C. *Theory of Unimolecular and Recombination Reactions*; Blackwell Scientific Publications: Oxford, 1990.

(8) Harding, L. B.; Schlegel, H. B.; Krishnan, R.; Pople, J. A. *J. Phys. Chem.* **1980**, *84*, 3394-3401.

(9) Hehre, W. J.; Radom, L.; Schleyer, P. R.; Pople, J. A. *Ab initio Molecular Orbital Theory*; Wiley & Sons: New York, 1986.

(10) Held, T. J.; Dryer, F. L. *Internation Journal of Chemical Kinetics* **1998**, *30*, 805-830.

(11) Kee, R. J.; Miller, J. A.; Jefferson, T. H. CHEMKIN: Fortran Chemical Kinetics Code Package, 1980.

(12) Lay, T. H.; Bozzelli, J. W.; Dean, A. M.; Ritter, E. R. *J. Phys. Chem.* **1995**, *99*, 14514-14527.

(13) Lee, C.; Yang, W.; Parr, R. G. *Phys. Rev. B* **1988**, *37*.

(14) Lee, J. W.; Bozzelli, J. W. "CH3CjO and CjCHO oxidation"; 5th International Conference on Chemical Kinetics, 2001, Gaithersburg, MD.

(15) Montgomery, J. A., Jr.; Ochterski, J. W.; Petersson, G. A. *J. Chem. Phys.* **1994**, *101*, 5900-5909.

(16) Ochterski, J. W.; Petersson, G. A.; Montgomery, J. A. *J. Chem. Phys.* **1996**, *104*, 2598.

(17) Pitzer, K. S.; Gwinn, W. D. *J. Chem. Phys.* **1942**, *10*, 428.

(18) Scott, A. P.; Radom, L. *J. Phys. Chem.* **1996**, *100*, 16502-16513.

(19) Sheng, C.; Bozzelli, J. W.; Dean, A. M.; Chang, A. Y. *Submitted to J. Phys. Chem. A* **2001**.

(20) Venkatesh, P. K.; Chang, A. Y.; Dean, A. M.; Cohen, M. H.; Carr, R. W. *AIChE Journal* **1997**, *43*, 1331-1339.

(21) Venkatesh, P. K.; Dean, A. M.; Cohen, M. H.; Carr, R. W. *Reviews in Chemical Engineering* **1997**, *13*.

(22) Walch, S. P. *J. of Chem. Phys.* **1993**, *98*, 3163-3167.

ADSORPTION PROPERTIES STUDIES OF THE NICKEL CATALYSTS FOR CARBON DIOXIDE REFORMING OF METHANE

Rong-Gang Ding[1, 2] *Zi-Feng Yan*[2]

[1]Department of Chemical Engineering, University of Queensland, Brisbane, 4072, Australia
[2]State Key Laboratory for Heavy Oil Processing, University of Petroleum, Dongying, Shandong 257062, CHINA

Introduction

Conversion of methane and carbon dioxide into useful products is an important area in the current catalytic research on hydrocarbon transformations. Carbon dioxide reforming with methane is not only very important for potential usefulness in industry and environment optimization[1-8] but also theoretically significant in understanding the nature of heterogeneous catalysis on hydrocarbon conversion. Heterogeneous catalysis occurs at active centers on a surface and it is recognized that a complete understanding of the catalytic process requires a detailed knowledge of the nature and function of active sites on the surface of the catalysts. The key to surveying the active centers of the metal catalysts is to evaluate and characterize the structure features and properties of the catalysts. The variation of the properties of catalysts can reflect the interaction among metal, support and promoter, and the agglomeration features of the active sites on the metal catalysts. The possible processes accompanying the carbon dioxide reforming with methane may be also speculated according to the changes of physical properties of catalysts. In this paper, physical and chemical adsorption methods are used to characterize the properties and structure of catalysts. The characterized results are used to correlate with the reforming reactivity on metal catalysts and to emphasize the importance of the special structure features in the reaction of this type.

Experimental

The surface properties such as surface area, average pore diameter, and pore volume are determined using an ASAP 2010 analyzer using N_2 adsorption at 77.5 K. Samples are degassed until the pressure in the tube was below 10 μmHg before analysis.

The total pore volume, V_t, is derived from the amount of adsorption at a relatively pressure close to unity, given that the pores were totally filled with the liquid adsorbate. The average pore size is estimated from the pore volume, assuming that a cylindrical pore geometry using the equation $D_p = 4V_t/S$. The mesopore distribution curve is obtained from the adsorption branch of the N_2 isotherm by BJH method. The micropore distribution is calculated from the gas adsorption using the Horvath-Kawazoe equation, with relative pressure (P/P_o) below 0.01.

The dispersion of nickel on the support is roughly estimated by static equilibrium chemisorption of H_2 at rather isothermal conditions of 308 K. A constant volume high-vacuum apparatus, ASAP 2010C, is used for this purpose. Samples are degassed until the pressure in the tube was below 10 μmHg before analysis.

The physisorbed gaseous impurities on the surfaces of the catalyst samples are cleaned away by ultra high pure N_2 (99.999%) at 973 K. Subsequently, the samples are reduced in ultra high pure H_2 (99.999%) flow at 973 K for 2 hrs. Finally, ultra high pure N_2 is introduced again to purge the samples for 30 minutes.

Results and Discussion

Effect of Active Component on Structure Variation of Catalysts. The catalysts are prepared by wetness impregnation method using $CoSO_4$ (Co-1), $Co(NO_3)_2$ (Co-2), and $Ni(NO_3)_2$ as the metal precursors, respectively. **Figure 1** shows the adsorption isotherms of the untreated alumina support and various calcined catalysts. All adsorption isotherms are similar to a type I isotherm. Impregnation results in an approached decrease in the amount adsorbed, with only slight modification of the knee corresponding to microporosity. A quantitative comparison of the variation of the textual structure, mesopore, and micropore distribution of the alumina support, fresh and used Co, Ni catalysts is given in **Table 1**. The results in **Table 1** show that impregnation of sulfate or nitrate on the support decreases its surface area and total pore volume. However, the average pore diameters of all catalysts are increased after impregnation and carbon dioxide reforming reaction. Of interest is that the mean micropore diameters of all catalysts are obviously decreased after impregnating of the metal component on the alumina support. It means that the impregnated metal species maybe mainly locate on the inner surface of the micropore of the alumina support and that the reforming active sites locate in these micropore metal sites. Simultaneously, the larger pores are generated after reaction.

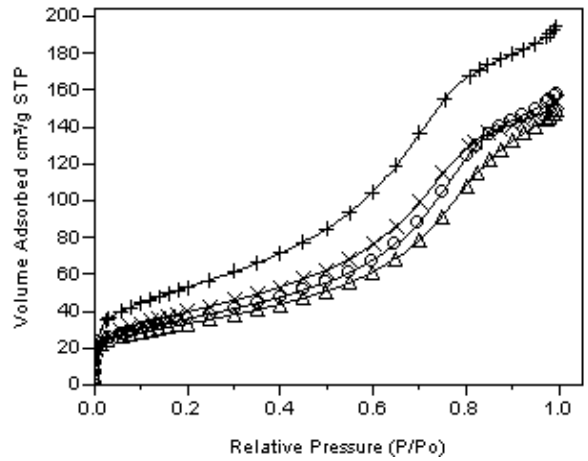

Figure 1. The adsorption isotherm of the untreated support and calcined catalysts.
×: 10 wt% Co-1/Al_2O_3 ($CoSO_4$ as the precursor) +: untreated γ-Al_2O_3 △ : 10 wt% Co-2/Al_2O_3 ($Co(NO_3)_2$ as the precursor) O: 10 wt% Ni/Al_2O_3

Table 1. Characterization of Catalyst Pore Structure*

Catalyst (10wt%)	state	S_{BET} (m^2/g)	D (Å)	D_{micro} (Å)	V_{total} (cm^3/g)
γ-Al_2O_3		192	62.5	7.20	0.300
Co-1/Al_2O_3	fresh	118	78.0	5.90	0.231
	used	114	85.7	6.31	0.244
Co-2/Al_2O_3	fresh	144	66.0	6.60	0.238
	used	174	97.1	6.67	0.422
Ni/Al_2O_3	fresh	130	75.2	6.50	0.244
	used	110	85.0	6.52	0.234

* D: average pore diameter $D_{micro:}$ mean micropore diameter

Effect of Promoter on Structure Variation of Catalysts. The variation of surface areas and total pore volumes of fresh and used catalysts with promoter addition are shown in **Table 2**. From the results shown in **Table 1**, it is deduced that nickel nitrate impregnate

is possibly distributed uniformly in the surface pores of the support with similar decrease in micropore and mesopore volume for various catalysts. Compared the results in **Table 2** with those in **Table 1**, it is easy to know that addition of oxide promoters results in the more decrease of the mesopore volume. Addition of promoters of $Mg(NO_3)_2$ and $Ce(NO_3)_2$ during the multiple-step impregnation process alters the deposition behaviors of $Ni(NO_3)_2$. The locations of the metal and oxide promoters are altered during the impregnation process and the oxide promoter are mostly concentrated on the outer layer of the alumina support while the nickel metal is generally dispersed in the support pores. Apparently, addition of promoters, which mostly deposit on the surface, contributes to more reduction in mesopore volume.

However, it is seen that the unpromoted and promoted 7wt% Ni catalysts show very slight difference in micro- and mesopore volume, but the variations are negligible and well within experimental errors. There is slight increase in surface area by promoter's addition. **Figure 2** indicates that the generation of the pores in the range of 10-30 Å results in the increase of surface area. The part blocking of the bigger mesopores by oxide promoters may be responsible for the generation of smaller mesopores.

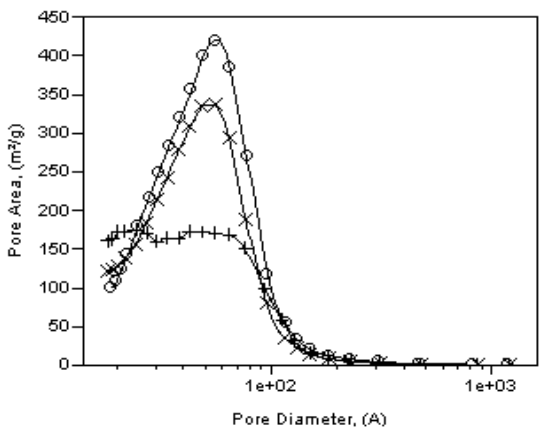

Figure 2. The mesopore distribution of the untreated support, fresh and used Ni supported catalysts.
O: untreated γ-Al_2O_3 ×: fresh 7wt%Ni/Al_2O_3 +: used 7wt%Ni/Al_2O_3

Table 2. Characterization of Catalyst Pore Structure*

Catalyst(wt%)	state	S_{BET} (m^2/g)	D (Å)	V_{total} (m^3/g)	V_{meso} (m^3/g)
γ-Al_2O_3		192	62.5	0.300	0.246
7%Ni/Al_2O_3	fresh	172	56.3	0.242	0.195
	used	143	53.6	0.192	0.154
7%Ni-1%Mg-1%Ce/Al_2O_3	fresh	180	55.3	0.240	0.195
8.5%Ni-2%Mg-3%Ce/Al_2O_3	fresh	150	59.4	0.227	0.189
	used	126	72.0	0.226	0.193
8.5%Ni-3%Mg-2%Ce/Al_2O_3	fresh	148	57.0	0.212	0.173
8.5%Ni-3%Mg-3%Ce/Al_2O_3	fresh	130	64.0	0.200	0.166
10%Ni-3%Mg-1%Ce/Al_2O_3	fresh	144	63.3	0.227	0.191
	used	123	69.0	0.212	0.181
11.5%Ni-1%Mg-2%Ce/Al_2O_3	fresh	145	61.7	0.223	0.186
	used	127	73.5	0.232	0.199
11.5%Ni-3%Ce/Al_2O_3	fresh	143	71.5	0.255	0.219

*D: average pore diameter

The pore structure variations of three kinds of 8.5 wt% Ni catalysts in **Table 2** show that more promoter addition results in more decrease in mesopore volume and the MgO addition exhibits stronger effect on this decrease. The data for 11.5 wt% Ni catalysts also indicate that MgO addition significantly influences pore structure. Too MgO addition may retard the reduction of NiO and cover the NiO layer on the support surface. Therefore, inappropriate MgO addition may decrease the nickel dispersion and surface nickel concentration, which will be described in the H_2 chemisorption.

Effect of Reaction on Structure Variation of Catalysts. Figure 2 shows that mesopore distribution of the untreated support, unpromoted and promoted catalysts before and after reaction. The variation of surface areas and total pore volumes of fresh and used catalysts are shown in **Table 2**.

Figure 2 indicates that the number of pores in catalysts decreases after nickel is loaded on the support remaining in approximately same range of pore diameters. However, the pore size distribution of various catalysts is quite different after reaction. **Figure 2** shows that the number of pores in the range of 30-80 Å in 7 wt%Ni/Al_2O_3 catalyst is significantly decreased after reaction. The total pore volume is also decreased from 0.242 to 0.192 cm^3/g. The mesopore volume decrease contributes primarily the decline of the total pore volume for 7 wt%Ni/Al_2O_3 catalyst. The pore volume decrease may be derived from the coverage of carbon deposition produced in the reforming reaction. That is to say, carbon deposition mainly covers the surface of the catalyst and blocks the mesopores. The unpromoted catalyst exhibits poor resistivity to carbon deposition compared with the alkaline oxide-promoted catalysts according to the pore volume results before and after reaction.

The results shown in **Table 2** indicate that the 8.5wt%Ni-2%MgO-3%CeO_2/Al_2O_3 provides almost unchanged total pore volume and decreased surface area after the reaction. The increased number of larger pores and decreased smaller pores generated in the reaction are responsible for these variations. The average pore diameter shifts toward larger pore size after reaction from 59.4 to 72.0 Å. The pore structure variation may be derived from the support crystalline phase change under high temperature.

H_2 Chemisorption. The metal dispersions of the nickel catalysts supported on alumina are estimated by assuming that each surface metal atom chemisorbs one hydrogen atom, i.e., $H/Ni_{surface}$= 1. Blank experiments show that the amount of H_2 chemisorbs on bare supports is negligibly small. The adsorption results are shown in **Table 3**.

It is found that the metal dispersions of Ni and metallic surface areas on all catalysts are not very high. The apparent low nickel dispersion on the high surface area of γ-Al_2O_3 carrier is probably due to the formation of $NiAl_2O_4$, which can not chemisorb hydrogen at room temperature. Incomplete reduction of Ni crystalline particles, as well as blocking and coverage of nickel crystallites by species originating from MgO and CeO_2 promoters, may also contribute to lowering the amount of hydrogen adsorbed.

Table 3. The Metal Dispersions of the Catalysts

Catalyst (wt %)	M_{disp} (%)	M_{sa} (m^2/g sample)	N_{sa} (m^2/g metal)
8.5%Ni-2%MgO-3%CeO_2/Al_2O_3	0.313	0.177	2.081
8.5%Ni-3%MgO-3%CeO_2/Al_2O_3	0.113	0.064	0.752
7%Ni-1%MgO-1%CeO_2/Al_2O_3	0.204	0.095	1.354
10%Ni-2%MgO/Al_2O_3	0.170	0.114	1.134

The results show that the 8.5%Ni-2%MgO-3%CeO_2/Al_2O_3 catalyst achieved best metal dispersion among the tested catalysts. The nickel dispersion declines form 0.313% to 0.113% with increased

MgO addition from 2 wt% to 3 wt%. This may be attributed partly to the catalyst preparation uncertainty. However, no doubt that the decrease of metal dispersion can be ascribed primarily to the inappropriate promoter addition.

Conclusions

1) The mean micropore diameters of all catalysts were obviously decreased after impregnating of the metal component on the alumina support. It means that the impregnated metal species maybe mainly locate on the inner surface of the micropore of the alumina support and that the reforming active sites also locate in these micropore metal sites.

2) The oxide promoter were mostly concentrated on the outer layer of the alumina support while the nickel metal was generally dispersed in the support pores. Addition of promoters contributed to more reduction in mesopore volume.

3) H_2 chemisorption revealed that the addition of the alkaline oxide MgO promoter significantly prohibits the metal dispersion on the catalyst. Inappropriate promoter addition can result in sharp decrease of the metal dispersion.

Acknowledgement. Financial supports by the Young Scientists Award Foundation of Shandong Province and China National Petroleum Corporation are gratefully acknowledged.

References

(1) Swaan, H. M.; Kroll, V. C. H.; Martin, G. A. and Mirodatos, C. *Catal. Today,* **1994**, *21,* 571.
(2) Hu, Y. H. and Ruckenstein, E. *Catal. Lett.,* **1997***, 43,* 71.
(3) Ruckenstein, E. and Hu, Y. H. *Appl. Catal*., **1995**, *133*, 149.
(4) Hu, Y. H. and Ruckenstein, E. *Catal. Lett,,* **1996**, *36,* 145.
(5) Horiuchi, T.; Sakuma, K.; Fukui, T.; Kubo, Y.; Osaki, T. and Mori, T. *Appl. Catal.,*. **1996**, *144*, 111.
(6) Zhang, Z. and Verykios, X. E. *Appl.Catal.,* **1996**, *138*, 109.
(7) Zhang, Z. and Verykios, X. E. *Catal. Today,* **1994**, *21*, 589.
(8) Tsipouriari, V. A.; Efstathiou, A. M. and Verkios, X. E. *Catal. Today,* **1994**, *21*, 579.

PRODUCTION OF RICH HYDROGEN GASES IN FUEL CELLS

Zhang Xinrong[1], Shi Pengfei[1], Zhao Jianxi[2], Zhao Mengyue[3], and Liu Chuntao[1]

1.Applied of Chemical Department
Harbin Institute of Technology
No 92 Xidazhi Street ,Harbin, China
2.78 Cedar St. #1R, Wakefield, MA 01880
3.College of Chemical Engineering
Zhengzhou University
Wenhua road, Zhengzhou, China

Introduction

Currently, increasing attention is being paid to the low temperature steam reforming of methanol to produce high purity hydrogen to use as fuels in fuel cells for on-board power generation for vehicles. The favor for methanol as a chemical carrier for hydrogen is mainly due to its ready availability, high energy density, and easy storage and transportation. Hydrogen can be extracted in three different processes from methanol: (i)methanol decomposition (ii)steam reforming of methanol(SRM) and (iii) partial oxidation of methanol (POM; equations (1) − (3),respectively):

$CH_3OH \rightleftharpoons 2H_2+CO$ (1)

$\triangle H^0_{298}= + 92.0$ kJ mol^{-1}

$CH_3OH+H_2O \rightleftharpoons 3H_2+CO_2$ (2)

$\triangle H^0_{298}= + 49.4$ kJ mol^{-1}

$CH_3OH +(1/2)O_2 \rightleftharpoons 2H_2+CO_2$ (3)

$\triangle H^0_{298}= - 192.2$ kJ mol^{-1}

So far, the steam reforming of methanol reaction (equation(2)) was the only process considered for hydrogen production for fuel cell applications. Unfortunately, the reaction produces a considerable amount of CO (＞100ppm) as a by-product. As for the application of PEFC, even traces of CO(＞20ppm) in the reformed gas deteriorate a Pt electrode and the cell performance is lowered dramatically. A second-stage catalytic reactor has been suggested to remove the CO by water-gas shift reaction($CO+H_2O \rightleftharpoons CO_2+H_2$,WGSR, equation (4)) or CO oxidation which, in turn , requires additional space and equipment cost.

An ideal method to produce high concentration hydrogen with lower amount of CO is by steam reforming of methanol reaction over the high activity and selectivity catalysts. Now the most widely used catalysts for this reaction are copper containing catalysts since copper has been found to be highly active and selective for hydrogen. In the present study, we have prepared $Cu/ZrO_2/Al_2O_3$ ternary catalyst by coprecipitation method. Our studies were aimed at investigating the effects of ZrO_2 concentration, reaction temperature, H_2O/CH_3OH molar ratio, methanol space velocity and reaction time on the activity and selectivity and stability of the cataysts. The results show that the catalysts display great activity for methanol conversion and high selectivity for hydrogen and long stability. Maximum conversion of methanol 95.0 %, 100 mol.% hydrogen selectivity and CO molar fraction 1.45×10^{-6} were obtained in the steam reforming reaction at 250 ℃ with the catalyst containing 15.0 wt.% ZrO_2.

Experimental

Catalyst preparation. A mixed aqueous solution of copper nitrate trihydrate ($Cu(NO_3)_2.3H_2O$), zirconium oxychloride octethydrate ($ZrOCl_2.8H_2O$) and aluminum nitrate nonahydrate ($Al(NO3)_3.9H_2O$) and a solution of sodium carbonate are added slowly and simultaneously into 100ml of deionized water at 60℃ with vigorous stirring. The pH is kept constant at 7.0−7.2. The precipitates are aged at 60 ℃ for 30 min under vigorous stirring and then filtered and thoroughly washed with hot deionized water. The precipitates are dried overnight in air at 110℃ and calcined on a muffle oven at 500℃ for 3h . Each calcined catalyst are pelletized in a hydraulic press, crushed, and sieved into particle size ranging from 0.45−0.50mm and used as catalysts for the steam reforming of methanol reaction.

Activity measurement. Catalytic experiments were performed in a continuous flow fixed-bed microreactor (4mm i.d.) placed in an electrically heated furnace. The furnace temperature was controlled by a PID temperature controller through a K−type thermocouple inserted into the furnace. A separate thermocouple was used to monitor the temperature of the catalyst bed. This arrangement was capable of ensuring an accuracy of (±1℃) for the catalyst bed temperature. All run were conducted at reaction temperature in the range of 180-250℃ at atmospheric pressure. About 300−500mg of the catalyst was loaded in the reactor. A typical run for methanol–steam reforming (methanol space velocity of 3.28h^{-1} and feed consisting of a 1:1 molar mixture of methanol and water) was performed as follows: The catalyst was first reduced in situ in a premixed H_2/Ar (5/95(v/v)) flow of 80 ml min^{-1} from 120℃ to 300 ℃ with a heating rate of 1℃ min^{-1} and kept at this temperature for 3h before cooling to the reaction temperature. The feed was then pumped at the desired methanol space velocity to the vaporizer maintained at about 240℃. The vaporized feed from the vaporizer entered the reactor in a stream of Ar gas. The reaction products were analyzed on-line using HP 5890 gas chromatograph with thermal conductivity detector. The GC equipped with a 3m long Porapak-Q column and a 3m long Porapak-R column was able to detect the liquid products such as water, methanol, formaldehyde, methyl formate and dimethyl ether and the gaseous products such as H_2, CO, CO_2 and CH_4. The catalytic activity was evaluated from the data collected between 2h and 4h of the continuous operations. In order to check the stability of the catalyst, the reaction was also performed for a period of 200 h the continuous operation at 250℃. Blank run conducted with an empty reactor in the temperature range 180-250℃ did not show any detectable methanol conversion.

Results and Discussion

Table 1 Effect of ZrO_2 concentration on catalytic activity

No	ZrO_2 Wt. /%	$X(CH_3OH)$ /%	$Y(H_2)$/ mol(h.g)$^{-1}$	$S(H_2)$/ %	$y(H_2)$/ %	y(CO)/ 10^{-6}
1#	0	81.4	0.2509	100	75.0	1.60
2#	5	87.5	0.2697	100	75.0	1.65
3#	10	90.0	0.2774	100	75.0	1.47
4#	15	95.0	0.2928	100	75.0	1.45
5#	20	92.5	0.2851	100	75.0	1.44

Reaction conditions: p=0.1Mpa ; t=250℃ ; X is methanol molar conversion; Y is hydrogen productivity; S is selectivity ; y is molar fraction.

Table 1 shows a typical behavior of methanol conversion with catalyst ZrO_2 concentration. It is seen that initially shows an increase in methanol conversion with catalyst ZrO_2 concentration increasing between 0 wt.% and 15 wt.%, beyond 15.0 wt% ZrO_2, methanol conversion begins to fall. Maximum methanol conversion of 95.0 % is attained over the catalyst containing 15.0 wt.% ZrO_2. H_2 selectivity

is 100 mol.% in the experiment conditions, and CO concentration in reformed rich hydrogen gases is relatively little.

The effect of reaction temperature on catalytic performance is depicted in **Table 2**. Methanol conversion and hydrogen productivity increase with temperature increasing, methanol has almost converted into H_2, CO, CO_2 entirely at 280℃. In the temperature range180−250 ℃, hydrogen concentration and selectivity remain unchanged ,CO concentration is relatively little. On the other hand, CO concentration in reformed rich hydrogen gases increases with reaction temperature increasing.

Table 2 Effect of reaction temperature on catalytic activity

Temperature /℃	$X(CH_3OH)$ /%	$Y(H_2)$/ mol(h.g)$^{-1}$	$S(H_2)$/ %	$y(H_2)$/ %	y(CO)/ 10^{-6}
180	30.2	0.0931	100	75.0	1.06
200	56.4	0.1738	100	75.0	1.14
230	82.5	0.2543	100	75.0	1.21
250	95.0	0.2928	100	75.0	1.45
280	99.8	0.3076	100	75.0	4.46

Reaction conditions: the same as **Table 1**.

Figure 1 shows the effect of H_2O/CH_3OH molar ratio on the catalytic performance at 250℃. It can be observed that the methanol conversion and hydrogen productivity increase with H_2O/CH_3OH molar ratio increasing, beyond 1.3, methanol conversion increases relatively slowly. CO concentration decreases with H_2O/CH_3OH molar ratio increasing, water gas shift reaction accelerates with H_2O/CH_3OH molar ratio increasing according to equation (4), which promotes CO shifting to CO_2, so the experiment result displays that CO concentration decreases with H_2O/CH_3OH molar ratio increasing.

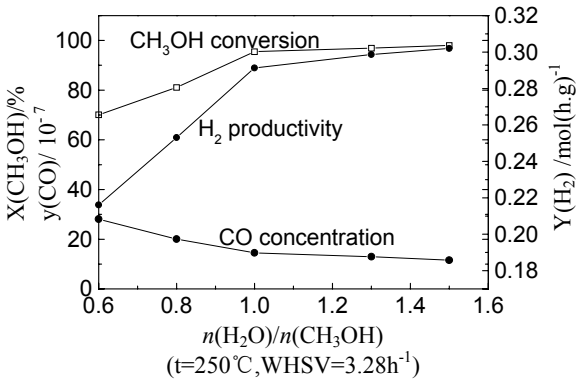

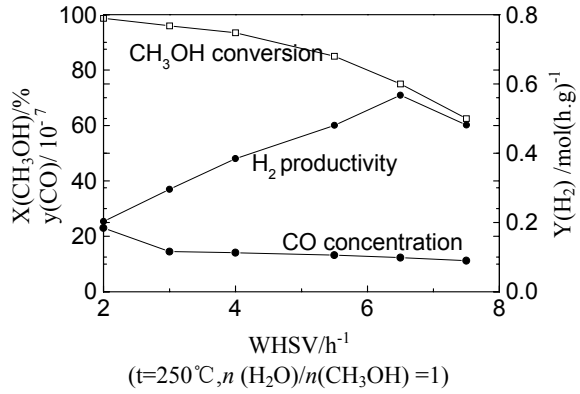

Figure1. Effect of H_2O/CH_3OH molar ratio on the reaction

Figure2. Effect of methanol space velocity on catalytic activity

Figure 2 shows the effect of methanol space velocity (WHSV) on the catalytic performance over $Cu/ZrO_2/Al_2O_3$ catalysts. Methanol conversion and CO concentration decrease with increasing methanol space velocity, hydrogen productivity has maximum in the experiment conditions. On the other hand, the methanol space velocity does not influence the selectivity of H_2, which remains 100% throughout the experiment. In the present study, a methanol space velocity of 3.28 h^{-1} has been chosen for the evaluation of the performance of the catalyst in the steam reforming reaction.

In order to investigate the stability of the catalyst during the steam reforming reaction, the continuous operation was performed at 250℃ over the catalyst with containing 15 wt. % ZrO_2 for a period of 200 h and the result is displayed in **Figure 3**. It can be seen that there is a small initial deactivation over the catalyst. After 30 hours of continuous operation, the methanol conversion remains almost unchanged throughout the period. As far as the product selectivity is concerned, there is no change in the selectivity of H_2, H_2 selectivity is still 100 mol.%.

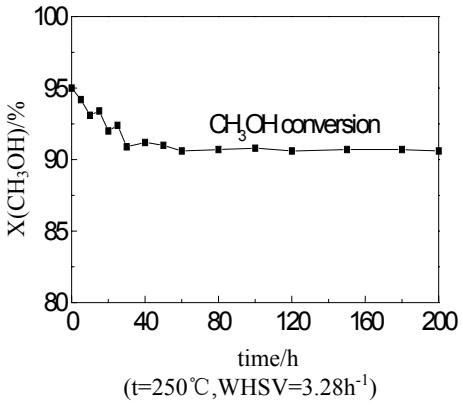

Figure 3.Effect of reaction time on catalytic activity

Conslusion

$Cu/ZrO_2/Al_2O_3$ ternary catalysts obtained from thermal decomposition of Cu/Zr/Al hydroxycarbonate precursors display great activity for methanol conversion and high selectivity for hydrogen and long stability. The catalytic activity increases with ZrO_2 concentration increasing between 0 wt.% and 15wt.%, the increase in the reaction temperature and H_2O/CH_3OH molar ratio also improves the catalytic activity, and the catalytic activity decreases with methanol space velocity increasing. Hydrogen selectivity and concentration remain unchanged in the experiment conditions, CO concentration in the reformed rich hydrogen gases is relatively little.

Acknowledgment

The authors acknowledge the financial support from the Guangyu Corp, China

References

1. Emonts B, Bogild J. *J Power Sources,* 1998**,** 71: 288-293.
2. Wies W,Emonts B. *J Power Sources,***1999**, 84: 187-193.
3. Amphlett J C, Mann R F. *J Power Sources,* **1998**, 71:179-184.
4. Velu S.Suzuki K, Kapoor M P. *Appl Catal A,* **2001**,213:47-64.
5. Dudfield CD,Chen R. *J Power Sources*, **2000**, 85:237-244.
6. Ledjeff−Hey K, Formanski V. *J Power Sources,* **1998**, 71:199.
7. Toshimasa U. Koshi S. *Appl Catal A*, **2000**,194:21-26.
8. Peppley B A, Amphlett J C. *Appl Catal A,* **1999**,179:21-29.

CHARACTERIZATION OF THE STRUCTURE FEATURES OF NICKEL CATALYSTS FOR CARBON DIOXIDE REFORMING OF METHANE

Rong-Gang Ding[1,2], and Zi-Feng Yan[2]

[1]Department of Chemical Engineering
University of Queensland, Brisbane 4072, AUSTRALIA
[2]State Key Laboratory for Heavy Oil Processing,
University of Petroleum,
Dongying, 257062, CHINA

Introduction

Conversion of methane and carbon dioxide into useful products is an important area in the current catalytic research on hydrocarbon transformations. Carbon dioxide reforming of methane is not only very important for potential usefulness in industry and environmental optimization[1-4] but also theoretically significant in understanding the nature of heterogeneous catalysis on hydrocarbon conversion. Heterogeneous catalysis occurs at active centers on a surface and it is recognized that a complete understanding of the catalytic process requires a detailed knowledge of the nature and function of active sites on the surface of the catalysts. The key to surveying the active centers of the metal catalysts is to evaluate and characterize the structure features and properties of the catalysts. The variation of the properties of catalysts can reflect the interaction among metal, support and promoter, and the agglomeration features of the active sites on the metal catalysts. The possible processes accompanying the carbon dioxide reforming of methane may be also speculated according to the changes of physical properties of catalysts. In this paper, XRD, TPR, SEM and EDX techniques are used to characterize the properties and structure of catalysts. The characterized results are used to correlate with the reforming reactivity on metal catalysts and to emphasize the importance of the special structure features in the reaction of this type.

Experimental

Catalyst preparation. Nickel catalysts were prepared by the incipient wetness impregnation method. The solids were dried overnight in air at 393K, then calcined at 773 K in air for 6 hrs for complete decomposition of the precursors. For the promoted catalysts, magnesium nitrate and cerous nitrate were added to the support by the same method.

Catalyst characterization. A BDX-3200 X-ray powder diffractometer was used to identify the main phases of nickel-based catalysts. Anode Cu Kα (40 kV, 20 mA) was employed as the X-ray radiation source, covering 2θ between 20° and 80°. The XRD patterns were monitored and processed by a computer.

The microscopic appearance observation was conducted using scanning electron microscope (JEM 5410LV, JEOL Technologies) with the accelerating voltage of 25 kV. The surface elemental composition of the catalysts was determined by energy distribution spectrum using X-ray microanalysis (ISIS, Oxford Instrument).

TPR experiments were carried out in an apparatus which consisted of a flow switching system, a heated reactor, and an analysis system. The reactor was a quartz tube of 6 mm diameter and 20 cm length. The outlet of the reactor was connected to a quadrupole mass spectrometer (DYCOR Quadrupole, Ametek Instrument) via a heated steel tube (diameter 3 cm). The pressure in the main chamber of the spectrometer was approximately 10^{-7} Pa. Calibration of the mass spectrometer was performed with a mixture of known composition. Ultra high purity gases (99.999%) were used in TPR experiments. The catalyst sample was firstly pretreated in a O_2 flow of 20 ml/min at 973 K for 30 min, then the sample was cooled to room temperature in the O_2 flow. Subsequently, the O_2 flow was switched to a H_2/He (10 ml/ 20ml) flow. After purging with H_2/He mixture for 10 min, temperature programming was initiated with a heating rate of 23 K/min and the TPR profiles were *on-line* recorded.

Results and Discussion

XRD characterization. The XRD patterns of support, promoted and unpromoted Ni-based catalysts were shown in **Figure 1**. From the XRD patterns of support and catalysts, it was clearly observed that NiO diffraction peak didn't appear in the patterns of unpromoted and promoted Ni-based catalysts. It was a good indication that high dispersion of nickel oxide was achieved over γ-Al_2O_3 support. However, it is difficult to estimate the effect of promoters on the metal dispersion on the support according to the XRD patterns.

As can be derived from the XRD patterns shown in **Figure 1**, no detectable solid reaction occurred between NiO and Al_2O_3 over promoted catalyst. However, certain amounts of nickel were found in the form of $NiAl_2O_4$, a compound resulting from the solid reaction between NiO and the acidic Al_2O_3 support in the Ni/Al_2O_3 catalyst. The $NiAl_2O_4$ crystalline phase, which has a stable spinel structure, is rather difficult to be reduced, as witnessed by the fact that it essentially survives H_2 reduction at 1023 K. However, addition of MgO (3 wt%) to γ-Al_2O_3 significantly affected the basicity/acidity of the support, leading to a profound change in the bulk phase composition. It was observed that the diffraction peak of $NiAl_2O_4$ disappeared over MgO-promoted catalyst. This is probably attributed the fact the basic MgO is preferably reacting with the acidic Al_2O_3 to form stable magnesium aluminate, thereby suppressing the reaction between NiO and Al_2O_3.

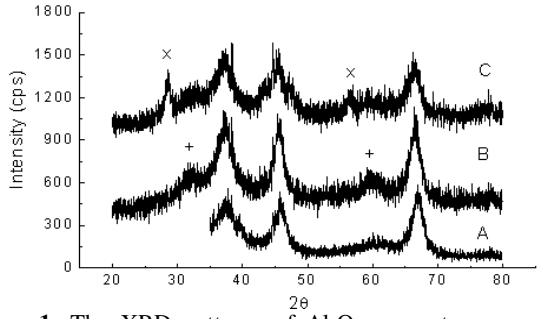

Figure 1. The XRD patterns of Al_2O_3 support, unpromoted and promoted catalysts. (+: $NiAl_2O_4$, ×: CeO_2) A: γ-Al_2O_3, B: 8.5wt%Ni/γ-Al_2O_3 C: 8.5wt%Ni-2wt%MgO-3wt%CeO_2/γ-Al_2O_3

The emergence of CeO_2 diffraction peak in Ni-Mg-Ce/Al_2O_3 catalyst indicated that the dispersion of CeO_2 was unsatisfactory. This may be related to the catalyst preparation processes and conditions. More series tests of the influence of CeO_2 addition on the dispersion of metal are absent now. The Ni-Mg-Ce/Al_2O_3 catalyst exhibited perfect performance in the catalyst evaluation experiments despite of unsatisfactory dispersion of CeO_2 promoter. The EDX analysis explains the emergence of the CeO_2 diffraction peak perfectly in following section. In the sharp contrast to CeO_2, the dispersion of MgO promoter was satisfactory and no diffraction peak appeared in the XRD patterns of the promoted catalyst.

SEM and EDX Analysis. The surface elemental compositions of the fresh and used catalysts were characterized by EDX analysis and the results were shown in **Table 1**. The high surface concentration of some element indicated that uniform dispersion of the element is achieved. The enrichment trend of the element may be effectively

retarded and various states of the element essentially exist in relatively small particles. From Table 1 it was observed that the surface concentration of the Ni over unpromoted catalyst significantly decreased by almost one time, from 5.29% to 2.37%, after carbon dioxide reforming reaction. The surface concentration of Ni element also declined to some extent, from 5.74% to 4.21% over the MgO-promoted catalyst after reaction. However, it was interesting that the surface concentrations of Ni element increased over CeO_2 promoted catalysts after reaction.

Table 1 Surface Composition of Fresh and Used Nickel Catalysts

catalyst(wt%)	state	Al (%)	Ni (%)	Mg (%)	Ce (%)
7 %Ni/Al_2O_3	fresh	94.71	5.29	-----	-----
	used	97.63	2.37	-----	-----
8.5%Ni-2%MgO-3%CeO_2/Al_2O_3	fresh	84.31	9.18	n.d.	6.51
	used	84.74	10.61	n.d.	4.65
10%Ni-2% MgO/Al_2O_3	fresh	94.26	5.74	n.d.	-----
	used	95.80	4.21	n.d.	-----
11.5%Ni-3% CeO_2/Al_2O_3	fresh	93.04	4.18	-----	2.78
	used	89.97	4.85	-----	5.19

Reaction conditions: P = 1 atm, T = 973 K, CH_4/ CO_2= 1.05, WHSV = 12.5 h^{-1}, used for 4 hrs. n.d.: not detected. %: atomic percentage

For the Ce-promoted catalysts, the nickel loadings on the support were higher than that of Ce-missing catalysts. High nickel loading does not favor the dispersion of Ni on the surface of the support. However, the surface concentration of Ni reached 4.18% on the fresh 11.5%Ni-3%Ce/Al_2O_3 catalyst, approached that on the fresh 7.5%Ni/Al_2O_3 catalyst. The uniform dispersion of nickel component over the 8.5%Ni loaded catalyst may be ascribed to appropriate nickel loading. Lu et al.[5] studied the optimum nickel loading on various supports. The results showed that two-dimensional surface compound was formed by the interaction between NiO and Al_2O_3 with nickl loading set at 9.0% under the specific conditions. The two-dimensional surface compound was highly dispersed on the surface of the support, and thus resulted in the maximum dispersion of Ni metal particles. Too high nickel loading may result in the formation of NiO crystalline phase on the support. The NiO crystalline phase submitted little contribution to the metal dispersion and large Ni particles were prone to formation in the reduction process. The large Ni particles provided less active metal surface area and caused rapid deactivation by carbon deposition on the Ni particles.

The high surface concentration of Ni on the 8.5%Ni-2%MgO-3%CeO_2/Al_2O_3 may be derived from two causes. The appropriate nickel loading was the key to obtaining uniform dispersion on the surface of the Al_2O_3 support. As mentioned above, two-dimensional surface compound may be formed by the interaction between NiO and Al_2O_3 on the catalyst and Ni particles were highly dispersed under the specific conditions. Additionally, the comparison of the surface compositions of the catalysts gave good indication that the addition of rare-earth metal oxide CeO_2 effectively promoted the Ni metal dispersion on the surface of the catalysts. Furthermore, the nickel component was gradually dispersed on the surface of the Ce-promoted catalysts following the exposure to reaction gas mixture for a period.

Chen et al.[6] investigated the influence of the rare-earth metal oxide on the nickel dispersion on the Al_2O_3 support. They reported that the active metal component was not directly sticked on the support, but adjacent to the surface of the rare-earth metal oxide. The interaction between them occurred and the specific filling structure was formed on the support. This structure inhibited the migration and enrichment of Ni and improved the nickel dispersion in the catalyst preparation and reaction processes. The formation of stable spinel $NiAl_2O_4$ was also retarded to a reasonable content.

It was also noteworthy that the variation of the self-dispersion of CeO_2 on the support. The surface concentration of Ce decreased from 6.51% to 4.65% on the MgO-containing catalyst and increased from 2.78% to 5.19% on the MgO-missing catalyst after reaction. The surface concentration of Ce decreased from 6.51% to 2.78% when the MgO addition increased from 2% to 3% for the fresh catalysts. Apparently, the addition of MgO inhibited the self-dispersion of CeO_2 on the catalysts. Therefore, the appearance of CeO_2 diffraction peak on the XRD patterns of 8.5% Ni-2%MgO-3%CeO_2/Al_2O_3 catalyst was indicative of the unsatisfactory self-dispersion of CeO_2 promoter. The EDX analysis result by scanning electron microscope was in good harmony with the XRD experiment result.

The surface concentration of Mg was not detected on the catalysts below 2% MgO-content added. It was observed that increased MgO addition inhibited the promotion effect of CeO_2 on Ni dispersion. Therefore, the optimum combination of the addition amount of the promoters is very important for perfect metal dispersion and desirable catalyst performance in the carbon dioxide reforming of methane.

TPR investigation. Figure 2, 3, and **4** showed the temperature programmed reduction profiles over promoted catalysts. Figure 2 indicated that appropriate MgO promoter may be a good solution to prohibiting the formation of $NiAl_2O_4$ spinnel phase. Addition of strong basic MgO significantly affected the basicity/acidity of the support, leading to a profound change in the bulk phase composition. It was observed that while the reduction peak of $NiAl_2O_4$ phase (1040 K) was significantly decreased, that of NiO (975 K) was greatly enhanced. This was probably ascribed to the fact that the basic MgO was preferably reacting with the acid Al_2O_3 to form stable magnesium aluminate, thereby suppressing the reaction between NiO and Al_2O_3. This was in agreement with the XRD results of promoted catalysts.

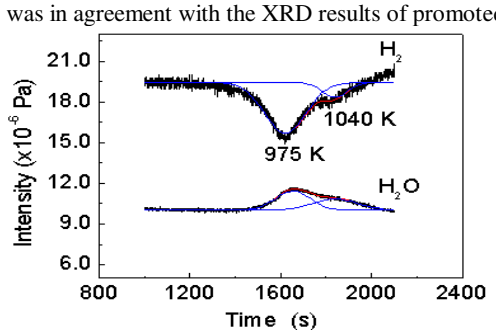

Figure 2. TPR profiles of 10wt% Ni-2wt%MgO/Al_2O_3 catalyst.

Addition of CeO_2 exhibited weak effect on retarding the formation of $NiAl_2O_4$ phase owing to its weak basicity (**Figure 3**). The reduction peak area of NiO was close to that of $NiAl_2O_4$ phase. However, the maximum reduction temperature of NiO on Ce-promoted catalyst was decreased from 975 K to 954 K, about 20 K reduction compared with that on Mg-promoted catalyst. The decreased reduction temperature may indicate that nickel dispersion on the support was improved by addition of CeO_2. The EDX analysis of the promoted nickel catalysts gave support for the description of promoting effect of CeO_2 on nickel dispersion.

The decreased reduction temperature of NiO and prohibition of formation of $NiAl_2O_4$ phase were obtained on the catalyst with appropriate addition amount of MgO and CeO_2 (**Figure 4).** It gave partial explanation for the perfect catalytic performance of the Mg-Ce-promoted catalyst. On the other side, the existence of appropriate amount of $NiAl_2O_4$ phase was beneficial to stabilization of Ni crystalline particles. Bolt et al.[7] reported that dispersed $NiAl_2O_4$ phase on the catalyst keep putting off the sintering and growth of nickel

particles. The backscattering spectra of specially treated catalyst with certain amount of $NiAl_2O_4$ on near-surface of the catalyst showed that unlapped Al_2O_3 reached 42%, while unlapped Al_2O_3 reached 83% on the near-surface of $NiAl_2O_4$-deficient catalyst. This indicated that the pronounced sintering of nickel particles on $NiAl_2O_4$-deficient catalyst occurred. The nickel particles were fixed and dispersed by $NiAl_2O_4$ and sintering was retarded on the treated catalyst.

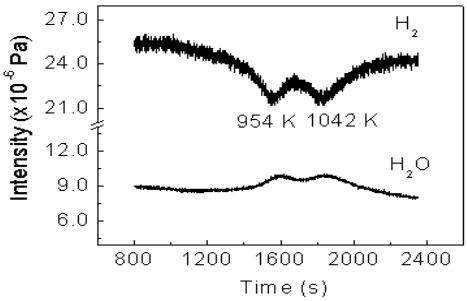

Figure 3. TPR profiles of 11.5wt% Ni-3wt%CeO_2/Al_2O_3 catalyst.

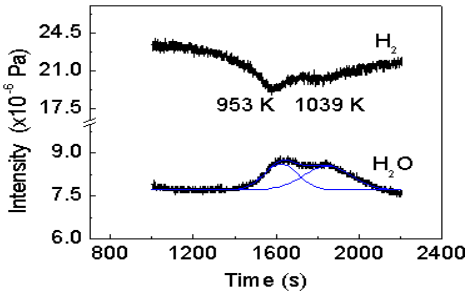

Figure 4. TPR profiles of 8.5wt% Ni-2wt%MgO-3wt%CeO_2/Al_2O_3 catalyst.

Conclusions

The chracterization results showed that addition of strong basic MgO promoter significantly retarded the formation of $NiAl_2O_4$ phase, while addition of rare-earth metal oxide CeO_2 effectively promoted the Ni metal dispersion on the surface of the catalysts despite of unsatisfactory self-dispersion of CeO_2 promoter. Furthermore, the nickel component was gradually dispersed on the surface of the support following the exposure to reaction gas mixture for a period. However, metal dispersion was not the unique factor that influenced the catalyst performance. Optimized combination of addition amount of different promoters was very important for perfect metal dispersion and desirable catalyst performance in the carbon dioxide reforming of methane.

Acknowledgement. Financial supports by the Young Scientists Award Foundation of Shandong Province and China National Petroleum Corporation are gratefully acknowledged.

References

(1) Trovarelli, A. *Catal. Rev. Sci. Eng.* **1996**, *38*, 439.
(2) Soria, J.; Coronado, J.M.; and Conesa, J.C. *J. Chem. Soc., Faraday Trans.* **1996**, *92*, 1619.
(3) Morterra C.; Bolis, V.; Magnacca, G. *J. Chem. Soc., Faraday Trans.* **1996**, *92*, 1991.
(4) Wang, C.Y.; Li, S.Y.; Yang, X.R.; Ren, J.; Chen, Y.G. *Energy Convers. Mgmt*. **1996**, *37*, 1357.
(5) Lu, Y.; Yu, C. C. *Chn. J. Catal.* **1996**, *17*(3), 212.
(6) Chen, Y. G.; Ren, J.; Wu, D.; Fan, W.H. *Petrochemical* **1994**, *23*(12), 771.
(7) Bolt P. H.; Habraken F. H. P. M.; Geus J. W. *J Catal.* **1995**, *151*, 300.

THE COUPLING OF CATALYTIC STEAM REFORMING AND OXIDATIVE REFORMING OF METHANE TO PRODUCE PURE HYDROGEN IN A NOVEL CIRCULATING FAST FLUIDIZATION BED MEMBRANE REFORMER

Zhongxiang Chen, Pradeep Prasad, and Said Elnashaie

Chemical Engineering Department
Auburn University, Auburn, AL 36849

Introduction

Steam reforming of natural gas represents the principal commercial route to hydrogen production. The classical industrial steam reformer (1st generation) consists of hundreds of parallel catalyst tubes of about 10 inches diameter, surrounded by a very large furnace. This process suffers from a number of limitations making it extremely inefficient e.g.:

(1) Diffusion Limitations: The effectiveness factors of the large catalyst pellets have been found to be as low as $10^{-2} - 10^{-3}$. [1,2]
(2) Thermodynamic Limitations: The reversibility of the reforming reactions limits the conversion to thermodynamic equilibrium.
(3) Catalyst Deactivation: Carbon formation increases with the increase in the temperature, leading to catalyst deactivation.

The most successful milestone to date in the development of a more efficient reformer was the bubbling fluidized bed membrane steam reformer (BFBMSR) for natural gas, where powdered catalyst was used to overcome the diffusion limitations and hydrogen selective membranes were used to overcome the thermodynamic equilibrium barrier.[3,4,5] Roy et al[6] have experimentally studied the addition of oxygen to the BFBMR to provide all of the heat required for the endothermic reforming reactions, and found that autothermal conditions could be reached and maintained.

The BFBMSR, although very efficient, still suffers from a number of important limitations. The present work suggests a novel, more efficient and flexible process consisting of a fast fluidization riser reactor where steam reforming and partial oxidation reactions are carried out. The riser reactor also has a number of hydrogen selective membranes for hydrogen removal and oxygen selective membranes to introduce a part of the oxygen into the reactor for partial oxidation of the feed. A gas solid separator is used to separate the solids and they are recycled to the riser reactor after regeneration of the catalyst. A preliminary schematic diagram of the proposed novel reformer is shown in Figure 1.

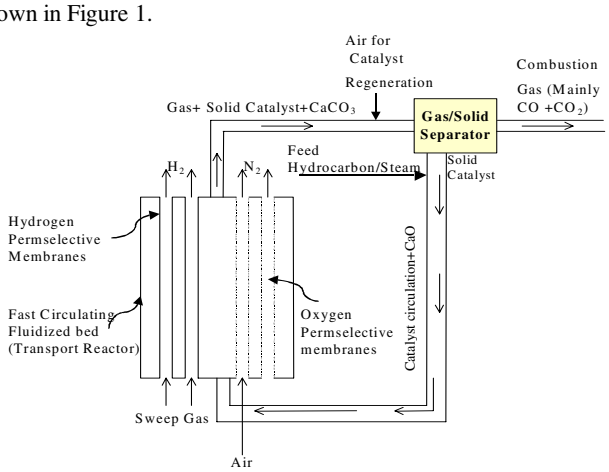

Figure 1. Schematic diagram of the proposed novel configuration.

Modeling

In the present paper, preliminary modeling and simulation are carried out on the reactor section alone of the circulating fast-fluidized bed reformer. The cases with and without hydrogen selective membranes are considered and are compared with industrial fixed bed reformers and bubbling fluidized bed reformers. Oxygen input to the reactor directly or through membranes is investigated.

Reaction Kinetics. The rate expressions proposed by Xu and Froment [7] for the steam reforming of methane using Ni/Al_2O_3 catalyst will be used in the present study. They were analyzed in some detail by Elnashaie et al [8] and found to be the most general rate equations.

A number of supported metal catalysts such as Ni, Rh, Pt, etc have been reported for partial oxidization of methane.[9] Dissanayake et al.[10] examined the oxidation state and phase composition of the Ni/Al_2O_3 catalyst as a function of axial position in the catalyst bed. Their results strongly support the mechanism of methane combustion followed by steam and carbon dioxide reforming.

Model Equations. The fast-fluidized bed reformer is modeled as a plug flow reactor with co-current flow in the reactor and membrane (sweep gas) sides. Ideal gas law is used to calculate the partial pressures on the reactor and the membrane sides. The mass and energy balances can be obtained at steady state as follows.

$$\frac{dF_i}{dl} = \rho_c A_c (1-\varepsilon) R_i + J_i \qquad (1)$$

$$\sum_i F_i \frac{d(H_i)}{dl} = A_c \rho_c (1-\varepsilon) \sum_j r_j (-\Delta H_j) + Q \qquad (2)$$

where $J_i=0$ for all components, except hydrogen and oxygen for which J_i is the corresponding molar permeation term depending on the type of membrane used. For a supported dense Pd membrane, the hydrogen permeation term is:[11]

$$J_{H_2} = -\frac{Q_{H_2}}{\delta_{H_2}} \exp\left(\frac{-E_{H_2}}{RT}\right)\left(\sqrt{p_{H_2,r}} - \sqrt{p_{H_2,m}}\right) \qquad (3)$$

For a dense perovskite oxygen permeable membrane, the oxygen permeation term is:[12]

$$J_{O_2} = Q_{O_2} \exp\left(\frac{-E_{O_2}}{RT}\right) \frac{T}{\delta_{O_2}} \ln\left(\frac{P_{O_2,m}}{P_{O_2,r}}\right) \qquad (4)$$

The set of initial value differential equations is solved using initial conditions to be the same as the feed conditions per tube of an industrial reactor described in Elnashaie and Elshishini.[13]

The method given by Kunii and Levenspiel[14] has been used to verify that the reactor is operating in the fast fluidization or the pneumatic transport regime.

Results and Discussion

Figure 2 shows the effect of the hydrogen permeable membrane on the conversion of methane in the isothermal reactor with only hydrogen selective membranes. The removal of hydrogen from the reactor side breaks the equilibrium barrier resulting in almost complete conversion of methane. This is achieved in a very short length of reactor (≈ 1 m) as compared to the much higher lengths (> 10 m) that are typically used for fixed bed steam reformers.

Table 1 compares the fast-fluidized membrane steam reformer (FFMSR) with the industrial fixed bed and the BFBMSR. The value hydrogen yield per m^3 of the reactor gives us a strong and direct indication of the improvement in the efficiency of the reactor.

Figure 3 shows the yield of hydrogen obtained for different amounts of oxygen introduced into an adiabatic reformer along with the feed, when no oxygen permeable membranes are present. Both, the cases with and without hydrogen permeable membranes are

investigated. We find a general increase in the yield of hydrogen for increased oxygen in the feed. The oxygen conversion via combustion causes an increase in hydrogen yield due to the higher equilibrium yield of the endothermic reforming reaction at higher temperatures. The use of hydrogen permeable membrane causes further increase in hydrogen yield by shifting the equilibrium.

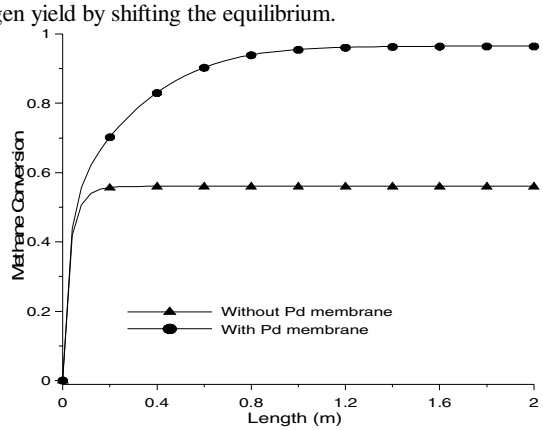

Figure 2. With membrane vs. without membrane for T=900 K, Reactor pressure=5atm, Membrane side pressure=1atm.

Table 1. Comparison between FFMSR and (a) Industrial Fixed Bed and (b) BFBMSR

(a)	Fixed Bed[12]	FFMSR	(b)	BFBMSR[5]	FFMSR
X_{CH4}	0.853	0.964	X_{CH4}	0.419	0.582
H_2 yield per m^3 of reactor	27.27	246.8	H_2 yield per m^3 of reactor	109	302.7

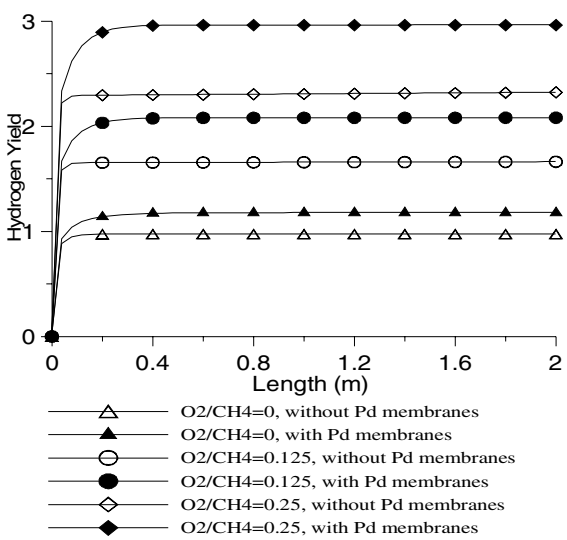

Figure 3. Yield of hydrogen with oxygen as part of reactor feed, T_{inlet}=1000K, Reactor pressure=5atm, Membrane side pressure=1atm.

An alternate approach is to introduce oxygen through oxygen permeable membranes. It allows us to distribute the supply of oxygen along the length of the reactor and thus optimize the extent of the oxidation reaction so as to maximize the productivity of hydrogen. Figure 4 shows the results of a simulation of an adiabatic reformer with both hydrogen and oxygen permeable membranes. Presently the permeability of the available oxygen permeable membranes seems to be a limiting factor. It necessitates the use of a reduced reactant feed rate as compared to the earlier cases, and high membrane surface area for oxygen permeation. The use of oxygen permeable membranes increases the yield of hydrogen because of the higher equilibrium conversion at higher temperature. The use of hydrogen permeable membrane causes a further increase in hydrogen yield by breaking the thermodynamic equilibrium barrier.

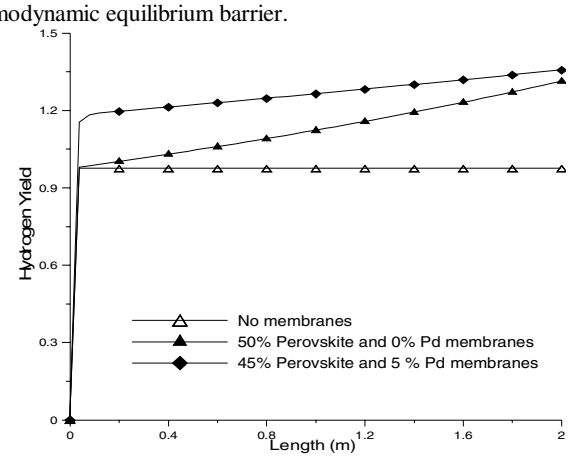

Figure 4. Yield of hydrogen vs length of reactor, T_{inlet}=1000K, Reactor pressure=5atm, Membrane side pressure=1atm. Percentage values denote percentage of reactor cross-sectional area occupied by the membrane.

Nomenclature

A_c	area of cross-section of the reactor (m^2)
E_i	apparent activation energy of membrane permeable to *i* ($kJ.mol^{-1}$)
F_i	molar flowrate of species *i* ($kmol.hr^{-1}$)
ΔH_j	heat of reaction for reaction *j* ($kJ.mol^{-1}$)
H_i	molar enthalpy of species *i* ($kJ.mol^{-1}$)
J_i	permeation flux of *i* ($kmol.hr^{-1}.m^{-2}$)
l	length of reactor (m)
P_i,r ,P_i,m	partial pressure of species *i* on the reaction and membrane sides respectively (kPa)
Q_i	pre-exponential factor in the Arrhenius relationships for permeability of hydrogen and oxygen ($kJ.m^{-1}.hr^{-1}.kpa^{-n}$)
Q	rate of heat input ($kJ.hr^{-1}.m^{-3}$)
R	gas constant (8.314 $kJ.kmol.^{-1}.K^{-1}$)
R_i	rate of production of species *i* ($kmol.hr^{-1}$)
T	temperature (K)
δ_i	thickness of membrane (m)
ε	void fraction
ρ_c	density of catalyst ($kg.m^{-3}$)

References

(1) De Deken, J.C.; Devos, E.F.; Froment,G.F., *Am. Chem. Soc. Symp. Ser.*, **1982**, 196, 181.
(2) Soliman, M.A.; Elnashaie, S.S.E.H.; Al-Ubaid, A.S.; Adris, A.M., *Chem. Eng. Sci.*, **1988**, 43, 1803.
(3) Adris, A.M.; Elnashaie, S.S.E.H.; Hughes, R., *Can. J. Chem. Eng.,*. **1991**, 69, 1061.
(4) Adris, A.M.; Lim, C.J.; Grace. J.R., *Chem. Eng. Sci.,*. **1994**, 49, 5833.
(5) Adris, A.M.; Lim, C.J.; Grace. J.R., *Chem. Eng. Sci.,*. **1997**, 52, 1609.
(6) Roy, S.; Pruden, B.B.; Adris, A.M.; Lim, C.J.; Grace, J.R., *Chem. Eng. Sci.* **1999**, 54, 2095.
(7) Xu, J.; Froment, G.F., *AIChE. J.*, **1989**, 35, 88.
(8) Elnashaie, S.S.E.H.; Adris, A.M.; Al-Ubaid, A.S.; Soliman, M.A., *Chem. Eng. Sci.*, **1990**, 45(2), 491.
(9) Ashcroft, A.T.; Cheetham, A.K.; Foord, J.S.; Green, M.L.H.; Grey, C.P.J.; Murrell , A. and Vernon, P.D.F., *Nature*, **1990**, 344, 319.
(10) Dissanayake, D.; Rosynek, M.P.; Kharas, K.C.C.; Lungsford, J.H., *J. Catal.*, **1991**, 132, 117.
(11) Barbieri, G.; Maio, F.P.D., *Ind. Eng. Chem. Res.* **1997**, 36, 2121.
(12) Tsai, C.; Dixon, A.G.; Moser, W.R.; Ma, Y.H., *J. AIChE*, **1997**, 43(11A), 2741.

(13) Elnashaie, S.S.E.H.; Elshishini, S.S., Modelling, simulation and optimization of industrial fixed bed catalytic reactors, Gordon and Breach Science Publishers: London, 1993.
(14) Kunii, D; Levenspiel, O., *Chem. Eng. Sci.*, **1997**, 52, 2471.

METHANE AND METHANOL STEAM REFORMING TO PRODUCE HYDROGEN USING CATALYTIC MICROCHANNEL REACTORS

Yong Wang, Robert Dagle, Ya-Huei Chin, Daniel Palo, Jianli Hu, and Jamie Holladay

Chemical and Biological Processing Group
Environmental Technology Division
Pacific Northwest National Laboratory
902 Battelle Blvd, Richland, WA 99352

Introduction

Steam reforming of hydrocarbons is conventionally used in fuel processing to produce hydrogen. A fuel processor is a critical reactor technology for the deployment of PEM-based fuel cells for portable, on-board, and stationary applications. Over the past several years, PNNL has developed microchannel chemical reactors for fuel processing applications, ranging from the power required for remote electronic device to that for automobile applications [1,2]. In particular, a series of steam reforming catalysts suitable for microchannel reactors have been developed [3-5]. In this presentation, we will present methane and methanol steam reforming catalyst work recently developed at PNNL.

Experimental

Pd/ZnO catalysts were prepared from impregnating aqueous $Pd(NO_3)$ solution containing 20.19 wt% Pd (Engelhard) onto ZnO powder (Aldrich, 99%) using a solution/solid ratio of 0.58 ml/g. The impregnated samples were dried under vacuum at 110 ^oC for at least 8 hrs prior to calcining in air. The calcination was conducted under a 2 ^oC/min ramp followed by holding isothermally at 350 ^oC for 3hs.

Activity tests were carried out in a 4 mm I.D. quartz tube reactor. Approximately 0.200 g of catalyst was loaded between two layers of quartz wool inside the reactor. A thermocouple was placed in the middle of the catalyst bed. A premixed 1:1wt % methanol-water feed was introduced into the reactor by using a syringe pump. The feed rate was adjusted such that the reaction was conducted under 100 ms contact time, which is in equivalent to a standard GHSV of 36000 h^{-1}. Prior to entering the reactor, the feed was fully vaporized through a vaporizer, operated at 200 ^oC. Prior to activity testings, the catalysts were reduced *in-situ* under a 10 % H_2/N_2 at 350 ^oC. A glass condenser at 0 ^oC was used to separate liquid products from gaseous products. The product gases, CO, CO_2, and H_2, were separated using MS-5A and PPQ columns, and analyzed on-line by means of a Hewlett Packard Quad Micro GC (Model Q30L) equipped with a TCD.

Results and Discussions

Methanol and methane are two popular and readily available hydrocarbons. One way to extract hydrogen from methanol or methane is via steam reforming reactions. Conventionally, CuZnAl catalysts are used for methanol steam reforming and methane steam reforming catalysts are based on Ni. Although these two types of catalysts are suitable for conventional fixed bed-type reactors where heat transfer is limiting, more active and selective catalysts are needed for mcirochannel reactor applications where heat and mass transfer advantages are exploited.

Methanol is a unique fuel since it is sulfur-free and can be activated at relatively low temperature (under 300 ^oC). This could be a significant advantage from system simplification and process heat recovery points of view. We have investigated the steam reforming of methanol with Pd/ZnO under high throughput conditions (GHSVs ranging from 18,000 to 144,000 hr^{-1}). Pd, like other transition metals (Pt, Rh), exhibits high methanol decomposition activity to CO and H_2. This is not surprising, since precious metal based catalysts typically exhibit different catalytic function than the Cu based catalytic materials. However, when supporting the Pd on ZnO, the catalytic function of Pd can be greatly modified, resulting in a highly active and selective catalyst for methanol steam reforming, which was not found previously on precious metal catalysts. Under steam reforming conditions, the Pd/ZnO catalyst produces mainly CO_2 and H_2 along with minimal amount of CO. The concentration of CO in the product stream was found to be at least as low as what reported for the well-studied Cu based catalyst. Hydrogen rich stream with low CO content is highly desired since the electrocatalyst at the anode is extremely sensitive to CO poisoning at the operating temperature of PEM fuel cells.

The methanol conversion and CO selectivity over 5, 10 and 20 wt% Pd/ZnO catalysts are shown in Figure 1a and 1b, respectively. The experiments were repeated with the same catalyst, and no noticeable catalyst deactivation was observed. As can be seen from Figure 1a and 1b that increasing Pd loading from 5 wt% to 20 wt% results in a 10 ^oC shift of the conversion profile to the lower temperatures. A complete conversion of methanol can be achieved at around 300 ^oC. The CO selectivities of these catalysts were less than 7 % over the entire temperature range studied. At 300 ^oC, this corresponds to a dry effluent consisting of approximately 1% CO, 26% CO_2, and 73% H_2. Of the three catalysts examined, the 20% Pd/ZnO catalyst exhibited the lowest CO selectivity. In addition to catalytic activity studies, we also attempted to elucidate the chemical and physical properties of Pd/ZnO catalysts using TPR, TEM, H_2 chemisorption and XRD. It was found that PdZn alloy formed under reducing environment at moderate temperatures (<300 ^oC). This species is highly selective for the steam reforming of methanol, which is not normally observed on precious metal based catalysts.

Methane steam reforming catalysts were also developed based on Rh [4]. This type of catalysts exhibited extremely high activity as evidenced by equilibrium conversion reached at a very high GHSV (as high as 1,000,000 hr^{-1}). Catalyst life was also evaluated under stoichiometric steam to carbon ratio, and no noticeable catalyst deactivation was observed under the conditions studied and the catalyst was shown to be coke resistance at low steam to carbon ratios.

Conclusions

A highly active and selective Pd/ZnO catalyst was developed for methanol steam reforming. Complete conversion was achieved at 300°C with a CO concentration in the dry effluent around 1%. This catalyst was evaluated by various catalyst characterization techiniqes including TEM, TPR, chemisorption, and XRD. It was found that PdZn alloy formed under reducing environment at moderate temperatures (<300 ^oC). This species is highly selective for the steam reforming of methanol, which is not normally observed on precious metal based catalysts. A highly active and coke resistant methane steam reforming catalyst was developed and its life performance was evaluated under low steam to carbon ratios.

Acknowledgement. This work was performed in the Environmental Molecular Sciences Laboratory, a national scientific

user facility sponsored by the US Department of Energy's Office of Biological and Environmental Research and located at Pacific Northwest National Laboratory in Richland, WA.

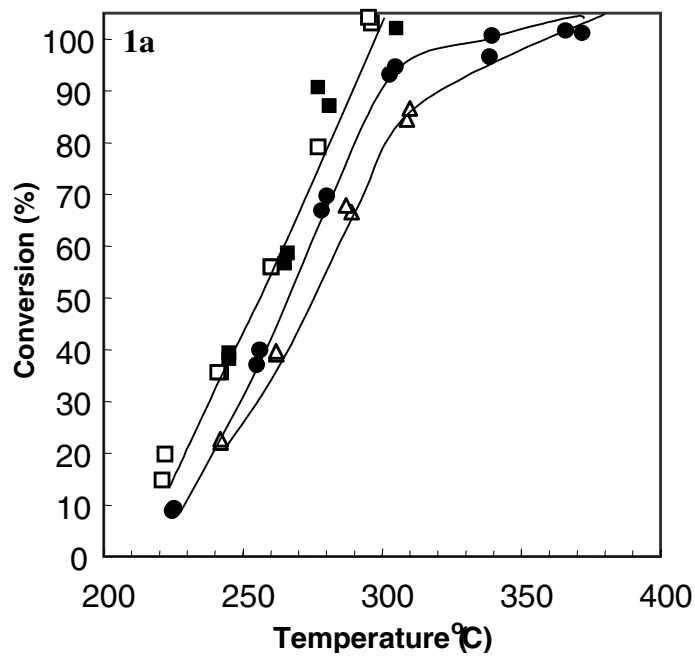

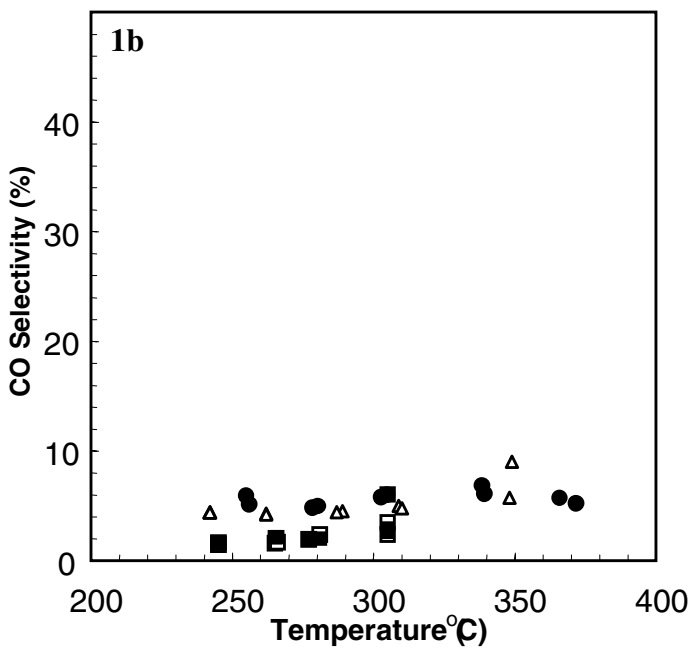

Figure 1a and 1b. Methanol conversion temperature profile under steam reforming of methanol (a) and the corresponded CO selectivity (b) for 5 wt% (triangle), 10 wt% (circle), and 20 wt% Pd on ZnO (both filled and open square). For 20%Pd/ZnO, the conversion profiles were acquired after two separate reduction temperatures: reduction at 125 °C (open square) and after reduction at 350 °C (filled square). All other catalysts were tested after reduction at 350 °C. Reaction conditions: 0.1925g catalyst, 100 ms contact time or 36000 GHSV, H_2O/C = 1.8, 1 atm.

References

1. D.R. Palo, J.D. Holladay, R.T. Rozmiarek, C.E. Guzman-Leong, Y. Wang, J.Hu, Y.Chin, R.A. Dagle, and E.G. Baker, *J. Power Sources* (in press).
2. J.D. Holladay, E.O. Jones, M.R. Phelps, and J. Hu, submitted to *Journal of Power Sources*
3. Y. Chin, R. Dagle, J. Hu, A. C. Dohnalkova, and Y. Wang, submitted to *Catalysis Today*.
4. Y. Wang, D. VanderWiel, A.L. Tonkovich, U.S. Pat., 6,284,17B1 (2001).
5. J.Hu , Y. Wang, D.P. VanderWiel, Y. Chin, D.R.Palo, R. Rozmiarek, R.A. Dagle, J.D. Holladay, and E.G.Baker, submitted to *Chemical Engineering and Technology.*
6. N. Iwasa, S. Masuda, N. Ogawa, N. Takezawa, *Appl. Catal*. 125 (1995) 145.

SURFACE REACTION MECHANISM DEVELOPMENT FOR PARTIAL OXIDATION OF METHANE TO SYNTHESIS GAS

Ashish B. Mhadeshwar[1], Preeti Aghalayam[2], Vasilis Papavassiliou[3], and Dionisios G. Vlachos[1]

[1]Department of Chemical Engineering, University of Delaware, Newark, DE 19716-3110
[2]Department of Chemical Engineering, University of Massachusetts-Amherst, MA 01003-3110
[3]Praxair Inc.

Introduction

Synthesis gas is an important chemical intermediate for many industrial processes. The need for synthetic fuels is increasing as the recovery of petroleum becomes increasingly difficult and expensive. Synthesis gas can be converted to paraffinic liquid fuels through Fischer-Tropsch synthesis. It helps to reduce environmental pollution, as fuels from synthesis gas are heteroatom free. Catalytic partial oxidation of methane (POX) offers a very promising route to convert natural gas to synthesis gas. POX over noble metal catalysts, including Pt and Rh, is in great demand due to the dual application for energy production[1] (complete combustion) and syngas production[2] (partial oxidation in short contact time microreactors). Although a considerable progress has been made in development of large detailed gas phase reaction mechanisms, the surface chemistry is not well established. In addition, surface reaction mechanisms proposed so far suffer from the disadvantage of violating thermodynamic consistency, lacking important reaction paths and surface coverage-dependent kinetic parameters.

In this work, an elementary surface reaction mechanism of methane oxidation is used, which is derived using a unique combination of surface science experiments, semi-empirical thermo chemistry calculations, and mathematical optimization. The ability of predicting experimental data over a wide range of operating conditions will be demonstrated. As an example, quantitative predictions of experimental data on fuel conversion vs. surface temperature, and selectivities to syngas will be shown.

Chemistry

Below we discuss the prominent features of our chemistry modeling.

Gas-phase Chemistry. The GRI 3.0 mechanism has been employed for gas phase chemistry[3]. This mechanism consists of 53 species and 325 chemical reactions. It is associated with a thermodynamic database as well as a transport database and is in the CHEMKIN format. This mechanism has been extensively validated against experimental data over a wide range of operating conditions and various types of experiments and is used without modifications.

Surface Chemistry. We have developed a C1 reaction mechanism for CH_4 oxidation on platinum consisting of 10 species among 62 surface reactions[4]. The surface reaction mechanism developed involves adsorption and desorption of reactants and intermediate species, pyrolytic hydrogen abstraction from CH_x species, oxygen-assisted and hydroxyl-assisted hydrogen abstraction from CH_x species as well as complete oxidation mechanisms of H_2 and CO on platinum[5,6]. The activation energies of the surface reactions are computed using the semi-empirical Bond Order Conservation (BOC), also known as Unity Bond Index Quadratic Exponential Potential (UBI-QEP) technique[7] that enables us to include the coverage dependence of activation energies in a systematic way. The entire BOC formulism has been incorporated within the SURFACE CHEMKIN Library itself for the first time to provide flexibility, clarity, and ease of use. Thermodynamic consistency is ensured, by using BOC for the calculations of activation energies.

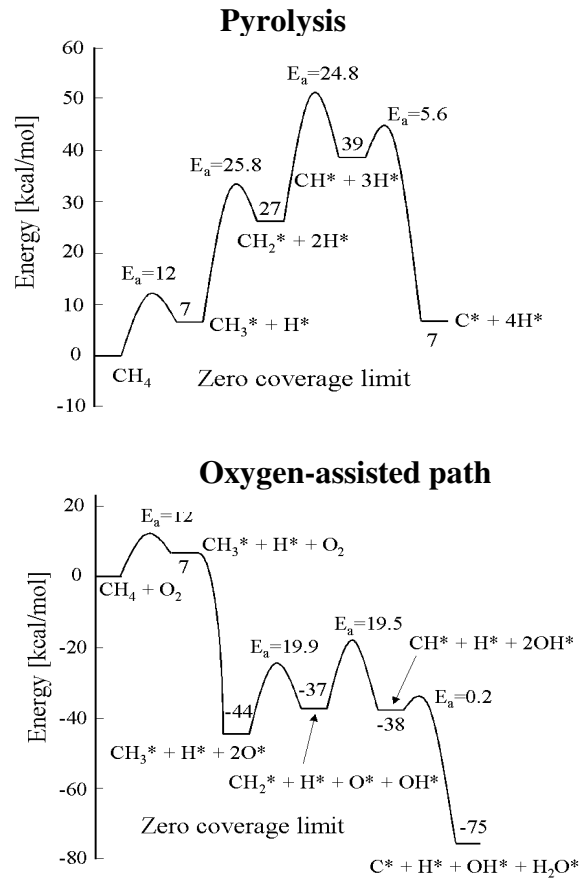

Figure 1. Selected energy diagrams for methane decomposition on Pt. The pyrolysis mechanism and oxygen-assisted mechanism are compared in terms of energetics at the zero coverage limit.

An example of reaction paths of the decomposition of methane on Pt is shown in Figure 1. In contrast to the previous assumption that methane decomposes in a simple step[2], $CH_4 \rightarrow C + 4H$, the energetics indicate that the rate determining step is the second or third hydrogen abstraction. Furthermore, in the presence of oxygen, lower activation energy paths will be preferred. The implications of these multiple reaction paths are that a change in the dominant path with composition as well as with operating conditions (e.g., prior and after ignition) have been observed in our simulations. Thus, the description of the all paths is essential to correctly describe both the entrance (prior to ignition) and main reactor zone (after ignition) of a monolith.

Numerics

In the case of steady state calculations, Newton's method and parametric arc-length continuation method are employed, whereas unsteady state simulations are carried out using the first order ordinary differential equation solver LSODA.

Reactor Scale Models

Depending on the reactor modeled, different reactor scale models have been implemented. Examples include a catalytic thin film plug flow reactor (PFR), a perfectly mixed fluidized bed reactor, a

temperature programmed desorption (TPD) model, and a catalytic stagnation flow micro-reactor.

Prediction of Conversion and Selectivity Data at Atmospheric Pressure

This section discusses the validation of the surface reaction mechanism by comparing with available experimental data in a fluidized bed reactor. In particular, Bharadwaj and Schmidt have carried out conversion and selectivity measurements as a function of operating temperature in a fluidized bed reactor with Pt-coated Al_2O_3 beads[8]. Figure 2 shows experimental as well as predicted methane conversion and selectivity to syngas for a mixture of 29.5% methane in air and conditions indicated in the figure caption.

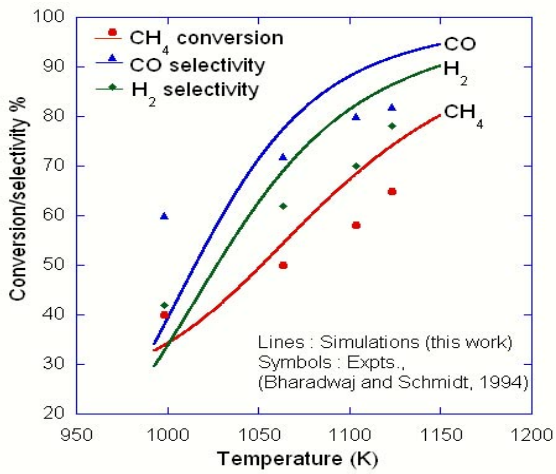

Figure 2. Comparison of predicted conversion and selectivity to syngas with experimental data of Bharadwaj and Schmidt.

The experiments have been conducted in a fluidized bed and the simulations using a catalytic CSTR, with an area per unit volume ratio of 15000 cm^{-1} and a residence time of 0.18 s. No optimization has been done for the reaction mechanism. Internal mass transfer limitations are not considered to be important. The concentration of OH, which is a main indicator of the role of gas phase chemistry, is very low ($<10^{-13}$) in this range. The negligible role of gas phase chemistry under these conditions has been further validated by excluding the gas phase chemistry from our calculations. The predicted data matches fairly well the experimental data except at lower temperatures, where the model underpredicts conversion as well as selectivities. Future work will address this last issue (see also below).

Surface Chemistry Optimization

From the preliminary simulations, we have observed fairly good agreement with available experimental data (see Figure 2). However, parameter optimization is necessary to accurately capture experimental data and have a reliable mechanism that can be used for reactor design. To accomplish the aim of optimizing the surface chemistry, we have concentrated on the ultra-high vacuum (UHV) conditions also where external mass transfer and heat effects are negligible. Developing a mechanism that is a valid over a wide range of pressure (pressure gap) is also important from a reactor design point of view, as most experiments have been conducted at relatively low pressures compared to the industrially desirable conditions. Results from these optimization studies along with illustration of the dominant reaction paths in syngas formation will be discussed.

Conclusion

A thermodynamically consistent detailed surface reaction mechanism with coverage-dependent activation energies and heats of reactions has been developed for methane oxidation simulations. Experimental data from literature are well captured by the proposed reaction mechanism.

Acknowledgement

This work was supported by the Department of Energy.

References

(1) Pfefferle, W. C.; and L. D. Pfefferle, *Prog. Energ. Combust. Sci.*, **1986**, 12, 25.
(2) Hickman, D. A.; and L. D. Schmidt, *J. Catal.*, **1992**, 138, 267.
(3) GRI-Mech 3.0 (1999) Gas Research- Institute mechanism for natural gas, taken from http://www.me.berkeley.edu/gri_mech.
(4) Aghalayam P.; Park Y.K.; Fernandes N.; Papavassiliou V.; and Vlachos D.G., *I&ECR*, **2001**, To be submitted.
(5) Aghalayam P.; Park Y.K.; and Vlachos D.G., *AIChE J.*, **2000**, 46(10), 2016.
(6) Aghalayam P.; Park Y.K.; and Vlachos D.G., *Symposium (International) on Combustion*, **2000**, 28, 1331.
(7) Shustorovich, E.; and Sellers, H., *Surf. Science Rep.*, **1998**, 31, 1.
(8) Bharadwaj S.S.; and Schmidt L.D., *J. Catal.* **1994**, 146, 11.

PRODUCTION OF SYN GAS / HIGH BTU GASEOUS FUEL FROM THE PYROLYSIS OF BIOMASS DERIVED OIL

S. Panigrahi, A. K. Dalai, and N. N. Bakhshi*

Catalysis and Reaction Engineering Laboratories
Department of Chemical Engineering
University of Saskatchewan
Saskatoon, SK. S7N 5C9, Canada
Phone: (306) 966-4771 Fax: (306) 966-4777
E- mail: Dalai@engr.usask.ca

Introduction

The gradual shortage of oil reserves has created considerable interest in using alternative source of energies, which are renewable in nature. As we enter the 21st century, new, clean burning, renewable fuels may revolutionize the energy industry. The renewable energy technologies (RET) of the European commission have the target of doubling their contribution from the present 5.6% to about 12% in the future[1]. Amongst all the renewable energy sources, biomass represents high potential and will play a vital role in the near future. Two approaches, namely pyrolysis and gasification of biomass, have been attempted to convert biomass into a useful form of energy[2,5]. The pyrolysis process is generally carried out by subjecting the biomass to a high temperature under an inert or oxygen deficient atmosphere. In the past, biomass was used for the production of hydrogen and medium Btu gas[6]. Extensive studies have been done on pyrolysis of cellulose, wood and biomass materials[7-12]. Waste biomass materials such as Kraft and Alcell lignins have been converted to hydrogen and medium Btu gas by steam gasification[6,13,14].

The fast pyrolysis process of biomass generally gives three products viz. gas, biomass-derived oil and char. The bio-oil thus produced contains unsaturated hydrocarbons and is thus highly unstable. This biomass-derived oil (BDO) has found a variety of applications in various areas. Unlike fossil fuels, BDO is renewable, cleanly burns, and is greenhouse gas neutral. It does not produce any SOx (sulfur dioxide) emission during combustion and produces approximately half the NOx (nitrogen oxide) emission in comparison with fossil fuels. Therefore, it is a potential raw material for renewable fuel and can be used as a fuel oil substitute[1-3]. However, several challenges are identified in bio-oil applications resulting from their properties. Extensive research on analyzing physical properties has been carried out earlier[15-20]. Rick and Vix have reviewed on product standards of BDO[21]. Most of the BDO are polar, viscous and corrosive, and contains 40-50 % oxygen. They have a high water content that is detrimental for ignition. Soltes and Lyn reported that most of the pyrolytic oils quickly form a solid mass when exposed to air[4]. Therefore, they can't be used as such as conventional fuel[5]. The conversion is due to the presence of organic acids in the oils. Over time, reactivity of some components in the oils leads to formation of larger molecules that result in high viscosity and in slower combustion[4]. Diebold and Czernik developed additives to stabilize the viscosity of biocrude during long-term storage, which demonstrated the ability to drastically reduce its aging rate, defined by the increase in viscosity with time[22].

Some research has been done on catalytic upgradation of BDO[14,23,24]. The product gas consisted of H_2 CO, CO_2. CH_4, C_2-C_4, higher hydrocarbons. The BDO has been converted to hydrogen via catalytic steam reforming followed by a shift conversion step[25,26]. The hydrogen yield was as high as 85%. Baker & Elliott have reported the catalytic upgrading of BDO produced at high-pressure conditions[27]. The yield of gasoline range hydrocarbons was 60-90%. The bio-oil thus produced contained unsaturated hydrocarbons and was highly unstable. An attempt has been made in this research to produce clean fuels including hydrogen, high Btu gaseous fuel and synthesis gas by pyrolysis of BDO in the absence of a catalyst. In this work, the reactor temperature and inert gas flow rate were varied from 650 to 800 ^{0}C, and from 18 to 54 ml/min, respectively. In all experiments, the BDO flow rate was maintained at 4.5-5.5 g/h.

Table 1. Properties of Biomass and BDO

Biomass Feedstock	Pine/ Spruce 100% wood[33]	Pine/ Spruce 53% Wood 47% bark [33]	Bagasse [33]	BDO (used in the present study)
Moisture, wt.%	2.4	3.5	2.1	-
Ash Content, wt.%	0.42	2.6	2.9	-
Bio-oil				
PH	2.3	2.4	2.6	2.5
Water Content, wt.%	23.3	23.4	20.8	21.5
Lignin Content, wt.%	24.7	24.9	23.5	25.0
Solids Content, wt.%	< 0.10	< 0.10	< 0.10	-
Ash content, wt.%	< 0.02	< 0.02	< 0.02	0.16-0.18
Density, g/cc @20°C	1.20	1.19	1.20	1.18-1.24
Calorific Value, MJ/kg	16.6	16.4	15.4	17.5-19.1
Kinematic Viscosity				
cSt @20°C	73	78	57	110
cSt @40°C	-	-	-	45.6
cSt @80°C	4.3	4.4	4.0	-

Experimental

Biomass-derived oil was obtained from DynaMotive, which was produced from Asphene wood materials using a patented technology[28]. On an average, 1 kg (dry) of biomass produces 0.75 kg of oil, 0.1 kg of char and 0.15 kg of gas[29]. Biomass derived oil is a liquid mixture of oxygenated compounds containing various chemical functional groups such as carbonyl, carboxyl and phenolic[30,31]. Biomass derived oil is made up of the following constituents: 20-25 % water, 25-30% water insoluble pyrolytic lignin, 5-12 % organic acids, 5-10% non polar hydrocarbons, 5-10% anhydrosugars and 10-25 % other oxygenated compounds[31].

The water includes those present in the wood 5-8% (see Table 1) as well as that is produced during the pyrolysis. Elemental analysis showed that the biomass-derived oil contained 43.6 wt % C, 8 wt. % H, 0.5 wt % N, and 47.9 wt% was O (obtained by difference). The viscosity of the fresh biomass-derived oil at 25 ^{0}C was $8x10^{-2}$ pa.s, which increased slowly upon storage[32].

Experimental Procedure. The experimental set-up used in our research consisted of an Inconel tubular continuous down flow micro reactor (12.7 mm i.d. and 200 mm long, placed co axially in the furnace). The reactor contained quartz chips (used for better temperature distribution and to avoid high pressure drop in the reactor) through which desired flow of an inert gas such as nitrogen was maintained through a Brooks mass flow controller (Model 0152/0154). The reactor temperature was controlled using a temperature controller using a thermocouple attached to the outer wall of the reactor and connected to the temperature controller. The temperature was measured by placing a thermocouple at the center of the quartz bed. A schematic diagram of the experimental set up used for the pyrolysis of BDO is shown in **Figure 1**. In this study, the reactor temperature was varied in the range of 650 to 800 ^{O}C where as the carrier gas flow rate was varied from 18 to 54 mL/min (STP). Biomass-derived oil was introduced at a predetermined rate using a micro metering syringe pump (Eldex, model A-60-S) at the rate of 4.5-5.5 ml/hr through a specially designed nozzle, which helped to spray liquids into the reactor along with the inert gas. Each experiment was performed at atmospheric pressure only for a period of 30-45 min, depending upon the operating conditions. In most cases, the run was terminated after 30 minute of operation. At the end of the run, the pump and the heating of furnace were shut off and the reactor was cooled down to the ambient temperature. The reactor was then removed from the reaction system and was weighed to determine the amount of coke formed. The product gas was cooled with a water-cooled heat exchanger and then with an ice-salt bath (to liquefy the condensable) before it was collected over saturated brine solution. The condensed liquid product was retained in a trap cooled by an ice-salt mixture and weighed. After each run, the mass of the gas, char and condensed liquid were calculated for bio oil conversion and mass balance.

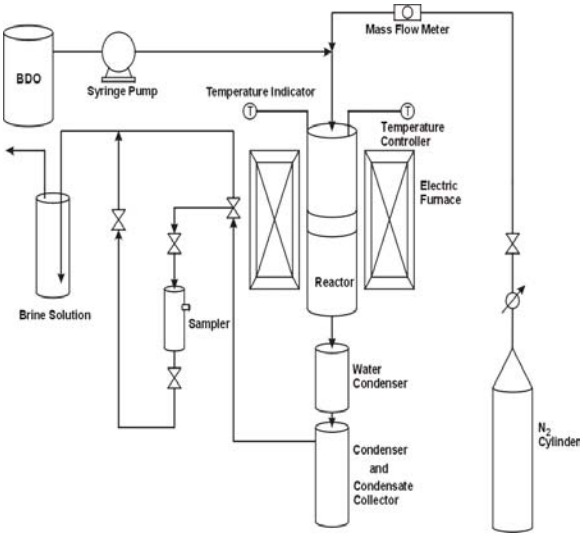

Figure 1: Schematic diagram of experimental setup for pyrolysis of BDO.

Product Gas Analysis. It may be noted that the reactor had a long preheating section. Thus, there was sufficient time for the BDO to achieve desired temperature in the reactor to crack and to produce gas, coke and liquid. The amount of the product gas was measured for each experiment, and was analyzed for its compositions using two GCs (Carle GC-500 series and HP5890). The HP5890 GC was equipped with a thermal conductivity detector and Carbosive S II column and analyzed H_2, CO, CO_2 and CH_4 where as the Carle GC, equipped with a flame ionization detector and combination of packed and capillary columns (Stable wax), analyzed hydrocarbons. Temperature programming of the oven was used in this case for analysis of the product gas.

Results and Discussion

The properties of BDO used in our study are compared to those reported in literature (see Table 1). The data in **Table 1** indicate that the properties of BDO are quite comparable to those obtained from other sources. In this investigation the effects of reactor temperature and the nitrogen flow rate on the BDO conversion and product gas composition was studied. The material balance for each experiment was found to be between 92-98wt.%.

Effect of Nitrogen Flow Rate. The effects of nitrogen flow rate (18 to 54 mL(STP)/min) on the conversion of BDO, product gas yield and its composition have been studied at constant pyrolysis temperature of 800 ^{0}C and contact BDO flow rate of 4.5 mL/h and the results are shown in **Figure 2**.

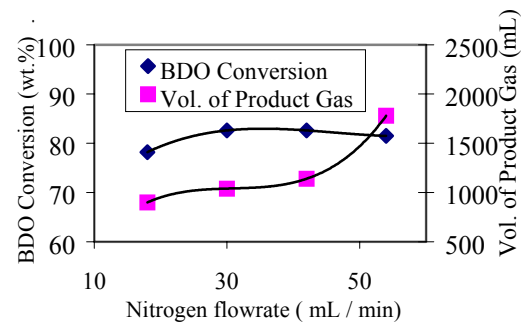

Figure 2 Effects of carrier (nitrogen) gas flow rate on conversion of BDO and volume of gas produced during pyrolysis of BDO at 800 0C and BDO flow rate of 4.5 mL/h

By varying nitrogen flow rate from 20 to 30mL/min, the conversion of BDO to gas and char was increased from 75 to 83wt.%. The increased conversion of BDO may be due to the increased heat and mass transfer caused due to the turbulences created by the higher flow rate of nitrogen. Beyond nitrogen flow rate of 30mL/min, the conversion of BDO was ~ 83wt.% and did not change with respect to nitrogen flow. It was also observed that with the increase in flow rate of nitrogen, the amount of gaseous product was increased. For example, the volume of product gas was increased from 900 to 1780 ml by changing the nitrogen flow rate from 18 to 54 ml/min i.e., from 100 grams of BDO, 39 l and 65 l of product gas were obtained at N_2 flow rates of 18 and 54 ml/min, respectively. Higher gas yield at higher nitrogen flow could be due to higher syn gas production, which is explained below.

The effect of nitrogen flow rate on product gas composition was also evaluated and is shown in **Figure 3**. It is observed that the production of hydrogen remained approximately constant with the

increase in nitrogen flow rate from 18 to 45 mL/min. However, there is a sharp increase in the hydrogen production with further increase in nitrogen flow rate. The formation of methane was high 30 mol% at lower nitrogen flow rate of 20 mL/min. Higher residence time due to low flow rate of nitrogen is responsible for cracking of BDO producing more methane. At higher flow rate (42-54 mL/min) of N_2, the concentration of methane was low (~20-24 mol%). At 800 ^{0}C methane could react due to partial oxidation and combustion producing more hydrogen. CO gas yield was increased when the nitrogen flow was increased from 18 to 54 ml and reached maximum for N_2 flow of 42 – 50 mL/min. This may be due to the reaction of CO_2 with carbonaceous material producing more CO. The total amount of synthesis gas (hydrogen and CO) also increased from 22 to 65 mol% as nitrogen flow increased from 18 to 54 mL/min. The effect of nitrogen flow rate on the production of other gases such as ethane and higher hydrocarbons was not very significant.

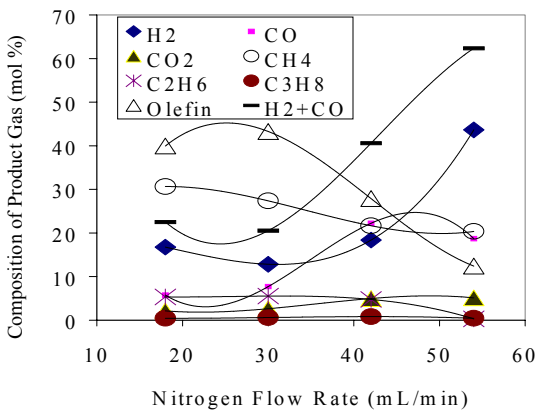

Figure 3. Effects of carrier (nitrogen) gas flow rate on product gas composition for pyrolysis of BDO at 800 0C and BDO flow rate of 4.5 ml/h

The effects of N_2 flow rate on total olefin production and its distribution are shown in **Figure 3** and **Table 2**, respectively. The production of olefins (mostly ethylene and propylene) initially after showing a slight increasing trend followed a decreasing pattern with nitrogen flow rate (see Figure 3). The olefin content of approximately ~ 43mol% was obtained corresponding to a nitrogen flow rate of 30mL/min (see Table 2). Probably at lower N_2 flow rate (20-30 mL/min) BDO had higher residence time for cracking and thus producing more olefins. At higher flow rate (42-54 mL/min) of N_2, the concentration of olefins was lower (~10-25 mol%) where as syn gas formation was higher.

Table 2. The Effects of N_2 Flow Rate on Total Olefin Production and its Distribution at a Reaction Temperature of 800 ^{0}C

Nitrogen flow	C_2H_4, mol%	C_3H_6, mol%	HigherC_3H_6 Olefins, mol%	Total olefins, mol%
18	31.5	3.8	3.6	38.9
30	31.1	3.1	9.0	43.2
42	18.4	2.4	7.1	27.9
54	6.9	0.1	4.4	11.4

The effect of nitrogen flow at 800 ^{0}C on the heating value of product gas is shown in **Figure 4**. Due to optimum production of hydrocarbons at a nitrogen flow rate of 30mL/min and 800 ^{0}C, the heating value of gas was high (1738 Btu/SCF). At these conditions, the conversions of bio-oil and olefin yield were as high as 83 wt.% and 43mol%, respectively. However, the syn gas yield of 65mol % was optimum at nitrogen flow rate of 54mL/min at 800 ^{0}C (See Figure 3).

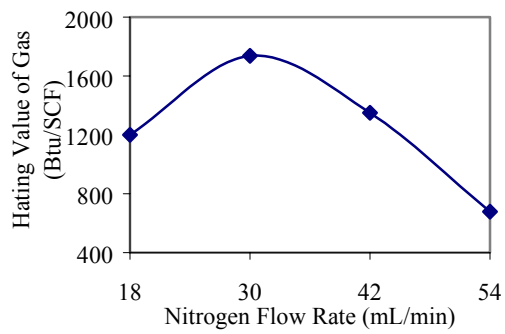

Figure 4. Effects of carrier (nitrogen) gas flow rate on total heating value of produt gas during pyrolysis of BDO at 800 ^{0}C

Effects of temperature. The effects of temperature (650-800 ^{0}C) on the conversion of bio-oil, gas yield and its composition have been studied keeping nitrogen and bio-oil flow rates constant, respectively, at 30mL/min and 4.5g/h. Effects of temperature on conversion of BDO and volume of gas produced are shown in **Figure 5**. The results show that as the temperature is increased from 650 to 800 ^{0}C, the conversion of bio-oil to gas and char is increased from 57 to 83 wt. %. Also, as expected, the production of gas is increased with temperature. For example, the product gas volumes obtained at 650 and 750 ^{0}C were 730 and 1020 mL, respectively. This corresponds to the fact that from 100 grams of BDO, 26 l to 45 l of gas could be produced with increase in temperature from 650 to 750 ^{0}C at constant N_2 flow rate of 30 mL/min. However, beyond this temperature, its effect on the gas production was negligible.

Table 3. The Composition Data as a Function on Temperature at Nitrogen Flow Rate of 30 mL/min

Temp., ^{0}C	H_2, mol %	CO, mol %	CO_2, mol %	CH_4, mol%	C_2H_6, mol%	C_3H_8, mol%	Total olefin, mol%	Total
650	12.8	17.0	2.5	19.2	7.2	0.9	40.3	99.9
700	16.3	9.2	3.4	21.6	7.2	1.1	41.2	99.8
750	9.3	6.5	2.1	23.2	9.0	1.3	48.5	99.9
800	12.8	7.7	2.6	27.4	5.5	0.6	43.2	99.8

The effects of temperature on the product gas composition and olefins formed from BDO are given in **Table 3**. It is also evident from data in this table that the production of maximum olefins is at 48.5 mol% at 750 ^{0}C. The methane concentration increases from 19.2 to 27.4 mol% as the temperature increases from 650 to 750^{0}C. Thus it is possible to produce a gas stream having an olefin content of as high as ~48-mol % from BDO. The results also show that the concentration of CO_2, C_2, C_3 paraffin do not change with temperature.

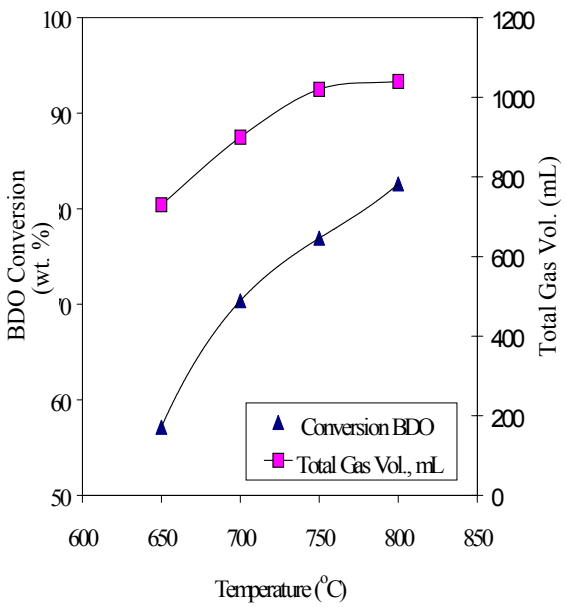

Figure 5. Effects of temperature on conversion of BDO and volume of gas produced during pyrolysis of BDO at a nitrogen flow rate of 30 mL (STP)/min

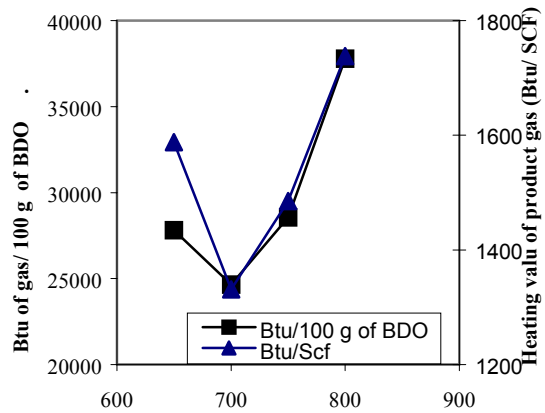

Figure 6. Effects of temperature on heating value of product gas for pyrolysis of BDO at nitrogen flow rate of 30 mL/min.

The effects of reaction temperature on the olefins composition are shown in **Table 4**. The effects of reaction temperature on the heating value and energy content of the gas produced at nitrogen flow rate of 30 mL/min are shown in **Figure 6**. The results indicate that the heating value of the product gas was increased from 1300 to 1700 Btu/SCF with increase in temperature from 700 to 800 ^{0}C. This could be due to increase in methane concentration from 19 to 27 mol % in the product gas.

Table 4. Effects of Temperature on Distribution Olefins Formed During the Pyrolysis of BDO at a Nitrogen Flow Rate of 30 mL/min and BDO Flow Rate of 4.5 –5.5 mL/h

Temperature ^{0}C	C_2H_4, mol%	C_3H_6, mol%	Higher C_3H_6Olefins, mol%	Total olefins, mol%
650	20.8	9.4	10.1	40.3
700	23.0	9.1	9.1	41.2
750	26.4	10.2	12.0	48.6
800	31.1	3.1	9.0	43.2

It is observed that the concentration of olefins (of which 60-70 mol % is ethylene) is varied in a range of 40 to 48mol % in the product gas with increase in temperature from 700 to 800 ^{0}C. However, syn gas production is decreased by 20 mol % in spite of higher production of hydrogen with the temperature increase. The increase in hydrogen production with increased temperature occurred probably because at high temperatures pyrolysis of the BDO sub-units, which evolved more hydrogen.

Conclusions

The present study identifies the pyrolysis of biomass-derived oil as a source of gaseous fuel. In this process, the product gases essentially consisted of H_2, CO, CO_2, CH_4, C_2H_4, C_2H_6, C_3H_8, and C_4^+ components. This process can be utilized for producing hydrocarbons and synthesis gas for various applications. By adjusting the parameters such as inert gas flow rate and reactor temperature, the composition of the product gas from biomass-derived oil can be tuned in the desired direction. The conversion of biomass-derived oil at a flow rate of 4.5 – 5.5 g/h could be increased from 57 to 83 wt.% due to increasing the reactor temperature from 650 to 800 ^{O}C at a nitrogen flow rate of 30

mL/min. At 800 ^{0}C and nitrogen flow rate of 30 mL/min, composition of various product gas components ranged between: Syn gas 16-30 mol %, CH_4 19-27 mol % and C_2H_4 23-31 mol %. A large amount of total product gas was obtained from BDO at 800 ^{0}C and N_2 flow rate of 30 mL/min. Heating values ranged between 1300 – 1700 Btu/SCF. Thus, the present study shows that there is a strong potential for making syn gas, methane, ethylene and high heating value gas from the pyrolysis of biomass-derived oil.

References

1. Chantal, P.D; Kaliaguine, S; Grandmaison, K.L; Mahay, A. *Appl. Catal*. **1984**, *10*, 317.
2. Sharma, R.K; Bakhshi, N.N. *DSS contract file # 23440-0-9467/01-SZ, Bio-energy Dev. Prog., Energy Mines and Resources, Ottawa,* **1992**
3. Diebold, J; Soltes, E.J; Miline, T.A. *ACS Symp. Ser.376, Amer. Chem. Soc., Washington, DC*, **1988**, 264.
4. Soltes, E.J; Lin, S.L. *ACS Symposium Series* **1987**, *264*, 178-185.
5. Churin, E.P; Grange, B. *Elseiver Appl. Sci., London, UK*, **1990**. *2,* 616
6. Chaudhari, S.T; Ferdous, D; Dalai, A.K; Bej. S.K; Thring, R.W; Bakhashi, N.N. *Fifth International conference on Biomass Conversion, Austria*, **2000**
7. Boutin, O; Ferrer, M; Lede, J. *J. Anal. Appl. Pyrol.* **1988** *47,* 13.
8. Radlein, A.G.D; Piskorz, J; Scott, S.D. *J.Anal. Appl. Pyrol.* **1987***,12*, 51.
9. Piskorz, J; Radlein, A.G.D; Scott, S.D; Czernik, S. J. *Anal. Appl. Pyrol.* **1989**, *16*, 127.
10. Liu, N.A; Fan, W.C. *Fire and Materials.* **1998**, *22,*103.
11. Koullas, D.P; Nikolaou, N; Koukios, E.G. *Bioresource Energy,* **1998**, 63: 261.
12. Maschio, G; Lucchesi, A; Stoppato, G. *Bioresource Technology,* **1994**, *48*, 119.
13. Iqbal, M; Dalai, A.K; Thring, R.W; Bakhshi N.N. *33rd International Engineering Conference on Energy Conversion, Colorado,* **1998**.
14. Bakhshi, N.N; Dalai, A.K; Thring R.W. *Division of Fuel Chemistry, 217th ACS National Meeting, California,* **1999**, *4,* 278.
15. Elliot, D.C. *IEA Co-operative project D1 Biomass liquefaction Test Facility project , Washington, Pacific Northwest Laboratory*, **1983,** *4*, 87.
16. Bridgwater, A.V; Kuester, J.L. *Research in thermo chemical biomass conversion, Phoenix, Arizona, New York: Elsevier Applied Science,* **1988,** 1177.
17. Milne, T.A; Brennan, A.H; Glenn, B.H. *Sourcebook of methods of analysis for biomass and biomass conversion process.* London, Elsevier Applied Science, **1990,** 327.
18. McKinley, J.W; Overend, R.P; Elliott, D.C. In *Proc. Biomass pyrolysis oil properties and combustion meetings,* Estes Park, CO. Golden, CO: NREL. NREL-CP-430-7215, **1994,** 34.
19. Diebold, J.P; Milne, T.A; Czernik, S; Oasmaa, A; Bridgwater, A.V; Cuevas, A; Gust, S; Huffman, D; Piskorz, J. *Development in thermo chemical biomass conversion. Banff.* Glasgow: Blackie Academic and professional, Eds.; **1997**,*1*, 533.
20. Piskorz, J; Radlein, D; Majerski, P; Scott, D.S. In *Proc. Biomass pyrolysis oil properties and combustion meetings*, Estes Park. CO. Golden. CO. NTIS, **1994**, 22.
21. Rick F, and Vix U. In Bridgwater, A.V; Grassi, G. *Biomass Pyrolysis liquids upgrading and utilization. London & New York: Elsevier Applied Science,* Eds.; **1991**. 177-218.
22. Diebold, J.P; Czernik, S. *Energy & Fuels,***1997***, 11(5)*, 1081.
23. Mathews JF, Tepylo MJ, Eager RL and Pepper JM. *Can. J. Chem. Eng.,* **1985**, *63*, 686.
24. Srinivas, S.T; Dalai, A.K; Bakhshi, N.N. Can. J. Chem. Eng., **1985,** *78*, 343.
25. Wang, D; Czernik, S; Montane, D; Mann, M; Chornet, E. *Industrial and Engineering Chemistry Research***, 1994,** *36(5)*, 1507.
26. Czernik, S; Wang, D; Chornet, E. *Proceedings of the 1998 U.S. DOE Hydrogen Program Review*, 28-30 April, Alexandria, Virginia. NREL/CP-570-25315. National Renewable Energy Laboratory,**1998,** *2*, 557.
27. Baker, E.G; Elliot, D.C. *Thermo chemical Biomass Conversion,* Eds.; Elsevier Appl. Sci., London UK, **1988,** 883-895.
28. Cottam, M.L; Bridgwater, A.V. *Thermo chemical Biomass Conversion,* Blackie Academic and Professional, London, Eds.; **1994**, *2*, 1343.
29. Bridgwater, A.V. *Advances in Thermo chemical Biomass Conversion* Blackie Academic and Professional, London,Eds.; **1994**, *2*, 1314.
30. Bridgwater AV, In *Fast Pyrolysis of Biomass: A handbook,* Eds.; PL Press. **1999**.
31. Morris, K.W. *4th Biomass conference of Americas,* **1999**.
32. Piskorz, J. *United States Patent* No. 5,728,271.
33. Morris, K.W; Johnson, W; Thamburaj, R**.** *1st World Conference and Exhibition on Biomass for Energy and Industry in Seville, Spain,* **2000**.

Temperature-Programmed Studies on Partial Oxidation of CH_4 to Syngas over a Ni/Al_2O_3 Catalyst

LI Chun-Yi [1], ZHANG Zhao-Bin [2], YU Chang-Chun [2], and SHEN Shi-Kong [2]

1. National Key Lab of Heavy Oil Processing, College of Chemistry & Chemical Engineering, University of Petroleum, Dongying, Shandong Province 257061
2. Catalytic Key Lab of CNPC, University of Petroleum, Changping, Beijing 102200

Introduction

Partial oxidation of CH_4 to syngas has been a hotspot of research for the advantages comparing to steam reforming process, such as low H_2/CO ratio (≈2), more energy-efficient, and high CH_4 conversion and selectivities to CO and H_2 with smaller reactor and short contact time (⩽10^{-2}s), etc [1-3]. Many metal catalysts have been studied, such as supported Rh, Pt, Pd, Ru, Re, Ir, Ni, Fe and Co, etc. The supported noble Rh catalyst exhibits excellent activity and selectivity [4], but its price is too expensive. The supported Ni catalysts have similar performance with supported Rh, and the price of Ni is far lower than that of Rh. So the studies on supported Ni catalyst have attracted a great number of researchers [5-14].

About the reaction mechanism, some authors [15,16-18] pointed out that partial oxidation of CH_4 to syngas proceeds via indirect oxidation mechanism, namely: complete combustion of CH_4 to CO_2 and H_2O and subsequently reforming reaction of the residual CH_4 with CO_2 and H_2O to CO and H_2. However, other authors [9,19,20,21] claimed that the reaction proceeds via direct oxidation mechanism: H_2 is from the decomposition of CH_4 and CO is the product of the reaction between surface carbon species and surface oxygen species.

Our work [22] on the reaction over a Ni/Al_2O_3 catalyst supports direct oxidation mechanism. CH_4 firstly decomposes on active metal Ni sites to H_2 and Ni_xC, and then Ni_xC reacts with NiO formed by oxidation of metallic Ni by O_2 to CO or CO_2 depending on the concentration of NiO around Ni_xC. Steady and non-steady state isotopic transient experiments showed that most of CO_2 during the reaction is from the surface reaction between Ni_xC and NiO, not from disproportionation of CO or further oxidation of CO [23]. This also proves the mechanism we suggested.

Furthermore, metal Ni is active sites of the Ni/Al_2O_3 catalyst. So the catalyst must be kept in reduced state, or the reaction mechanism will change and the conversion of CH_4 and the selectivities to H_2 and CO will be very low for CH_4 can't decompose on NiO [24].

In this paper, the Ni/Al_2O_3 catalyst was evaluated and the effects of temperature and space velocity were investigated with on-line chromatography analysis. In addition, temperature-programmed technique was used to investigate the change of the catalyst surface state during the reaction at different temperature and its influence on the conversion and selectivities.

Experimental

The preparation of the 8%(mol, $\frac{Ni}{Ni+Al}$) Ni/Al_2O_3 catalyst has been depicted elsewhere [22,24]. The granularity range is 0.30-0.45mm to eliminate the effect of inner diffusion. The BET surface area and the dispersion of Ni measured by ASAP2010 are $280m^2/g$ and about 5%, respectively.

The reactor for catalyst evaluation is a quartz tube with inner diameter 12mm. 450mg catalyst was placed in the middle and the other space of the reactor was filled with 0.45~0.9mm quartz sand. Before reaction the catalyst was reduced with pure H_2 at 700°C for 4h. The products were analyzed with on-line gas chromatography (GC) (HP5890). The analysis method called Double-column in Series Analysis was developed by Zhang et al [25], which permits to analyze all the effluents in partial oxidation of CH_4 to syngas with once sample injection.

The apparatus for temperature-programmed experiments has been introduced in the reference [22,24]. All experiments were carried out in a fixed bed quartz micro-reactor with inner diameter 5.5mm at atmospheric pressure, and the total flow rate was 30mL/min. For TPO (temperature-programmed oxidation) and TPR (temperature-programmed reduction), 200mg catalyst was used. For the other experiments, only 30mg catalyst was used. The effluents of the reactor were monitored by a quadrupole mass spectrometer (MS) (AMTEK QuadLink 1000) with the minimum dwell time of 3 milli-seconds.

Results and Discussion

Evaluation of the Ni/Al_2O_3 catalyst under different temperature and space velocity The performance of the catalyst for partial oxidation of CH_4 to syngas was investigated at 600°C, 700°C, and 800°C with different space velocity 53.3 h^{-1}, 65.2 h^{-1}, 77.0h^{-1}, respectively. After the reaction had proceeded for 1h over the catalyst pre-reduced for 4h at 700°C, we sampled and analyzed the products with on-line GC. The results of conversion and selectivity were listed in **table 1**. The conversion of CH_4 is all more than 80% except for at 600°C and 53.3h^{-1}, and even more than 90% at 800°C. Apparently, high temperature is favorable for CH_4 conversion. The selectivities to H_2 are in the range of 94.8% to 97%, very high at all the conditions. At higher space velocity, the selectivity to CO may exceed 90% at or above 700°C. At 800°C and 77h^{-1}, the selectivity to CO is 95.2%, approaches 96% the thermodynamic equilibrium value at the temperature [16]. Obviously, the catalyst exhibits very good performance. Zhang [26] gave even better results: the conversion of CH_4 95.6%, the selectivity to H_2 99.7%, and to CO 94.5%. These show that Ni base catalyst is the most promising one for partial oxidation of CH_4.

Table1. Results of partial oxidation of CH_4 over the catalyst

T (°C)	Space velocity (h^{-1}, wt/wt)	Conversion of CH_4 (%)	Selectivity to CO (%)	Selectivity to H_2 (%)
600	53.3	79.2	82.6	94.9
	65.2	81.1	85.4	94.8
	77.0	83.9	87.2	95.9
700	53.3	84.6	89.3	95.4
	65.2	85.8	90.5	95.5
	77.0	87.2	91.1	96.3
800	53.3	89.7	94.3	96.3
	65.2	91.0	94.8	96.8
	77.0	91.7	95.2	97.0

Based on the results listed in **Table 1**, temperature and space velocity affect the results significantly. At the same space velocity, the conversion of CH_4 and the selectivities to H_2 and CO all increase with temperature. From 600°C to 800°C, at space velocity 53.3h^{-1} they increase 10.5, 1.4, and 11.7 percentage points, respectively. At 77.0h^{-1}, however, they increase 7.8, 1.1, and 8.0 percentage points, respectively. Obviously, at low space velocity both the conversion and the selectivities are more sensitive to temperature, and the selectivity to H_2 is more inert to temperature. Furthermore, the conversion of CH_4 and the selectivities to H_2 and CO all increase with space velocity, too. At 600°C, they increase 4.7, 1.0, and 4.6 percentage points from 53.3h^{-1} to 77.0h^{-1}, respectively. However, at 800°C they increase only 2.0, 0.7, and 0.9 percentage points, respectively. So at low temperature they are sensitive to space velocity. Similarly, the selectivity to H_2 is insensitive to space velocity.

Temperature-programmed decomposition of CH_4 and temperature-programmed partial oxidation of CH_4 from 510°C to 800°C Temperature-programmed decomposition of CH_4

proceeded in pure CH_4 with the rate of 25°C/min over the catalyst that had been reduced in pure H_2 at 700°C for 4h. The results were shown in **figure 1**. When temperature increases to 330°C, that the intensities of CH_4 and H_2 begin to decrease and increase respectively shows that CH_4 can decompose at the temperature. Between 330°C and 490°C, CH_4 decomposed is only a little. When temperature exceeds 490°C, CH_4 can decompose quickly and a large quantity of H_2 is produced. With Ni on the surface of the catalyst converting to Ni_xC [18], CH_4 stops to decompose gradually.

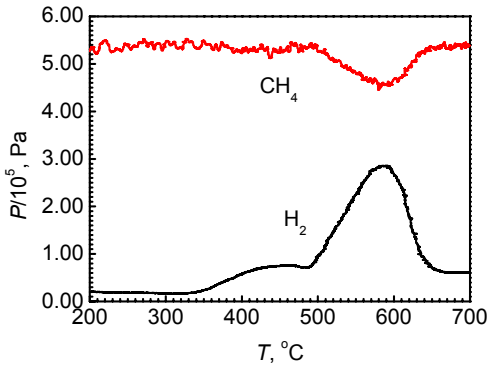

Figure 1. Curve for temperature programmed decomposition of CH_4 over the Ni/Al_2O_3 catalyst.

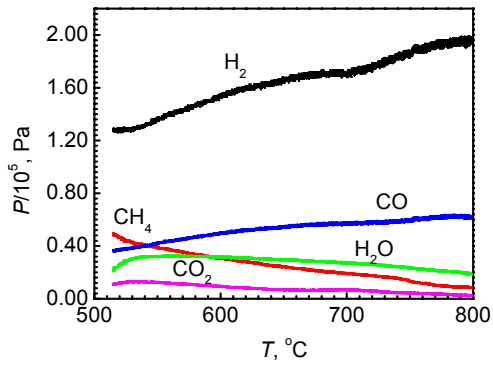

Figure 2. Curves for temperature-programmed partial oxidization of CH_4 from 500°C to 800°C over the Ni/Al_2O_3 catalyst reduced.

The catalyst was reduced firstly with pure H_2 for 4h at 700°C. In pure Ar, temperature was decreased to about 510°C, and then the atmosphere was switched from Ar to 2/1 (mol/mol) CH_4/O_2. After the switch, partial oxidation of CH_4 happens immediately. During the reaction, O_2 is consumed completely [15,26,27], and the conversion of CH_4 and the selectivities to H_2 and CO are changing with temperature. In **figure 2**, even at 510°C, the main products are H_2 and CO, but the conversion of CH_4 is very low (about 30%), and the selectivities to H_2 and CO are all not high (about 80% and 75%, respectively). With the increase of temperature, the conversion of CH_4 and the selectivities to H_2 and CO all increases gradually. At 800°C, the conversion of CH_4 and the selectivities to H_2 and CO are about 90%, 95% and 93%, consistent basically to that of catalyst evaluation.

The results of catalyst evaluation and **Figure 2** show that high temperature and high space velocity are all favorable for the conversion of CH_4 and the selectivities to CO and H_2. According to the mechanism we suggested, the decomposition of CH_4 over metal Ni sites to H_2 and Ni_xC is the precondition of the reaction [22]. In **figure 2**, No O_2 is detected during the process no matter how much the conversion of CH_4 is. As indicates that the conversion of CH_4 and the selectivities to H_2 and CO are dependent on the rate of CH_4 decomposition. High temperature can quicken the decomposition of CH_4 (**figure 1**), so the conversion of CH_4 increases with temperature. For CO and CO_2 are from the reactions between Ni_xC and NiO on the catalyst surface [22],

$$Ni_xC + NiO \rightarrow (x+1)Ni + CO$$

$$Ni_xC + 2NiO \rightarrow (x+2)Ni + CO_2$$

and O_2 is consumed completely. If the conversion of CH_4 is lower, CO_2 is easier to be produced due to more NiO and less Ni_xC on the catalyst surface. Therefore the selectivity to CO will be affected by the conversion of CH_4 seriously. H_2, however, is the product of CH_4 decomposition. The adsorption of H_2 on the catalyst is very weak at high temperature. Although more NiO on the catalyst surface will promote the reaction

$$H_{2(ad)} + NiO \rightarrow H_2O + Ni$$

to produce H_2O, the temperature effect on the selectivity to H_2 is very weak.

Partial oxidation of CH_4 is a mild exothermic reaction,

$$CH_4 + \frac{1}{2}O_2 \rightarrow 2H_2 + CO$$

$$\Delta H^o_{298K} = -35.7 kJ/mol$$

To enhance space velocity, the heat released per catalyst surface will increase. Although temperature of the catalyst bed is controlled, the increase of inner surface temperature of the catalyst granules is inevitable. It's obvious that enhancing space velocity is indirectly increasing the temperature. So the effect of space velocity on the reaction is similar to that of temperature.

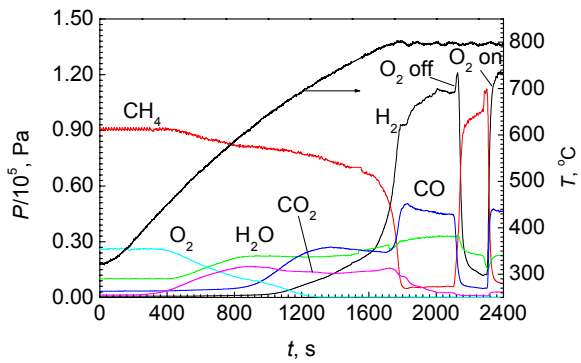

Figure 3. Curves for temperature-programmed reaction of partial oxidation of methane over the reduced Ni/Al_2O_3 catalyst under 30mL/min 2/1(mol/mol) CH_4/O_2 from room temperature to 800°C. Shut off O_2 for a few min and reopening at 800°C.

Transformation of the catalyst surface state during temperature-programmed partial oxidation of CH_4 If the other conditions were the same as that of **Figure 2** and temperature-programmed partial oxidation of CH_4 began from room temperature, the results are absolutely different from **Figure 2**. At about 430°C, CO_2 and H_2O are produced (**Figure 3**). When temperature increases to about 600°C, CO and H_2 appear. The intensities of these products increase with temperature. At 700°C, the conversions of CH_4 and the selectivities to H_2 and CO are about 8%, and 75%, 40% respectively, far lower than that in **Figure 2**. O_2 is not consumed completely here.

Continue to increase the temperature, when it exceeds 750 °C, the intensity of H_2 goes up quickly with temperature and O_2 is

consumed completely. Thereafter the intensity of CO also ascends rapidly. At 800 °C, the conversion of CH_4 and the selectivities to H_2 and CO reach or exceeds 90%. We closed O_2 for a while then reopened. It is can be seen that no evident change in the conversion of CH_4 and the selectivities to H_2 and CO happens before O_2 mass flow controller was closed and after it was reopened.

TPO and TPR of the catalyst show that the catalyst begins to be oxidized from about 250°C and the rate of oxidization is quickened with the increase of temperature, however, reducing the catalyst needs higher than 650°C. So the catalyst is easy to be oxidized and difficult to be reduced. In **figure 1**, CH_4 begins to decompose at 330°C. Thereby, if temperature-programmed partial oxidation of CH_4 begins from the temperature CH_4 can't decomposes rapidly, the catalyst surface will be oxidized. CH_4 can't decompose on the oxidized catalyst. We have discussed the effect of surface state and adsorbed oxygen on partial oxidation of CH_4 to syngas [24]. At or below 700°C, if the catalyst surface is oxidized, O_2 will not be able to be consumed completely and a certain amount of reversibly adsorbed oxygen will exist on the catalyst surface. Non-selective oxidation between CH_4 and reversibly adsorbed oxygen with high oxidation activity [28] occurs via Rideal-Eley mechanism, and both the conversion of reactants and the selectivities to H_2 and CO are very low.

With the increase of temperature, the reaction rate between CH_4 and adsorbed oxygen quickens. When temperature increases to around 750°C, O_2 is consumed completely, as can be seen clearly in **figure 3**. Then NiO on the catalyst surface has the chance to be reduced by hydrogen produced and metal Ni sites that are necessary for CH_4 decomposition form. Thereupon, CH_4 begins to decompose and the reaction mechanism changes to direct oxidation mechanism. Thus, when we closed O_2 for a while and then re-open, the conversion of CH_4 and the selectivities to H_2 and CO are almost unchanged for the catalyst surface has been reduced. Therefore, during partial oxidation of CH_4, the catalyst must be maintained in the reduced state, and CH_4 can react with O_2 via direct oxidation mechanism with high conversion and selectivity.

If partial oxidation of CH_4 proceeds at the temperature lower than 750°C, the catalyst must be kept reduced state. Otherwise, the conversion of CH_4 and the selectivities will be very low for CH_4 can't decompose and can only react with adsorbed oxygen on the oxidized catalyst surface via Rideal-Eley mechanism. However, if the reaction temperature is higher than 750°C, the catalyst is unnecessary to be reduced before reaction and metal Ni sites can form automatically during the reaction for O_2 is consumed completely.

Acknowledgement

This work is supported by the National Natural Science Foundation of China (Issue No. 29673027).

References

1 Tang S., Lin J., and Tan K.L. *Catal. Lett*. **1998**, *55*: 83.
2 Hickman D.A., Haupfear E.A., and Schmidt L.D. *Catal. Lett*. **1993**, *17*: 223.
3 Tsipouriari V.A., Zhang Z., and Verykios X.E. *J. Catal*. **1998**, *179*: 283.
4 Hickman D. A., and Schmidt L.D. *J. Catal.*, **1992**, *138*: 267.
5 Prettre M., Bichner C. H. and Perrin M. *Trans. Faraday Soc.*, **1946**, *43*: 335.
6 Hayakawa T., Anderson A. G., Shimizu M., and Suzuki K.. *Catal. Lett.*, **1993**, *22*: 307.
7 Lu Y., Deng C., Ding X.J., Shen S.K. *Chinese J. Catal.*, **1996**, *17(1)*: 28 (in Chinese).
8 Choudhary V. R., Rane V. H., and Rajput A. M. *Catal. Lett.*, **1993**, *22*: 289.
9 Choudhary V. R., Rajput A. M., and Prabhakar B. *J. Catal.*, **1993**, *139*: 326.
10 Choudhary V. R., Rajput A. M., and Prabhakar B. *Catal. lett.*, **1995**, *32*: 391.
11 Choudhary V. R., Rane V. H., and Rajput A. M. *Catal. Lett.*, **1992**, *16*: 269.
12 Choudhary V. R., Sansare S. D., and Maman A.S. *Appl. Catal.*, **1992**, *89*: 90.
13 Choudhary V. R., Rajput A. M., and Rane V. H. *J. Phys. Chem.*, **1992**, *96*: 8686.
14 Slagtern A., Swaan H.M., Olsbye U., Dahl I.M., and Mirodatos C. *Catal. Today*, **1998**, *46*: 107.
15 Ashcroft A. T., Cheetham A. K., Foord J. S., Green M. L. H., Grey C. P., Murrell A. J., and Vernon P.D. F. *Nature*, **1990**, *344*: 319.
16 Dissanayake D., Rosynek M.P., Kharas K.C.C., and Linsford J.H. *J. Catal*., **1991**, *132*: 117.
17 Looij F.V., Giezen J.C.V., Stobbe E.R., and Geus J.W. *Catal. Today*, **1994**, *21*: 495.
18 Ruiz A. G., Aparicio P. F., Baeza M.B. B., Ramos I. R. *Catal. Today*. **1998**, *46*: 99.
19 Hickman D. A., and Schmidt L.D. *Science*, **1993** , *259*: 343.
20 Mallens E.P.J., Hoebink J.H.B.J., and Marin G.B. *J. Catal*. **1997**, *167*: 43.
21 Matsumura Y., and Moffat J.B. *Catal. Lett*. **1994**, *24*: 59.
22 Shen S.K., Li C.Y. and Yu C.C. *Stud. Surf. Sci. Catal.*, **1998**, *119*: 765.
23 Li C.Y., Yu C.C., and Shen S.K. *Acta Physico-Chimica Sinica*, **2000**, *16*: 97.
24 Li C.Y., Yu C.C., and Shen S.K. *Catal. Lett.*, **2000**, *67(2-4)*: 139.
25 Zhang Z.B., Yu C.C., and Shen S.K. *Analysis and Measurement Technology & Instrument*, **1998**, *4*: 98. (in Chinese).
26 Zhang Z.B. *Studies on Ni Base Catalysts for Partial Oxidation of CH_4*, Ph. D. Thesis, University of Petroleum, Beijing, **1999** (in Chinese).
27 Huszar K. *Acta. Chim. Acad. Sci. Hungar*, **1971**, *70*: 287.
28 Li C.Y., Yu C.C., and Shen S.K. *Chinese J. Catal.*, **1998**, *19(5)*: 463 (in Chinese).

PRODUCT ANALYSIS OF A NOVEL SYN-CRUDE SYNTHESIS DIRECTLY FROM A COMBINED CONVERSION OF COAL AND METHANE

Yu Wang[1], Yang Li[1], Jijun Zou, Baldur Eliasson[2], and Chang-jun Liu[1]*

1. State Key Laboratory of C1 Chemistry and Chemical Technology,School of Chemical Engineering and Technology, Tianjin University,Tianjin 300072, China
2. Energy & Global Change, ABB Corporate Research Ltd., Baden, CH5405, Switzerland

Introduction

Mankind has been used to an ever-growing supply of cheap and abundant fossil energy including coal, oil and natural gas for more than 150 years. Especially, cheap oil has played an important role in the booming economic all over the world. The consumption of fossil energy is challenging us due to some global problems. The first problem is the degradation of the environment. The second one is the lack of availability and security of oil. To solve these problems, one has to improve the efficiency of energy consumption and develop alternative fuels simultaneously. Since the safe nuclear energy technology is still in the development, alternative fuels and renewable energy become very important in the present world.

Methane is a principal component of natural gas, coalbed methane, associated gas of oil field and some by-product gases of chemical plants. There is a plentiful resource of methane. The utilization of methane is very important to keep the safe and reliable energy supply in the coming new century. On the other hand, there is a huge reserve of coal all over the world. Especially, the major fossil fuel consumed in China is coal. An intensive investigation has been conducted to develop technologies for the clean use of coal in China. Due to its low H/C, it is still difficult to chemically utilize coal. Since methane owns a higher heat value, with its high H/C ratio, it is very promising to combine the utilization of methane and coal. Especially, it will be very promising if we can produce liquid fuels directly from conversions of coal and methane. However, few work has been conducted in this field.

The industrialized synthetic fuel production from coal or methane claims a multi-step process. First, the syngas ($CO+H_2$) is produced and the liquid fuel is then produced from syngas.

However, there exist some difficulties in such fuel production. First, the process of the production of syngas is an endothermic reaction and requires a high temper-ature for a favoured equilibrium. This is a very energy-intensive process. Second, further reactions of syngas, like F-T synthesis, need high-pressure operation for a reasonable conversion. Therefore, the produced syngas has to be compressed. This also consumes extra energy. For the comercialised set-up of fuel synthesis from syngas, more than 60% of the cost goes to the production and compression of syngas [1]. The high-energy consumption and high investment in set-up limit the application of multi-step conversion. Especially, such multi-step utilization is not suitable for *on site* coal or methane conversion at remote sites by far. It is very necessary to improve such multi-step utilization of coal or methane simultaneously exploits new techniques. Among all the new technologies under developing, the non-thermal plasma conversion is very promising. Since non-thermal plasma is a mixture of electrons, highly excited atoms and molecules, ions, radicals, photons, etc, the chemistry is very complex. A very selective product from this plasma chemistry could become very expensive. This character determines that non-thermal plasma is feasible for the synthesis of liquid fuel that is a mixture of higher hydrocarbons. Here we report a direct liquid fuel synthesis from the combination of conversions of coal and methane using dielectric-barrier discharge (DBD) that has led to a significantly high yield of higher hydrocarbons.

Experimental

The DBD reactor we used in this investigation was similar to that reported previously [2,3]. The gap for the discharge was 1.8 mm and the length of the discharge zone was 250 mm. The pure methane feed was used for this investigation. The flow rates of feed gas were about 20 ml/min and 40 ml/min, respectively. The high voltage electrode was an aluminum foil attached to the inner surface of the quartz tube. And a stainless steel tube around the quartz tube served as the grounded electrode. The width of discharge gap was equal to the distance between the steel tube and the quartz tube. The temperature of all the reactions was adjusted at about 65 °C with circulating oil. All the experiments were operated at atmospheric pressure.

The feed gas (methane) was introduced into the reactors via mass flow controllers. The gaseous products were analyzed using an online gas chromatograph (HP 5890, TCD and FID) with a mass selective detector (HP 5971) equipped with a HP-PLOT Q column (30 m × 0.53 mm). The liquid products were collected in a trap cooled by a mixture of ice and water. The liquid hydrocarbons were analyzed using the same GC with a CBP-1 column (50 m × 0.25 mm).

The loading of coal (anthracite coal; purchased from Beijing Institute of Coal Science,product code: GBW11103b) in the discharge space was the same as the approach described elsewhere [3,4].

Results

The product from such DBD plasma methane conversion in the presence of coal contains gaseous hydrocarbons (mainly ethane and propane with some small amount of ethylene, propylene, butane, iso-butane and benzene) and syn-crude. It is clear that the product includes products from the decomposition of methane, products from the conversion of coal and products of reactions of discharge species with components in the coal. The decomposition of methane leads to the formation of higher hydrocarbons. The conversion of coal principally leads to the formation of aromatics and also higher hydrocarbons (from the hydrogenation of coal). The reactions of discharge species and components of coal lead to the production of hydrocarbons and oxygen-containing and nitrogen-containing hydrocarbons. The formation of nitrogen-containing hydrocarbons will induce extra purification of syn-crude that is a major drawback of the present DBD conversions.

The decomposition of methane was initiated from the formation of methyl radicals in the DBD discharges

$$CH_4 + e \rightarrow CH_3 + H \quad (4)$$

The reactions of propagating the length of carbon chain, which took place in the bulk gases, could be expressed as:

$$CH_3 + CH_3 \rightarrow C_2H_6 \quad (5)$$

$$C_2H_6 + e \rightarrow CH_3 + CH_3 \quad (6)$$

$$C_2H_6 + e \rightarrow C_2H_5 + H \quad (7)$$

$$CH_3 + C_2H_5 \rightarrow C_3H_8 \quad (8)$$

$$C_3H_8 + e \rightarrow C_3H_7 + H \quad (9)$$

$$CH_3 + C_3H_7 \rightarrow C_4H_{10} \quad (10)$$

$$C_2H_5 + C_2H_5 \rightarrow C_4H_{10} \quad (11)$$

…… …… ……

The chain reactions lead to the formation of syn-crude. In the presence of coal, the components in the coal will also involve in the chain growth reactions for the syn-crude production to lead to the production of aromatics and nitrogen-containing hydrocarbons. Figure *1* shows a MS spectrum of syn-crude produced. The peaks at

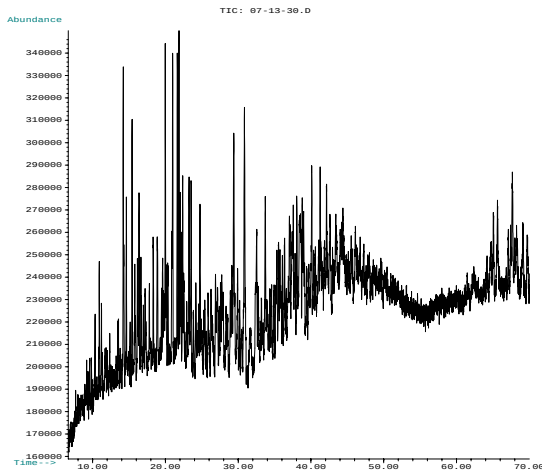

Figure*1*. MS spectra of syn-crude produced from the DBD plasma methane conversion in the presence of coal (*flow rate of feed methane: 20 Nml/min; Input power: 50 W; Conversion of methane: 28.2% (after 15 min); 35.0% (after 70 min)*)

the first 50 minutes in the Figure *1* are principally hydrocarbons. A large amount of branched hydrocarbons have been detected in these hydrocarbons, which means a better fuel production. The peaks present in the range of 60 to 70 minutes are mostly nitrogen-containing hydrocarbons. It is obviously that the nitrogen species in the coal are easily involved in the reactions for the production of higher hydrocarbons. Further investigation is being conducted for the understanding of reactive mechanisms.

Conclusion

The present investigation has confirmed a syn-crude production from the combined conversions of methane and coal. Such produced syn-crude contains a large amount of branched higher hydrocarbons. Some nitrogen-containing hydrocarbons have also been detected that requires a further purification of syn-crude. The syn-crude production from the combined conversions of methane and coal employs three kinds of reactions: (1) decomposition of methane; (2) conversion of coal, including hydrogenation, decomposition of volatiles under the condition of DBD plasmas (3) the reactions of methane plasma species with the components of coal. Compared to methane conversion in the absence of coal, the addition of coal in the discharge gap induces a significantly higher yield (more than 200% higher) of liquid fuel (syn-crude exactly). This means that the addition of coal is favoured for the syn-crude formation under the condition of DBD plasmas. This enhanced yield would be from the hydrogenation of coal (there is a plentiful of hydrogen species in the methane DBD plasmas). Since DBD plasma is a cold plasma phenomenon and can be operated at the ambient conditions, it is very potential to develop such combined conversions of coal and methane.

Acknowledgment

The support from the National Natural Science Foundation (under the contract number 29806011) is very appreciated. This investigation has been conducted using ABB donated instrument and the author is also grateful to ABB Corporate Research Ltd., Switzerland for the donation of instrument.

Reference

1. Pasquon, I. New trends in methane conversion and basic petrochemicals. *Bull. Soc. Chim. Fr.* **131**, 452-462(1994).
2. Liu, C.-J., Xue, B., Eliasson, B., He, F., Li, Y. and Xu, G.-H. Methane conversion to higher hydrocarbons in the presence of carbon dioxide using dielectric-barrier discharge plasmas, Plasma Chemistry & Plasma Processing，V.21, No.3,301-310, 2001
3. Eliasson, B., Liu, C.-J. and Kogelschatz, U. Direct Conversion of Methane and Carbon Dioxide to Higher Hydrocarbons Using Catalytic Dielectric-Barrier Discharges with Zeolites, Ind. Eng. Chem. Res., V.39, No.5, pp.1221-1227, 2000
4. Liu, C.-J., Eliasson, B., Xue, B., Li, Y. and Wang, Y.-Q. Zeolite-Enhanced Plasma Methane Conversion to Higher Hydrocarbons with Dielectric-barrier Discharges, Reaction Kinetics and Catalysis Letters (accepted)

Challenges and Progress in the Conversion of Natural Gas to Fuels and Chemicals

Enrique Iglesia
Department of Chemical Engineering
University of California at Berkeley, Berkeley, CA 94720

Introduction

Its low heteroatom concentration and high hydrogen content make natural gas an ideal fuel in our continuing efforts to minimize the local and global environmental impact of energy use and of chemical syntheses. Gas reserves are more uniformly distributed than oil reserves, making supplies less sensitive to local disruptions or manipulative practices. Many gas reserves are located far from markets; and their use as fuels and petrochemical feedstocks is currently restricted by the limited availability of technology and infrastructure for efficient conversion of methane to liquid fuels, petrochemicals, and even electricity. In remote locations, gas conversion will produce predominately liquid fuels, because economies of scale and required depletion rates will involve the processing of large gas throughputs. With time, methane conversion to liquid fuels will be mostly replaced by direct use of gas as a fuel, as pipelines and local infrastructures and economies develop. The concurrent production of commodity and intermediate chemicals in large gas conversion plants can influence economic incentives by increasing margins and it can lead to earlier profitable implementations of emerging technologies. The synthesis of chemicals will continue even after the gas conversion to fuels window and it will provide the cleanest and most economical routes to many of the chemicals currently produced from oil.

Activation and Conversion of Methane

Natural gas conversion costs depend on gas prices, on thermal efficiencies, on chemical selectivities, and on capital costs. Maximum attainable (theoretical) thermal efficiencies depend only on the stoichiometry of the products formed. They are unaffected by whether direct or indirect routes are used to form a given product slate. Highest theoretical efficiencies are reached when product H/C ratios resemble those in CH_4. Practical (in contrast with theoretical) thermal efficiencies and capital costs depend for the most part on the temperature and pressure changes required throughout the process and on the product yield per pass. Thus, direct processes tend to minimize temperature (and pressure) fluctuations and to decrease second-law efficiency losses and capital costs, which depend strongly on the required amounts of heat exchange. High yields minimize the energy and capital costs of separation, recompression, and recycle.

Methane conversion can proceed via direct or indirect paths. Direct paths require C-H bond activation and the conversion of the CH_x species formed to products within a single vessel. Pyrolysis, oxidative coupling, selective oxidation (to methanol or formaldehyde), partial oxidation (to CO/H_2), and steam reforming are direct (one-step) methane conversion routes. Only a few desired products (CO/H_2, acetylene, ethylene, aromatics, methanol, formaldehyde) can be formed via these direct routes. Invariably, CH_4 reaction products are much more reactive than CH_4 itself and they progress along reaction paths leading to thermodynamically more stable carbon or CO_2 products. High product yields in direct routes require the continuous removal of desired products from the reaction zone or the thermodynamic or kinetic protection of these products against further reactions. In general, maximum attainable yields depend on the thermodynamic tendency of a given products to oxidize to CO_2 or to dehydrogenate to solid carbon. Weaker C-H bonds in products tend to favor their activation at low reaction temperatures in the absence of thermodynamic or kinetic protection. Although at first glance counterintuitive, low temperatures actually disfavor the desired products, because their subsequent reactions have much lower activation energies that the primary CH_4 activation reactions that form these desired initial products.

Many direct paths become indirect when desired products are made via the initial formation of chemically-protected intermediates, which are subsequently converted to the desired products. The first step forms a protected form of methane, which resists further conversion to CO_2 or carbon, and the second step "de-protects" this intermediate and forms the desired products in higher yields than via the corresponding direct routes. For example, synthesis gas (H_2/CO) is in effect a protected form of activated methane and it can be used to form a broad range of hydrocarbons and oxygenates useful as fuels and chemicals. High temperature reactions of CH_4 with H_2O, CO_2 and even O_2 do not form large amounts of CO_2 because of thermodynamic constraints imposed by the high reaction temperature and the stoichiometry of the reactants used. Kinetic protection can be achieved using methyl bisulfate or methyl chloride intermediates, both of which can be used to form methanol or hydrocarbons in subsequent steps. Synthesis gas routes require two steps, including a thermally efficient but costly synthesis gas generation process, but the oxidants, however, are O_2 or H_2O, which are readily available and require only their extraction from the environment in purified form. The bisulfate and chloride routes use expensive and toxic reagents (H_2SO_4, Cl_2, or HCl), which require careful handling. They also involve costly chemical regeneration in an additional third step. To some extent, these considerations have lead to the accepted use of synthesis gas routes in currently envisioned gas conversion technologies.

Intermediates can also be protected using physical rather than chemical means. Physical protection schemes require a device that extracts desired products continuously or which can separate CH_4 and O_2 within a chemical reactor. This separation can occur spatially or temporally. High ethylene and benzene yields can be obtained by rapid quenching of pyrolysis products; two-step cyclic processes involving methane decomposition to CH_x species on metals and hydrogenation of these fragments lead to larger alkanes. Endothermic CH_4 dimerization and pyrolysis reactions can be carried out at low temperatures by continuously removing hydrogen using absorption onto solids, transport through membranes, or reactions with lattice oxygen. High ethylene yields can be achieved by its continuous removal from a stream, using external absorbers in recycle or moving bed reactors and by the use of lattice oxygen in cyclic reactors for oxidative coupling. In all cases, the approaches are technically sound and practically feasible from engineering considerations, but they increase the complexity and cost of the reactors because of the multi-functional or transient nature of their operation. As a result, they do not really deliver the intended simplicity and low capital costs of direct methane conversion processes.

Direct and Indirect Methanol and Formaldehyde Synthesis

One-step homogeneous oxidation of methane at high pressures and temperatures has led to the synthesis of methanol with yields of ~4%. The rapid subsequent combustion reactions of methanol to form CO_2 limit conversions in practice, while the explosive nature of the required reactant mixtures creates engineering challenges in the design of mixing schemes and pressure vessels. Solid catalysts have not led to yield improvements, because surface sites activate C-H bonds in both methane and methanol. Staged O_2 introduction using multiple injectors or dense oxygen conducting

membranes are also unlikely to increase yields, because the rates of activation of C-H bonds in CH_3OH and CH_4 appear to depend similarly on O_2 concentrations. Continuous extraction of methanol can prevent combustion, but requires its selective absorption, adsorption, or permeation above ambient temperatures, none of which are currently possible, as well as a low conversion per pass. The introduction of sites for methanol conversion to hydrocarbons into homogeneous methane to methanol oxidation reactors may provide a less costly product separation scheme, as well as the protection of activated CH_4 (as methanol) as aromatic molecules that are considerably less reactive than methanol.

The direct conversion of methane to formaldehyde using O_2 has also been widely studied on heterogeneous catalysts and formaldehyde yields have been typically even lower that those reported for the direct methane conversion to methanol. Two recent studies have reported higher formaldehyde yields; one study uses NO/O_2 mixtures as the oxidant and homogeneous pathways and the other O_2 as the oxidant and supported silicomolybdic acids as heterogeneous catalysts.

Biological routes that convert methane selectively to methanol are often mentioned as the ultimate replacement for these other routes. Progress in this area will require enzymes or microorganisms that function selectively and efficiently in concentrated aqueous methanol solutions and the replacement of the co-reagents currently needed for effective energy transfer in these biochemical reactions.

Commercial methanol synthesis processes use indirect routes based on synthesis gas intermediates. These processes lead to much higher methanol yields (25-30% yield per pass) and >99% CH_3OH selectivity. Synthesis gas generation requires high temperatures and large capital investments but recent process improvements that combine partial oxidation and steam reforming in a nearly thermoneutral process have led to practical thermal efficiencies (71-72%) for the overall methanol synthesis process very close to theoretical thermal efficiency values (84.2%). Recent development in the use of adiabatic monolith reactors for partial methane oxidation to synthesis gas have provided a novel and useful approach, especially for small-scale methanol synthesis applications that cannot exploit the beneficial economies of scale of steam reforming and autothermal reforming processes. The chemical and structural integrity of noble metal catalytic coatings in these monolith reactors and the mixing and handling of explosive CH_4/O_2 mixtures remain challenging issues in the design of the short contact time reactors for the production of synthesis gas. Recent advances in the design of ceramic membranes for oxygen and hydrogen transport may become useful in decreasing or eliminating air purification costs and in driving endothermic steam reforming reactions to higher conversions or lower operating temperatures. Such ceramic membranes have advanced beyond their status as a laboratory curiosity and into developmental consortia, but their reliable practical implementation will require additional advances in the synthesis and stabilization of thin metal oxide films within novel reactor geometries as well as the development of faster proton conductors for the case of hydrogen separation schemes.

Methanol can also be formed via other indirect routes, such as via processes involving the formation of methyl bisulfate on Hg complexes followed by its conversion to methanol via hydrolysis, and by the regeneration of the sulfuric acid oxidant by SO_2 oxidation. Methyl bisulfate yields can reach 70-80%, because of the low reactivity of methyl bisulfate relative to methanol and even methane. Turnover rates are very low in the temperature tolerated by these homogeneous catalysts and Hg organometallic complexes and sulfuric acid are very toxic and difficult to handle and to regenerate. More recent studies have increased the stability of these catalysts by introducing more stable ligands and eliminated Hg-based materials with Pt-based homogeneous catalysts. This approach involves a new type of protected intermediate (methyl bisulfate) and leads to higher methanol yields than in commercial routes based on synthesis gas. It is, however, neither a direct route to methanol nor a process with low capital investment. It involves three steps, including a very costly oxidant regeneration step and a deprotection step limited by thermodynamics.

Oxychlorination provides another indirect route to methanol and to hydrocarbons via acid-catalyzed hydration or oligomerization of methyl chloride. It involves the use and the costly regeneration of Cl_2 and it requires corrosion-resistant vessels and significant temperature cycling of process streams. CH_3Cl yields of 25-30% have been achieved with yield losses predominately to CO_2 and CH_2Cl_2. An additional chemical hurdle in these process is the low selectivity to monochlorinated products. Higher yields will require more selective monochlorination and lower combustion rates of these desired intermediates. These improvements appear unlikely because of the kinetic instability of CH_3Cl relative to CH_4 and of the thermodynamic stability of the sequential CO_2 and CH_2Cl_2 products.

Synthesis of Hydrocarbons via Pyrolysis Reactions

The pyrolysis of methane to form alkynes, alkenes, and arenes is highly endothermic and requires very high temperatures and concurrent combustion of methane as a fuel in order to provide the enthalpy of reaction in a heat exchange furnace. At these high temperatures, homogeneous pathways lead to acetylene, polynuclear aromatics and soot as the preferred products for both kinetics and thermodynamic reasons. Thermal efficiencies are low because of the extreme temperature cycling required of process streams and because of the rapid quenching protocols used to restrict chain growth and soot formation. The low pressures required by thermodynamics and the slow homogeneous reactions lead to large reactor vessels, which must be protected against carbon deposition and metal dusting corrosion by using coatings or specialized materials of construction.

Recently, several approaches have addressed these limitations and they have led to significant control of methane pyrolysis selectivity. One approach involves the synthesis of benzene and ethylene with 30-40% yields per pass using homogeneous pyrolysis reactors and the rapid thermal quenching of reaction products. Another improvement uses shape-selective catalysts based on MoC_x and WC_x species held within shape-selective channels in pentasil zeolites (H-ZSM5), where chain growth to form polynuclear aromatics is spatially restricted and the presence of CH_4 activation sites on the surface of carbide clusters leads to CH_4 pyrolysis reactions at much lower temperatures (700 ^{0}C) than for homogeneous pathways. The addition of small amounts of CO_2 during CH_4 pyrolysis on these catalysts and the selective deactivation of acid sites on external zeolite surfaces have led to marked improvements in catalyst stability and to lower selectivity to hydrocarbons larger than naphthalene. The combination of such catalysts with hydrogen removal by ceramic membranes remains a promising but challenging approach to the direct conversion of methane to larger hydrocarbons.

A two-step cyclic process involving the deposition of CH_x fragments from methane on metal surfaces at 200-300 ^{o}C and the coupling of such fragments during a subsequent hydrogenation cycle has led to very low yields of C_2+ hydrocarbons. Yields are unavoidably constrained by the unfavorable thermodynamics of this overall process at low temperatures and by the selectivity losses to surface carbon, which also cause rapid deactivation and loss of methane reactants. A more promising and thermodynamically feasible cyclic strategy involves the formation of relatively pure H_2 streams using CH_4-H_2O cyclic processes on solids that can generate reactive

carbon and H_2 during the CH_4 cycle and remove the carbon as CO while producing additional H_2 during subsequent contact with steam.

Oxidative Coupling of Methane

Oxidative coupling combines at the molecular level methane dimerization via radical-like pathways with the removal of the hydrogen formed, often before recombinative desorption to form H_2, via oxidation steps. Ethane and ethylene are the predominant hydrocarbons formed. Heterogeneous catalysts improve the yields and selectivity attainable in homogeneous coupling reactions, but the active surface sites in these materials also activate C-H bonds in ethane and ethylene, leading to secondary combustion reactions, which limit attainable yields to 20-25% and lead to significant formation of CO_2. These secondary pathways are very exothermic and they place significant heat transfer loads on the catalytic reactors. The use of cyclic strategies using lattice oxygen and moving or fluid bed reactors provides an attractive alternate option, which avoids unselective homogeneous combustion pathways and uses the heat capacity of the solids to increase the efficiency to heat removal during reaction. Protecting strategies in oxidative coupling can lead to two-step processes similar to those for methanol synthesis. In principle, synthesis gas, methyl bisulfate, or methyl chloride intermediates can be used to form ethylene, but ethylene formation from these protected intermediates is not very selective and the overall processes is not environmentally benign.

Other protecting strategies have been attempted, or at least proposed, in order to increase C_2 yields in oxidative methane coupling. The separation of ethylene from the reactor effluent using cation-exchange zeolites has been carried out and it has led to slight C_2 yield improvements. The low adsorption temperatures required and the lack of adsorption selectivity for ethane, however, limit the practical applications of these approaches. The in situ conversion of ethane and ethylene to aromatics using cation-exchange zeolites after oxidative coupling can lead to the simpler separation of aromatics from the product stream, but in a process for the synthesis of aromatics instead of ethylene. Finally, yields improvements can result from the separation of methane and oxygen reactants in space (via membranes) or in time (via cyclic reactors). The first approach exploits any differences in kinetic oxygen response between the coupling and the product combustion reactions. O_2 is introduced along the reactor via multiple injectors or oxygen-conducting membrane walls. Low O_2 concentrations can also be achieved using backmixed fluidized beds operated at high oxygen conversion levels. The staging of the oxidant along a tubular reactor has not led to significant improvements, apparently as a result of the similar kinetic dependences of CH_4 and C_2 activation steps on O_2 concentration. Detailed kinetic simulations have shown that distributed oxygen introduction is unlikely to give C_2 yields above 35-40%. Laboratory tests have shown that poor radial dispersion of the oxygen feed can lead to high local O_2 concentrations, which can cause stable flames and structural damage at membrane walls.

Detailed kinetic and process simulations have suggested that continuous ethylene removal from a recycle stream can lead to 75-85% C_2 yields during oxidative coupling of methane. When the removal of ethylene requires temperatures significantly lower than for oxidative coupling, the required recycle ratios become impractical, because extensive thermal cycling leads to second-law inefficiencies and to large capital and operating costs associated with heat exchange and recompression. These constraints can be overcome by designing absorbers or membranes that remove ethylene selectively from dilute streams containing ethane, CH_4, CO_2, H_2O, and O_2 at typical oxidative coupling temperatures. A reaction-separation protocol using simulated chromatographic reactors has led to 65-70% ethylene yields. The practical use of these reactors as moving beds, however, requires porous solids that separate C_2 from methane and oxygen at elevated temperatures using adsorption, capillary condensation, or diffusion differences among these components. Cation-exchanged zeolites and microporous carbons are promising as materials for the separation of ethylene from such mixtures, but optimum operating temperatures remain well below those required for oxidative coupling.

Oxidative coupling of methane can be carried out without contact between hydrocarbons and O_2 using cyclic reactors or hydrogen-conducting membranes. High C_2 yields (25-28%) can be achieved by cycling reducible oxides between a methane activation reactor and a solids re-oxidation vessel. This cyclic process can maintain constant temperatures during solids recycle and uses air (instead of pure O_2) as the oxidant, but the process requires complex handling of solids in fluidized beds. Such redox cycles can be carried out within a single vessel by internally segregating a fluid bed into a reaction zone and an oxidative regeneration zone. The appropriate desing oxygen donor solids can be used to the amount of and rate of reaction of the available lattice oxygen. These cyclic oxidative coupling scheme remain of fundamental and practical interest in the activation and conversion of methane via oxidative routes.

Another type of cyclic reactor uses hydrogen absorption into a solid during methane pyrolysis and the removal of the absorbed hydrogen as water in subsequent oxidation cycles. This approach has been recently reported for dehydrogenation reactions of higher alkanes. In such cyclic schemes, pyrolysis and oxidation are separated temporally. In the mathematically analogous catalytic membrane process, reactants are separated spatially using a diffusion barrier that permits only hydrogen transport. Experimental tests using thick membrane disks of hydrogen-conducting perovskites led to very low methane conversion rates and C_2 yields. Significant improvements are possible by combining cation-exchanged zeolites for selective methane pyrolysis at low temperatures with much thinner oxide films, the successful synthesis of which has been recently reported. Hydrogen transport rates at the H_2 pressures prevalent during methane pyrolysis, however, must be improved significantly before practical applications of such schemes can be seriously considered.

Synthesis Gas Conversion Routes to Fuels and Chemicals

Synthesis gas conversion processes are significantly more advanced in development than direct or other two-step methane conversion schemes. Indirect gas conversion processes are currently practiced for methanol synthesis and for hydrocarbon formation via the Fischer-Tropsch synthesis. Diesel-range hydrocarbons (via FT synthesis) and gasoline (via MTG processes) can be produced thermal efficiencies as high as ~80% of their respective theoretical values (78% and 75%). These indirect processes have continued to evolve as continuous improvements have come about from advances in synthesis gas generation, from the design and deployment of three-phase bubble columns for synthesis gas conversion, and from the development of improved catalytic materials for the selective synthesis of paraffins, intermediate size α-olefins, and higher alcohols. Small modular gas conversion plants using catalytic partial oxidation in monolith reactors and CO hydrogenation in bubble columns may also create future opportunities for combining H_2 and power generation with the "small-scale" synthesis of commodity petrochemicals and even of liquid fuels.

Selective pathways for ethylene and propylene from synthesis gas remain unavailable, because Flory-type chain growth kinetics lead to broad carbon number distributions. The most promising approach uses acid-catalyzed chain growth reactions of methanol within shape-selective channels in pentasil zeolites and silicoaluminophosphate microporous materials in a three-step process

requiring synthesis gas generation, methanol synthesis, and methanol to olefins (MTO) or gasoline (MTG) conversion. The latter must be carried out in fluid bed or moving bed reactors because of the need for frequent regeneration. Currently available technologies use silicoaluminophosphate materials or modified pentasil zeolites in order to provide optimum shape-selective environments for the synthesis of light olefins. Intermediate range α-olefins (C_5-C_{15}) can be produced with modest selectivity from CO and H_2 on promoted Fe-based catalysts. Maximum yields are limited by Flory-type chain growth kinetics, but the valuable mid-range paraffins and the smaller olefins formed as by-products are much more valuable than the paraffins formed and useful only as fuels.

Higher alcohol synthesis is also restricted to broad product distributions governed by stochastic chain growth kinetics. Recently, bifunctional catalysts consisting of metal sites for hydrogenation reactions and basic sites for alcohol coupling steps have led to high selectivity to branched alcohols. Chain growth appears to be restricted to C_4 and C_5 alcohols by the chemical constraints of base-catalyzed aldol condensation reactions. High 2-methyl-1-butanol yields (200-300 g/kg-cat-h) have been recently reported on Pd-based bifunctional catalysts, but at very high pressures (>200 bar) and temperatures (400-450 ^{o}C). Dimethylether isomerization and aldol condensation of olefins with methanol using acid-base bifunctional catalysts provide alternate but unexplored pathways to overcome the C_1 to C_2 conversion bottleneck during CO hydrogenation to form higher alcohols.

SUPPORTED BINARY CATALYSTS FOR DEHYDROGENATION OF METHANE

Naresh Shah[1], Frank E. Huggins[1], Devadas Panjala[1], Gerald P. Huffman[1], A. Punnoose[2], M.S. Seehra[2]

[1]University of Kentucky, Lexington, KY 40508-4005
[2]West Virginia University, Morgantown, WV 26506-6315

Introduction

Production of pure hydrogen from hydrocarbons, particularly methane, the major component of natural gas, has great practical importance. Traditionally, reforming and partial oxidation of methane are employed to produce synthesis gas, which, when followed by water-gas shift conversion of the CO in synthesis gas to CO_2 and the consequent removal of CO_2, produces a relatively pure hydrogen stream. However, this hydrogen stream still contains enough CO to poison the catalysts used in PEM electrochemical fuel cells. A reverse methanation reaction has to be carried out to reduce the CO concentration to sub-ppm levels.

Catalytic decomposition of undiluted methane to pure hydrogen and carbon was carried out in absence of any oxidizing medium with a variety of alumina supported binary metal catalysts. Nanoscale, binary, 0.5%M-4.5%Fe (M = Pd, Mo or Ni) catalysts supported on alumina reduced the decomposition temperature of undiluted methane by 400-500 °C relative to non-catalytic thermal decomposition. The product stream comprised of over 75-volume % of hydrogen and unconverted methane at reaction temperatures of 700 °C. The efficient removal of carbon from the catalyst surface in the form of nanotubes is believed to be the key factor influencing catalyst performance.[1]

Figure 1 is a plot of hydrogen production by catalytic decomposition of methane at various reactor temperatures using pure Fe, pure Mo and binary Mo-Fe catalysts. The role that binary metals play in methane decomposition is clearly evident. Similar plots of hydrogen production by methane decomposition using other binary metal catalysts (Ni-Fe and Pd-Fe) show significantly higher activity than either Fe or the other secondary metal (Ni, Pd) alone.[1]

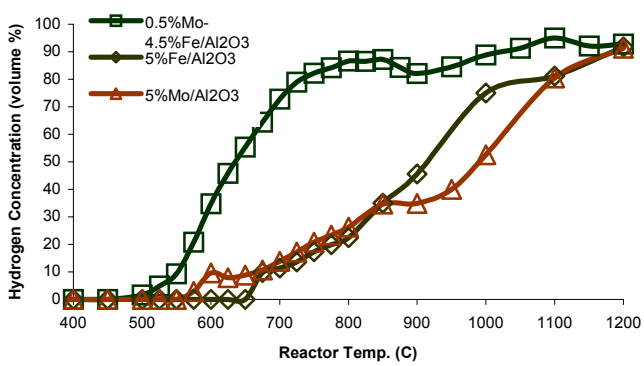

Figure 1. Comparison of alumina supported pure molybdenum and pure iron catalysts with binary Fe-Mo catalysts pre-reduced at 700 °C for hydrogen production.

This paper primarily deals with characterization of these highly active nanoscale binary alumina supported catalysts using a variety of analytical techniques, viz. x-ray absorption fine structure (XAFS) spectroscopy, x-ray diffraction (XRD), Mössbauer spectroscopy, and scanning (SEM) and transmission (TEM) electron microscopy. The synthesis and pre-treatment of the catalysts, as well as SEM/TEM characterization of the produced nanotubes, have been reported elsewhere[1].

As-prepared catalysts

Mössbauer and Fe K-edge XAFS spectroscopies confirmed that the iron in vacuum-dried, alumina-supported catalysts exists in the ferrihydrite structure.[2] The radial structure functions of the Pd and Ni EXAFS indicate the presence of only one nearest neighbor oxygen shell implying either very small particles of oxide on alumina or incorporation in ferrihydrite. XAFS analysis indicates that Mo exists in the +6 oxidation state, probably as MoO_4^{-2}.

Pre-reduced catalysts

The as-prepared or pre-oxidized catalysts were not active for methane decomposition[1]. The catalysts were activated by reduction at 700 °C for two hours and cooling in flowing hydrogen. However, Mössbauer and Fe EXAFS spectroscopic data showed that for all the catalysts, the reduction of Fe to the metallic state is not complete at 700 °C probably because iron reacted with the alumina support to form hercynite. Pre-reduction at 1000 °C is required to complete the reduction of all the Fe to metal. XRD studies of catalysts reduced at 700 °C only yielded lines due to the γ-alumina support, except for Pd-Fe, in which lines due to metallic Fe were also observed (figure 2). Both Pd XANES and Fe Mössbauer data showed that at 700 °C, Pd is easily reduced to metallic state and its presence appears to facilitate the reduction of Fe. Both Ni and Mo are partially reduced to the metallic state. Mössbauer spectroscopy showed the presence of a Fe_2Mo phase in Mo-Fe/Al_2O_3 catalysts and the enhanced formation of a NiFe austenitic phase in reduced Ni-Fe/Al_2O_3 catalysts. STEM investigation of the reduced catalyst further confirms the formation of alloy phase. Figure 3 shows a dark field STEM image and Al, Fe and Mo K-edge EDS maps of a pre-reduced Mo-Fe catalyst. Overlap of Mo and Fe images confirm formation of nanoscale Mo-Fe metallic alloy particles.

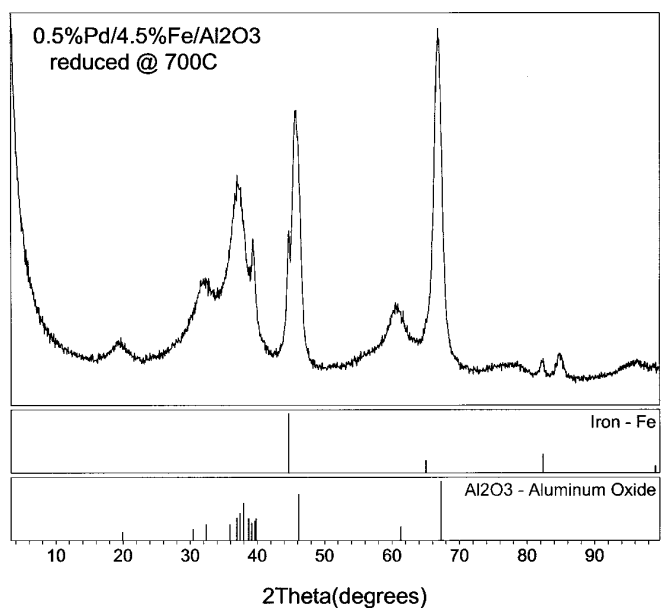

Figure 2. XRD spectra of 0.5%Pd/4.5%Fe/Al_2O_3 catalyst after reduction at 700C showing formation of metallic Fe phase.

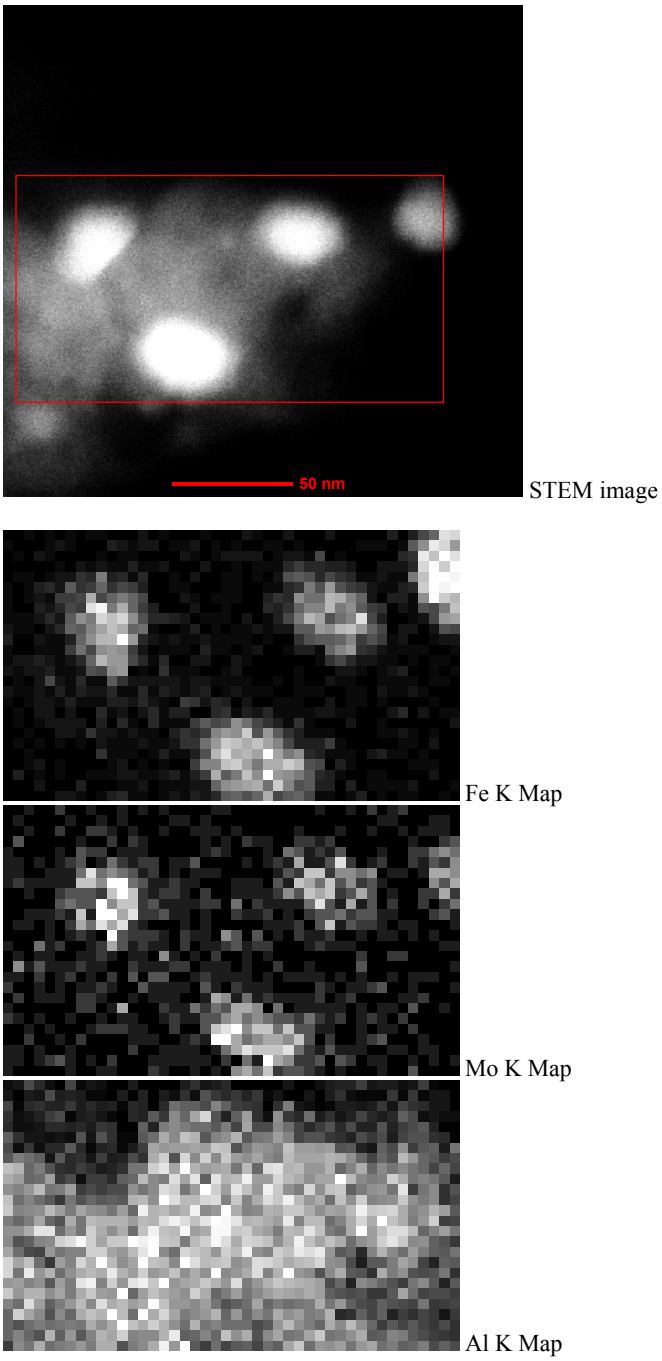

Figure 3. Dark field STEM image with Fe, Mo and Al K-edge EDS maps of the area mark in the STEM image of a Fe-Mo catalysts pre-reduced at 700 °C showing formation of nano-size binary metallic particles on alumina support.

Catalysts after on-stream exposure

Exposure of the pre-reduced catalysts to flowing methane at 700 °C did not result in any significant changes in the XAFS spectra. Although methane is a carburizing atmosphere and the catalysts are very active in decomposing methane to produce large amounts of elemental carbon in form of nanotubes, the catalysts retain their metallic states. As shown in figure 4, XRD studies indicate that γ-alumina undergoes a phase transformation to δ-alumina when the pre-reduction step is carried out at a higher temperature (1000 °C instead of 700 °C). Besides lines due to alumina, XRD studies showed lines due to graphite and Fe_3C in all samples after on-stream exposure. Mössbauer spectroscopy indicated formation of austenite phase possibly due to incorporation of carbon in iron and/or stabilization by the secondary metal. A small amount (0-20%) of iron was also found in metallic state. Substantial amounts of iron were still in unreduced Fe^{2+} state probably as hercynite ($FeAl_2O_4$) spinel due to reaction of the iron with the support.

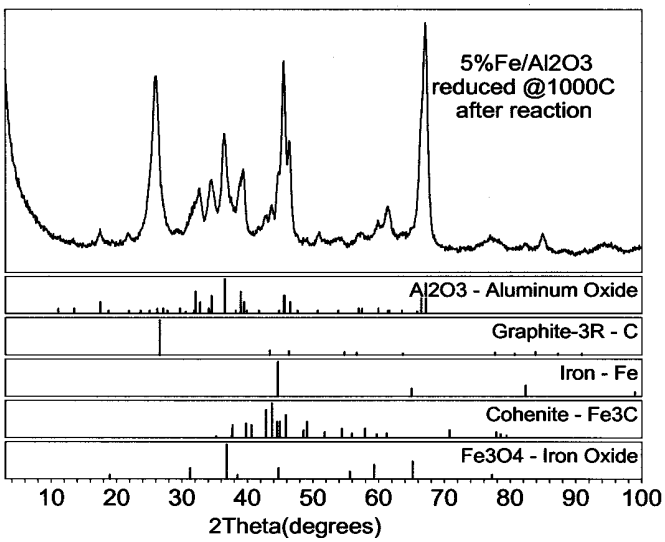

Figure 4. XRD spectra of 5%Fe/Al_2O_3 catalyst (reduced at 1000C) shows phase transformation of alumina support. Lines due to deposited graphitic carbon (in form of nanotubes) are also clearly evident. PDF files of different possible phases are also shown for comparison

Acknowledgement. This research was supported by the U.S. Department of Energy through both the Division of Fossil Energy (FE) under the National Energy Technology Laboratory (NETL) and the Division of Energy Efficiency and Renewable Energy (EE) under the Office of Advanced Automotive Technologies, under contract No. DE-FC26-99FT40540.

References

(1) Shah, N.; Panjala, D.; Huffman G. P. *Energy & Fuels,* **2001**, *15(6),* To be published.
(2) Shah, N.; Zhao, J.; Huggins, F. E.; Huffman, G. P. *Energy & Fuels*, **1996,** *10(2),* 417-420.

CHARACTERIZATION AND APPLICATION OF Cr_2O_3-ZnO CATALYSTS FOR METHANOL SYNTHESIS

Michael C.J. Bradford, Mahesh V. Konduru, and Digna X. Fuentes

CeraMem Corporation
12 Clematis Avenue
Waltham, MA 02453

Introduction

The synthesis of methanol from mixtures of hydrogen and carbon oxides using mixed metals and metal oxides has been under investigation since at least 1914.[1] Both zinc oxide and chromium oxide, with or without promotion by alkali metal hydroxides, are described as preferred materials for oxygenate synthesis in this BASF patent. In addition, two later patents from BASF issued in 1925 [2] and 1926 [3] focused on the use of CuO/ZnO and Cr_2O_3/ZnO catalysts. By 1932, the industrial production of methanol was primarily undertaken through the use of these two catalyst types.[4] During this time, a series of papers was published by Frolich and coworkers that focused on methanol synthesis over CuO/ZnO/Al_2O_3,[5] CuO/ZnO,[6-8] and Cr_2O_3/ZnO[9] catalysts. Additional investigations of methanol synthesis over Cr_2O_3/ZnO catalysts were undertaken contemporaneously by Brown and Galloway.[10-11] However, CuO/ZnO/Al_2O_3 is currently (and has been since *ca.* 1960) the preferred industrial catalyst for methanol synthesis,[12-15] and academic research efforts on CuO/ZnO[16-18] and CuO/ZnO/Al_2O_3 [19-20] catalysts for methanol synthesis have continued essentially unabated.

Nevertheless, the use of alkali-promoted, Cr_2O_3/ZnO-based catalysts for higher alcohol synthesis (which can be inferred from the early BASF patent)[1] has been explicitly under investigation since at least 1928.[21-33] Mixed Cr_2O_3-ZnO/H-ZSM-5 catalysts have also been studied for the direct conversion of synthesis gas to C_2+ hydrocarbons and aromatics.[34-41] The mechanism of higher alcohol synthesis is reported to occur through the interaction of intermediate surface species (formate and methoxy) that also have the potential (via hydrogenation) to form methanol.[29,33] In addition, the mechanism for C_2+ hydrocarbon and aromatic formation over physical mixtures of Cr_2O_3-ZnO and H-ZSM-5 catalysts presumably involves the generation of intermediate alcohol species on the Cr_2O_3-ZnO function that migrate and react at Brönsted acid sites on the zeolite via the established methanol-to-olefin and methanol-to-gasoline mechanisms.[34-41] A common feature of both the higher alcohol and aromatic synthesis catalytic systems is the necessity for surface formate and methoxy species formation on the Cr_2O_3-ZnO catalyst function. Therefore, understanding the role of the Cr_2O_3-ZnO catalyst function on the kinetics of methanol formation is of fundamental importance to both higher alcohol and aromatics syntheses from synthesis gas..

Cryder and Frolich, in an early report on methanol synthesis over Cr_2O_3/ZnO catalysts, postulated that the apparent synergy observed between chromium oxide and zinc oxide when co-precipitated, in comparison to the pure component oxides, was mainly due to an increase in the catalyst surface area per unit mass;[9] however, they also explicitly lamented that in 1929 no satisfactory means of estimating the catalyst surface areas was available in order to report methanol synthesis rates on an areal basis. The subsequent development of a suitable and reproducible technique for the measurement of catalyst surface areas by Brunauer, Emmett and Teller,[42] now referred to commonly as the BET method, has since enabled researchers to measure catalyst surface areas, and thus to report kinetic data on an areal basis. Despite this fact that the BET method is widely available and relatively inexpensive, and areal rates are ultimately more suitable toward the elucidation of catalyst properties,[43] much experimental work in the areas of methanol, higher alcohol, and aromatics syntheses continues to be reported on either conversion or specific activity (per mass of catalyst) bases.

In the investigation reported herein, several Cr_2O_3-ZnO catalysts prepared via co-precipitation with either K_2CO_3 or $(NH_4)_2CO_3$ were characterized by X-ray diffraction, N_2-BET and activity for methanol synthesis at 593 K. Through the use of BET and areal rates it is demonstrated that the catalyst specific activities can be described well by a simple linear combination of areal rate data for the pure component oxides, indicating that no synergy is likely present between chromia and zinc oxide in these catalysts.

Experimental

Catalyst Preparation. Several K-Cr_2O_3/ZnO catalysts were prepared via co-precipitation using a procedure adapted from that reported by Ereña et al..[39] After defining the desired catalyst composition, a 0.14 M cation solution was prepared via addition of appropriate quantities of $Cr(NO_3)_3 \cdot 9H_2O$ (Acros, 99.98% Purity) and $Zn(NO_3)_2 \cdot 3H_2O$ (Acros, 99+% Purity) to distilled H_2O. In addition, a 0.5 M solution of K_2CO_3 was prepared as a precipitating agent. The cation (Cr^{3+} / Zn^{2+}) and anion (CO_3^{2-}) solutions were simultaneously added dropwise to a stirred beaker of distilled H_2O maintained at 7.0 $\leq$ pH $\leq$ 7.5 and 338±5 K. Analogous Cr_2O_3/ZnO catalysts with substantially lower potassium contents were prepared using a 0.5 M solution of $(NH_4)_2CO_3$. Co-precipitated materials were filtered, washed repeatedly with distilled water, dried in static air at 383 K, and subsequently calcined at 473 K for 2 h using 10% oxygen in argon at a Gas Hourly Space Velocity (GHSV) of 600 $cm^3/h \cdot g_{cat}$. Additional samples were prepared via subsequent calcination in 10% oxygen for 2 h at temperatures between 373 and 973 K.

Catalyst Characterization. All catalysts were characterized using direct current plasma emission spectroscopy (DCPES) to quantify the composition of elemental chromium, zinc, and potassium. N_2 BET analysis was used to determine the surface areas of the calcined samples after evacuation for 3-5 h at 473-573 K. In addition, powder X-ray diffraction (XRD) spectra were obtained using filtered CuK_α radiation (Materials Characterization Laboratory at the Pennsylvania State University). Volume-weighted crystallite sizes (d_v) were estimated from XRD spectra using the Scherrer equation, $d_v = 0.9\ \lambda\ /\ B\ \cos\ \theta$, with Warren's correction for instrumental line broadening, $B = (B_M^2 - B_I^2)^{1/2}$, where λ = 1.54158 Å for weighted CuK_α radiation, B_M is the peak width at one-half maximum intensity, and B_I is the instrumental line broadening.

Selected catalyst samples were also characterized after reaction via temperature programmed oxidation (TPO). After reaction, catalysts were cooled to room temperature in flowing nitrogen, removed from the reactor, and subsequently transferred to a quartz tube packed with quartz wool. The quartz tube was placed in a horizontal tube furnace equipped with a carbon dioxide sensor (Vaisala) at the effluent. Catalyst TPO was thereafter performed using 10% oxygen in argon (GHSV = 100 $cm^3/h \cdot g_{cat}$) at *ca.* 4 K/min from 293 to 973 K to quantify total carbon deposition (as either carbonaceous deposits or adsorbed CO_x).

Apparatus for Methanol Synthesis. High purity N_2 (99.999%), H_2 (99.999%), and CO (99.3%) were used as-received without further purification and introduced independently using mass flow controllers (Porter) to a copper-lined, tubular reactor made of Inconel 600. The reactor was placed within a vertical split-tube furnace (Lindberg) equipped with a thermocouple for external reactor temperature control and a thermocouple inserted into the catalyst bed to monitor catalyst temperature. The temperature of the reactor effluent line was typically maintained at 240°C, and an electronic

back-pressure regulator (Tescom) was used to control reactor pressure up to 34 atm. The back-pressure regulator effluent was directly fed at 1 atm to the sampling valve of an on-line gas chromatograph (SRI Model 8610C), in which 0.2 cm^3 samples were subjected to simultaneous analysis with flame ionization (FID) and thermal conductivity (TCD) detectors. The FID was used for methanol, methane, and byproduct analyses, and the TCD was used for nitrogen, hydrogen, carbon monoxide, and methanol analyses. Carbon dioxide formation was not observed during the experiments reported herein. The absolute rate of methanol formation was determined with the TCD via reference to nitrogen, by-product formation rates were quantified via reference to methanol, and carbon monoxide conversion was quantified from an overall carbon balance assuming a negligible rate of carbon accumulation on the catalyst. TCD and FID response values obtained during in-house calibration were used in conjunction with those available in the literature.[44]

Procedures for Methanol Synthesis. Typically, *ca.* 1 gram of ground and sieved catalyst [0.125 ≤ particle diameter (mm) ≤ 0.25] was packed into the reactor between plugs of quartz wool, and thereafter purged for 15 min at 293 K in flowing nitrogen (1350 $cm^3/h \cdot g_{cat}$). The catalyst was then subject to a pretreatment procedure involving reduction for 2 h in flowing hydrogen (H_2/N_2 = 2/1; GHSV = 4050 $cm^3/h \cdot g_{cat}$) at 673 K. After completion of pretreatment, the reactor temperature was reduced to 393 K, and the catalyst was exposed to a mixture of hydrogen and carbon monoxide in nitrogen ($N_2/H_2/CO$ = 1/2/1, GHSV ≈ 5000 $cm^3/h \cdot g_{cat}$). After exposure to this gas composition for 15 min, the reactor pressure was raised at a rate of 0.34 atm/min from 1 to 34 atm, and then the reactor temperature was raised at a rate of 2.5 K/min to 593 K. Catalyst activity and selectivity at 593 K remained fairly constant during the initial 15 h on stream; therefore, time-weighted average of these data are reported herein.

Results and Discussion

Characterization of Prepared Catalysts. Catalyst chromium and zinc compositions determined via DCPES were in relatively good agreement with nominal composition values for the samples prepared with either ammonium or potassium carbonate. The potassium concentrations in the samples precipitated with ammonium carbonate are roughly three orders of magnitude lower than for those samples precipitated with potassium carbonate; however, the values are non-zero. Presumably, the trace potassium content in these ammonium-precipitated catalysts is a consequence of contamination from use of the same laboratory glassware for preparation of all samples.

Powder XRD spectra of the Cr_2O_3/ZnO catalysts after calcination for 2 h in flowing 10%O_2 at 973 K are shown in Figure 1. The bulk phase for the nominal Cr/Zn = 0 sample corresponds as expected to ZnO (JCPDS # 05-0664). Increase in catalyst Cr/Zn ratio from 0 to 1.86 resulted in a decrease in bulk ZnO and concomitant increase in bulk $ZnCr_2O_4$ (JCPDS #22-1107). Further increases in catalyst chromium content resulted in the appearance of Cr_2O_3 (JCPDS #6-0504) and a concomitant decrease in $ZnCr_2O_4$ content. Powder XRD spectra of the K-Cr_2O_3/ZnO catalysts after calcination for 2 h in flowing 10%O_2 at 973 K are similar (not shown), except that diffraction peaks due to the presence of K_2O (JCPDS 23-493) and $K_2Cr_2O_7$ (JCPDS 27-380) are also present.

Volume-weighted crystallite sizes for the catalysts were calculated through application of the Scherrer Equation to the (101)

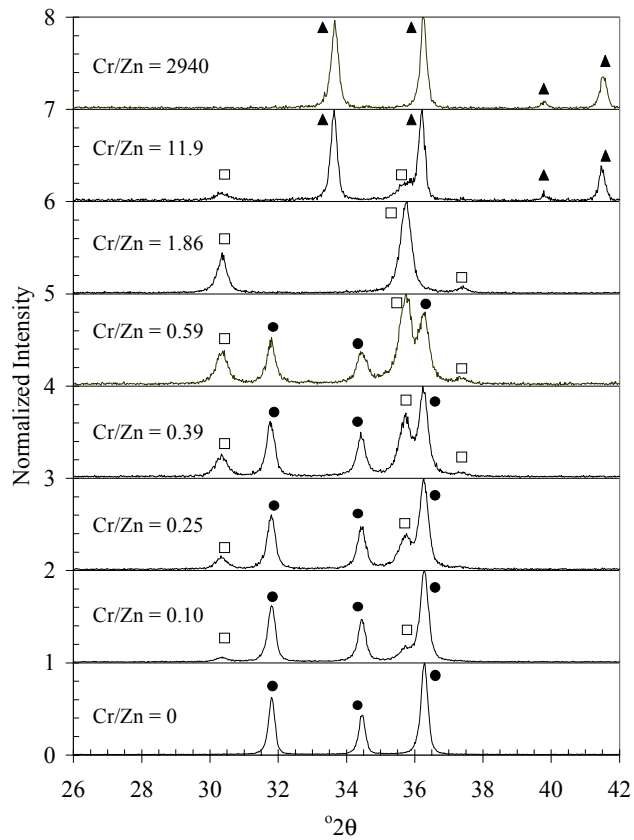

Figure 1. XRD spectra of Cr_2O_3/ZnO catalysts prepared via co-precipitation with $(NH_4)_2CO_3$ and calcined for 2 h in 10% O_2 at 973 K. Phases present include: (□) ZnO; (□) $ZnCr_2O_4$; and (□) Cr_2O_3.

diffraction peak for ZnO, the (311) diffraction peak for $ZnCr_2O_4$, and the (110) diffraction peak for Cr_2O_3. The data for Cr_2O_3/ZnO catalysts prepared via co-precipitation with $(NH_4)_2CO_3$ demonstrate that addition of chromium to ZnO results in a decrease in the ZnO crystallite size (for Cr/Zn ≤ 1.86), which however tends to increase with increasing calcination temperature, as shown in Figure 2. Similar trends were obtained for the K-Cr_2O_3/ZnO catalysts.

Surface areas for the Cr_2O_3/ZnO catalysts prepared via co-precipitation with $(NH_4)_2CO_3$ reveal a similar trend; i.e., the addition of chromium to ZnO (or conversely, zinc to Cr_2O_3) results in an increase in catalyst surface area (Table 1). Surface areas of analogous K-Cr_2O_3/ZnO catalysts exhibited lower surface areas, presumably indicating that potassium oxides and potassium chromates induce an intrinsically low hydrothermal stability.

Table 1. Catalyst surface area after calcination for 2 h at 973 K.

	S (m^2/g)	
~ Nominal Cr/Zn	**$(NH_4)_2CO_3$**	**K_2CO_3**
0.00	5.3 ± 0.3	4.1 ± 0.1
0.10	17.0 ± 0.3	3.3 ± 0.7
0.25	19.1 ± 1.0	1.8 ± 0.3
0.39	19.00 ± 0.01	0.5 ± 0.2
0.42	23.9 ± 0.1	---
0.59	24.9 ± 0.9	7.9 ± 0.4
2.00	27.2 ± 0.3	2.4 ± 0.1
15.0	18.7 ± 0.7	0.16 ±0.11
∞	14.4 ± 0.1	< 0.05

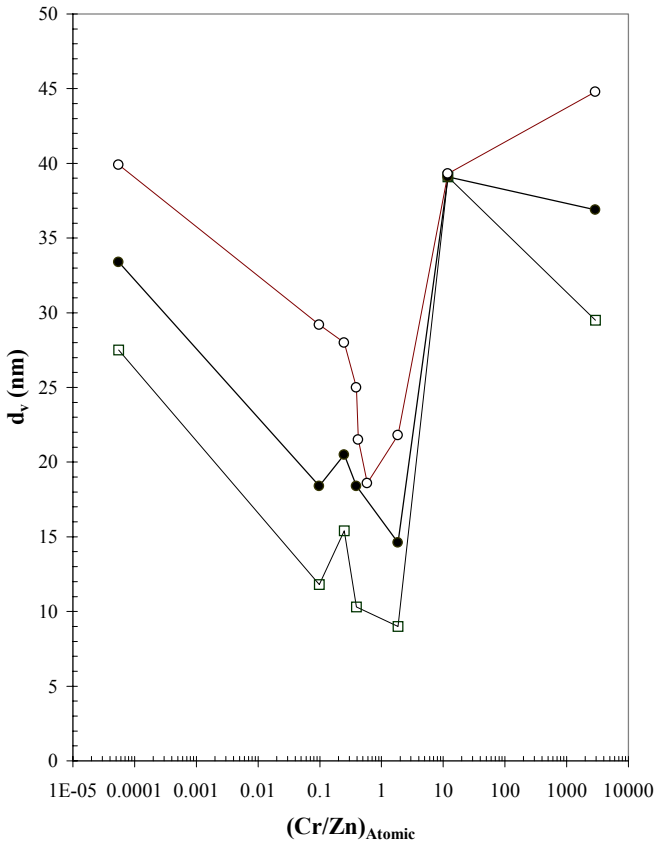

Figure 2. Catalyst volume-weighted crystallite size as a function of Cr/Zn ratio and calcination temperature for Cr_2O_3/ZnO catalysts prepared via co-precipitation with $(NH_4)_2CO_3$. (□) 773 K; (□) 873 K; (□) 973 K.

Catalyst activity for methanol synthesis was evaluated as a function of Cr/Zn ratio at 34 atm and 593 K, as shown in Tables 2-3 and Figure 3. It has been reported in the literature that internal mass transport limitations exist during methanol synthesis, and that the degree of this limitation increases with increasing catalyst particle diameter (> 1 mm) and temperature.[45] However, application of the Weisz-Prater criterion[46] indicated that the data reported herein are free from internal mass transfer limitations. Regardless, subject to the experimental conditions of this study, the maximum allowable conversion of CO to CH_3OH is only 4.2%. Therefore, although the conversions used in this study are low, the kinetic results for many catalysts are to some extent equilibrium-limited.

The specific activity of the Cr_2O_3/ZnO catalysts prepared via co-precipitation with $(NH_4)_2CO_3$ exhibited the expected volcano-type of relationship with the activity maximum observed for *ca.* Cr/Zn = 0.39 (Figure 3); however, the specific activity of the K/Cr_2O_3/ZnO catalysts decreased with increasing potassium content. Comparison of rates on an areal basis, however, reveals that the activities of ZnO and K/ZnO are effectively identical within experimental error, and that activities for catalysts with other Cr/Zn ratios are at least within an order of magnitude (Tables 2 and 3). In addition, it is important to note that the highest observed areal rate for catalysts prepared with either $(NH_4)_2CO_3$ or K_2CO_3 is for ZnO, and the lowest areal rate among the catalysts prepared with $(NH_4)_2CO_3$ is observed for Cr/Zn = 11.9 and Cr_2O_3. Although the limited analysis herein cannot preclude the formation and presence

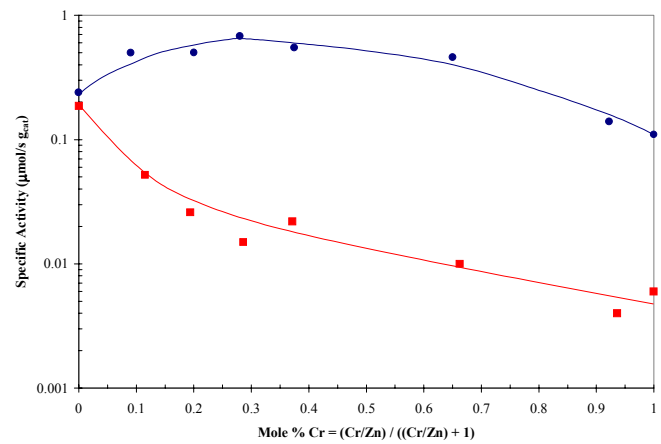

Figure 3. Specific activity of (□) K-free and (□) K-containing Cr_2O_3/ZnO catalysts for CH_3OH synthesis as a function of catalyst Cr/Zn content.

of active sites for methanol synthesis on the Cr_2O_3/ZnO catalysts that do not exist on either Cr_2O_3 or ZnO, the data indicate that, if they exist, they do not likely possess an intrinsic activity for methanol synthesis that exceeds the activity of sites present on the partially reduced ZnO surface.

Table 2.
Cr_2O_3/ZnO catalyst performance for CH_3OH synthesis.
(T=320±2°C, P=34.1±0.2 atm, $N_2/H_2/CO$=1/2/1, GHSV =5134±263 $cm^3/h \cdot g_{cat}$)

Cr/Zn (Actual)	CO Conversion (%)	Specific Activity (μmol/s·g_{cat})	Areal Rate (μmol/min·m^2)	Methanol In Product (wt%)
0.00	1.65	0.24 ± 0.01	2.72	97.8±0.1
0.10	2.98	0.50 ± 0.02	1.76	97.5±0.3
0.25	3.14	0.50 ± 0.03	1.57	97.5±0.2
0.39	4.13	0.68 ± 0.06	2.15	97.8±0.4
0.59	3.67	0.55 ± 0.02	1.32	96.7±0.4
1.86	2.72	0.46 ± 0.04	1.01	97.1±0.9
11.9	0.86	0.14 ± 0.04	0.45	96.5±0.7
2940	0.71	0.11 ± 0.02	0.46	91.6±0.3

Table 3.
K/Cr_2O_3/ZnO catalyst performance for CH_3OH synthesis.
(T=320±1°C, P=34.0±0.2 atm, $N_2/H_2/CO$=1/2/1, GHSV =5168±196 $cm^3/h \cdot g_{cat}$)

Cr/Zn (Actual)	CO Conversion (%)	Specific Activity (μmol/s·g_{cat})	Areal Rate (μmol/min·m^2)	Methanol In Product (wt%)
0.00	1.12	0.187±0.014	2.74	96.8 ± 0.3
0.13	0.31	0.052±0.003	0.94	74 ± 3
0.24	0.16	0.026±0.003	0.87	68 ± 6
0.40	0.09	0.015±0.002	1.80	42 ± 3
0.59	0.14	0.022±0.001	0.17	60 ± 4
1.96	0.06	0.010±0.006	0.25	67 ± 12
14.6	0.03	0.004±0.001	1.50	34 ± 6
1540	0.04	0.006±0.001	---	28 ± 3

Therefore, application of Occam's razor permits, to a first approximation, the expression of global reaction rates on a specific

activity basis as a linear combination of the intrinsic areal rates of the pure component oxides:

$$r_g = S_{ZnO} r_{ZnO} + (S_{Total} - S_{ZnO}) r_{Cr_2O_3}$$

where r_g is the observed global reaction rate (μmol/s·g_{cat}), r_{ZnO} is the intrinsic areal rate for ZnO (0.045 μmol/s·m^2), $r_{Cr_2O_3}$ is the intrinsic areal rate for Cr_2O_3 (0.008 μmol/s·m^2), S_{ZnO} is the surface area of ZnO, and S_{Total} is the total catalyst surface area measured via BET. Surface areas for ZnO in the Cr_2O_3/ZnO catalysts prepared via co-precipitation with $(NH_4)_2CO_3$ were calculated from this relationship using experimental values for r_g, r_{ZnO}, $r_{Cr_2O_3}$, and S_{Total}; see Table 4.

The results support the early hypothesis by Cryder and Frolich,[9] and indicate that the increase in the specific activity for CH_3OH synthesis observed for the Cr_2O_3/ZnO catalysts (for Cr/Zn ≤ 1.86) is due primarily to the increase in accessible ZnO surface area (Table 4). In addition, the results indicate that the observed decrease in specific activity for the Cr_2O_3/ZnO catalysts with Cr > 2 is likely due to the predominance of Cr_2O_3 on the catalyst surface.

Table 4. Estimated ZnO surface area in Cr_2O_3/ZnO catalysts.

	S (m^2/g)		
Cr/Zn	**Total**	**ZnO**	**Cr_2O_3**
0.00	5.3	5.3	0.0
0.10	17.0	9.8	7.2
0.25	19.1	9.4	9.7
0.39	19.0	14.2	4.8
0.59	24.9	9.5	15.4
1.86	27.2	6.7	20.5
11.9	18.7	0.0	18.7
2940	14.4	0.0	14.4

Summary

Several Cr_2O_3-ZnO catalysts prepared via co-precipitation with $(NH_4)_2CO_3$ were characterized by XRD, BET and activity for methanol synthesis at 593 K. Data reveal that addition of chromium to ZnO up to a level of Cr/Zn = 1.86 decreased the volume-weighted crystallite size of ZnO, increased the total catalyst surface area, and increased the available surface area of ZnO. It was also demonstrated that the catalyst specific activities could be described well by a simple linear combination of areal rate data for the pure component oxides. Although the limited analysis herein cannot preclude the formation and presence of active sites for methanol synthesis on the Cr_2O_3/ZnO catalysts that do not exist on either Cr_2O_3 or ZnO, the data indicate that, if they exist, they do not likely possess an intrinsic activity for methanol synthesis that exceeds the activity of sites present on the partially reduced ZnO surface. Therefore, there is likely no true synergy is present between chromia and zinc oxide in this catalyst system. Qualitatively similar results were obtained for catalysts prepared via co-precipitation with K_2CO_3. However, the presence of potassium in these catalysts induced hydrothermal instability and reduced the surface area for both the catalyst and ZnO, in comparison to the relatively K-free samples.

Acknowledgement

This work was funded by the U.S. Department of Energy under SBIR Grant No. DE-FG02-99ER82762. The authors thank CeraMem Corporation for permission to publish this work.

References

1. Mittasch, A. and Schneider, C., US Pat. 1,201,850, **1916.**
2. Mittasch, A., US Pat. 1,558,559, **1925**.
3. Mittasch, A., US Pat. 1,569,775, **1926**.
4. Dreyfus, H., US Pat. 1,868,096, **1932**.
5. Lewis,W.K. and Frolich,Per K., *Ind.Eng.Chem*., **1928**, *20(3),* 285.
6. Frolich,Per K., Fenske, M.R., and Quiggle,D., *Ind.Eng.Chem*., **1928**, *20(7)*, 694.
7. Frolich, Per K., Fenske,M.R., Taylor,P.S., and Southwich,C.A., *Ind.Eng.Chem*., **1928**, *20(12),* 1327.
8. Frolich,Per K., Davidson, R.L., and Fenske,,M.R., *Ind.Eng.Chem*., **1929**, *21(2),* 109.
9. Cryder, D.S.and Frolich,Per K., *Ind.Eng.Chem*., **1929**, *21(9),* 867.
10. Brown,R.L. and Galloway,A.E., *Ind.Eng.Chem*., **1928**, *20(9),* 960.
11. Brown,R.L. and Galloway,A.E., *Ind.Eng.Chem*., **1929**, *21(4),* 310.
12. Vannice,M.A., *Catal.Rev.-Sci.Eng*., **1976,** *14(2),*153.
13. Kung, H.H.,*Catal.Rev.-Sci.Eng*., **1980**, *22(2),* 235.
14. Rase,H.F., Handbook of Commercial Catalysts: Heterogeneous Catalysts, CRC Press: Boca Raton, 2000, p.432.
15. Synetix Brochure for the KATALCO 51-8 Methanol Synthesis Catalysts, available at: http://www.synetix.com/methanol/pdfs/productbulletins/pb51-8.pdf
16. King,D.S. and Nix,R.M., *J.Catal*., **1996,** *160,* 76.
17. Fujitani,T. and Nakamura,J., *Catal.Lett*., **1998**, *56,* 119.
18. Fujita,S.I., Moribe,S., Kanamori,Y., Kakudate,M. and Takezawa,N., *Appl.Catal.A.General*, **2001**, *207,* 121.
19. Skrzypek,J., Lachowska,M., Grzesik,M., S□oczy□ski,J. and Nowak,P., *Chem.Eng.J.,* **1995**, *58*, 101.
20. Lommerts,B.J., Graaf,G.H. and Beenackers,A.A.C.M., *Chem.Eng.Sci*., **2000**, *55*, 5589.
21. Frolich,Per K. and Lewis,W.K., *Ind.Eng.Chem*., **1928**, *20(4),* 354.
22. Frolich,Per K. and Cryder,D.S., *Ind.Eng.Chem*., **1930,** *22(10),*1051.
23. Graves, G.D., *Ind.Eng.Chem*., **1931**, *23(12),* 1382.
24. Anderson,R.B., Feldman,J. and Storch,H.H., *Ind.Eng.Chem*., **1952**, *44(10),* 2418.
25. Lunev,N.K., Artyukh,Y.N., Leonov,V.E., Yakubovich,M.N. and Ryzhak,I.A., *Kinet.Catal*., **1985**, *26(4)*, 752.
26. Tronconi,E., Ferlazzo,N., Forzatti,P. and Pasquon,I., *Ind.Eng.Chem.Res*., **1987,** *26,* 2122.
27. Lietti,L., Botta,D., Forzatti,P., Mantica,E., Tronconi,E. and Pasquon,I., *J.Catal*., **1988**, *111*, 360.
28. Calverley, E.M. and Smith,K.J., *J.Catal*., **1991**, *130,* 616.
29. Calverley, E.M. and Smith,K.J., *Ind.Eng.Chem.Res*., **1992**, *31,* 792.
30. Mawson,S., McCutchen,M.S., Lim,P.K. and Roberts,G.W., *Energy & Fuels*, **1993**, *7*, 257.
31. Campos-Martín,J.M., Guerrero-Ruiz,A. and Fierro,J.L.G., *J.Catal*., **1995**, *156*, 208.
32. Moser,W.R.and Connolly,K.E., *Chem.Eng.J*., **1996**, *64*, 239.
33. Beretta,A., Tronconi,E., Forzatti,P., Pasquon,I., Micheli,E., Tagliabue,L. and Antonelli,G.B., *Ind.Eng.Chem.Res*., **1996**, *35,* 2144.
34. Zahner,J.C., US Pat. 4,011,275, **1977.**
35. Chang,C.D.and Lang,W.H., US Pat. 4,180,516, **1979**.
36. Simard,F., Mahay,A., Ravella,A., Jean,G., and de Lasa,H., *Ind.Eng.Chem.Res*., **1991**, *30,*1448.
37. Simard,F., Mahay,A., Jean,G. and de Lasa,H., *Can.J.Chem.Eng*., **1991**, *69,* 898.
38. Simard,F., Sedran,U.A., Sepúlveda,J., Fígoli,N.S. and de Lasa,H.I., *Appl.Catal.A:General*, **1995**, *125,* 81.
39. Ereña,J., Arandes,J.M., Bilbao,J., Aguayo,A.T. and de Lasa,H., *AFINIDAD*, **1997**, *54(471),* 367.
40. Ereña,J., Arandes,J.M., Bilbao,J., Olazar,M. and de Lasa,H., *J.Chem.Technol.Biotechnol*., **1998**, *72,* 190.
41. Ereña,J., Arandes,J.M., Bilbao,J., Gayubo,A.G., and de Lasa,H., *Chem.Eng.Sci*., **2000**, *55,* 1845.
42. Brunauer,S., Emmett,P.H. and Teller,E., *J.Am.Chem.Soc*., **1938**, *60,* 309.
43. Boudart,M., *Chem.Rev*., **1995**, *95,* 661.
44. Dietz,W.A., *J.Gas Chromatography*, **1967**, *February*, 68.
45. Lommerts,B.J., Graaf,G.H. and Beenackers,A.A.C.M., *Chem.Eng.Sci*., **2000**, *55,* 5589.
46. Madon,R.J. and Boudart,M. *Ind.Eng.Chem.Fundam*., **1982**, *21*,438.

Selective Oxidesulfurization of C1-Organosulfur Compounds over Supported Metal Oxide Catalysts

Sukwon Choi and Israel E. Wachs

ZCSS and Department of Chemical Engineering,
Lehigh University,
Bethlehem, Pennsylvania 18015

Introduction

Recent analyses by EPA[1, 2] concluded that one of the highest priority needs of the Pulp and Paper industry is a new alternative to combustion (burning in power boilers and lime kilns using fossil fuels) and incineration (thermal oxidation systems operating at ~1500 °F) of concentrated process streams of totally reduced sulfur (TRS) compounds (H_2S, CS_2, CH_3SH, CH_3SCH_3 and CH_3SSCH_3) as well as CO that are currently converted to SO_2, CO_2 and H_2O. Consequently, the toxic TRS and CO emissions from the pulp and paper mills are converted to an undesirable acid rain precursor, SO_2, and a major contributor to global warming, CO_2, in very energy intensive non-catalytic processes. A novel catalytic process scheme has been developed to convert the by-products from the pulp and paper mills (TRS compounds, SO_2, CO and CO_2) to valuable chemical intermediates (CH_3OH, H_2CO and H_2SO_4) that are consumed in the Pulp and Paper Industry. A key catalytic intermediate reaction step in the catalytic process scheme is the selective catalytic oxidation of C1-organosulfur compounds:

$$COS + O_2 \rightarrow CO + SO_2 \quad [1]$$
$$CS_2 + 5/2\ O_2 \rightarrow CO + 2\ SO_2 \quad [2]$$
$$CH_3SH + 2\ O_2 \rightarrow H_2CO + SO_2 + H_2O \quad [3]$$

These reactions are the subject of this paper. The objective of the current studies is to establish the fundamental kinetics and mechanism of the selective oxidation of C_1-organosulfur compounds (COS, CS_2, and CH_3SH) over sulfur-tolerant metal oxide catalysts.

Experimental

Catalyst Preparation. The catalysts used in this study were prepared by the incipient wetness impregnation method. This technique is described in detail elsewhere[3-5]. The support materials used in this study are TiO_2 (55 m^2/g), ZrO_2 (39 m^2/g), Nb_2O_5 (55 m^2/g), CeO_2 (36 m^2/g), Al_2O_3 (γ, 180 m^2/g), and SiO_2 (300 m^2/g). Concentrations of the supported metal oxides were all prepared to exhibit below monolayer coverage.

Characterization. *In Situ* Raman spectroscopy was performed with a system comprised of an Ar+ laser (Spectra Physics, model 2020-50) set at 514.5 nm, and a Spex Triplemate spectrometer (model 1877) connected to a Princeton Applied Research (model 143) OMA III optical multichannel photodiode array detector. Samples were dehydrated by heating to 300 °C prior to any analyses. The entire procedure was performed in flowing oxygen to achieve complete oxidation of the catalyst. The reactivities of the catalysts were obtained from an isothermal fixed-bed reactor system operating at atmospheric pressure. The feed gas contained 1000 ppm of the reactant (COS, CS_2, or CH_3SH), 18% O_2 in He balance, and was introduced into the reactor at a flow rate of 150 ml/min. Sample runs were performed between 200-450 °C. Analysis of the reaction products was accomplished using a FTIR, (model #101250 Midac) or an on-line gas chromatograph (HP 5890A) equipped with a thermal conductivity detector (TCD) and a sulfur chemiluminescence detector (SCD 355, Sievers). Temperature Programmed Surface Reaction Mass Spectrometry (TPSR-MS) was carried out with an AMI-100 system equipped with an online mass spectrometer (Dycor DyMaxion). The adsorption was performed between 35-100 °C using 200 mg of catalyst and was ramped to 500 °C at a heating rate of 10 °C/min in 5% O_2/He or He at 30 mL/min.

Results and Discussion

Steady-state reactivity data showed that COS and CS_2 are selectively oxidized to CO and SO_2 over the sulfur tolerant supported vanadia catalysts via reactions [1] and [2] between 290-330 °C and 230-270 °C, respectively. CO selectivities as high as 98% and 90% were achieved for COS and CS_2 oxidation, respectively. The major byproduct from CS_2 oxidation is COS, which can be further selectively converted to CO via reaction step [1]. For the selective oxidation of CH_3SH to H_2CO and SO_2 via reaction [3] over a series of redox supported metal oxide catalysts (supported vanadia, molybdate, tungstates and niobates) also did not exhibit deactivation and were sulfur tolerant. The most selective catalysts for reaction step [3] between 350-400 °C were vanadia supported on ZrO_2, TiO_2 and SiO_2 (in the 84-89% range at high conversions).

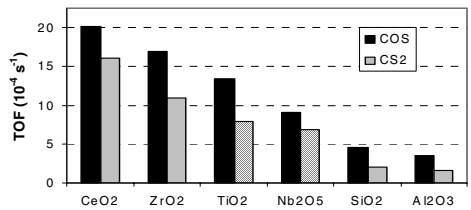

Figure 1. Variation of the TOF with the oxide support for COS and CS_2 oxidation at 330°C and 260°C, respectively, over supported vanadia catalysts with monolayer coverage.

Raman spectroscopy revealed that the supported metal oxide phases were 100% dispersed on the oxide substrate. Thus, the exclusive presence of surface metal oxide species allowed the determination of the number of active sites in the catalyst samples since dispersion was 100 %. As shown in **Figure 1** for monolayer surface vanadia coverage, where the oxide support cations are essentially not exposed to the reactant gases and are covered by the vanadia overlayer, the turnover frequencies (TOF: Activity per surface metal atom based on the yield of CO) for COS and CS_2 oxidation varied about one order of magnitude with the specific oxide support ($CeO_2 > ZrO_2 > TiO_2 > Nb_2O_5 > Al_2O_3 \sim SiO_2$). A similar phenomenon is shown in **Figure2** for TOFs (based on the yield of H_2CO) during CH_3SH oxidation over supported vanadia catalysts at 350 °C. The TOFs varied within one order of magnitude ($TiO_2 > ZrO_2 \sim Nb_2O_5 > Al_2O_3 \sim SiO_2$). These trends are inversely correlated with the electronegativity of the support cation in the bridging V-O-Support bond and suggests the bridging V-O-Support bond being the active site for these reactions since Raman revealed that the terminal V=O bonds were essentially the same in these supported vanadia catalysts[6]. Furthermore, all three reactions exhibited a zero-order dependence on the oxygen partial pressure

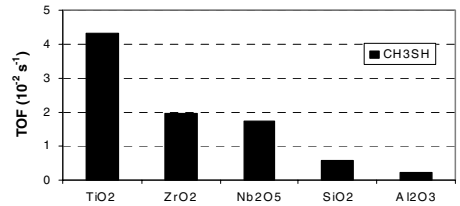

Figure 2. Variation of the TOF with the oxide support for CH_3SH oxidation at 350°C over supported vanadia catalysts (1% V_2O_5).

(0.5-20%) and a first-order dependence on the COS/CS_2 /CH_3SH partial pressures (<1%, due to safety concerns), which suggest that the surface vanadia species is essentially fully oxidized under the investigated reaction conditions. The apparent activation energies for COS, CS_2 and CH_3SH oxidation over the supported vanadia catalysts were found to be ~10, ~6 Kcal/mol and 17 Kcal/mol, respectively.

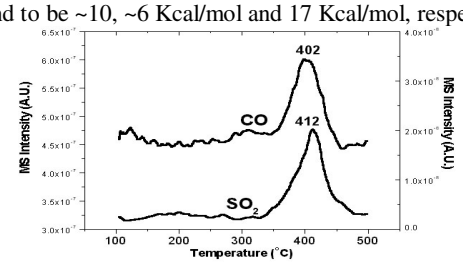

Figure 3. TPSR-MS profiles after *COS* adsorbed at 100 °C on the 5% V_2O_5/TiO_2 catalyst, under 5% O_2/He flow.

The desorption spectra of CO and SO_2 are shown in **Figure 3** from the 5% V_2O_5/TiO_2 catalyst following COS adsorption at 100 °C. The simultaneous desorption of CO and SO_2 suggests that the oxidation of COS proceeds via the rate-determining step involving cleavage of the C-S bond. The slight delay in the production of SO_2 is consistent with this conclusion since the remaining S(ads) requires the addition of two oxygen atoms. The above suggests the following mechanism for COS oxidation to CO and SO_2 over the 5 % V_2O_5/TiO_2 catalyst.

COS		↔	COS(ads)	[4]
COS(ads)	→	CO + S(ads)		[5] rds
S(ads) + O(ads)	→	SO(ads)		[6]
SO(ads) + O(ads)	→	SO_2		[7]

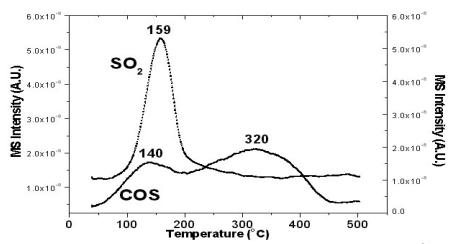

Figure 4. TPSR-MS profiles after *CS_2* adsorbed at 35 °C on the 5% V_2O_5/TiO_2 catalyst, under 5% O_2/He flow.

The desorption spectra of COS and SO_2 are shown in **Figure 4** from the 5% V_2O_5/TiO_2 catalyst following CS_2 adsorption at 35 °C. The presence of the COS species in the desorption spectra suggests CS_2 is oxidized to CO and SO_2 via the formation of COS as an intermediate species. Steady-state data obtained at low conversions also confirmed the presence of COS formation. In view of these findings the following mechanism is proposed for CS_2 oxidation.

CS_2 + O(ads)	↔	CS_2O(ads)		[8]
COS_2(ads)	→	COS + S(ads)		[9] rds
S(ads) + O(ads)	→	SO(ads)		[10]
SO(ads) + O(ads)	→	SO_2		[11]

The further oxidation of COS to CO and SO2 proceeds via reaction steps [4-7]. From comparison of the CH_3SH and CH_3OH TPSR desorption profiles in **Figures 5** and **6**, the peaks for H_2CO appear at the exact same temperature suggesting H_2CO is produced via the same surface reaction intermediate from both CH_3SH and CH_3OH.

The above suggests the following mechanism for reaction [3] over the 1 % V_2O_5/TiO_2 catalyst.

CH_3SH + O(ads)	↔	CH_3S(ads) + OH(ads)		[12]
CH_3S(ads) + O(ads)	→	CH_3SO(ads)		[13]
CH_3SO(ads)	→	CH_3O(ads) + S(ads)		[14]
CH_3O(ads)	→	H_2CO + H(ads)		[15] rds
H(ads) + OH(ads)	↔	H_2O		[16]
S(ads) + O(ads)	→	SO(ads)		[17]
SO(ads) + O(ads)	→	SO_2		[18]

The dissociative adsorption of CH_3SH to CH_3S(ads) and OH(ads), reaction step [12], was revealed by desorption of CH_3SSCH_3 into the gas phase during the adsorption step at 100 °C. All TPRS experiments repeated in the absence of flowing gas phase oxygen gave the same product desorption peaks, which demonstrate that the oxygen involved in the surface reaction steps [4-18] is oxygen from the surface vanadia species.

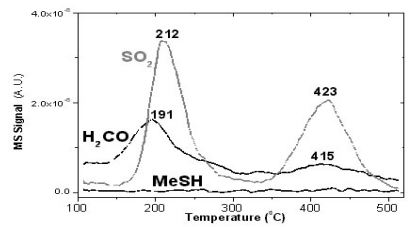

Figure 5. TPSR-MS profiles after *CH_3SH* adsorbed at 100 °C on the 1% V_2O_5/TiO_2 catalyst, under 5% O_2/He flow.

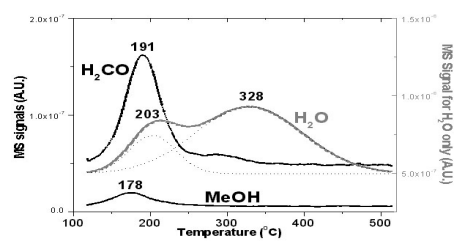

Figure 6. TPSR-MS profiles after *CH_3OH* adsorbed at 100 °C on the 5% V_2O_5/TiO_2 catalyst, under 5% O_2/He flow.

Acknowledgement

The authors gratefully acknowledge the National Science Foundation, Grant NSF-CTS-9626893, for financial support of this research.

References

1. "Pulp, Paper and Paperboard Industry - Background Information for Proposed Air Emission Standards," EPA, 453/R-93-050a (Oct. 23, 1993).
2. "Targeted Energy Performance Areas for 1999," American Forest and Paper Association Energy Performance Research Task Group (May 1998).
3. Deo, G., Wachs, I. E. J. Catal. 146 (1994) 323-334.
4. Wachs, I. E., Deo, G., Juskelis, M. V., Weckhuysen, B. M. in: Froment, G. F., Waugh (Eds.), K. C., Dynamics of Surfaces and Reaction Kinetics in Heterogeneous Catalysis, Elsevier, Amsterdam, 1997, pp. 305-314.
5. Wachs, I. E., in: Spivey(Ed.), J. J., Catalysis, vol. 13, The Royal Society of Chemistry, Cambridge, 1997, pp. 37-54.
6. Harcastle, F. D. and Wachs, I. E., J. Phys. Chem. **95** (1991) 5031-5041.

METHANOL SYNTHESIS ACTIVITY OF ALKALINE EARTH AND LANTHANOID METAL ADDED SULFIDED PD/SIO_2 AND THEIR SURFACE FINE STRUCTURES INVESTIGATED BY DRIFT SPECTROSCOPY

Naoto Koizumi, Kazuhito Murai, Satoshi Takasaki and Muneyoshi Yamada

Department of Applied Chemistry, Graduate School of Engineering, Tohoku University, 07Aoba, Aramaki, Aoba-ku, Sendai 980-8579, Japan

Introduction

Because of the potential use of dimethyl ether as a substituted diesel fuel, methanol synthesis from CO/H_2 (syngas) is one of attractive technologies for the production of high-quality transportation fuels. Cu/Zn-type catalyst is currently applied for the industrial methanol production using a feed containing both syngas and CO_2.[1] For a feed containing only the syngas, reduced Pd catalysts show a high activity. The turnover frequency of reduced Pd/CeO_2 at 443 K and 3.0 MPa has been reported to be equivalent to that of Cu/Zn catalyst at 523 K and 5.1 MPa from $CO/H_2/CO_2$ feed.[2]

To develop methanol synthesis catalysts with a sulfur tolerance, authors investigated CO hydrogenation activity of various transition metal sulfides and found that $Rh_{17}S_{15}$[3] and $Pd_{16}S_7$[4] yield methanol from the syngas feed even in the presence of H_2S. In the absence of H_2S, the space-time yield (STY) of methanol obtained with $Rh_{17}S_{15}$ reached 800 g/kg-cat/h at 593 K and 5.1 MPa, which is comparable with that obtained with a commercial Cu/Zn/Al catalyst at 523 K and 5.1 MPa from $CO/H_2/CO_2$ feed. $Pd_{16}S_7$, on the other hand, yielded only 77 g/kg-cat/h of methanol at 613 K and 5.1 MPa. To improve the methanol synthesis activity of Pd sulfide, authors investigated the activity of Pd sulfide supported on various metal oxides and found that SiO_2 is most effective support among the metal oxides examined. The STY of methanol obtained with sulfided Pd/SiO_2 was 1.6 times higher than that obtained with $Pd_{16}S_7$. Besides, the STY of methanol obtained with SiO_2 supported Pd sulfide changed depending on the kinds of SiO_2.[5] It was suggested that alkaline and alkaline earth metal impurities in SiO_2 act as promoters.

Thus, to improve the methanol synthesis activity of Pd sulfide further, the present work investigated effects of alkaline, alkaline earth or lanthanoid metal additives on the activity of SiO_2 supported Pd sulfide. DRIFT measurements under the reaction conditions were also performed to make clear active adsorbed species formed on SiO_2 supported Pd sulfide.

Experimental

Catalyst preparation. Precursor materials for SiO_2 supported Pd sulfide with or without the additive were prepared by the impregnation method. SiO_2 supported Pd oxide was prepared by impregnating pre-calcined SiO_2 powder (Fuji Silysia, 560 m^2/g) with an aqueous $Pd(NH_3)_4(NO_3)_2$ solution followed by drying and calcination (Pd/SiO_2). A weight ratio of Pd (as metal) to SiO_2 was 0.045. Then, Pd/SiO_2 with the additive was prepared by impregnating Pd/SiO_2 with an aqueous $M(NO_3)_x$ solution (M: Li, K, Cs, Mg, Ca, Sr, Ba, La or Nd) followed by drying (M-Pd/SiO_2 (D)). M/Pd atomic ratio was varied in a range from 0.1 to 1.0. To examine effects of calcination, part of M-Pd/SiO_2 (D) was calcined (M-Pd/SiO_2 (C)).

Activity measurement. The precursor material thus prepared was charged into a stainless steel reactor and was sulfided in a stream of H_2S 5%/H_2 at 673 K. The cumulative amount of H_2S fed during the sulfiding pretreatment was 160 mol-H_2S/mol-Pd. Methanol synthesis was then performed using the syngas feed (CO 33%/H_2 62%/Ar). Cu/Zn/Al catalyst supplied by ICI Corp. was also used as a reference.

DRIFT measurement. To obtain DRIFT spectra of adsorbed species formed under the high-pressure reaction conditions, DRIFT chamber equipped with ZnSe window (Spectra-Tech Inc.) was utilized in the present work. After the sulfidation of the precursor material in the chamber, methanol synthesis was performed at 613 K and 5.1 MPa using the same feed as that employed for the activity measurements. DRIFT spectra were recorded on FTS 6000 spectrometer (Digilab) with a resolution of 4 cm^{-1} and accumulation of 128.

Results and Discussion

Methanol synthesis was performed at 613 K, 5.1 MPa and 20 m^3 (STP)/kg-cat/h using sulfided Pd/SiO_2 and sulfided M-Pd/SiO_2 (D) having M/Pd atomic ratio of 0.5. Methanol, CH_4 and CO_2 were formed under these conditions. The products obtained with sulfided Pd/SiO_2 and sulfided M-Pd/SiO_2 (D) (M: Mg, Ca, Sr, La or Nd) were mainly composed of methanol while the remainder of the catalysts mainly yielded methane. Methanol selectivity of sulfided Pd/SiO_2 and M-Pd/SiO_2 (D) (M: Mg, Ca, Sr, La or Nd) was 90 mol% and 60-70 mol%, respectively. **Figure 1** shows the STY of methanol obtained with these catalysts. The STY of methanol obtained with sulfided M-Pd/SiO_2 (C) is also shown in **Figure 1**. Except for K and Cs additives, all the additives examined here show promoting effects. Especially, the higher STY is obtained with the sulfides containing Ca, Sr, La or Nd additive. The calcination of the precursor material increases the activity slightly in the case of sulfided Sr-Pd/SiO_2. Among the catalysts examined here, the maximum STY is obtained with sulfided Ca-Pd/SiO_2 (D), which is about 4 times higher than that obtained with sulfided Pd/SiO_2.

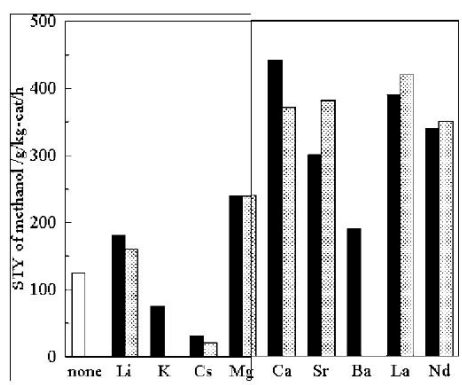

Figure 1. STY of methanol obtained with sulfided Pd/SiO_2 ( ), sulfided M-Pd/SiO_2 (D) ( ) and sulfided M-Pd/SiO_2 (C) ( ): Reaction conditions, CO 33%/H_2 62 %/Ar, 613 K, 5.1 MPa, 20 m^3 (STP)/kg-cat/h.

Then, methanol synthesis was performed using sulfided Ca-Pd/SiO_2 (D) at 5.1 MPa and 30 m^3 (STP)/kg-cat/h in a temperature range from 473 K to 613 K. The STY of methanol increases with increasing the temperature from 473 K to 593 K and was 700 g/kg-cat/h at 593 K. For comparison, the commercial Cu/Zn/Al catalyst was also subjected to the reaction. Cu/Zn/Al catalyst yielded 900 g/kg-cat/h of methanol at 523 K, 5.1 MPa and 6.0 m^3/kg-cat/h from $CO/H_2/CO_2$ feed. Thus, at the higher reaction temperature and gas-hourly space velocity, the STY of methanol obtained with sulfided Ca-Pd/SiO_2 (D) reaches 80% of that obtained with the commercial Cu/Zn/Al catalyst.

To make clear active species on sulfided Ca-Pd/SiO_2 (D), DRIFT spectra were recorded as a function of time when sulfided Ca-

Pd/SiO_2 (D) was exposed to the stream of the syngas at 613 K and 5.1 MPa (**Figure 2**). The spectra show IR bands at 1820, 1600, 1450, 1270, 1110, 1062, 1031, 1007 and 957 cm^{-1}. A shoulder band is also visible at 1304 cm^{-1}. The bands at 1062, 1031 and 1007 are assigned to C-O stretching vibration of the gas-phase methanol while the shoulder band at 1304 cm^{-1} is assigned to C-H bending vibration of the gas-phase methane. The appearance of the bands due to the gas-phase methanol clearly indicates that methanol synthesis takes place in the chamber.

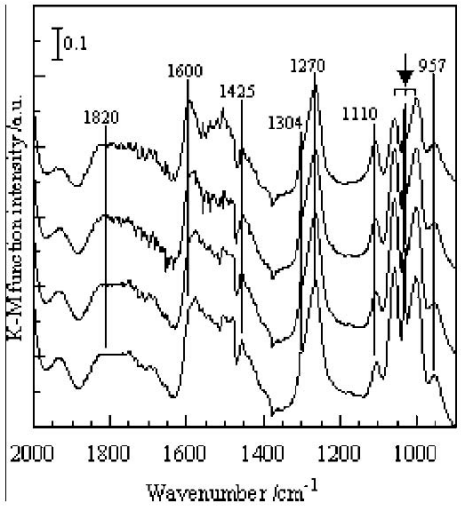

Figure 2. DRIFT spectra of sulfided Ca-Pd/SiO_2 (D) under the high-pressure methanol synthesis conditions as a function of time-on stream (from top to bottom, *t*=0, 5, 30, 93 min): The arrow indicates the IR bands due to the gas-phase methanol.

To facilitate assignments of the remainder of the bands observed during methanol synthesis, the catalyst temperature was reached down to 298 K under the high-pressure syngas flow and then the pressure of the syngas flow was reached down to 0.3 MPa followed by the flushing with helium. Although the bands of the gas-phase methanol, methane and CO completely disappeared, the bands at 1600, 1425 and 1270 cm^{-1} were still visible in the spectrum recorded under these conditions. IR bands were also visible at 2060 and 1925 cm^{-1}, which are assigned to C-O stretching vibration of adsorbed CO species. Thus, the bands at 1600, 1425 and 1270 cm^{-1} observed during methanol synthesis originate from adsorbed species, not the gas-phase products. Several authors have reported that IR bands of adsorbed formate species are observed when a reduced Na-Pd/SiO_2[6] or reduced PdCu/KL[7] is exposed to the stream of the syngas at elevated temperatures. The formate species shows IR bands at 1600-1550 cm^{-1}, 1400-1380 cm^{-1}, 1380-1340 cm^{-1} and 1090-1060 cm^{-1}.[8] The bands at 1600, 1425 and 1270 cm^{-1} observed during methanol synthesis, therefore, are not due to the adsorbed formate species. Except for the bands of the gas-phase methanol and methane, all the bands appeared in the spectra in **Figure 2** were also observed when sulfided SiO_2 was exposed to the stream of the syngas at 613 K and 5.1 MPa. This observation indicates that the bands at 1600, 1425 and 1270 cm^{-1} observed during methanol synthesis originate from some kinds of adsorbed species formed on SiO_2 and this species is not involved in the formation of methanol.

Then, attention was given to the nature of the adsorbed CO species. As mentioned above, IR bands of the adsorbed CO species appear at 2060 and 1925 cm^{-1} when sulfided Ca-Pd/SiO_2 (D) is exposed to the stream of helium after methanol synthesis. From the literature data,[8] these bands are assigned to CO species linearly adsorbed on Pd^0 sites (2060 cm^{-1}) and CO species adsorbed on Pd^0 sites in the form of bridge (1925 cm^{-1}), respectively. To investigate the reactivity of these adsorbed CO species toward hydrogen, helium flow was replaced by hydrogen flow. The catalyst temperature was then ramped from 298 to 613 K at the rate of 10 K/min. DRIFT spectra were recorded at each temperature (Temperature Programmed Surface Reaction, TPSR). The pressure of hydrogen flow was maintained at 1.6 MPa during the TPSR. The obtained spectra are shown in **Figure 3**. With increasing the temperature, the intensities of the bands of the adsorbed CO species decrease and disappear at the temperature above 473 K, which is accompanied with the increase of the intensities of the bands at 1271, 1099 and 950 cm^{-1}. Careful inspections of the spectra also show the appearance of the bands due to the gas-phase methanol at 1062, 1031 and 1007 cm^{-1}.

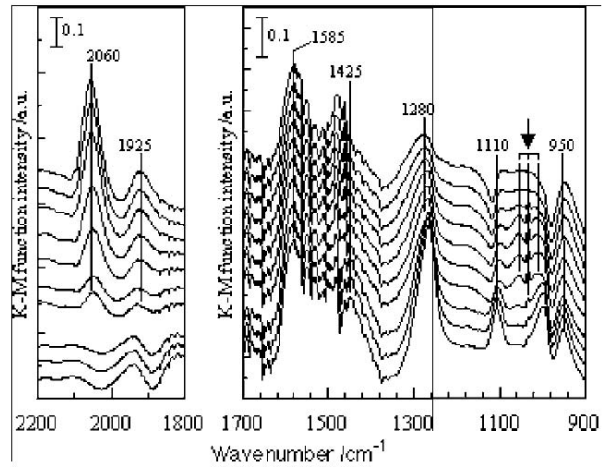

Figure 3. DRIFT spectra of sulfided Ca-Pd/SiO_2 during the TPSR (from top to bottom, *T*=303, 323, 343, 373, 393, 423, 473, 523, 573, 613 K): The arrow indicates the IR bands due to the gas-phase methanol.

The intensities of the bands at 1271, 1099 and 950 cm^{-1} increase with increasing the temperature until it reaches 613 K while those of the bands due to the gas-phase methanol showed the maximum at around 400 K. This indicates that the adsorbed CO species observed after methanol synthesis react with hydrogen to form the gas-phase methanol during the TPSR. It is suggested that Pd^0 sites are formed on sulfided Ca-Pd/SiO_2 under methanol synthesis conditions and CO species adsorbed on these sites is hydrogenated to yield methanol.

Acknowledgement

This work was supported by Research for the Future Program of JSPS under the project "Synthesis of Ecological High Quality of Transportation Fuels" (*JSPS-RFTF98P01001*).

References

(1) Chinchen, G. C.; Mansfield, K.; Spencer, M. S. *CHEMTECH* **1990**, 699.
(2) Matsumura, Y.; Shen, W. J.; Ichihashi Y.; Okumura, M. *J. Catal.* **2001**, *197*, 267.
(3) Yamada, M.; Koizumi, N.; Miyazawa, A.; Furukawa, T. *Catal. Lett.*, *in print*
(4) Koizumi, N.; Miyazawa, A.; Furukawa, T; Yamada, M. *Chem. Lett., in print.*
(5) Koizumi, N. ; Murai, K.; Takasaki, S.; Yamada, M. Prepr. Pap. - *Am. Chem. Soc., Div. Fuel Chem.*, **2001**, *46* (2), 437.
(6) Kikuzono, Y.; Kagami, S.; Naito, S.; Onishi T.; Tamaru, K. *Faraday Discuss. Chem. Soc.* **1981**, *72*, 135.
(7) Anderson, J. A.; Lopez-Granados, M.; Fernandez-Garcia, M. *J. Catal.* **1998**, *176*, 235.
(8) Gopal, P. G.; Schneider, R. L.; Watters, K. L. *J. Catal.*, **1987**, *105,* 366.
(9) Sheppard, N.; Nguyen, T. T. *Adv. IR and Raman Spectrosc.* **1987**, *5*, 67.

CONTINUOUS PRODUCTION OF DIETHYL CARBONATE OVER A SUPPORTED $CuCl_2/PdCl_2/KOH$ CATALYST

N. S. Roh, B. C. Dunn, and E. M. Eyring

Department of Chemistry
University of Utah
Salt Lake City, Utah 84112

J. Dworzanski, H. L. C. Meuzelaar, J. Z. Hu, M. S. Solum, and R. J. Pugmire

Department of Chemical and Fuels Engineering
University of Utah
Salt Lake City, Utah 84112

Introduction

Diethyl carbonate is a potential oxygen-containing additive for gasoline and diesel fuel to reduce pollutant emissions. Previous studies using a similar compound, dimethyl carbonate (DMC), as an oxygenate have shown reduction of carbon monoxide,[1] oxides of nitrogen,[2] hydrocarbons,[3] and particulate matter.[4] Our own research efforts[5] indicate that 5 wt. % DEC in diesel fuel can reduce the emission of particulate matter by as much as 50%. Additional factors make DEC an attractive oxygen-containing fuel additive, namely, its high oxygen content (40.6 wt. %), and more favorable gasoline/water distribution coefficient[3] when compared with ethanol or DMC. When in contact with soil, DEC should slowly decompose into ethanol and carbon dioxide,[6] two compounds with little or no environmental impact.

One promising method of producing DEC on an industrial scale is the oxidative carbonylation of ethanol using a heterogeneous catalyst. The overall reaction is:

$$2\,\mathrm{EtOH} + \mathrm{CO} + \frac{1}{2}\mathrm{O}_2 \xrightarrow{\mathrm{Cu}^{2+}/\mathrm{Pd}^{2+}} \mathrm{O{=}C(OEt)_2} + \mathrm{H_2O}$$

Previous studies[5] conducted with a batch reactor indicate an improvement in the yield of DEC when the $CuCl_2/PdCl_2$/activated carbon catalyst is treated with KOH after the support is loaded with the chloride salts. This post-treatment creates an additional phase of copper, atacamite, which creates a more active catalyst.[7]

Batch reactor studies[5] cannot predict the behavior of the chemical reaction due to the static nature of the system. Thus, studies employing a pulse-quench-flow reactor were conducted using the most active catalyst determined from the batch reactor experiments. These experiments have increased our understanding of the chemical reaction and may lead to the development of better catalysts.

Experimental

Pulse-quench-flow reactor. The reactor design was based on a previously published report[8] and consisted of three mass flow controllers (MKS) to deliver the gaseous reactants (CO and O_2) and N_2 carrier gas. The ethanol, with a 5 wt. % toluene internal standard, was delivered at a constant rate with a syringe pump (Isco) equipped with a preheater to ensure the ethanol was in the gas phase. The reactor consisted of a 5 inch long, ¼ inch id stainless steel tube, plugged at both ends with glass wool to contain the catalyst, and wrapped with a rope heater. A thermocouple was placed inside the catalyst bed for accurate temperature control. A backpressure regulator located downstream of the catalyst bed maintained pressure inside the system and the sampling port for the GC/MS was located on the low pressure side of the regulator. All components of the reactor were heated to maintain the reactants and products in the gas phase at all times. The GC/MS sampling line was also heated to prevent condensation.

Catalyst Preparation. The catalyst was prepared by dissolving suitable amounts of $CuCl_2$ and $PdCl_2$ in approximately 500 mL of methanol and adding sufficient activated carbon (Darco, 20-40 mesh) to yield 3 wt. % Cu and 0.25 wt. % Pd, both measured as metals. The mixture was refluxed for four hours to impregnate the carbon support and the methanol was removed by vacuum distillation. The catalyst was dried in a vacuum oven at 80 °C overnight. The catalyst was then treated with a methanolic solution of KOH, refluxed, vacuum distilled, and dried overnight. A fresh 2.00 g sample of the catalyst was loaded into the reactor for each experiment to ensure that any effects observed were due to the chemical reaction and not from catalyst deactivation.

Results and Discussion

The catalyst used for all of the studies consisted of $CuCl_2/PdCl_2/KOH$ supported on activated carbon. This catalyst has proven to be more active[5] than those prepared without $PdCl_2$, with other copper salts ($Cu(NO_3)_2$, $Cu(CH_3COO)_2$, etc), with other hydroxide sources (NaOH, $Ca(OH)_2$, etc), or on other supports (alumina, silica, etc). Even with the most active catalyst, the reaction is quite slow, such that long residence times must be used to produce a suitable amount of DEC for GC/MS detection. The continuous flow reactor allows for simple adjustment of the residence time by modifying the flow rate of the N_2 carrier gas. The influence of residence time on DEC production is presented in **Figure 1** which shows the conversion of ethanol into DEC reaches a maximum of 12.5% at τ=17.4 s. Shorter residence times simply result in less DEC produced, and the selectivity for DEC remains constant at 100%. No additional products were detected in the GC/MS; however, conversion of CO into CO_2 was not considered.

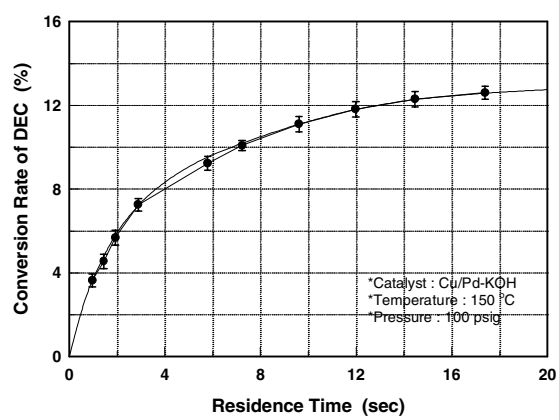

Figure 1. Influence of residence time on production of DEC. Conditions: 2.0 g catalyst, 3.2 standard cubic centimeters per minute (sccm) O_2, 48 sccm CO, 1.2 mL/hr ethanol (as liquid), 150 °C, 100 psig.

The reaction temperature was varied between 120 °C and 180 °C with five residence times and the results are presented in **Figure 2**. The two smallest residence times (1.44 s and 2.89 s) show very little temperature dependence presumably due to the short contact time with the catalyst, while the other three contact times show a linear dependence on the reaction temperature. No other organic products

were detected, thus the selectivity for DEC remained essentially constant at 100%. The maximum conversion of DEC reached almost 18% at 180 °C with 17.4 s contact time, and based on these data, further improvements may be possible with even higher temperatures.

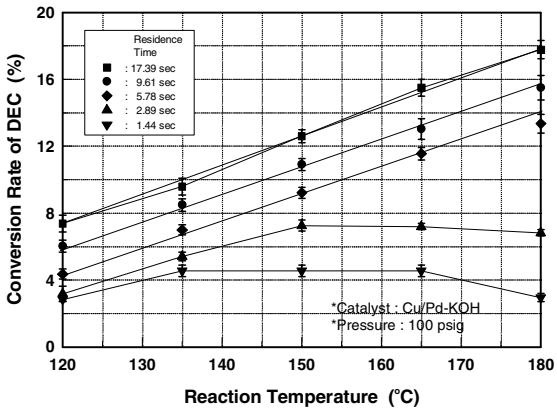

Figure 2. Impact of reaction temperature on the production of DEC. Conditions: 2.0 g catalyst, 3.2 sccm O_2, 48 sccm CO, 1.2 mL/hr ethanol (as liquid), 100 psig.

The flow rate of CO into the reactor showed unexpected behavior. As seen in **Figure 3**, the relationship between CO flow rate and production of DEC is not linear, but shows three distinct regions.

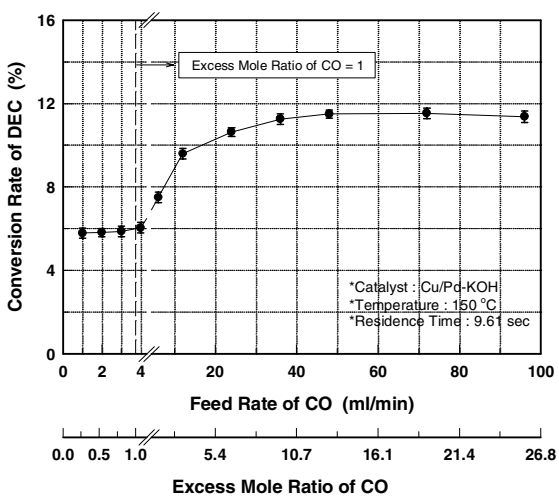

Figure 3. Influence of CO flow rate on conversion of ethanol to DEC. Conditions: 2.0 g catalyst, 3.2 sccm O_2, 1.2 mL/hr ethanol (as liquid), 150 °C, 9.61 s contact time.

In the region where CO is the limiting reactant, DEC production is independent of the flow rate of CO. Since the calculation of DEC conversion is based on the limiting CO reactant, this region indicates that a simple chemical equilibrium has been established. The ratio of DEC to CO is constant. At CO flow rates between 4 and 35 sccm, the results still indicate a simple chemical equilibrium because 100% conversion is based on ethanol rather than CO, as in the previous case. At CO flow rates above 35 sccm, the reaction has reached saturation in which all of the accessible catalytic sites are occupied by a CO molecule, and the yield is controlled by kinetics rather than by equilibrium.

The flow rate of ethanol was varied from 1.2 to 9.5 mL/hr while maintaining all other experimental parameters. The results can be seen in **Figure 4**. Rather than show simple chemical equilibrium as noted above, an additional product, diethoxymethane (DEM), is formed when ethanol is in stoichiometric excess. Since the amount of DEM increases independently of the amount of DEC, the reaction which produces DEM must be independent from the DEC reaction, not a sequential mechanism.

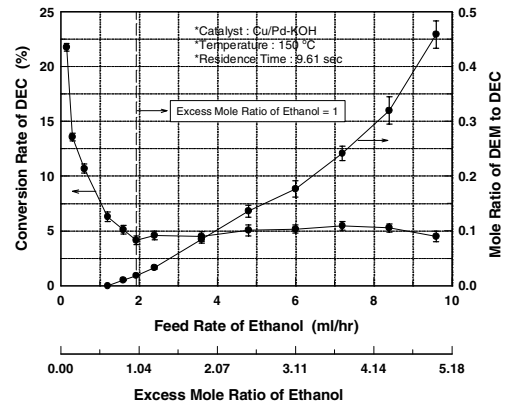

Figure 4. The impact of ethanol flow rate on DEC yield. Conditions: 2.0 g catalyst, 3.0 sccm O_2, 6.0 sccm CO, 150 °C, 9.61 s contact time.

Conclusions

Diethyl carbonate can be produced with high selectivity using a $CuCl_2/PdCl_2/KOH$ catalyst supported on activated carbon. The reaction behaves as predicted with respect to temperature and contact time, but unusual effects have been observed when the flow rate of CO and ethanol are varied. The reaction reaches kinetic saturation when CO is present in large excess, and when ethanol is in excess, the formation of a byproduct is favored.

Acknowledgement. Financial support by the US Department of Energy through the Consortium for Fossil Fuel Liquefaction Sciences (University of Kentucky, Lexington) is gratefully acknowledged.

References

1. Imoura, S.; Matsushita, D. Japan Patent 61[1986]-207496, **1986**
2. Stoner, M.; Litzinger, T. *SAE Technical Paper Series* **1999**, 1999-1901-1475.
3. Pacheco, M. A.; Marshall, C. L. *Energy & Fuels* **1997**, *11*, 2-29.
4. Dillon, D. M.; Iwamoto, R. Y. US Patent 4,891,049, **1990**
5. Dunn, B. C.; Guenneau, C.; Hilton, S. A.; Pahnke, J.; Eyring, E. M.; Dworzanski, J.; Meuzelaar, H. L. C.; Hu, J. Z.; Solum, M. S.; Pugmire, R. J. *Energy & Fuels* **2001**, *in press*.
6. Crandall, J. W.; Deitzler, J. E.; Kapicak, L. A.; Poppelsdorf, F. US Patent 4,663,477, **1987**
7. Punnoose, A.; Seehra, M. S.; Dunn, B. C.; Eyring, E. M. *Energy & Fuels* **2001**, *in press*.
8. Goguen, P. W.; Xu, T.; Barich, D. H.; Skloss, T. W.; Song, W.; Wang, Z.; Nicholas, J. B.; Haw, J. F. *J. Am. Chem. Soc.* **1998**, *120*, 2650-2651.

INVESTIGATION OF HYDROFORMYLATION OF OLEFINS IN SUPERCRITICAL CARBON DIOXIDE USING PHOSPHINE MODIFIED RHODIUM CATALYST

Can Erkey, Daniel R. Palo, and Shaker Haji

Department of Chemical Engineering
University of Connecticut
191 Auditorium Road, U-3222
Storrs, CT 06269

Introduction

Over 6 million tons of aldehydes are produced annually by homogeneous catalytic hydroformylation of olefins. The shares of various aldehydes are C_3 (2%), C_4 (73%), C_5-C_{13} (19%) and C_{13}-C_{18} (6%).[1] The catalysts are of the form $H_xM_y(CO)_zL_n$; the two transition metals utilized are rhodium and cobalt and the most commonly utilized ligands are phosphines (PR_3 where R=C_6H_5 or n-C_4H_9). Production of C_4 aldehydes from hydroformylation of propene are dominated by rhodium based catalysts whereas higher aldehydes are produced mainly by catalysts based on cobalt. Since rhodium is about 10,000 times more active than cobalt, processes based on Rh catalysts operate at significantly lower temperatures and pressures than processes based on Co catalysts. For example, the UCC liquid recycle process for hydroformylation of propene which uses $HRh(CO)(P(C_6H_5)_3)_3$ operates in the temperature range 85-90 ^oC and at 18 bar. On the other hand, the BASF process for hydroformylation of 1-octene which uses $HCo(CO)_4$ operates in the temperature range 160-190 ^oC and in the pressure range 250-300 bar. Therefore, substantial savings in operating and capital costs can be achieved if hydroformylation of higher olefins are conducted using Rh based catalysts.

One of the difficulties associated with switching to Rh is the difficulty of the separation of products and catalyst by distillation of the aldehydes. The high boiling points of aldehydes beyond C_7 makes such an operation impractical even under reduced pressure due to thermal stability considerations for the catalyst. A relatively recent development in this field has been the commercialization of a biphasic hydroformylation process by RCH/RP.[1] In this process, the hydroformylation reaction is conducted in the aqueous phase using water-soluble rhodium complexes as catalysts, thus eliminating the problem of separating the catalyst from the product mixture. The process is utilized for production of C_4 and C_5 aldehydes, however application of this concept to higher olefins is highly unlikely due to extremely low solubilities of higher olefins in water. An alternative may be to utilize supercritical fluids as solvents in hydroformylation reactions.

A supercritical fluid (SCF) is a fluid that has been heated and compressed above its critical temperature and pressure. At these conditions, SCFs have densities that are greater than those of gases but comparable to those of liquids, which enable them to function as solvents. Using SCFs as solvents may have great advantages in catalyst recovery. The solubility of solutes in SCFs are strong functions of temperature and pressure in the vicinity of the critical point. Therefore, the catalyst, products and reactants may be separated in an efficient manner through temperature and/or pressure programming. Among the SCFs, supercritical carbon dioxide ($scCO_2$) is particularly attractive as a solvent since it is non-toxic, environmentally acceptable, cheap, readily available in large quantities and has a low critical temperature and a moderate critical pressure. It is non-flammable unlike some other SCFs such as ethane and propane, thus its use does not constitute a safety hazard. Today, there are many $scCO_2$ extraction plants operating around the world thereby indicating the technical and economical feasibility of carbon dioxide based processes. In this preprint we report the results of our investigations of hydroformylation of higher olefins in $scCO_2$ using $HRh(CO)L_3$ where L is a fluoroalkyl- or fluoroalkoxy-substituted arylphosphine.

Experimental

Experimental apparatus. A schematic diagram of the experimental apparatus is given in Figure 1. Hydroformylation reactions were conducted batchwise in a custom manufactured, 51.5 mL stainless steel reactor fitted with two sapphire windows (1" ID, Sapphire Engineering, Inc.), poly-ether-ether-ketone o-rings (Valco Instruments, Inc.), a T-type thermocouple assembly (Omega Engineering, DP41-TC-MDSS), a pressure transducer (Omega Engineering, PX300-7.5KGV), a vent line, and a rupture disk assembly (Autoclave Engineers). The reactor rests on a magnetic stir plate and heated to appropriate temperatures by a circulating heater (Fisher Scientific) via a machined internal heating coil. The reactor is pressurized with CO_2 from a syringe pump (ISCO, 260D) equipped with a cooling jacket to the desired reaction pressure. Samples can be obtained via a sampling loop with the arrangement shown below. A high-pressure-high temperature FTIR sampling head can be screwed through the reactor body to reach inside the reactor.

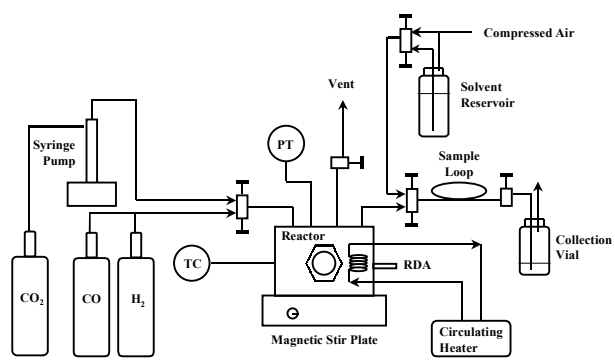

Figure 1. Schematic diagram of the experimental setup.

Catalysts preparation and the hydroformylation experiments. All the phosphines were synthesized from the corresponding perfluoroalkyl- or perfluoroalkoxy-substituted aryl bromides as described earlier.[2] The different forms of the catalyst $HRh(CO)L_3$ were formed in situ under hydroformylation conditions from $Rh(CO)_2(acac)$ and the specified ligand. For each hydroformylation experiment, $Rh(CO)_2(acac)$ (0.65 x 10^{-5} mol), ligand (2.0 x 10^{-5} mol), and 1-octene (0.054 mol) were charged to the reactor under nitrogen. The reactor was then sealed, heated to reaction temperature (50 ^oC), and charged with H_2/CO (0.055 mol each). Finally, CO_2 was charged to the reactor, bringing the total pressure to 273 atm. Periodic samples taken during each reaction were analyzed by gas chromatography.

Results and Discussion.

We synthesized and characterized several fluoroalkyl- or fluoroalkoxy-substituted arylphosphines and investigated the effect of ligand modification for homogeneous hydroformylation of 1-octene in $scCO_2$. The variation of 1-octene concentration with time for all the different phosphines are given in Figure 2.

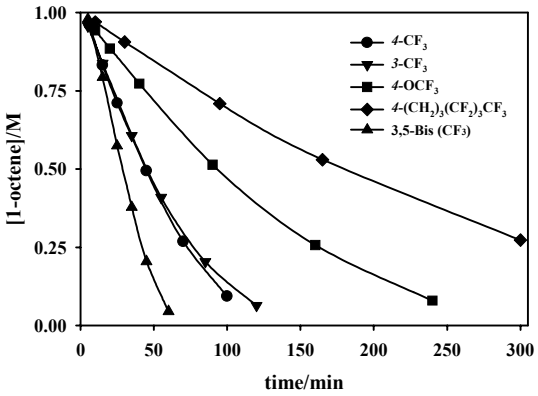

Figure 2. Hydroformylation of 1-octene using $HRh(CO)L_3$: P = 273 atm, T = 50 °C, $[1\text{-octene}]_0$ = 0.95 M, $[H_2]_0 = [CO]_0$ = 1.1 M, [Rh] = 1.27 mM, [P]/[Rh] = 3.0.

The activity of the rhodium complex (formed *in situ* from $Rh(CO)_2(acac)$ and L) increased with decreasing basicity of the phosphine according to the series $P[3,5\text{-}(CF_3)_2C_6H_3]_3$ > $P(4\text{-}CF_3C_6H_4)_3$ ≈ $P(3\text{-}CF_3C_6H_4)_3$ > $P(4\text{-}CF_3OC_6H_4)_3$ > $P[4\text{-}F(CF_2)_4(CH_2)_3C_6H_4]_3$. Among the various catalyst systems, the initial rates of reaction differed more than 5-fold between the fastest and the slowest. The rate of hydroformylation correlated very well with the IR stretching frequency of metal carbonyls, ν(CO), for the various catalysts, showing a linear dependence. The ν(CO) is a sensitive indicator of electron density at the metal center, yielding a relative measure of the amount of π-backbonding from an occupied metal d-orbital to the empty π*-orbital of the carbonyl. The trend in ν(CO) corresponded well with the amount and proximity of the electron-withdrawing fluoroalkyl or fluoroalkoxy groups of the phosphines, with $P[3,5\text{-}(CF_3)_2C_6H_3]_3$ having the greatest effect and $P[4\text{-}F(CF_2)_4(CH_2)_3C_6H_4]_3$ having the least effect relative to the value for PPh_3. The phosphines $P(4\text{-}CF_3C_6H_4)_3$ and $P(3\text{-}CF_3C_6H_4)_3$ showed identical electronic behavior, and almost identical activity/selectivity behavior, while $P[3,5\text{-}(CF_3)_2C_6H_3]_3$, with a much higher ν(CO) value also had a significantly higher activity. The results were in agreement with an earlier report that the electronic effect of trifluoromethyl-substitution is independent of *ortho*-, *meta*-, or *para*- placement, and that the effects of multiple trifluoromethyl-substitutions are cumulative.[3] The ability of oxygen and methylene groups to insulate against the electron-withdrawing effects of the fluoroalkyl moieties could be observed for phosphines $P(4\text{-}CF_3OC_6H_4)_3$ and $P[4\text{-}F(CF_2)_4(CH_2)_3C_6H_4]_3$, where significant decreases in ν(CO) were accompanied by 50% and 70% decreases in activity, respectively. The results confirmed the observation by Leitner that methylene spacers effectively insulated the phosphorus lone pair from the electron-withdrawing effect of the fluoroalkyl chain,[4] and also showed that oxygen spacers exhibited a similar though less profound effect. While these spacers are effective insulators, they actually decrease the catalytic activity relative to "non-insulated" phosphines.

Extensive in situ FTIR studies were carried out for the catalyst with the highest activity, the one with $P[3,5\text{-}(CF_3)_2C_6H_3]_3$ as ligand. The intermediates of the reactions of $RhH(CO)[P(3,5\text{-}(CF_3)_2C_6H_3)_3]_3$ **1** with CO, H_2, C_2H_4 and mixtures of these in dense carbon dioxide were monitored. The results were compared to the behavior of the conventional catalyst, $RhH(CO)(PPh_3)_3$ **2**, in organic solvents.[5,6,7] Comparing the IR spectra of **1** in solid form with that in solution in $scCO_2$ at 50 °C and 115 bar (2039 and 1952 cm^{-1} vs. 2041 and 1964 cm^{-1}), its concluded that $RhH(CO)L_3$ **1** does not dissociate in $scCO_2$ like **2** does in organic solvents. This indicates a stronger metal-ligand bond in **1** compared to **2**. The strong bond could be attributed to a strong π-backbonding from an occupied metal d-orbital to the empty π*-orbital of the ligand caused by the high electronegative trifluoromethyl groups attached to it. However, **1** was converted to $RhH(CO)_2L_2$ **3** and to $[Rh(CO)_2L_2]_2$ **4** in the presence of CO in $scCO_2$. When hydrogen was added to such mixture, $RhH(CO)L_2$ **5** was produced. The last three species (**3**,**4**, and **5**) existed in equilibrium with each other. Another strange behavior was noticed in the reaction of **1** with an equimolar mixture of CO and H_2. In the presence of 1:1 mixture of CO/H_2, **1** underwent ligand dissociation to form $RhH(CO)L_2$ **5**, however, the presence of equimolar H_2 prevented further coordination of CO to form the dicarbonyl species $RhH(CO)_2L_2$ **3**. In the presence of CO and C_2H_4, the peaks observed in the acyl region and the terminal carbonyl region indicated the formation of $Rh(CO)_2L_2(COEt)$ **6**. In the ethylene hydroformylation reaction, **6** was observed again at 14 °C, however, its concentration reduced as the reaction proceeded with heating. After the completion of the reaction both $RhH(CO)_2L_2$ **3** and $RhH(CO)L_2$ **5** co-existed in the presence of excess CO/H_2. After depressurizing the reaction mixture, NMR spectra showed that most of the catalyst species, presented in the reaction mixture, converted back to the original form of **1**. The carbonyl stretching frequencies of all of the rhodium-carbonyl species were shifted to higher wave numbers due to a reduction of electron density at the metal center by the CF_3 groups.

Acknowledgement

This work was partially supported by Petroleum Research Fund, administered by the ACS (ACS-PRF 32299-AC1). The authors also gratefully acknowledge the National Science Foundation for its grant (CTS-0080823).

References

[1] Frohning, C. D.; Kohlpaintner, C. W. In *Applied Homogeneous Catalysis with Organometallic Compounds*; Cornils, B., and Herrmann, W. A., Eds.; VCH: Weinheim, 1996; pp. 29.
[2] Palo, Daniel R.; Erkey. C. *Organometallics* **2000**, 19, 81.
[3] Howell, J. A. S.; Lovatt, J. D.; McArdle, P.; Cunningham, D.; Maimone, E.; Gottlieb, H. E.; Goldschmidt, Z. *Inorg. Chem. Commun.* **1998**, 1, 118.
[4] Kainz, S.; Koch, D.; Baumann, W.; Leitner, W. *Angew. Chem., Int. Ed. Engl.* **1997**, 36, 1628.
[5] Evans, D.; Wilkinson, G. *J. Chem. Soc. (A)* **1968**, 2660.
[6] Brown, C. K.; Wilkinson, G. *J. Chem. Soc. (A)* **1970**, 2753.
[7] Moser, W.R.; Papile, C.J.; Brannon, D.A.; Duwell, R.A.; Weininger, S.J. *J.Mol.Catal.* **1987**, 41, 271.

TRANSESTERIFICATION OF DIMETHYL OXALATE AND PHENOL OVER TS-1 CATALYST

Xinbin Ma, Shengping Wang, Hongli Guo, Genhui Xu

State Key Laboratory of C_1 Chemistry and Technology,
School of Chemical Engineering and Technology, Tianjin University,
Tianjin 30072, China

Introduction

Polycarbonates (PCs) are excellent engineering thermoplastics and substitutes for metals and glass because of their good impact strength and transparency [1]. In recent years, there has been an increasing demand for safer and environmentally friendly processes for PC synthesis. Non-phosgene based processes have been proposed to replace the traditional phosgene process [2]. One such process is composed of the synthesis of diphenyl carbonate (DPC) followed by the transesterification between DPC and bisphenol A. Several alternative methods for DPC synthesis have been developed or proposed. Among them, the transesterification of dimethyl oxalate (DMO) and phenol via three-step reaction has been considered as one of possible routes for DPC synthesis from the raw materials such as carbon monoxide, phenol and oxygen [3-4]. In the first step, dimethyl oxalate is produced by carbonylation of methanol, as shown in equation (1), and in the second step, diphenyl oxalate (DPO) is obtained from transesterification of dimethyl oxalate and phenol, as shown in equation (2), and in the third step, the decarbonylation of DPO, as shown in equation (3), is carried out to produce DPC and by-product carbon monoxide.

$$2CO + 2CH_3OH + 1/2O_2 \rightarrow (COOCH_3)_2 + H_2O \quad (1)$$

$$(COOCH_3)_2 + 2PhOH \rightarrow (COOPh)_2 + 2CH_3OH \quad (2)$$

$$(COOPh)_2 \rightarrow CO(OPh)_2 + CO \quad (3)$$

Usually, the transesterification of DMO and phenol in reaction (2) is carried out in the liquid phase using homogeneous catalysts such as Lewis acid and soluble organic Pb, Sn, or Ti compounds [3-4]. But the separation of the catalysts from the products will be complicated when these catalyst systems are applied to the industrial process. There are few reports on the development of active heterogeneous catalysts for the reaction. Hence we report that the titanium silicate molecular sieve TS-1 is an excellent solid catalyst for this reaction. It is well known that TS-1 is active in a variety of oxidation reactions. Reported herein is a new aspect of TS-1 as an acid catalyst.

Experimental

The TS-1 obtained from SINOPEC Research Institute of Petroleum Processing were dried in an oven at 393K for 2h to remove the absorbed water and calcined at different temperature for 2h in the air.

Ester change reactions were performed by mixing DMO, phenol and catalyst TS-1 1.8 g in a 250 ml glass flask equipped with a thermometer, a stirrer under refluxing conditions at atmosphere pressure. Identification and quantitative analysis of reaction products were carried out by a GC-MS spectrometer of HP 5890-HP5971MSD and a gas chromatograph equipped with a flame detector (FID). An OV-101 packed column was used to separate products for GC analysis.

The specific surface areas of the catalysts were determined using a constant volume adsorption apparatus (CHEMBET-3000) by the N_2 BET method at the liquid nitrogen temperature. Powder X-ray diffraction (XRD) measurements were conducted on a MAC Science Co. Model D/Max-2500 X-ray diffractometer using a radiation source of Cu Kα at 40 kV and 100 mA with a scanning rate of 8° min^{-1}.

Results and Discussion

In catalysts screening experiments, it was found that TS-1 is one of the most efficient catalysts for the transesterification of dimethyl oxalate and phenol. It was observed that methylphenyl oxalate (MPO) as an intermediate was produced, which is the same as the case with homogenous catalyst. It proved that DPO have been synthesized via a two-step reaction module from DMO and phenol since the direct synthesis of DPO is limited due to low equilibrium constants as the same as the transesterification of dimethyl carbonate and phenol. The first step, transesterification of DMO and phenol proceeds as shown in reaction (4) and formed MPO is disproportionated into DPO and DMO in reaction (5).

$$(COOCH_3)_2 + PhOH \rightarrow PhOOCOOCH_3 + CH_3OH \quad (4)$$

$$2PhOOCOOCH_3 \rightarrow (COOPh)_2 + (COOCH_3)_2 \quad (5)$$

The selectivity of the MPO and DPO (%) are defined as the moles of MPO and DPO produced per 100 mole of consumed DMO, and the yield of the MPO and DPO (%) are obtained from multiplication of phenol conversion by MPO selectivity and DPO selectivity, respectively.

It was observed that little by-products were anisole, which could be produced via methylation of phenol and DMO, when TS-1 was used in the ester change reaction of the DMO and phenol. The catalyst TS-1 performed significantly better than the other catalysts as shown in Table 1. The sum of the MPO selectivity and the DPO selectivity based on DMO of the catalyst TS-1 could reach 97.5% when the other catalyst only have 20~30%. Although the $Ti(OC_4H_9)_4$ and $AlCl_3$ showed good activities according to the conversion of the DMO, but the selectivity to MPO and DPO are poor. When the $Ti(OC_4H_9)_4$ was chosen as the catalyst of the transesterification of the DMO and phenol, the major by-products were n-butyl alcohol, n-butyl ether, butylphenyl oxalate and ethyl benzene, the selectivity to by-products was more than 76.5%. It was also observed the major by-products were anisole when the $AlCl_3$ and $MgCl_2$ as catalyst, the selectivity to anisole could reach 70%. Overall, the TS-1 was an efficient catalyst, giving a higher selectivity of MPO and little by-products were produced. However, the production of the DPO was much less than the MPO, indicating that DPO could not be obtained effectively through the disproportionation of MPO in the closed system.

Table 1. The Activities of the Different Materials

Catalyst	DMO conversion (%)	MPO selectivity (%)	DPO selectivity (%)
TS-1[a]	49.6	93.0	4.5
$Ti(OC_4H_9)_4$	92.5	20.6	2.8
$Zn(OAc)_2$	19.1	54.6	3.2
$MgCl_2$	30.5	19.7	0.0
$AlCl_3$	79.8	29.1	2.0

Reaction condition: 0.1 mol DMO, 0.5 mol phenol, 0.01 mol catalyst under refluxing conditions at 453K for 2h.
a: 1.8 g TS-1 calcined at 823K.

The activities of the transesterification reaction in the catalyst TS-1 calcined at 823K as function of the reaction time was shown in Table 2. The conversion of the DMO and the yield of MPO increased rapidly with the increase in the reaction time until 2 hours, beyond which the conversion of DMO didn't change and the yield of MPO decreased due to the disproportionation of MPO. The selectivity to

MPO was a constant of 92.6% at first, and then decreased slowly also due to the disproportionation of MPO. The yield and selectivity of DPO were not much more because the disproportionation of MPO is not favorable thermodynamically and the excessive phenol was used in the experiments. The yield and selectivity of DPO could be enhanced by combination of the common chemical method, such as the reactive distillation.

Table 2. Effect of the Reaction Time on the Activities for the Transesterification of DMO and Phenol over TS-1

Reaction time (h)	DMO conversion (%)	MPO selectivity (%)	MPO yield (%)	DPO selectivity (%)	DPO yield (%)
1	24.1	92.6	22.3	5.9	1.4
2	49.6	93.0	46.5	4.5	2.3
3	49.8	87.9	43.8	11.1	5.5
4	50.8	87.8	44.6	10.9	5.5

Reaction condition: 0.1 mol DMO, 0.5 mol phenol, 1.8 g TS-1 calcined at 823K under refluxing conditions at 453K.

Table 3 tabulates the activities of the catalysts TS-1for the ester change reaction of DMO and phenol as well as the calcination temperature. The selectivity to DPO decreased slowly with the increasing calcination temperature, and selectivity to MPO increased with the increase of the calcination temperature. The result showed that the conversion of DMO and the sum of selectivity to MPO and DPO did not show much variation with the calcination temperature. The conversion of DMO remained at 45~50%, and the sum of selectivity to MPO and DPO were more than 97.5%.

Table 3. Effect of the Calcination Temperature of TS-1 on the Activities for the Transesterification of DMO and Phenol

Calcination temperature (K)	DMO conversion (%)	MPO selectivity (%)	MPO yield (%)	DPO selectivity (%)	DPO yield (%)
723	47.7	86.8	41.4	11.9	5.7
773	50.6	89.0	45.0	9.0	4.6
823	49.6	93.0	46.5	4.5	2.3
873	45.1	93.0	41.9	4.6	2.1

Reaction condition: 0.1 mol DMO, 0.5 mol phenol, 1.8 g TS-1 under refluxing conditions at 453K for 2 hours.

It was also observed that the calcination temperature had not influence on the specific area of the catalyst TS-1, maybe one reason was because the TS-1 was also calcined at 773K for 4h in the factory in the past prior to catalyst thermal treatment by ourselves. The specific area of the catalyst TS-1 was generally 345 m^2/g. But after reaction the specific area of the catalyst TS-1 at calcined at 823K decreased to 295.5 m^2/g. The loss of the specific area of the catalyst TS-1 could be attributed to the carbon deposit. Studies on the influence of the coking on the activities of the catalyst TS-1 are ongoing to enhance and preserve the activity of the catalyst.

There are a large number of studies in the literature on the structure of TS-1 [5]. The XRD patterns of the sample TS-1 are similar too, and the calcination temperatures have no influence on the structure of the catalyst TS-1. The relation between the catalyst TS-1 structures and the activities for transesterification of dimethyl oxalate and phenol will be investigated in the future.

Conclusions

The titanium silicate molecular sieve TS-1 was an active heterogeneous catalyst for the transesterification of dimethyl oxalate and phenol. The sum of the methylphenyl oxalate selectivity and the diphenyl carbonate selectivity based on dimethyl oxalate of the catalyst TS-1 could reach 97.5%, with smaller by-product. The calcination had not obvious influence on the conversion of dimethyl oxalate and the sum of selectivity to methylphenyl oxalate and diphenyl oxalate.

Acknowledgement. This work was supported by foundation for University Key Teacher by the Ministry of Education and the Department of Science and Technology of Yunnan Province for the project on Technology Collaboration and Development in China.

References

(1) Freitag, D.; Grigo, U.; Müler, P.R.; Nouvertné, W. in: Mark, H.F.; Bikales, N.M.; Overberger, C.G.; Menges, G. (Eds.). Encyclopeia of Polymer Science and Engineering, Second ed., Vol. 11, Wiley, New York, 1988, p. 648
(2) Ono, Y. *Pure Appl. Chem.* **1996**, 68, 367.
(3) Keigo, N.; Shuji, T.; Katsumasa, H.; Ryoji, S.; U.S. Patent 5834651 (1998).
(4) Keigo, N.; Shuji, T.; Katsumasa, H.; Ryoji, S.; Akinori, S.; Katsutoshi, W.; U.S. Patent 55922827 (1999).
(5) Notari B. *Stud. Surf. Sci. Catal.* **1987**, 37, 413.

STRUCTURAL EVOLUTION AND SITE REQUIREMENTS FOR FISCHER-TROPSCH SYNTHESIS CATALYSTS BASED ON Fe OXIDES PROMOTED WITH Cu, Ru, OR K

Senzi Li, Sundaram Krishnamoorthy, George D. Meitzner, and Enrique Iglesia

Department of Chemical Engineering, University of California at Berkeley, Berkeley, CA 94720

The effects of different promoters (Ru, Cu, ZnO, and K_2CO_3) on the density and structure of active sites for the Fischer-Tropsch synthesis (FTS) was studied. The structure, reduction and carburization behavior, and catalytic properties of the catalysts were examined using a combination of isothermal kinetic transient and spectroscopic methods including on-line mass spectroscopy, *in-situ* X-ray absorption spectroscopy, and steady-state FTS catalytic rate measurements. Isotopic jump and site titration methods were used to estimate the density of active sites, to establish the identity and reversibility of elementary steps, and to confirm the structure-function rules suggested by the kinetic and spectroscopic methods.

Fe-based catalysts were prepared by co-precipitation of Fe and Zn (Zn/Fe=0.1) nitrates with $(NH_4)_2CO_3$ to form porous mixed oxides, which were subsequently impregnated with Cu (Ru) nitrate or K carbonate solutions (M/Fe=0-0.04, M=Cu, K, or Ru), similar to the procedure used in another study [1]. Displacing intrapore water with alcohol before drying the precipitate and decreasing the treatment temperature from 673 K to 543 K increased the surface area of Fe-Zn-K-Cu oxides from 65 to 120 m^2/g. These procedures appear to prevent pore mouth pinching during by decreasing the surface tension of intrapore liquids.

The reduction of Fe_2O_3 to Fe_3O_4 in H_2 in Fe-Zn-K-Cu (Ru) precursors is faster than on Fe-Zn-K samples; Cu and Ru reduce at low temperatures and provide H_2 dissociation sites unavailable on Fe_2O_3. Oxygen removal and carbon introduction rates during exposure of Fe-Zn-K-Cu (Ru) oxides to CO showed that such processes occur sequentially via Fe_2O_3 reduction to Fe_3O_4, incipient removal of a minority of the O-atoms in Fe_3O_4, and rapid carburization of such oxygen-deficient species to form a □-$Fe_{2.5}C$ and □-Fe_3C mixture at 540 K or pure □-Fe_3C at around 720 K. Cu and Ru increased the rate of oxygen removal from Fe_2O_3 and Fe_3O_4 and thus the rate of formation of FeC_x. K, present as a carbonate, inhibited oxygen removal but increased the rate of carbon introduction, apparently by increasing CO dissociation rates on FeO_x or FeC_x surfaces.

Mass spectrometric analysis of the products formed during initial exposure of oxide precursors to H_2/CO mixtures at 523 K detected the initial removal of oxygen and a concurrent increase in FTS rates as oxygen was removed and carbon introduced. Steady-state rates were obtained after an initial induction period during which only 1-2 equivalent oxygen monolayers are removed (10^{19} O-atoms/m^2) from the Fe_2O_3 precursors. Pre-reduced (Fe_3O_4) and pre-carburized FeC_x (Fe/C=2.5~3) did not show the induction period or the rapid initial removal of oxygen as H_2O and CO_2 observed on Fe_2O_3 precursors. FTS remained constant even as slow removal of oxygen and introduction of carbon continued to occur on Fe_3O_4. This indicates that the formation of an active surface occurs within a few FTS turnovers, irrespective of the initial presence of Fe_3O_4 or FeC_x (Fe/C=2.5~3). The catalytic properties of the resulting surface are not influenced by the remaining presence of an oxide or carbide bulk. This active surface is likely to consist of a steady-state mixture of vacancies, adsorbed CO, and carbon and oxygen atoms formed in CO dissociation steps. Their relative concentrations are rapidly established by FTS elementary steps and depend on the redox properties of the contacting gas phase, the reaction temperature, and the surface concentrations of chemical promoters.

In-situ Fe K-edge X-ray absorption (XAS) studies confirmed the phase transformation from Fe_2O_3 to Fe_3O_4 and then to FeC_x during the initial stages of FTS reactions. Only the incipient conversion of Fe_2O_3 to Fe_3O_4 and Fe_xC was required in order to reach steady-state FTS rates. The extent of carburization increased with time on stream without a detectable increase in FTS reaction rates, confirming that the catalytic properties of Fe carbides are not influenced by a remaining Fe oxide core or by its ultimate carburization. Cu, K and Ru all increased the rate and the extent of carbide formation. The promoting effects of K, Cu, and Ru on FTS reaction rates (described below) appear to correlate with their ability to increase the rate and the extent of reduction and carburization of Fe_2O_3 precursors. Localized Fe_2O_3 surface regions influenced by the presence of Cu, Ru, or K species may provide multiple nucleation sites for reduction and carburization within each Fe_2O_3 precursor crystallite with the eventual formation of smaller oxide and carbide particles from larger Fe_2O_3 precursor particles. This proposal is consistent with the greater extent of carburization obtained when K and Cu (Ru) are present.

The effects of promoters (K, Cu and Ru) on FTS rate and selectivity were determined using a fixed-bed reactor in the 493-543 K temperature range and 5-31.6 atm pressure with a H_2/CO mixture (2/1). Addition of Cu considerably improves FTS activity of the catalyst by decreasing the temperature required for the formation of active Fe_xC structures. At 508 K and 21.4 atm for example, the CO rate doubled with the addition of Cu (Cu/Fe=0.01) to a Fe-Zn-K (Zn/Fe=0.1, K/Fe=0.01) catalyst (1.3 to 2.6 mol/h-mol Fe at 20% CO conversion). Copper also promotes the hydrogen availability on the catalyst surface and hence decreases product molecular weight. Potassium improves both the activity and the selectivity of the FTS by increasing the amount of chemisorbed CO and decreasing the amount of chemisorbed H_2 on Fe-based catalysts. The promotion effect of K, however, is much more pronounced on a Cu-promoted catalyst than on a Cu-free catalyst, suggesting a synergistic effect of Cu and K, in agreement with a previous study [1]. Cu and K also significantly promote CO_2 formation during the FTS reaction. Replacement of the Cu by Ru in the Fe-Zn-K system led to a significant promotion of the FT rate (CO rates being 2.7 and 6.7 mol/h-mol Fe respectively at 20% CO conversion and 508 K) with negligible change in the product selectivities. This effect can be attributed to the better dispersion of the Fe_xC structure in the presence of Ru. Furthermore, an increase in surface area in the case of the Fe-Zn-Cu-K catalyst also markedly increases FT rates (CO rates being 2.7 and 6.8 mol/h-mol Fe respectively at 20% CO conversion and 508 K) due to a corresponding increase in the availability of the active Fe_xC sites.

Iron-based catalysts with high Fischer-Tropsch synthesis (FTS) rates were prepared by using promoters (K, Ru, Cu) and synthesis and activation protocols that favor the nucleation of small Fe carbide crystallites and inhibit sintering of oxide catalyst precursors during synthesis and activation. The effect of promoters on reduction/carburization behavior, on Fischer-Tropsch synthesis (FTS) rates, and on the number of CO binding sites formed during reaction

were examined by combining steady-state and transient rate measurements, titration of active sites, and X-ray absorption spectroscopy. K, Ru, and Cu promoters increased reduction/carburization rates of Fe-Zn oxide precursors, steady-state FTS rates, and the number of CO binding sites present after activation and FTS. These promoters increased the number of active sites formed during activation by favoring the nucleation of smaller Fe_3O_4 and Fe_xC domains as Fe_2O_3 precursors convert to active catalysts during initial contact of oxide precursors with synthesis gas. These smaller crystallites, in turn, provide higher surface areas, a larger number of CO binding sites, shorter diffusion distances for oxide-carbide transformations, and higher steady-state FTS rates. The number of active sites and the rates of FTS reactions were also increased by using surface-active alcohols to minimize sintering of Fe-Zn oxide precursors during thermal treatment of precipitated oxide precursors. The hydrocarbon synthesis rates using Fe-Zn-Cu-K catalysts prepared by this method were similar to those on representative Co-based catalysts (at 473 K; 2.0 MPa) when compared on the basis of catalyst mass and significantly higher on a volume basis. Fe-Zn-Cu-K catalysts showed significantly lower CH_4 selectivities than Co-based catalysts and much weaker effects of temperature and of synthesis gas composition on CH_4 and C_{5+} selectivities. The CO_2 selectivity is lower than on previously reported Fe-based catalysts, predominately because of the lower reaction temperatures made possible by the high FTS reaction rates on the promoted Fe catalysts reported in this study

1. S. Soled, E. Iglesia, S. Miseo, B. A. DeRites and R. A. Fiato, *Topics in Catalysis* 2 (1995) 193.

Reaction Behavior of Fischer-Tropsch Synthesis in Near Critical and Supercritical Hexane Media

*Xiwen Huang, Christine W. Curtis, Christopher B. Roberts**

Department of Chemical Engineering
Auburn University
Auburn, AL, 36849

Introduction

Supercritical fluids (SCFs) can offer certain advantages over traditional solvents for catalytic reactions including the ability to manipulate the reaction environment through simple changes in pressure to enhance solubility of reactants and products, to eliminate interphase transport limitations, and to integrate reaction and separation unit operations. SCF solvents offer attractive physical properties including; low viscosity and high diffusivity resulting in superior mass transfer characteristics; low surface tension enabling easy penetration into the pores of a solid matrix (catalyst) for extraction of nonvolatile materials from within the pores; high compressibility near the critical point inducing large changes in density with very small changes in pressure and/or temperature enabling separation of the dissolved material easily and completely. These unique properties of SCFs have been exploited to provide many opportunities for the design of heterogeneous catalytic reaction systems such as ethylene polymerization, ammonia synthesis and methanol synthesis.

The advantages of SCF-phase Fischer-Tropsch (FT) synthesis (SCF-FT) include gas-like diffusivities and liquid-like solubilities which together combine the desirable features of the gas- and liquid-phase FT synthesis routes[1-5]. The supercritical phase reaction can also (1) reduce production of undesirable products; produce less methane because of better distribution of heat in the reactor; (2) produce more long-chain olefins as a result of the enhanced solubility of these higher hydrocarbons in the SCF; (3) mitigate deactivation of the catalyst through better heat and mass transfer; (4) provide in-situ extraction of heavy hydrocarbons from the catalyst surface and their transport out of the pores thereby extending catalyst lifetimes; (5) enhance pore-transport of the reactants such as hydrogen to the catalyst surface thereby promoting desired reaction pathways; (6) enhance desorption of the primary products preventing secondary reactions that adversely affect product selectivity.

In this paper, we will investigate the FT reaction under supercritical hexane conditions in a continuous, high pressure, fix-bed reactor by employing a cobalt catalyst (15%Co-0.5%Pt-Al_2O_3). The effect of SCF conditions on syngas conversion, product distribution and olefin selectivity will be presented in order to demonstrate improvements in process parameters under SCF-FT operation versus gas phase operation. In addition, the effects of isothermal pressure-tuning on the catalyst activity, product distribution, and olefin selectivity will be examined. In the near critical and supercritical region, optimal combinations of product desorption and pore transport can be obtained. Finally, the syngas space velocity was varied to determine whether the primary and/or secondary reaction steps are diffusion controlled.

Experimental

Reactor Design. The reactor (HIP Equipment, Erie, Pa) used in this study is a conventional downflow fixed bed reactor. The cobalt catalyst (United Catalyst Inc.) is fixed in the middle of the fixed-bed. To fix the catalyst in place, a 15mm (diameter), 2-3mm (thickness) and 4-15micron (porosity) fused quartz disc (Quartz Plus, Inc.) is put inside the reactor. In order to position the disc in the middle of the reactor, the inner diameter of the reactor above the disc was machined exactly to match the disc diameter, which is a little larger than the section underneath the disc. The quartz disc was employed to avoid the use of any Fe-containing metal near the reaction zone. A profile thermocouple with 6 equally-spaced thermocouple probes(OMEGA) is located along the axial reactor tracking the temperature distribution in the reactor.

Delivery, Reaction and Analysis Systems. Syngas (AirProducts) flow rate was controlled by a mass-flow controller (5850E Brooks) and hexane was delivered through an HPLC pump (Acuflow Series III, Fisher). The hexane and syngas were combined in the static mixer (OMEGA) before entering the reactor. The reactor was situated in a furnace (Applied Test System Inc.) with a programmed temperature controller system. The reaction pressure is adjusted using a backpressure regulator (Tescom, Inc.) located between the reactor and a hot trap. After leaving the reactor, the products passed through a hot trap (200 ^oC) to condense some heavy components prior to the on-line GC analysis. All of the lines between the reactor outlet and the GC were heated to 200 ^oC preventing product condensation. Two GCs were used for the analysis system, which included; Varian 3300 GC with a capillary column (DB-5) and FID for the analysis of C2-C30 hydrocarbons and oxygenates; Varian CP-3800 with packed column (Hayes-DB100/120) and TCD for the analysis of permanent gases and C1-C3 hydrocarbons.

Reaction Procedure. The cobalt catalyst is so highly hygroscopic that it needed to be heated for an extended period of time (>24 h) at 150^oC to remove absorbed water. CO was used to reduce the catalyst at 280^oC, 100psi for 20hrs before the reaction initiated. Once the HPLC pump flow rate was checked to guarantee a steady-state flow rate, hexane flow is directed to the reaction system. With hexane flowing, the temperature and pressure of the reaction zone is raised to 250C and the particular pressure for the experiment. The hot trap and the transfer line to the GC were heated to 200C to absolutely insure the stream directed to the GC would experience no condensation while being directed to the GC.

Once the temperature and pressure were stabilized, the flow of syngas was initiated. The mass flow controller is set to the appropriate value and control commenced. All the reactions were continued until a steady-state with respect to conversion and selectivity are attained. When the reaction was halted, the syngas flow is stopped while maintaining the hexane flow. Once the FT products were no longer detected in the effluent, the pressure was reduced to 100psi and the flow of hexane is stopped, helium flow was started and the temperature of catalyst bed was allowed to drop to room temperature with helium flowing over it.

Reaction Conditions

Reactor	Stainless steel, D=1.27cm, L=25.4cm, V=32 cm^3
Catalyst	15%Co-0.5%Pt-Al_2O_3
Solvent	Hexane (Pc=29.7bar, Tc=233.7C), flowrate:1.0 ml/min
Syngas	Space velocity: 50 sccm/g cat; Ratio: H_2/CO: 2.0
Pretreatment	Reducing gas:CO; Flowrate: 50sccm; Time: 20 hr; Temperature: 280°C
Reaction Conditions	Temperature: 250^oC (1.07Tc); Pressure: 500psi, 600psi, 950psi, 1160psi Time: until steady state and keep steady state for 10h

Results and Discussion

1. Comparison of Gas-Phase and Supercritical Phase Fischer-Tropsch

1.1 Syngas Conversion. Figure 1 presents the syngas conversion in gas-phase and SCF-phase Fischer Tropsch synthesis. From this figure, we can see that the CO conversion is slightly higher in the supercritical phase than in the gas phase. This result suggests that the SCF-FT could increase the syngas conversion.

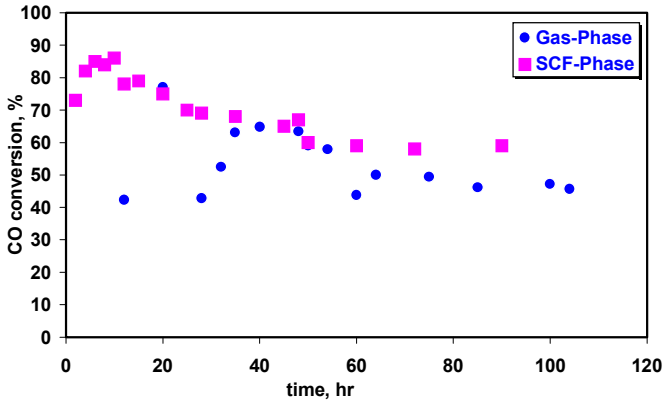

Figure 1. CO Conversion in Gas- and SCF-Phase Reaction. The pressure in the SCF phase reaction was 1160 psi and the pressure in the gas phase was 290 psi.

1.2 Hydrocarbon Distribution. Figure 2 and 3 presents the hydrocarbon distribution under gas- and SCF- phase operation. From these figures, we can see that in the supercritical phase, the whole hydrocarbon distribution diagram is shifted to a higher carbon number, and the methane content is decreased. Interestingly, the mass percents of C11 to C17 are fairly constant in the SCF experiment. The reason is that in the supercritical phase, the higher diffusivities and desorption rates of heavy hydrocarbons could cause the heavy product to diffuse easily from the catalyst bed along with the lighter compounds, rather than remaining in the catalyst.

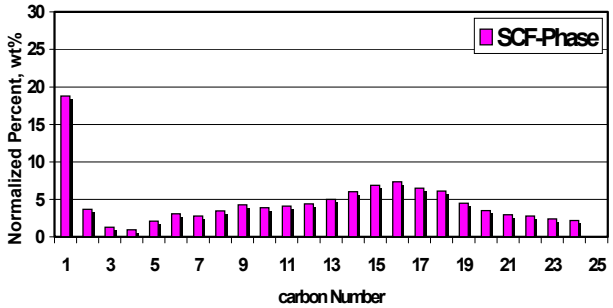

Figure 2. Hydrocarbon Distribution in SCF-Phase FT synthesis at 1160 psi.

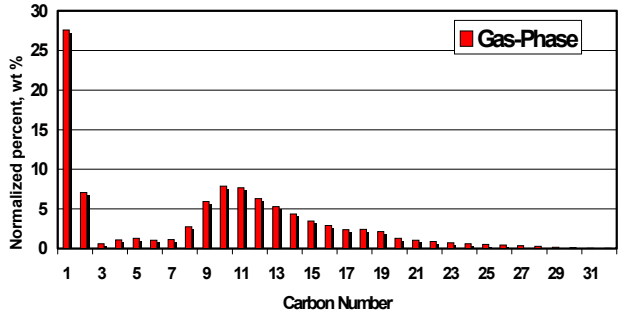

Figure 3. Hydrocarbon Distribution in Gas-Phase FT synthesis at 290 psi.

1.3 1-Olefin Selectivity. The initial product in the Fischer Tropsch reaction is the olefin species. In the case of mass transfer and heat transfer limitations, the olefin products can not flow out of the catalyst pores as soon as they are produced so as to cause many secondary reactions to take place, such as hydrogenation and isomerization to form paraffins. If the supercritical medium could improve the diffusivity and desorption rate of the product, then the secondary reactions would be reduced and the olefin selectivity would consequently increase. Figure 4 presents the olefin selectivity in the supercritical phase and gas phase. From this figure, we can see that the olefin selectivity in the SCF phase is obviously higher than in gas phase. This is in agreement with the situation discussed above. The enhanced selectivity of heavy olefins is due to the higher diffusivities and desorption rates. Without the intraparticle diffusion limitations, the primary products can leave the catalyst pores without undergoing secondary reactions.

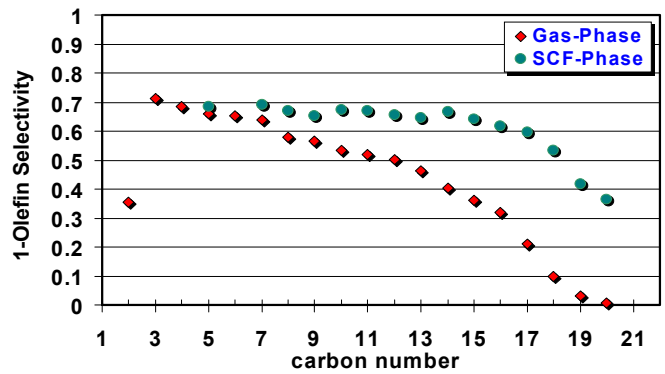

Figure 4. 1-Olefin Selectivity in Gas- and SCF-Phase FT synthesis

1.4 Temperature Distribution. The supercritical medium has a better heat removal ability compared to the gas phase. The FT reaction is an exothermic process in which a large amount of heat is given off during the reaction process. If the heat transfer process is so slow as to create excessive heat, then it will coke the catalyst shortening the catalyst lifetime. Figure 5 presents the temperature profile along the length of the reactor under both SCF phase and Gas phase operation. Thermocouple postion 3 is just above the catalyst bed and the distance between each thermocouple is 1.4 inches. The temperature deviation is from 247 to 261°C in the gas phase where the temperature deviation is only from 253 to 258°C in the SCF phase. Therefore, the temperature deviation is 3 times greater in the gas phase than in the SCF phase. It should also be noted that the CO conversion in the SCF phase experiment presented in Figure 5 was 70% where the conversion in the gas phase experiment was only 40%. Therefore, if the conversions were matched the temperature difference between the gas phase and SCF phase would be even more dramatic. From this we can conclude that a better heat transfer rate could be obtained in the supercritical reaction medium relative to the gas phase reaction.

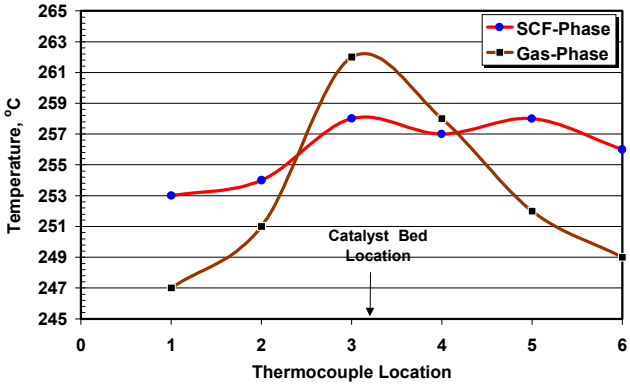

Figure 5. Temperature distribution in Gas- and SCF-Phase. The pressure in the SCF phase experiment was 1160 psi and the pressure in the gas phase experiment was 200 psi.

2. Effect of Pressure-tuning on the reaction behavior

According to Professor Subramaniam,[2] "the physical and transport properties of the fluid can be altered drastically from gas-like to liquid-like behavior, simply by isothermally varying the pressure around the critical pressure. At slightly above the critical pressure, while the fluid possesses roughly 70% of the liquid density, the diffusivity and viscosity are more gas-like. By pressure-tuning fluid properties around the critical pressure, optimal combinations of product desorption and pore transport can be obtained."

2.1 Syngas Conversion. Figure 6 presents the effect of pressure on the CO conversion. From this result we can see that the conversion increases with the pressure from 500psi to 950psi. As the pressure is increased the hexane medium posses a more liquid-like density enabling extraction of more heavy hydrocarbons from catalyst pores and maintains wider pore channels to reduce pore diffusion limitation. Meanwhile, this SCF environment maintains the high gas-like diffusivity. This combination results in the increase in conversion with increasing pressure up to 950psi. However, when the pressure is increased to a certain point (in our case 950psi), the conversion can not continue to increase. At this point it begins to decrease with a further increase in pressure. Beyond this transition point, the further increase in pressure still increased the hexane medium density which further increases the ability to extract heavy products. But, on the other hand, the bulk diffusivity decreases at these higher pressures and the comprehensive result is that the negative decrease in bulk diffusivity outweighs the positive enhancement in pore diffusivity. So, the conversion ceases to increase with further increases in pressure.

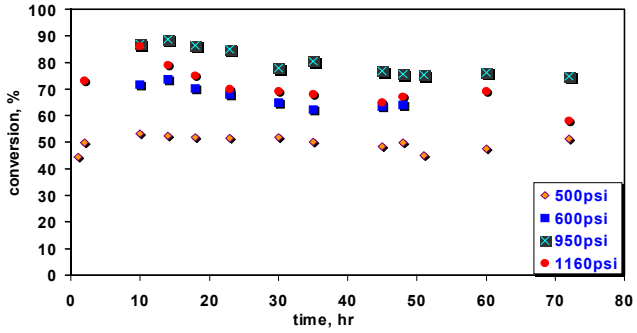

Figure 6. Effect of Pressure-Tuning on CO conversion.

2.2 Hydrocarbon Distribution Figure 7 presents the overall product carbon number distribution at different pressures in the SCF FT reaction. From this figure, we can see that at the higher operating pressure, more heavy hydrocarbon products could be obtained. This again supports the assertion that the decreased pore diffusion limitation at the high pressure is due to enhanced extraction of the heavier hydrocarbons by the more dense medium.

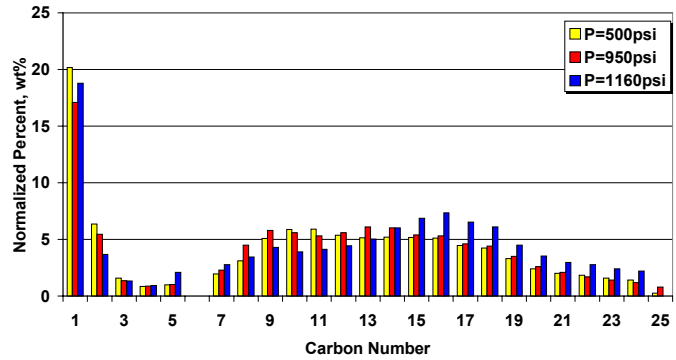

Figure 7. Effect of Pressure-Tuning on the Hydrocarbon Product Distribution in SCF FT synthesis.

2.3 1-Olefin Selectivity The effect of pressure on the olefin selectivity is also apparent in Figure 8. With an increase in pressure from 500 psi to 950 psi, the olefin content increases because of the improved extraction ability of the more dense medium. This results in an increase in pore diffusion efficiency, and an increase in the solubility of heavy products from the inner pores. This could result in a reduction in the readsorption of the 1-olefin thus reducing secondary reactions to form paraffin and 2-olefin products. Once the pressue was raised from 950 psi to 1160 psi, the 1-olefin content decreased. This also may be due to the decrease in bulk diffusivity of the product in the mole liquid-like medium at the highest pressure.

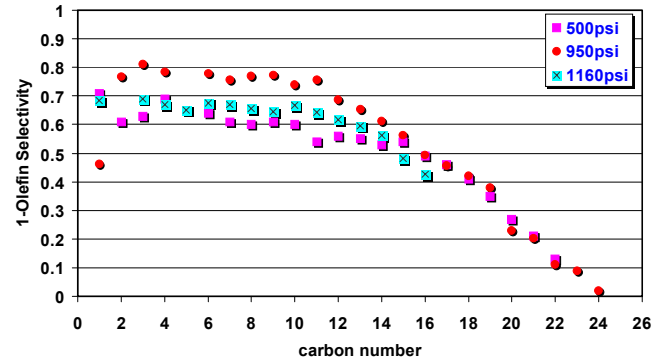

Figure 8. Effect of Pressure-Tuning on 1-olefin Selectivity

3. Gas Residence Time Effects

The effect of syngas residence time on the conversion was also examined. Figure 9 shows that there is no significant effect of syngas residence time on the CO conversion. This result is quite different from that obtained under gas-phase operation in which the conversion increases with a decrease in syngas residence time. The lack of effect of residence time on conversion in the supercritical phase reaction maybe a result of the improved pore diffusivity in the supercritical medium. Thus, the diffusion rate of product out of the catalyst pores is increase thereby leaving more active sites for CO and H2 causing the residence time effects become insignificant.

The effect of residence time on olefin selectivity is presented in Figure 10. Again, there is an insignificant effect of the residence time on the 1-olefin selectivity in the SCF phase. At high syngas

conversion, the effect of the solubility on the olefin selectivity is stronger than the effect of intraparticle diffusion. Therefore, there is little effect of residence time on the olefin selectivity. The olefin selectivity decreases with the increase in carbon number because the larger olefins spend more time in the catalyst pores than smaller ones due to the lower diffusivities. This increases the probability for secondary 1-olefin readsorption, double bond isomerization and hydrogenation reactions.[4] This suggests that the SCF-FT reaction is not diffusion controlled, however, the secondary olefin hydrogenation is diffusion limited.

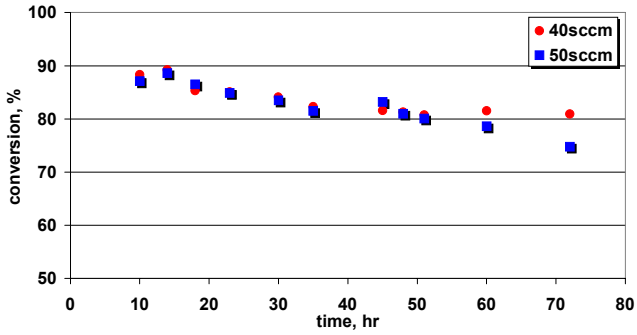

Figure 9. Effect of Syngas-Residence Time on CO Conversion at 950 psi.

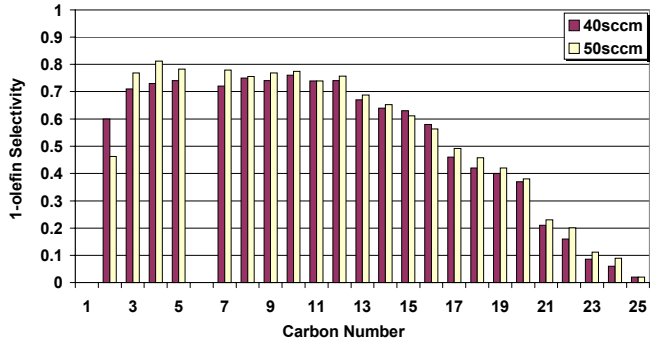

Figure10. Effect of Syngas-Residence Time on 1-olefin Selectivity at 950 psi.

Conclusions

Due to the increased diffusion and desorption rate of reactants and products in SCF phase Fischer Tropsch synthesis, the CO conversion and olefin content are higher than that in conventional FTS. Higher selectivity of the olefin products suggest that the SCF-FT operation results in higher pore diffusivities and more rapid removal of heavy 1-olefins from catalyst, thereby suppressing secondary hydrogenation and isomerization reactions. Over our experimental range, there exists an optimum operating pressure (P=950psi) that maximizes the conversion and the olefin selectivity. Better heat removal in SCF-FT compared to gas phase allows the catalyst bed temperature to be well controlled. There is little effect of syngas residence time on the syngas conversion and olefin selectivity in the SCF FT process. This demonstrates that the SCF-phase based Fischer-Tropsch reaction is not diffusion controlled.

Acknowledgement. Financial support by the U.S. Department of Energy, Fossil Energy Division, through the Consortium for Fossil Fuel Liquefaction Science is gratefully acknowledged. The authors would also like to thank Dr. Yoonkook Park for his valuable assistance in the reaction system built and other precious suggestions.

References

1. Li, F.; Fujimoto, K.; *Applied Catalysis A: General*; **1999**, 186, 343
2. Bala Subramaniam; *Energeia*; **1999**,10(3)1-4
3. Bala Subramaniam; *Industrial Engineering Chemistry Research;* **1997**, 36(10); 4413
4. Bukur, D.B.; Lang, X.; *Industrial Engineering Chemistry Research;* **1997;** 36(7); 2580-2587
5. Burt Davis; *Energeia*; **1997,** 8(3),1

Supercritical-phase process for selective synthesis of heavier hydrocarbons from syngas on cobalt catalysts

Jinglai Zhou[1] Shirun Yan[2] Zhixian Gao[1] Li Fan[3]
1: Institute of Coal Chemistry, Chinese Academy of Science. P.O. Box 165, Taiyuan, Shanxi030001, P.R. China
2: Department of Chemistry, Fudan University, Shanghai ,P.R. China
3: Department of Applied Chemistry, School of engineering, The University of Tokyo

Introduction

As an effective reaction for production of liquid fuels from coal and natural gas, Fischer-Tropsch (FT) synthesis has received great attention in past several decades. To be more promising and economically competitive, FT synthesis should be modified to shift the product spectrum from transportation fuel to valuable chemicals such as light olefin and heavier wax. Owing to its merits such as high melting point, low viscosity, as well as nitrogen-, sulfur-, and aromatics-free property, wax has been highly favored. However, selective synthesis of wax is not easy. It is believed that the readsorption and subsequent secondary reaction (hydrogenolysis, cracking, and reinsertion) of primary 1-olefin product are main reasons for the deviation from ASF distribution. To obtain an insight into secondary reactions of primary product, 1-olefin, and the mechanism of chain growing process, gas and liquid phase FT reaction over Fe, Co, Ru catalyst cofed with the 1-olefin ($C^{=}_2$, $C^{=}_3$, 1-$C^{=}_4$, 1-$C^{=}_6$, 1-$C^{=}_8$, 1-$C^{=}_{10}$, 1-$C^{=}_{20}$) have been studied extensively by many researchers[1-5]. It was found added 1-olefin, as a chain initiator, could combine CH_2 species on the catalyst surface, which lead to a decrease in methane formation and a increase in selectivity of hydrocarbons with one more carbon number than the added 1-olefin. But added olefin had no noticeable effect on the formation rate of heavier hydrocarbons and on the chain growth probability.

The supercritical phase FT synthesis cofed with medium-size 1-olefin (i.e. 1-tetradecene) over Co/SiO_2 catalyst, combining the characteristic of effective transportation of supercritical fluid and high readsorption probability of medium-size 1-olefin, have been carried out in our laboratory. Our results have shown that added 1-tetradecene could be remarkably involved in the chain growth process that was indistinguishable from the original chain growth. Consequently the formation rate of hydrocarbons larger than C_{14} increased markedly, while yield of C_1-C_{13} hydrocarbons decreased correspondingly. Effects of catalyst pore size, H_2/CO feed ratio, cofed olefin concentration were also investigated.

Experimental

Co/SiO_2 catalysts were prepared by impregnating SiO_2 with cobalt nitrate from its aqueous solution by incipient wetness method. The catalyst precursors were dried in air at 393K for 12hr and then calcined at 573K. Supercritical-phase FT reaction was carried out on a pressurized fixed-bed reactor system, accompanied with a high pressure pump which supplied the supercritical fluid (SCF) and 1-olefin during supercritical-phase reactions. Detailed description of reaction system was reported in our previous publication[6]. N-pentane was used as SCF., and Nitrogen was used as the balance material in gas phase reaction. The loading amount of catalyst was 0.5g. Prior to FT reaction, the catalyst was reduced with hydrogen under atmospheric pressure at 673K, 60ml/min for 12hr. Except noted, the reactions were conducted under standard conditions listed below. T=483K, P(total)=4.5Mpa, P(CO+H_2)=1.0MPa, W/F (syngas)=15g.h/mol. Argon was used as internal standard with concentration of 3% in the feed gas. The effluent gas was analyzed on line with two gas chromatographies. The condensed products were analyzed off-line with other two chromatographies.

Results and Discussion

1. Reaction Performance in Different Reaction Phase

Fig.1 and Table 1 present the effect of reaction phase on CO conversion and the hydrocarbon yield. It is found that CO conversion in supercritical phase was higher than that in gas phase and the yield of hydrocarbons, except methane, showed the same trend.

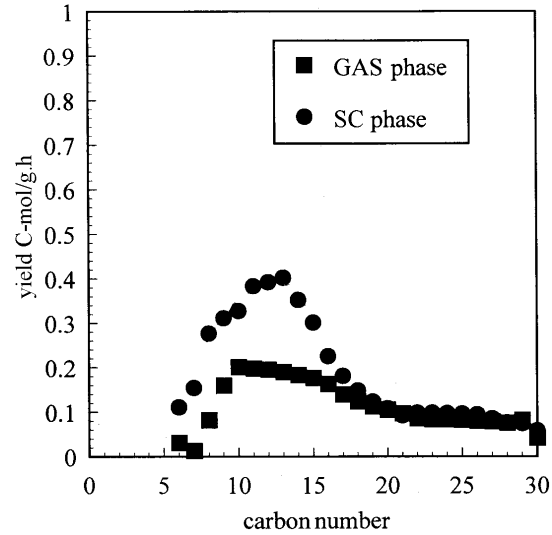

Fig.1. Phase effect on yield of hydrocarbons; Cat.3, W/F=15,210□, with out olefin addition

It is well known that in gas-phase FT reaction, after reaching the steady state, the catalyst pores were filled with heavier hydrocarbons in which CO and H_2 must be solved and subsequently diffused to reach the inner surface of catalyst. In supercritical phase FT reaction, due to the higher solubility of supercritical fluid, a large part of these heavier hydrocarbons could be solved and removed in situ by supercritical solvent whose density and viscosity are greatly smaller than those of the heavier hydrocarbons.

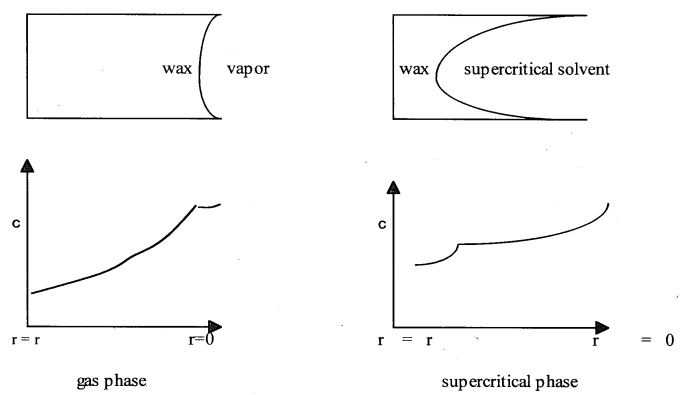

Fig.2. Visualized CO and H_2 concentration Profiles inside catalyst pores in different phases
Note: Represent the concentration of syngas inside pores

Consequently the transportation of CO and H_2 to the surface of catalyst was facilitated, and both the CO conversion and hydrocarbon yield were increased. CO and H_2 concentration profiles in different phase can be visualized in Fig.2. Meanwhile, because the large amount

of reaction heat could be removed efficiently by the SCF, formation of overheating spot on catalyst bed was prohibited and formation of methane, which was favored at high temperature, was also inhibited.

2. Effect of 1-tetradecene addition

Fig.3 and Table 2 exhibit the addition effect of 4 mole% (CO base) 1-tetradecene on CO conversion and hydrocarbons formation rate. It was found that CO conversion as well as light hydrocarbons (C_1-C_{13}) yield decreased, but the selectivity of hydrocarbons larger than C_{14} increased markedly with the addition of 1-tetradecene. As a result, C^+_{20} Yield was enhanced from 33.3% to 36.2% due to the addition of 1-olefin.

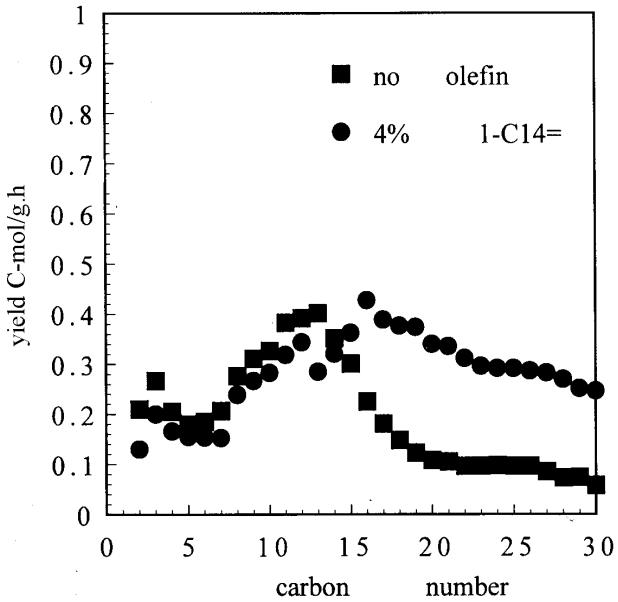

Fig.3. Effect of olefin addition on the distribution of products CO conversion: 85% (without olefin addition); 73% (with 4% 1-tetradecene addition);(CH_4 was not included)

Light olefin (C_2-C_{10}) addition to syngas and subsequent influence on reaction itself on cobalt catalysts had been well studied[17]. In recent years Iglesia[5] and kuipers[8,9] reported their cofeeding studies. Their results showed that 1-olefin addition of low concentration (5% mole) could inhibit the formation of methane but did not affect the value of the chain growth probability. But in our study where 1-olefin 4% mole was added increased the formation rate of heavier hydrocarbons noticeably as shown in Fig.3. The differences between previous olefin cofeeding studies and ours are molecule size of the added olefin and the reaction medium therein. In previous cofeeding studies, added light olefin was at gas phase under reaction conditions. In contrast, in our studies, supercritical fluid could greatly remove the wax in situ, which made the wax layer covered on the surface of catalyst much thinner than that for the gas phase reaction. And the added 1-tetradecene, which was at liquid state under reaction conditions, had higher solubility in wax layer than that of gaseous olefins. Thus the concentration of added 1-tetradecene in wax layer was relatively high and its adsorption probability on the catalyst surface and thus followed reinsertion reaction rate were also higher, which consequently increased the yield of hydrocarbons higher than C_{14}. Another interesting phenomenon in Fig.3 is that in the 1-tetradecene cofeeding experiment the yield of C_2 was much lower than that of C_3 while C_{16} were higher than C_{15}. This implies that probably species involved in growing chains was not limited to CH_2, and C_2H_4 may also be inserted. It is reported C_2H_4 is more active than C_3H_6[10], so the probability of being inserted was higher correspondingly. This phenomenon was also found by other investigators[3,11]. As for the CO conversion, since the adsorption of added 1-olefin would consume some H_2, and occupy some active sites which otherwise would be consumed and occupied by CO, the conversion level in the olefin-added reaction was lower than that of conventional reaction.

3. Influence catalyst pore size

The Co/SiO_2 catalysts with different pore size but the same amount of metal on specific surface area were also prepared and investigated. The properties and composition of catalysts and their reaction performance were compared in Fig.4 and Table 3. It is clear from the data in Fig.4 that the selectivity to the heavier hydrocarbons increased with increasing catalyst pore size, while the CO conversion decreased as shown in Table 3.

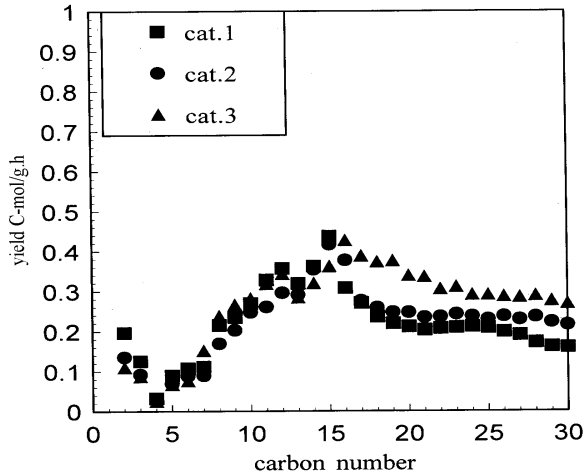

Fig.4. Catalyst pore size effect on yield of heavier hydrocarbon (see also Table3) Reaction conditions: T=483K, P(total)=4.5MPa, P(CO+H_2)=1.0MPa, W/F=15g.hr/mol, 4% (CO base) 1-tetradecene added

Because more effective mass transfer could be realized on the catalyst with large pores, it can be inferred that with the increase of pore size, the percentage of wax extracted in situ by the supercritical fluid increased correspondingly, while the thickness of wax layer covered on the surface of catalyst was reduced. Thus the diffusion of added 1-olefin inside the large-pore catalyst and its concentration in the wax layer was relatively higher than those for the catalyst with small pores, which consequently led to the higher adsorption probability of cofed olefin onto the catalytic sites. As a result, the selectivity to heavier hydrocarbons increased. One of the present authors have investigated the pore size effect on the performance of Ru/Al_2O_3 catalyst in supercritical phase FT synthesis, which proved that the chain growth probability increase with the increasing pore diameter of catalyst [6]. Meanwhile the acceleration in the heavier hydrocarbon formation may inhibit the formation of CO_2. So the CO_2 yield on catalyst with large-pore was greatly less than that on the small-pore catalyst.

4. Effect of olefin cofeeding concentration

Fig.5 shows olefin cofeeding concentration effect on the CO conversion and carbon number distribution of products. It was found that the yield of hydrocarbons heavier than C_{14} increased with increasing concentration of added 1-tetradecene while the CO conversion shown a reverse trend. This could be ascribed to the different probability of adsorption and thus-hence chain growth reaction of different cofed olefin concentrations. It is clear from the above discussion that addition of 1-tetradecene could enhance the

formation of hydrocarbons larger than C_{14}, while the formation of C_1-C_{13} was inhibit, thus increased the selectivity to heavier hydrocarbons. It can be deduced that with the increasing concentration of 1-tetradecene in the system, the concentration within wax layer increased, the probability of participation in the chain growth process also increased, and consequently the selectivity of hydrocarbons larger than C_{14} increased. Because the more adsorption of olefin would occupy more active sites and consume more H species, CO conversion was lowered correspondingly.

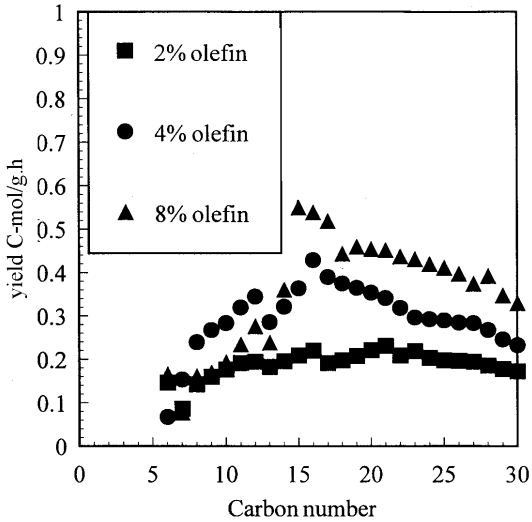

Fig.5 Olefin concentration effect on carbon number distribution of product Cat.3, T=210□, W/F=15g.hr/mol, P(total)=4.5MPa, P(CO+H_2)=1.0MPa, The percentages in figure are CO conversions

5. Investigation on the influence of H_2/CO feed ratio

Different gases with H_2/CO ratio of 1/1 and 2/1 have been used to investigated effect of H_2/CO ratio on the catalytic behavior of Co/SiO_2 catalyst. The main results are exhibited in Table 4. It can be found that for 1/1 syngas, CO conversion was obviously lower while the selectivity of wax was higher than that for 2/1 syngas. The reaction rate of FT synthesis is reported to be proportional to the partial pressure of H_2 over Co/SiO_2 catalyst[7]. The lower CO conversion may be interpreted easily by the stoichiometrical requirement of FT reaction as well as the properties of catalyst. The higher selectivity to wax in the case of 1/1 syngas might be ascribed to high surface concentration of CO, which would favor the adsorption and chain propagation reaction of added olefin[5].

6. Analysis and evaluation results of waxes

Table 5 presents some analytical results of wax. It could be found that the average molecule weight and the degree of saturation (H/C ratio) of wax increased greatly due to addition of 1-tetradecene. These strongly support that the incorporation of 1-tetradecene to chain growth reaction happened. This implies that added 1-tetradecene might inhibit the formation of oxygenates which is generally the products of hydroformylation reaction. Elemental analytical results also give some evidences to this point, because total percentage of (C+H) were increased from 98.65% to 99.55% after addition of 1-tetradecene. However, as for inhibition of oxygenates formation, the reaction mechanism was not clear.

Table 1. CO conversion and hydrocarbons distribution in different reaction phase

Reaction phase	CO conv. (%)	C_1-C_4 yield (C-mmol/g.hr)				C^+_{20} Selectivity (%)
		C_1	C_2	C_3	C_4	
Gas phase	70	2.91	0.218	0.551	0.607	13.4
SC phase	84	1.87	0.259	0.164	0.041	39.6

Rreaction conditions: T=483K, P(total)=45atm, W/F(CO+H_2)=15g/hr.mol

Table 2. Effect of 1-tetradecane addition

Item	CO conv. (%)	C_1-C_4 yield (C-mmol/g.hr)			
		C_1	C_2	C_3	C_4
Without 1-$C^=_{14}$	84	1.870	0.259	0.164	0.04
4% 1-$C^=_{14}$ added	73	1.235	0.128	0.302	0.16

tetradecane addition: 4 mol% CO base

Table 3. Effect of catalyst pore size on reaction performance of Co/SiO_2

Catalyst No.	Mean pore Diameter (Å)	Co loading (by weight) (%)	CO Conversion (%)	CO_2 Selectivity (%)	C^+_{20} Selectivity (%)
1	150	40	96	10	36.9
2	300	29	93	6	41.7
3	500	30	73	N.D*	49.5

Note: 4mol% 1-tetradecene added. * N.D. Non-detectable

Table 4. Effect of H_2/CO ratio on the reaction performance

H_2/CO	CO conv. (%)	Yield of C_1-C_4, C-mol/g.hr				C^+_{20} Selectivity
		C_1	C_2	C_3	C_4	
1/1	42	1.030	0.145	0.120	0.074	57.3
2/1	73	1.235	0.128	0.302	0.164	49.5

4 mol.% 1-tetradecene added

Table 5. Molecule weight and elemental composition of wax

Item	Sample 1	Sample 2
Mean molecule weight	873	1055
Composition (%)		
H	13.84	15.01
C	84.81	84.54
N	N. D	N. D
O	N. D	N.D
Ash	-	-
Total	98.65	99.55

Note: Sample 1: Co/SiO_2 catalyst, T=483K, W/F=15g.hr/mol; N. D: Non-detectable

Sample 2: reaction condition is same as the sample 1 except for 4% 1-tetradecene addition.

Molecule weight is the number mean molecule weight measured by Gel Permeation Chromatography (GPC).

Conclusions

1. Due to quick diffusion of reactant and product in supercritical phase, CO conversion and liquid hydrocarbon yield of the supercritical phase reaction are higher than those in gas phase reaction.
2. Added 1-tetradecene, as a chain initiator, could participate in the chain propagation process, and consequently promoted formation of hydrocarbons larger than C_{14}, inhibited the formation of C_1-C_{13} hydrocarbons, which made the carbon number distribution deviated from ASF distribution significantly.
3. Species involved in the chain growth process is not limited to the CH_2; it is found that C_2H_4 could be incorporated into carbon chain growth as well.
4. Because the effective transportation of reactant and product could be realized inside the larger pores, catalyst with large pores favored the formation of heavier hydrocarbons.
5. Because the high CO partial pressure could inhibit the hydrogenation and hydrogenolysis of olefin, CO-rich syngas favored the formation of heavier hydrocarbons.
6. In the studied cases, the more olefin added, the more wax produced.

References

1. Robert T. Hanlon and Carles N Satterfield, *Energy & Fuels*, 2 (1988), 196
2. Li-Min Tau, Hossein A. Dabbagh and Burtron H. Davis, *Energy & Fuels,* 4(1990)94
3. Ruichi Nakamura, Irura Takahashi, Chan Sieh Yong and Hiroo Niiyama, *9 th int. congr. Catal.*, 2(1988)759
4. A. T. Bell and P. Winslow, *Proc. 8 th Int. Congr. Catal.,* Berlin, 3(1984)175
5. Enrique Iglesia, Sebastain C. Reyes, Rostam J. Madon and Stuart L. Soled, *Advances in catalysis,* 39(1993)759
6. Li Fan, Kohshiroh Yokota, and Kaoru Fujimoto, *AIChE J.,* 38 (10), 1992, 1639
7. J. P. Hindermann, *Catal. Rev.-Sci. Eng.,* 35(1), 1993, 1
8. E. W. Kuipers, I. H. Vinkenburg and H Oosterbeek, *J. Catal.,* 152, 1995, 137
9. E. W. Kuipers, C. Scheper, J. H. Wilson, I. H. Vinkenburg and H. Oosterbeek, *J. Catal.,* 158, 1996, 288
10. Li-Min Tau, Hossein Dabbagh, Shiqi Bao et al., *9 th Int. Congr. Catal.,* 1988
11. Takashi Komaya and Alexis T. Bell, *J. Catal.*, 146, 1994, 237

Effect of Water on the Fischer-Tropsch Synthesis on Supported Cobalt Catalysts

S. Storsæter[1] ,Chr. Aaserud[1] A-.M.Hilmen[2] , O.A. Lindvåg[2] , E. Bergene[2] , D. Schanke[3] , S. Eri[3] and A. Holmen[1]

[1]Dept. of Chemical Engineering, Norwegian University of Science and Technology (NTNU). N-7491 Trondheim , Norway. [2]SINTEF Applied Chemistry, N-7465 Trondheim, Norway, [3]Statoil, R&D Centre, Postuttak, N-7005 Trondheim, Norway.

Introduction

The Fischer-Tropsch synthesis is an interesting pathway for converting natural gas to transportation fuels. A key element in improved Fischer-Tropsch processes is the development of active catalysts with high wax selectivity. Supported cobalt is the preferred catalysts for the Fischer-Tropsch synthesis of long chain paraffins from natural gas due to their high activity and selectivity, low water-gas shift activity and a comparatively low price. Water is produced during the Fischer-Tropsch synthesis and will be present in varying quantities during synthesis, depending on the conversion and reactor system.

Different results have been reported on the effect of water on the activity of cobalt Fischer-Tropsch catalysts[1,2,3]. The effect of water seems to depend mainly on the support although promoters may also be important. It has been shown that Al_2O_3-supported cobalt catalysts deactivate when water is added during the synthesis[4]. It has also been shown that water inhibits secondary hydrogenation of olefins on Al_2O_3-supported cobalt catalysts[5].

The present work aims at studying the effect of water on the activity and selectivity for cobalt catalysts using different supports and promoters as well as unsupported cobalt. In the following the main emphasis is on Al_2O_3 supported cobalt catalysts.

Experimental

Catalysts. The supported catalysts were prepared by incipient wetness (co)impregnation of the different supports as described elsewhere[6]. The unsupported cobalt catalyst was prepared by precipitation by adding NH_3 to an aqueous solution of $Co(NO_3)_2{\cdot}6H_2O$ with continuous stirring until there were an excess of NH_3. The precipitate was washed several times, dried and calcined in flowing air at 698 K for 3h.

Reactorsystem. The catalysts were tested in an isothermal fixed-bed microreactor[6] as shown below in **Figure 1**:

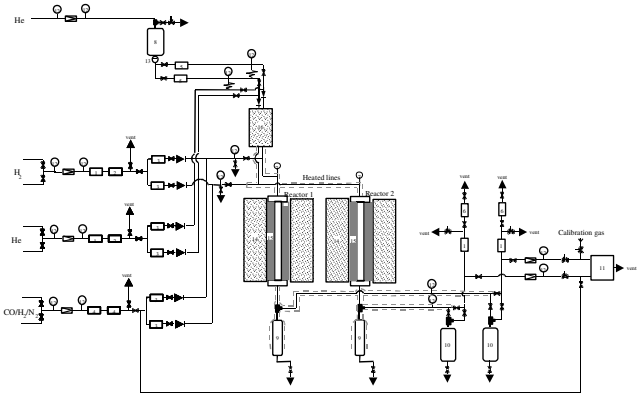

Figure 1. Experimental apparatus

Experimental procedure: The catalyst (1.0-1.6 g diluted with SiC) was loaded to the reactor, flushed with He and reduced in hydrogen at 350 ^{0}C for 16h. After reduction the reactor was cooled to 170 ^{o}C, the pressure increased to 20 bar and premixed synthesis gas (31.3 % CO, 65.7 % H_2 and 3 % N_2) was introduced. The reactor temperature was slowly increased to 483 K in order to prevent runaway. The feed and the products were analysed using an on-line HP 5890 gas chromatograph equipped with thermal conductivity (TCD) and flame ionization (FID) detectors.

Catalyst characterization: The catalysts were characterized by Temperature Programmed Reduction (TPR), chemisorption, and BET surface area. Model studies of catalysts exposed to different H_2O/H_2 ratios in a gravimetric microbalance have also been performed.

Results and Discussion

Previous results show that Co-Re/Al_2O_3 catalysts deactivate as a result of reoxidation of small cobalt particles. When water is added to the feed for Al_2O_3 supported cobalt catalysts the rate of deactivation increases. This behavior is clearly demonstrated in **Figure 2** below.

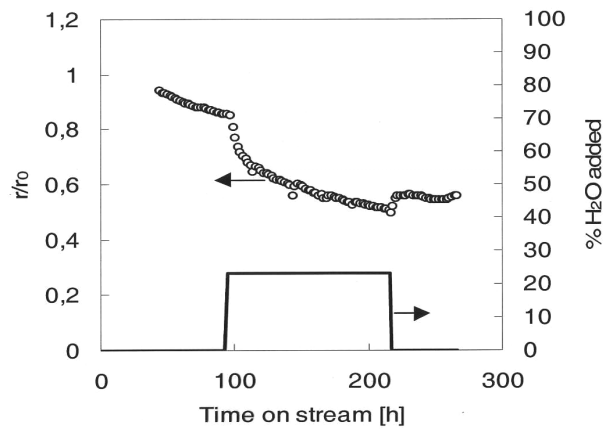

Figure 2. Rate of hydrocarbon formation relative to the initial rate for 20%Co-1%Re/Al_2O_3 at 210 ^{o}C, 20 bar and H_2/CO=2.1 [4].

Figure 2 also shows that the rate does not return to the same level as before water was added. It has been shown that the loss in activity can only partly be recovered by rereduction due to increased cobalt-alumina interactions. Both XPS and TPR indicate that a phase interacting more strongly with the alumina is formed upon exposure to water.

The effect of conversion on the selectivity is shown in **Figure 3**. The C_{5+} selectivity increases as the CO conversion is increased. It can also be added that the CH_4 selectivity decreases with increasing conversion and that the selectivity to olefins decreases with increasing CO conversion. In **Figure 3** the selectivity to C_{5+} is also given when water is added to the feed. The results show that the selectivity increases only slightly with the conversion when water is added. In the case of CH_4 the selectivity does almost not depend on the conversion when water is added to the feed (**Figure 4**).

It has been suggested[2] that the increase in C_{5+} selectivity as a function of conversion is to a large extent caused by secondary reactions of primary olefin products at longer residence times i.e.

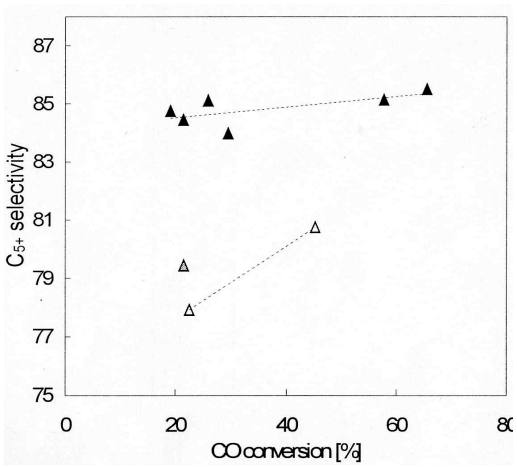

Figure 3. The effect of CO conversion on the selectivity of C_{5+} in the presence of added water (▲) compared with runs without water addition (Δ) for 12%CO-0.5%Re/Al_2O_3 at 210 °C, 20 bar and H_2/CO=2.1.

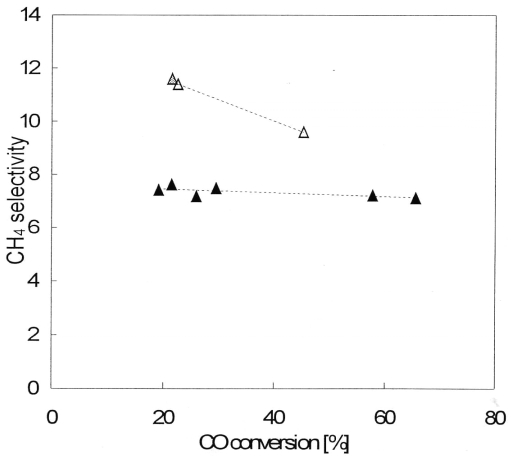

Figure 4. The effect of CO conversion on the selectivity of CH_4 in the presence of added water (▲) compared with runs without water addition (Δ) for 12%CO-0.5%Re/Al_2O_3 at 210 °C, 20 bar and H_2/CO=2.1.

readsorption and further chain growth. The present results also indicate that the increasing partial pressure of water with increasing CO conversion contributes to the increase in C_{5+} selectivity by inhibiting hydrogenation reactions.

The Fischer-Tropsch reaction network is indicated on **Figure 5** and the observed changes in selectivity can be interpreted in terms of the reaction network. It has been shown[5] that the hydrogenation reactions on active Fischer-Tropsch catalysts are inhibited by water. In one case the conversion of propene to propane dropped from 70% to below 40 % when water was added to the feed. (It should be noted that these results are obtained at different conditions (1 bar pressure, high dilution) but with an active Fischer-Tropsch cobalt catalyst). Even though the hydrogenation reactions are inhibited by water, the olefin selectivity decreases (except for C_2) suggesting also increased further chain growth.

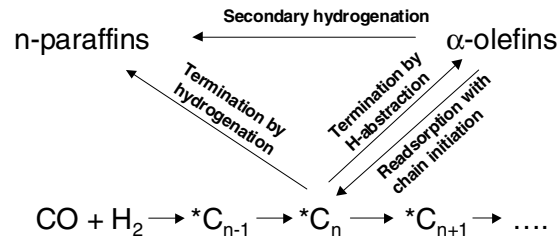

Figure 5. Fischer-Tropsch reaction network

Similar experiments have also been performed on different supports and on unsupported catalysts. The effect of water on the activity depends on the catalytic system, but the C_{5+} selectivity increases when water is added to the feed for all the systems studied.

Mass transfer effects are very important in Fischer-Tropsch synthesis. Even though the reactants are in the gas phase, the pores will be filled with liquids. Since diffusion in the liquid phase is about 3 order of magnitude slower than in the gas phase, even slow reactions may become mass transfer limited. For the Co/Al_2O_3 catalyst referred to above, the C_{5+} selectivity starts to decrease and the CH_4 selectivity increases at diffusion distances of roughly 0.2-0.3 mm[4].

Conclusions

- The C_{5+} selectivity increases with increasing conversion. Water is a main product of the Fischer-Tropsch synthesis and the amount increases with increasing conversion.
- Adding water to the feed increases the selectivity to C_{5+}. When water is added to the feed the selectivity to C_{5+} depends only slightly on the conversion
- The effect of water on the activity depends on the support. For cobalt supported on Al_2O_3 the addition of water results in deactivation.

Acknowledgement. Statoil and the Norwegian Research Council (NFR) are acknowledged for financial support and for the permission to publish these results.

References

(1) Hilmen, A.M.; Schanke, D.; Hanssen, K.F.; Holmen, A. Appl. Catal. A: General. **1999** 186, 169.
(2) Iglesia, E. Appl. Catal. A: General 1997, 161, 59.
(3) Schultz, M; Claeys, M; Harms, S. Stud. Surf. Sci. Catal. **1997** 107, 193.
(4) Hilmen, A.M.; Lindvåg, O.A.; Bergene, E.; Schanke, D; Eri, S.; Holmen. A. Stud. Surf. Sci. Catal, **2001** 136 295.
(5) Aaserud, Chr.; Hilmen, A.M.; Bergene, E.; Schanke, E.; Eri, S.; Holmen, A. Submitted.
(6) Schanke. D.; Hilmen, A.M.; Bergene, E.; Kinnari, K.; Rytter, E.; Ådnanes, E.; Holmen, A. Catal. Lett. **1995** 34 269.

Fischer-Tropsch Synthesis: Effect of Activation on Potassium Promoted Iron Catalysts

Mingsheng Luo and Burtron H. Davis

Center for Applied Energy Research,

2540 Research Park Drive, Lexington, KY 40511

Introduction

In the Fischer-Tropsch Synthesis (FTS) process, the hydrocarbon is produced from CO and H_2 by a reaction that can be expressed as

$$(2n+1)\ H_2 + n\ CO \rightarrow C_nH_{2n+2} + n\ H_2O \qquad (1)$$

When an iron catalyst is used for FTS, the water gas shift (WGS) reaction can also occur. This side reaction consumes CO and water formed by the FTS reaction and produces additional hydrogen as well as carbon dioxide.

$$H_2O + CO \rightarrow CO_2 + H_2 \qquad (2)$$

Potassium has long been used as a promoter for iron catalysts. It provides an increase in the alkene yield and a decrease in the CH_4 selectivity [1-3]. Potassium can also increase the catalytic activity for FTS and water-gas shift (WGS) reactions [3-9].

Pretreatment of iron catalysts can have important influence on FTS activity and selectivity. A cobalt catalyst is usually activated with H_2 and metallic cobalt is believe the active phase for FTS, but the pretreatment of iron catalyst is not as simple as that of a cobalt catalyst. Carbides are probably the active phase for FTS. Reduction of Fe_3O_4 with H_2 to zero valence was claimed by Rao and Bukur at al. [10-17]. It is also found that 20% metallic iron was obtained by treating iron catalyst with H_2 at 220EC. Pretreatment of iron catalyst with CO or syngas can result in the presence of P-carbide [13-15]. Bukur studied the activation effect on K/Fe=0.8/100 (mass) catalyst in a fixed bed reactor and concluded that CO activation at 280EC led to higher initial FTS activity and higher long chain hydrocarbons than H_2 activated catalysts.

Experimental

In this study, an Fe/Si/K=100/5.1/1.25 (atomic ratio) potassium promoted iron catalysts were pretreated with CO, syngas(H_2:CO=0.7) or H_2 at 230-270EC for 24 hours. Carbon monoxide activation was carried out at 1.3MPa while H_2 activation was at atmospheric pressure. To investigate the effect of syngas activation pressure on FTS activity, both atmospheric and 1.3MPa pressure were used. The CO flowed through a catalyst slurry containing 10% solids in 300 mL of Ethylflow (a mixture of decene trimers). A one-liter continuous stirred tank reactor (CSTR) was used in this study. A sintered metal filter was installed to remove the wax samples from the catalyst slurry. The wax sample was extracted through the internal filter and collected in the hot trap held at 200EC. A warm trap (100EC) and cold trap (0EC) were used to collect light wax and the water plus oil samples, respectively, by condensing from the vapor phase that was continuously withdrawn from the reactor vapor space.

Daily gas, water, oil, light and heavy wax samples were collected and analyzed. Table 1 gives a summary of the instruments for gas and liquid product analysis. A heavy wax sample was taken from the 200EC hot trap connected to the filter. The vapor phase above the slurry passed continuously to the warm (100EC) and the cold (0EC) traps outside the reactor. The light wax and water mixture was collected from the warm trap and an oil plus water sample from the cold trap. Tail gas from the cold trap was analyzed with an online HP Quad Series Micro GC, providing molar compositions of C_1-C_7 olefins and paraffins as well as for H_2, CO and CO_2. Hydrogen and carbon monoxide conversions were calculated based on the gas product GC analysis results and the gas flow measured at reactor outlet. The oil and light wax samples were mixed before analysis with an Agilent 6890 Series GC. The heavy wax was analyzed with an HP5890 Series II Plus GC while the water sample was analyzed using an HP5890 Series II GC.

Results and Discussion

Activity Carbon monoxide activated catalyst yielded the highest activity at 270EC, as indicated by Figure 1. A stabilized CO conversion of 80% was obtained at only 200 hours of time on stream and deactivated slightly after 600 hours of time on stream. Syngas activation yielded a stabilized CO conversion of 80% at 250 hours of time on stream while H_2 activation generated a CO conversion of 59% at 320 hours of time on stream. Increase in activation temperature from 250 to 270EC significantly improved the FTS activity regardless of the gas type used in the activation process, suggesting that higher temperature enhanced the activation process.

As claimed by other researchers, activation conditions can also influence the FTS activity [1, 3, 14]. Figure 2 shows the effect of activation pressure on FTS activity over syngas activated catalyst. Under atmospheric pressure, CO conversions of 42, 62 and 80% were achieved at 230, 250 and 270EC, respectively while a low CO conversion of less than 15% was obtained at all temperatures using 1.3MPa pressure. This result indicates that pressure had a detrimental effect on FTS activity with syngas activation. A higher temperature yielded a higher stabilized CO conversion. Figure 3 shows the effect of H_2 activation temperature on CO conversion. When temperature increased from 230 to 250EC, the peak CO conversion in the initial induction period was increased from 42 to 58%, while the stabilized CO conversion did not change. After 400 hours on stream, a stabilized CO conversion of 40% was obtained at both 230 and 250EC. At 270EC, however, both peak CO conversion and stabilized CO conversion were increased dramatically. A 76% initial peak conversion and a 55% stabilized CO conversion were generated at 270EC. Thus a higher activation temperature of 270EC is necessary for hydrogen activated iron catalyst.

Selectivity Higher activation temperature can produce a higher hydrocarbon rate when CO or syngas is used as activation gas, as shown in Figure 4. When CO was used as activation gas, hydrocarbon rate remained unchanged when activation temperature increased from 230 to 250EC. When activation temperature increased form 250 to 270EC, however, hydrocarbon rate improved from 1.67 to 1.75 g h^{-1} g-Fe^{-1}. Activation temperature with syngas showed a greater effect on hydrocarbon rate than for CO activation. An increase in activation temperature from 230 to 250EC improved the hydrocarbon rate form 1.16 to 1.29, and an increase in activation temperature from 250 to 270EC increased the hydrocarbon rate form 1.29 to 1.64. When H_2 was used as activation gas, an increase in activation temperature from 230 to 250EC resulted in little change in hydrocarbon rate, while an increase in activation temperature from

250 to 270EC yielded a significant hydrocarbon rate increase from 0.84 to 1.24. Carbon monoxide activation yielded a higher overall hydrocarbon rate than either syngas or H_2, regardless of the activation temperature.

Figure 5 gives the methane selectivity for the FTS with three different activation gases at 230, 250 and 270EC. With CO activation, methane selectivity did not change as activation temperature increased in the range of 230 to 270EC. Best overall methane selectivity was also obtained with CO activation and 8% methane was produced when CO was used as activation gas. Syngas activation gave 12.2% methane selectivity at 250EC and ~8% at 250 and 270EC. Hydrogen activation yielded a methane selectivity of 8, 9 and 10% at 230, 250 and 270EC, respectively. The lowest methane selectivity of 7.6% was obtained at 250EC with CO activation and 270EC with syngas activation while the highest methane selectivity of 12.2% was produced at 250EC with syngas activation

Highest olefin fraction was obtained from H_2 activation and the lowest from CO activation, as shown in Figure 6. With the exception of ethylene, all olefin ratios decreased linearly with increasing carbon number, regardless of the activation temperature. Ethylene is believed to possess rapid readsorption ability in the FTS system [18-20]. Other explanations for the low ethylene are incorporation of ethylene into the growing chain [21-22], hydrogenolysis of ethylene [19] and hydrogenation of ethene [20, 23-24].

Water gas shift Water-Gas shift (WGS) is an important reaction in an FTS process when iron catalyst was utilized. In this reaction, CO reacts with water, which is generated from FTS and produces CO_2 and H_2. WGS produces the majority of the CO_2 from FTS system, as given by equation [2]. Figure 7 shows the influence of activation temperature and activation gas type on CO_2 selectivity. This indicates that activation temperature did not affect the CO_2 selectivity with CO activation. With syngas and H_2 activation, however, CO_2 selectivity was affected by activation temperature. Carbon monoxide activation generated a CO_2 selectivity of 45% regardless of the activation temperature. As activation temperature increased from 230 to 250EC, CO_2 selectivity increased from 41to 45% with syngas activation, and from 43 to 47% with H_2 activation. Further increase in activation temperature slightly raised the CO_2 from 45 to 46% with syngas activation, but lowered the CO_2 selectivity from 47 to 44.5% with H_2 activation. The highest CO_2 of 47% was produced with H_2 activation at 250EC while the lowest of 41%obtained with syngas activation at 230EC.

Figure 8 shows that the effect of activation gas type and activation temperature on water-gas shift quotient. With syngas and H_2 activation, water-gas shift quotient increased monotonously as activation temperature increased from 230 to 270EC. Increase in activation temperature from 230 to 250EC shows a slight decrease in water-gas shift quotient from 12.6 to 11, but an increase of water-gas shift quotient from 11 to 15.8 as activation temperature increased from 250 to 270EC. The highest water-gas shift quotient was obtained with CO activation at 250EC while the lowest obtained with syngas activation at 230 to 250EC.

Conclusions

The highest CO conversion was obtained from CO activated catalyst, regardless of the activation temperature. Although higher initial CO conversion was obtained, stabilized CO conversion (80%) is independent of the activation temperature when CO was used as activation gas. In contrast, hydrogen activation yielded the lowest CO conversion among the three activation gases. Syngas activation temperature increased the CO conversion as activation temperature increased from 230 to 270EC. The results indicated that activation temperature and activation gas type showed a different influence on FTS activity. Syngas pretreatment showed a great dependency of FTS activity on the activation pressure. For high pressure, a low CO conversion was obtained, regardless of the activation temperature. At atmospheric pressure, however, FTS activity was noticeably increased and activation temperature showed a significantly influence on CO conversion

In addition to the FTS activity, CO activation showed the best overall hydrocarbon productivity and the best methane selectivity. The lowest hydrocarbon rate was obtained from H_2 activation.

Syngas activation generated the lowest water-gas shift activity while CO activation produced the highest. It was also found that activation temperature favored the WGS activity. The higher WGS activity from CO activated catalyst resulted in a lower H_2/CO usage as the WGS consumes CO and generated additional H_2 in the FTS system.

Acknowledgement. Funding from the Department of Energy (DE-FC-26-98FT40308) and the Commonwealth of Kentucky are acknowledged.

References

(1) Dry, M.E.; in *Catalysis: Science and Technology*, Vol. 1, 159-255, (1981)
(2) O'Brien, R.J.; Xu, L.;R. Spicer L; and Davis, *B.H; Symposium on Syngas Conversion to High Value Chemcials, 252-253*, Presented at the 211th ACS Annual Meeting, New Orleans, March 24-29, 1996.
(3) Dictor, R. A.; and Bell, A. T.; *J. Catal.*, 1986, 97, 121-136.
(4) Bukur, D. B.; Mukesh, D.; and Patel, S. A.; *Ind. Eng. Chem. Res.*, 1990, 29, 194.
(5) Dry, M. E. ; Shingles, T. ; Boshoff, L. J.; and Oosthuizen, G. J.; *J. Catal.* 1969, 15, 190.
(6) Benziger, J.; and Madix, R. J. ; *Surf. Sci.* 1980, 94, 119.
(7) Arakawa, H.; and Bell, A. T.; *I&EC Proc. Des. Dev.* 1993, 22, 97.
(8) Luo M; and Davis, B. H.; *in Studies in Surface Science and Catalysis*, Elsevier Science, 2001, 133, Vol. 139.
(9) O'Brien, R.J.; Xu, L.;R. Spicer L; and Davis, *B.H; Energy & Fuels*, 1996, 10, 921.
(10) Bukur, D. B.; Nowichi, L.; and Lang, X.; *Energy & Fuels*, 1995, 9, 620.
(11) Rao, K. R. P. M.; Huggins, F. E.; Mahajan, V.; Huffman, G. P.; Rao, B. L. Bhatt, V. U. S.; Bukur, D. B.; Davis, B.; and O'Brien, R. J.; *Top. Catal.*, 1995, 2, 71.
(12) Bukur, D. B.; Koranne, M.; Lang, X.; Rao, K. R. P. M.; and Huffman, G. P.; *Applied Catalysis A: General*, 1995, 126, 1, 85-113.
(13) E. S. Lox, G. B. Marin, E.De Graeve, and P. Bussiere, *Applied Catalysis A: General*, 40, 1, 197 (1988).
(14) O'Brien, R. J.; Zhang, Y.; Hamdeh, H. H.; Davis, B. H.; *"Mossbauer study of precipitated unpromoted iron Fischer-Tropsch catalyst," Preprints*, 44(1) ACS, Division of Petroleum Chemistry, Mar. 21-25, 1999, Anaheim, CA, 100-102.

(15) Raje, A. P.; O'Brien, R. J.; and Davis, B. H.; *J. Catal.*, 1998, 180, 36.
(16) Iglesia, E. ; Reyes, S. C.; and Madon, R. J.; *J. Catal.*, 1991, 129, 238.
(17) Komaya, T.; and Bell, A. T.; *J. Catal.*, 1994, 146, 237.
(18) Jordon, D. S.; and Bell, A. T.; *J. Phys. Chem.*, 1986, 90, 4797.
(19) Novak, S.; Madon, R. J.; and Shul, H.; *J. Catal.,* 1982, 77, 141.
(20) Novak, S.; Madon, R. J.; and Shul, H.; *J. Phys. Chem.,* 1981, 74, 6083.
(21) Kuiper, E. W.; Vinkenburg, I. H.; and Oosterbeek, H.; *J. Catal.,* 1995, 152, 137.
(22) Kuiper, E. W.; Scheper, C.; Wilson, J. H.; and Oosterbeek, H.; *J. Catal.,* 1996, 158, 288.
(23) Dry, M. E.; *Appl. Catal. A: General,* 1999, 189, 1850.
(24) Forney, A. J.; Haynes, W. P.; Elliot, J. J.; Zarochak, *Am. Chem. Soc., Div. Fuel*, 1975, 20, 3.

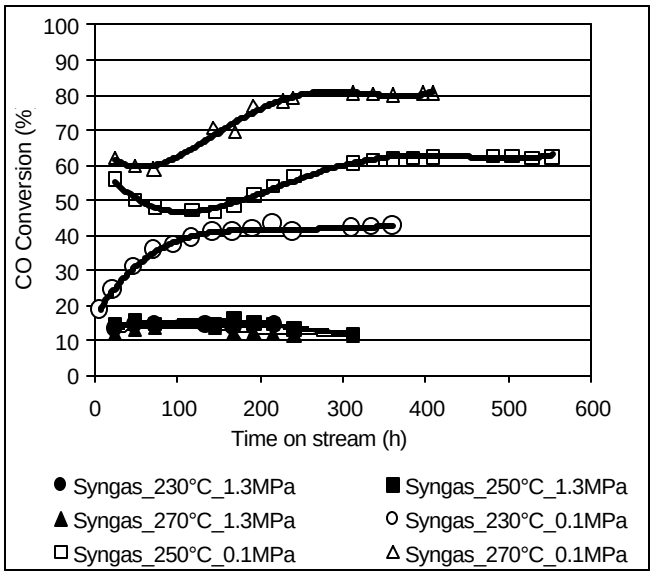

Figure 2. Influence of syngas activation pressure and temperature on CO conversion (FTS conditions: 270°C, 1.3MPa)

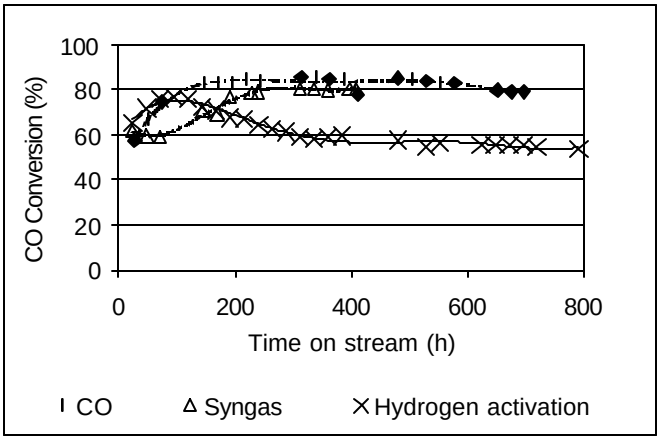

Figure 1. Influence of activation gas on CO conversion (activated at 270°C; FTS conditions: 270°C, 1.3MPa)

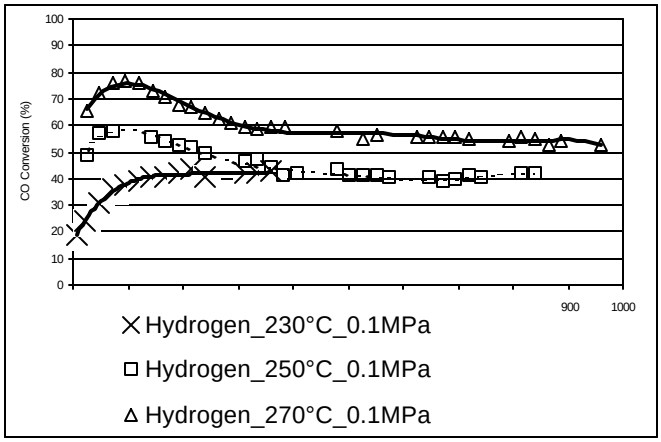

Figure 3. Influence of hydrogen activation temperature on CO conversion
(FTS conditions: 270°C, 1.3MPa)

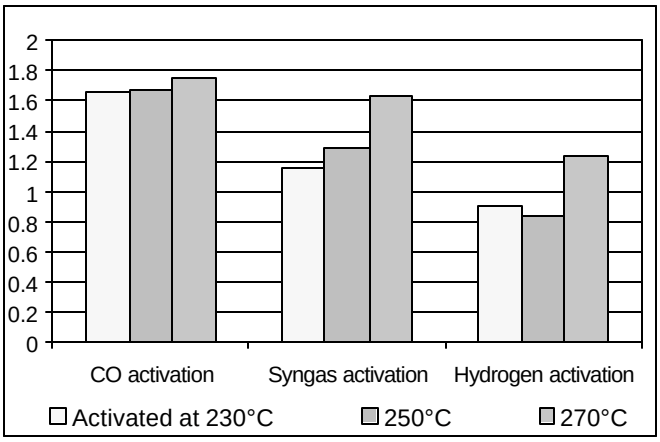

Figure 4. Influence of activation gas on hydrocarbon rate
(FTS conditions: 270°C, 1.3MPa)

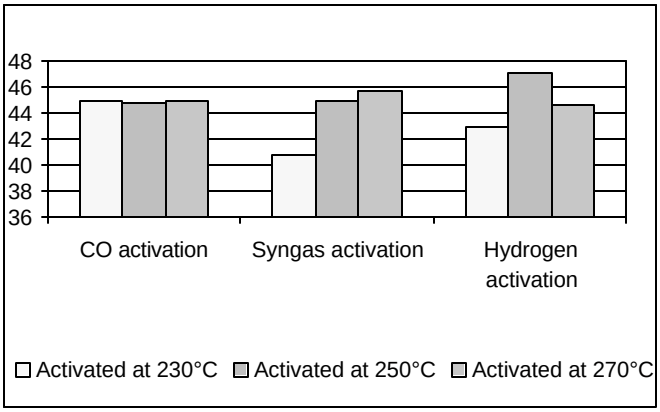

Figure 5. Influence of activation gas on methane selectivity
(FTS conditions: 270°C, 1.2MPa)

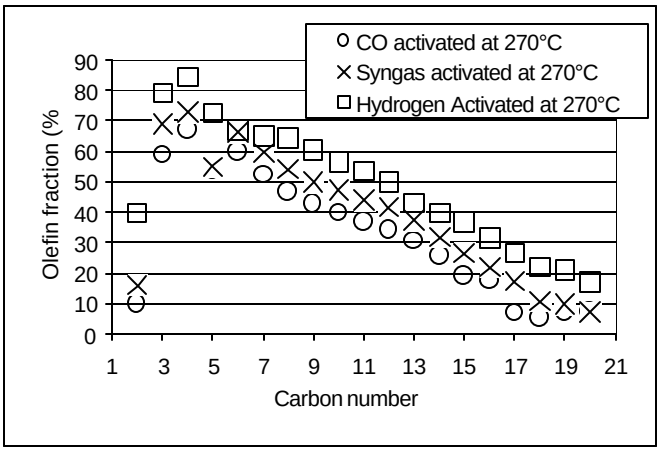

Figure 6. Influence of activation gas on olefin ratio
(FTS conditions: 270°C, 1.3MPa)

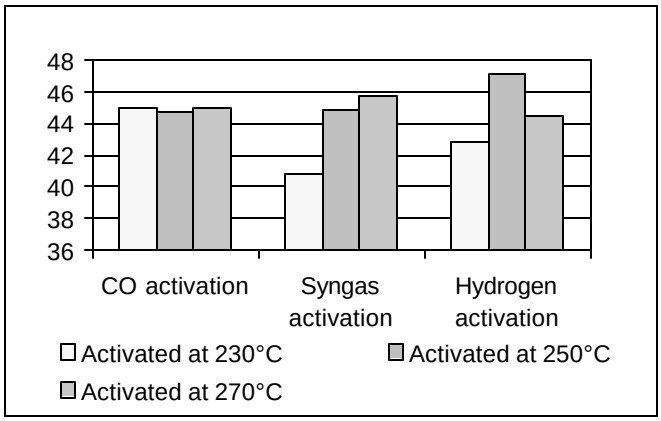

Figure 7. Influence of activation gas on CO_2 selectivity
(FTS conditions of 270°C, 1.3MPa)

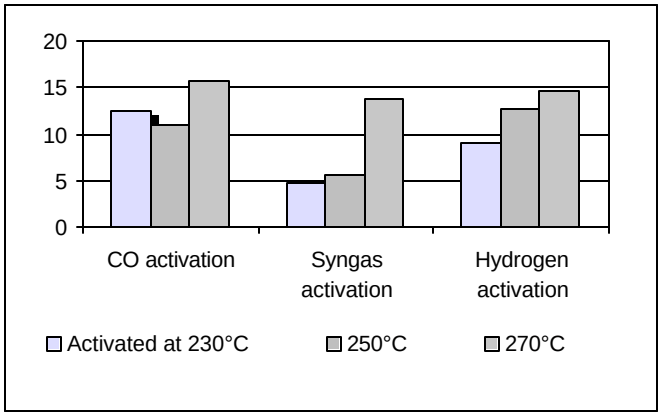

Figure 8. Influence of activation gas type on WGS quotient
$Q_{WGS} = P[CO_2]*P[H_2] / P[CO]*P[H_2O]$
(FTS conditions: 1.3MPa, 270°C)

STUDIES WITH A PRECIPITATED IRON FISCHER-TROPSCH CATALYST REDUCED BY H_2 OR CO

Guozhu Bian, Atsushi Oonuki, Norimasa Fujishita, Naoto Koizumi, Hiderou Nomoto, and Muneyoshi Yamada

Department of Applied Chemistry, Graduate School of Engineering, Tohoku University, Aoba 07, Aramaki, Aoba-ku, Sendai 980-8579, Japan

Introduction

Iron- based catalysts have been used in Fischer-Tropsch synthesis of hydrocarbons from syngas since 1923. It has been reported that the reducing pretreatments with H_2, CO or syngas often have significant effects on the catalytic activity and selectivity of the iron-based catalysts. For instance, for unsupported iron-based catalyst systems, H_2-reduced samples show obvious lower activities for FT synthesis than the CO- and syngas-reduced samples [1-2]. It has been regarded that reduction of the iron-based sample in hydrogen lead to a metallic state with serious sintering, and CO or syngas reduction lead to metallic state and small amounts of iron carbides without significant sintering. During performing FT synthesis, more iron carbides and iron oxides are formed. However, the purpose of the pretreatments of various catalyst systems have not been clearly understood, on which carefully investigations may deepen the understanding of the roles of the various iron phases in performing FT synthesis, and might be helpful to prepare catalysts with good activities.

Experimental

Precipitated Fe_2O_3 sample used in this study was prepared in the usual batch-wise manner by adding ammonia solution into a solution of $Fe(NO_3)_3 \cdot 9H_2O$. The obtained precipitates were calcined in air at 350°C for 2h. The reduced samples were obtained by calcination of the precipitated Fe_2O_3 samples in a 40ml/min flow of H_2 or CO/He (20/80) at 300°C and atmospheric pressure for 6h. The treated samples were obtained by calcination of the H_2-reduced sample in the CO/He flow or by calcination of the CO-reduced sample in the H_2 flow at 300°C for 6h.

The diffuse reflectance FTIR spectra were recorded with a resolution of 4cm^{-1} and accumulation of 20 on a Bio-Rad FTS 6000 FTIR spectrometer supplied with a MCT detector and a diffuse reflectance attachment. The infrared cell with ZnSe windows (Spectra-Tech Inc.) can be used at high pressures and high temperatures.

BET specific surface areas of the samples were measured by N_2 physisorption at 77K, using a QUANTACHROME MONOSORB surface area analyzer and one-point BET method.

Activities of the reduced and treated catalyst samples for FT synthesis from syngas were measured using a slurry phase reactor with a volume of 100ml. 30ml of n-$C_{16}H_{34}$ was used as liquid medium. 0.3g of oxidized catalyst sample was used for each experiment. The reaction was carried out in a 30ml/min flow of syngas with H_2/CO/Ar ratios of 62/33/5.0 at 1.0 MPa and 250°C. Analyses of the gas-phase products were performed by an on-line gas chromatography. The liquid products in the reactor and those collected in an on-line trap at 0°C were analyzed by an off-line gas chromatograph after the reaction. Chain growth probability, α, was calculated using the C_{10}-C_{25} data.

Results and Discussion

In- situ H_2-reduced iron sample was subjected to the adsorption experiment in a syngas flow (H_2/CO=2, 60ml/min) at 1.2MPa and room temperature. Figure 1a shows the spectrum recorded after the syngas adsorption was performed for 20min. Two very weak bands at 2013 and 2033cm^{-1} can be observed. With increasing time, the bands at 2013 and 2033 cm^{-1} slowly increase. According to the literature [3], these bands are assigned to linearly adsorbed CO on metallic iron particles.

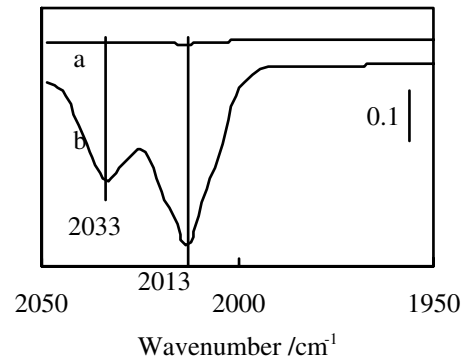

Figure 1. Infrared spectra recorded from syngas adsorption on H_2-reduced Fe catalyst at 1.2 MPa and room temperature for 20min (a), and followed by flashing the sample in the high-pressure syngas flow up to 100°C (b)

After syngas adsorption for 20 min, the sample was quickly heated up to 100°C in the high-pressure syngas flow. The bands at 2013 and 2033cm^{-1} become very stronger (Figure 1b). Thereafter, however, the bands gradually decrease in intensities. After remaining temperature at 100°C for 1h, the bands become as weak as those shown in Figure 1a. When the high-pressure syngas adsorption is directly performed at 100°C, the bands at 2013 and 2033cm^{-1} are even weaker than those observed by syngas adsorption at room temperature.

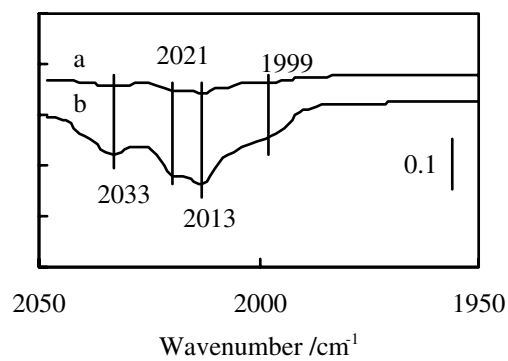

Figure 2. Infrared spectra recorded from syngas adsorption on CO-reduced Fe catalyst at 1.2MPa and room temperature for 20min (a), and followed by flashing the sample in the high-pressure syngas flow up to 100°C (b)

After high-pressure syngas adsorption at room temperature for 20min, pressure was reduced and then syngas was replaced by helium at atmosphere pressure. The bands of gaseous CO disappear by simple helium flushing for about 0.5min. The sample was flashed up to 100°C after helium flushing for 3min. By flashing sample to 100°C in the helium flow, the bands at 2013 and 2033cm^{-1} become stronger. It is

also seen that these bands quickly diminish in the helium flow at 100°C and disappear completely in about 2min.

These results suggest that the tremondous increase in intensities of the bands are not due to further adsorption of gaseous CO molecules, but due to recombination of the dissociative CO molecules bound on the catalyst surface at room temperature. The recombined CO molecules were initially adsorbed molecularly on the catalyst surface, followed by slowly desorption in the high-pressure syngas flow, or by quickly desorption in the helium flow at atmospheric pressure.

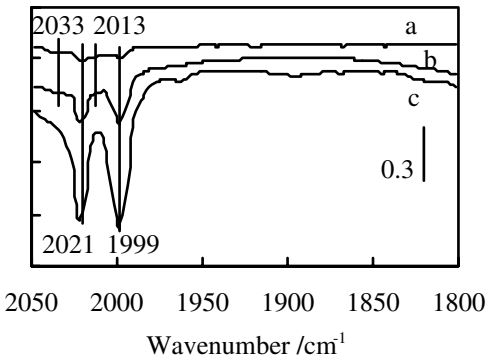

Figure 3. Infrared spectra recorded from syngas adsorption on H2-reduced Fe catalyst used for FT synthesis for 15min (a), 50min (b) and 3h (c). The adsorption was performed at 1.2MPa and room temperature for 20min.

As shown in Figure 2, on CO-reduced sample, high-pressure syngas adsorption at room temperature gives four weak bands at 1999, 2013, 2021 and 2033cm^{-1}. Compared to the spectra of syngas adsorption on the H_2-reduced sample, two new bands appear at 1999 and 2021 cm^{-1}. It is also observed that, as shown in Figure 2(b), quickly heating the sample up to 100°C in the syngas flow results in a great increase of all these four bands. Therefore, large quantities of CO molecules are dissociatively adsorbed on the CO-reduced catalyst at room temperature as well.

The bands at 1999 and 2021cm^{-1} may be assigned to CO adsorption on iron carbide species. The main reason for this assignment is that, as shown later in this paper, syngas adsorption on the samples used for FT synthesis gives rise to strong bands at 1999 and 2021cm^{-1}. This result strongly supports the above assignment, because during FT synthesis iron carbides are the only Fe^0 species to be formed in large quantities. More investigations were performed and it is found that iron carbides on the CO-reduced sample can be converted to metallic iron by H_2 treatment at 300°C, and metallic iron on the H_2-reduced sample can be partly converted to iron carbides by CO treatment at 300°C.

On the H_2-reduced sample used for FT synthesis for 15min, syngas adsorption gives rise to four obvious bands at 2013, 2033, 1999 and 2021cm^{-1}, as shown in Figure 3a, indicating that the metallic iron species on the surface are partly transformed to iron carbides. Figure 3b shows the spectrum of the syngas adsorption on the sample used for FT synthesis for 50min; the bands at 1999 and 2021cm^{-1} are growing, and the bands at 2013 and 2033cm^{-1} become very weaker. Figure 3c shows the spectrum of the syngas adsorption on the sample used for FT synthesis for 3h, the bands at 1999 and 2021cm^{-1} become very strong. These results clearly indicate that the metallic iron particles on the surface are gradually transformed to iron carbides. However, the iron carbides formed during FT synthesis exhibit very low ability for CO dissociation.

Syngas adsorption on the CO-reduced sample used for FT synthesis for 10min gives bands at 1999 and 2021cm^{-1} as well. Furthermore, it is noticed that the iron carbides formed on the CO-reduced samples during performing FT synthesis have relatively higher ability for CO dissociation than that on H_2-reduced sample.

BET surface area data are shown in Table 1. The surface area of the CO-reduced sample is near to that of the oxidized catalyst precursor, but the surface area of the H_2-reduced sample becomes very much low. The surface area of the CO-reduced sample is about 5 times higher than that of the H_2-reduced sample. After the H_2-reduced sample was treated with CO at 300°C, its surface area increases significantly. On the other hand, after the CO-reduced sample was treated with H_2, its surface area shows a slight decreae.

Table 1 BET surface areas of various iron samples

Sample	reduction conditions	Surface area (m^2*g^{-1})
Oxidized	-----	38
Reduced:	CO, 300°C	37
	H_2, 300°C	7
Treated:	CO, 300°C; H_2, 300°C	33
	H_2, 300°C; CO, 300°C	11

As shown in Table 2, H_2-reduced sample shows lower catalytic activity for FT synthesis than the CO-reduced sample. Over the CO-reduced sample treated with H_2, CO conversion becomes greatly reduced compared to that over the untreated sample. Conversely, over the H_2-reduced sample treated with CO, CO conversion shows a sharp increase. These results clearly indicate that high surface area of the CO-reduced sample is not the main cause for the sample to show high activity for FT synthesis. The fine iron carbides formed during CO reduction of the oxidized sample or during CO treatment of the H_2-reduced sample have played an important role in enhancing the activity of the sample.

Table 2 Activity data of the iron samples after reaction for 7h

Reduction Conditions	CO conv. (CO%)	Yields of CO_2 & HC (CO%) CO_2	C_1	C_2	C_{3-5}	α
H_2, 300°C	24.1	4.2	2.9	1.9	7.4	0.87
CO, 300°C	68.9	13.9	6.6	5.6	21.5	0.85
H_2, 300°C; CO, 300°C	46.9	8.6	4.1	3.6	16.7	0.85
CO, 300°C; H_2, 300°C	32.3	7.5	3.8	2.6	9.7	0.86

Acknowledgement. This work was supported by Research for the Future Program of Japan Society for the Promotion of Science under the project "Synthesis of Ecological High Quality Transportation Fuels" (JSPS-RFTF98P01001).

References

(1) Bukur, D. B.; Koranne, M.; Lang, X.; Rao, K. R. P. M.; Huffman, G. P. *Appl. Catal. A* **1995**, 126, 85.

(2) Bukur, D. B.; Lang, X.; Rossin, J. A.; Zimmerman, W. H.; Rosynek, M. P.; Yeh, E. B.; Li, C. *Ind. Eng. Chem. Res.* **1989,** 28, 1130.
(3) Guglielminotti, E. *J. Phys. Chem.* **1994**, 98, 4884.

STRUCTURAL REQUIREMENTS AND REACTION PATHWAYS FOR THE FISCHER-TROPSCH SYNTHESIS

Sundaram Krishnamoorthy, Senzi Li, Dario Pinna, Mai Tu, and Enrique Iglesia
Department of Chemical Engineering, University of California, Berkeley, CA 94720

Hydrocarbon synthesis from H_2/CO in the Fischer-Tropsch synthesis (FTS) is a critical step in the conversion of coal or natural gas to petrochemicals and fuels. On Co-based catalysts, crystallite size and support effects do not influence turnover rates, but small amounts of Ru increase rates and C_5+ selectivity. Co crystallites smaller than ~6 nm, however, tend to oxidize during FTS. Promotion by Ru requires its intimate contact with Co, induced by RuO_x migration and by formation of Co-Ru oxides. Ru domains on Co surfaces inhibit the formation of unreactive carbon species and preserve the initial number of Co surface atoms. Other promoters inhibit sintering (Re) or aid the reduction (Pt) of CoO_x precursors. Catalyst synthesis by contact of supports with saturated Co precursor solutions and the slow reduction of Co precursors without air treatment lead to small Co crystallites (6-10 nm), even at high Co concentrations.

Water is the primary oxygenate product during FTS reactions on Co-based catalysts. Higher water concentrations in the synthesis gas reactant stream lead to higher hydrocarbon synthesis rates. The C_{5+} selectivity and the olefin content in all hydrocarbons also increases with increases water content, while the CH_4 selectivity concurrently decreases. Kinetic isotope effects using CO/H_2 and CO/D_2 reactants showed that these changes do not arise from independent kinetically relevant steps introduced by water, since the observed isotope effects were not influenced by the reactant conversion level or by the water concentration. Reactant mixtures consisting of CO/H_2/D_2 and CO/H_2O/D_2O were used in order to probe the reversibility of hydrogen dissociation and water desorption steps. H_2 dissociation are quasi-equilibrated during FTS reactions, but water desorption steps are reversible but far from equilibrium. This leads to oxygen chemical potentials at Co surfaces that significantly exceed those set by the H_2O/H_2 ratios in the prevalent gas phase. This surface chemical potential become the controlling variable in establishing the extent of oxidation of Co surfaces during FTS, a process that can lead to deactivation especially for well-dispersed Co catalysts.

In-situ infrared studies of the CO coverage during FTS showed that the number of CO binding sites is not influenced by the presence of water concentrations that lead to greater than two-fold increases in FTS reaction rates. Thus, it appears that the role of water is not to increase the density of catalytic sites during FTS, a process that would have led to a rate increase, possibly via the scavenging of unreactive carbon-containing adsorbed species. The intensity of the linear adsorbed CO band did not change as H_2O partial pressures increased from 0 to 300 kPa, but the band disappeared and reaction rates became very low at H_2O/H_2 ratios greater than 0.8, apparently as a result of surface oxidation. Chemical transients effected by switching from H_2/CO to H_2 streams were used in order to measure the concentration of reactive adsorbed species during steady-state catalysis on Co/SiO_2 and Co/SiO_2. The concentration of these carbon species was not influenced by the presence of water at concentrations leading to significant changes in FTS reaction rates and selectivity. In situ X-ray absorption spectroscopy showed that at typical reaction conditions, Co metal was the only Co-containing structure present on Co/SiO_2 catalysts.

FTS reactions proceed on Co and Fe via surface polymerization using surface alkyls as growing chains and CH_x species as monomers. Olefin readsorption influences C_{5+} and olefin selectivities by reversing chain termination to olefins. Intrapellet and gas-liquid diffusional constraints increase the extent of readsorption and introduce catalyst design parameters (e.g., pellet diameter and void fraction, Co site density) unavailable in kinetic-limited pellets. The higher reactivity and lower diffusivity of larger olefins lead to an increase in growth probability and in paraffin content with increasing chain size. The pellet structure and the Co site density also influence CO diffusional restrictions, which decrease local monomer concentrations and inhibit chain growth. As a result, maximum C_{5+} yields are achieved using catalyst pellets with intermediate transport restrictions. In packed-bed reactors, these optimum pellets require eggshell Co distributions, which decouple the size of the pellets from their characteristic diffusion distance. Smaller uniform pellets with higher site densities lead to optimum transport restrictions in bubble column reactors.

Fe-based catalysts exhibit more complex structure-function relationships than Co and significant structural promotion by oxides (ZnO), metals (Cu, Ru), and alkali (K). In situ X-ray absorption and transient product analysis methods confirmed FeC_x as the active species and probed the kinetic details of the structural changes occurring during reaction. Controlled pH co-precipitation, surface active agents added during drying, and promoters that convert Fe oxide precursors to high surface area FeC_x at low temperatures led to Fe-based catalysts with higher productivity than reported Co-based catalysts (at 473 K, 2 MPa, H_2/CO=2.1). Although these Fe catalysts give higher CO_2 selectivities than Co catalysts (6-10% vs. <1%), their lower selectivities to CH_4 and to C_2-C_4 paraffins make them attractive catalysts, even for the synthesis of liquid fuels from H_2/CO mixtures derived from natural gas.

SELECTIVELY SYNTHESIZE ISOBUTENE FROM CO HYDROGENATION OVER ZRO_2 BASED CATALYSTS IN A SPECIALLY DESIGNED REACTOR

Yingwei Li, Dehua He*, Qiming Zhu
State Key Laboratory of C_1 Chemistry and Technology, Department of Chemistry,
Tsinghua University, Beijing 100084, China

*Corresponding author. Email: hedeh@mail.tsinghua.edu.cn Fax: +86-10-6279-2122

Introduction

Isosynthesis is the reaction that selectively converts syn-gas ($CO+H_2$) to isobutene (and isobutane). It has been widely investigated over ZrO_2 based catalysts in recent years [1-3]. The common problems in the isosynthesis are that it is difficult to obtain high activity and i-C_4 selectivity at the same time and suppress the percentage of CO_2 in the products (>40%). In this study, we report an effective catalyst loaded in a specially designed reactor that could selectively convert synthesis gas to i-C_4 hydrocarbons and in the meantime surely maintain a relative high CO conversion. Furthermore, the percentage of CO_2 in the products was largely suppressed.

Experimental

Preparation of zirconia-based catalysts has been described in our previous work [4]. The hydrogenation of CO was carried out in two types of reactors at 5.0 MPa, 648-723 K and 650 h^{-1}. One was a stainless steel tube (marked as Reactor A) that was normally used in most researches that performed at a high pressure [2,3]. Another was a specially designed reactor that contains a stainless steel line in which a quartz line was tightly fixed (marked as Reactor B). A Viton O-ring pressed by a locking nut was used to prevent the gas from leaking into the ringed gap so as to eliminate the influence of the metal wall. The reactor effluent was reduced to atmospheric pressure and then injected into two on-line gas chromatographs.

Results and Discussion

The results are presented in Table 1. Under the reaction conditions in this study, the products consisted primarily of hydrocarbons, CO_2, methanol and dimethyl ether. About 19.6% CO was converted with 36.7% C_4 selectivity in total hydrocarbons over ZrO_2 catalyst in the stainless steel tube. However, the percentage of CO_2 in the products was exceeding 60%, as normally reported in the literatures and the formation of C_1–C_3 was also remarkable. This would likely indicate that the metal wall of the stainless steel tube affected seriously the reactivity of the catalysts in the isosynthesis. The blank reactivity of the stainless steel tube also accounted for it. It can be seen from Table 1 that C_1-C_3 hydrocarbons were the predominant hydrocarbons products in the blank experiments. In order to eliminate the influence of the metal wall on the isosynthesis, the reaction was performed on the specially designed Reactor B (quartz lined). The blank experiment of the Reactor B showed that much fewer amount of CO was converted (lower than 0.1%) compared with the activity conducted on the reactor A. Although the CO conversion was a little lower than the reactor A, the i-C_4 selectivity in total hydrocarbons was largely enhanced (about 52.5%) with a much lower percentage of CO_2 in the products (37.7%) over ZrO_2 catalyst conducted on the reactor B. This would suggest that the quartz line reactor (reactor B) could eliminate the influence of metal wall, improving the performance of the catalysts in the isosynthesis.

Table 1. Influence of the Type of Reactor On the Performance of the Isosynthesis [a)]

Reactor	Catalyst	CO conv. / %	Selectivity of Products / %			Distribution of hydrocarbons / (C mol%)			
			H.C.[b)]	CHO [c)]	CO_2	C_1-C_3	C_4	C_5^+	i-C_4
A	-	1.8	81.7	0	18.3	83.6	15.1	1.2	2.8
B	-	< 0.1	51.7	0	48.3	100	0	0	0
A	ZrO_2	19.6	38.8	0	61.2	50.8	36.7	12.5	26.9
B	ZrO_2	16.3	51.5	10.8	37.7	19.6	58.1	22.3	52.5

A: Stainless steel tube; B: Stainless steel tube in which a quartz line was tightly fixed.
a) Reaction conditions: 673 K, 5.0 MPa, GHSV = 650 h^{-1}, CO/H_2 = 1.
b) $CH_3OH + CH_3OCH_3$ c) Hydrocarbons

The percentage of CO_2 in the products could be even more decreased over 15.3%Al_2O_3-0.5KOH-ZrO_2 catalyst conducted in the reactor B at 673 K. The NH_3, CO_2-TPD experiments revealed that the performance of the catalysts strongly depended on the acid-base properties of the catalysts. An appropriate amount of moderately strong acid - base sites and ratio of basic to acidic sites on the catalysts are significant for an active catalyst to selectively produce isobutene and isobutane from CO hydrogenation.

Conclusion

The metal wall of the stainless steel tube reactor would affect seriously the reactivity of the catalysts in the isosynthesis. The quartz tube reactor would be favorable for the formation of i-C_4 and decrease CO_2 formation. The amount of acid - base sites and ratio of basic to acidic sites on the catalysts are significant for an active catalyst to selectively produce isobutene and isobutane from CO hydrogenation.

Acknowledgement

We acknowledge the financial support from the Basic Research Foundation of Tsinghua University and the Analytical Foundation of Tsinghua University.

References

(1). [1] Maruya, K.; Komiya, T.; Hayakawa, T.; Lu, L. H.; Yashima, M. *J. Mol. Catal. A-Chem.* **2000**, *159*, 97.
(2). [2] Postula, W. S.; Feng, Z. T.; Philip, C. V.; Akgerman, A.; and Anthony, R. G. *J. Catal.* **1994**, *145*, 126.
(3). [3] Su, C. L.; Li, J. R.; He, D. H.; Cheng, Z. X.; Zhu, Q. M. *Appl. Catal. A-Gen.* **2000**, *202*, 81.
(4). [4] Li, Y. W.; He, D. H.; Cheng, Z. X.; Su, C. L.; Li, J. R.; Zhu, Q. M. *J. Mol. Catal. A-Chem.* **2001**, *175* (1-2), 267.

SIMULTANEOUS COAL GASIFICATION AND CO_2 SEQUESTRATION USING A FLUIDIZED BED OF ACTIVATED SERPENTINE

Zhong Tang, M. Mercedes Maroto-Valer, Yinzhi Zhang, Matthew E. Kuchta, John M. Andrésen and Scott A. Bair

209 Academic Projects Building, The Energy Institute
The Pennsylvania State University, University Park, PA 16803

Introduction

Coal has been the main energy supplier over a century and will continue being an important energy source in the 21st century. Unfortunately, all the coal utilization technologies used today, such as combustion and gasification, are inevitably associated with CO_2 emissions, and subsequently linked to the greenhouse effect and climate change by the public opinion. Therefore, the greatest challenge to achieve no environmental impact or zero emission in the 21st Century Energy Plant is probably the elimination of greenhouse gases emissions.[1]

Mineral carbonation, that involves the reaction of CO_2 with non-carbonate minerals, such as serpentine, to form stable mineral carbonates, has been lately proposed as a promising CO_2 sequestration technology due to the vast natural abundance of the raw minerals, the long term stability of the mineral carbonates formed, and the overall process being exothermic, and therefore, potentially economic viable.[2] Furthermore, mineral carbonation technologies could potentially provide a direct path to remove CO_2 when integrated with other systems, such as gasification processes. Using CO_2 sequestration as a part of the gasification process can be a highly efficient, environmental friendly and economical alternative to combustion technologies, since the volume of fuel gas in gasification is significantly lower than that of flue gas generated by combustion. In addition, the concentration of CO_2 is higher in fuel gas than in flue gas[3].

In the present study, a lab-scale fluidized bed gasification unit was used to investigate the effect of in-bed carbon dioxide removal during coal gasification using activated serpentine, which was produced by the novel active carbonation concept. [4]

Experimental

Char Samples. For this study, a char was chosen instead of a coal to prevent problems that may arise from the evolution of tars within the gasifier bed. The char used was collected from the cyclone of a coal combustor unit. Table 1 lists both the proximate and ultimate analysis for the coal char investigated. A petrographic study showed that the char contained mainly anisotropic carbon.[5] The char was grinded and the particle fraction between 60-100mesh (150~250μm) was collected and used for the gasification experiments.

Table 1. Proximate and ultimate analysis for the coal char investigated (dry ash basis).

C	H	N	S+O*	Moist.	Ash	VM	FC
84.76	0.02	1.22	0.26	0.17	13.74	1.97	84.30

* Calculated by difference.

Serpentine Samples. The serpentine samples come from the Cedar Hills, USA. The particle size of the serpentine was less than 100mesh. Both the raw serpentine and activated serpentine (A-SP) samples were characterized by N_2 adsorption isotherms using a Quantachrome Aotusorb-1 at 77K. The raw and activated serpentine samples were placed in the fluidized bed gasifier and used simultaneously as fluidizing and carbonation agents.

Gas analysis. An Agilent 3000A Micro GC was used to analyze on-line the gas composition. The instrument has two channels with thermal conductivity detectors (TCD) that are capable of performing gas analyses within seconds. There is a 10m×0.32mm MolSieve 5A PLOT column and an 8m×0.32mm PLOT U column in channel A and B, respectively. Channel A uses Argon as carrier gas and Channel B uses Helium as carrier gas. The column temperature is 100 and 90°C for channel A and B, respectively.

Gasification experiments. The gasification tests were conducted in a lab scale bench fluidized bed gasifier. The diameter of the gasifier was 45mm. Typically, around 20g char or 20g char and 2g serpentine was put into the gasifier for each run. The reactor was heated up to the desired temperature under N_2, and then steam mixed with N_2 was fed into the gasifier to conduct the gasification reaction. In present study, the operation temperature was 950°C and the total gas flow rate was 1,475mL/min (67.73%vol steam). The composition of the produced gas was on-line analyzed using the Agilent 3000A Micro GC.

Results and Discussion

Characterization of raw and activated serpentine samples. Figure 1 shows the N_2-77K adsorption isotherms for the raw and activated serpentine samples. For the activated serpentine, the adsorbed volume increases rapidly at low relative pressure, but it keeps increasing progressively, and there is a distinct hysteresis loop in the isotherm, which indicates that the sample porosity is a mixture of micropores (<2nm in width) and mesopores (2-50nm in width). Compared to the raw serpentine, the activated sample has developed significant microposity. The adsorbed volume increases significantly for the activated sample compared to that of the raw serpentine sample, indicating that the activation process has increased the surface area of the activated sample. Indeed, the BET surface area has gone up an order of magnitude to 142m^2/g compared to only~16m^2/g for the raw serpentine.

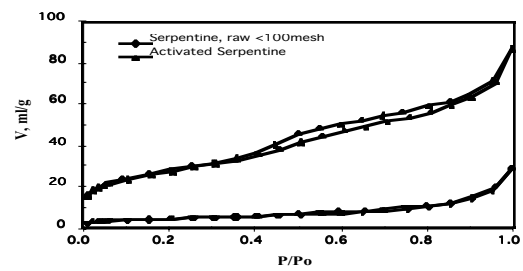

Figure 1. N_2 77K isotherms of the raw and activated serpentine samples.

Char gasification with and without activated serpentine addition. Figure 2 shows the variation of the gas composition with reaction time for the char gasification experiment without serpentine. It can be seen that the concentrations of H_2, CO and CO_2 are lower than previously reported by the authors for coal gasification.[6] This could be due to the low reactivity of the coal char used. The water decomposition ratio here was just 16.67%, which is much lower than average 30% level. [6] In addition, a gasification experiment of the char mixed with activated serpentine was conducted at the same operation conditions as for the char alone gasification (Figures 3-4).

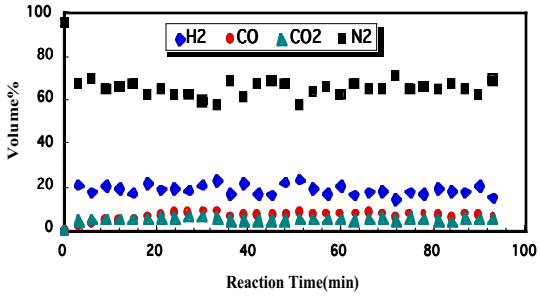

Figure 2. Variation of the gas concentration with reaction time for the char alone gasification experiment.

Figures 3 and 4 show the variation of CO_2 and $CO+H_2$ concentrations in the fuel gas with reaction time for the char and activated serpentine (A-SP) gasification compared to that of the char alone gasification. As expected, the CO_2 concentration decreased for the char+A-SP gasification experiment, and at the same time, the $CO+H_2$ concentration increased compared to that of the char alone gasification. During the relative steady gasification period (between 15~70mins), for the char+A-SP gasification, the average CO_2 concentration was 4.61%vol, and the average $CO+H_2$ concentration was 27.03%vol. For the char only gasification, the average CO_2 and $CO+H_2$ concentrations were 5.14%vol and 26.44%vol, respectively. Therefore, the CO_2 concentration decreased about 10% (from 5.14% to 4.61%), while the $CO+H_2$ concentration increased about 3.25% (from 26.44% to 27.30%) for the char gasification when activated serpentine was added. This indicates that the activated serpentine could have reduced the CO_2 concentration in the fuel gas, possibly due to mineral carbonation reactions. Further characterization studies of the activated serpentine minerals after gasification are being conducted to understand its role during the gasification process.

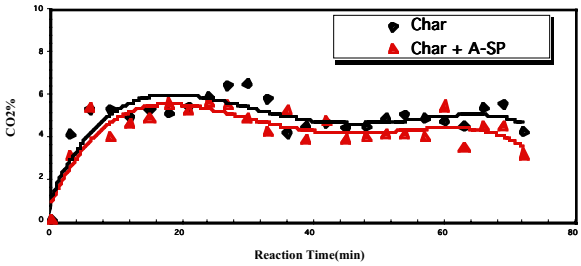

Figure 3. Variation of CO_2 concentration in the fuel gas with reaction time for the char and activated serpentine (A-SP) gasification compared to that of the char alone gasification.

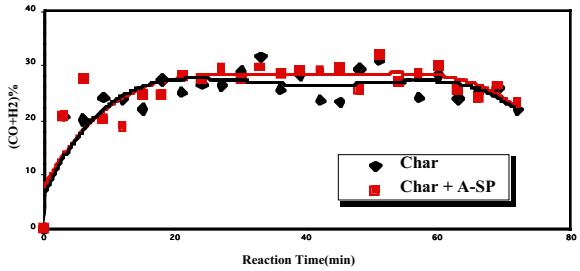

Figure 4. Variation of $CO+H_2$ concentrations in the fuel gas with reaction time for the char and activated serpentine (A-SP) gasification compared to that of the char alone gasification.

The water shift reaction ($H_2O + CO \leftrightarrow CO_2 + H_2$), which will determine the gas composition is a crucial reaction during gasification process. Accordingly, the rate constants of water gas shift for the char alone and char+A-SP gasification experiments were calculated, and Figure 5 shows the variation of the rate constant with reaction time. It was found that the rate constant was higher at the beginning of the gasification and then decreased slowly with gasification process, keeping virtually constant for reaction times over 75 minutes. The rate constant for the char+A-SP gasification is lower than that for the char alone gasification. The rate constants reported here are lower than the theoretical equilibrium constant (about 0.45 at 950°C). The variation of the reaction rate constant with different operation conditions indicates the magnitude of the driving force for the water gas shift reaction to occur in the positive direction. When activated serpentine is used in the gasifier bed, there is a reduction of the CO_2 concentration in the flue gas, suggesting that mineral carbonation of the activated serpentine during the gasification process could potentially produce high quality syngas ($CO+H_2$) with low CO_2 content.

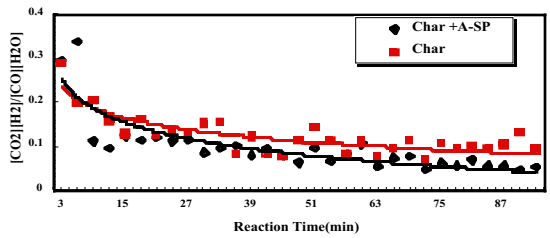

Figure 5. Variation of rate constant for the water shift reaction with reaction time.

Conclusions

In this work, a lab-scale fluidized bed gasification unit was used to investigate the effect of in-bed carbon dioxide removal during coal gasification using activated serpentine. There was an improvement in the quality of the fuel gas produced (reduction of CO_2 concentration and an increase in the $CO+H_2$ content) when activated serpentine was added in the gasifier bed. It seems that the carbonation reaction may have occurred during the gasification process in order to reduce the CO_2 concentrations. Further work is underway to study the reaction mechanisms of simultaneous gasification and carbonation, and to develop a process that can integrate gasification and sequestration in order to produce high purity H_2 with zero emission of CO_2.

Acknowledgements. The authors wish to thank the Department of Energy and Geo-Environmental Engineering and the at Penn State University for supporting this work.

References

1. DOE/NETL, Version 21 Program Plan, Office of Fossil Energy, U.S. DOE, 1999.
2. DOE/OS-FE, Carbon Sequestration. State of Science, Office of Fossil Energy, DOE, 1999
3. Tang, Z. and Wang, Y., *Fuel Processing Technology*, **2000**, *62(2-3)*, 137-141.
4. Maroto-Valer, M.M., Fauth, D., Kuchta, M., Zhang, Y., Andrésen, J. and Soong, Y., Eighteenth Annual International Pittsburgh Coal Conference, December 2001, Australia.
5. Maroto-Valer, M.M., Zhang, Y., Andrésen, J. and Morrison, J., Proc. of Carbon'01, July 14-19, 2001, CD paper 34-3.pdf.
6. Tang, Z., PhD dissertation, The Institute of Coal Chemistry, Chinese Academy of Sciences, 1997.

Hydrotreatment of tar formed in gasification of biomass

M. Hernelind[+] and B. Gevert[*]

Department of Applied Surface Chemistry, Chalmers University of Technology, S-412 96 Göteborg, Sweden.
[+]Present address: Perstorp AB, S-284 80 Perstorp, Sweden.
[*]Corresponding author. Tel.: +4631-7722956; fax: +4631-160062; e-mail: gevert@surfchem.chalmers.se

Introduction

Gasification of biomass leads to more or less production of a tar. A lot of research has bean done to crack this tar into carbon monoxide and hydrogen. In this paper we will present an alternative way of using the tar. The purpose with here is to present some results of stabilizing tar from gasification of biomass by hydrotreatment with a commercial CoMoS-catalyst. We are here focusing on finding the optimum temperature for hydrodeoxygenation (HDO) of the tar. The effects of pressure and liquid hourly space velocity (LHSV) are also studied. The results are based on five analysis methods: elemental analysis, ^{1}H-NMR, FT-IR, GC and water content analysis.

Experimental

The raw material for this study was tar formed in a gasification plant in Tervola, Finland. The type of gasifier was a mixture of up- and down-draught. To pump the tar through the continuous hydrotreating system a piston pump was used. The tar was filtered with three sieves with the mesh sizes of 710 µm, 125 µm and 45 µm. In this study a commercial CoMo catalyst called Akzo Ketjenfine 702 was used. The catalyst was sulfided in the reactor by exposing the catalyst to a gas mixture of H_2/H_2S 90/10% by volume. The hydroprocessing system study consisted of a feed tank, a reactor and a separator, which were connected to each other by _-inch stainless steel pipes (REF REACYTOR). Since Baker et al. (1) used up-flow mode for upgrading flash pyrolysis tar in their hydroprocessing apparatus to prevent reactor bed blocking, that mode was also used here. The reactor was filled with 40 ml of catalyst.

Results and Discussion

Analysis of the gasification tar. The properties of the feed tar formed in gasification of biomass are reported in Table 1. The water content was 8.14 %, which is relatively low compared to bio-oils produced by fast pyrolysis. The water in the tar together with the water produced by the hydrodeoxygenation reactions deactivates the hydrotreating catalyst in two ways. Water molecules may, according to Furimsky (3), adsorb to anion vacancies and thereby block active sites and Grange et al. (4) reports that water also alters the structure of γ-Al_2O_3 support materials. If the γ-Al_2O_3 is hydrated into the boehmite phase the characteristic porous structure will be lost. The reactants will then have reduced access to active elements in the support material. However, water in bio-oils also lowers the viscosity and makes the bio-oils more stable. Moreover the elemental analyses showed that the tar contained less oxygen than bio-oils from fast pyrolysis, which have a typical oxygen content of 44-46% by weight including the oxygen in the water. The GC analysis showed that the amount of compounds in the lighter fractions of the tar was relatively small. In the IR spectrum of the tar, which is reported in Fig. 2, it can be seen that the tar was a cocktail of different hydrocarbons. Since the objective was to remove as much organically combined oxygen as possible the most interesting peaks for this study were: alcohols at 3550-3200 cm^{-1} (O-H stretching) and above all carboxylic groups at 1780-1630 cm^{-1} (C=O stretching).

Table 1. Properties of gasification tar

Elemental analysis (on wet basis)	Weight percent	GC analysis	*Mole % of carbon*
C	64.46	Gasoline	~0
H	7.21	Kerosene	11.5
N	~0	Gas oil	61.0
O (by difference)	28.33	Residue. 369°C+	27.5

Hydrodeoxygenation of gasification tar by catalytic hydrotreatment. The first hydrotreating run was performed at high temperature (370°C) and pressure (10.0 MPa). The reactor was quickly blocked with coke and therefore it was confirmed that the tar must be pre-stabilized to be able to treat it at temperatures of about 400°C. In the last run the temperature and pressure were set to 300°C and 11.0 MPa. Then the reactor bed was also blocked by coke. Therefore the pre-Hydroprocessing of temperature of the tar must be in the temperature interval 200-300°C in similar way as for bio-oil produced by flash pyrolysis (1). The elemental analysis of untreated tar showed that it contained 28.3-weight percent oxygen, including the oxygen atoms in water. In Fig. 1 the elemental analyses show that the oxygen content of the tar clearly decreased with increasing hydrotreating temperature, as expected. The explanation for this result is that the higher the temperature the higher HDO reaction rates. The oxygen content decreased from 28.3 weight percent to 24.4% at the 7.0 MPa pressure level and to 21.6% at the 11.0 MPa pressure level when the temperature was increased from 200 to 280°C. It might seem like a small reduction of oxygen-containing compounds in the tar. But one must remember that the most reactive species have been deoxygenated. The influence of pressure on the HDO of tar, see the results from the elemental analyses in Fig. 1 was that the oxygen content decreased with increasing pressure. This is logical since the higher the hydrogen gas pressure the higher the concentration of active hydrogen atoms on the surface of the catalyst, which in turn leads to higher HDO reaction rates. The dependence of the pressure is not as strong as the temperature dependence.

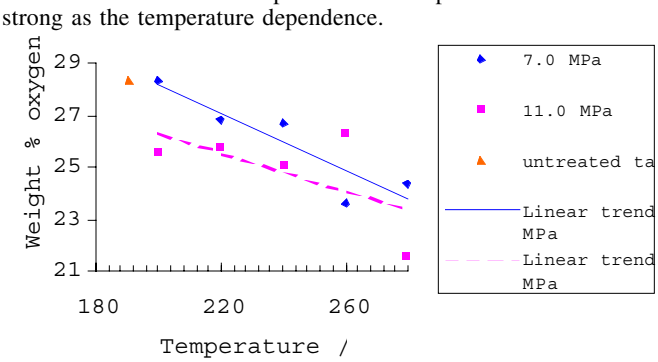

Figure 1. Elemental analysis: Effect of temperature on the oxygen content in hydrotreated tar. LHSV: 2.2 ± 0.3 h^{-1}.

At the lower pressure 7 MPa the same results were received as for the 11 MPa case. In Fig. 2 the carbonylic peaks in

the FT-IR spectra for untreated tar and hydrotreated tar at 7 MPa is zoomed in. It is clearly seen that the carbonylic absorption decreases with increasing hydrotreating temperature. Since the carbonylic absorption is a measure of the concentration of carbonylic compounds in the tar it is concluded that amount of C=O groups decrease with increasing temperature. For hydroprocessing at 11 MPa the results were similar.

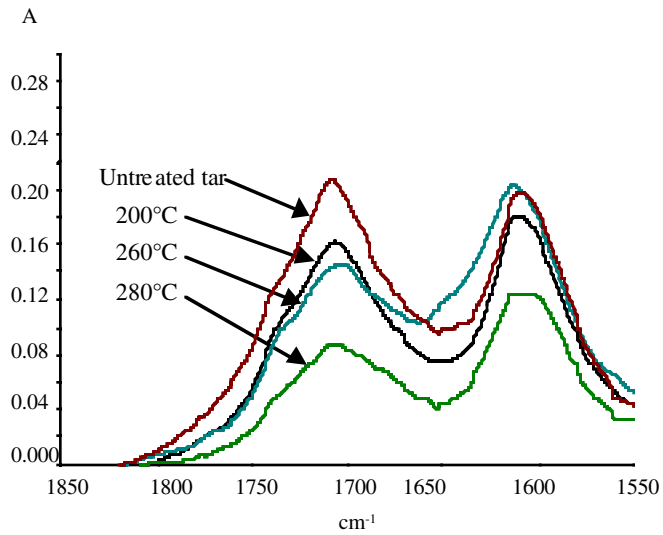

Figure 2.Comparison of FT-IR spectra for untreated tar and hydrotreated tar. Conditions: 7.0 MPa, LHSV= 2.2 ± 0.3 h^{-1}.

In the beginning of the test series a run with the following settings was performed: 10.0 MPa; 200°C; LHSV= 4.5 h^{-1}. To examine if the catalyst was deactivated during the experiments, a run with approximately the same hydrotreating conditions as above was carried out at the end of the test series: 10.0 MPa; 200°C; LHSV= 4.6 h^{-1}. The FT-IR analysis showed that the carbonylic peak heights of the two samples were 0.1995 and 0.1997 Absorbance units, respectively. Therefore approximately no deactivation of the catalyst could be indicated from the FT-IR analyses. Total time on tar stream was 42 hrs. When hydroprocessing tar from high-pressure liquefaction Gevert (5) found that the deactivation was quick during the first hours and leveled out to be constant. The same behavior is found here.

The results from the GC analyses in Fig. 3 show that the fraction of compounds with relatively low boiling points increase on the expense of compounds with high boiling points when the gasification tar was hydrotreated. This result is general for all this result is general for all hydroprocessing conditions analyzed. The explanation is that when the oxygen-containing compounds become hydrodeoxygenated the effect of hydrogen bonding and dipole-dipole interactions will decrease, which in turn means that the boiling points of hydrodeoxygenated compounds will be lowered. It is also interesting that the kerosene fraction increases from ~10 to ~20 mole percent already at 200°C, since the definite aim with this project is to produce aviation fuel from biomass. One possible reason to why the effects of LHSV and pressure from the FT-IR analyses were inconclusive could be that these effects only were studied at 200°C. At such mild conditions very few HDO reactions occur and it is therefore hard to say in what way different parameters influence the result. However, high hydrogen gas pressure and high LHSV counteracts coke formation and in that way the catalyst lifetime can be prolonged. The optimum hydrotreating condition for hydrodeoxygenation of the tar was thereby found to be 280°C, 11.0 MPa and LHSV=2.3 h^{-1}. Should the definite objective with this project fail, which is if it is difficult to produce aviation fuel components from tar formed in gasification of biomass with aid of hydrotreatment/hydrocracking, the product could be used to replace fuel oil. Then the value of the product would be lower but the environmental profits would remain.

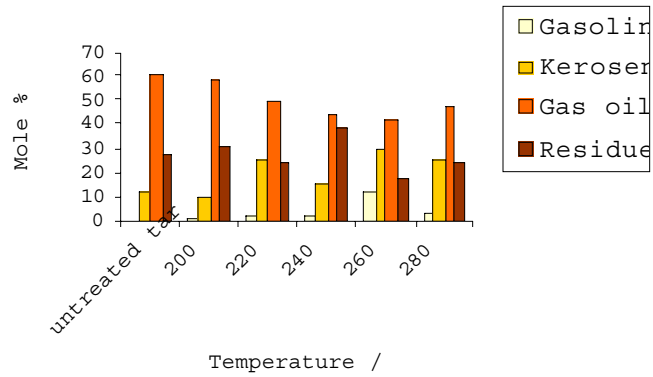

Figure 3. GC analysis: Effect of temperature on the yield of different fractions in hydrotreated tar and unhydrotreated tar. Pressure: 11.0 MPa, LHSV: 2.2 ± 0.3 h^{-1}

Conclusions

Tar from gasification of biomass can be hydroprocessed.. The oxygen content of the tar decreased with increasing hydrotreating temperature. At temperatures >300°C the hydrotreating reactor was blocked with coke. Therefore it was concluded that the maximum (optimum) hydrotreating temperature was 280°C.The elemental analysis showed a tendency for decreasing oxygen with increasing pressure.The FT-IR analyses could not indicate any deactivation of the catalyst.Optimum hydrotreating condition was found to be: 280°C; 11.0 MPa; LHSV = 2.3 h^{-1}.

Acknowledgement. The authors would like to thank Swedish National Board for Industrial and Technical Development (NUTEK) and CF's Environmental foundation for financial support, Long Feixiang for assistance with the hydrotreating apparatus and Anders Mårtensson for help with FT-IR analyses.

References

(1) Baker, E.; Elliott, D. In: Soltes, E.J.; Milne, T.A. (Eds). *Pyrolysis oils from biomass: producing analysing and upgrading*; ACS 376, Washington, DC, 1988; pp. 228-240.

(2) Ying Zhong-Shu, Börje Gevert, Jan-Erik Otterstedt, Johan Sterte, Applied Catalysis A, 153 (1997), 69-82.

(3) Furimsky, E., *Catalysis reviews science and engineering*. **1983**, *25*, 421-458.

(4) Grange, P.; Ceteno, A.; Maggi, R.; Delmon, B. In: Bridgwater, A.V.; Hogan, E. (Eds). *Bio-oil production and utilization*, 1996; pp. 186-197

(5) Gevert, B. In Bridgewater A.V. (Ed). Advances in Thermo Chemical Biomass Conversion, Blackie, London, 1994, 1424-1431.

A COMPARISON OF PRODUCT PROFILES FROM AQUEOUS PYROLYSIS OF SELECTED BIOMASS AND WASTE MATERIALS.

Tanja Barth

Department of Chemistry, University of Bergen, Allégaten 41, N-5007 Bergen, Norway

Introduction

Conversion of biomass and waste into fluids could provide a sustainable alternative to increased use of fossil fuels. Alternatively, synthetic chemicals could be produced from renewable resources instead of petroleum, with a positive environmental effect. However, many types of widely researched processes of biomass pyrolysis do not give liquid products that are compatible with petroleum fluids. Since this would make the introduction of alternative fuels and raw materials much easier, a study of pyrolysis in an aqueous reaction medium aimed at optimising the yield of hydrocarbon-rich fluid products has been made.

Three types of clean vegetable biomass and five types of organic rich waste materials have been pyrolysed in batch reactors in the presence of excess water. Experimental designs covering a range of conditions with regard to temperature, duration, water content and catalysts have been used with the aim of maximising the yields of liquids, and providing a maximum of the hydrocarbon fractions or petroleum compatible liquids. The gas, organic-, aqueous and solid phase products have been fractionated, quantified and analysed to provide yield profiles and mass balances.

Experimental

Batch pyrolysis experiments were performed in 21 ml stainless-steel autoclaves. The pyrolysis conditions were varied in the ranges given in Table 1. The biomass samples were clean wood and Miscanthus, various sewage sludges and industrial by-products. A fractional factorial design was used for each biomass type. 1 M aqueous solutions of KOH or NaOH were used as catalysts. Addition of zeolites and other solid catalysts were also tested. More than 200 experiments have been performed.

Table 1: Pyrolysis Conditions

Parameter	Range
Temperature	320 - 500 °C (mostly 340-380 °C)
Duration	3 - 96 hours (mostly 6 and 17 hours)
Amount of biomass	0.2 - 4 g (mostly 0.5 - 3 gram)
Amount of water	0.5 -15 ml (mostly 2.2 - 9 ml)
Catalysts	

The fluids were extracted and quantified gravimetrically, and fractionated into asphaltenes and oils by n-hexane precipitation and further separated in a silica micro-column to give hydrocarbons and a polar fraction. The coke yield was determined by weight and TOC measurements. The gas-phase and aqueous products were also analysed and quantified. A mass sum of recovered products was calculated from each experiment. Multivariate data analysis is used to relate the yield profiles to the experimental conditions.

Results and Discussion

The product profiles are a function of the experimental conditions, with a high water-to biomass ratio giving a high yield of liquids relative to coke. The biomass stating material is, however, the dominating factor for the products. The maximum liquid yields are obtained from degraded sludges with high organic contents, while vegetable biomass produces more coke and asphaltenes, and relatively more of the polar fractions in the liquids. Figure 1 shows the liquid yields from 1 gram of four biomass types after pyrolysis at 380 ºC for 17 hours.

The reaction conditions can alternatively be optimised to give aqueous short-chain organic acids as the major product. Addition of a base together with excess water suppresses coke formation completely, but increases thee yields of aqueous organic acids and CO_2 by "capture" in the aqueous phase. Hydrocarbon gases are minor products at all conditions tested.

Addition of homogenous and heterogeneous catalysts changes the yield profiles significantly, but the effects are often not the same for the different starting materials. The addition of a base improves the yields from the vegetable biomasses, but has a slight negative effect for the sludges. The presence of potassium ion results in significantly improved hydrocarbon yields in most systems.

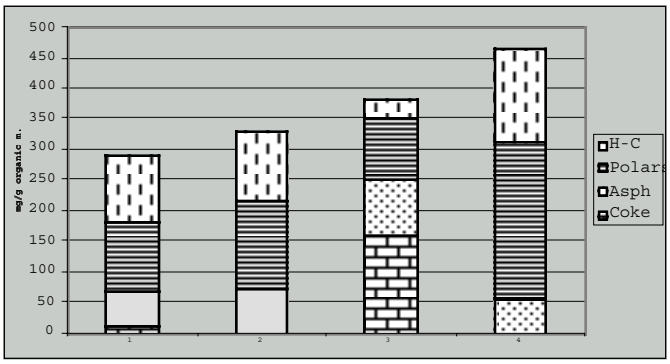

Figure 1. Examples of liquid yields from four biomass types at 380 ºC for 17 hours, with 1 g of dry biomass to 9 ml water in a 21 ml reactor.
H-C: Hydrocarbon fraction.
Sample 1: Clean woody biomass with 1 M KOH
Sample 2: Miscanthus stem with 1 M KOH
Sample 3: Sewage sludge from a chemical treatment plant with 1 M NaOH
Sample 4: Sludge from an industrial bio-filter with 1 M NaOH

Conclusions

Solid biomass and organic wastes are converted to liquids in high yields by pyrolysis in autoclaves in excess water. The product is a petroleum-like fluid, but contains more non-hydrocarbon compounds than crude oils. However, the composition of the fluid is very dependent upon which raw material is being used, and on the reaction conditions. The following systematic relationships are observed from the experimental designs:

- The initial biomass composition determines the reaction pathways and product spectrum in pyrolysis in aqueous conditions.
- Degraded biomasses give the highest yields of fluids.
- Excess water as reaction medium increases the fluid yields for most biomass types.
- High carbohydrate biomass types produce high coke yields in the absence of potassium and base.
- Degraded biomass gives high fluid yields with no base added.

Further optimisation on specific raw materials has a good potential for providing petroleum compatible sustainable fuels.

Acknowledgement. Funding from the European energy research program JOULE (Contract JOR3-CT97-0176) is gratefully acknowledged.

DEVELOPMENT OF GASIFICATION/MELTING PROCESS FOR COAL AND COMBUSTIBLE WASTES

Yongseung Yun and Ji Sun Ju

Plant Engineering Center
Institute for Advanced Engineering
633-2, Goan-ri, Baegam-myeon
Yongin, Gyeonggi-do, 449-863 Korea

Introduction

With recent widespread urgency in solving environmental problems, local environmental contamination in the past has become a serious worldwide problem in such forms as greenhouse effects, acid rain, and ozone depletion. In order to cope with these problems, many countries are trying to mandate to curb the amount of CO2 emission, to install facilities for reducing SOx, NOx in addition to regulate the use of CFC materials. Since the gasification can solve many of the current environmental problems even with energy recovery for wastes, many processes are unveiled during the last decade. In particular, recent interest in the gasification process itself that has been renewed in many developed countries yielded several noteworthy process developments for unconventional feedstock like biomass and municipal solid wastes.

Gasification research has been existed in Korea from late 1940's without much success. As in other developed countries, renewal of the technology starts just after the 1st oil crisis in the early 1970's even though they were basic studies. From 1990's, after the potential impact of IGCC (Integrated Gasification Combined Cycle) technology on the coal-utilizing power plants was recognized after the Cool Water project in USA, Korea started the small-scale process research. From 1993, pilot-scale gasification facilities were constructed in Korea and since then high-pressure gasification for the nine imported coals were performed. With the accumulated knowledge regarding the gasification, application area is being explored for waste feedstock from late 1990's in Korea.

Environmental concerns regarding the old-style coal-utilization and waste treatment technologies have prompted the development and application of gasification processes that produce far less pollutants like SOx, NOx and dioxins while recovering energy mainly as a chemical energy of CO and hydrogen. In Korea, coal needs to make up at least 1/3 of total generated electricity while waste incineration faces many challenges in convincing its environmental cleanness, especially with respect to dioxins and possibility of heavy metal leaching from the combustion ash. During the last eight years, Korea has prepared the application possibilities of gasification process into coal and wastes in that process cost and system availability were the main obstacles. In this paper, current research status of gasification research using coal and combustible wastes is discussed.

Gasification Facilities

A dry-feeding entrained-bed type gasification facility, that is located at Ajou University in Suwon, Korea and can treat 3 ton/day at maximum 30 bar, 1650°C has been built in April 1995. **Figure 1** shows the facility (8 m x 17 m x 20 m) located in 30 m x 50 m space and the corresponding 3-dimensional PDS (Process Design System) picture. Main target feeds are subbituminous and bituminous coals, but petroleum coke is also possible to gasify. Coal feed is identical size with that of conventional power plants using pulverized coal, as 80-90% passing -200 mesh. Pulverized coal is pneumatically conveyed with nitrogen gas at dense-phase into the feeding nozzle system, where 99%-purity oxygen and steam are mixed with the coal powder. Steam is injected separately from the oxygen and coal powder.

Normal operation consists of the preheating, pressurization, transient operation, normal gasification operation, and the shutdown steps. LPG burner at the bottom of the gasifier did preheating of the gasifier at least for 20 hours. Then, nitrogen is introduced to pressurize the gasifier till the operating pressure range in less than 30 min, after this step, oxygen and coal powder are being fed into the gasifier. Coal supply is first started at the low feeding range in order not to cause any sudden pressure buildup in the gasifier and thus causing any back pressurization into the coal feeding lines. This step takes normally less than one hour. Normal hot test operation step for obtaining gasification data is maintained at the steady state for at least 4 hours to provide enough gas, slag, and other process data.

Figure 2 show the view of the gasification facility that was being developed for the liquid or slurry type combustible wastes. Maximum pressure and temperature for the operation are 10 bar and 1550°C, respectively. Left-side view shows the waste-oil feeding facility including the heating lines for waste oils. Right-side view illustrates the main gasifier and the carbon scrubbing system.

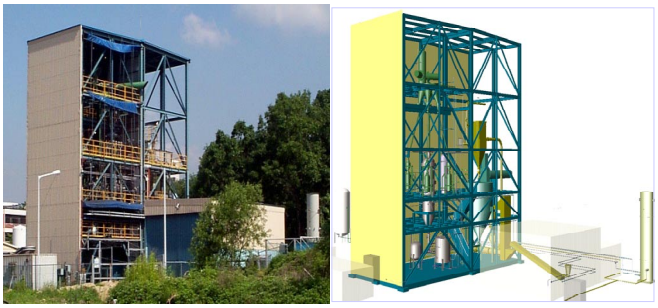

Figure 1. View of the 3 ton/day gasifier system and the corresponding 3-D design view.

Figure 2. Feeding facility (Left) and the gasifier section (Right) of the 1 ton/day-class waste-oil based gasification facility.

Results and Discussion

Total 9 coals were tested under the high-pressure conditions of 12-29 bars and high temperature of 1400-1550°C. Important gasification parameters like carbon conversion and cold gas efficiency for the tested coals showed above 95% and 65-80%, respectively, depending on the coal used. [1]

Among coal properties influencing the gasification process, the removal rate of surface moisture content after drying was more important than the total moisture content in the coal feeding system. In the aspect of ash in coal, since most gasifiers remove ash as a molten slag, ash characteristics are one of the most important

parameters. Among the attributes of ash characteristics grasped in the study, a certain amount of ash in coal exhibits more favorable performance when judging from the experimental point of view.

From experiments that applied in coals of 2-11% ash content, due to satisfactory slag shapes and reasonable shape in coating refractory wall by tested coals, ash content of the coals proved to be in reasonable range for the application in the dry-feeding gasifier. Also, ash-melting temperature applicable in the dry-feeding gasifier was estimated to be better in the range of 100°C lower value than the gasifier reaction zone temperature of 1400-1500°C. That is, coals showing ash-melting temperature in the range of 1300-1400°C were thought to be best candidate coals for the slagging gasifier.

Most coals of bituminous and subbituminous rank, except coals of high fuel ratio (fixed carbon/volatile matter) and high ash content like Australian Curragh (VM 20.0%, FC 56.8%, Ash 16.1% as-received) and Russian Denisovsky (VM 20.1%, FC 59.1%, Ash 12.1% as received) coals, were all successfully applicable in the dry-feeding slagging-type gasifier.

Wastewater sludge was melted under combustion conditions yielding slags as shown in **Figure 3**. Left-side slag was obtained from the as-received feed (CaO/SiO_2=0.11) whereas the right-side slag that exhibits lower flow viscosity was produced after adjusting CaO/SiO_2 ratio as 1.0. Through the tests, self-reacting calorific value for the waste water in the facility was determined as 4,100 kcal/kg-ds, which is more or less higher than reported 3,500 kcal/kg-ds [2] probably due to the insulation depth of the reactor.

Figure 3. Slags obtained from wastewater sludge (unit: cm).

Inner structure of slag after gasification and ash after combustion was analyzed by XRD for the samples obtained from Australian Drayton coal as shown in **Figure 4**. While combusted ash samples show the crystal structure of $CaSO_4$, SiO_2, etc., slag samples exhibit an amorphous structure where all crystal structures in mineral matter were melted without much crystalline nature. Slags that were formed after melting under high temperature gasification temperature and solidification by cooling appear to bind the heavy metal components into the slag structure during the process. As demonstrated in **Figure 4**, heavy metal components appear to be intertwined with melted mineral matter components, so that the inner structure of slag is amorphous. According to the leaching tests on slags, Cu, Cr, Pb, Cd, As, Hg that are regulated as a heavy metal pollutants in a leached water in Korea were not detected at all. Thereby, coal slag can be safely utilized as a construction material or filler for road asphalt and proves not to cause any secondary pollution. Usually coal flyash from a boiler causes a secondary pollution by leaching.

One of the main focuses in the waste-oil based gasification is in minimizing soot production with minimum additional fuel to treat heavy metal containing wastes. More than 50% of waste-oil is reused through simple distillation as a fuel oil in Korea only for the designated boilers as a public bath place. Current obtained carbon conversion was 93% while the cold gas efficiency reached 71% for the waste oil. Another point is the control of residence time for different waste characteristics of melting temperature and slag viscosity for smooth slag discharge.

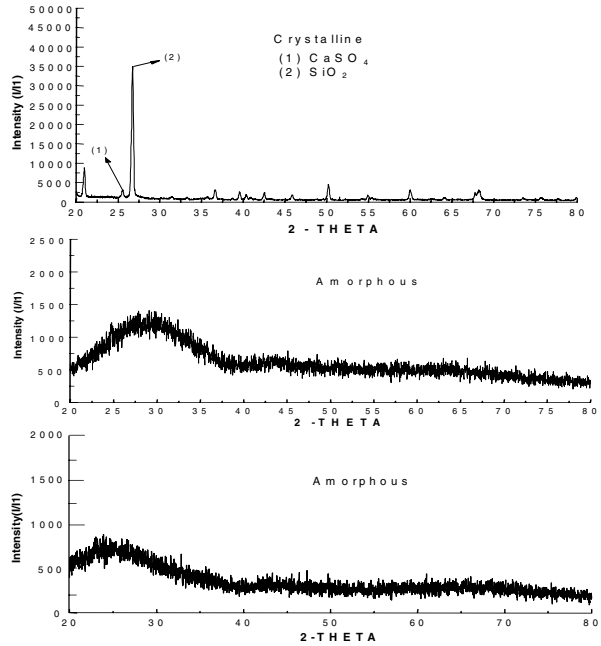

Figure. 4. XRD results of ash and slags from Drayton coal: combustion ash (Top) and slags (Middle: from 3 ton/day gasifier, Bottom: from commercial-scale gasifier).

Conclusions

Slagging coal gasification pilot plant has provided the fundamental technologies that was a basis for the development of slagging combustor/gasifier using the waste feed like a sludge and waste oil. Coal gasification system yielded carbon conversion of above 98% and above 70% cold gas efficiency for the Indonesian subbituminous coals that were the best-suitable coals for gasification among the tested nine imported coals. Wastewater sludge was successfully treated at the developed combustion/melting process with above 90% slag-conversion and without any leaching problems of heavy metal components in slags. Gasification/melting process utilizing the calorific value of waste oil as a heating energy in melting has been installed and tested, in that powder-type wastes are converted into environmentally benign products with minimum extra fuel consumption. Developed combustion/melting process proved that designated-waste sludges can be treated cheaply compared to incineration, although general-waste-class sludges are yet to be competitive with conventional land-filling. Wide application of the technology requires more stringent environmental regulation that will in turn stimulate advanced process developments.

Acknowledgement

This work was supported by KISTEP as one of National Research Lab. Projects in Korea under contract 2000-N-NL-01-C-224.

References

1. Yun, Y.; Yoo, Y.D., *Korean J. of Chem. Eng.*, **2001**, 18(5), 679-685.
2.Greenhut, D.A.; Prepr. Pap.-*Society of Mining Engineers of AIME*, 1991, pp. 1-12.

THE USE OF COAL PYROLYSIS PRODUCTS FOR THE DEVELOPMENT OF THERMALLY STABLE JET FUELS

James J. Strohm, Suchada Butnark, Terry L. Keyser, John M. Andrésen, Mark W. Badger, Harold H. Schobert and Chunshan Song

The Energy Institute and The Department of Energy and Geo-Environmental Engineering, The Pennsylvania State University, 209 Academic Project Bldg., University Park, PA 16802.

Introduction

Conventional paraffin based jet fuels are solely derived from petroleum and are, in addition to serving as the fuel source, designed to act as coolants for the engines and electrical parts of the aircraft at temperatures up to 300°C (1). Lately there has been a driving force towards the development of jet planes that can operate at speeds reaching several Mach (2). The increased heat-load generated by friction with air on the body of the jet plane, the need for compressed air during combustion and higher rate of fuel injection into the engine will result in the fuel experiencing extreme temperatures when acting as coolants (3). These temperatures can reach levels around 500°C or above, and can result in severe coking of the fuel in the fuel-line although the contact time will be on the order of a few seconds. This problem has been identified especially for paraffinic based jet fuels, while naphthenic based jet fuels with a natural content of hydrogen donor compounds have shown improved thermally stability at these high temperatures (4). Correspondingly, feedstocks that can yield both naphthenes and hydrogen donor compounds will yield jet fuels with improved thermal stability.

One such route is outlined in Scheme 1. Pyrolysis of coal generates tars and liquids with a high content of aromatic compounds. From the pyrolysis product a stream with a tailored composition of aromatic compounds can be obtained. Hydrotreating and hydrogenation of such streams can yield naphthenic (cycloalkane-rich) liquids that have jet fuel characteristics. One such example is refined chemical oil (RCO) that is obtained from coal tar from by-product coke ovens (5, 6). Although aromatic streams can also be obtained from petroleum, such as light cycle oils, the high degree of alkylation of the aromatic rings lowers the thermal stability of the hydro-treated products from these streams compared to coal derived streams (7). From Scheme 1 other possible routes for the use of coal pyrolysis products are also outlined. Partial hydro-treatment of the aromatic streams from coal pyrolysis generate streams high in hydrogen donor compounds, such as tetralin, that could either be used as a fuel on its own, or used as thermal stability boosters for paraffinic derived fuels from petroleum or synthesized from coal gasification products. In addition, fully saturated naphthenic streams may also show high thermally stability in itself, or when partially mixed with the hydrogen donor containing stream.

Accordingly, in this study a refined chemical oil and two hydro-treated products with varying contents of aromatic, hydroaromatic and naphthenic compounds, were characterized and probed for their thermally stable properties. The various chemical compositions of the hydrotreated pyrolysis products were tested for their function as thermally stable jet fuels in the pyrolytic regime. In particular, the coal-derived jet fuels were able to withstand temperatures up to 820°C at short contact times even in the presence of dissolved air, while the paraffinic structure of the petroleum-derived jet fuel started decomposing below 720°C. The role of the chemical composition of the coal pyrolysis product towards the thermal stability of the resultant hydrotreated liquids was also investigated.

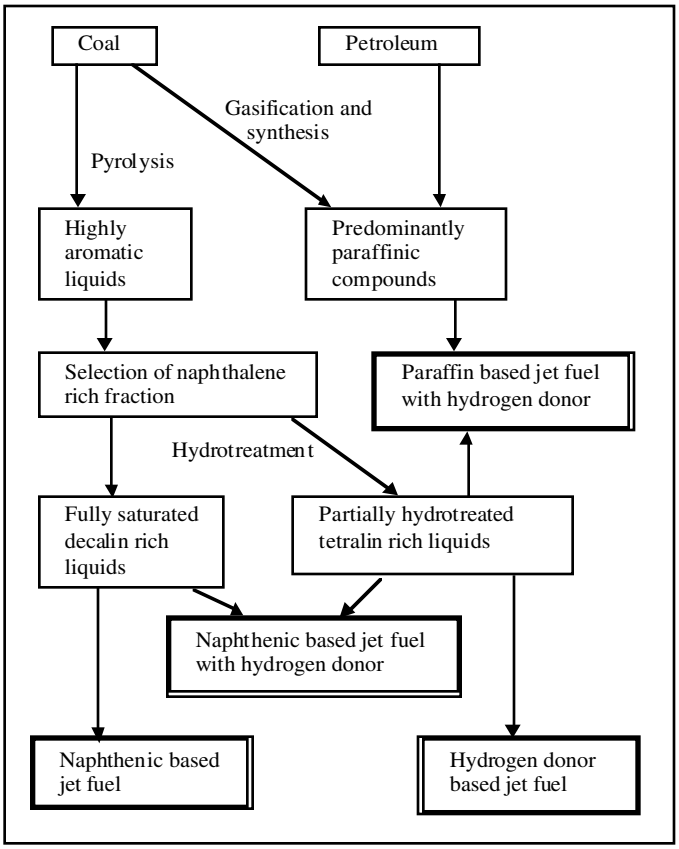

Scheme 1. Scheme of the possible use of coal and petroleum for the production of thermally stable jet fuels, highlighting the role of coal pyrolysis.

Experimental

A refined chemical oil (RCO) was hydro-treated in two steps: (i) severe hydro-treatment of the RCO at 385°C to produce the partially hydro-treated HDT-RCO, and (ii) further saturation and dearomatizing at 315°C to yield SAT-RCO. The jet fuel samples were produced in a pilot plant facility by PARC (8). The flow reactor setup has been characterized elsewhere (9). The GC-MS was performed on a Shimadzu GC-174 coupled with a Shimadzu QP-5000 MS detector.

Results and Discussion

Characterization of samples. The overall chemical makeup of the original refined chemical oil (RCO), its hydrotreated derivative (HDT-RCO) and its fully dearomatized fraction (SAT-RCO) is compared with the standard petroleum-derived jet fuel, JP-8P, in Figure 1. The original RCO is, as expected, highly aromatic and mainly a mixture of naphthalene and its alkylated derivatives, with about 10% alkylated benzenes and around 15% of aromatic compounds with three rings or more. The severe hydrotreatment at 385°C produces a range of hydroaromatics such as tetralin and hexahydroacenaphthalene (HDT-RCO). However, still there are some aromatic compounds remaining. Also, upon hydrotreatment virtually all of the 3+ aromatic rings compounds have one or more of the rings hydrogenated, transforming them into hydro-aromatics. A similar change was found for the naphthalenes, where the major hydroaromatic was tetralin and its alkylated derivatives. The alkyl-benzenes were transformed to cyclo-alkanes. When fully

dearomatized into SAT-RCO, essentially all the aromatics and hydroaromatics have been converted to cyclo-alkanes, which account for over 98% of this fraction. The dearomatization of the coal-derived liquid causes a dramatic conversion to decalins, mostly the *trans*-decalin isomer, but also a considerable content of the *cis*- isomer. Figure 1 also compares the chemical structure of the petroleum-derived jet fuel, JP-8P to that of the three coal-derived streams. As expected, the JP-8P is dominated by a high content of long-chain paraffins. Also, JP-8P does not contain any hydro-aromatic structures such as tetralin, and all the aromatic compounds are alkylated benzenes or alkylated naphthalenes.

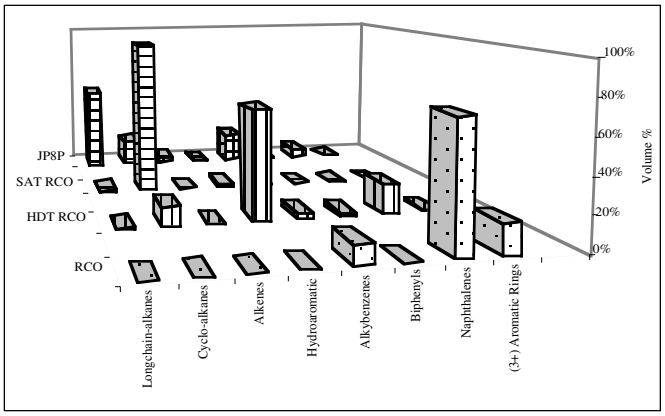

Figure 1. The overall chemical makeup of the coal-derived refined chemical oil (RCO), its hydro-treated (HDT-RCO) and fully dearomatized (SAT-RCO) fractions, compared to that of the standard petroleum derived jet fuel, JP-8P.

Thermal stability of the jet fuels. Figure 2 shows the changes in the chemical composition as detected by GC/MS of the saturated RCO stream when purged with oxygen and heated to 771°C in the flow reactor. The coal-derived fuel, SAT RCO, can be heated to these temperatures with very little thermal decomposition of the structure.

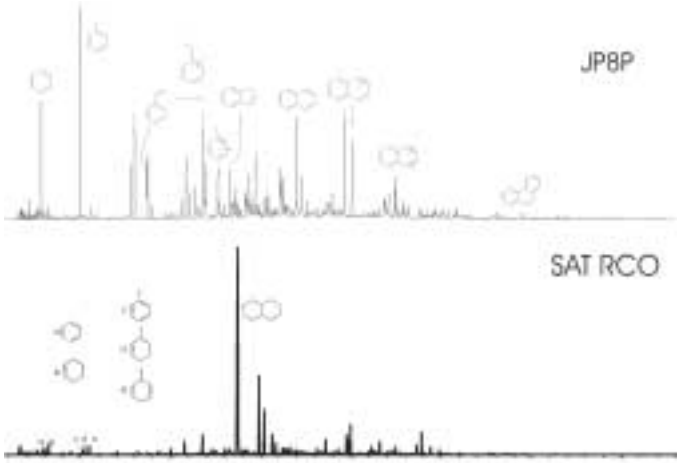

Figure 2. The change in chemical composition as detected by GC/MS of the saturated RCO stream when purged with oxygen and heated to 771°C in flow reactor.

In comparison, when the petroleum-derived jet fuel JP-8P is purged with oxygen and heated to 771°C in the flow reactor severe thermal cracking is observed resulting in a nearly complete transformation of long-chain paraffins into aromatic compounds.

Solid deposition in fuel line. Figure 3 compares the changes in coke deposits along the fuel line of the flow-reactor related to the bulk-fuel temperature. Very little solid deposition is observed in the tube in the temperature range 25 to 450°C. This was unexpected, since the fuels may form gums, especially JP-8P, due to the presence of oxygen in the fuel. The gums are formed in the autoxidative regime from 150 to 350°C. However, due to the high flow rate in the system (LHSP of 450) the gums may not precipitate before 500°C. This can explain the growth in solid deposit peak for JP-8P at 700°C and the subsequent decrease at 750°C before pyrolytic solid deposition increases rapidly at higher temperatures. The coal-derived SAT-RCO jet fuel may have formed some gums at 550°C but does not form pyrolytic solid deposit before 800°C.

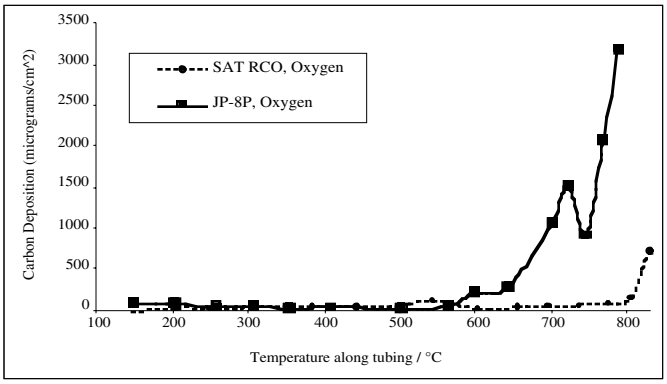

Figure 3. Changes in coke deposits along the fuel line of the flow-reactor related to the bulk-fuel temperature.

Conclusions

A jet fuel derived from a refined chemical oil, obtained from coal pyrolysis, was found to be thermally stable up to 771°C in a flow-reactor. Compared to the petroleum-derived jet fuel, JP-8P, that showed extensive thermal cracking at these temperatures, the coal-derived jet fuel was superior in suppressing the formation of solid deposit in the fuel line.

Acknowledgements. The authors wish to thank the USAF/WPAFB for their support, Koppers and PARC for the RCO sample and preparation.

References

(1) Yoon, E.M.; Selvaraj, L.; Song, C.; Stallman, J.B and Coleman, M.M., Energy & Fuels, **1996**,*10*, 806.
(2) Ben-Yakar, A. and Hanson, R.K., J. Propulsion and Power, **2001**, *17 (4)*, 869.
(3) Edwards, T., Prepr. Pap. - *Am. Chem. Soc., Div. Petr. Chem.*, **1996**, *41(2)*, 481.
(4) Song, C.; Eser, S.; Schobert, H.H.; and Hatcher, P.G. Energy & Fuels, **1993**, *7*, 234.
(5) Butnark, S.; Badger, M.W.; Schobert, H.H., Prepr. Pap. - *Am. Chem. Soc., Div. Fuel Chem.*, **1999**, *44* (3), 662.
(6) Butnark, S., Hydrogenation of Coal Tar Fractions and Refinery Streams. Master Thesis. Pennsylvania State University, December 1999.
(7) Andrésen; J.M., Strohm; J.J, Sun, L. and Song, C, Energy & Fuels, **2001**, *15*, 714.
(8) Wilson, G. R. Project Report on AFOSR-Subcontract for Advanced Thermally Stable Coal-Based Jet Fuels for the Pennsylvania State University. PARC Technical Services Inc. (Pittsburgh, PA) to Pennsylvania State University, May 2000.
(9) Andrésen, J.M.; Strohm, J.J.; Boyer, M. L.; Song, C.; Schobert, H.H.; and Butnark, S., *Am. Chem. Soc., Div. Fuel Chem.*, **2001**, 46(1), 208.

SIMULTANEOUS CO-CARBONIZATION OF COAL AND DECANT OIL: THE EFFECT OF VARYING PROCESS PARAMETERS

Mark Badger, Gareth Mitchell, Nate Herman, Brian Senger and Harold Schobert.

The Energy Institute,
The Pennsylvania State University,
University Park, PA, 16802.

Introduction

The practice and rationale behind the simultaneous co-carbonization of coal and decant oil, or co-coking, has been described at length elsewhere (1-5). However, the main goals of the research into co-coking at Penn State are to develop a coal-based liquid that may be upgraded into a thermally stable jet fuel, and to produce a value-added carbon product of unique properties. To this end, recent efforts have been undertaken to scale up the co-coking process from static small laboratory-scale tubing bomb experiments to a semi-continuous small pilot-scale delayed coker unit.

The delayed coker unit was designed and built in-house by researchers and staff at The Energy Institute after a similar unit operated by PARC Technical Services, Harmaville, PA. The unit has a coke drum with internal dimensions of 7.5cm ID by 102.5 cm high, giving a volume of around 4.5 liters. The unit is capable of operating under typical delayed coking process conditions. The system pressure, temperature and flow rates are monitored by a number of computer-controlled devices, and data from these devices is recorded throughout the run.

The data presented in this preprint concentrates on varying the processing parameters, and studying what affect this has on the yield and composition of the products.

Experimental

This study used Powellton coal, that had been deep cleaned to remove the majority of mineral matter, and low sulfur decant oil. Proximate and ultimate analyses for these feedstocks are shown in Table 1.

Table 1. Proximate and Ultimate Analysis of the Feeds Used in this Study.

	Coal	Decant Oil
Proximate analysis [a]		
Ash (%)	1.9	0.0
Volatile matter (%)	29.4	-
Fixed carbon (%)	68.7	-
Ultimate analysis [a]		
Carbon (%)	86.3	89.7
Hydrogen (%)	5.2	9.3
Nitrogen (%)	1.5	0.2
Sulfur (%)	0.9	0.8
Oxygen (by diff.) (%)	6.1	-

[a]. Values reported on a dry basis

Table 2 shows experimental conditions for each of the tests performed in this study. At least two runs were performed under each of the test conditions. During each run liquid samples were taken at selected intervals. Simulated distillation (SimDis) GC was performed on these samples to study what effect the conditions had over the time of the run on the boiling range. The instrument used was a HP 5890 GC-FID fitted with a MXT-500 Sim Dist column supplied by Restek Corp. After the conclusion of the run a coring bit was used to take a representative sample of the coke bed along its entire height. Proximate and ultimate analysis was performed on the coke samples. In addition, petrographic analysis was conducted on the coke formed in the runs, following a method described previously (5).

Table 2. Matrix of Tests Performed in this Study.

Coal (Wt%)	Decant Oil (Wt%)	Coke drum pressure (psig)	Water feed rate*	Sample set
10	90	25	2%	A
10	90	50	2%	B
20	80	25	2%	C
10	90	25	1%	D

* The water feed rate is a percentage of the feedstock feed rate. For the purposes of this study the feedstock feed rate was set to 1 kg/hr. The water is used for steam injection.

Results and Discussion

Table 3 shows data on the product yields derived for the co-coking under varying process conditions.

Table 3. Average Product Yields for Co-coking Runs with Varying Operating Conditions.

Sample set	Coke yield (wt%)	Liquid yield (wt%)
A	18.5	61.6
B	25.7	66.9
C	24.0	65.2
D	20.2	65.4

Taking sample set A as the base line set of runs observations can be made, with respect to the product yields. With an increase in coke drum pressure, there was an increase in coke yield. This is wholly consistent with results previously reported in the literature (2,6). The corresponding increase in liquid yield is an indication that there was an enhancement of cracking reactions of the higher molecular weight species. This is also exemplified in the data shown on Table 4. With an increase in coal in the feedstock, there was an increase in coke yield. This result is as expected. The ability to accurately determine how much of the coke is coal-derived has not yet been determined. The goal is to derive this value through yield calculations, with back up, concurring results from optical microscopy and other instrumental methods. With the increase in coal to the feedstock, there was an increase in the liquid yield. This result would indicate that the volatiles, from coal, evolved during the coking process were resistant to thermal cracking, and so did not decompose to gaseous compounds. A 50% decrease in water feed rate, and thus steam to the coker, resulted in an increase in coke and an increase in liquid yield. The coke increased because the lower steam rate resulted in less medium volatile compounds being swept from the coke drum. And so these medium volatiles subsequently coked. As there was an increase in liquid yield too, then the coking of the medium volatiles must have partially decomposed to intermediate lower boiling liquids, and to a lesser extent produce gaseous products.

Table 4 shows the results of SimDis GC analyses of liquid samples taken in successive periods during the different co-coking experiments.

Table 4. Yield of Liquids in Specific Boiling Ranges Sampled at Different Times During the Co-Coking Runs.

	Liquid Sample								
	1			2			3		
Sample	Boiling Range (°C)			Boiling Range (°C)			Boiling Range (°C)		
Set	-360	360-500	500+	-360	360-500	500+	-360	360-500	500+
A	22.1	65.8	8.6	29.5	61.1	5.8	31.9	59.3	5.5
B	36.9	51.6	3.9	38.9	49.0	4.3	40.3	50.8	4.7
C	31.7	58.7	4.9	30.2	58.3	6.2	28.9	61.7	7.4
D	27.3	63.1	6.6	28.4	61.6	5.2	32.4	58.9	5.7

For the decant oil feed –360 °C, 360-500 °C, and +500 °C cuts were 14.3%, 65.9% and 18.8%, respectively.

The most important observation that can be made from this data is that as the length of the run progresses the conversion of liquids to lighter boiling material is increased. The main reason for this phenomenon is that the coke bed facilitates the cracking of the high molecular weight species to lower molecular weight species, that boil at lower temperatures. As a run progresses the size of the bed increases, and therefore the time in which the liquids may be in contact with the bed also increases. Thus increasing the propensity for cracking reactions. The exception to this was when the coal loading was increased to 20 wt%. Although the overall liquid yield was increased, (see Table 3) the conversion to lower boiling species decreased over time. This may be because the increase in coal-derived material to liquid products may be resistant to decomposition through thermal cracking. As the majority of the coal-derived species may be of a high molecular weight this would explain the small increase in compounds boiling above 360 ^{0}C as the run progressed.

Petrographic analyses of coke textures derived from coal/ decant oil blends in the laboratory-scale delayed coker, suggested that coal materials were being concentrated near the inlet of the coker and decreased in concentration with increasing bed height (see Table 5). The presence of coal in increasing concentration locally decreased the size of the isochromatic textures derived from the decant oil. The Powellton coal appeared to interact both physically and chemically with decant oil during co-coking and resulted in a significant improvement in the size of the coal-derived isochromatic textures. Changes in other operating conditions with respect to steam injection rate, drum pressure and coal addition, appeared to have an influence. Reduction of steam rate from 2.8 to 0.3 mL/min had a profound influence on increasing the size of isochromatic areas derived from the decant oil. Coke generated at the lowest steam injection rate (0.14 mL/min) and with doubled drum pressure, resulted in a significant amount of isotropic carbon derived from the decant oil. However based on earlier results, it is unclear whether operating conditions alone can be blamed for these changes in coke properties. Increasing the amount of coal in the feed to 20 wt.% had a predictable effect on coke properties, in that more enhanced coal-derived material was observed near the bottom of the core and decreased in concentration and enhancement with increasing distance from the inlet.

Table 5. The Proportions of Textures Derived from Coal and Decant Oil Compared with the Normalized Concentration of Decant Oil Textures (Vol. %).

Distance from Bottom of Core, mm	% Coal derived	% Petrol. derived	% Isotropic	% Mosaic	% Small Dom.*	% Dom.*	% Flow Dom.*
10% Powellton Coal; 20 wt% water feed rate							
0 -21	11.6	88.4	0.0	37.3	60.6	1.6	0.5
26 - 44	11.3	88.7	0.3	27.6	67.7	2.4	2.0
Sample Set A							
0 - 14.5	25.9	74.1	0.0	38.5	50.5	8.6	2.4
102 - 127	12.6	87.4	0.3	10.1	61.9	22.1	5.6
280 - 305	5.6	94.4	0.0	5.6	72.1	19.2	3.1
356 - 381	4.2	95.8	0.0	14.2	52.0	14.6	19.2
Sample Set B							
0 - 34	5.4	94.6	28.9	21.0	42.2	7.1	0.8
45 - 70	4.1	95.9	12.9	17.7	55.8	8.8	4.8
115 - 140	5.4	94.6	17.3	17.3	59.8	3.7	1.9
Sample Set C							
0 - 20	17.7	82.3	0.1	67.2	27.5	3.9	1.3
70 - 95	3.5	96.5	0.3	19.0	65.4	9.3	6.0
356 - 381	0.1	99.9	0.0	7.9	80.3	7.1	4.7
Sample Set D							
0 - 26	14.4	85.6	3.9	45.2	47.9	2.2	0.8
52 - 72	7.2	92.8	85.1	12.7	2.0	0.2	0.0
127 - 150	5.8	94.2	4.8	20.9	57.6	13.6	3.1

*. Dom. = Domain

Conclusions.

Changing the experimental parameters can have a marked effect on the quality and yield of the products produced in the co-coking of coal and decant oil. Increasing the quantity of coal in the feed mix does not seem to have a detrimental effect. However, lowering the water feed rate results in a coke product of poor quality if it was to be used as a value-added carbon. Increasing the drum pressure has a disproportionate effect: The yield of liquids increases with increasing pressure, along with the yield of low boiling liquids. Conversely, the high degree of isotropic carbon reduces the quality of the coke.

References

(1) Badger, M.W.; Fickinger, A.E.; Martin, S.C.; Mitchell, G.D.; Schobert, H.H. Prepr. Pap. - *AIE 8th Australian Coal Science Conference*, **1998,** 245.

(2) Fickinger, A.E.; Badger, M.W.; Mitchell, G.D.; Schobert, H.H. Prepr. Pap. - *ACS Div. Of Fuel Chem.* **2000**, *45*, (3), 299.

(3) Fickinger A.E. "Laboratory-Scale Coking of Coal/Petroleum Mixtures" Masters Thesis. The Pennsylvania State University. July **2000**

(4) Badger, M.W.; Fickinger, A.E.; Mitchell, G.D.; Adams, A.A.; Schobert. H.H. *Proceeding of the 26th International Technical Conference on Coal Utilization and Fuel Systems.* **2001**, 149.

(5) Badger, M.W.; Mitchell, G.D,; Karacen, C.O.; Wincek, R.T. Prepr. Pap. - *ACS Div. Of Fuel Chem.* **2001**, *46*, (2), 564.

(6) Hossain, T., Zaman, N., Jahan, S.T., Podder, J., Rashid, M.A. *J. Mech. Eng. Res. & Dev.* **1994**, *16*, 47.

CATALYTIC PYROLYSIS OF N-HEXANE FOR ETHYLENE PRODUCTION OVER MORDENITE ZEOLITES MODIFIED BY METAL OXIDES

Jian Zheng[a], Jialu Dong[b], Weifeng Zhang[b], Qinhua Xu[b], Chunshan Song[a]

[a]The Energy Institute & Department of Energy & Geo-Environmental Engineering, Pennsylvania State University, 209 Academic Projects Building, University Park, PA16802
[b]Department of Chemistry, Nanjing University, Nanjing 210093, P.R. China

Introduction

Thermal cracking (pyrolysis, or so-called steam cracking) of various hydrocarbons at high temperature (1073-1123 K) for the production of lower C_2-C_4 olefins has been one of the core processes in the petrochemical industry. Besides the large amount of energy consumed in this pyrolysis process, another disadvantage is the difficulty for this process to control the olefins formed, especially the lower yield to ethylene. Therefore, pyrolysis of hydrocarbons in the presence of catalysts[1-6], allowing preparation of lower olefins at lower temperature and with higher selectivity, is a subject of some studies.

The search for catalysts that promote hydrocarbon cracking started in the late 1960s. Till now, the catalysts found active to different extent can be typically classified into three types, *i.e.*, acidic catalysts (amorphous silica-alumina or zeolite crystalline), basic catalysts (such as CaO-SrO-Al_2O_3, KVO_3/corundum etc.) and transition metal oxide catalysts (*e.g.*, Cr_2O_3/Al_2O_3), which are used under the non-aerobic or aerobic conditions[3]. Three catalytic pyrolysis processes, namely Vniios process in Russia (using KVO_3/corundum catalyst), Asahi process in Japan and the deep catalytic cracking (DCC) process in China (both using ZSM-5 zeolite modified with Al and Cr), have been developed[6]. However, they are still far from replacing the conventional pyrolysis technique, and it is therefore worthy exploring approaches to finding highly efficient catalyst system for preparing C_2-C_4 olefins.

In this work, we studied the acid-base and catalytic properties of a series of Mordenite zeolites for the pyrolysis of n-hexane, and modified the least acidic Na^+ type Mordenite by supporting basic metal (such as alkali, alkaline earth) and reductive transition metal oxides. The reaction mechanisms for different catalysts have been discussed.

Experimental

Sample Preparation. Sodium-type Mordinite zeolite (NaM, the unit cell composition: $Na_{6.23}H_{0.02}Al_{6.25}Si_{41.75}O_{96}$) was purchased from HongGuang Molecular Sieve Co., Dalian, China. Three NaHM zeolite samples with different H^+ content were produced by ammonium ion exchange of NaM zeolite at 353 K for different times, each time for one hour, followed by calcinations at 773 K for 5 hours. Proper amount of alkali (Li, K, Cs), alkaline earth (Mg, Ca, Sr), and transition metals (Cu, Mo, Mn, Ag, etc.) oxides were introduced into NaM zeolite by impregantion of the respective metal nitrate solutions at 353 K, followed by calcinations at 973 K for several hours.

Characterization. The acidic and basic properties of Mordenite zeolites with or without metal modification were analyzed using NH_3-TPD and CO_2-TPD, respectively. Before the TPD experiments, all samples had been treated at 773K in N_2 for several hours. The adsorption of NH_3 or CO_2 was saturated at room temperature, followed by purging with N_2 at 333 K for at least one hour. TPD was then carried out at a heating rate of 12 K/min. The reduction of transition metal oxides was characterized by conventional TPR. All temperature-programmed studies were carried out using a TCD detector, and the TPD or TPR peak signals were recorded and calculated quantitatively.

Catalysis. Catalytic pyrolysis of n-hexane was performed in a continuous flow micro-reactor. N-hexane flew continuously through the catalyst together with steam, with the steam/hydrocarbon weight ratio to be 0.9 and the space velocity (WHSV) to be 3.6 h^{-1}. The reactor temperature was 808K for bare zeolite catalysts and 890K for metal oxide modified NaM catalysts. The reaction products after TOS of 1 h were analyzed by on-line gas chromatography with a TCD detector and Porapak Q column. Results were reported as conversions calculated as the weight percent of n-hexane reacted, molecular selectivity and yields, especially to ethylene.

Results and Discussion

The curves of ammonia thermal desorption for NaM and three NaHM zeolites (figures not shown) exhibit mainly two peaks: low-temperature peak with T_{max} at 497 K, typically representative of weak Lewis acid centers or cationic sites, and high-temperature peak with T_{max} at 813 K, corresponding to strong Brönsted acid centers. It is found that, the higher temperature peak increases with the proton content in the NaHM zeolites, while the same peak can hardly be found in the case of NaM zeolite. **Figure 1** shows the catalytic pyrolysis results over the zeolites as a function of acidic amount, which was calculated from the amount of the NH_3-TPD peak at higher temperature. There is a clear trend that, with the increase of zeolite acidity, the activity increases while both the selectivity of ethylene and the ratio of $(C_1+C_2)/C_3$ decrease. This is due to the well-known cracking reaction on acidic catalysts, possibly via carbenium ion mechanism: the strong Brönsted acidic sites of NaHM zeolites protonate n-hexane to form carbenium ions, followed by β-scission to form smaller molecules. According to this mechanism, C_3 hydrocarbon and alkane would be the predominant cracking products rather than ethylene. Meanwhile, secondary undesirable reaction such as aromatization might occur between the olefin products and the carbenium ion intermediates, and coke formation becomes severe with the increase of strong acidity.

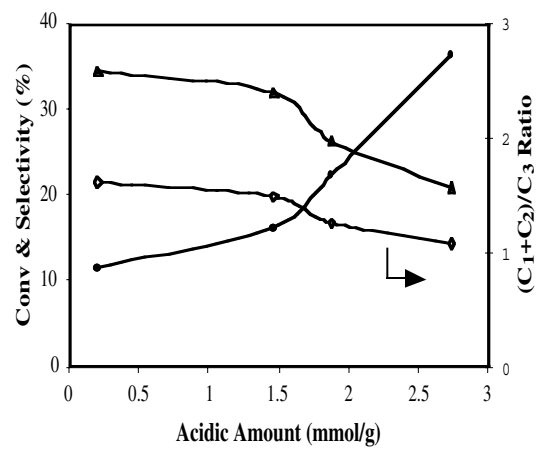

Figure 1. Catalytic pyrolysis (808 K) results of n-hexane over Mordenite zeolites with different acidic amount.
●: Conversion of n-hexane; ▲: Yield of ethylene
✧: $(C_1+C_2)/C_3$ Ratio.

In order to increase the ethylene selectivity, non-acidic NaM zeolite was selected, and basic metal oxide such as alkali (Li, K, Cs) and alkaline earth (Mg, Ca, Sr) were incorporated.

Figure 2 shows results of catalytic pyrolysis over metal supported NaM zeolite catalyst as a function of base amount, which was calculated from the peak amount of the CO_2-TPD (pictures not shown). It is interesting to find that with the increasing basic sites introduced, both the activity and the yield to ethylene increase. This is because the catalytic cracking over non-acidic or basic catalysts with steam conditions follows a free radical mechanism, where the selectivity to alkene, especially ethylene, increases when compared with the carbenium ion mechanism on acidic catalysts.

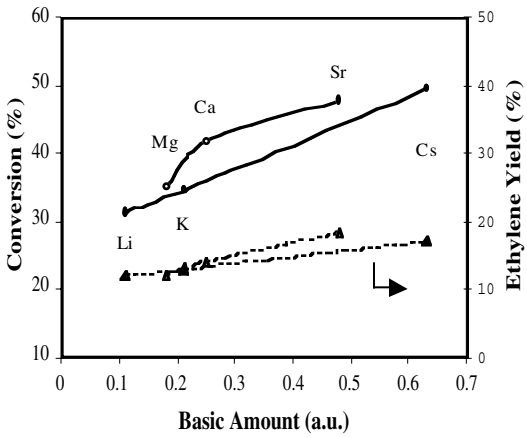

Figure 2. Catalytic pyrolysis (890 K) results of n-hexane over alkali and alkaline earth metal oxide supported Mordenite zeolites with different basic amount.
●: Conversion of n-hexane; ▲: Yield of ethylene.

TPR profiles of different transition metal oxide supported on NaM zeolites (pictures not shown) differ from one another because of the difference in both the electronic state and the reducibility of each metal oxide. For example, the reduction of CuO/NaM starts at about 500 K, while MoO_3/NaM can only be reduced at temperature higher than 870 K. It's therefore our intention to compare the catalytic cracking results of these catalysts as a function of their reducibility.

Figure 3 shows the results of the catalytic pyrolysis over transition metal (Ag, Cu, Mn, Mo) oxides supported NaM zeolite as a function of the starting temperature of respective TPR peaks. It can be found that, the metal oxides that are easier to be reduced (except MnO) show approximately higher catalytic acitivity and yields to alkenes including ethylene. It has been reported that, catalytic cracking over non-reducible transition metal oxide catalysts such as Cr_2O_3/Al_2O_3 under aerobic conditions, *i.e.*, oxidative catalytic cracking, follows a free radical mechanism, where activated oxygen species abstract hydrogen from hydrocarbons to form radicals[3]. Accordingly, high yields of ethylene would be expected[3]. The present work does not involve O_2 during the catalytic pyrolysis. However, lattice oxygen in reducible transition metal oxide supported catalysts may exhibit the similar free-radical oxidative catalytic cracking of n-hexane. The easier the metal oxide to be reduced, the higher extent of this oxidative effect might have.

We also found that, if the transition metal oxide was reduced to metal, the catalytic activity decreased greatly. For example, the conversion of n-hexane over PbO_2/NaM and VO_3/NaM catalysts are 57.2% and 37.0%, respectively. But for Pb/NaM and V/NaM, they are only 10.8% and 3.6%, respectively. This shows again the importance for the existence of oxidative cracking.

Table 1 shows the catalytic pyrolysis over the same transition metal oxide supported catalysts with or without steam. It can be seen that, in the presence of steam, the catalytic activity and ethylene selectivity decrease greatly. This indicates that steam plays an important role in keeping the transition metal oxides at higher oxidation state and therefore exhibiting the oxidative catalytic pyrolysis for n-hexane.

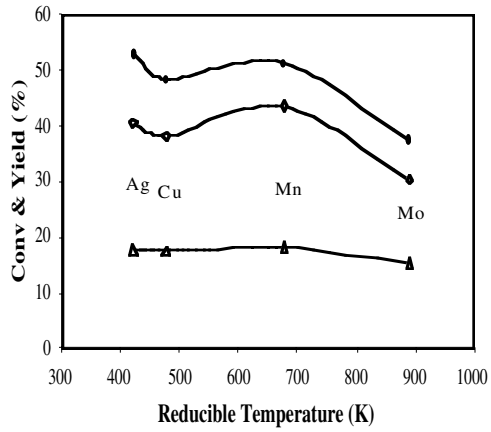

Figure 3. Catalytic pyrolysis (890 K) results of n-hexane over alkali and alkaline earth metal oxide supported Mordenite zeolites with different basic amount.
●: Conversion of n-hexane; ▲: Yield of ethylene.
✧: Total yields of alkenes.

Table 1. Results of catalytic pyrolysis of n-hexane over M_xO supported NaM in N_2 or H_2O (890 K, WHSV 3.6 h^{-1}, H_2O/henxae ratio 0.9, TOS 1h)

Cat.	Conversion (%)		X_{C2H4} (%)*		Y_{alkene} (%)*	
	a	b	a	b	a	b
Ag_2O/NaM	28.0	53.0	34.3	33.6	19.8	40.6
CuO/NaM	28.6	48.5	20.2	36.0	19.4	38.2
MnO/NaM	26.3	51.4	31.0	35.5	19.4	43.7
MoO/NaM	11.8	37.5	38.8	41.0	8.5	30.4

*X_{C2H4}: Selectivity to ethylene; Y_{alkene}: Yield of alkenes.
a: Reaction in N_2; b: Reaction in H_2O

Acknowledgement. We are grateful for the financial supports from National Natural Science Foundation of China, SINOPEC, and the Pennsylvania State University.

References

(1) Le Van Mao, R.; Melancon, S.; Gauthier-Campbell, C.; Kletnieks, P. *Catal. Lett*. **2001**, *73*, 181-186.
(2) Erofeev, V. I.; Adyaeva, L. V.; Ryabov, Yu. V. *Russ. J. Appl. Chem.* **2001**, *74*, 235-237.
(3) Yoshimura, Y. et. al. *Catal. Surv. Japan*, **2000**, *4*, 157-167.
(4) Shi, Z.; Zhang, F.; Liu, S. *U.S. Patent* 6,211,104, April 3, **2001**.
(5) Xie, C.; Li, Z.; Shi, W.; Wang, X. *U.S. Patent* 6,210,562, April 3, **2001**.
(6) Picciotti, M. *Oil & Gas J.* **1997**, *97*, 53-58.

Ruthenium ion catalyzed oxidation as a tool for the characterization of pyrolysis non-volatile products

Marco Antonio G. Teixeira, Maria Luísa A. Gonçalves, Rosana C. L. Pereira

PETROBRAS R&D Center/Chemistry
Cidade Universitária, 21949-900, Rio de Janeiro, RJ, Brazil
marcoa@cenpes.petrobras.com.br

Introduction

Processing high-density petroleum feeds, that are nowadays very important in the scenario of fossil fuel supplies, brings naturally the challenge of dealing with abundances of heavy ends and coke precursors. On the other hand, the optimization of refining facilities to deal with such feeds brings economical competitiveness, since these oils have low prices in the international market.

Studies on pyrolysis mechanisms are quite important under this aspect. Coking units, for example, which have traditionally been the second places among refining units, after FCC, may have their operation optimized with deeper knowledge on the pyrolysis mechanisms. Even the operation of FCC units, specially the ones processing distillation residua as part of their feed or its integrality, may take advantage of pyrolysis studies, since in these cases a meaningful portion of the coke formed in the reversible deactivation of the catalysts may come from thermal degradation of the feeds. In summary, as previouly stated by Speight (1), the key for optimization in the conversion of heavy residua lies on the understanding of coking phenomena, though the understanding of the main coke percursors, which are asphaltenes. In a previous study of thermal decomposition of asphaltenes, that author (2) had worked on the thermal decomposition of asphaltenes from 300 to 900ºC, and observed the occurrence of low molecular weight species in the volatile products. The most complex aromatic systems remain as coke, the non-volatile residue (45 % in weight).

Many efforts on the understanding of pyrolysis mechanisms can be found described in literature, and a main techinque for that is thermogravimetry, mainly if coupled to GC-MS; however, most of them are dedicated to the study of the volatile products formed (3-9). Of course those fractions are the most important ones from the economical point of view, since these are the ones that can be converted to valuable fuel products; nevertheless, the fact that completely established analytical approaches for the characterization of the coke formed do not exist is a major limitation to the study of this fraction, which is quite important to bring a full comprehensive analysis of pyrolysis phenomena.

This paper brings a novel approach for that aim. Ruthenium ion catalyzed oxidation (RICO) is employed to allow a better characterization of the coking process. That reagent allows selective oxidation of aromatic structures. CO_2 is the product of these oxidations in aromatic carbons. Alkyl side branches yield carboxylic acids, while naphtheno-aromatics and chains connecting two aromatic nuclei yield dicarboxylic acids. Condensed aromatics yield mainly dicarboxylic aromatic acids (*e. g.*, the main product of the oxidation of naphthalene is phthalic acid).

Since coke is basically constituted by aromatic nuclei with aliphatic branches, the relative yields and the distribution of products can be expected to be an indication of coke structure. This was confirmed in the present work. The application proposed was employed for the monitoration of the different structures of coke generated by the pyrolysis of asphaltenes at several decomposition temperatures.

So, conditions were proposed to execute the RICO reaction with coke. The strategy considered here is to employ this characterization scheme as a complimentary source of information to the study of volatile product formation, which can be monitored by some of the techniques mentioned above.

Experimental Procedures and Results

For a perfect control of the conditions of pyrolysis of asphaltenes, a TG oven was employed. The collection of volatile material was achieved by passing the effluent gas stream into dichloromethane. Previous experiences employing TG-GC-MS showed that interface optimization can be necessary for that. The scope of this work did not aim the characterization of these products; that has been discussed elsewhere (10).

Asphaltenes from a Brazilian oil obtained by IP-143 were the material chosen to undergo pyrolysis . Table 1 shows the elemental analysis and aromaticity (ratio of the area of the envelope in the range of 160-100 ppm and total area of solid state ^{13}C NMR spectra) of those asphaltenes and cokes obtained after their pyrolysis at several temperatures.

Table 1. Characterization of Asphaltenes Submitted to Pyrolysis and Cokes Obtained at Several Temperatures

Temperature (°C)	Coke (weight %)	%C	%H	% aromatic carbon	Atomic ratio (C/H)
-*	-*	85.8	8.4	55.5	0.85
320	94	85.9	7.8	60.9	0.92
380	90	86.2	7.6	66.8	0.95
400	87	86.3	7.2	67.8	1.00
440	65	85.7	6.2	75.5	1.15
480	53	88.7	4.1	82.3	1.80
550	51	87.0	3.3	97.8	2.20
580	50	86.4	2.7	99.0	2.67

*original asphaltenes

The RICO reaction was performed using an adaptation from literature (11,12). The procedure consists of stirring, 150 mg of asphaltenes or pyrolysis residues obtained at each temperature, at 40ºC for 24 hours with CCl_4 (20 mL), $NaIO_4$ (3.4 mg), H_2O (30 mL), acetonitrile (20 mL) and $RuCl_3.H_2O$ (7 mg).

The resulting two layers are separated and the organic phase, after being concentrated, was mixed with excess of ethereal diazomethane.

The ethereal solution was analyzed submitted by a gas chromatography/mass spectometry (GC/MS) for methyl ester analysis. Samples were injected with the previous addition of an internal standard in splitless mode using a 5%-phenyl 95%-methyl siloxane capillary column (30 m x 0.25 cm x 0.25 μm) and helium as carrier gas. Mass spectrometer was operated in electron impact ionization mode (70 eV) and scanned from 15 to 450 m/z.

As long as similar conditions were employed in all of the oxidation procedures, a comparison by the absorbance at the same wavenumber of the esters obtained after oxidation and reaction with diazomethane could be considered an indication of the relative yields. This was possible by doing equal dilutions of isolated materials after each reaction and recording the infrared spectra of the solutions.

Table 2 shows a comparison the ratios of the total responses of the esters of the cokes obtained at different temperatures to the

total responses of the esters obtained form the asphaltenes by GC/MS (total ion area with corrections were made using the areas of the internal standard) and infrared spectrophotometry (absorbances). These data cannot be taken as quantitative or strictly comparable ones, since it is well known that MS responses and infrared absortivities vary with the distribuiton of components in each sample, and the analyses refer to the reaction products, which are mixtures of different components depending on pyrolysis temperature. However, it can be seen that there are basically 3 groups into which the pyrolysis temperatures can be divided: before 380ºC there is no meaningful variation, while after 440ºC there are no more appreciable amounts of non polycondensed aromatic material. In fact, kinetic studies (10) show that the temperature in which pyrolysis has its maximum speed is 425°C.

Table 2. Indications Of Relative Yields Of Esters From The Oxidation Of Cokes (Ratio To The Responses From Asphaltene Oxidation) By 2 Techniques

Temperature (°C)	Infrared	MS
320	0,95	0,94
380	0,47	0,76
400	0,45	0,69
440	0,13	0,04
480	0,11	0,04
550	n.r.*	0,01
580	n.r.*	n.r.*

*negligible responses

Figure 1 summarizes the main classes of esters found by MS and shows the relative abundance of each of these classes, in terms of the ratios of their collective area in total ion chromatograms to the area of the internal standard (*raid*). It can be seen that linear chain esters are the most important ones in asphaltenes and in low temperature coke, indicating the abundance of linear aliphatic side chains in these samples.

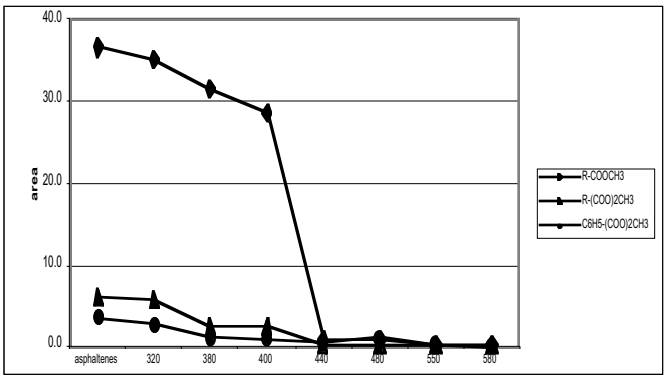

Figure 1. Yields of esters after RICO of cokes obtained by asphaltene pyrolysis at several temperatures

Figure 2 shows that, as a general tendency, the higher the number of carbons, the lower the temperature the side chains undergoes pyrolysis.

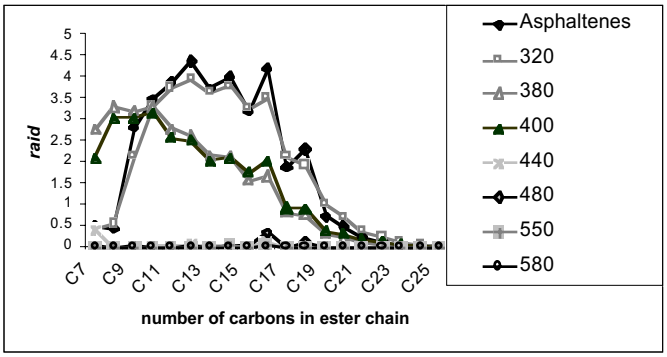

Figure 2. Distribution of monoesters after RICO of cokes obtained by asphaltene pyrolysis at several temperatures

Conclusions

RICO followed by esterification of the oxidation products is a useful tool to the study of pyrolysis material (coke). It allowed some important inferences, about the fact that the profile of remaining components after heating asphaltenes dramatically changes in temperatures above 440°C, about the distribution of aliphatic chain lengths in cokes obtained at different temperatures, and about the tendency of ease of the alkyl groups bonded to aromatic nuclei to undergo pyrolysis according to the number of carbons in the chain. Future studies by the authors aim the integration of the data into a reasonable pyrolysis pathway.

References

(1) Speight,, J. G., . Prepr. Pap. - Am. Chem. Soc., Div. Fuel Chem, **1994**, 39(2), 200.
(2) Speight, J.G., In Characterization of heavy crude oil and petroleum residue, Ed. Technip: Paris, 1984, pp.29-32.
(3) Wilhems, A., Larter, S.R., E Schulten, H.R., Org. Geochem., 20(7), **1993,** 1049.
(4) Skjevrak, I., Larter, S. Graas, G.V., Jones, M. Berger, E., Org. Geochem., **1993**, 22(3/5), 873.
(5) Eglinton,T.I., Larter, S.R., Boonmj.J., J. Anal. Appl. Pyr., **1991**, 20, 25.
(6) Jones, D.M., Douglas, A.G., Energy & Fuels, **1987**, 1, 468.
(7) Bestougeff, M.A., Guiochon, G., Jaqueé, J. Compt. Rend., **1962**, 254(2), 266.
(8) Nicksic, S.W., Jeffries-Harris, M. J., J. Inst. Petrol., **1968**, 54(532), 107.
(9) Calderon, J.L., Cotte, E., Rev. Tec. INTEVEP, **1983**,3(1), 69.
(10) Gonçalves, M. L. A., Teixeira, M. A. G., Pereira, R. C. L., Mercury, R. L. P., Matos, J. R., J. Therm. Anal. Cal., **2001**, 64, 697.
(11) Strausz, O.P., Mojelsky, T.W., Montgomery, D.S., Aostra J. Res.**,** **1985**, 2(2), 131
(12) Murata, S., U-Esaka, K., Ino-Eu, H. Nomura, M., Energy & Fuels**,** **1994**, 8(6), 1379.255-274.

PYROLYSIS YIELDS OF COAL TAR PITCHES: EFFECT OF POLYMERIZATION ADDITIVES

M. Mercedes Maroto-Valer, Yinzhi Zhang, Brandon N. Shaffer and John M. Andrésen

Department of Energy and Geo-Environmental Engineering and The Energy Institute, The Pennsylvania State University, University Park, PA 16802.

Introduction

The pyrolysis of coal tar pitches is associated with the emission of hazardous and carcinogenic polyaromatic hydrocarbons (PAHs) resulting in strong environmental and commercial challenges from the carbon industry (1). In order to prevent the shortcomings of the weight loss of coal tar pitches during pyrolysis, while optimizing their properties, a series of additives are routinely used to achieve high carbon yields upon baking or pyrolysis (2, 3). These additives typically include sulfur compounds that promote the polymerization of coal tar pitches and therefore increase the carbon yields. Although these sulfur additives effectively increase the carbon yields, they also evolve detrimental sulfur species upon baking. Accordingly, this work compares the pyrolysis yields of conventional sulfur additives as well as a series of alternative additives on basis of the pitch yield.

Experimental

The coal tar pitch and calcined coke samples used for this study were supplied by Carbone of America. The thermogravimetical analysis (TGA) were carried out on a Perkin Elmer TGA-7 with a heating rate of 5°C/min from ambient up to 900°C, using about 10 mg of sample under a flow of N_2. The production of green carbon bodies was conducted following a protocol previously established by the investigators (4). The paste mix was heated to ~130°C and pressed into pellets to produce carbon bodies with dimensions of ~ 27mm in diameter and 15mm in height. The absolute densities of the pellets were measured by using a Quantachrome MVP-1 Multi Pycnometer and employing helium as density medium. The green bodies were baked in a closed system by placing them inside crucibles and covering them with calcined petroleum coke. The crucibles were then placed inside a muffle furnace and the baking program used was as follows: (1) 25-500°C at 10°C/hour; (2) 500-1075°C at 25°C/hour; and (3) held at 1075°C for 16 hours, providing an overall length of around 5 days for a completed baking and cooling cycle. Closed environments and slower baking programs have been previously reported to result in significant higher pitch yields and apparent and helium densities than those reported for open systems (5).

Results and Discussion

Comparison of pyrolysis pitch yield. The thermal gravimetric profiles of the pitch alone and its mixtures with additives A1 and A2 are shown in Figure 1. The investigated pitch started losing weight at temperatures above 150°C and lost around 62 wt% during its carbonization at temperatures up to 850°C. When the pitch was mixed with different concentrations of the additive A1, the weight loss at 850°C was reduced, indicating an improvement in the solid yield, compared to that of the pitch alone. Furthermore, the pitch yield increased with the amount of additive at concentrations up to 10 wt% addition of A1 (3). The initial weight loss observed for the pitch/additive mixture was attributed to weight loss directly associated with the additive A1, as also indicated by the fact that the mixture with the highest additive content started losing weight at lower temperatures.

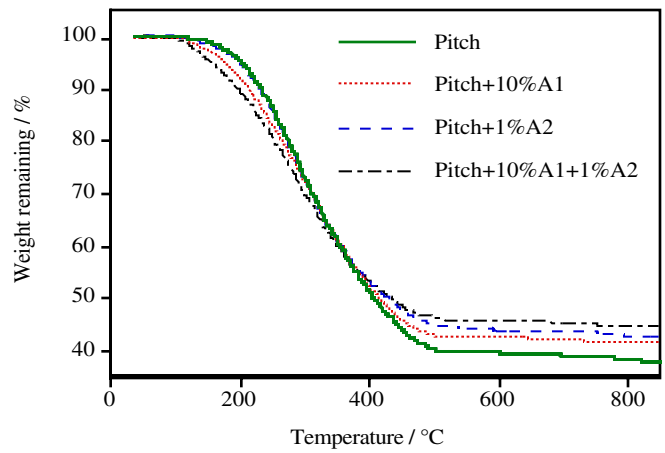

Figure 1. Comparison of the pyrolysis TGA traces for the coal tar pitch alone and mixed with additives A1 and A2.

A second additive A2 was also investigated and showed that when the pitch was mixed with only 1 wt% of A2, the weight loss at 850°C was reduced, indicating an improvement in the solid yield, compared to that of the pitch alone. Therefore, lower concentrations of additive A2 produced similar pitch yields to those observed at higher concentrations of additive A1. When the pitch is mixed with hybrid additives (10 wt% of A1 and 1 wt% of A2) the weight remaining at temperatures above 400°C is higher than when using only A1 or A2 (Figure 1). As previously observed for single additives, the pitch/additive A1+A2 mixture started to lose weight at temperatures lower than the pitch alone (120°C vs. 150°C) and presented larger weight loss than the pitch alone in the temperature range 120°C-300°C, due to weight loss directly associated with the additives (3). The pitch yields observed for the hybrid mixture were higher than those reported for the single additives, indicating that a possible synergistic effect takes place when adding both additives.

Sulfur additives, namely S1 and S2, were also tested to compare their performance with the alternative polymerization additives A1 and A2. When adding 1 wt% of S1, the pitch weight loss decreased from 62 wt% to around 58 wt% at 850°C. Similar pyrolysis pitch yield was reported when adding 1 wt% of A2, indicating that the additive A2 has similar performance in terms of pitch yield to S1. However, the mixture of pitch with sulfur additive S1 presents very similar weight loss profile to that of the pitch alone at temperatures <200°C, while the additives A1 and A2 presented higher weight loss in that temperature range. The pyrolysis pitch yields at 850°C of all the additives mixtures are compared in Figure 2. The alternative additives A1 and A2, have at least equal or superior performance in terms of pitch yields than conventional sulfur additives S1 and S2. Furthermore, the mixture of pitch with 10 wt% additive A1 presented higher pitch yield than the other mixtures, including those of the sulfur additives S1 and S2. The pitch yields observed for the hybrid mixture were higher than those reported for the sulfur additives. Finally, the pitch yields obtained from the thermogravimetric studies are generally low, due to the open system used as well as the high heating rates (5).

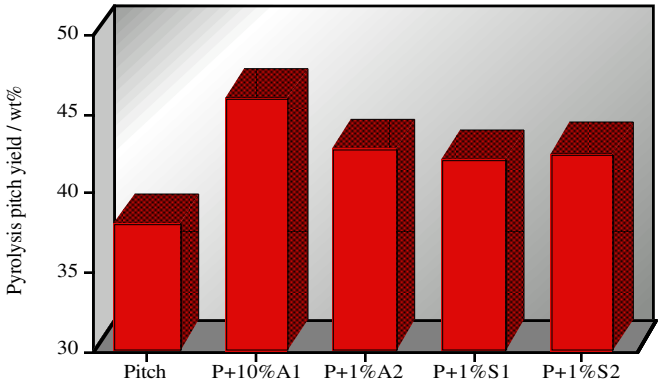

Figure 2. Pyrolysis pitch yields for the pitch alone and the mixtures with the different additives.

Comparison of pyrolysis pitch baking yields for alternative additives and sulfur additives. Carbon bodies were prepared using the alternative additives A1 and A2 as well as the sulfur additives S1 and S2 to compare their pitch yields. The green carbon bodies prepared with S1 and S2 contained seven different particle size coke fractions, while the green carbon bodies prepared with the A1 and A2 additives only contained two coke fractions. Table 1 shows that the apparent and helium densities of all the green carbon bodies prepared with the different additives were very similar, indicating that the additives did not have any impact in the density of the carbon body produced.

Table 1. Apparent and helium densities for the green carbon bodies.

I. D.	Apparent Density g/cc	Helium Density g/cc
CB	1.574	1.783
CB-A1*	1.762	1.829
CB-A2*	1.764	1.843
CB-S1	1.683	1.791
CB-S2	1.710	1.752

* Formulation comprises two coke fractions, while the other formulations comprise seven coke fractions.

Table 2 shows the pyrolysis pitch yields and the helium densities of the baked carbon bodies prepared with the additives A1, A2, S1 and S2. The baking temperature was 1075°C, as previously described. The helium densities of all the baked bodies are in the range 2.031-2.097g/cc (Table 2).

Table 2. Pyrolysis pitch baking yields and helium densities for the baked carbon bodies.

I. D.	Baking Temperature °C	Pitch Yield %	Helium Density g/cc
CB-1075	1075	69.5	2.077
CB-A1-1075*	1075	73.4	2.097
CB-A2-1075*	1075	75.8	2.093
CB-S1-1075	1075	72.7	2.057
CB-S2-1075	1075	72.5	2.031

* Formulation comprises two coke fractions, while the other formulations comprise seven coke fractions.

Figure 3 shows the pyrolysis pitch baking yields of the carbon bodies. When using the A1 and A2 additives, the pyrolysis yields are slightly higher than the yields of the bodies prepared using the S1 and S2 sulfur additives. One caveat in this comparison is the different formulations used, where the carbon bodies prepared with the S1 and S2 sulfur additives contained seven different coke fractions, while the green carbon bodies prepared with the A1 and A2 additives only contained two coke fractions. Accordingly, further studies will be conducted to assess the effect of the coke formulation and also to investigate higher concentrations of S1 and S2 additives.

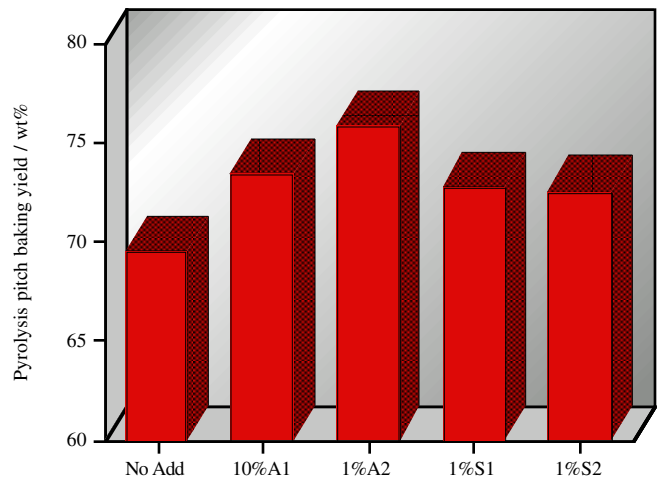

Figure 3. Pyrolysis pitch baking yields for the carbon bodies.

Conclusions

There is a clear need to reduce the emissions of PAHs from coal tar pitches by improving the pyrolysis yield. This study has shown that all the polymerization additives tested thus far increase the pitch yields, with the highest pitch yields corresponding to the hybrid additives A1+A2. The polymerization additives tested, A1 and A2, present higher yields than the S1 and S2 sulfur additives tested. The helium and apparent densities of the green and baked carbon bodies are very similar, regardless of the type of additive used.

Acknowledgements. The authors would like to acknowledge the Carbon Research Center of The Pennsylvania State University for support.

References

(1) Cirovic D.; Brereton R.G.; Walsh P.T., Ellwood J.A.; Scobbie E. *Analyst*, **1996**, 121(5), 575.
(2) Zhang, Y.; Maroto-Valer, M.M.; Andrésen, J., Proc. of Carbon'01, July 14-19, 2001, CD paper.
(3) Andrésen, J.M.; Zhang, Y.; Jensen, K.; Rusinko, F.J.; Schobert, H.H.; Prepr. Am. Chem. Soc. Div. Fuel Chem., 2001, 46(1), 292-293.
(4) Maroto-Valer, M.M.; Andrésen, J.M.; Andrésen, C.A; Battista, J.J., 1999 Int. Ash Utilization Symposium, 534-540.
(5) Maroto-Valer, M.M., Andrésen, J.M., and Zhang, Y., 2001, Carbon Research Center, Tech. Transfer Session Progress Report, The Pennsylvania State University, May, 2001.

ELECTROCHEMICAL PROPERTIES OF MCMBS AS ANODE FOR LITHIUM ION BATTERY

Baohua Li, Ruixia Guo, Kaixi Li, Chunxiang Lu, Licheng Ling

State Key Laboratory of Coal Conversion, Institute of Coal Chemistry, Chinese Academy of Sciences, P.O. Box 165, Taiyuan, Shanxi 030001, P.R. China

Introduction

It is recognized that lithium secondary batteries using lithium metal exhibit problems, which make it difficult for their wide usage in consumer market. The problem is the unsafe characteristic, such as combustion and explosion due to dendrites formed at the surface of lithium metal during charge-discharge cycles. To solve this problem, a "rocking-chair" battery, which uses another intercalation compound as the anode for the lithium secondary battery, has been proposed. Among the alternative materials, which could replace lithium metal as the anode, the carbon materials are very desirable from the viewpoints of being abundant. Carbon materials have received much attention as anode material for lithium ion batteries since 1990. Various carbon materials have been investigated and shown good performances as the host for lithium [1-7]. They have high reversible capacity, high cyclic efficiency(ca,100%) , low electrochemical potential (•1V vs .Li/Li^+) and long cycling life.

The theoretical lithium storage capacity of a graphite anode for a lithium secondary battery has been considered to be 372mAh/g, corresponding to the first stage Li-GIC (Lithium-graphite intercalation compound, LiC_6). To further increase the energy density of lithium secondary batteries requires increasing the specific capacities of the electrode materials. Mesophase microbead (MCMB) prepared from petroleum pitch or coal tar is one of the candidate carbon materials available commercially. since it has high specific capacity(•500 mAh/g) and a spherical structure[4] which can be easy for closely packing, resulting in high density of electrode. Its low surface area can also minimize the side reactions during charge-discharge process. The present work studied the charge-discharge properties of MCMBs with different mean diameter and size distribution.

2 Methods

2.1 Preparation of MCMB. MCMB was prepared by heat-treating coal tar pitch with 3.7%wt pyridine insoluble fraction (PI) at 723K for 1~4h under autogenous pressure. Mesophase pitch was filtrated at 423K. The residue was then extracted by pyridine to get MCMB, which was further carbonized at 973K for 1h under N_2.

2.2 Analyses of SEM. The surface morphology of the isolated spherule after heat-treatment at 973K was observed under scanning electron microscope (Hitach H-600).

2.3 Electrochemical measurement. Working electrodes were fabricated by mixing MCMB with 10% wt of binder poly-[tetrafluroethylene](PTFE) and were dried at 433K under vacuum for 12 h in a dry box.

Electrochemical measurements were performed by using three-electrode cells. Carbon electrode was used as work electrode. Lithium metal was used as a counter electrode and a reference electrode. The electrolyte was 1MLiPF6-EC/DEC (volume1: 1) solution. All the operations on the cells assembled were carried out in the glove box filled with argon gas. Galvanostatic cycle was carried out at a constant current density of 15mA/g, and the cut off range is from 0.001 to 2V vs Li/Li^+.

3 Results and discussion

3.1Features of isolated spherules (MCMB). SEM photographs of MCMBs prepared under different conditions are shown in Fig1 (a)-(d), and the diameter distributions of MCMBs are shown in Fig 2. Fig1 shows that the diameter of MCMBs increased significantly with increasing reaction time. Fig2 shows that the diameter distribution of samples a, b and d are almost normal frequency distribution, while sample c has a few small MCMBs and large number of relatively big MCMBs.

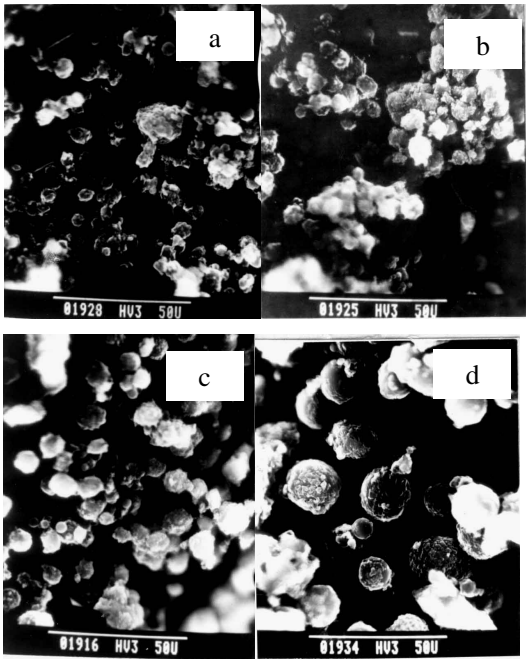

Fig. 1 SEM photographs of MCMBs prepared under At 723K for different time, a 1h, b 2h, c 3h, d 4h.

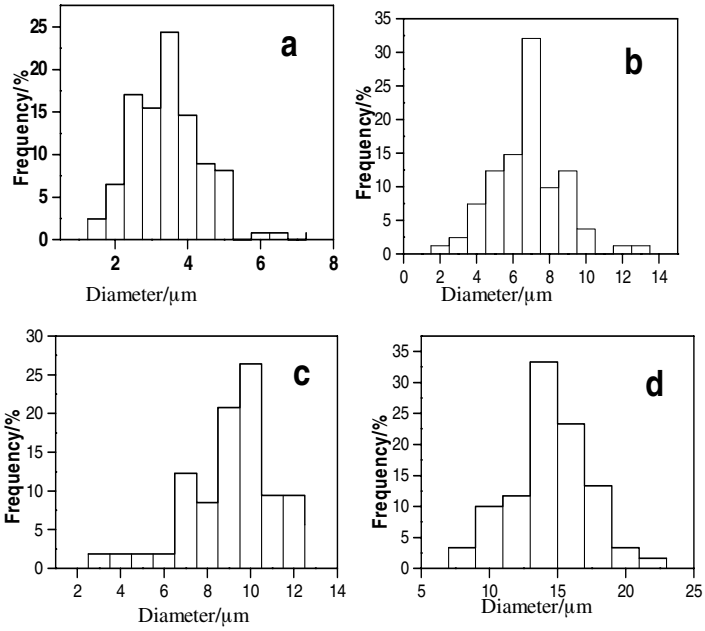

Fig 2. The diameter distribution of the MCMBs derived from coal tar pitch at 723K for different time, a 1h, b 2h, c 3h, d 4h.

3.2 Electrochemical properties of MCMBs . Fig 3 showed the first cycle charge-discharge profiles of MCMBs. The plateau observed at 0.8V vs Li/Li^+ during charge was attributed to the formation of solid electrolyte interface film (SEI) by the decomposition of electrolyte. Fig3 showed that the discharge profiles of MCMBs had a large hysteresis and a potential plateaus appearing at approximately 1V vs Li/Li^+, while the charge profiles had no potential plateaus appearing at approximately 1V vs Li/Li^+. Accordingly, the plateau is not due to a side reaction such as electrolyte decomposition but the cavities, which came into being when MCMBs were heat-treated at 973K. Lithium ions stored in the cavities were de-inserted at about 1V Li/Li^+[4].

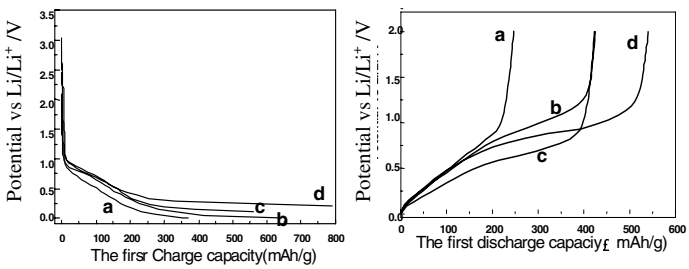

Fig 3. The first charge-discharge curves of MCMB heat-treated at 973K

Table 1 summarized some properties of MCMB anode., The first reversible capacity increased from 246 to 541 mAh/g with increasing of the mean diameter. And the first coulombic efficiencies were respectively 66.4%, 66.0%, 75.7%, and 68.3%. Since small MCMB has large specific surface area, resulting in more SEI, the first coulombic efficiencies increased with increasing of the mean diameter of MCMB. However, for the large MCMB, the numbers of rupture and defects will increase. When lithium ion diffuses into the large particle, it is probable to come across more ruptures and defects, making the diffusion dynamics process difficult. This gave rise to more irreversible capacity. Moreover, the interface of MCMBs decreases with increasing of particle size, which may reduce the electrical conductivity of MCMB. Consequently MCMB's cyclical property draws down. For example, the second discharge capacities of sample a, b, c and d, are respectively 8, 14, 22, 80 mAh/g less than the first cycle. If proper proportion of small MCMBs is added to big MCMBs, the electrical conductivity will be improved. This can be noted in Figure 3 and Table 1.The size distribution of sample c makes charge-discharge property fine. The first/second discharge capacity was 424/402 mAh/g and the first coulombic efficiency was 71.7%.

Table 1. Some properties of MCMBs prepared from coal tar at 723K

Code	Heattreatment time (h)	Mean diameter (μm)	First /second Cr(mAh/g)	First Cirr (mAh/g)	First coulomic efficiency(%)
a	1	3.2	246/238	124	66.4
b	2	6.5	425/411	219	66.0
c	3	8.9	424/402	167	71.7
d	4	13.8	541/461	243	68.3

Cr- reversible capacity Cirr-irreversible capacity

4 Conclusions

MCMB is one of the promising carbon materials as anode for lithium secondary battery among commercially available carbon materials. The MCMBs heat-treated at 973K had higher reversible capacity than the theoretical lithium storage capacity of a graphite anode. This suggests that there be a cavity mechanism for the charge-discharge reaction. The mean diameter and size distribution of MCMBs have influence on the charge-discharge properties of MCMBs.

Acknowledgements.The project is supported by Shanxi Province Natural Science Foundation • 991068 • and Chinese Academy of Sciences Foundation and State Key Laboratory of Heavy Oil Processing in the University of Petroleum• 199901 •

Reference

(1). Pled, E.; Menzchem,C.; BarTow, D. and Melman, A.. *J. Electrochem .Soc*, **1996**, *143*(1), L4-L7
(2). Ishikawa,M.; Kamobara,H.; Morita M. et al, *Journal of Power Sources*, **1996**, *62*, 229-232
(3). Buiel, E.; and Dahn, J.R. *J. Electrochem.Soc,* **1998**,*145*(6), 1977-1981
(4). Mabuchi,A.; Tokumisu, K.; Fujimoto, H.; and Kasuh, T. *J. Electrochem. Soc,* **1995**,*142*(4), 1041-1046
(5). Naji, A.; Willmann, P.; and Billaud, D. *Carbon*, **1995**,*33*(9), 1347-1352
(6). Liu,Y.; Xue, J.S.; Zheng, T.; and Dahn, J.R. *Carbon* , **1996**,*34*(2),193-200
(7). Bondarenko, G.N.; Nalimova,V.A.; Fateev, O.V. *Carbon*, **1998**,*36*(7-8), 1107-1112

NOVEL METHOD TO SYNTHESIZE CARBON MOLECULAR SIEVES WITH PETROLEUM COKES

Ya LIU, Zi-Feng YAN *

State Key Laboratory for Heavy Oil Processing,
Key Laboratory of Catalysis, CNPC,
University of Petroleum, Dongying 257061, P R China

Introduction

Since Emmet found carbon molecular sieves (CMS) in 1948, various starting materials, such as coal, polymer, nuts shell and so on, have been used to synthesize CMS. Generally, the preparation process consists of two steps as followed:

(1) Prepare carbon precursor with initial pore system by carbonization or activation.

(2) Modify the pore texture of precursor by carbon deposition of organic substance to satisfy different separation[1].

Petroleum cokes, especially ordinary cokes, are the main waste residue of refinery and have not been made full use of so far. Petroleum cokes contain high carbon content and low ash content, which are expected to be the potential carbon resources. Developing the application field of petroleum cokes is favorable to both of environment and economy.

By now, there are many reports concerning the preparation of high surface activated carbon from petroleum cokes. What we now are interested in is how to control the pore texture of the porous carbon for different purpose. In this paper, petroleum cokes were used as starting material to prepare microporous carbon with sieving ability and the product has been tentatively applied in air separation.

Experimental

Preparation of carbon precursor. The petroleum cokes were crashed to particle of 20~40 mesh and then impregnated in concentrated KOH aqueous solution in which the weight ratio of KOH to cokes was 1.5. The mixture was dried at 373 K in drying oven for several hours to form slurry and then moved into the reactor to activate thermally. In nitrogen atmosphere, the sample was heated at the rate of 10 K/min to a final temperature (1053~1123 K) and held isothermally for a period of time (60~120 min). Finally, the sample was cooled in nitrogen, washed to pH~7 and dried.

Modification of pore texture. The precursor was placed into tubular flowing reactor and was heated to 1053 K in nitrogen atmosphere and held isothermally for 60 min to get rid of surface functional groups from precursor. Afterward, the reactor was cooled to a certain pyrolysis temperature and then the hydrocarbon stream was introduced. The precursor was exposed to the hydrocarbon for a specified period. Following this treatment, the sample was degassed in nitrogen at the same temperature for 60 min and then cooled to ambient condition.[2]

Characterization of pore texture. The adsorption of nitrogen at 77 K was performed on Micromeritics ASAP2010 instrument to characterize the pore texture. Data of micropore and transitional pore were calculated by H-K and BJH method respectively.

Evaluation of sieving ability. Air separation was performed on small-scale single volume PSA apparatus to evaluate the sieving ability of the product. The size of the adsorption volume is 3.5×300 mm and the weight of adsorbent was about 1 g. The operating procedures were as followed:

(1) Vacuumize for 3min.

(2) Introduce air and perform adsorption at ambient pressure

(3) Repeat the above two steps for several times to attain the average result

Result and discussion

Influence of activation condition on the pore texture of carbon precursor. Effect of activation time. Fig.1 and 2 showed that micropore diameter of precursor increases initially and then decreases along with activation time while the micropore volume decreases at first and then increases with activation time. Furthermore, the activation time correspondent with the minimum micropore volume and the largest micropore diameter is coincidently in agreement. It was speculated that the micropore forms initially and then activation reagents gradually diffuse into the nanopore system and continue erode and enlarge the wall of the micropore during the activation, which leads to the increase of micropore volume and size. Meanwhile, some micropores become so larger that they could turn into transitional pore even macropores or connect with each other to become larger, so the micropore volume decreases and micropore becomes small. However, the subsequent corruption of the wall of the larger pores results in the new micropore with smaller size, which may increase micropore volume. The other reason why micropore

*Corresponding author. E-mail: zfyancat@hdpu.edu.cn

diameter decreased may be the fragment of organic substance from cokes blocked the micropore.

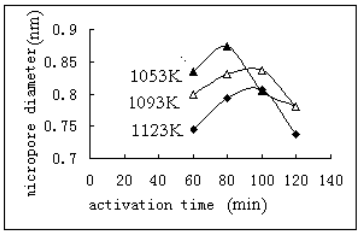

Fig. 1 The effect of activation time on the micropore size

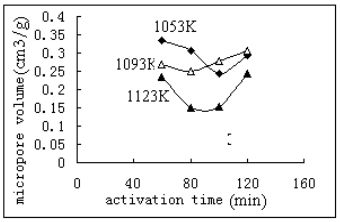

Fig. 2 The effect of activation time on the micropore volume

Effect of activation temperature. Fig.3 and 4 illustrated that both of micropore diameter and micropore volume increased initially and then decreased as temperature rose. However, the culmination temperature is not the same. It means that higher activation temperature accelerated the process of nanopore or micropore generation, but excessive high temperature resulted in the shrinkage of the micropore. The key to synthesize ideal precursor is to optimize activation temperature.

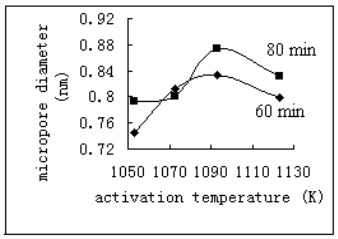

Fig. 3 The effect of activation temperature on the micropore size

Nanopore structure. Sample AC-3# bears abundant and smaller size micropore with rather narrower nanopore distribution (Table 1), which was the selected carbon precursor that subjected to further treatment. It means that thermal activation assisted by KOH is feasible to synthesize optimum carbon precursor with initial nanopore structure. Of course, the activation condition must be seriously controlled.

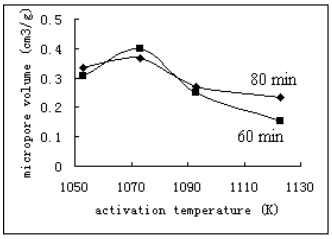

Fig. 4 Effect of activation temperature on the micropore volume

Modification of the textural properties by carbon deposition. Pyrolysis of LPG. While liquefied petroleum gas was applied as nanopore modifer of precursor, the operating condition, such as the concentration of LPG, the pyrolysis temperature and pyrolysis time were extensively investigated, unfortunately, it was in vain. The modified product showed very weak air separation ability. Meanwhile, it was found that the BET surface area and pore volume decrease with the increase of pyrolysis temperature or pyrolysis time. Of interests were that the loss of micropore volume is always more severe than that of transitional pore (illustrated by Fig. 5) and that micropore diameter became larger with the loss of micro pore volume after carbon deposition (illustrated by Fig. 6).

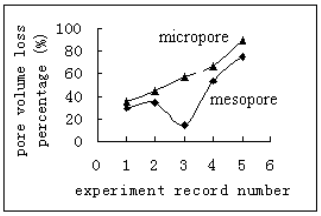

Fig. 5 Profile of pore volume loss percentage

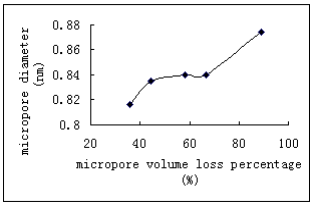

Fig. 6 Relation between micropore diameter and volume loss

According to a widely accepted pore texture modal, porous carbon bears macropore, transitional pore and micro pore. Transitional pore is branched off from macropore and micropore is branched off from transitional pore. Macropore and transitional pore serve as a passage of gas molecular and micropore practices separation in deed. Gas-solid heterogeneous reaction such as carbon deposition consists of external diffusion, internal diffusion,

adsorption, surface reaction, desorption, internal diffusion and external diffusion. Simultaneously, the homogeneous pyrolysis of hydrocarbon must be taken into account. So where the carbon deposition will occur depends on the relative speed of each step.[3] Therefore it was speculated that hydrocarbon molecular (or the product of homogenous pyrolysis) could easily enter the transitional and micropore. The carbon from pyrolysis either filled the micro pore or congested the opening of the micro pore located on the wall of the transitional pore. Moreover carbon molecular perhaps occurred on the wall of transitional pore, diminished the size of the pore and formed new micropore. Because smaller micropore tends to be blocked and the size of newly formed micropore is larger, so in general the average diameter of micropore increases.

Pyrolysis of butene. The available results were indicated in Table 2. Compared with the pyrolysis of LPG, butene is rather feasible to modify the nanopore of carbon molecular sieve samples. The nanoporous CMS sample indicated the favorable air separation ability. It means that the complexity of LPG constitute and too lighter lead to be difficult to control the pyrolysis reation.

The air separation performance of a commercial CMS was compared on the same apparatus under the same operating conditions. The concentration of nitrogen was 92.751%. We will also investigate the influences of butene concentration, flow velocity, cracking time and temperature.

Effect of carbon precursor. Another carbon precursor (AC-7, showed in Table 1) was used to repeat the above experiment of butene. The product exhibited no air separation ability. It means that the nanopore properties of precursor is very important to do subsequent modification of nanopore.

Conclusions

(1) Petroleum cokes were feasible to be the starting material for producing carbon molecular sieves.

(2) Nanoporous carbon precursor could be synthesized by thermal activation assisted by KOH activator.

(2) During the carbon deposition procedure, the kind of hydrocarbon and the pore texture of precursor are critical. Butene might be the optimum feed to modify the nanopore structure of CMS samples.

(3) The theory concerning the gas-solid heterogeneous reaction should be tentatively introduced to elucidate carbon deposition mechanism.

Acknowledgement. This program was financially supported by Key Teacher Foundation, Department of Education, China. Prof. Qian L., Song C.-M. And Dr. Liu X.-M., who give many beneficial discussions on this paper, were acknowledged.

Reference

(1) Shaoping, Xu; Shucai, Guo. *Coal Conversion,1995,18(3),43*

(2) S.K.Verma; P.L.Walker,Jr. Carbon, 1993, 31(7), 1203

(3) M.M.A.Fereitas; J.L.Figueiredo. Fuel, 2001, 80,1

Table 1. The Properties of Carbon Precursor

	Activation temp. (K)	Activation time (min)	Micro-pore diameter (nm)	Micro-pore Volume (cm^3/g)	Micropore volume/ total pore volume (%)
AC-3	1053	120	0.74	0.29	80.78
AC-7	1123	60	0.80	0.23	76.73

Table 2. The Carbon Deposition of Butene

Sample	Cracking temperature (K)	Concentration of nitrogen (vol.%)
CD-1	973	83.31
CD-2	993	84.67
CD-3	1013	83.52
CD-4	1033	83.79
Commercial CMS	----	92.75

COPROCESSING OF YANZHOU COAL WITH A FCC SLURRY

Z. J. Wang, J. L. Yang, Z. Y. Liu

State Key Lab. of Coal Conversion, Institute of Coal Chemistry
Chinese Academy of Sciences, P.O. Box 165, Taiyuan, P.R.China

Introduction

Although a number of processes for direct coal liquefaction and coprocessing of coal with petroleum resid have been developed to produce liquid fuels, the liquids produced are still expensive compared with petroleum[1]. Principal factors responsible for the high cost of coal derived liquids are the high cost of hydrogen, the severe liquefaction conditions and the use of expensive catalysts, which are essential for high yield of liquids[2]. Recently, a partial liquefaction concept was proposed [3]，with characteristics of low-severity conditions and comprehensive utilization of all liquefaction products. In the partial liquefaction concept, high coal conversion to liquids is no longer necessary, highly active but expensive catalysts are no longer needed, however, use of the heavy liquefaction product becomes a key issue in the overall process. Following this thought, we recently studied the heavy liquefaction product and found that asphalt produced from coprocessing of coal and fluidized catalytic cracking (FCC) slurry under mild conditions meets the properties of high grade paving asphalt[4]. FCC slurry, produced from fluidized catalytic cracking process at oil refineries, has a relatively high polycyclic aromatics content. It is costly to further process it to produce distillates, but it is an effective solvent for coal liquefaction and is good for production of high grade paving asphalt[4,5].

This work investigates the coprocessing of coal with a FCC slurry under different reaction conditions. Coal conversions and product yields are studied to reveal the interaction between the coal and the slurry. The roles of catalyst and hydrogen are also discussed.

Experimental

Yanzhou coal (Yanzhou, China) and a FCC slurry (Shijiazhuang oil refinery, China) were used. Their characteristics were shown in Tables 1 and 2.

Table 1. Proximate and Ultimate Analyses of Yanzhou Coal

Proximate anal. W/%			Ultimate anal.W/% daf					
Mad	Ad	Vdaf	C	H	N	S	O*	H/C
2.49	7.14	45.43	81.80	5.86	1.25	3.49	7.60	0.86

Table 2. Ultimate Analyses of FCC Slurry

C	H	N	S	O*	H/C
89.77	7.86	0.42	0.75	0.50	1.05

* by difference

Coprocessing experiments were performed under the following conditions: (1) N_2 atmosphere without catalyst, (2) N_2 atmosphere with a ferrous sulfate-based catalyst impregnated on coal[6], (3) H_2 atmosphere without catalyst, (4) H_2 atmosphere with a ferrous sulfate-based catalyst impregnated on coal. During a typical run, 100g mixture of coal and slurry were charged into a 1-liter autoclave. The reactor was filled with N_2 or H_2 to a pressure of 4 MPa and then heated up to 400 ^oC for reaction. After one hour reaction at 400 ^oC, the autoclave was cooled with a fan to room temperature and the gases were vented. The liquid and solid products were collected and extracted with tetrahydrofuran(THF) and toluene(T) in sequence. The products were divided into following fractions: THF i(THF insolubles), preasphaltene(THF solubles, T insolubles), asphalt(>320 ^oC fraction of T solubles), oil(220-320 ^oC fraction of T solubles) and <220 ^oC fraction(including gases).

The THF and T conversions of coal were calculated based on coal(dry and ash free) and by subtracting contributions of the slurry. Product yields were obtained based on overall feedstock.

Results and discussion

THF and T conversions of coal

In order to understand the interaction between coal and slurry, Yanzhou coal was coprocessed with the FCC slurry at two different coal/slurry ratios(2:1 and 1:2) under the four reaction conditions mentioned above. The THF and T conversions of coal alone and product yields (based on the overall feed) under different conditions were determined to reveal the effects of slurry. The conversions of the coal are summarized in Table 3.

Table 3. THF and T Conversion of Coal under Four Different Reaction Conditions

Conditions	THF conversion%			T conversion%		
	coal *	(2:1) *	(1:2) *	coal	(2:1)	(1:2)
N_2, without cat	16.9	17.3	32.0	15.8	16.5	1.5
N_2, with cat	15.5	16.5	21.1	14.4	15.3	8.2
H_2, without cat	38.3	62.8	71.8	35.3	44.8	27.4
H_2, with cat	57.5	70.8	85.2	44.2	48.2	42.7

* (coal) means the results determined coal alone , (2:1) and (1:2) denote the coal/slurry ratios in the feed.

It can be seen that the THF conversion increases with increasing slurry content in the feed concentration. The slurry enhanced dissolution and dispersion abilities to coal radicals and preventing them to combine together to form solid unreactive residue, which results in increased THF conversions. It is also observed that the increase in THF conversion is more obvious in H_2 atmosphere than in N_2 atmosphere, which may be caused by the good H-shuttling capacity of FCC slurry. However, it is somewhat surprising that the T conversion at coal/slurry of 1:2 is far lower than that at coal/slurry of 2:1. Possible reasons are that: At coal/slurry of 1:2 condition, the high content of slurry provides good dissolving and dispersing ability for coal and more coal radicals are stabilized as preasphaltene, which could not undergo further cracking and results in decrease of T conversion.

Change of product yields in coprocessing under different reaction conditions.

In order to further understand the interaction of coal and slurry in coprocessing, theoretical product yields are calculated according to the product yields when coal and slurry are treated individually under the same reaction conditions. The differences between the experimental and the theoretical values, obtained by subtracting the theoretic value from the experimental value, are summarized in Tables 4 and 5.

Table 4. Differences in product yields between experimental value and theoretical calculation in N_2 atmosphere

Condition	THF i	preasph-	asphalt	oil	<220^oC
(2:1)* without cat	-0.2	-0.1	-10.2	2.6	8.0
(2:1)* with cat	-0.6	0.1	-13.0	1.6	11.9
(1:2)* without cat	-4.8	9.5	-8.4	0.5	3.2
(1:2)* with cat	-1.7	3.7	-9.1	1.3	5.8

* The meaning of (2:1) and (1:2) are the same as in Table 3.

In N_2 atmosphere (Table 4), less asphalt and more oil and <220 ^oC fraction are obtained in coprocessing, which means that there is a synergistic effect between the coal and the FCC slurry on production of oil and <220 ^oC fraction. It is also observed that, at coal/slurry ratio of 1:2, less THF insolubles and more preasphaltene were obtained, compared to those at coal/slurry ratio of 2:1, which suggests increased stabilization ability for coal radicals at high slurry content. However, more slurry also confines further cracking of coal radicals and leads to increased preasphaltene yield. It was found that addition of catalyst had no significant effect on changes of product yields in N_2 atmosphere.

Table 5. Differences in product yields between experimental value and theoretical calculation in H_2 atmosphere

Condition	THF i	preasph-	asphalt	oil	<220^oC
(2:1)* without cat	-15.8	9.2	4.4	1.7	0.5
(2:1)* with cat	-7.7	5.6	4.5	-1.8	-0.6
(1:2)* without cat	-10.0	13.2	-0.5	-2.0	-0.7
(1:2)* with cat	-7.9	9.0	-5.8	0.4	4.3

* The meaning of (2:1) and (1:2) are the same as in Table 3.

Table 5 shows the differences in product yields in H_2 atmosphere. Results suggest that the coal and the FCC slurry have

a synergistic effect on decreasing THF insolubles. This is due not only to the increased dissolution and dispersion ability of slurry, but also to the good H-shuttling capacity of the slurry in the presence of H_2. It can also be observed that more preasphaltene was produced compared to that in the N_2 atmosphere. This again suggests that the enhanced H-donor ability hampered further cracking of preasphaltene. It is well known that the addition of catalyst can convert H_2 into active H atoms and promote the change of polyaromatics in the FCC slurry into hydroaromatics and the hydroaromatics promote cleavage of some strong bond in coal structure[7]. Therefore, in the presence of the catalyst, more hydroaromatics was produced from the slurry at coal/slurry ratio of 1:2 than at that of 2:1, which resulted in less asphalt and more oil and <220°C fraction at coal/slurry ratio of 1:2.

Conclusions

1. Addition of the FCC slurry greatly enhanced coal conversion, which is attributed to its good H-shuttling capacity and dissolution ability for coal radicals.
2. Decrease of T conversion are observed when more FCC slurry is used in the coprocessing, the excessive FCC slurry may hamper further cracking of preasphaltene by stabilizing coal radicals.
3. In the presence of N_2, coal and FCC slurry have a synergistic effect on production of oil and <220 ^{o}C fraction in coprocessing.
4. In the presence of H_2 and catalyst, polyaromatics of FCC slurry may be converted into hydroaromatics, which enhances H-donor ability and promotes the cleavage of strong bond of coal structure.

Acknowledgement. The authors gratefully acknowledge the financial support from the National Natural Science Foundation of China, the Chinese Academy of Sciences, and the Special Founds for Major State Basic Research Project. Mr. Yanti Wang of Shijiazhuang petroleum refinery is also acknowledged.

References

1 Osuma Okuma. Liquefaction process with bottom recycling for complete conversion of brown coal. Fuel, 2000,79,355-364
2 Derbyshire, F., Energy & Fuels, 1989,3,273-277
3 Liu Z. and Yang J. Proceedings of The Fifteenth Annual International Pittsburgh Coal Conference, September 14-18, 1998
4 Wang Z.J., Li Y. M., Zhang H. H. et al, Proceedings of the 10th International Conference of Coal Sciences [C]. 1999:1187-1190
5 Harrison G and Ross A B. Fuel, 1998,77,1421-1425
6 Zhang L.A., Yang J.L., Liu Z.Y., et al. Proceedings of the 10th International Conference of Coal Sciences [C]. 1999:965-968
7 Malhotra R, McMillen D F. Energy&Fuels, 1993,7:227-230

VOLATILIZATION OF Na DURING PYROLYSIS OF A VICTORIAN BROWN COAL AT ELEVATED PRESSURES

Chirag Sathe[a,b], Jun-ichiro Hayashi[b], Chun-Zhu Li[a] and Tadatoshi Chiba[b]

[a]CRC for Clean Power from Lignite, Department of Chemical Engineering, Monash University, Clayton, Australia
[b]Center for Advanced Research of Energy Technology Hokkaido University, Sapporo, Japan

Introduction

Volatilization of Na during pyrolysis/gasification has been known to cause severe problems of erosion/corrosion of heat-exchanger tubes and high-temperature rotating parts in a gas turbine, affecting the steady operation of the plant. On the other hand, retention of Na in the char would enhance combustion/gasification processes due to its catalytic activity. The volatilization of Na is likely to be dependent on the reaction conditions. This paper examines the effects of changes in pressure, heating rate and temperature on the release of Na during pyrolysis of a Victorian brown coal (Loy Yang).

Experimental

Coal sample. A sample of "as-mined" brown coal was obtained from the Loy Yang field in Latrobe Valley, Australia. The sample was partially dried at low temperature (<35°C) and then pulverized and sieved to obtain a fraction sample of particle sizes between 106 and 150 µm. The properties of the coal sample are: C, 68.5; H, 4.8; N, 0.6 and S, 0.3 wt% on a daf basis with 0.13 wt% of Na (db).

Pyrolysis. Pyrolysis experiments were carried out in a wire-mesh reactor[1]. For experiments at elevated pressures, a reactor vessel made of stainless steel (instead of glass) was used together with a specially designed gas distributor and a tar trap. Less than 10 mg of the air-dried sample was used in each experiment. The details of tar collection, char and tar quantification have been given elsewhere[2,3]. All the pyrolysis experiments were carried out in helium (purity >99.999%). A gas flow rate of 2.5 L min^{-1} (measured at 25°C and 1 bar) was used for experiments at atmospheric pressure. For experiments at pressures from 6 bar to 20 bar, a gas flow rate of 4 L min^{-1} (measured at 25°C and 1 bar) was used to maintain an upward flow direction of the volatiles. Experiments using a higher flow rate of 8 L min^{-1} at elevated pressures (20 bar) did not show any discernible changes in product yields. For very high pressure up to 61 bar, a gas flow rate of 10 L min^{-1} was used.

Quantification of Na. Detailed procedure for the quantification of Na is given elsewhere[2]. In brief, after the pyrolysis experiment, a portion of the char was ashed in a thermogravimetric analyzer at 600°C (with 30 min holding time) in O_2. The ashing conditions were controlled to ensure complete combustion without ignition[2]. The ash was then digested with a mixture of HNO_3 and HF solution. After evaporating HNO_3 and HF the sample was re-dissolved in 20 mM CH_3SO_3H prior to injection into an ion chromatograph to quantify Na concentrations.

Results and Discussion

Pyrolysis experiments using the raw coal sample were carried out at pressures of 1, 3, 6, 11, 20, 36 and 61 bar. Two heating rates were used: 1 and 1000°C s^{-1} with a holding time of 10 s. As indicated previously[4], the introduction of pressure greatly affects the mass-transport mechanism of volatiles and changes the tar yield. A brief summary on the effect of pressure on the tar yield is given here in the form of Figure 1 at 700 and 900°C. At the fast heating rate of 1000°C s^{-1} the tar yield decreases with increases in pressure up to 11 bar. Further increase in pressure to 20 bar results in substantial increases in the tar yield. At a slow heating rate of 1°C s^{-1}, the tar yield remains unaffected by pressure up to 6 bar, but nearly doubles at 11 bar and remains unchanged up to 20 bar.

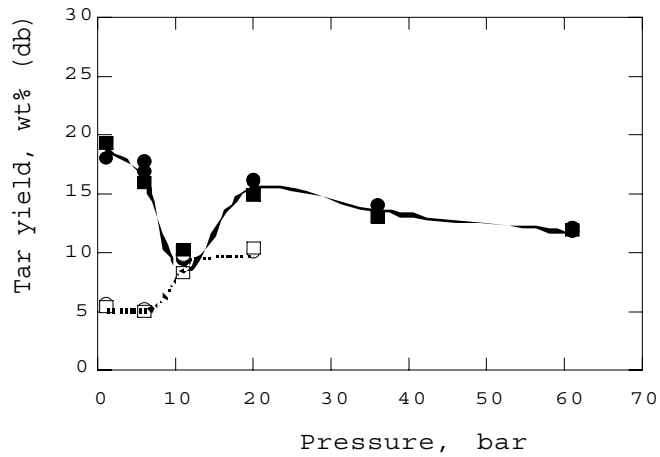

Figure 1. Effect of pressure on the tar yield at 700 (l and ◦) and 900°C (n and o) with a holding time of 10 s at: 1000°C s^{-1} (filled symbol) and 1°C s^{-1} (open symbol).

In our previous study[2] at atmospheric pressure, the volatilization of Na was found to be a function of temperature alone. Changes in the heating rate (1 and 1000°C s^{-1}) had no apparent effect on the release of Na. When the pressure is increased in the present study from 1 to 11 bar at 700°C at the fast heating rate, the Na retention in the char decreases gradually, as shown in Figure 2. When the pressure is increased to 20 bar, the Na retention increases substantially which is followed by no essential increase with pressure up to 61 bar. More than 85% of Na present in the coal sample is retained in the char at pressures of 20 bar and higher.

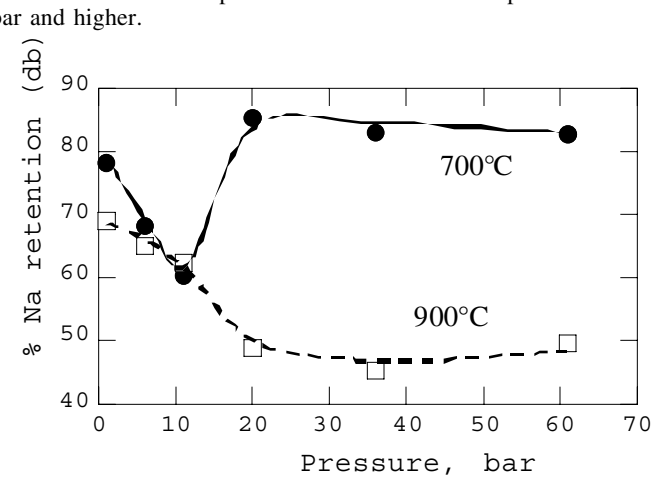

Figure 2. Na retention as a function of pressure at 700 and 900'C at a fast heating rate of 1000°C s^{-1} with a holding time of 10 s.

Interestingly, Figs. 1 and 2 suggest that at 700°C the Na retention followed the path of the tar yield with changes in pressure. At a higher temperature of 900°C, the Na retention shows similar behavior to that at 700°C with increases in pressure up to

11 bar. However, the difference between the Na retention at 700 and 900°C decreases with increases in pressure. At 11 bar, the Na retention is same at both temperatures. Further increase in pressure to 20 bar at 900°C causes a significant reduction in the retention and remains unchanged with further increases in pressure up to 61 bar. It appears from Figs. 1 and 2 that at a higher temperature of 900°C, the temperature has played a significant role in the volatilization of Na from the coal.

When the coal particles are heated slowly at 1°C s^{-1}, the Na retention for both temperatures decreases with pressure to 6 bar and then remains nearly unchanged up to 11 bar, as shown in Figure 3. However, at 20 bar the retention increases and matches the value at 1 bar. This behavior of Na at 900°C is in sharp contrast to that at fast heating rate. It is also to be noted that the difference between the retention at 700 and 900°C remained nearly unchanged with increasing pressure.

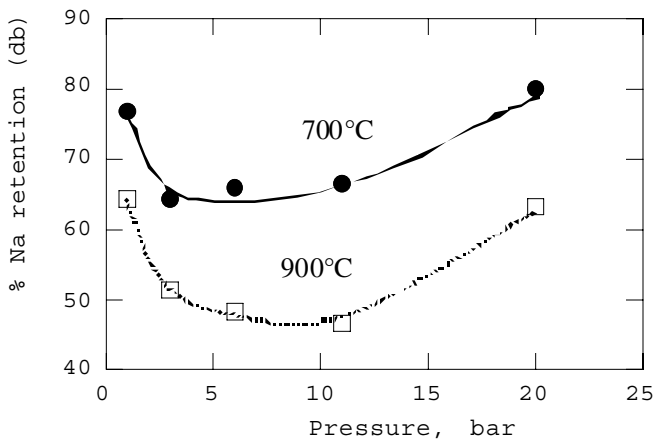

Figure 3. Na retention as a function of pressure at 700 and 900°C at a slow heating rate of 1°C s^{-1} with a holding time of 10 s.

It is supposed that when the generation of volatiles in the particle is rapid the evolution of the volatiles out of the particle can be affected by pressure[5]. As discussed in detail elsewhere[4], with changes in pressure, the diffusion flow due to the concentration gradient and/or the forced flow due to the pressure gradient would be the main mass transport mechanism for the release of volatiles out of the particle during rapid pyrolysis. This in turn could affect the release of alkali and alkaline earth metallic species (AAEM). Thus, the release of AAEM species was speculated to depend on their transformation during pyrolysis.

It is known that the carboxylates in coal will undergo decomposition at relatively low temperatures[6]. In the absence of oxygen, some AAEM species associated with the $-COO^-$ groups might leave the particle together with the –COO group. With the release of CO_2, Na originally associated with a –COO group might still be bonded to coal/char matrix (CM),

$$(\text{-COO-Na}) + (\text{CM'}) \Rightarrow \text{CM-Na} + CO_2 \qquad (1)$$

The strength of this newly formed bond will depend on the temperature alone. Increasing temperature would generate volatile matter (VM') from the coal/char matrix,

$$\text{CM-VM} \Rightarrow \text{CM'} + \text{VM'} \qquad (2)$$

and could also break the bond between CM and Na,

$$\text{CM-Na} \Rightarrow \text{CM'} + \text{Na'} \qquad (3)$$

In the diffusion controlled mass transport regime, the concentration of the VM inside the particle increases with increasing pressure. This will allow for the further interaction between the VM' and Na',

$$\text{VM'} + \text{Na'} \Rightarrow \text{VM-Na} \qquad (4)$$

It is speculated that the Na could be released along with VM. The chances of Na being released by reaction (3), even after the completion of the release of tar and major volatiles, are not excluded. On the other hand, if the forced flow is the main controlling mass transport mechanism for the release of volatiles, the concentration as well as the time spend by VM' inside the particle would reduce considerably. This, in turn, would reduce the possibility of the interaction between VM' and Na'.

At 700°C the thermal dissociation (reaction 3) would not be an important process for the volatilization of Na. In the diffusion controlled mass transport process regime (up to 11 bar), reactions (2) and (4) would play a vital role and result in more release of Na with increasing pressure. When forced flow becomes the main mass transport mechanism (at 20 bar), there are neither enough Na' species and/or the VM' nor the time available for the progress of reaction (4) to cause volatilization of Na. The Na retention increased substantially when the pressure is increased to 20 bar (Fig 2). At 900°C, the reaction (3) would intensify and irrespective of the mass transport regime would cause further volatilization of Na with increasing pressure (up to 20 bar). At higher pressures (36 and 61 bar), the data in Fig. 2 suggest that the release of Na has reached a plateau value at 900°C.

When the generation of volatiles is slow and is the rate-limiting process, as in the case with 1°C s^{-1}, increasing pressure would further increase the concentration of VM inside the particle. The net result of reactions (2), (3) and (4) is a gradual release of Na with increasing pressure. The data in Figs. 1 and 3 for 20 bar are somewhat ambiguous. The slow generation of volatiles is thought to negate the effect of increasing pressure on the release of volatiles. However, the increase in the tar yield as well as the Na retention at 20 bar suggest the forced flow could be the main mass transport mechanism for the release of volatiles, resulting in higher retention of Na during pyrolysis. Further work is being carried out to understand the effect of pressure on the release of Na during slow heating.

Conclusions

Tar yield is found to be sensitive to changes in pressure and heating rate. Volatilization of Na is found to depend on pressure, temperature and heating rate. At atmospheric pressure, the release of Na is only temperature dependent. Increasing pressure alters the mass transport mechanism of the generated volatiles and in turn affects the volatilization of Na. At fast heating rate, higher pressure and higher temperature result in substantial volatilization of Na. At slow heating rate, the volatilization of Na is mainly a function of temperature.

Acknowledgement. The financial and other support received for this research from the Cooperative Research Center (CRC) for Clean Power from Lignite (Australia) is gratefully acknowledged. The authors also thank the partial financial support by the New Energy and Industrial Technology Development Organisation (NEDO) in Japan.

References

(1) Sathe, C.; Pang, Y.; and Li, C.-Z. *Energy & fuels*, **1999**, *13*, 748-755.
(2) Li, C.-Z.; Sathe, C.; Kershaw, J. R.; and Pang, Y. *Fuel*, **2000**, *79*, 427.
(3) Kershaw, J. R.; Sathe, C.; Hayashi, J.-i.; Li, C.-Z; and Chiba, T. *Energy & Fuels*, **2000**, *14*, 476-482.
(4) Sathe, C.; Hayashi, J.-i.; Li, C.-Z. submitted to *Fuel*, **2001**.
(5) Gavalas, G.R. Coal Pyrolysis, Elsevier Scientific Publication: Amsterdam, 1982; Chapter 5.
(6) Schafer, H.N.S. The Science of Victorian brown coal, Editor, Durie, R.A.; Butterworth-Heinmann, 1991; Chapter 7.

NITROGEN AND SULFUR RELEASE DURING HIGH TEMPERATURE PYROLYSIS OF COALS

Naoto Tsubouchi and Yasuo Ohtsuka

Institute of Multidisciplinary Research for Advanced Materials
Tohoku University
Katahira, Aoba-ku, Sendai 980-8577, Japan

Introduction

The fate of the nitrogen and sulfur in coal during pyrolysis has been studied extensively with different reactors under various conditions[1-5], since it is related with NO_x and SO_x emissions in the subsequent combustion process. However, most of researchers have paid no attention to the release of these heteroatoms from char after devolatilization. There have been only a few papers on this topic so far[6-8].

It is of interest to make clear what factors can control such behavior during high temperature pyrolysis. The present work focuses on examining the influences of some factors on the nitrogen and sulfur release during coal pyrolysis at high temperatures of ≥ 1000°C, and on elucidating possible mechanisms.

Experimental

Coal Samples. Ten coals with different ranks from different countries were used in this work. All the samples were air-dried at room temperature, ground and sieved to coal particles with size fraction of 150-250 μm. Their carbon, nitrogen, and sulfur contents ranged from 66 to 80 wt%, 0.9 to 2.0 wt%, 0.1 to 1.3 wt% on a dry ash-free basis, respectively.

Ca catalyst was loaded on the coal by using a saturated aqueous solution of $Ca(OH)_2$ in a rotary evaporator at room temperature[9]. The Ca content in the dried sample was 3 wt%.

Pyrolysis. Pyrolysis runs were carried out with a fixed bed quartz reactor[4], except for the use of a free-fall type quartz pyrolyzer under rapid heating conditions (10^4-10^5°C/s). After precautions against leakage, about 0.5 g of the sample was heated in a stream of high purity He (>99.9999%) at 400°C/min up to 1000°C-1350°C, soaked for 2 min, and then quenched to room temperature.

Nitrogen and Sulfur Analysis. Pyrolysis products were separated into gas, tar, and char in the same manner as described elsewhere[4]. N_2 in the gas was detected with a micro gas chromatograph, and the HCN and NH_3 were analyzed with a FT-IR equipped with a long-path gas cell. The nitrogen in the tar (tar-N) or in the char (char-N) was determined with conventional combustion-type elemental analyzers. H_2S was analyzed by the Gastec standard tube. Yield of each nitrogen species or H_2S is expressed in percent of total nitrogen or sulfur in feed coal, respectively.

Char Characterization. The XRD measurements of samples after pyrolysis were carried out with Ni-filtered Cu-Kα radiation (40kV, 30mA) to clarify crystalline forms and dispersion states of inherent minerals and added Ca. The average crystalline size of CaO was calculated by the Debye-Scherrer method.

Results and Discussion

Pyrolysis Temperature. When the changes in yields of N-containing products between 1000°C and 1350°C were examined with all the coals used, N_2 was the dominant species and the yield increased almost linearly with increasing temperature with a corresponding decrease in char-N. On the other hand, yields of volatile-N (tar-N, HCN, and NH_3) were almost unchanged.

The increase in N_2 yield between 1000°C and 1350°C is plotted as a function of the decrease in char-N yield in **Figure 1**. There was a strong reverse correlation between N_2 and char-N, though some data were scattered at a larger extent of the decreased yield of char-N. The N/C ratios in the 1200°C and 1350°C chars, normalized to that in the 1000°C char, were lower at a higher temperature, irrespective of coal type. Thus, these observations point out that the N_2 increased arises mostly from char-N after devolatilization.

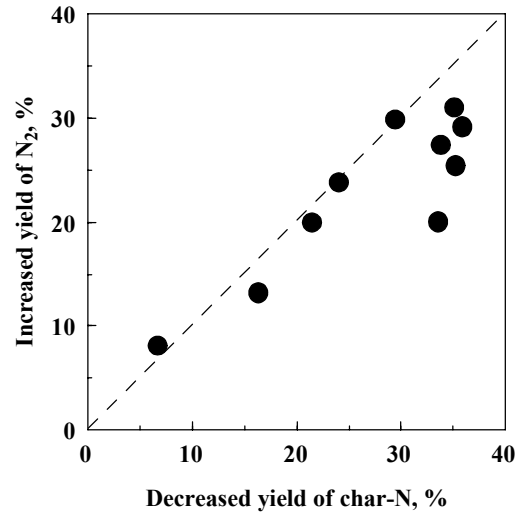

Figure 1. Relationship between N_2 and char-N.

Typical examples of H_2S release between 1000°C and 1350°C are illustrated in **Figure 2**, where H_2S yield is given for AD, LP, and TG coals. The yield increased with increasing temperature, and the increment depended on coal type. Although recent XPS and XANES studies have shown a clear trend of a larger proportion of thiophenic sulfur at a higher carbon content in coal[10], the increase in H_2S yield observed between 1000°C and 1350°C was almost independent of coal rank. It is suggested that H_2S formation under such conditions can not be correlated with the distribution of sulfur functional groups in coal.

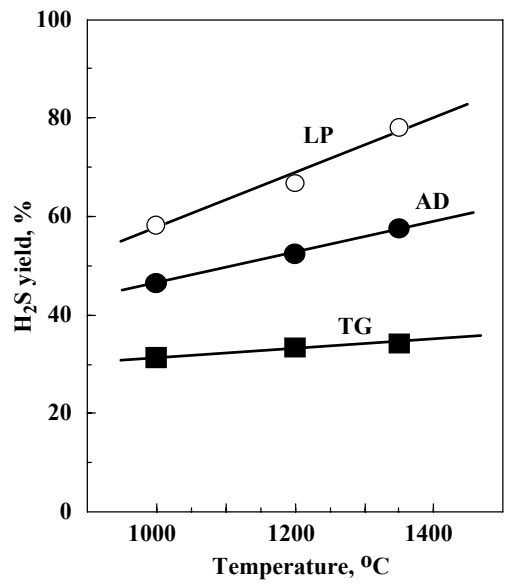

Figure 2. Temperature dependence of H_2S yield.

Solid Residence Time. The dependence of yields of N_2 and H_2S for AD coal on solid residence time at 1300°C is illustrated in **Figure 3**, where heating rate is 10^4-10^5°C/s. Weight loss was almost unchanged with the time. Volatile matter in the present rapid pyrolysis was the same as or higher than that from proximate analysis, indicating complete release of volatile matter.

As is seen in **Figure 3**, a small amount of N_2 was observed at time of 0 s. The yield increased with increasing time and reached 37% at 120 s. On the other hand, char-N decreased with time, as expected. H_2S showed almost the same time dependence as N_2, and H_2S yield increased considerably from 38% at 0 s to 82% at 120 s.

Figure 3 also shows the H/C ratio in the char after pyrolysis at time of 30 s or 120 s, normalized to that at 0 s. The ratio was smaller at a longer time. There was a reverse correlation between the decrease in H/C and formation of N_2 or H_2S. Since the decrease means the occurrence of aromatization reactions of char, it is likely that the formation of N_2 and H_2S proceeds in the process of carbon crystallization.

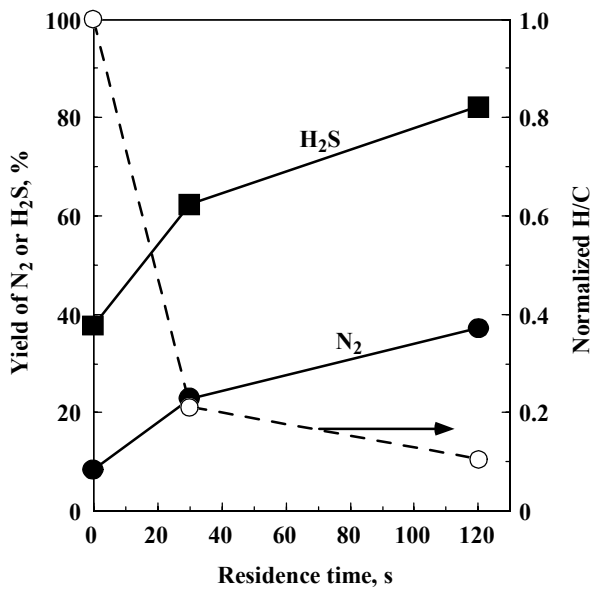

Figure 3. Effect of solid residence time on normalized H/C and yields of N_2 and H_2S under rapid heating conditions.

Calcium Addition. Table 1 shows the effect of Ca addition on the changes in yields of N_2, char-N, and H_2S between 1000°C and 1350°C. The Ca^{2+} ions added on AB and AD coals enhanced N_2 yield at high temperatures of ≥ 1000°C, but decreased char-N yield. The Ca on AD coal catalyzed N_2 formation more remarkably. This would be ascribed to the difference in the content of inherent Ca between both coals, that is, 1.8 wt%Ca for AB and 0.2 wt%Ca for AD, since the Ca added to a low rank coal with the higher content does not work efficiently. No changes in H_2S yield for AB and AD coals by Ca addition were observed. In other words, the Ca suppressed H_2S formation.

Table 1. Effect of Ca Addition on formation of N_2 and H_2S

Coal	Ca loading (%)	Change in yield between 1000°C-1350°C (%)		
		N_2	char-N	H_2S
AB	0	+13	-14	+4
AB	3	+15	-16	±0
AD	0	+27	-32	+11
AD	3	+32	-35	±0

The XRD measurements after pyrolysis revealed that the Ca existed predominantly as CaO with the average size of 15-30 nm in the 1000°C chars derived from Ca-loaded AB and AD coals and promoted carbon crystallization at high temperatures above 1000°C. When temperature was raised to 1350°C, the sizes increased slightly. Thus, the reaction between CaO particles and char-N may occur in the process of carbon crystallization. The small peaks of CaS were also observed. These observations indicate that the highly dispersed CaO catalyzes efficiently conversion reactions of char-N to N_2 at solid phase, and captures H_2S evolved and/or reacts organic sulfur in the char.

A small XRD peak of CaO was also detectable in the chars from AB coal, though it was not observed for AD coal because probably of low content of inherent Ca. Therefore, the mineral-derived CaO can catalyze carbon crystallization, as observed in **Figure 3**. It is likely that N_2 formation from char-N and sulfur capture by CaO occur through the same mechanism as in the pyrolysis of Ca-loaded coal.

Conclusions

To make clear nitrogen and sulfur release from char after devolatilization, ten coals have been pyrolyzed at high temperatures of ≥ 1000°C with both a fixed bed reactor and a free fall type reactor. Yields of N_2 and H_2S increase with increasing temperature and solid residence time, whereas char-N decreases. The addition of 3 wt%Ca to low rank coals enhances N_2, whereas it decreases yields of char-N and H_2S. The Ca is transformed to fine particles of CaO, which catalyzes carbon crystallization. CaO particles may not only promote N_2 formation through solid phase reactions of char-N but undergo sulfur capture reactions.

Acknowledgment

This work was supported in part by the Basic Research Associate for Innovative Coal Utilization (BRAIN-C) Program, sponsored by the New Energy and Industrial Development Organization (NEDO), Japan. The authors gratefully acknowledge Ms. Hazuki Satake for her assistance in carrying out experiments.

References

1. Solomon, P. R., Colket, M. B., *Fuel* 1978, **57**, 749-755.
2. Chen, J. C., Castagnoli, C., Niksa, S., *Energy Fuels* 1992, **6**, 264-271.
3. Bassilakis, R., Zhao, Y., Solomos, P. R., Serio, M. A., *Energy Fuels* 1993, 7, 710-720.
4. Wu, Z., Ohtsuka, Y., *Energy Fuels* 1997, **11**, 477-482.
5. Sugawara, T., Sugawara, K., Nishiyama, Y., Sholes, M. A., *Fuel* 1991, **70**, 1091.
6. Tsubouchi, N., Ohshima, Y., Xu, C., Ohtsuka, Y., *Energy Fuels* 2001, **15**, 158-162.
7. Tsubouchi, N., Ohtsuka, Y., *Fuel*, in press.
8. Garcia-Labiano, F., Hampartsoumian, E., Williams, A., *Fuel* 1995, **7**, 1072-1079.
9. Ohtsuka, Y., Asami, K., *Catal. Today* 1997, **39**, 111-125.
10. George, G. N., Gorbaty, M. L., Kelemen, S. R., Sansone, M., *Energy Fuels* 1991, **5**, 93-97.

EFFECT OF GASEOUS ADDITIVES ON DESULFURIZATION OF COAL THROUGH PYROLYSIS

Long Xu, Jianli Yang, Yunmei Li, Zhenyu Liu

State Key Laboratory of Coal Conversion,
Institute of Coal Chemistry, Chinese Academy of Sciences,
Taiyaun 030001 P. R. China

Introduction

With the increasing environmental concerns on SO_2 emission from coal combustion, use of high sulfur coals becomes more and more difficult. Development of sulfur removal process from coal prior to combustion is very important for continued used of high sulfur coals. Pyrolysis is likely to be an effective way to transform sulfur in coal to the gas and liquid phases, and to generate low sulfur content char for clean combustion.

Researches show that the efficiency of sulphur removal from coal through pyrolysis depends on many factors, such as temperature [1-3], heating rate [2], nature of atmosphere [3-6], residence time and coal type [6]. Pyrolysis of coals in nitrogen, hydrogen and steam indicates that H_2 atmosphere results in better sulphur removal efficiency than others, but the char yield is low, and the sulphur content of the char usually does not show significant decrease compared to the raw coal. To reach the goal of simultaneous sulphur removal and production of chars of high heating value, selective sulphur removal from coal is preferred. It is possible that addition of other chemicals are required to selectively reduce the strength of sulphur-carbon bonds and/or to stabilise the sulphur containing radicals to prevent them to form solid products, however, a little work is available in the literature in this field.

In this study, ethanol and acetone as well as nitrogen and hydrogen were used to constitute different atmospheres for pyrolysis of coal to evaluate their effect on sulphur removal. The results obtained are useful for understanding of sulphur removal mechanism from coal and for development of novel sulphur removal technologies.

Experimental

A Spanish coal (Mequinenza) and three Chinese coals (Yanzhou, Datong and Xianfeng) were used in this study. All samples were ground to less than 0.25mm before use. Ultimate and sulfur-form analyses of the coals are presented in Table 1.

Table 1. Ultimate and Sulfur-form analyses of sample coals

Samples	Yanzhou	Datong	Xianfeng	Mequinenza
Ultimate(wt%, daf)				
C	81.80	82.76	66.98	61.64
H	5.86	5.07	5.73	7.45
N	1.25	0.82	1.50	1.39
S	3.49	2.42	1.16	12.03
O (diff.)	7.60	8.93	25.63	17.49
Sulfur-form (wt% total)				
Pyritic	44.70	64.32	2.59	3.82
Sulfate	0.57	3.01	14.66	9.39
Organic	54.73	32.67	82.76	86.79

Pyrolysis runs were carried out in a fixed bed quartz tube reactor (70cm length, 1.4cm i.d.). Coal samples were heated from room temperature to 500°C or 700°C at a heating rate of 10°C/s. Ethanol or acetone was fed into the reactor by a pulseless pump, vaporised and then carried to the pyrolysis area by nitrogen. As a reference, hydrogen atmosphere was also used in the study. And the flow rate of nitrogen or hydrogen was 30ml/min. In order to compare the effects of different atmospheres, the same amount of organic reagents as that of hydrogen (in mol) were introduced. The amounts of these reagents actually fed into the reactor were 0.05ml/min for methanol, 0.08ml/min for ethanol and 0.10ml/min for acetone in the liquid state.

The sulfur content of raw coals and the pyrolysis chars were analysed by a sulfur detector (model WDL-3C).

Results and Discussion

Figures 1(a, b, c, d) is the desulfurization results of these four coals at 700°C. In the figure, X-axis represents the percentage changes of the weight loss of coal (weight lose%), and Y-axis is the corresponding efficiency of desulfurization (De-S%). By this way, the degree of desulfurization can be reasonable evaluated. For a pyrolysis in which De-S% is equal to the weight loss%, in other words, the sulfur content in char (S_{char}%) is as same as that in coal, then the result is represented by a point on the diagonal line.

Figure 1(a) is the effect of atmospheres on desulfurization of Yanzhou coal. It shows that for Yanzhou coal the order of the effect on De-S% is as following H_2>N_2> C_2H_5OH> CH_3COCH_3. However, the value of weight loss% is also with the similar order. Furthermore, the values of S_{char}% are 2.56% for H_2, 2.77% for N_2, 2.54% for ethanol, 2.79% for methanol, and 2.87% for acetone. Although the values of S_{char}% for hydrogen and ethanol atmospheres are very similar, the yield of char for ethanol is about 7 percentage points higher than that for H_2 atmosphere. This suggests that ethanol atmosphere is much more selective to sulfur removal than H_2 atmosphere. It is also interesting to note that introduction of acetone also results in higher char yields compared to that in H_2 and N_2 atmospheres. Figure 1(b) is the desulfurization results of Datong coal. Among the four atmospheres, ethanol results in the highest char yield and the highest De-S%. While De-S% and the char yield observed for H_2 atmosphere are nearly 20 and 7percentage points lower than that for ethanol, respectively. Figure 1(c) is the pyrolysis results of Xianfeng coal. Again, ethanol atmosphere results in almost the highest De-S% and nearly the lowest weight loss%. Figure 1(d) is the results of Mequinenza coal. Similar to the Chinese coals, ethanol atmosphere gives the highest char yield and the highest De-S%. Although H_2 atmosphere yields a De-S% value very close to that of ethanol atmosphere, its weight loss% and S_{char}% are higher than that in ethanol atmosphere.

In general, Figures 1 shows that introduction of ethanol and acetone does alter the pyrolysis of the coals, and usually results in the chars with high yields and low sulfur contents. Hydropyrolysis, on the other hand, usually promotes devolatillazation of coal but is ineffective to generate low sulfur-containing chars.

Although detailed mechanism on the effect of the atmospheres is not clear by now, it is certain that this effect is related to the state of sulfur in coal as well as the type of the coal. The differences in weight loss% between ethanol and hydrogen for Yanzhou, Datong, Xianfeng and Mequinenza are 7.21%, 6.94%, 3.17% and 3.18%, respectively. The four coals studied can be divided into two groups, one group are lignites, including Mequinenza and Xianfeng, the other are bituminous coals, while the differences mentioned can also be divided into two groups, 3% for lignites and 7% for bituminous coals. The phenomena may indicate that the influence of ethanol on yield of char is related to the type of coal or carbon content in raw coal. Comparing the desulfurization efficiency of these coals, it was observed that the improvement of De-S% by ethanol atmosphere is much more than those by hydrogen atmosphere for Datong coal. It suggests the possible existence of the special sulfur containing structures in Datong coal, which interact strongly with ethanol during pyrolysis.

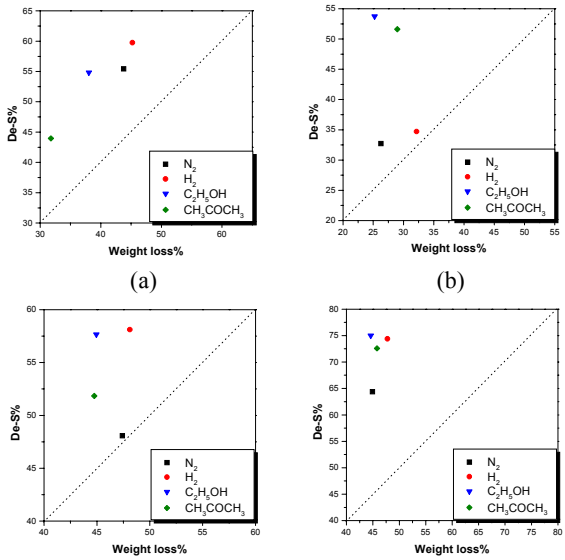

Figure 1. Effect of gaseous additives on desulfurization of four coals during pyrolysis. (a) Yanzhou coal (b) Datong coal (c) Xianfeng coal (d) Mequinenza coal

In order to see clearly the effects of the gaseous additives at different temperature ranges during pyrolysis, a variables F_T is used in this study. F_T and is calculated according to the following equation:

$F_T(T1\sim T2)=[(De\text{-}S\%_{T2}-De\text{-}S\%_{T1})/(Weight\ loss\%_{T2}-Weight\ loss\%_{T1})]-1$

Based on the equation, if the change of De-S% is dominant, then F_T will be more than zero, but if the change of Weight loss% is dominant, then it will be less than zero. Here two temperature ranges, ≤500°C and 500~700°C, are studied separately. Figure 2 is the change of F_T for Yanzhou coal in different pyrolysis atmospheres. It is observed that: (1) Below 500°C, the value of F_T is more than zero only for ethanol, zero for acetone and less than zero for the others. That is to say, in the atmosphere of ethanol more sulfur can release than volatile matter does. While in other atmospheres the emission of volatile matter is dominant; (2) From 500°C to 700°C, all F_T is more than zero. That is to say, sulfur releasing is dominant in this temperature range for all atmospheres. And in hydrogen the desulfurization effect is the best. In acetone and ethanol there are similar effect on desulfurization; (3) In hydrogen the gap of F_T between these two temperature ranges is the widest, while in ethanol the gap is the narrowest. The atmosphere of hydrogen is the most sensitive to temperature, while ethanol is a relative mild atmosphere for desulfurization. Of course, F_T is only the overall effect in the temperature range, and if the temperature range is narrow enough, the nature of each atmosphere will be discovered more clearly.

Figure 2. The change of F_T for Yanzhou coal under different

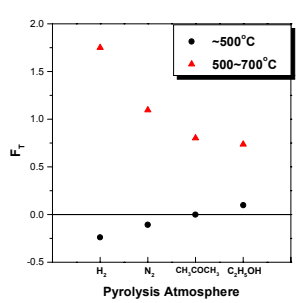

pyrolysis atmospheres.

The promotion on sulfur removal by the introduction of ethanol depends not only on the sulfur structure in coal, but also on the decomposition of itself during pyrolysis. As known, pyrolysis generates free radicals from coal under a broad range of temperatures. Combination of large radicals produces heavy products such as char, and combination of small radicals produces volatile products such as gas and tar. If there is not enough small radicals to stabilizing the sulfur-containing radicals from coal, the sulfur-containing radicals released from coal may react with large radicals to form char, which reduces the sulfur removal effect. Pyrolysis of the organic reagents added may produce more small radicals including hydrogen redicals, to stabilize the sulfur containing radicals, and to increase the amount of sulfur in the volatile products. The proposed decomposition mechanisms of ethanol and acetone are shown in the following along with the decomposition energy for each substance.

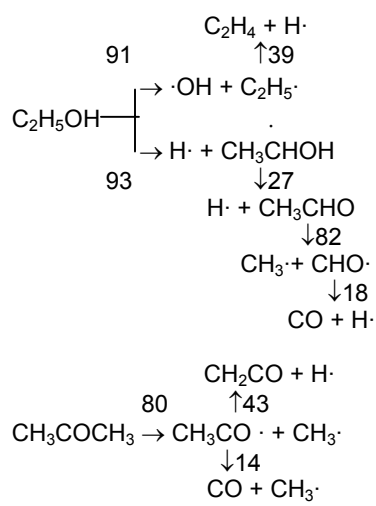

D_{298}^{o}(kcal •mol^{-1})

Comparing these reactions, it is observed that ethanol can generate more small free redicals, especially hydrogen redicals, than acetone. Among these free radicals, hydrogen redicals may be the main one promoting the sulfur removal reaction. Studies, however, are needed for further exploration on this subject.

Conclusions

Compared to pyrolysis and hydropyrolysis of coals, the introduction of ethanol and acetone into the reaction atmosphere selectively promotes sulfur removal from coal, which results in chars of low sulfur content and high yield, especially for ethanol. In addition, there is a symmetrical and promotive effect on desulfurization at a wide temperature range in ethanol.

Acknowledgement. The project is subsidised by the Special Founds for Major State Basic Research Project, the Chinese Academy of Sciences, and the Natural Science Foundation of China and Shanxi Province, and the State Key Laboratory of Coal Conversion.

References

(1) Kelemen, S. R.; Gorbaty, M. L.; Geoge, G. N.; Kwiatek, P. J.; Sansone, M. *Fuel*, 1991, ***70***, 396-402.
(2) Sugawara, K.; Tozuka, Y.; Sugawara, T.; Nishiyama, Y. *Fuel Processing Technology*, 1994, ***37***, 73-85.
(3) Liao, H. Q.; Li, B. Q.; and Zhang, B. J. *Fuel*, 1998, ***77***, 1643-1646.
(4) Chen, H. K.; Li, B. Q.; Yang, J. L.; Zhang, B. J. *Fuel*, 1998, ***77***, 487-493.

(5) Robert, S.; and VanMeurs, P. *Fuel*, 1980, ***59***,458-464.
(6) van Heek, K. H.; and Hodek, W. *Fuel*, 1994, ***73***, 886-896.

THE BEHAVIOR OF THE TRACE ELEMENTS IN COAL DURING PYROLYSIS

Ruixia Guo, Jianli Yang, Dongyan Liu and Zhenyu Liu

State Key Laboratory of Coal Conversion, Institute of Coal Chemistry
Chinese Academy of Sciences, P.O. Box 165, Taiyuan, Shanxi 030001, P.R. China

Introduction

Coal is a cheap and the most commonly fuel in China. However, coal contains trace hazardous elements of environmental concerns in ppm order, such as As, Pb, Cr, Cd, and Mn. The presence of the elements can have a great influence on coal utilization processes. The most important effects are related to coal combustion and the environmental impact resulted from the thousands of tonnes of solid emitted into the atmosphere. For example, the release of the trace elements from coal as vapor or fine particles during combustion causes causes potentially toxic to plants, animals and human health and pollution to ecological environment under certain conditions and concentrations[1-3]. The formation of the technology for the coal utilization units requires the understanding of their occurrence in coal, their behavior during and prior to combustion and their form in the stack gas.

Recently, many of researchers have concentrated on behavior of trace elements during combustion and post-combustion[3-7]. Their investigation on the transformation of trace elements during coal combustion have shown that the volatility of trace elements depends on their affinities and concentrations, and on the physical changes and chemical reaction of these elements with sulfur or other volatile elements during combustion. The main purpose of this study is to understand the transformation of As, Pb, Cr, Cd, and Mn during coal pyrolysis. The effects of pyrolysis temperature and coal type were investigated. In addition, thermodynamic analysis was also further carried out.

Experimental

Three Chinese coals, Datong, Shenhua and Yima, were used in this study. The coals were crushed and sieved to 0.16~0.27mm, and then dried under vacuum at 110°C with a nitrogen purge. The properties of coals are given in Table 1.

Table 1. Analysis of coal samples•wt%

Coal sample	Proximate analysis			Ultimate analysis•daf					Ash analysis	
	V_{ad}	A_d	M	C	H	N	S	O^a	Si	Al
Shenhua	30.71	6.61	0.51	63.77	3.81	0.79	0.57	31.06	27.8	5.9
Yima	30.24	15.79	0.79	58.88	2.94	0.65	1.94	35.62	30.1	10.0
Datong	26.86	13.58	0.61	67.62	4.18	0.72	2.03	25.45	25.4	11.3

Note: a: by difference

Pyrolysis experiment was conducted in a fixed bed quartz reactor under N_2 stream with a heating rate of 20°C/min. The temperature ranges from 500°C to 1000°C. As, Pb, Cr, Cd, and Mn contained in char and raw coal were measured by inductively coupled plasma-atomic spectroscopy (ICP-AES). The concentrations of elements in three raw coals are presented in table 2. Bleeding ratio (BR) was defined as:

$$BR(\%) = \frac{\text{concentration in coal} - \text{concentration in char} \times \text{char yield}}{\text{concentration in coal}} \times 100\%$$

It was used to evaluate the change of the trace elements in coal during the treatment.

Table 2. The concentration of trace elements in three coals•μg/g coal

Coal sample	As	Pb	Cr	Cd	Mn
Shenhua	-	6.2	3.2	-	70.5
Yima	40.3	12.6	15.6	1.28	40.4
Datong	8.6	8.8	6.2	0.25	49

Results and discussion

Transformation of trace elements with temperature. As shown in Fig 1(a), the large amount of As and Cd is released from Datong coal at relative low temperatures of 500°C, while the temperature for lead release is above 800°C. The lesser emission of Cr and Mn during pyrolysis implies that these elements may be retained by aluminosilicate, or was initially existed as more stable forms in raw coal[8].

The bleeding ratio was plotted versus the yield of volatiles (tar +gas) in Fig 1(b) for Datong coal. The points are divided into two parts by the diagonal line l. The points at the upper part represent the char with a concentration of trace elements lower than that in raw coal and the points at the lower part represent the char with a concentration of the trace elements higher than that in raw coal. As shows that the concentration of As, Cd and Pb in char decreased to lower than that in raw coal with increasing the yield of volatiles. This indicates that the majority of these elements vaporized by heat treatment. Cr and Mn concentration in all the chars, however, are higher than that in raw coal, which indicate their relative non-volatility.

Effect of coal type. The bleeding ratio of trace elements in 1000°C char with coal type is shown in Fig 2. This was examined for Pb, Cr, Mn in three coals and for As, Cd in Yima and Datong coals.

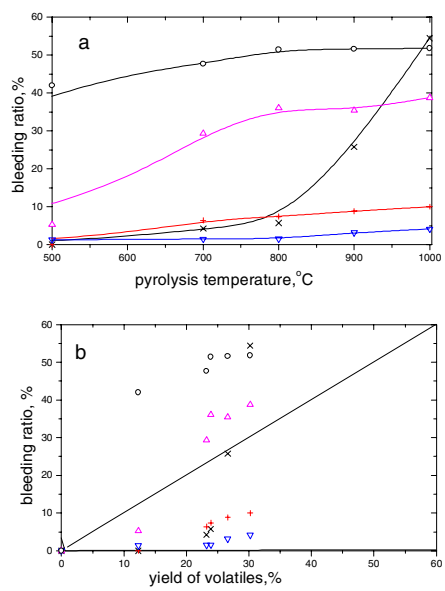

Fig. 1 Effect of temperature on release of trace elements for Datong coal (o) As; (Δ) Cd; (×) Pb; (+) Cr; (∇) Mn

As indicated the bleeding ratios of Pb, Cr, Mn for Shenhua coal were the highest. Among the five trace elements considered, Lead was the most volatile element at pyrolysis temperature of 1000°C. Arsenic and cadmium were next volatile elements with bleeding ratio of 51.8% and 38.8% for Datong coal and 30.1% and 27.2% for Yima coal. For a given element, the bleeding ratio varies with the coal type. This may be caused by the difference in the chemical composition of the raw coal, both element-containing compounds and the relative compounds

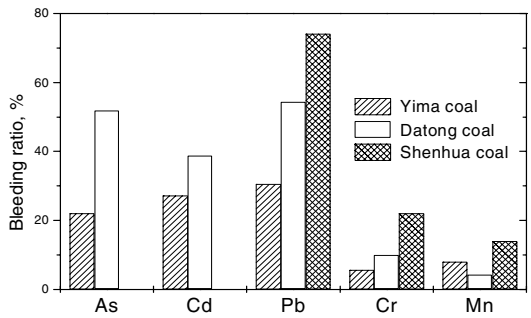

Fig. 2 Effect of coal type on bleeding ratio of trace elements

Thermodynamic behavior of trace elements.

The element volatility behavior is related with boiling point of the element and of the relative compounds. The high volatility of the element is often related to the low boiling points and compounds. Boiling points of trace elements considered and their relative important compounds are presented in table 3. It can be seen that boiling points for Mn element and compounds are higher than the pyrolysis temperature studied. It is consistent with the lower bleeding ratio of Mn. Although the high boiling points of oxides, sulfides for Pb, Cr and Cd are relatively high, the boiling points of chlorides for these elements plus As are lower than the pyrolysis temperature range studied. Thus it may conclude that the formation of chlorides during pyrolysis promotes the emission of the elements. Due to high boiling points of element, oxide and sulfide, Pb is non-volatility. However, it can be transformed into Chloride at high temperature of 1100K by gasification-agglomeration effect[9]. This accelerates Pb emission. Moreover, this is consistent with the experimental result that bleeding ratio of Pb increased quickly above 800°C. As and Cd are both volatile elements based on the boiling points of elements and their oxides.

Table.3. Boiling point of trace elementsand their compounds, °C

kind	Element	Oxide	Sulfide	Chloride
Pb	1740	1535	1281	953
As	814	461	707	130
Cd	765	>920	1382	964
Cr	2672	2275	1550	950
Mn	1900	1650		1190

Furthermore, formation of their chlorides can also result in more emission for As and Cd from coal. However, the elements did not release completely during pyrolysis. This suggests that some of As and Cd may be existed in more stable structure in coal or chlorine content in coal is limited. Compared with Pb, As, and Cd, however, Cr is non-volatility element. This accords with the fact that high boiling points of element and compounds for Cr, especially that its chlorides is hardly to be formed at 1100K.

Conclusions

The behavior of trace elements observed in this study was dependent upon both coal type and pyrolysis parameters. The amount of trace elements emissed during pyrolysis increased with increasing temperature. Although Pb, As and Cd were volatile, their volatility varies with coal type. This indicates that the volatility is related with the form of the elements occurred in raw coal. Cr and Mn were relatively non-volatile elements under the conditions tested.

Further work identifying the relationship between volatile and elemental form in raw coal, particularly for the elements Pb, As, and Cd is clearly needed.

Acknowledgement. The authors gratefully acknowledge the financial support from the Special Founds for Major State Basic Research Project, the Chinese Academy of Sciences, and the Natural Science Foundation of China

References

(1) Eble, C. F.; and Hower, J. C. *Fuel*, **1997**, *76* (8), 711
(2) Feng, Xinbin.; Ni, Jianyu.; and Hong, Yetang. *Environmental Chemistry*, **1998**, *17* (2), 148.
(3) Swaine, D.J. *J. Coal Qual*. **1989**, *8*, 63
(4) Constance, L.S.; Lawrence, E.; Joseph, R.M. *Fuel Processing Technology*, **2000**, *63*, 109
(5) Querol, X.; Fernandez-Turiel, J.L.; and Lopez-Soler, A. *Fuel*, **1995**, *74* (3), 331
(6) Querol, X.; Juan, R.; Lopez-Soler, A.; and etc. *Fuel*, **1996,** *75*, 821
(7) Palmer, C.A.; Mroczkowski, S.J.; Finkelman, R.B.; Crowley, S.S.; and Bullock, J.H. In *Proceedings of the Fifteenth Pittsburgh Coal Conference (CD-ROM)*; 1998
(8) Raask, E. In *Mineral Impurities in Coal Combustion*; Hemisphere Publishing; London, 1985; pp.293-312.
(9) Wang, Xifen.; Sun, Xuexin.; and Li, Min. *Coal Conversion*, **1999**, *22*(1), 58

Influence of thermal treatment conditions on transformation behavior of trace elements in coals

Ruixia Guo, Jianli Yang, Baohua Li, Dongyan Liu, Zhenyu Liu

State Key Laboratory of Coal Conversion, Institute of Coal Chemistry, Chinese Academy of Sciences, P.O. Box 165, Taiyuan, Shanxi 030001, P.R. China

Introduction

Coal contains harmful elements of environmental concerns in ppm order, such as Na, K, Pb and Mn. Release of these elements from coal as vapor or fine particles during coal combustion causes severe problems to the turbine blades, human health and ecological environment [1-3]. Therefore, a full detailed understanding on the chemical and thermal stability of Na, K, Pb and Mn during coal processing is desirable in guiding their effective control prior to combustion.

Recently, many researchers have studied the forms of Na, K, Pb and Mn in coal and their fate during coal combustion [3-7]. However, the information on the transformation of the elements during pyrolysis is limited. The attempt was made in this paper is to understand the transformation of Na, K, Pb and Mn during thermal treatments under different conditions. The effects of the temperature, pressure, and atmosphere were investigated. The pyrolysis temperature was found to be the most influential factor for Na, K, Pb and Mn evolution.

Experimental

2.1 Coal sample. Two Chinese coals, Shenhua and Yima, were used in this study. The coals were crushed and sieved to 0.16~0.27mm, and then dried under vacuum at 110°C with a nitrogen purge. The properties of the coals are given in Table 1.

Table 1. Analysis of coal samples，wt%

Coal sample	Proximate analysis			Ultimate analysis，daf					Ash analysis	
	V_{ad}	A_d	M	C	H	N	S	O^a	Si	Al
Shenhua	30.71	6.61	0.51	63.77	3.81	0.79	0.57	31.06	27.8	5.9
Yima	30.24	15.79	0.79	58.88	2.94	0.65	1.94	35.62	30.1	10.0

2.2 Apparatus and Procedure. A schematic representation of experimental apparatus is shown in Fig 1. It consists mainly of a rotary furnace and a pyrolysis reactor. Prior to a reaction，about 5g of coal sample was placed at the top of the reactor. Then it was sealed and filled with a desired gas to a pressure of 0.1 MPa or 5.0 MPa. During these processes, the reactor was maintained at horizontal position. After heating up the reactor to a desired temperature, the furnace, along with the reactor, was quickly turned to vertical position to allow fast pyrolysis. After 2 minutes, the reactor was pulled out from the furnace and quenched in the cold water. Char was collected from the bottom of the reactor. Amount of gases produced was determined by the weight difference of the reactor with the samples before and after the reaction. Amount of tar produced was calculated by subtraction.

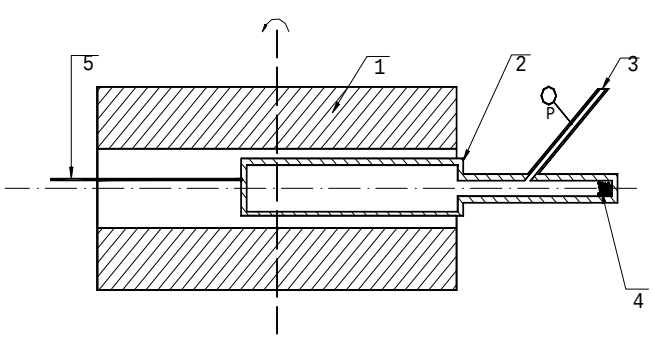

1 furnace, 2 reactor, 3 gas in and out, 4 coal sample 5 thermocouple

Fig 1. The schematic of high pressure closed fast pyrolysis apparatus

2.3 Trace element analysis. The forms of Pb and Mn contained in the coals were defined as the following: H_2O solubles, HCl solubles and residues. Deionised water and aqueous solutions of 1N hydrochloric acid (HCl) were used for H_2O solubles and HCl solubles seperation. The use of HCl removed acid soluble minerals such as calcite ($CaCO_3$), dolomite (CaMg $[CO_3]_2$), and siderite ($FeCO_3$). Clay (aluminosilicates), quartz (SiO_2), and pyrite (FeS_2) as residue remained in the solid. The content of Na, K, Pb and Mn in raw coal, char and solutions was measured by inductively coupled plasma – atomic emission spectroscopy (ICP-AES).

Results and Discussion

3.1 Release behavior of the elements in Shenhua and Yima coal. Tables 2 and 3 show changes of Na, K, Pb and Mn content in chars with temperature during pyrolysis in a nitrogen atmosphere. Although contents of all the four elements decreased with increasing pyrolysis temperature, the initial emission temperature for Shenhua coal (400°C) is lower than that for Yima coal (600°C). The content of Na, K, Pb and Mn in chars varies with coal type. This indicates that the transformation of the elements is related to their forms in the coals and the environment around them. Larger amounts of Si, Al and S in Yima coal than those in Shenhua coal suggests that the elements in Yima coal may be existed as sulphate, aluminate and silicate of thermal stable forms. Due to high boiling point of these thermally stable compounds, their decomposition and transformation are difficult [6,7,11]. This resulted in the lower emission of the elements from Yima coal.

Table 2. char yield (wt%) and the contents of elements for Shenhua coal（μg/g coal）

Temperature ℃	Raw coal	400	500	600	700
Char yield		97.75	93.65	87.80	81.41
Na	1334.2	1334.2	1331.5	1328.9	1299.1
K	2963.1	2963.1	2963.1	2960.1	2927.5
Pb	13.1	13.1	13.1	12.5	11.8
Mn	41.8	41.8	41.8	41.7	40.8

Table 3. char yield (wt%) and the contents of elements for Yima coal（μg/g coal）

Temperature ℃	Raw coal	400	500	600	700
Char yield		93.61	91.41	86.70	81.00
Na	893.2	846.6	843.0	835.0	823.3
K	627.0	610.1	605.7	604.4	595.7
Pb	6.2	5.8	5.7	5.5	5.3
Mn	70.6	67.2	67.1	66.9	66.5

In order to further demonstrate the relationships between the behavior of the elements during heating and their chemical forms in the coals, the distribution of the forms for the elements in Yima and Shenhua coals were investigated. Results obtained for the elements Pb and Mn are presented in Table 4. It can be seen that Pb is predominantly present as H_2O solubles and residues in Shenhua coal. However, the residues are the main forms of Pb in Yima coal. It is consistent with that Pb is often reported to be strongly associated with sulfur and Pb sulfides are H_2O insoluble. In the experimental temperature range, residues are non-volatile compounds. This may lead to lower release of the elements from coals. H_2O solubles of Pb were found in Shenhua coal but not in Yima coal. This results in the difference of initial emission temperature between two coals. However, percentage of Pb emitted (14.1%) up to 700°C is lower than that of H_2O solubles (23%) based on total content in Shenhua coal. This suggests that the H_2O solubles of Pb is not released to gas completely and partly converted into other forms during thermal treatment. In addition, Mn in both coals is distributed in all the three forms but H_2O solubles fraction is negligible. This agrees with the non-volatile behavior of Mn.

Table 4. Analysis of elements forms（μ g/g coal）

solubles	Pb		Mn	
	Shenhua	Yima	Shenhua	Yima
H_2O	1.7	0	1.2	0.1
HCl	0	1.1	57.8	0.3
Residue	4.6	11.8	11.6	40.3

3.2 Influence of atmosphere. Fig 2 (a) and (b) show the changes in content of Na, K, Pb and Mn in Shenhua coal during pyrolysis in N_2, H_2 and CO_2 atmospheres. Among the three atmospheres, H_2 results in the least elements retention and CO_2 the highest elements retention. The polymerization between siliceous char and volatile compounds is favorable in oxidizing atmosphere [8]. This may transform volatile compounds of Na, K, Pb and Mn into thermally stable compounds. In contrast, the high yield of volatile compounds (gas +tar) under H_2 (shown in Fig 3) increases the emission of the elements by transferring thermally stable compounds into low boiling point of compounds (such as chloride) [9]. As a result, H_2 and CO_2 resulted in obvious distinction on emission of the four elements.

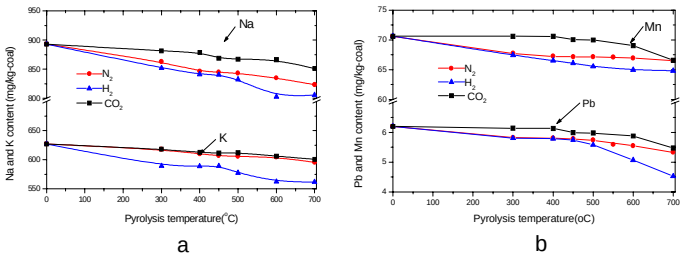

Fig 2. The effect of atmosphere on evolve of elements in Shenhua coal
a：The effect on Na and K　　b：The effect on Pb and Mn

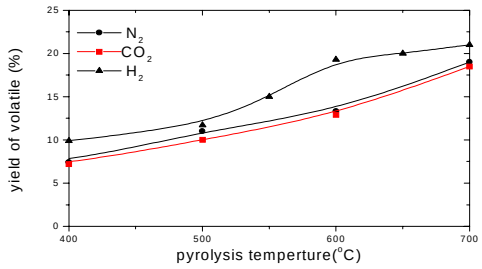

Fig 3. Yield of volatile for Shenhua coal during pyrolysis at 0.1MPa

3.3 Influence of pressure. The effects of pressure on the retention of Na, K, Pb and Mn in Shenhua coal during pyrolysis were given in Fig 4. Although lesser amounts of the elements were released at 5MPa than at 0.1MPa, the effect of pressure is small. Two important steps may affect the release of the elements: breaking of chemical bonds and transfer of the volatiles from the coal pore to the gas phase. Generally speaking, the former is not sensitive to the pressure, but the latter is affected by the pressure. The higher pressure restrains the transfer of volatile compounds from the pore of coal and increases the possibility of the element retention in the char. The thermodynamic analysis also confirmed this [10].

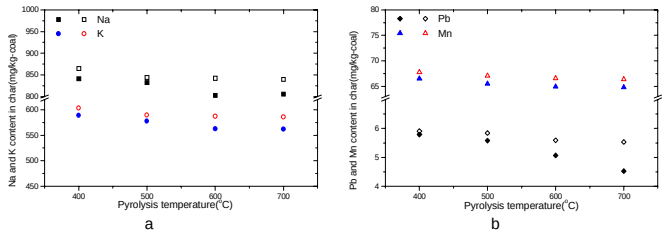

Fig 4. The effects of temperature and pressure on evolve of elements for Shenhua coal in H_2: Filled symbol, 0.1MPa; Open symbol：5Mpa.
a: The effect on Na and K; b: The effect on Pb and Mn

Conclusions

The effects of atmosphere, pressure and temperature on trace elements release behavior during thermal treatment were investigated. The elements studied are Na, K, Pb, and Mn. The order of atmosphere influence on the emission of the elements is H2> N2> CO_2. Although the effect of pressure is not significant, the higher pressure results in the lesser element emission. The emission of the four elements is mainly dependent on temperature and their forms in coal.

Acknowledgement. The authors gratefully acknowledge the financial support from the Special Founds for Major State Basic Research Project, the Chinese Academy of Sciences, and the Natural Science Foundation of China.

References

(1). Manzoori, A. R.; Pradeep, K.; and Agarwal. *Fuel,* **1992**, *71* (5), 513.
(2). Peterson, J. R.; Lucke, V. H. *Combustion*, **1979**, *50* (7), 29.
(3). Feng, X.B.; Ni, J.Y.; Hong, Y.T.; Zhu, J.M.; Zhou, B.; Wang, Y. *Environmental Chemistry*, **1998**, *17* (2), 148.
(4). Helble, J.J. *Fuel Processing Technology*, **1994**, 39(1), 159
(5). John Hodges, N. D.; and Richards, G. *Fuel,* **1989,** *68*(1), 440.
(6). Han, C.l.; Zhang, J.; Liu, K.L.; Xu, Y.Q. *Journal of fuel chemistry and technology*, **1999,** *27*(6), 575.
(7). Huang, W.H.; and Yang, Q. *Geological Science and technology information,* **1999**, *18*(1), 71.
(8). Zhang, J.; Han, C.L.; and Liu, K.L. *Journal of Engineering for Thermal Energy and Power,* **1999**, *14*(2), 83.
(9). Enders, M.; Wilenborg, W.; Albrecht, J.; Putnis, A *Fuel Processing Technology,* **2000**, *68*(1), 57.
(10) Wang, X.F.; Sun, X.B.; and Li, M. *Coal Conversion*, **1999**, *22*(1), 58.
(11). Sugawara, K.; Inoue, H.; Enda, Y.; Sugawara, T.; Shirai, M.In *The 7th China-Japan Symposium on Coal and C_1 Chemistry Proceedings*; P.R.China, 2001; pp.367-370

MODELING OF A SMOLDERING CARBONACEOUS ROD

Ali Rostami[1], Jayathi Murthy[2] and Mohammad Hajaligol[1]

(1) Philip Morris USA, Research Center
P.O. Box 26583, Richmond, VA 23261

(2) Department of Mechanical Engineering,
Carnegie Mellon University, Pittsburgh, PA 15213

ABSTRACT

A transient 2-D model based on the first principles has been developed for the natural smoldering of a porous carbonaceous rod. Heat transfer is represented by the use of a two-temperature formulation whereby the solid and gas phases are considered to have separate and distinct temperatures interacting through an inter-phase heat exchange. The starting material first undergoes pyrolysis prior to oxidation of the remaining carbonaceous residue. The pyrolysis is assumed to consist of a set of reactions. Oxidation of the carbonaceous residue is accompanied by the formation of gas-phase combustion products, whose concentration is also computed. Calculations under unsteady conditions are done for a variety of smoldering cases with varying operating and boundary conditions. The model was validated by comparing the predictions with the experimental data on the smoldering burn rate and the maximum gas and solid temperatures. The computation captures the development of a steady combustion regime in which the burn front moves at a constant rate. More information can be obtained from the model including coal shape, gas and solid temperature profiles, product yields, solid density variations, and the effects of ignition conditions. The results are shown to be very sensitive to the availability of oxygen as well as heat losses.

INTRODUCTION

Smoldering of a porous carbonaceous rod is normally controlled by two main parameters: availability of oxygen to the combustion front and heat losses form it. The velocity of the combustion front into the carbonaceous fuel after the ignition by an external heat source and the peak temperature are two indicators of the sustenance of combustion. It is a transient process which is controlled by a combination of endothermic and exothermic chemical reactions in the pyrolysis and combustion zones, diffusion of oxygen to the combustion zone, diffusion of reaction products away from the sources, and heat transfer as well.

Since the early 1980's, several works on smoldering of cellulosic materials have been reported [1-7]. These works were focused on the generalization of combustion modeling in porous media. Both forward and reverse smoldering were considered, where a forced flow of air is resumed either in the direction of (forward) the smolder propagation or opposite to that (reverse). Analytical and numerical solutions were obtained for 1-D case of a semi-infinite packed fuel bed. In an attempt to model the steady state smoldering of a burning rod, Kinbara et al [8] used the a diffusion controlled approach to model the smoldering of a cylindrical fuel. The model was 1 D and the predicted behavior was in agreement with the measured burn rate. Ohlemiller [1] considered a burning cigarette as forward smoldering case, in which the air flow is in the same direction as the travelling combustion front. A comprehensive description of the mathematical formulation was presented by Ohlemiller [1], but no attempt was made to develop a solution technique for the multi-phase and multi-component system of equations.

We have recently embarked on an effort to develop comprehensive modeling software for the prediction of flow, heat transfer and chemical reaction in a burning porous rod. In this paper we present the natural smoldering combustion of the rod where no forced flow exists within the rod. A two-temperature formulation for the solid phase and the gas phase is then developed. In the subsequent sections, the model is described, followed by a description of the governing equations and the boundary conditions. Finally, the computed results are evaluated and recommendations are made.

MODEL DISCRIPTION

The modeling of pyrolysis and combustion in a smoldering fuel bed requires the solution of flow, heat and mass transfer through porous media. The gas and solid phases are treated separately. Pyrolysis occurs in the starting material through a set of pyrolysis reactions. The pyrolysis reactions result in the formation of a series of products. The pyrolysis products leave the solid phase, while the remaining carbonaceous residue is oxidized when exposed to high temperatures and oxygen. Some species in the gas phase may undergo further degradation reactions into other gas phase species, which is not considered in this study. In addition, we must also account for the evaporation of water, other volatile materials, and ash formation reactions as well.

The combustion process is initiated by applying a high temperature or a high heat flux at one end of the fuel rod for a fixed time. This initiates the pyrolysis reactions in a very narrow, nearly one-dimensional zone, followed by the oxidation of the carbonaceous residue. It is followed by combustion reactions in a larger two-dimensional cone, sustained by the diffusion of oxygen from the surrounding air through the porous fuel rod under smoldering conditions. The burn front moves axially, so does the combustion cone. For a given smoldering condition, the burn front is expected to travel at a constant velocity away from the lighted end of the rod.

Following the ignition, the instantaneous density of the starting material is calculated using a set of pyrolysis reactions and water evaporation represented by Arrhenius expression. The remaining solid residues react with oxygen at high temperatures which is assumed to follow Arrhenius relation as well. The kinetic parameters for the material of interest are obtained from literature.

The gas-phase transport equation is expressed as

$$\frac{\partial\ \rho(1-\phi)Y_i}{\partial t} + \nabla.(\rho V Y_i) = \nabla \bullet (\rho D(1-\phi)\nabla Y_i) + R_i\phi \qquad (1)$$

where, ϕ is the porosity of the porous bed, ρ is the gas-phase mixture density, D is the diffusion coefficient of the species in the mixture and R_i is the volumetric rate of species production due to the oxidation reaction. All terms involving velocity V will be omitted for the case of smoldering.

The solid and gas phase energy equations are given as

$$(1-\phi)\rho_S C_{ps}\frac{\partial T_S}{\partial t} = \nabla \bullet \left(k_{s,eff}(1-\phi)\nabla T_S \right) + h_{S-g}\left(\frac{A}{V}\right)\left(T_g - T_S\right) + S_{solid} \qquad (2)$$

and

$$\frac{\partial}{\partial t}\left(\rho\ \phi h_g\right) + \nabla \bullet (\rho V h_g) = \nabla \bullet (k_g \phi \nabla T_g) + h_{S-g}\left(\frac{A}{V}\right)\left(T_S - T_g\right) + S_{gas} \qquad (3)$$

respectively. For the solid phase equation, the source term S_{solid} would include the heat of reactions. $k_{s,eff}$ includes the radiation contribution to heat transfer in the solid by using Rosseland approximation to augment the solid conductivity. The interface heat exchange between the solid and gas phases is prescribed empirically by assuming a pore geometry. The correlation by Wakao and Kaguei [9] has been used in this study.

Boundary Conditions

For smoldering, the internal flow in the porous media is assumed to be negligible. The temperature for both the solid and gas phases at the inlet is held at T=1000 K until combustion starts; this typically takes 10-30 seconds depending on the conditions. After this, the temperature for both phases is set to T=300 K. All gas-phase species are assumed to have zero mass fraction at the inlet except oxygen, which assumed a mass fraction of 0.23 and nitrogen, which assumes a value of 0.77 throughout the smoldering process. At the outlet, a zero gradient condition is assumed for temperature and species mass fraction.

For smoldering, no flow boundary conditions are required. The gas and solid phase temperatures are subjected to a convective boundary condition at the lateral cylindrical boundary. All gas-phase species except oxygen are subjected to zero gradient conditions at the lateral boundary. For oxygen, different boundary conditions have been used for smoldering calculations, ranging from fully impermeable, to having a specified mass transfer coefficient.

Initially, both the gas and solid phase temperatures are set at 300 K throughout the domain. The mass fractions of oxygen and nitrogen are set at their environmental values of 0.23 and 0.77 respectively.

Details of the model as well as the numerical implementation appear in a manuscript submitted to *Journal of Applied Analytical Pyrolysis* and in another manuscript to be submitted to *Combustion and Flame*.

NUMERICAL IMPLEMENTATION

The geometry of the calculation domain is shown in Figure 1. A cylindrical axisymmetric fuel rod is assumed. A non-uniform structured mesh of 82x22 control volumes is used in the x and r directions respectively. The computational domain is set to be a porous zone in Fluent parlance.

The implementation of the models is done in a custom version of Fluent's structured mesh solver, Fluent 4.5. The domain is discretized into structured control volumes over which the conservation equations for mass, momentum, energy and chemical species are discretized.

A variable time step is used to do the calculations, with relatively large time steps of between 0.1-0.01 seconds during the initial passive heat-up stage followed by very smaller time steps once combustion commences. The size of the time step is controlled by the time scale of the oxidation reaction which is very fast.

RESULTS AND DISCUSSIONS

Numerous calculations were performed to identify the effects of the appropriate model parameters, numerical parameters and boundary conditions. A number of results including the effects of the surface heat transfer coefficient, overall mass transfer coefficient and the lighting conditions are reported here. The overall mass transfer coefficient, to which the results are very sensitive, depends on the convective coefficient on the surface as well as the diffusion coefficient in the porous wrapper if exists. In practice, the air velocity on the surface, hence the heat transfer and mass transfer coefficients, are highly unpredictable and vary significantly depending on the conditions of the air surrounding the rod. Therefore, an accurate comparison between the experimental results and the predictions was impossible, because most of the data available in the literature do not provide sufficient information on either the operating conditions or the physical properties.

Figure 2 shows the gas-phase temperature contours at steady state conditions for smoldering of a fuel rod made of cellulose. The steady state conditions prevail approximately 100 seconds after ignition. The kinetic parameters for this run were obtained from Kashiwagi and Numbu [10] and the thermophysical properties form Moussa et al. [11] and Dosanjh et al. [12]. The temperature at one end of the fuel rod was raised to 1000 K for 3 seconds. Combustion is initiated at this time and the temperature is set back to 300 K. The maximum temperature that normally occurs at the centerline (see Figure 1) strongly depends on the surface heat and mass transfer coefficients. The corresponding values for this run are 80 W/m^2K and 0.008 kg/m^2s respectively. The oxygen concentration for this case at the same time is shown in Figure 3. An oxygen-depleted region can be clearly seen in this figure.

The temperature of solid phase is slightly higher than the gas temperature (not shown in the figure). The difference is due to the fact that heat is generated in the solid phase as a result of chemical reactions and has to be transferred from the solid to the gas phase through the gas-solid interface. Therefore a solid-to-gas phase temperature gradient is required to keep the flow of heat, which is caused by the thermal resistance associated with the interface. The actual temperature difference between the two phases depends on the gas-solid interface resistance as well as the interface area, both of which are difficult to be accurately evaluated. The predicted temperature difference is generally between 1 and 2% of the gas temperature. For the case of Figures 2 and 3, the maximum solid temperature is generally 10 to 20 K higher than the maximum gas temperature depending on time and location.

The effects of peripheral heat losses are shown in Figure 4. For a given set of kinetic parameters, the fate of combustion is tied to the oxygen availability to as well as heat losses from the combustion zone. Having discussed the oxygen supply, we now turn to the heat transfer effects. The heat transfer mechanisms that are relevant to the combustion zone are axial and radial conduction and radiation in the porous rod as well as convection and thermal radiation form the surfaces. The first two are incorporated in the governing equations. An overall heat transfer coefficient is assigned to the lateral surface that includes the surface convection and radiation. The value of overall heat transfer coefficient, *h*, is varied from 20 to 100 W/m^2K. Fig. 5 shows the effects of the overall heat transfer coefficient on the steady state smoldering velocity and the gas maximum temperature respectively. The smoldering velocity reaches a high value of 16 mm/min for h=20 W/m^2K, while the maximum temperature reaches 1660 K for the same conditions. As h increases to 100 W/m^2 K, they drop to 5.3 mm/min and 850 K respectively.

CONCLUSIONS

Smoldering combustion of a cylindrical porous rod has been computed using Fluent 4.5. A variety of models have been incorporated for pyrolysis and oxidation as well as for heat transfer in porous media, including a two-temperature model for thermal non-equilibrium between gas and solid. Predictions of temperature and species concentration have been made. The results establish that the overall physics of the smoldering process is captured by the simulation, and the actual values of the gas and solid temperatures and the rate of burn are in reasonable agreement with the experimental data. The accuracy of the results depends strongly on a number of empirical parameters. The most significant parameters are the lateral mass transfer boundary condition for oxygen. The effects of these parameters are being studied and will be reported later. The numerics have proved to be stable and convergent and allow us to do computations with relative ease.
Though the effort has been successful in capturing the broad features of smoldering, as discussed above a number of improvements to the current model needs to be made.

REFERENCES

1. Ohlemiller, T. J., Modeling of Smoldering Combustion Propagation, *Prog. Energy Combust. Sci.*, Vol. 11, pp. 277-310, 1985.
2. Ohlemiller, T. J., and Lucca D. A., An Experimental Comparison of Forward and Reverse Smolder Propagation of Permeable Fuel Beds, *Combust. Flame* 54:131-147, 1983.
3. Leach, S. V., Rein, G., Ellzey, J. L., and Ezekoye, O. A., and Torero, J.L., Kinetics and Fuel Property Effects on Forward Smoldering Combustion, *Combust. Flame* 120: 346-358, 2000.
4. Torero, J. L., and Fernandez-Pello, A., Forward Smolder of Polyurethane Foam in a Forced Air Flow, *Combust. Flame* 106:89-109, 1996.
5. Buckmaster, J. and Lozinski, D., An Elementary Discussion of Forward Smoldering, *Combust. Flame* 104:300-310, 1996.
6. Ohlemiller, T. J., Bellan, J., and Rogers, F., A Model of Smoldering Combustion Applied to Flexible Polyurethane Foams, *Combust. Flame* 36:197-215, 1979.
7. Di Blasi, C, Modeling and Simulation of Combustion Processes, of Charring and Non-Charring Solid Fuels, *Prog. Energy Combust. Sci*., Vol. 19, pp. 71-104, 1993.
8. Kinbara, T., Endo, H. and Sega, S, Downward Propagation of Smoldering Combustion through Solid Materials, *11th Symp. Combust*., Pittsburgh, Pennsylvania, pp 525-531, 1967.
9. Wakao, N., and Kaguei S., "Heat and Mass Transfer in Packed Beds," Gordon and Breach, New York, 1982.
10. Kashiwagi T. and Nambu H., Global Kinetic Constants for Thermal Oxidative Degradation of Cellulosic Paper, Combustion and Flame, 88: 345-368, 1992.
11. Moussa, N. A., Toong, T. Y., and Garris, C. A., 16th Symposium on Combustion, The Combustion nstitute, Pittsburgh, p. 1447, 1976.
12. Dosanjh, S. S., Pagni, P. J., and Fernandez-pello, A. C, Forced Cocurrent Smoldering Combustion, Combustion and Flame, 68: 131-142, 1987.

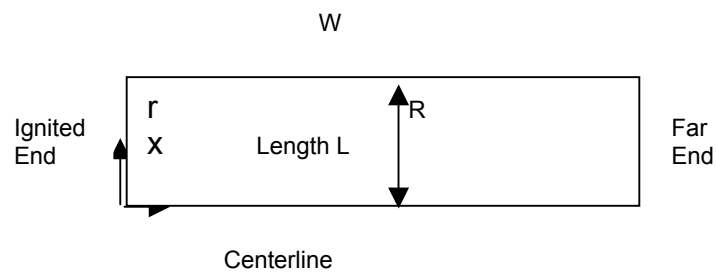

Figure 1 Geometry of Computational Domain

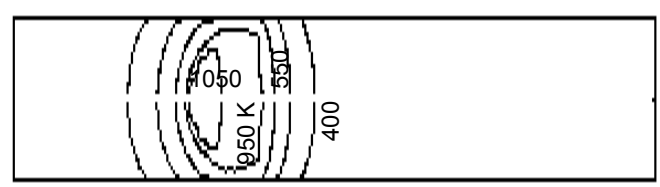

Figure 2. Gas Temperature Contours at 153 s after Initiation of smoldering

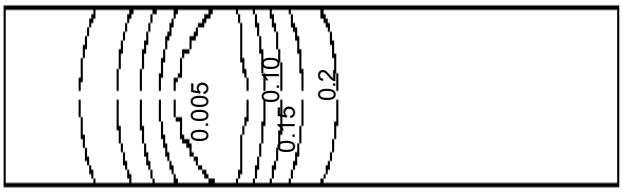

Figure 3. Oxygen Concentration Contours at 153 s after Initiation of Smoldering.

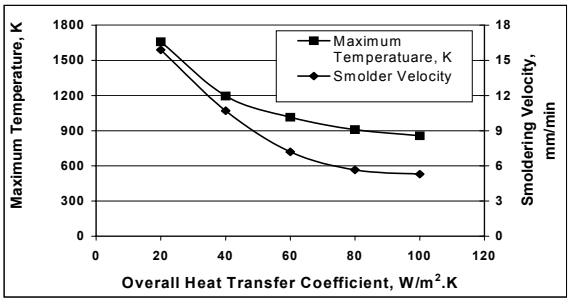

Figure 4. Effects of Heat Dissipation on Smoldering Velocity and Peak Temperature

DEVELOPMENT OF MODEL FUELS WITH VOLATILITIES THAT RESEMBLE THOSE OF REAL FUELS

Michael L. Greenfield

Chemistry and Environmental Science Department
Ford Motor Company
P.O. Box 2053, mail drop 3083/SRL
Dearborn, MI 48121

Introduction

Commercial fuels are typically hydrocarbon mixtures that contain tens to hundreds of components [1]. The many chemical compounds found in gasoline fuels range from light ends, such as propane and butane, to heavy ends that boil at temperatures above 450 K. The wide range of compounds in fuel lead to it boiling and evaporating over a range of temperatures.

Vehicle performance depends in part on the fuel used. For example, the range of vaporization temperatures has been correlated with an empirical "drivability" parameter, which roughly describes how well a vehicle drives when using a particular fuel. It is thus desirable for engine and vehicle models to have clear mechanisms for incorporating differences among many different fuels. However, incorporating complete chemical detail into large-scale engine models becomes intractable for a fuel that contains hundreds of species. Fuels with only 5–10 components must be used instead.

Fuel volatility is typically measured using the ASTM D86 procedure [2]. In this test, 100 mL of fuel are heated. Fuel vapors are collected via a condenser, and enough heat is applied such that 4 mL of fuel condensate is collected each minute. The result of the measurement is data for the fuel vapor temperature as a function of the percent of fuel evaporated. The shape of the resulting plot—the so-called "D86 curve"—is a characteristic of any particular fuel. In practice, the composition of a commercial fuel varies to some extent from batch to batch, leading to slight changes in the D86 curve. In this sense, the D86 curve is not a true physical property; instead it is a mixture property tunable to meet prescribed specifications.

In previous work, we developed a computer model that predicts the D86 curve for a fuel, given the identity of each fuel component and its concentration [3]. In this work, we have used that model to develop model hydrocarbon mixtures whose compositions, vapor pressures, and distillation properties resemble those of two real fuels. These mixtures are both simple enough to use in analytical engine models and complicated enough to use in interpreting measurements of fuel volatility, fuel evaporation, and fuel permeation. Their research octane numbers also allow them to be used in an engine.

Modeling Approach

Two fuels were modeled in this study. Certification fuel (sometimes called indolene, a trademark of BP) is used in vehicle emissions certification tests, making this fuel important to include in engine models. The second fuel is an oxygenated fuel, included to illustrate the level of physicochemical nonideality that can arise.

The compounds to use in the model fuels were chosen using a variety of criteria. Beginning with a speciation of certification fuel, eight compounds were selected to span the range of boiling points found in the real fuel. Their molecular architecture (straight vs branched vs cyclic, alkane vs aromatic) and molecular weight were chosen to span the range found in a PIANO (paraffin, isoparaffin, aromatic, naphthenic, olefin) analysis of the same fuel. Ethanol was added to the component list for the oxygenated fuel.

The model requires several parameters for each component in the fuel, such as critical properties, solubility parameter, ideal gas heat capacity, and vapor pressure. We used correlations to estimate other required properties. Instrument-related model parameters were determined by matching the predicted D86 curve to experimental results for a 7-component synthetic fuel available at Ford. All the molecular and instrument parameters are described in detail in our previous work [3]. We modeled the fugacity of each component in each phase using either an ideal or nonideal approach. An ideal solution and vapor approach has the advantage that each component's volatility depends only on its concentration and pure-component properties; its volatility is independent of the identity and relative concentrations of all other compounds. Nonideal behavior was represented using vapor-phase fugacity coefficients, calculated via critical-property-based correlations [4], and liquid-phase activity coefficients, calculated using the group-contribution-based UNIFAC model [5,6]. The nonideal phase behavior approach is more realistic from a chemical viewpoint but leads to the volatility of each component being a function of temperature and of the concentration of all species in the same phase. For a fuel of known composition, predictions using a fully nonideal approach would be most likely to agree with experimental results.

Results and Discussion

The ultimate results from running our calculations are compositions of model fuels with volatilities representative of those of real fuel mixtures. These compositions depend on the fuel of interest, since different fuels have different volatilities, and on whether an ideal or nonideal approach is used for the phase equilibrium. Table 1 contains recommended compositions for use in ideal solution-based models. Each model fuel is made up of 7 or 8 compounds. These compositions, as shown in the figures below, are predicted to vaporize within an ideal model in very similar ways to how real fuel vaporizes in a real experiment. However, if the volatility of a mixture with a listed fuel composition was measured in a lab, the measured D86 curve is not expected to agree with the experimental D86 curve for the corresponding fuel. This disagreement would occur because no mixture of fuel components would behave exactly like an ideal solution in equilibrium with an ideal gas mixture.

Table 1. Amounts of Each Component in Model Fuels for Use in Ideal Liquid and Vapor Models.

Fuel	nC_4	iC_5	EtOH	nC_6	iC_8	nC_8	tol[a]	124-TMB[b]	nC_{13}
Certification	4	16		2.5	32		25.5	18	2
Oxygenated	6	34	5	10		11	20	12	2

Compound descriptions: (a) toluene, (b) 1,2,4-trimethylbenzene

Table 2 contains model fuel compositions recommended for use in nonideal solution models or in experimental applications in which a simplified fuel of fewer than 10 compounds is required. We expect that the fuel volatility of these mixtures, if mixed in the lab and measured experimentally, would show reasonably good agreement with the experimental D86 curve for their corresponding fuels. The predicted D86 curves are in excellent agreement with the experimental curves for the corresponding fuels, as shown below.

The experimental D86 curve and predictions from the ideal and nonideal models for certification fuel are shown in Figure 1. Experimental results are indicated by squares and circles. Throughout the measurement, the vaporization temperature increases with respect to the volume fraction distilled. Below 40 volume % distilled, there is slight disagreement of order 6°C between the two data sets. At 80 vol%, the vapor temperature begins to increase at a faster rate relative to the vaporization, causing a kink in the D86 curve. Our model predictions, calculated using a nonideal or ideal model, are shown by the dashed and solid lines, respectively. At low

vol%, the model results pass between the two data sets. At higher vol%, they are in good agreement with both sets and follow the kink at 80 vol%. The model fuel compositions from both approaches are close to one another, indicating near-ideal behavior.

Lines with filled points indicate mass fractions for model fuel components remaining in the liquid phase, using the nonideal model. These compositions provide an estimate of the composition that remains after partial evaporation (useful from the perspective of fuel handling). At low to moderate vol% distilled, the concentrations of n-butane, isopentane, and n-hexane decrease. Their disappearance is followed by increases and then decreases in isooctane, toluene, and 1,2,4-trimethylbenzene concentrations. The peaks indicate that isooctane, for example, is a larger fraction of the continuously decreasing amount of liquid in the flask. The kink in the D86 curve is predicted to occur when the toluene concentration approaches zero. In this model fuel, the kink occurs because there is a 60°C difference in boiling point between toluene and 1,2,4-trimethylbenzene. For real certification fuel, this suggests that few compounds are present with boiling temperatures between 111 and 170°C.

Table 2. Amounts of Each Component in Model Fuels for Use in Nonideal Liquid and Vapor Models or in Experiments Using Fuel Mixtures that Mimic Real Fuels.

Fuel	nC_4	iC_5	EtOH	C_6	iC_8	nC_8	Tol	124-TMB	nC_{13}
Certifi-cation	5	13		3[a]	31		27	19	2
Oxygen-ated	5.25	23.75	13	10[b]		10	24	12	2

a) n-hexane, b) cyclohexane

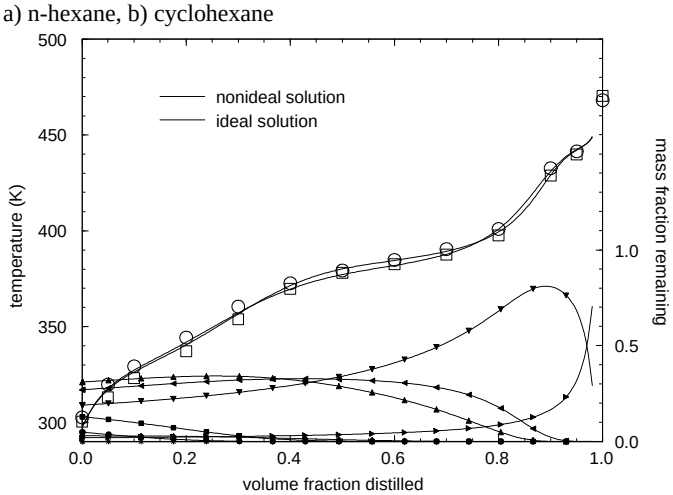

Figure 1. Distillation curve for real certification fuel and predictions using the D86 fuel distillation model. Model fuel compositions are based on ideal (straight line) and nonideal (dashed line) phase behavior. Dashed lines below the D86 data indicate the mass fractions of nC_4 (circles), iC_5 (squares), nC_6 (diamonds), iC_8 (up triangles), toluene (left triangles), 124-trimethylbenzene (down triangles), and nC_{13} (right triangles) in the undistilled fuel.

Figure 2 indicates the corresponding results for the oxygenated fuel. We find qualitatively similar results for this fuel. Here the kink (at 60 vol%) is due to the disappearance of ethanol, which is very nonideal (activity coefficient near 4). The nonideal solution model can capture this kink well. Our ideal solution model is tuned to follow the approximate curvature, but it deviates from the real fuel in two ways. First, no kink is present, because the fuel compounds are too close to one another in boiling point. Second, the required concentrations are significantly different from those in the real fuel. This is especially seen for ethanol: only 5% is optimal for the ideal model, compared to 13% in the nonideal model (and in the real fuel).

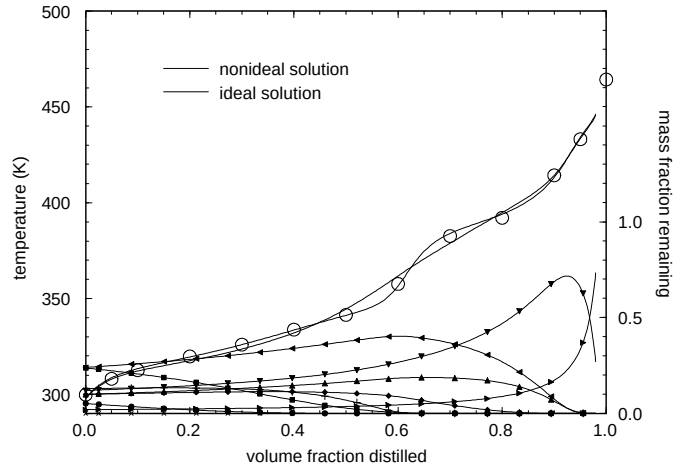

Figure 2. Distillation curve for oxygenated fuel and predictions using the D86 fuel distillation model. Model fuel compositions are based on ideal and nonideal phase behavior. Dashed lines below the D86 data indicate the mass fractions. Labels are the same as in Figure 1, with ethanol indicated by a plus (+).

The compounds used in this work do not represent the full spectrum of compounds found in a real fuel. For some compounds (typically n-butane and isopentane), the concentration in a model fuel is near the amount found in real fuel. This is because there are few compounds of comparable size and boiling point. For other compounds (isooctane, 1,2,4-trimethylbenzene, decane, tridecane), there is a significantly larger mass fraction in the model fuel than in a real fuel. This is because a single compound in the model fuel vaporizes in place of several compounds with similar structures and boiling points. For example, isooctane (2,2,4-trimethylpentane) represents other trimethylpentanes, assorted dimethylhexanes, and methylheptanes. It also represents compounds of similar molecular weight, such as dimethylpentanes and trimethylhexanes.

Conclusions

A macroscopic model of the D86 fuel distillation process can be used to create model fuels that display volatilities that equal those of real fuels used in vehicle testing and operation. Using less than 10 components in the mixture, it is possible to reproduce the entire distillation curve. Results are presented here for two fuels: a certification fuel and an oxygenated fuel. For the certification fuel, similar model fuel compositions result from using nonideal or ideal thermodynamics. For the oxygenated fuel, these approaches lead to qualitatively different fuel compositions and distillation curves. The resulting compositions can be used in engine models or in studies of fuel volatility, evaporation, or permeation.

Acknowledgement. We thank George Lavoie, Eric Curtis, Pete Misangyi, and Mira Burbaroska of Ford Motor Company for assistance with the properties of the real fuels.

References

(1) Owen, K.; Coley, T. *Automotive Fuels Handbook*; Society of Automotive Engineers: Warrendale, PA, 1990.
(2) *Standard Test Method for Distillation of Petroleum Products*, American Society for Testing and Materials: Philadelphia, *5.01*, 237–242.
(3) Greenfield, M.L.; Lavoie, G. A.; Smith, C. S.; Curtis, E. W. *SAE paper* **1998**, *982724*, 1–15.
(4) Smith, J. M.; Van Ness, H. C. *Introduction to Chemical Engineering Thermodynamics, 4th edition*, McGraw-Hill: New York, 1987.
(5) Prausnitz, J. M.; Lichtenthaler, R.; Azevedo, E. G. *Molecular Thermodynamics of Fluid-Phase Equilibria*, Prentice-Hall: Englewood Cliffs, NJ, 1986.
(6) Fredenslund, A; Jones, R. L., Prausnitz, J. M. *AIChE J.* **1975**, *21*, 1086.

A NOVEL APPROACH TO MOLECULAR MODELING OF TRANSPORT THROUGH INORGANIC NANOPOROUS MEMBRANES

M. A. Snyder[1], D. G. Vlachos[1], M. A. Katsoulakis[2]*

[1]Department of Chemical Engineering and Center for Catalytic Science and Technology (CCST), University of Delaware, Newark, DE 19716-3110

[2]Department of Mathematics and Statistics, University of Massachusetts, Amherst, MA 01003

Introduction

Numerous growth and permeation studies of nanoporous films have led to their attractiveness for application in separating gas mixtures with permselectivities approaching unprecedented subnanometer molecular resolution. The understanding and ability required for predicting macroscopic transport characteristics for diffusion of interacting molecular species through the complex lattices of these nanoporous inorganic membranes is key to the ultimate development of both traditional applications of this technology such as integrated reaction and separations devices, and more novel ones, such as substrates for growth of nanowires and chemical sensors.

Molecular simulations, specifically molecular dynamics and Monte Carlo algorithms, have emerged in the past few decades as preeminent computational tools for science and engineering research. Despite their widespread use and unprecedented insights into microscopic dynamics, such molecular simulations are computationally limited to short length and time scales, while inorganic membranes, such as zeolite films, invoke much larger scales (e.g., [1]) by way of macroscopic heterogeneities and imposed gradients.

On the opposite end of the modeling spectrum, continuum, Maxwell-Stefan models have been proposed in attempts to describe experimentally observed diffusion behavior. While these models have proven beneficial in fitting single and multi-component diffusion data, their phenomenological derivation does not capture the underlying microscopic diffusion dynamics and restricts their applicability to unrealistically simple diffusion lattices. Consequently, their accuracy as *a priori* predictive models is severely limited.

A major obstacle in addressing this multiscale modeling challenge is the lack of a rigorous mathematical and computational framework directly linking atomistic simulations and scales to complex mesoscopic and macroscopic phenomena dictated by microscopic intermolecular forces and material microstructure. A new mathematical framework has been introduced and validated through comparison with gradient Monte Carlo simulations, for modeling diffusion of interacting species in nanoporous materials over large length scales while retaining molecular scale information typically captured only by molecular simulations [2, 3].

Physical System and Microscopic Dynamics

Nanoporous membrane systems under imposed macroscopic gradients in concentration are the focus of this modeling work. In particular diffusion through inorganic membranes such as MFI and Faujasite zeolites is modeled. The mesoscopic framework is derived for systems characterized by intermolecular interactions between the adsorbed molecules (guests) and adsorbent (host) as well as between adsorbates (guest-guest interactions). Such diffusion systems are characterized by activation energies of duffusion that exceed the thermal energy of the system. As a result, diffusing molecules spend a significant amount of time at binding sites along the length of the pore, resulting in an activated hopping, or configurational diffusion mechanism. Fickian constitutive relations are rendered inadequate in this diffusion regime, the modeling of which is complicated by macroscopic gradients and material heterogeneities. An Arrhenius formalism is applied in this work to describe the microscopic diffusion dynamics of these systems. Such a mechanism[4] is characterized by an activation energy for diffusion depending only upon the energy of the departing site.

Validation of Mesoscopic Framework

Features of the mesoscopic framework. This new mathematical framework proposed to link microsopic properties to macroscopic diffusion phenomena, entails the use of newly developed mesoscopic equations derived rigorously from underlying master equations by coarse-graining statistical mechanics techniques in the case that diffusion occurs by a hopping mechanism. As a result of its fundamental derivation, the framework preserves microscopic dynamics. It has been shown mathematically that these equations are exact in the limit of long-range intermolecular interactions[2]. Furthermore, the coarse-grained continuum form of this framework results in the ultimate computational tractability for systems of realistic length and time scales through application of continuum numerical solution methods.

Steady state comparison to G-CTMC solutions. The validity of the mesoscopic model was first assessed in the microscopic limit for steady state behavior by comparing its solution to the corresponding solution obtained from Gradient-Continuous Time Monte Carlo (G-CTMC) simulations. Excellent agreement between the mesoscopic and MC steady state concentration profiles is depicted in **Figure1(a)** for longer-range potentials.

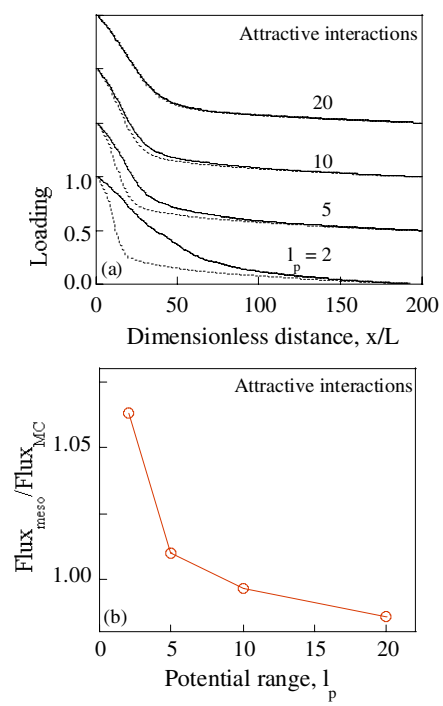

Figure 1. (a) Concentration profiles for Arrhenius dynamics obtained in 1D from MC (solid lines) and mesoscopic framework (dotted lines) using a piecewise constant interaction potential, with $\beta w = 4$ (attractive interaction strength) and different values of the interaction range, l_p. Note that the profiles have been shifted upward on the loading axis for the purpose of clarity. (b) Ratio of fluxes versus the potential range l_p.

Interestingly, the deviations seen in the predicted concentration profiles in **Figure 1(a)** for short-range potentials are not reflected in the predicted flux, **Figure 1(b)**. Similar validation of the mesoscopic solution was observed for systems with repulsive interactions, where the agreement between the G-CTMC and mesoscopic solutions is closer than the attractive case even for short potential lengths. It is important to note that all deviations between the mesoscopic and G-CTMC fluxes are smaller than those reported from one membrane to another in experiments, consequently suggesting the capability of mesoscopic models to accurately predict macroscopic permeation properties such as fluxes.

As seen in **Figure 1**, the concentration profiles for these systems, characterized by intermolecular interactions, are highly non-Fickian. That is, the profiles are highly non-linear. More dramatically, however, is the strong influence that interactions have upon the flux as depicted in **Figure 2**.

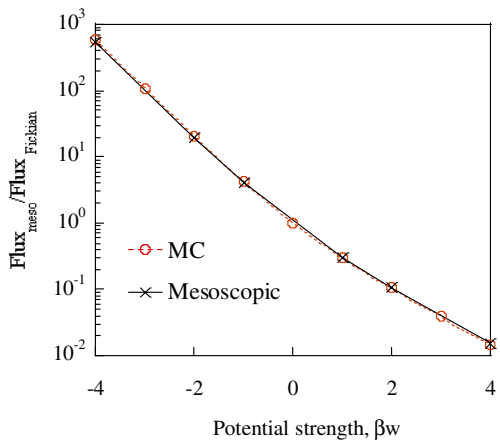

Figure 2. Steady-state fluxes versus potential strength in 1D for a piecewise constant potential with an interaction length of l_p=20.

As expected, repulsive interactions (negative *w*) greatly enhance the flux due to a reduction in activation energy of hopping, and attractive interactions (positive *w*) significantly inhibit diffusion due to an increase in the hopping activation energy caused by adsorbate-adsorbate interactions.

This drastic influence of intermolecular interactions upon the steady state flux further motivates development of the *fundamentally* derived mesoscopic framework to preserve the underlying microscopics while providing insight into macroscopic permeation properties at realistic length and time scales.

Extension of the Mesoscopic Framework

Multi-component diffusion. The extension of this mesoscopic framework to account for multi-component diffusion is shown in this work, focusing on mixtures of cyclohexane and benzene in faujasite through comparison to recently published multicomponent data[1]. Validation of the binary mesoscopic framework will be shown on the microscopic scale through comparison with multi-component G-CTMC simulation results.

Complex zeolite lattices. This rigorously derived mesoscopic framework allows for further extension of the mesoscopic models to account for complex zeolite lattice structures (e.g., MFI, Faujasite) defined by a variety of active sites available for diffusion, each uniquely contributing to the system energetics. We show here that the geometry and orientation of the pores of these three-dimensional materials strongly influence the ultimate membrane permeation characteristics and, consequently, begin to develop critical relations between microscopic properties and macroscopic diffusion phenomena within nanoporous membranes.

Acknowledgements

The work presented here has partially been supported by the National Science Foundation Career Award.

References

(1) Nikolakis, V.; Xomeritakis, G.; Abibi, A.; Dickson, M.; Tsapatsis, M.; Vlachos, D.G. *J. Membrane Sci.* **2000**, *84*, 209.

(2) Vlachos, D. G.; Katsoulakis, M. A. *Phys. Rev. Letters* **2001**, 85(18), 3898.

(3) Lam, R.; Basak, T.; Vlachos, D. G.; Katsoulakis, M. A. *J. Chem. Phys.* **2001**, 115(21), (*in press*).

(4) Metropolis, N.; Rosenbluth, A. W.; Rosenbluth, M. N.; Teller, A. H.; Teller, E.; *J. Chem. Phys.* **1953**, *21*, 1087.

CHARACTERIZING THE HIGH PRESSURE BEHAVIOUR OF LUBRICANT BASESTOCKS

Clare McCabe[1], Peter T. Cummings[2,3], Scott Bair[4], Charles W. Manke[5]

[1]Department of Chemical Engineering, Colorado School of Mines, Golden CO 80401
[2]Departments of Chemical Engineering, Chemistry and Computer Science, University of Tennessee, Knoxville TN 37996
[3]Chemical Sciences Division, Oak Ridge National Laboratory, Oak Ridge TN
[4]George W. Woodruff School of Mechanical Engineering, Georgia Institute of Technology, Atlanta GA 30332
[5]Department of Chemical Engineering and Materials Science, Wayne State University, Detroit MI 48202

Introduction

Given the range of operating conditions lubricants are subjected to in practical applications (for example, in an automobile engine) a lubricant is often required to be effective over a wide range of temperature, speeds, and loads. Hence, a consideration of not only the viscosity, but also the viscosity-temperature and viscosity-pressure behaviour is needed to determine if a fluid would make a good lubricant component for a particular application. For example, it is essential that a lubricant retain a sufficiently high viscosity at normal operating temperatures (e.g., temperatures up to 100°C in the case of an automobile engine), whilst not being excessively high at the lowest temperatures (e.g., a cold start). The ideal lubricant would be one whose viscosity was minimally affected by the range of operating temperatures and pressures encountered. In reality, viscosity changes substantially with both temperature and pressure, though the extent of change depends on the chemistry and architecture of the lubricant molecules. Certain general trends in the structure–property relationships of hydrocarbon molecules are well known, for example while linear alkanes have very favourable viscosity-temperature behaviour they are solids at room temperature and so usually removed from the basestock during refining to improve the low temperature performance. By contrast, branched alkanes have a lower melting point, making them more suitable as lubricants, but have poorer viscosity-temperature behaviour. Hence obtaining the right balance is an important consideration.

Much of what is known about the physical properties of hydrocarbons is based on API Research Project 42 [1], a database of physical properties for pure hydrocarbons. Although API 42 contains some 273 entries, less than a quarter are in the C_{20}–C_{40} mass range, representing a minuscule fraction of the total number of possible structural isomers. Furthermore, very little experimental data is available in the literature on the high-pressure rheological properties of hydrocarbons, especially in the mass range of interest. The most comprehensive experimental study of the viscosity of lubricants to high pressures was undertaken at Harvard University [2] in the late 1940s, though more recently Bair and co-workers have measured the pressure-viscosity behaviour of liquid lubricants to pressures in the GPa range [3-4]. Hence, in order to provide a more complete datebase and obtain a clearer understanding of the influence of molecular architecture on viscous behaviour further experimentation is needed, though it is both costly and time consuming, especially at the severe conditions commonly found in engines and other machinery (e.g. film thickness < 1 micrometer, shear rates > 10^7 s^{-1}, pressure approximately = 10^9 Pa) which are extremely difficult to study experimentally.

Method

Over the last decade, with the exponential increase in computing power simulation techniques are proving to be an attractive and valuable means with which to "fill in the gaps" in the experimental data and obtain important structure-property information for lubricant basestocks. Using the non-equilibrium molecular dynamics (NEMD) technique, which is particularly suited to studying dynamic behaviour, there have been a number of simulation studies reported in the literature on the rheological properties of industrially important molecules [5]. For hydrocarbons, early work was limited to short, mainly linear molecules. However, with the recent advances in algorithms and the development of more realistic models it is now possible to perform simulations of more complex systems and more recently longer chains and branched molecules have been examined.

Results and Discussion

We present the results of non-equilibrium molecular dynamics simulations of alkanes in the C_{20}-C_{40} mass range, as this mass range form main constituents of lubricant basestocks, and hence their rheological properties are of great concern in industrial lubricant applications. The united atom model of Siepmann et al. [6] and Mondello and Grest [7], which has been shown to be successful in similar work, is used to describe the alkane molecules. From NEMD simulations at giga-pascal pressures and over a range of state conditions for each molecule studied we determine the strain rate dependant viscosity and the pressure-viscosity coefficient [8]. We show that the simulation results obey corresponding states behavior as seen in the rheology of polymer melts [9].

State Point	Temperature/K	Pressure/ GPa	Density/ gcm^{-3}
A	310.93	1.01E-04	0.791
B	372.04	1.01E-04	0.751
C	372.04	0.682	0.943
D	372.04	0.829	0.964
E	372.04	0.958	0.980

Table 1. State points studied for 9-octylheptadecane.

Through the generation of a "*master curve*", as illustrated in Figure 1 for 9-octylheptadecane at the state conditions given in Table 1, this

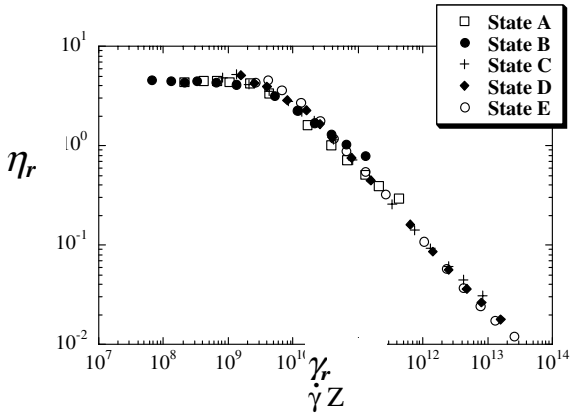

Figure 1. Reduced strain rate dependent viscosity for 9-octylheptadecane at state points given in Table 1. Taken from Reference 10.

yields the capability of quickly and efficiently predicting the Newtonian viscosity of lubricant components. Additionally, using low temperature shear-thinning viscosity measurements at GPa pressures, for the first time we demonstrate consistency between simulation and experiment in the Newtonian and non- Newtonian regimes [10].

Acknowledgement. This work was supported in part by the Division of Materials Sciences of the U. S. Department of Energy. The Oak Ridge National Laboratory is managed by UT-Battelle, LLC, for the Department of Energy under contract number DE-AC05-00OR22725. Additional funding was provided by Mobil Technology Company.

References

(1) *API 42: Properties of Hydrocarbons of High Molecular Weight*. American Petroleum Institute, New York, 1966.
(2) *ASME Research Committee on Lubrication, Pressure Viscosity Report*. Harvard University, New York, 1953.
(3) Bair, S. and Winer, W. O. (1992), 'The High Pressure High Shear Stress Rheology of Liquid Lubricants,' *Journal of Tribology*, **114**, 1-13.
(4) Bair, S. (2000), 'Pressure-Viscosity Behaviour of Lubricants to 1.4GPa and its Relation to EHD Traction,' *Tribology Transactions*, **43**, 91-99.
(5) Cummings, P. T. and Evans, D. J. (1992), 'Nonequilibrium Molecular Dynamics Approaches to Transport Properties and Non-Newtonian Fluid Rheology,' *I&EC Research*, **31**, 1237-1252.
(6) Smit, B., Karaborni, S. and I., S. J. (1995), 'Computer Simulations of the Vapor-Liquid Phase Equilibria of N-Alkanes,' *J. Chem. Phys.,* **102**, 2126.
(7) Mondello, M. and Grest, G. S. (1995), 'Molecular Dynamics of Linear and Branched Alkanes,' *J. Chem. Phys.*, **103**, 7156.
(8) McCabe, C., Cui, S. T., Cummings, P. T., Gordon, P. A. and Saeger, R. B. (2001), 'Examining the Rheology of 9-Octylheptadecane to Giga-Pascal Pressures,' *J. Chem. Phys.*, **114**, 1887-1891.
(9) S. Bair, C. McCabe, and P. T. Cummings, "Comparison of Non-Equilibrium Molecular Dynamics with Experimental Measurements in the Nonlinear Shear-Thinning Regime", *Physical Review Letters,* submitted for publication (2001).
(10) C. McCabe, C. W. Manke and P. T. Cummings, "Predicting the Newtonian Viscosity of Complex Fluids from High Strain Rate Molecular Simulations", *Journal of Chemical Physics,* accepted for publication.

Physical properties of supported and unsupported transition metal nanoclusters

Shi-Ping Wang, Daniela S. Mainardi, and Perla B. Balbuena

Department of Chemical Engineering, University of South Carolina, Columbia, SC 29208

Introduction

Supported nanoclusters play a major role in many physical and chemical processes, such as those in heterogeneous catalysis and in the fabrication of nanostructured materials tailored to specific technological applications, e.g., micro and nanoelectronics, optoelectronics, and magnetic devices. Physical and electronic properties of metal nanoclusters deposited on various substrates have recently received a great deal of attention. [1] In particular, carbon-supported platinum particles are commonly used as catalytic materials in gas and liquid reactions. [2-4] Due to the high cost of platinum, many efforts are directed to optimizing its catalytic performance, which in turn requires a substantial understanding of the catalyst/substrate interactions,[5] and of the relationships between size, shape, and activity of the nanocatalysts [6,7] To minimize costs, alternative bi- and tri-metallic catalysts are proposed for several catalytic processes. In these cases, the mixing of the different elements on the surface of the nanoparticle gives rise to unexpected electronic and physical effects.

Computational methods

We use molecular dynamics (MD) simulations to compute the time evolution of a system consisting of a metal cluster of nanodimensions either in vacuum or deposited on a graphite substrate. The metal-metal interactions are treated within the Sutton-Chen potential model,[8] whereas the metal-graphite interactions are described by a Lennard-Jones potential. Details of the computational methods are given in a previous study. [9]

Heating and cooling curves are determined for each nanocluster and the melting temperature is obtained by the transition observed in the potential energy curve versus temperature. The melting/freezing characteristics are obtained for different cluster sizes and shapes.

Bimetallic systems are studied using a combination of Monte Carlo (MC) and MD methods. The MC technique is used to obtain the equilibrium atomic distribution on a bimetallic cluster of a given shape and size.[10,11] This equilibrium distribution is used as input to MD simulations where the dynamics of the system is investigated.

Results and Discussion

Figure 1 shows the variation of the potential energy for the 256-atom cube-shaped Pt cluster. In the heating process (squares), there is a clear energy jump in the temperature range from 1000 to 1100 K, this is due to the melting transition, note that the cluster melting temperature is much lower than that of bulk Pt metal (2041.15 K as determined experimentally). [12] The second set of data in Figure 1a corresponds to the cooling curve (circles), where the temperature is lowered starting from 1800 K down to 300 K. The system also shows a sharp liquid-solid transition, the freezing temperature, at T between 1000 and 900 K. The same time step was used for heating and cooling processes. Note that the portion of the curves corresponding to T > 1000 K are coincident for the cooling and heating processes, whereas for the portion below the melting temperature the potential energy is higher for the heating than for the cooling process. This indicates that the annealing process can easily find the lowest energy state for a given temperature, whereas during the heating process the system gets trapped in metastable states. Eventually, for simulation times sufficiently long, both curves should also agree at $T < T_{melting}$. Similar phenomena have been observed in simulations of unsupported gold nanoclusters.[13] Another interesting behavior is observed also in the heating curve (Figure 2a), where the potential energy decreases from its value at 600 K to a lower value at 700 K and then increases again when T reaches 800 K. At 600 K, the cluster changes shape due to surface melting and surface atomic diffusion, adopting a semi-spherical shape. This change has also been observed in the experiment using high-resolution transmission electron microscopy, [14] and it is attributed to a structural solid-solid transition.

The melting behavior depends on the shape and size of the cluster. A spherical cluster constructed by carving the surface of a fcc cluster and deposited on the static surface of graphite is also studied. The potential energy for the 260-atom ball-shaped cluster is displayed in Figure 1b for the heating and cooling processes. Upon heating, the ball cluster also undergoes a solid-liquid jump in the temperature range from 1000 to 1100 K (squares), although the slope of the heating curve changes again at 1200 K. Practically no hysteresis is found between the heating and cooling curves at the liquid-solid transition for the ball-shaped cluster, as opposed to the case of the cubic cluster. This suggests that hysteresis loops may be more likely to be found in local minimum structures. The ball-shaped cluster also exhibits a behavior similar as that calculated for the cubic cluster at a temperature right below the melting transition, at T between 800 and 900 K, where the potential energy changes to a lower energy state presumably due to a solid-solid transition. [13] We suggest that the clusters undergo surface melting and surface atomic diffusion to form a lower energy structure before melting, as discussed in more detail below. Upon cooling, as in the case of the cubic cluster, the potential energy (circles) in the liquid range approaches values close to those of the heating process, whereas it reaches lower values in the solid region.

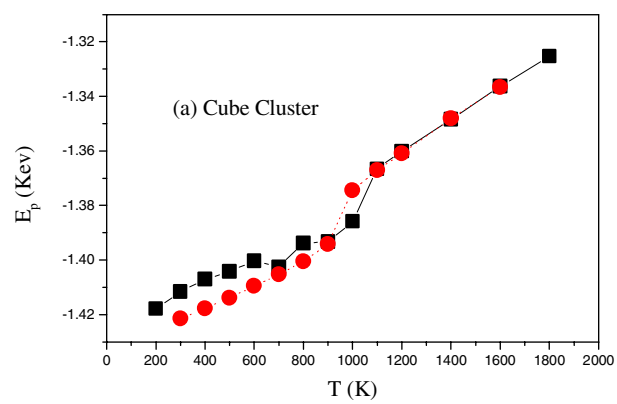

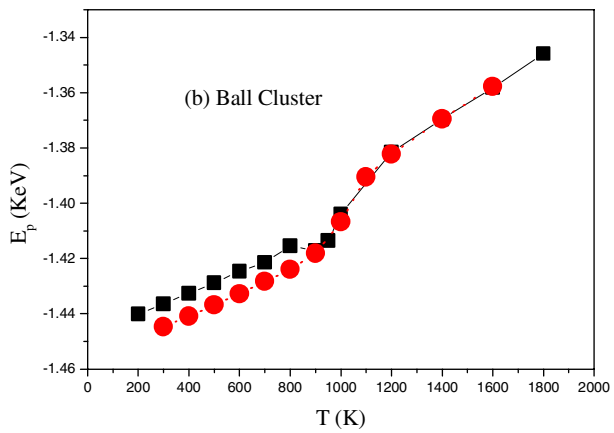

Figure 1. Calculated potential energy (E_p) variation, in KeV, for the heating (squares) and cooling (circles) curves. (a) Cube-shaped cluster. (b) Ball-shaped cluster.

Conclusions

The melting transition for a 256-atom Pt cluster of cubic shape deposited on a static graphite substrate is found in the range between 1000 and 1100 K, and the freezing temperature between 900 and 1000 K. At 600 K the cubic cluster starts experiencing a structural transformation, which is evidenced at 700 K by an increase in the interlayer separations from 1.83 to 2.13 Å, the outermost surface layers melt, and their atoms migrate to the layers closer to the substrate, a temperature-induced wetting phenomenon. At temperatures higher than 1000 K, melting takes place.

Results on bimetallic systems will be presented at the meeting.

Acknowledgement. This work is supported by the National Science Foundation (CTS-9876065), the Army Research Office (DAAD-19-00-1-0087), and the Department of Energy (DE-FG02-1ER15249)

References

(1) Jensen, P. *Rev. Mod. Phys.* **1999**, 1695-1735.
(2) Adzic, R. In *Electrocatalysis*; Lipkowski, J., Ross, P. N., Eds.; Wiley-VCH: New York, 1998, pp 197-242.
(3) Gunter, P. L.; Niemantsverdriet, J. W.; Ribiero, F. H.; Somorjai, G. A. *Catal. Rev. Sci. Eng.* **1997**, *39*, 77.
(4) Lambert, R. M.; Pacchioni, G., Eds. *Chemisorption and Reactivity on Supported Clusters and Thin Films: Towards an Understanding of Microscopic Processes in Catalysis*; Kluwer Academic Publishers: Dordrecht, 1997; Vol. 331.
(5) Zhu, J.; Somorjai, G. A. *Nano Letters* **2001**, *1*, 8-13.
(6) Joo, S. H.; Choi, S. J.; Oh, I.; Kwak, J.; Liu, Z.; Terasaki, O.; Ryoo, R. *Nature* **2001**, *412*, 169-172.
(7) Combe, N.; Jensen, P.; Pimpinelli, A. *Phys. Rev. Lett.* **2000**, *85*, 110-113.
(8) Sutton, A. P.; Chen, J. *Phil. Mag. Lett.* **1990**, *61*, 139-146.
(9) Huang, S.-P.; Balbuena, P. B. *Mol. Phys.* **2001**, in press.
(10) Mainardi, D. S.; Balbuena, P. B. *Langmuir* **2001**, *17*, 2047-2050.
(11) Mainardi, D. S.; Balbuena, P. B. *Int. J. Quant. Chem.* **2001**, in press.
(12) Benfield, R. E.; Filipponi, A.; Morgante, N.; Schmid, G. *J. of Organometallic Chemistry* **1999**, *573*, 299-304.
(13) Lewis, L. J.; Jensen, P.; Barrat, J. L. *Phys. Rev. B* **1997**, *56*, 2248-2257.
(14) Wang, Z. L.; Petroski, J. M.; Green, T. C.; El-Sayed, M. A. *J. Phys. Chem. B* **1998**, *102*, 6145-6150.

CO chemisorption on flat and stepped Ni surfaces: A density functional study

Vaishali Shah[*], *Tao Li*[*,#] *Hansong Cheng*[%], *Kenneth Baumert*[%], *and David S. Sholl*[*,#]

[*]Department of Chemical Engineering, Carnegie Mellon University, Pittsburgh, PA 15213
[#]U. S. Department of Energy, National Energy Technology Laboratory, P. O. Box 10940, Pittsburgh PA 15236
[%]Air Products and Chemicals Inc., Allentown, PA 18195

Introduction

The adsorption of CO molecules on transition metal surfaces is one of the most widely studied problems in surface chemistry. CO is an important industrial gas. For example, mixtures of CO and H_2 (syngas) are used as precursors to liquid fuels and also to hydrogen fuels. Adsorption and desorption of CO on metal surfaces can lead to a range of desirable and undesirable chemical reactions. For example, contact between CO and Ni can corrode the solid phase nickel with the formation of gaseous nickel carbonyl. In the same system, adsorbed CO can dissociate to form carbonaceous surface species. This latter reaction is a serious problem in reforming applications where Ni is used as a catalyst. Many experimental and some theoretical studies have been performed to characterize and understand the CO interaction on Ni surfaces.[1,2] Despite this effort, there are a number of open problems and controversial issues concerning not only the preferred adsorption site, the structure of the CO layer at low and high coverages but also the nature of CO bond on these surfaces.[3-5] There is consensus however regarding the fact that steps and other surface defects are considerably more reactive than atomically flat surfaces.

In the present work we have examined the adsorption of CO on Ni(110) and Ni(210) surfaces using first principles density functional theory. Ni(110) is the least coordinated atomically flat Miller index surface and Ni(210) is characterized by a series of atomically straight step edges with (100) and (110) coordinations on either side of the step edge. CO adsorption at three sites, top, bridge and hollow is investigated. The purpose of this work is to gain insight into the preferred adsorption site for CO that can be then used in understanding the surface reactions available to CO on Ni surfaces.

Computational Method

Our density functional theory calculations are performed using the VASP (Vienna Ab initio simulation package) code[6-8] which is based on the Kohn-Sham density functional theory (DFT) formulation.[9] The electron-ion interactions are described by ultra soft pseudopotentials and exchange correlation energies are calculated with the generalized gradient approximation (GGA) as parameterized by Perdew and Wang.[10] A spin polarized computational scheme is employed since Ni is ferromagnetic. The bulk lattice constant of Ni was calculated to be 3.53 Å, in good agreement with experimental data.[11] The bond length of a gaseous CO molecule was calculated to be 1.15 Å, agreeing well with the calculations of Norskov *et. al.* [12]

The calculated bulk lattice constant was used to define the Ni(110) and Ni(210) surfaces. A (1x1) surface unit cell was chosen to minimize the number of atoms in the calculations and the surfaces were modeled by a slab consisting of five layers. The bottom two layers of the slab were held fixed allowing the top three layers to relax. CO was adsorbed on the topmost surface layer. We also performed these calculations with slabs consisting of three layers to check the minimum number of layers required for accurate results. In the three layer calculations the bottom layer was held fixed and the top two layers were allowed to relax. In the fully optimized five layer and three layer calculations good agreement is seen in the general trends observed in the interlayer separations as well as the percentage of contraction observed in the topmost layer. In each case, CO coverages corresponding to 1 molecule per surface atom were examined. The vacuum between the slabs when adsorbates are included is greater than 11 Å, large enough to ensure no significant interaction between the slabs.

The Brillouin zone of the surface unit cells was sampled with 5x5x1 Monkhorst-Pack mesh. An energy cutoff of 396.0 eV was used for the bare Ni surface as well as CO adsorbates on Ni surfaces. Full geometry optimizations were performed with the symmetry constraint using the conjugate gradient minimization scheme for systems consisting of less than 20 atoms and the quasi-Newton minimization scheme for systems consisting of more than 20 atoms. These two minimization methods were used solely for reasons of numerical efficiency. Calculations without the symmetry constraint for the atop and bridge sites on Ni(110) yielded equivalent results. The adsorption energy in each case is calculated according to the following equation $E_{ads} = E_{CO} + E_{Ni\ slab} - E_{CO/Ni\ slab}$, where E_{CO} is the total energy of an isolated CO molecule, $E_{Ni\ slab}$ is the total energy of the bare Ni(110) or Ni(210) surface and $E_{CO/Ni\ slab}$ is the total energy of the adsorbate on slab system. A positive E_{ads} corresponds to a stable adsorbate/slab system. The same Brillouin-zone sampling and energy cutoff were used in calculating the energies of the bare slab and adsorbate on slab system.

Results and Discussion

We have performed geometry optimizations for CO adsorbed at top, bridge and hollow site for Ni(110) and Ni(210) surfaces. These calculations were performed with both five layer surfaces and three layer surfaces. During these calculations all the atoms are allowed to relax completely except for the atoms in the fixed layers. In all the cases CO bonds to the surfaces via the C atom.

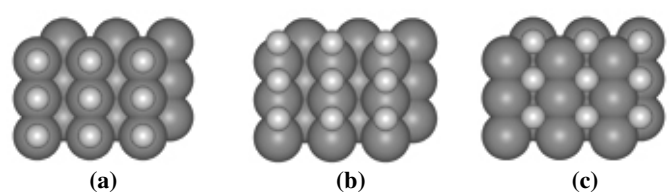

Figure 1. Adsorbate sites on Ni(110) surfaces. (a) top site, (b) bridge site and (c) hollow site.

The top view of the three adsorbate sites: top, short bridge (henceforth referred to as bridge) and four-fold hollow site for Ni(110) surface is shown in Figure 1. There is an additional adsorption site on Ni(110) surfaces, the long bridge site for which we have not reported any calculations in this work. The small light spheres correspond to the CO molecule and the large dark spheres correspond to the Ni(110) surface. Examining the energetics of the bare surface and the adsorbate on the Ni(110) surface, we observe that the net magnetic moment of the surface is slightly reduced in the presence of CO. The interlayer separations in the completely optimized five layer and three layer calculations agree with respect to the general trends observed as well as the percentage of contraction seen in the topmost layer.

Table 1 lists the adsorption energies at these three sites on Ni(110) and Ni(210) surfaces. The top site calculation was performed

with both five layer and three layer slabs. As can be seen, the agreement in the adsorption energy between these two calculations is very good. The distance between the Ni-C and C-O atoms also shows excellent agreement. Comparing the adsorption energies at the three sites, we observe that the bridge site is the most stable and the four-fold hollow site is the least stable. This trend in the adsorption energies and bond lengths of CO/Ni(110) is in agreement with that observed by Jenkins *et al*.[13] At the top and bridge site the C-O bond length is unchanged from its gas phase value but at the hollow site the C-O bond length has stretched by 1.8%. Our Ni-C and C-O bond lengths are again in good agreement with the spin polarized results of Jenkins *et al*.[13] Experimental investigation of CO adsorption on Ni(110) above atmospheric pressure[14] using x-ray diffraction measurements show that CO forms a (2x1) structure consisting of ordered zigzag arrangement of tilted molecules on short-bridge sites of the substrate with the Ni-C and C-O bond lengths to be 1.83 Å and 1.21 Å respectively. King *et. al.* have measured the calorimetric heat of adsorption of CO on single crystal Ni(110) surfaces at 0.12 monolayer (ML) to be 1.38 eV. [15]

Table 1. The adsorption energies, Ni-C and C-O bond lengths at the three sites for the 5 layer and 3 layer calculations on Ni(110) and Ni(210) surfaces.

	Site	# of layers	Eads (eV)	Ni-C Å	C-O Å
CO/Ni(110)	top	5	1.147	1.774	1.158
CO/Ni(110)	top	3	1.150	1.772	1.157
CO/Ni(110)	bridge	5	1.579	1.883	1.170
CO/Ni(110)	hollow	5	0.954	1.878	1.203
CO/Ni(210)	top	5	1.745	1.764	1.159
CO/Ni(210)	top	3	1.728	1.764	1.159
CO/Ni(210)	bridge	5	1.746	1.762	1.154
CO/Ni(210)	hollow	5	0.097	1.934	1.181

Our calculations on the Ni(210) surface with five layer and three layer slabs again agree with regard to the trends in the interlayer separations, the percentage contraction of the topmost layer, the adsorption energy and the distance between the Ni-C and C-O atoms, as seen from Table 1. As observed for CO/Ni(110), the presence of CO on Ni(210) slightly reduces the magnetic moment of the surface. The adsorption energies on the top and the bridge site are almost identical on Ni(210). The C-O bond length is once again unchanged from the gas phase value. The calculated adsorption energies show that the four fold hollow site is the least stable as also seen in the case of Ni(110) with the C-O bond length elongated by 3.4%.

Unlike Ni(110) there are no experimental or theoretical calculations performed to our knowledge on Ni(210) surfaces to compare our results with. There are however a wide variety of experiments performed on Ni(111) and Ni(100) surfaces. On Ni(100) experimental results show that CO is found in either the top or bridge site[4,16] for coverages < 0.5 ML LEED pattern studies and Extended Hückel Molecular Orbital calculations of CO at two fold and three-fold sites on Ni(111) surfaces[3] indicate that the three fold site is preferred at low coverages and as coverages increase the two-fold site and for higher coverages the top site is preferred for adsorption. On stepped Ni surfaces,[17,18] at low coverages CO is adsorbed in the step region and at increased coverages CO starts to adsorb on the terraces. CO adsorption on Pd(111) follows the same trend observed in Ni(111), however in Pt(111) at low coverages CO adsorbs at the top site and two fold bridge site and at high coverages CO is adsorbed exclusively at the top site similar to that seen in Ni(111) and Pd(111) surfaces.[3]

Conclusions and Ongoing Work

We have used DFT to study the adsorption of CO on flat Ni(110) and stepped Ni(210) surfaces. The adsorption energies are calculated from spin polarized plane wave calculations. Three adsorption sites were examined, namely the top, bridge and hollow sites. On both surfaces, the hollow site is found to be the least stable and the bridge site is found to be the most stable. The C-O and Ni-C bonds are elongated at the hollow site in comparison with the top site. Our calculations on five layer and three layer surfaces show good agreement in adsorption energies and bond lengths for both flat and stepped surfaces. Thus these surfaces can be successfully modeled using only three layers in the slabs.

We are currently extending these preliminary studies to look at several issues relevant to the chemical reactions available to CO on Ni surfaces. Specifically, we are examining the thermochemistry of Ni-carbonyl formation on atomically flat and stepped Ni surfaces. We are also applying DFT with the aim of quantitatively understanding the experimental observation that CO dissociates much more readily at surface steps and defects than on atomically flat planes.[19]

Acknowledgement. We gratefully acknowledge financial support from the Pennsylvania Infrastructure Technology Alliance and the National Energy Technology Laboratory and computing resources at the Pittsburgh Supercomputer Center.

References

(1) Dorsey, H. E.; Reutt-Robey, J. E. *Surf. Sci.,* **1997**, 380, 165.
(2) Brown, Robinson A.; Sinniah, K.; Reutt-Robey, J. E.; Doren, D. J.,*J. Chem. Phys*., **1994**, 101, 764.
(3) Wong, Y-T.; Hoffmann., R. *J. Phys. Chem*., **1991**, 95, 859.
(4) Föhlish, A.; Nyberg, M.; Bennich, P.; Triguero, L.; Hasselström, J.; Karis, O.; Petterson L. G. M.; Nilsson., A. *J. Chem. Phys*., **2000** 112, 1946.
(5) Hasselström, J.; Karis, O.; Petterson, L. G. M.; Föhlish, A.; Nyberg M.; Nilsson, A. *Phys. Rev. Lett*., **2000**, 85, 3309.
(6) Kresse, G.; Hafner, J. *Phys. Rev.*, **1993**, B 48, 13115.
(7) Kresse, G.; Furthmüller, J. *Comput. Mat. Sci*. **1996**, 6, 15.
(8) Kresse, G.; Furthmüller, *Phys. Rev*.. **1996**, B 54, 11169.
(9) Kohn, W.; Sham, L. J. *Phys. Rev*., **1965**, 140, A1133.
(10) Perdew, J. P.; Wang, Y. *Phys. Rev.*, **1992**, B 45, 13244.
(11) Kittel, C. *Introduction to Solid State Physic*s, John Wiley & Sons, 1976.
(12) Hammer, B.; Morikawa, Y.; Mortensen, J. J; Norskov, J. K. *Surf. Sci*., **1997**, 386, 66.
(13) Jenkins, S. J.; Ge, Q.; King, D. A. *Chem. Phys. Lett*., **2000**, 327, 125.
(14) Peters, K. F.; Walker, C. J.; Steadman, P.; Robach, O.; Isern, H.; Ferrer, S. *Phys. Rev. Lett*., **2001**, 86, 5325.
(15) Stuckless, J. T.; Al-Sararaf, N.; Wartnaby, C.; King, D. A. *J. Chem. Phys*., **1993**, 99, 2202.
(16) Pacchioni, G.; Chung, S-C.; Krüger, S.; Rösch, N. *Surf. Sci*., **1997**, 392, 173
(17) Sinniah, K.; Dorsett, H. E.; Reutt-Robey, J. E. *J. Chem. Phys*., **2000**, 112, 1958.
(18) Svensson, K.; Rickardsson, I.; Nyberg, C.; Andersoon, S. *Surf. Sci*., **1996**, 366, 140.
(19) Nakano, H.; Nakamura, J., *Surf. Sci*. **2001**, 482, 341.

Thermochemistry and Kinetics for Alkyl + O2 Reactions in Hydrocarbon Oxidation.

Joseph W. Bozzelli, Chiung-Ju Chen, Chad Sheng
Dept of Chem Engrg, Chem and Envir. Sci.
New Jersey Institute of Technology, Newark, NJ 07102

Anthony M. Dean
Chemical Engineering Dept.,
Colorado School of Mines, Golden, CO 80401

ABSTRACT

Hydrocarbon radical reactions with oxygen are important in ignition and low temperature oxidation. Thermodynamic properties of reactants, products and transition states are determined by *ab initio* methods at the CBS-Q and G2 levels of theory based on the optimized geometry using B3LYP/6-31G(d,p) DFT and isodesmic reaction analysis. Rate coefficients for reactions of the energized adducts are obtained from canonical transition state theory. The reaction of an alkyl radical with O_2 typically forms an energized peroxy adduct with a calculated well depth of about 35 kcal/mole. This energized adduct can undergo isomerization, dissociate to new products or react back to reactants before stabilization. The stabilized adduct can also react through these same paths. Reactions of the adduct involve intramolecular hydrogen shifts, concerted HO2 molecular elimination, and subsequent reactions of the isomers formed include epoxide formation. Important product formation pathways involve pathways that are lower in energy than the initial reactants. The kinetics of the chemically-activated reaction between alkyl radicals and molecular oxygen are analyzed using quantum Rice-Ramsperger-Kassel (QRRK) theory for *k(E)* and a master equation analysis for collisional deactivation. Temperature and pressure dependent rate coefficients for the chemically-activated and the thermal reaction of the adducts and isomers are assembled into a mechanism and compared with experimental data for several systems. The predictions, using unadjusted rate coefficients, are consistent with literature observations over extended temperature and pressure ranges. Important new kinetic implications for chain branching and low-temperature ignition are discussed.

INTRODUCTION

Reactions of hydrocarbon radicals with molecular oxygen are important in atmospheric chemistry as well as in combustion processes. This type of elementary reaction is still under active investigation. The initially-formed energized peroxy radical has multiple reaction possibilities. The $C_2H_5 + O_2$ reaction represents an important model system to explore the kinetic consequences of these reactions; it contains many of the complexities of larger systems, yet is more amenable to detailed electronic structure calculations. An added advantage is that this reaction has been extensively studied experimentally. (Kaiser, 1995; Clifford et al., 2000, and references therein) There have also been several theoretical analyses of this system. Recent high-level *ab initio* calculations (Rienstra-Kiracofe et al., 2000) have characterized a new reaction pathway, concerted elimination to directly produce C_2H_4 and HO_2 from the initially-formed ethylperoxy adduct. This pathway was not considered in earlier kinetic analyses of the ethyl + O_2 system (Bozzelli et al., 1990; Wagner et al., 1990), but was included in a recent study. (Miller et al., 2000) One important aspect of this system is that most of the reaction channels of the energized adduct are higher in energy than the entrance channel and the concerted elimination channel is only a few kcal/mole lower. Thus, adduct stabilization is likely over an extended temperature range. Both Kaiser and Clifford et al. recognized the need to consider the kinetic consequences of subsequent thermal dissociation of this adduct in analyzing their experimental data. This reaction becomes increasingly important at higher temperatures, where the dissociation rate coefficient is larger.

METHODS

We used electronic structure theory to generate most of the input parameters needed to analyze this chemically-activated system. We wanted to assess whether this approach could accurately predict the temperature and pressure dependence of the various reaction channels. The potential energy surface was calculated at relatively high levels, and the rate coefficients for reactions of the energized adducts were obtained from canonical transition state theory (CTST). The rate coefficient for initial formation of ethylperoxy was calculated using variational transition state theory (VTST). We compared two models for collisional deactivation in conjunction with use of QRRK theory to estimate k(E). Finally, we incorporated the predictions for the individual branching fractions of the energized adducts and those for thermal dissociation of the stabilized adducts into a mechanism to illustrate where it is necessary to account for thermal dissociation. We conclude that this approach, with no adjustments to any of the parameters, permits a reasonably accurate description of this system. We also explore the kinetic implications of the direct formation of ethylene and HO_2 from CCOO•.

TABLE 1. Isodesmic Working Reactions

Isodesmic Reaction	ΔH^f_{298}	Method
CH_3CH_2OOH + CH_3OH = CH_3CH_2OH + CH_3OOH	-39.89	CBS-Q
CH_3CH_2OOH + CH_3OH = CH_3CH_2OH + CH_3OOH	-40.06	G2
CH_3CH_2OOH + CH_3OH = CH_3CH_2OH + CH_3OOH	-39.96	G2//B3
CH_3CH_2OO• + CH_3OOH = CH_3OO• + CH_3CH_2OOH	-6.72	CBS-Q
CH_3CH_2OO• + CH_3OOH = CH_3OO• + CH_3CH_2OOH	-6.77	G2
•CH_2CH_2OOH + CH_3OH = CH_3CH_2OOH + C•H_2OH	10.92	CBS-Q
•CH_2CH_2OOH + CH_3OH = CH_3CH_2OOH + C•H_2OH	10.49	G2
(Specie Calculated Are In Bold.)	**kcal/mol**	

DISCUSSION OF RESULTS

The calculated apparent rate coefficients for direct formation of the major product channels of chemically-activated CCOO•, including both the master equation and modified strong collision results, are shown in Fig. 2 for P = 1 atm N_2. Both models give remarkably similar predictions. In this case, the barriers for the major channels are reasonably close in energy, and this would be expected to minimize the differences between the two deactivation models. The dominant reaction up to almost 1000K is formation of the ethylperoxy adduct, while the direct formation of ethylene and HO_2 from the energized adduct dominates above 1000 K. The production of ethylene and HO_2 via the sequential pathway is much less important, due to the higher barrier for isomerization.

At 750K, the ethylene channel decreases with pressure, as expected, but the overall predicted pressure effect is quite small. Stabilization becomes the dominant channel at higher pressures. The

production of the hydroperoxyethyl isomer is much less likely than ethylperoxy, reflecting the lower energy pathway from ethylperoxy directly to ethylene, which bypasses hydroperoxyethyl. Significant differences between the collisional deactivation models only appear at very low pressures, with the master equation model showing less stabilization. The smaller number of collisions at lower pressures enhances the energy-dependent reaction channels. Since the master equation model allows multiple deactivation steps prior to "complete" deactivation, this increases the probability for reaction with this model and thus decreases the stabilization rate coefficient.

Table 2 QRRK Input Parameters

Reaction	A	n	Ea
$C_2H_5 + O_2 = C_2H_5OO\bullet$	8.82×10^{9}	1.12	0.0
$C_2H_5OO\bullet = C_2H_5 + O_2$	2.46×10^{18}	-1.07	35.32
$C_2H_5OO\bullet = H_2C\bullet CH_2OOH$	7.90×10^{6}	1.79	35.82
$H_2C\bullet CH_2OOH = C_2H_5OO\bullet$	5.89×10^{6}	1.04	18.01
$C_2H_5OO\bullet = CH_3CHO + OH$	1.32×10^{9}	1.37	41.59
$C_2H_5OO\bullet = C_2H_4 + HO_2$	8.80×10^{5}	2.24	29.61
$C_2H_5OO\bullet = CH_3CH_2O\bullet + O\bullet$	2.98×10^{15}	-0.09	61.6
$H_2C\bullet CH_2OOH = C_2H_4 + HO_2$	6.44×10^{10}	0.52	16.18
$H_2C\bullet CH_2OOH = H_2COCH_2 + OH$	6.62×10^{9}	0.72	15.41

$C_2H_5OO\bullet$ ν_1=373 cm^{-1} (degen=4.13) ν_2 = 1256 cm^{-1} (10.53) ν_3 = 3053 cm^{-1} (5.34)

$H_2C\bullet CH_2OOH$: ν_1=289 cm^{-1} (degen=6.10) ν_2 = 1161 cm^{-1} (8.16) ν_3 = 3179 cm^{-1} (5.23)

σ = 4.94 Å ε/k = 450.

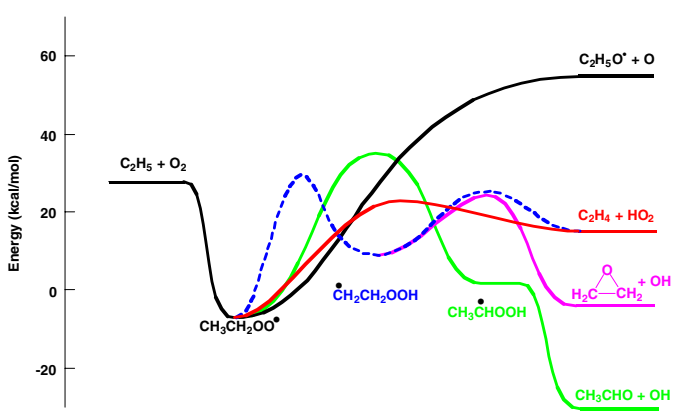

Fig. 1 Potential energy diagram for the C_2H_5 +O_2 reaction. There are the two pathways to C_2H_4 + HO_2. The red line represents the direct elimination, while the blue dashed line represents a sequential pathway–first isomerization to hydroperoxyethyl, which is followed by β-scission

Fig. 3 compares the predictions of the ethylene yield as a function of pressure at 298K to that measured by Kaiser. The sharp decrease with pressure, due to increased stabilization of the energized adduct prior to the concerted elimination, is well predicted with both collisional deactivation models. The predictions indicate that virtually all of the ethylene is produced via the direct elimination channel, as opposed to that produced via isomerization to hydroperoxyethyl followed by β-scission.

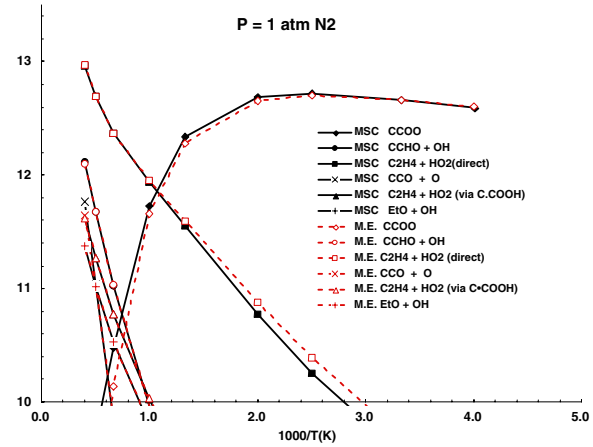

Fig. 2 The predicted effect of temperature upon the apparent rate coefficients for the major channels of the chemically-activated reaction C_2H_5+O_2, using both the modified strong collision model and a master equation model for collisional deactivation.

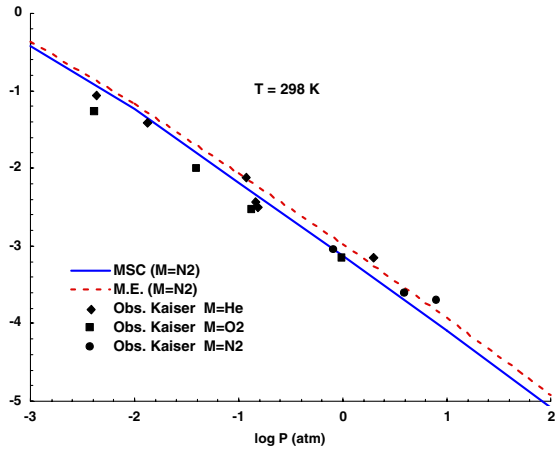

Fig 3. Comparison of Ethylene Yield at 298K between Kaiser's experimental data with model predictions.

At this low temperature, it is possible to compute to ethylene yield directly by taking the ratio of the sum of the predicted rate coefficients for "direct", i.e., chemically-activated, ethylene production to the total predicted "direct" rate coefficient. The temperature is sufficiently low that any contribution from dissociation of the stabilized adduct is insignificant. However, as the temperature is increased and the thermal dissociation rate coefficient increases, it is necessary to generate a small mechanism to allow comparison to the data. The reactions considered includes all the "direct" reactions, as well as further reactions of the stabilized adducts formed in the direct reactions. Also included are the other reactions used by Kaiser to model his data. Since the QRRK rate coefficients are dependent on both temperature and pressure, we needed to use different sets of coefficients for each set of experimental conditions with different T and P. (This is a good example of the utility of using Chebyshev fits (Venkatesh et al., 1997) to capture k(T,P) so that one set of rate coefficients could be used for all conditions.)

The importance of the subsequent reactions of the stabilized adducts can be seen in Fig. 4, where predictions of the temperature dependence of the ethylene yield are compared to Kaiser's data. At

253 K and 373 K, the ethylene yield computed by only considering the direct channels is identical to that obtained by numerical integration of the complete mechanism. However, at 513K, the direct yield is significantly smaller than that obtained by the mechanism. Here the temperature is sufficiently high that thermal dissociation of ethylperoxy contributes substantially to the overall ethylene yield. Predictions based on the overall mechanism are in good agreement with Kaiser's observations.

In addition to capturing the temperature and pressure dependence of the ethylene yield, the predicted rate coefficient for overall ethyl decay is also in reasonable agreement with Kaiser's data. There is little difference in the "direct" QRRK result and that obtained via numerical integration. For the integration, we used Kaiser's method (comparing the computed consumption of ethane to the formation of ethyl chloride) to obtain k_{tot}. This approach lead to slightly different values at different times, and the results were averaged. The agreement with Kaiser's data is encouraging. The increase in predicted rate coefficient at the lower temperatures reflects the temperature dependence of adduct formation rate, while the decrease seen in most cases at 460K reflects the onset of falloff. Here the apparent rate coefficient decreases as the adduct begins to react back to reactants.

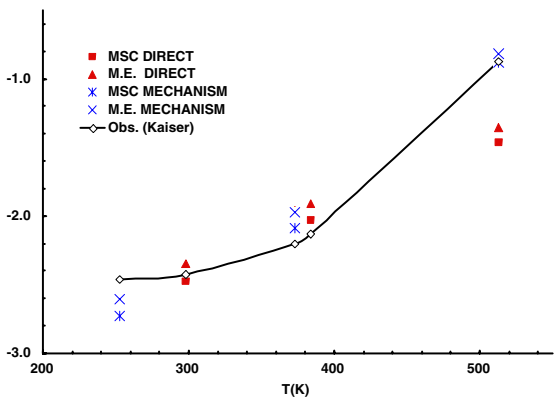

Fig. 4 Comparison of predicted effect of temperature on the ethylene yield to the observations of Kaiser. Points labeled "DIRECT" are obtained by taking the ratio of the chemically-activated rate coefficients for production of ethylene to the total apparent chemically-activated rate coefficient. Points labeled "MECHANISM" were calculated from the results of numerically integrating the systems of reactions.

We have also used our approach to compare predicted HO_2 yields to those measured in the recent measurements of Clifford et al. (2000). Those experiments were done over a wider temperature range at lower pressures and lower radical concentrations than Kaiser's. The temporal evolution of HO_2 was measured. Biexponential time behavior for HO_2 formation was observed and attributed to the reactions of the stabilized peroxy adduct. These researchers were able to extract both a total and a prompt HO_2 yield. The prompt yield should correspond to that obtained from the QRRK chemical-activation analysis, while the total yield corresponds to that obtained using the mechanism, which accounts for these reactions as well as the reactions of the stabilized adduct. Clifford et al. obtained the HO_2 yield by comparing the HO_2 signal obtained with ethane to that obtained with methanol, where the yield is expected to be unity. This was necessitated by the importance of HO_2 recombination under the experimental conditions. We obtained our predicted yields in an analogous manner. We found that the yields were not always constant with time, especially at lower temperatures, and the values reported represent an average over the time scale of the Clifford et al. experiments. We used both collisional deactivation models for our comparisons.

Fig. 5 compares the predicted total HO_2 yield as a function of temperature to that measured by Clifford et al. Again we obtain similar results with both the modified strong collision assumption and the master equation, and both sets of predictions agree nicely with the observations of Clifford et al. Particularly encouraging was the correct prediction of the observed rapid increase above 500K. It is essential to include the dissociation of the ethylperoxy adduct at 650K, as can be seen by the comparison of the results for direct HO_2 production to those obtained using the mechanism. Only approximately one-third of the overall HO_2 yield can be seen to come directly from the energized adduct. On the other hand, at 500K virtually all of the yield can be attributed to the direct reaction. At this lower temperature, the contribution from dissociation of the stabilized adduct is negligible.

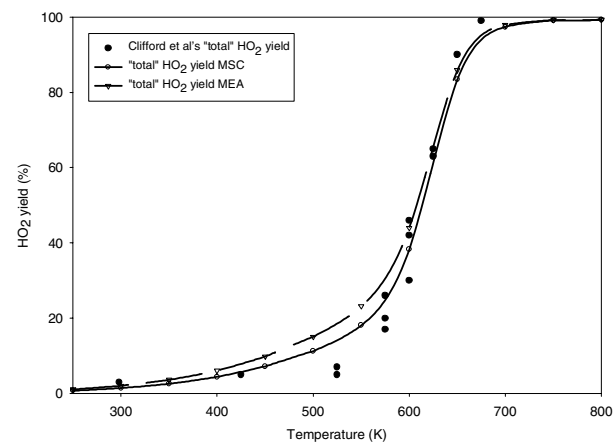

Fig. 5 Comparison of predicted total yield of HO_2 to that observed by Clifford et al.

IMPLICATIONS FOR LOW TEMPERATURE IGNITION

The conventional approach to describe low-temperature ignition kinetics, especially the region of negative temperature coefficient, considers the following reactions (Walker et al., 1997):

$$R^{\bullet} + O_2 \rightleftharpoons ROO^{\bullet} \quad (1)$$

$$ROO^{\bullet} + RH \longrightarrow ROOH + R^{\bullet} \quad (2)$$

$$ROOH \longrightarrow RO^{\bullet} + HO^{\bullet} \quad (3)$$

$$ROO^{\bullet} \longrightarrow R^{\bullet}OOH \quad (4)$$

$$R^{\bullet}OOH \longrightarrow RO + HO^{\bullet} \quad (5)$$

$$R^{\bullet}OOH + O_2 \longrightarrow \text{branching} \quad (6)$$

($R^{\bullet}$ is an alkyl radical, $RO^{\bullet}$ is an alkoxy radical and RO is generally a cyclic ether. $R^{\bullet}OOH$ is often written as QOOH, but we use the $R^{\bullet}OOH$ notation to emphasize the free radical character of this species.) If the temperature is sufficiently low that the equilibrium in (1) is shifted to the right, the subsequent reactions of RO_2 can lead to the chain-branching (Rxns. 3 and 6) needed for ignition. However, as

the temperature rises, the equilibrium in (1) shifts to the left, reducing the RO_2 concentration and thus slowing down the overall rate, i.e., producing a negative temperature coefficient of reaction rate. Particularly noteworthy in this mechanism is the importance of the isomerization reaction (Rxn. 4); without this, chain branching via Rxn. (6) cannot occur. In ethane oxidation, the *newly-identified* direct pathway for production of ethylene and HO_2 from ethylperoxy is much faster than Rxn. 4. This competing fast reaction necessarily reduces the amount of $R^{\bullet}OOH$ that can be produced via Rxn. 4. Here the amount of chain branching via Rxn. 6 will be substantially reduced. Although more complex fuels might well have lower barriers to isomerization [by having the internal hydrogen transfer via a less strained ring (6- vs. 5-member) or by abstracting secondary or tertiary hydrogens rather than the primary hydrogens in ethyl], the possibility of concerted elimination of HO_2 from RO_2 in these fuels will generally result in formation of less $R^{\bullet}OOH$, thus reducing the overall branching rates. Thus there is a need to revisit these systems to see if new branching pathways are needed to accurately describe low-temperature ignition.

REFERENCES

(1) Bozzelli, J. W.; Dean, A. M. *J. Phys. Chem.* **1990**, *94*, 3313-3317.
(2) Clifford, E. P.; Farrell, J. T.; DeSain, J. D.; Taatjes, C. A. *J. Phys. Chem A* **2000**, *104*, 11549-11560.
(3) Kaiser, E. W. *J. Phys. Chem.* **1995**, *99*, 707-711.
(4) Miller, J. A.; Klippenstein, S. J.; Robertson, S. H. "A Theoretical Analysis of the Reaction Between Ethyl and Molecular Oxygen"; 28th International Symposium on Combustion, 2000, Edinburgh, Scotland.
(5) Rienstra-Kiracofe, J. C.; Allen, W. D.; Schaefer III, H. F. *J. Phys. Chem. A* **2000**, *104*, 9823-9840.
(6) Venkatesh, P. K.; Dean, A. M.; Cohen, M. H.; Carr, R. W. *Reviews in Chemical Engineering* **1997**, *13*.
(7) Wagner, A. F.; Slagle, I. R.; Sarzynski, D.; Gutman, D. *J. Phys. Chem.* **1990**, *94*, 1853-1868.
(8) Walker, R. W.; Morley, C. Basic Chemistry of Combustion. In *Low-Temperature Combustion and Autoignition*; Pilling, M. J., Ed.; Elsevier: Amsterdam; New York, 1997; pp 1-124.

O_2 dissociation on transition metals: Insights from first-principles calculations

Manos Mavrikakis and Ye Xu

Department of Chemical Engineering
University of Wisconsin - Madison,
Madison, WI 53706

Introduction

Dioxygen (O_2) dissociation on transition metal surfaces is of considerable research and practical interest both because many important industrial oxidation processes are heterogeneously *catalyzed* by transition metals and feature O_2 as the oxidizing agent and because O_2 dissociation is the first step toward the *corrosion* of various metals. Different mechanisms for O_2 dissociation have been identified on different metal surfaces. In the chemisorbed-precursor mechanism, the incident O_2 molecule initially chemisorbs intact [1]. Subsequent thermally driven kinetics determines selectivity between desorption and dissociation. On a number of transition metal surfaces, including Pt(111), Pd(111), Ni(111), Ag(110) and Cu(110), chemisorbed molecular oxygen species have been detected at temperatures below ~150 K. Two molecular states are frequently observed in vibrational spectroscopy: a peroxo form (O_2^{2-}), with an O-O stretching frequency of 610-650 cm^{-1}, and a superoxo (O_2^{-}) form, with a stretching frequency of 810-870 cm^{-1}. The precursors generally adopt the di-π orientation in which their molecular axes are parallel to the surface. Significant charge transfer from the substrate to the O_2 π_{2p}* orbital weakens the O-O bond, which makes them likely precursors to O_2 dissociation. Because the existence of molecular O_2 precursors influences surface reaction kinetics, it is important to ascertain their characteristics and behavior. In this presentation, we will discuss our findings on O_2 dissociation on flat and stepped Cu and Au surfaces, but we will focus on our results on the O_2/Cu(111) system for the rest of this document.

The adsorption of atomic oxygen on Cu(111) has been studied extensively under a variety of experimental conditions. Threefold hollows are found to be the preferred adsorption sites for O atoms. The estimated saturation coverage of atomic oxygen ranges from 0.3 to 0.5 ML at room temperature. Extensive surface reconstruction is observed at medium to high oxygen coverage and at room temperature and above. There is no conclusive evidence for ordered overlayer structures until much higher temperature, probably with the onset of Cu_2O formation [2].

Molecularly adsorbed O_2 has also been detected on the Cu(111) surface. Several techniques, including UPS, XPS and HREELS, have revealed two chemisorbed molecular O_2 species, characterized by O-O stretching frequencies of 610 cm^{-1} and 820-870 cm^{-1} [3,4]. At low temperature a mixture of chemisorbed molecular oxygen and atomic oxygen species are found on the surface. The molecular species are not detected at temperatures above 170 K. The structural and electronic properties of these species are still not well understood, and the dissociation of O_2 on Cu(111) has not yet been studied theoretically.

We have performed periodic self-consistent DFT calculations to investigate the characteristics of various molecular and atomic oxygen configurations on Cu(111) and to explore the most likely pathways of O_2 dissociation. Because industrial heterogeneous catalysts consist of nanometer-sized metal particles supported on metal oxides that often induce strain on the surfaces of the metals [5], we have also examined the effect of strain on the thermochemistry and on the reaction barrier for O_2 dissociation on Cu(111) [6].

Methods

The calculations were performed using DACAPO [7]. Adsorption was allowed on only one of the two surfaces of a (2×2) unit cell used to construct the Cu(111) surface. The metal slab consists of four layers of Cu atoms. Successive slabs are separated by a vacuum equivalent to six layers of Cu. The Kohn-Sham one-electron valence states are expanded in a basis of plane waves with kinetic energies below 25 Ry. The exchange-correlation energy and potential are described by the generalized gradient approximation (GGA-PW91), and ionic cores are described by ultrasoft pseudopotentials. The surface Brillouin zone is sampled at 18 special *k* points. The calculated equilibrium PW91 lattice constant for bulk Cu is a = 3.66 Å, in good agreement with the experimental value of 3.62 Å.

Adsorption of atomic and molecular oxygen, and O_2 dissociation pathways are explored first on a fixed bulk-truncated surface at the equilibrium lattice constant. The effect of surface relaxation is investigated by relaxing the top two layers of the fixed surface. The fixed bulk-truncated surface is then compressed or stretched in the plane of the surface, whereon various properties are calculated again. The O-O bond length is chosen as the reaction coordinate in the determination of the dissociation pathway. The O-O stretching frequency is calculated using the harmonic oscillator approximation.

Results and Discussion

Atomic oxygen on Cu(111) The properties of adsorbed atomic oxygen are calculated at _ ML coverage. fcc sites are clearly preferred with a binding energy of -4.3 eV/O. For adsorption in an fcc or hcp site, the Cu atoms bound to the O atom relax outward by ~0.01 Å and move ~0.05 Å laterally away from the O atom to accommodate its presence. The energy barrier to diffusion is estimated to be ~0.45 eV on both the fixed and the relaxed surface. Increase in the surface work function suggests a net charge transfer to the O atoms, which makes these species ionic in character.

Molecular oxygen precursors on Cu(111) Calculations for molecular oxygen precursors are carried out with one O_2 molecule in every (2×2) unit

cell. Perpendicular O_2 precursors are calculated to be only marginally stable on Cu(111). The parallel (di-□) O_2 precursors are more strongly bound than the perpendicular precursors by ~0.5 eV/O_2 each. The di-□ precursors exist in several configurations on Cu(111). (For brevity, site names are abbreviated to their first letters. Thus, for instance, t-f-b stands for top-fcc-bridge). These include t-b-t, t-h(f)-b, and b-h(f)-b. Their binding energies are, respectively, -0.45, -0.52, and -0.56 eV/O_2 on a relaxed surface and are about 0.03 eV/O_2 less on a static surface. Charge transfer from the substrate quenches the magnetic moment of all but the t-b-t state, which still carries half (1.0 μ_B) of what a gas-phase O_2 molecule possesses. The O-O bond of the parallel precursors on Cu(111) is lengthened up to about 18% of the gas-phase O_2 bond length. Cu atoms not bound to the precursors sink between 0.05 to 0.14 Å in place. Those that are directly bound to the precursors do not show appreciable vertical displacement but move away from the precursors by ~0.05 Å horizontally. The O-O stretching frequencies of t-b-t, t-h-b and b-h-b states are found to be, respectively, 954, 789, and 729 cm^{-1}. The calculated frequencies are higher than experimental findings, but the two are in reasonable agreement given that GGA-PW91 calculations regularly over-predict vibrational frequencies by 5-10%. Based on their bond lengths and magnetic properties, the t-b-t precursor can be viewed as superoxo-like, and the t-h(f)-b and b-h(f)-b precursors can be viewed as peroxo-like.

O_2 dissociation on Cu(111) The most probable pathway starts with the most thermodynamically

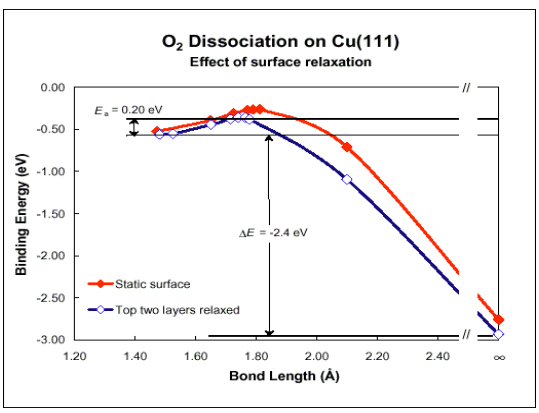

Figure 1. Reaction pathway for O_2 dissociation from b-h-b to fcc□2. The indicated activation energy and heat of reaction are those calculated on the relaxed surface.

,favorable precursor, b-h-b. The O-O bond would stretch until it breaks, upon which the two separated O atoms would fall into two adjacent fcc sites. The energy evolution along this pathway, both on the fixed and on the relaxed surface, is given in **Figure 1**. It can be seen that the transition state occurs early in the process, with a small activation energy barrier of 0.26 eV/O_2 above the initial b-h-b state on the fixed surface. On the relaxed surface the barrier is lowered to 0.20 eV/O_2. The overall O_2 dissociation process on Cu(111) is very exothermic, releasing 2.4 eV/O_2 of heat. Given the relative magnitudes of the precursor binding energy, activation energy and overall reaction exothermicity, O_2 precursor molecules will dissociate, rather than desorb, upon heating of the surface to yield chemisorbed O species. This agrees well with previous experimental findings [4]. The relaxed surface displays a high level of flexibility in the dissociation process, particularly after the transition state, indicating substantial involvement of surface Cu atoms in facilitating the breaking of the O-O bond.

Effect of strain We used a lattice constant of 3.50 Å (4.4% less than the equilibrium value of 3.66 Å) to model a compressed surface and 3.80 Å (3.8% more) to model a stretched surface. Lattice expansion leads to increased stability for all adsorbates. The binding energy of both atomic oxygen and molecular precursors are modified by ~∓0.1 eV by ~±4% strain. Roughly, for a 1% increase in the lattice constant, the binding energies of various adsorbates increase by ~0.03 eV. We also calculated the position of the *d*-band center of the Cu(111) surface as a function of strain. The results show a consistent up-shift of the *d*-band center with lattice expansion and thus increasingly strong surface-adsorbate interaction. This is in good agreement with the findings of previous theoretical studies on the effect of strain on the reactivity of several metal surfaces [8].

Figure 2 shows our results for the effect of strain

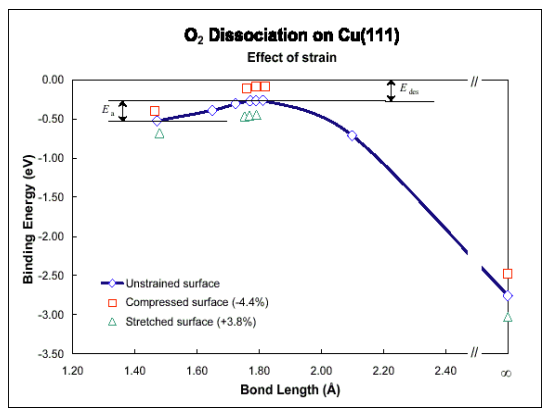

Figure 2. Effect of strain on O_2 dissociation from O_2 (b-h-b) to fcc□2 on a Cu(111) surface. Surface is not relaxed.

along the O_2 dissociation reaction path. Stretched surfaces stabilize the initial, transition, and final states. Because the transition state becomes significantly more stable in going from a = 3.66 to 3.80 Å, making the desorption barrier for the transition state correspondingly higher, the rate of O_2 dissociation can outperform the rate of O_2 desorption by 1-2 orders of magnitude depending on the temperature. Thus small supported Cu particles can show enhanced reactivity,

both because of strain and because of higher concentration of under-coordinated sites.

Acknowledgements

This research was supported in part by NSF cooperative agreement ACI-9619020 through computing resources provided by the National Partnership for Advanced Computational Infrastructure. Part of the calculations was performed on DOE supercomputing facilities (NERSC). YX gratefully acknowledges partial financial support from an NSF-GRT grant (Contract # EHR-9554586). MM thanks Shell Oil Company Foundation for a Faculty Career Initiation Award, which provided partial financial support.

References

(1) Nolan, P. D.; Wheeler, M. C.; Davis, J. E.; Mullins, C. B.; *Acc. Chem. Res.* **1998**, *31*, 798.
(2) Besenbacher, F.; Sprunger, P.T.; Ruan, L.; Olesen, L.; Stensgaard, I.; Lægsgaard, E. *Top. Catal.* **1994**, *1*, 325.
(3) Rajumon, M. K.; Prabhakaran, K.; Rao, C. N. R. *Surf. Sci.* **1990**, *233*, L237.
(4) Sueyoshi, T.; Sasaki, T.; Iwasawa, Y. *Surf. Sci.* **1996**, *365*, 310.
(5) Knop-Gericke, A.; Hävecker, M.; Schedel-Niedrig, T.; Schlögl, R. *Top. Catal.* **2000**, *10*, 187.
(6) Xu, Y.; Mavrikakis, M.; *Surf. Sci.* **2001**, *494*, 131.
(7) Hammer, B.; Hansen, L. B.; Nørskov, J. K. *Phys. Rev. B* **1999**, *59*, 7414.
(8) Mavrikakis, M.; Hammer, B.; Nørskov, J. K.; *Phys. Rev. Lett.* **1998**, *81*, 2819.

Density Functional Theory Studies of Chemisorption and Diffusion Properties of Ni and Ni Complexes on MoS_2 Basal Planes

D. C. Sorescu, A. V. Cugini* and D. S. Sholl*,#*

*U. S. Department of Energy, National Energy Technology Laboratory, P. O. Box 10940, Pittsburgh, PA 15236.
#Dept. of Chemical Engineering, Carnegie Mellon University, Pittsburgh, PA. 15213

Introduction

Among various sulfide catalysts proposed for the hydrodesulfurization (HDS) process, molybdenum sulfide is one of most promising candidates for technological applications.[1,2] In practice it is used as well-dispersed MoS_2 nanocrystallites supported on γ-alumina and can be used both as an unpromoted or promoted catalyst[1] with Co or Ni atoms.

Despite a relative large number of experimental studies the role of the metallic promoters in HDS processes is still under intense debate. Recently, Weiss *et al.*[3-5] provided new insight based on low-temperature scanning tunneling microscopy investigations of the dynamics of Ni and Co clusters on MoS_2 basal planes. These studies indicate that both these species have a low barrier for surface diffusion. It was suggested that these promoters can be used to increase the sticking probability of sulfur-containing hydrocarbons and to transport these hydrocarbons to the active sites for reaction. However, several issues were not clarified by these studies. For example the location of the promoters on the basal plane or the electronic modifications induced upon adsorption of these metallic atoms is not well established. Moreover, the transport properties, particularly the diffusion characteristics as well as the clustering processes of these promoters on MoS_2 have not yet been well characterized and understood. Another issue raised by experimental investigations is that of the role played by various sulfur defects on the chemisorption properties of promoter atoms. In general, it would be very useful to understand how the adsorption and dissociation of various hydrocarbon species containing sulfur are changed in the presence of the promoters and of the vacancies on MoS_2 surface.

The properties of promoted MoS_2 catalysts have also been considered in several recent theoretical studies based on density functional theory (DFT) calculations.[6-7] However, these studies have focused exclusively on description of the binding properties of promoter species at edge surfaces where the catalytic activity is the highest but have not analyzed the properties of basal surfaces. In the present study we describe a DFT study that focuses on analyzing the interaction of Ni promoters with the basal plane of MoS_2 in an effort to clarify some of the mechanisms proposed by Weiss *et al.*[3-5] based on their STM investigations.

Computational Method

The calculations performed in this study were done using the Vienna *ab initio* simulation package (VASP).[8-10] This program evaluates the total energy of periodically repeating geometries based on density-functional theory and the pseudopotential approximation. In this case the electron-ion interaction is described by fully non-local optimized ultrasoft pseudopotentials similar to those introduced by Vanderbilt.[11,12] Periodic boundary conditions are used, with the one electron pseudo-orbitals expanded over a plane-wave basis set. The expansion includes all plane waves whose kinetic energy, $\hbar^2 k^2 / 2m < E_{cut}$ where k is the wave vector, m the electronic mass and E_{cut} is the chosen cutoff energy. A cutoff energy of 242 eV has been used in our studies.

Calculations have been done using the spin polarized PW91 generalized gradient approximation (GGA) of Perdew *et al.*[13] The sampling of the Brillouin zone was performed using a Monkhorst-Pack scheme.[14] The minimization of the electronic free energy was performed using an efficient iterative matrix-diagonalization routine based on a sequential band-by band residuum minimization method (RMM) or alternatively, based on preconditioned band-by-band conjugate-gradient (CG) minimization.[15] The optimization of different atomic configurations was performed based on a conjugate-gradient minimization of the total energy.

The minimum energy paths between different minima were optimized by use of the nudged elastic band (NEB) method of Jónsson and Mills.[16] In this approach the reaction path is "discretized", with the discrete configurations, or images, between minima being connected by elastic springs to prevent the images from sliding to the minima in the optimization. In the NEB searches either 8 or 16 images were employed between minima.

The periodic nature of the surface was represented in our simulations using a supercell model with periodic boundary conditions in all three directions. Most calculations have been done using a slab model consisting of one S-Mo-S layer. However, additional tests have been performed for the case of supercells with three S-Mo-S trilayers. In all calculations a vacuum layer of at least 10 Å has been used parallel to the MoS_2 basal plane

Results and Discussions

Based on full optimizations of the Ni atoms on the MoS_2 basal plane we have identified three stable adsorption configurations. The first one (1F) (see Fig.1a) corresponds to Ni atoms adsorbed on top of the sulfur atoms, the second one (6F) corresponds to a six-fold configuration of Ni (see Fig.1b).The last one (3F) is represented by adsorption on top of Mo atom with a three-fold binding to neighbor sulfur atoms (see Fig.1c).

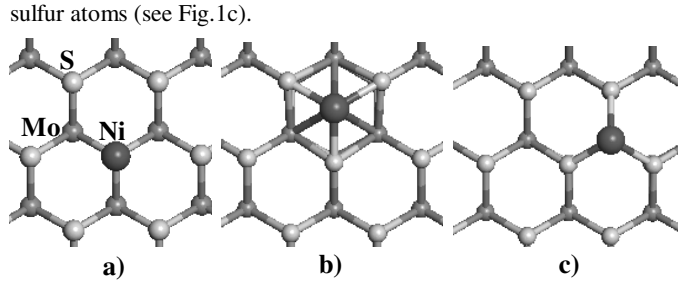

Figure 1. Adsorption configurations of Ni on $MoS_2(0001)$ surface: (a) 1F on top of S atoms, (b) 6F in a six-fold configuration and (c) 3F on top of Mo atom.

Our results indicate a stability order E(3F) > E(6F) > E(1F). For the most stable adsorption configuration (3F), the adsorption energy, 77 kcal/mol, is large. In this configuration the Ni atom sits above the Mo atom at a distance of 2.59 Å while the Ni-S distances are 2.13 Å.

We have also investigated the minimum energy paths for diffusion of a Ni atom between different adsorption configurations using NEB calculations. In particular, we have analyzed three diffusion pathways suggested by the surface symmetry: 3F→6F→3F, 3F→6F→1F and 3F→1F. Our calculations indicate that among these the 3F→6F→3F pathway has the smallest barrier for diffusion. The corresponding profile determined in our studies is represented in Figure 2. As can be seen from this figure the barrier height is about 20 kcal/mol. This value is about 3.8 times smaller than the corresponding adsorption energy at the 3F site. This ratio of the

diffusion barrier to the adsorption energy is consistent with values obtained for other adsorbate/surface systems.[17] However, our results indicate much larger diffusion barriers than those expected from the analysis of STM data by Weiss et al.[3,4]

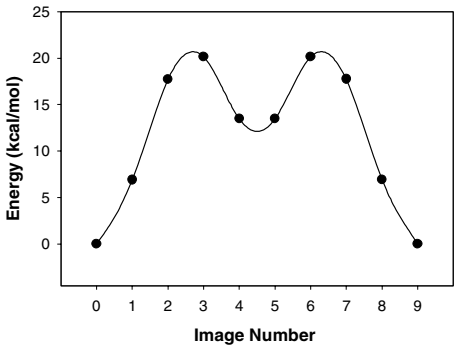

Figure 2. Minimum energy path for diffusion of Ni atom between two 3F sites and passing through the 6F configuration.

We have also analyzed the case when a Ni_3 cluster adsorbs on MoS_2 basal plane. We have identified an adsorption configuration on top of S atoms in which the adsorption energy per Ni atom decreases significantly to about 20.4 kcal/mol. However when this cluster is moved away from the on-top position the Ni atoms are adsorbed at the corresponding 3F sites, leading to cluster deformation and dissolution at the surface sites.

Another set of investigations we have pursued is related to adsorption of Ni atoms at S vacancy sites. Our calculations indicate that independent on the starting optimization configuration the Ni atom will adsorb at the position of S vacancy on the basal plane. The corresponding adsorption energy increases for this configuration to about 98.5 kcal/mol, indicating the existence of a very stable adsorption configuration.

As indicated by Weiss et al.[3-5] the presence of Ni atoms on MoS_2 surface is important to increase the sticking of sulfur-containing hydrocarbons. We have analyzed this aspect by performing studies of the adsorption of thiophene molecules on the promoted and unpromoted surfaces.

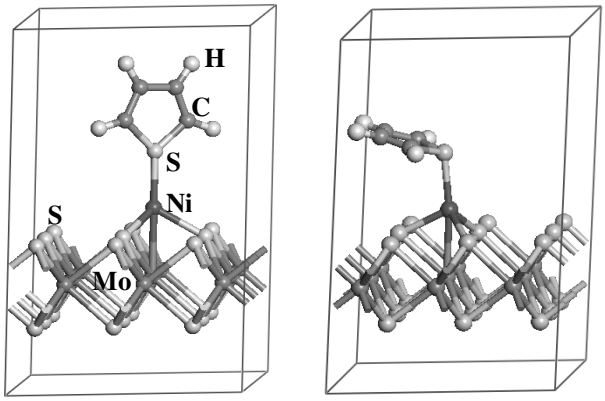

Figure 3. Vertical and tilted adsorption configurations of thiophene on Ni promoted MoS_2 basal plane.

In the case of adsorption of thiophene molecules on the unpromoted surface the calculated adsorption energies of thiophene are very small indicating a physisorption interaction mechanism. This result is in agreement with previous experimental findings determined by Salmeron et al.[18] based on TPD investigations. However, when Ni atoms are present on the surface the binding energies significantly increase. For example, in Figure 3 we present two possible adsorption configurations of thiophene molecule on Ni atoms positions at 3F sites. Our calculations indicate adsorption energies of about 20 kcal/mol for thiophene on the promoted surface. These results support the experimental findings related to the increased sticking probability of sulfur-containing hydrocarbons on basal surface.

Conclusions

The main results of our investigations related to adsorption and diffusion studies of Ni and Ni complexes on $MoS_2(0001)$ surface can be summarized as follows:

a) there are several adsorption configuration of Ni atoms on MoS_2 basal planes with large adsorption energies.

b) a simple hopping mechanism of Ni atoms between different adsorption sites indicate diffusion barriers in excess of 20 kcal/mol. This results contradict the experimental findings of Weiss et.al.[3,4] where metallic promoters were found to move easily on the surface even in the case of low temperatures.

c) the binding energy of Ni atoms to the surface increases when S vacancies are present.

d) the Ni promoter species increase the binding of thiophene molecule to the surface. In the absence of these promoters, thiophene physisorbs on the surface.

Acknowledgement. We gratefully acknowledge the supercomputer allocation provided by Pittsburgh Supercomputer Center under the SC^2 partnership program.

References

(1) Topsøe, H.; Clausen, B. S.; Franklin, F. E.; Massoth, E. in *Science and Technology in Catalysis: Hydrotreating Catalysis*; Anderson, J. R. Boudart, M., Ed.; vol. 11, Springer: Berlin, 1996.
(2) Kabe, T.; Ishihara, A.; Qqian, W. in *Hydrodesulfurization and Hydrogenation*, Wiley, New York, 1999.
(3) Kushmerick, J. G.; Weiss, P. S. *J. Phys. Chem.* B **1998**, 102, 10094.
(4) Kushmerick, J. G.; Han, K. P.; Johnson, J. A.; Weiss, P. S. *J. Phys. Chem.* B **2000**, 104, 2980.
(5) Kandell, S. A.; Weiss, P. S. *J. Phys. Chem.* B **2001**, 105, 8102.
(6) Byskov, L. S.; Nørskov, J. K.; Clausen, B. S.; Topsøe, H. *J. Catal*. **1999**, 187, 109.
(7) Raybaud, P.; Hafner, J.; Kresse, G.; Kasztelan, S.; Toulhoat, H. *J. Catal.* **2000**, 190, 128.
(8) Kresse, G.; Hafner, J. *Phys. Rev*. **1993**, B 48, 13115.
(9) Kresse, G. ; Furthmüller, J. *Comput. Mat. Sci*. **1996**, 6, 15.
(10) Kresse, G.; Furthmüller, J. *Phys. Rev.* **1996**, B 54, 11169.
(11) Vanderbilt, D. *Phys. Rev*. **1990**, B 41, 7892.
(12) Kresse, G; Hafner, J. *J. Phys. Condens. Matter* **1994**, 6, 8245.
(13) Perdew, J. P.; Chevary, J. A.; Vosko, S. H.; Jackson, K. A.; Pedersen, M. R.; Singh, D. J. and Frolhais, C. *Phys. Rev.* **1992**, B 46, 6671.
(14) Monkhorst, H. J.; Pack, J. D. *Phys. Rev*. **1976**, B 13, 5188.
(15) Kresse, G; Hafner, J. *Phys. Rev*. **1993**, B 47, 588.
(16) Mills, G.; Jónsson, H.; Schenter, G. K. *Surf. Sci.* **1995**, 324, 305.
(17) Gomer, R.; Rep. Prog. Phys. **1990**, 53, 917.
(18) Salmeron, M.; Somorjai, G.A.; Wold, A. Chianelli, R.; Liang K. S. Chem. Phys. Lett. **1982**, 90, 105.

CATALYTIC DEHYDROGENATION OF PHENOLICS AND POLYCYCLIC OLEFINS IN THE PRESENCE OF HYDROAROMATIC COMPOUNDS

Irving Wender

Chemical and Petroleum Engineering Department,
University of Pittsburgh

Introduction

The dehydrogenation of coal is a reaction that likely plays an important role in direct coal liquefaction and in various stages of coalification. Reggel, Wender and Raymond,[1] in what has been termed a classic study,[2] dehydrogenated coals using a 1%Pd on calcium carbonate catalyst in refluxing phenanthridine. For 24 vitrains, all obtained from coals ranging in rank from high volatile C bituminous to low-volatile bituminous, the data scatter about a reasonably smooth curve, in which the hydrogen evolution decreases gradually as the carbon content increases from 75.7% m.a.f. to 91.0% m.a.f. Three other points for semi-anthracite and anthracite show that hydrogen evolution decreases rapidly for ranks above low-volatile bituminous. The authors suggested that these findings were an indication of hydroaromatic structures in coal. It is important to note that the catalyst support, $CaCO_3$, and most of the phenanthridine could be removed by treatment with HCl, allowing examination of the dehydrogenation residues.

This paper looks into the possible effects of two structures in coal that could play a role in influencing the results obtained by Reggel et al.: the part played by phenolic structures and the effect of polynuclear olefinic entities.

Experimental

The original dehydrogenation apparatus[1] was modified so that the pressure difference between the reaction flask and the ambient pressure was controlled by a computer linked to the apparatus. Reaction products were removed from the flask and ground to a fine powder to achieve uniformity. A sample of this ground mixture, dissolved in $CDCl_3$, was analyzed in a 300 mHz Bruker spectrometer interfaced with a Silicon Graphics workstation. Gases were analyzed using an HP-5890 GC. Illinois #6 coal was from the Argonne Premium Coal Sample Bank. Oils from the dehydrogenation of coals were analyzed using simulated distillation

Results and Discussion

It is known that about half of the oxygen in bituminous coals occurs in phenolic structures[3,4]. Skowronski et al.[5] have suggested that secondary reactions involving oxygenated structures could have a significant impact on the catalytic dehydrogenation results using the Pd/phenanthridine system. Reggel et al. raised the question in their original papers in regard to the effect of phenolic groups on their catalytic dehydrogenation of coals. They found that certain phenolic compounds (not designated) yielded hydrogen on catalytic dehydrogenation "probably by reactions of the type"

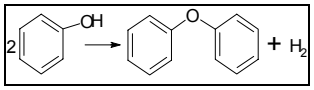

Figure 1. Postulated dehydrogenation of phenol[1].

Phenol as such does not exist in coal. We chose to investigate the catalytic dehydrogenation of 9-phenanthrol which has a phenolic group on a phenanthrene structure, in the absence and in the presence of coal. 9-Phenanthrol is a type of structure likely to exist in bituminous coal. Similar catalytic dehydrogenations, all in the Pd/$CaCO_3$-phenanthridine system, were carried out with "- and $-naphthols.

Analysis by GCMS of the residue from 9-phenanthrol dehydrogenation showed that evolution of hydrogen was due to reaction between two phenanthrol molecules to form aromatic ethers, by the reaction of a phenolic OH group with the aromatic ring in another phenanthrol molecule. The structure of this ether was confirmed by NMR spectroscopy and the overall reaction is given in Figure 2.

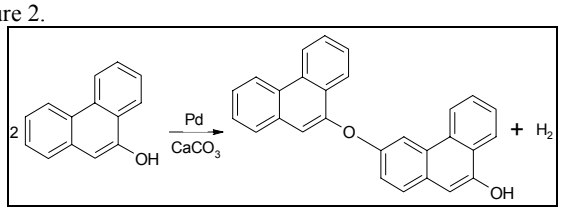

Figure 2. Dehydrogenation of 9-phenanthrol with Pd/$CaCO_3$ to form aromatic ethers.

The bond dissociation energy of a hydrogen atom attached to a benzene ring is about 103 kcal/mole; that of a benzylic hydrogen is about 85 kcal/mole. Hydrogens attached to the 9,10 position of 9,10-dihydroanthracene (9,10-DHA) or the 9,10 position in 9,10-dihydrophenanthrene (9,10-DHP) have much lower bond dissociation energies.

We therefore dehydrogenated mixtures of 9-phenanthrol with 9,10-DHA and also with 9,10-DHP. The amounts of hydrogen evolved were consistently lower than those which would be obtained by simple addition of the amount of hydrogen from the phenol plus that from the hydroaromatic compound.

The interaction has a negative influence on the rate of H_2 evolution and the final H_2 yield so that the actual yield is always less than theoretical. Proton NMR of the residue from the dehydrogenation of 9,10-DHA and 9-phenanthrol showed that there is a peak in the region of 4.9-5 ppm which is attributed to the formation of an aliphatic aromatic ether.

To determine if there was any interaction between 9-phenanthrol and coal during the catalytic dehydrogenation process, a mixture of 0.2 g of Illinois #6 coal was dehydrogenated, along with 0.2 g of 9-phenanthrol, using 0.3 g of Pd/$CaCO_3$ in phenanthridine. The results are shown in Figure 3. The final volume of hydrogen evolved for the mixture is less than that which would be obtained by adding the two individual volumes obtained from coal and 9-phenanthrol. This is an indication of the influence of phenolic structures likely to be present in coal on the evolution of hydrogen from what may be hydroaromatic substrates in coal.

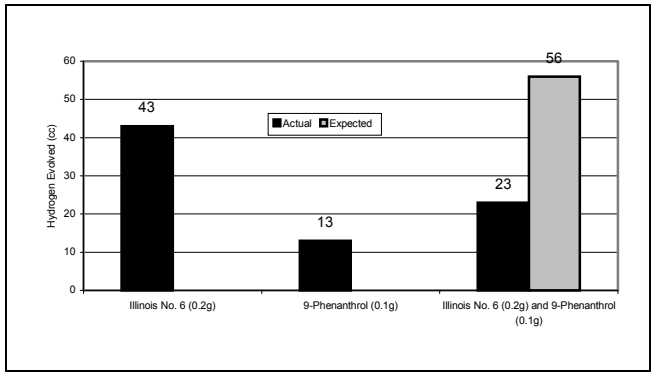

Figure 3. Final hydrogen yields from Illinois #6 coal, 9-phenanthrol and a mixture of the two.

Effect of Polycyclic Olefinic Structures. It is known that all petroleum contains optically active structures. Zahn et al. found that oils from the hydrogenation of coal at 450-525°C and 8000 psig still

contained distillates that were indeed still optically active. They postulated that part of these structures were probably derived from various steroids and terpenes.[6]

Many of the cyclic triterpenoid substances occur in organisms and their fate is of considerable interest as coal precursors. These include the tetracyclic steroids such as cholesterol in animals and sitosterol in plants; these compounds differ in structure only near the end of the aliphatic side chain.[7] All sterols are unsaturated alcohols, generally with an olefinic bond in one ring

We chose to investigate the dehydrogenation of the readily available cholesterol (Figure 4) in the same catalytic dehydrogenation system. No hydrogen was evolved from cholestane, a fully saturated naphthene. Cholesterol, with a single double bond evolved seven moles of hydrogen plus some methane per mole of cholesterol. When the hydroxyl group in cholesterol was blocked by formation of its silyl ether, only six moles of hydrogen were evolved. The one mole difference in the amount of hydrogen evolution indicated that two naphthenic hydrogens in ring A cannot be removed if the hydroxyl group is blocked.

It was not surprising to find that cholesterol is a very good vehicle for the dehydrogenation of coal; a better dehydrogenation solvent that even 9,10-DHA.

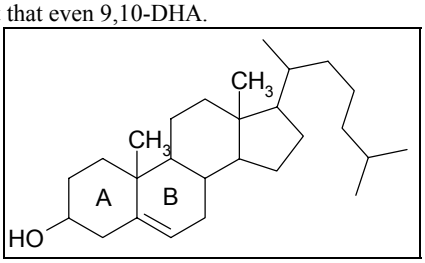

Figure 4. Structure of cholesterol.

It appeared possible that structures resembling cholesterol could be good hydrogen donors in direct coal liquefaction. We liquefied Illinois No. 6 coal using cholesterol as a donor solvent (400°C, 1000 psig of He). As shown in Table 1, the use of cholesterol in coal liquefaction resulted in both a high conversion and a higher oil yield as compared to the use of 9,10-DHA. Even partially dehydrogenated cholesterol gave higher conversions (THF solubles) and oil yields (pentane solubles) than did 9,10-DHA. The oils were characterized by simulated distillation. Lighter oils were obtained from the reaction of coal with cholesterol as solvent than with 9,10-DHA, indicating that naphthenic structures containing a single double bond in a ring can be superior hydrogen donors.

Acknowledgement. Support from the United States Department of Energy is gratefully acknowledged.

Table 1. Comparison of Hydrogen Donor Ability of Cholesterol with 9,10-DHA in Liquefaction of Illinois #6 Coal at 400°C.

Donor Solvent	Conversion (%)	Oil Yield (%)
9,10-DHA	66.7	18.8
Cholesterol	78.2	22.1
Partially Dehydrogenated Cholesterol	75.4	20.3

[1] Reggel, L;, Wender, I.; Raymond, R. *Science* **1962**, ***137,*** 681**.** *Fuel***, 1964**, *47*, 373; **1970**, *49*, 287; **1971**, *50,* 152*;* **1973***, 52*, 162.
[2]Larsen, J.W.; Ozik, M.; Lapucha,A.; Li, S. *Energy & Fuels*, **2001**,*15*, 801.
[3]Blom, L.; Edelhausen, L.; van Krevelen, D.W. *Fuel* **1959,** *38*, 537.
[4]Friedman, S.; Kaufman, M.L.; Steiner, W.A.; and Wender, I. *Fuel*, **1961**, *40*, 33.
[5] Skowronski, R.P.; Heredy, L.A.; Ratto, J.J.; Neuworth, M.B. *Am. Chem. Soc., Fuel Chem.Div. Reprints*, **1985**, 30(4), 333.
[6] Zahn, C.; Langer, S.H.; Blaustein, B.D.; Wender, I. *Nature*, **1963**, *200*, 53.
[7] Given, P.H. in *Coal Science*, Vol. 3, edited by Gorbaty, M.L., Larsen, J.W., and Wender I., "An Essay on the Organic Geochemistry of Coal", **1984**, 63.

Shape-Selective Catalysis for Specialty Chemicals from Coal-Derived Polycyclic Hydrocarbons

Chunshan Song

Clean Fuels and Catalysis Program, The Energy Institute, and Department of Energy & Geo-Environmental Engineering, The Pennsylvania State University, 209 Academic Projects Building, University Park, PA 16802-5000, USA
E-mail: csong@psu.edu; Fax: 814-865-3248

Introrduction

Coal-derived liquids, such as distillates from coal liquefaction, pyrolysis, and carbonization, are rich in polycyclic aromatic hydrocarbons. These PAHs are not desirable components of conventional liquid fuels such as gasoline or diesel fuels. However, they can be converted into value-added chemicals and advanced polymer materials.

There are some exciting developments in advanced polymer materials and specialty chemicals which present new opportunities for catalytic research on selective conversion of polycyclic compounds that can be obtained from coal-derived liquids and some refinery steams [1-4].

PAH Conversion

This presentation is a review of our recent studies on synthesis of value-added organic chemicals from 2-ring and 3-ring polycyclic hydrocarbons by selective conversion over certain 12-MR or 10-MR zeolite catalysts or zeolite-supported metal catalysts [4-7].

Early studies and publications on chemicals from coal till 1980s seem to be dominated by the approaches to obtain chemical feedstocks or commodity chemicals or alternate chemicals from coal in connection with alternate fuels from coal (as an alternative to petroleum-based fuels and chemicals). Such chemicals typically include olefins, BTX and phenol, which are currently produced in petrochemical industry.

However, our attention has been focused on how to make use of the unique structural features of the aromatic compounds, particularly polycyclic compounds, in coal-derived liquids for producing value-added organic chemicals.

Specifically, this review will discuss the new developments in the following catalytic reactions over large-pore zeolite catalysts:

(1) ring-shift isomerization of phenanthrene derivatives to anthracene derivatives;

(2) shape-selective alkylation of naphthalene for synthesizing 2,6-dialkylnaphthalene;

(3) shape-selective alkylation of biphenyl for synthesizing 4,4'-dialkylbiphenyl;

(4) conformational isomerization of cis-decahydronaphthalene into trans-decahydronaphthalene;

(5) shape-selective hydrogenation of naphthalene into either cis- or trans-decalin, and

(6) regio-selective hydrogenation of 1-naphthol and quinoline for synthesizing specialty fuel additives.

Schemes 1 to 8 illustrate these reactions. In most case, the selectivity strongly depends on the type and nature of catalysts, as well as reaction conditions.

Scheme 1. Ring-Shift Isomerization

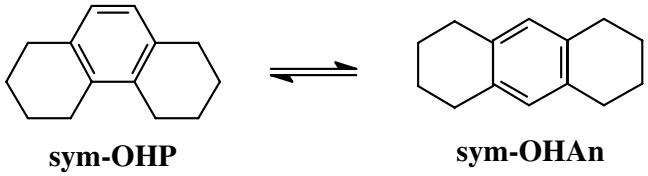

Scheme 2. Reaction Pathways for Ring-Shift of sym-OHP

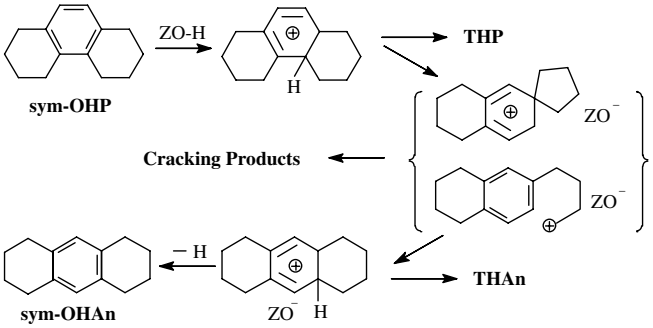

Scheme 3. Alkylation of Naphthalene

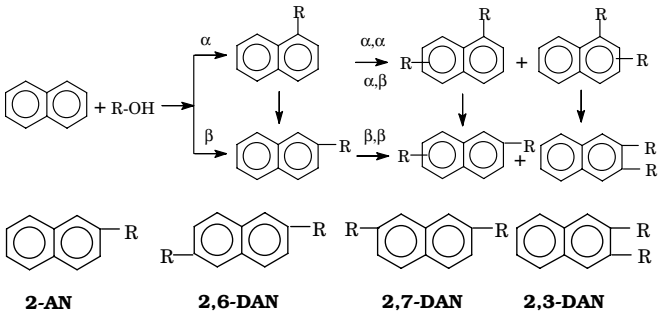

Scheme 4. Alkylation of Biphenyl

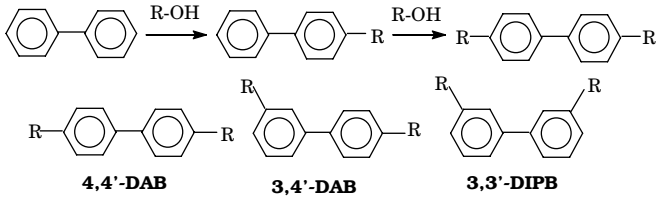

Scheme 5. Conformational Isomerization of cis-DeHN

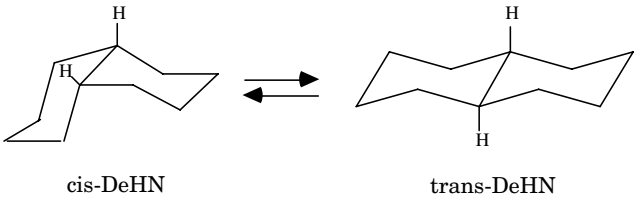

Scheme 6. Proposed reaction pathway for isomerization of cis-DeHN into trans-DeHN.

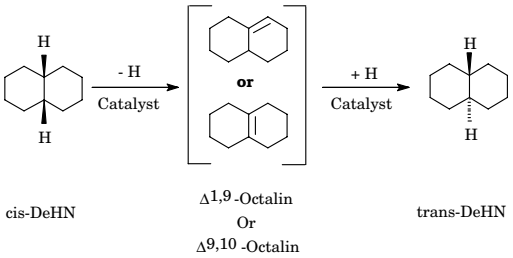

Scheme 7. Selective Hydrogenation of Naphthalene.

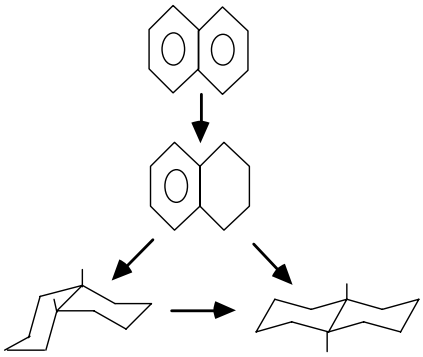

Scheme 8. Regio-selective Hydrogenation

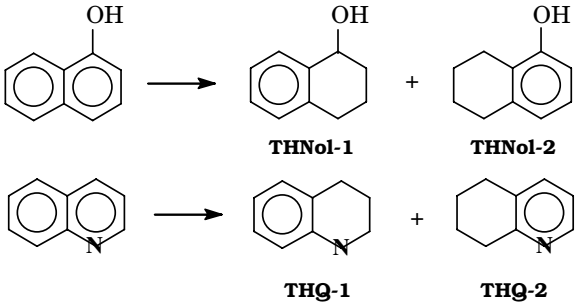

The products of the selective catalytic reactions discussed above are intermediates for making specialty chemicals, monomers of advanced polymer materials such as high-performance polyesters including polyethylene naphthalate, polybutylene naphthalate, and liquid crystalline polymers, and components of advanced thermally stable aviation jet fuels for high-Mach aircraft. The possible reaction mechanisms, pathways and factors affecting the selectivity have also been discussed [5-7].

Concluding Remarks

This presentation is a selective review based on recent studies in our laboratory. Selective catalytic conversion of PAHs can be very useful for making polycyclic specialty chemicals that have potential industrial applications.

Because of the presence of two or more isomers of polycyclic compounds, a major challenge is to direct the reaction along a very specific pathway to the desired isomer.

Substantial progress has been made in the applied fundamental research in the past several years. In many cases, further improvement in catalyst selectivity and stability is needed, and many fundamental questions concerning mechanistic aspects remain to be answered by future study.

Acknowledgments. The author is very grateful to Prof. Harold H. Schobert for encouragement and support for catalytic research, to his former and current coworkers including Drs. Andrew D. Schmitz, Wei-Chuan Lai, Shawn D. Lin, K. Madhusudan Reddy, Stephan Kirby, and Jian-Ping Shen for many helpful discussions, and to Prof. Paul B. Weisz of PSU and the late Dr. Werner O. Haag of Mobil for their encouragement. The author also wishes to thank Dr. Michael Ford of Air Products & Chemicals Inc. and Prof. John W. Larsen of Lehigh University for helpful discussions on the possible mechanism of sym-OHP ring-shift isomerization, and Dr. Juan M. Garces of Dow Chemical Company and Prof. Y. Sugi for general discussions on PAH conversion over zeolites. Various portions of our research were supported through funding or donations of special samples from the U.S. Department of Energy/National Energy Technology Laboratory, U.S. Air Force/Wright Laboratories, Air Products and Chemicals Inc., and PQ Co.

References

(1) Song, C.; Schobert, H. H. *Fuel Process. Technol.*, **1993**, 34, 157.
(2) Song, C.; Schobert, H. H. *Fuel*, **1996**, 75, 724.
(3) Sugi, Y.; Toba, M., *Catal. Today*, **1994**, 19, 187.
(4) C. Song, Stud. Surf. Sci. Catal., 1998, **113**, 163.
(5) Song, C.; Garces, J. M.; Sugi, Y. (Eds). Shape-Selective Catalysis. Chemicals Synthesis and Hydrocarbon Processing. American Chemical Society, Washington DC, ACS Symposium Series, Vol. 738, **1999**, 410 pp.

(6) Song, C. *Comptes Rendus de l'Academie des Sciences Series IIC Chemistry,* **2000**, 3, 477.
(7) Song, C. *Catalysis-Specialist Periodical Report*, RSC, **2001**, 16, in press.

Promoted Pt catalysts for the dry reforming of methane in the presence of oxygen

Venkatesh Phadnavis, Bakul Pant, and Susan M. Stagg-Williams

Chemical and Petroleum Engineering Department
4006 Learned Hall, University of Kansas, Lawrence, KS 66045

Introduction

The production of synthesis gas via CO_2 reforming of CH_4 received significant attention over the past decade as the push for environmentally friendly processes and the elimination of greenhouse gases became a major focus in industry. Even though it has been shown that the reduction of CO_2 is not a valid argument for dry reforming, interest in the reaction and finding stable catalytic materials has remained high. Reasons for this interest include the simultaneous presence of both reactants in natural gas reservoirs [1] and the ability to combine the dry reforming reaction with partial oxidation and steam reforming to obtain any ratio of H_2:CO in the synthesis gas [2].

Catalyst deactivation continues to be an obstacle at high temperatures and the majority of the research has focused on finding materials capable of withstanding the reaction conditions. Previous studies have shown that Pt metal supported on ZrO_2 promoted with La^{3+} and Ce^{4+} can be stable for the reforming reaction at 800°C and a 2:1 ratio of CH_4:CO_2 [3]. These results demonstrated that the reaction proceeded through a bifunctional mechanism in which methane decomposes on the metal resulting in the formation of hydrogen and carbon adsorbed on the metal. This carbon can react with oxygen from the support to produce carbon monoxide and create an oxygen vacancy in the support near the perimeter of the particle. Carbon dioxide adsorbs at the vacancy site and dissociates to form CO and replenish the support oxygen. The balance between the rate of decomposition and dissociation determines the overall activity of the catalyst. The addition of the promoters resulted in a support that facilitated the reaction mechanism and substantially improved the stability and overall catalytic performance. The Ce-promoted catalysts were found to be more readily reducible which aided in the removal of the carbon species from the metal. The La-promoted catalysts helped to retard particle growth and had increased CO_2 adsorption and dissociation capability.

More recent studies have shown that the loading of Ce in the support impacts the catalytic performance, and the activity can be correlated to the reducibility of the oxide [4]. XPS studies have shown that catalysts with 50% Ce and 50% Zr exhibited the highest degree of Ce reduction and the highest activity. Previous studies have shown that the addition of Ce and La to ZrO_2 does not result in a significant increase in catalytic performance [5] however; no investigations to explain the observed activity have been performed.

In this contribution we are focusing on the promotion of ZrO_2 with both Ce and La and the effect of the components on the Pt metal. We have prepared 0.5 wt% Pt supported on Ce-, La-, and CeLa-doped ZrO_2 and characterized the materials using TPR, BET surface area measurements, H_2 chemisorption, and pulse studies. The activity and stability of these materials has been compared to a 0.5 wt% and 1.5 wt% Pt/ZrO_2 catalyst for the dry reforming reaction in the presence and absence of oxygen.

Experimental

The ZrO_2, lanthanum (5 wt%)–doped ZrO_2, cerium (18 wt%)-doped ZrO_2, and lanthanum (5 wt%)-cerium (18 wt%)-doped ZrO_2 were all obtained from Magnesium Elektron Inc. Prior to the addition of the metal the supports were calcined at 800°C in stagnant air for 4 hours. Pt was added to the supports using incipient wetness impregnation of an aqueous solution of $H_2PtCL_6 \cdot 6H_2O$. The metal loading on the promoted catalysts was 0.5 wt%. Two un-promoted samples were made, with metal loadings of 0.5 wt% and 1.5 wt%. The nomenclature for the unpromoted catalysts will be 0.5PZ and 1.5PZ, respectively. All of the catalysts were dried overnight at 110°C, and then reduced *in-situ* in H_2 (30 cm^3/min) at 500°C for 1.5 h, prior to reaction.

Dry reforming activity measurements were performed in a quartz flow reactor at 800°C using a CH_4:CO_2 ratio of 1:1 and a GSHV of 180,000 h^{-1}. For the experiments in the presence of oxygen, the composition of the feedstock was 61.5 % CH_4, 10.5 % CO_2, and 28 % O_2. The GSHV for these reactions was 85,000 h^{-1}. Temperature-programmed reduction (TPR) experiments were performed on each sample. The samples were heated to 800°C at a rate of 6.5 °C/min in a stream of 5% H_2/Ar (30 cm^3/min).

Pulse studies were performed on each sample at 800°C following the pretreatment described for the activity experiments. The catalysts were exposed to 100 μL pulses of CH_4 followed by pulses of CO_2 and then CH_4. Information about the H_2 and CO production during each pulse was obtained using a mass spectrometer (Pfeiffer Vacuum).

Results and Discussion

Table 1 shows the BET surface area and the H_2 chemisorption measurements for the various catalysts. Chemisorption values were taken after reduction at 500°C and heating to 800°C in He, to simulate the particle size at the beginning of the reaction. The surface area for the promoted catalysts was much higher than the observed surface area of the unpromoted ZrO_2. The support containing both Ce and La had a surface area greater then 200 m^2/g. These results are in agreement with previous studies [4], in which x-ray diffraction was used to demonstrate that the promoters stabilize the tetragonal form of the ZrO_2 leading to increased surface areas after high temperature calcination.

Table 1. BET Surface Area and Chemisorption Measurements of the Catalysts Investigated

Catalyst	BET surface Area (m^2/g)	Dispersion (%)
0.5PZ	24.862	35.012
1.5PZ	24.862	17.669
PCZ	49.257	23.96
PLC	53.997	9.19
PLCZ	224.92	14.98

Pulse studies performed on the various catalysts allow for the probing of the degree of support reduction and the ability of the support to facilitate CO_2 dissociation. The degree of reducibility of the support can be observed by monitoring CO production during pulses of pure CH_4, while the CO_2 dissociation can be monitored by the CO produced during pulses of CO_2. The ability of the catalyst to remove carbon deposited during the reaction can be observed by comparing the amount of H_2 produced in the first pulse of each series of CH_4 pulses. Pulse studies performed on the PCZ, PLZ, and PLCZ, showed that the presence of Ce results in more CO produced during CH_4 pulses, and thus a more readily reducible oxide. The catalysts containing La showed more CO_2 dissociation capability which agrees with TPD results reported elsewhere [6]. Finally, unlike the 0.5PZ catalyst, the promoted catalysts all show the ability to effectively remove carbon from the metal by exhibiting similar hydrogen production during the first pulse of each set of CH_4 pulses.

Based on the BET surface area, the measured dispersion, and the knowledge of the role of the promoters we anticipated that the

addition of both promoters would utilize the increased reducibility of ceria and the enhanced CO_2 dissociation of La to improve the catalytic performance. Contrary to what we anticipated, Figure 1 shows that the PLCZ catalysts did not exhibit improved performance for the dry reforming reaction. The methane conversion on the dual promoted material was less than the La- or Ce-doped material as well as the unpromoted catalysts. Figure 1 also shows that the PCZ and PLZ catalysts were more active than the 1.5PZ catalyst even with three times less Pt. Finally, the 0.5PZ catalyst, although having the highest initial activity, experienced significant deactivation during the 15 hour reaction. The conversion of methane observed after 15 hours was less than the 1.5PZ catalyst and was still decreasing.

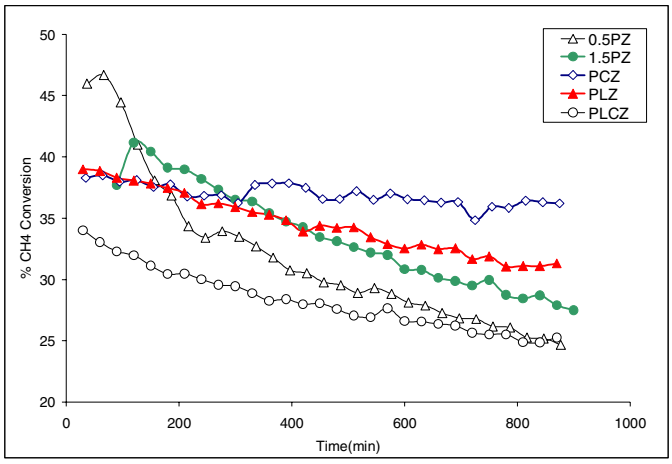

Figure 1. CH_4 conversion during dry reforming reaction at 800°C with 1:1 feed ratio of CH_4:CO_2 (GHSV=180,000 h^{-1}).

The high initial activity of the 0.5PZ catalyst is not surprising based on the dispersion values measured by chemisorption. Using the chemisorption information and assuming that all particles on the catalyst were uniform in size and shape, an average particle size was determined for each catalyst. Using the particle size, an estimate was made of the perimeter of the particle and ultimately the total contact area of the metal and support. If the catalyst with the higher loading of Pt had more total interfacial area this might explain the observed higher stability. However, our results show that based on the pre-reaction chemisorption, the 0.5% Pt catalyst had the most interfacial area, and therefore should exhibit the highest stability. X-ray absorption studies have suggested that sintering of the Pt particles at 800°C may be responsible for the deactivation of the Pt/ZrO_2 catalyst due to the loss of the metal-support interfacial area [6]. Our chemisorption results suggest that if particle size is the primary factor in determining long-term activity, then sintering of the metal particle not during the pretreatment, but during the reaction, resulting in a dramatic decrease in activity. In addition, the 1.5 wt% Pt/ZrO_2 catalyst appears to be more resistant to sintering resulting in a more stable catalyst with higher long-term activity. Further investigations are being performed to determine the optimal Pt metal loading for the dry reforming reaction.

TPR experiments performed on the 0.5PZ and 1.5PZ catalysts show that the reduction of PtO to metallic Pt occurs in the temperature range of 180-200°C. Similar results were obtained on the PCZ catalyst. A shift in the reduction temperature was observed on the catalysts containing La. On the PLZ catalyst the reduction of PtO appears at 220°C, while on the PLCZ catalyst the shift is even greater with complete reduction not occurring until 300°C. The shift in reduction temperature indicates a modification of the Pt by the support. XPS studies are currently being performed to determine if the Pt is being altered due to the presence of the La and Ce.

Figure 2 shows the results of the reaction of CH_4 and CO_2 in the presence of O_2. The promoted catalysts still perform better than the unpromoted catalyst with the same loading of metal. The performance of the promoted catalysts in the presence of O_2 is very similar, with a final conversion of CH_4 after 15 hours within 2%. It is interesting to note that unlike the dry reforming reaction, the CH_4 conversion observed on the 1.5PZ catalyst in the presence of O_2 was higher than the promoted materials. These results suggest that the beneficial effect of the promoters in facilitating the two path mechanism may not be as significant when oxygen is present to assist in carbon removal from the metal.

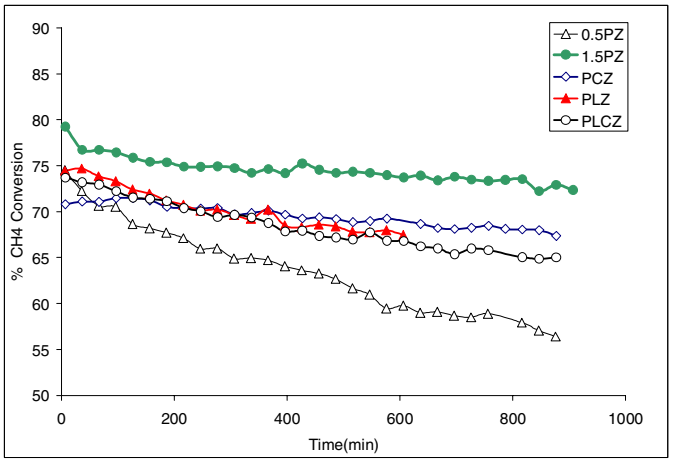

Figure 2. CH_4 conversion during dry reforming reaction in the presence of oxygen at 800°C with a feed composition of 61.5% CH_4, 28% O_2, and 10.5% CO_2 (GHSV=85,000 h^{-1}).

Conclusions

The results of this work have shown that the addition of both La and Ce to Pt/ZrO_2 catalysts does not result in improved performance for the dry reforming reaction. Although the material does show high surface area, good metal dispersion, increased reducibility, and increased CO_2 dissociation capabilities, the methane conversion observed is significantly lower than that observed on the $LaZrO_2$ and $CeZrO_2$ supports. The decreased activity could be due to modification of the Pt by the support as observed through TPR studies. XPS characterization is being performed to further explain the source of the modification. In the presence of O_2, the beneficial effects of the promoters may not be as significant due to the ability of the O_2 to aid in carbon removal from the metal.

References

(1) Takano, A.; Tagawa, T.; and Goto, S., *J. Chem. Eng. Jpn.*, **1994**, *27*, 727.
(2) Choudhary, V. R.; Uphade, B. S.; and Mamman, A. S., *Appl. Catal. A,* **168**, 33 (1998).
(3) Stagg-Williams S, M; Noronha, F. B; and Resasco, D. E., *J. Catal.*, **2000**, *194(2)*, 240.4
(4) Noronha, F. B.; Fendley, E.C; Soares, R. R; Alvarez, W. E; and Resasco, D. E, *Chem. Eng. Journal,* **2001**, *82*, 21.
(5) Stagg-Williams, S. M.; Soares, R. R,; Romero, E.; Alvarez, W. E; and Resasco, D. E , *Stud. in Surf. Sci. and Catal.*, **2000**, *130,* 3663.
(6) Stagg, S. M.; and Resasco, D. E , *Stud. in Surf. Sci. and Catal.*, **1998**, *119,* 813.

GAS-TO-LIQUIDS TECHNOLOGY
- FT CATALYSIS IN EXXONMOBIL'S AGC-21 PROCESS -

R. A. Fiato, E. Iglesia and S. L. Soled,*
ExxonMobil Research and Engineering Company
1545 Route 22 East
Annandale NJ 08801

Abstract. Conversion of natural gas to liquids (GTL) utilizing Fischer-Tropsch (FT) hydrocarbon synthesis technology is an attractive option to bring static gas resources to market. ExxonMobil's Advanced Gas Conversion for the 21st Century (AGC-21)[1] is state-of-the-art GTL technology that provides an important commercial option for utilization of stranded natural gas around the world. Continuing research at ExxonMobil is leading to additional catalyst and technology improvements that will further reduce the cost of producing liquids from natural gas. This article discusses advances in ExxonMobil's AGC-21 technology achieved over the years as a result of an ongoing, comprehensive research, development and engineering program.

INTRODUCTION

Over the last decade, there has been renewed interest in the production of synthetic fuels via Fischer-Tropsch synthesis, using synthesis gas produced from remote natural gas.[2] Emphasis is being placed on use of cobalt catalysts in fixed bed and slurry reactors to achieve high yields of paraffinic wax that can be further converted to other products.

ExxonMobil's three step AGC-21 process is shown in Figure 1.[4-9]

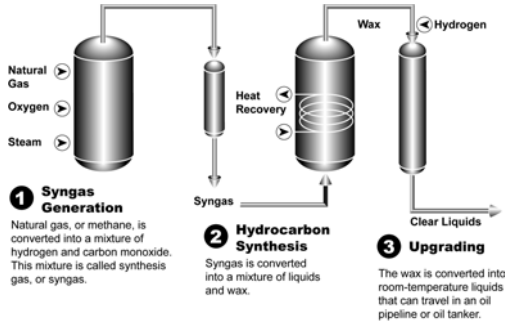

Figure 1 – AGC-21 Flow Scheme

HYDROCARBON SYNTHESIS

ExxonMobil's Fischer-Tropsch HCS technology operates in a novel slurry reactor, using new, high-activity thin layer cobalt catalysts under controlled hydrodynamic operating conditions. The combination of the slurry reactor design with advanced catalyst tailored for slurry reactor operation has resulted in higher hydrocarbon productivity levels and selectivity to 650°F+ boiling material than previously thought possible.

Over the past two decades ExxonMobil has pioneered the development of cobalt catalysts and advanced slurry reactors for high productivity wax synthesis.

The high performance HCS process is characterized by the achievement of high catalyst activity, high selectivity to C10+ hydrocarbon yield and low rate of catalyst deactivation, resulting in sustained operations at high productivity and high yield. While improvements in either activity, selectivity or activity maintenance have been reported in the literature, AGC-21 technology is unique in having achieved all three of these attributes simultaneously.

ExxonMobil has patented cobalt catalyst systems consisting of cobalt on inorganic oxide supports, including titania, alumina, silica and silica-alumina. The preferred formulation consists of cobalt on modified titania, specifically tailored for slurry Fischer-Tropsch operation, to achieve high C10+ productivity[7-8] The catalyst is designed to avoid diffusion limitations associated with intraparticle mass transfer, which is particularly important when operating at high productivities. Performance tests have shown that by maintaining cobalt in a dispersed RIM or thin layer on the outer surface of the catalyst, it is possible to achieve very high productivity with minimum gas make. The thin cobalt layer minimizes relative H_2 and CO diffusion rates and also avoids particle overheating.

The catalyst composition and activation procedures provide high activity and the manner in which it is fabricated results in high selectivity to desired high molecular weight products under moderate slurry reactor operating pressures. The catalyst is also highly resistant to attrition, which is particularly important for efficient separation of the catalyst from the HCS reactor product.

As shown in Figure 3 Current HCS reactor productivity is more than double previously reported ExxonMobil performance, and more than four times recently reported iron slurry results. Progress in increasing reactor productivity, which translates into fewer reactors required to achieve desired plant capacity, is continuing, with the ongoing research advancing new catalysts that show promise of further substantial increases in productivity.

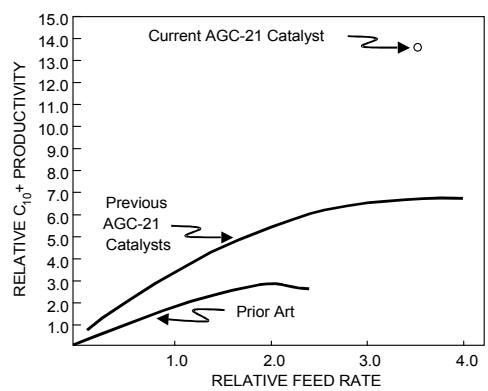

Figure 3 – Relative Productivity vs. Relative Feed Rate

A plot of HCS reactor performance during a large scale pilot plant run is shown in Figure 4. High levels of productivity with low methane yield were demonstrated in extended operations. This was achieved through use of a proprietary catalyst rejuvenation system that maintains a high level of catalyst activity by stripping reaction inhibitors from the catalyst surface, coupled with good catalyst fluidization.

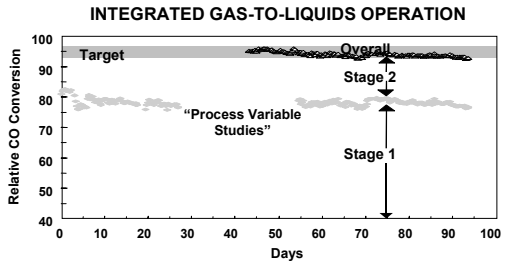

Figure 4 – Days of Operation vs. CO Conversion

This high level of performance is consistent with the fundamental understanding developed over years of research in the areas of reaction kinetics, hydrodynamics and catalytic surface chemistry relationships that impact activity maintenance. This understanding is used to set conditions and operating procedures that have extended previously accepted performance limitations and identified additional process improvement opportunities.

* Current Address: Department of Chemical Engineering, University of California, Berkeley.

REFERENCES

1. AGC-21 is a proprietary process name of ExxonMobil Research and Engineering Company, Florham Park, New Jersey, U.S.A. 07932.
2. Storch, H. H., Golumbic, N., Anderson, R. B., *The Fischer-Tropsch and Related Syntheses,* John Wiley & Sons, New York, 1951; and references therein.
3. Tower, A.W., III, "Fischer-Tropsch Technology," published by Howard, Weil Labouisse, Friedrichs, December 1998; and references therein.
4. Eidt, C.M., Jr., "Emerging Technologies for Fossil Fuel Processing and Products", presented at the Agency for Assessment and Application of Technology (BPPT) Conference, Jakarta, Indonesia, August 25, 1993.
5. Eisenberg, B., Lahn, G.C., Fiato, R.A., and Say, G.R., "Exxon's AGC-21 Advanced Gas Conversion Technology", presented at Alternate Energy '93, Council on Alternate Fuels, April 27-30, 1993.
6. Ansell, L.L., Eisenberg, B., Bauman, R.F., and Say, G.R., "Liquid Fuels From Natural Gas -- An Update of the Exxon Process", presented at Alternate Energy '94. Council on Alternate Fuels, April 26-29, 1994.
7. See for example: Arcuri, K. B., Behrmann, W. C. and Mauldin, C. H., US Patent 5,128,377, 1992 and US Patent 5,545,674, 1996.
8. See for example: Baumgartner, J., Fiato, R. A., Iglesia, E., Soled, S. L., Vroman, H., US Patent 5,036,032, 1991.
9. Everett, B.M., Eisenberg, B., and Bauman, R.F., "Advanced Gas Conversion Technology: A New Option for Natural Gas Development", presented at the First Doha Conference on Natural Gas, March 14, 1995.

FISCHER-TROPSCH SYNTHESIS MECHANISM – STORCH WAS CORRECT?

Burtron H. Davis
Center for Applied Energy Research
University of Kentucky
2540 Research Park Dr.
Lexington, KY 40511

Storch experienced during a brief period the best of times and the worst of times. The U.S. had just experienced WW II and a demonstration of the impact of a plentiful fuel supply. To overcome the lack of a supply of petroleum, Germany developed a synfuels industry based on direct and indirect coal liquefaction during the 1930's. The German synfuels industry developed to the extent that it made a significant contribution to the overall supply of transportation fuel until production was severely hampered by Allied bombing. The U.S. petroleum production was not significantly hampered by the war effort and the industry expanded to provide about four of the five billion barrels of fuel needed for the Allied effort in Europe. Research efforts were rapidly utilized in various efforts, including the Manhattan Project and the petroleum industry. At the end of WW II, the research directors were very positive in their attitude toward the benefit of research (1,2). There was a general consensus that the world was facing a severe shortage of petroleum crude. For example, Dobie Keith founded Hydrocarbon Research, Inc. to develop a commercial Fischer-Tropsch plant at Brownville, Texas. Because of the anticipated shortage, the U.S. Bureau of Mines was able to develop a major research effort in both direct and indirect coal liquefaction. This effort, headed by Henry H. Storch, led to the development of major pilot plants for direct and indirect coal liquefaction In 1944, the 78th Congress passed an act authorizing the construction and operation of demonstration plants to produce synthetic liquid fuels from coal, oil shales, agricultural and forestry products, and other substances, in order to aid the prosecution of the war, to conserve and increase the oil resources of the Nation, and for other purposes (3). The funding authorization was $30 million, and this was increased to $87 million, with $85 million actually appropriated. Approximately $10 million was expended to construct direct and indirect coal liquefaction pilot plants at Louisiana, Missouri; this was a major project at that time. In addition to the major funding devoted to both basic and development research, the Bureau worked to compile the literature and to provide major reviews, including translations of the materials obtained in Germany and Japan following WW II. In 1945 Storch headed a group of more than 300.

Storch, together with Norma Golumbic and Robert B. Anderson, wrote the definitive book on Fischer-Tropsch in 1951 (4). In subsequent years, Pichler is reported to have indicated that this book was flawed since the Germans, following WW II, did not provide accurate data to the U.S. scientists (5). However, considering the extensive reviews of German work prior to, and the primary documents obtained following, WW II, this assertion does not appear to be valid. Thus, in 1950 Storch was in an enviable position, heading an exceptionally well-funded research and development activity.

With the recognition of the vast reserves of petroleum available in the Middle Eastern countries in the early 1950s, governments of developed countries lost interest in a synfuels industry. In the U.S., there was a dramatic reduction in funding of research by the government for synfuels research and Storch faced the unpleasant task of having his research activities dramatically reduced.

The mechanisms predating 1950 were reviewed in Storch's book and then the mechanism supported by the Bureau's work, and reinforced by the ^{14}C tracer studies, was presented. In this mechanism it was assumed that (a) hydrogen is chemisorbed as atoms; (b) carbon monoxide is chemisorbed on surface metal atoms in a manner similar to that postulated for bonds in metal carbonyls; and (c) the adsorbed carbon monoxide is partially hydrogenated according to equation 1. Chain-building reactions occur in two ways: (a) by addition to end carbon atoms (equations 2 and 3) and (b) by addition to adjacent-to-end carbons (equations 4 and 5). It was postulated that double bonds between carbon and metal atoms were more resistant to hydrogenation if the carbon atom is also attached to a hydroxyl group. Intermediate β may grow by reaction 5 to produce a product with a methyl side chain while intermediate α will grow to produce normal products. Equations 6 and 7 illustrate ways of terminating the growth of chains. According to equation 6, aldehydes and alcohols result from desorption and hydrogenation of the alcohol-like groups at the surface. Equation 7 leads to olefin and paraffin products.

Chain Initiation

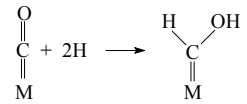

(1)

Chain Growth

a. At end carbon

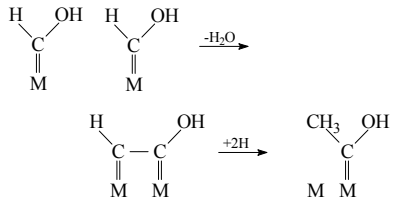

(2)

and for the general case

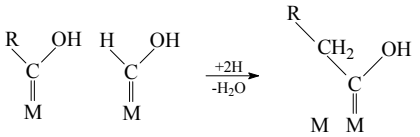

(3)

b. At adjacent-to-end carbon

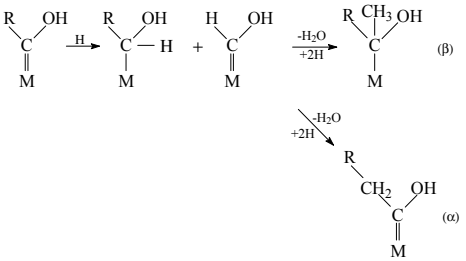

(4)

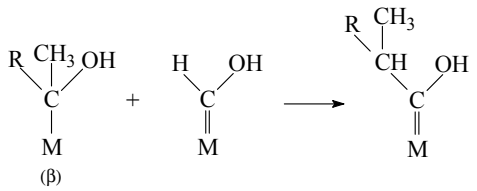

(5)

Chain Ending

a.

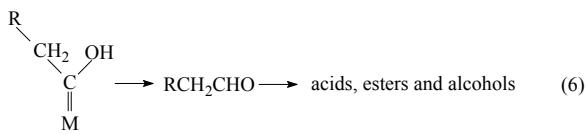

(6)

b.

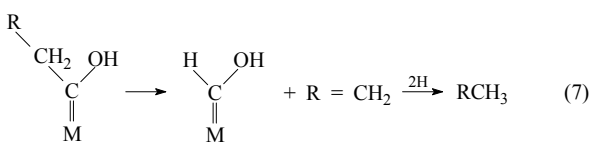

(7)

The popularity of this mechanism outlived Storch but the widespread utilization of surface science instruments in the 1970's produced results that led to abandonment of the oxygenate mechanism in favor of a surface carbide mechanism. For example, measurements of the surface concentrations following adsorption of the reactants, always at low pressure, showed a surface rich in carbon but very low, or undetectable, levels of oxygen. These results were interpreted to indicate that adsorbed CO rapidly dissociated to form adsorbed carbon and oxygen. Hydrogenation of adsorbed oxygen was considered to be very rapid, as was the desorption of the water that formed, in order to account for the low levels of oxygen. The hydrogenation of adsorbed carbon to form adsorbed CH_x species was slow compared to the hydrogenation of O. In fact, this was used to explain the inverse kinetic isotope effect obtained with deuterium. We have also obtained an inverse kinetic isotope effect with an iron catalyst but when all products are considered rather than just the disappearance of CO, the situation is very complex. Today the surface carbide mechanism is the one that is almost universally accepted.

We have obtained data, using ^{14}C tracers, that agree with the Storch mechanism better than with the surface carbide mechanism. Some of these results are outlined below.

We have determined the ^{14}C distribution in the products obtained when ^{14}C-1-propanol or ^{14}C-2-propanol is fed together with the syngas. The surprising conclusion is that 1-propanol produces predominantly n-products. 2-Propanol contributes to the products to a lesser degree than 1-propanol and produces predominantly iso-products (branched chain products). The loss of the oxygenate group from either alcohol would lead to the same intermediate if the half-hydrogenated intermediate is able to isomerize:

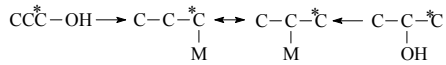

(8)

Since obtaining data with these ^{14}C-labeled alcohols, we have obtained conclusive evidence to show that the isomerization shown above for the half-hydrogenated state does occur at a rate that is rapid compared to FTS (6). The simplest explanation for these observations is that the oxygenate species is retained until the irreversible reaction leading to the final product occurs.

Another observation was the conversion of 1-^{14}C-1-pentanol. Here, the CO_2 produced had a significantly higher concentration of ^{14}C than CO. If the reverse hydrocarbonylation reaction had occurred, as shown in equation 9, this could not have happened.

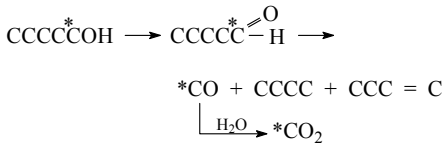

(9)

For the CO_2 to have been formed from CO, the radioactivity/mole of the CO_2 could only be equal to that of CO but could never exceed that of CO. Experimentally, it was found that the ^{14}C in CO was very much lower than in the CO_2. Furthermore, the activity in CO and CO_2 that was formed from 2-^{14}C-1-hexanol was very low, indicating that the carbonyl carbon was lost predominantly as CO_2. It is proposed that the adsorbed n-alcohol reacts with surface oxygen to form a species that is similar to, or the same as, an adsorbed carboxylic acid which then undergoes conversion by eliminating CO_2 as shown below:

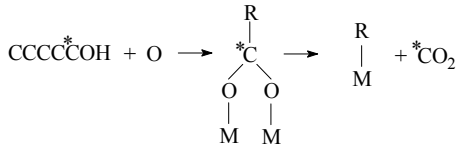

(10)

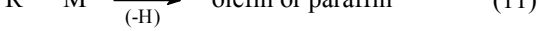

(11)

Another experiment that provided data to support an oxygenate mechanism was obtained during the conversion of $^{14}CO_2$, added to the syngas at about 2% of the CO. The results are shown in Figure 1. If the hydrocarbon products are formed only from CO, the methane could never have a greater ^{14}C content than the CO. As shown, this is not the case. Furthermore, the C_2 products can only have a ^{14}C content that is two times that of the CO; again, this is not the case. All hydrocarbon products have a much higher ^{14}C content that the CO. It therefore appears that the CO_2 that is converted to hydrocarbons does so not by first being converted to CO and then hydrocarbons but by being initiated by a species that is formed from CO_2. Based on the data shown in figure 1, it appears that about half of the CO_2 that is converted goes to produce hydrocarbons and the other

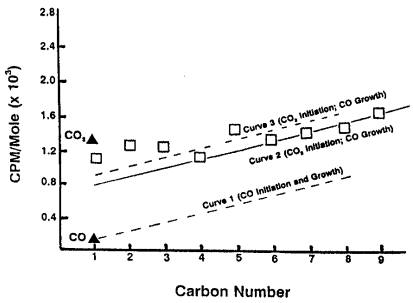

Figure 1. Radioactivity in products when $^{14}CO_2$ is added to the synthesis gas.

half to produce CO by the reverse water-gas-shift reaction. To account for this observation, it is proposed that the intermediate responsible for the water-gas-shift reaction also initiates FTS. A likely intermediate resembles an adsorbed formate.

In summary, we have gone through at least three cycles of intense interest followed by neglect for indirect liquefaction since Storch's best period. The interest in FTS now appears to be one of optimism. It also appears that at least for an iron catalyst the FTS mechanism involves an oxygenate species and not a surface carbide intermediate. In this respect, we believe that the Storch mechanism is more appropriate for an iron catalyst than the carbide mechanism.

Acknowledgment. This work was supported by U.S. DOE contract number DE-FC26-98FT40308 and the Commonwealth of Kentucky. The author is especially appreciative of the effort expended by several members of the Fuel Chemistry Division to keep the Storch Award alive - this has not been an easy task even though Storch certainly merits the continued recognition the award provides.

References

(1) The Future of Industrial Research, Papers and Discussion, Standard Oil Development Co., 1945.
(2) R. P. Eischens, personal communication to B. Davis.
(3) The Bureau of Mines Synthetic Liquid Fuels Program, 1944-55, Report of Investigations 5506, 1959.
(4) H. H. Storch, N. Golumbic and R. B. Anderson, "The Fischer-Tropsch and Related Syntheses," John Wiley & Sons, Inc, New York, 1951.
(5) A. Geertsema, private communication to B. Davis.
(6) B. Shi, R. J. O'Brien, S. Bao and B. H. Davis, J. Catal., 199, 202 (2001).

Asphalt from co-hydrogenation of coal and catalytic cracking residue

Yongbing Xue, Jianli Yang, Zhenyu Liu, Zhiyu Wang

State Key Laboratory of Coal Conversion, Institute of Coal Chemistry, Chinese Academy of Sciences, P.O. Box 165, Taiyuan, Shanxi 030001, P.R. China

Introduction

Coal, as a primary energy resource and air pollution source in China, is demanded to be used as efficient and clean as possible. Catalytic cracking residues (CCR) from petroleum refineries, with an annual production of more than 2 million tones in China, is difficult to be further processed because it contains large amounts of aromatics and heavy metals. Recently, it has been demonstrated that asphalt produced by hydrogenation of coal with CCR may be used as high grade paving asphalt[1-4]. This is important since the need of high grade paving asphalt is increasing with the fast growing of the highway construction in China. In addition, oil can also be produced to make the co-hydrogenation process economical. In this paper, asphalt produced from hydrogenation of Yanzhou coal with three CCRs was studied. The yield, and the chemical and rheology properties of the asphalt were included.

Experimental

Yanzhou coal from Shandong China was used, its properties are listed in Table 1. Three catalytic cracking residues named as CCR1, CCR2 and CCR3 were used. CCR1 and CCR2 were from Shijiazhuang petroleum refinery and CCR3 was from Shenghua petroleum refinery. The properties of the CCRs are given in Table 2. An iron catalyst was impregnated on the coal. The hydrogenation was carried out at 400 ^{o}C for 1 hour under a hydrogen pressure of 7 MPa (cold) in an 1-liter autoclave.

Table 1. The proximate and ultimate analyses of Yanzhou coal

Proximate anal. wt%			Ultimate anal. wt%				
Mad	A_{ad}	V_{daf}	C_{daf}	H_{daf}	O^{*}_{daf}	N_{daf}	S_{daf}
2.5	6.7	43.9	80.8	5.1	1.2	3.7	9.2

*: by difference; ad: air dry; daf: dry ash free.

Table 2. The properties of the catalytic crack residue(CCR)

	Ultimate analysis wt%				
	C	H	O	N	S
CCR1	88.92	8.12	0.37	0.32	1.14
CCR2	87.81	9.34	0.36	0.41	0.96
CCR3	85.33	10.88	0.48	0.25	0.96
	Group compositions wt%				
	Saturates	aromatic	resin	asphalte	
CCR1	8.1	60.4	27.3	4.2	
CCR2	39.36	36.82	18.24	5.58	
CCR3	10.07	35.00	33.38	21.55	

The hydrogenation products were separated into residues, preasphaltene and toluene solubles by using tetrahydrofuran (THF) and toluene as extraction solvent[1]. Asphalt was obtained by distilling out the light products from the toluene solubles.

Thin layer chromatograph coupled with a flame ionized detector (TLC-FID) was used for group composition analysis. Hexane, toluene, and trichloromethane(95%) + methanol (5%) were used to separate the asphalt into four compositions: saturates, aromatics, resin and asphaltenes. The rheology properties were measured by Cannon Rotary Viscometers.

Results and Discussion

Effects on conversions and yields: The coal and the CCRs were hydrogenated at the reaction conditions separately. Results are shown in Figure 1. It can be seen that both the THF conversion and the asphalt yield of the coal and the CCRs are significantly different. All the CCRs show high THF conversions (>95%) and high asphalt yields.

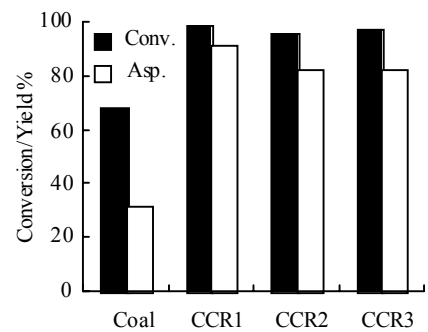

Fig. 1 Conversion/Yield of coal and CCRs

Co-Hydrogenation of the coal and a CCR was carried out at different coal-to-CCR ratios. Synergic effect on the asphalt yield is defined as the difference in asphalt yield between experimental data and the theoretical calculation. The theoretical calculation was made through mathematical addition of the results from individual hydrogenation runs weighted by the coal-to-CCR ratio. Figure 2 gives the experimental and calculated asphalt yields along with the synergic effects for the co-hydrogenation of Yanzhou coal with CCR1. The co-hydrogenation results of the coal and the other two CCRs are similar.

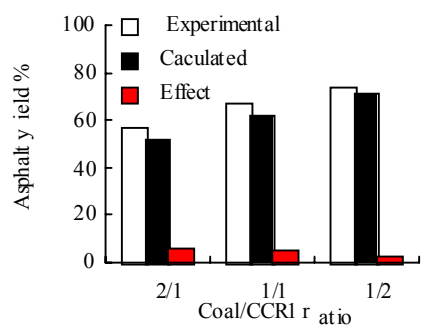

Fig. 2 Asphalt yields and synergic effects

Compared to the hydrogenation of the coal and the CCR alone, the synergic effect is obvious although the effect level is different for different CCRs. The main reason may be that the CCR is not only functioning as a reactant but also a reaction solvent during the co-hydrogenaction. Coal particles can be solved, swollen and dispersed by the reaction solvent. Hydrogen can be supplied and transferred by a hydrogen donor solvent[5]. All the three CCRs contain over 30% aromatic compounds. The group compositions (see Table 2) are closed to that of the coal liquids. From chemistry point of view, these CCRs are good hydrogen transfer and coal dissolution solvents.

Effects on group compositions of the asphalt: Results of group composition analysis for the asphalt produced are given in Table 3. Generally, saturates and aromatics increase with the increase of the CCR concentration in the feed stock. Resin and asphaltenes decrease with the increase of the CCR concentration. These results suggest that the saturates and aromatics are mainly from CCRs and resins asphaltenes are mainly from the coal.

Table 3. The group compositions of the asphalt produced

	Coal:CCR	Saturates	Aromatics	Resin	Asphaltene
CCR1	2:1	4.90	12.80	57.20	25.70
	1:1	5.13	24.51	59.05	11.31
	1:2	25.07	29.92	29.83	15.18
CCR2	2:1	16.73	13.39	44.57	25.31
	1:1	26.63	14.82	34.28	21.77
	1:2	10.92	18.10	52.78	18.20
CCR3	2:1	3.04	6.21	60.88	29.87
	1:1	35.94	17.33	33.12	13.61
	1:2	45.53	27.15	23.27	4.05

In the view of paving asphalt[6], saturates components worsen asphalt property. The less the saturate content is, the better the asphalt quality is. The saturate concentration must be controlled to a limited amount in high grade paving asphalts. Aromatic component can dissolve micelles formed by resins and asphaltenes and is a necessary component to make asphalt in the sol-gel state that has high viscous-elastic effects. Resin is the key component for the good viscous-elastic property. Asphaltenes act as enters for promoting the formation of the micelles. It also adsorbs resin. So a certain amount of asphaltenes is also necessary to form micelles. But excessive amount of asphaltenes will result to low penetration, high softening point and low ductility. In fact, the first two products listed in Table 3 (rows 2 and 3) have demonstrated their satisfaction in meeting the Chinese National Standard (GB/T 15180-94) for high grade paving asphalt in terms of penetration, softening point and ductility.

Rheological properties of the asphalts: Rheology properties are important in determination of asphalt application, especially in road paving[7]. The changes in viscosity of a number of asphalts with temperature at a number of spin rates were measured. Figure 3 shows viscosities of three asphalts, a commercial product and two co-hydrogenation products, at various temperatures and a spin rate of 1 rpm. The latter two were obtained from co-hydrogenation of Yanzhou coal with CCR1 and CCR2 at a coal-to-CCR ratio of 1/1.

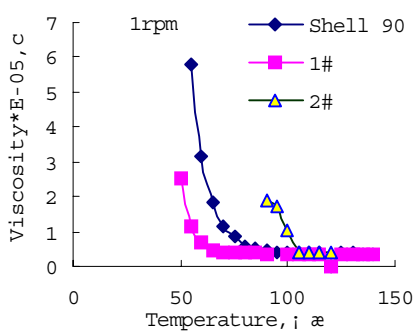

Fig. 3 Viscosity of asphalts

Generally, viscosities of the asphalts decrease with increases in temperature and in spin rate, but the temperature ranges where the viscosity changes the most are different. The curve in Fig. 3 for asphalt #1, which meets the Chinese national standard for high way asphalt, falls in the left side of Shell 90; while the curve for asphalt #2, which does not meet the Chinese national standard for high way asphalt, falls in the right side of Shell 90. Clearly, The rheological properties of the co-hydrogenation asphalts can be controlled by varying CCRs and the hydrogenation conditions. It is important to point out that, compared to Shell 90, no additives were added in the co-hydrogenation asphalts.

4. Conclusions

Co-hydrogenation of Yanzhou coal and CCR at mild conditions may produce asphalt with properties similar to that of petroleum derived high quality paving asphalt. Synergetic effects in asphalt yield between the coal and CCR were observed. Compared to individual hydrogenation of the coal and the CCR, the asphalt yield was enhanced greatly. The properties of the asphalt produced can be controlled by adjusting the CCR and the co-hydrogenation conditions. High aromatic CCR can produce asphalt of good rheology properties to meet the highway requirements.

Acknowledgement: The authors gratefully acknowledge the financial support from the National Natural Science Foundation of China, the Chinese Academy of Sciences, and the Special Founds for Major State Basic Research Project. Mr. Yanti Wang of Shijiazhuang petroleum refinery is also acknowledged.

References

1. Yunmei Li, Ruiping Yan, Jianli Yang, Zhenyu Liu, Zhe Wang, Proceedings of The 14th Annual International Pittsburgh Coal Conference & Workshop,1997, CD-ROM
2. Hong Cui, Jianli Yang, Yunmei Li, Yongda Gu, Zhenyu Liu, Proceedings of The 14th Annual International Pittsburgh Coal Conference & Workshop, 1997, CD-ROM
3. Zhenyu Liu, Jianli Yang, Proceedings of The 15th Annual International Pittsburgh Coal Conference & Workshop,1998, CD-ROM
4. Zhijie Wang, Ruiping Yan, Yunmei Li, H. Zhang, J. Yang, Z. Liu, 3rd China-Korea Joint Workshop on Coal &Clean Energy Utilization Technology, taiyuan, Shanxi, P.R.China, 2000
5. Yongbing Xue, Kaicheng Lin, Gangming Zou, Coal Conversion 22(3): 1-4, 1999
6. Edwin J. Barth, Asphalt science and technology, Gordon and Breach Science Publishers, New York 1962
7 D. Mastrofini, M. Scarsella, Fuel 79(2000),1005-1015

MORPHOLOGY AND REACTIVITY OF BED MATERIALS IN PFBC BOILER AT DIFFERENT LOAD

F. Ishom[1], T. Harada[2], T. Aoyagi[3], Y. Korai[1], I. Mochida[1]

[1]Institute of Advanced material Study, Kyushu University
[2]Nishinippon Environmental Energy
[3]Kyushu Electric Power

Abstract:

Bed materials in pressurized fluidized bed combustion (PFBC) at various combustion conditions were characterized by SEM and TGA to describe their morphology and reactivity. 270 MW output conditions were found to keep bed material uniform, whereas 285 MW output conditions produced sintered egg (SE), sintered grain (SG), and unburnt char (UC) among the bed materials. Normal fluidization of uniform bed materials mainly at 270 MW output level combustion. Poor fluidization at 285 MW caused several types of adhering and agglomerating of bed materials was produced in the boiler. Local heating during poor fluidization was suggested to cause the formation spherical particle through the melting and melted surface particle of SE to be flat. Fine particles of aluminasilicate adhered to the melted surface to form porous surface.

Introduction

Pressurized fluidized bed combustion (PFBC) of coal has been recognized as an advanced coal firing process to achieve high thermal efficiency through combined cycles, high combustion efficiency for poor coals of low reactivity, and environmental protection using calcium minerals as bed material [1].

Several PFBC plants have been operated in Japan. There are reported several problems in PFBC operation. One of the problems is reported poor fluidization at the high-level load operation producing agglomerates among bed materials.

In the present report, bed materials at two combustion conditions (270 and 285 MW outputs) were recovered from the bottom of a commercial PFBC boiler to be characterized by SEM-EDAX and TGA in terms of its morphology and weight loss change by the heat treatment. Through such analysis, mechanism of formation is discussed to propose way how to reduce such problems.

Experimental

Bed materials (BM) in PFBC operated at load levels 270 and 285 MW were recovered from the bottom of 360 MW PFBC boiler were used as samples. Uniform particle of BM at 270 MW output level was called BM270. Bed materials at 285 MW output level were separated by hand picking up into similar particles being called BM285. BM285 carried sintered egg (SE), sintered grain (SG), and unburnt char (UC). BM270, BM285, SG, SE, and UC were characterized by SEM-EDAX (JEOL JSM-6320F) and TGA (Seiko Instruments 220).

Result and Discussion

270 MW output level

Bed materials produced from PFBC at 270 MW output level contained uniform particles as shown in Figure 1a. Morphology of BM270 shows porous on the surface of the $CaCO_3$ as shown in Figures 2a and 2e. Around 1 □m calcium aluminasilicate particles were melted and bonded together to form outer face of BM270 particle. Uniform surface of BM270 showed no local heating during combustion. TG/DTG profile of BM270 showed weight loss 35%wt at 700°C suggesting $CaCO_3$ decomposition. BM270 commonly contained $CaCO_3$ and small amount of calcium aluminasilicate on the outer surface. Limestone as raw bed materials of PFBC was suggested to be core particle of BM270. Its surface react with SO_x released from coal combustion and was covered by aluminasilicate particle from coal ash.

285 MW output level

285 output level of PFBC produced several kinds of bed materials which could be separated by hand picking up BM285, carried sintered egg (SE), sintered grain (SG), and unburnt char (UC) as shown in Figure 1b

Major part of BM285carried similar outer face to that of BM270, carrying porous faces. TG/DTG showed 40% weight loss at 700°C like BM270, indicating major core of limestone. Some spheres were unusually observation on surface of BM285. Such spheres were of CaO, SiO_2 and Al_2O_3 fine particles, which were fused together to form sphere and to be adhered onto the surface of limestone.

Sintered egg (SE) found at BM285 was shown in figure 1c. The morphology of SE shows melted surface with several fine particles adhered on the outer surface. TG/DTG profile of SE shows only 5% weight loss during heating in the air atmosphere. Small amount of $CaCO_3$ contained in SE. Melted surface of calcium aluminasilicate suggested fusion and adhesion of fine particle of CaO, SiO_2 and Al_2O_3 to for SE at the high indicating temperature due to local heating.

Figure 1d shows sintered grain (SG) particle. Very fine particle (around 0.1 □m) sintered and bonded together to form SG. No weight loss occurred during heat treatment to 1000°C in air atmosphere. A very fine particle of aluminasilicate was suggesting to form SG.

Unburnt char (UC) was also picked up among BM285. It was combusted completely in TGA. Insufficient oxygen or short time residence in the boiler may cause the production of UC.

References

[1] Anderson, J., Anderson, L., Energy and Fuel, 1998; 39(3): p.207

[2] Abe R, Sasatsu H, Harada T, Misawa N, Saito I, Fuel, 2001; 80(1): p.135-144.

[3] Qiu, Kuanrong; Steenari, Britt-Marie, Energy and Fuel, 2000; 14(5): p.973-979

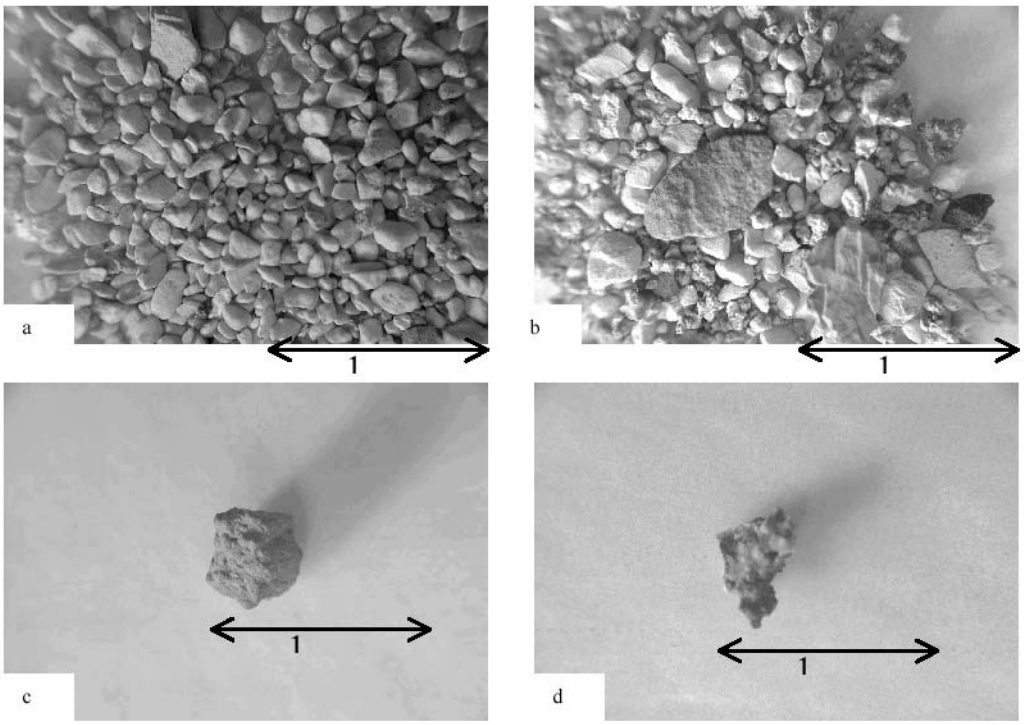

Figure 1. Photograph of bed material (BM) recovered from PFBC boiler: (a) BM 270/360 MW, (b) BM 285/360 MW, (c) Sintered egg, and (d) Sintered grain.

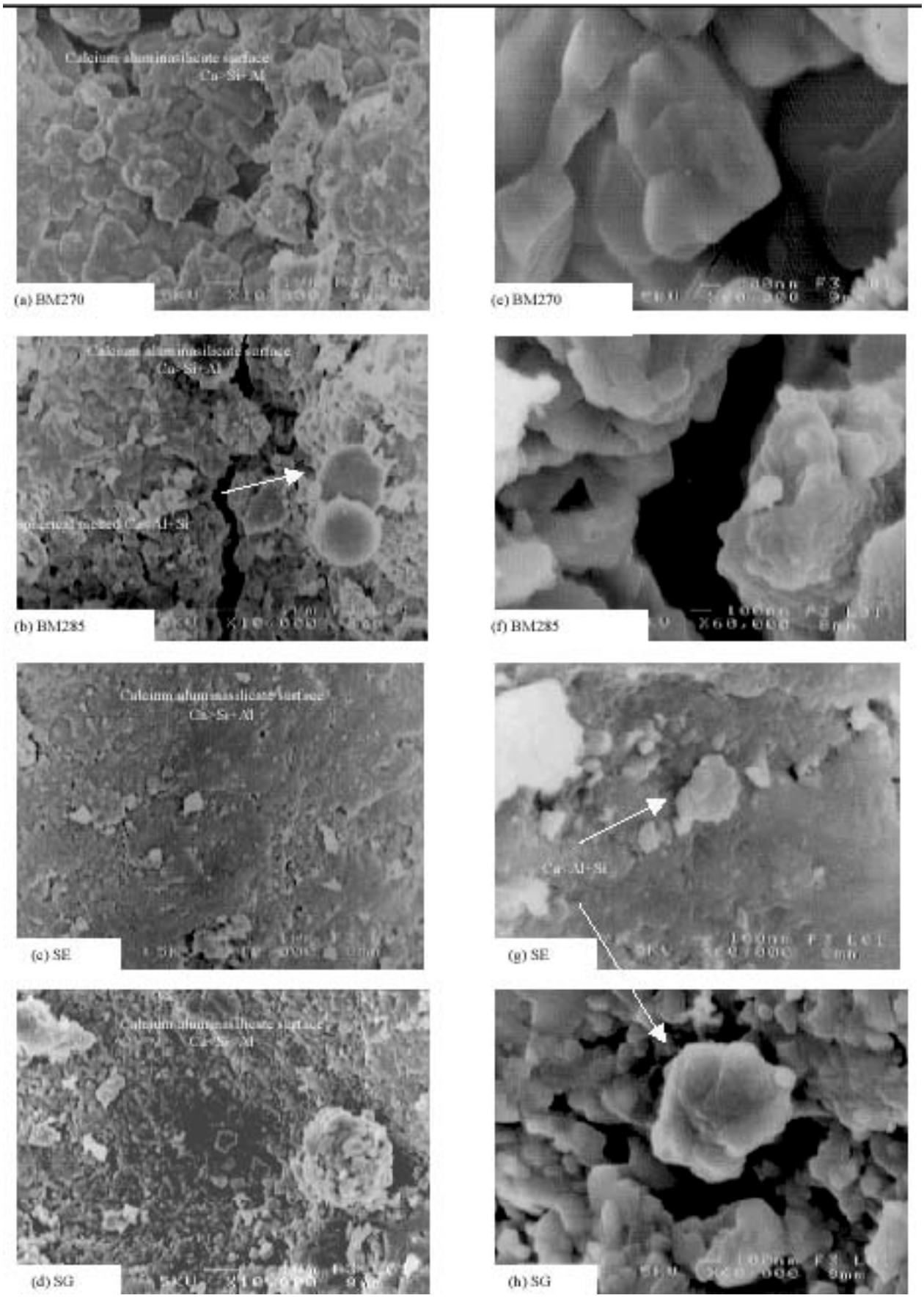

Figure 2. SEM photograph of: 10,000 x magnification of (a) BM270, (b) BM285, (c) SE, and (d) SG; and 60,000 x magnification of (e) BM270, (f) BM285, (g) SE, and (h) SG

EFFECT OF PRE-REDUCTION ON CARBON FORMATION DURING STEAM REFORMING OF METHANE OVER PROMOTED AND UNPROMOTED NI/AL_2O_3 CATALYSTS

*Jian Zheng, Wei Pan, Chunshan Song**

Clean Fuels and Catalysis Program, Energy Institute and
Department of Energy & Geo-Environmental Engineering,
Pennsylvania State University, University Park, PA 16802
Email: csong@psu.edu; Tel: 814-863-4466; Fax: 814-865-3248

Introduction

The steam reforming of methane is a well established industrial process for the production of synthesis gas ($CO + H_2$)[1]. The reaction is favored at high temperature, where coke formation is also a problem[2]. As a result, nickel – the most cost-effective catalyst – is loaded on support material with additional promoters that catalyze gasification of carbon (coke or of intermediates leading to coke). Potassia[3] and magnesia[1] etc are known to promote gasification by steam. However, catalyst deactivation due to carbon deposition still exits in industrial production after several months or years reforming reactions even with high steam/carbon ratio[4].

Many studies have been done on the mechanism of carbon formation and the promoting effect of basic alkali, alkaline earth metal oxides for decreasing of coke formation[3]. However, most of the studies concentrated on what happened on the surface of Ni metals, since most of the catalysts had been reduced at high temperature to achieve fully reduction. Little is known therefore about the effect of un-reduced Ni on the catalytic properties and carbon formation.

Based on a previous research, a pretreatment procedure, where the Ni supported catalysts were pre-reduced at 450˚C, was found to give good catalyst performance[5]. However, the reduction of NiO may become more difficult in the presence of Ca or K, etc. Therefore, this work aims at studying the effects of pre-reduction of K_2O and CaO promoted Ni/Al_2O_3 catalyst on the reforming catalysis and carbon formation. This kind of study may shed some light on the causes of and ways to eliminate carbon formation.

A commercial reforming catalyst promoted with K_2O and CaO was chosen in this study for the steam reforming of methane at different temperatures with different pre-reduction treatments. Interesting results have been found that carbon formation is more severe in the case of partially reduced Ni catalysts.

Experimental

Sample. Two commercial catalysts were obtained from Süd Chemie, one is the un-promoted (C11-9-09) with 1-15% NiO, 85-99% Al_2O_3 (as per the data provided by vendor) and the other is the promoted (G-91) with 15-25% NiO, 45-60% Al_2O_3, 5-15% $CaAlO_2$, 5-15% CaO and 1-10% K_2O.

Characterization. XRD patterns of the catalysts were obtained using a Scintag powder Diffractometer with Cu Kα as the radiation source. The reduction of the fresh catalysts were characterized by conventional TPR with a heating rate of 10˚C/min in argon (Ar, 30 ml/min). H_2-TPD was carried out on the catalysts reduced in situ at different temperature followed by purging with Ar. TPD profiles were then recorded by TCD detector at 10˚C/min in Ar. Carbon formation on the used catalysts was characterized by using a highly sensitive LECO RC-412 Multiphase Carbon Determinator, where the CO_2 produced during TPO was monitored by means of IR. SEM/EDX was also done for the information of surface images and compositions of used catalysts using HITACHI S-3500N Scanning Electron Microscope.

Reforming. The reaction of steam reforming of CH_4 was studied at three different temperatures, 450˚C (842˚F), 538°C (1000˚F) and 649°C (1200˚F), under pressure of 200 psi (13.6 atm) with the feed H_2O/CH_4 molar ratio of 0.5. Space velocity (WHSV) was kept at 30,000 $cm^3.g^{-1}.h^{-1}$. About 0.1g catalyst sample was placed in the middle of an Inconel 800 H alloy tubular reactor (0.54" O.D. x 0.375" I.D. and about 16" in length). α-Al_2O_3 spheres (2 mm I.D.) were filled up to the rest of the reactor.

Before admitting the reactants the catalysts were pre-reduced in H_2 (10 ml/min)-Ar gas flow (30 ml/min) at different temperature for 75 min. Then the reaction run was started by introducing H_2O followed by CH_4 feed (10 ml/min). A condenser was used to remove un-reacted H_2O after the reaction. Reaction products were analyzed by on-line GC (SRI GC 8610C) using a packed silica gel column and TCD detector. GC data were recorded every 30 min during a time-on-stream (TOS) period of 300 min after the steady state conditions were reached (15-30 min).

Results and Discussion

An intense XRD peak attributing to the diffraction of NiO (012) still exits on the promoted G-91 catalyst after reduction at 450˚C, which disappears at higher reduction temperature.

TPR profiles as shown in **Figure 1** confirm that the promoters (K_2O and CaO) make the reduction of NiO harder. In the absence of promoter (curve **a**), the reduction of NiO starts at 300˚C and peaks at 460˚C, so the pretreatment procedure that we developed previously[5] is suitable to achieve full reduction of NiO. On the contrary, the reduction of same metal oxide over G-91 catalyst could not occur until temperatures higher than 400˚C, and the T_{max} of the first TPR peak (curve **b**) is around 500˚C. A second TPR peak appears and is probably due to the reduction of less reducible NiO-CaO-K_2O solid solution. Therefore, partly reduced NiOx ($x \leq 1$) remains after pre-reduction at 450˚C.

H_2-TPD of G-91 catalyst after 450˚C reduction shows relatively smaller peak at around 120˚C than those reduced at higher temperature (figures not shown). However, two additional H_2-TPD peaks at higher temperature (350˚C and 600˚C) can be found in the case of 450˚C reduction, which might be due to the desorption of H_2 bounded to NiOx during the purging process in Ar.

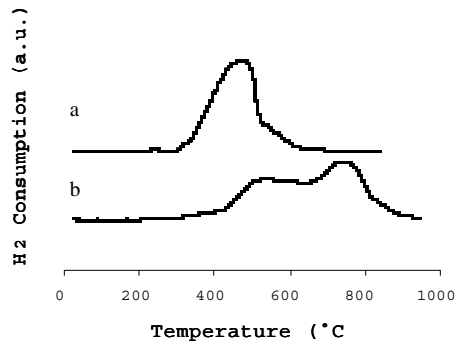

Figure 1. TPR profiles of un-promoted C11-9-09 (a) and promoted G-91 (b) catalysts.

Table 1. Results of Methane Steam Reforming on G-91 Catalysts (H_2O/CH_4: 0.5, 200 psi, TOS: 5 h)

T_{rex} (˚C)	450		538			649		
	$T_{red.}$ (˚C)		$T_{red.}$ (˚C)			$T_{red.}$ (˚C)		
	450	850	538	649	850	450	649	850
Conv (%)	25.1	17.3	14.6	7.1	28.7	22.9	24.0	23.4
Yield H_2	6.5	6.6	15.0	12.0	13.0	27.5	27.2	28.3
CO	0	0	0	0	0	4.2	3.8	4.4
CO_2	3.3	3.5	7.3	2.2	6.2	9.1	9.5	9.7

* $T_{rex.}$: Reaction temperature, $T_{red.}$: Pre-reduction temperature.

Steam reforming catalysis results of G-91 catalyst (TOS = 5 h) are listed in **Table 1**. There are no big differences among the activity and product yields of the same catalyst after different pre-reduction treatments, especially at reaction temperature of 649˚C. This is probably because that the H_2 produced during the steam reforming will eventually reduce the NiOx to Ni, which therefore acts as the same active sites for methane steam reforming as the case of pre-reduction at higher temperature.

However, it is worth noting that, there is a trend of the decreasing amount of carbon deposition with the increase of pre-reduction temperature as analyzing the used catalysts by TPO-IR.

Figure 2 shows the TPO-IR patterns of G-91 catalyst pre-reduced at different temperature followed by 5 h reforming reaction of methane at 649˚C. Several peaks are presented in all samples, as noticing that the curves in Figure 2 are drawn in different scales. The amount of the peaks at lower temperature (<400˚C) almost keep constant in all cases, which are probably due to the desorption of CO_2 chemisorbed on Ni supported catalysts during reforming reaction. Therefore these peaks may not relate directly to the carbon deposited. The peak with T_{max} at 600˚C is the oxidation of carbon filament, which is in accordance with literature work[6].

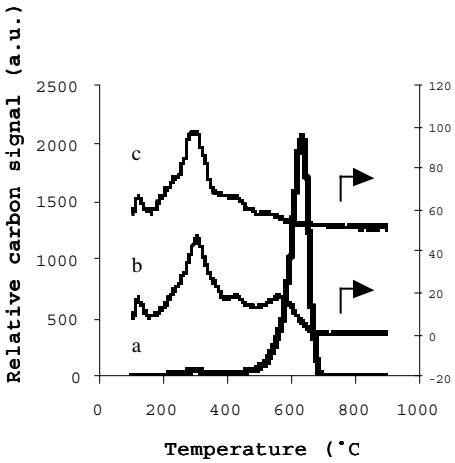

Figure 2. TPO-IR spectra of G-91 catalyst pre-reduced at 450˚C (a), 649˚C (b), and 850˚C (c) followed by steam reforming of methane at 649˚C for 5 hours.

It is very interesting to note that the amount of filament carbon significantly increases with decreasing temperature of pre-reduction, especially at reduction temperature of 450˚C where NiO has not been fully reduced.

This observation indicates that formation of carbon filament can be enhanced on partially reduced $NiOx/Al_2O_3$ catalyst when compared to fully reduced Ni/Al_2O_3 catalyst.

Figure 3 shows the SEM pictures of the used G-91 (after 5 h TOS) catalysts that were pre-reduced at 450˚C and 649˚C, respectively. Significant amount of carbon filament can be easily found in the case of lower-temperature pre-reduction, while it is less obvious in the case of higher reduction temperature.

All these results seem to correlate well with each other. Although the partially reduced NiOx in the promoted reforming catalyst can be eventually fully reduced under high temperature reaction conditions, certain species in partially reduced catalyst may act as an active site for the initial carbon formation, which could be accumulated to become severe. Therefore, care should be taken to achieve full reduction of the promoted Ni catalysts before the reforming reaction, particularly when using lower steam/carbon ratios.

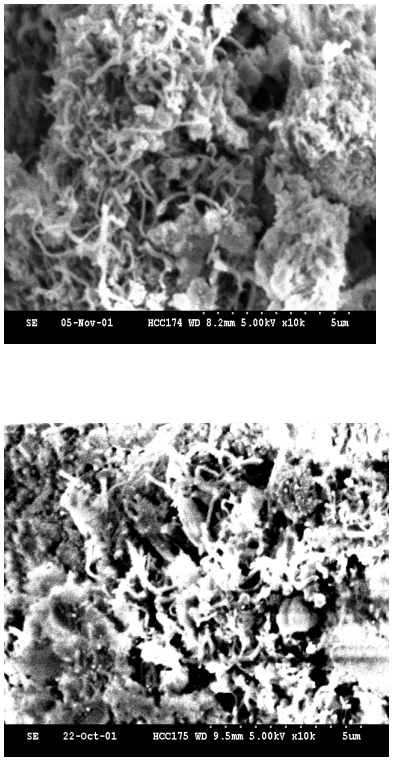

Figure 3. SEM pictures of G-91 catalyst pre-reduced at 450˚C (above) and 649˚C (below) followed by steam reforming at 649˚C for 5 hours.

Conclusions

The present work reveals that there is a significant effect of pre-reduction treatment on the carbon formation during steam reforming of methane over promoted Ni/Al_2O_3 catalyst. The partially reduced catalyst enhances carbon formation when compared to fully reduced catalyst, possibly because some species

in partially reduced catalyst (NiOx?) acts to promote the initial carbon formation.

Acknowledgement. We are grateful to Air Product and Chemicals Inc. and to the Pennsylvania State University for partial financial supports. We also wish to thank United Catalyst Inc./Süd Chemie for providing the catalyst samples. JZ would like to thank Dr. M. Klimkiewicz for help with the use of SEM/EDX, to Ms. N. Wonderling for help in the XRD, and to Dr. A. Orhan for help with the use of TPO-IR instrument.

References

(1) Rostrup Nielsen, J. *Steam Reforming Catalysts,* **1975**, Danish Technical Press, Copenhagen.
(2) Bartholomew, C. H. *Catal. Rev. - Sci. Eng.,* **1982**, *24*, 67-112.
(3) Trim, D. L. *Catal. Rev. – Sci. Eng.*, **1977**, *16*, 155-167.
(4) Arakawa, H.; et al. *Chem. Rev*., **2001**, *101*, 953-996.
(5) Song, C., Murata, S., Srinivas, S.T., Sun, L., Scaroni, A.W. *Am. Chem. Soc. Div. Petrol. Chem. Prepr.*, **1999**, *44*, 160.
(6) Wang, S.; Lu, G. Q. *J. Chem. Tech. Biotechnol*., **2000**, *75*, 589-595.

HYDRODEMETALLATION OF NICKEL AND VANADYL OCTAETHYLPORPHYRINS IN THE ABSENCE OF A CATALYST

Hai Xu, Daoyong Yu, Guohe Que, Zongxian Wang
State Key Laboratory of Heavy Oil Processing, Faculty of Chemistry and Chemical Engineering, University of Petroleum, Dongying 257061, China

Introduction

Metals in petroleum (mainly nickel and vanadium) often cause serious problems in the catalytic cracking and the hydrodesulfurization units, such as blocking the pores, fouling the active sites and changing the selectivity of the catalyst. So it is necessary to remove these metals in advance. And a better understanding of the chemical properties of metal containing compounds in petroleum would lead to develop an effective and economic demetallation process.

At present, as only some nickel and vanadyl porphyrins have been isolated from petroleum and identified, and a little is known about other metal containing compounds, so most of demetallation studies have been devoted to metal porphyrins. Many investigators (1-4) have studied the catalytic hydrodematllation of nickel and vanadyl porphyrins and a sequential HDM mechanism has been proposed, but the demetallation reaction mechanism in the absence of a catalyst seems to be unclear. In the present study, the demetallation reaction mechanism of nickel and vanadyl 2,3,7,8,12,13,17,18-octaethylporphyrins (NiOEP and VOOEP) in the absence of a catalyst at temperature from 613 to 653 K and pressure of 3 and 9 MPa H_2 is described.

Experimental

NiOEP and VOOEP (Aldrich, >97%) were employed as model compounds. A liquid paraffin free of sulfur, nitrogen and metals was used as a solvent and purchased from Beijing Chemicals. The method of dissolving the model compounds in the liquid paraffin was based on the description by Hung and Wei (1).

All experiments were performed in a high-pressure and high-temperature reactor system, which was previously described (5). The flow of gas feeds (H_2 or N_2) was controlled through a gas flow meter, and liquid feeds (metal porphyrin solutions) was pumped into the reactor and mixed with hydrogen at the top of the reactor tube. The reactor tube had a length of 50cm and inside diameter of 0.6cm, and it was packed with 20~40 mesh inert silica. Although the temperature distribution of the reactor tube was not uniform, there was a constant temperature zone of about 5 mL in the middle of the reactor tube. Therefore this zone was used as the working section. The system operated in a down flow mode.

HDM experimental conditions in the absence of a catalyst are listed in table 1, and the volume ratio of H_2 to liquid feed is 250:1 for all the runs. In addition, in order to examine whether there are thermolysis reactions for NiOEP and VOOEP at the temperature ranging from 613K to 653K, H_2 is replaced with N_2. The volume ratio of N_2 to liquid feed is also 250:1, and the other experimental conditions are given in table 2.

Liquid samples were subjected to atomic absorption spectrophotometry (AAS) and ultraviolet-visible (Uv-vis) spectrophotometry. A flame atomic absorption spectrophotometer (WFX-1F2B) was used to determine the total nickel concentration and a nonflame atomic absorption spectrophotometer (HITACHI Z-8000) with a graphite furnace system the total vanadium content. The metal porphyrin or porphyrinic metal concentration measurement was made on an Uv-vis spectrophotometer (VARIAN CARY 50) according to the characteristic peaks of metal porphyrins, and simultaneously their electronic spectra were recorded on this instrument.

Table 1 HDM Conditions

Run no.	Porphyrin type	Ni or V concn in feeds, ppm	Temp, K	H_2 pressure, MPa
1	NiOEP	7.06	613	9
2	NiOEP	7.92	633	9
3	NiOEP	8.46	653	9
4	NiOEP	7.92	633	6
5	NiOEP	7.92	633	3
6	VOOEP	8.21	633	9

Table 2 Thermal Reaction Conditions

Run no.	Porphyrin type	Ni or V concn in feeds, ppm	Temp, K	N_2 pressure, MPa
7	NiOEP	2.40	633	6
8	NiOEP	2.40	653	6
9	VOOEP	2.44	633	6

Results and Discussion

In our experiments, there was no gas resultant and the liquid product yield was 100w%. Metal porphyrin conversion (MPC) was defined as

$$MPC = \frac{C_{MP,feed} - C_{MP,product}}{C_{MP,feed}} \times 100\%$$

where $C_{MP,feed}$ represents the metal porphyrin concentration in feeds and $C_{MP,product}$ the metal porphyrin concentration in liquid products. The demetallation yield (DMY) of metal porphyrin was defined as

$$DMY = \frac{C_{M,feed} - C_{M,product}}{C_{M,feed}} \times 100\%$$

where $C_{M,feed}$ represents the metal concentration in feeds and $C_{MP,product}$ the metal concentration in liquid products.

Table 3 MPC and DMY
(The liquid feed flow was 0.3mL/min)

Run no.	MPC	DMY
1	29.1	27.5
2	33.4	30.6
3	47.0	39.5
4	27.7	25.8
5	19.9	18.3
6	38.5	34.6
7	0	0
8	0	0
9	0	0

For all the runs, when the liquid feed flow was 0.3ml/min, MPC and DMY are given in table 3. In the presence of H_2, even without a catalyst, the two metal porphyrins can be demetallated. By contrast, when H_2 was replaced with N_2, their MPC and DMC are both zero, and they don't decompose thermally. Based on the above findings, it is conclude that H_2 plays a key role during the demetallation reaction of the two metal porphyrins in the absence of a catalyst.

For NiOEP and VOOEP, although MPC and DMY of the non-catalytic HDM are lower than that of the catalytic HDM (5-6), their demetallation reaction mechanism appears to be same, i.e., the sequential HDM mechanism. This would be confirmed by the following facts.

For every HDM run, MPC is always higher than DMY (table 3). This means that the concentration of total metal is larger than that of porphyrinic metal in liquid products, but the former is identical with the latter in feeds. Obviously there are newly formed metallorganics in liquid products. Figure 1 and 2 are the typical Uv-vis spectra of the feed and the liquid product during the non-catalytic HDM of NiOEP

respectively. Evidently, a new peak at 615nm occurs for the product (figure 3). Similarly, the typical Uv-vis spectra of the feed and the liquid product are shown respectively in figure 3 and 4 during the non-catalytic HDM of VOOEP, and a new peak at 629nm appears for the product (figure 4). It is believed that the peak at 615 nm is of nickel octaethylchlorin and the peak at 629 nm is of vanadyl octaethylchlorin. The nickel or vanadyl octaethylchlorin is a dihydroporphyrin in which the peripheral double bond of one pyrrole group is hydrogenated; their structures are shown in figure5.

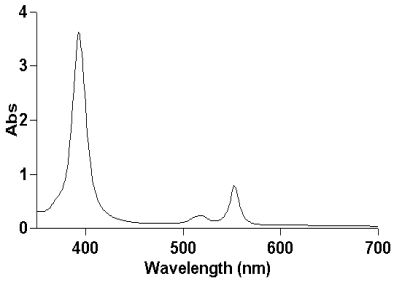

Figure 1. Uv-vis Spectrum of the NiOEP Feed (Diluted with Liquid Paraffin)

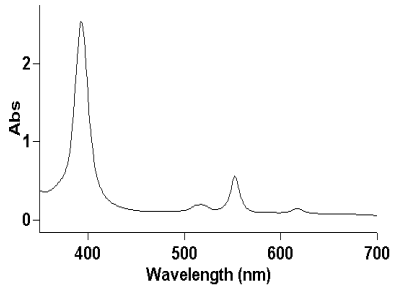

Figure 2. Uv-vis Spectrum of the Liquid Product during the Non-catalytic of NiOEP (Diluted with Liquid Paraffin)

To provide much proof that the two new peaks belong to nickel and vandyl chlorins respectively and they are the main stable intermediates during the non-catalytic HDM, we separated the reaction intermediates from liquid products by alumina adsorption chromatograph. The detailed procedure is as follows: (a) 25mL product was diluted with 25 mL n-heptane, then placed on the top of neutral alumina (100~200mesh, 1%H_2O) in a glass column (15X250 mm). As the purple liquid completely entered the alumina column, a little fresh alumina was placed on its top to cover it. (b) At first, elution with n-heptane removed a colorless metal-free fraction in which the unreacted liquid paraffin may be concentrated, and a purple fraction containing metal was adsorbed on the upper portion of the column. Secondly, when toluene (for the product of NiOEP HDM) or 1:1 dichloromethane/toluene (for the product of VOOEP HDM) was used to elute the purple fraction, it was made into two colored fractions. A blue fraction for NiOEP or a green fraction for VOOEP came out of the column firstly, and a red band then was effluent.

The above colored fractions were subjected to Uv-vis and MS analysis. The spectra of the red fractions are the same as that of feeds. The spectrum of the blue fraction is shown in figure 6, and the spectrum of the green fraction is given in figure 7. In figure 6, the ratio of the Soret band (397nm) to the 615nm band is about 2, which was found to be one of the most typical characteristics of nickel octaethylchlorin (7). MS measurement indicated that NiOEP and the blue fraction have the molecular weights of 590 and 592 respectively, and VOOEP and the green fraction have the molecular weights of 600 and 602 respectively.

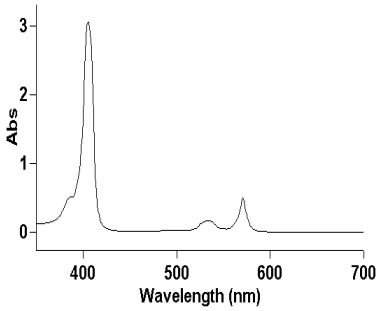

Figure 3. Uv-vis Spectrum of the VOOEP Feed (Diluted with Liquid Paraffin)

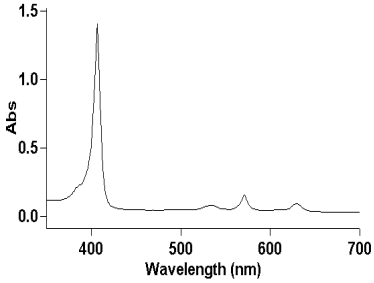

Figure 4. Uv-vis Spectrum of the Liquid Product during the Non-catalytic of VOOEP (Diluted with Liquid Paraffin)

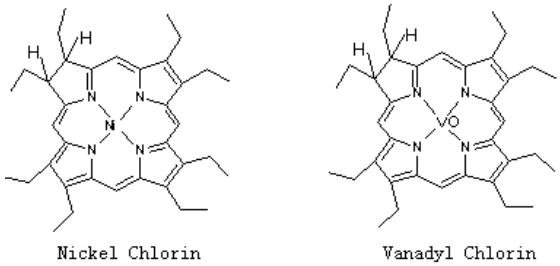

Figure 5 Structures of Nickel and Vanadyl Octaethylchlorin

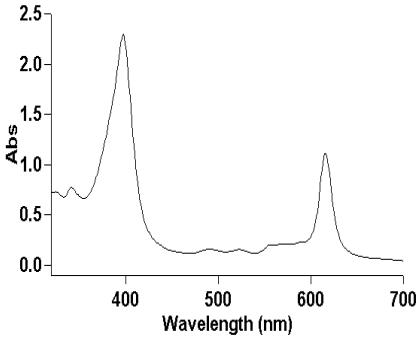

Figure 6. Uv-vis Spectrum of Nickel Octaethylporphyrin in Toluene

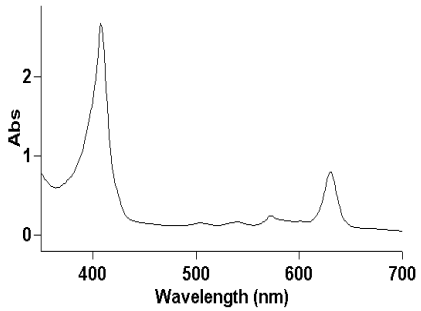

Figure 7. Uv-vis Spectrum of Vanadyl Octaethylporphyrin in dichloromethane/toluene

Table 4. C_M, $C_{M, MP}$ and $C_{M, MC}$ of the Liquid Products of Run 3

Liquid feed flow, mL/min	C_M, ppm	$C_{M, MP}$, ppm	$C_{M, MC}$, ppm
0.1	2.94	2.47	0.46
0.3	5.14	4.49	0.62
0.6	6.30	5.73	0.58
1.0	7.13	6.68	0.48
2.0	7.76	7.42	0.38

The separated metal chlorins were dissolved in the liquid paraffin. Their absorption coefficients were determined through AAS and Uv-vis. According to the coefficients, the chlorinic metal concentration was measured during the non-catalytic HDM. The sum of porphyrinic metal concentration ($C_{M, MP}$) and chlorinic metal concentration ($C_{M, MC}$) is approximately equal to the total metal content (C_M) in liquid products, which is shown in table 4. All the above findings confirm that the metal chlorins are the main stable intermediates during the non-catalytic HDM of NiOEP and VOOEP.

Conclusions

In the presence of N_2, NiOEP and VOOEP are stable at the temperature ranging from 513K to 653K. In H_2, however, even without a catalyst, they are not stable and metals are demetallated. The non-catalytic HDM reaction mechanisms of NiOEP and VOOEP are similar to their catalytic HDM mechanisms, firstly being the hydrogenation of metal porphyrin to metal chlorin, followed by the hydrogenolysis of metal chlorin which fragments ring system and results in demetallation.

Acknowledgement. The authors thank B. H. Zhang, L. Q. Wang for their effective assistance in experimental work, and are grateful to SINOPEC for necessary fund support.

References

(1) Hung, C. W.; Wei, J. *Ind. Eng. Chem. Process Des. Dev.* **1980**, 19 (2), 250.
(2) Agrawal, C. W.; Wei, J. *Ind. Eng. Chem. Process Des. Dev.* **1984**, 23 (3), 505.
(3) Ware, R. A.; Wei, J. *J. of Catal.* **1985**, 93(1), 100.
(4) Bonne, R. L. C.; van Steenderen, P. V.; van Langeveld, A. D.; Moulijin, J. A. *Ind. Eng. Chem. Res.* **1995**, 34, 3801.
(5) Xu, H.; Que, G. H.; Yu, D. Y.; Wang, Z. X. Prepr. Pap. – *Am. Chem. Soc., Div. Pet. Chem.* **2001**, 46(4), 84.
(6) Xu, H.; Yu, D. Y.; Wang, Z. X.; Que, G. H. *Acta Petrolei Sinica (Peroleum Processing Section)* **2001**, 17(4), 18
(7) Fuhrhop, J. H. Z. *Naturforsh* **1970**, 25b, 255

Thermal-cracking and catalytic hydro-cracking reaction of tetralin and normal eicosane with steady isotope

SHI Bin QUE GuoHe

(National Laboratory of Heavy Oil Processing, University of Petroleum, Dongying, 257062;PRC)

Introduction

Hydrogen donors were used in coal liquefaction(1) and residue conversion(2), in which hydrogen donors were important in inhibiting the coke formation. Because coal and petroleum residue structures have been unclear, a study of the reactions of coal- or petroleum residue-related model compounds is a powerful approach in hydrogen-transfer between hydrogen donors and complex macromolecule. This paper reports the effects of hydrogen donor and H_2 on thermal-, hydro-, catalytic hydrocracking of n-C_{20} and hydrogen transferring between normal hydrocarbon and hydrogen donor.

Experimental

Normal C_{20} was used as reagent, and 1-methylnaphthelene (98%pure) as aromatic solvent, tetralin$C_{10}H_{12}$ (99.3%) as hydrogen donor, detuerated tetralin $C_{10}D_{12}$ (98%D, Aldrich provided) as deuterated H-donor for tracking the hydrogen-transfer between hydrogen donors and normal hydrocarbon. The experimental procedure was as literature (4). The reaction products were recovered with chloroform and analysed by GC and GC-MS.

Results and Discussion

Thermal-, hydro-cracking, catalytic hydro-cracking of n-C_{20} was performed, while thermal- or hydro- cracking of n-C_{20} in hydrogen donor (tetralin,THN) or aromatic solvent(1-methylnaphthelene ,1-MN) were also carried out as comparison . Distribution of the reaction products was displayed in Figure1. It seems that distribution in carbonic number of the products in the four cracking reaction have not changed, however, the catalytic hydrocracking of n-C_{20} could crack more than hydrocracking and thermal cracking of n-C_{20}. On the other hand, it is clear that in the presence of H-donor or aromatic solvent, especially in the presence of H-donor, inhibited cracking of n-C20. What is different was that the ratio of n-alkanes to α–olefins in thermal cracking and thermal-cracking with aromatic solvent was about 1:1, and that in thermal–cracking in H-donor decreased to about 1:0.5. The proportion of α–olefins in hydrocracking of n-C_{20} remained about 15~10% and hydrocracking of n-C_{20} with H-donor hardly gave α–olefins. Catalytic hydrocracking of n-C_{20} without or with THN brought about no α–olefins. It is obvious that hydrogen-in-gas and hydrogen provided from H-donor could have hydrogenated the olefins resulted from cracking of n-C_{20} and the former could enhance cracking of n-C_{20} and the latter could inhibit cracking.

Deuteron as steady isotope of hydrogen could be used to investigate the mechanism of hydrogen–transferring (3). In the following experiment, $C_{10}D_{12}$ was used as deuterated H-donor for tracking hydrogen-transferring between hydrogen donors and hydrocarbon. From Table2, it is found that deuterated H-donor existed a substantial isotopic kinetic effect in the thermal cracking system and that the isotopic kinetic effect was reduced in the hydrocracking and catalytic hydrocracking system. H- or D-donating yields at high temperature were more than in low temperature since more radicals could yield by high temperature and get scavenged by H-donor.

During initialization or propagation of the thermal radicals of n-C_{20}, hydrogen donation from tetralin for s cavenging thermal radicals of n-C_{20} could strongly affect the thermal cracking of n-C_{20}. That is to say, the hydrogen from tetralin could scavenge the radicals of n-C_{20} and the cracking of n-C_{20} would be inhibited. This reaction could also affect hydrocracking and catalytic hydrocracking of n-C_{20}.

Fig 2~4 show the GC-MS of the recovered n-C_{20}. From the M+1or M+2 peak, there existed one deuterium in the paraffinic chain, except that there were two deuteriums in the catalytic hydrocracking system. It is clear that deuterium was from deuterium-donor and could be used to scavenge radicals of n-C_{20}. The MS of the recovered

$C_{10}D_{12}$ showed $C_{10}D_{12}$ had experienced H-D exchange in Fig 5~7. Except the molecular peak144, the peaks from 143 to132 were the molecular peaks of tetralin, which had experienced H-D exchange. It is clear that H-D exchange in catalytic hydrocracking system was the most, and in hydrogen atmosphere was stronger than in nitrogen atmosphere.

^{2}H-NMR analysis of D_{12} -THN, which was separated and recovered by small-scale liquid chromatography showed that the 2.63ppm peak of Dα of recovered D_{12} -THN, was smaller than that of 1.70ppm Dβ from Fig 8. The ratio of Dα and Dβ was 0.856 (thermal cracking), 0.726(hydro-cracking), 0.695 (catalytic hydro-cracking). It is clear that the dehydrogenation of tetralin was selective and the α-hydrogen of naphthenic ring was easier to dehydrogenate than the β-hydrogen.

^{1}H-NMR analysis of D_{12} -THN displayed the same trend of the dehydrogenation of tetralin. It is shown that dehydrogenation of tetralin was stepwise and α hydrogen could be abstracted by the radicals and then β could be continued, when H_2 atmosphere could rehydrogenation on the abstracted tetralin, this is the "hydrogen shuttle" in the catalytic hydrocracking system.

The scheme of reaction mechanism between eicosane and D_{12} -THN in the cracking system would be suggested in Fig.9. Fig.9 shows the H-D exchange reaction between tetralin and n-C20 in the thermal cracking have been transformed into the rehydrogenation of tetralin in hydrocracking and catalytic hydrocracking system under H_2 atmosphere.

Conclusion

1. It is found that the effect of hydrogen donor was inhibition of cracking reaction and hydrogen atmosphere and dispersed catalysts were enhancement of cracking.

2. Hydrogen donor or H_2/dispersed catalyst could perform the saturation of the radicals and decrease the yield of olefins.

3. Inhibition of cracking of normal hydrocarbon with tetralin was ascribed to the dehydrogenation of tetralin for scavenging the thermal radicals.

4. There existed a substantial isotopic kinetic effect of deuterated tetralin in the cracking system under nitrogen and under hydrogen, and the isotopic kinetic effect could reduce in the cracking system under hydrogen.

5. Hydrogen (or deuterium) donation of hydrogen donor depended on reaction temperature and number of radicals in reaction system.

6.The dehydrogenation of tetralin was stepwise and the α-hydrogen of naphthenic ring was easier to dehydrogenate than the β-hydrogen.

Acknowledgement. The authors thank Wang LuoQiu and Wang Jing for their effective assistance in experimental work, and are grateful to University of Petroleum and National Laboratory of Heavy Oil Processing for fund support.

References:

(1). Yanlong Shi, Lian Shao, Willian F. Olson Coprecessing coal with hydrogenated vacuum pyrolyzed tire oil [J].Fuel processing Technology, 1999,(58):135~150

(2). Shi Bin, Li PeiPei, Que GuoHe. New developments in deep hydro conversion of heavy oil residues with dispersed catalysts [J] Preprints, div. fuel chem., ACS, 1998, 43(3): 558-562.

(3). R. P. Skowronski, and J. J. Ratto, I. B. Goldberg et al Hydrogen incorporation during coal liquefaction [J] Fuel 1984(63) 4,440-448.

(4). Shi Bin,Wang Luoqiu,Weng Ping,et al. Reaction of H-donor and paraffinic series as model compounds for residue oil with steady isotope method [J] J. of Fuel Chem. and Tech. (China) 2001(29) 5,400-403.

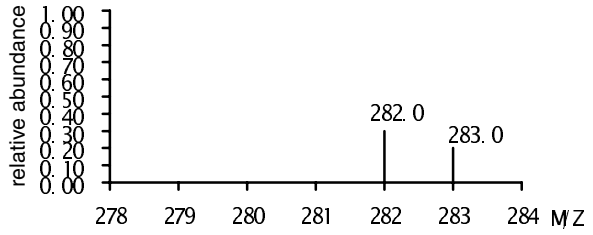

Figure2 M+1 peak of recovered eicosane scavenged by deuterium under nitrogen

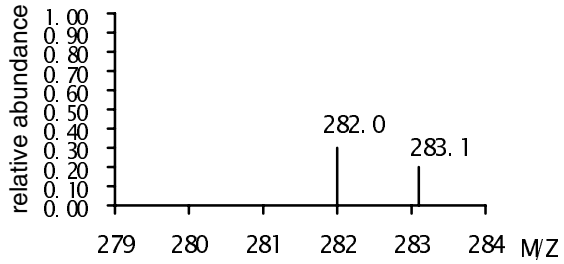

Figure3 M+1 peak of recovered eicosane scavenged by deuterium under hydrogen

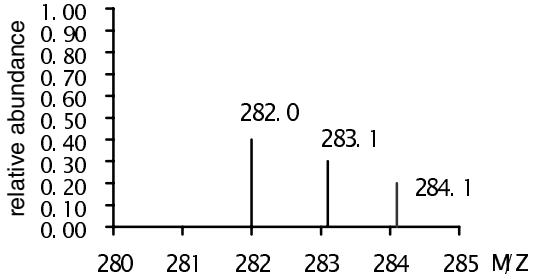

Figure 4 M+1 and M+2 peak of recovered eicosane scavenged by deuterium in catalytic hydrocracking system

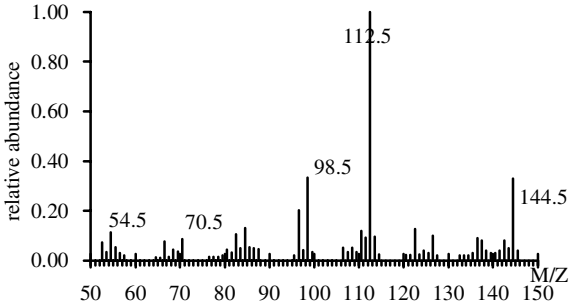

Figure5 MS of recovered D_{12}-THN in thermal-cracking system

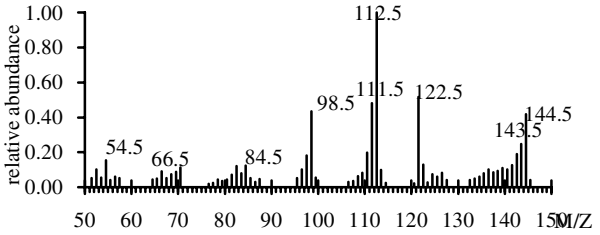

Figure 6 MS of recovered D_{12}-THN in hydrocracking system

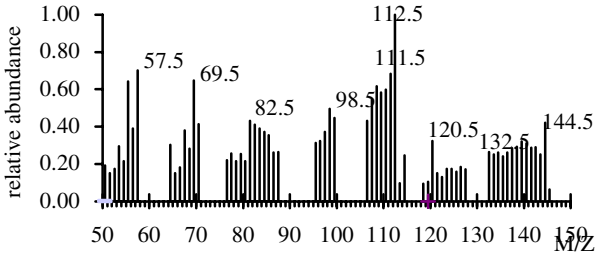

Figure 7 MS of recovered D_{12}-THN in catalytic hydrocracking system

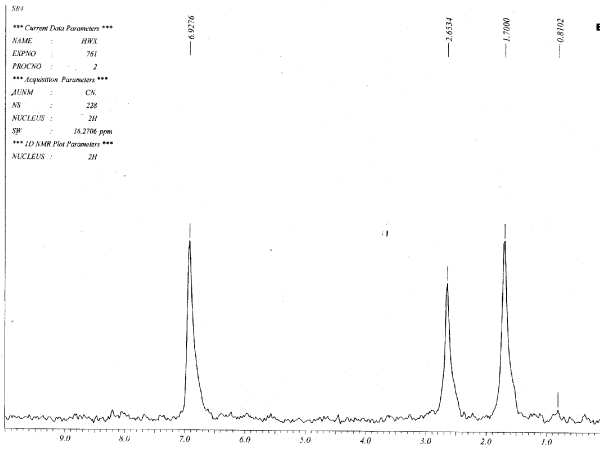

Figure8 ^{2}H-NMR of recovered D_{12}-THN in the cracking system

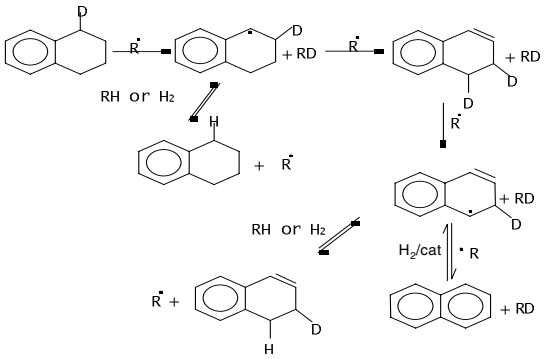

Figure9 Scheme of reaction mechanism between eicosane and D_{12} -THN in the cracking system

Table 1 Hydrogen(or deuterium) donating yields of THN reacted with eicosane /W%

T(°C)	N_2	N_2	H_2	H_2	H_2+Mo	H_2+Mo
	H_{12}-THN	D_{12}-THN	H_{12}-THN	D_{12}-THN	H_{12}-THN	D_{12}-THN
430	6.14	2.96	18.43	10.31	11.79	8.38
440	11.62	7.17	30.36	22.78	23.10	19.45

Note: eicosane /THN=0.100 g /0.100g;initial nitrogen pressure 7.0Mpa; durance time:1hr; Mo/ eicosane=1.0w%

Table2 ^{2}H-NMR of recovered D_{12} -THN experienced different hydrocracking

	D_{12} -THN Dα	D_{12} -THN Dβ	D_{12} -THN A_D
Peak shift (ppm)	2.63	1.70	6.93
thermal-cracking system	0.267	0.312	0.421
hydro-cracking system	0.244	0.336	0.420
catalytic hydro-cracking system	0.248	0.357	0.395

Table 3 ^{1}H-NMR of recovered D_{12} -THN experienced different cracking

	D_{12} -THN Hα	D_{12} -THN Hβ	D_{12} -THN A_H
Peak shift (ppm)	2.60	1.70	7.02
thermal-cracking system	0.40	0.35	0.25
hydro-cracking system	0.46	0.35	0.26
catalytic hydro-cracking system	0.40	0.30	0.35

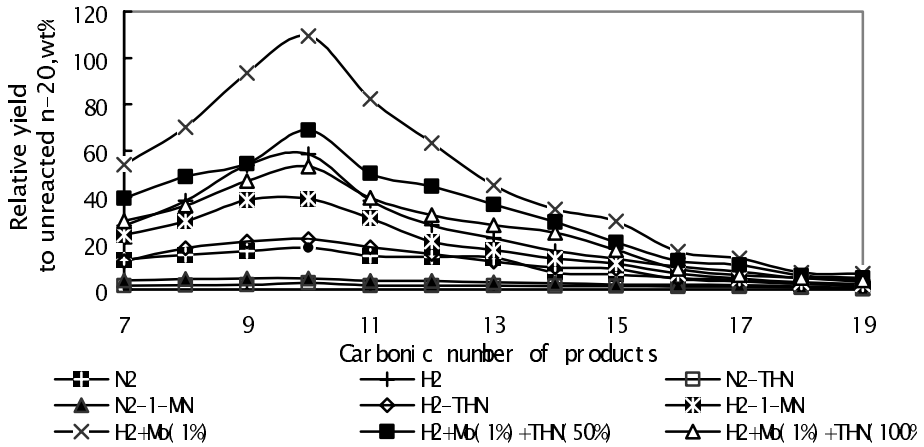

Figure1 Distribution of carbonic number in thermal-, hydro-and catalytic cracking of n-C_{20} in 440 °C

CARBON DIOXIDE: AN EFFECTIVE SOURCE OF CARBON FOR THE CHEMICAL INDUSTRY

Michele Aresta

University of Bari and METEA Research Center
Department of Chemistry, Campus Universitario, 70126 - Bari, Italy,
fax +39 080 544 2083, e-mail:aresta@metea.uniba.it

Introduction

The overall CO_2 mass used in industrial (chemical and technological) applications is at present limited to ca. 100 Mt per year[1]. Only four industrial processes based on carbon dioxide are on stream, two of which are more than one century old [synthesis of urea and salicylic acid] and do not require any catalyst. The two other processes are: the carboxylation of epoxides, and methanol synthesis, which require both metal catalysts.

However, the utilisation of carbon dioxide as a source of carbon in synthetic chemistry appears very attractive in view of the fact that, if recovery of carbon dioxide will be adopted as a technology for controlling its emission into the atmosphere, large amounts will be easily available. The products that can be conveniently obtained from carbon dioxide can be categorized as:

i) *Fine or commodity chemicals*, i.e. molecules containing functionalities such as: -C(O)O- acids, esters, lactones; -O-C(O)O- organic carbonates; -N-C(O)O- carbamates; -N-C(O)- ureas, amides;

ii) *Products for the energy industry*, i.e., energy-rich C1 molecules (HCOOH, CO, CH_3OH) and C_n hydrocarbons or their derivatives.

Developing industrial processes in these areas would produce the following advantages:

i) replacement of multistep processes with more direct synthetic procedures with waste reduction at source and atom economy, ii) implementation of alternative ways to processes presently based on more toxic or expensive materials, iii) raw materials diversification, and iv) recycling of carbon.

A point that must be emphasized is that speaking of "avoided CO_2", one should consider not only the amount of CO_2 recycled through its fixation in chemicals, but also the amount of CO_2 not produced by implementing the atom efficiency and waste minimization principles.

Results and Discussion

The carbon dioxide-utilizing reactions mentioned so far, can be divided into two main categories from the energetic point of view.[2]

Class 1

Reactions in which the whole carbon dioxide molecule is used. The substrate (amines, unsaturated hydrocarbons) is the energy vector and the amount of extra energy, if required, is usually very low. These reactions include the carboxylation reactions with the formation of a C-C or C-heteroatom bond (C-E; E=O, N, P, other element).

Class 2

Reduction reactions to C1 or C_n species, using dihydrogen, electrons, or heat as energy source.

All these reactions are common to, and very important in, biological systems (plants and bacteria), in which several enzymes involved in carbon dioxide utilisation are metal enzymes with the metal acting as the active site.

A great emphasis has been put on elucidating the role of CO_2-metal complexes, in which CO_2 is either η^2-C, O or μ-bonded to one or more metal centres, in carbon dioxide reduction or in its reaction with olefins to afford carboxylates. This issue is relevant to the more general question if the coordination of CO_2 to a metal is a necessary prerequisite for CO_2 fixation onto an organic substrate. Available data suggest that such co-ordination is necessary in the reduction to CO.

In carboxylation reactions either the olefin is activated first, or a concerted three-centre mechanism may operate. The carboxylation of unsaturated hydrocarbons (alkenes, alkynes, butadienes, allenes) has been recently developed with interesting yield and selectivity (>90%) using transition metal complexes as catalysts. In all cases the homo coupling of substrates is a concurrent process with the hetero-coupling substrate-CO_2. The solvent and the carbon dioxide concentration in solution play an important role in driving the reaction in either directions.

Methanol may have a large market as fuel or intermediate and its synthesis from carbon dioxide attracts the attention and interest of several research groups all over the world in order to define its potential. The use of carbon dioxide (Eq. 1) has as major draw-back the higher consumption of dihydrogen with respect to CO.

$$CO_2 + 3\,H_2 \longrightarrow CH_3OH + H_2O \qquad (1)$$

However, higher selectivity and better yields may counterbalance such apparent negative point.

The implementation of innovative synthetic technologies based on CO_2 can considerably contribute to the reduction of carbon dioxide emission. The avoided amount is not simply represented by the amount of fixed CO_2. New synthetic methodologies implementing the principles of atom economy, solvent shift, waste minimisation at source, use of less noxious materials and carbon recycling, contribute to CO_2 reduction in many different ways, which cannot be discovered and quantified by simply looking at the stoichiometry of a reaction.[3]

Acknowledgement. This work was supported by MURST, Project no. 9803026360 and MM03027791

References

(1) Aresta, M.; Quaranta , E. – *ChemTech.*, **1997**, 32-40.
(2) Aresta, M.; Dibenedetto, A. - ACS Book on *CO_2 Conversion and Utilisation*, **2001**
(3) Aresta M.; Tommasi I.; Dibenedetto A. - *Energy&Fuels*, **2001**, 15, 2, 269-273.

HYDROGEN ABSTRACTION FROM ALKYLAROMATICS WITH CO_2

Sang-Eon Park

Catalysis Center for Molecular Engineering,
Korea Research Institute of Chemical Technology (KRICT),
P.O. Box 107, Yusung, Taejon 305-600, Korea

Introduction

Catalytic conversion of CO_2 has been extensively studied as an important issue for last decade. However, utilization of carbon dioxide as an oxidant evokes emerging interest on new way of chemical fixation of CO_2.[1,2] Several examples have proved that CO_2 can play as soft oxidant in the various catalytic oxidative reactions by CO_2 alone or together with O_2, resulting in improved activities and selectivities.[3]

Dehydrogenation of aromatic hydrocarbons with benzylic hydrogen leads easily to aromatic hydrocarbons with α-olefin group through the hydrogen abstraction of benzylic C-H bond by surface oxygen of heterogeneous catalyst. This step is considered to be a rate-determining one. A representative example of such reactions is the dehydrogenation of ethylbenzene to styrene. It has been already proposed that for this reaction CO_2 plays a role as the soft oxidant to abstract the hydrogen atom from ethylbenzene.[4,5] It is worth verifying if carbon dioxide acts on dehydrogenation of other aromatic hydrocarbons.

The oxidation of alkylaromatics is an important commercial reaction. Discovery of bromide promoted metal catalysts in 1954[6] for the oxidation in presence of molecular oxygen evolved into one of the major industrial processes. The cobalt-based catalysts have been developed with different promoters (Br, Mn, Zr, Mo, Hf, Ni, Cr etc.) for the last four decades.[7] The promotional effects of several transition metal promoters have been reported for the oxidation reactions.[7] On the other hand, the unexpected function of CO_2 as a co-oxidant and/or oxidation promoter was reported in the early 1990s for the vapor phase oxidation of aromatic compounds,[8] and recently the similar effect has been found for the MC-type oxidation of xylenes to the corresponding dicarboxylic acids with Co/Mn/HBr in the liquid phase.[9]

Here, the effect of carbon dioxide as the soft oxidant is demonstrated in both oxidative dehydrogenation of alkylaromatics to corresponding olefins and oxidation of alkylaromatics to corresponding aldehydes and acids.

Experimental

For dehydrogenation of aromatic hydrocarbons with CO_2, Al_2O_3-supported vanadium-antimony binary oxide ($V\text{-}SbO_x/Al_2O_3$) catalyst was prepared by impregnation of aqueous solutions of ammonium metavanadate and antimony (III) chloride onto activated alumina. The impregnated sample was dried at 100°C and then calcined in air at 600°C for 4 h. The content of V_2O_5 and Sb_2O_3 was 7.5 wt% and 15.5 wt%, respectively. Dehydrogenation of alkylaromatics was carried out in a micro-activity test unit (Zeton, MAT 2000) with a fixed bed reactor at 600°C under atmospheric pressure. The liquid and gas products were analyzed by GC (Donam Corp., DS6200) equipped with FID and TCD, respectively. Effluent gases from the reactor were analyzed by a gas chromatograph (Chrompack CP9001) equipped with a thermal conductivity detector (TCD).

For oxidation of alkylaromatics, the required quantity of the catalyst and reaction the mixture was taken in a 150 ml Teflon-lined reactor and pressurised either with CO_2 or N_2 and raised the temperature to its optimum level and the optimum pressure was balanced by N_2. The O_2 was admitted to the reactor and measured the O_2 consumption with the help of pressure transducer connected to the oxygen chamber. The products were analysed by GC using DB-1 capillary column and FID. The solid products (carboxylic acids) were esterified and analysed as methyl esters. The products were confirmed by GC-MS. $CoBr_2$ (0.54mmol) / $Mn(OAc)_2{\cdot}4H_2O$ (0.65mmol) / *p*-xylene (48.6mmol) / AcOH (420.6mmol) was exposed to reaction conditions with and without CO_2 for ESR analysis. ESR measurements were conducted on Bruker ESR (EMX model) at 77K and DPPH was used as a g-marker.

Results and Discussion

Dehydrogenation of Alkylaromatics with CO_2. The effect of CO_2 in dehydrogenation of aromatic hydrocarbons such as ethylbenzene, 4-ethyltoluene, and cumene was examined at 500°C as shown in **Table 1**. Indeed, it is certain that carbon dioxide works very well in dehydrogenation of other aromatic hydrocarbons as the soft oxidant to increase the conversion as well as selectivity. Thus, CO_2 stream gave beneficial effect on dehydrogenation of aromatic hydrocarbons in terms of reactant conversion, indicating the oxidant role of CO_2 in abstraction of hydrogen atom from the benzylic C-H bond. The dehydrogenation of ethylbenzene showed very high selectivity even under nitrogen stream, but other two reactants exhibited the increased selectivity to their dehydrogenated products in the presence of CO_2. The enhancement of the dehydrogenation activity and the selectivity is certainly ascribed to the promotional effect to the oxidative process by excess carbon dioxide since high conversion of CO_2 comparable with the conversion values of aromatic reactants was obtained. This result implies that the initial hydrogen abstraction of aromatic hydrocarbons was much facilitated by carbon dioxide. Dehydrogenation of cumene to α-methyl styrene was easier than those of other reactants and, especially, this reaction was much accelerated by carbon dioxide.

Table 1. Effect of carbon dioxide for dehydrogenation of alkylaromatics[a]

Reactant	Carrier	Conv. (%)	Selec. (%)	$X(CO_2)$ (%)	H_2O/H_2[b]
Ethylbenzene	N_2	28.6	98.3	-	-
	CO_2	38.3	98.1	30.2	2.8
4-Ethyltoluene	N_2	23.1	89.7	-	-
	CO_2	33.9	91.8	27.5	4.7
Cumene	N_2	33.4	93.6	-	-
	CO_2	50.7	95.8	42.2	3.8

[a]Reaction conditions: Catalyst: $V\text{-}SbO_x/Al_2O_3$, [c]Temp. = 500°C, LHSV = 1.0 h^{-1}, CO_2/reactant = 10/1, Time-on-stream = 2 h. [b]molar ratio of H_2O/H_2 estimated in the gaseous products.
*Notation: Conv., reactant conversion; Selec., selectivity of target product; $X(CO_2)$, CO_2 conversion based on the reactant.

In gas phase distribution of products, carbon monoxide, water, and hydrogen are observed together with a trace of methane. The ratio of H_2O/H_2 in the product stream is estimated to be 2.8, 4.8, and 3.8 for ethylbenzene, 4-ethyltoluene, and cumene, respectively, after 2 h on stream. The formation of water as well as carbon monoxide implies that on the $V\text{-}SbO_x/Al_2O_3$ catalyst CO_2 molecule dissociates CO and surface oxygen which can abstract hydrogen from aromatic hydrocarbons, and then results in the generation of water. Taking into account the formation of large amount of water, high activity for supported $V\text{-}SbO_x$ catalyst under CO_2 carrier may be mainly ascribed to oxygen species dissociated from carbon dioxide molecule, thus due to the promotion of the oxidative process by carbon dioxide. In other words, this indicates that carbon dioxide plays a role as the soft oxidant in dehydrogenation

of alkylaromatics.

Oxidation of Alkylaromatics with O_2/CO_2. The effect of CO_2 in the liquid phase of alkylaromatics over Co/Mn catalyst has been shown in the **Table 2**. Initially the reaction was carried out with *p*-xylene which indicate s that the yields of acids are considerably increased in the presence of CO_2 under the similar reaction conditions. The study has been extended to other aromatic hydrocarbons such as toluene, *p*-toluic acid and ethyl benzene. The promotional effect of CO_2 on toluene is shown in **Figure 1**, in each time interval the conversions are higher with CO_2 and in the case of 3h run the yield of benzoic acid is about 80% in the presence of CO_2 where as in the absence of CO_2 it is about 60% - the yield enhancement by the CO_2 is about 20%. Further investigation of CO_2 promotional effect has been made on *p*-toluic acid and found that the yield of terephthalic acid is 65 % with CO_2 but in the absence of CO_2 it is only 58 %. The catalytic activity in the oxidation of toluene and *p*-toluic acid followed the similar trend of *p*-xylene but in the case of ethyl benzene we observed different trend regarding product distribution. In the presence of CO_2 acetophenone is the main product whereas in the absence of CO_2 it is benzoic acid. It is proposed that the abstraction of hydrogen (α-C-H bond fission) from the ethylbenzene produces acetophenone via ethyl benzene free radical. In the absence of CO_2 benzoic acid was produced by the C-C bond cleavage from the ethyl benzene. Aresta *et al.*[10] observed the similar behavior in the oxidation of double carbon side chain alkylaromatics (styrene).

Table 2. Effect of CO_2 in the liquid phase oxidation of alkylaromatics with Co/Mn catalyst

Substrate	P_{CO2} (atm)	Temp. (°C)	Time (h)	Yield (mol %)
p-Xylene	4	170	3.0	TPA (34.8), *p*-TA (36.9), TPAL (2.4), *p*-TAL (1.7), others (24.2)
p-Xylene	0	170	3.0	TPA (17.7), *p*-TA (47.9), TPAL (1.7), *p*-TAL (2.8), others (29.2)
p-TA	4	190	3.0	TPA (64.9), others (10.6)
p-TA	0	190	3.0	TPA (58.1), others (3.7)
Toluene	4	150	3.0	BA (78.7), others (0.7)
Tolune	0	150	3.0	BA (58.6), others (13.7)
EB[a]	6	100	2.5	AP (52.6), BA (36.9), others (10.5)
EB[a]	0	100	2.5	AP (19.4), BA (56.5), others (9.6)

Conditions: Substrate = 48.6mmol, Acetic acid = 420.6mmol, Co = 0.54mmol, Mn = 0.65mmol, Br =1.08mmol, P_{total} = 12atm (P_{O2} = 2atm, P_{N2} = Balance), [a]P_{total} = 10atm (P_{O2} =2).
Abbreviations: TPA (Terephthalic acid), *p*-TA (*p*-Toluic acid), TPAL (Terephthaldehyde), *p*-TAL (*p*-Tolualdehyde), BA (Benzoic acid), EB (Ethyl benzene), AP (Acetophenone).

In conclusion, typical oxidative dehydrogenation catalysts were proved to be utilized under the CO_2 stream alone instead of O_2 to get alpha olefin substituted aromatics from alkylaromatics such as ethylbenzene, 4-ethyltoluene, and cumene. Carbon dioxide

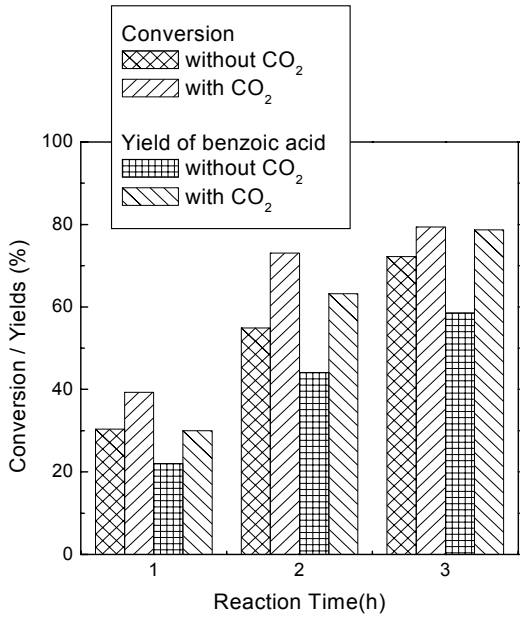

Figure 1. Effect of CO_2 in the liquid phase oxidation of toluene with Co/Mn catalyst. Conditions: Touene = 48.6 mmol, Acetic acid = 420.6 mmol, $CoBr_2$ = 0.54 mmol, $Mn(OAc)_2{\cdot}4H_2O$ = 0.65 mmol, P_{total} = 12 atm(P_{CO2} = 0 or 4, P_{O2} = 2, N_2 = Balance), Temp. = 150°C.

contributes to highly improved activities together with selectivities on one hydrogen molecule abstracted aromatics. The conventional cobalt and manganese catalyst was utilized for the oxidation of alkylaromatic hydrocarbons with O_2/CO_2 as co-oxidants. Carbon dioxide co-fed with O_2 led to the selective control to produce the corresponding aldehydes and acids with the enhanced rates. Therefore, the main roles of CO_2 in these oxidative reactions are found to enhance the selective hydrogen abstraction with the improved activities.

Acknowledgment

This work was performed for the Greenhouse Gas Research Center, one of the Critical Technology-21 Programs, funded by the Ministry of Science and Technology of Korea (MOST). I also thank my colleagues including Dr. K.W. Jun for their contributions to this work.

References

1. Yoo, J.S., *Catal. Today*, **1998**, 41, 49.
2. Park, S.-E., Yoo, J.S., Chang, J.-S., Environmental Challenges and Greenhouse Gas Control for Fossil Fuel Utilization in the 21st Century (eds. M.M. Maroto-Valer, Y. Song, C. Song), Chapter 33, Kluwer Academic/Plenum: New York, 2002.
3. Park, S.-E., Yoo, J.S., Chang, J.-S., Lee, K.Y., Park, M.S., *Prep. ACS Fuel Chem. Div.*, **2001**, 46(1), 115.
4. Chang, J.-S., Park, S.-E., Park, M.S., *Chem. Lett.*, **1997**, 1123.
5. Mimura, N.,Saito, M., *Catal. Lett.*, **1999**, 58, 59.
6. Landau, R., Saffer, A., *Chem. Eng. Proc.*, **1968**, 48, 20.
7. Partenheimer, W., *Catal. Today*, **1995**, 23, 69 and the references cited therein.
8. Yoo, J.S., Lin, P.S., Elfine, S.D., *Appl. Catal. A*, **1993**, 105, 259.
9. Jhung, S.-W., Lee, K.-W., Park, Y.-S., Yoo, J.S., US patent **2001**, 6,180,822.
10. Aresta, M., Tommasi, I., Quaranta, E., Fragale, C., Mascetti, J., Tranquille, M., Galan, F., Fouassier, M., *Inorg. Chem.*, **1966**, 35, 4254.

A NOVEL HIGHLY ACTIVE REFORMING CATALYST SYSTEM AND PRODUCTION OF PURE HYDROGEN FROM THE GREENHOUSE GASES OF CH_4 AND CO_2 AT MILD TEMPERATURES WITH A MEMBRANE REACTOR

Linsheng Wang, Kazuhisa Murata, Megumu Inaba

Research Institute for Green Technology, National Institute of Advanced Industrial Science and Technology,
AIST Tsukuba Central 5, Tsukuba, Ibaraki 305, Japan
E-mail: linsheng.wang@aist.go.jp

Introduction

Conversion of methane and carbon dioxide into synthesis gas (CO/H_2) is an important route for reasonable utilization of natural gas resource. Carbon dioxide reforming reaction of methane was first studied by Fischer and Tropsch using Ni and Co based catalysts in 1928 [1]. Recently the reforming reaction of methane with carbon dioxide on supported Ru, Rh, Pd, Ir, Pt, Mo or W carbide based catalysts has been studied by many other authors [2-10]. SiO_2, Al_2O_3, TiO_2, MgO, ZrO_2, La_2O_3, NaY, NaZSM-5 were used as supporting materials of the catalysts for the reforming reaction. The Bronsted acid sites of the supports are not necessary for the reforming reaction on the traditional catalysts [8]. The reported traditional reforming catalysts are also active for the two-step homologation of methane [11-13]. It has recently been reported that Re/HZSM-5 is a promising catalyst for one-step activation of methane into aromatics and C_2 hydrocarbons [14,15]. However, the catalytic performance of Re/HZSM-5 for the reforming reaction of methane with carbon dioxide has not been studied so far. In the present paper, the reforming reaction of methane with carbon dioxide on the bifunctional Re/HZSM-5 and Mo/HZSM-5 catalysts has been studied. In addition, High pure hydrogen was directly produced from the two greenhouse gases of methane and carbon dioxide on the novel catalyst at mild temperatures by integration of the reforming reaction and H_2 separation with a Pd membrane reactor.

Experimental

Re/HZSM-5 and Rh/HZSM-5 were prepared by impregnating $NH_4ZSM\text{-}5 \bullet SiO_2/Al_2O_3=30 \bullet$ with NH_4ReO_4 and $RhCl_3$ aqueous solution respectively, followed by drying at 383 K for 4 h and calcination at 773 K for 4 h. The sample was finally pressed, crushed and sorted into 20-40 meshes. Catalytic tests were carried out with about 200-2000 mg catalyst placed in a fixed bed continuous-flow membrane reactor. The catalysts were reduced by hydrogen at 623-673K for 2h. The membrane reactor is with 5/8" diameter and by 10" tall. It contains four membrane tubes with 1/8" diameter and by 7" tall. H_2 was permeated through the membrane into the tubes and removed by pump immediately after produced. The selectivity for hydrogen permeation through the membrane is 100% and ultra high pure H_2 was produced as a result. Conversion, selectivity and formation rate of products were calculated by an internal standard analyzing method described as previously. About 11.1% N_2 was added into ethane feed as internal standard. Catalytic conversion of ethane on Re/HZSM-5 was conducted at a reaction temperature range of 773-858K and a wide SV range.

Results and discussion

Catalytic performance of the novel Re based catalysts has been compared with traditional noble metal Rh based catalyst for the carbon dioxide reforming reaction of methane and results are listed in table 1. HZSM-5 supported Re catalyst exhibits a quite high activity for the reforming reaction and even better than the traditional noble metal Rh based catalyst as shown in table 1.

Table 1. The bifunctional effect of catalysts in activation of CH_4 and CO_2

Catalyst	Conversion (%) CH_4	CO_2	CH_4/CO_2 consumed	H_2/CO ratio in product
Re/HZSM-5	83	80	1.07	0.81
Rh/HZSM-5	78	72	0.96	0.80
Re/KZSM-5	17	9	1.74	0.43
Mo/HZSM-5	22	15	0.68	0.38

Methane SV=5000 ml/h/g; Feed ratio (CH_4/CO_2)=1.05; Temperature=973K

The high methane and CO_2 conversions of 83% and 80% were attained on Re/HZSM-5 at 973K. Conversions of methane and carbon dioxide on Rh/HZSM-5 are 78% and 72% at the exactly same reaction conditions. The high activity of the novel bifunctional Re/HZSM-5 for the reforming reaction is due to its high activity for one-step activation of methane. It is also indicated in table 1 that both metal Re and Bronsted acid of ZSM-5 support are necessary for the high activity of Re/HZSM-5. The monofunctional Re/KZSM-5 (B acid sites of HZSM-5 support were poisoned by K) and bifunctional Mo/HZSM-5 give much lower activity for carbon dioxide reforming of methane although Mo/HZSM-5 is also an excellent catalyst for one step activation of pure methane. This is due to the active phase of Mo/HZSM-5 for methane active phase is unstable when it is exposure to CO_2. Table 2 gives the effect of feed ratio (CH_4/CO_2) on the conversions of CH_4 and CO_2. It is indicated in table 2 that the maximum methane conversion is obtained when the feed ratio (CH_4/CO_2) is near 1. However, CO_2 conversion increases with increasing the ratio of CH_4/CO_2 in feed. The H_2/CO ratio is near unity is at the higher CH_4/CO_2 ratio. In addition, the ratio of the consumption rates of methane and carbon dioxide is about 1 even at the different feed ratio (CH_4/CO_2).

Table 2. Dependence of CH_4 and CO_2 conversions on the feed ratio (CH_4/CO_2)

Feed ratio CH_4/CO_2	Conversion (%) CH_4	CO_2	CH_4/CO_2 consumed	H_2/CO ratio in product
0.81	77	59	0.89	0.67
0.91	83	64	1.01	0.71
1.05	83	80	1.07	0.81
1.47	66	83	0.99	0.84
1.64	45	94	0.99	0.92

Methane SV=5000 ml/h/g; Temperature=973K

The low-temperature activity of Re/HZSM-5 catalyst for the dry reforming reaction is also evaluated and the result is listed in table 3.

Table 3. The lower temperature activity of Re/HZSM-5 for the reforming reaction CH_4 and CO_2

Temperature (K)	Conversion (%) CH_4	CO_2	CH_4/CO_2 consumed	H_2/CO ratio in product
773	15	26	0.61	0.15
818	30	44	0.70	0.60
858	41	49	0.85	0.66
973	83	80	1.07	0.81

Methane SV=5000 ml/h/g; Feed ratio (CH_4/CO_2)=1.05

It is indicated in table 3 that the Re/HZSM-5 exhibits a considerable activity even at as low as 773-858K and the conversions of methane and CO_2 are 41% and 49% at 858K. The excellent low temperature activity of Re/HZSM-5 makes it have many advantages for the integration of the catalytic reaction of the reforming and hydrogen separation because the Pd type membrane is limited to use only at relatively mild temperatures.

Although Re/HZSM-5 is quite active for the carbon dioxide reforming of methane even at the lower temperatures, the conversions of methane and carbon dioxide are constrained by thermodynamic equilibrium. To transform methane and CO_2 into pure hydrogen and CO at the conversions beyond the thermodynamic equilibrium, a Pd type membrane reactor was used for integration of the reforming reaction and hydrogen separation. The conversions of CH_4 and CO_2 when hydrogen is separated and not separated at 858K and different methane SV are compared in table 4. It is shown in table 4 that methane conversion for the dry reforming reaction is about 47-48% and it changes little with varying methane SV from 1300 to 325 ml/h/g when hydrogen was not separated from product. However, the much higher methane conversion of about 77% has been achieved at the low temperature of 858K as shown in table 4. CO_2 conversion is also enhanced by the hydrogen separation at the same time. In addition, the ratio of feed consumption rates (CH_4/CO_2) is more near unity when hydrogen is separated from product. This is because some side reaction such as reduction of CO_2 by H_2 in to CO is effectively suppressed by the continuously hydrogen separation from product with the membrane.

Table 4. Effect of H_2 separation on the conversions of CH_4 and CO_2 at different SV

SV of CH_4 (ml/h/g)	Permeability of H_2 (%)	Conv. (%) CH_4	CO_2	CH_4/CO_2 consumed	H_2/CO ratio
325	92	76.9	60.5	1.15	*
	0	48.3	48.0	0.91	0.63
650	92	69.2	45.6	0.98	*
	0	47.9	34.4	0.90	0.71
1300	90	62.7	42.6	0.95	*
	0	47.1	33.3	0.92	0.71

Feed ratio (CH_4/CO_2)=0.69; Temperature=858K; * H_2 separated

Conclusion

Re/HZSM-5 is a novel reforming catalyst for the conversion of methane and carbon dioxide into hydrogen and CO. The novel catalyst system exhibits a quite high activity for the carbon dioxide reforming reaction of methane even at mild temperatures and it is different from the traditional reforming catalysts because both Re metal and the Bronsted acid on the novel catalyst are contributed to the methane activation. On the novel catalyst system, high pure hydrogen are directly produced from the greenhouse gases of methane and carbon dioxide by integration of the reforming reaction and hydrogen separation with a Pd type membrane reactor. In addition, much higher conversions of methane and CO_2 beyond the thermodynamic equilibrium are attained because hydrogen is separated from the product.

References

1. F. Fischer and H. Tropsch, Brennst. Chem. 3 (1928) 39
2. F. Solymosi, Gy. Kutsan and A. Erdohelyi, Catalysis Letters, 11 (2000) 149
3. Z. L. Zhang, V. A. Tsipouriari, A. M. Efstathiou and X. E. Verykios, Journal of Catalysis, 158 (1996) 51
4. M. C. J. Bradford and M. A. Vannice, Journal of Catalysis,173 (1998) 157
5. M. C. J. Bradford and M. A. Vannice, Journal of Catalysis,183 (1999) 69
6. M. F. Mark and W. F. Maier, Journal of Catalysis,164 (1996) 122
7. J. H. Bitter, K. Seshan and J. A. Lercher, Journal of Catalysis,176 (1998) 93
8. R. N. Bhat and W. M. H. Sachtler, Applied Catalysis A: General 150 (1997) 279
9. M. Tsuji, T. Miyao and S. Naito, Catalysis Letters, 69 (2000) 195
10. A. J. Brungs, A. P. E. York, J. B. Claridge, C. Marquez-Alvarez and M. L. H. Green, Catalysis Letters, 70 (2000) 117
11. L. Guczi, K. V. Sarma and L. Borko, Journal of Catalysis,167 (1997) 495
12. M. Belgued, A. Amariglio, L. Lefort, P. Pareja and H. Amariglio, Journal of Catalysis,161 (1996) 282
13. T. Koerts, M. J. A. G. Deelen and R. A. Van Santen, Journal of Catalysis,138 (1992) 101
14. L. Wang, R. Ohnishi and M. Ichikawa, Journal of Catalysis,190 (2000) 276
15. L. Wang, K. Murata, A. Sayari, B. Grandjean and M. Inaba, ChemComm., in press (2001)

Dry reforming of ethane on tri-metallic perovskites ($LaCo_xFe_{1-x}O_3$). Characterisations and reactivity.

G. Rodriguez[1], A.C. Roger[1], L. Bedel[1], L. Udron[1], L. Carballo*, A. Kiennemann[1]*

[1]LMSPC-ECPM, UMR 7515 25, rue Becquerel 67087 Strasbourg Cedex 2 France

*Universitad National Colombia, Santa Fé de Bogota Colombia.

1. INTRODUCTION

The study of the catalytic dry reforming of light hydrocarbons (C_1, saturated C_2) is of interest for syngas ($CO-H_2$) production. The obtained $CO-H_2$ mixture can be used for hydroformylation, methanol or Fischer-Tropsch synthesis. The fast deactivation by excess of carbon deposits is the main drawback of metal supported systems (Ni, Co, Pt, Pd, Rh) [1]. Basic supports like MgO, La_2O_3 have been used to increase the catalyst live by lowering the rate of carbon deposition [2]. A second way has been explored through formation of well defined structure containing an active metal (nickel). For example, we have shown that the partial substitution of Ni by Fe in $LaNiO_3$ increases the Ni reduction temperature close to the reaction temperature. Strong Ni-tri-metallic perovskite interactions both improve lifetime and dispersion of nickel particles and decrease carbon formation and sintering of metal by formation of a Ni-Fe alloy [3,4,5]. Due to the good ability of perovskite-type oxides to be B-site substituted, Ni could be replaced by other metal such as Co.

The aim of the present study is to point out the interest of these defined Co-containing structures in reforming of ethane.

2. EXPERIMENTAL PART

2.1. Preparation. The mixed $LaCo_xFe_{1-x}O_3$ perovskites with x values varying from 0 to 1 (x = 0, 0.3, 0.5, 0.7, 1) were prepared from La acetate, Co acetate and Fe powder via a sol-gel related method [6]. The starting materials were separately dissolved in hot propionic acid under stirring and then mixed. After 30 minutes stirring, the boiling resulting solution was evaporated until a resin is obtained. This resin was heated 4 hours at 750°C with a ramping of $3°C.mn^{-1}$. BET surface areas were in the range of 3 (x=0) to 6 $m^2.g^{-1}$ (x=1).

2.2. Characterization The nature of the obtained phases and the lattice parameters were determined by powder X-Ray diffraction (XRD) recorded on a Siemens D-5000 diffractometer using the CuKα radiation.

Transmission electron microscopy (TEM) was performed on a TOPCON-EM002B apparatus coupled with an energy dispersive X-Ray device (EDS).

Temperature programmed reduction (TPR) was performed with a 50 mg sample placed in a U-shaped quartz tube (6.6 mm ID), the temperature was increased from 25 to 900°C with a slope of 15°C min^{-1}. The reducing mixture was 3 vol.% hydrogen in helium (50 mL min^{-1}). Hydrogen consumption was quantified by a TC detector after trapping on molecular sieve of the formed water.

2.3. Reaction conditions The operating conditions were the following : fixed bed quartz reactor (6.6 mm I.D.), inlet temperature : 400-800°C; feed flow rate : 0.15 $L.h^{-1}$ ethane, 0.3 $L.h^{-1}$ CO_2 and 2.55 $L.h^{-1}$ Ar; catalyst amount: 100 mg. The outlet gas was analyzed by two on line gas chromatographs: one for C_2H_6, CO and CO_2; and a second one for CO and H_2.

3. RESULTS

3.1. Characterization of $LaCo_xFe_{1-x}O_3$ systems before catalytic test

XRD pattern of $LaCo_xFe_{1-x}O_3$ (x=0.3, 0.5 and 0.7) shows that a solid solution is formed in all proportions. A split of the main reflection line for x ≥ 0.5 is characteristic of the rhombohedral system (R) of $LaCoO_3$ isomorphs. Compounds without split reflection crystallize in the orthorhombic (O) system such as $LaFeO_3$ [7].

The different catalysts have been analysed by TEM-EDS to confirm the initial composition of the structures and the homogeneity of the preparation (figure 1).

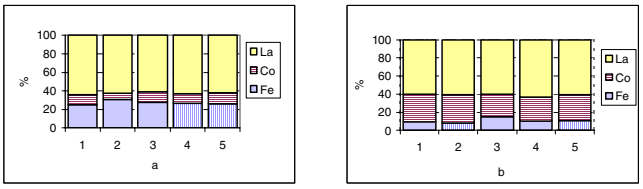

Figure 1. Elemental distribution observed by energy dispersive X-ray spectroscopy before catalytic test for: (a) $LaCo_{0.3}Fe_{0.7}O_3$ and (b) $LaCo_{0.7}Fe_{0.3}O_3$. (1) Broad focused beam 200nm (2-5) Narrow focused beam 14 nm.

The characterization (with broad and narrow focussed beam) shows a good homogeneity of each preparation which is formed of grains of around 50 nm each. The reducibility of the perovskites was studied by T.P.R.. The hydrogen consumption is given versus temperature for four different materials (figure 2).

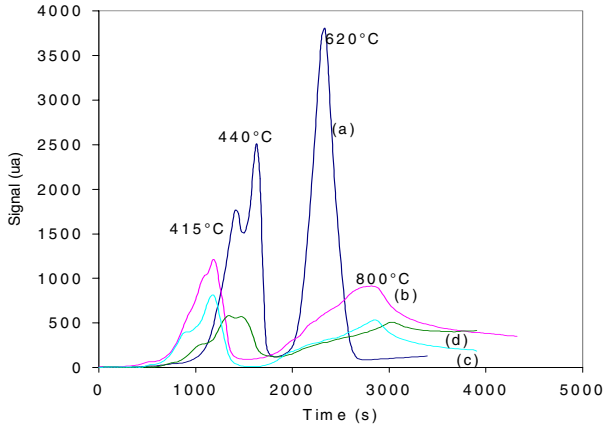

Figure 2. TPR before catalytic test for (a) $LaCoO_3$, (b) $LaCo_{0.7}Fe_{0.3}O_3$, (c) $LaCo_{0.5}Fe_{0.5}O_3$ and (d) $LaCo_{0.3}Fe_{0.7}O_3$.

The T.P.R. shape reveals two reduction areas. The first between 350°C and 500°C, the second with a maximum between 620°C ($LaCoO_3$) and 810°C ($LaCo_{0.3}Fe_{0.7}O_3$). The temperature of the second maximum increases with iron content. So it is possible to control the perovskite reduction temperature by varying the Co/Fe ratio, and to correlate it with the ethane reforming temperature.

3.2. Catalytic tests. Figures 3 and 4 show respectively the ethane conversion and the CO yield versus x for temperatures between 600°C and 800°C. Ethane conversion increases with increasing x values and temperatures. There is an important change in conversion and CO yield when x is equal or higher than 0.5. This value corresponds to a change of the structure from orthorhombic to rhombohedral. $LaCoO_3$ shows excellent results too, but deactivated very fast. On the other hand, catalysts containing cobalt and iron showed very good stability in addition to performance.

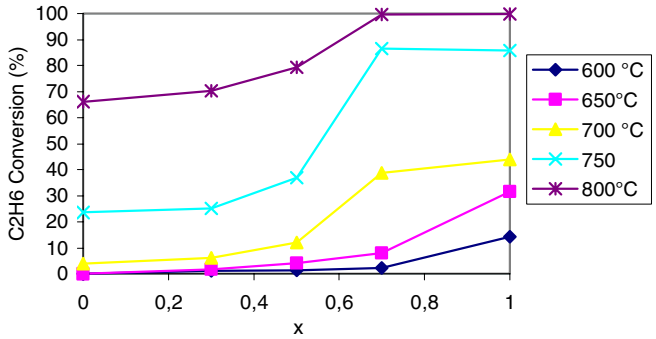

Figure 3. C_2H_6 Conversion at various temperatures versus x with a CO_2/C_2H_6=2 for $LaCo_xFe_{1-x}O_3$ perovskite.

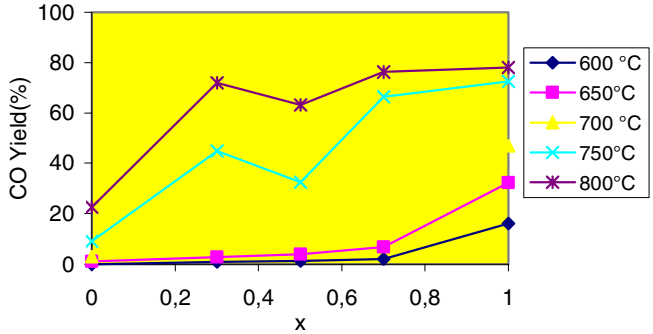

Figure 4. CO yield (%) at various temperatures versus x with a CO_2/C_2H_6=2 for $LaCo_xFe_{1-x}O_3$ perovskite.

The interest of the tri-metallic perovskite La-Co-Fe compared to the bi-metallic La-Co is better understood by characterization of the catalysts after test.

3.3. Characterization after test. XRD diffraction patterns after test show different phases depending on x values as summarised in Table 1.

x	Crystalline phases detected by XRD after catalytic test					
0	$LaFeO_3$					
0.3		$LaCo_wFe_{1-w}O_3$	La_2O_3			
0.5		$LaCo_zFe_{1-z}O_3$	La_2O_3			
0.7			La_2O_3	$LaFeO_3$	Co	
1			La_2O_3		Co	CoO

Table 1. Crystalline phases detected by XRD after test for $LaCo_xFe_{1-x}O_3$ perovskite oxides.

For higher cobalt contents (x > 0.5) the three-metal perovskite structure is destroyed and the most stable $LaFeO_3$ perovskite is formed together with lanthanum oxide and cobalt. $LaFeO_3$ perovskite could also be characterised by FT-IR (555 cm^{-1}). For low cobalt content, the La-Co-Fe perovskite is preserved, although cobalt content is less than in the initial structure.

The LaCoFe elemental distributions (EDS) are given in figure 5 and the La/Fe ratios in figure 6 for x = 0.3 and 0.7. Figure 5 shows a higher heterogeneity of $LaCo_{0.7}Fe_{0.3}O_3$ compared to $LaCo_{0.3}Fe_{0.7}O_3$. For x = 0.3, almost the same ratio La/Co/Fe or La/Fe are observed in different parts of the sample, no free cobalt has been seen confirming that the tri-metallic structure was preserved. However, analyses show clearly that part of cobalt has left the perovskite and w and z (Table 1) are lower than the initial value of x. For x = 0.7, the tri-metallic perovskite is destroyed, free cobalt particles are evidenced and the La/Fe ratio changed. The change in La/Fe ratio indicates the presence of free lanthanum (as oxide or hydroxide). In the latter case, in agreement with XRD results, it can be concluded that the $LaFeO_3$ perovskite behaves as a support for cobalt metal particles of 10 to 50 nm (TEM).

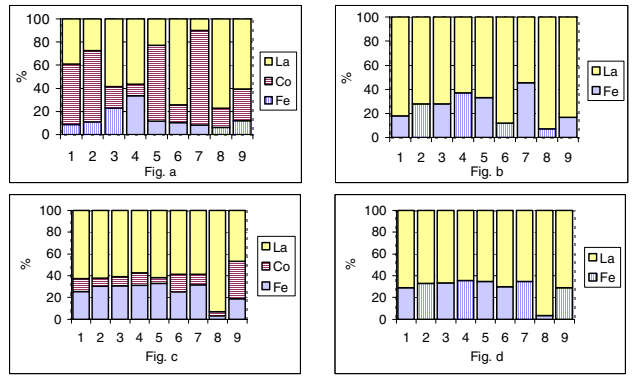

Figure 5. Elemental distribution observed by energy dispersive X-ray sprectroscopy after catalytic test for: $LaCo_{0.7}Fe_{0.3}O_3$ (a) La, Co and Fe. (b) La and Fe. $LaCo_{0.3}Fe_{0.7}O_3$ (c) La, Co and Fe. (d) La and Fe. (1) Broad focused beam 200nm (2-9) Narrow focused beam 14 nm.

4. DISCUSSION AND CONCLUSIONS

In the present study, we can see that whatever the x value (until 0.7), the perovskite structure is preserved : as LaCoFe for x ≤ 0.5 and as a LaFe system for x ~ 0.7.

The catalytic results have shown an increase of reactivity with the increase of the x value and of the reaction temperature. Moreover a gap of activity corresponds to a change of the perovskite structure from orthorhombic to rhombohedral. Such a change has also been seen in Fischer-Tropsch reaction (7). Good aging for the catalysts suggests that coke formation is limited as confirmed by elemental analyses. Different explanations could be given : formation of small Co metal particles in strong interaction with the perovskite support or formation of a Co-Fe alloy and dilution effect. With La-Fe-Co catalysts alloy formation was not seen. For 0.3 ≤ x ≤ 0.7, we suggest that the presence of cobalt inside the partially reduced perovskite network is in strong interaction with the free cobalt and then avoids an excessive coke formation, resulting in a good aging. This strong interaction is confirmed by the possibility of regeneration of the used catalyst by heating at high temperatures (900°C). Another contribution to decreasing coke formation is the performance of $LaFeO_3$ in total oxidation of hydrocarbons. Thus it is postulated that $LaFeO_3$ as well as La_2O_3 will participate in the oxidation of coke precursors.

Acknowledgement. The authors are deeply grateful to ECOS-NORD for providing fellowship to G. Rodriguez and to the European Community through the RUCADI program.

REFERENCES

(1) J.R. Rostrup-Nielsen, *Catalysis Science and Technology 5* **1984**, *1*, J.R. Anderson, and M. Boudart (eds) Springer (Berlin).
(2) F. Frusteri, F. Arena, G. Calogero, T. Torre, A. Parmaliana, *Catalysis Communications* **2001** *2* 49.
(3) H. Provendier, C. Petit, C. Estournes, S. Libs, A. Kiennemann, *Appl. Catal. A* **1999** *180* 163.
(4) C. Petit, A. Kiennemann, P. Chaumette, O. Clause, *U.S. Patent 5447705* **1995**.
(5) H. Provendier, C. Petit, C. Estournes, A. Kiennemann, *Stud. Surf. Sci. Catal.* **1998** *119* 741.
(6) H. Provendier, C. Petit, J.L. Schmidt, A. Kiennemann, C. Chaumont, *J. Mater. Sci.* **1999** *34* 4121.
(7) L. Bedel, A.C. Roger, A. Kiennemann, C. Estournes, Prepr. Pap. ~ *Am. Chem. Soc., Div. Petroleum Chem.*, **2000**, *45*, 236.

Catalytic Tri-reforming of Methane Using Flue Gas from Fossil Fuel-based Power Plants

*Wei Pan, Jian Zheng, Chunshan Song**

Clean Fuels and Catalysis Program, Energy Institute and
Department of Energy & Geo-Environmental Engineering,
The Pennsylvania State University, University Park, PA 16802
*Email: csong@psu.edu; Tel: 814-863-4466; Fax:814-865-3248

Introduction

The present work is an exploratory study on a new process for the production of synthesis gas ($CO + H_2$) using CO_2 in flue gas from fossil fuel-based electric power plants. The existing processes for synthesis gas production from methane or natural gas include steam reforming, CO_2 reforming, auto-thermal reforming, and partial oxidation, of methane or natural gas. The new process is called tri-reforming of methane, referring to simultaneous oxy-CO_2-steam reforming.

Tri-reforming is a new process designed for the direct production of synthesis gas with desirable H_2/CO ratios by reforming methane or natural gas using flue gas from fossil fuel-based electric power plants without pre-separation of CO_2. These flue gases are regarded as major source of CO_2 emission in the U.S. Generally the compositions of flue gases depend on the types of fossil fuels used in power plants. Flue gases from natural gas-fired power plants typically contain 8-10% CO_2, 18-20% H_2O, 2-3% O_2, and 67-72% N_2; flue gases from coal-fired boilers primarily contain 12-14% CO_2, 8-10% H_2O, 3-5% O_2, 72-77% N_2, and trace amount of NOx, SOx, and particulates [1].

It is hypothesized that tri-reforming be a synergetic combination of CO_2 reforming (Eq.1), steam reforming (Eq. 2), and methane oxidation reactions (Eqs. 3 and 4). Therefore, tri-reforming is expected to encompass a number of unique features. One major feature is its ability to convert CO_2 in flue gas without CO_2 separation while avoiding the use of pure CO_2 and the severe problem of carbon deposition encountered in CO_2 reforming system [2-6]. Currently most of pure CO_2 is obtained from CO_2 separation processes (e.g. absorption, adsorption, and membrane separation) that are often energy-intensive and costly. Some separation processes could lower the power plant energy output as much as 20% [7].

Other features of tri-reforming include that there is no need to handle pure oxygen and it directly produces synthesis gas with a desirable H_2/CO ratio (e.g. $H_2/CO = 1.5 \sim 2$). Furthermore, oxygen in flue gas may help to ease the reaction energy requirement as encountered in CO_2 reforming alone or steam reforming alone. In general, the new tri-reforming process concept is consistent with the goals of DOE Vision 21 for power plants with respect to decreasing greenhouse gas emission, improving power generation efficiency and co-producing fuels and chemicals [8].

$$CO_2 + CH_4 = 2CO + 2H_2 \quad \Delta H° = 247.3 \text{ kJ/mol} \qquad (1)$$
$$H_2O + CH_4 = CO + 3H_2 \quad \Delta H° = 206.3 \text{ kJ/mol} \qquad (2)$$
$$(1/2)\, O_2 + CH_4 = CO + 2H_2 \quad \Delta H° = -35.6 \text{ kJ/mol} \qquad (3)$$
$$2O_2 + CH_4 = CO_2 + 2H_2O \quad \Delta H° = -880 \text{ kJ/mol} \qquad (4)$$

It should be pointed out that the H_2/CO ratio in synthesis gas is important since synthesis gas with different H_2/CO ratios has different applications in industry. The current major applications of synthesis gas (not hydrogen) include methanol synthesis and Fischer-Tropsch (F-T) synthesis that require synthesis gas with a H_2/CO ratio close to 2. However, synthesis gas directly produced from CO_2 reforming of methane has H_2/CO ratio close to 1. Hence this kind of synthesis gas (H_2/CO ratio ≤ 1) requires further treatment in order to be applied in methanol and F-T synthesis. Similarly synthesis gas produced from steam reforming can not be directly applied in methanol or F-T synthesis either since the H_2/CO ratio of synthesis gas produced from steam reforming is usually larger than 3. Although methane partial oxidation produces synthesis gas with a H_2/CO ratio of 2, methane partial oxidation is difficult to control due to its exothermic feature and is dangerous and expensive due to the handling of pure oxygen. Tri-reforming, however, is expected to readily produce synthesis gas with the desired H_2/CO ratios of $1.5 \sim 2$ by manipulating tri-reforming reactant compositions under relatively mild reaction conditions.

Unlike steam reforming, CO_2 reforming, or methane partial oxidation, tri-reforming has not been systematically studied. The concept of tri-reforming using power plant flue gas was first proposed by Song in 1999 [1,9]. Before 1999, several papers were published on the study of combined CO_2 reforming and partial oxidation reaction [10-12] and simultaneous steam and CO_2 reforming of methane in the presence of oxygen [13]. The results in these papers have indicated that combined reforming is feasible. However, the new tri-reforming process still faces a number of challenges. The future challenges include, for example, effective conversion of CO_2 in the presence of O_2 and H_2O; the heat management; the minimization of the effect of SOx and NOx in flue gas on tri-reforming process; the management of inert gas N_2 in flue gas; and the integration of new process into power plants. The tasks in the current work of tri-reforming include the computational study of equilibrium properties of tri-reforming at various feedstock compositions and reaction conditions, the design of operation parameters, and the development of catalysts tailored for tri-reforming. In a real tri-reforming reaction, steam, CO_2, and O_2 all compete to react with methane over catalysts. Improvement of CO_2 conversion in the presence of steam and O_2 would depend on the catalysts and reaction conditions.

Experimental

Computational Analysis. The theoretical analysis was based on thermodynamic calculations. The purpose of this analysis is to establish thermodynamic equilibrium conversions of reactants, equilibrium product distributions under different reaction conditions (such as feedstock compositions, temperatures, and pressures) in tri-reforming reaction system.

The equilibrium compositions were calculated based on the principle of atom and mass balance and Gibbs Energy Minimization Method (GEMM). Before calculation, it was critical to identify stable reactants and products in the reaction system. The calculation employed HSC Chemistry software developed by Outokumpu Research Oy, Finland.

Catalyst preparation. Catalysts studied in this work included 8 wt% Ni and 2 wt% Pt catalysts supported on Ce-Zr oxides with or without CaO or MgO promoters. Ce-Zr oxides were prepared according to the method of "soft chemistry" [14]. Zirconium n-propoxide ($Zr(OC_3H_7)_4$) dissolved in 20 ml of iso-propyl alcohol was gradually added into an aqueous solution (20ml) of $Ce(NO_3)_2.6H_2O$, leading to the immediate hydrolysis and the formation of a pseudo gel. The pseudo gel was dried at 60ºC for 1 h and then at 120ºC overnight. The dried sample was finally calcined in air at 870ºC for 4 h and ready for use as a support.

Ni and Pt catalysts supported on Ce-Zr oxides were prepared by wet impregnation. $Ni(NO_3)_2 \bullet 6H_2O$ or $Pt(NH_3)_4Cl_2 \bullet xH_2O$ (MW = 334.12) was dissolved in 5 ml of H_2O. Ce-Zr oxide powder was then added into the solution under stirring. The mixture was dried at 60ºC overnight, followed by calcination at 870ºC for 4 h. The calcined sample was then pressed into disks and crushed and sieved. The particles between 18-35 meshes were collected for use

in reaction test. When preparing MgO or CaO promoted catalysts, $Ca(NO_3)_2 \bullet 4H_2O$ or $Mg(NO_3)_2 \bullet 6H_2O$ was dissolved in the same solution as $Ni(NO_3)_2$ or $Pt(NH_3)_4Cl_2$ and followed the same procedures as described above.

Tri-reforming experiments. The tri-reforming reaction was studied in a fixed-bed reactor at 850ºC under 1 atm. The reactor was made of an Inconel 800H alloy tube with the dimension of 0.54" o.d., 0.375" i.d., and 16" in length. In each tri-reforming, about 0.1 g of catalyst sample was placed in the middle section of the reactor. The reactor was interfaced with GC by a ten-port gas sampling valve, which enables online product analysis. The GC included a packed silica gel column, a molecular sieve column, and a TCD detector. Before each reaction the catalyst was reduced in H_2 following the temperature program: keeping the reactor temperature at 100ºC for 15 minutes, at 450ºC for 75 minutes, and at 850ºC for 10 minutes with a temperature ramp of 12ºC/min. Then H_2 was stopped and the reactor temperature was kept at 850ºC under Ar flow for another 20minutes. Steam was first introduced into the reactor. After 20 minutes of steam flow (0.02ml(l)/min), CH_4, CO_2, and O_2 were then introduced into the reactor. The flow rates of CH_4, CO_2, and O_2 were maintained by mass flow controllers (Brooks Instruments Corporation, USA); steam flow was controlled by an ISCO liquid pump. The reaction effluent except steam was analyzed by an on-line GC in every 30 minutes during a time-on-stream (TOS) period of 300 minutes. Steam was condensed before the GC.

Results and Discussion

It is expected that steam reforming, CO_2 reforming, and methane oxidation take place simultaneously in tri-reforming system. Table 1 compares equilibrium methane conversions, CO_2 and steam conversions, and H_2/CO ratios in steam reforming, CO_2 reforming, and combined CO_2 and steam reforming with the $(CO_2+H_2O)/CH_4$ ratio of 1. When steam is gradually replaced by CO_2, H_2/CO ratios in products decrease monotonically from 3.06 in steam reforming to 1.03 in CO_2 reforming at 850ºC and 1 atm while methane conversions and CO_2 conversions have only minor changes.

Table 1. Equilibrium H_2/CO Ratios and Equilibrium Conversions of Methane, Steam, and CO_2 at 850ºC and 1 atm

	CH_4 Conv. (%)	CO_2 conv. (%)	Steam conv. (%)	H_2/CO ratio
$CH_4:H_2O:CO_2$ =1:1:0	94.0	-	95.4	3.06
$CH_4:H_2O:CO_2$ =1:0.75:0.25	94.9	91.3	93.1	2.25
$CH_4:H_2O:CO_2$ =1:0. 5:0.5	95.8	93.7	88.7	1.66
$CH_4:H_2O:CO_2$ =1:0.25:0.75	96.6	94.3	76.4	1.32
$CH_4:H_2O:CO_2$ =1:0:1	97.4	95.0	-	1.03
$CH_4:H_2O:CO_2:O_2$ =1:0.475:0.475:0.1	97.9	87.0	77.0	1.67
$CH_4:H_2O:CO_2:O_2$ =1:0.45:0.45:0.2	99.0	75.2	56.0	1.69
$CH_4:H_2O:CO_2:O_2$ =1:0.375:0.375:0.5	99.8	28.4	-29.0	1.71
$CH_4:H_2O:CO_2:O_2$ =1:1:1:0.1	99.8	53.1	26.7	1.48

The calculation also predicts a decrease of steam conversions with increasing CO_2 and O_2 concentrations in the feed.

When O_2 is introduced, the ratio of $(CO_2+H_2O+0.5O_2)/CH_4$ is kept at 1 for comparison with steam reforming, CO_2 reforming, and combined reforming (Table 1). Although both CO_2 and steam conversions decrease with O_2 concentrations in the tri-reforming system, steam conversions decrease more dramatically than CO_2 conversions. This may be contributed to the reverse water gas shift reaction at high temperatures. Methane conversions only have a slight increase (close to 100%) with the increase of O_2 and a constant H_2/CO ratio is predicted with the addition of O_2.

When the same amount of CO_2 and H_2O is present in tri-reforming as in the cases of $CH_4:CO_2:H_2O:O_2$=1:0.475:0.475:0.1 and $CH_4:CO_2:H_2O:O_2$=1:1:1:0.1 (Table 1), CO_2 show higher equilibrium conversions (87% and 53.1% , respectively) than the steam conversions (77% and 26.7%, respectively).

Although thermodynamic analysis predicts CO_2 is more preferably converted than steam when same amounts of CO_2 and steam are present in tri-reforming system, one of the major challenges in the study of tri-reforming is the development of new catalysts that are able to efficiently convert CO_2 in the presence of H_2O and O_2. We have prepared and tested a number of Ni and Pt-based catalysts. Some of the preliminary results are listed in Table 2.

Table 2. Experimental Results of Tri-reforming at 850ºC and 1 atm ($CH_4:CO_2:H_2O:O_2$=1:1:1:0.1)

	CH_4 Conv. (%)	CO_2 conv. (%)	H_2/CO ratio
8%Ni/Ce-Zr-O	77.0	26.9	1.60
8%Ni/CaO/Ce-Zr-O	86.2	36.6	1.48
8%Ni/MgO/Ce-Zr-O	89.1	38.8	1.49
2%Pt/ /Ce-Zr-O	80.4	36.2	1.44
2%Pt/CaO/Ce-Zr-O	64.5	26.5	1.52
2%Pt/MgO/Ce-Zr-O	83.5	32.7	1.57
Equilibrium values	99.8	53.1	1.48

Note: all the experimental data in this table are average values during TOS of 300 minutes.

These experimental results show that CaO and MgO promote methane and CO_2 conversions over Ni-based catalysts although methane and CO_2 conversions over these catalysts are still lower than those predicted from thermodynamic analysis. On the contrary, CaO and MgO in Pt-based catalyst lower CO_2 conversions. These results indicate that catalysts still play an important role in tri-reforming. More catalysts are under investigation.

Conclusions

Equilibrium properties of tri-reforming under different conditions were analyzed by thermodynamics. O_2 in tri-reforming system could lead to the decrease of both CO_2 and steam conversions. CO_2 usually has a higher equilibrium conversion than steam when same amounts of steam and CO_2 co-exist in tri-reforming.

To achieve higher CO_2 conversions in catalytic tri-reforming of methane, a tailored catalyst for tri-reforming is desired.

Acknowledgement. The authors are grateful for the financial support from National Energy Technology Laboratory, US DOE (UCR Innovative Concepts Program, DE-FG26-00NT40829) and Department of Energy and Geo-Environmental Engineering (Graduate assistantship to WP) at Penn State University.

References

(1) Song, C. Tri-reforming: A new process for reducing CO_2 emission. *Chemical Innovation*. **2001**, 31(1), 21-26.

(2) Rostrup-Nielsen, J. R. Aspects of CO_2-reforming of Methane. *Studies in Surface Science and Catalysis - Natural Gas Conversion II*; Curry-Hyde, H. E. ; Howe, R.F. Elsevier: Amsterdam, **1994**; 81, 25-41.

(3) Rostrup-Nielsen, J. R.; Bak Hansen, J. H. CO_2-reforming of methane over transition metals. *J. Catal.* **1993**, 144,38-49.

(4) Wang, S.; Lu, G. Q. M. Carbon dioxide reforming of methane to produce synthesis gas over metal-supported catalysts: State of art. *Energy & Fuels* **1996**, 10(4), 896-904.

(5) Bradford, M. C. J.; Vannice, M. A. CO_2 reforming of CH4. *Catal. Rev.Sci. Eng.* **1999**, 40(1), 1-42.

(6) Tomishige, K.; Himeno, Y.; Yamazaki, O.; Chen, Y.; Wakatsuki, T.; Fujimoto, K. Development of a New Generation Reforming Catalyst: Catalytic Performance and Carbon Deposition Behavior on Nickel-Magnesia Catalysts. *Kinet. and Catal.* **1999**, 40(3), 432-439.

(7) DOE/FE . *Capturing Carbon Dioxide*. Office of Fossil Energy, U.S. Department of Energy, Washington, D.C., **1999**;

(8) FETC (Federal Energy Technology Center). *Vision 21 Program Plan - Clean Energy Plants for the 21st Century*. Office of Fossil Energy, U.S. Department of Energy, Washington, D.C., **1999**;

(9) Song, C. Chemicals, fuels and electricity from coal. A proposed tri-generation concept for utilization of CO_2 from power plants. *16th International Pittsburgh Coal Conference*, Pittsburgh, USA, **1999**; Paper No., 16-6.

(10) Ashcroft, A. T.; Cheetham, A. K.; Green, M. L. H.; Vernon, P. D. F. Partial Oxidation of Methane to Synthesis Gas Using Carbon Dioxide. *Nature* **1991**, 352(6332), 225-226.

(11) Inui, T.; Saigo, K.; Fujii, Y.; Fujioka, K. Catalytic combustion of natural gas as the role of one-site heat supply in rapid catalytic CO_2-H_2O reforming of methane. *Catal. Today* **1995**, 26(3/4), 295-302.

(12) O' Connor, A. M.; Ross, J. R. H. The effect of O_2 addition on the carbon dioxide reforming of methane over Pt/ZrO_2 catalysts. *Catal. Today* **1998**, 46,203-210.

(13) Choudhary, V. R.; Rajput, A. M.; Prabhakar, B. NiO/CaO-catalyzed formation of syngas by coupled exothermic oxidation conversion and endothermic CO_2 and steam reforming of methane. *Angewandte Chemie* **1994**, 33(20), 2104-2106.

(14) Rossigonol, S.; Madier, Y.; Duprez, D. Preparation of zirconia-ceria meterials by soft chemistry. *Catal. Today* **1999**, 50, 261-270.

APPLICATION OF HIGH-PRESSURE PHASE BEHAVIOR TO OPTIMIZE THE PLATINUM CATALYZED SELECTIVE OXIDATION OF 2-PROPANOL IN "SUPERCRITCAL" CARBON DIOXIDE

Roger Gläser[a], Jörg Williardt[a], David Bush[b], and Charles A. Eckert[b]

[a] Institute of Chemical Technology
University of Stuttgart
D-70550 Stuttgart
Germany

[b] School of Chemical Engineering
Georgia Institute of Technology
778 Atlantic Drive
Atlanta, GA 30332-0100
USA

Introduction

A promising utilization of the greenhouse gas carbon dioxide is its application as an environmentally benign, non-toxic and abundantly available reaction medium for organic synthesis at conditions above its critical point (T_c = 31.1 °C, p_c = 73.8 bar).[1] Supercritical carbon dioxide exhibits unique solvent properties between those of typical liquids or gases that can be sensitively tuned by pressure and temperature. The use of supercritical carbon dioxide is particularly attractive as a solvent for selective oxidation reactions. Not only is carbon dioxide chemically inert and non-flammable, but it is miscible with both oxygen (or air) and organic reactants over a very broad range of compositions and reaction conditions. Therefore, limitations of oxygen mass transfer as often encountered in conventional liquid-phase oxidations can be eliminated by operating in a "supercritical", single-phase region. To capitalize on this advantage, the experimental conditions for existence of the single-phase region of a given reaction system have to be accurately known.[2] In spite of its utmost importance, this issue of high-pressure phase behavior is often not sufficiently addressed in studies of reactions at "supercritical" conditions.

An example where the beneficial properties of "supercritical" carbon dioxide as a reaction medium have been successfully applied is the selective oxidation of secondary alcohols with molecular oxygen to ketones over supported noble metal catalysts.[3,4] Conventionally, this conversion is conducted in aqueous solution of the alcohol and, in many cases, the reaction rate is restricted by oxygen transport from the gas into the liquid reaction phase.[5,6]

In the present study, we report on the peculiarities and the prediction of the high-pressure phase behavior of the multi-component reaction mixture related to the oxidative dehydrogenation of 2-propanol (IPOH) with molecular oxygen to acetone (AC) and water in "supercritical" carbon dioxide. The results of these predictions are then applied to choose reaction conditions for experimentally investigating the conversion over a carbon-supported platinum catalyst in a single, homogeneous phase.

Experimental

Phase Behavior. Calculations of the phase behavior were based on the Patel-Teja equation-of-state.[7] Interaction parameters (k_{ij}) were fit to binary vapor-liquid equilibria (VLE) data from the literature and were used to predict the multi-component phase equilibria. It should be stressed that the term "supercritical" in its strict sense refers to single components only, and is used here for the multi-component mixture in quotation marks as suggested previously.[8]

Materials. 2-Propanol (Fluka, puriss. p.a., over molecular sieve), 1,4-dioxane (Merck, p.a., ACS reagent) and carbon dioxide (Air Products, 99.995 %) were used as received. A carbon-supported platinum catalyst (5 Pt/C, 5 wt.-% Pt, precious metal surface 14.5 m^2/g, specific surface area 1000 m^2/g) available from Chempur was applied in the oxidation reactions.

Catalytic Experiments. The catalytic conversions were carried out at 40 °C in a 100 ml batch reactor equipped with a magnetic stirrer (1000 min^{-1}) and a heating jacket. Prior to the experiments, the catalyst was placed in the reactor and dried in vacuum. After adding carbon dioxide, liquid 1,4-dioxane and 2-propanol were introduced into the reactor by means of an injection loop. 1,4-Dioxane (DO) served as an internal standard for closing the mass balance. The mixture was heated to reaction temperature and further carbon dioxide was added, if necessary. The reaction was started by adding oxygen to the reaction vessel to the desired reaction pressure. To monitor the progress of the reaction a small amount of the reaction mixture was continuously removed, expanded to ambient pressure through heated tubing and a needle valve and periodically analyzed by temperature-programmed capillary gas chromatography. *Generally, care must be exercised in carrying out oxidation experiments, especially at increased reactant concentrations.*

Results and Discussion

The VLE curves for the four-component reaction system IPOH/ O_2/CO_2/DO, have been calculated at fixed molar ratios of oxygen to carbon dioxide for the temperature of 40 °C. This temperature was chosen for the experiments due to its proximity to the critical temperature of pure CO_2 and to demonstrate the feasibility of selective alcohol oxidations at mild conditions. As depicted in **Figure 1**, the single-phase region for the reaction system is reached at pressures above the equilibrium line indicated for each O_2/CO_2 molar ratio. As expected, a higher pressure is needed to reach the single phase when the oxygen to carbon dioxide ratio is increased.

In **Figure 2**, the oxygen mole fraction is presented at a constant oxygen to carbon dioxide molar ratio of 5.3 %. The addition of carbon dioxide allows for high concentrations of oxygen in the liquid or the "supercritical" phase without going to high partial pressures of oxygen.

It is noteworthy, that, although the reactant concentration were quite low, the presence of 1,4-dioxane which was added to the

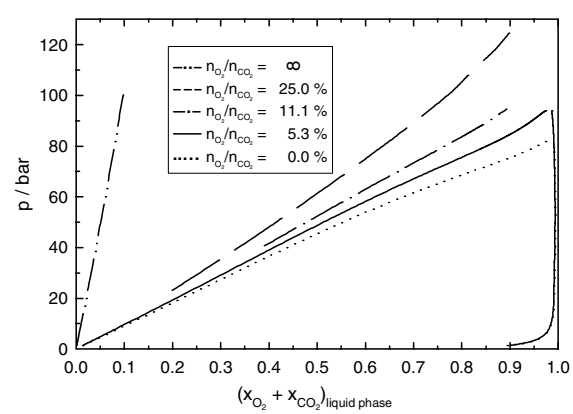

Figure 1. Vapor-liquid equilibrium of the oxygen/carbon dioxide/IPOH/DO mixture at 40 °C for different oxygen/carbon dioxide mole fractions.

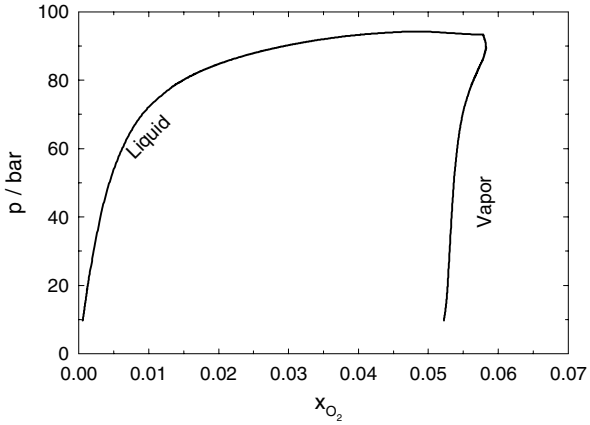

Figure 2. Oxygen mole fraction in the two-phase region for a fixed O_2/CO_2 molar ratio of 5.3 % at 40 °C.

mixture as an internal analytical standard in a comparable amount as the alcohol, decreases the pressure required for single-phase operation compared to the system containing oxygen, 2-propanol and carbon dioxide only. This is perhaps due to CO_2/1,4-dioxane interactions, which exhibit negative deviations from Raoult's law in the binary mixture.

Pertinent results of the catalytic conversion of 2-propanol over 5 Pt/C with oxygen at 150 bar, i.e., sufficiently above the one corresponding to the VLE, are displayed in **Figure 3**. In all cases, acetone was the only detectable oxidation product indicating the high selectivity of the reaction at the mild reaction temperature. Within the single-phase region, the initial amount of 2-propanol relative to the catalyst mass could be increased above 6 mmol / 125 mg, a typical value for the reaction in aqueous solution where catalyst deactivation was observed.[6] While no catalyst deactivation occurs at a fourfold increase of the IPOH/catalyst ratio, the conversion remains incomplete when eight times the initial amount of 2-propanol was present in the reactor. Nevertheless, and although the initial reaction rate r_0 was lower for the increased IPOH/catalyst ratios, a considerably higher amount of reactant could be converted with the same amount of catalyst in the high-pressure reaction medium.

To assess the influence of the oxygen mole fraction on the catalytic conversion, increasing amounts of oxygen were added to the

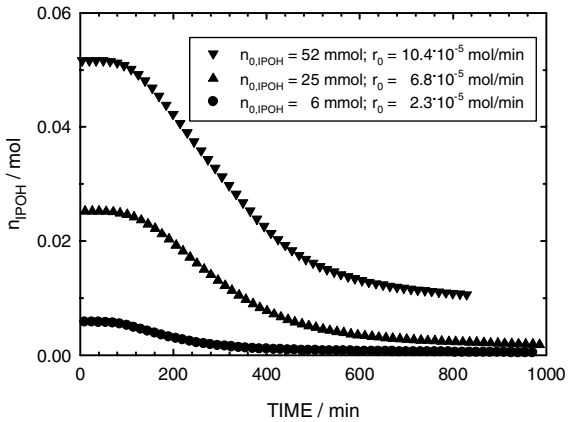

Figure 3. Conversion of increasing amounts of 2-propanol with molecular oxygen over 5 Pt/C in "supercritical" carbon dioxide (x_{O_2} = 2.8 %, $p_{0,CO2}$ = 150 bar, m_{cat} = 125 mg, r_0: initial reaction rate).

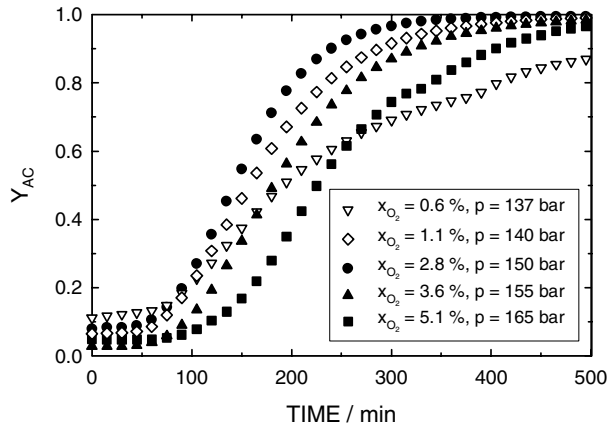

Figure 4. Influence of oxygen mole fraction on the acetone yield in the 2-propanol conversion with molecular oxygen over 5 Pt/C ($p_{0,CO2}$ = 135 bar, $n_{0,IPOH}$ = 13 mmol, m_{cat} = 250 mg).

same mixture of the catalyst, carbon dioxide, 2-propanol and the standard 1,4-dioxane. It is observed, that the rate of acetone formation increases with the oxygen mole fraction from 0.6 (substoichiometric with respect to IPOH) to 2.8 % and, for higher oxygen concentrations, decreases again (**Figure 4**). This finding is in accordance with results reported by Jenzer et al.[3] and can be rationalized by poisoning of the platinum surface due to partial over-oxidation. Although increasing oxygen mole fractions shift the VLE line to higher pressures (**Figure 1**), the reaction pressure in these experiments may be assumed to be high enough to avoid the occurrence of two separate phases.

In summary, the prediction of multi-component high-pressure phase behavior is helpful to devise reaction conditions for carrying out catalytic oxidation reactions in a single phase with "supercritical" carbon dioxide as a reaction medium. So far, only the initial reactant mixture has been considered. Further research will therefore be directed towards incorporating the changes in the compositions of the reaction mixture due to the consumption of the reactants and formation of the products into the phase behavior predictions. These changes are especially important for oxidation reactions, since highly polar and hydrogen-bonding products, such as acids or water, are among the products, and these will have a pronounced effect on the phase behavior, especially when the reactant concentrations and the conversion levels are high.

Acknowledgment

R.G. acknowledges a stipend from the Dr. Leni Schöninger foundation and Prof. Dr.-Ing. J. Weitkamp for generous support.

References

1. Kaupp, G., *Angew. Chem., Int. Ed. Engl.*, **1993**, *33*, 1452-1455.
2. McHugh, M.A., Subramaniam, B., *Ind. Eng. Chem. Proc. Des. Dev.*, **1986**, *25*, 1-12.
3. Jenzer, G., Sueur, D., Mallat, T., Baiker, A., *Chem. Commun.*, **2000**, 2247-2248.
4. Steele, A.M., Zhu, J. Tsang, S.C., *Catal. Lett.*, **2001**, *73*, 9-13.
5. Kluytmans, J.H.J., Markusse, A.P., Kuster, B.F.M., Marin, G.B., Schouten, J.C., *Catal. Today*, **2000**, *57*, 143-155.
6. Nicoletti, J.W., Whitesides, G.M., *J. Phys. Chem.,* **1989***, 93*, 759-767.
7. Patel, N.C., Teja, A.S., *Chem. Eng. Sci.*, **1982**, *37*, 463-473.
8. Jenzer, G., Mallat, T., Baiker, A., *Catal. Lett.*, **2001**, *73*, 5-8.

SYNTHESIS OF DIMETHYL CARBONATE BY SUPERCRITICAL CO_2-FEEDING METHANOL AND DIMETHYL ETHER

Tian Yiling, Qin Ying, Chen Li, Fang Jingang and Wang Li*

Department of Chemistry, Tianjin University, Tianjin, 300072, China

Albert S.C. Chan

Department of applied Biology and Chemical Technology,

Polytechnic University, Hong Kong ,China

1. Introduction

Dimethyl carbonate is an important methylating agent which replaces former toxic methylating agent $(Me)_2SO_4$ in the synthesis of medicines. It is also an intermediate of synthesis of higher carbonates and fuel oil additive. Many outhors reported the synthetic methods of DMC[1-5], most of them used organometal compounds as catalysts.It would be difficult to separate product mixture, then it was spreaded difficultly in industry. Our technological process is a heterogeneous catalysis. This method has many obvious advantages. The product fractionation and purification are then esaier and more economical.

There are many CO_2 resources in China, for example, Victory Oil Field has about ten billions m^3 of CO_2 deposits, which is a nature carbon resource and is yet not exploited and used. The super-critical CO_2 (SC-CO_2) is non-toxic, nonflammable and cheep solvent. The high diffusility, low viscosity and low surface tension of SC CO_2 is expected to spead up mass-transfer controlled reations. In[1] this work, SC CO_2 is both reactant and solvent.

2. Experimental

2.1 Chemicals

CO_2, with a minimum purity 99.99%, was obtained from Tianjin Special Gas Limited Company, China.

Absolute alcohls was obtained from Tianjin Reagent company, China, with a stated purity of 99.8%. It was used as receiled without further purification.

The carbonylation catalyst of MeOH is a mechanical mixture of CuI, MgO and other addend powders, the purities of them are all C.P. Before use they were dried and activated.

The hydrolyst of DME, HZMS molecular sieve, was obtained from Nankai University, China. The specific surface of HZMS is 30 $\pm 2m^2/g$. Before use it was activated for 4h at temperature of 280℃.

DME with purity of 99.9% was obtained from Shanxi Institute of Coal Chemistry, China. It was used without further purification.

2.2 Procedure

The experiments were carried out in a high-pressure autoclave of $0.5dm^3$ equipped with stirring. The temperature of the autoclave was adjusted by a heating jacket and was measured directly by a shielded chromel-to-alumel thermocouple inside the autolave. The chemical equilibrium, indicated by reaching a constant pressure (changed with the added amounts of chemicals), was reached typically 4h after terminating stirring.

After feeding catalysts, MeOH was introduced into the evacuated autoclave from tared sample bottle and the mass determined by weighing. DME and CO_2 were pressured respectively into the autoclave from two little light-alloy flask, which were cooled before falling CO_2 and DME in the presence of ice and salt. The reactant mixture was stirred at established temperature for 4h. After that, the autoclave was cooled to room temperature and let the left gases out of the autoclave. The product mixture was analyzed by a gas chromatography equipped with integrator. All analysis were carried out under the same conditions: hydrogen (99.99%) as carrier gas, flowing rate $35cm^3min^{-1}$, FID detector, 2m column(i.d 3mm) packed with silicone elastomer. Column temperature 80℃, injection port temperature 220℃, n-butanol was used as internal standard. The bridge current was 100mA, The amount of injected sample was 2μ dm^3 for each.

3. Results and discussion

The total reaction can written as

(1) $CO_2+2MeOH=DMC+H_2O$

(2) $H_2O+DME=2MeOH$

Owing to the present of reaction (2), the water produced by reaction

$$y = \frac{\text{n(DMC) in product mixture}}{\text{n(MeOH) in reactant mixture}}$$

(1) was consumed and then equilibrium of (1) was removed to right hand. The yield of DMC was increased. In this paper the yield of DMC was defined as

3.1 The effect of temperature on the yield of DMC

The reaction(2) is an endothermic but reaction(1) is exothermic reaction. We selected temperature range was from 100℃ to 150℃. Table 1 gives this effect. The reaction conditions were: MeOH, $160cm^3$(4mol); DME, 115g(2.5mol). CO_2, 44g(2.0mol), HZMS+CuI+MgO+other, 100g. Here the "other" is a kind of solid initiator.

Table 1 Effect of temperature on the yield of DMC

t/℃	yield of DMC /%	*t*/℃	yield of DMC /%
100	11.26	130	28.58
110	19.83	140	21.74
120	24.17	150	17.36

Table 1 shows that along with increasing temperature the yield of DMC was changed. Initially it was increased and then decreased. At temperature of 130℃ shows a maximum of 28.58%. Two reasons account for the occurrence. Higher temperature is favorable to (2) and could increase reaction rate of (1). Since (1) is an endothermic reaction. The higher temperature is unfavorable to equilibrium of (1).

3.2 The effect of the ratio of reactants on the yield of DMC

Table 2 gives this effect. The reaction conditions were:130℃, HZMS+CuI+MgO+other, 100g,reaction period 4h.

[1] To whom correpondencel should be addressed. Email: tianyiling@eyou.com

Table 2 The effect of the rato of reactants on the yield of DMC

(*n* of reactants)/mol			yield of DMC/%	(*n* of reactants)/mol			yield of DMC/%
MeOH	DME			MeOH	DME	CO_2	
4	0	4	1.07	4	2	2	26.52
4	1	3	9.41	4	2.5	2	28.58
4	1.5	2.5	14.34	4	3	2	22.73

The main problem for the synthesis of DMC is the removal of product water. DME has proved to be aid to this synthesis. When the amount of DME was excess, then concentrations of CO_2 and MeOH would be diluted, so that reaction rate of (1) would be decreased. If the amount of DME was too few, the hydrolysis reaction (2) would not be successful. Therefore the decided optimal ratio is *n*(MeOH): *n*(DME): *n*(CO_2)=4:2.5:2

3.3 The effect of catalysts on the yield of DMC

Changing the amounts and ratios of catalysts would affect the yield of DMC. The results are gives in Table 3. The experimental conditions were:

the temperature 130 ℃

n(MeOH):*n*(DME):*n*(CO_2)=4:2.5:2. The reaction period was 4h.

Table 3 The effect of catalysts on the yield of DMC

m (catalysts)/g		Yield of DMC/%	*m* (catalysts)/g		Yield of DMC/%
CuI+MgO +other	HZMS		CuI+MgO +other	HZMS	
10	90	9.09	60	40	28.58
20	80	19.43	80	20	21.23
40	60	22.89	90	10	21.47
50	50	24.79	100	0	7.29

Table 3 shows that yield of DMC were initially increased with increasing amounts of (CuI+MgO+other) and then decreased. The optimum ratio is 60:40.

We have found during the analysis that besides DMC was formed, the by-products present in reaction mixture. They are methy carbamate and other unknown substances. Their total content was about 5%. The little amounts of solved DME and CO_2 in producted mixture were analyzed out.

References

(1). Bolton [J]. Chem. Eng. **1992**,517,13

(2). Yamazaki N, Nakahama S. , Ind. Chem. Prod. Res. Dev. **1979**,18,249

(3). Kizlink J, Pastucha I, Collect. Czech. Chem. Commun. **1994**,59,2116

(4). U.S.Patent 5902894

(5). Kizlink J, and Pastucha I, Collect. Czech. Chem.Comun. **1995**,2,687

CARBON DIOXIDE REFORMING WITH METHANE IN LOW TEMPERATURE PLASMAS

Korada Supat, Sumaeth Chavadej*, Lance L. Lobban** and Richard G. Mallinson***

*The Petroleum and Petrochemical College,
Chulalongkorn University
Bangkok 10330, Thailand
**Institute for Gas Utilization Technologies and
School of Chemical Engineering and Materials Science
University of Oklahoma,
100 E. Boyd St., Rm.T-335, Norman, OK 73019, USA

Introduction

With increasing population and rapid technology development, it is possible that we have begun to encounter alteration of the climate. Greenhouse gases, that include carbon dioxide, methane, ozone, halocarbons and nitrous oxide, to a significant extent come from the combustion of fossil fuels (coal, oil, and natural gas) for power generation and transportation. A potentially useful reaction for reducing the impact of carbon dioxide (reducing net emissions), a major component in many natural gas resources, especially in Asia, is carbon dioxide reforming with methane (reaction 1) for production of synthesis gas (carbon monoxide and hydrogen) at a lower H_2/CO ratio compared to steam reforming of methane (reaction 2), which is the conventional process for synthesis gas production. However, as with steam reforming, the highly endothermic reaction requires significant high temperature (ca. 800 ^oC) energy input that is usually provided by combustion that releases CO_2. Also, the 1:1 H_2/CO ratio produced from CO_2 reforming requires, for GTL applications, the use of the water gas shift reaction, in which much of the potential net consumption of CO_2 is lost. The alternative is to combine CO_2 reforming with steam reforming and its similar low net CO_2 reduction due to combustion to provide the required heat of reaction. Thus any net reduction of CO_2 impact from the process must be compared with the partial oxidation or combined/autothermal reforming which are exothermic or self heating, but require the production of oxygen that is itself energy intensive.

$$CH_4 + CO_2 \longrightarrow 2\,CO + 2\,H_2 \qquad \Delta H_1 = 247.0 \text{ kJ mol}^{-} \qquad (1)$$

$$CH_4 + H_2O \longrightarrow CO + 3\,H_2 \qquad \Delta H_1 = 229.7 \text{ kJ mol}^{-} \qquad (2)$$

Therefore, rather than considering the net CO_2 reduction as the driver, other factors must be considered. For example, The previously mentioned high CO_2 natural gas resources may be stranded by the high cost of CO_2 removal, which may be reduced or eliminated by use of CO_2 reforming. Additionally, the possible lower capital investment and operating costs due to the elimination of the requirement for oxygen makes consideration of this technology worthwhile. However, a major problem with CO_2 reforming to this point in time is the deactivation of the catalyst due to carbon deposition (reaction 3 and 4) at the desired reaction conditions.

$$CH_4 \longrightarrow C + 2H_2 \qquad \Delta H = 75 \text{ kJ mol}^{-1} \qquad (3)$$

$$2CO \longrightarrow C + CO_2 \qquad \Delta H = -171 \text{ kJ mol}^{-1} \qquad (4)$$

So far, no effective commercial catalyst exists which can operate without carbon formation [1]. Therefore, solving these problems to find ways to operate this process at milder reaction conditions is of great interest.

In this work, a low temperature plasma reactor was used to facilitate this reaction by itself and in combination with steam, at low temperatures. This has been shown to be possible in other methane conversion studies without carbon dioxide, such as helping in the conversion of methane over Sr/La_2O_3 [2] and other materials. The disadvantage of using electrical energy, that at best may only be about 60 percent efficient, may be offset by process simplicity and cost, lower carbon formation and less excess energy that must be recovered and utilized only with considerable cost.

A plasma is a quasineutral gas consisting of charged and neutral gas molecules with a collective behavior in which the charged molecules follow the path of the electric field. It is in equilibrium when the kinetic energy of the charged particles and neutral species are the same. The non-thermal, also called cold, plasma, and its non-equilibrium properties, high electron temperature and low bulk gas temperature, provide the capability for initiating chemical reactions at low temperature and with lower energy input.

Corona discharge and dielectric barrier discharge (DBD) techniques are two of the commonly used methods for producing non-equilibrium plasmas at atmospheric pressure [3], [4], [5]. Because the corona is particularly easy to establish, it has had wide application in a variety of processes such as electrostatic precipitation, electro-photography and also synthesis of chemicals [3]. The electron energy, which corresponds to the electron temperature, is restricted to less than 6 eV in the corona discharge [6]. These relatively low-energy electrons have insufficient energy to ionize methane, which has an ionization potential greater than 12 eV [7], but high enough to dissociate CH_4 and CO_2 molecules with dissociation energies of 4.5 and 5.5 eV, respectively (reaction 5 and 6) [1].

$$e^- + CH_4 \longrightarrow CH_3 + H + e^- \qquad (5)$$

$$e^- + CO_2 \longrightarrow CO + O + e^- \qquad (6)$$

The utilization of non-equilibrium plasma techniques for carbon dioxide reforming with methane has been studied in the dielectric barrier discharge. The combination of solid catalysts with a dielectric-barrier discharge was studied for carbon dioxide reforming of methane. It is shown that the use of a catalytic coating in the discharge can have a promoting effect on the plasma chemistry and the use of the ceramic foams improved the temperature and lowered the undesired temperature increase [4]. The dielectric barrier discharge has also been used to investigate the effect of a non-equilibrium discharge on the production of synthesis gas from two major greenhouse gases carbon dioxide and methane. A pronounced synergistic effect caused by free radical reactions was observed using these two gases simultaneously with a minimum required specific energy of 40 eV/molecule for the production of syngas and the highest energy efficiency (electric energy converted to chemical energy in the syngas) reached so far was about 7%[1]. The effect of a third body (helium) was also investigated in the DBD for carbon dioxide reforming [8].

Experimental

The flow rate of feed gases, methane and carbon dioxide, were controlled by a set of mass flow controllers supplied by Porter Instrument, Inc. All experiments were carried out at atmosphere pressure. The feed gases were introduced downward through the reactor and analyzed on-line by a Carle AGC 400 gas chromatograph, with thermal conductivity detector. To provide the water vapor in the feed, the feed gas was bubbled through a water

saturation system in a water bath maintained at the temperature needed to provide the desired vapor pressure of water. All inlet and exit lines were heat traced and the reactor tube was placed in a heater and maintained at 100°C. The exhaust gas from the reactor was introduced into a condenser cooled by a mixture of dry ice and acetone that was used to remove the condensable products. The power supply unit consisted of an AC power supply for converting domestic AC power 120V, 60 Hz, using a function generator for varying the frequency in the range of 300 to 600 Hz with a sinusoidal waveform. The output was then transmitted to a high voltage alternating current (HVAC) transformer. The HVAC could step up the low side voltage to the high side voltage by nominal factor of 125 at 60 Hz. This factor may not be constant with changes in frequency due to changes in power factor because of the capacitive nature of the reactor system. The discharge occurred in a quartz tube with an i.d. of 7 mm between two stainless steel electrodes. The upper wire electrode is centered axially within the reactor tube, while the lower electrode is a circular plate with four holes to allow gas to pass through the reactor and is positioned perpendicular to the reactor axis

For this system, the conversions are defined as:

Conversion of methane = (moles of CH_4 consumed/moles of CH_4 introduced) x 100 %

Conversion of carbon dioxide = (moles of CO_2 consumed/moles of CO_2 introduced) x 100 %

H_2/CO mole ratio = moles of H_2 produced/moles of CO produced

CO/C_2 mole ratio = moles of CO produced/moles of ethane, ethylene and acetylene produced

In some cases, at lower methane conversions, the product material balances could be below 80%, however in most cases the product carbon balance was in the 80-90% range. Water was not quantified.

Results and Discussion

In Table 1, It may be seen that in an excess of CO_2, without water, the methane conversion is low and little CO_2 is converted even as power is substantially increased. In the last column, with addition of water, much higher conversion of both CO_2 and methane is achieved at otherwise similar conditions. Power is somewhat higher, but eV/mol of carbon converted is lower despite a 50 percent dilution of CO_2 and CH_4 by the water. With the excess CO_2, little C_2 formation occurs and the H_2/CO is quite low.

At a CO_2:CH_4 ratio of 5:1, methane conversion is substantially increased with a more modest increase in CO_2 conversion. With less water, at 30 %, energy consumption per C converted is substantially reduced compared to 50 % water. Also noticeable is a substantial suppression of C_2 production with increased water content. At 30 percent water in the feed, are increases in both conversions but hydrogen production appears to be significantly reduced.

The results at the stoichiometric CO_2:CH_4 ratio of 1:1 and 50% water vapor are shown in Table 3. The conversions are similar to those at the 3:1 ratio with the same power and water content, but Energy consumption per C converted is lower due to decreased CO_2 dilution since methane conversion is the higher of the two. Increased power at 1:1 ratio shows increased conversion except when the frequency is increased. The increase in frequency essentially "detunes" the system, reducing the power factor and the power actually applied to the plasma. Power is actually measured on the low voltage side and therefore includes all high voltage system losses. A system designed to properly match impedances and operate at a high power could significantly lower the real power usage over that reported here. The lower CO_2:CH_4 ratio results in greater C_2 production. C_2's may be undesirable components of synthesis gas,

Table 1. Effect of Power and Water on CO_2 Reforming at a 3:1 CO_2: CH_4 Ratio

Flowrate (sccm)	100	100	100	100
CO2:CH4	3	3	3	3
% vapor	0	0	0	50
Gas gap (cm)	1	1	1	1
Low side Voltage(V)	57	68	79	62
Frequency	300	400	500	400
Power (W)	11	11	11	14
Power Factor	0.56	0.48	0.42	0.78
Current (Amp)	0.35	0.34	0.33	0.29
X_{CH4}	11.5	19.2	14.0	34.4
XCO_2	1.5	4.1	2.0	13.0
S_{CO}	63.4	52.9	47.8	99.9
S_{H2}	-	-	-	-
S_{C2H6}	13.8	5.9	11.6	1.0
S_{C2H4}	13.6	9.1	13.0	1.0
S_{C2H2}	18.8	17.6	14.9	4.5
S_{total}	109.6	85.5	87.3	106.3
$eV/m_{C(CO2+CH4)}$	41.4	21.0	33.0	23.3
H2/CO	1.28	1.26	1.31	0.65
CO/C2	2.74	3.24	2.42	31.07

Table 2. Effect of Power and Water on CO_2 Reforming with Water at a 5:1 CO_2:CH_4 Ratio

Flowrate (sccm)	100	100	100
CO2:CH4	5	5	5
% vapor	30	30	50
Gas gap (cm)	1	1	1
Low side Voltage(V)	62	75	79
Frequency	300	300	400
Power (W)	11	13	14
Power Factor	0.43	0.35	0.43
Current (Amp)	0.41	0.50	0.41
X_{CH4}	51.1	57.4	58.1
XCO_2	13.2	17.1	18.2
S_{CO}	85.3	86.4	100.2
S_{H2}	-	-	-
S_{C2H6}	0.0	0.0	0.0
S_{C2H4}	2.3	1.6	0.0
S_{C2H2}	13.2	9.9	2.9

S_{total}	100.8	97.9	103.1
$eV/m_{C(CO2+CH4)}$	12.1	11.7	17.1
H2/CO	5.00	0.44	0.41
CO/C2	11.05	14.97	68.83

but the olefinic nature of those produced here are reactive on Fischer Tropsch catalyst systems and therefore may be suitable for feeds to a Fischer Tropsch Synthesis Reactor. The H_2/CO ratio is close to that desired for Fischer Tropsch or methanol and may be controllable by altering the water content.

Table 3. Effect of Power on CO_2 Reforming with Water at a 1:1 CO_2: CH_4 Ratio

Flowrate (sccm)	100	100	100	100
CO2:CH4	1	1	1	1
% vapor	50	50	50	50
Gas gap (cm)	1	1	1	1
Low side Voltage(V)	57	66	88	97
Frequency	300	300	400	600
Power (W)	11	13	14	14
Power Factor	0.54	0.45	0.34	0.40
Current (Amp)	0.36	0.43	0.47	0.36
X_{CH4}	40.5	44.3	47	30
XCO_2	19.6	20.9	21	12
S_{CO}	55.5	60.2	56	72
S_{H2}	-	-	-	-
S_{C2H6}	1.5	1.4	1	3
S_{C2H4}	4.6	4.5	5	5
S_{C2H2}	22.7	23.8	26	21
S_{total}	84.3	89.9	88	101
$eV/m_{C(CO2+CH4)}$	11.0	12.0	12.3	19.7
H2/CO	1.90	1.85	1.9	1.7
CO/C2	3.85	4.05	3.5	4.9

Table 4. Water Gas Shift Reaction Pathway

Flowrate (sccm)	100	100
CO2:CH4	50%CO	50%CO_2
% vapor	50	50
Gas gap (cm)	1	1
Low side Voltage(V)	63	85
Frequency	600	400
Power (W)	7	10
Power Factor	0.49	0.27
Current (Amp)	0.23	0.44
X_{CH4}	Xco = 6.03	0
XCO_2	0	1
S_{CO}	-	112
S_{H2}	-	-
S_{C2H6}	0	0
S_{C2H4}	0	0
S_{C2H2}	Sco_2 = 105.05	0
S_{total}	105	112
$eV/m_{C(CO2+CH4)}$	34.6	352.7
H2/CO	H_2/CO_2 = 0.87	0.0
CO/C2	-	-

Lastly, in Table 4, results of reacting with CO or CO_2 with water are shown. CO_2 and water are essentially unreactive under the conditions of this experiment, where of course both species are strongly favored by thermodynamics. CO and water or converted to some extent with the expected production of hydrogen and CO_2. Power consumption is high under these conditions, but a lower value might be feasible under optimal conditions.

Conclusions

CO_2 combined with steam reforming at moderate conversion levels has been demonstrated at near ambient conditions with moderate power consumption. Under most conditions, carbon formation was not an operational problem. If long term operation with high conversions can be demonstrated, a process can be envisaged wherein the cost and efficiency of using electricity to drive the reaction is counter-balanced by lower costs and simpler operation (without oxygen). For smaller resources and more remote locations, these tradeoffs may be highly advantageous. Whether there is a net reduction in CO_2 impact compared to more conventional reforming/partial oxidation syn gas generation processes can only be determined by a detailed life cycle analysis and not simply by the reaction equations.

Acknowledgements

ChevronTexaco, Inc. and The Thailand Research Fund are gratefully acknowledged for supporting this research. Helpful discussions with Terence A. Caldwell are also acknowledged.

References

(1) Kogelschatz, U., Zhou, L.M., Xue, B., & Eliasson, B. (1998), 'Production of synthesis gas through plasma – assisted reforming of greenhouse gases', Proceedings of the 4th International conference on greenhouse gas control technologies, Interlaken, Switzerland, 385-390

(2) Marafee, A., Liu, C., Xu, G., Mallinson, R., & Lobban, L. (1997), 'An Experimental Study on the Oxidative Coupling of Methane in a Direct Current Corona Discharge Reactor over Sr/La_2O_3 Catalyst', *Industrial and Engineering Chemistry Research*, **36**, 632-637

(3) Chang, J., Lawless, P.A., Yamamoto, T. (1991), 'Corona Discharge Processes', *IEEE Transactions on plasma science*, **19**, 1152

(4) Kraus, M., Eliasson, B., Kogelschatz, U., & Wokaun, A. (2001),'CO_2 reforming of methane by the combination of dielectric-barrier discharge and catalysis' *Physical Chemistry & Chemical Physics*, **3**, 294-300

(5) Lui, L., Marafee, A., Hill, B., Xu, G., Mallinson, R., & Lobban, L. (1996), 'Oxidative Coupling of Methane with ac and dc Corona Discharge', *Industrial and Engineering Chemistry Research*, **35**, 3295-3301

(6) Eliasson, B., & Kogelschatz, U. (1991), 'Nonequilibrium Volume Plasma Chemical Processing', *IEEE Transactions on plasma science*, **19**, 1063

(7) Sorensen, S. L., Karawajczyk, A., Stromholm, C., Kirm, M. (1995), 'Dissociative Photo excitation of CH_4 and CD_4', *Chemical Physics Letters*, **232**, 554

(8) Larkin, D.W., Leethochawalit, M., Chavadej, S., Caldwell, T. A., Lobban, L.L., & Mallinson, R.G. (1998), 'Carbon Pathways, CO_2 Utilization, and In Situ Production Removal in Low Temperature Plasma Methane Conversion to Methanol', Proceedings of the 4th International conference on greenhouse gas control technologies, Interlaken, Switzerland, 397-402

FREQUENCY EFFECTS IN THE CATALYTIC OLIGOMERIZATION OF METHANE VIA MICROWAVE HEATING

L. Daniel Conde, Carolina Marún, Steven L. Suib, Zak Fathi*

University of Connecticut
Department of Chemistry
55 North Eagleville Rd. U3060
Storrs, CT 06269-3060

Introduction

Many efforts have been focused on the activation of methane to more valuable products in the last two decades. Many studies have been done in order to produce more valuable products from natural gas, of which methane is the major constituent. Natural gas is an inexpensive and abundant energy resource. Therefore, effective and economic processes to obtain higher hydrocarbons, methanol and/or synthesis gas would be valuable.

Thermal,[1-3] homogeneous,[4-6] and heterogeneous[7-10] catalytic conversions of methane to higher hydrocarbons have been studied by many authors. Due to the high thermodynamic stability of methane compared with that of higher hydrocarbons, methane can only be thermally converted to C_{2+} hydrocarbons at temperatures higher than 1400 K. The products are unsaturated and unstable hydrocarbons such as acetylene. Therefore, appropriate temperature, residence time control, and rapid reaction quenching are necessary to achieve selectivity to desired products. Otherwise, carbon and hydrogen will be the only products.

The use of microwave heating to induce chemical reactions has been studied for several years. Over the past decade microwave heating has been employed extensively in organic[37-41] and inorganic synthesis.[41-55] Microwave-induced catalytic reactions have been studied extensively by Wan and coworkers.[25,35,27-29,58-61] We have studied the oligomerization of methane to higher hydrocarbons using Ni powder, Fe powder, and activated carbon.[62] Oligomers ranging from C_2 to C_6 hydrocarbons have been produced in a relatively high selectivity depending on the nature of the catalyst, power level, and the presence of He as a diluent gas.

Nickel catalysts have been shown to be highly selective and effective catalysts to lower the activation energy of breaking the carbon-hydrogen bond. Although microwave heating has been studied very systematically for the oligomerization of methane it is not clear yet what other factors might affect the activity and product distribution of this reaction. In this work, we studied the systematic effects of frequency and magnitude of the applied microwave radiation on the conversion and product distribution of methane oligomerization using nickel catalysts in the presence and absence of He as a diluent gas.

Experimental Section

Microwave Apparatus and Gas System. Oligomerization of methane was carried out in a flow reactor system. A Lambda Technologies variable frequency unit, Vari-Wave model VW-2750 was used for these experiments. The reactor, a straight 3/8 in-quartz tube, was mounted horizontally inside the cavity. Methane gas as well as He diluent gas was mixed in a panel when necessary and flowed into the quartz reactor. High Purity (HP) grade methane obtained from Matheson and Ultra High Purity (UHP) helium purchased from Airgas were used.

Various frequencies and modes were produced in the microwave cavity. This cavity allows TM_{01n} modes (n = 2 to 9) over a frequency range of 2.400 to 5.056 GHz. The cavity was designed by Lambda Technologies to have different modes for each frequency. Our experiments were done with and without diluent at 2.40 GHz at TM_{012} and also at 4.60 GHz at TM_{018} for comparison. Thermal paper was inserted into the microwave cavity and used to map the heating patterns of the various modes.

The length of the aluminum cavity was 29.5 cm and the radius was 5.15 cm. In order to ensure microwave absorption for a specific frequency value and power level, the reflected power had to be minimized first by means of a tuning knob and the frequency tuning control on the main panel. Therefore, the working frequency is a result of the tuning process. Reflected power higher than 60 W makes the safety feature of the unit shut off. Thus, not all frequencies are possible for a particular system.

Catalyst. Nickel powder catalyst with morphology of branched filaments was used for these experiments. The diameters of the filaments were 2.5 μm as measured in a Scanning Electron Microscopy (SEM) photograph. Clusters of nickel metal particles were aggregated to form the filaments. The catalyst (100 mg) was placed inside the reactor with high purity quartz wool on either side of the catalyst bed. The reactor was placed in the center of the aluminum cavity. Helium was flushed for 30 min through the reactor to purge the atmosphere.

The experiments were run at two different flow rates: 3 mL/min of pure methane; and 12 mL/min of a 3:1 mixture of helium and pure methane respectively at atmospheric pressure. Samples for analyses were taken after 3 min of irradiation time for each power level (100, 130, 170, 210, 300, and 370 W).

Product Analysis. Products were trapped using a 4 way-gas sampling valve and analyzed by using an HP5890 Series II Chromatograph equipped with a mass detector. Details about the Gas Chromatographer/Mass Spectrometer (GC/MS) were published elsewhere.[62]

Results

Microwave Induced-Oligomerization (MIO) of methane was performed at two different frequency levels (2.40 and 4.60 GHz). It was not possible to set the unit to operate under other frequencies. The effect of power and the presence of helium as diluent gas on conversion and product distribution were also studied at these two different frequency values. A summary of the results can be seen in **Table 1**.

Feed	Flow rate (mL/min)	Time (min)	Power[(a)] (W)	Astex Unit	Var. Freq. Unit[(b)]	
				2.45 GHz	2.40 GHz	4.60 GHz
CH_4	3	3	130	N.R.	N.R	Y
			370	Y	N.R	Y
CH_4:He	3:9	3	130	N.R.	N.R	Y
			370	Y	Y	Y

Table 1. Summary Results. N.R. = no reaction; Y = see Fig. 4 - 7 for product distribution. [(a)] 100, 130, 170, 210, 300, 370 Watts of power level were used. Those not shown in the table were neither relevant nor reaction detected at any frequency. [(b)] It was not possible to set other frequency values with successful microwave absorption.

No visible arc formation was detected during these runs and the catalyst bed remained the same after reaction (checked by SEM photographs). Ethylene, acetylene and ethane were the major C_2 products observed for the oligomerization of methane via microwave

heating using Ni powder as a catalyst. Benzene was also formed with selectivities that ranged from 10 to 29%. In the case of 25% diluted methane as a feed and low frequencies (2.45 GHz), low selectivities of benzene were detected (2 to 5%).

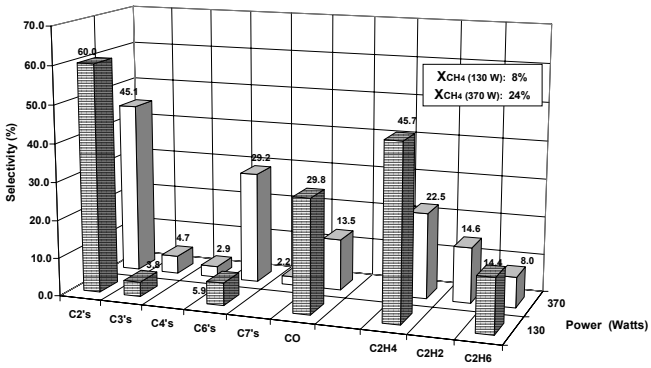

Figure 1. Effect of applied power on product distribution at 4.60 GHz using pure methane as a feed and nickel powder catalyst

Pure Methane as Reactant. When using pure methane as reactant, as power increased from 130 to 370 W at 4.60 GHz, conversion increased from 8 to 24%. Selectivities towards C_{2s} decreased from 60 to 45% and selectivities to C_{6s} increased from 6 to 29% (**Figure 1**). Acetylene was not detected at low power (130 W). At 370 W, the relative proportions of C_2 products were ethylene > acetylene > ethane. At a low frequency (2.45GHz), when using pure methane as reactant, oligomerization was not achievable using the variable frequency unit. Therefore, for pure methane, the effect of frequency was compared using an ASTEX unit at the same conditions except at a fixed 2.45 GHz frequency (for more detail see previous publication).[62] The selectivities towards C_{2s} decreased from 71 to 45% and the selectivities towards benzene (C_{6s}) increased from 20 to 29% when the frequency was increased from 2.45 to 4.60 GHz at 370 W. The selectivities towards ethylene, acetylene, and ethane decreased as frequency increased, maintaining their relative proportions (**Figure 2**).

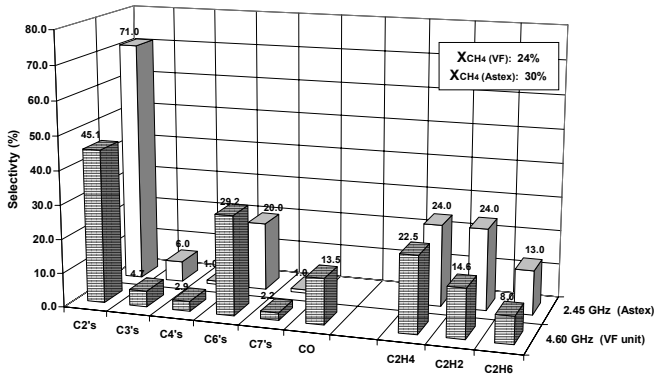

Figure 2. Frequency effect on product distribution at 370 W using pure methane as a feed and nickel powder catalyst

Methane Diluted in He (25%). When the feed was changed to 25% methane in helium, as power was increased from 130 to 370 W at 4.60 GHz, conversion increased from 6 to 8%, selectivities towards C_{2s} decreased from 83 to 72%, and selectivity towards benzene increased from 1 to 10%. Conversion levels were lower than those in the case of using pure methane as a feed (6 and 8% compared to 8 and 24%). Also, while increasing power, less drastic changes in selectivity towards C_{2s} and C_{6s} were observed than those when using pure methane (See **Figures 1** and **3**).

Acetylene was not detected at 130 W and 4.60 GHz frequency. The relative proportion of C_{2s} changed from ethylene > ethane to ethane > ethylene > acetylene as power was increased from 130 to 370 W (**Figure 3**), which was different from the proportion of C_{2s} in the case of pure methane as a feed (ethylene > acetylene > ethane). The systematic effect of frequency was studied using the Lambda variable frequency unit and comparisons were also made when using the fixed frequency ASTEX unit in order to check for reproducibility of results at low frequency (2.45 GHz).

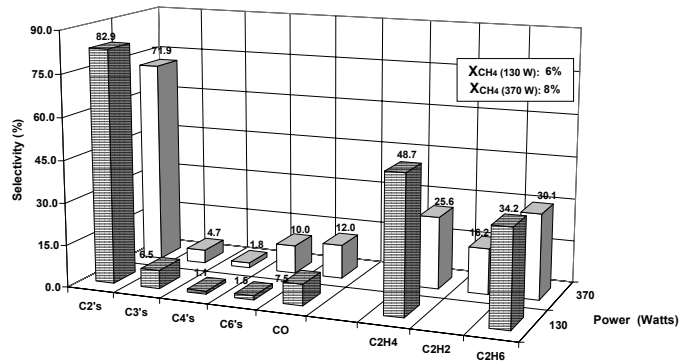

Figure 3. Effect of applied power on product distribution at 4.60 GHz using methane diluted in helium (25%) and nickel powder catalyst.

The data here show that both the ASTEX fixed frequency and the Lambda variable frequency systems behave almost the same when comparing data at low frequency (2.45 GHz) with respect to conversion levels (about 7%) and product distributions (Figure 7) at 370 W. As frequency was increased from 2.45 to 4.60 GHz, selectivities towards C_{2s} decreased from 81 to 72% and selectivity towards benzene increased from 5 to 10% (**Figure 4**). When using He as diluent at 370 W, the only C_2 detected was ethane at a low frequency value (2.45 GHz). As frequency was increased from 2.45 to 4.60 GHz, the proportion of C_2 products changed from ethane to ethane > ethylene > acetylene (**Figure 4**). The effect of frequency on product distribution among C_{2s} was different with respect to the case of pure methane in the feed as seen in Figures 5 and 7. The proportion of C_{2s} changed from ethylene > acetylene > ethane to ethane > ethylene > acetylene at 4.60 GHz. At 4.60 GHz and pure methane, selectivity of benzene was higher than that at 4.60 GHz and diluted methane (29 *vs*. 10% respectively).

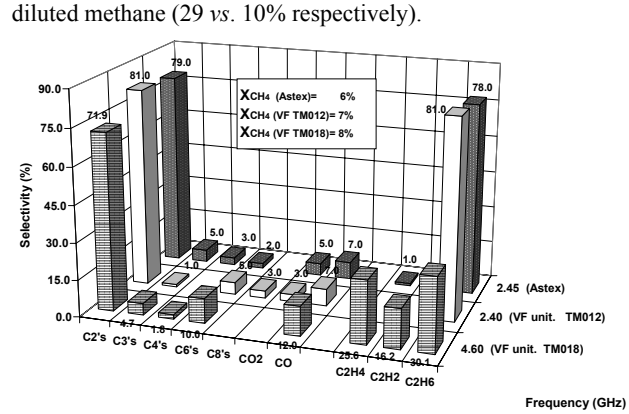

Figure 4. Frequency effect on product distribution at 370 W using methane diluted in helium (25%) and nickel powder catalyst

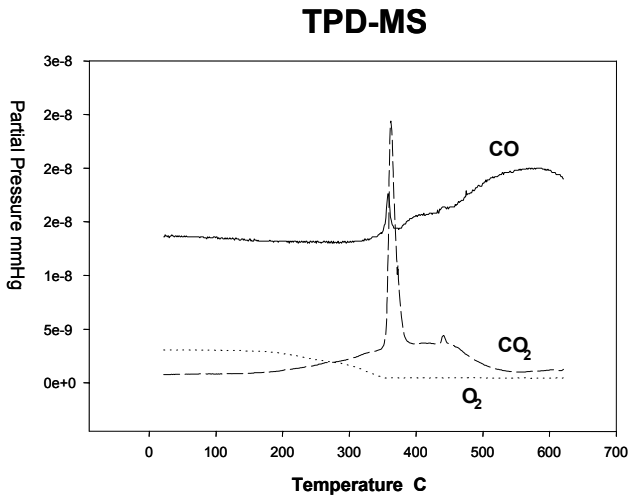

Figure 5. Fresh nickel catalyst Temperature-Programmed Desorption analysis

There are different sources of oxygen that account for the formation of carbon monoxide and carbon dioxide detected. Nickel catalyst was used as received for the experiments. Subsequent temperature-programmed desorption analysis revealed the presence of oxygenated species in the catalyst as seen in **Figure 5**.

Discussion

Microwave radiation does not have sufficient energy to cause any chemical changes, such as breaking bonds and transferring electrons. Nickel catalyst strongly absorbs microwave energy providing the necessary kinetic energy for the surface electrons to enhance the surface chemical reaction. The energy absorbed by the metallic sites is transformed from a rapid oscillating electric field into thermal energy. Since only the catalyst surface site is heated, there is a large temperature gradient between the surface and the bulk of the gas phase. The reaction pathway most likely proceeds via formation of free radical intermediates as shown by Wan et. al.[56] The primary decomposition fragment from methane is the methylene radical which recombines on very hot surfaces to yield acetylene, whereas on cooler surfaces it leads to the formation of ethylene. This finding is in agreement with our results as seen in Figures 4 and 6, which show formation of acetylene as power increased. Equations 1-7 summarize some of the proposed reactions:

$$CH_4 \rightarrow :CH_2 + H_2 \quad (1)$$
$$2\,CH_4 \rightarrow C_2H_4 + 2\,H_2 \quad (2)$$
$$2\,CH_4 \rightarrow C_2H_2 + 3\,H_2 \quad (3)$$
$$C_2H_4 + H_2 \rightarrow C_2H_6 \quad (4)$$
$$3\,C_2H_2 \rightarrow C_6H_6 \quad (5)$$

The presence of H_2 from reaction (1) leads to hydrogenation of olefins and production of ethane as shown in reaction (4). The highly reactive methylene ($:CH_2$) intermediate can be used to elucidate the formation of ethylene and acetylene as indicated in reactions (2) and (3). The formation of benzene may be explained by the well-known cyclization reaction given in Equation (5). This is in agreement with the fact that selectivity of benzene increases as selectivity of acetylene also increases. Another viable mechanism for ethylene and acetylene formation could involve the dehydrogenation of secondary hydrocarbons:

$$C_2H_6 \rightarrow C_2H_4 + H_2 \quad (6)$$
$$C_2H_4 \rightarrow C_2H_2 + H_2 \quad (7)$$

The increase in the duration of the pulse in order to achieve a certain average power and therefore an increase in the surface temperature of the catalyst explains the general trend where conversion increases as power increases. Conversion levels were smaller when using He as a diluent in the feed due to the fact that the residence time was about four times smaller than that when using pure methane in the feed (0.08 vs. 0.33 min^{-1} respectively). Allowing the reactant to spend more time in the reaction zone will permit the methane molecules to find adequate sites for reaction to occur. Since the irradiation time of the catalyst was small (3 min), the bulk temperature was not completely homogeneous. That is, there were hot spots, cold spots, and intermediate temperature spots. Methane will only react on those sites that have reached the proper temperature. Thermodynamic analysis has indicated that a catalyst particle surface temperature on the order of 1400°C – 1600°C is required to yield C_2 products from methane.[67] The proportion of C_2 products changed from ethylene > acetylene > ethane when using pure methane to ethylene > ethane > acetylene when using methane and He in the feed. More benzene was also formed when using pure methane. These observable facts can be explained by both the difference in reagent residence time and the difference in concentration of methane. Wan found that sudden cooling of products would favor the formation of ethylene and ethane. [67] For the case of CH_4:He feed, low concentration of active intermediates and products, relatively cold He molecules combined with low residence time, would give the molecules more likelihood for rapid quenching. As mentioned previously, benzene very likely comes from the trimerization of acetylene. High concentrations of methane will statistically favor the formation of acetylene and benzene. Including a diluent in the feed will help prevent the coupling of intermediates to these products.[63-66]

At present, the issue of microwave effects is very controversial. Unfortunately, many of the expected results from microwave processing such as rapid and uniform heating, more uniform microstructures, inverse temperature profiles, and selective heating are included in the general category of microwave effects. However, only those anomalies that cannot be predicted or easily explained based on our present understanding of differences between thermal and microwave heating should be referred to as microwave effects.[44,68] "Microwave specific" activation has been a debated concept which actually refers to a unique interaction, reaction, or activation, specific to the microwave radiation. Two models of the chemical mechanisms in such reactions have emerged from research work done so far on microwave induced reaction chemistry. One model assumes that rate enhancement is simply due to thermal dielectric heating and the other assumes that there is a specific activation due to microwave radiation that occurs in addition to the dielectric heating mentioned earlier.[69]

Our work is unique in the sense that systematic frequency effects have been found to markedly influence conversion and selectivity under microwave radiation in the oligomerization of methane. The effect of frequency on product distribution for the oligomerization of methane was studied with and without He as a diluent. It is a fact that when increasing microwave frequency, selectivities towards C_{2s} decreased and selectivity towards C_6 increased for both cases (with and without diluent).

All C_2 hydrocarbons decreased as frequency increased when using pure methane feed. When using He as a diluent, ethylene and acetylene increased as frequency increased while ethane decreased (see Figures 4 and 7). These effects on product distribution are related to the transverse magnetic modes at different frequencies that would generate diverse transient heating patterns. The two parameters that define the dielectric properties of materials and

concomitant heating patterns are dielectric constant and dielectric loss.

As quenching of intermediates has an important role in ethylene formation, different transient heating patterns would affect the environment in which the reaction is taking place, consequently affecting the selectivities of the final products. The dielectric constant, e', describes the ability of the molecules to be polarized by the electric field. At low frequencies this value will reach a maximum as the maximum amount of energy that can be stored in the material. As frequency increases e' decreases as shown by Mingos et al.[70] The dielectric loss, e", measures the efficiency at which microwave energy can be converted into heat and goes through a maximum as frequency increases.[70] The relationship between these two parameters e"/e' defines the dielectric loss tangent, tan δ, which measures the ability of a material to convert electromagnetic energy into heat at a given frequency and temperature. The dielectric loss also goes through a maximum as frequency increases. Therefore, higher formation of benzene-acetylene at higher frequency in our experiments can be explained by the increase of the dielectric loss as frequency increases before going through the maximum. Greater dielectric loss is directly related to greater temperatures, consequently related to acetylene formation.[56] Acetylene is later consumed in the trimerization reaction to obtain benzene, which is detected in the final products.

Conclusions

Systematic effects of power level, He as diluent, and microwave frequency were studied for the microwave oligomerization of methane using Ni powder catalyst with branched filament morphology. We are not aware of other heterogeneous catalysis studies where either direct or indirect frequency effects have been observed under microwave radiation. As frequency increased, selectivity towards benzene also increased. When using He as a diluent, as frequency increased, selectivities towards ethylene and acetylene also increased. When pure methane was used, the opposite result was observed. These changes in product distribution are most likely due to different transverse modes that generate different transient heating patterns and changes in dielectric constant and loss of the catalyst.

Acknowledgment

The authors thank the National Science Foundation and the Electrical Power Research Institute under Grant CTS-9413394 of the joint NSF/EPRI Initiative on Microwave Induced Reactions. We thank Lambda Technology Inc. for support of this research. We also thank Todd Ellis and Denise Tucker of Lambda Technology Inc. for their advice and technical support. We thank Professor G. Roussy of LSTM Université de NANCY 1, and Professor J.K.S Wan of Queen's University for helpful discussions.

References

(1)Anderson, J. R., *Appl. Catal.* **47**, 177 (1989)
(2) Mimoun, H., *New J. Chem*. **11**, 7, 513 (1987)
(3) Pitchai, R., Klier, K., *Catal. Rev. –Sci. Eng.* **28**, 1, 13 (1986)
(4) Janowicz, A. J., Periana, R. A., Buchanan, C. A., Kovac, C. A., Stryker, J. M., Wax, M. J., Bergman, R. G., *Pure Appl. Chem.* **56**, 13 (1984)
(5) Hoyano, J. K., McMaster, A. D., Graham, W. A. G., *J. Am.Chem. Soc.* **105**, 7190 (1993)
(6) Kao, L. C., Hutson, A. C., Sen, A., *J. Am.Chem. Soc.* **113**, 700 (1991)
(7) Scurrell, M. S., *App. Catal*. **32**, 1 (1987)
(8) Lee, J. S., Oyama, S. T., *Catal. Rev. –Sci. Eng.* **30**, 2, 249 (1988)
(9) Hutchings, G. J., Scurrell, M. S., Woodhouse, *J. R., Chem. Soc. Rev*. **18**, 251 (1989)
(10) Amenomiya, Y., Birss V. I., Goledzinowski, J., Galuszka, J., Sanger, A. R., *Catal. Rev. –Sci. Eng*. **32**,163 (1990)
(11) Shepelev S. S., Gesser H.D., Hunter N. R., *Plasma Chem. and Plasma Proc*. **13**, 3, 479 (1993)
(12) Shilov A. E., "The Activation of Saturated Hydrocarbon by Transition Metal Complexes." Reidel D. and Dordrecht, The Netherlands, 1984.
(13) Wada K., Yoshida K., Watanabe Y., Suzuki T., *J. Chem. Soc. Chem. Commun.* 726 (1991)
(14) Otsuka K., Komatsu T., *J. Chem. Soc. Chem Commun*. 388 (1987)
(15) Ogura K., Kataoka M., *J. Mol. Catal.* **43**, 371 (1988)
(16) Sayyel B. A., Stair P. C., *J. Phys. Chem.* **94**, 409(1990)
(17) Hill C.L., "Activation and Functionalization of Alkanes." Wiley, New York, 1989.
(18) Ryabov A. D., *Chem. Rev*. **90**, 403 (1990)
(19) Wolf E. E., "Methane Conversion by Oxidative Process." Van Nostrand Reinhold: New York, 1992.
(20) Huang J., Suib S. L., *J. Phys. Chem*. **97**, 37, 9403 (1993)
(21) Huang J., Suib S. L., *Res. Chem. Intermed*. **20**,1, 133 (1994)
(22) Suib S. L., Zerger R.P., Zhang Z., "Proceedings, Symposium on Natural Gas Upgrading II", p 344, Petroleum Chem., ACS, Washingtong DC, 1992.
(23) Suib S. L., Zerger R. P., *J. Catal.* **139**, 383 (1993)
(24) Huang J., Badani M. V., Suib S. L., Harrinson J. B., Kablauoi M., *J. Phys. Chem*. **98**, 1, 206 (1994)
(25) Tse, M. Y., Depew, M. C., Wan, J. K. S., *Res. Chem. Intermed*. **13**, 221 (1990)
(26) Cameron K. L., Depew M. C., Wan J. K. S., *Res. Chem . Intermed*. **16**, 57 (1991)
(27) Bamwenda, G., Moore, E., Wan, J. K. S., *Res. Chem. Intermed*. **17**, 243 (1992)
(28) Bamwenda, G., Depew, M. C., Wan, J. K. S., *Res. Chem. Intermed*. **19**, 6, 553 (1993)
(29) Ioffe, M. S., Pollington, S. D., Wan, J. K. S., *J. Catal*. **151**, 349 (1995)
(30) Dinesen T. R. J., Tse M. Y., Depew M. C., Wan J. K. S., *Res. Chem. Intermed.* **15**, 113 (1991)
(31) Cameron K. L., Depew M. C., Wan J. K. S., *Res. Chem. Intermed.* **16**, 57 (1991)
(32) Depew M. C., Lem S., Wan J. K. S., *Res. Chem. Intermed.* **16**, 213 (1991)
(33) Wan J. K. S., *Res. Chem. Intermed.* **16**, 147 (1991)
(34) Wan J. K. S., Ioffe M. S., *Res. Chem. Intermed*. **20**, 1, 115 (1994)
(35) Pollington, S. D., Ioffe, M. S., Westergaard, M., Wan, J. K. S., *Res. Chem. Intermed*. **21**, 1, 59 (1995)
(36) G. Roussy, J. A. Pearce, "Foundations and Industrial Applications of Microwaves and Radiofrequency Fields." John Wiley, New York, 1995.
(37) Caddick, S., T*etrahedron* **51**, 38, 10401 (1995)
(38) Strauss, C. R., Trainor, R. W., *Aust. J. Chem*. **48**, 1665 (1995)
(39) Majetich, G., Hicks, R., *J. of Microwave Power and Electromagnetic Energy* **30**, 1, 27 (1995)
(40) Bram, G., Loupy, A., Villemin, D., in "Solid Supports Catal. Org. Synth." Chapter 12, Microwave activation of reaction on inorganic solid supports Eds. Smith, K., p302, 1992
(41) Whittaker, A. G., Mingos, D. M. P., *Journal of Microwave Power and Electromagnetic Energy* **29,** 4, 195 (1994)
(42) Mingos, D. M. P., Baghurst, D. R., *British Ceramic Transactions and Journal* **91**, 4, 124 (1992)

(43) Sutton, W., *Ceramic Bulletin* **68**, 2, 376 (1989)
(44) Clark, D. E., Sutton, W. H., *Annu. Rev. Mater. Sci*. **26**, 299 (1996)
(45) Rao, K. J., Ramesh, P. D., *Bull. Mater. Sci*. **18**, 4, 447 (1995)
(46) Mingos, D. M. P., Baghurst, D. R., *Chem. Soc. Rev*. **20**, 1 (1991)
(47) Baghurst, D. R., Chippindale, A. M., Mingos, D. M. P., *Nature* **332**, 311 (1988)
(48) Baghurst, D. R., Mingos, D. M. P., *J. Chem. Soc. Chem. Comm*. 829 (1988)
(49) Chatakondu, K., Green, M. L. H., Mingos, D. M. P., Reynolds, S. M., *J. Chem. Soc. Chem. Comm*. 1515 (1989)
(50) Baghurst, D. R., Cooper, S. R., Greene, D. L., Mingos, D. M. P., Reynolds, S. M. *Polyhedr*. **9**, 893 (1990)
(51) Baghurst, D. R., Mingos, D. M. P., *J. Chem. Soc. Dalton Trans*. 1151 (1992)
(52) Baghurst, D. R., Mingos, D. M. P., Watson, M. J., *J. Organomet. Chem*. **368**, C43 (1989)
(53) Baghurst, D. R., Mingos, D. M. P., *J. Organomet. Chem*. **384**, C57 (1990)
(54) Whittaker, A. G., Mingos, D. M. P., *J. Chem. Soc. Dalton Trans*. 275 (1992)
(55) Whittaker, A. G., Mingos, D. M. P., *J. Chem. Soc. Dalton Trans*. 2541 (1993)
(56) Wan, J. K. S., Tse, M. Y., Husby, H., Depew, M. C., *J. of Microwave Power and Electromagnetic Energy* **25**, 1, 32 (1990)
(57) Gourari, S., Roussy, G., Thiebaut, J. M., Zoulalian, A., *The Chemical Eng. J*. **49**, 79 (1992)
(58) Roussy, G., Thiebaut, J. M., Souiri, M., Marchal, E., Kiennemann, A., Maire, G. *Catal. Today* **21**, 349 (1994)
(59) Seyfried, L., Ganh, F., Maire, G., Thiebaut, J. M., Roussy, G., *J Catal*. **148**, 281 (1994)
(60) Chen, C., Hong, D., Dai, S., Kan, J., *J. Chem. Soc. Faraday Frans*. **91**, 7, 1179 (1995)
(61) Bond, G., Moyes, R. B., Whan, D. A., *Catal. Today* **17**, 427 (1993)
(62) C. Marun, L. D. Conde, S. L. Suib., *J. Phys. Chem. A* **103**, 4332 (1999)
(63) Maitlis, *J. Organomet. Chem*. **200**, 161 (1980)
(64) Maitlis, *Acc. Chem. Res*. **9**, 93 (1976)
(65) Vollhardt, *Acc. Chem. Res*. **10**, 1 (1977)
(66) Reppe, Kutepow, and Magin, *Angew. Chem. Int. Ed. Engl*. **8**, 727 (1969)
(67) Wan, J.K.S., US Patent 4574038 (1986)
(68) Lewis D.A., *Microwave Processing of Materials III, Mater. Res. Soc. Symp. Proc., 269, Pittsburg: Mater. Res. Soc.* 21 (1992)
(69) Jacob J, Chia L. H. L., Boey F. Y. C., *J. Mat. Soc*. **30**, 5321 (1995)
(70) Mingos, D. M. P., Baghurst, D. R., in "Microwave-Enhance chemistry." Kingston, H. M. and Haswell, S. J. p. 1. Am. Chem. Soc., Washington, DC, 1997

PLASMA CATALYTIC HYBRID REFORMING OF METHANE

Thomas Hammer, Thomas Kappes, Wolfgang Schiene

Siemens AG, Corporate Technology Department Plasma- and Switching Technology, POB 3220, 91050 Erlangen, Germany

Introduction

Hydrogen enriched fuel gases offer the potential for efficient low NOx combustion processes. The reduction of NOx-emission is caused by a reduction of the adiabatic flame temperature due to stable, lean combustion and in some cases due to steam addition or exhaust gas recirculation. In the past reduced NOx-emissions both from gas turbines[1,2] and internal combustion engines[3] were reported. At the same time the energy efficiency of internal combustion engines[3] was improved for 15-50 % compared to pure gasoline operation. In stationary applications there is an additional potential for the reduction of specific CO_2-emissions: If the hydrogen is generated by integrated reforming of fossil fuels, carbonaceous products of the reforming reaction like CO_2[4], solid carbon[5] or in the case of methane higher hydrocarbons[6] may be separated prior to combustion and utilized as raw material e.g. in the chemical industry. For mobile application of PEM fuel cells requiring hydrogen as a fuel on-board generation of hydrogen is desirable because of the high energy storage density of gasoline or diesel fuel.

Large scale production of hydrogen is performed e.g. by catalytic steam reforming of methane. However, this process requires a temperature of about 900 °C. At lower temperatures catalyst coking and poisoning can get a problem. For the generation of hydrogen enriched fuel gases a low temperature reforming process which is not sensitive to coking or poisoning would be desirable.

Recently plasma reforming has been proposed for the efficient generation of hydrogen and higher hydrocarbons in a compact, light weight reactor. For large scale application arc based plasma torches heating the gas very rapidly to temperatures of several thousand degrees Celsius for complete fuel conversion are utilized. However, for small scale application and for incomplete fuel conversion non-thermal plasmas which avoid excessive gas heating are a much better choice. Non-thermal plasma (NTP) reforming induced by dielectric barrier discharges (DBD) has been shown to have the potential for the generation of hydrogen and higher hydrocarbons.

In facilities where waste heat can be utilized to support NTP-reforming an endothermic reforming process like methane steam reforming

$$CH_4 + H_2O \rightarrow CO + 3\ H_2,\ \Delta H^0 = 206\ \text{kJ/mole} \qquad (1)$$

rather than an exothermic one will be applied: However, neither the selectivity nor the energy efficiency of DBD induced methane steam reforming showed to be sufficient for practical application. For this reason plasma catalytic hybrid steam reforming of methane was investigated in the temperature range 200-600 °C.

Experiments on Plasma Induced Steam Reforming of Methane

The conversion of methane and water as well as the yields of hydrogen, carbon monoxide, carbon dioxide, methanole, and higher hydrocarbons up to C_4H_n were investigated as a function of the gas temperature, plasma input power, gas flow, and feed ratio of methane to water. Methane was fed from a pressurized gas cylinder using a mass flow controller, water was spray injected and evaporated at 250 °C. The gas mixture was heated to the desired temperature using a tubular heat exchanger.

For gas analysis a gas chromatograph (GC: Shimadzu GC 14B equipped with a combination of a HayeSep R/Q column and a mole sieve 13X column) and an FTIR-absorption spectrometer (FTIR: Perkin Elmer System 2000 with a 1 m White cell heated to 190 °C) were applied. Prior to FTIR-analysis the gas was diluted for a factor 10 with pure nitrogen.

Dielectric Barrier Discharge Reactor. Reference measurements on NTP-induced steam reforming of methane were performed using a coaxial DBD-reactor (Figure 1) which was thermally isolated and thermostatically heated to the desired temperature. An alumina tube with an outer diameter of 25 mm and an inner diameter of 20 mm was applied as a dielectric barrier between the ground electrode and the high voltage electrode. The ground electrode was manufactured by flame coating the outer tube surface. The structured high voltage electrode consisted of sharp edged circular discs with a diameter of 16 mm fed on a stainless steel rod. The number and spacing of the discs was chosen such that the active region of the reactor had a length of 200 mm.

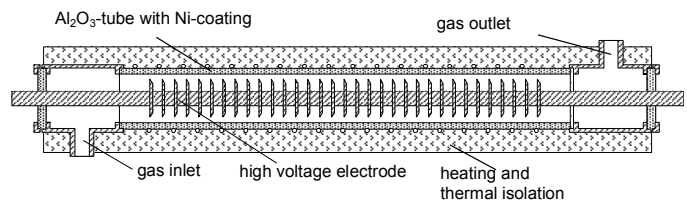

Figure 1. DBD-reactor set-up for methane steam reforming.

Dielectric Packed Bed Reactor. Plasma catalytic experiments were carried out in a thermostatically heated dielectric packed bed (DPB) reactor, which combines the features of a catalytic fixed bed tube reactor and of a DBD reactor (Figure 2). Its ground electrode and barrier were identical to those of the DBD-reactor. A stainless steel tube with an outer diameter of 10 mm was used as inner electrode. Thus a discharge gap 10 mm was obtained, which was filled with the catalyst packing consisting of nickel dispersed on ceramic pellets having diameters between 2 and 4 mm. For electrical discharge excitation a sinusoidal high voltage power supply with a maximum output power of 600 W was applied.

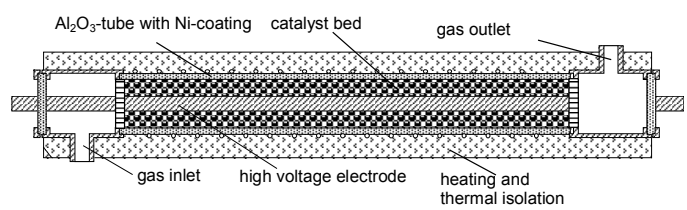

Figure 2. DPB-reactor set-up for methane steam reforming.

Experimental Results

DBD-Induced Reforming. We found that DBD-induced CH_4-conversion and product yields depended on all parameters under investigation. As a reference the dependencies on temperature and plasma input power are shown in Table 1 and Table 2, respectively.

Because the net water conversion was negligibly small, the hydrogen yield was calculated under the assumption that only CH_4 but not H_2O contributes to H_2-formation. It depends much stronger on power than on temperature. The conversion of CH_4 is roughly proportional both to temperature and plasma input power, however, the yields of H_2 and higher hydrocarbons (mainly C_2H_6) are not.

Increasing the CH_4:H_2O feed ratio from 1:3 to 1:1 reduced the yields, however, the molar flows of the reaction products remained nearly unchanged. When the flow rate was increased at constant specific plasma energy input (ratio of power to gas flow rate) both the CH_4-conversion rate and the product yields increased.

The energy requirements for H_2-generation did not depend substantially on the specific plasma energy input and decreased with increasing temperature. They ranged from 2 to 8 MJ/mole H_2.

Table 1. Dependence of Conversion and Product Yields on the Temperature

T [°C]	CH_4-conversion and product yields [%]									
	CH_4	H_2	CH_3OH	CO	CO_2	C_2H_6	C_2H_4	C_3H_8	C_3H_6	C_4H_{10}
200	2.3	1.3	0.23	0.43	0.02	1.4	0.03	0.39	0.00	0.45
400	4.9	1.7	0.11	0.31	0.05	2.6	0.11	0.68	0.01	0.37
600	7.9	2.7	0.00	0.21	0.19	4.1	0.71	0.73	0.12	0.26

Experimental conditions: Plasma input power 50 W, flow rate 1 Nliter/min, feed ratio CH_4:H_2O = 1:2

Table 2. Dependence of Conversion and Product Yields on the Plasma Input Power

P [W]	CH_4-conversion and product yields [%]									
	CH_4	H_2	CH_3OH	CO	CO_2	C_2H_6	C_2H_4	C_3H_8	C_3H_6	C_4H_{10}
50	2.3	1.3	0.23	0.43	0.02	1.4	0.03	0.39	0.00	0.45
100	6.9	2.4	0.43	0.79	0.06	2.2	0.06	0.67	0.00	1.03
150	12.1	4.1	0.46	0.96	0.12	3.8	0.12	1.20	0.04	1.78
200	17.3	6.5	0.57	1.12	0.22	5.1	0.28	1.64	0.12	1.35

Experimental conditions: Temperature 200 °C, flow rate 1 Nliter/min, feed ratio CH_4:H_2O = 1:2

Plasma-Catalytic Hybrid Reforming. In contrast, when plasma-catalytic hybrid treatment was applied both methane and water were converted (Figure 3). Therefore now the H_2-yield was calculated taking into account both the CH_4 and the H_2O-feed. At temperatures below 400 °C no catalytic conversion was observed when the plasma was switched off. In this temperature range mainly H_2, CO_2, and small amounts of C_2H_6 were formed by plasma-catalytic hybrid reforming. At temperatures above 400 °C substantial CO-yields were achieved, and the CO_2-yield dropped relative to the H_2-yield. In contrast to DBD-reforming the C_2H_6-yield gets negligible at higher temperatures.

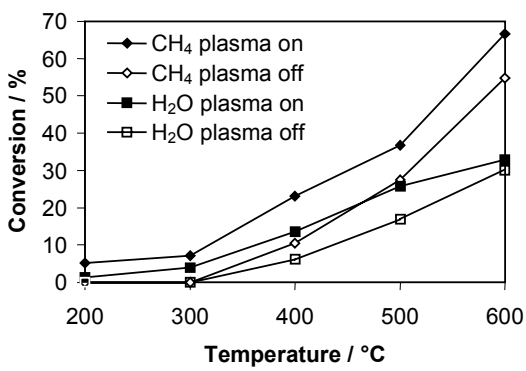

Figure 3. Plasma-catalytic hybrid reforming of methane – conversion as a function of the temperature (flow rate 1 Nliter/min, plasma input power 150 W, feed ratio CH_4:H_2O = 1:2)

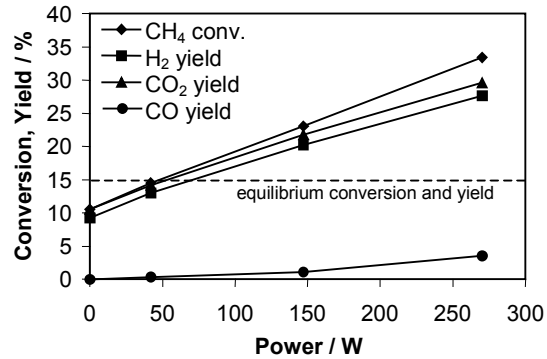

Figure 4. Plasma-catalytic hybrid reforming of methane – conversion as a function of the plasma input power (flow rate 1 Nliter/min, temperature 400 °C, feed ratio CH_4:H_2O = 1:2)

Conversion and yields increased linearly with the plasma input power. At temperatures around 400 °C and input powers above 60 W the yields of H_2 and CO_2 exceeded the values calculated from thermodynamic equilibrium relations. With increasing power an increasing selectivity towards CO-formation was observed whereas the selectivity for CO_2-formation decreased.

The dependency of CO- and CO_2-concentrations on specific energy and temperature may be explained by the assumption that CO is formed by plasma induced gas phase processes and by catalytic processes, whereas CO_2 is mainly formed due to a low temperature catalytic water shift reaction converting CO to CO_2.

At temperatures above 200 °C by the combination of plasma and catalyst the energy requirements were reduced compared to DBD-treatment. Values as low as 315 kJ/mole H_2 were achieved at 600 °C.

Conclusions

NTP-reforming of methane in CH_4-H_2O-mixtures was investigated. Dielectric barrier discharges mainly induce formation of H_2 and C_2H_6 by decomposition of CH_4 at negligible H_2O-conversion. Numerical simulations of the DBD-induced chemical kinetics showed that 38 % and 7 % of the energy dissipated in discharge filaments are spend for CH_4- and H_2O-dissociation respectively.

By the combination of the DPB-plasma and a Ni-catalyst high H_2O-conversion rates and selectivities towards H_2- and CO_2-formation were achieved. For temperatures above 200 °C the energy requirements dropped for an order of magnitude down to values as low as 315 kJ/mole H_2 at 600 °C. Further improvements can be expected if thermal losses e.g. due to barrier heating could be avoided, which may be well above 60 % of the plasma input power.

References

[1] Phillips, J.N.; Roby, R.J. *Power Engineering* **2000**, *May*, 36-40.

[2] Maughan, J.R.; Bowen, J.H.; Cooke, D.H.; Tuzson, J.J. *Proc. ASME Cogen-Turbo Conference*, **1994**, 381-390.

[3] Jamal, Y.; Wyszynski, M.L. *Int. J. Hydrogen Energy*, **1994**, *19(7)*, 557-572

[4] Nihous, G.C.; Mori, Y.; Masutani, S.M.; Vega, L.A.; Kinoshita, C.M. *Int. J. Hydrogen Energy*, **1994**, *19(4)*, 387-94.

[5] Fulcheri, L.; Schwob, Y. *Int. J. Hydrogen Energy*, **1995**, *20(3)*, 197-202.

[6] Kogelschatz, U.; Zhou, L. M.; Xue, B.; Eliasson, B. In *Greenhouse Gas Control Technologies*, Proc. 4th Int. Conf., Meeting Date 1998; Eliasson, Baldur; Riemer, Pierce; Wokaun, Alexander, Eds.; Elsevier, Oxford, UK, **1999**, pp. 385-390.

REFORMING OF METHANE INTO SYNGAS IN A PLASMA-ASSISTED REACTOR

Albin Czernichowski [(1)], Mieczyslaw Czernichowski [(2)], Piotr Czernichowski [(1)], and Thomas E. Cooley [(1)]

(1) Synergy Technologies Corporation,
335 25th St. S.E., Calgary, Alberta, T2A 7H8
(2) Etudes Chimiques et Physiques
21 François Marchand, 45100 Orléans, France

Introduction

A mixture of H_2 + CO (called "synthesis gas" or "syngas") is an important bridge to several chemical syntheses like methanol or synthetic liquid fuels through the Fischer-Tropsch syntheses. Nowadays, syngas starts to be also considered as simple fuel that can be converted to electric energy in Solid Oxide or Molten Carbonate Fuel Cells (FC). These two kinds of FC use both H_2 and CO as fuel while other cells accept only pure hydrogen; in addition other cells are poisoned by traces of CO. syngas is almost certain to play a major role in the massive production of pure hydrogen in the near- to medium-term future. This production, for exclusively H_2-based FC or other chemical, petrochemical, metallurgical or space applications, would go through hydrogen separation from the syngas, followed by the "water shift" in which remaining CO is converted to H_2 then polished using a less or more deep purification.

It also appears that in the near- to medium-term future most of syngas production will be based on fossil fuel reforming, mostly Natural Gas (NG). Small- and medium-scale reforming would allow using a pipeline distributed NG as well as numerous small NG sources. However, conventional reformers require careful attention to heat management, feed introduction, catalysts, etc., and entail solution of a set of difficult problems.

Our SynGen reformer based upon the gliding discharges (GlidArc) plasma principle solves many of these problems when using the electrically assisted Partial Oxidation (POX) of NG. For the sake of simplicity and economics, the unique oxidant (oxygen) source we use is atmospheric air. Although enriched oxygen up to and including "pure" oxygen can be used.

Thermodynamics and Energetics

The exothermic chemical reaction describing the POX of a mixture of HC contained in NG can be written as:

$$C_nH_{2n+2} + {}^{n}/_{2}\, O_2 \rightarrow n\, CO + (n+1)\, H_2 . \quad (1)$$

For pure methane the reaction is:

$$CH_4 + 0.5\, O_2 \rightarrow CO + 2\, H_2 \quad (2)$$

with a weak exothermic effect of $\Delta H° = -36.1$ kJ per mol of converted methane. This heat of reaction is insufficient to keep moving it properly; it represents less than 5% of the methane full combustion heat so that extra heat and/or catalysts are necessary in classical technologies. For example, an O_2/CH_4 » 0.5 ratio could be used to burn a part of the methane feed. However, this adds steam and CO_2 into the syngas. As a compromise, we install gliding discharges directly in the reacting mixture; they add an active electric energy and catalytic species.

Experimental

A bench scale GlidArc stainless steel reactor, similar to those previously described[1,2] was used as reformer; it is shown schematically on the Fig. 1.

The reactor /1/ uses six steel electrodes /2/ (only two electrodes are shown) that delimit a nozzle-shaped volume /3/ where gliding electric discharges /4/ may develop. This reactor contains a nozzle /5/ blowing the premixed NG + air mixture /6/ to be converted in the space /7/ between the electrodes arranged so that the mixture flows along the central part of these electrodes exposed to the discharges.

The discharges pre-ionize the gas at the point /9/, glide on the electrodes and disappear at the point /10/ near the end of the electrodes, to appear once again at the initial point. The process is sequential and the lifetime of a single discharge /4/ ranges from 1 to 20 ms, depending on the linear speed of the fluid in zones /7/, /9/, /3/ and /10/. Given the moderate temperature of the electrodes (not cooled) and a very short contact time of the discharge root /8/ with the electrodes, we do not observe any deterioration that may prevent the gliding of these current-limited discharges.

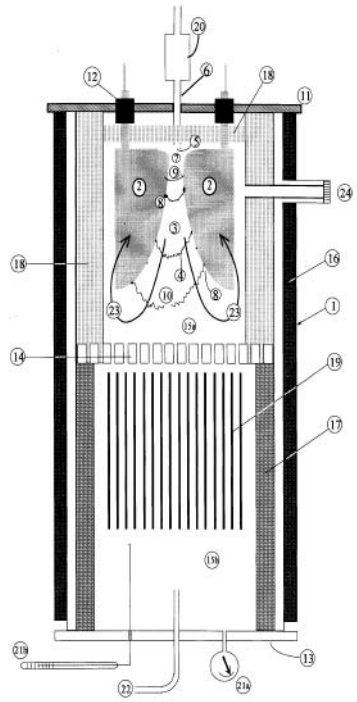

Figure 1. Schematic view of the GlidArc reformer.

Two flanges close the tubular reactor. One /11/ supports the electrodes through with high voltage connectors /12/. The other one /13/ closes the reactor on the other side and comprises a product output tube /22/. The entire structure is tight; it can support a pressure of 0.6 MPa (measured at point /21a/) but for the present tests we worked at slightly higher than atmospheric pressure.

A perforated plate /14/ separates a void plasma zone /15a/ and a post-plasma zone /15b/ which is partially filled with metallic Ni pads. The plate /14/ makes it possible to run products from the plasma treatment to the post-plasma zone. The reactor is insulated externally and internally by ceramic felts and tube /16/ and /17/ in order to keep it hot. The plasma zone is also insulated by a heat resisting felt /18/. The total free volume (in terms of fluid) inside the reactor is about 2 L. No part of the reactor is cooled in a forced manner. Two holes in the flange /13/ provide for the connection of a pressure gauge /21a/ and for the insertion of a thermocouple /21b/ measuring the downstream temperature.

With almost punctual injection of the fluid between the electrodes we already provoke a phenomenon of re-circulation /23/ of the reactants in the gliding discharge zone. In order to reinforce this re-circulation, we also add this separating plate /14/, thus dividing the reactor in two parts. The perforated plate provides for the flow of

reactants (partially consumed) and "long-living" active species resulting from the excitation of the gases by the gliding discharges. In the post-plasma zone, the conversion is thus completed in the presence of that space filling. The luminous zone of the gliding electric discharges, as well as part of the wall of the zone, can be observed through a window /24/ in order to verify the proper operation of the reactor and to determine (through a pyrometer) the temperature in the compartment /15a/.

The reactor is fed by controlled (through mass flow meters) flows of compressed air and NG. Both flows were mixed together before their injection into the reactor.

A high voltage system provides both the pre-ionization of the medium and then the transfer of electric energy into the gliding discharges. The 6-phase system is composed of neon transformers. The time-averaged electric power of the reactor was measured using a 3-phase kWh-meter and a chronometer. We are taking into account a power consumption of the transformers themselves. The net GlidArc power during our tests was up to 0.85 kW.

The reforming products were flared. The flame spectrum gave us an important indication of the process. When the flame was satisfying we sucked a sample of the gas product through anhydrous $CaCl_2$ and analyzed immediately using gas chromatography methods. We use two chromatographs, each dedicated to individual dry gases: H_2, N_2, O_2, CO, CO_2 and CH_4 for the first, and all the HC for the second.

The gas from the town pipeline has the following composition (in vol. %) according to our analysis: CH_4 84.5, C_2H_6 10.4, C_3H_8 2.2, C_4H_{10} 0.7, C_{5+} 0.1, N_2 1.6, and CO_2 0.6. We sucked it from the low-pressure pipeline and than compressed it. The flow-rate from our "source" could be well stabilized at the levels from 19 to 25 L(n)/h.

Results and Discussion

Continuous run times for NG were 160 min and 560 min. During these two long runs we fully analyzed syngas samples as well as input air/NG and pure NG samples. Table 1 shows some parameters and results from these runs. For soot presence checking we installed a quartz filter at the stream of the produced syngas. Then, after a certain time, the filter was removed for appreciation. The mass increase of the filter was always less than 0.1 mg. A gray or white color of the filter indicated a very little or no soot presence.

Table 1. Results of completely non-sooting reforming of NG.

Flow rate input	air	L(n)/min	81
	NG	L(n)/min	23
O/C atomic ratio @ input		mol/mol	1.3
Electric power injected		kW_e	0.79
Output gas conc. (vol. %)		CH_4	4.5
		C_2H_6	0.02
		C_2H_4	none
		CO_2	4.0
		CO	13
		H_2	26
		N_2	51
Output gas flow rate in m^3(n)/h		Total	7.4
		H_2+CO	2.9
kWh_e spent to produce 1 m^3(n) of H_2+CO			0.27

We observe a certain slippage of CH_4 while ethane, propane, and butane (all initially totalizing 13 vol. % in NG) are completely converted. No soot was observed for NG reforming at a sufficient O/C ratio. We are not yet at the limits of possible optimization of the process; from the given reactor we can probably obtain a much higher flow of syngas when working at higher pressures… To increase the reactor throughput we can also preheat both air and NG (we have a heat available from the hot output syngas).

Conclusions

This contribution presents some of the experimental data from our work thus far in 2001. Pipeline grade natural gas is almost completely reformed in the SynGen reactor at atmospheric pressure and at quite low electric power GlidArc assistance. We have successfully engineered novel technologies in developing a fossil fuel reformer. Synergy Technologies Corporation's SynGen based on non-catalytic, plasma-assisted POX reforming offers the following competitive advantages:

- We produce syngas in quality and quantity that may be applied to an ideal 10-kW Solid Oxide or Molten Carbonate FC.
- For other applications, the reformer can also be a part of pure H_2 generators after a classical water-shift.
- It is a Sulfur-tolerant, non-catalytic reforming technology and can therefore process any acid NG.
- Any soot is produced.
- SynGen reformers are compact and easily scalable.
- No additional water or steam circuits, heaters, etc are necessary.
- Electrical consumption for process assistance is low.
- The process starts after only 15 min warm-up and can re-start after about 1 min.

Further developments are in progress. Our on-road development includes systems to generate 15 m^3(n)/h of H_2+CO mix. A much bigger SynGen reformer for NG conversion is currently under development in Alberta as a part of Synergy's Gas-to-Ultra Clean Diesel and Gasoline advanced technology. Synergy's technology incorporates various proprietary and/or licensed components and is covered by appropriate US and PCT patents.

References

1. A. Czernichowski, P. Czernichowski, French Pat., No. 2,768,424, **1997**; see also US6007742, EP1012113 and WO9911572 patents.
2. A. Czernichowski, Oil & Gas Science and Technology - Revue de l'IFP, **2001.** 56(2) p. 181-98.

Acknowledgement

Participation of Michal Mlotek (Warsaw Technical University, Poland) in initial experiments is highly appreciated.

CARBON DIOXIDE AS A SOLVENT FOR POLYMERIZATION AND CROSS COUPLING REACTIONS

A. B. Holmes, T. R. Early, R. S. Gordon, L. M. Stamp*

Melville Laboratory for Polymer Synthesis, University of Cambridge, Pembroke Street, Cambridge, CB2 3RA UK

R. E. Shute

Astra Zeneca, Mereside, Alderley Park, Macclesfield, Cheshire SK10 4TG

I. F. McConvey

Astra Zeneca Process Research, Silk Business Park, Macclesfield, Cheshire SK10 4NA

Introduction

Modern organic synthesis has entered a phase in which there is a desire to achieve rapid parallel reactions. Obviously this places more demands on the use of volatile organic solvents. There is therefore an increasing interest in using readily available carbon dioxide (for example from the combustion of fossil fuels) as an alternative solvent. There have been several significant recent reviews on the use of carbon dioxide as a solvent for organic synthesis.[1-3]

In this paper we describe the applications of supercritical carbon dioxide ($scCO_2$) as a solvent for various organometallic cross coupling reactions. In particular we focus on the Heck[4] and Suzuki[5] cross coupling reactions which have emerged as some of the most powerful methods of forming a bond between sp^2 carbon atoms. We[6] and Tumas[7] had previously demonstrated the first palladium-mediated examples of these reactions in $scCO_2$, using perfluorinated phosphines to solubilize the palladium(0) complexes in the solvent medium. Subsequently Rayner found that certain commercially available non-fluorinated ligands were moderately reactive in the presence of trifluoroacetate counterion.[8] Arai used phase transfer catalysis,[9] and most recently Bannwarth obtained promising results in a Stille coupling with triphenylphosphine as ligand, although the results were still inferior to those in which the phosphine carried fluorinated chains.[10]

Results and Discussion

Cross Coupling Reactions. We have now found that tri-*tert*-butylphosphine [P(*t*-Bu)$_3$] in the presence of palladium(II) acetate is a very effective catalyst for Heck and Suzuki reactions in $scCO_2$, thus dispensing completely with the need for fluorinated solubilizing groups.[11] The ligand [P(*t*-Bu)$_3$] has been popularized by Fu and colleagues[12,13] as a very powerful partner in catalytic Suzuki reactions with unreactive substrates such as aryl chlorides.

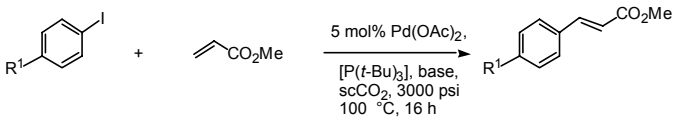

Scheme 1 Heck reaction in $scCO_2$

Both aryl iodides and bromides underwent the Suzuki reaction, although lower yields were obtained with the less reactive bromide coupling partners. A variety of different bases were investigated and shown to be effective in $scCO_2$. Surprisingly these reactions proceeded effectively in the presence of solid tetra-alkylammonium acetate salts without addition of any other base. Jeffrey has reported the use of tetra-alkylammonium salts for the Heck reaction in conventional solvents.[14] Herrman has also used the corresponding bromide salts as neat molten solvents.[15]

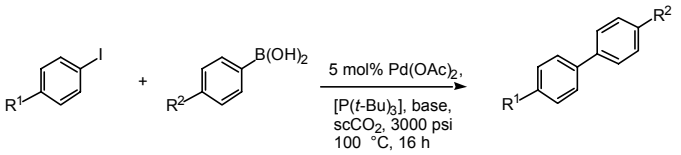

Scheme 2 Suzuki cross coupling reaction in $scCO_2$

Supported catalysts have been extensively developed for use in organic synthesis[16] and for palladium-mediated reactions on a solid phase support.[17-18] We have also developed variants of the solid phase synthesis of cinnamate derivatives by carrying out Heck reactions on a REM resin in $scCO_2$.[11]

Polycarbonate Synthesis. Another area of interest is the synthesis of polycarbonates in which carbon dioxide behaves as both solvent and reactant. This work was pioneered by Darensbourg[19] and Beckman[20-21] and it shows the power of various catalysts for this process. We recently employed a Cr(III)-tetra(pentafluorophenyl)porphyrin catalyst which was soluble in $scCO_2$ as a catalyst for polycarbonate synthesis using cyclohexene epoxide as the monomer.[22] This afforded low polydispersity polymer in excellent yields, but had the disadvantage that the porphyrin catalyst contaminated the final product (Scheme 3).

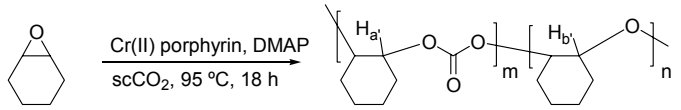

1 **2**

Scheme 3 Preparation of polycarbonate **2**

It is now shown that an Argogel® supported chromium porphyrin **3**[23] is effective in the copolymerization of 1,2-cyclohexene oxide (CHO) **1** and CO_2 (Scheme 4).

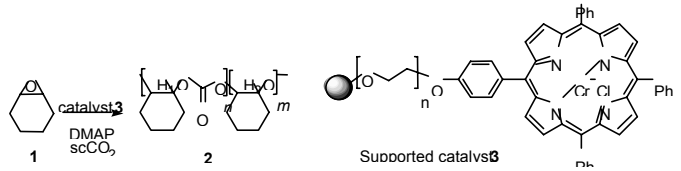

Scheme 4 Copolymerization of cyclohexene oxide and carbon dioxide in the presence of the Argogel catalyst **3** and dimethylaminopyridine

The ring opening copolymerization of cyclohexene oxide (CHO) **1** and CO_2 to form the copolymer poly(cyclohexenecarbonate-*co*-cyclohexene ether) **2** was investigated using catalyst **3** under various reaction conditions. Polymerizations were also carried out using an Irori Kan™ reactor[25] to separate the porphyrin beads from

the product polymer. This technique offered the opportunity to stir the reaction mixture with a magnetic stir bar and to study the recyclability of the catalyst. In fact the catalyst could be used for several cycles without loss of activity, and produced the polymer with increased yield compared with the unsupported catalyst.

Conclusions

This work has demonstrated that palladium-mediated cross coupling reactions can be carried out with commercially available phosphines and on solid phase supports in $scCO_2$. In a second aspect of this work it has been demonstratedd that copolymers of cyclohexene oxide and carbon dioxide can be prepared under supercritical conditions in the presence of a polymer-suppported Cr(III) porphyrin catalyst.

Acknowledgement. We thank Astra Zeneca (T. R. Early, L. Stamp,), the Engineering and Physical Sciences Research Council UK (Swansea Mass Spectrometry Service), the Isaac Newton Trust (R. Gordon), and the Commission of the EU (Brite-Euram BRRT-CT98-5089 'RUCADI') for generous financial support. We are grateful for the collaboration with K. Knights and Y. R. de Miguel (King's College, London).

References

(1) Oakes, R. S.; Clifford, A. A.; Rayner, C. M. *J. Chem. Soc., Perkin Trans. 1* **2001**, 917.
(2) Darr, J. A.; Poliakoff, M. *Chem. Rev.* **1999**, *99*, 495.
(3) Jessop, P. G; Leitner, W. *Chemical Synthesis Using Supercritical Fluids*; Wiley-VCH: Weinheim, 1999.
(4) Beletskaya, I.; Cheprakov, A. V. *Chem. Rev.* **2000**, *100*, 3009.
(5) Suzuki, A. *J. Organomet. Chem.* **1999**, *576*, 147.
(6) Carroll, M. A.; Holmes, A. B. *Chem. Commun.* **1998**, 1395.
(7) Morita, D. K.; Pesiri, D. R.; David, S. A.; Glaze, W. H.; Tumas, W. *Chem.Commun.* **1998**, 1397.
(8) Shezad, N.; Oakes, R. S.; Clifford, A. A.; Rayner, C. M. *Tetrahedron Lett.* **1999**, *40*, 2221.
(9) Bhanage, B. M.; Ikushima, Y.; Shirai, M.; Arai, M. *Tetrahedron Lett.* **1999**, *40*, 2221.
(10) Osswald, T.; Schneider, S.; Wang, S.; Bannwarth, W. *Tetrahedron Lett.* **2001**, *42*, 2965.
(11) Early, T. R.; Gordon, R. S.; Carroll. M. A.; Holmes A. B.; Shute, R. E.; McConvey, I. *Chem. Commun.* **2001**, 1966.
(12) Littke, A. F.; Fu, G. C. *J. Org. C hem.* **1999**, *64*, 10.
(13) Littke, A. F.; Fu. G. C. *J. Am. Chem. Soc.* **2001**, *123*, 6989 and references cited therein.
(14) Jeffrey, T. *Tetrahedron* **1996**, *30*, 10113.
(15) Böhm, V. P. W.; Herrmann, W. A. *Chem. Eur. J.* **2000**, *6*, 1017.
(16) Ley, S. V.; Baxendale, I. R.; Bream, R. N.; Jackson, P. S.; Leach, A. G.; Longbottom, D. A.; Nesi, M.; Scott, J. S.; Storer, R. I.; Taylor, S. J. *J. Chem. Soc., Perkin Trans. 1* **2000**, 3815.
(17) Kingsbury, C. L.; Mehrman, S. J.; Takacs, J. M. *Curr. Org. Chem.* **1999**, *3*, 497.
(18) Franzen, R. *Can.. J. Chem.* **2000**, *78*, 957.
(19) Darensbourg, D. J.; Stafford, N. W.; T.Katsurao, T. J. *J. Mol. Catal.,* A **1995**, *104*, L1.
(20) Super, M.; Berluche, E.; Costello, C.; Beckman, E. *Macromolecules* **1997**, *30,* 368.
(21) Sarbu, T.; Styranec, T.; Beckman, E. J. *Nature* **2000**, *405*, 165.
(22) Mang, S.; Cooper, A. I.; Colclough, M. E.; Chauhan, N.; Holmes, A. B. *Macromolecules* **2000**, *33*, 303.
(23) This supported catalyst was prepared as part of a collaboration with Mr K.. A. Knights and Dr Y. R. de Miguel (ref. 24).
(24) Stamp, L. M.; Mang, S. A.; Holmes, A. B.; Knights, K. A.; de Miguel, Y. R.; McConvey, I. F. *Chem. Commun.* **2001**, *in press*.
(25) Nicolaou, K. C.; Pfefferkorn, J. A.; Mitchell, H. J.; Roecker, A. J.; Barluenga, S.; Cao, G.-Q.; Affleck, R. L.; Lillig, J. E. *J. Am. Chem. Soc.* **2000**, *122*, 9954.

METHANOL SYNTHESIS FROM $H_2/CO/CO_2$ OVER CNTs-PROMOTED Cu-ZnO-Al_2O_3 CATALYST

Hongbin Zhang, Xin Dong, Guodong Lin, Youzhu Yuan, K. R. Tsai

Department of Chemistry & State Key Lab of Physical Chemistry for the Solid Surfaces, Xiamen University, Xiamen 361005, CHINA

Introduction

Among C_1 chemicals, methanol is the species most widely used in various chemical applications. More recently, it has been used as a clean synthetic fuel additive. Serious considerations have been given to it as an alternate fuel source [1], including as a convenient hydrogen carrier for PEM fuel cells. More active catalysts and corresponding lower-temperature processes with high syngas single-pass conversion have been the objective for many research and development efforts.

Carbon-nanotubes (CNTs) are drawing increasing attention recently[2]. This kind of new carbon material possesses a series of peculiarities, such as, its nanosize channel, the highly conductive graphite-like tube-wall, the sp^2-carbons constructed surface, as well as its excellent performance of hydrogen adsorption, which make the CNTs full of promise to be a novel catalyst carrier[3] or even promoter. In the present work, a CNTs-supported/promoted Cu-ZnO-Al_2O_3 catalyst was prepared. Its catalytic performance for CO/CO_2 hydrogenation to methanol was investigated and compared with those of the Cu-ZnO-Al_2O_3 systems supported by AC (active carbon) and γ-Al_2O_3. The results shed some light on the understanding the nature of promoter action by the CNTs and the prospect of developing highly active catalysts.

Experimental

The CNTs were synthesized by the catalytic method reported previously[4]. The prepared CNTs were multi-walled carbon nanotubes, with O.D. of 15-45 nm and I.D. of ~3 nm. The N_2-BET surface area is ~130 m^2g^{-1}. The supported catalyst, Cu-ZnO-Al_2O_3/CNTs (or AC or γ-Al_2O_3), symbolized as wt%$Cu_iZn_jAl_k$-O_X/CNTs (or /AC, γ-Al_2O_3), was prepared by impregnating a certain amount of CNTs (or AC, γ-Al_2O_3) with aqueous or ethanol solution containing a calculated amount of nitrates of Cu, Zn, and Al, followed by drying at 373 K for 6 h, and calcining at 473 K for 4 h.

The catalyst test for methanol synthesis was carried out in a continuous flow micro-reactor-GC combination system. 0.25 g of catalyst sample was used for each test. Prior to the reaction, catalyst sample was programmedly pre-reduced by 5%H_2+N_2 for 12 h. Methanol synthesis from $H_2/CO/CO_2$ over the catalysts was conducted at a stationary state with feedgas composition of $H_2/CO/CO_2/N_2$ = 62/30/5/3 (v/v) under 463-563 K and 2.0 MPa. The reactants and products were determined by an on-line GC (Model 102-GD) equipped with a TC detector and dual columns filled with 5A zeolite molecular sieve and 401-porous polymer, respectively. The former column was used for analysis of CO and N_2 (as internal standard), and the latter for CH_3OH, CO/N_2, CO_2, MF, and DMC. CO conversion was calculated by an internal standard analysis method, and space-time-yield (STY) of methanol evaluated by an external standard (i.e., working curve) method.

BET-surface area of catalyst carriers was measured by N_2 adsorption using a SORPTOMATIC-1900 (CARLO ERBA) system. H_2-TPR and H_2-TPD test of catalyst was conducted on a fixed-bed continuous flow micro-reactor or adsorption-desorption system. 20 mg of catalyst sample was used for each test. The rate of temperature increase was 10 K/min. Change of hydrogen-signal was monitored using an on-line GC with a TC detector.

Results and Discussion

Study of effect of the feedgas GHSV on the reactivity of methanol synthesis over the 40wt%$Cu_6Zn_3Al_1$-O_X/CNTs catalyst showed that, at a certain temperature (e.g. 503 K), CO conversion increased with increasing GHSV from zero to ~3000 ml (STP) h^{-1} (g-catal.)$^{-1}$, and reached a maximum at GHSV close to 3000 ml (STP) h^{-1} (g-catal.)$^{-1}$. It then started to decrease with further increasing GHSV. It was believed that, as the GHSV approached 3000 ml (STP) h^{-1} (g-catal.)$^{-1}$, the reaction of methanol formation was in the kinetics-controlled region. In the present work, all reactivity tests of methanol synthesis were performed under the reaction condition of GHSV=3000 ml (STP) h^{-1} (g-catal.)$^{-1}$.

It is well known that CO_2 in the feedgas is a participant component indispensable for continuous fast conversion of the syngas to methanol. Whereas the net-conversion of CO_2 indicated by GC analysis of the inlet and exit gases of the reactor was quite low, all assay results of the catalyst activity in the present work are shown with CO conversion and methanol STY. The reactivity of methanol synthesis over a series of wt%$Cu_iZn_jAl_k$-O_X/CNTs catalysts has been evaluated, and the results are shown in Table 1.

Table 1 Reactivity of CH_3OH Synthesis From $H_2/CO/CO_2$ Over A Series of Catalysts of wt%$Cu_iZn_jAl_k$-O_X/CNTs *

Catalyst sample	STY at initiating temperature		STY at the optimum working temp.	
	T/K	STY	T/K	STY
40%Cu_5Zn_5-O_X/CNTs	473	55.1	523	182
40%Cu_6Zn_3-O_X/CNTs	463	69.3	513	189
40%$Cu_{4.5}Zn_{4.5}Al_1$-O_X/CNTs	473	63.4	523	220
40%$Cu_5Zn_5Al_{0.5}$-O_X/CNTs	463	49.8	523	232
40%$Cu_6Zn_3Al_1$-O_X/CNTs	463	79.4	508	240
42%$Cu_6Zn_3Al_1$-O_X/CNTs	473	73.0	523	238
38%$Cu_6Zn_3Al_1$-O_X/CNTs	463	101	508	261
32%$Cu_6Zn_3Al_1$-O_X/CNTs	463	110.	508	287
24t%$Cu_6Zn_3Al_1$-O_X/CNTs	463	78.4	508	239
32%$Cu_6Zn_3Al_1$-O_X/CNTs**	463	100	513	307

*Reaction conditions: 2.0MPa, $H_2/CO/CO_2/N_2$=60/30/5/5(v/v), GHSV=3000ml(STP) h^{-1} (g-catal.)$^{-1}$; and STY at mg-CH_3OH h^{-1} (g-catal.)$^{-1}$. **Prepared from ethanol solution of the precursor.

It appears from the results shown in Table 1 that the optimum formula of catalyst composition is 32wt%$Cu_6Zn_3Al_1$-O_X/CNTs, i.e., with Cu/Zn/Al molar ratio at 6/3/1 and the corresponding loading amount of the $Cu_6Zn_3Al_1$ at 32wt%. On this catalyst, the STY of methanol reached 287 mg h^{-1} (g-catal.)$^{-1}$, which is considerably superior to catalysts of other formulae, under the reaction conditions shown in Table 1.

Fig. 1 shows the results of activity evaluation of methanol synthesis over the catalysts of Cu-ZnO-Al_2O_3 supported by CNTs, AC, and γ-Al_2O_3, respectively. On all three catalysts, CO conversion and methanol STY both first went up with increasing temperature, reached a maximum at their respective optimum operating temperature, and then went down as temperature further increased. This could be understood considering that at the lower temperatures before the maximum, the methanol synthesis reaction was controlled by kinetics, and after the maximum, the reaction turned to be limited by thermodynamics equilibrium due to the high reaction temperature.

It is experimentally found that the support can significantly affect the activity of methanol synthesis. Over the 32wt%$Cu_6Zn_3Al_1$-O_X/CNTs catalyst, the methanol synthesis exhibited considerable reactivity at operating temperature as low as 463 K, and reached the highest STY, 287 mg-CH_3OH h^{-1} (g-catal.)$^{-1}$, at 508 K, which was 1.9

and 2.5 times of those over the catalysts supported by AC and γ-Al_2O_3 (i.e., 150 and 114 mg h^{-1} (g-catal.)$^{-1}$ obtained at the respective optimum operating temperatures, 523 and 543 K).

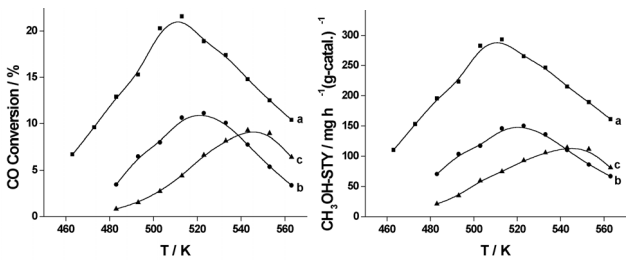

Fig.1 Activity of CH_3OH synthesis on: a) 32%$Cu_6Zn_3Al_1$-O_X/CNTs; b) 32%$Cu_6Zn_3Al_1$-O_X/AC; c) 32%$Cu_6Zn_3Al_1$-O_X/γ-Al_2O_3.

It is conceivable that the dispersion of Cu-Zn-Al components on the hydrophobic surface of CNTs constructed by sp^2-C could be improved by using proper organic solvent (e.g., ethanol), instead of water, for the preparation of the catalyst precursor solution, which would be conducive to enhancing the catalyst activity. That turned out to be the case. On the 32wt%$Cu_6Zn_3Al_1$-O_X/CNTs catalyst prepared from the corresponding ethanol solution, the highest CO conversion and methanol STY attained were 23.1% and 307 mg h^{-1} (g-catal.)$^{-1}$, ~7% higher as compared to that prepared from the corresponding aqueous solution.

Fig. 2 shows the H_2-TPR spectra of the oxidation precursors of the three catalysts. For the 32wt%$Cu_6Zn_3Al_1$-O_X/CNTs, the H_2 started to react from ~463 K, with the main H_2-TPR peak centred round 530 K. The two samples supported by AC and γ-Al_2O_3 were not reduced by H_2 until ~500 K, and each reached the reduction-peak round 578 K, which was ~48 degrees (K) higher than that of the CNTs-supported system. The observed reducibility sequence of the three samples was as follows: $Cu_6Zn_3Al_1O_X$/CNTs >> $Cu_6Zn_3Al_1O_X$/AC ≅ $Cu_6Zn_3Al_1O_X$/γ-Al_2O_3, in line with the sequence of their catalytic activity for the methanol synthesis.

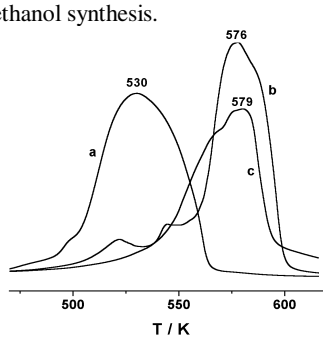

Fig. 2 H_2-TPR spectra on the catalyst precursor: a) 32%$Cu_6Zn_3Al_1$-O_X/CNTs; b) 32%$Cu_6Zn_3Al_1$-O_X/AC; c) 32%$Cu_6Zn_3Al_1$-O_X/γ-Al_2O_3.

It is quite evident that the much better performance of the CNTs-supported catalyst for methanol synthesis from $H_2/CO/CO_2$ is closely related to the peculiar structure and properties of the CNTs carrier. Fig. 3 shows TEM image of the CNTs grown catalytically from CH_4 decomposition. The results of XRD measurements revealed that their main XRD feature at 2θ= 26.1° was close to that of graphite at 2θ= 26.5°, but somewhat broadened, implying that the degree of long-range order of these nanostructures was relatively low compared to that of graphite. HRTEM observation revealed that they were constructed by superimposure of many layers of carbon with conical graphite-like platelets along a common central hollow.

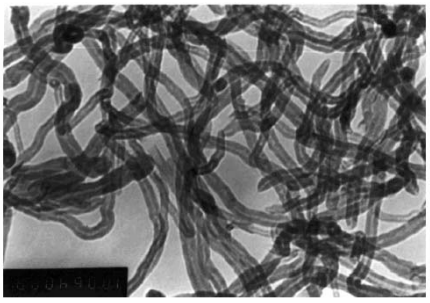

Fig. 3. TEM image of the CNTs grown catalytically from CH_4 decomposition.

From the viewpoint of chemical catalysis, in addition to its high mechanical strength, nanoscale channel, sp^2-C constructed surface, and graphite-like tube-wall, the excellent performance of the CNTs in hydrogen-adsorption/storage and electron transportability is also very attractive. Fig. 4 displays H_2-TPD spectrum of hydrogen adsorption on the CNTs. The main TPD peaks appeared at 400 K and 990 K. The lower-temperature peak was contributed from H_2-desorption, while the higher-temperature peak involved desorption of CH_4, C_2H_4, C_2H_2, and H_2. Conceivably, there would exist a considerable amount of hydrogen-adspecies on the CNTs carrier under the condition of methanol-synthesis used in the present study. This would lead to higher stationary-state concentration of hydrogen-adspecies on the surface of the functioning catalyst, and would in turn favor a series of surface hydrogenation reactions in the process of CO/CO_2 hydrogenation to methanol. On the other hand, the operation temperature of the $Cu_6Zn_3Al_1$-O_X/CNTs catalyst for methanol synthesis can be 20~30 K lower than those of the 32wt%$Cu_6Zn_3Al_1$-O_X/γ-Al_2O_3 (or /AC). That would contribute considerably to an increase in equilibrium conversion of CO and space-time-yield of CH_3OH. The results of the present study indicated that the CNTs served not only as carrier, but also as an excellent promoter, and that its peculiarity of adsorbing H_2 may play an important role in promoting the methanol synthesis activity more effectively.

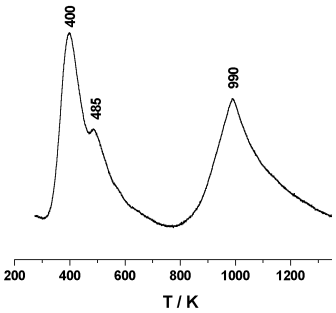

Fig. 4. TPD spectrum of hydrogen adsorbed on the CNTs material.

Acknowledgment

This work was supported by National Nat. Sci. Foundation (Project No. 50072021) and Fujian Provincial Nat. Sci. Foundation (Project No. 2001H017) of China.

References

[1] MacDougall, L. V., *Catal. Today*, **1991**, *8*, 337.
[2] De Jong, K. P.; Geus, J. W., *Catal. Rev.-Sci. Eng.* **2000**, *42*, 481.
[3] Zhang, Y.; Zhang, H.-B.; Lin, G.-D.; Chen, P.; Yuan, Y.-Z.; Tsai, K.R., *Appl. Catal. A: General,* **1999**, *187*, 213.
[4] Chen, P.; Zhang, H.-B.; Lin, G.-D.; Hong, Q.; Tsai, K. R., *Carbon,* **1997**, *35 (10-11)*, 1495.

Effect of H_2S on the Reaction of CH_4 with CO_2 over Titania Supported Noble Metal Catalysts

András Erdőhelyi, Tamás Szailer and Éva Novák

Institute of Solid Sate and Radiochemistry, University of Szeged, P.O. Box 168, H-6701 Szeged, Hungary

Introduction

Great efforts are made in the last decade in the catalytic transformation of methane and carbon dioxide, the cheapest carbon containing materials, into more valuable compounds. One of the possibilities to achieve this goal is to react CH_4 with CO_2 to produce synthesis gas. All of the Group VIII metals on a variety of supports have been studied as a dry reforming catalyst [1]. The high efficiency of supported noble metals in this reaction was confirmed by our studies [2-4]. Relatively little attention was paid to the effect of sulphur on the CO_2 + CH_4 reaction although natural gases always contain more or less amount of sulphur compounds.

The present report gives an account of the effect of H_2S on the CO_2 + CH_4 reaction in the presence of different titania supported noble metal catalysts. This reaction can be described as the sum of different reactions, for example the steam reforming and the reverse water gas shift reactions. For comparison the CO_2 hydrogenation was also studied in the presence of H_2S. Great attention was paid to the formation of surface species during the reaction and to the effect of H_2S on it.

Experimental

Materials. The catalysts were prepared by impregnating the TiO_2 support (Degussa P25) with the solution of Pt metal salts to yield a nominal 1 % metal loading. The following salts were used: H_2PtCl_6*$6H_2O$, $PdCl_2$, $RhCl_3$*$3H_2O$ and $RuCl_3$*$3H_2O$. The impregnated powders were dried at 383 K. Before any measurements the fragments of catalyst pellets were oxidized at 473 K for 30 min and reduced at 673 K in the catalytic reactor for 1 hour.

Methods. The adsorption and interaction of the reacting gas mixtures were studied by FTIR spectroscopy.

The catalytic reactions were carried out in a fixed bed continuous-flow reactor (100mm x 27 mm o.d.). The ratio of CH_4/CO_2 in the reacting gas mixture was 1:1 and that of CO_2/H_2 was 1:4. The inlet gas mixture contained 20 % of Ar or He as diluents and 22 ppm or 116 ppm of H_2S when the effect of H_2S was studied. The amount of catalysts used was usually 0.3 - 0.5 g. The flow rate of the reactants was 80 ml/min. Analyses of the gases were performed with gas chromatograph (Chrompack 9001) using Porapak QS column. The products were detected simultaneously by TCD and FID detectors. The amount and the reactivity of surface carbon formed in the catalytic reactions were determined by temperature-programmed reduction. After the catalytic run the reactor was flushed with Ar, the sample was cooled to room temperature, then the Ar flow was changed to H_2 and the sample was heated up to 1173 K with a 10 K/min heating rate and the hydrocarbons were determined.

Temperature programmed desorption experiments were carried out in a quartz reactor (8 mm o.d.) filled with 0.3 g of samples. The products were analysed by an online mass spectrometer (Balzers QMS 200).

The dispersions of the supported metals were determined by H_2-O_2 titration at 298 K using the pulse technique.

Results and Discussion

Infrared spectroscopy measurements revealed that CO is formed in the interaction of CH_4 + CO_2 and of CO_2 + H_2 far below the reaction temperature. The CO spectra obtained in the interactions were compared with those of clean CO, adsorbed on the same catalyst after the same pre-treatment. In the presence of H_2S after the adsorption of CO nearly the same features were registered, only the intensity of the absorption bands decreased. Zhang et al. also found that the presence of S does not significantly influence the geometrical structure and chemisorption energy of CO adsorbed on Rh(111) surface [5]. In the interaction or in the reaction of CH_4 + CO_2 or CO_2 + H_2 the CO band appeared at significantly higher temperature on the spectra than in the absence of H_2S, although in the case of Rh/TiO_2 the gas phase spectra of CH_4, which was the main product in the H_2 + CO_2 reaction, were detectable with the same intensities.

The reaction between CO_2 and CH_4 proceeded rapidly above 673 K on TiO_2 supported noble metals to give CO and H_2 with different ratios. The reaction occurred at the highest rate (rates per unit surface area of metals) in the first minutes of the reaction on Ru followed by Pd, Rh and Pt. This is practically the same as the sequences for CH_4 + CO_2 reaction on alumina supported noble metals [2]. The conversion of CO_2 exceeded that of CH_4 for every catalyst sample. The CO/H_2 ratio was between 2 and 3 in the first minutes of the reaction (Table 1). In the presence of H_2S the initial rate of H_2 or CO formation and the conversion of the reactants decreased in time in all cases (Fig. 1 and Table1). The deactivation rate was the highest on supported Rh catalyst, and the lowest on Ru/TiO_2.

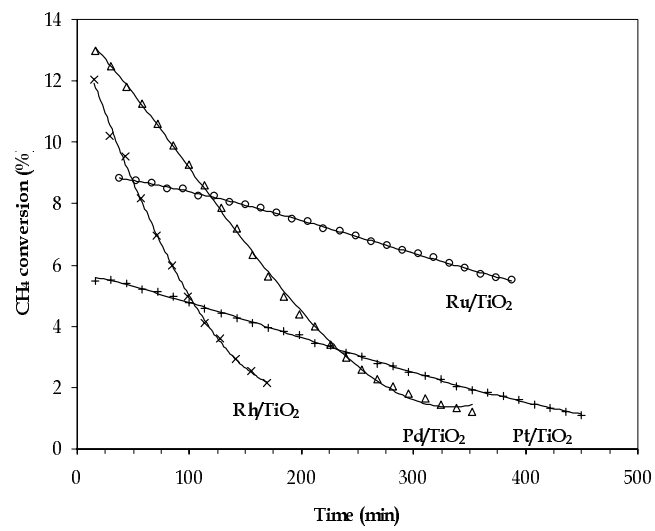

Figure 1. The conversion of methane in the CH_4 + CO_2 reaction on different TiO_2 supported catalysts at 773K in the presence of 22 ppm H_2S

The initial conversion of methane at 773 K was 12 % on Rh/TiO_2 but after 3 hours of the reaction it was only 2.1 %. On Ru/TiO_2 this value changed only from 8.8 % to 7.7 %. While the rate of products formation decreased, the CO/H_2 ratio surprisingly increased continuously in all cases (Fig. 2).

The enhancement of the CO/H_2 ratio at the beginning of the reaction was relatively low, but after a time lag it increased considerably. The length of this time depends on the metal; it was about 50 minutes on Rh/TiO_2 and more than 100 minutes on titania supported Pt catalyst. In the presence of Rh/TiO_2 after 180 minutes of the reaction the CO/H_2 ratio was more than 8 (Table 1). The most stable catalyst was Ru/TiO_2 on this sample the CO/H_2 was only 2.7 after 400 minutes.

When the H_2S concentration was increased in the reacting gas mixture (116 ppm) the conversion of CH_4 or CO_2 decreased more

rapidly. After 180 minutes the CH_4 conversion was less than the initial value by more than one order of magnitude in all cases. The CO/H_2 ratio increased as was observed earlier.

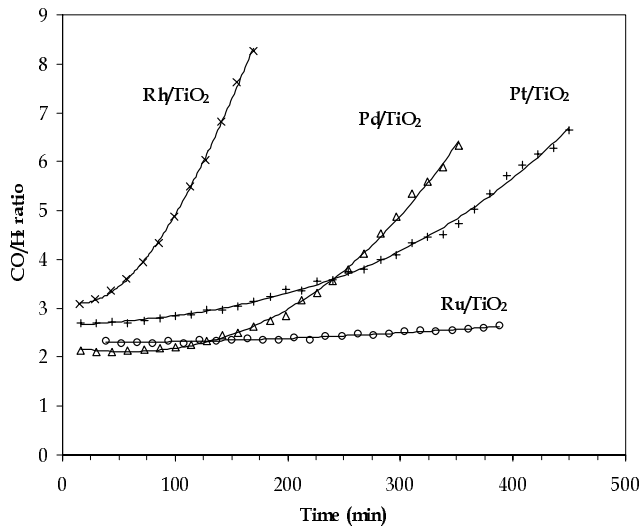

Figure 2. Changes of the CO/H_2 ratio in the $CH_4 + CO_2$ reaction on different TiO_2 supported catalysts at 773K in the presence 22 ppm of H_2S

The amount of surface carbon was determined after the catalytic reaction. In the case of Rh/TiO_2 in the presence of H_2S the amount of surface carbon was lower than the absence of it. The reactivity of this carbonaceous deposit did not change significantly. These results agree well with the observation found in the Sparg process [6] when the supported Ni catalyst was pre-sulphided to decrease the surface carbon formation.

In the absence of H_2S on TiO_2 supported samples the CH_4, CO_2 conversion and the CO/H_2 ratio did not change significantly during the reaction. On silica-supported samples in the presence of H_2S although the conversion decreased as mentioned above, the CO/H_2 ratio remained nearly the same.

Table 1. Some Characteristic Data for $CH_4 + CO_2$ Reaction on Titania Supported Noble Metal Catalysts at 773 K in the Presence of 22 ppm H_2S.

	D%	Conversion				CO/H_2	
Samples		CH_4		CO_2			
		15	360	15	360	15	360
		Minutes					
1%Ru/TiO_2	9.4	8.8	5.5	14.9	10.8	2.32	2.65
1%Rh/TiO_2	41	12.0	2.1*	17.9	4.9*	3.0	8.2*
1%Pd/TiO_2	16	12.9	1.2	20.8	2.2	2.1	6.3
1%Pt/TiO_2	38	5.5	1.7	10.4	4.2	2.7	5.0

* Data were obtained in the 180 minutes of the reaction

We found that CO_2 conversion was higher than that of methane in all cases and that the CO/H_2 ratio increased in time in the presence of H_2S. These observations indicated that the reaction

$$CH_4 + CO_2 = 2\ CO + 2\ H_2$$

was followed by several secondary processes, including the hydrogenation of CO and CO_2, the water gas shift reaction and the Boudouard reaction.

CO_2 hydrogenation was studied in the presence of 22 ppm H_2S at 548 K. The main product of the reaction was methane on Ru and Rh catalysts; its selectivity was near 100 %. On Pt and Pd samples mainly CO was formed. The methane selectivity was about 20% at the beginning of the reaction. These results agree well with our earlier results [7-9] obtained on different supported noble metal catalysts. In spite of the 22 ppm H_2S concentration of the reacting gas mixture the rate of product formation or the CO_2 conversion changed only slightly in all cases. The highest decrease was in the case of Pd catalyst when the initial conversion decreased from 10.0 % to 6.54 % during 6 hour of the reaction. It has to be mentioned that during the same time in the $CO_2 + CH_4$ reaction the CO_2 conversion decreased from 20.8 to 2.9%. When the reaction was studied at 773 K at the same temperature, where the $CO_2 + CH_4$ reaction was followed the same results were obtained. In this case the contact time was lower, so the conversion was in the same range.

These observations suggest that H_2S poisons the $CO_2 + CH_4$ reaction, while the $CO_2 + H_2$ reaction was only effected slightly by the same amount of H_2S. This finding results the changes of the CO/H_2 ratio. The rate of hydrogen formation in the $CO_2 + CH_4$ reaction decreased while the consumption rate of it in a secondary reaction remained the same. In some cases CO is also formed in this process so the CO/H_2 ratio has to increase during the $CO_2 + CH_4$ reaction.

On SiO_2 supported samples in the $CO_2 + CH_4$ reaction the CO/H_2 ratio does not change significantly, so the effect observed on TiO_2 supported metals depends on the support.

The interaction of H_2S with the titania supported metals was studied by temperature programmed desorption method. The adsorption was performed on the reduced samples by exposure to Ar flow containing 110 ppm of H_2S for 30 min at 373 K. Afterwards the reactor was flushed with Ar for 10 min, cooled down to room temperature and the sample was heated at a rate of 20 K/min up to 1073 K. The products were analysed by an online mass spectrometer. After H_2S adsorption on titania supported noble metals only SO_2 desorption was detected in two stages nearly at the same temperatures. H_2S evolution was not observed. Fig. 3 shows the TPD curve in the case of Pd/TiO_2 sample.

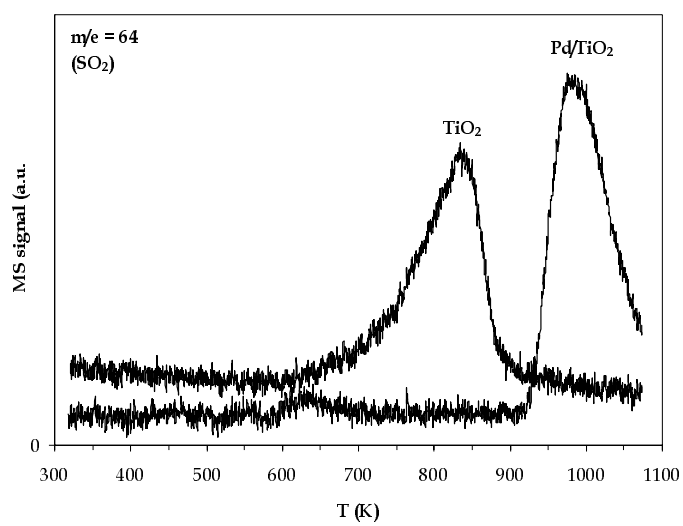

Figure 3. Temperature programmed desorption spectra of adsorbed H_2S at 373 K

A small peak was detected above 580 K (T_{Max}=631 K), but at higher temperature, above 920 K, great amount of SO_2 desorption was observed (T_{max}= 988 K). For comparison the TPD of adsorbed H_2S on clean TiO_2 is also presented on Fig. 3. In this case, too, only SO_2 was desorbed, but in one stage in the temperature range 630 – 910 K (T_{Max}= 840 K). Beck and White [10] and Chen et al. [11] found nearly the same picture on clean TiO_2.

These results clearly show that the most part of the adsorbed H_2S desorbed from the TiO_2 and from the TiO_2 supported noble metals as SO_2. From these results we may suppose that sulphur was built into the oxygen vacancies of the TiO_2 [11] and created new catalytic centres on the metal-support interface. These sites have different catalytic activities in the secondary reactions of the dry reforming of methane and this is the reason why the CO/H_2 ratio increased in the reaction in the presence of H_2S.

Acknowledgement.

Financial support of this work by OTKA (contract number T 034270) is gratefully acknowledged

References

(1) Bradford, M.C.J., Vannice, M.A., *Catal. Rev.* **1999,** *41*, 1.
(2) Solymosi, F., Kutsán, Gy., Erdőhelyi, A., *Catal. Letters* **1991,** *11,* 149.
(3) Erdőhelyi, A., Cserényi, J., Solymosi, F., *J. Catal.* **1993,** *141,* 287.
(4) Erdőhelyi, A., Cserényi, J., Papp, E., Solymosi, F., *Appl. Catal. A General* **1994,** *108,* 205.
(5) Zhang, C.J., Hu, P., Lee, M.-H., *Surface Sci.* **1999,** *432,* 305.
(6) Dibbern, H.C., Olesen, P., Rostrup-Nilsen, J.R., Toettrup, P.B., *Hydrocarbon Proc.* **1986,** *65,* 71.
(7) Solymosi F., Erdőhelyi, A., *J. Mol. Catal.***1980,** *8,* 471.
(8) Solymosi F., Erdőhelyi, A., Bánsági, T., *J. Catal.* **1981,** *68,* 371.
(9) Erdőhelyi, A., Pásztor, M., Solymosi, F., *J Catal.* **1986,** *98,* 166.
(10) Beck, D.D., White, J.M., *J. Phys. Chem.* **1986,** *90,* 3123.
(11) Chen, Y., Jiang, Y., Li, W., Jin, R., Tang, S., Hu, W., *Catal. Today,* **1999,** *50,*39.

A NEW ROUTE FOR CARBON DIXODE CYCLOADDITION TO PROPYLENE CARBONATE

*Wei Wei Wei Tong Yuhan Sun**

State Key Laboratory of Coal Conversion, Institute of Coal Chemistry Chinese Academy of Sciences, Taiyuan, 030001, China

Introduction: The formation of five-cyclic carbonate (such as propylene carbonate) via cycloaddition between CO_2 and epoxides is not only one of the routes for CO_2 chemical fixation [1], but also the cycloaddition of propylene oxide (PO) with CO_2 is the first step for synthesis of dimethyl carbonate (DMC) via transterification[2]. Furthermore, propylene carbonate (PC) itself was a nontoxic and versatile intermediates in environmentally begin organic synthesis. Hence, the green synthesis route of propylene carbonate has being expected in the half century.

Nemirovsky firstly reported the synthesis of alkyl carbonate by phosgenation method in a century ago[3], but the method has gradually given up for using toxic and hazardous phosgene. After 1960s many methods have been published by patents, particularly, much attention has been paid attention to the cycloaddition between PO and CO_2, and the main catalytic systems included organometallic halides-Lewis base[4], organotin halde-tetraalkyphosphonium halide [5], alkali metal halide-crown ether[6] or polyethylene glycol-400[7]. But the catalytic performance and the severely reaction conditions limited their further utilization. In addition, a variety of solvents or promoters must be used, resulting in high separating cost or low purity of PC. Moreover, the reaction was carried out in a intermission autoclave, and leading to low production capacity. Thus, a new heterogeneous catalysts with high catalytic performance at moderate conditions (i.e. KI supported on different supports was firstly studied. In order to further improve the lifetime of the catalysts and productivity capability and avoid the hot spot of the catalysts, a new continual structural reactor was investigated. Combing the new heterogeneous catalysts and the new continual structural reactor, a new method for cycloaddition between PO and CO_2 in the heterogeneous process was developed in the present work.

Experimental: The purity of CO_2 was higher than 99.5%. Commercially available PO was used without further purification. Catalysts were prepared by impregnating the supports with an aqueous solution of KI, and then dried at 60℃ for 10 h.

The catalysts were firstly evaluated in conventional intermission autoclave. For the cycloaddition between CO_2 and PO was intense exothermal reaction (≈30kcal/mol), this led to the difficult operation in heterogeneous catalytic process and the higher local temperature and the limitation of the lifetime of catalyst. Thus, a new structural reactor was designed. In this reactor the lifetime of the catalysts were further studied.

Results and discussion: In the heterogeneous process, KI supported on different supports was investigated (see Table 1). Firstly, the reaction conditions (reaction temperature,120℃, pressure, 4.0MPa) were very moderate, particularly, the pressure was lower than the saturate pressure of carbon dioxide at room temperature. Secondly, both PO conversion and PC selectivity were nearly 100% although neither solvents nor promoters in this catalytic synthsis were used. Thus, the product must not be separated and simplified the production of PC. In addition, the space hour yield of PC was much higher than the conventional heterogeneous process (< 5g/(g(cat.) hr)), in particular, for KI supported activated carbon the space hour yield could reach to 12.0.

Table.1 Effect of several supports on catalytic activity of cycloaddition

Catalysts	PO Conv(%)	PC yield(%)	Space hour yield (kg/(kg(cat.) hr
KI/γ-Al_2O_3 [a]	100.0	99.0	7.0
KI/acativated carbon[a]	100.0	99.3	12.0
KI/SiO_2[a]	100.0	99.0	7.4

a-temperature, 120℃, pressure, 4.0MPa

In 1L conventional intermission autoclave, both the conversion of PO and the selectivity of PC were shown in Fig. 1 in 100 hours. The catalytic performance sharply decreased in 100 hours. The BET surface area of fresh catalyst and after reaction catalyst was showed in table 2. Obviously, the fouling of the catalyst pore was very severe in reaction process in the conventional intermission autoclave. In addition, we also found that the product color was wine. This indicated that KI in the catalysts was partly oxidized in reaction process because reaction heat could not removed and existed local hot spot.

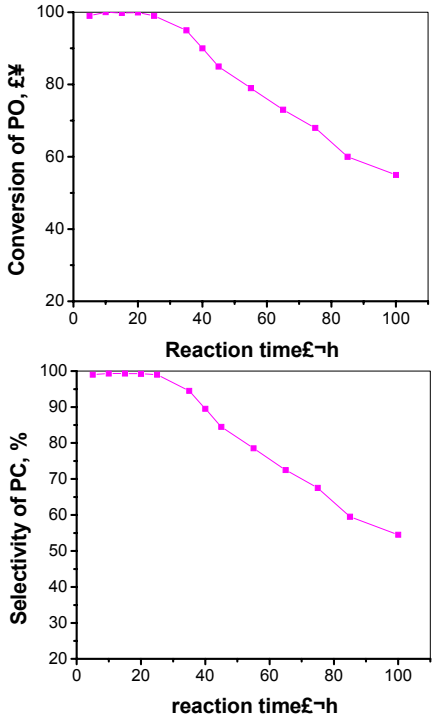

Fig. 1 Both the conversion of PO and the selectivity of PC in 1 L conventional intermission(autoclave in 100 hours)

Table 2 The characters of the fresh catalyst and after the reaction

catalyst	BET surface	m^2/g pore size[a], A	pore vol., cc/g
fresh catalyst	394.3	22.2	0.22
after reaction	40.7	56.8	0.06

a-average pore diameter

* To whom correspondence should be addressed: weiwei@sxicc.ac.cn or yhsun@sxicc.ac.cn

In order to further improve the lifetime of the catalysts and productivity capability and avoid the hot spot of the catalysts, a new continual structural reactor was designed[8]. The advantages of the continual structural reactor included: (1) In this reactor the PC could be immediately removed from the surface of the catalysts as soon as it was produced, and avoided the deposition of the catalyst pore; (2) The catalysts were particularly loaded in this reactor and the reaction heat could be efficiently removed. Thus, the lifetime of catalyst could be improved; (3) The reaction was continual in this reactor, and improved its production capacity. Figure 2 demonstrated that in the new continual structural reactor both the PO conversion and PC selectivity hardly decreased in 400h. And the product was not color.

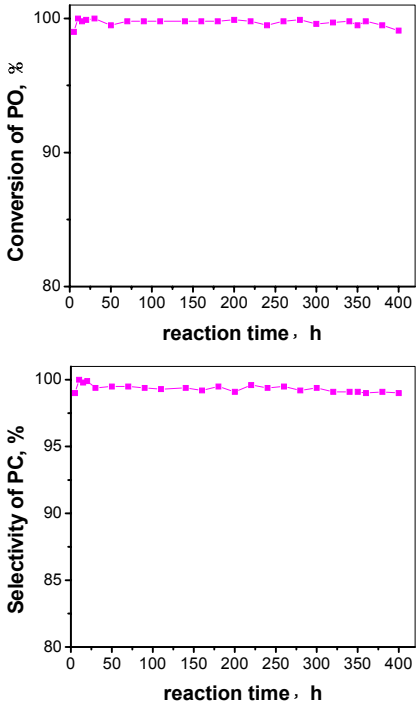

Fig. 2 Both the conversion of PO and the selectivity of PC in 20 L new continual structural(reactor in 400 hours)

Conclusion: For the new heterogeneous catalysts, both PO conversion and PC selectivity, especially, KI/A.C. catalyst, were nearly 100% at moderate conditions; the STY of PC was also very high. In the 1L intermission autoclave the fouling of the catalyst pore led to the deactivation of the catalysts, and the reaction heat could not be removed. Both the PO conversion and PC selectivity hardly decreased in 400h in the new continual structural reactor. In general, the new method provided an economically advantageous process for the production of propylene carbonate under milder reaction temperature and pressure condition in high yield.

Reference:

[1] R. Nomura, M. Kimura, S, Teshima, etc., *Bull. Chem. Soc. Jpn.,* 1982. 55. 3200.

[2] A. Baba, T. Nozaki, T.Miki, *Bull. Chem. Soc. Jpn.,* 1987. 60. 1552.

[3] I. Nemirovsky, J. Prakt Chem., 1883. 28. 439.

[4] R. Nomura, M. Kimura, S, Teshima, etc., *Bull. Chem. Soc. Jpn.,* 1982. 55. 3200.

[5] A. Baba, T. Nozaki, T.Miki, *Bull. Chem. Soc. Jpn.,* 1987. 60. 1552.

[6] G.Rokicji and W. Kuran, *Bull. Chem. Soc. Jpn.,* 1984. 57. 1662.

[7] Z.Z.Tang, Y.Chen, Z.J.Qu, etc, *J. Peterochem Technol.* (China), 1996. 25. 409.

[8] Yuhan Sun, Xiaoping Chen, Wei Wei, China patent: 01108814.1.

SUPPORTED Pd CATALYSTS FOR HIGH-TEMPERATURE METHANE COMBUSTION – EXAMINING THE COMBUSTION SYNTHESIS PREPARATION METHOD

M.A. Fraga, M.C. Greca, L.G. Appel

Instituto Nacional de Tecnologia – Laboratório de Catálise, Av. Venezuela, 82/sala509, CEP 20081-310 – Centro, Rio de Janeiro/RJ, Brazil – appel@uol.com.br

Introduction

Catalytic combustion of hydrocarbons, especially methane, has been widely investigated as an alternative technology for power generation (1). This process is also environmentally attractive as it produces less carbon dioxide, a greenhouse gas, per unit of power generated when compared to the combustion of other hydrocarbons. Furthermore, low amounts of NO_x emissions are formed as the combustion proceeds bellow 1400 ºC (2). However, as far as the use of gas turbines is involved in the process, temperatures as high as 1200 ºC can still be achieved and, therefore, the use of thermostable catalysts is compulsory.

Ceramic oxides obtained by a high temperature process arises as feasible materials to be used as catalysts supports. Indeed, the preparation of simple ceramic oxides via a route known as combustion synthesis has been gaining reputation as a straightforward process to produce homogeneous, very fine and crystalline powders (3,4). The synthesis explores an exothermic, generally very fast and self-sustaining chemical reaction between the desired metal salts and a suitable organic fuel, which is ignited at a temperature much lower than the actual phase formation one. The major drawback of such a route is that it leads to low surface area materials.

This work focuses on the preparation of Pd-based catalysts used on the methane combustion whose supports were obtained by combustion synthesis. Alumina was taken as the reference support and the effects brought about by the addition of different lanthanides, namely La and Ce, in the support texture and the catalytic activity are reported.

Experimental

In the combustion synthesis the appropriate amounts of the cations precursors (nitrates) and an organic fuel (urea) dissolved in water were heated in a wide-mouth vitreous silica basin up to boiling and self-ignition. The basin was then transferred to a muffle furnace preheated at 600 ºC and kept for 30 min producing a fragile foam that easily crumbles into powder. The reactant proportions were calculated in order to obtain oxides with 4 and 12%wt. La or Ce. Different cerium precursors were used in order to evaluate the cerium oxidation influence, namely $Ce(NO_3)_3$ and $(NH_4)_2Ce(NO_3)_6$. These samples are denoted according to their chemical composition, lanthanide loading and cerium oxidation number, e.g Al12Ce3 (alumina-ceria mixed oxide containing 12 %wt. Ce prepared from cerium nitrate III). Pure Al_2O_3, La_2O_3 and CeO_2 were also synthesized to be taken as reference.

The catalysts were prepared by contacting the supports and an aqueous solution of $Pd(NO_3)_2$ in a rotary evaporator for 8 h. The solvent was then slowly evaporated under vacuum at 80 ºC; the powder obtained was dried overnight at 110 ºC and lastly calcined at 500 ºC for 4 h in air. These samples will be referred in the same way as their parent supports preceded by Pd, e.g. PdAl12Ce3.

X-ray diffraction (XRD) analyses were also carried out just after the powders synthesis in order to identify the oxides phases. The diffractograms were collected in a Rigaku Denki, CuK_α/Ni, 2º/min from 15 to 75º/2θ. Specific surface area was determined by the BET method using nitrogen adsorption in a Micromeritics ASAP 2000 equipment.

UV-Vis diffuse reflectance (DRS) spectra in the range of 200 – 800 nm were recorded in a Varian Cary 5 spectrometer using a Harrick diffuse reflectance accessory. Spectra of the catalysts were obtained using pure alumina as a reference. In order to support the species identification, spectra of CeO_2, La_2O_3 and $LaAlO_3$ samples prepared by combustion synthesis were also recorded. Such spectra were collected from a 2% mixture in alumina to overcome specular reflectance.

Catalytic tests were performed at atmospheric pressure in a conventional system with fixed bed reactor, monitored by on-line chromatography. A gas mixture containing 2.5% methane and 10% oxygen (N_2 to balance) was fed at 100 ml/min on the catalyst bed (100 mg). Prior to reaction, the catalysts were reduced in situ at 300 ºC for 2 h. The activity data were collected just after the catalysts have achieved the steady-state at 500 ºC

Results and Discussion

The synthesized supports were first characterized by XRD. The lanthanides-containing supports diffractograms presented the same pattern as in α-Al_2O_3 although their peaks were less intense. On the lanthanum-based support (Al12La) the disturbance detected by XRD was even more pronounced as no α-Al_2O_3 could be detected. No phase related to Ce or La compounds were identified.

The UV-Vis spectra of La-containing samples presented two peaks at 210 and 300 nm. These absorbance bands are placed between those related to La_2O_3 and $LaAlO_3$ not allowing a faithful distinction between such compounds. The existence of both species, therefore, can not be ruled out.

The spectra of Ce-based supports were identical irrespective the loading or precursor used. The spectra exhibited basically two peaks centered at 240 and 300 nm, which can be associated with CeO_2. The absorbance at higher wavenumber is commonly attributed to three dimensional array of cerium and oxygen atoms while the peak at 240 nm is related to the presence of small crystallites (5). Therefore, it can be concluded that the cerium oxide crystallites on the prepared supports are rather small, which is consistent with the XRD results that were not able to detect the CeO_2 phase.

Table 1 collects the BET surface area data of both supports and catalysts as well as the crystallite average size calculated with the Scherrer equation (2θ = 43.4º). As previously referred, low surface area powder are typically obtained through combustion synthesis method. The values determined by alumina is quite consistent with those reported in the literature (3,4). It can be easily seen that textural changes were induced by adding low contents of lanthanides in the formulation as a dramatic surface area increase was detected. Such disturbance appears to be more significant when $(NH_4)_2Ce(NO_3)_6$ is used as cerium precursor. The results might suggest that the presence of small CeO_2 crystallites disturbs the crystallization process leading to a decrease in the alumina crystallite size and consequently improving the surface area. On the other hand, high Ce loading does not interfere the samples textural features, which might be related to the formation of CeO_2 agglomerates allowing phase segregation. As for La-based sample, a completely different behavior was observed; even at high loading the surface area was improved. As no alumina reflections were recorded by XRD it is reasonable to assume the formation of a mixed compound, $LaAlO_3$. Indeed, the formation of such aluminate has been reported in the literature under similar conditions (6).

Table 1. Surface Area and α-Al_2O_3 Crystallite Size

Sample	S_{BET} (m^2/g) Supports	Catalysts	d (nm)
Al	3	3	36
Al4La	23	22	25
Al4Ce3	14	12	28
Al4Ce4	28	24	27
Al12La	20	18	-
Al12Ce3	5	5	37
Al12Ce4	7	6	42

Catalytic activity data for methane combustion are collected in Table 2. It was characterized by the temperatures at which methane conversion achieved 5 and 10% and is given as T_5 and T_{10} respectively. It should be stressed that carbon dioxide and water were the only reaction products detected.

It can be seen that the catalytic activity markedly depend on the nature of the support. Pd/Al_2O_3 catalyst presents low activity which could be related to the specific features of such system, especially the rather low surface area, as mentioned above. Alongside the enhancement in the support texture, the addition of lanthanides appears to improve the catalyst performance especially when low contents is used. Ce revealed to be a better promoter than La irrespective its content. These results are in close agreement with the literature regarding the promoting effects of CeO_2 in noble metal-based combustion catalysts (7).

The catalytic activity of the La-based systems are dependent on the lanthanide concentration, being favored at low La loading. As a matter of fact, the difference in the temperature to reach methane conversion of 5% is quite significant, practically 30 ºC.

Similar DRS spectra obtained for both samples suggested the presence of the same La species, which would be naturally associated with $LaAlO_3$ based on the XRD results. Nevertheless, the catalytic performance do not support such assignment. The activity data evidences a different La species distribution. At low concentration (PdAl4La) the promoting effect on the methane combustion may arise from the La-doped alumina support. On the other hand, the poor performance registered over PdAl12La might be ascribed to the nature of the support, that is, the intrinsic activity of the $LaAlO_3$-supported catalyst.

Table 2. Methane Combustion over Pd Catalysts Prepared by Combustion Synthesis Method

Catalyst	Catalytic Activity T_5 (ºC)	T_{10} (ºC)
PdAl	483	-
PdAl4La	441	473
PdAl4Ce3	415	447
PdAl4Ce4	429	460
PdAl12La	470	-
PdAl12Ce3	441	473
PdAl12Ce4	440	472

The different performance observed amongst the catalysts with low and high Ce content could be explained by the different distribution of CeO_2 crystallites on the alumina support as previously suggested. High concentration seems to lead to a CeO_2 and Al_2O_3 phase segregation which would allow the existence of different sites, namely Pd/Al_2O_3 and Pd/CeO_2. It is reasonable, thus, that the catalytic activity diminishes due to the intrinsic behavior of Al_2O_3-supported catalyst. As the segregation occurs as a consequence of lanthanide loading, it may be expected that whatever the cerium precursor used, the prepared catalyst will present the same behavior. The results obtained over PdAl12Ce3 and PdAl12Ce4 indeed follow such a trend.

As for PdAl4Ce samples, a model of small CeO_2 crystallites uniformly spread on alumina could be accepted. Such a model is in line with the support textural modifications previously observed (Table 1). Nevertheless, differently from what is seen over PdAl12Ce3 sample, the catalytic performance is fairly distinct between samples with low Ce concentration prepared from different salt precursors (PdAl4Ce3 and PdAl4Ce4). Indeed it has been reported that the formation of CeO_2 aggregate crystallites on alumina surface is connected with the salt precursor (8). CeO_2 obtained from cerium (IV) ammonium nitrate allows the formation of small aggregate crystallites at concentrations as low as 1.7 %wt. Hence, taking into account the difference in CeO_2 dispersion, its promoting effects is softened on PdAl4Ce4 catalyst.

Conclusions

The texture of oxides prepared by combustion synthesis can be effectively enhanced by adding low contents of lanthanides, especially Ce. La does not seem to be a very suitable additive as it reacts with alumina forming $LaAlO_3$.

Low loading of cerium oxide well dispersed on alumina revealed to be the most effective promoter for the methane combustion.

Acknowledgement. The authors are indebted to Mr. F. Cano and IME for carrying out the BET measurements. The financial support from CTPETRO/FINEP is gratefully acknowledged.

References

(1) Groppi, G.; Cristiani, C.; Lietti, L.; Ramella, C.; Valentini, M.; Forzatti, P.; *Catal. Today,* **1999***, 50*, 399.
(2) Garten, R.L.; Dalla Betta, R.A.; Schlatter, J.C. In *Handbook of Heterogeneous Catalysis*; Ertl, G.; Knözinger, H.; Weitkamp, J.; Ed.; Wiley-VCH: New York, 1997; pp. 1668-1677.
(3) Greca, M.C.; Moraes, C.; Morelli, M.R.; Segadães, A.M.; *Appl. Catal. A*, **1999**, *179*, 87.
(4) Greca, M.C.; Moraes, C.; Segadães, A.M.; *Appl. Catal. A,* **2001**, *216*, 267.
(5) Bensalem, A.; Muller, J.C.; Bozon-Verduraz, F.; *J. Chem. Soc. Faraday Trans*., **1992**, *88*, 153.
(6) Kingsley, J.J.; Patil, K.C.; *Mater. Lett*., **1988**, *6*, 427.
(7) Trovarelli, A.; *Catal. Ver.-Sci. Eng.*, **1996**, *38*, 439.
(8) Appel, L.G.; Frydman, A.; Perez, C.A.C.; Eon, J.G.; Castner, D.G.; Campbell, C.T.; Schmal, M.; *Phys. Stat. Sol. B*, **1995**, *192*, 477.

CO_2 hydrogenation over copper-based hybrid catalysts for the synthesis of oxygenates

*Young-Kwon Park, Se-Won Baek and Son-Ki Ihm**

National Research Laboratory for Environmental Catalysis,
Dept. of Chem. Eng., Korea Advanced Institute of
Science and Technology
373-1 Kusong-dong, Yusong-gu, Taejon 305-701, Korea
Tel : +82-42-869-3915, FAX : +82-42-869-5955
e-mail : skihm@mail.kaist.ac.kr

1. Introduction

Catalytic hydrogenation of CO_2 has been recently attracting considerable attention as one of the chemical fixation and recycling technologies for emitted CO_2. DME is a useful building block for making important chemicals, including dimethyl sulfate and high-valued oxygenated compounds. DME can easily be obtained through dehydration of methanol over solid acids[1], while methanol is commercially manufactured from syngas by using Cu-based catalysts. In this regard many investigations have been made on the combination of the methanol synthesis and methanol conversion process in a single step by using hybrid catalysts to obtain hydrocarbons or oxygenates directly either from syn-gas or from CO_2[2-5]. However, methanol synthesis from CO_2 hydrogenation has a severe limitation of thermodynamic equilibrium compared with that from CO hydrogenation. To overcome such a limitation, *in situ* transformation of methanol to dimethyl ether(DME) is a reasonable way to improve the total oxygenates yield (methanol + DME). However, very few studies were made on the direct synthesis of DME from CO_2 hydrogenation, while Dubois et al.[2] demonstrated that combination of Cu-based catalyst with a solid acid, which enhanced the DME formation, really provided a strong driving force for CO_2 conversion In the present work, hybrid catalysts made of Cu-based methanol synthesis catalyst and a zeolite were used for the direct formation of oxygenates(methanol + DME) from CO_2 hydrogenation, and the catalytic behaviors were investigated in terms of their reducibility and oxygen coverage.

2. Experimental

Catalyst preparation Cu/ZnO based catalysts were prepared by co-precipitation. ZSM-5 was obtained through a three day hydrothermal synthesis at 170°C in a Teflon-lined 450ml Parr bomb by following the procedures in a US patent [3]. H-Ga-Silicate were synthesized according to the procedure similar to that of HZSM-5 except that Al source was substituted with Ga nitrate. SAPO-34 was hydrothermally prepared from reactive gels containing a silicon source (Ludox HS-30), an aluminum source (pseudoboehmite), phosphoric acid, morpholine and water [4]. Hybrid catalysts were prepared by physically mixing equal weight of a copper based catalyst and a zeolite.

Catalyst characterization The exposed copper surface area was measured by titration with nitrous oxide. The copper surface area (Cu_{react}) of used catalyst after 1hr of reaction was measured first, and the total copper surface area (Cu_{total}) was obtained from the same catalyst after complete reduction of copper. The oxygen coverage was calculated by the following equation [5] : $\bullet_O = (Cu_{total}-Cu_{react})/(Cu_{total} \times 2)$.

Temperature programmed reduction (TPR) was performed to determine the reduction temperature peak of catalyst. And Temperature programmed desorption(TPD) measurements by using ammonia as an adsorbate were carried out to determine the acidic properties of zeolites.

Catalytic activity for the synthesis of DME Carbon dioxide hydrogenation was performed in a continuous-flow fixed bed microreactor system made of a stainless-steel tube. In a typical experiment, 1.0g of hybrid catalyst was loaded in the reactor. It should be noted that the amount of Cu-based catalyst in the hybrid catalyst was 0.5g. After the catalyst bed was reduced with hydrogen at 280 °C, the reactor was pressurized to 28atm with helium, and CO_2 and H_2 were introduced into the reactor. CO_2 hydrogenation products were passed throughh a heated transfer line to a gas chromatograph with TCD and FID detectors.

3. Results and Discussion

In our previous work, it was found that $Cu/ZnO/ZrO_2$ and $Cu/ZnO/Ga_2O_3$ showed higher methanol yields. It was previously reported [5, 6] that ZrO_2 improved the dispersion of Cu, and that Ga_2O_3 increased the specific activity by optimizing the ratio of Cu^{1+}/Cu^0 on the surface of Cu particles. Since it is believed that Cu^{1+} species plays an important role in methanol synthesis [5], the optimization of the ratio Cu^{1+}/Cu^0 should be made for high yield of methanol. Table 1 shows the results of oxygenates synthesis from CO_2 hydrogenation over different hybrid catalysts. It can be seen that the catalysts including different zeolites had different catalytic activities. The activity of hybrid catalyst with NaZSM-5 was the lowest among hybrid catalysts due to its weakest acidity. To convert methanol into DME, moderate acidity rather than weak acidity is preferable. The hybrid catalyst from $Cu/ZnO/ZrO_2$ and H-Ga-silicate showed the highest yield of oxygenates. Even if $Cu/ZnO/Ga_2O_3$ showed a good activity for methanol synthesis, its hybrid counterpart showed a lower activity for oxygenates and a higher selectivity for CO. The temperature at which the maximum of TPR curve is located (defined as peak temperature) could be a measure of reducibility or the degree of interaction, and the peak temperatures are listed in Table 2. It can be seen that the peak temperature of the original methanol synthesis catalysts changed through hybridization with zeolite. Some interactions between methanol synthesis catalyst and zeolite might modify the properties of each component in the hybrid catalyst such as the reducibility of methanol synthesis catalyst and the acidity of zeolite. The peak temperatures of hybrid catalysts were found to be higher than that of the original methanol synthesis catalysts such as $Cu/ZnO/ZrO_2$ or $Cu/ZnO/Ga_2O_3$. The increase in the peak temperature for the hybrid catalyst containing $Cu/ZnO/ZrO_2$ was rather small (about 20°C), while that for the hybrid catalyst with $Cu/ZnO/Ga_2O_3$ was quite large (about 60°C). This difference in the peak temperature seems to be related with the ability of oxygenate synthesis. Saito et al. [5] suggested that oxygen coverage is a measure of Cu^{1+}/Cu^0 ratio and that the specific activity increased linearly with

Table 1. Comparison of different types of hybrid catalysts for oxygenates synthesis

Catalyst	Conv. (%)	Selectivities (wt%)			Yield of Oxygenates (wt%)
		CO	MeOH	DME	
A + NaZSM-5	15.4	50.6	19.5	29.9	7.6
A + HZSM-5	17.2	42.4	22.7	34.9	9.9
A + H-Ga-silicate	19.0	33.7	21.0	45.3	12.6
A + SAPO-34	17.5	44.0	21.1	34.9	9.8
B + NaZSM-5	18.2	73.0	10.5	16.5	4.9
B + HZSM-5	19.1	68.6	12.0	19.4	6.0
B + H-Ga-silicate	19.4	67.2	12.9	19.9	6.4
B + SAPO-34	19.6	67.9	12.7	19.4	6.3

Reaction conditions : 28 atm, 250°C, W/F = 20g-cat•hr/mol, H_2/CO_2 = 3
A : $Cu/ZnO/ZrO_2$(6:3:1), B : $Cu/ZnO/Ga_2O_3$(6:3:1)

Table 2. TPR peak temperatures and oxygen coverages

Catalyst	A	A + NaZSM-5	A + HZSM-5	A + H-Ga-silicate	A + SAPO-34
Peak temp. (°C)	280 (•0)	300 (•20)	300 (•20)	289 (•9)	300 (•20)
Oxygen coverage	0.21	0.24	0.24	0.19	0.24
Catalyst	B	B + NaZSM-5	B + HZSM-5	B + H-Ga-silicate	B + SAPO-34
Peak temp. (°C)	250 (•0)	310 (•60)	310 (•60)	310 (•60)	310 (•60)
Oxygen coverage	0.15	0.30	0.30	0.30	0.30

A : $Cu/ZnO/ZrO_2$(6:3:1), B : $Cu/ZnO/Ga_2O_3$(6:3:1)

the coverage below 0.16, reached a maximum at 0.17 and then decreased above 0.18. As shown in Figure 1, the oxygen coverage of hybrid catalysts with $Cu/ZnO/Ga_2O_3$ (data point 7,8,9 and 10) were much larger than that of original $Cu/ZnO/Ga_2O_3$ i.e., (0.15) and their oxygenate yields were smaller. If the optimum oxygen coverage is 0.15, the higher oxygen coverage of hybrid catalysts with $Cu/ZnO/Ga_2O_3$ may indicate that the hybridization made copper components less active and resulted in poor yield of oxygenates. Among hybrid catalysts with $Cu/ZnO/ZrO_2$, the hybrid catalyst containing H-Ga-silicate (data point 4) showed the highest yield of oxygenates probably due to weak interaction. Its oxygen coverage (0.19) was also not much different from that(0.15) of $Cu/ZnO/Ga_2O_3$. The Ga oxide inside the pore of H-Ga-silicate seems to make Cu species in the hybrid catalyst more active by balancing the ratio Cu^{1+}/Cu^0. Table 3 shows that the increase of calcination temperature resulted in higher yield of oxygenates because the larger amount of Ga oxide, formed inside the pore, optimized the oxygen coverage. It is preferable to use H-Ga-silicate as a Ga source rather than $Cu/ZnO/Ga_2O_3$ to regulate the Cu ion state for a higher production of oxygenates. Another kind of interaction, i.e., acidity modification, seems to be more beneficial for hydrocarbon synthesis, while not good for oxygenates synthesis. The hybrid catalyst with SAPO-34 or HZSM-5 which had higher acid amount due to solid-solid interaction showed a poor yield of oxygenates but a higher yield of hydrocarbons than that with H-Ga-silicate [7]. It is believed that the reducibility should affect the synthesis of oxygenates and that the acidity should influence the hydrocarbon synthesis. The moderate acidity of H-Ga-silicate seems to be sufficient for oxygenate synthesis. Figure 2 shows the effect of mixing ratio on the yield of oxygenates over the hybrid catalyst from $Cu/ZnO/ZrO_2$ and H-Ga-silicate. It can be seen that the hybrid catalysts with low fraction of zeolite showed better yield for oxygenates. It was reported that for DME synthesis the rate limiting step is methanol formation [8], and accordingly it is desirable to increase the weight fraction of methanol synthesis catalyst. Relatively small amount of acid sites were sufficient to convert methanol into DME because the rate of dehydration due to H-Ga-silicate is much faster. Campbell et al. [9] showed that only a small active site concentration was necessary for HZSM-5 to be an efficient and effective methanol conversion catalyst.

Table 3. Effect of calcination temperature of H-Ga-silicate on oxygenates yield

Calcination temperature(°C)	550	600	650
Oxygenates yield* (Oxygen coverage)	12.6 (0.19)	13.4 (0.18)	13.8 (0.16)

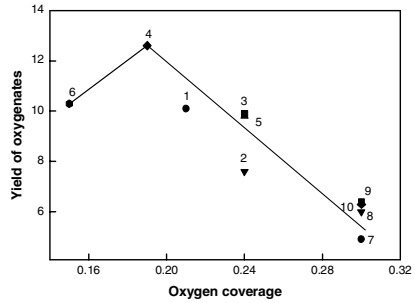

Figure 1. Yield of oxygenates vs. oxygen coverage;
1: $CuO/ZnO/ZrO_2$ (A),2:A+NaZSM-5,3:A+HZSM-5, 4:A+Ga-silicate,5:A+SAPO-34, 6: $CuO/ZnO/Ga_2O_3$(B),7:B+NaZSM-5,8:B+HZSM-5, 9:B+Ga-silicate,10:B+SAPO-34

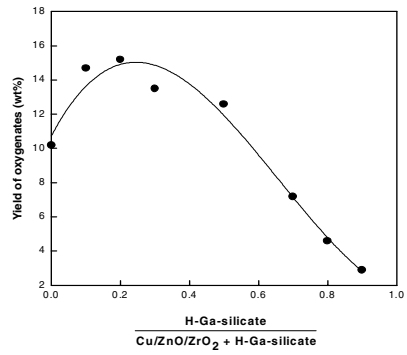

Figure 2. Effect of mixing ratio of hybrid catalyst on oxygenates yield

Conclusions

Since methanol synthesis from CO_2 hydrogenation has a severe limitation of thermodynamic equilibrium, *in situ* transformation of methanol to dimethyl ether (DME) was investigated by using hybrid catalyst composed of Cu-based methanol synthesis catalyst and a zeolite to improve the total oxygenates yield (methanol + DME).

Hybrid catalysts composed of $Cu/ZnO/ZrO_2$ showed higher yield of oxygenates than those of $Cu/ZnO/Ga_2O_3$. Among them the hybrid catalyst of $Cu/ZnO/ZrO_2$ and H-Ga-silicate showed the highest yield of oxygenates in CO_2 hydrogenation. The modification of reducibility or oxygen coverage due to the interactions between methanol synthesis catalyst and zeolite was believed to determine the ability of oxygenate synthesis.

References

(1) Spivey, J. J. *Chem. Eng. Commun.,* **1991,** 110, 123.
(2) Dubois, J.L.; Sayama, K. ; and Arakawa, H. *Chem. Lett.* **1992**, 1115.
(3) Argauer, R.J.; and Landolt, G.R.; **U.S. Patent** 3 702 886.
(4) Ashtekar, S.; Chilukuri, S.V.V.; and Chakrabarty, D.K. *J. Phy. Chem.* **1994,** 98, 4878.
(5) Saito, M.; Fujitani, T.; Takeguchi, M.; and Watanabe, T. *Appl. Catal. A : General,* **1996,** 138, 311.
(6) Ihm, S.K.; Park, Y.K.; Jeon, J.K.; Park, K.C.; and Lee, D.K. *Stud. Surf. Sci. Catal.* **1998**, 114, 505.
(7) Park, Y.K.; Park, K.C.; and Ihm, S.K. *Catal. Today* **1998**, 44, 165.
(8) Fujimoto, K.; Asami, K.; Saima, H.; Shikada, T.; and Tominaga, H. *Ind. Eng. Chem. Prod. Res. Dev.,* **1986,** 25, 262.
(9) Campbell, S.M.; Bibby, D.M.; Coddington, J.M.; and Howe, R.F. *J. Catal.,* 1996, 161, 350.

CATALYTIC ESTERIFICATION OF CARBON DIOXIDE AND METHANOL FOR THE PREPARATION OF DIMETHYL CARBONATE

Fa-hai CAO[+] *Ding-ye FANG* *Dian-hua LIU* *and* *Wei-yong YING*

Department of Chemical Engineering, East China University of Science and Technology, Shanghai 200237, China

Keywords: carbon dioxide; dimethyl carbonate; methanol; reaction on supercritical condition

1. Introduction

In the global warming imbroglio, carbon dioxide is number one enemy. It is mainly liberated from combustion of fossil fuels (coal, oil and natural gas). Conversely, carbon dioxide is also one of the cheapest and most abundant carbon source in the world. Carbon dioxide can be converted into a lot of useful organic compounds by effectively activation. Thus, the recycle and utilization of carbon dioxide seem to be a fundamental task from environmental protection and economics points of view. For these reasons, we proposed a process by which dimethyl carbonate could be prepared by catalytic esterification of carbon dioxide and methanol.

Dimethyl carbonate has attracted much attention in terms of a non-toxic substitute for dmethyl sulfate and phosgene, which are toxic and corrosive methylating or carbonylating agents. In addition, DMC is considered to be an option for meeting the oxygenate specification for transportation fuels.

The conventional synthesis of DMC is via the reaction of methanol and phosgene. Owing to the high toxicity of the raw material and severe corrosity, this method has fallen out of use gradually. The other two widely used methods of synthesis of DMC are ester exchange process[1-2] and the process of oxidative carbonylation of methanol[3-5]. Recently, a more challenging method[6-9] is the direct synthesis from carbon dioxide and methanol. Although metallic magnesium powder, Sn(Ⅳ) and Tl(Ⅳ) alkoxides have been used the catalysts, respectively, unfortunately, the yield of DMC was low even in the presence of chemical dehydrates because mainly of thermodynamic limit.

The near critical regions are considered as the most significant regions that have the supercritical characteristics that affect the reactions to the greatest extent. The supercritical conditions would play a crucial role in carbon dioxide effectively activation and conversion. In this paper, we studied the process for the continuous preparation of DMC near the critical regions of carbon dioxide, in which carbon dioxide acted not only as a medium of the supercritical fluid, but also as one of the reactants.

2. Experimental

Chemicals. Methanol (analytical grade purity, 99.5%), dimethyl carbonate (99.8% purity) and CH_3I and K_2CO_3 (analytical grade purity, 99.8%) were all made in China. Compressed carbon dioxide (used as a food agent, purity min. 99.9%) was used.

Apparatus and Analysis. The experimental configuration is shown in Figure 1. The reactor was a stainless steel autoclave (FYX-5A, made in Dalian, China) with an inner volume of 500mL, a magnetic stirrer and an electric heater. When a given amount of CH_3I and K_2CO_3 were mixed with methanol (150mL) in the autoclave, the autoclave was sealed. After flushing with nitrogen and then purging with CO_2+N_2 to a given pressure at room temperature, the autoclave was heated and stirred constantly at a specific temperature and pressure for a given period of time. The reaction products, which were collected to a proper volume from the tap hole, were cooled to the ambient temperature. The samples so obtained were analyzed by gas chromatograph and organic 402 was used as monomer columns (60-80 mesh). After condensation, gas-liquid separation, depressure, the reaction products are continuously monitored on-line by double-column GC-900B （made in Shanghai, china） with a thermal conductivity detector, a TDX-02 column (80-100 mesh) was for the analyzing of the gas phase.

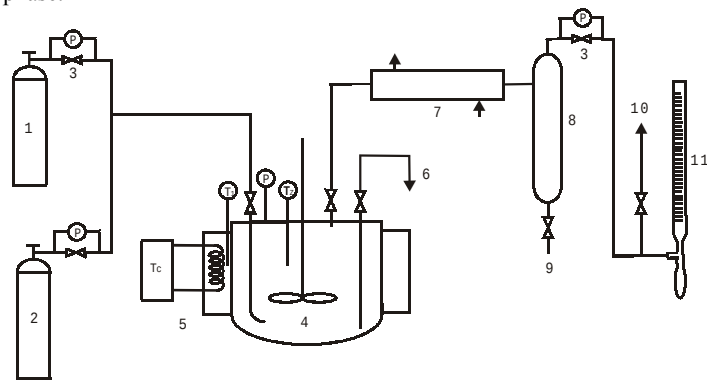

Fig. 1 The schematic diagram of the experimental apparatus

1－Cylinder of feed gas; 2—Cylinder of N_2; 3—Reducing pressure valve; 4—Autoclave; 5—Heater; 6—Tap hole; 7—Condenser; 8—Gas-liquid separator; 9—Gas chromatograph; 10-Vent; 11—Soap film flowmeter

3. Results and Discussions

In the all experiments, the constitute of feed gas is CO_2:N_2＝3:5, the velocity of magnetic stirrer was controlled at 250 rmp. The preliminary tests showed that the dosages of CH_3I and K_2CO_3 were 10.0mL and 8.0g, respectively. If one of the two compounds was absence, the other compound had no activity for the catalytic reaction.

The x_D is defined as the mole fractional of DMC in liquid-phase product.

3.1 Reaction pressure and temperature

Figures 2 and 3 show the effects of the reaction pressure (P) and the temperature (T) on x_D, respectively. From Figure 2 it could be seen that x_D increases with increase of the reaction pressure. When the reaction pressure approaches about 7.3MPa, x_D reaches the maximum value. Then, x_D decreases. The change tendency of Figure 3 is similar to that of Figure 2, in which the peak value of x_D is at approximately 80~100℃. Obviously, it is near the critical regions of carbon dioxide that carbon dioxide can be converted effectively into DMC.

[+] Author to whom correspondence should be addressed.

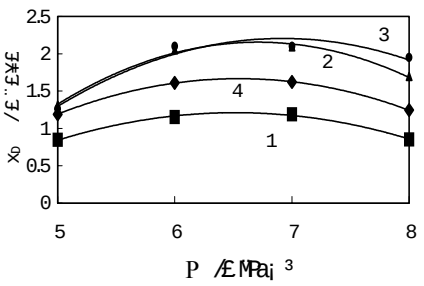

Fig.2 Effects of the reaction pressure on x_D

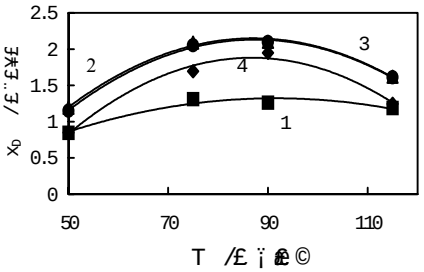

Fig.3 Effects of the reaction temperature on x_D

1—50.0℃；2—75.0℃；3—90.0℃；4—115.0℃

1—5.0MPa；2—6.0MPa；3—7.0MPa；4—8.0MPa

3.2 Supercritical phenomena and reaction pathway[10-12]

There is a conjugated double bond in the molecule of carbon dioxide. Near the critical regions of carbon dioxide, the reaction rate varies with the change of the electric polarization of the conjugated system of the molecule, so that carbon dioxide can take part in an addition reaction. Furthermore, carbon dioxide has a Lewis -acid carbon atom and two weakly Lewis basic oxygen atoms, it is therefore not surprising that it can undergo various reactions, such as firstly bound "abnormally" to form the intermediate. The basic function is useful for the activation of methanol and formation of CH_3O^-, the nucleophilic attack of CH_3O^- upon CO_2 led to the formation of DMC. Methyl idoide is only involved in the catalytic cycle. Based on above analysis, near the critical point of carbon dioxide, x_D reaches the maximum value.

3.3 Tentative ideas for the commercial production of DMC

In the system of preparation DMC from carbon dioxide and methanol, besides the product such as DMC and water, there are large number of feed gas and a little of by-product like dimethyl ether. In order to obtain pure product of DMC, two-steps method can be utilized to separate dimethyl carbonate from reaction product. The first step is forerunning, it most fully used the azeotropic feature of methanol with dimethyl carbonate, the azeotropic mixture of CH_3OH－DMC can be separated from by-product and feed gas in packed column. The second is refining step, extractive distillation method was adopted. Based on the feature, of which DMC is difficult to dissolve into water, water was used as an extraction reagent to extract and separate DMC from azeotrope, we put forward the tentative ideas for the commercial production of DMC.

Figure 4 showed the schematic diagram of the tentative ideas for the commercial production of DMC. After forerunning, the gasified azeotrope was added into extractive distillation column (3) at central section and water was sprayed from top of column. Distillate contained two layers, the upper layer was organic phase which contained 97% of DMC, the lower was aqueous phase which contained 5% of water and 0.05% of DMC, respectively. The water phase was discharged from bottom of separator (5) and mixed with first runnings.

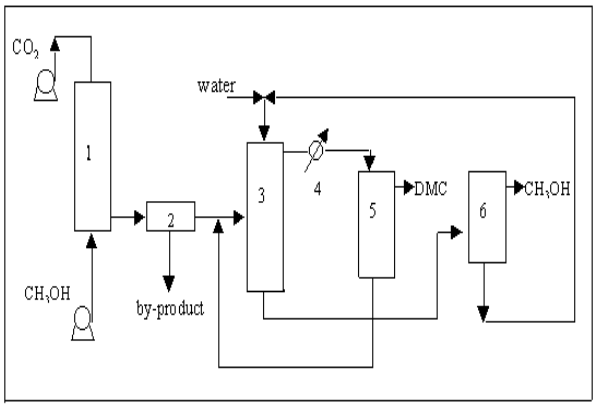

Fig. 4 The schematic diagram of the tentative ideas for the commercial production of DMC

1—reactor; 2—primary tower; 3—extractive distillation; 4—condensor; 5—separator; 6—fractionating town

The weak point of this preparation from methanol and CO_2 is that the conversion is limited by the reaction equilibrium at low level. But this limitation is avoidable by the removal of water from the reaction system, for example, by introducing trimethyl orthoformate. If it is possible to get a suitable method for the removal of water, DMC yield will be improved drastically.

4. Conclusions

The continuous catalytic synthesis of dimethyl carbonate from carbon dioxide and methanol in the presence of CH_3I and K_2CO_3 near the critical point of carbon dioxide was studied in an agitated reactor. The optimal x_D was obtained under the conditions of reaction temperature 80~100℃, reaction pressure 7.3MPa. The value of the reaction pressure was near the critical point of carbon dioxide. It could be concluded that under the supercritical condition carbon dioxide was effectively activated. A possible reaction pathway was suggested from the viewpoint of supercritical phenomena. Finally we put forward the tentative ideas for the commercial production of DMC, the results will be useful to the esterification of carbon dioxide and methanol.

Acknowledgments

Our work is supported by the Research Fund for the Doctoral Program of Higher Education (97025105) and the Basic Research Project of SINOPEC (598013).

References

(1). Knifton, J. F. *"Process for co-synthesis of ethylene glycol and DMC"*; assigned to Texaco;1987, US Patent 4,661,609;

(2). Duranleau, R. G.; Nieh, E. C. Y.; Knifton, J. F. *"Process for production of ethylene glycol and dimethyl carbonate"*; assigned to Texaco,1986 US Patent 4,691,041;

(3). Romano, U., et al. *Synthesis of DMC from methanol, CO, and O_2 catalyzed by copper compounds.* Ind. Eng. Chem. Prod. Res. Dev. 1980,**19**,396-403

(4). Fenton, D. M.; Steinward, P. J. Noble Metal Catalysis, Ⅲ: *Preparation of dialkyl oxalates by oxidative carbonylation*; Union Oil. J. Org. Chem, 1974, **39**, 701-704

(5). WO Patent 07601; Curnutt, G. L. "*Catalytic Vapor Phase Process for Producing Dihydrocarbyl Carbonates"*; assigned to Dow Chemical Company; 1987

(6). Kizlink J. *Synthesis of dimethyl carbonate from carbon dioxide and methanol in the presence of organotin compounds*. J Collect Czech Chem Commun, 1993，**58**：1399

(7). Jiang Q，Lin Q H and Huang Z T. *A new catalytic process for the direct synthesis of dimethyl carbonate from carbon dioxide and methanol.* Cuihua Xuebao，1996，**17**（2）：91 (in Chinese)

(8). Fang S.，Fujimoto K. *Direct synthesis of dimethyl carbonate from carbon dioxide and methanol catalyzed by base. Applied catalysis* A：General，1996，**142**：L1-L3

(9). Gui X S, Cao F H, Liu D H and Fang D Y. *Synthesis of dimethyl carbonate from methanol and carbon dioxide in the autoclave. Journal of east china university of science and technology,* 1998, **24** (1): 7 (in Chinese)

(10). Savage P. E.; Gopalan S.; Mizan T. I.; Martino C. J. and Brock E. E. *Reactions at supercritical conditions: Applications and fundamental.* AICHE Journal, 1995, **41**(7): 1723

(11). Xu X. D.; Moulijn J. A. *Mitigation of carbon dioxide by chemical conversion: Plausible chemical reactions and promising products.* Energy & Fuels. 1996, **10**: 305

(12). Brounstein P, Matt D and Noble D. *Reactions of carbon dioxide with carbon-carbon bond formation catalyzed by transition-metal complexes.* Chem Rev. 1988, **88**: 747

BRIDGING NATURAL FACTS WITH INDUSTRIAL PROCESSES FOR CARBON DIOXIDE UTILIZATION: METAL ENZYMES AND TRANSITION METAL SYSTEMS

Michele Aresta and Angela Dibenedetto

University of Bari and METEA Research Center
Department of Chemistry, Campus Universitario, 70126 - Bari, Italy,
fax +39 080 544 2083, e-mail:aresta@metea.uniba.it

Introduction

The direct use of carbon dioxide in the carboxylation of organic substrates finds a quite extensive application in Nature,[1] while only few processes based on carbon dioxide are industrially exploited: the Kolbe-Schmitt reaction[2] (Eq.1) and the synthesis of urea [3] (Eq.2), that are known since more than one century, and the recent carboxylation of epoxide.

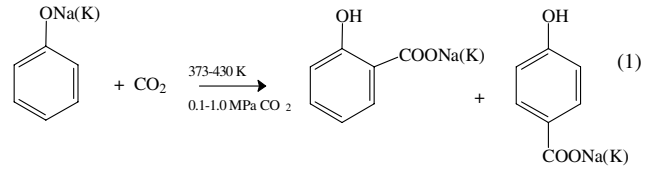

I **II** **III**

$$2\ NH_3 + CO_2 = H_2NCONH_2 + H_2O \qquad (2)$$

IV

Also, carbon dioxide is the electron acceptor in metabolic paths characteristic of anaerobic microrganisms, methanogens and acetogens[4] among others. Their enzymatic reaction mechanism shows in some cases a surprising similarity with chemical processes.

The conversion of organic compounds into methane requires a complex metabolic food chain[5] as the biomass undergoes several steps (depolymerization, acidogenesis, acetate formation, methanogenesis, methanation of CO_2) that opens new perspectives for the development of biotechnologies and environmental friendly innovative synthetic methodologies based on carbon dioxide.[1,6]

Results and Discussion

Biotechnological carboxylation of phenol

The Kolbe-Schmitt reaction (Eq.1) is industrially used since long time for the synthesis of 2-OH-benzoic acid and 4-OH-benzoic acid but the selectivity and yield are not completely mastered. However, it is highly wished to dispose of a selective process working under mild conditions.

We have found that the pathway for phenol degradation follows the route, quite usual in Nature, of "increasing the complexity of the molecule for its easier degradation".[7] In fact, as shown in Scheme 1, phenol (V) is first phosphorylated (VI), then carboxylated to 4-OH-benzoic acid (VII), which is converted into the active form 4-OH-benzoyl-CoA (VIII) subsequently, dehydroxylated to benzoyl-CoA (IX), the active form of benzoic acid. The latter is eventually converted into CO_2 and H_2O (X).

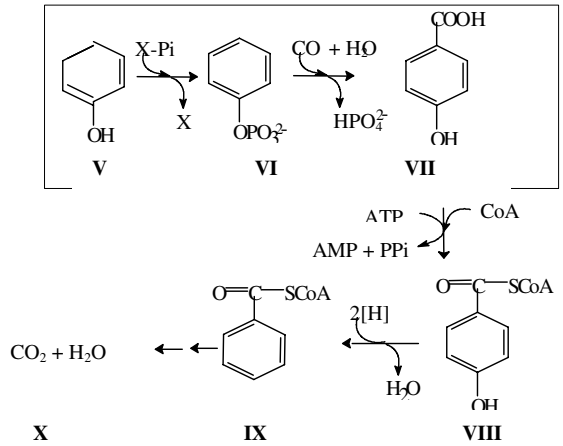

Scheme 1. Phenol biodegradation pathway by Thauera aromatica

The carboxylase enzyme responsible for the carboxylation of phenol is Mn(II) dependent[6,8] and affords very selectively the 4-OH-benzoic acid isomer, a compound that finds application in material science. We have developed a biotechnological synthesis of it, solving, thus, the problem of purity. The enzyme was supported on low-melting agar on which it has a life from several days to weeks.

A recent modification of this system makes use of a membrane for the separation of the reaction space where the enzyme is kept, from the space where the reaction product is extracted.

Such first application of the Phenol carboxylase enzyme for the functionalisation of organic substrates, is clean and affords an interesting turnover number of ca. 16 000.

CO_2 reduction to CO and the synthesis of acetic acid.

The reduction of CO_2 to CO (Eq.3) is the first step in the bacterial production of acetic acid from CO^2.

$$CO_2 + 2\ H^+ + 2e^- \rightarrow CO + H_2O \qquad (3)$$

It recalls the "reverse gas shift reaction" occurring in industrial CO_2 reduction with H_2, that is believed to take place in the synthesis of methanol from CO_2. (Eq. 4)

$$CO_2 + 3\ H_2 \rightarrow CH_3OH + H_2O \qquad (4)$$

In bacteria, the CO_2 reduction is mediated by the enzyme CODH (Carbon monoxide dehydrogenase), that contains both Ni and Fe. Once formed, CO is coupled with a methyl group generated from CO_2 (Scheme 2) with the intervention of the tetrahydrofolate enzyme.

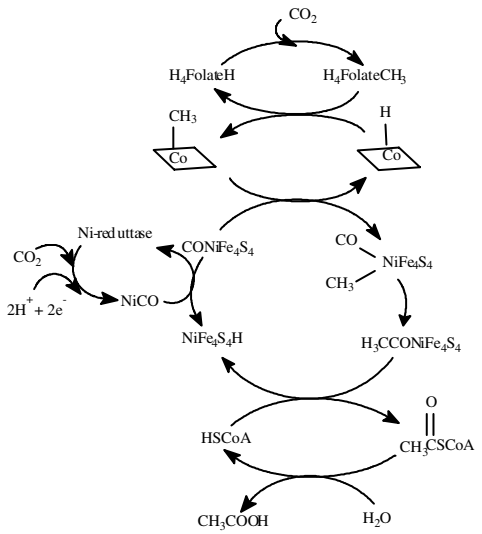

Scheme 2. Cycle of CODH

Such coupling generates the acetyl-moiety, CH_3-CO- that generates acetic acid. It is amazing the similarity of the bacterial synthesis of acetic acid with the industrial Monsanto process. (Scheme 3)

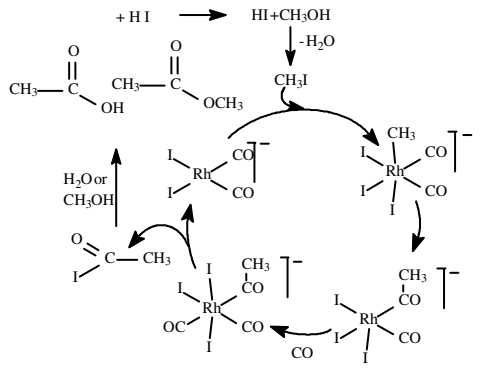

Scheme 3. Monsanto process

For a long time, Ni has been considered to be, in the enzymatic system, the metal center binding CO and probably catalysing the CO_2 reduction.[9] It has been proposed that CO is bound to Fe, where the acetyl moiety is generated.[10]

Chemical model systems indicate that both Ni[11] and Fe[12] complexes are able to bind carbon dioxide. Concerning the CO_2 reduction to CO, at the present time only evidence that the Ni complex $(PCy_3)_2Ni(CO_2)$ (**XI**) catalyses the CO_2 reduction reaction in the presence of proton and electron donors has been collected.[13] The fluxional behaviour of the carbon dioxide moiety co-ordinated to the metal has been unambiguously established in the case of **XI**, for which the limit forms and the rotational free energy barrier have been determined ($\Delta G^{\neq}$ = 39.6 kcal/mol).[14]

XI in toluene, under dinitrogen atmosphere, reacts with several Broensted acids, under electron transfer conditions with formation of the carbonyl-bound species $(PCy_3)_2Ni(CO)_2$ (**XII**) isolated from the reaction mixture as thermodynamic products, while $(PCy_3)_2Ni(CO)$ (**XIII**) is a kinetic product.

The so formed CO is able to react with one olefin and Ph-SS-Ph to afford a thioacetyl moiety, fully mimicking the bacterial process (Scheme 4).

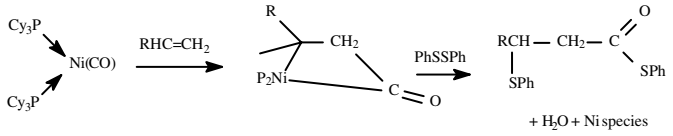

Scheme 4. Biomimetic synthesis of thioesters

These findings prompted us to propose the alternative acetyl formation based on Ni (Scheme 2).

The influence of Fe, Co, Ni on the production of methane

We have studied the influence of the concentration of Ni, Fe, Co on the methanation of fermentable vegetables and found that they influence at different extent the H_2 production, the CO_2 reduction to methane and, thus, the CH_4/CO_2 ratio that may reach quite high values (more than 4.5). This finding suggests that the natural biogas composition may have been influenced by the nature of the rocks that constitute the walls of the reservoirs. The presence of Ni, Fe, Co ions may have made available the metal ions to the bacterial pool for a better biogas quality.

Acknowledgement. The financial support by MURST (Project no. 9803026360) is gratefully

References

(1) Aresta, M. and Forti, G. (Eds), in *Carbon Dioxide as a Source of Carbon*, Elsevier Publ. **1987**; Aresta, M. and Schloss, J. V. (Eds), in *Enzymatic and Model Reaction for Carbon Dioxide Carboxylation and Reduction Reactions*, Elsevier Publ. **1990**.
(2) Kolbe, H., Lautemann, E. *Ann.* **1869**, 113, 125; Ota, K. *Bull. Chem. Soc. Jpn.,* **1974**, 47, 2343.
(3) Fumasoni, S.; Pochetti, F.; Roberti, G. Ger. Offen. **1974**, 2,318,327, C.A., 80, 14593j; Fromm, D.; Luetzow, D. *Chem. Unserer Zeit*, **1979**, 13, 78.
(4) Wood, H.G., Ragsdale, S.W., Pezacka, E. *Biochem. Int.* **1986**, 12, 421; Ragsdale, S.W., Wood, H.G., Morton, T.A., Ljungdahl, L.G., Der Vartanian D.V. in *The bioinorganic chemistry of Nickel*, VHC, New York, **1988**, 311.
(5) Zehnder, A. J. B., In *Water pollution Microbiology*, **1978**, vol. 2, John Wiley & Sons, Inc., New York; Zeikus, J. G. In *Microbes and Their Natural Environments*, Slater, J. H. and Whittenbury J. W. Eds., **1983**, Cambridge University Press, London; Schink, B. In *Environmental Microbiology of Anaerobes* **1983**, Zehnder, A. J. B. Ed., Wiley, New York.
(6) Lack, A., Fuchs, G. Aresta, M., Tommasi, I., *Eur. J. Biochem*. **1991**, 197, 473.
(7) Platen, H., Schink, B. *Arch Microbiol*. **1987**, 149, 136; Schnell, S., Bak, F., Pfenng, N. *Arch. Microbiol*. **1989**, 152, 556.
(8) Aresta, M., Tommasi I., Dileo C., Dibenedetto A., Narracci, M., Ziolkowski J., Jezierski A. *Canad. J. Chem*. **2001**, In press.
(9) Cramer, S.P., Eidsness, M.K., Pan, W.-H., Morton, T.A., Ragsdale, S.W., DerVartanian, D.V., Ljungdahl, L.G., Scott, R.A. *Inorg. Chem*., **1987**, 26, 2477.
(10) Qui, D., Kumar, M. Ragsdale S.W., Spiro, T.G. *Science* **1994**, 264, 817; Kumar, M., Lu, W.-P., Ragsdale, S.W. *Biochemistry*, **1994**, 33, 9769.
(11) Aresta, M., Nobile, C.F., Albano, V.G., Forni, E., Manassero, M. *J. C. S. Chem. Comm.*, **1975**, 636.
(12) Karsh, H.H. *Chem. Ber*., **1977**, 110, 2213; Komiya, S., Kasuga, N., Hirano, M., Fukuoka, A. *J. Chem. Soc. Chem. Commun*., **1994**, 1115.
(13) Aresta, M., Quaranta, E., Tommasi, I. *J. Chem Soc. Chem. Commun*., **1988**, 450; Aresta, M., Tommasi, I., Giannoccaro, P., Quaranta, E., Fragale, C. *Inorg. Chim. Acta*, **1998**, 272, 38.
(14) Aresta, M., Quaranta, E., Tommasi, I., Gobetto, R., *Inorg. Chem.* **1992**, 31, pp. 4286-4290; Jegat, C., Fouassier, M., Tranquille, M., Mascetti, J., Tommasi, I., Aresta, M., Ingold, F., Dedieu, A. *Inorg. Chem*., **1993**, 32, 1279.

SYNTHESIS AND EPR STUDY OF RU-MN DIMER COMPLEXES AS CATALYSTS FOR LIGHT-DRIVEN WATER OXIDATION: TOWARDS SOLAR ENERGY CONVERSION INTO FUELS

Licheng Sun[a], Anh Tran[a], Yunhua Xu[a], Reiner Lomoth[b], Ping Huang Kenéz[c], Ann Magnuson Styring[c], Björn Åkermark[a], Leif Hammarström[b], Stenbjörn Styring[c]

[a] Department of Organic Chemistry, Arrheniuslab, Stockholm University, SWEDEN
[b] Department of Physical Chemistry, Uppsala University, Box 532, 751 21 Uppsala, SWEDEN
[c] Department of Biochemistry, Center for Chemistry and Chemical Engineering, University of Lund, Box 124, S-221 00 Lund, SWEDEN

Introduction

In Photosystem II (PSII),[1] solar energy is used to extract the electrons needed to reduce CO_2 (the greenhouse gas) from water. Thereby, the biosphere is provided with an inexhaustible electron source, making water oxidation in PSII a key process in nature. Under illumination, the chlorophylls in the primary donor in PSII (P_{680}) are transiently excited to P_{680}^* which, within picoseconds, ejects an electron to a chain of protein-bound electron acceptors. The photo-oxidized P_{680}^+ has a potential of E_m P_{680}^+/P_{680} ≈1.18V *vs*. NHE, and retrieves its electron from a series of electron donors and ultimately from water.

Water oxidation is catalyzed by a domain within PSII called the water oxidizing complex (WOC), which involves a tyrosine residue, denoted Tyr_Z, and a cluster of four Mn ions functioning as a charge storing device for oxidizing equivalents. In each turnover of the enzyme, four electrons are extracted from two water molecules. The reaction is catalyzed by the manganese cluster in close conjunction with Tyr_Z.

In attempts to mimic the WOC and the redox reactions involved in photosynthetic water oxidation, we have incorporated principles from PSII into supramolecular complexes. Our strategy is to couple a photoactive Ru^{II} *tris*-bipyridine ($Ru^{II}(bpy)_3$ center (which mimics P_{680}) to a redox active moiety containing manganese or tyrosine.[2] Others and we have synthesized several multinuclear Ru-Mn systems.[3, 4] In all these systems, it has been possible to observe light induced electron transfer from the Mn ion(s) to the photo-oxidized Ru center when the molecules are exposed to laser flashes in the presence of an external electron acceptor. We have also shown that tyrosine can be coupled to the Ru-complex and function as a redox-active intermediate.[3] However, to more completely mimic the reaction sequence, a higher degree of complexity is required.

To increase the similarities between our supramolecular complexes and the donor side of PSII, we have synthesized a triad system complex **2** (Figure 1) containing a $Ru^{II}(bpy)_3$ center coupled *via* a modified *L*-tyrosine to a $Mn_2^{II,II}$-bpmp dimer(**1**),[17,18] (bpmp = 2,6-bis[[*N, N*-di(2-pyridylmethyl)amino]methyl]-4-methylphenol). In our first study of this complex,[3] we described the synthesis and a few of the chemical and spectroscopic properties of **2**. We showed that under illumination, the excited Ru^{II}* can reduce an external electron acceptor. The photo-generated Ru^{III} then retrieves an electron very rapidly ($k>1 \times 10^7 s^{-1}$) *via* intramolecular electron transfer. In this paper we want to show the photo-induced multistep electron transfer in **1** and the synthesis of its derivatives **3** and **4**.

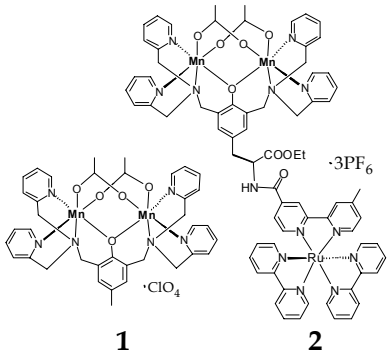

Figure 1. Structures of one Mn dimer complex **1** containing a $Mn_2^{II,II}$ moiety and one trinuclear complex **2** containing the same dimer covalently linked to a $Ru^{II}(bpy)_3$ *via* an amide bond.

Experimental

Chemicals and Synthesis: Penta-aminechlorocobalt^{III} chloride (here denoted Co^{III}) was purchased from Aldrich. Ru^{II} *tris*-(2,2´-bipyridyl) dichloride ($[Ru^{II}(bpy)_3^{2+}$) was prepared according to Sullivan *et al*. [5] Complex **1** in the $Mn_2^{II,II}$ and $Mn_2^{II,III}$ states was synthesized according to Diril et al.[6] and complex **2** was prepared as described by Sun *et al*.[7]

EPR Spectroscopy*:* X-band EPR measurements were performed on a Bruker ESP 380E spectrometer equipped with a TE_{102} cavity and an Oxford Instruments liquid helium flow system. EPR spectra were analyzed using the software package WinEPR. Laser flashes at 532 nm (6ns pulse width, ~250 mJ/flash) were given at room temperature from a Spectra Physics DCR 3G Nd:YAG laser. The incident laser light was adjusted with lenses to cover the entire EPR sample volume. In flash photolysis experiments, saturating laser flashes (1 Hz repetition rate) were applied to the EPR samples at room temperature. After the designated number of flashes, the sample was first frozen in a 200 K ethanol/dry ice bath within 2 seconds and then quickly transferred to liquid N_2 until further use. X-band EPR spectra were recorded before and after flashing of the EPR samples.

Electrochemistry*:* Electrochemical measurements were performed using a three-electrode system connected to a potentiostat from Eco Chimie with an Autolab/GPES electrochemical interface. The working electrode was a glassy carbon disc (diameter 2 mm, freshly polished) for voltammetry or a platinum grid for bulk electrolysis respectively. A platinum spiral was in a separate compartment was used as counter electrode. The reference electrode was an $Ag/AgNO_3$ electrode (10 mM $AgNO_3$ in acetonitrile). The electrolyte was prepared from dry acetonitrile (molecular sieves 3 Å) with 0.1 M tetrabutylammonium perchlorate ($TBAClO_4$, Aldrich) that had been dried at 413 K. For the aqueous electrolytes, 1% or 10% water (v/v%) was added. Before the measurements, oxygen was removed from the solution by purging for 10 minutes with solvent saturated nitrogen.

Results and discussions

Electrochemical Studies.

The redox potentials for the sequential oxidation of **1** and **2** were determined by cyclic voltammetry. Complex **1** was studied in both dry acetonitrile and mixtures of acetonitrile and water, whereas **2** was only studied in dry acetonitrile due to its low stability in water. The voltammogram of **1** in dry acetonitrile (Figure 2A) displays two reversible redox processes at $E_{1/2}$= 0.50 V and 1.06 V vs. SCE. These potentials are in good agreement with the data previously reported by Chang et al[6] who assigned the first anodic peak to the $Mn_2^{II,II/II,III}$ redox couple and the second to the $Mn_2^{II,III/III,III}$ redox couple.

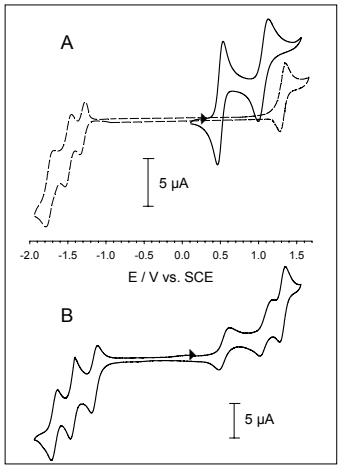

Figure 2. Cyclic voltammograms obtained in dry acetonitrile of **A**, 1.5 mM complex **1** (—) and 1 mM $Ru^{II}(bpy)_3$ (---) and **B**, 1 mM complex **2**. Conditions: scan rate 10mV/s. Otherwise, see experimental section.

The cyclic voltammogram of complex **2** in dry acetonitrile is shown in Figure 2B. The reversible anodic process at 1.35 V vs. SCE and the three cathodic peaks at negative potentials, are typical for $Ru^{II/III}$ oxidation and ligand reduction in $Ru^{II}(bpy)_3$ complexes.[21] By comparison with the voltammogram of complex **1** (Fig 2A) the additional quasi-reversible anodic processes can be assigned to the Mn moiety, i.e. to the $Mn_2^{II,II/II,III}$ and $Mn_2^{II,III/III,III}$ couples respectively. The peak potentials for these two processes are identical within 20 mV for **1** and **2**.

Photo-induced, Stepwise Oxidation of $Mn_2^{II,II}$.

Figures 3 and 4A demonstrate chemical reactions in complexs **1** and **2** when they are subject to flash illumination in the presence of $Ru^{II}(bpy)_3$ (in **1**) and Co^{III} in deareated solution. The EPR spectrum of a mixture of complex **1** and $Ru^{II}(bpy)_3$ in buffered (20 mM MES, pH 7, saturated with Co^{III}) water solution containing 10% acetonitrile was recorded at 10 K. Previous to any illumination (Figure 4, top spectrum), **1** displays two spectroscopic species. The main part of the spectrum represents the $Mn_2^{II,II}$ dimer, distinguishable by the broad peak at 2628 G (indicated by a bar) and by the broad trough at 3648 G (see above). However, because of the presence of 90% water a small fraction of the Mn dimers are destabilized to monomeric Mn^{II}. This fraction is visible as a set of 6 lines centered around 3384 G ($g \approx 2$), and was estimated to be less than 20%, measured from the peak-to-trough height. To steer clear of interference from this signal in our quantitative measurements of **1**, we have used the peak at 2628 G which only belongs to the coupled $Mn_2^{II,II}$ spectrum.

The EPR spectrum of **2** prior to illumination is similar to that published earlier and is also dominated by the $Mn_2^{II,II}$ dimer spectrum from two antiferromagnetically coupled Mn^{II} ions (top spectrum in Figure 4A). Notably, due to the lower water content (10%) in the measurement, there is no or negligible contamination from uncoupled Mn^{II} in the spectrum of **2**. Interestingly, there is an 11-line hyperfine pattern observable in **2** between ≈ 2400 to 2850 G with a splitting constant ≈ 40 to 45 G which is also typical for $Mn_2^{II,II}$ [8] but which was not observed in **1**.

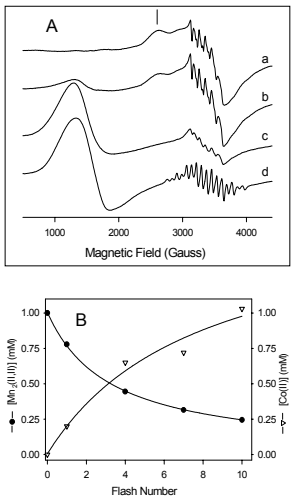

Figure 3. EPR spectra showing the flash dependent oxidation of **1** from the $Mn_2^{II,II}$ to the $Mn_2^{III,IV}$ oxidation state. Spectra **a**, **b**, **c** and **d** are recorded in samples that were exposed to 0, 1, 10 and 20 flashes respectively. EPR conditions: T= 10 K; microwave power, 3.3 mW; modulation amplitude, 10 G; microwave frequency, 9.47 GHz; modulation frequency, 100 kHz.

Spectra b, c and d in Figure 3 show the results of flash illumination at 532 nm of a mixture of complex **1**, $Ru^{II}(bpy)_3$ and Co^{III}. When one flash was applied (Figure 3 spectrum b) the maximum peak height of the $Mn_2^{II,II}$ signal decreased compared to the spectrum recorded before flash illumination (Figure 3, a). Simultaneously a new signal at ≈1300 G, originating from Co^{II} arose. By increasing the number of flashes, the Co^{II} signal increased while the $Mn_2^{II,II}$ signal amplitude decreased (Figure 3, b to d). The increase of the EPR signal from Co^{II} indicates that Co^{III} was reduced in a flash-dependent fashion. Spectra c and d in Figure 3 represent samples that were given 10 or 20 flashes respectively. It is clear that the EPR signal from $Mn_2^{II,II}$ decreased, and already after 10 flashes most of the $Mn_2^{II,II}$ features, as well as those from the uncoupled Mn^{II}, disappeared from the EPR spectrum (Figure 3 c). After 20 flashes (Figure 3, d), a well-resolved 16 line EPR signal appeared in the spectrum. The new signal is centered around $g \approx 2$ and has a width of approximately 1220 G, ranging from 2880 to 4100 G, with a hyperfine coupling constant of 78 to 80 G. This hyperfine pattern makes it clear that the signal originates from Mn, and EPR signals of this type with 16 lines are characteristic for a strongly spin coupled $Mn_2^{III,IV}$ dimer.[9]

The photo-induced oxidation of **1** to the $Mn_2^{III,IV}$ state is an interesting reaction, but it occurs *via* intermolecular electron transfer. We were therefore interested in whether a similar reaction could be achieved in **2**, where the $Mn_2^{II,II}$ dimer is covalently linked to the $Ru^{II}(bpy)_3$ center. We have earlier described very rapid reduction of photo-oxidized Ru^{III} in **2** ($k > 1 \times 10^7 s^{-1}$) and we proposed that the electron originated from the Mn-dimer in **2**[14]. Here, we expand these optical studies of Ru^{III} reduction with EPR studies aimed at following the redox chemistry in the Mn moiety of **2**.

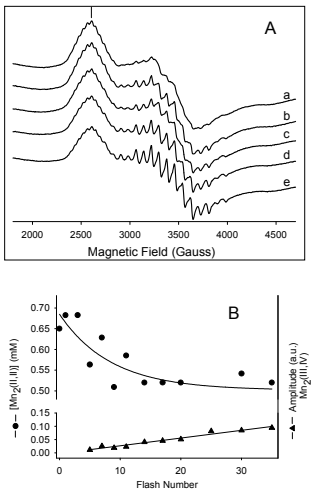

Figure 4. **A**, EPR spectra showing the oxidation of **2** from the $Mn_2^{II,II}$ to the $Mn_2^{III,IV}$ oxidation state. **B**, Decrease of the $Mn_2^{II,II}$ (●) and increase of the $Mn_2^{III,IV}$ (▲) signal amplitude from **2** as a function of flash number. Spectrum **a** was recorded in the dark. Spectra **b** through **e** were recorded after the sample was exposed to 7, 11, 20 and 25 flashes respectively. The EPR conditions as in Figure 3.

In the low temperature EPR spectrum of **2** (Figure 4A, spectrum a) the main spectral features from the $Mn_2^{II,II}$ dimer are clearly observable at 2605 G and 3680 G. Photo-oxidation experiments were carried out in the presence of 10% water. Figure 4A shows the results when **2** was exposed to laser flashes in the presence of Co^{III} as electron acceptor. A small, but significant, fraction of the signal amplitude from $Mn_2^{II,II}$ (indicated with a bar) disappeared as a function of number of flashes applied. After 10 and 35 flashes, about 15% and 25% respectively of the EPR signal amplitude had disappeared (Figure 4A,B). The spectra in Figure 4A also clearly reveal that continuous flashing results in the formation of a new dominating EPR feature centered around 3380 G ($g \approx 2$). This spectrum consists of 16 lines with a hyperfine coupling constant ≈78 to 80 G and is essentially identical to the $Mn_2^{III,IV}$ spectrum from **1**. We conclude that the $Mn_2^{II,II}$ moiety in **2** can also be photo-oxidized to the $Mn_2^{III,IV}$ state. Because of the rapid electron transfer to photo-generated Ru^{III} in **2** observed earlier, we propose that the photo-oxidation is an intramolecular electron transfer reaction.

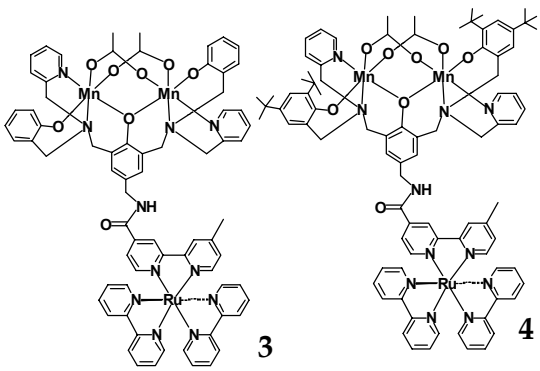

Figure 5. The structures of high valence Mn(III/III) dimer covalently linked to ruthenium tris-bipyridine complexes.

To drive the photo-oxidation of a Mn dimer to a higher oxidation state, such as $Mn_2^{IV,IV}$, complex **2** was modified. The complex **3** and **4** in Figure 5 have been synthesized recently. Two pyridine groups were replaced by phenol groups. Preliminary measurements show that the new ligands can stabilize $Mn_2^{III,III}$ state from beginning. Photo-induced multi-step electron transfer study is underway.

Conclusions

The photochemistry and electrochemistry in two model complexes complex **1** and **2** were investigated. The EPR spectra revealed that both complexs underwent photo-induced, stepwise manganese oxidation by electron transfer to a photosensitizer. Figure 6 describes the reactions involved. The electron transfer is intermolecular for complex **1** and intramolecular in **2**. In the presence of water, the $Mn_2^{II,II}$ moiety was successively oxidized to the mixed-valence $Mn_2^{III,IV}$ state. Electrochemical studies indicate that ligand exchange in the $Mn_2^{III,III}$ state, e.g. substitution of the acetate bridges by water molecules, is most likely a prerequisite for oxidation to the $Mn_2^{III,IV}$ state.

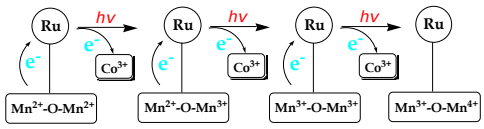

Figure 6. Photo-induced three step electron transfer in trinuclear complex **2**.

The light induced Ru oxidation to the highly oxidizing Ru^{III} species involves an oxidizing potential quite similar to that of P_{680}^{+} in the PSII reaction center. The redox potentials of the different manganese oxidation states of **1** and **2** are also quite comparable to those involved in the donor side chemistry in PSII, with the potential of the highest oxidation state remarkably close to that which is necessary for oxidizing water. The successive recovery of Ru^{II} accompanied by stepwise Mn oxidation, possibly mediated by the tyrosine derivative in **2**, thereby highly resembles important steps in the function of the WOC in PSII.

Acknowledgements

This work was supported by grants from the Knut and Alice Wallenberg Foundation, the Swedish Natural Science Research Council, the Swedish Council for Engineering Science, the European TMR Program (TMR Network CT96-0031), and the Nordic Energy Research Program. We acknowledge valuable discussions with Prof. Jean-Jacques Girerd and colleagues, Orsay, France and Prof. Karl Wieghardt, Mulheim an der Ruhr, Germany.

References

(1). (a) Britt, R. D. *Oxygenic Photosynthesis: The Light Reactions*; Ort, D. R. and Yocum, C. F., Ed.; Kluwer Academic Publishers: Netherlands, **1996**, pp 137-164. (b) Diner, B. A.; Babcock, G. T. *Oxygenic Photosynthesis: The Light Reactions*; Ort, D. R. and Yocum, C. F., Ed.; Kluwer Academic Publishers: Netherlands, **1996**, pp 213-247. (c) Barber, J.; Kuhlbrandt, V. *Current Opinion in Structural Biology* **1999**, *9*, 469-475.

(2). Sun, L., Hammarström, L., Åkermark, B., Styring, S., *Chem. Soc. Rev.* **2001**, *30*, 36-49.

(3). (a) Magnuson, A.; Berglund, H.; Korall, P.; Hammarström, L.; Åkermark, B.; Styring, S.; Sun, L. *J. Am. Chem. Soc.* **1997**, *119*, 10720-10725. (b) Magnuson, A.; Frapart, Y.; Abrahamsson, M.; Horner, O.; Åkermark, B.; Sun, L.; Girerd, J. J.; Hammarström, L. & Styring, S. *J. Am. Chem. Soc.* **1999**, *121*, 89-96. (c) Sjödin, M., Styring, S., Åkermark, B., Sun, L.; Hammarström, L. *J. Am.Chem. Soc.* **2000**, in press (d) Sun, L.; Berglund, H.; Davydov, R.; Norrby, T.; Hammarström, L.; Korall, A.; Börje, A.; Philouze, C.; Berg, K.; Tran, A.; Andersson, M.; Stenhagen, G.; Mårtensson, J.; Almgren, M.; Styring, S.; Åkermark, B. *J. Am. Chem. Soc.* **1997**, *119*, 6996-7004. (e) Berglund-Baudin, H.; Sun, L.; Davidov, R.; Sundahl, M.;

Styring, S.; Åkermark, B.; Almgren, M.; Hammarström, L. *J. Phys. Chem. A* **1998**, *102*, 2512-2518. (f) Sun, L.; Raymond, M.; Magnuson, A.; LeGourrierec, D.; Tamm, M.; Abrahamsson, M.; Huang Kenéz, P.; Mårtensson, J.; Stenhagen, G.; Hammarström, L.; Styring, S.; Åkermark , B. *J. Inorg. Biochem.* **2000**, *78*, 15-22.

(4). (a) Burdinski, D., Wieghardt, K.,; Steenken, S. *J. Am. Chem. Soc*. **1999**, 10781-10787. (b) Burdinski, D., Bothe, E.,; Wieghardt, K. *Inorg. Chem*. **2000**, 105-116

(5). Sullivan, D. J.; Meyer, T. J. *Inorg. Chem* **1978**, *17*, 3334.

(6). (a) Diril, H.; Chang, H.-R.; Zhang, X.; Larsen, S. K.; Potenza, J. A.; Piepont, C. G.; Schugar, H. J.; Isied, S. S.; Hendrickson, D. N. *J. Am. Chem. Soc.* **1987**, *109*, 6207-6208. (b) Chang, H.-R.; Larsen, S. K.; Boyd, P. D. W.; Pierpont, C. G.; Hendrickson, D. N. *J. Am. Chem. Soc.* **1988**, *110*, 4565-4576.

(7). Sun, L.; Burkitt, M.; Tamm, M.; Raymond, M. K.; Abrahamsson, M.; LeGourrierec, D.; Frapart, Y.; Magnuson, A.; Huang Kenéz, P.; Brandt, P.; Tran, A.; Hammarström, L.; Styring, S.; Åkermark, B. *J. Am. Chem. Soc*. **1999**, *121*, 6834-6842.

(8). Khangulov, S. V.; Pessiki, P. J.; Barynin, V. V.; Ash, D. E.; Dismukes, G. C. *Biochemistry* **1995**, *34*, 2015-2025.

(9). (a) Dismukes, G. C.; Siderer, Y. *Proc. Natl. Acad. Sci. USA* **1981**, *78*, 274-278. (b) Zheng, M.; Khangulov, S. V.; Dismukes, G. C.; Barynin, V. V. *Inorg. Chem.* **1994**, *33*, 382-387. (c) Schäfer, K.-O.; Bittl, R.; Zweygart, W.; Lendzian, F.; Haselhorst, G.; Weyhermüller, T.; Wieghardt, K.; Lubitz, W. *J. Am. Chem. Soc.* **1998**, *120*, 13104-13120.

DE NOVO SIMULATION AND SPECTROSCOPIC STUDY OF IRON SPECIATION IN MICRO- AND MESOPOROUS BIOMIMETIC MATERIALS ACTIVE IN THE SELECTIVE OXIDATION OF METHANE

Peter-Paul H.J.M. Knops-Gerrits

Département de Chimie, Université Catholique de Louvain (UCL), Batiment LAVOISIER, Place L. Pasteur n°1, B-1348 Louvain-la-Neuve, Belgium

Introduction

Methane Mono-Oxygenase (MMO) and Deoxyhemerythrin are examples of diiron enzymes that catalyze the dissociative and non-dissociative binding of molecular oxygen [1-5]. Dissociative binding of oxygen via a peroxo intermediate to a diamond core structure leads to a reactive species active in the oxidation of alkanes [1-2]. Non-dissociative binding of oxygen via a side-on peroxo intermediate such as in the active site of deoxyhemerythrin does not allow the splitting and allows binding/release of oxygen as a function of the physiological conditions. Such active sites are among the growing list related to (hydr)oxo-bridged di- or poly-iron cores in biological systems. Methane mono-oxygenase has a binuclear active site in which two histidines and four glutarates are present. Both iron ions are coordinated by a histidine, an oxygen from a bridging carboxylate and a μ-oxo bridge [1]. Theoretical modeling of these enzyme active sites has been recently reported. Yoshizawa *et al.* studied the dioxygen cleavage and methane activation on diiron enzyme models with the extended Hückel method, an approximate molecular orbital method, the $\mu\text{-}\eta^1{:}\eta^1\text{-}O_2$ or $\mu\text{-}\eta^2{:}\eta^2\text{-}O_2$ binding modes are distorted to the corresponding dioxygen complex [4].Shestakov and Shilov showed that the synchronous insertion of O atom mechanism is found to be significantly less contradictory (for example in methane) if it is supplemented by the stage of formation of the five-coordinate carbon intermediate complex of a hydrocarbon molecule via oxygen atom of an active center[5].

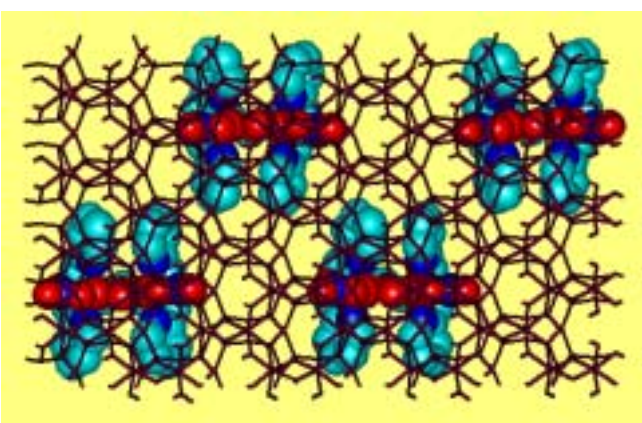

Figure 1. $[Fe_2(HPTP)(OH)(NO_3)_2]$ in montmorillonite clays.

Methane can be converted into methanol with binuclear iron(IV)-model complexes

To mimic the MMO active site with a finite cluster we chose to study the binuclear heptapodate coordinated iron (III)-complexes of *N,N,N',N'*-tetrakis(2-benzimidazolylmethyl)-2-hydroxy- 1,3-diamino -propane (HPTB) and *N,N,N',N'*,-Tetrakis(2-pyridylmethyl)-2-hydroxy-1,3-diamino-propane (HPTP). These have active sites of the form $[Fe_2(HPTP)(\mu\text{-}OH)]^{4+}$ (1) and $[Fe_2(HPTB)(\mu\text{-}OH)]^{4+}$ (2). As supports for such complexes we use mesoporous materials such as MCM-41, FSM-16, HMS (Hexagonal Molecular Sieve) [7-8] and clays (Fig 1) [9] since these materials have large surface areas and large pore sizes that can be tuned from 1.5 to 10 nm. We characterized these complexes using Quantum Mechanics (QM) and EXAFS, Mössbauer and Catalysis and studied the effect of the support.

The QM was at the *ab initio* and DFT (B3LYP) levels [3]. All chelating N-atoms and the ligand backbone were included in the QM determination of the geometry and electronic properties of the ground and excited states of the active site. The geometries of the supported complexes were determined with MD using the Universal FF (UFF) [6] supplemented with a FF based on the quantum mechanics. For the O_2 binding on the reduced active site the $\mu\text{-}\eta^1{:}\eta^1\text{-}O_2$ mode seems to preceed formation of the O=Fe-O-Fe=O bis-ferryl active site that reacts exothermally with methane by 50.56 kcal/mol. After the H splitting from methane, the methyl recombines with the FeO center via a weak $Fe\text{-}OCH_3$ bond in this model. The consecutive reaction with water protonates the methoxy group to form methanol and the substitution at the active site by a hydroxo group is endothermic by 7.50 kcal/mol. The regeneration of the active site with H_2O_2 is again endothermic by 3.24 kcal/mol. After the loss of methanol $Fe^{(III)}$- O- $Fe^{(III)}$ is formed which is reduced to the Fe(II,II) form. Ferryl groups are reactive two center three electron bonds. The solvation calculations are very important to obtain good quantitative data. Siegbahn *et al.* [1] uses gas-phase values as the dielectric constant of an enzyme is low ($\varepsilon = 4$) compared to this of water ($\varepsilon = 80$). For the solvation of small model compounds in water such effects are not negligable. The solvation energies are about 150, 300 and 500 kcal/mol for the 2+, 3+ and 4+ complexes.

Mössbauer spectroscopy allows the oxidation and spin states of the iron atoms to be assessed. Thus the isomer shifts relative to metallic iron at 300 K in the range 0.35-0.60 mm/s are characteristic of 5- or 6-coordinate high-spin di-ferric μ-OH complexes, the smaller quadrupolar splitting < 1 mm/s, in the hydroxo-bridged complexes is due to the lengthening of the Fe-O bond upon protonation of the oxo bridge. The Mössbauer pattern of the supported complexes becomes more complex due to complex lattice interactions. The EXAFS shows lengthening of the Fe-Fe distances for benzimidazole compared to pyridine containing complexes. When the complexes are supported on mesoporous oxides, the EXAFS finds a lengthening of the Fe-Fe distances. The EXAFS data on the model compounds gives longer Fe-Fe distances than the QM. This may be due to neglecting in the QM the large counterbalancing anions associated with the structure of $[Fe_2(HPTP)(\mu\text{-}OH)(NO_3)_2](ClO_4)_2$ and $[Fe_2(HPTB)(\mu\text{-}OH)(NO_3)_2](ClO_4)_2$.

Methane can be converted into methanol with α-Oxygen on iron in ZSM5 type zeolites

α-Oxygen can be formed on such iron sites by nitrous oxide N_2O decomposition at elevated temperature. Nitrous oxides are formed in the industrial synthesis of adipic acid. In nitrous oxide decomposition several routes exist depending on pressure and temperature. In order to study the pretreatment, activation, reaction and extraction effects the Fe containing topologies such as CHA, MFI, MOR and CFI [10] are tested in the methane to methanol conversion. Pretreatment performed with O_2 at 550°C and vacuum at 800°C to 900°C is optimal. Activation with N_2O at 250°C is optimal and reaction with CH_4 occurs from 20°C, extraction is best with H_2O and quantification of methanol is performed by GC, GC-MS and NMR. Structure/activity effects rquire the notion of new structural parameters related to the introduction of iron in zeolite topologies such as CHA, MFI, MOR and CFI [10-11], performed via direct

synthesis and post-synthetic modification. When iron concentrations are kept low framework iron is seen (Fig 2).

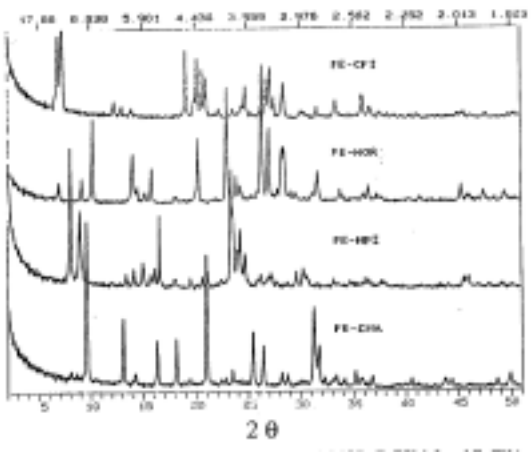

Figure 2. X-Ray Diffraction patterns of FeCIT-5, FeMOR, FeZSM-5 and FeCHA.

Extra-framework iron oxides are occluded after calcination of framework iron zeolites with high iron loading or physical mixtures of aluminum containing zeolites with iron salts or sublimation of iron by mixing zeolites with $Fe(acac)_2$ followed by an oxygen calcination procedure. The recent structure of CIT-5 is composed of 1D, extra-large pores of nearly circular cross section (center of O to center of O distance 9.91Å x 9.87Å) circumscribed by 14 T-atoms. The asymmetric unit contains 10 T-atoms and 19 oxygen atoms resulting in a unit cell content of $[Si_{32}O_{64}]$, a framework density of 18.3 T-atoms/1000 $Å^3$ and a density of 1.821 g/cm^3. The topology consists of zigzag ladders of 4-rings with pendant 5-rings interconnected through single zigzag chains. For CIT-5 (CFI) all structural parameters are within reasonable ranges for silicate materials (d(Si-O) 1.591 Å with a range of 1.555-1.641 Å, a Si-O-Si angle of 149.4° with a range of 168.7°-140.6°, and an O-Si-O angle of 109.4° with a range of 113.8° - 104.2°. These values are appended to the molecular mechanics Universal Force Field (UFF) [3]. The UFF functional forms, parameters, and generating formulas for the full periodic table

Table 1. Partial oxidation of methane with α-Fe sites in ZSM-5 and other Zeolites.

Zeolite	%wt Fe in	Oxidation	μmol Fe in sample	μmol. MeOH (oxygenate)
Fe-ZSM-5 Si/Al 11	0.5%	5 Torr N_2O/ 250°C	75	-
Fe-ZSM-5 Si/Al 11	2.0%	5 Torr N_2O/ 250°C	360	97
Fe-ZSM-5 Si/Al 11	5.0%	5 Torr N_2O/ 250°C	800	163
Fe-ZSM-5 Si/Al 11	5.0%	10Torr N_2O/250°C	800	208
Fe-CHA (0.1 μm)	5.0%	5 Torr N_2O/ 250°C	800	10
Fe-MOR (1-3 μm)	5.0%	5 Torr N_2O/ 250°C	800	10 (33)
Fe-CIT-5 (3-7 μm)	5.0%	5 Torr N_2O/ 250°C	800	4 (39)

are used to model these structures. XRD, EXAFS, Mossbauer, DRS, magnetic measurements and EPR can resolve and attribute presence of lattice iron and extra-framework clusters. XRD for as made and calcined materials with iron in the lattice reveals α-Fe_2O_3 particles are absent (no α-Fe_2O_3 reflection, d_{104} = 2.70 Å). From EXAFS structural parameters obtained in the k^3 weighted optimization give 1.7, 2.7 and 3.4Å distances for $Fe^{(III)}$-oxygen, $Fe^{(III)}$- $Fe^{(III)}$ and $Fe^{(III)}$-Si bonds. In the EPR spectra the ratio of octahedral/tetrahedral iron can be assumed from the presence of lines at g= 2/4.3, and depends on sample hydration. In mononuclear iron complexes the Fe-O bond distances of 1.86 Å (2+, O_h) 6 coordinated and 1.90 Å (3+, T_d) 4 coordinated. For tetrahedral iron and silicon atoms bond distances of 1.65 for Si-O and 1.90 Å for Fe-O obtained from QM seen in the direction of the Fe-O-Si bridge, with Fe-O-Si angles close to the 131.2° and to a O-Fe-O angles of 109.47°.

CONCLUSION.

The reaction of the MMO binuclear heptapodate coordinated iron (III)-complexes of *N,N,N',N'*-tetrakis(iminomethyl)-2-hydroxy-1,3-diamino-propane model with methane is exothermic The σ- and π-bonds of the ferryl Fe=O in the plane of the Fe-O-Fe bridge, have the properties of a two atom three electron bond. After the H splitting from methane, the methyl recombines with the FeO center via a weak Fe-OCH_3 bond in this model.

Methane can also be converted into methanol with α-Oxygen at room temperature using N_2O as a selective oxidant inside the pores of various zeolites. Extraction of the catalysts with water is preferred over acetonitrile-water mixtures. The dinuclear iron oxide clusters realize the sub-stoichiometric (based on a diiron sites) oxidation of methane after N_2O activation, the small dinuclear Fe sites favor oxygen insertion chemistry over coupling chemistry.

Acknowledgement.
PPKG thanks ESA, FNRS and FSR Belgium for financial support, A.Fukuoka & M.Ichikawa from the CRC, at Hokkaido University, Sapporo, Japan for a collaboration on EXAFS. PPKG thanks WAGoddard III from the Material & Process Simulation Center, Beckman Institute (139-74), California Inst. of Technology, Pasadena CA, USA, WAG thanks BP Amoco for financial support.

References

(1) R.H. Crabtree, *Chem.Rev*., **1995**, 95, 987.
(2) P.E. Siegbahn, R.H.Crabtree, *J.Am.Chem.Soc*., **1997**,*119*, 3103.
(3) P.P. Knops-Gerrits , P.A. Jacobs, A.Fukuoka, M.Ichikawa, F.Faglinoni, W.A. Goddard III, *J.Mol.Cat., A*, 166 (2001) 3, P.P. Knops-Gerrits, M. Witko, W.A.Goddard III, R. Millini Eds.
(4) K. Yoshizawa, K. Ohta, T. Yamabe, R. Hoffmann, *J. Am. Chem. Soc.*, **1997**, *119*, 12311.
(5) A.E.Shestakov, A.E.Shilov, *J.Mol.Cat., A*, 105 (1996) 1.
(6) A.K. Rappe, C.J. Casewit, K.S. Colwell, W.A. Goddard, W.M. Skiff, *J. Am. Chem. Soc.*, 114 (1992) 10024.; A.K. Rappe, W.A. Goddard, *J. Chem. Phys*., **1991**, 95, 3358.
(7) P.P. Knops-Gerrits, A.M. Van Bavel, G. Langouche, P.A. Jacobs, NATO ASI, **1998**, Derouane Eds., 3.44, 215.
(8) P.P. Knops-Gerrits, A. Verberckmoes, R.A. Schoonheydt, M. Ichikawa, P.A. Jacobs, *Micro- Mesop. Mat.*, **1998**, *21*: 4-6, 475.
(9) P.P. Knops-Gerrits, A. Weiss, S. Dick, P.A. Jacobs, *Stud.Surf.Sci.Catal*., **1997**, *110*, 1061.
(10) P.P. Knops-Gerrits, W.A. Goddard III, *J.Mol.Cat., A*, **2001**, 166, 1 & 135.
(11) Y. Oumi, M. Yamadaya, T. Kanougi, M. Kubo, A. Stirling, R. Vetrivel, E. Broclawik, A. Miyamoto, Catal. Lett., **1997**,45, 21.
(12) G.I., Panov, V.I., Sobolev, K.A. Dubkov,.A.E., Parmon, N.S., Ovanyesan, A.E., Shilov, A.A., Shteinman, *React. Kinet. Catal.Lett.*, **1997**, *61*, 251 .

ENZYMATIC CONVERSION OF CARBON DIOXIDE TO METHANOL BY DEHYDROGENASES ENCAPSULATED IN SOL-GEL MATRIX

Zhongyi JIANG , Hong WU , Songwei XU , Shufang HUANG

State Key Lab. of C1 Chemistry and Chemical Technolgy, School of Chemical Engineering and Technology, Tianjin University, Tianjin 300072, China

Introduction

Due to the abundance of CO_2 as the major greenhouse and the most oxidized form of carbon, the efficient utilization of CO_2 has aroused much interest from fundamental research to application application.

Herein, we report a novel and promising approach to convert carbon dioxide into methanol through consecutive reduction catalyzed by three different dehydrogenases. The whole process consists of three steps: reduction of CO_2 to formate catalyzed by formate dehydrogenase ($F_{ate}DH$), reduction of formate to formaldehyde by formaldehyde dehydrogenase ($F_{ald}DH$), and reduction of formaldehyde to methanol by alcohol dehydrogenase (ADH). Reduced nicotinamide adenine dinucleotide (NADH) acts as a terminal electron donor for each dehydrogenase-catalyzed reduction.

It is now well established that a wide variety of enzymes retain their characteristic reactivities and chemical functions when they are confined within the pores of the silica sol-gel derived matrix. The porosity of sol-gel glasses allows small molecules and ions to diffuse into the matrix while the enzymes remain physically trapped in the pores, and thus resulting in an enhanced probability of reaction due to an increase in local concentration of substrates within the nanopores. Our experiments demonstrated that when the above-mentioned three enzymes are encapsulated in the silica sol-gel matrix, the yield of methanol is considerably increased as compared to that in solution phase.

Experimental

The reaction was studied in the solution phase by using an enzyme stock solution that was comprised of 7mg/mL of $F_{ate}DH$, 2mg/mL of $F_{ald}DH$, 2mg/mL of ADH dissolved in 0.1M phosphate buffer at pH7. Add 1.0 mL of the enzyme stock solution to 1.0 mL of NADH solution in a polystyrene cuvette such that the final concentration of NADH varied from 0.025 to 0.1M . The cuvette was covered with Parafilm to prevent the evaporation loss of methanol produced, and CO_2 was then bubbled through the solution for 8 h to ensure that the reaction equilibrium was established.

The concentration of methanol was determined by gas chromatography. A calibration curve was established for methanol aqueous solutions with known concentration of methanol ranging from 0.001 to 0.005M . To evaluate the concentration of methanol produced as a result of the enzyme-catalyzed reaction. 1.0μL of the final reaction solution was used for GC measurements. The concentration of methanol was calculated by using peak areas for the characteristic methanol band in the chromatogram.

The sol-gel encapsulated samples were prepared as follows: Tetraethoxysilane (TEOS) was used as precursor for making the silica sol-gel. The initial sol was prepared by mixing 2.60g of TEOS , 1.10g of 3%(v/v) of HCl solution . The mixture was then vigorously mixed for 10 min to form sol. The gel were prepared by adding 1.0 mL of the stock enzyme solution to 1.0mL of the sol in a polystyrene cuvette. Typical gelation times are on the order of 10-30s. The cuvette was then covered with Parafilm and gel was allowed to age at 4℃ for 24 h. The aged gel was then put into a dialysis membrane using 250 mL of 0.1M phosphate buffer at pH7 as dialysis solution , and placed in refrigerator at 4℃ with frequent change of 0.1M phosphate buffer at pH7 The dialysis lasted 24-48 h to completely remove ethanol generated in the sol-gel process. 0.1 mL of NADH solution diffused into the gel by dialysis in the similar manner (the final concentration of NADH varied from 0.025 to 0.1M), the sample containing the gel and the NADH solution was left undisturbed for 48h. To this mixture , CO_2 was then bubbled for 8h for production of methanol. The concentration of methanol produced was determined using GC by taking a 1.0μL aliquot of the solution.

Results and Discussion

Table 1 shows the preliminary methanol yields in solution and sol-gel matrix. The overall yield of the reaction in solution is near to 100%. In sol-gels, the production yield of methanol is substantially decreased due to the distribution effect, stereo hindrance, diffusion resistance.

Table1 Representative methanol yields in solution and sol-gel matrix

	Reaction Temperature ℃	NADH（μmol）	Methanol yield（%）
Solution	25	100	98.0
	37	100	100
	37	150	94.8
Solution	25	100	30.0
	37	100	91.9
	37	150	42.2

It is also found that all four species (i.e. $F_{ate}DH$, F_{ald} DH, ADH,NADH) must be present to generate methanol.

The introduction of chemical modification to the enzymes and the creation of mesoporous structure of gel by biomimetic synsthesis is under investigation.

To sum up, the feasibility of enzymatic conversion of carbon dioxide to methanol is tentatively explored. The consecutive reduction of carbon dioxide by three different dehydrogenases encapsulated in sol-gel matrix results in enhanced yields for generation of methanol. This will open up a new avenue not only for on-site production of methanol from cheap raw material but also for efficient fixation of the greenhouse carbon dioxide.

Acknowledgment

This work was supported by the National Natural Science Foundation of China, under the contract 20176039

References

(1). Obert R., Dave B.C.. *J.Am.Chem.Soc.,*1999,121,12192-12193.

(2). Gill I., Ballesteros A.. *Trends in Biotechnology* ,2000,18:282-296.

(3). Ellerby L M, Nishida C R, Nishida F et al. *Science*, 1992,255:1113-1115

DEHYDRO-AROMATIZATION OF CH_4 OVER W/HZSM-5-BASED CATALYSTS

Youzhu Yuan, Zhitao Xiong, Jinlong Zeng, Guodong Lin, Hongbin Zhang

Department of Chemistry & State Key Lab of Physical Chemistry for the Solid Surfaces, Xiamen University, Xiamen 361005, CHINA

Introduction

Direct catalytic dehydrogenation and aromatization of methane to aromatics and H_2 (DHAM) in the absence of O_2 has drawn increasing attention in the recent years with the development of a series of new catalysts[1-5]. For practical uses, W-loaded HZSM-5 zeolite is among the most promising DHAM catalysts[6-7]. Recent studies in our lab have shown that, following an initial induction period, a methane conversion of ca.20% could be achieved at a benzene selectivity of ca.58% at 1073 K over Zn (or Mn, Li)-promoted W/HZSM-5-based catalysts. Compared to Mo-based catalyst, the W-based catalysts can operate at 1073 K, and gain a methane conversion approximately 2 times as high as that of the Mo(or W)-based catalyst operating at 973 K. It can also operate at 973 K and have about the same methane conversion as that of the Mo-based catalysts at the same temperature. Its main advantage is its highly heat–resistant performance; the high reaction temperature did not lead to loss of W-component by sublimation. The present results shed light on the design and development of the practical W-based catalysts for DHAM reaction.

Experimental

The W/HZSM-5 catalyst was prepared by conventional method of impregnation with H_2SO_4-acidified $(NH_4)_2WO_4$ aqueous solution (pH=2~3) as precursor. The Zn (or Mn, Li)-promoted catalyst was prepared by firstly impregnating a certain amount of the HZSM-5 zeolite carrier (with Si/Al molar ratio of 38) with a calculated amount of $ZnSO_4$ (or $MnSO_4$, or Li_2SO_4) in aqueous solutions, followed by drying at 393 K for 2 h and calcining at 673 K for 4 h, and subsequently impregnating with a calculated amount of H_2SO_4-acidified $(NH_4)_2WO_4$ aqueous solution (pH=2~3), and finally drying at 393 K for 2 h and calcining at 773 K in air for 5 h.

The activity evaluation of catalyst was carried out in a fixed-bed continuous flow reactor-GC combination system. DHAM reaction was conducted at 0.1 MPa and 973-1173 K, with a gaseous mixture of CH_4 (of 99.99 % purity) +10%Ar (served as internal standard for GC analysis, of 99.99 % purity) as feed-gas. Conversion of CH_4 and selectivities of hydrocarbon products were evaluated with an internal standard analyzing method. The amounts of coke formed on catalyst were determined by TG-DTA method. In most cases, the results of calculation for carbon equilibrium may reach approximately 85% after 1 h of reaction. XPS measurements were done on a VG ESCA LAB MK-2 system under UHV (1×10^{-7} Pa), calibrated internally by the Si(2p) (B. E.) at 103.3 eV.

Results and Discussion

DHAM Activity of W/HZSM-5-based catalysts The results of activity assay of a series of catalysts for DHAM reaction were shown in Table 1. Over the Mn (or Zn, or Li)-promoted W/HZSM-5 catalysts, a methane conversion of ca.21% and a benzene selectivity of a value of 52-61% could be achieved in the initial 2 h of reaction at 1073 K. Addition of a minor amount of CO_2 (≤ 2%) to the feed-gas was found to significantly enhance methane conversion and selectivity of benzene and to improve the performance of coke-resistance of W/HZSM-5-based catalysts. The results of monitoring the changes of methane conversion and selectivities to hydrocarbon products with time on stream of the reaction over a 3%W-1.36%Zn/HZSM-5 catalyst is shown in Fig.1, from which it can be seen that, in the initial 2 h of reaction, ~22% conversion of methane and ~62% selectivity of benzene were reached, and after 6 h of reaction, methane conversion still maintained at ~10%, with the corresponding benzene selectivity at ~38%. The lifetime of the catalyst was thus prolonged to a great extent.

Table 1. DHAM Reactivity over Catalyst Systems with Different Promoters*

Catalyst	Convers. of CH_4(%)		Selectivity (%)			
			Ben.		C_2H_4	
	105th min.	300th min.	105th min.	300th min.	105th min.	300th min.
3%W/HZSM-5	19.5	6.2	48.2	22.0	9.2	12.4
3%W-1.5%Zn/ HZSM-5	21.5	11.0	52.0	25.0	8.0	12.8
3%W-0.1%Mg-1.5%Zn/HZSM-5	21.0	15.0	55.0	42.0	12.0	13.5
3%W-1.5%Mn/ HZSM-5	21.5	12.5	59.5	40.0	10.0	13.0
3%W-1.5%Li/ HZSM-5	21.0	17.0	61.5	50.0	9.0	12.5

* The activity data of each catalyst taken at the 105th min. and the 300th min. of the reaction, respectively, under reaction conditions: 0.1MPa, 1073 K, GHSV of feed-gas CH_4+10%Ar at 960 h^{-1}.

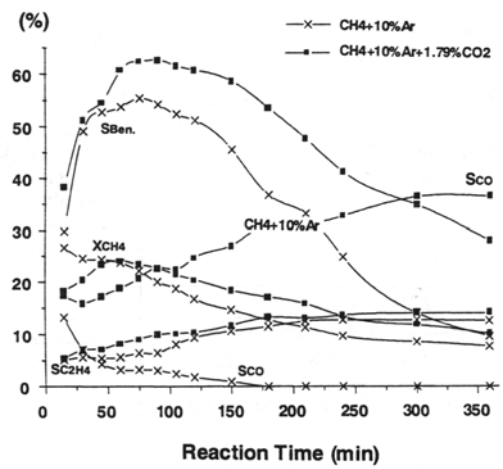

Fig. 3. Comparison between the assay results of DHAM reaction activity over the 3%W-1.36%Zn/HZSM-5 catalyst at 0.1 MPa, 1073 K, feed-gas: CH_4+10%Ar vs. CH_4+10%Ar+1.8%CO_2, both GHSV = 960 h^{-1}.

The promoting effect of the added CO_2 originated most probably from the role that it played as scavenger of functioning surface of the catalyst via Boudart reaction: CO_2 + C (deposited C at surface) →2CO, thus in favor of alleviating the deposition of carbon and inhibiting the formation of coke at the catalyst surface to a greater extent.

Carbon Deposition and Catalyst Regeneration Fig.2-I shows the changes of W(4f)-XPS spectrum of the 3%W/HZSM-5 catalyst with time on stream of the reaction. Detailed analysis and computer fitting of these W(4f)-XPS spectra revealed the existence of W-species in mixed valence-states at the surface of functioning catalyst, with the $W(4f)_{7/2}$ binding energy of W^{6+}, W^{5+}, W^{4+}, W^{2+} and WC at 36.0, 35.3, 34.5, 33.2 and 32.2 eV, respectively, and after the

reaction for 6 h, the WC had been the predominant W-containing species (See Table 2).

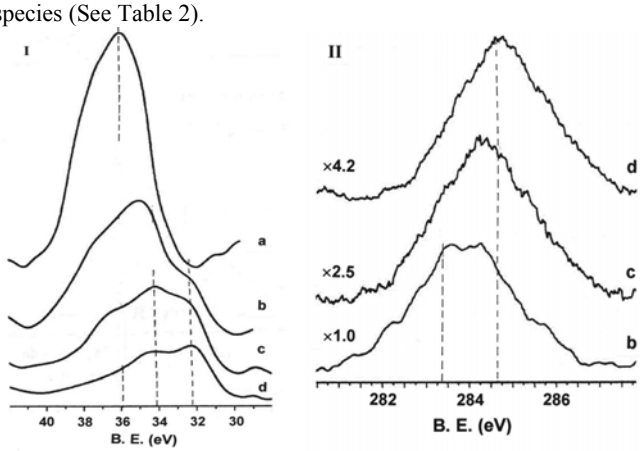

Fig.2 W(4f)-XPS spectra (I) and C(1s)-XPS spectra (II) of the 3%W/HZSM-5 catalyst with time on stream of the reaction.

Table 2 Composition of W-containing Species at the Surface of functioning 3%W/HZSM-5 Catalyst

Time (h) on stream of the reaction	Percentage of different W-Species in the total surface W (%)			
	W^{6+}	W^{5+}	W^{4+}	WC
1	19.1	13.5	28.8	18.6
3	12.5	24.2	32.1	31.2
6	7.5	18.2	20.1	54.2

Formation of the WC species was also evidenced from C(1s)-XPS spectra (Fig.2-II) taken on the functioning catalyst in different stages of the reaction; the dominant C-containing surface species was WC (B.E.of C(1s) at 283.3 eV) in the initial 1 h of reaction, while was amorphous carbon deposits (B.E. of C(1s) at 284.7 eV) after 6 h of reaction. By analysis and computer fitting of the XPS spectra taken on the catalyst samples with different time on stream of the reaction, it has been shown that the molar ratio of the component elements at the surface of 3%W/HZSM-5 catalyst was Al/C/O/Si/W= 1.2/~0/63.1/34.4/1.3 for the oxidation precursor, and 1.5/41.7/35.5/20.8/0.5 for the functioning catalyst after 1 h of reaction. It changed to Al/C/O/Si/W= 0.6/82.7/10/6.6/0.1 after 6 h of reaction, revealing that most portion of the surface of the functioning catalyst was covered by carbon deposits at that time.

NH_3-TPD measurements revealed that *ca*.80% of strong and medium-strong acidic sites were lost after 5 hours of reaction. N_2-BET measurements demonstrated that, after 1 h reaction, specific surface area of the functioning catalyst decreased to 302 m^2g^{-1} from 368 m^2g^{-1} for the oxidation precursor of catalyst. It further came down to 75 m^2g^{-1} after 5 h of reaction, implying that carbon deposits blocked most of the zeolite pores, thus resulting in the loss of a greater part of the surface. In fact, heavy deposition of carbon on the surface of functioning catalyst was the main reason leading to deactivation of the catalyst.

Reoxidation by air can regenerate the deactivated 3%W/HZSM-5 catalyst effectively, with the Al/C/O/Si/W molar ratio at the renewed surface recovered to 1.8/~0/64.7/31.7/1.9 and the X_{CH4} and S_{C6H6} regained to 20-18% and *ca*.50%, respectively, after undergoing an induction period of 20 minutes. The results of activity evaluation of the 3%W-1.5%Mn/HZSM-5 catalyst for DHAM reaction after a series of operation/regeneration (by air-oxidation each time for 1 h at 873 K) showed that, it is not until after ten times of regeneration that a small decrease in the catalyst activity was observed (See Fig.3). It seems that the reason leading to the decrease in the catalyst activity was probably due to dealuminization to some degree of the framework structure of HZSM-5 zeolite caused by aqueous vapor resulting from the coke combustion in air-regeneration processes over and over again.

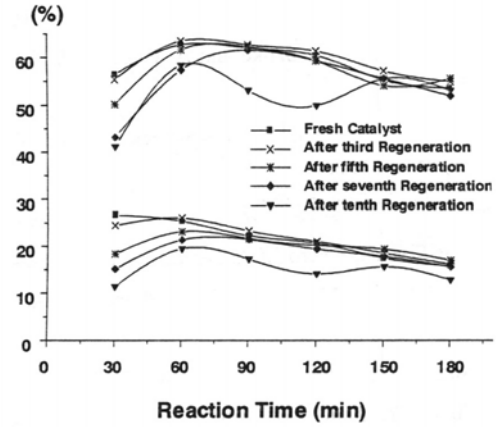

Fig.3 DHAM reactivity over the 3%W-1.5%Mn/HZSM-5 catalyst after undergoing a series of operation/air-regeneration; the below curves for CH_4 conversion and the upper curves for C_6H_6 selectivity.

Action of Promoters Zn, Mn and Li NH_3-TPD study of the W/HZSM-5-based catalysts confirmed that the intensity and concentration of the surface B-acid sites have pronounced effects on the catalyst performance for DHAM reaction. It was found experimentally that, by addition of a proper amount of Mg^{2+}, the strong B-acid sites at the catalyst surface could be effectively eliminated, whereas the addition of a proper amount of Zn^{2+} or Li^+ resulted not only in eliminating most of the strong surface B-acid sites but also in generating a kind of new medium-strong acid sites, mostly B-acid sites, simultaneously. The latter could serve as the catalytically active sites for DHAM reaction. On such medium-strong surface B-acid sites, the formation of coke would be also alleviated to a greater extent. By simultaneous addition of Mg^{2+} and Zn^{2+}, optimized adjustment in surface acidity of the catalyst could be realized. On the other hand, it was indicated experimentally that the doping of the Zn^{2+} or Li^+-component to WO_X matrix would facilitate inhibiting aggregation of the W-containing species and improving dispersion of the W-component at the surface of catalyst, thus bringing about decreasing in the reduction-temperature for the hard-to-be-reduced W^{6+}-species and increasing in quantity of the reducible W^{6+}-species, as has been evidenced by the results of H_2-TPR study on the reducibility of the Zn^{2+}(or Li^+, Mn^{2+})-promoted W/HZSM-5 system. The above two roles that Zn^{2+}, Mn^{2+} and Li^+ as promoters played both contributed to the persistence of high methane conversion and benzene selectivity, and the alleviation of coke deposition, as well as the prolongation of the catalyst lifetime.

Acknowledgment

This work was supported by the National Priority Fundamental Research Project (No: G1999022400) of China.

References

[1] Wang, L.; Tao, L.; Xie, M.; *et al.*, *Catal. Lett.*, 1993, *21*, 35.
[2] Wang, D. J.; Lunsford, J. H.; Rosynek, M.P., *J. Catal.*, 1997, *169*, 347.
[3] Solymosi, F.; Szoke, A.; Cserenyi, J., *Catal. Lett.*, 1996, *39*, 157.
[4] Ohnishi, R.; Liu, S.; Ichikawa, M., *J. Catal.*, 1999, *182*, 92.
[5] Zeng, J.-L.; Xiong, Z.-T.; Zhang, H.-B.; *et al.*, *Catal. Lett.*, 1998, *53,* 119.
[6] Xiong, Z.-T.; Zhang, H.-B.; *et al.*, *Catal. Lett.*, 2001, *74(3-4)*, 227.
[7] Xiong, Z.-T.; Zhang, H.-B.; *et al.*, *Catal. Lett.*, 2001, *74(3-4)*, 233.

CATALYTIC DEHYDROGENATION OF AROMATIC HYDROCARBON WITH CARBON DIOXIDE AS AN OXIDANT

Jong-San Chang, Min Seok Park, Vladislav P. Vislovskiy, Sang-Eon Park, and Jin S. Yoo

Catalysis Center for Molecular Engineering,
Korea Research Institute of Chemical Technology (KRICT),
P.O. Box 107, Yusung, Taejon 305-600, Korea

Introduction

For the mitigation of global warming due to carbon dioxide, catalytic conversion of CO_2 has been extensively studied for last decade.[1] Most of studies on this field have been concentrated on the utilization of carbon dioxide as a carbon source through catalytic reduction processes with various kinds of reductants.[1] Particularly, hydrogen has long been used to abstract the oxygen atom of CO_2 for catalytic conversion into useful chemicals.[2] However, catalytic hydrogenation is confronted with some limitations to be commercialized because in most cases the cost of hydrogen from conventional sources such as steam reforming of hydrocarbons is not cheaper than that of chemicals obtained from catalytic hydrogenation. However, the utilization of CO_2 as a mild oxidant and an oxygen transfer agent is recently attracting considerable attention.[3-5] This approach is expected to open new technology for CO_2 utilization. It has been proposed that the oxygen species of carbon dioxide is useful for oxidative conversions of hydrocarbons.[6-8] Krylov and Mamedov have studied on the oxidative conversions of alkanes, alkenes, and alcohols with carbon dioxide over Mn oxide-based catalysts.[9] Yoo *et al*. showed that Fe/Mo/borosilicate catalyst could activate CO_2 which could be functioning as a promoter and co-oxidant for the gas-phase oxidation of alkylaromatics with oxygen as well.[2]

Styrene is commercially produced by dehydrogenation of ethylbenzene (EB) using potassium-promoted iron oxide catalysts with a large excess of superheated steam. However, the use of steam has a drawback of losing latent heat of condensation during subsequent separation in the commercial process. The energy consumption required for the EB dehydrogenation using carbon dioxide is estimated to be much lower than that for the currently operating process using steam.[10] In addition to energy saving, the use of CO_2 with replacement of steam can give a beneficial advantage for increase in equilibrium conversion. Considering these aspects, it is desirable to design a new catalytic system based on the use of carbon dioxide instead of steam. Some selected catalytic systems show promoting effects in the presence of carbon dioxide.[4,6,11] In particular, we have reported that, in the case of zeolite-supported iron oxide catalysts, carbon dioxide exhibits beneficial effects on improving catalytic activity and preventing coke formation.[6]

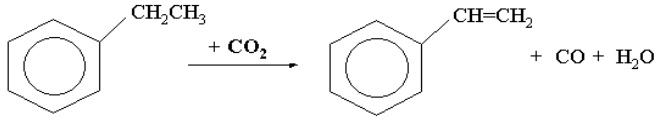

This work deals with dehydrogenation of aromatic hydrocarbons, especially ethylbenzene using CO_2 as an oxidant. We suggest catalysts to exhibit high activity and excellent selectivity for styrene with the help of carbon dioxide as an oxidant.

Experimental

Catalyst Preparation. γ-Al_2O_3-supported iron oxide catalyst (Fe/γ-Al_2O_3) was prepared by depositing iron(II) sulfate solution onto supports at the temperature range 60 - 70°C under nitrogen atmosphere to prevent the dissolution of oxygen.[6] It was precipitated at pH = 10 - 11 with ammonia water. The precipitates were filtered, dried at 80°C in vacuum oven, and calcined under a nitrogen stream at 700°C for 4 h. Al_2O_3-supported vanadium oxide (V_2O_5/Al_2O_3) or vanadium-antimony binary oxide (V-SbO_x/Al_2O_3) catalysts were prepared by impregnation of aqueous solutions of ammonium metavanadate and antimony (III) chloride onto activated alumina. The impregnated sample was dried at 100°C and then calcined in air at 600°C for 4 h. For V_2O_5/Al_2O_3, the content of V_2O_5 was 20.0 wt%. For V-SbO_x/Al_2O_3, the content of V_2O_5 and Sb_2O_3 was 7.5 wt% and 15.5 wt%, respectively.

Catalytic Measurement. The EB dehydrogenation into styrene was carried out in a micro-activity test unit (Zeton, MAT 2000) with a fixed bed reactor at 600°C under atmospheric pressure. A sample of 1g was placed on a fritted metal disk in the reactor. Before reaction, the catalyst was treated in a nitrogen stream from RT to 600°C with a heating rate of 10°C/min. Ethylbenzene was introduced by syringe pump and supplied into the reactor by a carrier gas with flow rate of 20 ml/min. The liquid and gas products were analyzed by GC (Donam Corp., DS6200) equipped with FID and TCD, respectively. Effluent gases from the reactor were analyzed by a gas chromatograph (Chrompack CP9001) equipped with a thermal conductivity detector (TCD).

Results and Discussion

Steam is generally utilized as diluent in dehydrogenation of aromatic hydrocarbonds and oxygen works as strong oxidant in oxidative reactions of aromatic hydrocarbons. However, carbon dioxide can be utilized as both oxidant and diluent since it can release oxygen as surface oxygen species upon activation on reduced or oxygen-deficient catalyst surface and it has high heat capacity. It can be confirmed that CO_2 plays a key roles as oxidant and diluent in EB dehydrogenation using carbon dioxide instead of steam. **Table 1** displays the effect of carrier gas in EB dehydrogenation over 5 wt% Fe/γ-Al_2O_3 catalyst. It is clearly seen that carbon dioxide works very well in EB dehydrogenation as the soft oxidant and diluent to increase the conversion as well as selectivity. The order of catalytic activity and selectivity for styrene according to carrier gas was CO_2 > N_2 > H_2O. Such dependence of the activity on carrier gas is just contrary to that of commercial catalyst. Considering that conversion of CO_2 took place together with EB conversion, the enhancement of the dehydrogenation activity and the selectivity is certainly ascribed to the promotional effect of excess carbon dioxide to the oxidative process. This result implies that the initial hydrogen abstraction at benzylic C-H bond of EB was much facilitated by carbon dioxide.

Table 1. Effect of carrier gas in EB dehydrogenation over Fe/γ-Al_2O_3 catalyst[a]

Carrier Gas	X(EB), %	S(SM), %	X(CO_2), %	H_2O/H_2[b]
N_2	63.7	95.8	-	-
H_2O	25.0	88.8	-	-
CO_2	68.5	97.2	47.4	1.7

[a]Reaction conditions: Temp. = 600°C, LHSV = 1.0 h^{-1}, CO_2(N_2 or H_2O)/EB = 10/1, Time-on-stream = 4 h. [b]relative concentration to EB.

Crystalline iron oxides have not been apeared on XRD pattern of Fe/γ-Al_2O_3 catalyst, suggesting that iron oxide phase is amorphous and is well dispersed. Characterization results revealed that the oxidation state of iron oxide over γ-alumina is between γ-Fe_2O_3 and Fe_3O_4. These two phases in the catalyst seem to be interconvertible during EB dehydrogenation with CO_2. There may be optimal population of iron oxide phase between γ-Fe_2O_3 and Fe_3O_4 to show high activity. The surface basicity upon the introduction of iron oxide onto γ -Al_2O_3 support was not changed so much. It is known that a Fe_3O_4 spinel oxide, so-called magnetite is basically oxygen deficient enough to activate carbon dioxide at elevated temperature.[12] In our previous work, it has been considered that oxygen deficiency of iron oxide in the supported catalyst is one of the most important factors on promoting the catalytic activity in the presence of CO_2.[6] Oxygen-deficient sites of the supported iron oxide catalyst seem to produce CO efficiently from the CO_2 dissociation, and the adsorbed oxygen on the catalyst surface can also play a role on hydrogen abstraction from EB. Dispersion of the oxygen-deficient sites or oxygen defects in the supported iron oxide catalysts appears to be more efficient for the CO_2 dissociation and thereby the oxidative dehydrogenation of EB. Therefore, it is assumed that high activity of Fe/γ-Al_2O_3 in the presence of CO_2 is mainly due to the presence of Fe^{2+} species and its oxygen deficiency.

Figure 1 displays the catalytic results for EB dehydrogenation with CO_2 over V_2O_5/Al_2O_3 and V-SbO_x/Al_2O_3 catalysts at 600°C. These catalysts exhibited very high conversion (>75%) and high selectivity (>95%) at initial stage. However, catalytic activity of V-SbO_x/Al_2O_3 was higher than that of V_2O_5/Al_2O_3 and, moreover, its stability was much better than that of the unpromoted one. It has been proposed that redox behavior of vanadium oxide-based catalysts played a key role in accordance with Mars-van-Krevelen mechanism in oxidative dehydrogenation of alkylaromatics.[13] Likewise, EB dehydrogenation with CO_2 is expected to follow the same mechanism. Vanadium oxide with V^{5+} is generally considered as an active component. Deactivation of supported vanadium oxide catalysts was

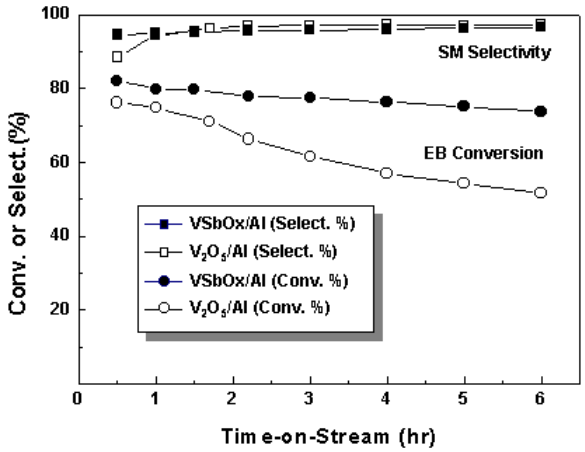

Figure 1. Comparison of catalytic activities of V_2O_5/Al_2O_3 and V-SbO_x/Al_2O_3 catalysts. Reaction conditions: Temp. = 600°C, LHSV = 1.0 h^{-1}, CO_2/EB = 1/1.

occurred by deep reduction of V^{5+} into V^{3+} and coke formation. The introduction of Sb oxide into V_2O_5/Al_2O_3 led to preventing the deep reduction of the oxidation state of vanadium and facilitating the redox cycle, resulting in enhancement of the catalyst stability as well as the catalytic activity. Carbon dioxide for this reaction acted as the soft oxidant to provide oxygen species on reduced catalyst surface and, consequently, reoxidize the reduced vanadium species.

There are two possible pathways for EB dehydrogenation to styrene. The simple dehydrogenation of EB that produces styrene and hydrogen occurs under nitrogen or even carbon dioxide atmosphere, while the oxidative dehydrogenation of EB that produces styrene, carbon monoxide, and water occurs under carbon dioxide atmosphere. During the reaction, carbon monoxide and hydrogen in the gas phase were observed together with a trace of methane. Considering the gas product distribution, the ratio of H_2O/H_2 in the product stream is estimated to be 1.7 for Fe/γ-Al_2O_3 and 1.4 for V-SbO_x/Al_2O_3, respectively, after 4 h on stream. The formation of water as well as carbon monoxide implies that CO_2 molecule over catalyst surface is dissociated with CO and surface oxygen, which can abstract hydrogen from EB and then results in the generation of water. Taking into account the formation of large amount of water, high activity for supported iron oxide and supported vanadium catalysts under CO_2 carrier may be mainly ascribed to oxygen species dissociated from carbon dioxide molecule, thus due to the promotion of the oxidative process by carbon dioxide. In other words, this indicates that carbon dioxide plays a role as an oxidant in EB dehydrogenation on supported iron oxide and vanadium oxide catalysts.

Conclusions

This work demonstrates that the utilization of carbon dioxide as an oxidant is very useful for oxidative dehydrogenation of aromatic hydrocarbon such as ethlbenzene. In dehydrogenation of ethylbenzene over supported iron oxide and vanadium oxide catalysts, carbon dioxide plays a key role as an oxidant to increase catalytic activity and selectivity to styrene.

Acknowledgment

This work was performed for the Greenhouse Gas Research Center, one of the Critical Technology-21 Programs, funded by the Ministry of Science and Technology of Korea (MOST). VPV thanks the MOST for the visiting scientist fellowship. We also thank Daebo Industries Co.(Korea) for financial support.

References

1. Delmon, B., Yates, J.T., Advantages in Chemical Conversions for Mitigating Carbon Dioxide, Studies in Surface Science and Catalysis, Vol. 114, Elsevier: Amsterdam, 1998.
2. Arakawa, H., *Stud. Surf. Sci. Catal*., **1998**, 114, 19.
3. Yoo, J.S., *Catal. Today*, **1998**, 41, 49.
4. Park, S.-E., Yoo, J.S., Chang, J.-S., Environmental Challenges and Greenhouse Gas Control for Fossil Fuel Utilization in the 21st Century (eds. M.M. Maroto-Valer, Y. Song, C. Song), Chapter 33, Kluwer Academic/Plenum: New York, 2002.
5. Aresta M., Tommasi I., Quaranta E., Fragale C., Mascetti J., Tranquille M., Galan F., Fouassier M., *Inorg. Chem*., **1996**, 35, 4254.
6. Chang, J.-S., Park, S.-E., Park, M.S., *Chem. Lett.*, **1997**, 1123.
7. Choi, Y.-S., Park, Y.-K., Chang, J.-S., Park, S.-E., Cheetham, A.K., *Catal. Lett*., **2000**, 69, 93.
8. Ohtsuka, Y, *J. Catal.,* **1999**, 186, 160.
9. Krylov, O.V., Mamedov, A. Kh., *Ind. Eng. Chem. Res.,* **1995**, 34, 474.
10. Mimura, N., Takahara, I., Saito, M., Hattori, T., Ohkuma, K., Ando, M., *Catal. Today*, **1998**, 45, 61.
11. Mimura, N., Saito, M., *Catal. Lett*., **1999**, 58, 59.
12. Tamaura, Y., Tabata M., *Nature*, **1990**, 346, 255.

13. Rizayev, R.G., Mamedov, E.A., Vislovskii, V.P., Sheinin, V.E., *Appl. Catal. A*., **1992**, 83, 103.

CATALYTIC BEHAVIOR OF CALCIUM OXIDE FOR SYNTHESIS OF DIMETHYL CARBONATE FROM PROPYLENE CARBONATE AND METHANOL

Tong Wei, Wei Wei, Mouhua Wang, Yuhan Sun, Bing Zhong*

State Key Laboratory of Coal Conversion Institute of Coal Chemistry Chinese Academic of Sciences, Taiyuan, 030001

*To whom corresponding should be addressed.
Fax: +86 351 4041153
E-Mail: yhsun@sxicc.ac.cn or weiwei@sxicc.ac.cn

Introduction

Dimethyl carbonate (DMC) is an important precursor of polycarbonate resins as well as a useful carbonylation and methylation agent [1]. Because of the negligible toxicity of DMC, it is promising as a substitute for phosgene, dimethyl sulfate, or methyl iodide. DMC can be prepared by the oxidative carbonylation of methanol, carbonylation of methyl nitrite or transesterification of cyclic carbonate with methanol [2]. Because of the moderate reaction conditions and the use of CO_2 as raw material, transesterification method, as shown follow, has gained increasing attention in recent years.

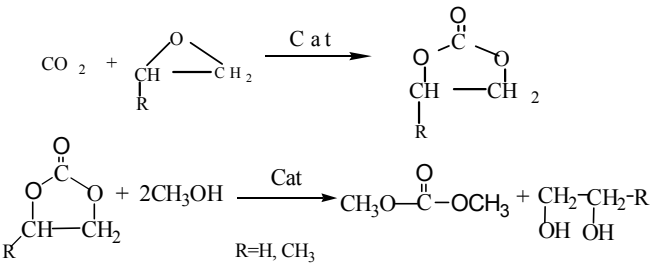

In present paper, CaO calcined from $CaCO_3$, which shows excellent catalytic activity, is used as solid base catalyst for the rudimental investigation of its catalytic behavior for synthesis of DMC from propylene carbonate (PC) and methanol (MeOH) as well as the mechanism of this reaction over CaO.

Experimental

CaO was prepared from $CaCO_3$ calcined at 1173K in N_2 atmosphere. The reaction was carried out in a 250mL flask equipped with reflux condenser, water bath and magnetic stirring. Except particular description, catalyst was added into the flask accompanied with violent magnetic stirring after the temperature reached to the expected one. Reaction product was analyzed by Gas Chromatograph after centrifugal separation of solid catalyst from liquid.

Result and discussion

Fig.1and Fig.2 shows the effect of temperature on DMC yield and DMC selectivity. It can be seen that CaO shows excellent catalytic activity for synthesis of DMC from PC and MeOH so that the reaction even can reach equilibrium in 60 minutes at 10℃. With the increase of temperature, equilibrium DMC yields decrease gradually. As for DMC selectivity, while it increase firstly then decrease gradually at 10℃ and 20℃, it decrease gradually all along at 30℃,40℃ and 50℃with the prolong of reaction time. This reaction is a little exothermic with $\Delta_r H$=-7.092kJ/mol [3-6], therefore, the increase of temperature would result in equilibrium constant decrease and the consequent decrease of equilibrium DMC yield. Since Knifton reported that hydroxyethyl methyl carbonate, which could be detected only at short reaction time and/or low temperature, was intermediate when MeOH reacted with ethylene carbonate to generate DMC and ethylene glycol, hydroxypropyl methyl carbonate (HMC) may be the intermediate of reaction in present paper. On the other hand, the intermediate can also react with PC continually to generate polymeric propylene carbonate (PPC) with the rate much slower than that of subject reaction. Thus the by-product is mainly intermediate--HMC before the reaction reach equilibrium, and is mainly PPC after reaction reach equilibrium, which is good explanation of white colloidal solid produced from MeOH and PC reacting 2hr at 120℃.The increase of temperature can promote the polymerization of PC and consequently result in the decrease of DMC selectivity.

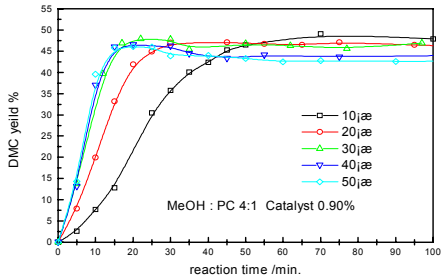

Fig.1 Effect of temperature on DMC yield

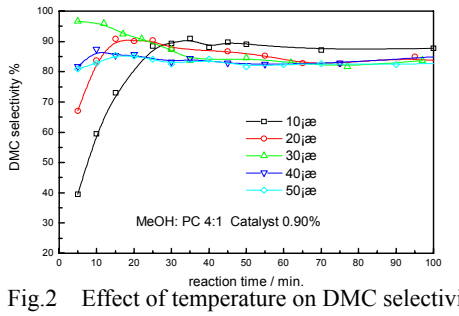

Fig.2 Effect of temperature on DMC selectivity

The effect of catalyst concentration on DMC yield and DMC selectivity is illustrated in Fig. 3 and Fig. 4. It can be seen that DMC equilibrium yield keep constant as catalyst concentration increase from 0.61% to 1.80%, which means that catalyst concentration have no effect on reaction equilibrium but can increase reaction rate. On the other hand, when catalyst concentration is 0.61% and 0.91, the variance of DMC selectivity with the prolong of reaction time like that at low temperature, which means that the decrease of catalyst concentration can decrease the reaction rate of HMC with MeOH and thus increase the concentration of HMC at short time. Furthermore, the increase of catalyst can promote the polymerization of PC and consequently result in the decrease of DMC selectivity.

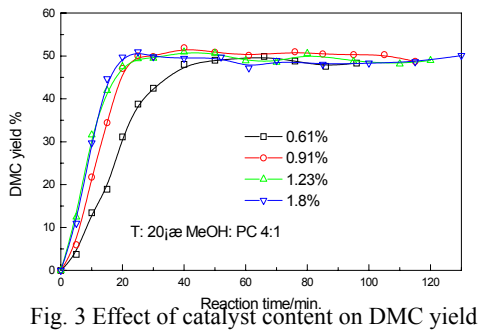

Fig. 3 Effect of catalyst content on DMC yield

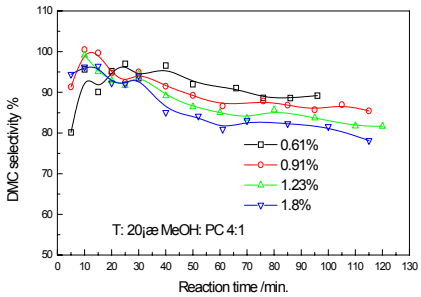

Fig. 4 Effect of catalyst content on DMC selectivity

The effect of the ratio of MeOH and PC on DMC yield and DMC selectivity is shown in Fig.5 and Fig. 6. It can be seen that equilibrium DMC yield increase gradually with the increase of the ratio of MeOH and PC. This reaction is reversible; therefore the increase of MeOH concentration can make equilibrium PC conversion increase and the subsequent increase of equilibrium DMC yield. From Fig. 6 we can see that on the one hand, DMC selectivity-time curve, liking that at low temperature, increase firstly then decrease gradually with low ratio of MeOH and PC, on the other hand, DMC selectivity increase gradually with the increase of the ratio of MeOH and PC after the reach of equilibrium. The decrease of the ratio of MeOH and PC means the decrease of MeOH concentration, which makes the reaction rate of HMC and MeOH decrease and consequent increase of HMC concentration at short time. At the same time the polymerization of PC is competitive with subject reaction. The increase of MeOH concentration can inhibit this side reaction and make DMC selectivity increase.

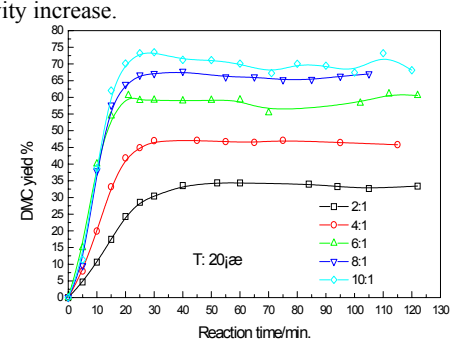

Fig. 5 Effect of MeOH to PC ratio on DMC yield

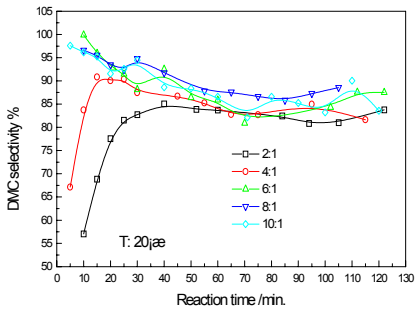

Fig 6. Effect of MeOH to PC ratio on DMC selectiviy

In order to further understand the mechanism of this reaction on the catalyst, the effect of addition method, temperature, catalyst concentration and the ratio of MeOH and PC on reaction rate are studied. Fig. 7 shows that there is an induction period in rate-time curve when MeOH and PC was added first as well as the PC and catalyst was added first, which means that the induction period comes from the activation of MeOH on solid base catalyst. On the other hand, the reaction rate is faster for MeOH and PC being added firstly than that of PC and catalyst being added firstly, which may be caused by activation of PC by H-bond between PC and MeOH. Therefore the catalytic mechanism of CaO may be as follow:.

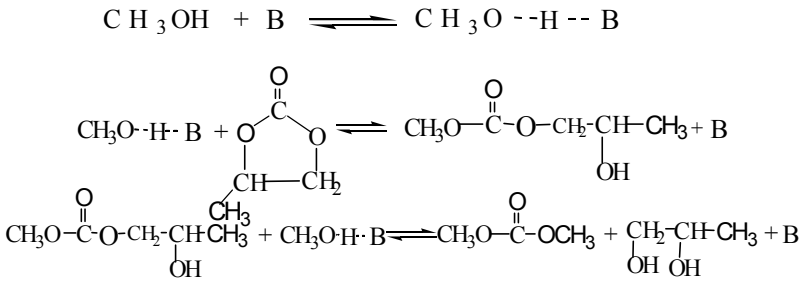

Fig. 8 shows the effect of temperature on reaction rate. The maximum rate increase and the induction period is shortened with the increase of temperature. At the beginning of the reaction, the concentration of activated MeOH is low, so the activation of MeOH has an important effect on DMC production rate, then after the activation step reach equilibrium, the surface reaction of activated MeOH with PC becomes an important factor that influence the rate of DMC production. The increase of temperature can promote the rate of all steps and consequently result in the maximum rate increase and the induction time shortened.

As for effect of catalyst concentration shown in Fig.9, the maximum rate increase and the induction period is shortened with catalyst concentration increase from 0.61% to 1.23%, but the rate-time curve almost unchanged when catalyst concentration increase from 1.23% to 1.84%. The increase of catalyst concentration can result in the increase of both MeOH activation rate and equilibrium activated MeOH concentration, so the maximum rate increase and the induction time is shortened with the increase of catalyst content. However, when the catalyst concentration reach certain amount, it is not an important factor that affect MeOH activation rate and equilibrium activated MeOH any more, therefore the reaction rate-time curve doesn't change with the continue increase of catalyst concentration.

As far as the effect of the ratio of MeOH and PC is concerned, the induction period is shortened with the increase of the ratio of MeOH and PC, but the maximum rate increase when the ratio of MeOH and PC increase from 2:1 to 6:1first, and then decrease when MeOH to PC ratio continual increasing from 6:1 to 10:1. With the increase of MeOH to PC ratio both MeOH activation rate and equilibrium activated MeOH concentration increase, but PC concentration decrease, thus although the induction time was shorten due to the increase of the ratio of MeOH and PC ratio, but the surface raction rate of activated MeOH with PC increase first then decrease with the increase of the ratio of MeOH and PC.

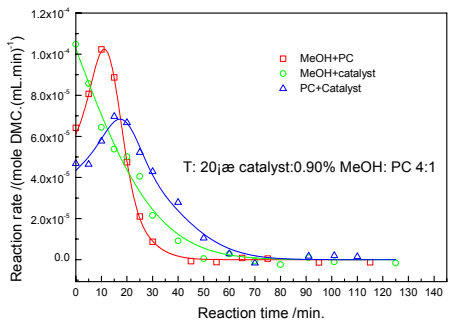

Fig. 7 Effect of addition method on reaction rate

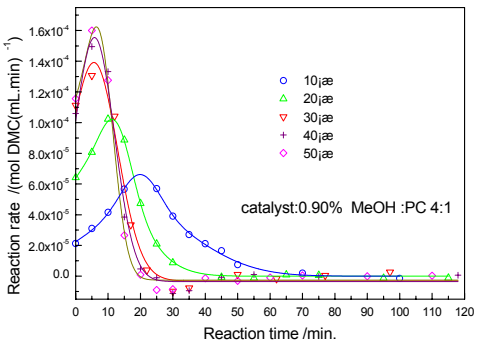

Fig 8 Effect of temperature on reaction rate

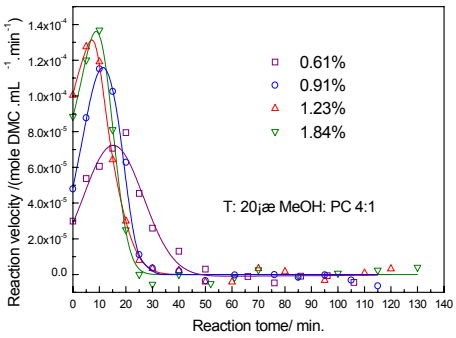

Fig. 9 Effect of catalyst content on reaction rate

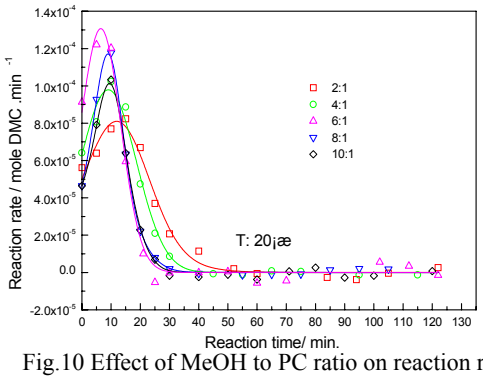

Fig.10 Effect of MeOH to PC ratio on reaction rate

Conclusion

1 CaO calcined from $CaCO_3$ shows excellent catalytic activity for synthesis of DMC from MeOH and PC. The reaction even can reach equilibrium in 60 minutes at 10℃。

2 The main function of CaO is the activation of MeOH and the consequent promotion of MeOH and PC reaction. The H-bound between MeOH and PC can activate PC and make reaction rate increase.

3 Relative low temperature and high ratio of MeOH and PC is preferable for high DMC yield and selectivity. Increase of catalyst concentration has little effect on DMC yield but make DMC selectivity decrease.

Reference

(1)Watanabe, Y.; Tatsumi, T. Microporous and mesoporous materials 1998, 22,399~407

(2) Pacheco, M. A.; Marshall, C. L. *Energy & Fuels* 1991, 11, 2~29

(3) Yin,Y.; Xi, Zh.; Li, D. *Physical Chemistry*. 3rd edition, Higher Education Press, Beijing, 1994, PP. 569

(4) Dong, Z. *Hangzhou Chemical Engineering* 1979, 3, 39~96

(5) Reid, R.C.; Prausnitz, J.M.; Poling, B.E. *The properties of Gases and Liquids*, 4th edition, McGraw-Hill Company, 1987, PP.683

(6) Steele, V.; Chirico, R. P.; Knipmeyer, S. E.; Nguyen, A.; Smith, N. K. *J. Chem. Eng. Data*. 1997, 42, 1031~1052

(7) Knifton, J.F., Duranleau, R.G. *Journal of molecular Catalysis*, 1991, 67, 389~399

TOWARDS AN UNDERSTANDING OF CATALYSIS FOR THE SIMULTANEOUS CONVERSION OF GREENHOUSE GASES

Yuan Kou

College of Chemistry and Molecular Engineering, Peking University, Beijing 100871, China

1. NO_X-catalyzed homogeneous partial oxidation of CH_4 to syngas

Our recent studies show that under both weak and strong oxidizing conditions (O_2/CH_4 = 1.5-5.0), NO_x can act as a good catalyst for the partial oxidation of methane to CO without the use of any solid catalyst. Under weak oxidizing conditions (O_2/CH_4 = 1.5) in the absence of NO_X, the oxidation of CH_4 requires temperatures higher than 850 °C. Addition of NO initiates the reaction at a much lower temperature arround 550 °C, and the selectivity to CO is about 40% at a temperature of 650 °C.

Table 1 CH_4 conversion and CO selectivity in the partial oxidation of methane [a]

NO /ppm	Flow rate /ml min^{-1}	Temperature range of CO formation /°C	CO selectivity (maximum)[b] (%)	CH_4 conversion at CO maximum (%)	Temperature of CO maximum /°C	$T_{50\%}$ /°C	TOF[d] $/s^{-1}$
/	20	800-880	16	79	868	866	/
/	40	840-920	25	42	910	911	/
/	80	875-	30[c]	54[c]	>950	950	/
200	40	540-760	66	88	630	595	5
600	20	520-760	68	83	610	590	9
600	40	560-780	69	90	645	612	9
600	80	570-840	67	94	680	635	13

[a] Reaction conditions: CH_4 : 0.4 mol%; O_2 : 2 mol%; temperatures: 200-950 °C. [b] CO selectivity: mol CO · (mol CO + mol CO_2 + mol CH_4)$^{-1}$ [c] Values measured at 950 °C [d] Values measured at 650 °C

Under strong oxidizing conditions (O_2/CH_4 = 5.0), NO_X also exhibits considerable catalytic activities and selectivities for the conversion of methane to CO. The results are summarized in Table 1. It can be seen that, in the absence of NO, the initial temperatures required for the activation of CH_4 are higher than 800 °C. In the presence of NO, however, the temperatures required are reduced to below 570 °C. The lowest temperature for the activation of CH_4 is only 520 °C. In all the experiments shown in Table 1, no decrease in NO/NO_2 concentration (based on the area of infrared absorption peak) is observed up to 950 °C, indicating that NO_2 and other possible nitrogen oxides cannot be reduced by CH_4 without a solid catalyst. NO-catalyzed partial oxidation of methane is a highly selective reaction for production of CO (68%). The highest TOF value (40 methane molecules converted per second per NO) is obtained at an NO concentration of 100 ppm, suggesting that the reactions described here are a gas-phase homogeneous catalytic reaction.

2. Biomass-based partial reduction of SO_2

$Na_2CO_3/\gamma\text{-}Al_2O_3$ has been employed as a regeneratable sorbent for SO_2 removal. Utilization of biomaterials or abandoned biomaterials (BIOM), treatments of which usually produces a great amount of CO_2, to take the place of alumina is a creative new approach to this problem. The BIOM includes farmland straw, rice husks and stalks, dried branches and leaves, waste paper and similar materials,. The breakthrough and stoichiometric SO_2 adsorption efficiencies of a biomass supported Na_2CO_3 system (80wt%Na_2CO_3/straw) reached 48.9% and 80.6% respectively at a desulfurization temperature of 80 °C. It should be noted that the reduction properties of cellulose-based materials like BIOM have been reported previously. Based on previous work and this study, a more efficient and complete flue gas desulfurization (FGD) process can be proposed. The key steps in the proposed process are the enrichment of SO_2 by Na_2CO_3/BIOM, and the subsequent reduction of SO_2 to S by BIOM via reaction (1):

(1) $C_6H_{10}O_5 + 6SO_2 \longrightarrow 6S + 6CO_2 + 5H_2O$ A suitable catalyst will be needed for this reaction, and further studies are being carried out in this laboratory.

3. CO_2-related aromatization of lower alkanes including methane

Conversion of C_1-C_3 alkanes in the presence of CO_2 has been investigated for years. What role the CO_2 plays under the reaction conditions and what products may be obtained from the reaction is still unclear however. Thermodynamic analyses as well as reaction studies have shown that both SAMCA (simultaneous activation of methane and carbon dioxide to aromatics) and SCACA (simultaneous conversion of alkanes and carbon dioxide to aromatics) are more thermodynamically favorable than other reactions reported to occur in the CH_4 (C_2H_6/C_3H_8)-CO_2 co-feed. For example, in comparison with aromatization of CH_4 without free-oxygen or oxidation of CH_4 by CO_2 to produce C_2H_4, reactions (2) and (3) are more thermodynamically feasible, suggesting that all studies of the conversion of lower alkanes in the presence of CO_2 as either an additive or a by-product should carefully check whether some aromatics are formed in the product mixture.

(2) $4CH_4 + 2CO_2 \rightarrow C_6H_6 + 4H_2O + H_2$ (ΔH_{1073} = 218.5 kJ/mol C_6)

(3) $5CH_4 + 2CO_2 \rightarrow C_7H_8 + 4H_2O + 2H_2$ (ΔH_{1073} = 272.2 kJ/mol C_7)

CO_2 AND CO METHANATION OVER TWO DIFFERENT NICKEL LOADING NI/TIO_2 CATALYSTS

Changwei Hu[*], *Dong-mei Tong*

Faculty of Chemistry
Sichuan University
Chengdu, 610064, China

Introduction

Ni-based catalysts can catalyze the methanation of both CO and CO_2. Adsorbed carbon species C(a) and CO(a) formed in CO methanation on nickel can be transformed into CH_4 through the same way as those in CO_2 methanation[1]. It is also found that different active phases which exhibit different methanation activities for CO with CO_2 can form on Ni/Al_2O_3 catalysts under different activation conditions[2]. TiO_2 supported metal catalyst is typical to exhibit strong metal-support interaction, and the methanation of CO on Ni/TiO_2 is widely studied. However, the methanation of CO_2 on Ni/TiO_2 as well as the effect of treatment under reaction conditions on the structure and properties of Ni/TiO_2 has rarely been studied. In present work, two different nickel loading Ni/TiO_2 catalysts are used to study comparatively the methanation of CO and CO_2. The structure and properties changes of the samples under thermal treatment in CO+H_2 and CO_2+H_2 ambience are also studied.

Experimental Section

The catalysts were prepared by wet impregnation on which the amount of the nickel loading was controlled by concentration of nickel nitrate solution. The amount of nickel loading on the two catalysts was 3.53mass% and 9.31mass%, and named catalyst-1 and catalyst-2 respectively. Hydrogen adsorbance on reduced catalysts was detected by pulse chromatographic technique[2,3]. Methanation experiments were carried out in a fixed-bed quartz reactor with the same method described previously[2]. Catalysts were activated stepwisely at 523K, 573K, 673K and 723K under CO_2+H_2 mixture, and then switched to CO+H_2 mixture. Another cycle was carried out first in CO+H_2 mixture, and then in CO_2+H_2 mixture.

Results and Discussion

Catalyst-1 can be activated at 573K under CO_2+H_2 mixture to show CO_2 methanation activity. High temperature(723K) destroys the active phase formed at low temperature(523K) because CO_2 methanation activity at low temperature over the catalyst activated at 723K is lower than that when activated at 523K, as shown in **Figure 1(I)**. The active phase formed at 723K in CO_2+H_2 flow shows low activity of CO methanation. The same fresh sample does not show CO methantion activity (about 3.4μmol/min•g) until activated at 723K in CO+H_2 ambience, and the active phase thus formed cannot catalyze CO_2 to form CH_4. It suggests that the active phase formed in CO_2+H_2 ambience at 723K can catalyze CO methanation, but the active phase formed in CO+H_2 ambience at 723K cannot show CO_2 methanation activity. In another word, CO_2 and CO methanation can proceed on different active phases.

The results obtained over catalyst-2 for CO_2 and CO methanation are shown in **Figure 2,** they are similar to those on catalyst-1. Catalyst-2 can be activated at lower temperature(523K) to show methanation activity than catalyst-1 in CO_2+H_2 ambience. It is attributed to the high nickel loading. When the same sample is activated first under CO+H_2 ambience, then switched to CO_2+H_2 mixture, the similar phenomenon to catalyst-1 is observed. It also suggests that CO_2 and CO methanation can be catalyzed by different active phases formed on nickel loading Ni/TiO_2 catalyst.

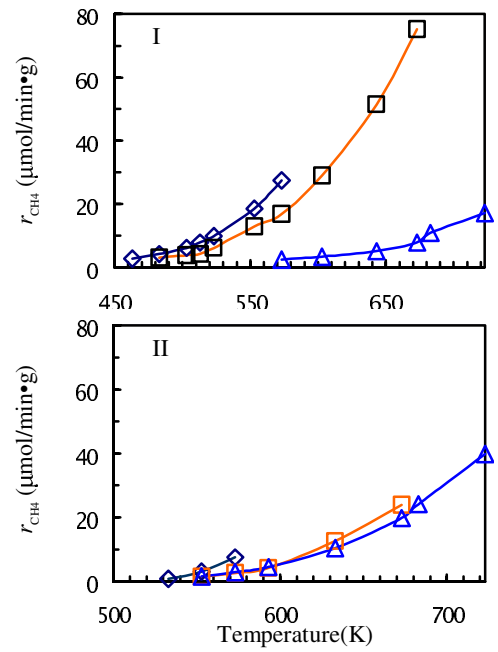

Figure 1. The methanation activity in terms of the formation of CH_4 on catalyst-1 activated under CO_2 +H_2 mixture(I), then switched to CO+H_2 mixture(II) at◇573K, □673K, △723K.

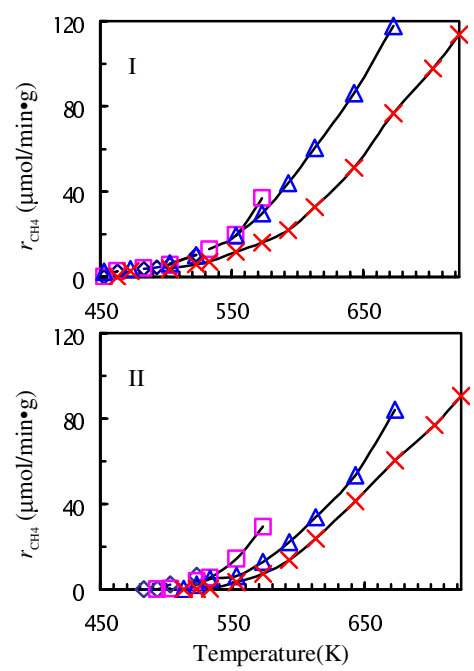

Figure 2. The methanation activity in terms of the formation of CH_4 on catalyst-2 activated unαder CO_2 +H_2 mixture(I), then switched to CO+H_2 mixture(II) at.523K, .573K, .673K, .723K

[*] Corresponding author. E-mail:chewhu@mail.sc.cninfo.net

Hydrogen adsorbance at room temperature on catalyst-1 decreases with reduction temperature, while it increases with reduction temperature on catalyst-2, as shown in **Table 1**. It indicates that the initiation of strong metal-support interaction at low temperature(573K) on low nickel loading catalyst is more easier than on high nickel loading catalyst, and the SMSI is affected by the nickel loading. The results of the hydrogen adsorbance could be compared with the results of methanation, it is seen that SMSI is one of the reasons for the methanation activities to decrease when the catalysts are activated at high temperature. The phenomenon could be explained by electronic effect, the extent of electron transfer from support to a small metal particle is much easier than that to a large one[4].

Table 1. The hydrogen adsorbance at room temperature over catalysts after reduction at different temperature.

reduction temperature (K)		523	573	673	723
H_2 adsorbance (mol/gcatal.)	catalyst-1	0.0344	0.0333	0.0209	0.0081
	catalyst-2	0.0123	0.0172	0.0206	0.0215

Conclusion

The active phase formed in CO_2+H_2 ambience can catalyze CO methanation, but the active phase formed in CO+H_2 ambience cannot show CO_2 methanation activity on nickel loading Ni/TiO_2 catalyst. CO_2 and CO methanation can be catalyzed by different active phases. A Ni/TiO_2 catalyst with a low nickel loading can fall into SMSI state more easily than that with a higher one.

Acknowledgment

The authors are grateful for the financial support by the Special Research Foundation of Doctoral Education of China (No. 2000061028) and the Foundation of Science and Technology of Sichuan Province (No. 200018-16).

References

1. Shin-ichiro Fujita, Hiroyuki Terunuma, Masato Nakamura, and Nobutsune Takezawa, Ind. Eng. Chem. Res. 1991,30,1146-1151.
2. Chang-Wei Hu, Jie Yao, Hua-Qing Yang, Yu Chen, and An-Min Tian, J.Catal.,1997, 166,1
3. Wang Hua-Ming, Lu Quan-Jie, Zhou Xue-Kai, Huaxue Tongbao, 1987,(1),30-32.
4. Di Li, Nobuyuki Ichikuni, Shogo Shimazu, and Takayoshi Uematsu, Appl.Catal.A:General, 1999, (180), 227-235.

CATALYTIC OXIDATION OF METHANE OVER Co/Mn MIXED OXIDES: THE WATER EFFECT

W. B. Li, Y. Lin, and Y. Zhang

Department of Environmental Science and Engineering
Tsinghua University
Beijing 100084, P. R. China

Introduction

Natural gas has been used as clean fuels in a variety of combustion processes, such as electrical utilities and motor vehicles. Catalytic combustion of methane without flame can not only improve the energy efficiency but also reduce the formation of thermal nitric oxide by lowering combustion temperatures.

Pd based noble metals have been reported as active catalysts for methane combustion. Besides high cost concerns, supported Pd catalysts usually deactivated by water vapor regardless of the type of the supports used, such as Pd/Al_2O_3,[1] Pd/SnO_2[2] and Pd/ZrO_2[3,4]. Most of the research works on metal oxides have been focussed on perovskite oxides[5], only few studies have been devoted to single oxides such as Au, Ag, Fe, and Mn containing metal oxides partly because of their relatively easy deactivation by sintering. On the other hand, considering a great number of literatures on methane oxidation, inhibition by the reaction products, viz., CO_2 and water has not been given much attention.[1] It is recently found in our laboratory that the reaction activity of methane combustion on Co/Mn mixed oxides can be improved by the presence of water vapor at low temperatures.[6]

In this presentation, a series of Co/Mn Mixed Metal Oxides was prepared by a sol-gel process, and then the Ce modified Co-Mn oxides and the Co-Mn supported catalysts, $Co\text{-}Mn/Al_2O_3\text{-}SiO_2$, were prepared by homogeneous precipitation, respectively. The water effect on methane oxidation was investigated in an attempt to improve the thermal stability of these catalysts in the presence of water vapor.

Experimental

Synthesis of Co/Mn oxides. A citrate solution was added to a mixed aqueous solution of $Mn(CH_3COO)_2{\cdot}4H_2O$ and $Co(NO_3)_2{\cdot}6H_2O$ under strongly stirring conditions. 2M aqueous ammonia was slowly added to the above solution until the pH value reached 6.5-7.0. Subsequently, the above transparent solution was water bathed at 95 °C for 10 h and then dried at 120 °C for 12 h to obtain a gel powder, which was further calcined at 450 °C in nitrogen for 1 h and then in oxygen for next 2 h. The available powders were ready for the oxidation activity measurements after being crushed and sieved. The obtained metal oxide samples are denoted as MnOx, CoMn and $CoMn_2$, in which the subscript number stand for the molar ratio of Mn and Co in the samples.

Synthesis of cerium doped Co/Mn oxides and Co/Mn oxide supported catalysts. Cerium doped Co/Mn oxides were prepared in the similar procedure above except that urea was used to precipitate a mixed aqueous solution of $Ce(NO_3)_3$, $Mn(CH_3COO)_2$ and $Co(NO_3)_2$ at 120 °C in an autoclave. The resulting sample was then obtained after being washed by distilled water, dried at 120 °C and calcined at 450 °C or 850 °C for 2 h. The powder sample was denoted as Ce-CoMn, in which the molar ratio of Ce:Co:Mn is 0.1:0.9:1.

The Co/Mn supported catalyst was prepared from a mixed aqueous solution of $Mn(CH_3COO)_2$ and $Co(NO_3)_2$ and urea through adding an appropriate amount of $Al_2O_3\text{-}SiO_2$ (BET surface area is ca. 1000 m^2/g) powders into the autoclave under the same procedure above. The obtained powder sample was denoted CoMn/SiAl, which contained 10 wt. % Co-Mn oxides with the molar ratio of Co to Mn as being 1:1.

Catalytic activity measurements Catalytic activities were measured in a fixed bed quartz tubular reactor. A gas mixture of CH_4 (0.5% by volume), O_2 (1.5% by volume) and argon was passed continuously through a 0.1 g catalyst sample bed with a total flow rate of 100 ml/min of argon. The inlet and outlet gas compositions were analyzed after stepwise changes in the reaction temperatures by on-line gas chromatograph.

Results and Discussion

Methane conversion was monitored between 300 °C and 800 °C. **Figure 1** shows methane conversion as a function of reaction temperature on the Co-Mn mixed oxides. It is observed that Co containing catalysts gave higher methane conversion than the bare Mn catalyst. The reaction activities at low temperatures followed the order of $CoMn_2$>CoMn>MnOx. For example, methane conversion at 400 °C in the absence of water vapor on $CoMn_2$, CoMn and MnOx was found to be 70%, 59% and 47%, respectively. When adding 5% water vapor into the reaction feed, methane conversion on MnOx was decreased in line with the previous report on Pd based catalysts. However, a remarkable increase in methane conversion was seen CoMn and $CoMn_2$ in presence of water vapor. It is shown that methane conversion at 500 °C on $CoMn_2$ was increased from 70% to 83% by the presence of 5% water vapor, and the value on CoMn was increased from 59% to 86% under the similar conditions. It was also noted that such a water enhancement effect became weak at high temperatures. The further work to understand the enhancement mechanism may help to develop a type of water-resistant catalysts for methane combustion.

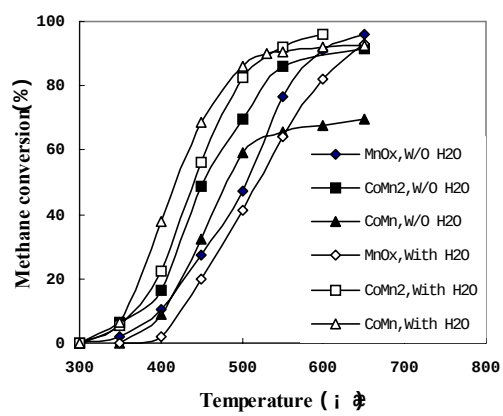

Figure 1. Methane conversion on Co/Mn mixed metal oxides calcined at 450℃ in the absence (solid symbols) and presence (open symbols) of water vapor.

In order to improve the thermal stability of the Co-Mn mixed oxides, cerium oxide was used to dope the catalyst. **Figure 2** shows methane conversion on Ce-CoMn calcined at 850 °C for 2 h. It was observed that a complete oxidation of methane occurred at 720 °C or higher on the cerium-doped catalyst as opposed to <10% of methane conversion on the catalyst without cerium, which indicates addition of cerium components can improve the thermal stability of the Co-Mn catalyst. Meanwhile, the enhancement of the reaction activity was also observed on Ce-CoMn in the presence of 5% water vapor.

A high surface area $Al_2O_3\text{-}SiO_2$ material was used as a

support for the Co-Mn oxide in an attempt to improve the thermal stability. The results were shown in **Figure 3**. As compared with the results on the CoMn sample in **Figure 1**, it can be seen that the reaction activities were improved on CoMn/SiAl in the absence or presence of water vapor, which might be related with the better dispersion of Co and Mn species on the support with a high specific surface area. Moreover, after the sample being calcined at 850 ^{o}C for 2 h, a similar water enhancement effect was still found on the CoMn/SiAl sample. For example, methane conversion at 700 ^{o}C reached ca. 100% in the presence of 5% water vapor as compared to the value of 74% in the absence of water vapor. Clearly, the thermal stability was improved after Co-Mn oxides being supported on an Al_2O_3-SiO_2 support.

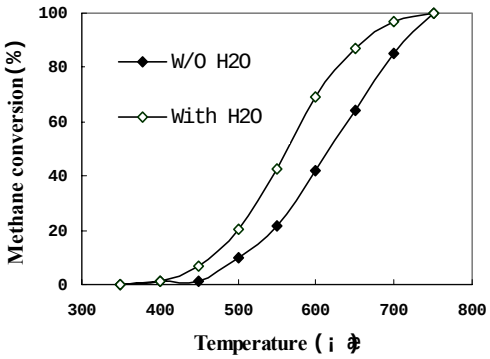

Figure 2. Methane conversion over Ce-CoMn calcined at 850℃.

Figure 4 shows the Changes in the catalyst activity of methane oxidation with time monitored at 500 ^{o}C in the presence of 5% water vapor over CoMn/SiAl calcined at 450 ^{o}C. It was demonstrated that methane conversion first slightly decreased from 96% to 89% after the reaction running for 1.5 h, and then the conversion was stabilized at ca. 85% for the next 24 h, which was indicating a better thermal stability in the presence of water vapor might be achieved by supporting Co-Mn components onto a support with a high surface area. An attempt to further improve thermal stability of the catalyst is in progress in our laboratory.

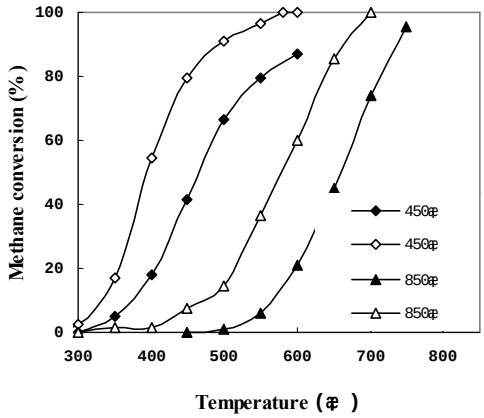

Figure 3. Methane conversion versus reaction temperature on CoMn/SiAl calcined at 450℃ (diamonds) or 850℃(triangles) in the absence (solid symbols) or presence (open symbols) of water vapor.

In conclusion, a variety of Co/Mn mixed oxides has been investigated in this presentation for catalytic oxidation of methane. The results showed that the catalytic activity was increased on Mn/Co mixed oxide catalysts by the presence of water vapor. The positive effect of water vapor was also observed after the Mn/Co oxide was doped with cerium oxide or supported on Al_2O_3-SiO_2, and the thermal stability of these catalysts was improved by these treatments to Mn/Co mixed oxides.

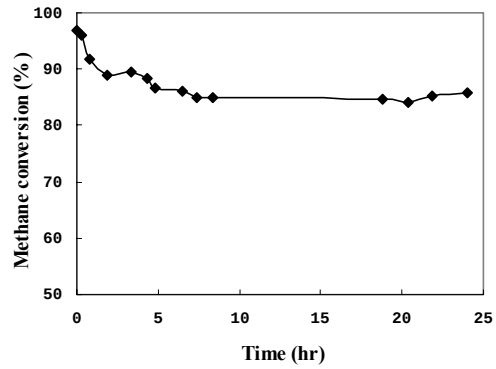

Figure 4. Methane conversion versus reaction time over CoMn/SiAl at 550 ℃ in presence of 5% water vapor.

Acknowledgment

This work was supported by the Basic Research Foundation of Tsinghua University (NO. JC1999009) and National Natural Science Foundation of China (NO. 29907003).

References

1 Van Giezen, J. C., Van den Berg,F. R., Kleinen,J., Van Dillen, L. A. J., Geus, J. W., Catal. Today , **1999**, *47*, 287.
2 Sekizawa,K., Widjaja,H., Machida, S., Ozawa, Y., Eguchi,K., Appl. Catal. A: General, **2000**, *200*, 211.
3 K. Nomura, K. Noro, Y. Nakamura, H. Yoshida, A. Satsuma, and T. Hattori, Catal. Lett., **1999**, 58.
4 K. Fujimoto, F. H. Ribeiro, M. Avalos-Borja, and E. Iglesia, J. Catal., **1998**, *179*, 431.
5 T. Seiyama, Catal. Review, **1992**, *34*, 281.

THEORETICAL STUDY OF THE CO-INTERACTION OF CO_2 AND H_2 WITH NICKEL

Changwei Hu, Song Qin, Huaqing Yang, Dongmei Tong ,Anmin Tian*
Faculty of Chemistry, Sichuan University, Chengdu, 610064, China

Ning-Bew Wong
Department of Biology and Chemistry, City University of Hong Kong, Kowloon, HK

Introduction

The activation of carbon dioxide is a very active research area by experimental and theoretical approaches.[1-3] The reactions of nickel atom with carbon dioxide have been widely investigated.[4-6] The hydrogenation of CO_2 is one of the most important ways for the effective use of CO_2. However, up to now, to our knowledge no studies of the co-interaction of carbon dioxide and H_2 with nickel have been performed theoretically. The ab initio calculation reported in this paper is intended to study the possible reaction path of carbon dioxide and hydrogen on nickel, including their reliable structures of the intermediates and transition states.

Computational Details

Full-parametric geometry optimizations and the final energy evaluation for all structures are performed at B3LYP level. The 6-311+G(2d,2p) basis set is employed for carbon, hydrogen and oxygen, and the SDD basis set and the corresponding ECP are used for nickel. The intrinsic reaction coordinate IRC method was used to track minimum energy paths from transition states to corresponding intermediates. All the ab initio calculations are performed using the Guassian 98 programs.

Results and Discussion

The calculated energy profile is shown in **Figure 1**. The optimized geometry of various intermediates and transition states along the predicted pathway of this reaction and their corresponding ZPE corrected relative energies are shown in **Figure 2**.

As seen in **Figure 1** and **Figure 2**, when CO_2 molecule and H_2 molecule attaches to Ni atom, intermediate A of C_1 geometry forms, the calculated OCO angle is 178.1° and the distances between carbon atom and oxygen atoms are 1.171Å(C1-O3) and 1.152Å(C1-O4), respectively, which are similar to those of free CO_2 molecule(1.160 Å). In addition, the distance between Ni atom and O(3) of CO_2 molecule is 2.094Å which is close to the Ni-O distance(2.09Å) in NiO crystal,[7] indicating the interaction of CO_2 molecule with Ni atom.

From the non-planer complex A, the reaction proceeds via transition state TS1 to form an intermediate B of C_1 geometry. The OCO angle in TS1 is slightly bend to 169.0° and the Ni-O(2) bond length is shortened to 2.022Å. Meanwhile C-O bonds in TS1 are larger than those in intermediate A, which indicates that the C-O bonds are weakened. However, there is little difference in structure between intermediate A and TS1. The calculated activation energy is 0.28 kJ mol^{-1}. IRC confirmed that TS1 connects intermediate A and intermediate B.

Compared with intermediate A, the structure of intermediate B is much different. The O(3)-Ni distance is 1.853Å which is obviously shorter than that of intermediate A. Furthermore, the C-Ni bond forms (1.903Å). The calculated its relative energy is –49.1 kJ mol^{-1}. From those data, we may say the reaction proceeds via a formation of co-adsorption of CO_2 and H_2 on nickel atom. Since the activation energy of this step is so small, it may occur easily.

From intermediate B, the reaction proceeds via the transition state TS2 to form another intermediate C of C_s geometry. Compared with intermediate B, the central Ni-C and C-O(4) bonds (1.827Å and 1.266Å) in TS2 are slightly larger and the distance between Ni atom and H(6)(1.567Å) becomes larger, meanwhile O(4)-H(5) bond (1.351Å) becomes shorter, indicating the H(6)H(5)NiCO(4) five-members ring structure is formed. The calculated energy places the transition state TS2 156.1 kJ mol^{-1} higher than intermediate B, it may stem from the congested structure of TS2. IRC calculation confirmed that TS2 does connect the intermediate B and intermediate C.

The differences in structure between TS2 and intermediate C are also obvious. The most distinct change is H(5) has transferred from Ni to O(5). The distance between Ni-H(5) is 2.924Å and the distance between O(4) and H(5) is 0.966 Å in intermediate C, revealing the Ni-H(5) bond is broken and the O(4)-H(5) bond is formed.

The overall endothermic of this reaction is calculated to be about 6.42 kJ mol^{-1}. Because the calculated energy between intermediate B and TS2 is much larger than that between intermediate A and TS1, we can consider the step from intermediate B to TS2 as the rate-determining-step (RDS) of the reaction.

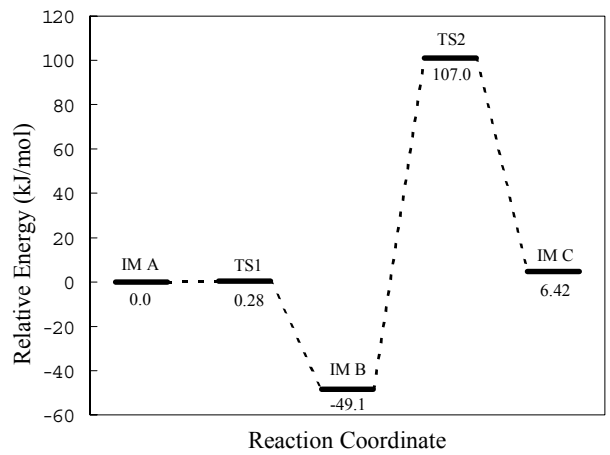

Figure1. Potential energy diagram for the reaction calculated at the B3LYP level. All energies are given in kJ mol^{-1} with respected to intermediate A.

Conclusion

The co-interaction of CO_2 and H_2 on Ni atom and then the reaction $H_2NiOCO \rightarrow HNiCOOH$ are studied by DFT method. The reaction of Ni with CO_2 and H_2 proceeds by forming co-adsorption complex of CO_2 and H_2 on Ni at the first stage. Reaction continues by forming the H(6)H(5)NiCO(4) five-members ring in TS2. Ab initio B3LYP method calculation reveals that overall endothermic of this reaction is calculated to be about 6.42 kJ mol^{-1} and the activation of intermediate B is RDS of it.

Acknowledgments

This work has been financially supported by the Key Project of National Fundamental Research and Development of China (973) (*No.* G1999022407), NNSF (*No.* 29873028), the Special Research Foundation of Doctoral Education of China (*No.* 2000061028) and

* Corresponding author. E-mail:chewhu@mail.sc.cninfo.net

the Foundation of Science and Technology of Sichuan Province (*No.* 200018-16).

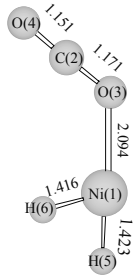

θ(5-1-6)=80.3
θ(3-2-4)=178.1
τ(5-1-6-3)=-179.4
τ(3-2-4-1)=177.7

Intermediate A
C_1 0.0kJ/mol

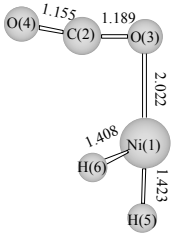

θ(5-1-6)=77.4
θ(3-2-4)=160.0
τ(5-1-6-3)=-175.2
τ(3-2-4-1)=177.3

TS1
C_1 0.28kJ/mol

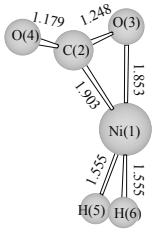

θ(5-1-6)=31.3
θ(3-2-4)=149.1
τ(5-1-6-3)=-138.5
τ(3-2-4-1)=179.7

Intermediate B
C_1 -49.1kJ/mol

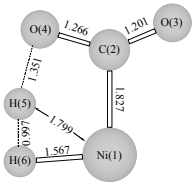

θ(5-1-6)=33.6
θ(3-2-4)=140.4
θ(3-2-1)=113.1

TS2
C_s 107.0 kJ mol^{-1}

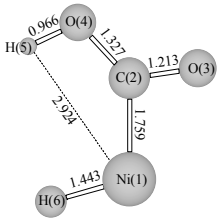

θ(5-4-2)=108.1
θ(3-2-4)=124.8
θ(3-2-1)=98.4

Intermediate C
C_s 6.42 kJ mol^{-1}

Figure 2. Geometries of intermediates and transition states in the reaction. Bond lengths are in Å and angles are in degrees.

Reference

1. F.Galan, M.Fourssier, M.Tranquille, and J.Mascetti., *J. Phys. Chem*. A. **1997**, 101, 2626
2. Gorge C.Schatz.,*J.Chem.Phys*.**1980**, 72(2), 3929
3. Luis Rodriguez-Sanatiago, Mariona Sodupe, and Vicenc Branchadell., *J.Chem.Phys.* **1996**, 105(22), 9966
4. Alexander M. Mebel and Der-Yan Hwang., *J. Phys. Chem*. A. **2000**, 101, 11622
5. Der-Yan Hwang, Alexander M. Medel., *Chemical Physics Letter*. **2000**, 325, 639
6. D.E.Peebles,D.W.Goodman., *J. Phys. Chem.* **1983**, 87, 4378
7. Hu Changwei, Chen Yu, Wang Wenzuo, Lu Guang, Ma Lidun, Shen Xiaoling., *J. Mol. Catal (China)* **1992**, 6(4),263

METHYL ACTIVATION BY NAKED Ni^+ ATOM. THEORETICAL STUDY

Chang-Wei Hu[a], Hua-Qing Yang[a], Yao-Qiang Chen[a], Mao-Chu Gong[a], An-Min Tian[a] and Ning-Bew Wong[b]*

[a] Faculty of Chemistry, Sichuan University, Chengdu, 610064, China
[b] Department Of Biology and Chemistry, City University of Hongkong, Kowloon, HK, China

Introduction

Methylidyne, methylene, and methyl fragments have been proposed to be key intermediates in the fuel reforming, methanation and the dissociation of methane processes.[1-3] Many transition metal catalysts have been synthesized, and Ni-based catalyst has been found to be one of the most active. In these processes, for example, the following steps have been suggested,[4, 5]

$$CH_3 = CH_2 + H = CH + 2H$$

Due to the low concentration and relatively instability of CH_x fragments, direct experimental determinations have proved elusive. Information on stability and interaction of these intermediates, therefore, has to be taken from theoretical calculations. The main objective of the calculations presented in this study is to investigate the deliberate reaction mechanism between Ni^+ and methyl.

Computational Details

The full-parametric geometry optimizations, the final energy evaluation and vibrational frequency analysis for all intermediates and transition states were calculated using two levels of theory, B3LYP with the 6-31G** basis sets for carbon and hydrogen and the SDD basis sets and the corresponding ECP for the nickel, and the larger 6-311+G(2d, 2p) basis set for all atoms, in the GAUSSIAN 98 programs.

Results and Discussion

For the intermediates and transition states, the calculated structures are displayed in Figure 1. The potential curve including both equilibria and transition states is shown in Figure 2. It is found that the calculated geometry structures, energies and vibrational frequencies of all compounds have little discrepancies using the two kinds of basis sets as mentioned above. For terseness, the results below are mainly at the B3LYP/6-311+G(2d, 2p) level. It should be emphasized that all transition states have been verified by IRC approach.

The initial interaction between Ni^+ and $CH_3\cdot$ is the formation of $NiCH_3^+$ species, with a stabilization energy of 129.4 kJ mol^{-1}. For $NiCH_3^+$, with C_{3V} symmetry, the C-H distance (1.091 Å) is longer than that for free $CH_3\cdot$ (1.078 Å). The planar $CH_3\cdot$ has been bent by its interaction with Ni^+. It is indicated that the C-H bond of - $CH_3\cdot$ moiety has been activated by Ni^+ atom.

The second step is an oxidative addition from $NiCH_3^+$ via TS1, yielding the insertion product $HNiCH_2^+$. This step involves an activation energy of 112.0 kJ mol^{-1}, with an endothermicity of 112.7 kJ mol^{-1}.

For transition state TS1, the C-H(5) distance is notably longer than that for $NiCH_3^+$, while their overlap population is remarkably smaller. Meanwhile, the Ni-H(5) distance is considerably shorter than that for $NiCH_3^+$. These indicate that the C-H(5) bond has been activated and the interaction of Ni-H(5) has been strengthened.

For $HNiCH_2^+$, the C-H(5) distance is longer than that for TS1, while their overlap population is smaller. Meanwhile, the Ni-H(5) distance is shorter than that for TS1. This is characteristic of Ni-H(5) single bond. Obviously, the bond of C-H(5) has been completely cleaved and Ni^+ atom has inserted into C-H bond of $CH_3\cdot$.

The third step is the formation of molecular hydrogen complex of the nickel methylidyne H_2NiCH^+, with an activation energy of 198.2 kJ mol^{-1} and an endothermicity of 94.6 kJ mol^{-1}. From the whole potential energy curve, this barrier is the highest. It is indicated that this step is the rate-determination step in the whole reaction.

For transition state TS2, the C-H(4) distance is strikingly

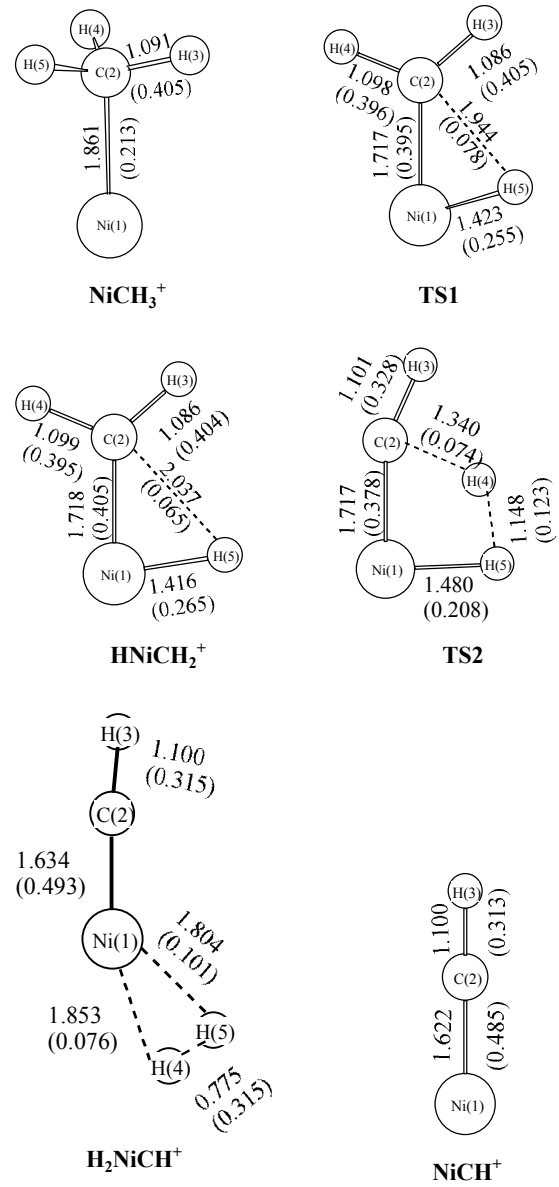

Figure 1. Calculated structures for intermediates and transition states on the potential energy surface at B3LYP/6-311+G(2d, 2p) level. Bond lengths are reported in Å and the overlap populations from the Mulliken Population are in parentheses.

* Corresponding author. E-mail: chwehu@mail.sc. cninfo. net

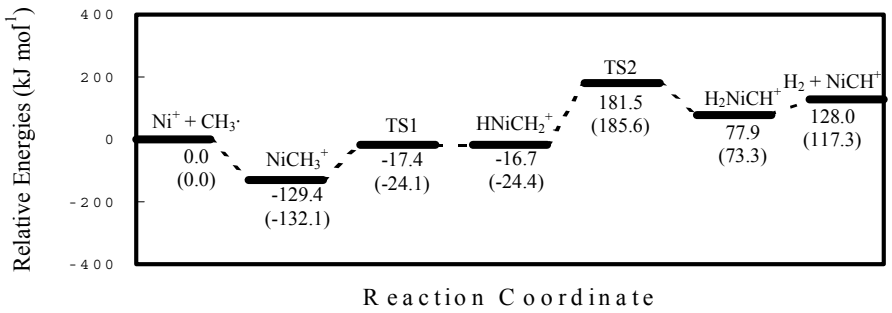

Figure2. The singlet potential energy surface for the reaction $Ni^+ + CH_3\cdot \rightarrow H_2 + NiCH^+$ at 6-311+G(2d, 2p) level. The values in parentheses are the relative energies at the 6-31G** basis sets for carbon and hydrogen and the SDD basis sets and the corresponding ECP for the nickel.

longer than that for H_2NiCH^+, while their overlap population is clearly smaller. Meanwhile, the H(4)-H(5) distance is significantly shorter than that for H_2NiCH^+. These indicate that the C-H(4) bond has been activated and the interaction of H(4)-H(5) has been increased.

For H_2NiCH^+, the C-H(4), Ni-H(4) and Ni-H(5) distances are longer than those for TS2, while the H(4)-H(5) and Ni-C distances are shorter. These are representative of H(4)-H(5) single bond and Ni=C double bond. Furthermore, the H(4)-H(5) distance (0.775 Å) is slightly longer that for free H_2 (0.743 Å), indicating that the H_2 molecularly adsorbed on $NiCH^+$.

The final step is the release of H_2 molecule yielding nickel methylidyne $NiCH^+$ at cost of 50.1 kJ mol^{-1}.

Among all species on the potential energy curve, $NiCH_3^+$ has the lowest energy. On the other hand, $HNiCH_2^+$ does not appear to be a very stable entity, and is easily hydrogenated to $NiCH_3^+$. This is in accordance with that obtained on Pd(111) surface by Paul et al.[6]

In general, our best estimate from the corrected calculations is that the reaction:

$$Ni^+ + CH_3\cdot \rightarrow H_2 + NiCH^+$$

is endothermic by about 128.0 kJ mol^{-1}.

Conclusion

The initial interaction between Ni^+ and $CH_3\cdot$ is the formation of $NiCH_3^+$ species with C_{3V} symmetry. The second step is an oxidative addition, yielding the insertion product $HNiCH_2^+$. The third step is the formation of molecular hydrogen complex of the nickel methylidyne H_2NiCH^+. This step is predicted to be the rate-determining step in the whole reaction process. The final step is the release of hydrogen molecule yielding nickel methylidyne $NiCH^+$. Subsequently, the overall reaction of $Ni^+ + CH_3\cdot \rightarrow H_2 + NiCH^+$ is endothermic by about 128.0 kJ mol^{-1}.

Acknowledgments

The authors are grateful for the financial support by the Key Project of National Fundamental Research and Development of China (973) (*No.* G1999022407), NNSF (*No.* 29873028), the Special Research Foundation of Doctoral Education of China (*No.* 2000061028) and the Foundation of Science and Technology of Sichuan Province (*No.* 200018-16).

References

1. Kaminsky M. P.; Winograd N.; Geoffroy G. L. *J. Am. Chem. Soc.* **1986**, *108*, 1315.
2. Koster A. D.; Santen R. A. V. *J. Catal.* **1991**, *127*, 141.
3. Yang H.; Whitten J. L. *J. Chem. Phys.* **1989**, *91*, 126.
4. Yang H. -Q.; Chen Y. -Q.; Hu C. -W.; Hu H. -R.; Gong M. -C.; Tian A. -M.; Wong N. -B. *J. Mol. Struc. (THEOCHEM)* **2001**, *574,* 57.
5. Michaelides A.; Hu P. *J. Chem. Phys.* **2000**, *112*, 6006.
6. Paul J. -F.; Sautet P. *J. Phys. Chem. B* **1998**, *102*, 1578.

OH RADICAL GENERATION BY ATMOSPHERIC PRESSURE PLASMA AND ITS QUANTITATIVE ANALYSIS BY MONITORING CO OXIDATION

Zhen-Zhou SU, Kohei ITO**, Hyun-Ha KIM***, Kazunori TAKASHIMA*, and Akira MIZUNO**

*Department of Ecological Engineering, Toyohashi University of Technology, Tempaku-cho, Toyohashi, Aichi, 441-8580, Japan
**Department of Electrical Engineering, Toyohashi University of Technology, Tempaku-cho, Toyohashi, Aichi, 441-8580, Japan
***Japan Atomic Energy Research Institute, Takasaki, 370-1292, Japan

Introduction

Applications of non-thermal plasma for gaseous pollution control or methanol synthesis have been carried out by several researchers [1,2]. In these plasma chemical reactions, OH radicals play a very important role for their strong oxidation capability. In understanding the mechanism of plasma chemical reactions, the behavior of the OH radical in both formation process and the subsequent chemical reaction process is required to be known. The measurement of OH radicals in discharge plasma, however, is very difficult, especially under the atmospheric condition. There are several methods such as LIF (Laser-induced fluorescence) or OES (Optical emission spectroscopy). These methods require rather complicated measurement system.

In the atmospheric chemistry, the CO oxidation monitoring method has been used to measure OH radicals concentration [3]. In this paper, the application of CO oxidation monitoring method to the OH radicals measurement in a pulsed discharge plasma in argon and H_2O mixture at atmospheric pressure was examined.

When a pulsed discharge plasma is generated in H_2O/Ar, OH radicals are formed by the collisions of electrons or the excited Ar molecules with H_2O. If CO was added to H_2O/Ar, it will be rapidly oxidized by OH radicals as shown in reaction (1). According to this reaction, the concentration of OH radicals can be determined by the amount of produced CO_2.

$$CO + OH \rightarrow CO_2 + H \qquad (1)$$

In order to apply this method in the discharged plasma, it is necessary to consider both the dissociation of CO_2 due to the next pulse discharge and the loss reactions of OH radicals. Under a condition where these influences can be ignored, the concentration of OH radicals can be determined as CO_2 concentration. In this work, gas residence time and initial CO concentration necessary to ignore the dissociation of CO_2 was studied with experiment and calculation. On the basis of this method, the concentration of OH radicals in the H_2O/Ar plasma was measured to study the effect of H_2O content, SIE on the formation of OH radicals.

Experimental

The gas mixture of Ar (99.999%)and CO (99.95%) was adjusted using mass flow controllers (Estec Inc., SEC-410 and DS-3). The H_2O concentration was controlled by evaporating a constant rate of H_2O fed by a microfeeder. The gas temperature was controlled by a convection oven (SIBATA, SPF-600) and a ribbon heater. The gas-residence time was adjusted by changing the flow rate of gas. A square pulse high voltage (peak voltage 15-22kV, frequency 230- 240Hz) was used to form non-thermal pulsed discharge plasma.

The reaction products were analyzed by FT-IR (BIO- RAD, FTS- 30) and found to be CO and CO_2. A GC-FID (Shimazu, GC-8A) equipped with a methanizer (GL Sciences, MT-221) was used for quantitative measurement of CO and CO_2. The voltage and current waveform were recorded with a digital oscilloscope (Tektronix, TDS-644A), a voltage divider (Tektronix, P6015) and a current probe (Tektronix, P6021). The discharge power was calculated with voltage and current waveform.

Results and Discussion

A. Criteria of the method

Dissociation of CO_2 due to discharge. In the case of the pulsed discharge plasma, the dissociation of products is mainly caused when the products are exposed to the plasma. For the purpose of quantitative measurement of OH radicals, unless otherwise noted, experiments were carried out in a single pulse condition, to avoid the dissociation of products. The single pulsed discharge process was realized by adjusting the gas-residence time to the period of the applied voltage. Consequently, there will be no dissociation of CO_2 caused by the next pulse. The time evolution of CO_2 production of the reaction of CO and OH was calculated. **Fig. 1** indicates that 130μs was necessary for the reaction to reach an equilibrium state when the OH concentration was 50ppm and the CO concentration was 1%. Because the FWHM (Full width at half-maximum) of the pulse current was 40ns, the reaction of CO and OH ran at the interval term of two successive pulsed discharges. The oxidation of CO by OH can be considered as a chemical reaction, and it is not affected from discharge in the single pulsed discharge.

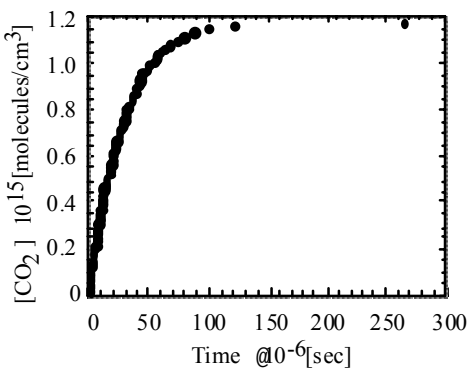

Fig.1 Calculation for the reaction time of CO_2 production.

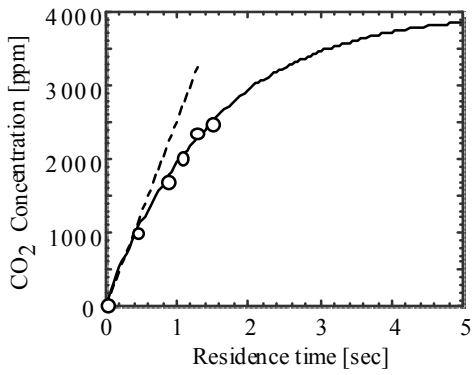

Fig. 2 Influences of the dissociation of CO_2 by discharge. (Discharge power=3.1W, H_2O/CO/Ar=1/1/98)

Under extended gas residence time, however, both processes of CO_2 formation and CO_2 dissociation take place at the same time. In this sense, we should consider these both processes to estimate the produced CO_2 concentration. Assuming that the production of CO_2 per each single pulse is constant and the dissociation of CO_2 is caused by reaction (2), then we can obtain the concentration of produced CO_2 after exposed to number of pulse as Eq. (3).

$$CO_2 + e^* \rightarrow CO + O + e \qquad (2)$$

$$[CO_2]_n = [CO_2]_{n-1} + [CO_2] - k[CO_2]_{n-1} \qquad (3)$$

Where

$[CO_2]$= CO_2 production by a single pulse

$[CO_2]_{n-1}$= CO_2 production by n-1 times of pulses

k = The rate of the dissociation of CO_2 by a single pulse discharge

Eq. (3) is transformed into Eq. (4).

$$[CO_2]_n = [CO_2] \times k^{-1} \times [1-(1-k)^n] \quad (4)$$

It indicates that $[CO_2]_n$ increases with the number of pulse (the residence time) nonlinearly. **Fig.2** shows the experimental results of the gas residence time up to 1.6sec. CO_2 production, $[CO_2]_n$, tends to increase linearly with the residence time up to 0.5sec, and then begin to saturate. The appearance of the linear increasing of CO_2 indicates that, the influence of the dissociation of CO_2 caused by succeeding discharges can be ignored when the residence time smaller than 0.5sec in this experimental condition.

The influences of loss reactions of OH radicals. Differing from the chemistry of atmospheric space, concentration of OH radical in the discharge plasma is very high. In the conditions where the concentration of OH radical is high, the loss-reaction mainly due to recombination may take place. Reactions (5)-(10) are regarded main reactions in the discharge space where H_2O exists. Reactions (5)-(8) are the loss-reactions of OH radicals. These reactions compete with the reaction (1), and affect the CO oxidation by OH radicals. OH radicals branching depends on the rate constants and initial concentrations of CO and OH. The variation of CO_2 production with the variation of the CO initial concentration was measured by the experiment. Calculation was also made using a simulation software (IBM, CKS version 1.0).

$$OH + OH \rightarrow H_2O + O \quad (5)$$

$$OH + OH \rightarrow H_2O_2 \quad (6)$$

$$H + OH \rightarrow H_2O \quad (7)$$

$$H + OH \rightarrow O + H_2 \quad (8)$$

$$H + H_2O \rightarrow H_2 + OH \quad (9)$$

$$H + H \rightarrow H_2 \quad (10)$$

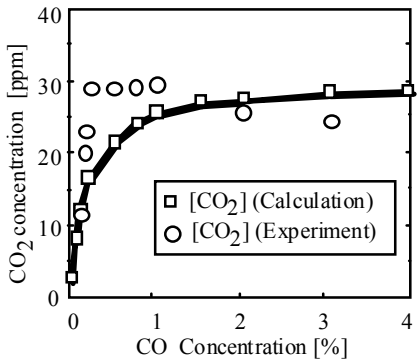

Fig.3 The influence of OH loss reactions. (Calculation condition: reaction (1), (5) -(10) were used. $[OH]_0=[H]_0=8.1 \times 10^{14}$ molecules/cm^3, $[CO]_0=2.7\times10^{14}$ molecules/cm^3, $[H2O]_0=2.7\times10^{14}$ molecules/cm^3, Experimental condition: Content of H_2O=1%, Residence time=4.2ms, Discharge power=1.8W, T=50 degree)

Fig.3 shows the results of the experiment and the simulation. In the experiment, the CO_2 production was observed while the initial concentration of CO was varied from 800ppm to 4%. When $[CO]_0$ < 2000ppm, the CO_2 production was increased with increasing $[CO]_0$. When $[CO]_0 \geqq$ 2000ppm, the CO_2 concentration became constant. This result indicated that the influence of the loss-reactions of OH radicals could be ignored when initial CO concentration is higher than 2000ppm. However, when CO concentration exceeded 1%, the CO_2 concentration began to decrease because the peak discharge current decreased.

The result shows the similar tendency in the variation of the CO_2 formation. It indicates that the influence of loss reactions much depends on the initial concentration of CO.

B. Influences of H_2O content and discharge power on OH formation

Fig.4 shows the relation between the H_2O content and the OH formation. It shows that production of OH radicals increased when the H_2O content increased under the same SIE (Specific Input Energy: energy to unit volume of gas, kJ/m^3). The production of OH radical increased with the SIE value when the H_2O content was kept constant. These results agree with other measurements on spectroscopic analysis of OH formation in DBD (dielectric barrier discharges) of $Ar/O_2/H_2O$ [4].

In our experiment, under the conditions with the SIE value of 9 kJ/m^3 and H_2O content of 1.5%, the maximum OH production 30ppm (9.4×10^{14} cm^{-3}) was obtained. The value is about the same as that observed in DBD [5]. In our experiment, the G value, which is defined as the number of OH produced per 100 eV, is 1.9. Penetrante calculated the G value for OH generation using DEGARD in the case of pure H_2O, and obtained 1.42[1]. It should be noted that a comparable OH yield-value has been obtained in our experiment using the simple equipment.

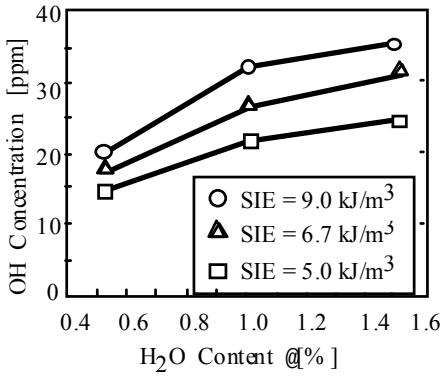

Fig.4 Influences of OH formation according to the variation of content of H_2O and discharge power. (CO/Ar=1%,T=50 degree)

Acknowledgment.

The authors are grateful to Professor H. Matsui, Professor K. Onda and Assistant T. Tatsuo of Toyohashi University of Technology for their valuable discussions.

References

[1] B. M. Penetrante, *NATO ASI Series*, **1993**, G34, Part A, pp.65.

[2] Liu, C. J., A. Marafee, R.G, Mallinson, and L.L. Loban, *Applied Catalysis A*, **1997**, 164, pp.21.

[3] Campbell M J, Farmer J C, Fitzner C A, Heavy N M, Sheppard J C, Hardly R J, Hopper J F and Muralidhar V, *J. Atmos. Chem.*, **1986**, 4, pp.413.

[4] Zoran Falkenstein, *J.Appl.Phys.*, **1997**, 81 (11), pp.7158.

[5] C. Hibert, I. Gaurand, O. Motret, J.M. Pouvesle, *J. Appl. Phys.*, **1999**, 85 (10), pp.7070-7075.

METHANE COUPLING AND REFORMING USING NON-EQUILIBRIUM PULSED DISCHARGE AT ROOM TEMPERATURE

Shigeru Kado[†], *Kohei Urasaki*[†], *Yasushi Sekine*[‡]

[†] Department of Applied Chemistry, School of Engineering, The University of Tokyo, Hongo, Bunkyo-ku, Tokyo 113-8656, Japan
[‡] Department of Applied Chemistry, School of Science and Engineering, Waseda University, Okubo, Shinjyuku, Tokyo 169-8555, Japan

Introduction

Methane, which is a major component of natural gas and one of the greenhouse gases, is so stable that high reaction temperature such as 1273 K or higher is required for its pyrolysis to ethylene or acetylene. Although high reaction temperature is favorable for high conversion, high reaction temperature promotes the consecutive decomposition of the products to carbon or complete combustion to CO_2 in the oxidative activation of methane. The utilization of natural gas as a chemical resource is limited in producing hydrogen and synthesis gas by steam reforming process, which requires higher operating temperature than 1073 K in the presence of catalysts.

Recently, methane conversion using non-equilibrium plasma technique has been studied at low temperature. For example, using 8 kPPS (pulse per second) high-frequency pulsed plasma produced acetylene selectively with relatively high energy efficiency.[1] A cogeneration of syngas and higher hydrocarbons can be achieved using a catalytic dielectric-barrier discharge (DBD).[2] In this study, selective formation of C2 hydrocarbon and/or carbon monoxide was achieved using a periodic pulsed spark discharge[3,4] with and without catalyst at room temperature.

Experimental

A schematic diagram of the experimental setup was almost the same as that reported previously.[3] A flow type reaction apparatus composed of a Pyrex glass tube with 4.0 mm internal diameter was used as the reactor. All experiments were conducted under the conditions of ambient temperature and atmospheric pressure. Stainless steel electrodes of 1.0 mm diameter were inserted from each end of the reactor and fixed with a certain distance. In the catalytic reaction, a quartz tube with 6.0 mm internal diameter was used, and the gap distance was fixed at 10 mm. The catalyst bed was put between stainless meshes.

The discharge was initiated by supplying a negative high voltage with a DC power generator (MATSUSADA Precision Inc. HAR-30R10). Figure 1-a shows examples of the waveforms of discharge current and voltage measured by digital oscilloscope (LeCroy Japan Corp. 9314C, 400 MHz bandwidth) using a voltage probe (PMK-20kV, 100 MHz, LeCroy) and current transformer (AP015, 50 MHz, LeCroy). The current width of one pulse was far shorter than 1 μs as shown in Fig. 1-b, and the peak value of the pulse current reached about 40 A. The reason why the current pulses did not have the same frequency as the voltage oscillations in Fig. 2-a was the low sampling rate of the oscilloscope. Owing to the short width of current, the pulsed spark discharge belongs to the non-equilibrium plasma.

A catalyst of 1 wt% Pt/SiO_2 was prepared by the incipient wetness method using $[Pt(C_5H_7O_2)_2]$ and CARiACT Q-15 SiO_2 (10-20 mesh, Fuji Silysia Chemical Ltd.), and $Ni_{0.1}Mg_{0.9}O$ solid solution catalyst was prepared by the same method as Tomishige et al..[5]

All products were analyzed with two gas chromatographs of FID-GC-14A and TCD-GC-8A.

The conversions of the reactants were defined as follows.
Reactant conversion (%) = (moles of reactant consumed) / (moles of reactant introduced) ∗ 100

The selectivities were defined as follows.
Product selectivity (%) = (carbon based moles of product dericed from methane) / (moles of CH_4 consumed) ∗ 100

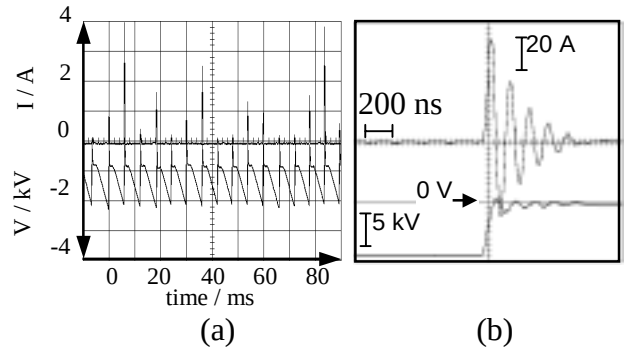

Figure 1. Typical waveform of pulsed spark discharge.

Results and Discussion

Selective Formation of C2 hydrocarbon. Investigations of the activation of methane with the non-equilibrium pulsed spark discharge were made under the condition of feeding pure methane at the flow rate of 10 cm^3min^{-1} while increasing the pulse frequency. As shown in Fig. 2, methane was activated to form acetylene with a selectivity of more than 90% in the absence of a catalyst. Hydrogen was abstracted from methane directly by the collision between electrons and methane molecules. Even when methane conversion increased up to 52%, acetylene selectivity was very stable at about 95%, while the other C_2 products were ethane and ethylene (selectivity of ~ 4%). Other higher hydrocarbons such as prop-1-yne (C_3H_4) and buta-1,3-diyne (C_4H_2) were produced with a selectivity of less than 1%. These results are quite different from those of simple gas-phase reactions.

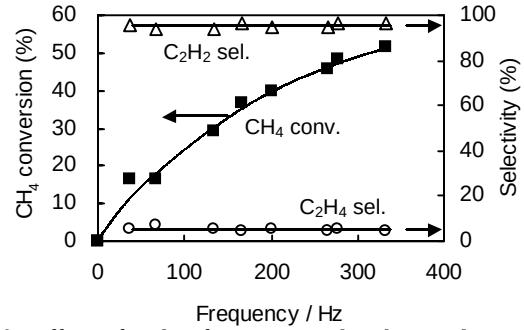

Figure 2. Effect of pulse frequency under the conditions of 10 cm^3min^{-1} total flow rate, CH_4 100%, room temperature, 0.1 MPa, 1.5 mm gap distance.

To investigate the catalytic spark discharge reaction, 1 wt% Pt/SiO_2 was inserted between the electrodes. The height of catalyst bed from the downstream electrode was varied from 0 to 10 mm. The results are shown in Fig. 3. The height of 0 mm means non-catalytic reaction, and the discharge region was filled with the catalyst at 10 mm height (0.1 g-Cat.). Pt/SiO_2 was used without pretreatment like reduction by H_2. To prevent the carbon deposition, CH_4 was diluted with 80% H_2.

As compared with results in Fig. 2, to lengthen the gap distance and to dilute CH_4 with H_2 did not affect the selectivity so much. The selectivity to C_2H_2 in Fig. 3 was 87% in non-catalytic reaction. On the other hand, the use of Pt/SiO_2 had a great influence on the product composition, and the selectivity to C_2H_6 increased drastically, while the conversion decreased. Under the condition of CH_4/H_2=8/32 cm^3min^{-1}, CH_4 conversion was 46% in non-catalytic reaction, which

decreased to 14.5% when the discharge region was filled with SiO_2 (void fraction: 65%). When the discharge region was filled with Pt/SiO_2, C_2H_6 was produced with the selectivity of 94% and the conversion of 10.5%. CH_4 conversion increased to 33% by decreasing the amount of the catalyst (2.5 mm height), and 25% yield of C_2H_6 was obtained.

Under the condition of CH_4/H_2=2/8 cm^3min^{-1}, the decrease in the conversion by the insertion of catalyst was not so large compared with that under condition of higher flow rate. Although CH_4 conversion at 5 mm and 2.5 mm height were almost the same at 51%, the selectivity to C_2H_4 slightly increased to 15%. The highest C_2H_6 yield of 49% was obtained at 5 mm height of catalyst, much higher than 30% that is the upper limit in the conventional thermal chemistry.

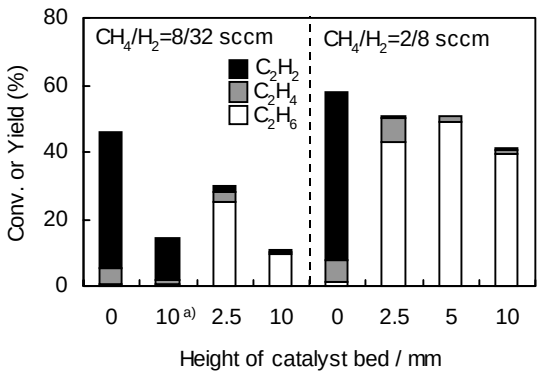

Figure 3. Effect of 1 wt% Pt/SiO_2 under the conditions of room temperature, 0.1 MPa, 10 mm gap distance, 100 Hz frequency. [a]: SiO_2 without Pt.

Selective Formation of Synthesis Gas by CO_2 Reforming or Partial Oxidation of CH_4. Fig. 4 shows the effect of CO_2 content in the feed gas on the conversion, the selectivity and H_2/CO ratio. In the presence of CO_2, carbon deposition on the electrodes and the wall of the reactor was not observed. With increasing CO_2 content, CH_4 conversion rose and reached 76 % at CH_4/CO_2=1/4 while CO_2 conversion remained almost stable with *ca*. 40 %. The selectivity strongly depended on the feed gas composition. With the increase of CO_2 content, C_2 selectivity decreased sharply while CO selectivity increased drastically. Under the condition of high CH_4 concentration, the formation of C_2H_2 was predominant, whereas under the condition of high CO_2 concentration, CO became the main product. The feed gas composition also had a great influence on H_2/CO molar ratio, which was in inverse proportion to CO_2 content. Synthesis gas with H_2/CO ratio of 2 was obtained at 40 % CO_2 content, which is suitable for the catalytic methanol synthesis.

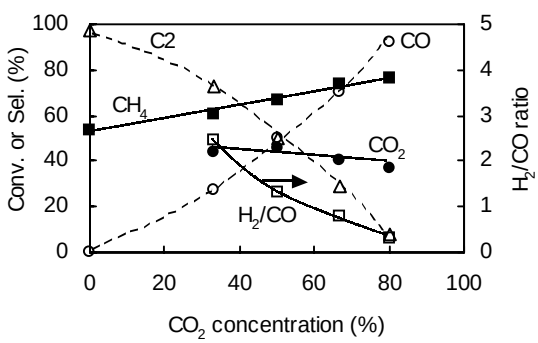

Figure 4. Effect of CO_2 concentration under the conditions of 10 cm^3min^{-1} total flow rate, room temperature, 0.1 MPa, 1.5 mm gap distance.

The use of pretreated NiNgO solid solution catalyst increased CO selectivity to 85% at CH_4/CO_2=1, while no remarkable effect was observed by using without pretreated one as shown in Table 1. The content of C_2H_4 in C2 hydrocarbons was 78% with pretreated NiMgO, and that of C_2H_2 was 77% with non- pretreated one. NiMgO and discharge combined system promoted CO_2 reforming of CH_4 at room temperature without dilution.

Table 1. Effect of $Ni_{0.1}Mg_{0.9}O$ with and without Pretreatment*

Catalyst	Frequency / Hz	Conv.(%) CH_4	Conv.(%) CO_2	Sel.(%) C2	Sel.(%) CO	H_2/CO ratio
non	50	62.8	50.0	44.1	55.9	1.1
NiMgO[a]	200	29.6	23.9	37.0	63.0	1.1
NiMgO[b]	91	29.5	26.2	15.5	84.5	1.0

* Reaction conditions: CH_4/CO_2=10/10 cm^3min^{-1}, room temperature, 0.1 MPa, 10 mm gap distance. [a]: without pretreatment, [b]: pretreated by H_2 reduction at 1123 K.

The partial oxidation of CH_4 was examined by varying the partial pressure of O_2 as shown in Fig. 5. CH_4 conversion increased from 24% to 76% in proportion to an increase in the partial pressure of O_2. CO selectivity increased from 0% to 79% while C2 compounds selectivity decreased from 99% to 7% with an increase in the O_2 content from 0% to 50%. The content of C_2H_2 in C2 compounds, however, decreased slightly from 98% (CH_4/O_2=10) to 68% (CH_4/O_2=1). And CO_2 selectivity increased slightly by the consecutive oxidation of product. The pulsed spark discharge reaction of CH_4 in the presence of O_2 produced CO and C_2H_2 at room temperature while suppressing carbon deposition and CO_2 formation.

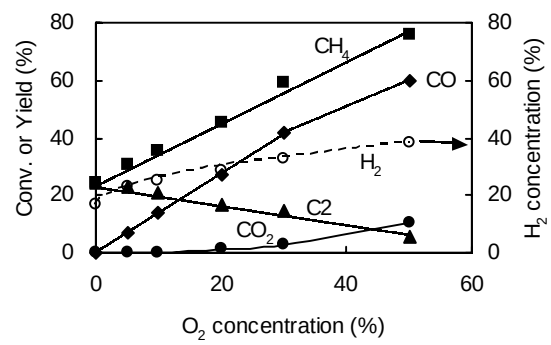

Figure 5. Effect of partial pressure of O_2 under the conditions of 50 cm^3min^{-1} total flow rate, 50% CH_4 concentration, balance gas of Ar, 45 Hz frequency, room temperature, 0.1 MPa, 10 mm gap distance.

Conclusion

The use of non-equilibrium pulsed spark discharge could activate CH_4 at room temperature. The selective formation of C_2H_2 with high conversion was achieved, and 49% yield of C_2H_6 was obtained in Pt/SiO_2 and discharge combined system. This method could be applied to the formation of synthesis gas, and has a possibility to be applied to the utilization of not only natural gas but also biogas, which is composed of CH_4 and CO_2.

References

[1] Yao, S. L.; Nakayama, A.; Suzuki, E., *AIChE Journal,* **2001**, *47*, 419.
[2] Eliasson, B.; Liu, C. J.; Kogelschatz, U., *Ind. Eng. Chem. Res.,* **2000**, *39*, 1221.
[3] Kado, S.; Sekine, Y.; Fujimoto, K., *Chem. Commun.,* **1999**, *24*, 2485.
[4] Kado, S.; Urasaki, K.; Sekine, Y.; Fujimoto, K., *Chem. Commun.,* **2001**, *5,* 415.
[5] Tomishige, K.; Himeno, Y.; Matsuo, Y.; Yoshinaga, Y.; Fujimoto, K., *Ind. Eng. Chem. Res.,* **2000,** *39,* 1891.

OXYGENATE SYNTHESIS FROM METHANE AND CARBON DIOXIDE USING DIELECTRIC-BARRIER DISCHARGES

Ming-xia He,[1,2] Ji-jun Zou,[2,3] Yang Li[2,3], Baldur Eliasson[2,4] and Chang-jun Liu[2,3]*

[1] School of Chemical Engineering and Technology, [2]Tianjin University-ABB Plasma Greenhouse Gas Chemistry Laboratory and [3] State Key Laboratory of C1 Chemical Technology, Tianjin University, Tianjin 300072, China
[4] Energy and Global Change, ABB Corporate Research Ltd., Baden, CH5405, Switzerland

Introduction

Plasmas, including thermal and non-thermal plasmas, have been extensively investigated for methane conversion. The thermal plasma normally was used for the production of acetylene or carbon black from methane, with hydrogen as a by-product. There have been much more investigations on methane conversion using non-thermal plasmas recently. An important characteristic of non-thermal plasma is its high electron temperature (as high as 10^5 K) while the bulk gas temperature remains as low as room temperature. This characteristic makes it suitable for chemical synthesis of higher hydrocarbons and oxygenates. Most of products produced using corona, microwave, and radio frequency discharge are some little molecules, like ethylene, acetylene, hydrogen and carbon monoxide. Under the condition of dielectric-barrier discharge, product could be more complex for its large volume of discharges. Light hydrocarbons, liquid fuels, alcohols and acids can be produced. Furthermore, some operation parameters in dielectric-barrier discharges can be easily changed including dielectric material, length and distance of discharge gap and electrode configuration. The distribution of products will be different with the different parameters in dielectric-barrier discharges. Due to the poor understanding of plasma chemistry, the present status of plasma methane conversion is still in the laboratory test. More intensive fundamental investigations are required, esp., at the time when the direct catalytic methane conversion still remains as a challenge to the scientists all over the world.

On the other hand, the combination of utilizations of methane and carbon dioxide is very promising, even with the plasma methane conversion. As a co-reactant for methane conversion, CO_2 is a soft oxidant and can provide extra carbon atom for the conversion. Oxygenates can be generated including methanol, formic acid and others upon the operative conditions applied.[1-3] The metal electrode material has also an effect on the product distribution from methane and carbon dioxide.[4] The previous investigation focused on the formation of higher hydrocarbons (including liquid fuels) using the high voltage electrode covered by the dielectric material.[5] In this work, we investigated the synthesis of oxygenates directly from CH_4 and CO_2 under the conditions of dielectric-barrier discharges with the grounded electrode covered dielectric material layer. This means the high voltage electrode will expose directly to plasma phase. A big difference induced by this change in the electrode configuration is that only oxygenates are produced in the liquid products (no liquid hydrocarbons) in the present reactor design.

Experimental

The schematic configuration of the discharge reactor used in this investigation is shown in Figure 1. A quartz tube with the inner diameter of 14 mm served as the dielectric barrier. A transparent conductive (silver) film deposited on the quartz tube was used as the grounded electrode. The high voltage tubular electrode with the outer diameter of 12 mm was made of aluminum foil and located in the center of quartz tube. The discharge zone was formed within a gap of 1 mm between the aluminum electrode and the quartz tube with the length of 200 mm. The feed gases passed through the gap and were converted within the discharge zone. The reaction was terminated at the end of discharge region. The high voltage generator supplied about 10 kV sinusoidal signals at frequency of 25 kHz to the discharge reactor. The voltage and current were measured with a high voltage probe (Tektronix P6015 A) and a pulse current transformer (Pearson Electronics 411) via a digital oscilloscope (Tektronix 2440). The discharge power was measured via a digital multimeter (Keithley 2000). The discharge power was fixed at 100 W in this investigation.

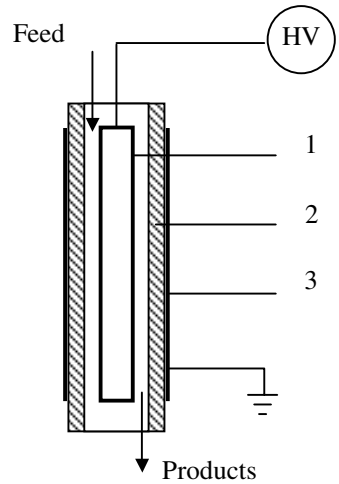

Figure 1. Schematic configuration of DBD reactor
(1-HV electrode; 2-Quartz tube; 3-Grounded electrode)

The reactants, methane and carbon dioxide, were introduced into the reactor via mass flow controllers. The total flow rates were fixed at 60 ml/min with the retention time of about 12 second. The feed and products were analyzed with a GC (HP 5890) equipped with a thermal conductivity detector (TCD) and a flame ionization detector (FID) via a HP-PLOT Q (30 m × 0.53 mm × 40 μm) column. A mass selective detector (HP 5971) was used to identify the products. Liquid products were collected in a cold trap cooled with a mixture of ice and water. All the investigations were carried out at ambient conditions.

Results

Conversions of Methane and Carbon Dioxide. The conversions of CH_4 and CO_2 are shown in Figure 2. Conversion of carbon dioxide nearly proportionally increased with increasing of methane concentration in the feed. Methane conversion increased with the increasing of carbon dioxide conversion while methane concentration was less than 60 v% in the feed. However, the conversion of methane reached a saturated value when methane was more than 60 v% in the feed. The trend of the change of methane conversion is different from that reported previously.[5] It suggested that the conversion of methane is strongly affected by the conversion of carbon dioxide in this case, especially when carbon dioxide was the principal component in the feed.

Figure 2. Effect of composition of feed on conversions

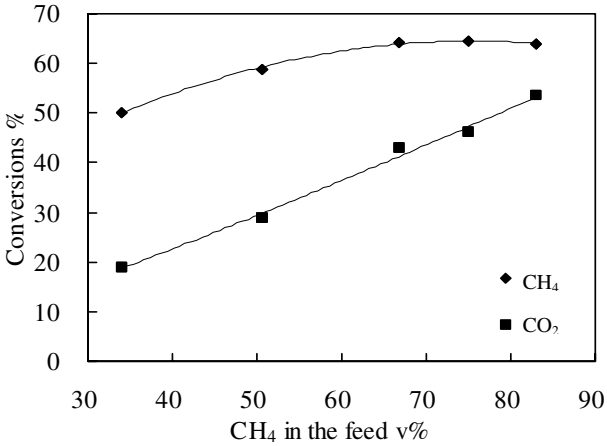

(Discharge power of 100 W; Flow rate of 60 ml/min)

Analysis of Gaseous Products. Gaseous products contain hydrocarbons (from C_2 to C_5) and CO. The selectivities of gaseous products are shown in Table 1. The selectivities of hydrocarbons were sharply decreased with the increasing carbon atom numbers in

Table 1. Selectivities of gaseous products
(Discharge power of 100 W; Flow rate of 60 ml/min)

CH_4 in the feed v%	34.0	50.6	66.8	75.1	83.1
	Selectivity based on carbon atoms /%				
Ethene	0.4	0.5	0.6	0.8	1.1
Acetylene	0.5	0.8	0.9	1.1	1.3
Ethane	11.1	11.5	11.7	12.4	14.2
Propene	0.2	0.3	0.5	0.5	0.7
Propane	5.0	6.1	6.9	6.8	8.6
Isobutane	1.2	1.8	2.2	2.1	2.8
Butane	1.4	2.0	2.4	2.3	3.1
Neopentane	0.7	0.9	1.0	1.0	1.1
Isopentane	0.1	0.4	0.5	1.9	2.6
Pentane	0.2	0.3	0.4	0.8	1.1
CO	64.9	49.0	32.2	22.6	17.3

the molecules. The selectivities of unsaturated hydrocarbons were much less than those of paraffins. It was considered that the formation of C_2 hydrocarbons from plasma methane conversion using dielectric-barrier discharges consists of the following three sequential steps [6]:

$$CH_4 \rightarrow C_2H_6 \rightarrow C_2H_4 \rightarrow C_2H_2 \qquad (1)$$

As shown in Table 1, CO selectivity decreased with the increasing methane concentration in the feed. And there existed a nearly linear relationship between selectivity of CO and CH_4 concentration in the feed.

Distribution of Components of Liquid Products. Oxygenates, including methanol, ethanol, acetic acid and other alcohols and acids containing more than two carbon atoms, were the major products in the condensate as shown in Table 2. Acetic acid was the primary product in the condensate with the highest selectivity of 5.2% at 66.8 v% of methane in the feed. There existed an optimum component of feed for the selectivities of ethanol, 1-propanol and acids, respectively.

Table 2. Selectivities of liquid products
(Discharge power of 100 W; Flow rate of 60 ml/min)

CH_4 in the feed v%	34.0	50.6	66.8	75.1	83.1
	Selectivity based on carbon atoms/%				
Methanol	1.1	1.0	0.3	0.3	0.1
Ethanol	2.6	4.9	1.8	1.7	0.8
Isopropyl alcohol	0.2	0.2	0.2	0.2	0.1
1-Propanol	0.2	0.3	0.1	0.1	0.1
Acetic acid	2.8	4.6	5.2	4.8	2.4
Propanoic acid	0.8	1.3	1.0	0.9	0.5
Isobutanoic acid	0.1	0.2	0.1	0.1	0.1
Butanoic acid	0.2	0.2	0.2	0.1	0.1

Conclusions

Direct synthesis of oxygenates, including acetic acid, propanoic acid, methanol and ethanol, from methane in the presence of carbon dioxide was conducted under the condition of dielectric-barrier discharges in this work. The present reactor design suggests the surface status of electrodes played an important role in the formation of oxygenates. The selectivities of acetic acid, propanoic acid, methanol and ethanol were 5.2%, 1.0%, 0.3% and 1.8%, respectively, with the conversions of methane and carbon dioxide of 64.3% and 43.1%, respectively, while methane of 66.8v% in the feed. From the obtained results, CO, gaseous and solid hydrocarbons are still the major product. To get a higher yield of oxygenates, it is better to remove the oxygenate product as soon as it is produced. Further investigation is being performed to achieve a better production of oxygenates directly from methane and carbon dioxide using plasmas (with special catalyst and typical reactor design).

Acknowledgement. Supports from the Key Foundation of Tianjin City Committee of Science and Technology and ABB Corporate Research Ltd., Switzerland are very appreciated.

References

1. Larkin, D. W.; Lobban, L.L. and Mallinson, R.; *Ind. Eng. Chem. Res.*, **2001**, 40, 1594.
2. Matsumoto, H.; Tanabe, S.; Okitsu, K.; Hayashi, Y. and Suib, S.L.; *J. Phys. Chem. A*, **2001**, 105, 5304.
3. Okumoto, M.; Su, Z.; Katsura, S. and Mizuno, A.; *IEEE Tran. Ind. Appl.*, **1999**, 35, 1205.
4. Li, Y.; Xu, G.-H.; Liu, C.-J.; Eliasson, B.; and Xue, B.; *Energy & Fuels*, **2001**, 15, 299.
5. Liu, C.-J.; Xue, B.; Eliasson, B.; He, F.; Li, Y.; and Xu, G.-H.; *Plasma Chem. Plasma Process.*, **2001**, 21, 301.
6. Kozlov, K. V.; Michel, P.; and Wagner, H.E.; *Plasmas and Polymers*, **2000**, 5, 129.

DE NOVO SIMULATION AND SPECTROSCOPIC STUDY OF IRON SPECIATION IN MICRO- AND MESOPOROUS BIOMIMETIC MATERIALS ACTIVE IN THE SELECTIVE OXIDATION OF METHANE

Peter-Paul H.J.M. Knops-Gerrits

Département de Chimie, Université Catholique de Louvain (UCL), Batiment LAVOISIER, Place L. Pasteur n°1, B-1348 Louvain-la-Neuve, Belgium

Introduction

Methane Mono-Oxygenase (MMO) and Deoxyhemerythrin are examples of diiron enzymes that catalyze the dissociative and non-dissociative binding of molecular oxygen [1-5]. Dissociative binding of oxygen via a peroxo intermediate to a diamond core structure leads to a reactive species active in the oxidation of alkanes [1-2]. Non-dissociative binding of oxygen via a side-on peroxo intermediate such as in the active site of deoxyhemerythrin does not allow the splitting and allows binding/release of oxygen as a function of the physiological conditions. Such active sites are among the growing list related to (hydr)oxo-bridged di- or poly-iron cores in biological systems. Methane mono-oxygenase has a binuclear active site in which two histidines and four glutarates are present. Both iron ions are coordinated by a histidine, an oxygen from a bridging carboxylate and a μ-oxo bridge [1]. Theoretical modeling of these enzyme active sites has been recently reported. Yoshizawa *et al.* studied the dioxygen cleavage and methane activation on diiron enzyme models with the extended Hückel method, an approximate molecular orbital method, the $\mu\text{-}\eta^1{:}\eta^1\text{-}O_2$ or $\mu\text{-}\eta^2{:}\eta^2\text{-}O_2$ binding modes are distorted to the corresponding dioxygen complex [4].Shestakov and Shilov showed that the synchronous insertion of O atom mechanism is found to be significantly less contradictory (for example in methane) if it is supplemented by the stage of formation of the five-coordinate carbon intermediate complex of a hydrocarbon molecule via oxygen atom of an active center[5].

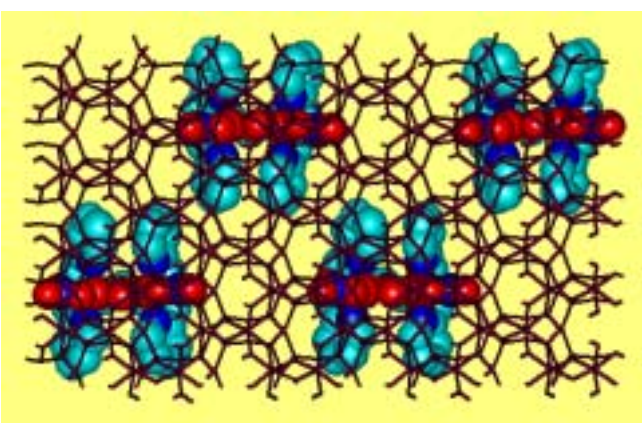

Figure 1. $[Fe_2(HPTP)(OH)(NO_3)_2]$ in montmorillonite clays.

Methane can be converted into methanol with binuclear iron(IV)-model complexes

To mimic the MMO active site with a finite cluster we chose to study the binuclear heptapodate coordinated iron (III)-complexes of *N,N,N',N'*-tetrakis(2-benzimidazolylmethyl)-2-hydroxy- 1,3-diamino -propane (HPTB) and *N,N,N',N'*,-Tetrakis(2-pyridylmethyl)-2-hydroxy-1,3-diamino-propane (HPTP). These have active sites of the form $[Fe_2(HPTP)(\mu\text{-}OH)]^{4+}$ (1) and $[Fe_2(HPTB)(\mu\text{-}OH)]^{4+}$ (2). As supports for such complexes we use mesoporous materials such as MCM-41, FSM-16, HMS (Hexagonal Molecular Sieve) [7-8] and clays (Fig 1) [9] since these materials have large surface areas and large pore sizes that can be tuned from 1.5 to 10 nm. We characterized these complexes using Quantum Mechanics (QM) and EXAFS, Mössbauer and Catalysis and studied the effect of the support.

The QM was at the *ab initio* and DFT (B3LYP) levels [3]. All chelating N-atoms and the ligand backbone were included in the QM determination of the geometry and electronic properties of the ground and excited states of the active site. The geometries of the supported complexes were determined with MD using the Universal FF (UFF) [6] supplemented with a FF based on the quantum mechanics. For the O_2 binding on the reduced active site the $\mu\text{-}\eta^1{:}\eta^1\text{-}O_2$ mode seems to preceed formation of the O=Fe-O-Fe=O bis-ferryl active site that reacts exothermally with methane by 50.56 kcal/mol. After the H splitting from methane, the methyl recombines with the FeO center via a weak $Fe\text{-}OCH_3$ bond in this model. The consecutive reaction with water protonates the methoxy group to form methanol and the substitution at the active site by a hydroxo group is endothermic by 7.50 kcal/mol. The regeneration of the active site with H_2O_2 is again endothermic by 3.24 kcal/mol. After the loss of methanol $Fe^{(III)}$- O- $Fe^{(III)}$ is formed which is reduced to the Fe(II,II) form. Ferryl groups are reactive two center three electron bonds. The solvation calculations are very important to obtain good quantitative data. Siegbahn *et al.* [1] uses gas-phase values as the dielectric constant of an enzyme is low ($\varepsilon = 4$) compared to this of water ($\varepsilon = 80$). For the solvation of small model compounds in water such effects are not negligable. The solvation energies are about 150, 300 and 500 kcal/mol for the 2+, 3+ and 4+ complexes.

Mössbauer spectroscopy allows the oxidation and spin states of the iron atoms to be assessed. Thus the isomer shifts relative to metallic iron at 300 K in the range 0.35-0.60 mm/s are characteristic of 5- or 6-coordinate high-spin di-ferric μ-OH complexes, the smaller quadrupolar splitting < 1 mm/s, in the hydroxo-bridged complexes is due to the lengthening of the Fe-O bond upon protonation of the oxo bridge. The Mössbauer pattern of the supported complexes becomes more complex due to complex lattice interactions. The EXAFS shows lengthening of the Fe-Fe distances for benzimidazole compared to pyridine containing complexes. When the complexes are supported on mesoporous oxides, the EXAFS finds a lengthening of the Fe-Fe distances. The EXAFS data on the model compounds gives longer Fe-Fe distances than the QM. This may be due to neglecting in the QM the large counterbalancing anions associated with the structure of $[Fe_2(HPTP)(\mu\text{-}OH)(NO_3)_2](ClO_4)_2$ and $[Fe_2(HPTB)(\mu\text{-}OH)(NO_3)_2](ClO_4)_2$.

Methane can be converted into methanol with α-Oxygen on iron in ZSM5 type zeolites

α-Oxygen can be formed on such iron sites by nitrous oxide N_2O decomposition at elevated temperature. Nitrous oxides are formed in the industrial synthesis of adipic acid. In nitrous oxide decomposition several routes exist depending on pressure and temperature. In order to study the pretreatment, activation, reaction and extraction effects the Fe containing topologies such as CHA, MFI, MOR and CFI [10] are tested in the methane to methanol conversion. Pretreatment performed with O_2 at 550°C and vacuum at 800°C to 900°C is optimal. Activation with N_2O at 250°C is optimal and reaction with CH_4 occurs from 20°C, extraction is best with H_2O and quantification of methanol is performed by GC, GC-MS and NMR. Structure/activity effects rquire the notion of new structural parameters related to the introduction of iron in zeolite topologies such as CHA, MFI, MOR and CFI [10-11], performed via direct

DECOMPOSITION OF CF_4 BY MICROWAVE HEATING

Franz-Josef Spiess and Steven L. Suib

Department of Chemistry, University of Connecticut,
55 N.Eagleville Rd., Storrs, CT 06268

Introduction

Carbon tetrafluoride is an inert gas that is also a greenhouse gas with a very high global warming potential. It is a by-product in the aluminum production and used in the semiconductor industry. The exceptionally long atmospheric lifetime of carbon tetrafluoride makes it imperative to find solutions to destroy this potent greenhouse gas.

So far mostly catalytic and plasma discharge methods have been used to decompose CF_4.[1-3] Grytsinin et al. showed effective decomposition using a slipping surface discharge.[1] Whereas Takita et al. used $AlPO_4$-rare earth phosphate catalysts to decompose CF_4 at conversions of about 50 %.[2] Several papers like Jacobsohn et al. describe the decomposition as a means to deposit fluorinated amorphous-carbon films.[3]

In this research, we studied the effective decomposition of carbon tetrafluoride using microwave heating at medium power (0-1200 W) using water as a supplement and activated carbon as a catalyst. The experiments were carried out using an ASTEK microwave unit.

Experimental

A simple setup was used as shown in Fig. 1. The feed is a mixture of carbon tetrafluoride, water (introduced by a bubbler), and nitrogen. The content of the feed gas is 4 % CF_4, 3 % water and balance nitrogen at a flow a rate of 15 mL/min. The active carbon (100 mg) was placed in a quartz tube and secured with quartz wool. This tube was then placed into the ASTEK microwave cavity (Fig 2.). The reaction mixture was continuously monitored with a MKS-UTI PPT quadrupole residual gas analyzer mass spectrometer with a Faraday cup detector and a variable high-pressure sampling manifold. The system was equilibrated at the beginning and then the power was turned on to the desired level and continued until an equilibrium value was achieved. The catalysts used were either prepared in our research group or used as obtained from commercial vendors.

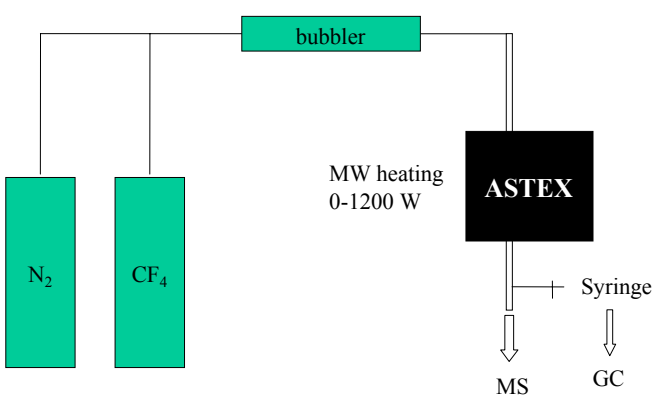

Figure 1. Schematic of the experimental setup for CF_4 decomposition.

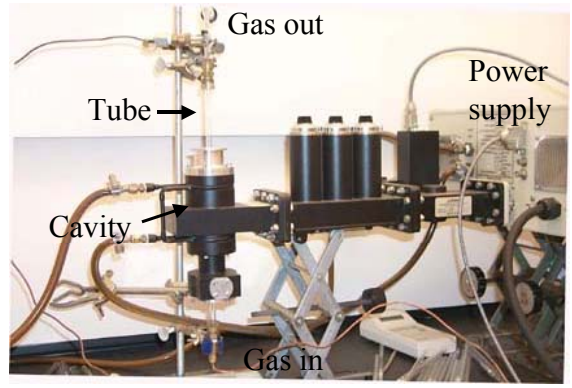

Figure 2. Photograph of the reaction setup

Results and Discussion

Initial studies using discharge plasmas yielded only low conversions (up to 12 %). Additionally, MS studies suggest that CF_4 alone or CF_4 and water are the most suited systems. Studies using microwave heating exhibited promising results under similar conditions and were therefore pursued.

The reactions were carried out with the setup presented before at a constant flow rate of 15 mL/min. Several catalysts were tested in this line of experiments. The catalysts tested were several different kinds of activated carbon, Ni filament type catalyst, V_2O_5 Supported on Al_2O_3, and a zeolite/active carbon mixture.

Of these catalysts, only the activated carbon exhibited any change in the CF_4 concentration in these experiments. It was furthermore observed that no reaction takes place without the presence of water vapor.

In the case of activated carbon, several kinds of activated carbon were used, but the results presented here are the ones for a commercial brand available from Sigma-Aldrich. A typical decomposition versus time plot is shown in Fig. 3 as obtained with the mass spectrometer.

Figure 3. Plot of CF_4 decomposition versus time, top plot is the CF_4 plot, bottom plot is the CO_2 plot, power was turned on to 480 W (arrow= time of power on)

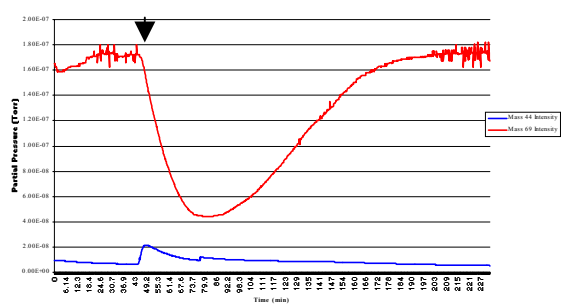

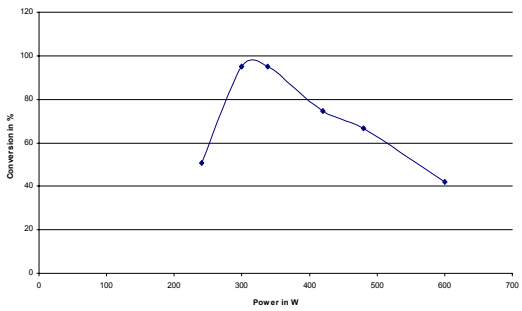

Figure 4. Plot of Conversion of CF_4 versus Power in Watts

The conversion was studied was a function of power. As shown in Fig. 4., the maximum conversion is achieved at medium power levels of 300-400 W (whole range 0-1200 W). The maximum conversion observed is 95 % measured as the disappearance of the CF_4 in the MS plot. As seen in the time versus conversion plot, the activated carbon deactivates rather quickly.

Furthermore, the reaction produces significant amounts of hydrogen, about 100,000 ppm. The extent of the reaction can also be seen on how the reaction tube looks after the reaction. The higher the extent of the reaction is, the more "decomposed" is the reaction tube due to the r\glow and HF production. The surface area of the activated carbon was determined to 653 m^2/g. It consists of meso- and micropores. The surface area below 20 Angstrom is 349 m^2/g, and between 20 and 200 Angstrom, it is 280 m^2/g.

The role of the water in this reaction is twofold. It is the primary energy absorber for the microwave radiation, but also it is the hydrogen and oxygen source needed in this reaction. It is believed that the carbon tetrafluoride reacts with the water under the use of the supplied microwave energy to yield hydrogen fluoride and carbon dioxide (The formed hydrogen fluoride is absorbed by a scrubber before it enters the mass spectrometer.). The reaction mechanism is believed to include the attack of hydrogen radicals on the CF_4 molecule; this is indicated by the formation of hydrogen in the reaction. Furthermore, the catalyst deactivation is thought to be due to the formation of hydrogen fluoride.

Conclusions

The destruction of carbon tertrafluoride by microwave heating represents an efficient and easy means to get rid of this greenhouse gas. Carbon tetrafluoride is almost completely decomposed. The main products are hydrogen fluoride, carbon dioxide and hydrogen. The activated carbon catalyst deactivates after a short period of time. The deactivation time has to be prolonged. Furthermore it was found out that water is essential in these reaction and a reaction scheme was proposed.

Acknowledgement. The authors thank JFCC and Planet Japan for support of this research. We also thank Daniel Conde for assistance in the power measurements and reactor setup.

References

(1) Grytsinin, S.I.; Korchagina, E.G.; Kossyi, I..A.; Misakyan, M.A.; Silakov, V.P.; Tarasov, N.M.; Temchin, S.M. *Plasma Sources Sci. Technol.* **10 (2001),** 125-133.
(2) Takita, Y.; Ninomiya, M.; Miyake, H.; Wakamatsu, H.; Yoshinaga, Y.; Ishihara, T. *Phys. Chem. Chem. Phys.* **1999, 1,** 4501-4504.
(3) Jacobsohn, L.G.; Franceschini, D.F.; Maia da Costa, M.E.H.; Freire Jr. F.L. *J. Vac. Sci. Technol. A* **18(5), Sept/Oct 2000,** 2230-2238.

synthesis and post-synthetic modification. When iron concentrations are kept low framework iron is seen (Fig 2).

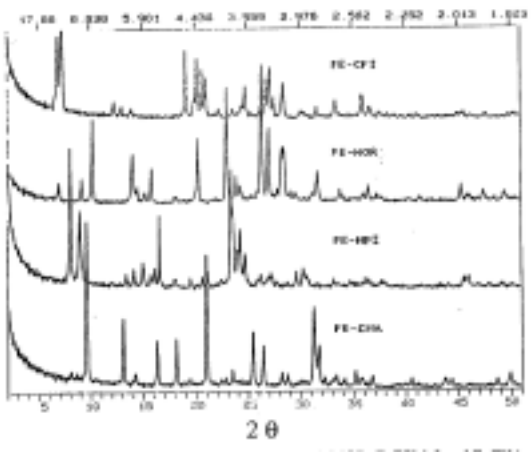

Figure 2. X-Ray Diffraction patterns of FeCIT-5, FeMOR, FeZSM-5 and FeCHA.

Extra-framework iron oxides are occluded after calcination of framework iron zeolites with high iron loading or physical mixtures of aluminum containing zeolites with iron salts or sublimation of iron by mixing zeolites with $Fe(acac)_2$ followed by an oxygen calcination procedure. The recent structure of CIT-5 is composed of 1D, extra-large pores of nearly circular cross section (center of O to center of O distance 9.91Å x 9.87Å) circumscribed by 14 T-atoms. The asymmetric unit contains 10 T-atoms and 19 oxygen atoms resulting in a unit cell content of $[Si_{32}O_{64}]$, a framework density of 18.3 T-atoms/1000 $Å^3$ and a density of 1.821 g/cm^3. The topology consists of zigzag ladders of 4-rings with pendant 5-rings interconnected through single zigzag chains. For CIT-5 (CFI) all structural parameters are within reasonable ranges for silicate materials (d(Si-O) 1.591 Å with a range of 1.555-1.641 Å, a Si-O-Si angle of 149.4° with a range of 168.7°-140.6°, and an O-Si-O angle of 109.4° with a range of 113.8° - 104.2°. These values are appended to the molecular mechanics Universal Force Field (UFF) [3]. The UFF functional forms, parameters, and generating formulas for the full periodic table

Table 1. Partial oxidation of methane with α-Fe sites in ZSM-5 and other Zeolites.

Zeolite	%wt Fe in	Oxidation	μmol Fe in sample	μmol. MeOH (oxygenate)
Fe-ZSM-5 Si/Al 11	0.5%	5 Torr N_2O/ 250°C	75	-
Fe-ZSM-5 Si/Al 11	2.0%	5 Torr N_2O/ 250°C	360	97
Fe-ZSM-5 Si/Al 11	5.0%	5 Torr N_2O/ 250°C	800	163
Fe-ZSM-5 Si/Al 11	5.0%	10Torr N_2O/250°C	800	208
Fe-CHA (0.1 μm)	5.0%	5 Torr N_2O/ 250°C	800	10
Fe-MOR (1-3 μm)	5.0%	5 Torr N_2O/ 250°C	800	10 (33)
Fe-CIT-5 (3-7 μm)	5.0%	5 Torr N_2O/ 250°C	800	4 (39)

are used to model these structures. XRD, EXAFS, Mossbauer, DRS, magnetic measurements and EPR can resolve and attribute presence of lattice iron and extra-framework clusters. XRD for as made and calcined materials with iron in the lattice reveals α-Fe_2O_3 particles are absent (no α-Fe_2O_3 reflection, d_{104} = 2.70 Å). From EXAFS structural parameters obtained in the k^3 weighted optimization give 1.7, 2.7 and 3.4Å distances for $Fe^{(III)}$-oxygen, $Fe^{(III)}$- $Fe^{(III)}$ and $Fe^{(III)}$-Si bonds. In the EPR spectra the ratio of octahedral/tetrahedral iron can be assumed from the presence of lines at g= 2/4.3, and depends on sample hydration. In mononuclear iron complexes the Fe-O bond distances of 1.86 Å (2+, O_h) 6 coordinated and 1.90 Å (3+, T_d) 4 coordinated. For tetrahedral iron and silicon atoms bond distances of 1.65 for Si-O and 1.90 Å for Fe-O obtained from QM seen in the direction of the Fe-O-Si bridge, with Fe-O-Si angles close to the 131.2° and to a O-Fe-O angles of 109.47°.

CONCLUSION.

The reaction of the MMO binuclear heptapodate coordinated iron (III)-complexes of *N,N,N',N'*-tetrakis(iminomethyl)-2-hydroxy-1,3-diamino-propane model with methane is exothermic The σ- and π-bonds of the ferryl Fe=O in the plane of the Fe-O-Fe bridge, have the properties of a two atom three electron bond. After the H splitting from methane, the methyl recombines with the FeO center via a weak Fe-OCH_3 bond in this model.

Methane can also be converted into methanol with α-Oxygen at room temperature using N_2O as a selective oxidant inside the pores of various zeolites. Extraction of the catalysts with water is preferred over acetonitrile-water mixtures. The dinuclear iron oxide clusters realize the sub-stoichiometric (based on a diiron sites) oxidation of methane after N_2O activation, the small dinuclear Fe sites favor oxygen insertion chemistry over coupling chemistry.

Acknowledgement.
PPKG thanks ESA, FNRS and FSR Belgium for financial support, A.Fukuoka & M.Ichikawa from the CRC, at Hokkaido University, Sapporo, Japan for a collaboration on EXAFS. PPKG thanks WAGoddard III from the Material & Process Simulation Center, Beckman Institute (139-74), California Inst. of Technology, Pasadena CA, USA, WAG thanks BP Amoco for financial support.

References

(1) R.H. Crabtree, *Chem.Rev*., **1995**, 95, 987.
(2) P.E. Siegbahn, R.H.Crabtree, *J.Am.Chem.Soc*., **1997**,*119,* 3103.
(3) P.P. Knops-Gerrits , P.A. Jacobs, A.Fukuoka, M.Ichikawa, F.Faglinoni, W.A. Goddard III, *J.Mol.Cat., A*, 166 (2001) 3, P.P. Knops-Gerrits, M. Witko, W.A.Goddard III, R. Millini Eds.
(4) K. Yoshizawa, K. Ohta, T. Yamabe, R. Hoffmann, *J. Am. Chem. Soc.,* **1997**, *119*, 12311.
(5) A.E.Shestakov, A.E.Shilov, *J.Mol.Cat., A,* 105 (1996) 1.
(6) A.K. Rappe, C.J. Casewit, K.S. Colwell, W.A. Goddard, W.M. Skiff, *J. Am. Chem. Soc.,* 114 (1992) 10024.; A.K. Rappe, W.A. Goddard, *J. Chem. Phys*., **1991**, 95, 3358.
(7) P.P. Knops-Gerrits, A.M. Van Bavel, G. Langouche, P.A. Jacobs, NATO ASI, **1998**, Derouane Eds., 3.44, 215.
(8) P.P. Knops-Gerrits, A. Verberckmoes, R.A. Schoonheydt, M. Ichikawa, P.A. Jacobs, *Micro- Mesop. Mat.,* **1998**, *21*: 4-6, 475.
(9) P.P. Knops-Gerrits, A. Weiss, S. Dick, P.A. Jacobs, *Stud.Surf.Sci.Catal*., **1997**, *110*, 1061.
(10) P.P. Knops-Gerrits, W.A. Goddard III, *J.Mol.Cat., A,* **2001**, 166, 1 & 135.
(11) Y. Oumi, M. Yamadaya, T. Kanougi, M. Kubo, A. Stirling, R. Vetrivel, E. Broclawik, A. Miyamoto, Catal. Lett., **1997**,45, 21.
(12) G.I., Panov, V.I., Sobolev, K.A. Dubkov,.A.E., Parmon, N.S., Ovanyesan, A.E., Shilov, A.A., Shteinman, *React. Kinet. Catal.Lett.,* **1997**, *61*, 251 .

A REMARKABLE ENHANCEMENT OF FORMATION OF DIAMOND-LIKE CARBON FILM FROM METHANE USING DIELECTRIC-BARRIER DISCHARGES

Yue-ping Zhang[1], Hai-yan Du[2], Yang Li[3], Baldur Eliasson[3,4], Fei He[3] and Chang-jun Liu[3]*

[1] Department of Chemistry, Tianjin University, Tianjin 300072, China; [2] Analysis Center, Tianjin University, Tianjin 300072, China; [3] Tianjin Univ.-ABB Plasma Greenhouse Gas Chemistry Laboratory, State Key Laboratory of C1 Chemical Technology, Tianjin University, Tianjin 300072, China; [4] Energy and Global Change, ABB Corporate Research Center, Baden, CH5405, Switzerland

Introduction

Plasma can create polymer films or diamond like carbon film from monomers (e.g. methane) that do not form polymers by conventional chemical technologies [1,2]. Such plasma-polymerized films exhibit excellent properties and have a great potential as electronic, optical and biomedical materials. There is an increasing interest at plasma polymerization of methane. DC glow, low frequency (50 or 60 Hz), radio frequency (13.56 MHz) or microwave (2.45 GHz) radiation usually induces plasma for such plasma polymerization. Mostly, a vacuum or low-pressure condition is required. Recently, we have achieved a fabrication of diamond like carbon film from methane and carbon dioxide or methane and carbon monoxide feed using dielectric-barrier discharge at atmospheric pressure. We have also observed a remarkable enhancement of production of diamond like carbon film if methane and carbon monoxide were used as co-feeds under the condition of dielectric-barrier discharges.

Experimental

The experimental setup has been shown in Figure 1 and has been discussed in detail elsewhere [3-5].

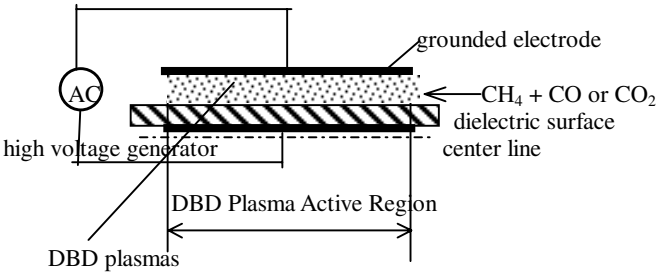

Figure 1. Schematic diagram of the DBD plasma polymerization reactor

Discharge zone lies between a dielectric-barrier made of quartz and a stainless steel tube serving as grounded electrode with a length of 250 mm and a gap width of 1.1 mm. An aluminum foil is connected with a high voltage generator, which output a sinuous signal at a frequency of 25 kHz. Methane and carbon monoxide or carbon dioxide were introduced into the discharge gap (between the grounded electrode and the quartz surface) both at 20 ml/min via two mass flow controllers. The voltage and current were measured with an on-line oscilloscope (Tektronix 2440) connecting a high voltage probe (Tektronix P6015 A) and a pulse current transformer (Pearson Electronics 411). The discharge power was read out with a multimeter (Keithley 2000). The discharge power in this work was fixed at 100 W. The temperature of reaction was adjusted at about 338 K with circling oil. The experiments were operated at atmospheric pressure. The feed gases and gaseous products were analyzed with an on-line gas chromatograph (HP 5890 with TCD and FID) and mass selective detector (HP 5971). The plasma-polymerized film was formed first on the surface of the dielectric tube (quartz) close to the exit of plasma active region. Such formed film continues to grow up the dielectric tube with reactions. After reaction, a piece of quartz tube with plasma-polymerized film was cut as a sample for IR characteristics. The morphology of solid products on the quartz tube was analyzed using a scanning electron microscopy (SEM, PHILIPS XL-30). A FT-IR (VECTOR 22, Bruker Instrument Ltd.) was also used to characterize the functional groups of the plasma-polymerized film. The surface analysis of the chemical structure was performed by ESCA, also known as XPS with a Perkin Elmer PHI1600 system. The angle-resolved ESCA analysis was conducted using a monochromated Mg Kα radiation at 250 w, by assuming a binding energy (BE) of adventitious carbon equal to 284.6 eV.

As discussed above, the reaction for the fabrication of carbon film occurs on the surface of dielectric material (quartz). A hard and dense uniform film has been observed after the reaction. It has been also observed that the hard carbon film was just formed within the discharge region. The formation of such carbon film was terminated right away out of the discharge region. It suggests that the gas discharge is a basic for the fabrication of carbon film. The hardness of the produced carbon film is 53.5 kgf/mm^2 (or 5.35×10^8 Pa) detected using a HVA-10A Vickers Hardness Measurement Instrument.

Results and Discussion

We have reported a production of plasma polymerized carbon film from methane and carbon dioxide using dielectric-barrier discharges [5]. The selectivity of such produced carbon film is from 30 to 40% upon the feed ratio of CH_4/CO_2. In this work, we feed carbon monoxide, instead of carbon dioxide, for the fabrication of plasma polymerized carbon film from methane. The selectivity of the carbon film was significantly increased. Table 1 shows the results of such a production.

Table 1. Conversions of Methane and CO and Selectivities
(Temperature of reaction: 338K; flow rate of feed: 40 ml/min)

Ratio of CH4/CO	2/1	2/1	1/1
Input power/W	50	100	100
Conversion of CH_4	43.74	62.45	72.92
Conversion of CO	14.70	20.02	18.51
Selectivity of diamond like carbon film	60.14	65.88	72.99
Selectivity of gaseous hydrocarbons	38.33	32.31	23.38
Selectivity of liquid products	1.54	1.81	3.63

Table 1 shows more feed amount of carbon monoxide will lead to higher selectivity of diamond carbon film. This suggests the presence of carbon monoxide tends to induce the plasma polymerization from methane under the condition of dielectric-barrier discharges. The result of FT-IR characteristics of plasma-polymerized film from methane and carbon monoxide is shown in Figure 2. There are two

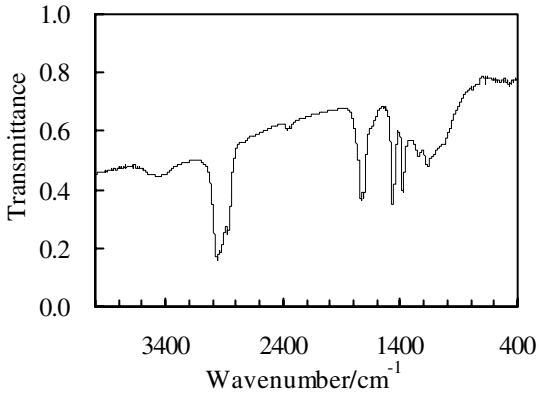

Figure 2. FTIR spectra of the carbon film sample

peaks at 1712 cm^{-1} and 1732 cm^{-1}, respectively, in the FT-IR spectrum. This splitting was assigned to the effect of coupling of α or β di-carbonyl. The presence of a band at nearly 3350 cm^{-1} was attributed to hydroxyl group. The bands at 2962 cm^{-1}, 2930 cm^{-1} and 2870 cm^{-1} were observed for CH_3 asymmetrical stretching vibration, CH_2 asymmetrical stretching vibration and CH_3 symmetrical stretching vibration, respectively. The bands at 1462 cm^{-1} and 1380 cm^{-1} were due to CH_3 asymmetrical bending or CH_2 scissoring vibration and CH_3 symmetrical bending vibration, respectively. The morphology of the polymer film on the quartz tube was studied by SEM microscope, as shown in Figure 3. Figure 3 shows the carbon film was consisted of small irregular units with the size from 5 μm to 10 μm. All the units were closely aggregated to compose the dense film on the quartz tube The polymer film produced from methane and carbon dioxide in Reference 5 was much more complex than the film produced in this work. It is considered that carbon monoxide is a better monomer for co-polymerization with methane using dielectric-barrier discharges. The plasma-polymerized film attained was also with relative simple structures that would lead many an application for coatings and others.

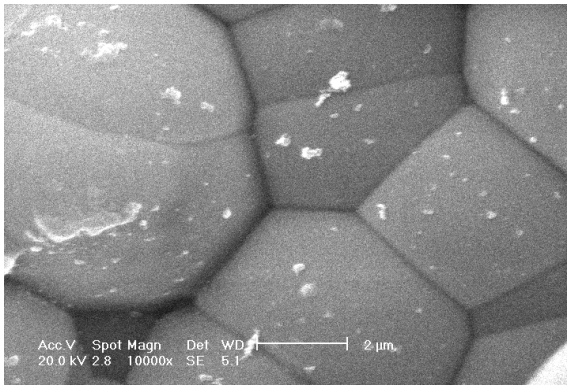

Figure 3. SEM images of polymer film on the quartz tube. (Discharge power of 100 W; the ratio of CH_4/CO: 1/1)

The angle-resolved ESCA allows an analyst to change the depth of analysis so that the depth information becomes available. The ESCA spectrum of plasma polymerized carbon film suggests another species in the binding energy of around 102.1 eV in addition to the Si species contributed from quartz (with a Binding Energy of 103.7 eV). This strange Si species could not be considered as a possible C-Si species in the polymerized film, upon the Angle-resolved ESCA analysis, since $Si_{102.1eV}/Si_{103.7eV}$ is very small at the small take-off angle (close to the top layer of surface). The ratio of these two kinds of Si species reduces with the decrease in the take-off angle, as shown in Table 2. This suggests the quartz becomes electrically active under the condition of gas discharge plasmas and is reduced slightly. It has been considered that the electrically active quartz will provide active sites for plasma polymerization.

Table 2. $Si_{102.1eV}/Si_{103.7eV}$ Reduces with the Decrease in the Take-off Angle

$Si_{102.1eV}/Si_{103.7eV}$	*Take-off angle θ*
0.7	90
0.4	60
0.2	30

Conclusion

The co-feed of methane and carbon monoxide has led to a remarkable enhancement of the formation of diamond-like carbon film from methane using dielectric-barrier discharges, compared to that obtained from the co-feed of methane and carbon dioxide. Due to the easy operation of dielectric-barrier discharge at atmospheric pressure, the present method would lead to a significant improvement in the fabrication of diamond-like carbon film. The present investigation is also helpful for the understanding of the formation of plasma-polymerized carbon film from plasma methane conversion using dielectric-barrier discharge in the presence of carbon dioxide because carbon monoxide will present as a major by-product with it.

Acknowledgement The supports from The Research Fund for the Doctoral Program of Higher Education of China and ABB Corporate Research Ltd., Switzerland are very appreciated.

References

1. Suwa, T.; Jikei, M.; Kakimoto, M.-A.; Imai, Y.; Tanaka, A.; and Yoneda, Y. *Thin Solid Films*. **1996**, 273, 258.
2. Biederman, H.; and Osada, Y. *Plasma Polymerization Processes*, Elsevier, 1992.
3. Eliasson, B.; Liu, C.-J.; and Kogelschatz, U. *Ind. Eng. Chem. Res*. **2000**, 39, 1221.
4. Eliasson, B.; Kogelschatz, U.; Xue, B.; and Zhou, L.M. *Ind. Eng. Chem. Res*. **1998**, 37, 3350.
5. Liu, C.-J.; Xue, B.; Eliasson, B.; He, F.; Li, Y.; and Xu, G.-H. *Plasma Chem. Plasma Process.*, **2001**, 21, 301.

METHANOL PRODUCTION FROM PARTIAL OXIDATION OF METHANE IN A SPECIALLY DESIGNED REACTOR

Qijian Zhang, Dehua He, Xin Zhang and Qiming Zhu*

State key Laboratory of C1 Chemistry and technology
Department of Chemistry, Tsinghua University, Beijing 100084, China

*Corresponding author. Email:
hedeh@mail.tsinghua.edu.cn
Fax: +86-10-6279-2122

Introduction

Research on direct partial oxidation of methane to methanol has last for a long time because of its great industrial potential. Unfortunately, in most literatures CH_3OH yield was always below 5%. The molecular of methanol is far more reactive than methane under similar condition. Methanol is easily oxidized to CO and/or CO_2. Therefore, the selectivity of methanol was always poor. Participation of catalyst has not improved methanol selectivity till now. The temperature and pressure for catalytic oxidation of methane were in the range of gas phase homogeneous oxidation. Then the gas phase homogeneous reaction was inevitable in the catalytic reaction. Therefore, it is necessary to continue the exploration on the gas phase homogeneous oxidation of methane.

Experimental

The gas phase partial oxidation of methane was investigated in a specially designed quartz lined tubular reactor. The quartz line was tightly fitted in the stainless steel line using an O-ring of fluoride rubber pressed by a locking nut to avoid contact of feed gas with metal wall so as to diminish the wall effect. And a spacer (quartz tube) was placed in the reactor to ensure the product mixture leave out the high temperature reaction zone rapidly so as to terminate the free radical reaction and minimize the deep oxidation of required product.

Results and discussion

In the specially designed reactor, a yield of CH_3OH about 7-8% (60-63% CH_3OH selectivity at 11-13% CH_4 conversion) could be obtained at 430-470°C, 5.0MPa and $CH_4/O_2/N_2$=100/10/10 (ml/min, STP), while O_2 was completely consumed. The selectivity of CO was about 30% and the selectivity of CO_2 was kept less than 5-10%. Production of H_2 was also observed, its concentration in the gas mixture was just less than that of CO. Since no HCHO was detected, it is believed that it decomposed quickly to CO and H_2 if it was formed in the reaction system.

In most literatures, high CH_3OH selectivity could be obtained when methane conversion was very low; however the selectivity would fall down quickly while increasing the methane conversion. The yield of methanol was always less than 5%. Comparison of the reaction conditions with that in our early work[1] and other literatures[2,3,4], the most difference lies in the reactor structure.

In order to verify what makes high methanol yield possible, some experiments were carried out by adjusting the structure of the reactor. Without O-ring for sealing the gap between quartz tube and stainless tube in the reactor, the methanol selectivity decreased sharply from 62% to 31%, and methanol yield fell from 8% down to only 3%. Instead of quartz line with silicate glass line, the selectivity only decreased slightly. The spacer (quartz tube) in the reactor does have some effect on the reaction because the methanol selectivity decreased from 62% to 41% (Table 1).

Table 1 Effect of the varying of the reactor structure on the partial oxidation of methane

Case*	Methane Conversion/%	Selectivity /%			Methanol Yield/%
		CH_3OH	CO	CO_2	
A	13.1	62.3	32.6	4.8	8.2
B	9.1	31.6	50.0	18.8	2.9
C	11.7	41.2	41.5	15.4	4.8
D	13.0	54.5	33.0	12.0	7.1

P=50atm, T=450℃, $CH_4/O_2/N_2$=100/10/10(ml/min)

*A-the original structure, B-without O-ring; C-without spacer; D-silicate glass line instead of quartz glass line

Conclusion

A yield of CH_3OH about 7-8% could be obtained in the specially designed reactor. It is supposed that the high CH_3OH yield should be attributed to the encapsulation of the ringed gap between the quartz line and the SS line. Higher CH_3OH selectivity could be achieved by improving the reactor design.

Acknowledgement

We acknowledge the financial support from the Key Project of National Fundamental Research and Development of China (973) and the Analytical Foundation of Tsinghua University.

References:

[1] Han, Z.S.; Pan, W.; Li, J.L.; Zhu, Q.M. Tsinghua Sci. Tech. 1996, 1(4):420-424
[2] Foulds, G.A.; Gray, B.F.; Miller, S.A.; Walker, G.S.; Ind. Eng. Chem. Res. 1993, 32:780-787
[3] Omata, K.; Fukuoka, N., Fujimoto, K.; *Ind. Eng. Chem. Res.* 1994, 33:784-789
[4] Chellappa, A.S.; Fuangfoo, S.; Viswanath, D.S.; *Ind. Eng. Chem. Res.* 1997, 36:1401-1409

CATALYTIC STABILITY OF NI CATALYST FOR PARTIAL OXIDATION OF METHANE TO SYNGAS

Li Zhenhua, Zhang Xiangyu, He Fei and Xu Genhui

State Key Lab of C_1 Chemistry and Technology, School of Chemical Engineering and Technology, Tianjin University, Tianjin 300072, P.R.China

Introduction

In recent years, catalytic partial oxidation of methane to synthesis gas (POM) attracted an extensive attention. Of the reported catalysts, supported Ni catalyst is a promising catalyst for POM industrial production since its high activity and low price[1-4]. However, the catalytic stability of Ni catalyst is not so good as noble catalysts such as Rh or Pt. In this paper, 10% (wt%) Ni catalysts supported on 5 mm α-Al_2O_3, β-Al_2O_3 and γ-Al_2O_3 pellets were prepared by impregnation method. The catalytic activity and stability were measured in a continuous fixed bed reactor.

Experimental

A quartz tube of dimension of 5mm o.d.× 3 mm i.d. ×300mm length was used as a reactor. The catalyst loaded was 60 mg. High purity Argon was used as a carrier gas for GC analysis of inlet and outlet gas mixture. The conversion and selectivity were calculated from GC analysis results based on the C, H, O and N balance.

The specific surface area of the support and the catalyst before and after reaction were measured using a Pulse Chemisorption (CHEMBET-3000) Instrument. The catalyst amounts were 30 mg. The adsorption at liquid nitrogen and desorption at room temperature were recorded when partial pressure of N_2 in He is 0.1, 0.2 and 0.3 respectively.

XPS characterization has been done to analyze the carbon deposit and the dispersion of Ni on the support. XPS analyses employed a multi-pass analyzer (PHI 5600) with pass energy of 188 eV for survey spectra and 29 eV for high-resolution spectra. X-rays were generated using a Mg K_α X-ray source.

Results and Discussion

Three catalysts were tested for POM process after reduced at 800 °C for 2 hours. As shown in Table 1, all catalysts exhibit good activity for POM process and 10% Ni/β-Al_2O_3 catalyst shows the best activity. It can be seen that the catalytic activity and the product selectivity increase in the order of 10% Ni/α-Al_2O_3< Ni/γ-Al_2O_3< Ni/β-Al_2O_3. The results were different from the reported results when the powder alumina was used. It was once reported[5] that the 8% Ni/α-Al_2O_3 is the best catalyst and the catalytic activity and the product selectivity increase in the order of 8% Ni/γ-Al_2O_3<Ni/β-Al_2O_3<Ni/θ-Al_2O_3 ≈Ni/α-Al_2O_3. It can be attributed to the differences of the support and the preparation method applied.

Table 1 Catalytic activities of 3 catalysts after reduced at 800 °C for POM process

Reaction condition / Catalyst	O_2, N_2, CH_4 flow rate: 19, 70, 38ml/min					O_2, N_2, CH_4 flow rate: 37, 140, 74ml/min				
	X_{CH4} %	X_{O2} %	S_{CO} %	Y_{CO} %	H_2 / CO	X_{CH4} %	X_{O2} %	S_{CO} %	Y_{CO} %	H_2 / CO
10%Ni/α-Al_2O_3	50.64	98.80	75.72	38.30	2.03	62.42	98.59	82.75	51.67	2.02
10%Ni/β-Al_2O_3	69.33	98.59	82.85	57.45	2.08	73.57	98.59	87.21	64.18	2.05
10%Ni/γ-Al_2O_3	64.56	98.36	85.00	54.91	2.05	68.73	98.66	88.10	60.52	2.03

Note: reaction temperature: 650 °C, pressure: atmospheric pressure

Three catalysts were continuously tested for 100 hours at reaction temperature 700 °C and space velocity of 1.5×10^5 hr^{-1} with the molar ratio of CH_4:N_2:O_2=2:4:1. The results showed that the catalytic stability increases in the order of 10% Ni/γ-Al_2O_3< Ni/β-Al_2O_3< Ni/α-Al_2O_3.

The above results indicated that the property of support alumina is a major factor of affecting the catalytic activity and stability. It is necessary to investigate this effect. The specific surface area of the catalysts and the supports were measured and shown in Table 2. It was found that for 10% Ni/β-Al_2O_3 and Ni/γ-Al_2O_3 catalysts, the specific surface area decreased as the order of support>(the catalyst before reduced at 800 °C) >(the catalyst after reaction at 650 °C for 4 hrs). As for 10% Ni/α-Al_2O_3 catalyst, its specific surface area has a little increase compared to that of the support.

Table 2 Specific surface area of the support and the 10% Ni catalysts

Catalyst	10% Ni/α-Al_2O_3			10% Ni/β-Al_2O_3			10%Ni/γ-Al_2O_3		
	1	2	3	1	2	3	1	2	3
specific surface area, m^2/g	8.6	11.9	10.8	71.3	47.0	43.8	251.1	107.6	66.2

Note: 1.support, 2.catalyst before reduction, 3.catalyst after reaction at 650 °C for 4 hrs

XPS characterization was done for three catalysts before reduction and after reaction at 700 °C for 100 hrs. The XPS spectra for 10% Ni/α-Al_2O_3 catalyst, which is similar with the spectra for the other two catalysts, was shown in Fig. 1.

The surface compositions for the three catalysts before reduction and after reaction at 700 °C for 100 hrs were determined by XPS and shown in Table 3. It was noted that the carbon on the 10%Ni/α-Al_2O_3 and 10% Ni/γ-Al_2O_3 catalysts before reduction are almost the same, which is about double the carbon on the 10% Ni/β-Al_2O_3 catalyst. After these catalysts were reduced at 800 °C by hydrogen for 2 hrs and reacted at 700 °C for 100 hrs, the carbon deposits on the catalysts all increased in the order of Ni/α-Al_2O_3<Ni/γ-Al_2O_3<10%Ni/β-Al_2O_3. Combined with the 100 hrs POM reaction result, it is clear that the carbon deposit is a major factor resulting in the deactivation of Ni catalyst for POM process. The Ni atomic ratio data indicated that the dispersion of Ni on these three supports are different and may be another factor affecting the stability.

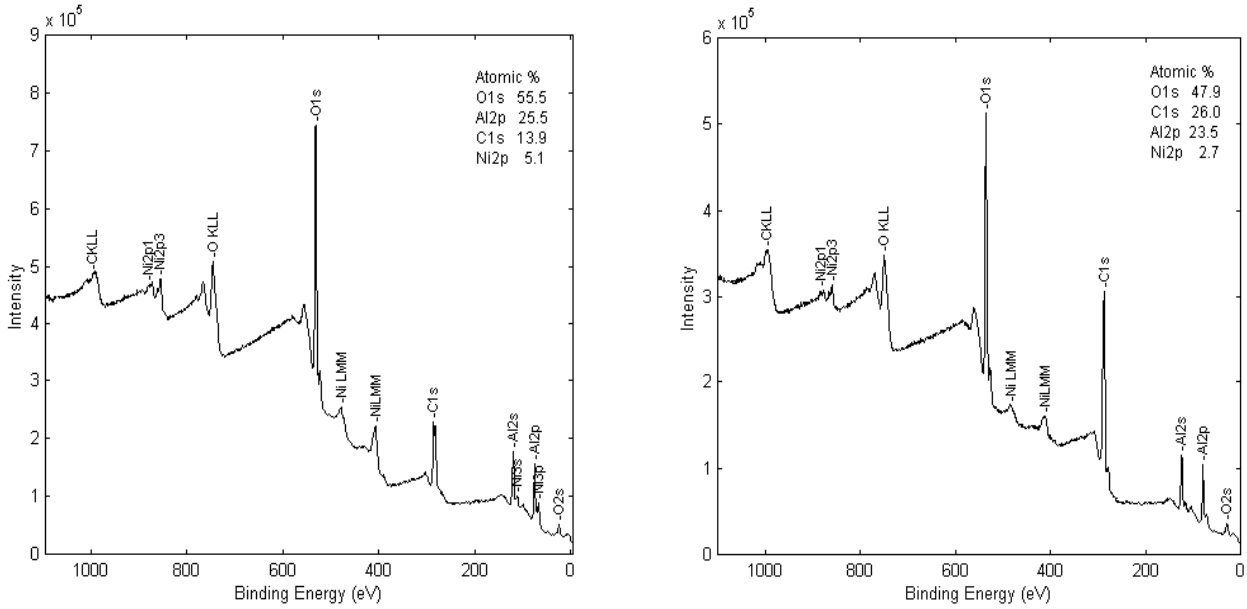

(a) (b)

Figure.1 The XPS survey spectra for 10% Ni/α-Al_2O_3 catalyst (a) before reduction; (b) after reaction at 700°C for 100 hrs.

Table 3 Surface compositions obtained from XPS for 3 catalysts

	Atomic ratio, %					
	10%Ni/α-Al_2O_3		10% Ni/β-Al_2O_3		10% Ni/γ-Al_2O_3	
	Before reduction	After reaction	Before reduction	After reaction	Before reduction	After reaction
O1s	55.5	47.9	59.7	49.2	56.3	44.1
Al2p	25.5	23.5	30.8	26.7	28.2	22.5
Ni2p	5.1	2.7	2.1	0.9	1.1	0.8
C1s	13.9	26.0	7.4	23.2	14.4	32.6

Conclusions

(1) 10% Ni/β-Al_2O_3 catalyst is better than 10%Ni/α-Al_2O_3 and 10%Ni/γ-Al_2O_3 catalysts considering both of the activity and stability.

(2) The dispersion of Ni and the carbon deposit are the major factors affecting the catalytic activity and stability for POM process.

Acknowledgement. We appreciate the financial support from Chinese National Natural Science Foundation (No: 20106013) and State Key Laboratory of C_1 Chemical Technology of Tianjin University.

References

(1) Ashcroft A T, Cheetham A K, Foord J S et al., *Nature(London)*, 1990, 344(6264)•319

(2) Hickman D A, Schmidt L D, *J Catal*, 1992, 138(1)•267

(3) Torniainen P M, Chu X, Schmidt L D, *J Catal.*, 1994, 146(1)•1

(4) Zhenhua L., Xiangyu Zh., Xinbin M., *Huaxue Fanying Gongcheng Yu Gongyi(Chinese)*, In press

(5) Lin Y., Shuhua Y., Jiuying T., et. al., *Chinese Journal of Catalysis*, 2001, 22(4)•383

Gas Hydrate Crystal Growth and Decomposition

C.A. Koh*[a] , S.C. Nyburg[a], A.K. Soper[b], S. Parker[b], R.E. Westacott[c], J. Creek[d], S. Subramanian[d]

[a]*King's College London, Department of Chemistry, Strand, London WC2R 2LS, U.K.*
[b]*ISIS Facility, Rutherford Appleton Laboratory, Chilton, Didcot, Oxon., OX11 0QX, U.K.*
[c]*Heriot-Watt University, Department of Mechanical & Chemical Engineering, Edinburgh, EH14 4AS, U.K.*
[d]*Chevron Petroleum Technology, Houston, TX 77082, U.S.A.*

The formation and decomposition of gas hydrates are of both fundamental and industrial importance.[1-3] Further insight into these processes is needed in order to control hydrate crystallisation in gas/oil pipelines, or for the extraction of methane hydrate from marine sediments.

Crystal growth[4] and decomposition processes have been examined for methane hydrate using *in situ* neutron diffraction measurements. The methane hydrate samples were synthesized by charging a high pressure variable temperature TiZr cell with D_2O and pressurising with CH_4 and CD_4. The liquid in the reaction cell was cooled using a recirculating glycol bath. Fine temperature control of the cell was achieved using electrical heating, with thermocouples placed within the copper cooling jackets at the top and bottom of the cell. The D_2O/methane mixture was allowed to equilibrate at around 18°C and 14.5 MPa while agitating the fluid within the cell vigorously to ensure effective interfacial mixing. The temperature was lowered in stages such that the system was driven towards methane hydrate formation. On complete hydrate conversion of the liquid within the neutron beam (indicated by the absence of any diffuse scattering), the temperature was subsequently increased in stages until the methane hydrate was completely decomposed. At this stage, the temperature was well outside the hydrate formation region and the neutron diffraction pattern gave no indication of Bragg reflections due to hydrate crystals (see Figure 1).

These neutron diffraction measurements were coupled with simultaneous gas consumption measurements, which were performed throughout the duration of the experiments. This is the first molecular-level study of methane hydrate decomposition and is expected to provide insight into the structure of the liquid phase immediately after dissociation of the hydrate crystal lattice.

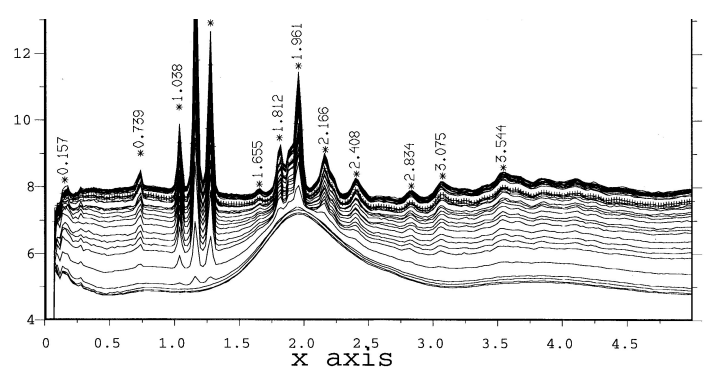

Figure 1. Neutron scattering cross-section data during methane hydrate decomposition (CH_4/D_2O).

The phonon density of states of methane hydrate and THF hydrate (a model sII hydrate) has also been measured using inelastic neutron scattering. Methane hydrate samples were prepared from fine particles of H_2O and D_2O ice pressurised with methane gas. The effect of a thermodynamic inhibitor, methanol, on the structure and dynamics of these systems has been investigated. Important structural information on methane hydrate and carbon dioxide hydrate has also been extracted from *in situ* neutron and X-ray diffraction data.

References

(1) Sloan, E.D. *Clathrate Hydrates of Natural Gases,* 2nd Edition, 1997, Marcel Dekker, N.Y.
(2) Englezos, P. *Ind. Eng. Chem. Res.,* **1993**, 32, 1251.
(3) Koh, C.A.; Westacott, R.E.; Zhang, W.; Hirachand, K.; Creek, J.L.; Soper, A.K. *Fluid Phase Equilibria*, **2001**, 4848, 1.
(4) Koh, C.A.; Wisbey, R.P.; Wu, X.; Westacott, R.E.; Soper, A.K. *J. Chem. Phys*. **2000**, 113, 6390.

SIMULATIONS OF METHANE HYDRATE PHENOMENA OVER GEOLOGIC TIMESCALES: EFFECT OF MARINE BASIN PARAMETERS

Kevin L. Gering, PhD

Fossil Energy Technologies
Idaho National Engineering and Environmental Laboratory
P. O. Box 1625
Idaho Falls, ID 83415-3625

Introduction

The complex behavior tied to formation and accumulation of methane hydrate and free gas within dynamic marine sediments has been investigated using a new model that includes physical, mechanical, biological, and thermodynamic contributions. An early paper provided a detailed analysis of phase equilibria for the seawater-methane system within the context of having variable seafloor depths and geothermal gradients.[1] The paper that followed presented initial results of the newest model that incorporates accurate phase equilibria, sediment compaction, liquid advection, and methane biogenesis.[2] Rates of key processes are described in terms of geologic time, making possible simulations covering several million years.

This work extends our focus to look at the effects of marine basin parameters on the occurrence of solid methane hydrate and free gas. Foremost parameters include the geothermal gradient (GTG) and the depth of the seafloor, which are key to establishing the thermodynamic state of the seawater-methane system at a given sediment depth below the seafloor. Other basin parameters include the rate of sediment deposition and compaction, average pore diameters within the sediments, and the shape of sediment particles. Determination of conditions for maximum occurrence of methane hydrate is facilitated by a comprehensive study of these basin parameters. Hence, resource determination is made possible by this model, whereas other applications could include seafloor stability issues, and environmental release of methane from marine systems.

Methods

Sediment Dynamics. Marine sediments are porous media whose porosity profiles change over time due to a number of influences. Herein, the sediment compaction rate is defined as the change in sediment porosity over time as a function of sediment depth, where this rate dictates the downward migration of the sediment solids and the upward liquid advection rate. This work developed an analytical expression for porosity as a function of depth and time that is essentially a time-modified version of the well-accepted Athy equation,[3] which has seen wide use in sedimentary geophysics because it can provide good estimates of porosity profiles for some marine basins.[4-7] Sediment compaction and liquid advection are heavily influenced by the physical characteristics of the sediment, and seawater advection due to compaction is the primary transport mechanism for moving methane to locations within the sediment where it can be formed into methane hydrate or free gas.

Key Basin Parameters. The depth of the seafloor and value of the GTG have profound effects on the amount of methane available from advecting liquid for hydrate formation or gas exsolution. Consider the idealized phase equilibria represented in **Figure 1**, wherein the phases are liquid seawater (L), methane hydrate (H), and free methane gas (G). If the GTG is assumed to be constant, then liquid advection pathways along a GTG are represented by straight lines on a depth versus temperature plot. Three such lines are shown in Fig. 1. Lines A and B represent the comparison of basins that have different seafloor depths, but have identical GTGs. Lines B and C represent the scenario of two basins that have the same seafloor depth, but differing GTGs. The potential magnitude and location of hydrate and free gas formations will vary between lines A, B, and C because the phase equilibria (as reflected by soluble methane concentrations) differs among these paths.

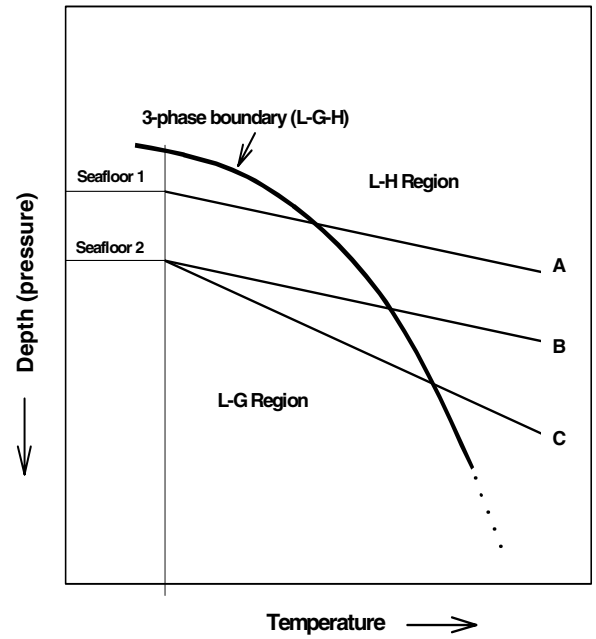

Figure 1. Idealized plot of phase equilibria for the seawater-methane system, contrasting the upward liquid advection paths taken along the same GTG with different seafloor depths (lines A and B) and different GTGs with the same seafloor depth (lines B and C).

Other parameters include rate of sediment deposition and compaction, average pore diameters between sediment particles, and the shape of sediment particles. Sediment deposition and compaction have a direct effect on the upward flux of advecting seawater, and hence influence the net migration of methane through the sediments over time. Pore sizes and particle shapes affect the frictional flow characteristics of the advecting liquid, and are key influences on liquid overpressures (those pressures experienced by advecting liquid that are greater than hydrostatic values).

Methane Biogenesis. A source term for biogenic methane has been incorporated into the model, which yields the production rate of methane as a function of depth and temperature. Predictions of methane generation within marine sediments are based on laboratory data gathered using isolated methanogens found in natural marine systems, assigning an average population of these microbes within the total microbial consortium. A previous paper should be consulted for further details concerning this biogenic source term.[2]

Results and Discussion

Methane within advecting liquid is considered available for hydrate or free gas formation if the advection path involves a change of thermodynamic states from higher to lower methane equilibrium concentrations. **Figure 2** shows the cumulative change of soluble (saturated) methane concentrations for seafloors at 500, 1000, and 2000m deep, and for GTGs of 20 and 40 °C per km. The inflection points represent crossing from the L-G region into the L-H region. It

is interesting to note that deeper seafloors actually cause methane to become subsaturated within advecting liquid until the three-phase boundary is reached, based solely on thermodynamic considerations. Shallower seafloors generally promote supersaturation of methane within seawater along the GTG-defined advection path. These observations lead to the assertions that bottom simulating reflectors (BSRs) would likely be absent for basins having deeper seafloors, since thermodynamic conditions along the GTG does not favor gas exsolution. Conversely, BSRs are more probable for shallower seafloors since it is thermodynamically feasible to produce free gas. All scenarios in Fig. 2 indicate that hydrate formation is possible for the advection paths within the L-H region, where more hydrate will be formed at higher GTG values.

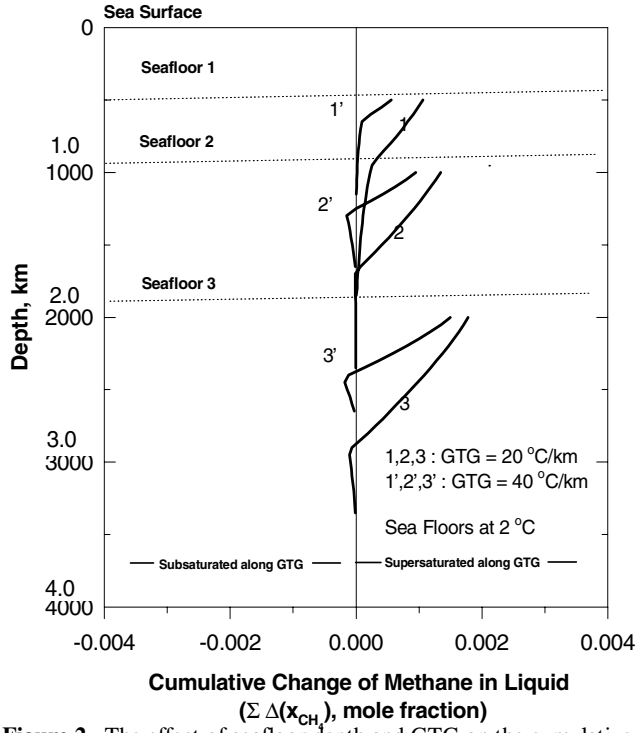

Figure 2. The effect of seafloor depth and GTG on the cumulative change of soluble methane in seawater along upward advection paths.

Up to this point considerations in Figs. 1 and 2 have been restricted to thermodynamic equilibrium conditions. However, it is necessary to superimpose phase equilibria upon a sediment compaction framework to quantify the amounts of soluble methane converted to hydrate and free gas over time. This was done for the case of having a constant seafloor depth, allowing simulations to run out to 20 Ma. **Figure 3** shows the velocity profiles for advecting liquid and settling sediment solids under conditions of a moderate sediment compaction rate. The fluid velocities are a key parameter in Darcian analyses of flow through the sediments, since they have a direct influence on liquid overpressures.

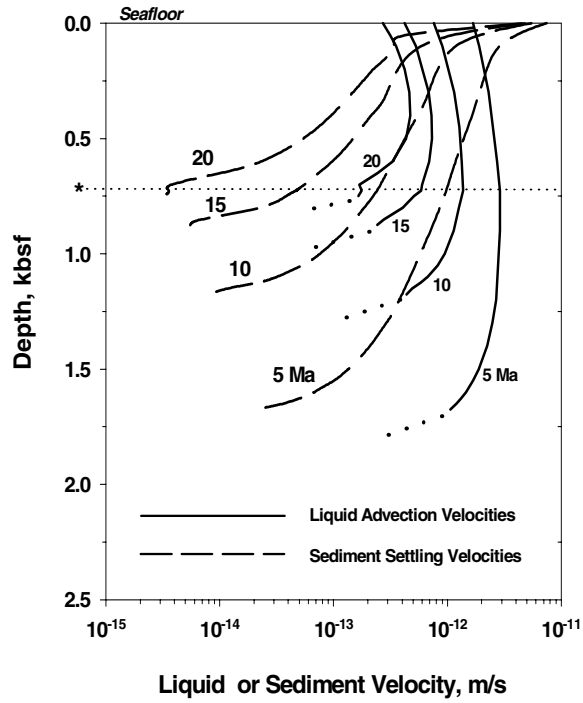

Figure 3. Velocity profiles of advecting liquid and sediment solids for the case of a "moderate" sediment compaction rate. The * represents the depth of greatest hydrate occurrence**.**

Figure 4 shows the net amounts of methane hydrate and free gas that have formed after 10 and 20 Ma, based on advection represented in Fig. 3. A GTG of 20 °C/km and a seafloor at 1000m were used in generating Fig. 4. It is seen in this figure that the greatest occurrences of hydrate and free gas lie within narrow bands of depth, which are generally located in the vicinity of where the advection path (GTG) crosses the three-phase boundary. Also shown is that the volume of free gas present at 10 Ma (5% by vol) disappears by 20 Ma. This disappearance is due to liquid overpressures that increase between 10 and 20 Ma as a consequence of lowered sediment porosity over time. These higher overpressures cause the local pressure experienced by the advecting liquid to shift from the L-G region into the L-H region, effectively enabling the free gas to be converted into hydrate. The amounts of hydrate shown in Fig. 4 are in good agreement with other investigators who have estimated hydrate occurrences in reasonably homogeneous sediments to fall between 1 and 12% by volume, depending on the age of the marine basin.[8-13]

Based on Fig. 2, we can speculate how the plots in Fig. 4 would change as the seafloor depth and GTG are changed. For example, shallower seafloors would yield shallower hydrate deposits with underlying free gas deposits. Deeper seafloors would correspond to deeper hydrate deposits that may be of a greater magnitude, with minimal free gas beneath. However, the shape and magnitude of the plots in Fig. 4 are also influenced by the sediment compaction rate. A faster compaction rate will yield somewhat different hydrate and free gas profiles (than a slower rate) because the higher liquid velocities will yield higher liquid overpressures that will cause a localized shift in phase equilibria conditions.

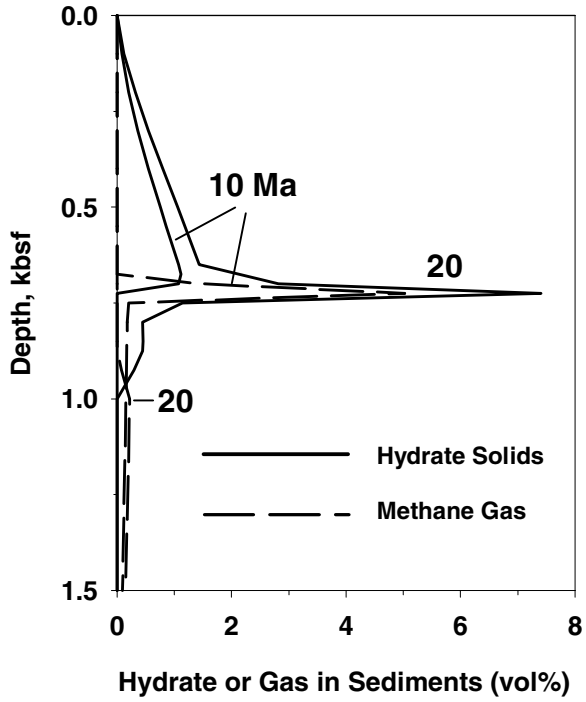

Figure 4. Predicted accumulation of methane hydrate and free gas within simulated compacting sediments undergoing a moderate compaction rate.

Conclusions

Occurrence of methane hydrate and exsolved methane gas within compacting marine sediments has been described by a advanced model incorporating accurate phase equilibria, sediment compaction, liquid advection, and methane biogenesis. Key parameters affecting the formation of hydrate and gas were discussed, which included the GTG and seafloor depth. Other parameters currently under investigation include the rate of sediment deposition and compaction, average pore diameters between sediment particles, and the shape of sediment particles. A large parameterized study can yield the optimal set of conditions for maximum hydrate and free gas formation. Results from a large-scale parameterized study will be given in the full presentation.

Acknowledgement. The author wishes to gratefully acknowledge that this work was funded by the United States Department of Energy under contract DE-AC07-99ID13727.

References

(1) Gering, K. L.; Cherry, R. S.; and Weinberg, D. M., *Ann. N.Y. Acad. Sci*., **2000**, *912,* 623.
(2) Gering, K. L., "Simulations of Methane Hydrate Phenomena over Geologic Timescales. Part I: Effect of Sediment Compaction Rates on Methane Hydrate and Free Gas Accumulations", submitted July 2001 to *Earth & Planetary Science Letters.*
(3) Athy, L. F., *Am. Assoc. Pet. Geol. Bull.*, **1930**, *14*, 1.
(4) Shi, Y.; and Wang, C., *J. Geophys. Res.,* **1986**, *91* (B2), 2153.
(5) Magara, K., *Soc. Pet. Eng. J*., **1971**, *2896*, 236.
(6) Hart, B. S.; Flemings, P. B.; and Deshpande, A., *Geology*, **1995**, *23* (1) 45.
(7) Yuan, T.; Spence, G. D.; and Hyndman, R. D., *J. Geophys. Res.*, **1994**, *99* (B3) 4413.
(8) Rempel, A. W.; and Buffett, B. A., *J. Geophys. Res*., **1997**, *102* (B5) 10,151.
(9) Rempel, A. W.; and Buffett, B. A., In *Gas Hydrates: Relevance to World Margin Stability and Climate Change*, J.-P. Henriet, J. Mienert, Eds.,Geological Society, London, Special Publications, **1998**, *137,* 63.
(10) Zatsepina, O. Ye.; and Buffett, B. A., *J. Geophys. Res*., **1998**, *103* (B10) 24,127.
(11) Buffett, B. A., *Annu. Rev. Earth Planet. Sci*., **2000**, *28,* 477.
(12) Davie, M. K.; and Buffett, B. A., *J. Geophys. Res.*, **2001**, *106* (B1) 497.
(13) Guerin, G.; Goldberg, D.; and Meltser, A., *J. Geophys. Res*., **1999**, *104* (B8) 17,781.

PHYSICAL PROPERTIES AND CONVERSION OF METHANE HYDRATES

Dirk D. Link, Edward P. Ladner, Heather A. Elsen, and Charles E. Taylor

U.S. Department of Energy
National Energy Technology Laboratory
P.O. Box 10940
Pittsburgh, PA 15236-0940

Introduction

Methane hydrates were first observed in the laboratory in 1810. It wasn't until nearly 150 years later that they were observed in nature. Hydrates can occur in permafrost, in sediment where gas exists under moderate to high pressure and low temperatures, and offshore beneath deep water. Hydrates are a problem in the oil and gas production industry because they can form in the well or pipelines, thereby blocking the flow of fuel. Estimates by the U.S. Geological Survey project that world hydrate deposits contain approximately 2 x 10^4 trillion cubic meters of methane [1]. Estimates of methane hydrate deposits off the coast of the United States is approximately 9 x 10^3 trillion cubic meters of methane with an additional 17 trillion cubic meters of methane in the permafrost on the north slope of Alaska [1].

Recent publications have indicated that photochemical oxidation of methane may be a commercially feasible route to methanol [2,3]. Previous research in our laboratory [4] has shown that, methane, dissolved in water, at temperatures > 70 °C, with a semiconductor catalyst, can be converted to methanol and hydrogen. The limiting factor for conversion of methane appears to be the solubility of methane in water. We hypothesized that if the concentration of methane in water can be increased, conversion should also increase. Methane hydrates might provide a method of increasing the amount of methane dissolved in water, because at standard temperature and pressure (STP), one volume of saturated methane hydrates contains approximately 180 volumes of methane.

Our vision is to immobilize methane and water in close proximity by formation of the methane hydrate. The reaction will involve the formation of hydroxyl radical (•OH) within the methane hydrate by photochemical means. The proximity and restricted mobility of the •OH and the CH_4 would then favor the formation of CH_3OH. Successful demonstration of this principle would then open the possibility of using hydrates to immobilize reactants in a way that favors the desired selectivity. This is the basis of our Patent [5].

EXPERIMENTAL

All reactions were conducted in a high-pressure view cell. The cell is constructed of 316 stainless steel 6.35 cm (2.5 inches) OD and 27.4 cm (11 inches) in length. The internal volume of the cell is ~ 40 mL. The cell is fitted with 2 machined endcaps, one which contains a sapphire window to allow for observation of the contents of the cell using a CCD camera. The cell is fitted with ports to accommodate the fill gas inlet and reaction product outlet, a pressure transducer to monitor the internal pressure of the gas inside the cell, and a thermocouple that terminates inside the cavity of the cell to monitor the temperature of the liquid/hydrate mixture. While the working pressure of the cell is rated at 220 MPa (32,000 psia), all experiments were conducted at 13.8 MPa (2000 psig) or less. The temperature of the cell is controlled by the flow of a glycol/water solution from an external circulating temperature bath through a coil of 0.64 cm (¼ inch) copper tubing that is wrapped around the outside of the cell. Several layers of insulating material are wrapped around the cell to help maintain constant temperature.

A typical experiment involves filling the cell with 40 mL of double-distilled water. A Teflon® coated stir bar is added, followed by portions of the photocatalyst. The endcap is placed on the cell and tightened to specifications. An external magnetic stirrer is used to obtain a high degree of vortex mixing inside the cell. The cell is connected to the gas manifold and purged several times with methane. Following the purge procedure, the cell is charged with methane at pressures of 5.5 – 13.8 MPa (800-2000 psig). Using the external circulating temperature bath, the temperature of the water in the cell is lowered until formation of the methane hydrate is observed. After formation of the hydrate, the temperature of the cell is lowered to -5 °C and held constant. Illumination of the hydrate is then performed using a high-pressure 350-watt mercury-vapor lamp, with the light directed toward the sapphire window. After illumination for a set period of time, the cell is allowed to warm slowly to room temperature. When the cell and its contents have reached room temperature, the contents of the cell are vented and a gas chromatograph and/or a mass spectrometer are used to analyze the products.

Multiple hydrate formation experiments were conducted using the following solutions: 30 mL of double distilled water, 30 mL of simulated seawater (made by by dissolving 26.8 grams of sodium chloride and 5.3 grams of magnesium chloride in 1 liter of double-distilled water), or water with surfactant (added at a concentration of 224 ppm). The cell was connected to the reactor manifold and charged with methane as described above. The temperature of the cell was reduced to 5°C and held constant until the methane hydrate formed. After formation of the methane hydrate, the cell's temperature was increased to 15°C. After the methane hydrate had dissociated, as observed through the cell's view port and the return of the cell pressure to that prior to hydrate formation, the temperature of the cell was reduced to 5°C. This procedure was repeated several times.

The experiments to determine maximum uptake of methane by the hydrate were conducted by filling the cell with 15 mL of double-distilled water and surfactant, adding the Teflon® coated stir bar, and sealing the cell, all as described above. The cell was connected to a modified gas manifold containing two single-stage high-pressure regulators in series and purged several times with methane. However, after the last purge, the valves connecting the cell to the manifold were not closed at this point. Rather, the regulators were set to deliver methane at 9.7 MPa (1400 psig), in order to allow the experiment to proceed at a constant head pressure of 9.7 MPa (1400 psig) during the formation of the hydrate. Again, an external magnetic stirrer was used to obtain a high degree of vortex mixing inside the cell. Temperature of the water in the cell was lowered until formation of the methane hydrate is observed. Following formation of the hydrate, the temperature of the cell is lowered to -5 °C to minimize the dissociation of the hydrate in the subsequent depressurization step. After 8 hours at -5 °C, the cell is isolated from the manifold and the head pressure released. After release of the head pressure, the cell was re-sealed and warmed to room temperature.

RESULTS

Our first experiments were to study the formation and dissociation of methane hydrates. Figure 1 shows a typical pressure/temperature profile for this process. During the initial stages of cooling, the pressure inside the cell mirrors that which would be predicted from the ideal gas law. However, as the hydrate begins to form, a sharp decrease in the cell pressure is observed, indicating that methane is being absorbed from the headspace. Visually, the initial

hydrate formation appears as ice crystals suspended in the water. As formation of the hydrate continues, the hydrate begins to agglomerate, forming a slush. Within a few seconds, the slush is transformed into a solid mass.

Figure 1. Pressure and temperature profile as a function of time for the formation of a methane hydrate from double distilled water.

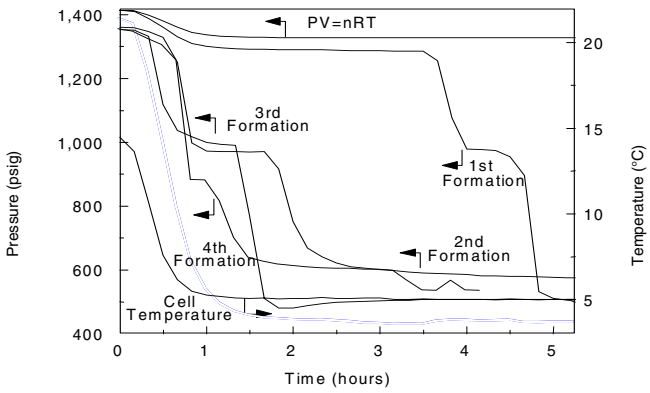

Even after formation of the solid mass, over time the hydrate incorporates more of the free methane into the crystal structure. This is evident by a decrease in the pressure in the cell over time as shown in Figure 1. Upon warming, the hydrate dissociates with evolution of methane from the slush. After dissociation of the hydrate, subsequently decreasing the temperature can reform the methane hydrate. This is also shown in **Figure 1.** Note that the hydrate forms notably faster during the second formation (1 hour as opposed to 4 hours). The third and forth formation of the hydrate occur at times slightly less than the second formation. This decrease in formation time may be due to microscopic hydrate crystals that are still present in the solution, even at 15 °C. These crystals would act as seeds for future formations. The formation of methane hydrates in water that contains the suspended photocatalyst followed the same physical changes as that observed for hydrate formed in pure water.

Formation of methane hydrates in double-distilled water, simulated sea water and double-distilled with a surfactant added is shown in Figure 2. As is shown in the figure, methane uptake by both double-distilled and simulated seawater is ~1.4 MPa (200 psig). Also of note is that the onset of hydrate formation in the simulated seawater is 3°C lower than that of the double-distilled water. When surfactant is adder to the water, methane uptake by the hydrate is ~5.6 MPa (800 psig), a four-fold increase. The increase observed in the uptake of methane when the surfactant is present can be explained what happens when hydrates form. Since methane hydrate is less dense than water, hydrates form on the surface of the water. Even with stirring, soon enough hydrate is present that the entire surface of the water is covered by the hydrate. This prevents additional methane from dissolving in the water. When the surfactant is present, the hydrate formed is forced to the edges of the surface, allowing the water-methane contact to be present longer, allowing the concentration of methane in the water to remain constant throughout formation.

In order to determine the maximum amount of methane that we could have taken up by the hydrate, we formed methane hydrate in double-distilled water containing 224-ppm surfactant under a constant head pressure of 9.7 MPa (1400 psig). The results are shown in Figure 3. During this experiment, the hydrate was formed under a constant head pressure of 1400 psig, with formation beginning at approximately 3.5 °C. The temperature of the cell was further decreased to -5 °C, in order to preserve the hydrate during the subsequent depressurization of the cell. Following depressurization at -5 °C, the cell was armed to room temperature, accompanied by an increase in cell pressure due to methane outgassing from the melting hydrate. As Figure 3 shows, the cell pressure reached approximately 1350 psig. The hydrate formed by this method contained over 96% of the maximum theoretical amount of methane.

Figure 2. Pressure as a function of temperature for the formation of a methane hydrate in double-distilled water, simulated seawater, and water with 224-ppm surfactant added.

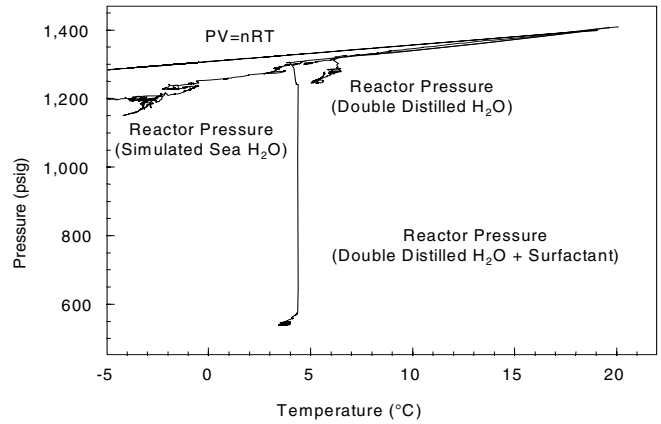

After the hydrate had formed and the pressure in the cell equilibrated, the UV lamp was turned on to initiate the photocatalytic conversion process. During illumination, a decrease in the pressure of the cell is observed. Following illumination, the cell was maintained at -2 °C for several hours before warming to room temperature. Also of note is that the final pressure of methane is less than the starting methane pressure due to conversion of the methane within the hydrate.

Figure 3. Pressure and temperature profile as a function of time for the formation of a methane hydrate with 224 ppm surfactant added.

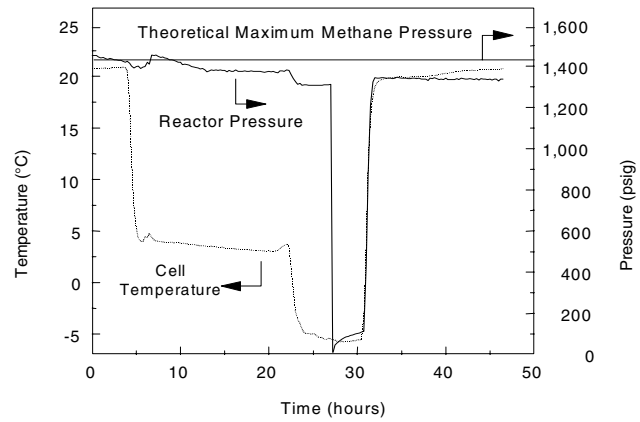

Mass spectrometric analysis of the gas vented from the cell after illumination revealed the presence of methanol, hydrogen, ethane, oxygen, formic acid, and carbon dioxide, as shown in Figure 4. Side reactions that occur during the photocatalytic conversion process are responsible for producing these additional species. Photocatalytic

splitting of water forms oxygen, ethane is formed by the combination of two methyl radicals, and the formic acid and carbon dioxide are the result of further reactions of methanol.

Attempts to use GC to identify products dissolved in the water after reaction were of limited value. In an effort to detect these products dissolved in the water, the cell and its contents were heated to 70°C prior to venting. Analysis of the gas headspace resulted in the detection of similar products as those obtained at room temperature. If products dissolved in the water were present, their concentration was too low to be detected with our setup. We are currently refining our detection system to correct this problem.

Figure 4. Product analysis for the photoconversion of methane hydrate.

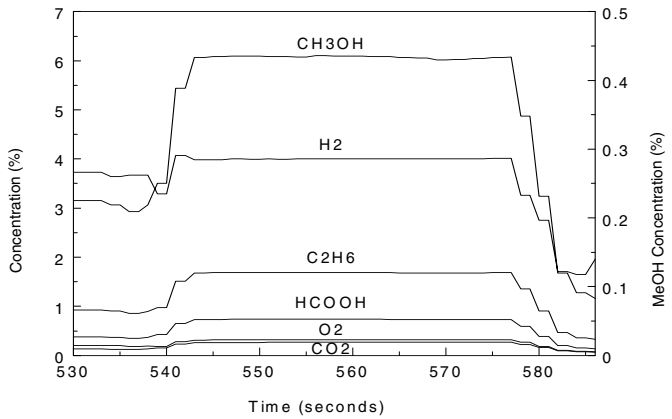

Experiments were also performed where the double-distilled water was replaced with simulated seawater. The results of these experiments were similar to those performed with double-distilled water.

CONCLUSIONS

We have produced methane hydrates in our laboratory. The temperature and pressure profiles for hydrate formation for several different starting pressures of methane, as well as different aqueous media, have been determined. Using a photocatalytic process, we have been able to convert the methane hydrate to methanol and hydrogen. We also observe several side reactions of methane hydrates, producing ethane, oxygen, formic acid and carbon dioxide.

Previous research [4] in our laboratory had shown that the photocatalytic reaction of methane and water did not occur below 70°C. However, current studies have demonstrated effective conversion of methane hydrates using the same catalyst at temperatures below 0°C [5].

The addition of a surfactant improves the uptake of methane during formation of the hydrate. The amount of methane uptake obtained using the surfactant has reached greater than 96% of the theoretical limit.

This process, while still in its infancy, may provide a method for recovering the methane contained within hydrate deposits. In addition, it may provide an effective method for removing hydrate plugs from pipelines and wells.

DISCLAIMER

Reference in this report to any specific commercial product, process, or service is to facilitate understanding and does not necessarily imply its endorsement or favoring by the United States Department of Energy.

ACKNOWLEDGEMENTS

The authors would like to acknowledge the technical assistance of Jennifer Bennett.

REFERENCES

(1) Collett, T.S. and Kuuskraa, V.A. *Oil and Gas J.* **May 11, 1998**, 90.
(2) Ashokkumar, M. and Maruthamuthu, P. *J. Mat. Sci. Le*tt.**1988**, 24, 2135-39.
(3) Ogura, K. and Kataoka, M. *J. Mol. Cat.* **1988**, 43, 371-79.
(4) Noceti, R.P. and Taylor, C.E. U.S. Patent 5,720,858 **February 24, 1998**.
(5) Taylor, C.E., Noceti, R.P., and Bockrath, B.C. U.S. Patent *6,267,849* **July 31, 2001**.

A Field Oriented Natural Gas Hydrate Research Project for The Alaska North Slope – Resource Evaluation And Possible Testing

Keith Millheim and Jonathan Kwan

Anadarko Petroleum Corporation
17001 Northchase Dr. Houston, TX 77060

Williams Maurer

Maurer Technology Inc.
2916 West T.C. Jester, Houston, TX 77018

Abstract

For years natural gas hydrates have portended potential multi-trillion cubic feet of primarily methane reserves both onshore and offshore. Recently, two major events have moved the hydrate curiosity to serious hydrate interest: (1) The perceived ensuing shortage of accessible cost effective energy for North America and other countries like Japan, and (2) The stimulus by the National Energy Technology Laboratory/US Department of Energy (NETL/DOE) hydrate program to fast forward hydrate technology.

Anadarko Petroleum Corp. along with Mauerer Technology and Noble Engineering are participating in the recent Alaska hydrate research program sponsored by NETL/DOE. This unique field oriented research project will apply known oil and gas technology with modification to recognize and access North Slope hydrate gas accumulations with a further plan to attempt long term well production testing of the wells that will be drilled during the project. The research program incorporated some of the unique approaches to the coring, core retrievable core assessment, well bore evaluation, including the various testing scenarios. On-site laboratory testing will be done when appropriated to understand the time function on some of the physical properties. Thermodynamics and kinetics data will be obtained from off-site measurements

Introduction

Gas hydrates occur naturally in permafrost and deep marine environments around the globe. It is estimated that methane in gas hydrates worldwide is more than 10^{13} tons of methane-carbon [1]. This quantity is equivalent to ~2.10^{16} cubic meters of methane gas, or about twice as much as all other fossil fuels, taken together. and about 370 times as much as all of the natural gas ever likely to be produced from conventional sources in North America [2]. Potentially, this resource could be the backbone for the world's energy sector during the 21st century.

Background

Several major factors have so far prevented the commercialization of gas hydrates to produce clean burning, environmentally friendly fuel. These factors are:

- Remoteness of the hydrate resources from major natural gas markets, except in several cases (offshore the East Coast of the United States, offshore Japan, offshore India, in the Black Sea, and offshore Australia);
- Insufficient knowledge about the in-situ properties of gas hydrates;
- Absence of economical and proven technology for the production of natural gas from gas hydrates;

Remoteness of the resource - no more. Even gas hydrates have been recovered in at least 90 locations in marine environments globally and in many cases in permafrost conditions onshore, these sites are often situated far from the major natural gas markets. For example, it would take a 5,000 km pipeline to bring gas from Alaska to the continental United States, and even if gas hydrates were to be successfully developed, the cost of transportation may be prohibitive. However, the situation changed when the N. America gas market get tight and several plans on gas pipeline from Alaska and Canada to the United States have been under intensive debate. The known gas resource on the North Slope, 35 trillion cubic feet (Tcf) are the energy equivalent to six billion barrels of oil, half the oil reserves in Prudhoe Bay. Up to 100 Tcf of gas could eventually be developed on the slope. This is not including the potential hydrate deposit under the permafrost and offshore Beaufort Sea. Due to its shallow depositional environment, hydrate can be a low cost energy source.

To evaluate the costs and benefits of bringing natural gas from gas hydrates to markets, the knowledge of the hydrate physical properties and the technologies for their production would first have to be developed and tested. Significant laboratory knowledge in gas hydrates is available, but the hands-on field experiences are few.

Insufficient knowledge – Improving. While it is easy to create gas hydrates in laboratory experiments, there are few hydrate samples (both in pressurized and non-pressurized containers) from natural deposits. In 1998, the completion of a 1150 meters hydrate test well Mallik 2L-38 in the MacKenzie Delta, NWT, Canada have made significant improvement in the knowledge base of naturally occurring hydrates [3]. The scientific project focused on geophysical measurements with limited hydrate coring. Approximately 37 meters of hydrate cores were recovered with very scarce publications on their test results. Such research requires the ability to recover, transport, prepare and analyze samples under controlled conditions identical to the ones in-situ. Currently there is no comprehensive program of this kind. The insufficient knowledge about gas hydrates properties in natural environments is a serious handicap for the development of technologies to produce methane from gas hydrates.

Absence of proven technologies – adopted and modified from existing industry. The Mallik well have employed several new and innovative coring designs and procedures with reasonable but limited success. There are several known technologies to extract natural gas from gas hydrates, mostly based on the use of techniques leading to the decomposition of the hydrates in-situ and the subsequent production of the gas by conventional or adapted gas wells. For example, gas hydrates decompose when the pressure and temperature are beyond certain limits, or when inhibitors are injected, and the gas is released and can be produced by wells.

There is one known case where natural gas has been commercially produced from gas hydrates for a sustained period of time. In permafrost onshore North Siberia in Russia, inhibitors were injected to cause the decomposition of the gas hydrates, and the released gas was produced at the Messoyakha gas field. Production was discontinued when it was judged uneconomic. In recent publications, the claim that the produced gas did actually originate from the gas hydrates, and not from free gas trapped under the gas hydrates in the Messoyakha field, has been disputed. It is inevitable that the hydrate production technology will be derived from the well-developed oil and gas practices. Under the contract terms with NETL/DOE, this research program will focus on the identification of the hydrate area, coring operation, test hydrate properties and monitor the wellbore. Production is only a secondary objective.

Site Selection and Permitting

Site selection is based on Anadarko proprietary seismic data and available public information from various well logs and temperature logs. The current selections of possible site are a balance between easy access to roads, potential hydrate thickness and safe operation conditions. Due to environmental concerns and regulatory stipulations in the Alaska Coastal and Foothill areas; the permitting processes are very lengthy. Other than the permitting requirements from the Federal and State agencies, local authorities, native and various citizen groups have to be informed of all drilling activities. The drilling season in the Arctic is only opened for the few months in winter. With all the logistic of mobilizing the equipment, the actual drilling window is very limited. Water and gravel usage to build ice road and site preparation is under rigorous control.

Drilling and Coring

Three straight holes will be drill and core from the permafrost through the hydrate zone. A small-footprint mining/coring rig will be used in the drilling and coring operation to minimize the environmental impacts in the tundra. Selection of coring equipment is underway with carefully planned operation procedures that meet all environmental and safety requirements. Fluid chilling will be used if the operational time frame will destabilize the hydrate core. Other than the thermodynamic properties, the kinetics reaction during coring of the hydrate is critical. The time-dependent hydrate freeze and thaw cycle in the presence of coring fluid may provide a self-preservation mechanism. Several drilling/coring fluids will be tested in the laboratory for its compatibility with the hydrate (laboratory simulated). The stringent requirement of the coring fluid will ensure and maximize core recovery. The data from laboratory measurement will feed into a computer wellbore simulator to ensure a safe operation. All equipment will be tested prior moving on location. Mud logging will be used to identify the hydrate stabilization zone. Gas and fluid compositions are good indicators.

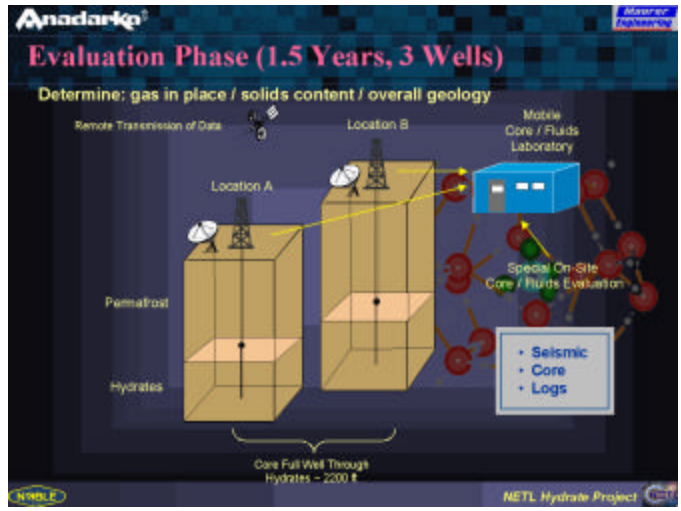

Fig. 1 Hydrate Evaluation Phase

Core Preservation and Laboratory Testing

The stability of gas hydrate is dependent on pressure, temperature and the solubility of gas as a function of pressure and temperature in the system. Understanding of the thermodynamic data of methane and other gas hydrates is very important from the view-point of preserving cores and exploiting natural gas production from hydrate wells. The hydrate handling experiences from various National Laboratories and the USGS indicated the stability of hydrate is more susceptible to changes in temperature than pressure during the time of coring and core preservation at the well site. During the coring operation, recovered cores will be kept at a specific (low) temperature to preserve its original properties by means of an insulated core holder. For longer term core storage, the hydrate cores will be kept in pressure core storage barrels and under proper temperature. Appropriate tests on-site and off-site using known laboratory techniques.

Geophysical and Petrophysical Properties. While the centerpiece of laboratory testing has been to understand the seismic response of hydrate and fluids and seismic relationships with petrophysical parameters, data can also be generated for reservoir quality evaluation, seismic characterization, petrophysical evaluation, and hydrate reservoir mechanical/chemical stability evaluation. The laboratory is highly automated with high sample throughput capability.

Thermal Properties. The basic properties important for understanding the thermal state of the hydrate reservoir are temperature, thermal conductivity and thermal diffusivity [4]. Time Temperature Transformation (TTT) profiles can be constructed from isothermal Differential Scanning Calorimetry (DSC) data. It will provide information about the complex nucleation and growth mechanism. This simple technique can be used to screen the efficiency of different chemical inhibitors. Results can provide heat flow Vs reference temperatures data with heats of fusion and crystallization resolving Ice and Hydrates distinctly

Table 1. Hydrate Core Characterization Measurements

Seismic	**Compression & Shear Velocities @various *P* & *T***
	Elastic Anisotropy
Petro -	**Porosity & Permeability @ various *P* &*T* (NMR)**
Physical	**Bulk and Grain Density**
	X-ray & FTIR Mineralogy
	Laser Particle Size Analysis
Engineering	**Compressive strength**
	Young's Modulus
Thermal	**Conductivity & Diffusivity**
	Heat of fusion
Chemical	**Carbon Isotope**
	Fluid & Gas Composition

Open Hole Logging and Completion

The basic sonic, SP and Gamma logs will be run after the cores are recovered. NMR is rather unique to apply in the investigation of hydrates. There are only two companies that can provide the NMR tool. Currently, only one will service the Alaska North Slope. The electronic logs will be analyzed in conjunction with the laboratory core testing results, the mud log data and seismic data. After the logs are done, these wells will be equipped with temperature strips and downhole pressure gauges for temperature and pressure profile monitoring. Various precautions will be observed to log the borehole temperature if fluids are accumulated inside the wellbore. Time will allow to let the wellbore to get in equilibrium with the surrounding formation. Simple techniques such as thermal stimulation will be applied to the wellbore to observe its respond.

Conclusions

The objective of this research project is to develop technologies that can be used for the continuation of a long-term product test at one or more hydrate sites in the arctic environment, and upon the confirmation of its viability, the immediate commercialization of the technology. The project is also expected to assess the natural gas reserves of gas hydrates resources in the arctic and the elaboration of recommendations to facilitate the commercialization of a vast, environmentally friendly source of fossil energy in Alaska and worldwide.

Acknowledgement. The authors like to thank the National Energy Technology Laboratory (NETL), Department of Energy for their generous support with contract # DE-PS26-01NT40869-2, and the management support of Anadarko Petroleum Corporation, Maurer Technology Inc., a unit of Noble Drilling Company.

References

(1) Kvenvolden, K.A., Ginsburg, G.D. and Soloviev, V.A. – *Geo-Marine Letters.*, **1993**, *13*, pp.32-40.

(2) Kvenvolden, K.A., *Natural Gas Hydrate: Introduction and History of Discovery* Chapter 2 in *Natural Gas Hydrate in Oceanic and Permafrost Environments*, Max, M.D., Ed.; Kluwer Academic Publishers, **2000**; pp. 9-16.

(3) Dallimore, S.R., Uchida, T. and Collett, T.S., *GSC Bulletin 544 Scientific Results from JAPEX/JNOC/GSC Mallik 2L-38 Gas Hydrate Research Well, Mackenzie Delta, Northwest Territories, Canada,* **1999**.

(4) Ruppel, C., *Thermal State of the Gas Hydrate Reservoir*, in *Natural Gas Hydrate, Chapter4 in Oceanic and Permafrost Environments*, Max, M.D., Ed.; Kluwer Academic Publishers, **2000**; pp.29-42

METHANE STORAGE IN HYDRATE FORM USING CALCIUM HYPOCHLORITE AS ADDITIVE

Shuan-Shi Fan, Yan-Kun Guo, Kai-Hua Guo, Yong Chen

Guangzhou Institute of Energy Conversion, The Chinese Academy of Sciences, 81 Center Martyr's Road, Guangzhou 510070, China

Introduction

Natural gas storage is a subject of great interest to many industries and particularly for transportation. Compressed natural gas, liquefied natural gas and adsorbent natural gas are widely techniques used. The possibility of developing a convenient storage system based on hydrate has been explored for about ten years around the world [1-6]. Gudmundsson[2] has focused on the storage and transportation of gas as hydrate at atmospheric pressure since 1990. Khokhar[3] used 1,3-dimethylcyclohexane and polyvinylpyrrolidone as additives to lower hydrate formation pressure. Also, Saito[4] used tetrahydrofuran or acetone, Rogers [5] used sodium dodecyl sulfate as accelerator to natural gas hydrates formation respectively. In this work, the effects of calcium hypochlorite on hydrate formation are investigated. The data shows that it can lower the degree of supercooling and enhance the relative cage occupancies.

Experimental

The schematic diagram of the apparatus is shown in Fig.1. The cell is cylindrical, immersed in a constant temperature water bath. Its inside diameter is 2.5cm, and the length is 4.5 cm, with a total volume of 24.3cc. A constant pressure regulator is equipped. The temperature of the cell was monitored with a platinum resistance probe accurate to ±0.1℃, and pressure was monitored via a 6.0Mpa gauge accurate to 0.4% of full scale. An electronic balance accurate to ±0.01g was used to detect the mass increment of the cell through the experiment.

The methane was produced by Guangzhou Gas Factory, with a purity of 99.9%. Doubly re-distilled water was used. The calcium hypochlorite was pure grade, purchased from Shanghai Fouth Reagent Factory.

All the experiments were carried out under 4.0MPa at 273.3K. Water, weights m_w, and 1% (mass fraction) of calcium hypochlorite was loaded into the cell as condensed phase. Vacuum the system and weight the cell's mass, expressed as m_1. After the system was refrigerated to 273.3K, charge methane in. Then weight the cell every 3 hours until the mass, expressed as m_2, does not change perceptible. The mass increments, $\Delta m=m_2-m_1$, in a series of experiments are listed in Table 1.

For compare, data for water/methane binary system under the referred pressure and temperature were tested also.

1. Results

2.1 data processing[6]

To calculate the storage capacity expressed as volume gas/volume hydrate (Vol/Vol) from the experimental data, trail and error procedures were applied.

For ideal structure I hydrates, if all of the cavities were filled, the hydration number (water molecules per guest molecular) would be n =46/8. For methane, which formed structure I hydrate, the hydration number is related to the fractional filling of the large and small cavities, y_L and y_s, respectively as:

$$n = \frac{46}{6y_L + 2y_s} \qquad (1)$$

And for a simple hydrate at 273.15K, y_L and y_s interrelates as:

$$-0.4885 = \frac{3}{23}\ln(1-y_L) + \frac{1}{23}\ln(1-y_s) \qquad (2)$$

The methane hydrate density(ρ) may be calculated by the formula:

$$\rho = \frac{\frac{N_w}{N_{Ava}}\left[M_{H2O} + (y_L\upsilon_L + y_s\upsilon_S)M_{CH4}\right]}{V_{Cell}} \qquad (3)$$

where, N_w is the number of water molecules per unit cell; N_{Ava}, Avagadro's number, 6.023×10^{23} molecules/mol; $M_{H2O,CH4}$, molecular weight of H_2O and CH_4;y_L, y_s, fractional occupation of large/small cavity by CH_4; ν_L, ν_s, number of large/small cavities per water molecule in unit cell; V_{cell}, volume of unit cell.

A value of n may be estimated at 4.0MPa corresponding to 273.15K for CH_4. Equations (1) and (2) may then be solved simultaneously for y_L and y_s. Hydrate density can be calculated by Equation (3).

$$\Delta m = \Delta m_H + \Delta m_C \qquad (4)$$

Where $\Delta m=m_2-m_1$, is measured mass increment; Δm_H, the mass of the methane trapped in hydrate; Δm_C, the mass of the methane over the hydrate as compressed gas.

Estimated a value of Δm_H, m_w and ρ are known quantity, the volume of hydrate can be calculated. Then Δm_C can be calculated by van der Waals equation, and get a new value of Δm_H. Use trail and error procedure to get the value of Δm_H corresponding to the hypothetical hydrate number.

Then the hydration number corresponding to Δm_H can be calculated. Substitute the calculated n value to Equations (1),(2),(3) to calculate the density of the hydrate, Δm_H, until a new n. Go on the iteration utile the hydration number n is ultimately calculated. After n is calculated, Δm_H and Vol/Vol were calculated for each experiment.

2.2 Results

The experimental data and calculation results are listed in Table 1. Fig 2 describes the Vol/Vol value of a series of experiments. It is showed that m_w range from 3.73 to 16.51, correspond to about 15% to 68% of the cell volume. When m_w exceeds 8 grams, the Vol/Vol value tends to reduce slightly with the increasing of m_w. It shows that the formation reaction was mass-transfer limited. As shown in figure 2, the Vol/Vol value varies from 134 to 176. Averagely, 151 volumes of methane (standard pressure and temperature) were trapped in one volume hydrate. Calcium hypochlorite has two evident effects on methane hydrate formation. Firstly, it reduces the degree of supercooling. In these experiments for water/methane binary system, no hydrates were observed in 20 hours under the mentioned temperature. After calcium hypoclorite is introduced, typically the formation begin in 6 hours, but it seems to be stochastic. Secondly, calcium hypochlorite helps most of the water

molecules to form hydrates in a relatively short time under moderate conditions. For different experiments, hydration number lies between 6.11 and 8.32. Its average magnitude is 7.36, indicating 78% of the large and small cavities in the lattices were occupied by methane molecules. The satisfactory effect of this compound makes the stabilization and transportation of natural gas as hydrates more feasible.

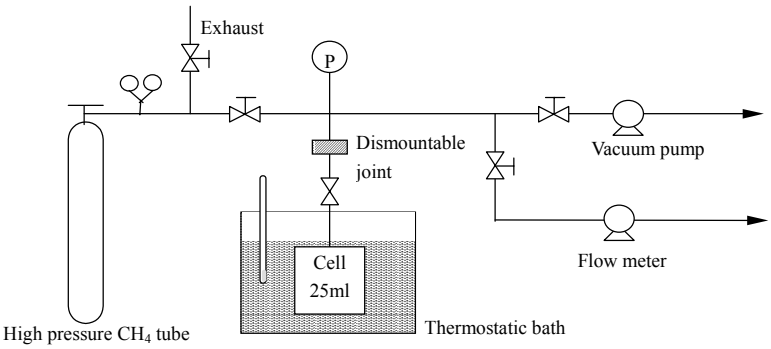

Fig 1. Schematic diagram of the experimental apparatus

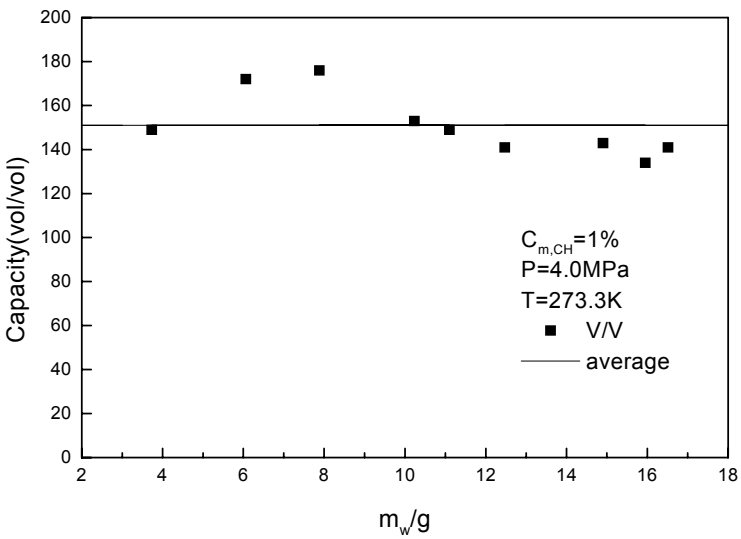

Fig. 2. Volume gas(standard conditions)/volume hydrate in a series of experiments

Table 1. Summary of experimental data and results

m_w	Δ m	Δ m_H	Vol/Vol	Hydration Number
3.73	1.07	0.45	149	7.40
6.06	1.38	0.85	172	6.32
7.88	1.6	1.14	176	6.11
10.23	1.64	1.27	153	7.15
11.1	1.67	1.33	149	7.40
12.47	1.69	1.4	141	7.90
14.9	1.9	1.71	143	7.75
15.95	1.86	1.7	134	8.32
16.51	2	1.87	141	7.85

Conclusion

The potential of methane storage in hydrate form with calcium hypochlorite as additive was investigated. Calcium hypochlorite reduced the degree of supercooling on methane hydrate formation. It also helped most of the water molecules to form hydrates in a relatively short time under moderate conditions.

The formed gas hydrates had the ability to store 134 to 176 volumes of methane per volume of hydrate, averagely, 151, at 273.3K and 4.0MPa. The hydration numbers of which were between 6.11 and 8.32.

References

(1). 2001. Peking. Century Petroleum Forum.

(2). Gudmundsson J S, et al, In: AIChE Spring National Meeting, New Orleans, March(1992)

(3). Khokhar A A, et al, Fluid Phase Equilibria 150-151(1998):383

(4). Saito Y, et al, In: 2nd International conference on natural gas hydrates, Toulouse France, June2-6,1996

(5). Rogers R E, et al, In: 3rd International conference on natural gas hydrates, Salt Lake City, Utah, USA, July, 18-29, 1999

(6). Sloan E D, Clathrate Hydrate of Natural Gases, 2nd edn., Marcel Dekker, New York, 1998

EFFECT OF POROUS MEDIA ON THE CONDITIONS OF DICHLORODIFLUOROMETHANE HYDRATE DISSOCIATION

E. A. Bondarev, A. Z. Savvin

Institute of Oil and Gas Problems
October Str., 1
677891 Yakutsk, Russia

Introduction

Study of gas hydrates in porous media became a matter of interest for the following reasons. Practice of developing natural gas fields, in the regions of permafrost particularly, has revealed the probability of hydrate formation in the bottom hole zone that reduces the well productivity. Also, thermodynamic conditions in the Earth's crust and in the World Ocean sediments may be such that they will favor the formation of large accumulations of hydrocarbon gases in a hydrate form.

Among the factors influencing the equilibrium conditions of hydrate formation (temperature and pressure) in porous media, aside from gas composition and pore water salinity, one can point out mineralogical and granulometric composition and moisture content of a medium. Numerous investigations have been carried out in order to determine the equilibrium conditions of hydrate formation in the absence of a porous medium. Their detailed review is presented in [1]. However, the analysis of the few works where the effect of rock properties on the phase equilibrium of hydrates has been studied reveals the absence of reliable experimental data, the available ones contradicting each other in some cases [2 - 6]. For example, it was stated in one of the first works that hydrate formation temperature in the sand rocks is 2-5 K lower then that for a pure hydrate (in the absence of a porous medium) [2]. The experiments with the tetrahydrofuran hydrate have shown that the porous medium consisting of sand and glass spheres with the diameter of 1.0 and 0.1 mm does not affect its thermophysical properties as well as its melting temperature [3]. A considerable shift of the phase equilibrium curve toward the lower pressure (about 50%) is observed during hydrate formation in water bentonite suspension [4]. On the other hand, a slight excess of the equilibrium pressure by 78 kPa in comparison with a pure hydrate at the same temperature has been observed during the experiments on methane hydrate formation and dissociation in natural water-saturated cores [5]. The experiments on hydrate formation in the clay rock have shown that the water layer the most tightly bound to the surface of particles has not been involved in hydrate formation [6]. Pressure and temperature of freon-12 and propane hydrate dissociation in porous media have been determined during the experiments on moisture migration during hydrate formation [7]. It has been established that dissociation pressure for the propane hydrate in the sand with the grain fraction of 0.1-0.25 mm and moisture of 20% is 10-20 kPa higher than that for a pure hydrate.

The aim of the present study is to investigate the effect of a type and moisture content of the porous medium on the phase equilibrium in the system hydrate – gas – water.

Experiment

Temperature of hydrate dissociation at a given pressure has been determined by the differential thermal analysis with the help of the laboratory device shown in Figure 1. In the duralumin heat unit 1 there are two symmetric cells 2, 3 in the form of a cylinder where polytetrafluoroethylene ampules with the primary standard and the sample under the study are placed. The heat unit is inserted in a steel high-pressure chamber 4 where gas is injected through the input system consisting of a container 9 with a gas, valves 10, 11 and high pressure pipes. Pressure in the chamber is measured with the manometer 13. To measure temperature in the sample and temperature difference between the standard and the sample we use the combined thermocouple consisting of two differential copper-constantan thermocouples 7, 8, cold junctions of which are placed in the Dewar vessel 6 at 273.15 K. Thermocouple readings are amplified (amplifiers 14, 15) and then, by means of the matching facilities, are transferred to the input of the multichannel potentiometer 16. Instrumental error of temperature measurements is determined by the error of the thermocouple graduation and that of thermoEMF (electromotive force) measurements and does not exceed $\pm$ 0.1K. Pressure in the chamber is measured by manometers, the error being less than $\pm$ 4 kPa.

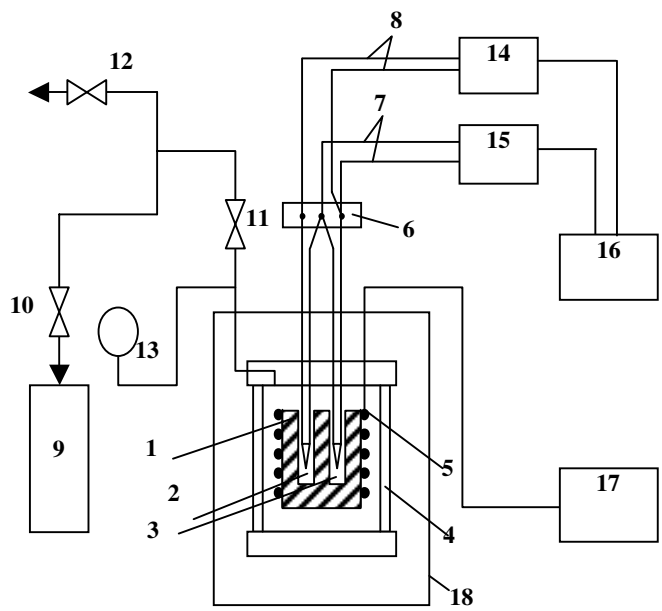

Figure 1. Sheme of the experimental device

At this stage of the study we used, as a hydrate former, the dichlorodifluoromethane CCl_2F_2 (freon-12) with the volume content of 99.5 %. Freon-12 forms the hydrate of Structure II. The porous medium is the quartz and river sand with the fraction of 0.15-0.25 mm, sand and clay mixture, obtained from the natural rock by sieving through the 0.08 mm sieve, and bentonite. According to the granulometric classification of dispersion media [8,9] the clay and sand mixture contains clay (<0.001 mm) and dust (0.001-0.05 mm) particles and fine-grained sand (0.05-0.08 mm). Bentonite is classified as highly disperse clay and consists of particles of <0.001mm size (85-90%). To remove water-soluble salts the samples are washed with hot distilled water followed by the analysis of the water extract in order to detect corresponding ions. Hygroscopic moisture of the samples is obtained by sorption during their keeping desiccators with pure water and solutions of sulfuric acid or kalium sulfate at 293 K within a month. The above method of moisture setting provides the most uniform distribution of water through the rock volume. Moisture content of the samples exceeding the maximum hygroscopic one is obtained by the contact method followed by their keeping in the in the desiccators with the distilled water within one or two weeks. Maximum hygroscopic moisture content is considered as

water quantity which rock absorbs from the environment at a relative moisture content φ =1.0. Moisture content of the samples (i.e. percentage relation of water mass in the rock sample to the mass of the dry sample) is measured by weighing. Mass of the dry sample is determined after its drying at 378 K. to a constant value.

The experiments have been performed in the following way. The heat unit with a sample of a porous medium at a given moisture content and the standard are placed into the high-pressure chamber. Then, with the help of the pump through the valve 12 vacuum is created in the chamber after that it has been filled with the gas under pressure of 0.4-0.5 MPa. The chamber is slowly cooled in the thermostat 18 to 276 K, at which freon is in liquid state. Hydrate formation is initiated by the evaporation of liquid freon. As a result, the pressure of the gaseous freon exceeding that of hydrate dissociation at the given temperature is set in the working chamber. After two or three days the standard and the sample are subjected to heating so that the linear temperature growth occurs. In our experiments the rate of heating has been about 10^{-3} K/s. Hydrate dissociation is revealed by a sharp peak-like deviation of the curve of the temperature difference between the sample and the standard. It is known that in this case the sample temperature at the same moment is the temperature of the phase transition [10,11].

Results and discussion

The data obtained for the temperature of the CCl_2F_2 hydrate dissociation are presented in Tables 1, 2. The experimental data show that at the same pressure the dissociation temperatures of the pure hydrate and the hydrate in the quartz and river sand are equal within the limits of a measurement error at moisture content of the sand being higher than that of the maximum hygroscopic one (W_{mg} = 0.96 %). Moisture content interval under study is 0.96-20.0 %. At W_{mg} = 0.96 % there is the drop of the temperature of hydrate dissociation in sand to $\Delta T = T_0 - T$ = 0.8 K (T_0 =279.4 K is the temperature of pure hydrate dissociation at P_0 =123 kPa).

Table 1. Conditions of CCl_2F_2 hydrate dissociation in the sand and clay and sand mixture

P, kPa	*T*, K (pure hydrate)	*T*, K (sand, *W*=3.2 %)	*T*, K (clay and sand mixture at moisture content *W*, %)		
			29.8	11.2	8.3
105	278.7	278.7	278.6	277.8	-
123	279.4	279.4	279.4	278.6	277.5
184	280.9	281.0	-	280.1	278.9
255	282.4	282.5	282.4	281.6	280.8

Similar dependence between the dissociation temperature and moisture content of the rock is observed for the hydrate formed from the pore water contained in the clay and sand mixture and bentonite. At moisture content $W > W_{mg}$=12.2 % for the clay and sand mixture and $W > W_{mg}$=43.3 % for bentonite dissociation temperatures of the pure hydrate and the hydrate formed from pore water are equal within the limits of a measurement error. At moisture content being less than that of the maximum hygroscopic one temperature drop of hydrate dissociation occurs, the lower the moisture content, the lower the temperature. If the dissociation temperature in the clay and sand mixture drops approximately by 2 K at *W*=8.3%, that in such a highly dispersion medium as bentonite drops by 2 K at *W*=39.8%.

Statistical processing of the experimental data shows that the total error at measuring the dissociation temperature, represented by a confidence limit, is not more than $\pm$ 0.3 K at probability being equal to 0.95.

Table 2. Conditions of CCl_2F_2 hydrate dissociation in bentonite

P, kPa	*T*, K at moisture content of the rock *W*, %		
	49.4	39.8	34.7
105	278.7	276.8	275.7
123	279.4	277.6	276.3
184	280.8	279.4	278.1
255	282.4	280.8	279.9

There is a certain relation between the maximum hygroscopic moisture content and the specific surface of the porous media under study, i.e. the larger the specific surface, the higher W_{mg}. Thus, W_{mg} may serve as some peculiar characteristics of the rock dispersion.

In the region of the hygroscopic moisture content of porous media water occupies mesopores due to the capillary condensation, i.e. at the pressure of the water vapor over the concave meniscus which is less than that of the saturated vapor over the flat surface. The reduced pressure of water vapor in such capillaries causes a temperature drop of hydrate dissociation in the porous medium as compared with the dissociation temperature of the pure hydrate. Thus, porous media at moisture content being less than that of the maximum hygroscopic one affect the phase equilibrium in the system hydrate – gas – water. The above effect manifests itself by a shift of the phase equilibrium curve in the direction of lower temperatures. The lower moisture content of the porous medium, the lower hydrate dissociation temperature.

References

1. Byk S.Sh., Fomina V.I. Gas hydrates. M.: Khimiya, 1980.
2. Makogon Yu.F. Hydrates of natural gases. M.: Nedra, 1974.
3. Rueff R.M., Sloan E.D Ind. Eng. Chem. Process Des. Dev., 1985, v. 24, No. 3, p. 882-885.
4. Cha S.B., Ouar H., Wildeman T.R., Sloan E.D. J. Chem Phys., 1988, v. 92, No. 23, p. 6492-6494.
5. Yousif M.H., Sloan E.D. SPE Reservoir Engineering, 1991, No. 12, p. 452-458.
6. Yakushev V.S. In: Natural and Technogenic Gas Hydrates. M.: VNIIGAS, 1990, p. 174-187.
7. Melnikov V.P., Nesterov A.N. Ground Freezing 97, Knutsson (ed), Balkema, Rotterdam, 1997, p. 391-395.
8. Efimov S.S. Moisture of hygroscopic materials. Novosibirsk: Nauka, 1986.
9. Soil Science/Edited by Sergeiev E.M. M.: Moscow State Univ. Publ., 1983.
10. Berg L.G. Introduction to thermography. M.: Nauka, 1969.
11. Piloyan G.O. Introduction to the theory of thermal analysis. M.: Nauka, 1964.

Dissociation of Methane clathrate hydrate in Viscous fluid

Taro Kawamura, Kotaro Ohga, and Kiyoshi Higuchi

Graduate school of engineering
Hokkaido University
North 13 south 8, Kitaku, Sapporo, Hokkaido, 060-8628, Japan

Takeshi Komai, Yoshitaka Yamamoto, and Hironori Haneda

National institute of advanced industrial science and technology,
Onogawa 16-1, Tsukuba, Ibaraki, 305-8569, Japan

Introduction

Natural gas clathrate hydrates, which exist under sea ground, are recently known as big natural gas reservoir, and then expected as near future energy resources[1]. In order to recover natural gas from them commercially, in-situ dissociation of hydrate under sea ground is needed. Moreover, in case of conventional petroleum drilling (riser drilling), viscous fluids called "drilling mud" are used[2], then dissociating front of hydrate is prospected to contact with such fluids. Therefore, the information about dynamic behavior of hydrate under such condition is required. Though there are some fundamental studies about hydrate dissociation[3], practical behavior under such condition is not well understood.

In this study, dissociation kinetics of methane hydrates in viscous fluid, which have various viscosities, was investigated experimentally. Artificial pellet shaped methane hydrates were dissociated under isothermal, isobaric condition. The dissociating boundaries were directly observed, and the dissociation rates were obtained.

Experimental

Methane Hydrate Samples. The starting material was methane hydrate powder prepared by ice-gas interface method at 270K and 10MPa for about 2 days. Spectroscopic analysis of the sample material determined that more than 98% of cavities were filled with methane gas[4]. With this hydrate powder, 12-mm-o.d. and 6-mm-thickness pellets of methane hydrate were produced under pressure and temperature conditions of 30MPa and 193K, respectively. The photograph of prepared hydrate pellet is shown in **Figure 1**. Moreover, simple ice pellet was also prepared from pure ice powder to confirm the adjustment of this experimental method.

XANVIS Solution. In case of raiser drilling system, viscous fluid called "drilling mud" is used. Drilling mud usually consists of water, some salts and viscous additive material made from a kind of biopolymer. In this work, viscous additive material, XANVIS, was supplied from TELNITE CO., LTD., and its solution in distilled water was used as model mixture of drilling mud for ease. As shown in **Figure 2**, XANVIS solution has non-Newtonian flow. And it also suggests 1.0% solution had about twice viscosity to 0.4%solution at whole shear rate.

Procedure. The schematic illustration of experimental apparatus used in this work is shown in **Figure 3**. The optical cell has an inner volume of about 2ml, maximum pressure of 15MPa and is covered with sapphire window. The gas-liquid inlet, outlet and a thermo-couple are also equipped with it. Prepared pallet was set in it, and liquid cell was filled with XANVIS solution or water. Under isothermal- isobaric conditions, sample pellet was dissociated in XANVIS solution or water. The dissociating boundaries were directly observed though optical window, and the time from start of dissociation to disappearance of pellet was measured. Dissociation rate was estimated from it.

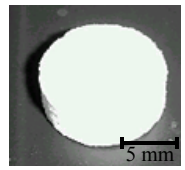

Figure 1.
Methane hydrate pellet
Height; 6 mm,
Diameter; 12 mm
Weight; 0.48-0.52 g
Porosity; 0.16-0.23

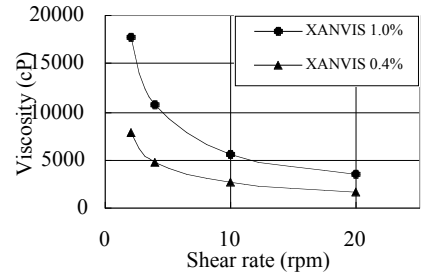

Figure 2. Viscosity of XANVIS solution. Viscosity was measured by rotary type viscometer at 279.15K.

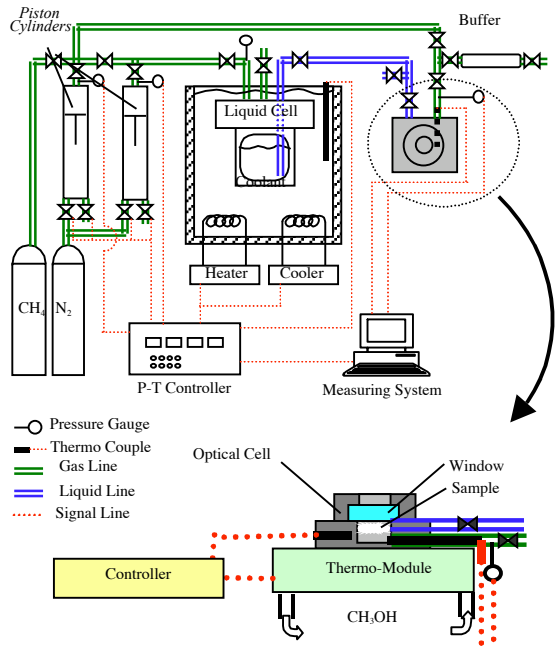

Figure 3. Schematic illustration of experimental apparatus.

Results and Discussion

Mathematical model. The mathematical model used in this work is based on simple one-dimensional thermal conduction[5]. Heat supplied from inner wall of optical cell conduct though water to hydrate (or ice) surface. Dissociation can be assumed to occur only at the surface and the surface temperature can be assumed to be its equilibrium temperature at each pressure condition. Thus, movement of the water-hydrate (or ice) interface, X, with time, t, is given by,

$$X = \lambda\sqrt{4\alpha_W \cdot t} \qquad (1)$$

$$\frac{e^{-\lambda^2}}{\mathrm{erf}\,\lambda} = (1-\lambda)\sqrt{\pi}\,\frac{\rho_H}{\rho_W}\,\frac{\Delta H}{C_{P,W}(T_0 - T_D)} \qquad (2)$$

Here, α_W is thermal diffusivity of water, ρ_H is density of hydrate (or ice), ρ_W is density of water, ΔH is heat of dissociation of hydrate (or ice), and $C_{P,W}$ is heat capacity of water. The measured porosity of

hydrate β was about 0.195. T_0 is the experimental temperature, and T_D, the hydrate (or ice) dissociation temperature, is set by the applied pressure. The adjustments of this model to experimental results, which were obtained from ice-water (XANVIS 0%) system, hydrate-water (XANVIS 0%) system, and hydrate-XANVIS solution system, were evaluated below.

Dissociation rate of Ice-Water system. Time required for vanish the ice pellet at each temperature is shown in **Figure 4**. Experimental result shows exponential trend; the time become long, as dissociating condition become close to equilibrium (273.15K, 0.1MPa). Vanishing time obtained from experiment and calculated value with eq. (1) show same trend and each value show reasonable agreement in error by 1.3min.

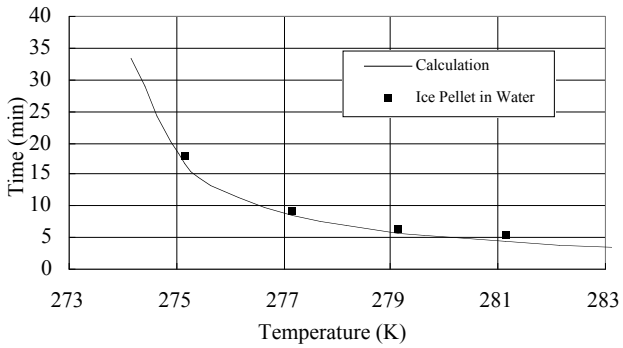

Figure 4. Time required for vanish the ice pellet at each temperature under atmospheric condition.

Dissociation rate of Hydrate-XANVIS Solution system. Figure 5 shows time required for vanish the hydrate pellet in each pressure-temperature-viscous condition. Each symbol represents experimental value. Lines represent obtained value from model calculation of hydrate-water (XANVIS 0%) system. Each value shows same exponential trend; the time become long, as dissociating condition become close to its equilibrium condition. On hydrate-water system, experimental results and calculated value show reasonable agreement at relatively low-pressure. However, experimental results show larger value than calculation, as the condition become cloth to equilibrium. At higher XANVIS concentration, obtained vanishing time took large value. This trend is shown at whole pressure condition.

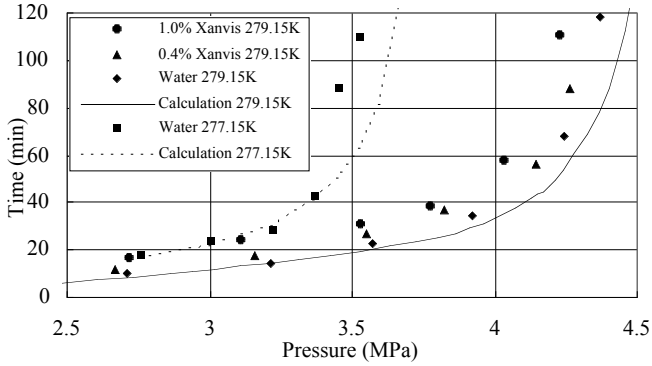

Figure 5. Time required for vanish the hydrate pellet at each condition.

Observed Dissociating boundary. Dissociating hydrate surfaces in three different viscous fluids are shown in **Figure 6**. Dissociating surface of ice is appended for comparison. During dissociation, though almost no bubble were shown on ice surface (see **Fig.6 a**), whole surface of each hydrate was covered with methane bubbles, which were generated by hydrate dissociation. In case of hydrate-water system (XANVIS 0%), small bubbles moved away from hydrate surfaces rapidly (see **Fig.6 b**). For 0.4% XANVIS solution, generating bubbles moved through the fluid slowly, then small bubbles combined each other to become relatively large one (see **Fig.6 c**). In case of 1.0%, bubbles moved very slowly on hydrate surfaces, and its sizes became large compared with former two cases (see **Fig.6 d**).

Since existence of bubbles causes thermal resistance, vanishing time is considered to become late. On the contrary, moving bubbles draw convection heat transfer. Then, it seems to accelerate the dissociation. On the other hand, influences of bubbles are neglected in the mathematical model. Therefore, it is considered that influence of bubbles is one of primary factor of misfit of calculated value to experimental results in hydrate-water system. At higher XANVIS concentration, it was also considered that the trend; vanishing time shift to long as concentration, was caused by the bubbles. Of course, the influence of heat capacity change of solution needs to be investigated.

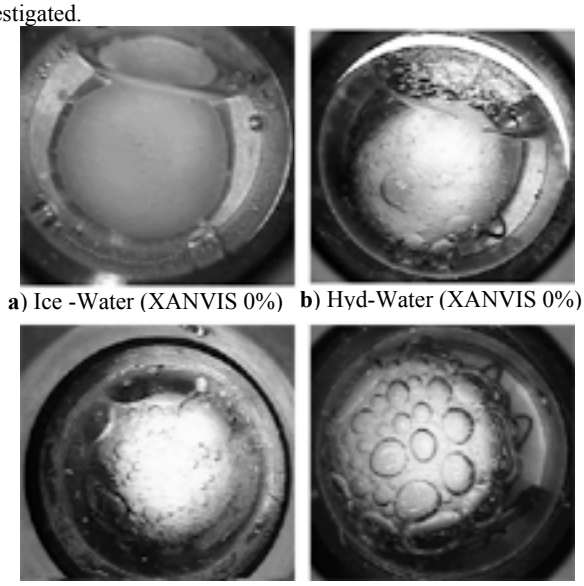

a) Ice -Water (XANVIS 0%) **b**) Hyd-Water (XANVIS 0%)

c) Hyd-XANVIS 0.4% **d**) Hyd- XANVIS 1.0%

Figure 6. Snapshots of dissociating pellet surfaces. Ice pallet was at 275.15K, hydrate pellets were at 279.15K, 3.8MPa respectively.

Conclusion

Experimental results, which were obtained from simple ice-water system, fitted well to model calculation. In case of hydrate-water system, it was considered that influence of bubbles is one of primary factor of the misfit of them. The bubble influence was also seemed to affect on dissociation in hydrate-XANVIS solution system. We attempt to construct more practical model, considering to the influence of bubbles and so on.

References

1. Sloan, E. D., Clathrate hydrates of natural gas, Marcel Dekker, New York, **1998**
2. Berthezene, N., de Hemptinne, J. C., Audibert, A., Argillier, J. F., J. Petro. Sci. Eng., **1999**, 23, 71-81
3. Clarke, M., Bishnoi, P. R., Chem. Eng. Sci., **2000**, 55, 4869-4883
4. Hirai, H., Kondo, T., Hasegawa, M., Yagi, T., Yamamoto, Y., Komai, T., Nagashima, K., Sakashita, M., Fujihisa, H., & Aoki, K., J. Phys. Chem. B, **2000**, 104, 1429-1433
5. Keikar, S. K., Selim, M. S., Sloan. E. D., Fluid Phase Equilibria, **1998**, 150, 371-382

KINETICS OF CO_2 HYDRATE FORMATION BELOW MELTING POINT OF ICE

Takeshi Komai, Taro Kawamura, and Yoshitaka Yamamoto

National Institute for Advanced industrial
Science and Technology
16-1 Onogawa, Tsukuba
305-8569 Japan

Introduction

Gas hydrates are very attractive from both resources and environmental aspects. CO_2 gas hydrate can be utilized to develop methane gas hydrate as an important energy source in the near future. When producing methane gas from gas hydrate reservoirs at permafrost area, the injection of CO_2 might be used to promote the gas production by replacement, and to maintain the stability of strata due to the formation of CO_2 gas hydrate. In addition, the sequestration of CO_2 mass can be performed in the process of gas hydrate production. An experiment on the formation of CO_2 gas hydrates was carried out under low temperature below melting point of ice, using a specially designed cell-type apparatus. To observe the nucleation and formation process, CO_2 gas was introduced to the ice crystals in a pressure cell at a condition of high pressure. Raman spectrometry was used to measure the rate of formation based on Raman analysis due to the dynamic behavior of guest molecules. As a result, it was found that the rate of formation of CO_2 gas hydrate depends on various conditions, such as temperature, pressure and diameter of ice crystals. The mechanism of the formation of CO_2 gas hydrate under low temperature was also discussed, based on the results of Raman analysis.

Experimental

Apparatus. The experimental apparatus was specially designed and equipped for the formation and replacement of gas hydrates. It can be used under the various conditions that pressure, temperature and concentration of gases are precisely controlled. **Fig.1** illustrates the schematic diagram of the apparatus and measuring system used in the experiment. The pressure cell, made of stainless steel with a 3.2 ml internal volume, can be used at a pressure condition of up to 20 MPa. It contains a glass window for observing Raman scattering of monochromatic lights, a thermoelectric temperature control module, and some nozzles for the introduction of gas and liquid components. The pressure cell is installed on a constant temperature plate filled with a cooling agent methanol, where the temperature can be controlled with an accuracy of ± 0.1 K. It is equipped with transducers for detecting and controlling pressures with an accuracy of ± 0.05 MPa.

Measuring Methods. The observation system of the Raman spectroscopy and a CCD camera are mounted in the apparatus. The mechanism and theoretical background of Raman analysis are described in **Fig.2**. The figure also shows the molecular model of CO_2 gas hydrate. Macro mode is applied for the measurement of Raman spectroscopy, in which Ar laser is emitted to the sample. In this experiment powder-like fine ice crystals were placed in the pressure cell for the starter of gas hydrate. The average diameter of the crystals is about 9 micro meters. CO_2 gas was introduced into the cell and the pressure was controlled to a value of a little higher than the equilibrium pressure. During the nucleation and crystal growth of CO_2 gas hydrate, Raman spectra were measured and analyzed to get the data of Raman shifts. As the strength of Raman shift is proportional to the concentration of guest component, the formation rate can be calculated by the relative strength. In this experiment temperature condition was changed to the range between –18.5 deg. C. and 0 deg. C.. The pressure condition in the formation process of gas hydrate was set to a constant value of 1.6 MPa.

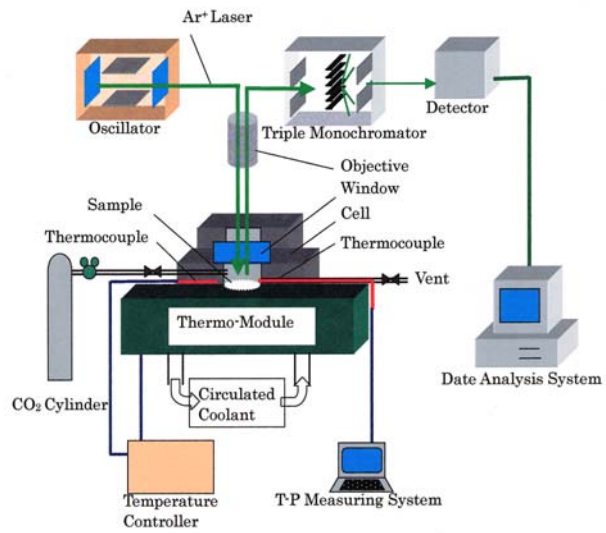

Fig.1 Experimental apparatus and measuring system of Raman spectroscopy.

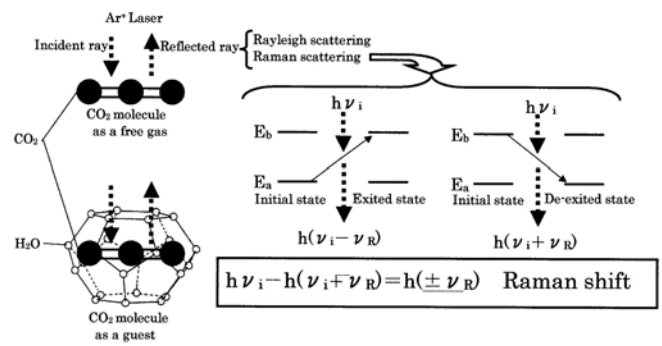

Fig. 2 Molecular model of CO_2 gas hydrate and the mechanism of Raman measurement.

Results and Discussion

In-situ measurement of formation process. As a typical result of measurement, **Fig.3** shows the trend of Raman shifts observed in the formation of CO_2 gas hydrate under a condition of –8.7 deg. C. and 1.6 MPa. Four peaks of Raman shift appeared as a result of Raman analysis in the process of guest molecule trap into the cages. The left hand peaks reveal the existence of CO_2 in large cage. It was found that the strength of the peaks gradually increased with time, and especially the rate of increase was quite large in the first stage of the formation, such as within 10 minutes. In this duration the formation mechanism is nucleation or transformation from ice to gas hydrate.

Formation rate of CO_2 hydrate vs Temperature. The comparison of time growth of the strength was made for the formation of CO_2 gas hydrate under the temperature condition that was changed between –18.5 deg C. and 0.5 deg. C.. **Fig.4** shows the relative strength of Raman shifts, in which the effect of temperature on the formation rate of CO_2 gas hydrate from ice crystals was described. From the result it was found that the rate of formation was very large in a condition of -0.5 deg C., compared with other conditions below –3.8 deg. C..

The result suggests that the nucleation phenomena or mechanism of CO_2 gas hydrate formation dramatically changes around the melting point of ice. This kind of effect is very much singular because in a normal situation the formation rate might increase as the temperature becomes lower. It is considered that the effect is caused by the existence of quasi-liquid layer at the interface of gas and hydrate sample. The liquid-like layer might accelerate the nucleation of gas hydrate and the rate of formation has a close relation with the thickness of the layer.

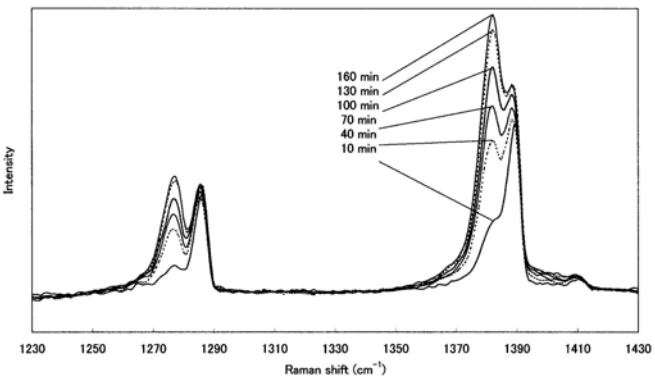

Fig.3 Raman spectra of CO2 gas hydrate obtained every 30 minutes.

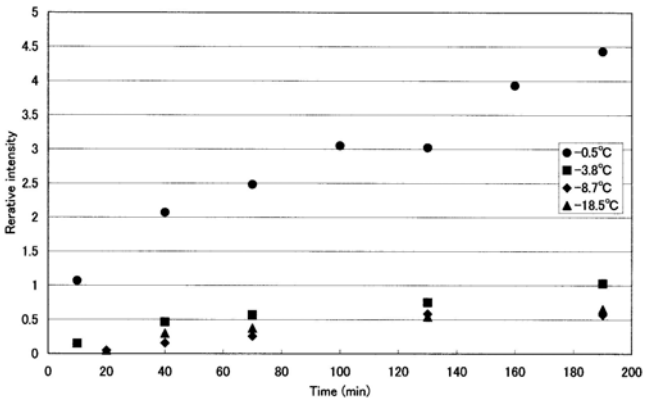

Fig.4 Time growth of relative strength obtained by Raman analysis as a parameter of temperature.

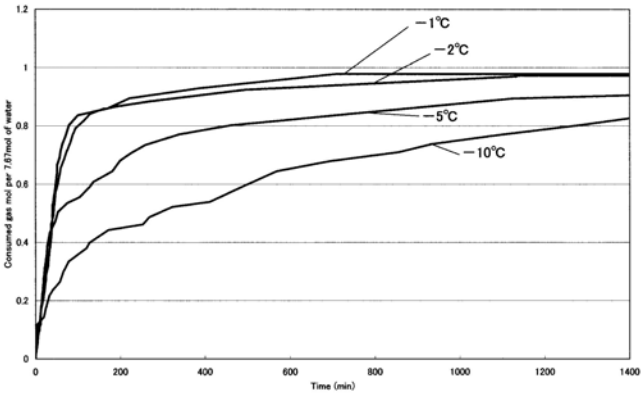

Fig.5 The formation rate of CO_2 gas hydrate obtained in bulk-scale experiment as a parameter of temperature.

Growth rate by bulk-scale experiment. The bulk-scale experiment for the formation of CO_2 hydrate was conducted using a pressure vessel with a volume of 200 mL. The rate of formation was obtained to measure the consumption of CO_2 in the process of transformation into gas hydrate. **Fig.5** illustrates the time growth of CO_2 gas hydrate for the bulk-scale experiment. The vertical axis means the consumed gas mole per mole of water. It is clear that the process of formation divides into two stages, especially in the case of temperature around meting point of ice. In other words, the formation of gas hydrate is very fast in the first stage of time growth within 200 minutes. However, the rate of formation became slower in the second stage of time growth. The result of this experiment agrees well with the result of Raman analysis, so that the rate of formation shows the maximum under a temperature condition between –1 to –2 deg. C.

The mechanism of time growth. Based on the results of Raman analysis and bulk-scale experiment, the mechanism of crystal growth and the resulted rate of formation of CO_2 gas hydrate can be qualitatively discussed. The most important factor in the first stage is considered to be the existence of liquid-like layer around the nucleation area. The thickness of the layer depends on the condition of temperature and ice surface. It makes sense to explain the effect of temperature on the formation rate of gas hydrate. On the contrary, the controlled factor might be the diffusion coefficient of gas between ice and hydrate, because the rate of formation became slower with time due to the blocking of gas transport through media. By the quantitative evaluation using a mathematical model, the rate of formation can be calculated as factors of temperature, pressure and other parameters. These kinetic data and the mechanism of crystal growth are very important to evaluate the formation behaviors of CO_2 gas hydrate under the real environment, such as marine sediments and permafrost.

Conclusions

The direct measurement by Raman spectroscopy is very effective to obtain kinetic data of gas hydrate formation. The rates of CO_2 gas hydrate formation were measured by Raman analysis and bulk-scale experiment as a fuction of temperature. The result showed that the effect of temperature on the gas hydrate formation was nonlinear and singular. It is suggested that the effect is due to the kinetic behavior of ice crystal and gas hydrate. The rate of CO_2 gas hydrate formation can be estimated to develop the kinetic model of ice and hydrate. More scientific research is needed to make clear the phenonenon.

Acknowledgment

We acknowledge Dr. S. P. Kang to conduct the measurement of Raman spectroscopy in this work, and thank Dr. K. Nagashima to carry out the data analysis of Raman spectra.

References

1. Furukawa, Y.,Yamamoto, M., Kuroda, T., J. Crystal Growth, 82, p.655, (1987)
2. Takeya, S., Hondo, T., Uchida, T., Ann. New York Academy Sci., 912, p.973, (2000)
3. Ikeda, T., Mae, S., Uchida, T., Chem. Phys., 108, p.1352, (1998)
4. Komai, T., Yamamoto, Y., Ohga, K., Ann. New York academy Sci., 912, 272, (2000)
5. Nakano, S., Moritoki, M., Ohgaki, K., J. Chem. Eng. Data, 43, p.807, (1998)

Corresponding author: Dr. Takeshi Komai, Thsukuba-West, AIST, 16-1 Onogawa, Tsukuba, 305-8569 Japan <koma@ni.aist.go.jp>

KINETIC INHIBITION OF METHANE HYDRATE BY POLYMERS

Ugur Karaaslan and Mahmut Parlaktuna

Department of Petroleum and Natural Gas Engineering,
Middle East Technical University, 06531 Ankara, Turkey

Introduction

Gas hydrates are ice-like crystalline compounds that are formed by the combination of water molecules with gas molecules under suitable conditions of pressure and temperature. Water molecules form a lattice structure with cavities that are occupied by gas molecules. There is no chemical union between the water and gas molecules. The water molecules that form the lattice are strongly hydrogen bonded with each other and the gas molecule interacts with water molecules through van der Waals type dispersion force[1].

In the industry, there is an increasing tendency to exploit hydrocarbon reserves at increasing depths in the oceans and with increasing distances for pipeline transportation in both horizontal and vertical directions. Due to this extended exposure of the water-containing unprocessed hydrocarbon fluid to low temperatures and high pressures, the handling of the hydrate problems in such transport lines has become a more integral part of the petroleum industry. Since large percentages of alcohol have to be added, an economic incitement towards more effective inhibitors has evolved. The focus over the last few years has been directed towards slowing down the process of hydrate formation, kinetic inhibition. In this context studying the fundamental kinetics of hydrate formation is importance.

Hydrate inhibitors are classified into three groups: Thermodynamic inhibitors, kinetic inhibitors and anti-agglomerates. Thermodynamic inhibitors are used at high concentrations (10-60 wt %), kinetic inhibitors and anti-agglomerates are added at low concentrations (<1 wt %). The latter do not affect the thermodynamics of hydrate formation, however, they do delay hydrate nucleation and/or crystal growth. Anti-agglomerates prevent the agglomeration of hydrates so that all the hydrate crystals are transportable in a pipeline. Both kinetic inhibitors and anti-agglomerates are usually polymers with surfactant properties[2].

The inhibition mechanism of polymers and surfactants is proposed as follows: Active molecules are found to adsorb strongly to the surface of a propagating hydrate crystal or pre-nuclear hydrate like clusters. In this process, they change the energy of the surface of hydrate crystal or cluster and so change its growth characteristics[3]. The poly(N-vinyl pyrrolidone) (PVP), poly(N-vinylcaprolactam) (PVCap), poly(N-methyl-N-vinylacetamide) (VIMA), poly(N-vinylvalerolactam) (PVVam) and poly(acryoylpyrrolidine) (PAPYD) are some examples of known and patented inhibitors[4].

In this study hydrate inhibition potential of different polymers have been tested in a high-pressure apparatus at high pressures and low temperatures with varying polymer concentration. A known hydrate inhibitor, poly(N-vinylpyrrolidone) (PVP) and a water soluble thermoplastic polymer (PEO) were determined the best kinetic inhibitors among them.

Experimental

Set-Up. A high-pressure system, whose schematic diagram is given in **Figure 1**, is used to carry out hydrate formation tests. A cylindrical high-pressure reactor with dimensions of 3.4 cm in diameter, 15 cm in length is the main piece of experimental set-up. Its total available volume is 142 cm^3 including connections. It is made of brass and tested up to 1200 psi. The high-pressure cell is placed into a constant temperature bath made by plexiglass allowing the observation of the system easily. A temperature controller and a refrigerated chiller are immersed into the water bath to provide temperature control during tests. A thermocouple (with an accuracy of ±0.2 °C) and a pressure transducer (with an accuracy of ±1 psig) are connected into the high-pressure cell to measure cell temperature and pressure. They are connected to a data-logger and a personal computer to record the temperature and pressure as functions of time. A motor at the outside of the bath is attached to the cell to provide rocking, and a glass marble is placed into the cell to stir and agitate the liquid inside. The speed of the rocking system was kept at 30 RPM; temperature and pressure are recorded every 10 seconds throughout this study. Methane gas that has 99.5 % purity was used as hydrate former gas. Aqueous polymer solutions were prepared in pure water.

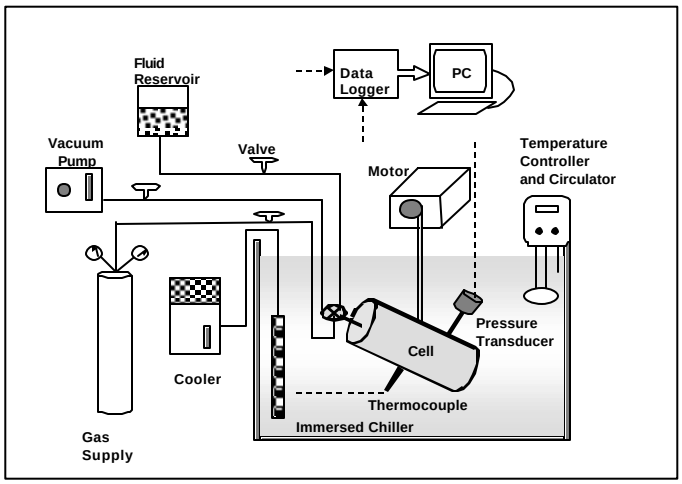

Figure 1. Schematic representation of experimental set-up.

Procedure. After making the necessary connections (gas, water, and vacuum lines, thermocouple and pressure transducer connections) to the high-pressure cell, the system is evacuated. Then, aqueous phase is injected into cell and the cell is pressurised by methane gas. After reaching in equilibrium at initial pressure and temperature conditions (**Table 1**), the system is cooled down to hydrate formation temperature without rocking meanwhile data collection is started. Rocking process is started to agitate the solution in the cell to initiate hydrate formation at predetermined hydrate formation temperature. At that point, the cell pressure already decreased from 700 psig to 662 psig due to cooling and dissolution of methane gas at low temperature. Details of the experimental procedure can be found from Karaaslan[5].

Table 1 Experimental Conditions

Test No	weight (%)	$T_{initial}$ (°C)	$P_{initial}$ (psig)	$T_{rocking}$ (°C)	$P_{rocking}$ (psig)

T-1	pure water	15	700	3	662
T-2	0.010 PVP	15	700	3	662
T-3	0.100 PVP	15	700	3	662
T-4	0.500 PVP	15	700	3	662
T-5	1.000 PVP	15	700	3	662
T-6	0.010 PEO	15	700	3	662
T-7	0.025 PEO	15	700	3	662
T-8	0.050 PEO	15	700	3	662
T-9	0.100 PEO	15	700	3	662
T-10	1.000 PEO	15	700	3	662

Results and Discussion

Kinetics. Rocking of cell inside hydrate formation region triggers hydrate formation and a decrease in pressure is observed. Pressure-temperature data of each test through real gas law are used to calculate the moles of remaining free gas in the cell during methane hydrate formation. Moles of free gas in the high-pressure cell as function of time for pure water (0.00 %), PVP and PEO solutions are given in **Figure 2** and **Figure 3,** respectively. As it is seen from the Figure 2, number of moles of free gas decreases with time for pure water due to hydrate formation. On the other hand, there is almost no change in moles of free gas when 0.1, 0.5 and 1 weight % of PVP solutions are used as hydrate forming media. Although 0.01 weight % PVP solution retarded the hydrate formation for a period of 40-45 minutes, after that time the hydrate formation accelerated, indicating that the inhibitor lost its efficiency.

As seen from Figure 3, the tests with PEO solutions show the same behavior as PVP tests. It is obvious from figure that PEO is an effective inhibitor as compared to the pure water experiment. Free gas consumption is less for all concentrations than observed with pure water (0 weight %). The highest inhibitor efficiency was determined at and higher concentrations of 0.1 weight % PEO solution. Free gas versus time plots also show that hydrate inhibition efficiency of PEO increases with increasing concentration.

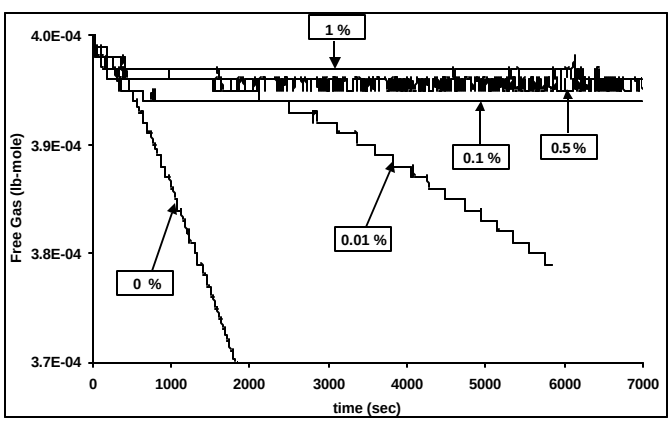

Figure 2. Methane hydrate formation with 0, 0.01, 0.1, 0.5 and 1 weight % PVP solutions.

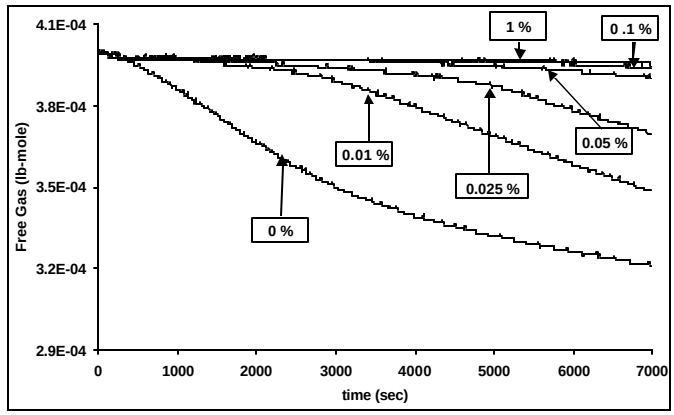

Figure 3. Methane hydrate formation in 0, 0.01, 0.025, 0.05, 0.1 and 1% PEO solutions.

Hydrate Formation Rates. Rate of change of free gas mole is used as an indicator for the hydrate formation rate. If the Cartesian plot of free gas mole versus time shows an exponential behavior it is an indication of a first order reaction. If the same data is plotted as natural logarithm of free gas mole versus time, the resulting line should fit a straight line. **Figure 4** gives the Cartesian plot of the experimental data for the test with pure-water (T-1). As observed, it exhibits an exponential behavior from which a first order reaction can be assumed.

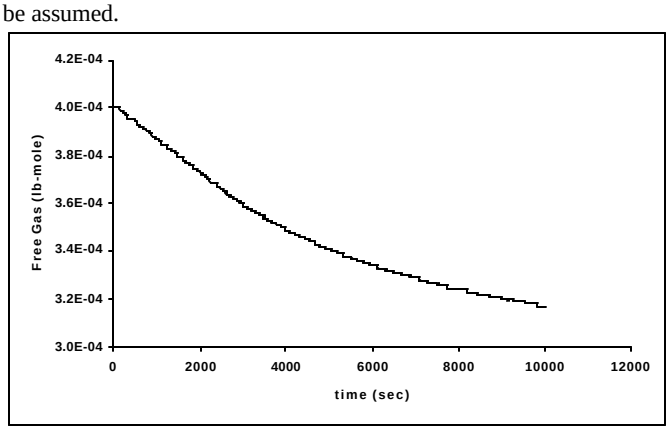

Figure 4. Cartesian plot of free gas versus time for the test with pure water (T-1)

A first order reaction equation is defined with the following expression;

$$N = N_0 e^{-kt} \qquad \text{(Equation-1)}$$

Where, N: Total number of moles at any time t; N_0: Initial number of moles; k: Rate constant, sec^{-1}; t: Time, sec.

When the natural logarithm of above equation is taken, the slope of ln(N) versus time graph is equal to rate constant k. When the derivative of the N with respect to time is taken, it will give the decrease in free gas content rate and it is relative to the hydrate formation rate so after that point it is going to be called hydrate formation rate.

$$\frac{dN}{dt} = -N_0 k e^{-kt} \qquad \text{(Equation-2)}$$

Thus, hydrate formation rate can be calculated at a specified time by Equation 2. First 30 minutes data of all experiments after the start of rocking are used to estimate the rate constants and hydrate formation rates.

Semi-logarithmic plot of the same data of Figure 4 is presented in **Figure 5** showing a linear behavior. Its best fit as a straight line has a correlation coefficient very close to unity. The slope of the straight line, 3.653E-05 for this case, is the rate constant with a unit of sec^{-1}. The rate constants and hydrate formation rates for all of the PVP and PEO experiments were determined and they are tabulated in **Table 2** and **Table 3**, respectively.

Table 2. Methane Hydrate Formation Rates with PVP Solutions

PVP (weight %)	k (sec^{-1})	Rate (lb-mole/sec)
0.000	3.653E-5	1.37E-8
0.010	3.540E-6	1.37E-9
0.100	4.735E-6	1.83E-9
0.500	2.457E-6	9.54E-10
1.000	2.398E-6	9.65E-10

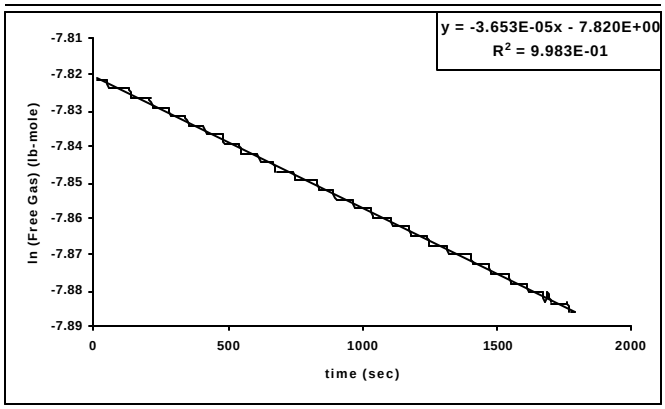

Figure 5. Semi-logarithmic plot of free gas versus time for the test with pure water (T-1)

Table 3. Methane Hydrate Formation Rates with PEO Solutions

PEO (weight %)	k (sec^{-1})	Rate (lb-mole/sec)
0.000	3.65E-5	1.37E-8
0.010	5.94E-6	2.35E-9
0.025	3.00E-6	1.19E-9
0.050	1.90E-6	7.58E-10
0.100	2.39E-6	9.52E-10
1.000	2.83E-6	1.12E-9

Hydrate formation rates in tables are in ascending order. As it is seen, for all of the concentrations of PVP and PEO formation rates are less than that of pure water. **Figure 6** and **Figure 7** present the hydrate formation rates in graphical form. As seen from Figure 6 and 7, the lowest methane hydrate formation rate (calculated from first 30 minutes of data) is about 14 times for PVP and about 18 times for PEO less than pure water experiment. Those results show that PEO is a good candidate of hydrate inhibitor.

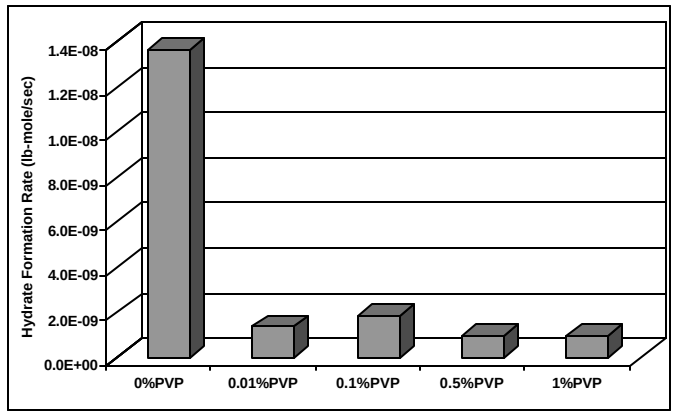

Figure 6. Methane hydrate formation rate with 0, 0.01, 0.1, 0.5 and 1 weight % PVP solutions.

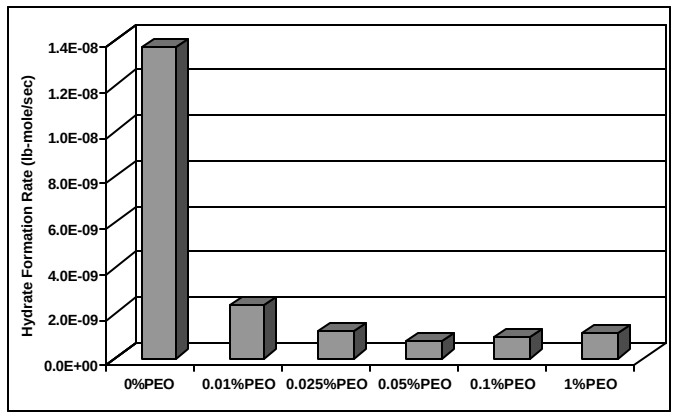

Figure 7. Methane hydrate formation rate within 0, 0.01, 0.025, 0.05, 0.1 and 1% PEO solutions

Conclusions

The following conclusions can be drawn from the analysis of experimental data of this study.

A known, patented hydrate inhibitor, PVP, was used to test the performance of experimental set-up and procedure of this study. The results showed that PVP is a good methane hydrate inhibitor and the experimental set-up and procedure are suitable for testing hydrate inhibition analysis.

PEO exhibits hydrate inhibition characteristics as a concentration of as low as 0.1 weight % and has not been known as a hydrate inhibitor until this study. This study shows that PEO prevents the methane hydrate formation within the first 60 minutes period from the start of rocking. After that period of time hydrate formation rate is still very low with respect to experiment carried out with pure water and methane gas. As a result, PEO is a good candidate of methane hydrate formation.

Since PVP is labelled as carciogenic, PEO can be a better candidate for hydrate inhibition in terms of health and safety considerations.

Acknowledgment. The authors wish to express their thankfulness to The Scientific and Technical Research Council of Turkey (TÜBITAK) for the financial support of this work.

References

(1) Sloan E.D., Jr. *Energy and Fuels*, **1998**, *12*, pp. 191-196.
(2) Kelland M.A.; Svartaas T.M.;and Dybvik L. *SPE 30695, Proceedings of the SPE Annual Technical Conference*, **1995**, pp. 529-537.
(3) Phillips N.J. and Kelland M.A. *Industrial Applications of Surfactants IV*; Karsa D.R., Royal Society of Chemistry, **1999**, pp. 244-259.
(4) Freer E.M. and Sloan E.D. *Ann. N.Y. Acad. Sci*., **2000**, *912*, pp. 651-657.
(5) Karaaslan U. *Ph.D. Thesis*, Middle East Technical University, Ankara, 2001.

New Chemicals and Polymers from Renewable Resources

Joseph J. Bozell, Stephen Kelley, Wanxuan Kang, Darrin Miller, and Mark Davis
National Renewable Energy Laboratory
1617 Cole Boulevard
Golden, CO 80401

Introduction

Biochemical pathways offer a rich source of new biomass derived building blocks. For example, the well known citric acid cycle is the central process in cellular respiration, and proceeds through 2-ketoglutaric acid (2-KGA) as a key intermediate. In most organisms, 2-KGA is a relatively transient intermediate in the metabolic process. However, some organisms do not possess a complete cycle, and stop at 2-KGA, allowing it to accumulate. Certain bacteria have been described as useful for the production of 2-KGA.[1] In addition, 2-KGA is an intermediate in the fermentative production of MSG, a large scale commercial bioproduct.[2] We wish to describe our preliminary results in the use of 2-KGA as a monomer in the production of new polyesters, and as a starting material for the synthesis of new renewables based chemical building blocks.

Experimental

Materials and Methods. All reagents were commercially available and used as received. GPC was carried out using 3 columns (300 x 7.8 mm each, Polymer Laboratories) connected in series, containing polystyrene-divinylbenzene copolymer gel (10 µm diameter particles) with nominal pore diameters of 10^4, 10^3, and 50 Å. The samples (about 50 µg sample/injection) were eluted with HPLC grade THF, at a flow rate of 1.0 mL/minute and were monitored by UV (220-400 nm) and RI. The columns were calibrated with polystyrene standards ranging in molecular weight from 580 to 2 x 10^6 (Polymer Laboratories). M_n and M_w were calculated using PL Caliber GPC/SEC Software (Polymer Laboratories). Glass transition temperatures (T_g) were measured on a DSC instrument (TA Instruments), using the transient method between -100 and 200°C at a scanning rate of 20°/min. T_g was designated as the temperature at half height of the transition shift. Variable amplitude cross polarization ^{13}NMR spectra were taken using a 2ms contact pulse ramped 1dB and a 1s recycle delay time. Single pulse ^{13}C spectra were acquired using a 90° tip pulse and a 50 sec recycle delay time. For the single pulse experiments, the longest relaxation times were measured to be 10s using an inverse recovery pulse sequence.

General procedure for the production of 2-KGA based polyesters. 2-KGA (1 eq) was mixed neat with the diol components (1.01 eq) and 1% p-TsOH. The mixture was heated for three sequential 24h periods, first at 105°C, then 130°C, and finally 150°C.

Background

The use of renewable raw materials as feedstocks for chemical production is continually suggested as offering several advantages over conventional petrochemical feedstocks, including a lowered demand for diminishing crude oil supplies, greater sustainability of the raw material source, the ability to recycle CO_2, the security of domestic feedstock supplies, and a source of new, structurally interesting building blocks with new properties and applications.[3]

Yet, despite these advantages, the huge majority of chemicals in the marketplace is not biomass derived. Although there are a few large scale examples of renewables based industrial production (the corn wet milling industry, production of EtOH, or the pulp and paper industry),[4] most chemical production is still based on petrochemicals. Frequently, the dearth of renewables in the chemical feedstock stream is blamed on cost. Biomass based materials are normally assumed to be more expensive to use than existing petrochemicals. However, a closer examination indicates that cost is not nearly as large an issue as is commonly assumed. Many of the chemical building blocks available from biomass can be obtained at costs that are very competitive with existing building blocks in the chemical industry. Moreover, even the primary raw materials can be competitive on both an energy and weight basis when raw material costs are considered. Other factors, such as processing, collection, or transportation may be important, but are frequently minimal in comparison to the raw material costs.[5]

Other issues have been seen as hindrances to the existence of a large scale biobased products industry. In a very broad sense, either a petrochemical based industry or a biomass based industry faces issues of supply, separation, and conversion. To a first approximation, issues of supply and separation are solved for both the biomass and petrochemical industry. In contrast, processes for raw material or building block conversion are significantly better understood for petrochemical based starting materials. Many of these processes are highly efficient, and proceed in very high yield. Many of the products can be made from several different routes. Importantly, most of these processes are thoroughly understood at the molecular level. The amazing process control that is the hallmark of many industrial processes is achieved through a deep understanding of discrete chemical mechanism of transformation. Most of these features are not well developed in the biobased products industry.

Accordingly, we have been investigating new methodology to improve the technology available for the conversion of renewable building blocks into chemicals. This investigation includes the identification of new building blocks, and new synthetic methodology to convert these building blocks into chemicals. We have recently started to investigate production of new polymeric materials based on the synthetic roadmap shown in **Figure 1**.

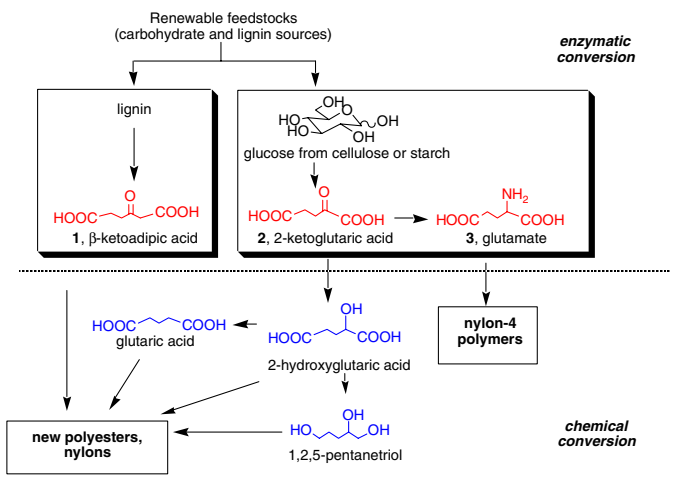

Figure 1. Reaction matrix for 2-KGA and derivatives

Results and Discussion

The renewable raw materials used for this scheme are carbohydrates, leading to 2-KGA or glutamic acid, available through bioprocessing.[6] Importantly, these initial building blocks can be converted into an even larger family of renewables based materials through simple chemical transformations. Our initial investigation has looked at the use of these materials in the production of renewables based polyesters (**Figure 2**).

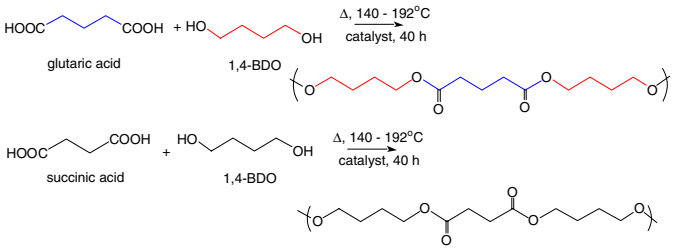

Figure 2. Production of linear polymers

Reaction of glutaric acid with 1, 4-butanediol between 140 – 190°C in the presence of catalytic p-TsOH results in the formation of a clear, light yellow rubbery material, presumably with the linear structure shown. Substitution of succinic acid as the diacid component leads to a stiffer material. We have carried out a number of polymerizations under these conditions, varying both the diacid and diol component, and find that we can produce polymers with reasonable molecular weights (M_w ~20,000 – 40,000; M_n ~10,000 – 20,000).

Substitution of the diacid component with 2-KGA introduces some profound changes in the polymerization process. The presence of the 2-keto group would be expected to introduce new electronic and structural variations in the process, leading to differences in reactivity. For example, the conditions initially used for production of the linear polymers of **Figure 2** lead to formation of dark intractable materials when 2-KGA is reacted with 1,4-butanediol. We have found that a three stage process (see Experimental Section) is much more effective for production of polymers based on 2-KGA (**Figure 3**).

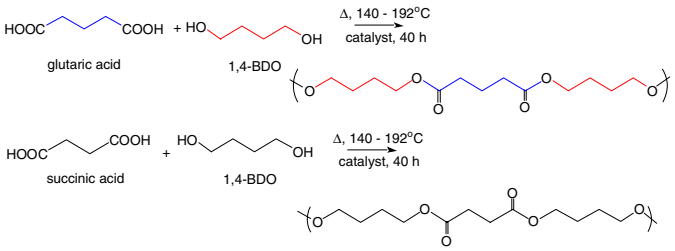

Figure 3. Polyester formation from 2-KGA and possible crosslinking mechanism

Changing the diol component from 1,4-butanediol to 1,3-propanediol leads to a stiffer material. As with the linear polymers, the molecular weights of these materials are also reasonable. Further heating of these materials to 165°C for several days results in a steady increase in the T_g.

In contrast to the initial linear polymers, polyesters based on 2-KGA become insoluble after heating for about 5 hours, indicating the presence of a crosslinking process. Several possible mechanisms to account for this crosslinking are possible, each centering upon a proposed initial reaction between the keto group of 2-KGA and the diol component of the polymerization.[7] We have investigated this reaction by solid state NMR, and observe a fairly smooth transition with time from the starting monomeric components to a crosslinked material that gives signals consistent with this mechanism. We have also tried to identify the initial reactions of the polymerization process by studying the solution esterification of 2-KGA with n-BuOH. Preliminary results indicate that the BuOH component shows little preference for one acid group over the other.

Finally, we have been studying the chemical conversion of 2-KGA into other building blocks (**Figure 4**) and find that some simple transformations can lead to a much wider family of starting monomers for chemical production. Future work will include incorporation of these monomers into new renewables based polymeric materials.

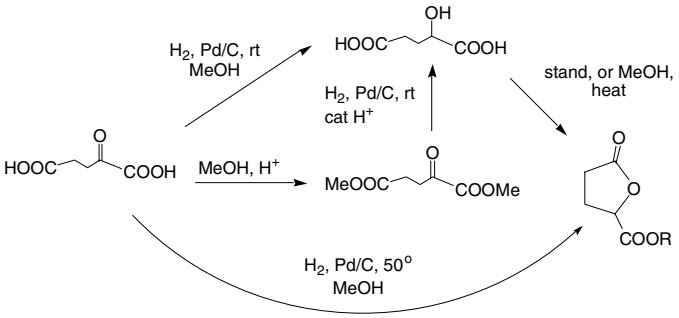

Figure 4. Transformations of 2-KGA into additional building blocks

Conclusions

Renewable feedstocks derived from well known biochemical pathways can be useful building blocks in the production of new materials. 2-KGA forms novel crosslinked polyesters upon reaction with diols. Future work will expand this process to a wider range of monomers and polymers.

Acknowledgement. This work was supported by the NREL Director's Discretionary Research and Development program.

References

(1) Katagiri, H., Tochikura, T., Imai, K., *Bull. Agr. Chem. Soc. Japan*, **1957**, *21*, 210.
(2) 3 billion lb/yr of MSG is produced worldwide at a cost of $0.75 - 0.80/lb; Bizzari, S., Janshekar, H., Yoneyama, M., Chemical Economics Handbook, July 2000, p. 543.6000.
(3) Chemicals and Materials from Renewable Resources, Bozell, J. J., ed., ACS Symposium Series, **2001**, 784.
(4) Several good smaller scale examples of commercial renewables based bioprocesses exist, but at a scale much smaller than a typical petrochemical based process; Wilke, D., *Appl. Microbiol. Biotechnol.*, **1999**, *52*, 135.
(5) Lynd, L. R. Wyman, C. E. Gerngross, T. U. *Biotechnol. Prog.,* **1999**, *15*, 777.
(6) We are also studying the β-ketoadipate pathway, a process used by many organisms for the metabolism of aromatic compounds, and a possible route for the use of lignin as a renewable feedstock. This path provides β-ketoadipic acid, which will be described in future publications; Harwood, C. S., Parales, R.E., *Annual Rev. Microbiol.*, **1996**, *50*, 553
(7) β-Keto acids form hydrates, and undergo condensation; Cooper, A. J. L., Ginos, J. Z., Meister, A., *Chem. Rev.*, **1983**, *83*, 321.

BIOREFINERY CONCEPT DEVELOPMENT BASED ON WHEAT FLOUR MILLING

Douglas C. Elliott[a], Rick J. Orth[a], Johnway Gao[a], Todd A. Werpy[a], David E. Eakin[a], Andrew J. Schmidt[a], Gary G. Neuenschwander[a], Anthony J. Flagg[b], Jim Murry[b], Lyle Lahman[c], C.J. Lin[c], Donald L. Mennel[c], Ron Landucci[d]

[a]Pacific Northwest National Laboratory, P.O. Box 999, Richland, Washington, USA 99352
[b]Pendleton Flour Mills, LLC., P.O. Box 1427, Pendleton, Oregon, USA 97801
[c]The Mennel Milling Company, P.O. Box 806, Fostoria, Ohio, USA 44830-0806
[d]ProForma Systems, Inc., 13902 W. 20th Place, Golden, Colorado, USA 80401-2193

Introduction

Wheat is the second largest agricultural commodity in the United States, with a net production of 56.1 million tonnes in 1995 (2.1 billion bushels). About half is exported, and, of the balance, 85% is dry-milled within the U.S. to produce 17.8 million tonnes of flour. The remaining 5.9 million tonnes consist of low-value byproducts, which are mostly disposed as animal feed. These byproducts, collectively referred to as millfeed, are made up of the bran, the germ, and a portion of the endosperm, which also contains a significant amount of starch not recovered in the milling process. A rough calculation suggests that millfeed is composed of up to 35% starch that originated from the endosperm.

Millfeed is not a single homogeneous stream but a collection of several streams from the process of making flour. It contains about 75% carbohydrate, 17% protein, 3% fat, and 5% mineral matter, but its composition varies, depending on the variety of wheat being processed. Millfeed production also varies slightly, depending on mill operation and variety of wheat. Flour extraction ranges from 73 to 77%; thus, the average amount of millfeed generated is about 25% by weight of the wheat introduced to the mill.

The process described in this paper is being developed to recover the starch-rich product from millfeed; process it to glucose; and convert the glucose into a commodity product, such as polyol or lactic acid. Processing the glucose from the extracted starch for polyol production is based on catalytic hydrogenation to sorbitol. Lactic acid production is based on fermentation of the millfeed-derived glucose.

In either pathway (catalytic or fermentation) to value-added products, the residual millfeed will also be an important consideration. By extracting the starch from the millfeed, the quality of the remaining material as animal feed may actually be increased by concentrating the protein content. The improved value of this starch-extracted millfeed has undergone preliminary evaluation, but needs to be validated in animal feeding tests.

Experimental

Glucose Production from Wheat Millfeed. Bench-scale testing was conducted to optimize the process and provide the foundation for a process to effectively recover the starch and convert it to glucose. The process optimization testing incorporated a systematic approach of evaluating each key processing step in the order that it appears in the process; **Figure 1** illustrates those steps. The millfeed used for these tests was a soft white winter wheat all inclusive without screenings. Once the individual unit operations were tested separately, the optimized conditions were tested together to arrive at an integrated starch extraction process.

A specified amount of water was added to a 250-mL flask, and then placed in an incubator (and constantly shaken) for heat-up to a predetermined temperature. Millfeed was then added to the 250-mL flask, and it was placed back into the incubator for a predetermined time (**initial water wash**). The millfeed slurry was then removed from the incubator and **coarse filtered** via vacuum filtration for 10 min through a 4-in. Buchner filter (no filter paper used). The filter-cake from the coarse filtration was dried and retained for analyses. The filtrate was collected, pH-adjusted if necessary, and placed back into the incubator for heat-up to a predetermined **liquefaction** temperature. After reaching, the specified liquefaction temperature, α-amylase was added, and liquefaction was initiated.

Following the liquefaction step, the incubator temperature was adjusted to a predetermined **saccharification** temperature, and pH adjustments were made if necessary. After the desired saccarification temperature was reached, glucoamylase was added to the solution, and it was placed in the incubator for a specified saccharification time.

Following a specified time, the product from saccharification was removed, and again filtered. This second filtering operation, termed fine filtration, was conducted via vacuum filtration for 10 min, using a 4-in. Buchner funnel with Whatman #4 filter paper. Following fine filtration, the filtercake was dried and retained for analyses. The filtrate from the fine filtration step was also collected for analyses.

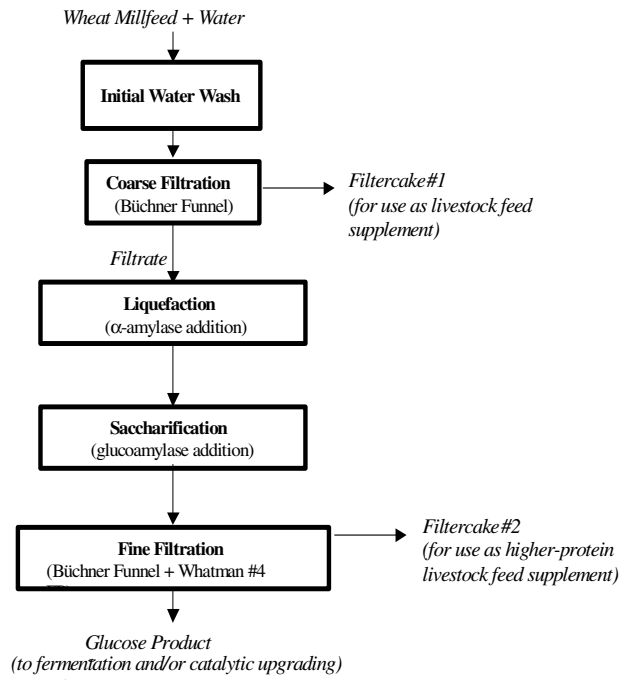

Figure 1. Starch Extraction Key Processing Steps

Fermentation Development Process. Batch and semi-batch modes were used for the lactic acid fermentation tests. In all the tests, bacterial strains of *Lactobacillus* species were selected for developing the lactic acid fermentation process. Pre-test results showed the fungal strain *Rhizopus oryzae* was unable to produce a substantial amount of lactic acid in the culture medium containing the wheat millfeed hydrolysate. However, *Lactobacillus* species were able to produce a large amount of lactic acid in the hydrolysate medium.

Fermentation media containing either reagent glucose or wheat millfeed hydrolysate were prepared. The pH of each medium was adjusted to 6.5 to 6.8 using 1 N KOH. Aliquots of 50-mL

fermentation medium were dispensed into 125-mL serum bottles, which were capped with Teflon-lined rubber septa and then wrapped with two layers of aluminum foil. After being autoclaved at 121°C for 15 min and cooled down to room temperature, each bottle was supplemented with 2 to 3 g of calcium carbonate powder, which was sterilized by baking in an oven at 121°C for at least 3 hr. The amount of added calcium carbonate depended on the glucose concentration in the hydrolysate. The medium bottles were capped with sterile septa and aluminum seals using a hand crimper, and the headspace of each bottle was purged with deoxygenated nitrogen for 5 to 10 min through a 0.2-µm sterile filter (VWR Scientific). The ready bottles with fermentation medium were then inoculated with mature seed culture and subsequently incubated in an orbital shaker at 140 rpm. The fermentation temperature was controlled at 40°C to 45°C, depending on the testing conditions.

Catalytic Process Development. Glucose hydrogenation to sorbitol was chosen as the catalytic processing test case for the wheat millfeed-derived glucose. The reactor was a stirred batch reactor made of 316 stainless steel. The reactor volume was typically 300 mL with the vessel filled half full of aqueous sugar solution. The catalyst was a ruthenium on titania (rutile form) extrudate ground to powder (5 g per 150 g of feed solution). The processing conditions were 100°C and 1500 psig with hydrogen atmosphere. The slurry of feed solution and catalyst particles was stirred to maximize hydrogen contact. The reaction was allowed to proceed for 6 hr, typically, with multiple samples of product solution withdrawn throughout the reaction period. The product solutions were analyzed by liquid chromatography to determine primarily the glucose and sorbitol concentrations, but also to monitor for byproducts. The vented gas product at the end of the test was analyzed by gas chromatography to determine other byproducts (hydrocarbons or carbon oxides).

Results and Discussion

Glucose Production from Wheat Millfeed. A baseline starch extraction process was developed that consists of hot water extraction of starch and filtration of fibrous animal coproduct, followed by enzymatic liquefaction and saccharification of the extracted starch with filtration of a high-protein and a lower-protein coproduct. With this process, a glucose yield of approximately 20% on a dry millfeed basis was achieved. Improvements to the baseline process, including thorough filtercake rinsing and countercurrent extraction, yielded nearly 30% glucose on a dry millfeed basis, corresponding to recovery of essentially all of the glucose value in the millfeed. Following bench-scale testing, pilot-scale testing was conducted, in which approximately 150 lb of wheat millfeed were processed. The glucose yields obtained in the pilot-scale testing were comparable to those obtained during the bench-scale testing; however, filtration was more difficult. The residual fibrous material from the pilot-scale testing was evaluated as animal feed, and the glucose-containing hydrolysate was evaluated as a feedstock for catalytic upgrading (with and without upstream separations) and fermentation.

Fermentation Development Process. Wheat millfeed hydrolysate was used as the primary carbon source for the lactic acid fermentation process development. Batch cultures of lactic acid fermentation were used to assess the feasibility of the fermentation process development. Three lactic acid producing strains [purchased from American Type Culture Collection (ATCC), Manassas, Virginia] were tested: *Lactobacillus rhamnosus* (ATCC 10863), *Lactobacillus delbrueckii subsp. lactis* (ATCC 12315), and *Lactobacillus rhamnosus* (ATCC 11443). All strains showed favorable lactic acid production rates at the temperature of 43°C.

Based on a mineral analysis, manganese was the only critical element lacking in the hydrolysate medium. Without the addition of manganese, the fermentation batch culture could result in lower lactic acid yield. Under the testing conditions, the hydrolysate medium with only minimal manganese addition performed better than the culture medium containing reagent-grade glucose and other nutrients such as yeast extract and peptone. The superior performance of the hydrolysate medium is probably due to the presence of various amino acids and other nutrients.

Catalytic Process Development. Three versions of the wheat millfeed-derived glucose solution were used for the testing: the hydrolysis filter press product, the ultrafiltration permeate derived from the filter press product, and the nanofiltration concentrate from the ultrafiltration permeate. Results showed that further cleanup of the wheat millfeed-derived glucose stream was required before it could be used as feedstock for catalytic processing. Therefore, the ultrafiltration permeate was treated in an activated carbon bed prior to the hydrogenation to sorbitol step in order to avoid catalyst inhibition. Nanofiltration (reverse osmosis) was also demonstrated as a means to concentrate the ultrafiltration permeate prior to carbon treatment and catalytic processing.

Support of Commercialization Efforts. Under a contract from Pendleton Flour Mills, LCC, the process economic model was developed by ProForma Systems, Inc., with input from Pacific Northwest National Laboratory. The model development included material and energy balances built into a virtual process simulator based on Excel™ and Visual Basic™. Equipment sizing and costing calculations were dynamic in nature and adjusted with changes in the mass balance. Capital investment costs and operating costs were also estimated. Using the model, sensitivity analyses could be undertaken as well as comparisons with other technology options.

The model was used to cost a midwest green field site processing a moderate 227,273 tonne per year of millfeed. The yield of glucose was 68,182 tonne per year with 149,091 tonne per year of animal feed and 17,727 tonne per year of high-protein feed supplement. The plant capital cost estimate was $34 million. Using a range of values for the byproducts, the range of costs and prices for the millfeed-derived glucose product was determined. These costs and prices range around the current costs and prices for corn-derived glucose. The corn costs and prices are based on a much larger (typical) corn wet mill producing 1,081,818 tonne per year of glucose. Capital cost at the different scales of operation is the major differentiating factor between the two glucose sources. According to the model, using a $70/ton for millfeed, the glucose from wheat millfeed would cost 8.1 cents per pound.

Acknowledgment

This development effort was conducted under a Cooperative Research and Development Agreement (CRADA) among Pacific Northwest National Laboratory; the U.S. Department of Energy; The Mennel Milling Company; and Pendleton Flour Mills, LLC. Pacific Northwest National Laboratory is operated by Battelle for the U.S. Department of Energy under Contract DE-AC06-76RL0 1830.

Production of ethyl esters from crude soybean oil: Optimization of reaction yields using a 2^3 experimental design and development of a new analytical strategy for reaction control.

Zagonel, G. F., Peralta-Zamora, P. G. and Ramos, L. P.*

Research Center in Applied Chemistry (CEPESQ), Department of Chemistry, Federal University of Paraná – P. O. Box 19.081 – Curitiba, Paraná, Brazil – 81531-990 – fax (55) (41) 361-3186; phone (55) (41) 361-3175 – lramos@quimica.ufpr.br

Introduction

In Brazil, as in many other countries, the first oil crisis in 1973 led to political initiatives to allocate funds for the development of alternative motor fuels. Initially, this program dealt with various types of raw materials and studied different conversion technologies to produce different liquid fuels from renewable resources (*e.g.*, ethanol). In all of its diversity, this broad national program also included efforts to develop vegetable oils and their derivatives for fuels applications. Indeed, this research area received governmental funding up to 1985, when it was discontinued from a general perception that the cost of making biofuels such as biodiesel from vegetable oils would always be greater than the products derived from the already well established petroleum chemistry and technology (MIC, 1985).

In recent years, ever since the Middle East crisis initiated a new cycle, the concept of producing biofuels from renewable resources regained international attention. In a direct attempt to contribute to this process, several projects were initiated in our country to evaluate the production of biodiesel from agro-commodities available nationwide, that is, ethanol and vegetable oils. In this work, the production of ethyl esters from crude soybean oil has been optimized and new analytical methods for process control have been designed to facilitate the *in situ* evaluation of reaction yields.

Experimental

Synthesis. The optimization study developed herein was based on an experimental design in which three process parameters were assessed in two levels (2^3 experimental design): the ethanol:oil molar ratio used for transesterification (6:1 to 10:1), the concentration of the alkaline catalyst (KOH, 0.2 to 0.6% in relation to the oil mass) and the reaction temperature (40 and 70°C). A further expansion of the experimental design was performed at 40°C, with the ethanol:oil molar ratio ranging from 6:1 to 14:1, whereas the KOH concentration varied from 0.2 to 1% (Zagonel, 2001).

Methods. The reaction yields were initially monitored by size exclusion chromatography (SEC) and, at the latter stage of the project, by Fourier-transformed infrared spectroscopy (FTIR) (Zagonel, 2001). This method was successfully used to develop a mathematical model which could easily predict *in situ* reaction yields, thus allowing for a direct monitoring of conversion rates inside the transesterification vessel. Development and validation of the proposed model was carried out by multivariate analysis and the data was treated by principal component analysis and partial least squares regression.

Size exclusion chromatography was carried out using a Shimadzu LC10AD workstation provided with a SIL10A autosampler and detection by differential reffractometry (RID10A). Samples placed in THF were filtered through a Teflon membrane with a pore size of 0.45 µm and analysed using a series of one guard column and two Tosoh TSK-GEL columns (TSK 2000HXL and TSK 1000HXL). Tetrahidrofuran (THF) was used as the eluting solvent at a flow rate of 1 $mL.min^{-1}$. A minimal of three analyses were carried out for each replicate and calibration was based on injection of external standards including ethyl oleate and mono, di and triolein.

FTIR spectroscopy. Standards (3 to 30 mg/mL) and reaction aliquots were also analysed by Fourier-transformed infrared spectroscopy (FTIR) using a Reagen KBr cell for liquid samples. The FTIR spectra were collected using a Bomem FTIR MB-100 spectrophotometer within the region of 500 to 4000 cm^{-1}, with a resolution of 4 cm^{-1}, 32 scans and triangular apodization.

Results and Discussion

The optimal conditions for the one-step transesterification of crude soya oil with ethanol, in which an actual ester yield of 95% was obtained, were: ethanol:oil molar ratio of 12:1, KOH concentration of 0.8% in relation to the oil mass and reaction temperatures of 40°C. These conditions were shown to be adequate for the transesterification of used cooking oil as well, and a first scale up experiment, carried out by a factor of 50 in relation to the bench scale, was also proven perfectly feasible. Lower molar ratios were also proven adequate when reaction times longer than 1 h were used.

Four replicates were carried out at the center point of the experimental design to validate the analytical data generated throughout its execution. The relative standard deviation of the process, including all steps ranging from sampling to SEC analysis, was shown to be only 1.6%. Hence, the overall trends demonstrated by the experimental data were considered of sufficient statistical significance to back-up the proposed conclusions and process recommendations.

In respect to the experimental design, there was a certain limitation in increasing both the ethanol:oil molar ratio and the concentration of the alkaline catalyst (KOH) for further increases in reaction yield. Also, for reactions carried out for more than 20 minutes, temperatures above 40°C were detrimental to the amount of ester produced. In this regard, since the reaction was always carried out in one single step, it seemed that yields could be increased if a two-step transesterification strategy is included, probably using lower ethanol:oil molar ratios.

The FTIR model developed in this work to follow up *in situ* reaction yields was proven very useful and much more effective than traditional methods such as gas-liquid, size exclusion (SEC) and reverse-phase chromatography. The model matched almost perfectly the experimental data obtained by SEC, with a R^2 of 0.984 (Figure 1). This is certainly one outstanding achievement because both methods, regardless of differences in their principles, provided almost identical reaction yields for most of the time in which the reaction was followed.

The ethyl esters produced in this work were proven very appropriate for fuels applications. Tests were recently conducted in stationary diesel engines and the results were very promising in both fuel performance and emissions. Longer field tests, similar to those previously done in Curitiba (PR) with methyl esters produced from soybean oil (B20 mixtures), are solely awaiting for a greater local availability of this biofuel, which is now being synthesized in amounts by far below the least requirements for field trials. Therefore, viability

of the process is still depending upon a reasonable scale up to a pilot plant level, whereby a suitable cost assessment should indicate how far are we from implementing this process in our country.

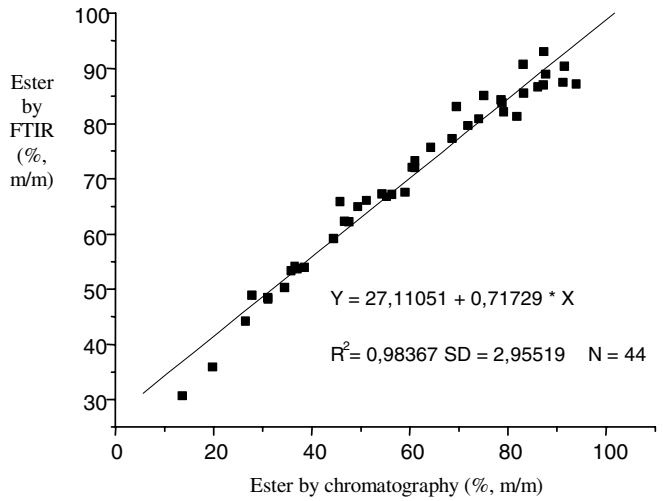

Figure 1. Correlation among reaction yields obtained by infrared spectroscopy and size exclusion chromatography

Future Perspectives

Biodiesel is, by many, one almost irresistible alternative to diesel oil since many environmental as well as social and economic benefits would readily arise from its utilization in both transportation and energy generation. In Brazil, there has been an increasing interest in developing such an alternative but the economics of producing biodiesel from vegetable oils have always been negative. However, several factors are indicating that changes are just around the corner. These include the severe retraction recently observed in the soybean oil market, the competition of the soybean oil with vegetable oils derived from other sources (e.g., rapeseed, sunflower, palm, dendê and others), the recent decline in exportation of the edible oil to Asian markets such as China, and the several consecutive annual records recently attained in soybean production in Brazil (with the concomitant increase in productivity as well).

To our knowledge, only five Brazilian institutions are now directly involved with biodiesel: The State University of Santa Cruz (Ilhéus, BA), The COPPE School of Engineering (Rio de Janeiro, RJ), The Tecnology Institute of Paraná (TECPAR, Curitiba, PR), The National Institute of Technology (INT, Rio de Janeiro, RJ) and our institution. Some local representatives of the private sector are also investigating this new business opportunity, such as Risotolândia Indústria e Comércio de Alimentos Ltda. and the State Association of Sugar and Alcool Producers (ALCOPAR, Curitiba, PR), among others. Therefore, there is an increasing perception that biodiesel will soon become competitive and its use in replacement to diesel oil will increase steadily (Chang *et al*., 1996; Ma and Hanna, 1999; Zagonel and Ramos, 2001). However, cost barriers among with powerful lobbies are still dominating the area and only a strong political support from all Brazilian soybean producers to these new market opportunities will possibly overcome these barriers (Ramos, 2000). Besides, how could biodiesel be produced if no oil is available to do so? Therefore, the future of biodiesel (and its environmental benefits) in Brazil now resides with the farmers and their sight to the immediate needs of our economy and/or society.

Acknowledgement. The authors acknowledge the collaboration of Prof. José Carlos Laurindo, as well as to the technical and financial support of Risotolândia Indústria e Comércio de Alimentos Ltda., Alcopar, Abiove, Imcopa Indústria e Comércio de Óleos Vegetais SA, Fundação Araucária e Instituto de Tecnologia do Paraná (Tecpar).

References

1. Ministério da Indústria e do Comércio, MIC; *Produção de Combustíveis Líquidos a Partir de Óleos Vegetais*. Secretaria de Tecnologia Industrial, Coordenadoria de Informações Tecnológicas, Brasília, DF, Brasil, **1985**
2. Zagonel, G. F., *Obtenção e Caracterização de Biocombustíveis a partir da Transesterificação Etílica de Óleo de Soja*, Mestrado (M.Sc.), Programa de Pós-graduação em Química, Universidade Federal do Paraná, **2001**
3. Zagonel, G. F.; Ramos, L. P. - *Revista de Química Industrial* **2001**, *717*, 17-26
4. Ramos, L. P. - In: *Anais do Congresso Tecnologia e Competitividade da Soja no Mercado Global*; Cuiabá, MT, August 28-30, **2000**, p. 111-113.
5. Ma, F.; Hanna, M. A. - *Biores. Technol.* **1999**, *70*, 1-15
6. Chang, Y. Z. D., Gerpen, V. H. J., Lee, I., Johnson, A. L., Hammond, G. E., Marley, J. S. - *J. Am. Oil Chem. Soc*, **1996**, *73*, 1549-1555.

AGTANE (AGricultural ceTANE): An economically viable bioenergy product for compression ignited engines

*A. Spataru**

*The ADEPT Group, Inc., 1575 Westwood Boulevard, Suite 200, Los Angeles, CA 90024-5620
Fax: (310) 478-5658; adept@adeptgroup.net

Introduction

Scientists at the Canadian Centre for Mineral and Energy Technology (CANMET) laboratory, Ontario, Canada, have proven at lab scale a process to convert yellow grease (YG), tallows and poultry fat to a **low sulfur**, **high cetane premium diesel blending stock**. This proprietary high-temperature and high-pressure process is based on a refining technology called hydrotreating. The principal output is a diesel blending stock called AGTANE (for AGricultural ceTANE).

What is AGTANE and its purpose?

AGTANE , a mix of long-chained paraffins, is *not* a biodiesel (e.g. methyl ester). California refiners who analyzed the final product classify AGTANE as a "synthetic diesel." Paraffins are a family of hydrocarbons normally found in commercial diesel blends; esters are not. When AGTANE is blended with regular diesels, the resulting fuel burns more efficiently and with cleaner emissions. Particulate matter (PM), and NOx emissions are lowered. AGTANE compliments and reduces the volume of traditional cetane improvers.[1]

Global Trends. Convergent global trends favor production of AGTANE from discarded fats and waste oils and greases. There is also regulatory pressure towards the use of on-road diesels with low sulfur and high cetane value.

Recent research has proved synergy between AGTANE and "traditional" cetane improvers.[2] This synergy increases AGTANE's value. It is thought that AGTANE will be added from 3 to 12% of volume in final commercial diesel mixes.

Test Results show that AGTANE:

(1) linearly raises the cetane of unadditized diesel ***without*** a top-end limit;[3]
(2) is synergistic with traditional cetane improvers;
(3) has a low sulfur content (~15 ± 5ppm[4]); and
(4) increases end-product volume by the added AGTANE volume.

Discussion and Application

There is a growing trend to exclude YG and tallow out of the food and feed chains due to ***bovine spongiform encepholapathy***, commonly known as "mad cow disease." Because YG contains a significant amount of animal fat, its sales as an animal feed component are increasingly restricted. There is an unprecedented worldwide surplus of YG. Smaller rendering plants have closed, raising health and environmental concerns in areas where other renderers have been unable to service.

Conclusion

Large-scale production and commercialization of AGTANE allows the rendering industry the option to become a significant pollution remediator. The broad use of AGTANE in on-road and off-road applications will significantly reduce both NOx and PM, something not possible by burning YG in rendering plant boilers.

AGTANE production is most likely to be conducted in major urban areas where large rendering operations are located within 50 miles of petroleum refining facilities. The profitability of AGTANE plants can be further enhanced by tax breaks/incentives currently extended to biodiesel. Exchanges with leading petroleum refiners indicate on-going strong interest in AGTANE.

AGTANE may prove to be a timely solution to help meet US energy and environmental needs, while helping the agricultural sector deal with food chain concerns. As it proportionally reduces the use of petroleum-derived diesel fuel, AGTANE can reduce dependence on foreign oil and increase domestic energy security.

---

[1] Cetane improvers are man-made chemicals that are added at the refinery level to diesel blends to raise the blend's cetane number. These compounds are also called "ignition improvers" Cetane is an indicator of a diesel blend's combustion performance in compression-ignited engines (same as "octane" for spark-ignited engines). As with octane, higher numbers are desirable.

[2] The cetane improver used in these tests was Octel CI-0801.

[3] The cetane value enhancing effects of traditional cetane improvers level off at some point (after an 8 or 9 point rise in cetane value).

[4] 15-ppm max. S_2 in on-road diesel is a South Coast Air Quality Management District requirement by 2005.

LIQUID SMOKE: PRODUCT OF HARDWOOD PYROLYSIS

S. Ramakrishnan, Patrick Moeller

Hickory Specialties, Inc, 1619 Service Merchandise Blvd, Brentwood –TN-37027, U.S.A

Introduction

Liquid smoke compositions are obtained from pyrolysis of hardwood. These solutions are used to impart flavor, color, texture and in certain cases provide enhanced shelf life for food products. The constituents of liquid smoke are obtained from thermal degradation reactions of cellulose, hemicellulose and lignin. More than four hundred compounds have been detected in wood smoke.[1] In order to express the composition from an application stand point, the compounds in liquid smoke have been lumped together as three functional groups: carboxylic acids, phenols, and carbonyls. Cellulose and hemicellulose degradation are the primary sources of carbonyls and carboxylic acids, while phenols are obtained from lignin pyrolysis. In addition to these functional classes, there are other products like alcohols, lactones, and hydrocarbons.

The main variables that control liquid smoke product yield and characteristics are temperature, rate of heat transfer, particle size, atmosphere of pyrolysis, vapor and particle residence times, and composition of biomass. The developments related to control of these variables for improved product and process capabilities have resulted in several patents and publications over the last two decades in the field of liquid smoke. The difference in heat transfer rates results in different product yields. Rapid heat transfer rates are associated with fast pyrolysis systems.[2] Further liquid smoke flavors with different attributes can be made by varying the feedstock.[3] Experiments were done in a bench scale reactor system under conditions of slow pyrolysis. The characteristics of liquid obtained from such bench scale experiments were compared with commercial product.

Experimental

Bench-scale Pyrolysis of Dried Saw-dust Under Atmospheric Conditions:[3]

Dried mixed hard wood saw-dust (150 gm, 8 % moisture) was weighed into a 4-inch diameter, 14 inch long laboratory size quartz rotary kiln and placed in a heated tube furnace. The reaction tube was rotated, so as to mimic the industrial process of a horizontal rotary kiln. The vapors from pyrolysis were then condensed in two vertical condensers in series. The first condenser was held at 65 ^{o}C and the second was held at 5 ^{o}C. The non-condensible vapors were then passed through filters for removing any aerosols, before being vented off. The liquids collected in the condensers were weighed. The test time was dependent on the time required for the char bed to attain the desired bed temperature. The test was stopped when gas evolution was not observed at the desired char bed temperature.

Analysis of Aqueous Condensate:[3]

The condensates were diluted with water, and analyzed for their overall composition for acid and phenol content.[4] The procedures used for composition analysis were those used in the liquid smoke industry. The acid content was determined by titration and expressed as percentage acetic acid. The phenols were determined by colorimetric methods using 2,6-dimethoxy phenol (Aldrich Chemical Co., U.S.A) as standard.[3] In this procedure liquid smoke solutions and standard solutions are complexed with 2,6-dichloroquinine-4-chloroimide (Aldrich Chemical Co. U.S.A) in a borate buffer solution at a pH of 8.3. The reaction is allowed to proceed for 30 minutes at room temperature. The color of the resulting complex is measured at 580 nm. The performance characteristics for the ability of carbonyls in liquid smoke to react with proteins was measured by staining index.[3] This index is obtained by measuring the net absorbance of a reacted sample of glycine and liquid smoke at 440 nm in a glacial acetic acid solution.[3]

Results and Discussion

The product yields from bench scale experiments at various temperatures are presented in table 1.

Table 1. Hardwood Saw-dust Pyrolysis Product Yields from Bench scale Experiment:

Temperature ^{o}C	Liquid yield (%)	Char yield (%)
350	45.7	37.5
400	51.5	28.8
475	59.6	22.8
600	54.7	18.9

The yield values indicate an increase in liquefaction type reactions with increasing temperature. For similar temperatures, higher liquid and lower char yields are obtained from fast pyrolysis type process. The mechanisms involved in the degradation process of the saw dust components to various products have been presented by various researchers. [4,5,6] The composition analysis of the aqueous fraction from bench scale experiments for liquid smoke type characteristics are presented in table 2.

Table 2. Composition Analysis (range) for Aqueous Fraction from Bench Scale Pyrolysis Experiments

Temperature range ^{o}C	400 –600°C
Acidity %	6.1 – 7.2
Phenol (mg/ml)	9.9 – 11.1
Stain index	69.6 – 81.5

The composition analysis indicates an increase in smoke components in the aqueous fraction with increase in temperature. In a traditional liquid smoke manufacture saw-dust is pyrolyzed in temperature ranges of 350-600^{0}C, under atmospheric pressure conditions. The vapors from pyrolysis are condensed and contacted with water. The aqueous condensate is allowed to settle for a period of ten to fourteen days. During this period, an insoluble organic fraction referred to as tar separates out. This fraction carries with it particulates and PAH compounds that are generated and condensed during the manufacturing process. The benzo(a)pyrene content of the resulting aqueous smoke is less than 2ppb. PAH characterization of liquid smoke can be done by HPLC –fluorescence spectroscopy or GC-MS.[7] A typical liquid smoke product from slow pyrolysis has the following average composition[4]: acidity =10.8%, phenol = 17.8 mg/ml, stain index =91.6. The acid and phenol concentration in liquid smoke indicate the flavor strength. The stain index value, provides information on the reactivity of the carbonyl compounds in liquid smoke towards non-enzymatic maillard type browning reactions with amino acids when applied on protein substrates. Thus it is observed that the aqueous extract from bench scale experiments have characteristics similar to a commercial liquid smoke product.

Conclusion:

The similarities in compositional analysis data from bench scale experiments and commercial product indicate suitability of the bench scale experiments to study biomass pyrolysis chemistry for liquid smoke manufacture. Liquid smoke, a product of the biomass pyrolysis provides a safe alternative to food processors over conventional smoke houses. The clean up steps used in the manufacturing process makes it a safe ingredient.

References:

(1) Maga, J.A. *Smoke in Food Processing*; CRC Press: Boca Raton, FL 1988
(2) Graham, R.J.; Bergougnou, M.A., *Journal of Analytical and Applied Pyrolysis* **1984** (6) , 95-135.
(3) Moeller, P.W.; Ramakrishnan, S., *U.S. Patent 6214395* **2001.**
(4) Mark R. Nimolos; Eun –Jae Shin; Alex L. Brown; Robert J. Evans, John W. Daily, *Prep. Pap.-Am. Chem.Soc ., Div Fuel Chem* **2001**, 46 (1) 185.
(5) Evans R.J.; Thomas A. Milne, *Energy Fuels* **1987,** 1, 123
(6) Jan Piskorz; Desmond Radlein, *Journal of Analytical and Applied Pyrolysis* **1986** (9) , 121-137.
(7) Mario Dolores Guillen, Patricia Sopelana, Aranzazu Partearroyo., *J. Agri. Food Chem*, **2000,** 48, 126.

ISOSORBIDE ESTERS: ENANTIOPURE ALCOHOLS DERIVED FROM GLUCOSE

Walter S. Trahanovsky and Yu Wang

Department of Chemistry
Iowa State University
Ames, IA 50011

Introduction

The catalytic hydrogenation of glucose (**1**) produces sorbitol (**2**)[1] which can be easily converted to enantiopure isosorbide by dehydration.[2] Isosorbide (**3**) has two hydroxy groups, one *exo*

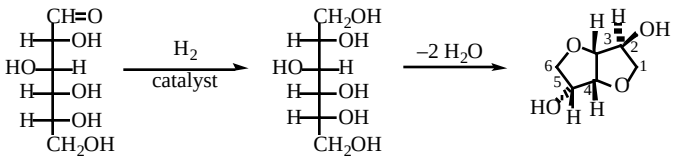

1 **2** **3**

(the 2-OH) and one *endo* (the 5-OH). Conversion of one of the hydroxy groups to an ester gives rise to a large class of enantiopure chiral alcohols. Enantiopure chiral alcohols have been used as chiral auxiliaries in asymmetric synthesis.[3] Moreover, the carboxylic acid portion of the ester can have other functional groups and this allows the synthesis of polyfunctional compounds that could function as complexing agents.

We have undertaken a study of the esterification of isosorbide (**3**) with the goals of a) determining how to effectively and efficiently prepare the *exo* and/or *endo* esters and b) developing convenient spectroscopic methods to determine whether the *exo* or the *endo* hydroxy group has been esterified.

Our first objective was to make and to fully characterize a pair of *exo* and *endo* esters of isosorbide (**3**). In this paper we report the preparation and characterization by ^{1}H and ^{13}C NMR spectroscopy of the mono *exo*- (**4**), the mono *endo*- (**5**), and the di (**6**) *para*-methylbenzoates of isosorbide (**3**).

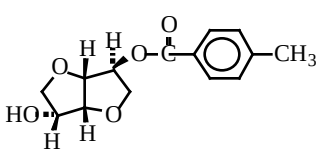

4

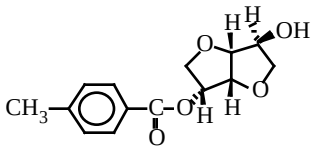

5

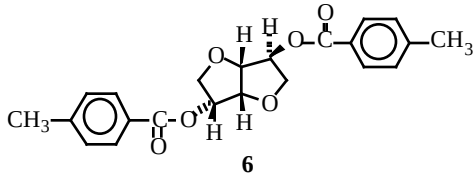

6

Results

Esters **4**, **5**, and **6** were prepared from isosorbide (**3**) and either *para*-methylbenzoic acid or its acid chloride. The esters were purified by column chromatography and the ^{1}H and ^{13}C NMR spectra of the esters were obtained. The chemical shifts of the ^{1}H and ^{13}C NMR data for these esters are presented in Tables 1 and 2.

Table 1. The ^{1}H NMR Chemical Shifts of Esters 4, 5 and 6 (in $CDCl_3$).

	4	5	6
H_{1exo}	4.171	4.016	4.116
H_{1endo}	4.130	3.982	4.106
H_2	5.465	4.375	5.474
H_3	4.633	4.454	4.667
H_4	4.722	4.983	5.054
H_5	4.354	5.395	5.412
H_{6exo}	3.938	3.946	4.038
H_{6endo}	3.618	3.921	4.022
$H_{aromatic}$ [a]	7.58	7.60	7.61
H_{CH_3}	2.417	2.417	2.410
			2.421

[a] center of aromatic signals

Table 2. The ^{13}C NMR Chemical Shifts of Esters 4, 5 and 6 (in $CDCl_3$).

	4	5	6
C_1	73.96	75.78	70.4
C_2	78.91	76.53	78.3
C_3	85.99	88.56	86.4
C_4	82.3	80.94	81.3
C_5	73.84	74.58	73.5
C_6	72.64	71.04	74.3
C_{CO}	165.82	166.24	166.03
			165.67
$C_{aromatic}$	133.6[a]	134.7[a]	133.7[b]
C_{CH_3}	165.82	166.24	166.03
			165.67

[a] center of 4 signals
[b] center of 8 signals

Discussion

The reaction of isosorbide (**3**) with *p*-methylbenzoyl chloride in pyridine gives all three esters, the mono *exo* (**4**), the mono *endo* (**5**), and the di (**6**). All three esters can be purified by column chromatography. The dominant mono ester is the *endo* isomer **5**.

The *exo* ester **4** is the dominant isomer when isosorbide (**3**) is allowed to react with *p*-methylbenzoic acid in the presence of dicyclohexylcarbodiimide. This is consistent with the report by Cekovic and Tokic who used this method to synthesize the isosorbide (**3**) mono *exo* benzoate.[4]

The ^{1}H NMR data of esters **4**, **5**, and **6** show that the proton on the carbon atom bearing the hydroxy group shifts downfield by *ca.* 1 ppm when converted to the ester. Changes of the other proton signals and of the ^{13}C signals are relatively small. The changes we observed in the ^{1}H NMR spectra of esters **4**, **5**, and **6** are consistent with the ^{1}H NMR spectrum of the benzoic acid mono *exo* ester of isosorbide (**3**) reported by Cekovic and Tokic[4] (the isomeric *endo* mono ester or the diester of benzoic acid is not described in this report).

Experimental

Preparation of mono *endo*- (5) and di (6) para-Methylbenzoates of Isosorbide. A 50-mL, round-bottomed flask equipped with a stir bar was charged with 0.3 g (2 mmol) of isosorbide (**3**) and 0.5 g of dry pyridine. The reaction was heated to 90 °C for 20 min and then *p*-methylbenzoyl chloride (0.67 g, 4 mmol) was added to the solution. The reaction was allowed to stand for 20 h. The mixture was treated with 2M HCl until the pH of the solution reached 1. The acidified mixture was extracted

three times with 5-mL portions of ethyl acetate. The organic layers were combined and dried over anhydrous $MgSO_4$, and the mixture was filtered. The solvent was removed under reduced pressure. A white solid (657 mg) was obtained. After recrystallization from toluene, white needle-like crystals (126 mg) were obtained, mp = 145-152 °C. Analysis of its ^{1}H NMR spectrum showed it to be the mono *endo* ester (**5**). After evaporating the solvent of the mother liquor, ethyl ether was added to dissolve the white solid which remained. The solution was cooled with ice. White needle-shaped crystals (300 mg) was obtained, mp = 102.0-102.5 °C. Analysis of the ^{1}H NMR, ^{13}C NMR, IR, and cosy spectra of these crystals showed it to be the di ester (**6**).

When the reaction was repeated but with a reaction time of only 3 h, a mixture of all three esters was obtained: mono *exo* (**4**), mono *endo* (**5**), and di (**6**). All three esters can be separated by column chromatography. The major mono ester was the *endo* isomer (**5**).

Preparation of mono *exo*- *para*-Methylbenzoate of Isosorbide (4). A 50-mL, round-bottomed flask equipped with a stir bar was charged with 0.29 g (2 mmol) of isosorbide (**3**), 0.3 g (2.2 mmol) of *p*-methylbenzoic acid, and 5 mL of CH_2Cl_2. The solution was cooled to 0 °C and 454 mg (2.2 mmol) of dicyclohexylcarbodiimide, and 2.44 mg (0.02 mmol) of 4-dimethylaminopyridine were added with stirring. The reaction was allowed to stand at room temperature for 5 h. The mixture was filtered to remove N,N′-dicyclohexylurea. The filtrate was washed with 2 mL of H_2O, and then 2 mL of 5% aqueous AcOH. The washed organic layer was dried over anhydrous $MgSO_4$ and the mixture was filtered. The solvent was removed under reduced pressure to yield 379 mg white crystals, mp = 155.0-155.5 °C. Analysis of this product's ^{1}H NMR spectrum showed it to be the mono *exo*-ester (**4**). The ester can be purified by column chromatography

Acknowledgement. The authors would like to thank the Iowa Energy Center for financial support of this research.

References

(1) Noller, C. R. *Chemistry of Organic Compounds*. W. B. Saunders Company, Philadelphia, 1965, p. 434.
(2) (a) Jasinski, W.; Ropuszynski, S. *Przegl. Nauk. Inst. Technol. Org.*, Tworzyw Sztucznych Politech. Wroclaw, 1973, 12, 3-29. (b) Fleche, G.; Huchette, M. *Starch/Staerke* **1986**, *38*, 26.
(3) (a) March, J. *Advanced Organic Chemistry*, 4th ed; John Wiley & Sons, 1992, p. 843. (b) Tamion, R.; Marsais, F.; Ribereau, P. and Queguiner, G. *Tetrahedron: Asymmetry* **1993**, *4*, 1879.
(4) Cekovic, Z.; Tokic, Z. *Synthesis* **1989**, *8*, 610.

A ^{1}H NMR Pulse Gradient Spin-Echo (PGSE) Mass Transport Study of Dimethyl Oxalate and Ethylene Glycol: New Fuels for the DOFC

S. Suarez-Gustave, S. Greenbaum* , S.H. Chung** ,E. Peled***, T. Duvdevani***, A. Aharon*** and A. Melman****

*Department of Physics
Hunter College of CUNY
New York, NY 10021
**Department of Chemistry and Physics
William Paterson University
Wayne, NJ, 07470
***School of Chemistry
Tel Aviv University
Tel Aviv, Israel 69978

Introduction

Fuel Cells are electrochemical devices that convert chemical energy into electrical energy. Of the many different types of fuel cells being investigated we focused on the Direct Oxidation Fuel Cell (DOFC). In the DOFC organic fuel is fed directly into the fuel cell without the need for prior modification. This makes the DOFC very attractive as the power source for electric vehicles as it offers reduce weight and volume advantages over the indirect fuel cell, which is based on the modification (reformation) of organic fuels into hydrogen.

Presently methanol is the fuel used in the DOFC. However, because of its toxicity, low boiling point and high permeability in *Nafion* - the proton conducting membrane (PCM) currently used, replacement fuels are being considered[2].

To aid in the development of the DOFC, we investigated the mass transport represented by the self-diffusion coefficients (D) of methanol and two alternative fuels - dimethyl oxalate (DMO) and ethylene glycol (EG) in new low-cost nanoporous PCM's. The NP-PCM's are based on commercial poly(vinylidene fluoride), with variable pore size determined by addition of nanoscale SiO_2 or Al_2O_3 particles[1]. EG is the most promising candidate to replace Methanol, as it is already a ubiquitous product within the automotive industry. The advantage of DMO is that it is a solid at room temperature and therefore may be added directly to the fuel cell without the need for separate fuel tank.

The use of the NP-PCM's offer several advantages over *Nafion* including: lower membrane cost, lower permeability to methanol due to smaller pores, and higher room temperature conductivities that are unaffected by metal-ion impurities (*Nafion's* conductivity decreases significantly with added impurities)[1].

Nuclear Magnetic Resonance Pulse Gradient Spin-Echo technique (NMR PGSE) was used to determine the self-diffusion of diffusing species in the systems[3]. The PGSE technique allows quick non-invasive measurements of the species self-diffusion and has the advantage of measuring mass transport irrespective of the number of chemical components in the diffusing specie.

Experimental

The NMR PGSE experiments were performed using a multiply-tuned PGSE NMR probe in a 7.1T superconducting magnet interfaced with a CMX-300 spectrometer. The NMR diffusion measurements use the Hahn spin echo pulse sequence ($\pi/2$-τ-π) with a pair of square-shaped gradient field pulses (separated by time Δ) of magnitude g and duration δ - the first applied between the two rf pulses and the other after the π pulse. The echo amplitude is attenuated by an amount dependent on the change in the spins position by the process of self-diffusion in the time interval Δ. This change may be represented by

$$A(g) = \exp[-\gamma^2 D g^2 \delta^2 (\Delta - \delta/3)]$$

where D is the self-diffusion coefficient and γ is the magnetogyric ratio of the spin. By fitting this equation to the echo amplitudes for a series of gradient strengths g, D is extracted[3].

Fuel/Acid mixtures consisting of 3M H_2SO_4 and 2M of the above named fuels were prepared. Strips of the NP-PCM's were placed in each of the fuel/acid mixtures and allowed to equilibrate for 48 hours. Measurements were collected over the temperature range of 30-90°C with 20-30min sample equilibration time after each temperature change. An Oxford ITC533 temperature accessory in conjunction with a stream of dry N2 gas was used to regulate the temperature to within ±1K.

Results

Proton NMR spectroscopy results for the fuel/acid systems revealed multiple components - OH and CH, identifiable by their respective chemical shifts, as shown in **Fig. 1**. Of the three fuel/acid solutions DMO gave OH and CH self-diffusion coefficients lower by about a factor of two both in solution and in the NP-PCM's. EG solution had OH and CH self-diffusion values comparable to Methanol over the entire temperature range.

However, results for the EG equilibrated NP-PCM's gave OH and CH diffusion values lower by about a factor of two compared with the Methanol equilibrated membranes. Of the five NP-PCM's investigated, one particular membrane that exhibited low crossover in electrochemical evaluations gave the highest OH and CH self-diffusion values, almost independent of fuel type. **Figures 2** and **3** show Arrhenius plots of D for both the OH and CH peaks components of the equilibrated NP-PCM's and fuel/acid solutions.

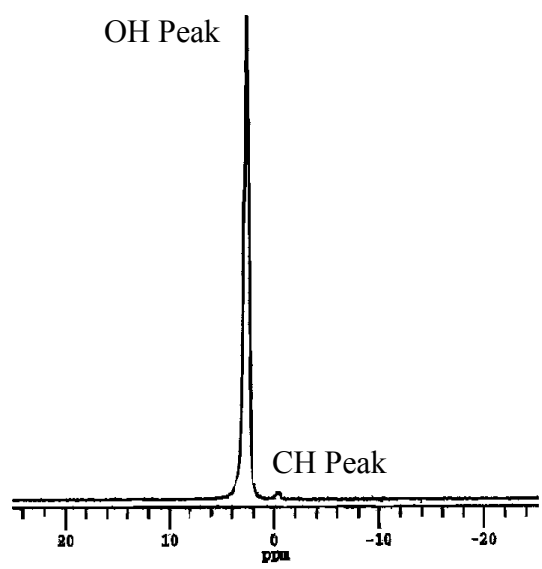

Figure 1. 1H NMR spectrum acquired at 333K indicating the OH and CH components of the system.

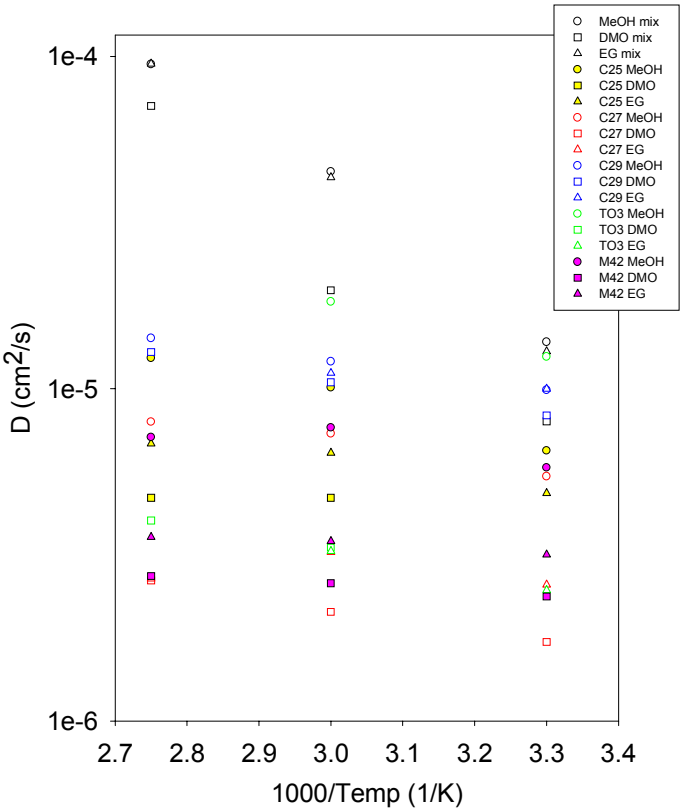

Figure 2. Arrhenius plot of the OH D values.

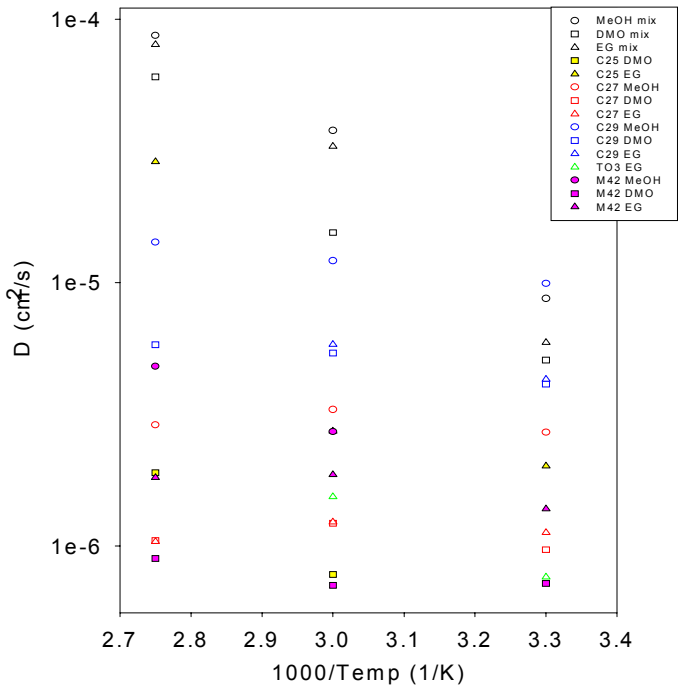

Figure 3. Arrhenius plot of the CH D values.

Conclusion

As replacement fuels for methanol, EG and DMO offers lower membrane permeability indicated by the lower values of CH self-diffusion coefficients obtained for the equilibrated NP-PCM's. Electrochemical measurements[1] indicate that the NP-PCM's exhibit low crossover while retaining high protonic conductivity. Although we expect to find correlations between the former and NMR-determined CH D values, and between the latter and OH D values, the present results suggest that proton transport may not be strongly correlated with OH mobility.

Acknowledgement.

This research is supported in part by ONR.

References

1. Peled, E.; Duvdevani, T; Aharan, A; Melman, A. Electrochemical and Solid-State Letters, **2000**,12 (3), 525-528.
2. Peled, E.; Duvdevani, T; Aharan, A; Melman, A. Electrochemical and Solid-State Letters, **2001**,4 43), A38-A41.
3. Chung, S.H; Bajue, S; Greenbaum, S.G. J. Chem. Phys. **2000**, 112(19), 8515-8521.

PRODUCTION OF HYDROGEN BY CO-REFORMING BIOMASS PYROLYSIS LIQUIDS AND NATURAL GAS

S. Czernik, R. French, C. Feik, E. Chornet

National Renewable Energy Laboratory
1617 Cole Blvd., Golden, Colorado, USA 80401

Introduction

At present, hydrogen is produced almost entirely from fossil fuels such as natural gas, naphtha, and coal. We believe that in the future biomass can become an important sustainable source of hydrogen. As a renewable resource, it has an advantage of low environmental impact (almost zero net CO_2 emissions) compared to that for fossil fuels. However, the price of hydrogen obtained by direct gasification of lignocellulosic biomass is at least three times higher than that for hydrogen produced by steam reforming of natural gas [1]. Over the last several years we have been developing a method for producing hydrogen from biomass [2-4] and concluded that only a hydrogen/co-products strategy could compete with the cost of the commercial hydrocarbon-based technologies.

The proposed process combines two stages: fast pyrolysis of biomass to generate bio-oil and catalytic steam reforming of the bio-oil to hydrogen and carbon dioxide. This concept has several advantages over the traditional gasification/water-gas shift technology. First, bio-oil is much easier to transport than solid biomass and therefore, pyrolysis and reforming can be carried out, if needed, at different locations. A second advantage is the potential production and recovery of higher-value co-products from bio-oil. For example, the lignin-derived fraction can be separated from bio-oil and used as a phenol substitute in phenol-formaldehyde adhesives while the carbohydrate-derived fraction is catalytically steam reformed to produce hydrogen. Assuming that the phenolic fraction could be sold for $0.44/kg (approximately half of the price of phenol), the estimated cost of hydrogen from the proposed process would be $7.7/GJ [5], which is at the low end of the current selling prices.

The yield of hydrogen that can be produced from biomass is relatively low, 12-14% based on the biomass weight. It is even lower when only the carbohydrate-derived bio-oil fraction undergoes reforming while the lignin part is used for other applications. At present, the amount of biomass-derived liquids available for reforming is rather limited but a viable way to increase the production of hydrogen in a biomass-based plant could be co-reforming of pyrolysis liquid with natural gas. This approach, similar to co-firing of biomass with coal for power generation, would add environmental benefits to the traditionally fossil-based technology. The objective of this work was to investigate the co-reforming process and validate the concept.

Experimental

C11-NK catalyst obtained from Süd-Chemie, Inc. was ground to the particle size of 300-500 μ and used for co-reforming in the 2"-diameter fluidized bed reformer system that was described in our earlier paper [4]. Bio-oil used for this study was generated from pine sawdust using the NREL fast pyrolysis vortex reactor system. The oil comprised 47.7% carbon, 7.4% hydrogen, and 44.8% oxygen with a water content of 26.7%. It was separated into aqueous (carbohydrate-derived) and organic (lignin-derived) fractions by adding water to the oil at a weight ratio of 1.5:1. The aqueous fraction contained 20.0 wt.% organics and 80.0% water and consisted of 11.8% carbon, 9.6% hydrogen, and 78.6% oxygen. Natural gas from the public utility was compressed and fed to the fluidized bed reformer at the rate of 0.75 L_{STP}/min, while the pyrolysis liquid feed rate was 2 g/min. The reactor operated at 850°C with a methane-equivalent gas hourly space velocity $G_{C1}HSV$ of app. 1000 h^{-1} and a molar steam-to-carbon ratio of 4.6. The test was carried out for 56 hours alternating between the co-reforming and the bio-oil-only reforming. The concentration of major gas components as a function of time is shown in Figure 1.

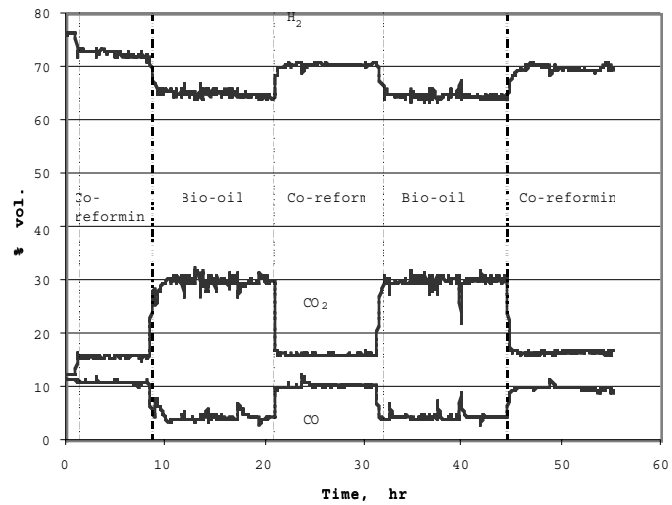

Figure 1. Composition of gas obtained from reforming of bio-oil and from co-reforming of bio-oil with natural gas.

The gas composition was almost constant during the stages of reforming and co-reforming, though a small decrease in hydrogen and increase in methane concentration were observed between the first and the second co-reforming cycle. Interestingly, co-feeding of natural gas helped maintain and restore the catalyst activity that was slowly declining during reforming the bio-oil fraction. An evidence of the catalyst deactivation is a sharp increase in methane concentration that was observed at the beginning of the second and third cycles of co-reforming but significantly decreased after 0.5-1 hour (Figure 2).

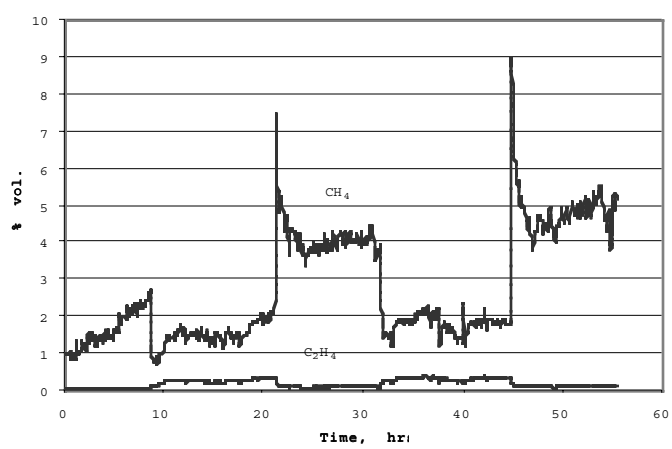

Figure 2. Concentration of hydrocarbons in the gas obtained from reforming of bio-oil and from co-reforming of bio-oil with natural gas.

Discussion

We believe that the mechanism of metal-catalyzed reforming of oxygenated organic molecules is similar to that proposed for hydrocarbons [6]. Dehydrogenation of the organic molecules adsorbed on the metal (nickel) sites produces hydrogen and smaller organic fragments that react with hydroxyl groups migrating from alumina sites to form first intermediate compounds and, eventually, carbon oxides. The above main processes are accompanied by side reactions leading to the formation of carbon deposits on the catalyst surface. This unwanted effect is enhanced by higher non-saturation, molecular weight, and aromaticity of the organic molecules [7]. Biomass-derived liquids are on one hand more reactive than hydrocarbons because they already have some carbon-oxygen bonds. On the other hand, they show greater tendency to form carbon deposits because of the large size of certain molecules (oligomeric carbohydrates and phenols) and thermal instability leading to carbonization at elevated temperatures.

The overall steam reforming of any oxygenated organic compound proceeds according to the following reaction:

$$C_nH_mO_k + (n-k)H_2O \leftrightarrow nCO + (n+m/2-k)H_2$$

Because of the excess steam used in the process, at least a part of carbon monoxide undergoes a consecutive water-gas shift reaction:

$$nCO + nH_2O \leftrightarrow nCO_2 + nH_2$$

Thus the maximum yield of hydrogen that can be obtained by reforming/water-gas shift (corresponding to the complete conversion of organic carbon to CO_2) equals 2+(m-2k)/2n moles per mole of carbon in the feed material. During reforming of the bio-oil fraction the yield of hydrogen was initially 82% then decreased to 75% of the stoichiometric potential. For co-reforming the hydrogen yield was about 85% of the theoretical maximum (Figure 3). These values could increase by additional 10% if a secondary water-gas shift reactor followed the reformer. During co-reforming, 23-26% of the hydrogen was generated from bio-oil and 77-73% from natural gas.

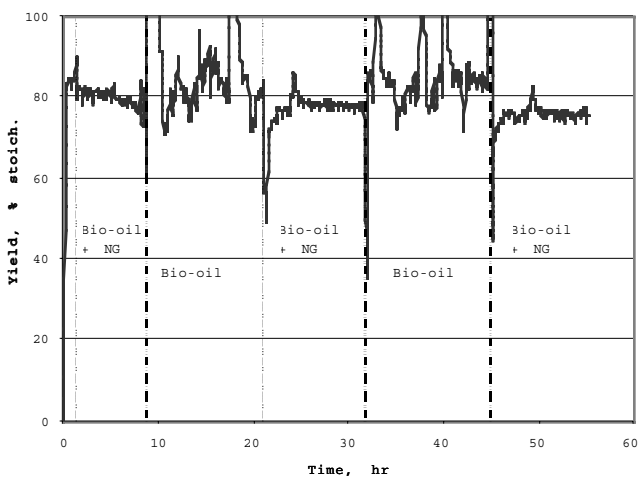

Figure 3. Yield of hydrogen obtained from reforming of bio-oil and from co-reforming of bio-oil with natural gas.

The decrease in the yield of hydrogen was a consequence of the declining conversion of methane that was initially 92.5% then decreased to 80% at the end of the test. All these clearly show a gradual loss of activity of the catalyst. We believe (though we do not have direct evidence) that the catalyst deactivation progressed because of two types of reactions: formation of carbon deposits on the catalyst surface and oxidation of nickel due to a high excess of steam (S/C=13), which was used for bio-oil reforming to remove those deposits. During co-reforming, the steam excess was much lower and the hydrogen production was greater, which prevented oxidation of the catalyst and slowed down the deactivation.

Conclusions

The technical feasibility of co-reforming bio-oil and natural gas has been demonstrated. Co-reforming can be an attractive opportunity that enhances the flexibility of the biomass-to-hydrogen process.

Acknowledgement. The authors are thankful to the U.S. Department of Energy Hydrogen Program for financial support of this work

References

(1) Spath, P.; Lane, J.; Mann. M.; Amos, W., *Update of Hydrogen from Biomass – Determination of the Delivered Cost of Hydrogen. NREL Milestone Report, April 2000.*

(2) Wang, D.; Czernik, S.; Montané, D.; Mann, M.; Chornet, E., *I&EC Research,* **1997,** 36, 1507-1518.

(3) Wang, D.; Czernik, S.; Chornet, E., *Energy & Fuels*, **1998,** 12, 19-24.

(4) Czernik, S.; French, R.; Feik, C.; Chornet, In *Advances in Hydrogen Energy*, Gregoire-Padró, C. and Lau, F., Eds., Kluwer Academic/Plenum Publishers, pp. 87-91.

(5) Mann, M.; Spath, P.; Kadam, K., In *Proceedings of the 1996 U.S. DOE Hydrogen Program Review*, NREL/CP-430-21968, pp. 249-272.

(6) Ross, J.R.H, Steel, M.C.F., Zeini-Isfahani, A., *J. Catal.*, **1978,** 52, 280.

(7) Trim, D.L., *Catal. Today*, **1997,** 37, 233.

FRACTIONAL PYROLYSIS OF BIOMASS FOR HIGH-VALUED PRODUCTS

*F. A. Agblevor and S. Besler-Guran**

Department of Biological Systems Engineering
Virginia Polytechnic Institute & State University
Blacksburg, VA 24061
*New Jersey Department of Environmental Protection,
Air Quality Management, Trenton, NJ.

Introduction

Conventional rapid pyrolysis (RP) of biomass is a thermal treatment process in the absence of air, which produces solid, liquid, and gaseous products.[1-4] In these processes, the pyrolysis temperatures range from 450 - 600°C and vapor residence times are one to five seconds. In the RP process, liquid production is maximized at the expense of gaseous and solid products. The liquid product (bio-oil) is generally unstable, acidic, corrosive, viscous, and has high moisture content.[5-6] The poor stability of bio-crude oils is attributed to the char and alkali metals in the oil, which catalyze secondary reactions during storage. However, if the hot pyrolysis vapors are filtered to reduce the char content before condensation, the stability of the oil is improved considerably.[1,5]

Bio-crude oils are complex mixtures of carbohydrate and lignin thermal decomposition products, which cannot be used for most bio-based products and fuel applications except after considerable secondary processing. Catalytic studies of biomass pyrolysis products have focused on post pyrolysis catalysis to higher value products[7-8], but most of these studies reported low yields of hydrocarbons, high coke/char yields and rapid deactivation of the catalysts. Fractional pyrolysis has not been reported.

Biomass feedstocks are composed of structural (lignin, cellulose, and hemicellulose) and non-structural (extractives) components, which have distinct chemical properties. It is conceivable to selectively convert the biomass constituents to a defined slate of chemicals and separate these products *in situ* (fractional pyrolysis) without necessarily going through secondary extraction and upgrading processes. Fractional pyrolysis is defined as a selective *in situ* conversion of biopolymers to desired products. This approach is aided by catalysts and can produce a narrow slate of pyrolysis products, which can be tailored to specific applications.

The goal of this research is to selectively convert biomass components *in situ* into suitable products using suitable catalysts and thus eliminating potential secondary processing steps. In this paper, we report the fractional catalytic conversion of the carbohydrate components of hybrid poplar wood into gaseous products and depolymerization of lignin into phenol, cresols, and catechols.

Experimental

Feedstock and Catalyst. The feedstock used for this experiment was a hybrid poplar whole wood ground in a Wiley mill to pass a 1-mm screen. The moisture content of the feed was 5%. 200 g batches of a proprietary catalyst (VPISU-001) were used in each experiment.

Fluidized Bed Pyrolysis. The reactor consisted of a 50 mm schedule 40 stainless steel pipe, 500 mm high (including a 140-mm pre-heater zone below the gas distribution plate) and equipped with a 100-µm porous metal gas distributor. The reactor was externally heated with a three-zone electric furnace. The biomass was conveyed by a twin-screw feeder into a compartment from where high-velocity nitrogen entrained the feed and carried it through a jacketed air-cooled tube into the fluidized bed. The pyrolysis temperature was maintained at 500°C and the apparent pyrolysis vapor residence time was about 1 s. A typical run lasted for 2-3 h, and the feed rate was 100 g/h. Pyrolysis gases and vapors exiting the reactor passed through a heated hot gas filter unit to separate char/ash and any entrained catalyst. The pyrolysis liquids were collected in two condensers and an electrostatic precipitator (ESP). The amount of char/coke was determined by weighing the reactor/catalyst and hot gas filter before and after each run. No attempt was made to differentiate between the char and coke and no further analysis was done.

Results and Discussion

Pyrolysis Products. During first half hour of pyrolysis, there was very little condensation of pyrolysis products. The absence of liquid condensate in any significant quantities suggested that during this phase the catalyst was extremely active and the major reaction was gasification. The material balances for two catalytic pyrolysis runs are shown in Table 1. Compared to rapid non-catalytic pyrolysis (RP), the total liquid yields were very low (30%), and the gas yields were very high (60%). The char/coke yields (11.5%) were comparable to those reported for conventional pyrolysis of hybrid poplar wood.[2]

Table 1. Material balance on catalytic pyrolysis of hybrid poplar (on as received basis).

Fractions	Run 1461-40 #4	Run 1461-42 #5		
Gas Yield (%)	60	55.0		
Total Liquids (%)	30.6	30.1		
Char/Coke (%)	11.5	11.9		
Total	102.1	97.0		
Liquid Fractions collected			**Color**	**# Phases**
Chilled Water Condenser (g)	19.9	18.9	Brown	1
Ice/Water Condenser (g)	14.7	16.8	Yellow	1
ESP (g)	25.7	25.3	Brown	1
Total Liquids (g)	60.3	61		
Total Biomass Pyrolyzed (g)	197	202		

About 90% by weight of the gaseous products was CO and CO_2 and the rest was a mixture of hydrocarbons. Butene was the most abundant hydrocarbon and in some cases constituted 30% of the total hydrocarbon products.

The liquids from the first condenser and the ESP were both brown, with extremely low viscosity. The liquids composition included almost exclusively phenolics (phenol, cresols, guaiacol, methyl-substituted phenols), small quantities of indene and substituted naphthalenes, with no detectable carbohydrate pyrolysis products. No benzene, toluene or xylenes were detected in any of the products. The elemental composition of the liquids had high carbon (71%) and relatively low oxygen content (21%) compared to non-catalytic pyrolysis oils. The HHV was consequently high (30.5 MJ/kg) compared to 23 MJ/kg for the non-catalytic pyrolysis oil. The liquid from the second condenser was light yellow, also had very low viscosity and appeared to be 95% water and 5% dissolved organics.

Molecular Weight Distribution of Liquid Products. Gel permeation chromatography (GPC) showed very low molecular mass distribution of the liquid products. The number average molecular weights (Mn) of the liquids from the ESP and the chilled water

condenser were both 160 while the weight average molecular weight (Mw) were 215 and 220 respectively. These molecular weights are about half of those reported for phenol/neutral fraction from conventional rapid pyrolysis products (Mn = 290, Mw = 440) (Fig 1).

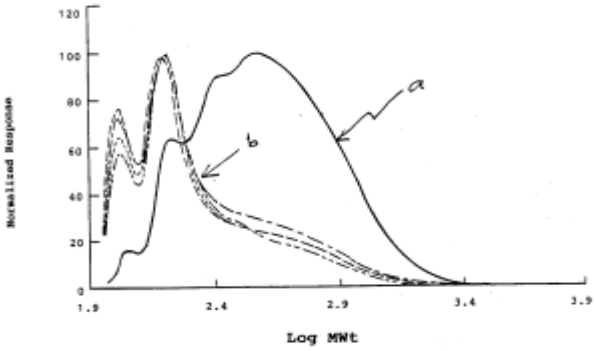

Figure 1. Molecular weight distribution of (a) phenol/neutral fraction extracted from sugar cane bagasse conventional rapid pyrolysis oils and (b) hybrid poplar catalytic pyrolysis liquids.

Catalyst Activity. The CO and CO_2 concentrations appeared to vary with time during the catalytic pyrolysis. The variation was probably due to catalyst deactivation. In these studies we attempted to monitor catalyst activity by following the variation in CO and CO_2 concentration in the gaseous product and compared CO/CO_2 ratio for the catalytic pyrolysis with a non-catalytic process carried out in a silica sand media. The CO/CO_2 ratio decreased with time and appeared to approach the value for non-catalytic pyrolysis (Fig 2). If we assume that this ratio is a true monitor of catalytic activity, then the catalyst was still active after three hours run albeit less active than the fresh catalyst.

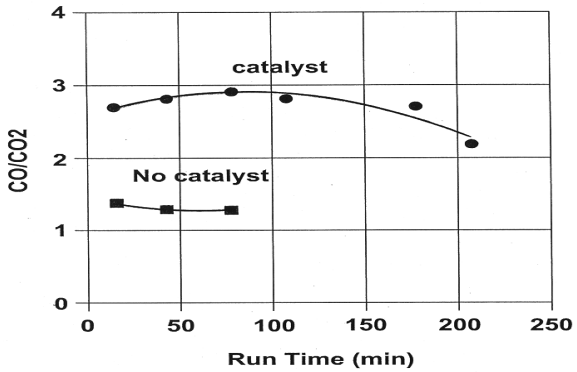

Figure 2. Variation of carbon monoxide and carbon dioxide during fractional and conventional pyrolysis of hybrid poplar wood

Under post-pyrolysis catalysis conditions, biomass feedstocks tend to produce very high coke yields, which rapidly deactivate the catalyst. The post-pyrolysis catalysis liquid products usually contain benzene, toluene, xylene, naphthalenes, substituted benzene, and naphthalenic compounds. On the contrary, in the catalytic pyrolysis, where the catalyst and the biomass feed were contacted, the catalyst was still active after 3 hours on steam and the product slate was quite different from that reported for post-pyrolysis catalysis. Coke formation seemed to be very low because the total yield of solids from the process was only 12%, which is equivalent to the coke yield alone from the post-pyrolysis catalysis runs. This could be attributed to the minimal secondary conversion of the primary lignin pyrolysis products to hydrocarbons, which is mostly responsible for the coke formation and thus strongly contribute to the deactivation of the catalyst as observed in post-pyrolysis catalysis. Deactivation of the catalyst seems to be followed by a decrease in CO concentration in the product gas as shown in Fig 2.

Clearly in the fractional catalytic process appeared to be selective pyrolysis and gasification of the biomass components. The carbohydrate degradation products are more labile than the lignin degradation compounds and thus were rapidly converted into gases while the more refractory lignin-derived components mostly formed the liquids. The total liquid yield was 30% with a water fraction of 30-40%. This implies that the organic liquid yield was only 18-21%, which coincides with the lignin content of hybrid poplar wood. Thus, the catalytic pyrolysis appeared to favor production of modified liquid phenolics from the lignin fraction of the biomass while converting the carbohydrate fraction to gases. The presence of high proportions of cresols and dihydroxy phenols (catechol) suggested that demethylation, demethoxylation and cleavage of the lignin decomposition products occurred. As the catalyst slowly deactivated, also some carbohydrate pyrolysis products such as hydroxyacetaldehyde, ethanedial, and hydroxyacetone were not cracked and condensed with the aqueous phase in the chilled water condenser.

Conclusions

We have demonstrated the concept of fractional pyrolysis of biomass. The most important factor is the choice of catalyst. By selecting a suitable catalyst, various components of the biomass feedstocks can be converted *in situ* into desirable products. In this work we showed that the lignin fraction of the biomass could be effectively converted into phenolics with low char yield when catalysis and pyrolysis reactions were performed simultaneously. Char yields for this process were similar to those obtained from conventional rapid pyrolysis. The molecular mass distribution of fractional catalytic pyrolysis process were about one half that obtained for phenol/neutral fraction in a conventional pyrolysis and there appeared to be considerable demethylation and demethoxylation reactions. The liquid product appeared to be stable with minimal repolymerization reaction.

References

1. Agblevor F.A., Besler, S., Wiselogel, A.E. *Energy and Fuels,* **1995,** 9(4), 635-640.
2. Scott D.S., Piskorz, J. *Can. J. Chem. Eng*. **1982,** 60, 666.
3. Graham, R.G. and Bergougnou. *J. Anal. Appl. Pyrolysis* **1984**, 6, 95-135.
4. Diebold, J.P., Scahill, J. In Pyrolysis Oils from Biomass, Soltes, E.J. and Milne T.A., Eds. ACS Symposium Series 376; American Chemical Society, Washington DC. **1988;** pp 31-40.
5. Diebold, J.P. and Czernik, S. *Energy and Fuels* **1997**, 11(5), 1081-1091.
6. Aubin, H. and Roy, C. *Fuel Science International* **1990,** 8(1), 77-86.
7. Sharma, RK, Bakhshi NN,. *Bioresource Technol*. **1991,** 35(1), 57-66.
8. Horne, P.A. and Williams, P.T. *J. Anal. Appl. Pyrol.* **1995**, 34, 65-85.

THE CATALYTIC EFFECT OF CARBON-SUPPORTED RUTHENIUM ON THE DEPOLYMERIZATION OF HYDROLYTIC LIGNIN

Caroline E. Burgess, David J. Clifford, and Justin R. Horvath

Penn State University, The Energy Institute,
209 Academic Projects Bldg., University Park, PA 16803

Introduction

Biomass consists of an assortment of recalcitrant polymers such as cellulose and lignin. Prior to use in gasification streams, these polymers are subjected to degradation/depolymerization reactions for the purpose of liberating smaller, more volatile and reactive species.

It is well known that carbohydrates can be depolymerized in an acid hydrolysis reaction with the depolymerization effectively catalyzed using a carbon-supported ruthenium catalyst (1-5). Under relatively mild conditions, carbon-supported ruthenium can also effectively catalyze the hydrogenation of highly hindered aromatic rings, such as those found in rosin (6, 7). More recently, alumina-supported ruthenium and other forms of ruthenium have been studied as hydrodesulfurization and coal liquefaction catalysts (8-11).

While it is known that ruthenium can catalyze carbohydrate depolymerization, less is understood when reacting whole biomass, as hydrolytic lignin remains and must be separated from the catalyst. Base hydrolysis at 280-320°C has been used to solubilize and react the hydrolytic lignin to phenolic compounds (2, 12). However, little is known about the effect of the ruthenium on the hydrolytic lignin under the base hydrolysis reaction conditions. In this study, the catalytic effect of ruthenium on the degradation of lignin polymers has been explored.

Experimental

Commercially available hydrolytic lignin was obtained from Aldrich Chemical Co. and used as the starting material. Reagent grade sodium hydroxide and concentrated hydrochloric acid were also obtained from Aldrich. The ruthenium catalyst (5% ruthenium loaded on a carbon support) was obtained from Aldrich.

Reactions were performed with and without ruthenium catalyst. For the latter, the catalyst loading was a 1% metal loading. Tubing reactors (~25 mL) were loaded with 1.5 g of hydrolytic lignin and 10 mL of 10% aqueous sodium hydroxide. The reactors were initially purged with nitrogen to remove air and charged to 4.5 MPa with hydrogen gas. An ebulating sand bath was utilized to obtain temperatures of 280, 300 and 320°C in three experiments, each of which had a residence time of 1 hour.

The reacted materials were processed according to the flow chart shown in Figure 1. Solid and liquid products were separated by filtration. The liquid material was then acidified to a pH of approximately 2.0 and separated into acid-soluble and acid-insoluble fractions. Acid-soluble compounds were then extracted with diethyl ether, which was then evaporated to determine yield. Not all acid soluble compounds were soluble in diethyl ether. The yield of residual acid-solubles and gases were determined by difference.

The ether soluble fraction was analyzed by gas chromatography-mass spectrometry (GC-MS) using a Shimadzu QP-5000 mass spectrometer. The acid-soluble fraction was analyzed using a Chemagnetics M100S solid-state nuclear magnetic resonance (NMR) spectrometer operating at a field strength of 2.4 T and utilizing a spinning speed of 3.5 kHz. The technique of cross polarization with magic angle spinning was employed.

To simplify the discussion, the ether-soluble fraction will be referred to as LMW (low molecular weight), the acid-insoluble as HMW (high molecular weight), and the residual soluble material following extraction with diethyl ether as AS-LMW (acid-soluble-low molecular weight) materials.

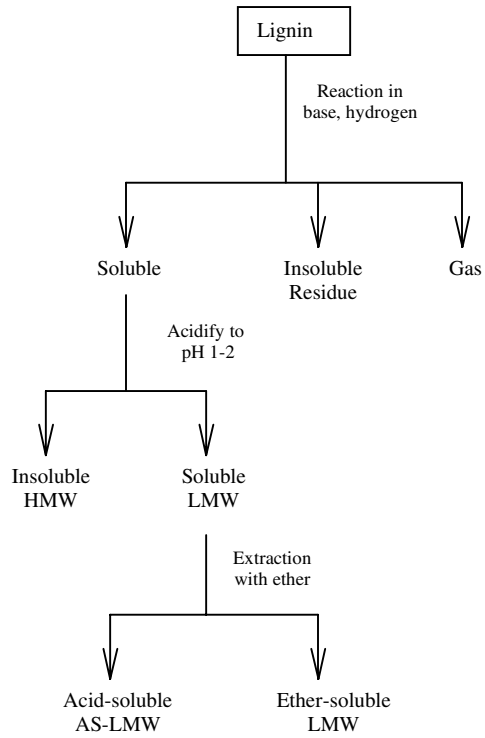

Figure 1: Schematic of procedure to separate products.

Results and Discussion

Non-catalytic Reactions. Table 1 shows the conversions and yields of HMW, LMW and AS-LMW/gas fractions for 280, 300 and 320°C reaction conditions. In each case, conversion to either LMW, HMW, or AS-LMW/gas was nearly complete. Shown in Figure 2 are the GC-MS chromatograms for the LMW fraction and in Figure 4 are solid-state ^{13}C-NMR spectra for the HMW fraction. Relative yields, which are listed in Table 1, indicate that as the reaction severity increases, the yield of HMW product and LMW product decreases, while the AS-LMW/gas yield increases, particularly at 320°C.

Table 1. Conversion and Yield Data for Reaction of Hydrolytic Lignin With and Without Ruthenium Catalyst

Reaction Temp (°C)[a]	Catalyst	Conversion (wt %)	Yield HMW (wt %)	Yield LMW (wt %)	Yield AS-LMW /Gas (wt%)[b]
280	none	99.7	52.0	22.1	25.6
300	none	98.1	38.2	14.6	45.3
320	none	98.6	24.0	8.1	66.5
280	Ru	97.6	22.6	27.5	47.5
300	Ru	90.4	23.6	23.7	43.1
320	Ru	93.5	21.2	16.9	55.4

a All reactions were run for 1 hour, under 4.5 MPa of hydrogen.
b Yield determined by difference.

GC-MS analyses of the LMW fraction (Figure 2) show a product distribution of primarily phenols and catechols, which are compounds typical of lignin degradation reactions. At 280°C, guaiacol is a major product, as well as other methoxyl-substituted aromatic compounds. As the reaction temperature increases, the abundance of methoxyl-substituted aromatics dramatically decreases, with 2,6-di-tert-butyl-p-cresol surviving the more degradative conditions.

Based on the solid-state NMR data (Figure 4), the HMW fraction was found to undergo reactions consistent with those previously reported in lignin maturation investigations (13-19). The primary reaction results in the loss of methoxyl (Figure 4: 74 ppm) and catechol (Figure 4: 148 ppm) functionality with some preservation of phenol-like moieties (Figure 4: 154 ppm).

Catalytic Reactions. When reactions were carried out in the presence of ruthenium catalyst, the conversion was slightly lower than for the corresponding reactions without ruthenium. At all three reaction temperatures, yield of HMW does not change significantly, while the LMW decreases with increasing reaction temperature. However, the depolymerization of the starting material appears to be suppressed under the catalytic reaction conditions at the higher reaction temperature.

GC-MS analyses of the LMW fraction (Figure 3) show the fraction is composed primarily of phenols and catechols, similar to non-catalytic reaction conditions. At 280°C, guaiacol is a major product, as well as other methoxyl-substituted aromatic compounds. As the reaction temperature increases, the methoxyl-substituted aromatics dramatically decrease, with 2,6-di-tert-butyl-p-cresol surviving the more degradative conditions.

The HMW fraction yield did not change as significantly with temperature. The most notable effect on functional group distributions was the loss of the methoxyl (Figure 5: 74 ppm) moieties, while there was some preservation of catechol (Figure 5: 148 ppm) and phenol (Figure 5: 154 ppm) groups within the structure.

Comparison of Non-catalytic and Catalytic Reactions. At 280°C, the extent of depolymerization appears greater for the catalytic reactions. The AS-LMW/gas yield is higher for the catalyzed reaction, and NMR of the HMW fraction shows a greater loss of oxygen functionality when catalyst is in the reaction. The GC-MS data for the LMW also shows fewer oxygen substituted compounds compared to the non-catalytic reaction, another indication of an increased rate of reaction.

However, at 300 and 320 °C, the ruthenium appears to suppress the depolymerization of the hydrolytic lignin compared to the non-catalyzed reactions. The AS-LWM/gas yield is lower for the catalytic reactions. Results of NMR analyses suggest that for the non-catalyzed reactions, the HMW fraction loses more oxygen functionality, particularly as phenols and catechols while the aromaticity increases, compared to the catalytic reactions. The GC-MS data obtained for the LMW fractions indicates a lower percentage of oxygenated compounds, with relatively more substituted aromatics, than in the catalytic reactions.

So what is the role of the ruthenium under these reaction conditions? Ruthenium is a known hydrogenation catalyst, particularly selective for hydrogenating carbonyl functional groups and hindered aromatics (1, 6, 7). However, the hydrogenation activity is highest at 25-200°C. At temperatures of 200-300°C, it has been reported that dehydrogenation activity of aromatics is more dominant (20-21). The reaction system we are investigating is slightly different in that it is a base hydrolysis as well as a hydrogenation reaction.

As observed in the non-catalytic reaction, it is thought that the base participates in breaking the β-O-4 bonds. As radicals are generated through the reaction of the hydrolytic lignin, at 280°C, the ruthenium may be catalyzing the capping of methoxyl radicals with hydrogen and keeping the radicals from re-reacting with the HMW structure. At higher temperatures, the ruthenium appears to promote hydrogenation of the oxygen radicals on the aromatic structures and preserve the phenols and catechols in the HMW structure. It may also function to hydrogenate the carbonyl groups on the generated monomers.

While ruthenium catalyst might suppress the complete gasification of the hydrolytic lignin, it does appear to selectively hydrogenate and retain some oxygen in the solid carbonaceous material. The possible result would be less oxygen in the gas products and less CO/CO_2 generation. Rather than focusing on the complete depolymerization of lignin, the goal could be to focus on finding value-added applications for the products in order to improve the economics for the entire process.

Conclusions

Results indicate that the overall lignin conversion is reduced slightly with increasing temperature compared to non-catalytic reactions. Acid-insoluble compounds retain oxygen functionality, as determined by solid state ^{13}C NMR, when compared to their non-catalytic counterparts. For all reactions, the NMR data showed the oxygen is lost as ether, phenol, and catechol moieties. However, in the non-catalytic reactions, the rate of loss of these moieties and the increase is aromaticity is greater than in the catalytic reactions. If the ruthenium does act to suppress the depolymerization of hydrolytic lignin at higher temperatures, it may selectively suppress loss of oxygen and therefore produce less CO/CO_2. In that case, making value added materials from the remaining material could increase the viability of the entire process. Future work will include using an inert gas, such as N_2 in the reaction, determining the gas composition and yield with and without hydrogen, and searching for uses of the remaining solid.

Acknowledgement. Funding for the project has been provided by the Energy Institute and the Center for Environmental Chemistry and Geochemistry at Penn State University.

References

(1) Gilman, G. and Cohn, G., *Adv. Catalysis,* **1957**, *9*, 733.
(2) Vasyunina, N.A., Balandin, A.A., Chepigo, S.V., and Barysheva, G.S., Bull. *Acad. Sciences USSR (Chem.),* **1960,** 1419.
(3) Robinson, J.M., Banuelos, E., Barber, W.C., Burgess, C.E., Chau, C., Chesser, A.A., Garrett, M.H., Goodwin, C.H., Holland, P.L., Horne, B.O., Marrufo, L.D., Mechalke, E.J., Rashidi, J.R., Reynolds, B.D., Rogers, T. E., Sanchez, E.H., Villarreal, J.S., *ACS Div. of Fuel Chem. Preprints,* **1999**, *44* (2), 224-227.
(4) Robinson, J.M., Herndon, P.T., Holland, P.L., Marrufo, L.D., *Org. Proc. Res. & Dev.,* **1999,** *3* (5), 352-356.
(5) Robinson, J.M., *U.S. Patent No. 5,516,960,* "Process for producing hydrocarbon fuels," **May 14, 1996**.
(6) Glasebrook, A.L., Hoffman, A.N., and Montgomery, J.B., *U.S. Patent No. 2,776, 276,* "Rosin hydrogenation," **Jan. 1, 1957** ((as reported by A.E. Rea and M. Bebbington in "Annotated Bibliography on Ruthenium, Rhodium, and Iridium as Catalysts," International Nickel Company: New York, 1959).
(7) Montgomery, J.B., Hoffman, A.N., Glasebrook, A.L., Thigpen, J.I., *Ind. Eng. Chem.,* **1958**, *50*, 313.
(8) Liaw, S.J., Lin, R.G., Raje, A., and Davis, B.H., *Appl. Catalysis A-Gen.,* **1997**, *151* (2), 423.
(9) Wojciechowska, M., Pietrowski, M., and Czajka, B., *Catalysis Today,* **2001,** *65* (2-4), 349.
(10) Suzuki, T., Yamada, H., Yunoki, K., and Yamaguchi, H., *Energy Fuels,* **1992**, *6* (4), 352.

(11) Kondo, K., Kawanishi, T., Ikenaga, N., and Suzuki, T., *Fuel,* **2001**, *80* (7), 1015.
(12) Burgess, C.E., Robinson, J.M., O'Hara, K., Rashidi, J.R., Sanchez, E.H., and Greenwood, P.F., *ACS Div. of Fuel Chem. Preprints,* **1998**, *43* (2), 335-339.
(13) Hayatsu, R., McBeth, R.L., Scott, R.G., Botto, R.E., and Winans, R.E., *Org. Geochem.,* **1984**, *6*, 463.
(14) Pang, L.S., Vassallo, AM., and Wilson, M.A., *Org. Geochem.*, **1990**, *16* (4-6), 853.
(15) Hatcher, P.G., *Org. Geochem.* **1990,** *16* (4-6), 959.
(16) Hatcher, P.G., Faulon, J-L., Wenzel, K.A., and Cody, G.D., *Energy Fuels,* **1992**, *6*, 813.
(17) Behar, F. and Hatcher, P.G., *Energy Fuels,* **1995**, *9*, 984.
(18) Buchanan, III, A.C., Britt, P.F., and Struss, J.A., *Energy Fuels*, **1997**, *11*, 247.
(19) Freitas, J.C.C., Bonagamba, T.J., and Emmerich, F.G., *Energy Fuels*, **1999,** *13*, 53.
(20) Borisov, P.R., and Stepanov, S.S., *Sci. Reports Moscow State University*, **1936**, *No. 6*, 347 (as reported by A.E. Rea and M. Bebbington in "Annotated Bibliography on Ruthenium, Rhodium, and Iridium as Catalysts," International Nickel Company: New York, 1959).
(21) Holroyd, R., and Peel, D.H.P., U.S. Patent No. 2,411,726, "Catalytic dehydrogenation," **Nov. 26, 1946** ((as reported by A.E. Rea and M. Bebbington in "Annotated Bibliography on Ruthenium, Rhodium, and Iridium as Catalysts," International Nickel Company: New York, 1959).

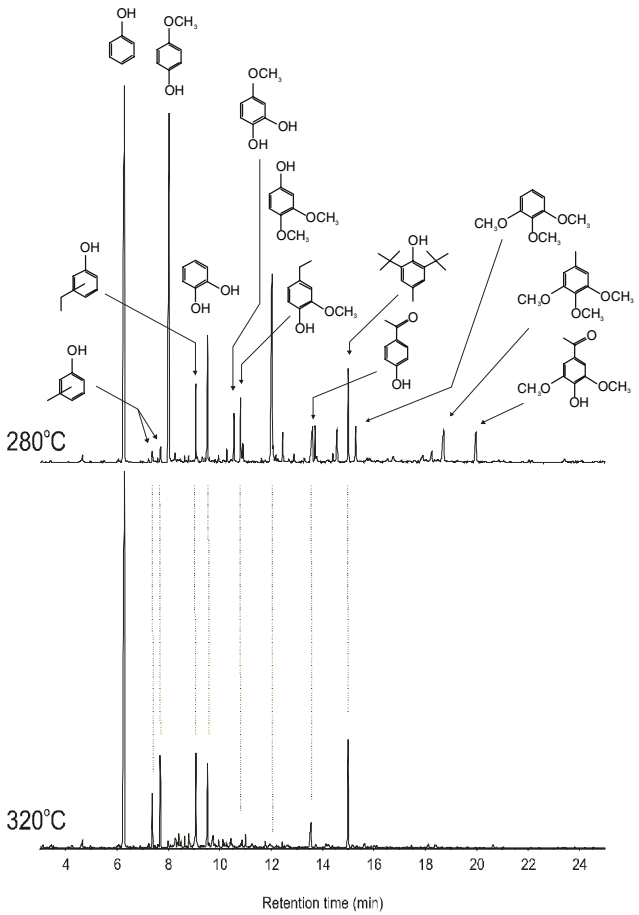

Figure 2: GC-MS spectra of LMW for non-catalytic reactions at 280 and 320°C.

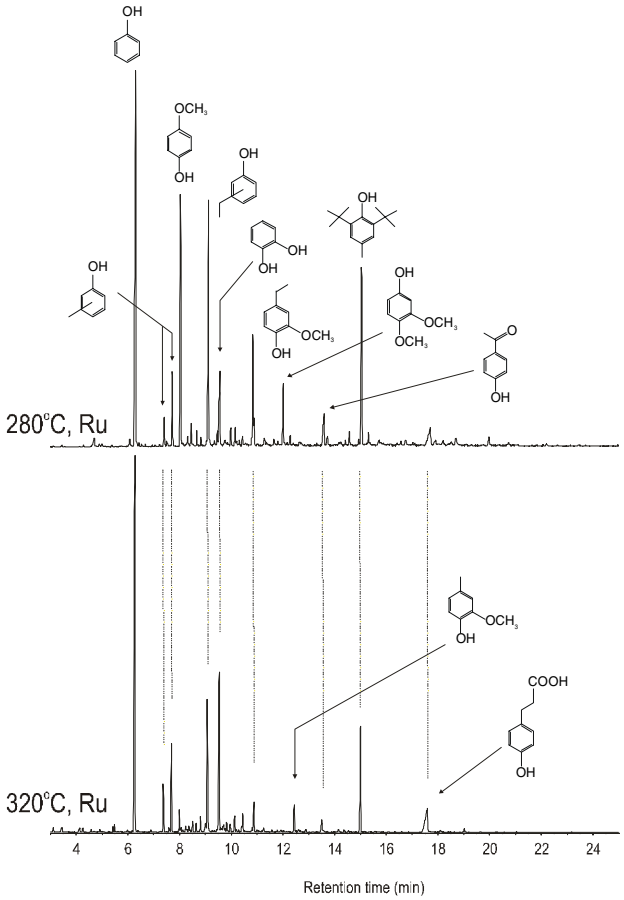

Figure 3: GC-MS spectra of LMW for catalytic reactions at 280 and 320°C.

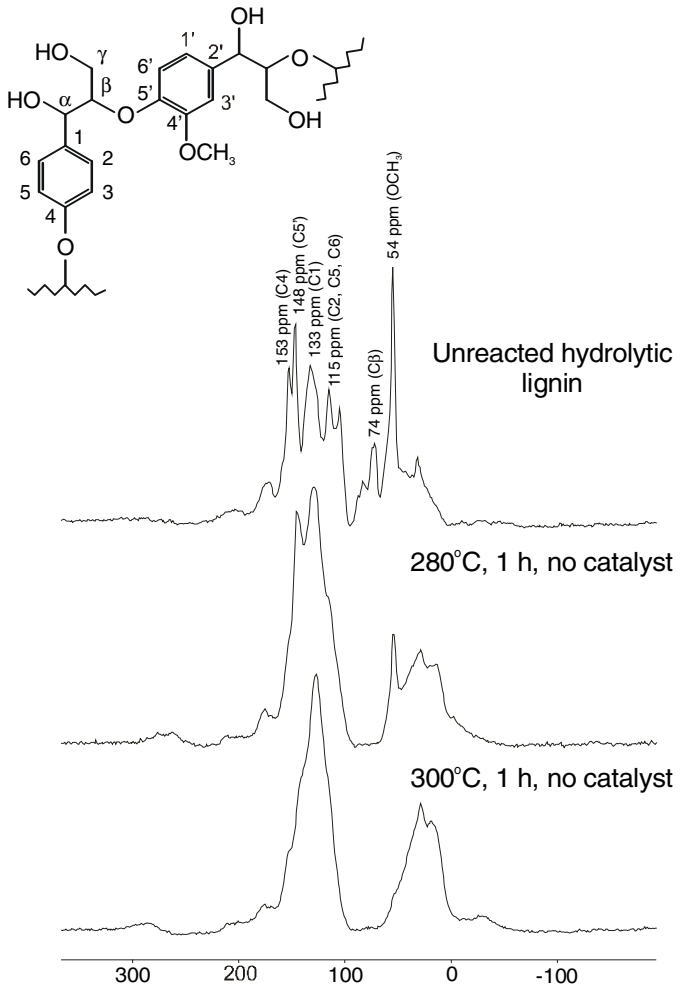

Figure 4: ^{13}C NMR spectra of unreacted lignin and catalytically reacted HMW at 280 and 300°C.

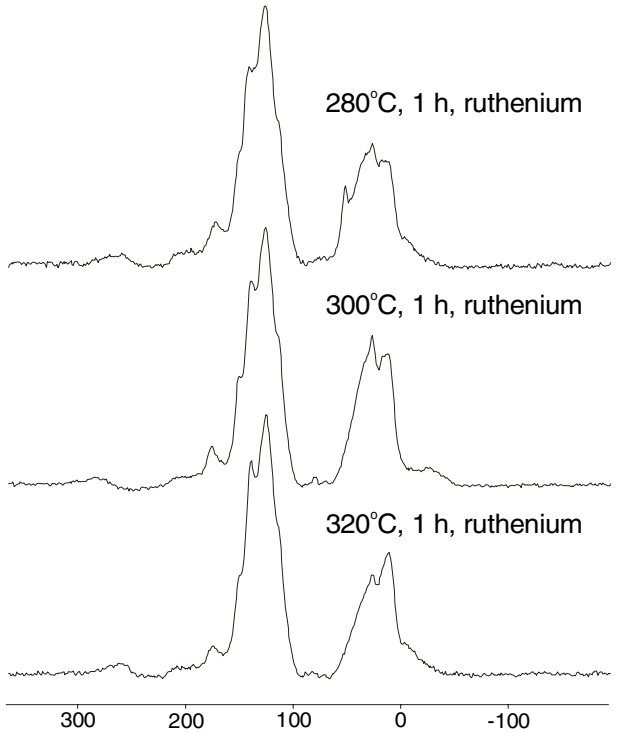

Figure 5: ^{13}C NMR spectra of reacted HMW from catalytic reactions at 280, 300, and 320°C.

CONVERSION OF LIGNIN INTO A HYDROCARBON PRODUCT FOR BLENDING WITH GASOLINE

David K. Johnson [a], Esteban Chornet [a,b], Wlodzimierz Zmierczak [c] and Joseph Shabtai [c]

[a] National Renewable Energy Laboratory, 1617 Cole Blvd., Golden, CO, USA 80401 Fax: 303-384-6363; david_johnson@nrel.gov; [b] University of Sherbrooke, Canada; [c] Department of Chemical and Fuels Engineering, University of Utah, Salt Lake City, UT 84112

Introduction

Lignin is present (15-30 wt%) in all lignocellulosic biomass. Ethanol production from biomass feedstocks will always generate lignin containing residues. Thus, lignin supply will progressively increase as ethanol plants using straw, forest residues, etc., are implemented in the future[1]. Adding value to this residue will significantly enhance the competitiveness of biomass-to-ethanol conversion. Lignin, a cross-linked amorphous phenolic polymer, is the biomass component with highest energy content (9000 - 11000 Btu/lb compared to 7300 - 7500 for cellulose). Lignin can be combusted to provide heat and/or power for the ethanol process, and could provide some excess power to generate additional revenue. Given the molecular nature of lignin it is also conceivable to convert lignin into added value end products, especially fuel components. Previous process development studies in our project have focused on converting lignin to reformulated gasolines and gasoline blending components[2,3].

Lignin-derived products must be compatible with the evolving regulations for transportation fuels. There are specific compositional requirements for gasoline limiting the level of aromatic compounds in gasoline[4]. For Federal Phase II Reformulated Gasoline (RFG), the limits are 1 percent benzene and 25 percent by volume total aromatics. In California, the Phase III RFG specification is an average of 22 percent aromatics or less. For non-RFG gasoline, the aromatic content is limited to the refinery's 1990 baseline level. Gasoline volatility (90% should distill below 167 ^{o}C) and Reid Vapor Pressure (RVP, should be 48-56 kPa) are also important specifications. Octane number ((R+M)/2) determines gasoline fuel grade and ranges from 85 to 93. It is the current goal of this project to convert lignin into a hydrocarbon product compatible with blending in gasoline that has an octane number greater than 110.

The sulfur-in-gasoline rule, issued in December 1999, greatly reduced the amount of sulfur to be allowed in gasoline by 2005. The new regulations for light-duty vehicles greatly reduced the allowable emissions of NO_x, NMOG and particulates. Automakers say these standards can only be achieved if virtually sulfur-free gasoline is available. It is estimated that the required desulfurization of gasoline could reduce aromatics levels in gasoline and create a loss of 0.5 octane numbers. The predicted phase-out of MTBE, an oxygenate and octane enhancer, will exacerbate the nationwide shortage of octane. This may permit introduction of an aromatic octane-blending agent without an increase in permitted aromatics levels. If the lignin-derived octane enhancer has the same octane number as xylene (i.e., 106), then 1.7 percent could be blended to remedy the octane loss without exceeding the original aromatics content of gasoline. On this basis, the potential US market for a lignin-derived octane enhancer could be 142,800 barrels per day or 2.2 billion gallons per year[4].

This project is thus targeted to obtain the necessary scientific and technological data with which to evaluate the economics and markets for converting lignin into valuable fuel components.

The main source of lignin from Biomass-to-Ethanol processes is the high molecular weight lignin remaining in the solid residue after saccharification and fermentation (SSF) of the dilute acid pretreated biomass. The lignin is soluble in aqueous basic solutions, and can be readily separated by solubilization from the protein, unconverted carbohydrate, and other non-lignin materials present in the residue.

The process strategy is to depolymerize the lignin by base catalysis, using moderately high temperatures and short reaction times. To minimize the cost of base recovery only low levels of soluble base are used, just sufficient to dissolve the lignin. The resulting intermediate is a base catalyzed depolymerized (BCD) product that consists of monomeric and oligomeric phenolics. The BCD product is isolated by acidification and then solvent extraction of the raw BCD product. Catalytic hydroprocessing (HPR) is then used to convert the extracted BCD product into a mixture of monomeric aromatic hydrocarbons very similar to components already found in gasoline. HPR utilizes catalysts with hydrodeoxygenation (HDO) and hydrocracking (HCR) activity to remove all remaining oxygen and break the interaromatic C-C linkages.

The target characteristics for the hydrocarbon product are:

Distillation characteristics
- –95% should distill <200 ^{O}C

Chemical composition
- –C + H > 99.5%
- –S content <0.01% (100ppm)
- –Aromatic hydrocarbons > 65%
- –No detectable phenols

Octane value
- –Blending octane number ((R+M)/2) > 110

Reed Vapor Pressure
- -Mandated limits vary
- -Maximum levels range from 7 - 10 psi

A process flow sheet has been constructed for the process of converting lignin into a high-octane hydrocarbon fuel blending component. From this the production cost for the BCD-HPR product has been estimated at $0.60 – 0.75/gallon. This estimate assumed the plant received a fraction of the lignin from a 600 tpd ethanol plant. Performance targets used in the calculations included that 100% of the lignin in the SSF residue could be solubilized to give a feed with an 8% lignin concentration. The cost of base recovery was minimized by limiting the soluble base concentration to 1% or less in the lignin depolymerization step. The overall yield of hydrocarbon product in the gasoline boiling range was assumed to be 70% of the theoretical yield, equivalent to about 50% on a mass basis. Extraction of the depolymerized lignin intermediate assumed that it could be performed with a relatively low cost solvent such as the BCD-HPR product or a process stream found in a petroleum refinery.

The value of high-octane ((R+M)/2 = 110) hydrocarbon fuel blending components has been estimated based on the Annual Energy Outlook projection of $20 – 25 / bbl for crude oil in 2010, and that the value of an octane boosting product is in the range of 0.7 – 1.4 cents per octane gallon[5]. The value of the lignin-derived gasoline blending component should be in the range of $0.97 – 1.14 per gallon based on these assumptions. Thus if performance targets can be met it should be possible to utilize the lignin from a bioethanol plant to enhance the competitiveness of biomass-to-ethanol conversion.

Results and Discussion

Base Catalyzed Depolymerization. Initially, systematic studies on the BCD reaction were performed at the U of U using stirred autoclaves. The effects of reaction time, temperature, and pressure, base type and concentration, and the solvent used, were examined. High yields of depolymerized lignin (60%–80%) were obtained at moderate temperatures and short reaction times.

Table 1. Comparison of Starting Lignin to BCD Products

	Alcell Lignin	LZD-7	LZD-19
Volatiles (by GC)	0%	36% ± 14%	33% ± 13%
Mn	870	470	530
Mw	2400	680	830
^{13}C NMR data (Number of Cs per 6 C_{Ar})			
Aliphatic C	2.9	2.6	2.5
Methoxyls	1.3	0.7	0.3
Methyls	0.6	0.9	0.9
Ar-OH	0.8	1.7	1.6
C=O	0.1	0.4	0.5
Elemental Analysis Data			
C%	66.6	68.8	70.9
H%	5.9	6.5	6.4
O% by difference	27.5	24.5	22.6

Mn = Number-average molecular weight of peracetylated BCD;
Mw = Weight-average molecular weight of peracetylated BCD.

As can be seen from the data in Table 1 the BCD reaction causes the lignin to be partially depolymerized from a mixture of dimers through nonamers into a mixture of monomers through trimers. Chemical analysis indicates that demethoxylation occurs during the BCD reaction, mostly through loss of the methyl group. The largest identifiable component of the BCD products is normally catechol. Analyses also indicate that all oxygen containing functionalities in the lignin side-chain are lost apart from a few that are converted to carbonyls. Figure 1 shows the average reaction chemistry that occurs during a BCD reaction.

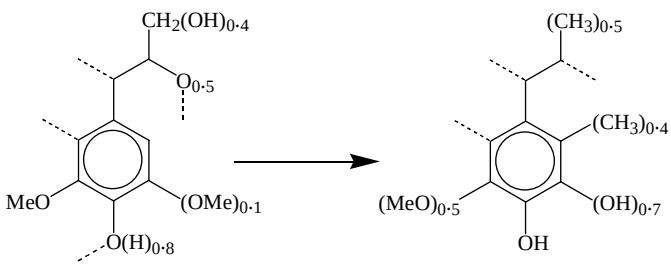

Alcell Lignin
66.8% C 5.9% H 27.0% O
$C_{8.9}H_{6.3}O_{0.7}(CH_3)_{0.6}(OH_{Ph})_{0.8}$
$(OH)_{0.4}(OMe)_{1.1}(CO)_{0.1}$
Repeat Unit MWt. = 182,
Oligomer range 2-mer to 9-mer

Depolymerized Lignin
70% C 6.5% H 23.5% O
$C_{8.2}H_{4.8}(CH_3)_{0.9}(OH_{Ph})_{1.7}$
$(OMe)_{0.5}(CO)_{0.4}$
Repeat Unit MWt. = 170,
Oligomer range1-mer to 3-mer

Figure 1. Average reaction chemistry for BCD reactions performed under aqueous conditions.

The depolymerization reaction has been scaled up into a flow reactor at the U. of Utah capable of processing 100g of lignin per hour.

Hydroprocessing Depolymerized lignin samples have been hydroprocessed at the U. of Utah into products that are predominately mixtures of aromatic and naphthenic hydrocarbons that could be blended with gasoline. Catalysts and reaction conditions are still being optimized so that the product meets all target specifications. Analyses of the BCD-HPR products, performed at NREL (Figure 2), indicate that complete deoxygenation with minimal hydrogenation is not easily attained.

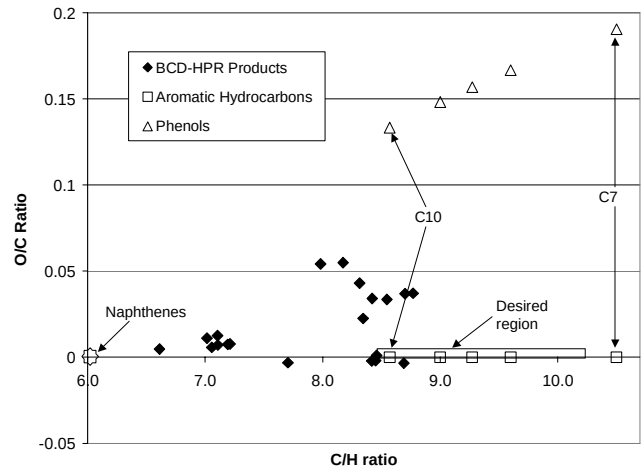

Figure 2. Variation of O/C ratio with C/H ratio for BCD-HPR products made at the U. of Utah.

A flow reactor has been brought into operation at the U. of Utah for production of sufficiently large samples (up to 1L) so that fuel property tests can be performed on lignin-derived hydrocarbon products. Standard tests for distillation (ASTM D86) and vapor pressure (ASTM D5191) have shown that the products are close to meeting these gasoline specifications. Standard tests (ASTM D2700 and D2699) of 10 – 50% blends of HPR-BCD products with unoxygenated gasoline have given blending octane numbers for the products of 82 – 97. Higher values are obtained when hydrogenation is limited, minimizing formation of naphthenes.

Conclusions

A process for converting the lignin in residues from biomass-to-ethanol processes is being developed. Significant progress has been made towards developing a process that has commercial potential. Increased yields, better control of hydroprocessing, and decreasing the cost of base recovery are the most important improvements that still need to be made.

Acknowledgement. We wish to thank the US DOE OTT Office of Fuels Development (Director John Ferrell) for funding this work, and NREL and DOE Ethanol Program managers, Robert Wooley and Gerson Santos-Leon, for their support.

We would also like to thank several of our colleagues at NREL., including Mark Davis and Justin Sluiter for their assistance in performing some of the analyses of the samples, plus Kelly Ibsen, and the Process Engineering group for technoeconomic analyses.

References

[1] Handbook on Bioethanol: Production and Utilization. Wyman, C.E. Ed., Taylor & Francis, Washington, DC: 1996; pp 105-118.
[2] Shabtai, J., Zmierczak, W., and Chornet, E. Proc. 3rd Biomass Conf. of the Americas, Elsevier, 1997, Vol. 2, pp 1037-1040.
[3] Shabtai, J., Zmierczak, W., and Chornet, E. U.S. Patent 5,959,167.
[4] Sinor, J.E. "Review of Market for Octane Enhancers" NREL report (NREL/SR-580-28193), May 2000.
[5] Unzelman, G.H., Natl. Petrol. Ref. Assn. Ann. Mtng., San Fransisco, CA, March 1995.

CATALYST DEVELOPMENT FOR THE CELLULOSE GASIFICATION AND OPTIMIZATION OF THE OPERATION VARIABLES

Mohammad Asadullah, Shin-ichi Ito, Kimio Kunimori, and Keiichi Tomishige

Institute of Materials Science, University of Tsukuba, 1-1-1, Tennodai, Tsukuba-shi, Ibaraki 305-8573, Japan

Introduction

Biomass gasification to synthesis gas is the most promising approach to share renewable energy, compared with its use as a combustion fuel. This is because the synthesis gas can be converted to clean liquid fuels or to many important bulk chemicals such as methanol, acetic acid, dimethyl ether, oxo alchohols, etc.[1, 2] Synthetic diesel and dimethyl ether, which are promising superclean fuels in the future, can be produced with high efficiency from the synthesis gas and contribute significantly to the reduction of the net CO_2 emission into the atmosphere.[3] Furthermore, the use of renewable energy resources, agricultural and forestall biomass, would decrease the petroleum dependence of many countries. However, the biomass gasification remains problematic because of the formation of tar, a complex mixture of aromatics, during the gasification of biomass even if the process is operated at very high temperatures.[4-6] Although the high gasification temperature decreases the tar formation, the process is unsuitable because of high energy consumption, causing high production costs of the synthesis gas. From the economic point of view, the process should be operated at low temperature, which allows a significant savings of energy, resulting the decrease of the production costs. However, the formation of tar and char is more severe at temperatures lower than 1023 K.[7] The use of an efficient catalyst in the gasification reactor can solve the tar and char formation problem by cracking them to gases even at low temperature. However, some reports have demonstrated that the use of nickel based catalyst in the primary reactor unit resulted in rapid deactivation of catalyst because of carbon deposition on catalyst surface.[8] This challenge can be overcome by developing a suitable catalyst, which can completely convert the carbonaceous materials without the formation of any residue. We already have reported such a catalyst (Rh/CeO_2), which is efficient for complete gasification of cellulose at low temperature (823 K).[9] This paper describes the performance of Rh catalysts on various supports, details of operating variables, and the catalyst characterization.

Experimental

Procedure. The general operating system has been described in a previous paper.[9] However, the dependence of operating conditions was investigated here. The amounts of cellulose feedings were varied from 25 to 150 mg in a batch. In each case, 0.5 g of catalyst was used. The total flow rate of air and Ar was varied from 110 to 200 $cm^3\ min^{-1}$ (STP) (W/F = 1 - 1.8 g.h/mol, where W = weight of the catalyst in grams and F = flow rate of the inlet gas in moles per hour) where their ratio was always maintained at 1.2. The reactions were carried out between 723 and 873 K. Temperature difference between outside of the reactor wall and inside of the catalyst bed and also between the bottom of the distributor and the center of the catalyst bed was continuously monitored by thermocouples. Product gases in the sampling gas were calculated as concentration such as, (amount of product gas / total amount in the effluent gas) x 100.

Catalyst. Catalysts used in this process were Rh, Ru, Pt, Pd, and Ni loaded on CeO_2 and Rh loaded on various supports prepared in our laboratory by a conventional impregnation method using an acetone solution of metal acetylacetonate such as $Rh(C_5H_7O_2)_3$, $Ru(C_5H_7O_2)_3$, $Pt(C_5H_7O_2)_2$, $Pd(C_5H_7O_2)_2$, and $Ni(C_5H_7O_2)_2$. All of the acetylacetonate salts with purity higher than 99% were purchased from Soekawa Chemicals. CeO_2 was purchased from Daiichi Kigenso Kagaku. In each case, the solution was added into the CeO_2 powder and stirred properly. Then the mixture was kept undisturbed for an hour. The acetone solvent was then evaporated with stirring at around 323 K, and the catalysts thus prepared were dried at around 393 K overnight. The metal loading for all catalysts was 1.2×10^{-4} mol (g of catalyst)$^{-1}$. In the case of the Rh/CeO_2 catalyst, the catalysts with 0.4×10^{-4}, 0.8×10^{-4}, 1.6×10^{-4}, and 2.5×10^{-4} mol (g of catalyst)$^{-1}$ were also prepared. Granules of the catalysts (60-100 mesh) were obtained by pressing, crushing, and sieving. The catalysts were pretreated before each run at 773 K under the flow of H_2 of 40 $cm^3\ min^{-1}$ for 0.5 h. The Brunaurer-Emmett-Teller (BET) surface areas of fresh (after H_2 treatment) and used Rh/CeO_2 catalysts were determined by a Gemini (Micrometrics).

Results and Discussion

We have previously investigated various types of support materials and supported metal catalysts for cellulose gasification in a batch-feeding and fluidized-bed reactor at 823 K (Table 1).[9] In this paper we also investigated the performance of Rh catalyst on various supports and the results are included in Table 1. In the noncatalytic reaction the C conversion was only 53% which was remarkably increased by the presence of CeO_2, ZrO_2, TiO_2, or MgO support materials on the bed. However, the synthesis gas formation increased only by the presence of CeO_2. Because CeO_2 has shown the performance for cellulose gasification on the basis of the C conversion as well as the formation of synthesis gas, we prepared CeO_2-supported various types of metal catalysts and tested them in the gasification reaction. As shown in Table 1 only Rh/CeO_2 promoted the C conversion as well as the formation of CO and H_2 drastically. Interestingly enough, complete C conversion was achieved when Rh/CeO_2 was used as a catalyst. The loading of Rh on other supports caused lower C conversion and higher methane formation that ultimately decreased the amounts of CO and H_2. The promoting effect of metals supported on CeO_2 is as follows: Rh >> Ru > Pt ≈ Pd > Ni.

It is a fact that the temperature of the catalyst bed greatly affects the cellulose gasification. In this work the influence of temperature on the C conversion and product distribution has been evaluated in the interval of 723-873 K and is shown in Figure 1. As expected, the C conversion increased with increasing reaction temperature, and became 100% at 823 K. At or above this temperature, the product gas analysis revealed that the total C in cellulose converted to gas. At lower temperatures than 823 K, some of the tar and/or char did not take part in either the combustion or the reforming reaction. On the other hand, the gas composition was greatly varied with increasing temperature. The amounts of H_2 and CO increased remarkably, however, the amount of CH_4 increased slightly with increasing temperature. Furthermore, the amount of CO_2 expectedly decreased with increasing temperature.

The variation of the C conversion and product distribution with the cellulose feeding amount in a batch is shown in Figure 2. It can be seen that 100% C conversion was achieved until 50 mg of cellulose was used in a batch. A higher amount of cellulose than 50 mg caused a decrease of C conversion. Although the CO_2 formation slightly increased when 150 mg of cellulose was used, the formation of CO and H_2 decreased.

Table 1. Effects of Various Supports and Supported Metal Catalysts on the Gasification of Cellulose [a]

Catalyst	Yield of gases /μmol				H_2/CO	C to gas wt%
	CO	H_2	CO_2	CH_4		
None	160	90	790	30	0.6	53
CeO_2	330	630	860	120	1.9	71
MgO	260	430	960	60	1.7	70
TiO_2	240	560	1040	40	2.3	71
ZrO_2	180	490	1020	110	2.7	71
Al_2O_3	200	480	720	60	2.4	53
SiO_2	220	230	680	60	1.0	52
Rh/CeO_2	670	1290	1060	120	1.9	100
Ru/CeO_2	490	1010	1050	130	2.1	91
Pd/CeO_2	360	830	1180	70	2.3	87
Pt/CeO_2	360	850	1080	120	2.3	85
Ni/CeO_2	280	740	1150	50	2.6	80
G-91[b]	450	760	990	180	1.7	87
Rh/CeO_2[c]	370	920	1160	300	2.5	100
Rh/ZrO_2	450	680	1150	250	1.5	98
Rh/Al_2O_3	340	660	1210	260	1.9	98
Rh/TiO_2	220	800	960	370	3.6	84
Rh/MgO	360	820	1010	170	2.3	83
Rh/SiO_2	400	720	698	160	1.8	68

[a]50 mg cellulose (C, 1850 μmol; H_2, 1543 μmol and O_2, 772 μmol). [b]Commercial steam reforming catalyst: Ni, 14%; Al_2O_3, 65-70%; CaO, 10-14% and K_2O, 1.4-1.8%. [c]Catalyst was placed in a secondary bed.

Table 2. Effect of W/F on the Carbon Conversion and Product Distribution [a]

W/F gh mol^{-1}	O_2 supply within 50 s/μmol	Yield of gases /μmol				C to gas %
		CO	H_2	CO_2	CH_4	
1	696	1534	2930	2523	268	78
1.2	578	1595	3101	2605	304	81
1.4	496	1398	2880	2534	204	75
1.8	409	1044	2226	2149	154	61

[a] Cellulose 150 mg (C, 5555 μmol; H_2, 4629 μmol and O, 4629 μmol).

The influence of *W/F* on the C conversion and product distribution has been studied at 823 K using 150 mg of cellulose, and the results are summarized in Table 2. An increase of *W/F* caused the variation of two factors in this system: an increase of the residence time and a decrease of oxygen supply. The highest C conversion (81%) and product yield were achieved in the case of *W/F* = 1.2 g.h mol^{-1}.

Figure 3 shows the performance of the Rh/CeO_2 catalyst with various loading amounts for the gasification of 50 mg of cellulose in a batch at 823 K. The C conversion and synthesis gas yield dramatically increased with an increase in the loading amount and reached 100% C conversion when the Rh loading of 1.2 x 10^{-4} mol (g of catalyst)$^{-1}$ was used. However, it is contrary to the fact that the higher loading amount of Rh than 1.2 x 10^{-4} mol (g of catalyst)$^{-1}$ decreased the C conversion. On the other hand, the formation of CH_4 increased with an increasing in the Rh loading, which ultimately decreased the yield of synthesis gas. Ceria alone also gave the higher amount of methane. Actually, ceria is an effective catalyst for CO hydrogenation giving mainly C_1-C_5 hydrocarbons.[10,11] In fact Ce^{3+}, which is generated under reducing atmosphere has been recognized as an active site for CO hydrogenation reaction.[12]

Table 3. BET surface area of Rh/CeO_2 catalyst

No. of batch reaction	BET surface area/ m^2 g^{-1}
0	59
1	24
5	24
10	23
20	21

Table 3 shows the BET surface area of Rh/CeO_2 of both fresh and used catalysts. This value was 59 m^2 g^{-1} before reaction, however, it was decreased drastically to 24 m^2g^{-1} during the first batch of cellulose gasification reaction. However, fortunately the decreasing trend of surface area was very slow and it was almost constant in successive reactions. The catalytic activity did not change significantly even after 20 times of batch feeding of cellulose.

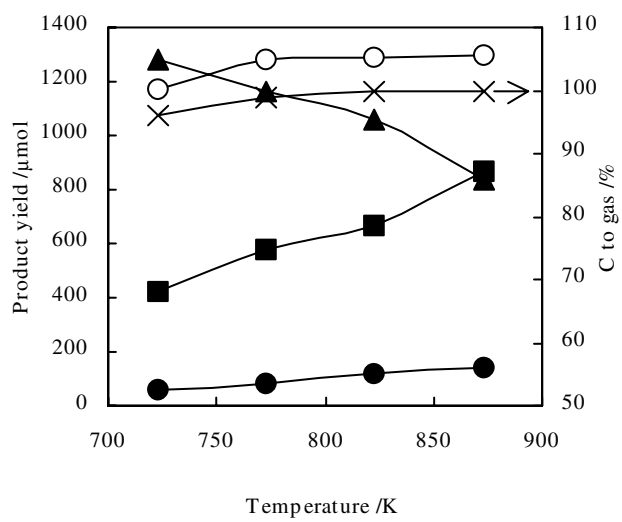

Figure 1. Effect of temperature on the Rh/CeO_2 (0.5 g) catalyzed gasification of cellulose (50 mg; C, 1850 μmol; H_2, 1543 μmol and O_2, 772 μmol) with air (60 cm^3 min^{-1}). ■ : CO, O: H_2, ●: CH_4, ▲: CO_2 and X : C-conversion.

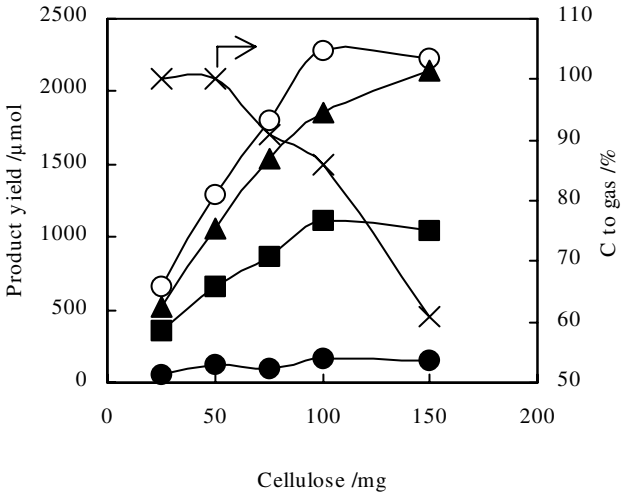

Figure 2. Effect of cellulose feeding amount in a batch on the C conversion and product distribution at 823 K. ■ : CO, O: H_2, ●: CH_4, ▲: CO_2 and X, C conversion.

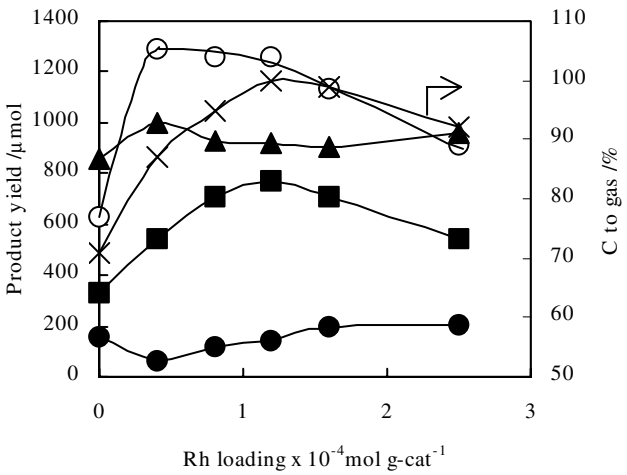

Figure 3. Effect of the amount of metal loading on the C-conversion and product distribution. ■ : CO, O: H_2, ●: CH_4, ▲: CO_2 and X : C-conversion.

Conclusions

Rh supported on CeO_2 only exhibited multifunction in this reaction such as increasing the C conversion as well as CO and H_2 formation. On the other hand, the formation of methane was inhibited on the catalyst. Total carbon conversion was achieved at temperatures above 823 K when up to 50 mg cellulose was used in a batch on Rh/CeO_2 catalyst of Rh loading 1.2 x 10^{-4} mol (g of catalyst)$^{-1}$. Although the surface area decreased suddenly in the first reaction, it was almost constant in the successive reactions and the reactivity remained constant.

Acknowledgement

This research was supported by the Future Program of Japan Society for the Promotion of Sciences under the Project "Synthesis of Ecological High Quality of Transportation Fuels" (JSPS-RFTF98P01001).

References

1. Tanaka, Y.; Yamaguchi, T.; Yamasaki, K.; Ueno, A.; Kotera, Y. *Ind. Eng. Chem. Res.* **1984**, *23*, 225.
2. Beaker, E. G.; Mitchell, D. H.; Mudge, L. K.; Brown, M. D. *Energy Progress* **1983**, *3*, 226.
3. Shikada, T.; Ohno, Y.; Ono, M.; Mizuguchi, M.; Tomura, K.; Fujimoto, K, *Stud. Surf. Sci. Catal.* **1998**, *119*, 515.
4. Caballero, M. A.; Corella, J.; Aznar, M. P.; Gil, J. *Ind. Eng. Chem. Res.* **2000**, *39*, 1143.
5. Miccio, F; Moersch,O; Spliethoff, H; Hein, K.R.G. *Fuel* **1999**, *78,* 1473.
6. Brage, C.; Yu, Q.; Chen, G.; SjOstrom, K. *Biomass Bioenergy* **2000**, *18*, 87.
7. Bangala, D. N.; Abatzoglou, N.; Martin, J.-P.; Chornet, E. *Ind. Eng. Chem. Res.* **1997**, *36*, 4184.
8. Baker, E. G.; Mudge, L. K.; Brown, M. D. *Ind. Eng. Chem. Res.* **1987**, *26*, 1335.
9. Asadullah, M.; Tomishige, K.; Fujimoto, K. *Catal. Commun.* **2001**, *2*, 63.
10. Maruya, K.; Inaba, A.; Maehashi, T.; Domen, K.; Onishi, T. *J. Chem. Soc., Chem. Commun.* **1985**, 487.
11. Arai, T.; Maruya, K.; Domen, K.; Onishi, T. *Bull. Chem. Soc. Jpn.* **1989**, *62*, 349.
12. Arai, T.; Maruya, K.; Domen, K.; Onishi, T. *J. Catal.* **1993**, *141*, 533.

EXHAUST EMISSIONS FROM A SI ENGINE FUELED WITH PYROLYSIS GAS

M. Ratcliff, C. Baca-Overly, S. Deutch, C. Feik, J. Graham and S. Phillips*

National Renewable Energy Laboratory, 1617 Cole Blvd, Golden, Colorado, USA 80401
Fax: 303-384-6363; matthew_ratcliff@nrel.gov

Introduction

A 4-cylinder, 4-stroke, spark ignition (SI) engine of 2.5L displacement and 9.4 compression ratio was operated for over 100 hours on wood-derived pyrolysis gas to measure exhaust emissions and performance characteristics. The pyrolysis gas (15-16.5 MJ/Nm^3) was produced from mixed hardwood and softwood pellets, in NREL's Thermochemical Process Development Unit (TCPDU) using a two-step, indirect gasification process [1]. A typical fuel gas composition is shown in Table 1. In addition, light gasifier "tar" that escaped the pyrolysis gas clean-up train was consumed as fuel. These "tar" components were principally benzene (~1 vol. %) and smaller amounts of toluene, naphthalene and related aromatics.

Table 1. Pyrolysis Gas Composition from TCPDU in Volume %

H_2	CO	CH_4	C_2H_4	C_2H_2	C_2H_6	CO_2	N_2
17.9	34.9	15.8	4.7	1.0	0.5	17.3	6.0

The manufacturer's rated output for the engine-generator on natural gas (~37 MJ/Nm^3) was 17 kW. The engine-generator also achieved 17 kW on pyrolysis gas, albeit with slightly less stable performance. This is in contrast to spark ignition engines fueled with producer gas (5.5-7.0 MJ/Nm^3), which typically must be derated 30-40% compared to natural gas [2]. At loads # 13 kW, the genset's performance on pyrolysis gas was as good or better than natural gas, as measured by the ability to maintain 60 ∀ 0.3 Hz.

Results and Discussion

The regulated exhaust emissions from both natural and pyrolysis gas are compared in Figure 1, as a function of Lambda (λ = actual Air/Fuel) stoichiometric Air/Fuel) at a load of 13 kW and ignition timing of 30° Before Top Dead Center (BTDC). NOx from natural gas peaked (44.3 lb/MWh) at λ = 1.10, then decreased with leaner air/fuel mixtures. The lean operating limit for natural gas (i.e. for a generator frequency = 60 ∀ 0.3 Hz) was λ = 1.18. At this setting, the CO and total hydrocarbon (THC) exhaust emissions were similar to those from pyrolysis gas. However, the NOx emitted from natural gas was 29.2 lb/MWh, in contrast to ∃82 lb/MWh from pyrolysis gas. There are three possible explanations for this large, fuel dependent, difference in NOx. Fuel-bound nitrogen in the wood, which produces NOx upon combustion, contributes to the total. However, given that the nitrogen content in the wood pellet feedstock was < 0.03 wt %, this can not explain a significant amount. Thermal NOx enhancement, due to higher localized flame temperatures within the combustion chambers, is another contributing mechanism. This hypothesis may be supported by the exhaust port temperature data. For the comparison in Figure 1, the average exhaust port temperature from natural gas at λ = 1.18 was 588°C; while the average was 592°C from pyrolysis gas at λ = 1.22. The slightly higher average exhaust port temperature was measured despite the presence of ~17% CO_2 in the pyrolysis gas. The CO_2 would be expected to reduce the combustion and exhaust temperatures relative to natural gas, due to its high heat capacity. This is the key mechanism by which exhaust gas recirculation (EGR) affects NOx reductions in reciprocating internal combustion engines [3]. Finally, the prompt NOx mechanism may be the principal explanation for the higher NOx emissions from pyrolysis gas, due to the presence of ethylene and acetylene in the fuel, typically 5% and 1%, respectively. The prompt NOx chemistry depends on the presence of CH radicals, which may arise in significant amounts from cleavage reactions of unsaturated hydrocarbons [4].

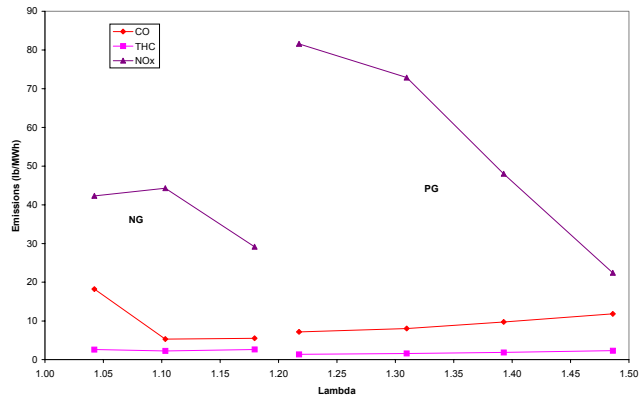

Figure 1. Regulated exhaust emissions from natural gas (NG) and pyrolysis gas (PG) at a load of 13 kW and ignition timing of 30° BTDC.

Figure 1 also shows that λ could be increased with pyrolysis gas to a lean operability limit of 1.49 (generator frequency = 60 ∀ 0.3 Hz), resulting in a NOx emission of 22.4 lb/MWh. At this condition, the averaged exhaust port temperature was 541°C, or 50°C lower than at λ = 1.22. Both CO and THC emissions from pyrolysis gas began to increase with increasing λ. This trend was expected, because unburned-fuel emissions increase as combustion temperatures decrease, or the engine enters lean-misfire conditions [5]. Because carbon monoxide is a major fuel component in pyrolysis gas, and CO oxidation kinetics are relatively slow, much of the CO in the exhaust should be considered to be unburned fuel.

In order to reduce NOx emissions, the limits of lean-burn operation and ignition timing were explored. Figure 2 shows NOx versus load curves from pyrolysis gas and natural gas. The top pyrolysis gas curve is from λ = 1.30, and 24° BTDC. Up to approximately 9 kW, the pyrolysis gas NOx emissions from this setting were very similar to the best natural gas results (λ = 1.03, 24° BTDC). At higher loads there was an increase in NOx compared to natural gas, despite the much leaner air-fuel mixture. The next lower pyrolysis gas curve in Figure 2 was obtained by optimizing the air-fuel ratio and ignition timing for each load tested. These data show that reducing NOx from pyrolysis gas combustion was most effectively done by lean operation, even when the ignition timing had to be advanced to maintain stable engine operation. The broad air flammability limits of pyrolysis gas are due to the presence of hydrogen in the fuel, as well as the relatively low concentration of nitrogen (compared to producer-gas). By exploiting this quality with lean-burn operation, we were able to achieve significantly lower, part-load NOx emissions using pyrolysis gas. Nevertheless, it appears that some form of exhaust after-treatment will be necessary

for both pyrolysis and natural gas fueled, spark ignition engine-generator systems, in order to achieve some existing and proposed NOx standards [6]. The "Lean-NOx" catalysts being developed for diesel engines may be ideal for pyrolysis gas, in order to achieve NOx standards and maintain high energy efficiency. However, those catalytic converters are not commercially available. Therefore, stoichiometric operation with conventional 3-way catalysts is the best approach.

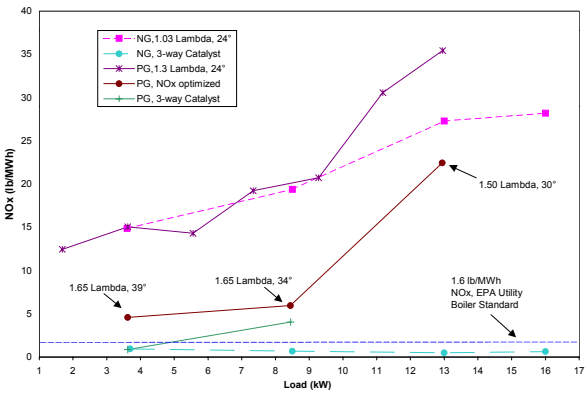

Figure 2. NOx emissions from pyrolysis gas and natural gas as a function of load, Lambda, ignition timing and 3-way exhaust catalyst.

At the bottom of Figure 2 is a two-point NOx line from pyrolysis gas fueled operation with a 3-way catalyst. Difficulties maintaining stoichiometric operation prevented collection of quality data, especially at higher loads. This was principally due to a lack of feedback air-fuel ratio control. The data presented suggest that NOx levels similar to those from natural gas with the 3-way catalyst (also shown in Figure 2) are possible using this strategy. A larger catalytic converter would perhaps be necessary, because of the higher raw NOx emissions from pyrolysis gas during stoichiometric operation. In either fuel case, a larger 3-way catalyst, or additional engine NOx control, such as EGR, would be required to meet present and future NOx standards for states such as Texas (0.14 lb/MWh in east Texas after January 1, 2005) [6].

At a given λ, NOx from pyrolysis gas fueling was higher than from natural gas. However, because the of the ability to operate the engine at higher air/fuel ratios on pyrolysis gas at comparable outputs, the differences in NOx emissions between the two fuels can be negligible. Regardless, the lowest measured NOx value at a load of 9 kW is still an order of magnitude higher than proposed U.S. emissions standards for small generators. Further reductions in NOx emissions from SI engines will have to come from enhanced lean-burn performance and/or addition of exhaust after-treatment technologies. Alternatively, engines could run stoichiometrically with feedback control and a 3-way exhaust catalyst, as developed by the automotive industry.

References

1) Ratcliff, M. A.; et. al. *Biosyngas Characterization Tests*, NREL/TP-510-31224. **1998**.
2) Shashikantha, Parikh, P. P. *Spark Ignition Producer Gas Engine and Dedicated Compressed Natural Gas Engine Technology Development and Experimental Performance Optimization*. SAE 1999-01-3515, **1999**.
3) Tomazic, D. *A Primer on Exhaust Gas Recirculation*. Diesel Progress. **October 2001**, 26-30.
4) Miller, J. A.; Bowman, C. T. *Prog. Energy Combust.* Sci. **1989**, *15*, 287-338.
5) Abdel-Rahman, A.A. *Int. J. Energy Res.* **1998**, *22*, 483-513.
6) *Air Quality Standard Permit for Electric Generating Units*. Air Permits Division, Office of Permitting, Registration & Remediation. Texas Natural Resource Conservation Commission. **2001**.

Substituent Effects in the Pyrolysis of Lignin Model Compounds

Michelle K. Kidder, Phillip F. Britt, and A. C. Buchanan, III

Chemical Sciences Division
Oak Ridge National Laboratory
P.O. Box 2008, MS-6197
Oak Ridge, Tennessee 37831-6197

Introduction

Lignin is the second most abundant natural biopolymer found in vascular plants and a potential source for renewable chemicals and fuel. Lignin is also a byproduct from pulping processes in paper mills, and over 975 million solid tons of lignosulfonate are produced each year.[1] However, lignin is underutilized because the decomposition of the polymeric structure yields crude mixtures of products and bio-oils that are highly oxygenated and typically need to be upgraded before it can be used. As a consequence of the poor quality of the bio-oils, a large fraction of lignin is burned. Thus, more control is needed over the depolymerization of this complex heterogeneous polymer into higher valued products, Our goal is to provide a better understanding of the chemical reactions that occur during the thermal processing of lignin, to control the product selectivities and yields.

The dominant backbone unit of the lignin structure is the β-O-4 linkage (47-60%). The simplest model of the β-O-4 linkage is phenethyl phenyl ether (PPE). Recently, our group studied the decomposition of PPE, in the gas and liquid phases, to clarify the primary reaction pathways.[2] This study resolved that PPE decomposed by a free radical chain pathway rather than a concerted retro-ene reaction[3] that was previously proposed. The free radical chain pathway also explained the formation of two previously unreported primary products, toluene and benzaldehyde, which were formed in a 1:1 ratio and accounted for 25% of the product mixture. These products were formed by hydrogen abstraction at the β-carbon, followed by 1, 2-O, C-phenyl shift and β-scission as shown in Figure 1.

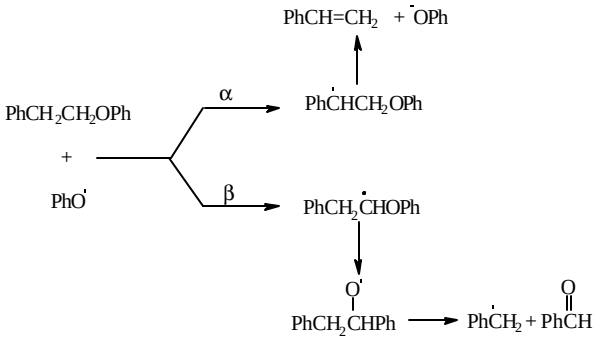

Figure 1. Hydrogen abstraction reactions in the free radical decomposition of PPE.

To determine if this free radical chain pathway occurs for substituted PPE's, a systematic study of the impact of substituents on the thermal decomposition of lignin model compounds was initiated. As a consequence of the complexity of the reaction mixtures and the reactivity of the products, the thermolysis was studied in the liquid phase with biphenyl as a solvent to minimize secondary reactions of the primary products. This study will focus on the impact of substituents on the rate of decomposition and selectivity of hydrogen abstraction at the α and β-positions, which is determined by the ratio of products formed from the subsequent reactions (see Figure 1).

Unfortunately, a substituent can affect many steps in a reaction. For example, an *o*-methoxy substituent is predicted to weaken the β-O-4 linkage (hence accelerate the rate of decomposition), alter the selectivity of hydrogen abstraction at the α and β-position (which will alter the product distribution) and alter the rate of 1, 2-O, C-phenyl shift. Thus, a systematic study of the impact of substituents on the rate of decomposition and product selectivity is needed to unravel the substituent effect on the reaction steps. This investigation will focus on oxygen containing substituents and the compounds to be studied are shown in Figure 2.

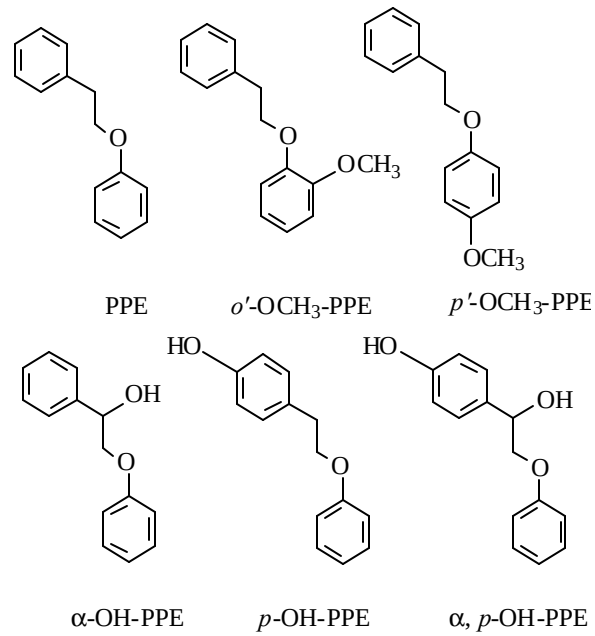

Figure 2. Substituted PPE compounds investigated.

Experimental

Materials. Standards were purified to > 99.9% by GC analysis. Biphenyl was purified by recrystallization from ethanol. Cumene is purified by fractional distillation and 2, 5-dimethylphenol was recrystallized from ethanol. Benzyl phenyl ether (Aldrich) did not require further purification.

The synthesis and purification of PPE (99.9% pure by GC),[2] α-OH-PPE (99.9%),[4] *o'*-OCH_3-PPE (99.6%),[5] *p*-OH-PPE (99.9%),[6] has been previously reported. The procedure for the synthesis of *p'*-OCH_3-PPE (99.9%) was similar to *o'*-OCH_3-PPE, except that *p*-methoxyphenol was used rather than guaiacol. The procedure for the synthesis of α, *p*-OH-PPE (99.4%) was similar to that for α-OH-PPE, except a benzyl protected *p*-hydroxyacetophenone was used as the starting material.

Thermolysis procedure. Pyrex tubes with an internal volume of ca. 3.1 mL were washed with detergent then rinsed extensively with distilled water, acetone, CH_2Cl_2, and ethanol and dried in an oven at 120 °C. The tubes are cooled under argon and loaded with the ca. 30.0 mg of the substituted ether and diluted 8-fold with biphenyl. The tubes were connected to a high vacuum line via Swagelok fittings with Teflon ferrules, degassed by a minimum of three freeze-pump-thaw cycles and sealed at < 2.5 x 10^{-5} Torr. The tubes were placed into a boat (2.54 cm x 35.6 cm) beside a RTD thermocouple, and slid into the center of a Carbolite three-zone furnace (45 cm x 3.8 cm i.d.) where the temperature was maintained within ±1ºC of the setpoint. Sample heat up times were ca. 3 minutes.

At the end of the reaction time, the tubes were removed from the oven, cooled to room temperature and frozen in liquid nitrogen. The tubes were opened and the samples dissolved in the minimum amount of high purity acetone (EM Scientific, Omni Solve, typically 200 μL),

and the standards (cumene, dimethylphenol and benzyl phenyl ether) were added in acetone.

Analytical Methods. Product analysis was performed on a Hewlett-Packard 5890 Series II gas chromatograph equipped with a flame ionization detector, and the identification of products was confirmed by comparison of retention times and mass spectral fragmentation patterns with authentic samples using a Hewlett-Packard 5972A/5890 Series II GC-MS (EI 70 eV). Both instruments were equipped with a J&W DB-5 5% diphenyl- 95% dimethylpolysiloxane capillary column (30 m x 0.25 mm i.d. with 0.25 μm film thickness). The injector temperature was 280 ºC, and the detector temperature was 305 ºC. The oven was programmed with an initial temperature of 45 ºC, and the temperature was ramped to 300 ºC at 10 ºC/ min and held for 20 minutes. The carrier gas, helium, was set at a constant flow rate of 1.0 mL/min.

Samples were injected four times onto the GC using a HP 7673 autosampler. The products were quantitated, and the data was averaged using the GC-FID output relative to the internal standards. Typical shot to shot reproducibility was ±2%. Response factors were measured with authentic samples or estimated from measured response factors for structurally related compounds and based on carbon number relative to the internal standards. Reaction mixtures were also silylated to the trimethysilyl ether derivatives with *N,O*-bis(trimethylsilyl)trifluoroacetamide in pyridine (1:2) to determine if the products contained an alcohol functional group. Conversion calculations were based on the recovered products and the charge of the substituted PPE. The rate of reaction was calculated from the conversion over the corrected reaction time.

Results and Discussion

Thermolysis of the substituted PPE model compounds was run at 345 °C diluted in biphenyl (8-fold) and the reaction time was varied to keep the conversion low (<10%) so the primary products could be observed. Products from the reactions were consistent with the free radical chain mechanism proposed for PPE (see Figure 1). The selectivity for products formed from hydrogen abstraction at the α- and β- carbons is referred to as α/β selectivity. The selectivity is calculated from the products containing (C_6 + C_8 fragments)/C_7 fragments for the PPE backbone. By the reaction stoichiometry, the ratio of the number of moles of C_6 fragment (analogous to PhOH in PPE), to the C_8 fragment (analogous to $PhCH{=}CH_2$ in PPE and products derived from $PhCH{=}CH_2$) and the C_{7Tol} to C_{7ald} (analogous to $PhCH_3$ and PhCHO respectively) should be unity if all the primary and secondary products are taken into consideration. The C_6/C_8 and the C_{7Tol}/C_{7Ald} balances for the liquid phase runs and their mass balances will be discussed on an individual basis for the substituted PPE's.

All runs were made in duplicate, and their rates, selectivities and product distributions were in excellent agreement (±10%, unless otherwise noted) between the runs. For PPE, the mass balance was 99.7%, and the fragment balances were 1.02 ± 0.05 and 1.01 ± 0.01 (C_6/C_8 and C_{7Tol}/C_{7Ald} respectively). The α/β selectivity for PPE at 345 °C is was found to be 3.9 when diluted in biphenyl (Table 1), but only 2.9 as neat solution.[2] This indicates that there is a slight concentration dependence to the product selectivity which is surprising since no concentration dependence was observed at 375 °C.[2]

Table 1. Reaction Rates and Product Selectivity from the Thermolysis of Substituted PPE's at 345 °C in Biphenyl

Compound	% Conversion	Rate (%/h)	a / b
PPE	3.8	1.7	3.9
o'-OCH_3-PPE	3.6	8.5	4.6
p'-OCH_3-PPE	4.6	10.7	3.0
α-OH-PPE	1.9	2.0	3.4
p-OH-PPE	2.1	10.4	5.0
a, p-OH-PPE	-*	-*	-*

-* Fragment balances were not close to unity, see text. %Conversion based on reaction products and starting charge of material. Rate based on %conversion over the corrected reaction time (see experimental).

***o'*-OCH_3-PPE.** The pyrolysis of the *o'*-OCH_3-PPE produced products consistent with the proposed free radical pathway described for PPE. The major products include styrene and guaiacol in a 1:1 ratio, and less than 10 mol % each of toluene, ethyl benzene, anisole, phenol, and *o*-anisaldehyde. The mass balance was 95.3% at 3.6% conversion. The reaction rate increased 5-fold for *o'*-OCH_3-PPE compared to PPE. It has been reported that the *o*-methoxy substituent weakens the C-O bond by ca. 4 *k*cal mol[7] so a rate enhancement was expected. In the FVP of *o'*-OCH_3-PPE (where only unimolecular reactions can occur), the *o*-methoxy substituent enhanced the rate of decomposition by 4-fold compared to PPE.[5]

The α/β selectivity increased 20 % for *o'*-OCH_3-PPE compared to PPE. This increase in selectivity could be a consequence of a reduction in the hydrogen abstraction rate constant for hydrogen abstraction at the β-carbon or a reduced rate constant for the 1,2-O, C-phenyl shift (so that bimolecular hydrogen transfer between the α and β-carbons competes) because of steric or electronic effects. In the neophyl rearrangement, electron donating substituents were found to decrease the rate of rearrangement while electron withdrawing substituents increased the rate of rearrangement.[8] Thus, the *o'*-methoxy substituent is expected to reduce the rate of the 1,2-phenyl shift. To investigate the potential role of steric effects in the reaction, the *p'*-methoxy substituted PPE was studied since this substituent should have similar electronic properties but different steric interactions.

***p'*-OCH_3-PPE.** Products from the pyrolysis of the *p'*-OCH_3-PPE were analogous to those proposed from the free radical pathway. The major products were styrene and 4-methoxyphenol produced in a 1:1 ratio, analogous to *o'*-OCH_3-PPE. The mass balance was 97.9 % for a conversion of 4.6%. The reaction rate increased 6.3-fold compared to PPE (and 1.3-fold compared to *o'*-OCH_3-PPE).

The α/β selectivity for *p'*-OCH3PPE was 35 % smaller than that found for *o'*-OCH_3-PPE. This indicates that the *o'*-methoxy substituent does impose steric constraints on the reaction. The methoxy-substituent also appears to enhance hydrogen abstraction at the β-carbon.

***a*-OH-PPE.** Acetophenone and phenol were the dominant products formed (25.5 and 39.6 mol % respectively) in the thermolysis of α-OH-PPE. Benzene, toluene styrene, benzaldehyde, phenol, benzyl alcohol, phenylacetaldehyde, and dehydrated α-OH-PPE were formed in smaller amounts (0.80-7.0 mol %). The mass balance was 95.7% at a conversion of 1.9 %. It is seen from Table 1, that the selectivity of α-OH-PPE is only 13% smaller than PPE, and the reaction rate only 1.2x larger than PPE, indicating that the α-hydroxy substituent has little impact on the reaction selectivity.

To account for the additional products found in the reaction mixture, there are two possible phenyl shifts that cam follow hydrogen abstraction at the β-carbon. If the aryl ring connected to the oxygen shifts, then the products of the β-scission are benzaldehyde and the α-hydroxybenzyl radical (Figure 3a). The α-hydroxybenzyl radical can either abstract hydrogen from the starting material (which is the most likely source of hydrogen at low conversions) to give benzyl alcohol, or it may lose a hydrogen atom to give benzaldehyde. If the other aryl ring shifts, i.e., 1,2 phenyl shift, the phenoxy radical and the tautomer of phenylacetaldehyde are formed following β-scission (Figure 3b). All of these compounds were detected in the reaction mixture. Again this is difficult to predict without further exploration for the decomposition of the α-hydroxybenzyl radical.

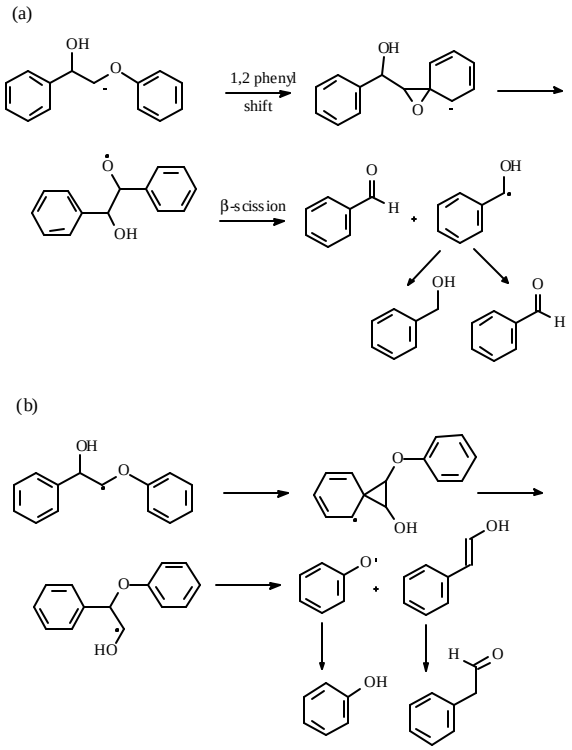

Figure 3. Possible pathways following β-hydrogen abstraction.

***p*-OH-PPE.** Products from the pyrolysis of *p*-OH-PPE are analogous to those that follow the free radical pathway. Phenol and *p*-vinylphenol make up the largest fraction of the product mixture, 41.4 mol % and 37.2 mol % respectively, from the hydrogen abstraction at the α-carbon. Benzaldehyde and *p*-cresol (8.3 mol% and 7.3 mol% respectively), which are formed from the β-hydrogen abstraction, followed by the 1,2-O, C-phenyl shift and β-scission, were formed in ca. a 1:1 ratio. However, the *p*-OH-PPE had a low, and slightly irreproducible mass balance of 88.5% at a conversion of 2.1%. The fragment balances showed reasonable agreement with a C_6/C_8 value of 1.07 ± 0.05, and C_7/C_7 value of 1.14 ± 0.0. The rate was enhanced by 5.8x, but the selectivity was only enhanced by 1.3x for *p*-OH-PPE compared to that of PPE. The increase in reaction rate may be attributed to participation of the *p*-hydroxy group in the hydrogen abstraction reactions, however no new products are seen. This is under additional investigation.

***a*, *p*-OH-PPE.** The pyrolysis of the α,*p*-OH-PPE left many unanswered questions. This compound was completely consumed in 15 minutes at 345 °C. The mass balance was ca. 60.8 %, and the fragment balances were poor, which indicate that many of the primary products undergo secondary reactions. One problem is the reactivity of the hydroxybenzyl alcohol, which is a potential product in the reaction but was not observed. A preliminary investigation of the reactivity of hydroxy and methoxy substituted benzyl alcohols at 345 °C, indicates that these compounds are not stable under the reaction conditions and undergo ionic and free radical reactions.

Conclusions

In general, the free radical chain mechanism proposed for PPE explains most of the pyrolysis products formed from the substituted PPE's. The rate of reaction increases if the substituent can stabilize the radicals formed from the C-O homolysis (such as a methoxy group), or if the substituent increases the rate constant for hydrogen abstraction. A subtle balance between rates for competitive hydrogen abstraction, 1,2-phenyl shift, and β-scission steps controls the product selectivities. Unfortunately, the rate constants for hydrogen abstraction by phenoxy or substituted phenoxy radical from hydrocarbons are not known, and as a consequence of polar effects in the hydrogen abstraction reaction, they cannot be reliably estimated by standard thermochemical kinetic techniques. Similarly, rate constants for the O, C-phenyl shift are not known. To predict the decomposition of the oxygenated materials, the rate constants for these processes are needed. Future studies include the study of the fast pyrolysis of the lignin model compounds by atmospheric pressure flow pyrolysis with on-line monitoring of products by molecular beam mass spectrometry to address these issues through direct kinetic measurements.

Acknowledgement. This research was sponsored by the Division of Chemical Sciences, Geosciences, and Biosciences, Office of Basic Energy Sciences, U.S. Department of Energy under contract DE-AC05-00OR22725 with Oak Ridge National Laboratory, managed and operated by UT-Battelle, LLC. MKK was supported by an appointment to ORNL Postdoctoral Research Associated program administered jointly by Oak Ridge Institute for Science and Education and ORNL.

References

(1) *Lignin: Historical, Biological, and Materials Perspectives*; Glasser, W. G., Northey, R. A., Schultz, T. P., Eds.; ACS Symposium Series 742: American Chemical Society: Washington, DC, 2000. Chapter 15.
(2) Britt, P. F.; Buchanan, A. C. III; Malcolm, E. A.*; J. Org. Chem*. **1995**, *60*, 6523.
(3) Klein, M. T.; Virk, P. S.; *Ind. Eng. Chem. Fundam*. **1983**, *22*, 35.
(4) Cooney, M. J.; Britt, P. F.; Buchanan, A. C. III *Prepr. Pap.-Am. Chem. Soc., Div. Fuel Chem*. **1997**, *42*, 89.
(5) Britt, P. F.; Buchanan, A. C. III; Cooney, M. J.; Martineau, D. R; *J. Org. Chem.* **2000**, *65*, 1376.
(6) Britt, P. F.; Buchanan, A. C. III; Hitsman, V. H.; *Prepr. Pap.-Chem. Soc., Div. Fuel Chem.,* **1991**, *36*, 529
(7) Stein, S. E. *J. Am. Chem. Soc.* **1989**, *111*, 1423.
(8) *Reactive Molecules;* Wentrup, C.; John Wiley & Sons, Inc.: Canada, 1984.

HYDROGEN TRANSFER REACTIONS OF PHENOXY RADICALS STUDIED BY LASER FLASH PHOTOLYSIS TECHNIQUE

Reza Dabestani, Ilia N. Ivanov, Phillip F. Britt, Michael E. Sigman, and A. C. Buchanan, III*

Chemical Sciences Division, Oak Ridge National Laboratory, Oak Ridge, TN 37831

Introduction

Aryloxy radicals are important intermediates in the thermal decomposition of lignin and low rank coals. Their rate of formation, termination, hydrogen abstraction, and addition (i.e. cross-linking) have a significant impact on the product yields and distributions. The Arrhenius parameters of hydrogen abstraction reactions of phenoxy radicals with substituted phenols and hydroperoxides have been reported.[1] However, there are only a few reports of Arrhenius parameters for hydrogen abstraction by phenoxy radicals from hydrocarbons. This is mainly due to the experimental challenges associated with the slow relative rates of hydrogen abstraction by phenoxy radical from hydrocarbons and the very rapid recombination rates of phenoxy radicals. In previous studies Britt et al.[2] have assumed that the Arrhenius parameters for hydrogen abstraction by phenoxy radicals from hydrocarbons are similar to that of benzyl radical. However, this does not take into account the well-known polar effects in free radical reactions.[3] Since hydrogen abstraction reactions of aryloxy radicals plays an important role in the processing of energy resources, such as lignin and low rank coal, we have undertaken this study to investigate the kinetics of hydrogen abstraction by phenoxy and substituted phenoxy radicals from hydrocarbons structures found in energy resources, such as toluene, diphenylmethane and fluorene. The data obtained from such studies will serve as a benchmark for thermochemical kinetic estimates on related systems.

Experimental

Diphenyl oxalate (DPO), di-(4-methoxy)-phenyl oxalate (PMPO), and di-(2,6-dimethoxy)-phenyl oxalate (DMPO) were synthesized (Scheme I) as precursors for this study using a literature method.[4] Laser flash photolysis set-up has been described elswhere.[5] For the excitation light, 308 nm line of an excimer laser (Lambda Physik, 20 ns pulse width) or the third harmonic (355 nm, 5 ns pulse width) of a Minilite II ND:YAG (Continuum) was employed. The excitation beam was overlapped with the probe beam (450-W xenon) delivered to the sample at right angle to the excitation. Changes in the relative transmission of the probe beam, which was directed into the entrance port of a monochrometer, as a function of time due to transient formation were detected by a photomultiplier tube (PMT) attached to the exit port of monochrometer. The output of PMT was amplified by a two-stage amplifier and the signal was fed into a LeCroy 9354A transient digitizer for data acquisition. All digitized kinetic signals from the transient digitizer were fed to a GPIB board (National Instruments) and stored as ASCII files. The data were then transformed to time-resolved absorption spectra using Origin 6.0 software (Microcal). A thermostated cell holder was employed to study the effect of temperature on hydrogen abstraction rate for phenoxy radicals. For room temperature experiments, we used a flow cell to pump new solution into the cell for each laser shot to avoid interference from the excitation of products formed during the first laser pulse. For high temperature studies, solutions of the oxalates in dimethoxy ethyl ether with and without the hydrocarbon (H-donor, e.g. diphenylmethane, fluorene, etc.) were placed in a 1-cm quartz cell. After exposure to a single laser shot, the solution was discarded and replaced with a fresh solution, allowed to equilibrate to the desired temperature, then flashed. This procedure was repeated for all the kinetic data reported in this study. Purging of the samples with argon had no effect on the kinetics of the observed transients suggesting oxygen does not quench these transients.

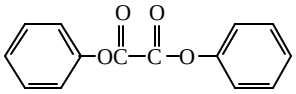

Diphenyl Oxalate (DPO)

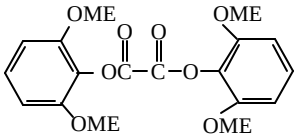

Di-(2,6-Dimethoxy)- Phenyl Oxalate (DMPO)

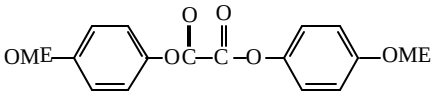

Di-(4-methoxy)-Phenyl Oxalate (PMPO)

Scheme I

Results and Discussion

Introduction of methoxy substituents into the phenoxy ring of DPO causes a red shifting of the absorption spectrum. Although DMPO contains two methoxy substituents in the *ortho*-position, the absorption spectra of PMPO which bears only one methoxy group in the *para*-position is considerably more red-shifted (~ 10 nm) than DMPO. Time-resolved transient absorption spectra of DPO, DMPO, and PMPO obtained at various time intervals after the laser pulse (308 nm) show the formation of a transient in the 300-450 nm region (due to phenoxy radical)[6] which slowly decays to produce a longer lived transient(s) with absorption in the 500-650 nm region. Because excited state lifetime of the initially formed triplet states is most likely in the pico-second time regime (which is outside of our time resolution limit), we only observe the appearance of phenoxy radical (us time domain) which absorb around 400 nm. The phenoxy radical can form from the breaking of carbon-oxygen bond in the triplet excited state of the oxalate. The observed red-shifting of the transient absorption, upon the addition of methoxy groups on the phenyl ring, further supports the notion that the observed transient is due to phenoxy radical formation.[6] Figure 1 shows the time-resolved transient absorption spectra of DPO obtained at 50 us time intervals after the laser pulse. The decay of the 395 nm peak with time is accompanied by the evolution of the 530, 560, and 600 nm peaks. Single exponential fit of both the rise for 560 nm peak (Fig. 2) and the decay for 395 nm peak (Fig. 3) gives a lifetime of 20 us.

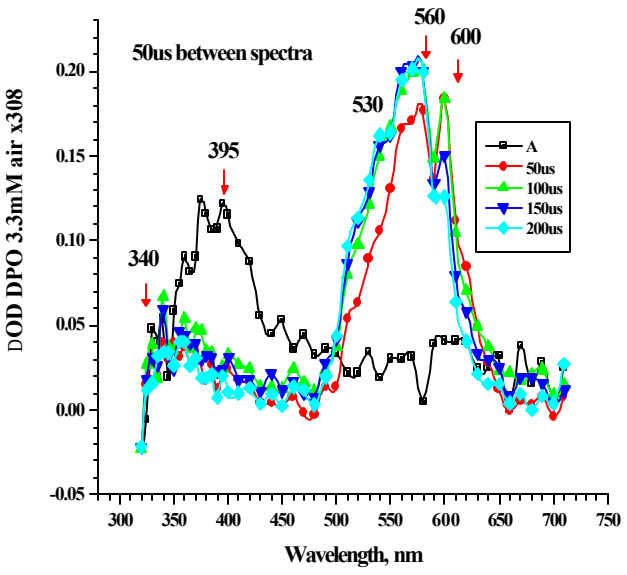

Figure 1. Time-resolved transient absorption spectra of DPO in air-saturated dimethoxy ethyl ether taken at 50 us time intervals after the 308 nm laser pulse.

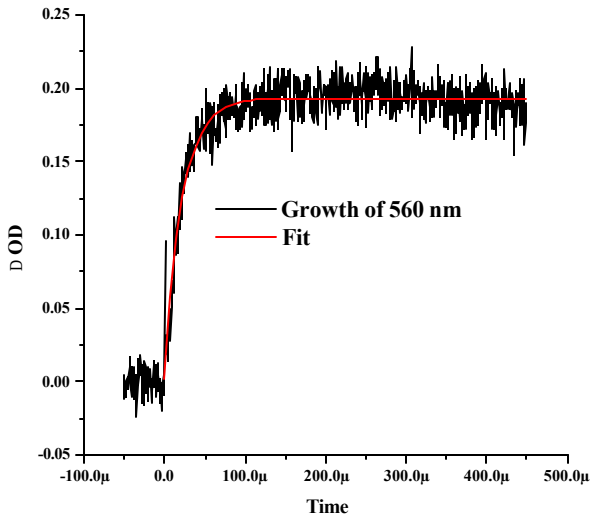

Figure 2. Growth of the 560 nm peak with time and its single exponential fit observed for DPO in air-saturated dimethoxy ethyl ether.

Time-resolved transient absorption spectra of PMPO and DMPO show similar behavior, but are red shifted. The quenching of phenoxy radical by various hydrocarbons (e.g. diphenylmethane, fluorene, and toluene) is currently under investigation to obtain the rate constants for H-abstraction by phenoxy radicals. The rate constant for H-abstraction will be measured at various temperatures in order to determine the Arrhenius parameters. One of the limiting factors in such studies is thermal stability of the oxalate at higher temperatures. Thermal stability studies are currently being conducted on DPO, DMPO, and PMPO to determine the feasibility of using the laser flash photolysis technique to study H-abstraction rates at higher temperatures. The results of this investigation will be presented at the meeting.

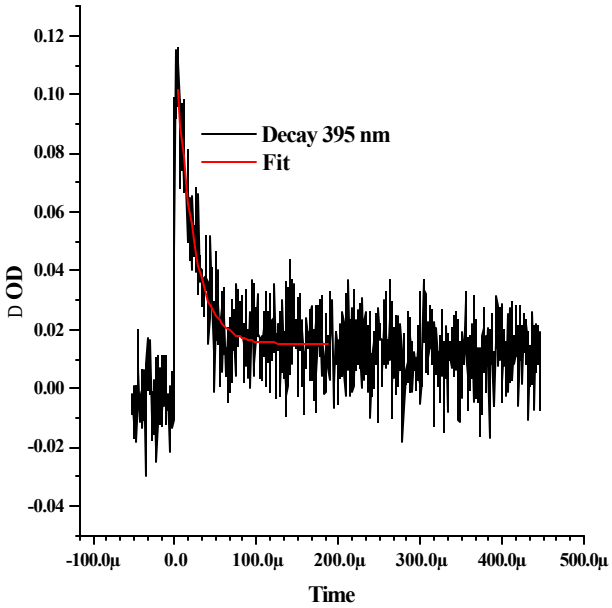

Figure 3. Decay profile for 395 nm transient and its single exponential fit observed for DPO in air-saturated dimethoxy ethyl ether.

Conclusions

Laser flash photolysis of a number of light sensitive oxalates proceeds to produce the corresponding phenoxy radicals. Time-resolved transient absorption spectra of these oxalates show strong absorption around 400 nm in good agreement with the reported literature values. The initially formed transient (due to phenoxy radical) slowly decays to produce a new transient(s) with strong absorption in the 500-600 nm region. The nature and identity of the newly formed transient(s) is currently under investigation Studies are also underway to determine the effect of concentration on the formation of new transient(s) and the rate constant for H-abstraction from hydrocarbons by phenoxy radicals.

Acknowledgements

This research was sponsored by the Division of Chemical Sciences, Geosciences, and Biosciences, Office of Basic Energy Sciences, U. S. Department of Energy under contract DE-AC05-96OR22464 with Oak Ridge National Laboratory, managed by UT-Battelle for the Department of Energy. I. Ivanov is supported by the ORNL Postdoctoral Research Associates program, which is administered jointly by Oak Ridge Institute of Science and Education and ORNL

References:

1. Denisov, E., *Handbook of Antioxidants*; CRC Press: Boca Raton FL, 1995; Chapter 3.
2. Britt, P. F.; Buchanan, A. C., III; Malcolm, E. A. *J. Org. Chem*. **1995**, *60*, 6523.
3. Minisci, F.; Fontana, F.; Recupero, F.; Bravo, A.; Agano, E.; Rinaldi, C.; Di Luca, M.; Grossi, F.; Bjorsvik, H-R. *J. Am. Chem. Soc.* **1999**, *121*, 7760.

4. Lahti, P. M.; Modarelli, D. A.; Rossitto, F. C.; Inceli, A. L.; Ichimura, A. S.; Ivatury, S. *J. Org. Chem*. **1996**, *61*, 1730.
5. Dabestani, R.; Higgin, J.; Stephenson, D.; Ivanov, I. N.; Sigman, M. E. *J. Phys. Chem. B* **2000**, *104*, 10235.
6. Das, P. K.; Encinas, M. V.; Steenken, S.; Scaiano, J. C. *J. Am. Chem. Soc*. **1981**, *103*, 4162.

LEVOGLUCOSAN PYROLYSIS

Mark R. Nimlos and Robert J. Evans

National Renewable Energy Laboratory
1617 Cole Blvd.
Golden, Colorado 80401
Email: mark_nimlos@nrel.gov

Introduction

Levoglucosan 1,6-anhydro-β-D-glucopyranose is known to be an important intermediate in the pyrolysis of cellulose, but little is known about its subsequent thermal degradation. Levoglucosan is formed in high yields (up to 60 %) by the pyrolytic unzipping of cellulose.

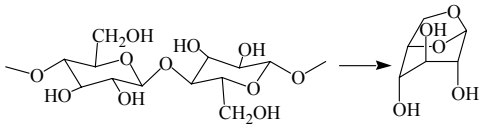

(1)

Section of cellulose ***Levoglucosan***

In a study of the thermal degradation of levoglucosan (600°C residence time = 8 min.), Shafizadeh and Lai[1] measured small molecular products such as 2-furaldehyde, 2,3-butanedione, pyruvaldehyde, acetaldehyde and glyoxal. They attempted to identify reaction mechanisms for the degradation of levoglucosan through radioactive labeling (^{14}C) of the 1,2 and 6 carbon of levoglucosan and measurements the incorporation of this radioactivity into the pyrolysis products. Based upon earlier work by Gardiner[2] on cellulose pyrolysis, Shafizadeh and Lai proposed that levoglucosan is initially converted to 3,6-anhydro-D-glucose.

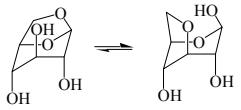

(2)

3,6-anhydro-D-glucose

Gardiner's work[2] also showed that this product can be thermally converted into 1,4:3,6-dianhydro-D-glucose.

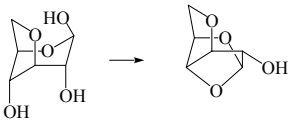

(3)

1,4:3,6-dianhydro-D-glucose

Recently Li *et al.*[3] measured the evolution of CH_2O, CO and CO_2 from the thermal degradation of levoglucosan using gas phase infrared (IR) spectroscopy. Finally, we have measured the global kinetics of the pyrolysis of levoglucosan using molecular beam mass spectrometry.[4]

Here we will report some of our work on the pyrolysis of levoglucosan in which we measure products by matrix isolation IR spectroscopy. Our studies are aided by electronic structure calculations (B3LYP/cc-pVDZ), which will allow us to accurately estimate reaction energies and occasionally reaction barriers. These values will be essential for estimating reaction kinetics.

Experimental

Pyrolysis experiments are conducted in flowing argon in a two-stage alumina tubular reactor (1 cm ID) and the products are deposited on a cold (8 K) salt window at the tip of cryostat. Levoglucosan is volatilized in the first stage of the reactor (resistively heated with nichrome wire) and pyrolyzed in the second stage (resistively heated with tungsten wire). The maximum practical temperature for the second stage is roughly 1200 °C. We estimate that the pressure in the reactor is about 100 mtorr and the residence time is about 1 ms. The levoglucosan is fed into the first stage of the reactor in a quartz boat that is fastened to the end of a thermocouple. The temperature of the sample is controlled so that sufficient levoglucosan is volatilized but so that the concentration is low enough that bimolecular reactions are minimized and good isolation is obtained. Once a sample has been deposited, IR absorption spectra are recorded using a Nicolet Magna 550 spectrometer.

Results and Discussion

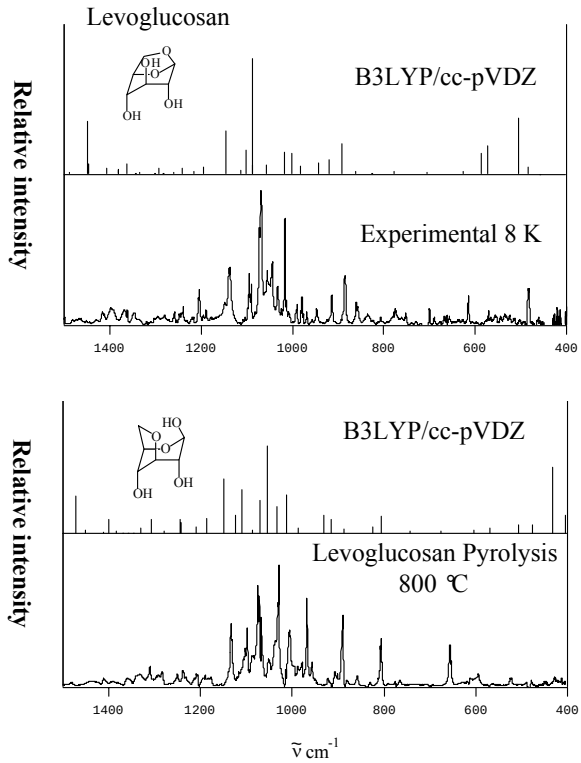

Figure 1 Matrix isolation IR spectra of levoglucosan (top half) and its pyrolysis products (bottom half). The top experimental spectrum of levoglucosan is compared to that computed with B3LYP/cc-pVDZ calculations. In the bottom half, the measured spectrum is compared to the calculated spectrum of 3,6-anhydro-D-glucose.

Figure 1 shows the matrix isolation infrared absorption spectra of a typical pyrolysis experiment involving levoglucosan. The top half of the figure compares the experimentally measured IR spectrum of levoglucosan with the IR spectrum calculated using B3LYP/cc-pVDZ. The experimental spectrum was collected by heating the levoglucosan to about 60 °C as measured by the thermocouple near the sample boat. At this temperature the vapor pressure of levoglucosan[5] is about 10^{-5} torr and a mixing ratio with the argon of about 1/10,000. The calculated spectrum is uncorrected and was obtained using the Gaussian98 program suite[6] running on a SGI super cluster at the National Center for Supercomputing Applications. The B3LYP technique has been shown[7] to produce reasonable frequencies and IR intensities. Since the calculated transitions are harmonic frequencies, they are typically shifted to a higher energy than the experimentally observed transitions by roughly 3%. As can be seen from this figure, the fit of the calculated spectrum to the experimental spectrum is good.

The bottom half of **Figure 1** shows the experimental spectrum obtained when the second stage of the reactor is heated to 800 °C, while the sample is held at 60 °C in the first stage. The observed spectrum contains only gas phase pyrolysis products as well as some remaining levoglucosan, which has been subtracted from the spectrum presented in the figure. Since the concentration of the levoglucosan is low, this spectrum contains products that are primarily a result of unimolecular decomposition of levoglucosan. We tested this by changing the vaporization temperature and thus, the concentration of the levoglucosan. We saw no change in the IR spectrum when the concentration was lowered.

The infrared spectrum that we obtain by pyrolyzing levoglucosan at 800 °C is suggestive of that calculated for 3,6-anhydro-D-glucose. This calculated spectrum is shown in the bottom half of **Figure 1**, above the experimental spectrum. As can be seen there is a good fit of most of the features to this calculated spectrum to the experimental spectrum. There is an intense peak at 1075 cm^{-1}, which may result from 1,4:3,6-dianhydro-D-glucose. Our calculations show that this molecule should have two intense transitions at 1068 cm^{-1} and 1103 cm^{-1} (harmonic frequencies). Further evidence for the formation of these two molecules lies in the fact that no IR transitions were observed in the region from 1650 cm^{-1} to 1850 cm^{-1}. Elimination of water or formaldehyde should result in intense peaks in this region. The absence of intense transitions in this region suggests that the products are unsaturated.

Calculations of Reaction Pathways In order investigate possible decomposition pathways for levoglucosan further, we used density functional theory (B3LYP) to estimate reaction energies for some like decomposition reactions. This technique has an RMS accuracy of about 3 kcal mol^{-1} compared to the G2 set of molecules.[8] Figure 2 shows the relative energies of some of the potential products from the unimolecular decomposition of levoglucosan and their calculated energies. These will be discussed below.

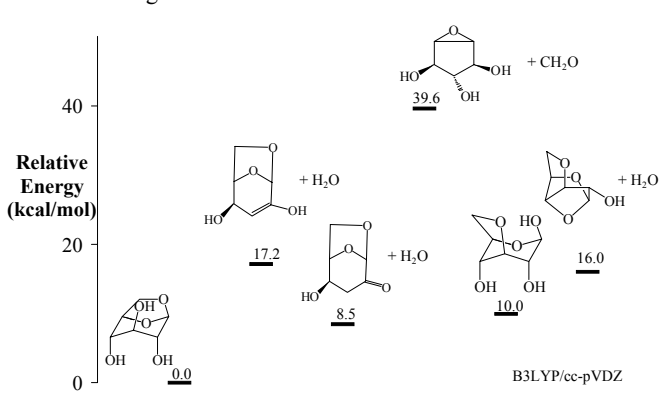

Figure 2 Calculated relative energies of different products from the pyrolysis of levoglucosan.

Homolytic bond dissociation in levoglucosan will not be important under typical pyrolysis conditions because the bond strengths are too high. The weakest bonds are the C–O ether bonds which will have bond energies[9] of about 82 kcal mol^{-1}. With a large pre-exponential factor of 10^{15} s^{-1}, which is typical for bond scissions, the rate constant for these reactions at 600°C would be smaller than 10^{-6} s^{-1}. This is much smaller than the observed global rate constant (0.45 s^{-1}) for levoglucosan destruction.[4]

Concerted reaction mechanisms are more likely. Dehydration of the alcohol groups to form alkenes is an example of this type of reaction. Loss of water from levoglucosan can result in the formation of a vinyl alcohol. For example, loss of the OH from the number 3 carbon can form the following vinyl alcohol.

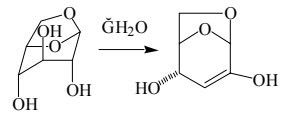

(4)

We calculate a reaction enthalpy for reaction (4) of $\Delta_{react}H_{298\ K}$ = 14.0 kcal mol^{-1}. The same reaction enthalpy is calculated for loss of the OH from the number 2 carbon, suggesting that all of the possible dehydration reactions involving the three OH groups in levoglucosan have a similar reaction enthalpy. We have conducted an exhaustive study of these types of dehydration reactions using electronic structure techniques[10] and found that the reaction barriers are about 69 kcal mol^{-1}. Vinyl alcohols formed by dehydration reactions such as are shown in reactions (4) are likely to be quickly followed by enol-keto tautomerizations such as

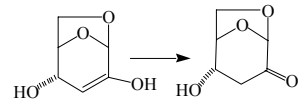

(5)

We calculate a reaction enthalpy of $\Delta_{react}H_{298\ K}$ = –12.6 kcal mol^{-1} a reaction barrier of 56.2 kcal mol^{-1} for this type of reaction. From the computed barriers and vibrational frequencies, we obtain a rate constant of about 10^{-4} s^{-1} (at 600°C) for reaction (4) and 10^{0} s^{-1} (at 600°C) for reaction (5). Since the first rate constant is low compared to the global rate constants for levoglucosan (0.45 s^{-1}),[4] reactions (4) and (5) should not be important. Indeed we do not observe IR transitions for these products.

We are considering a mechanism for (2) and (3) involving an oxonium ion. For instance, reaction (2) may involve the following steps.

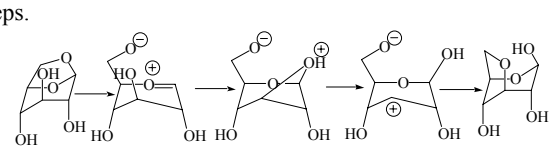

(6)

Our calculations suggest that formation of the oxonium ion, the first intermediate in (6), may require less than 50 kcal mol^{-1}. This could make reaction (2) possible under pyrolysis conditions. Furthermore the anhydro product from reaction (3) may be formed directly from this oxonium ion.

Acknowledgement

We would like to acknowledge the support of Phillip Morris and Mohammad Hajoligol the Nactional Center for Supercomputer Applications (NCSA Grant # CHE-980028N).

References

1. Shafizadeh, F.; Lai, Y. Z. *J. Org. Chem.* **1972**, *37*, 278.
2. Gardiner, D. *J. Chem. Soc. C* **1966**, 1473.
3. Li, S.; Lyons-Hart, J.; Banyasz, J.; Shafer, K. *Fuel* **2001**, *80*, 1809.
4. Shin, E-J.; Nimlos, M. R.; Evans, R. J. *Fuel* **2001**, *80*, 1697.
5. Oja, V.; Suuberg, E. M. *J. Chem. Eng. Data* **1999**, *44*, 26.
6. Gaussian 98 (Revision A.1x), Gaussian, Inc., Pittsburgh PA, 2001.
7. Koch, W.; Holthausen, M. C. "A Chemist's Guide to Density Functional Theory," 2nd Edition, Wiley, New York, 2001.
8. Foresman, J. B.; Frisch, Æ. "Exploring Chemistry with Electronic Structure Methods," 2nd Ed. Gaussian, Inc, Pittsburg, 1995.
9. Benson, S. W. "Thermochemical Kinetics," 2nd Ed., Wiley, New York, 1976.
10. Nimlos, M. R.; Blanksby, S. J.; Evans, R. J. *J. Anal. Applied Pyrol.* Submitted.

INVESTIGATION OF THE GAS-PHASE PYROLYSIS OF LIGNIN MODEL COMPOUNDS BY MOLECULAR BEAM MASS SPECTROMETRY

Phillip F. Britt,[1] A. C. Buchanan, III,[1] Robert J. Evans,[2] Michael Looker[2], and Mark R. Nimlos[2]

[1]Oak Ridge National Laboratory, P.O. Box 2008, Oak Ridge, TN 37831
[2]National Renewable Energy Laboratory, 1617 Cole Blvd., Golden, CO 80401

Introduction

The production of fuels and chemicals from the thermochemical processing of biomass depends on an understanding of the complex pathways and underlying mechanisms.[1] Unfortunately, the reaction pathways that lead to the complex array of products are still not resolved, and there is little insight into controlling product selectivity. To gain fundamental mechanistic insight into the pyrolysis of lignin, a major component of biomass,[2] our research has focused on the pyrolysis of model compounds that contain key structural elements found in native lignins.[3-5] The flash vacuum pyrolysis of lignin model compounds containing the β–O-4 linkage, which is the dominant linkage in lignin, has been reported.[4,5] These studies provided insight into the primary gas-phase reaction that occurs at 500 °C under low concentration conditions that favor unimolecular reactions. The reaction pathways were significantly more complex than expected, and the dominant reaction was C–O homolysis followed by intramolecular hydrogen abstraction, 1,2-phenyl shift, and/or β–scission of subsequent radicals to form stable products. In this study, the fast pyrolysis of lignin model compounds was investigated at atmospheric pressure in a stream of helium with real time sampling of the products by mass spectrometry. Under these reaction conditions, bimolecular reactions can compete with the unimolecular reactions for the formation of products. In this investigation, the pyrolysis of phenethyl phenyl ether (PPE) and its methoxy derivatives, *o*-CH_3O-PPE and (*o*-$CH_3O)_2$-PPE, was studied at 500 – 650 °C with residence times of 0.3 and 0.6 s.

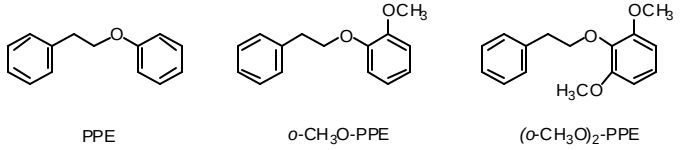

Experimental

The synthesis of the model compounds has been previously described.[3,5]

The study of pyrolysis by MBMS has been described previously.[6,7] All reactions were carried out at atmospheric pressure in a quartz tube reactor from 500 °C to 650 °C. A schematic diagram of reactor coupled to a molecular-beam mass spectrometer sampling system is shown in Figure 1. The quartz reactor consisted of inner and outer tubes, with pyrolysis occurring in the inner tube and the outer tube providing additional helium flow to satisfy the demands of the MBMS. The length of the inner tube from the sample to the end was 37 cm while the length of the mixing regime was 13 cm. A reactor with a spiral reaction section was used, so longer length and higher gas linear velocities could be achieved, which improved the flow characteristics. A fraction of the sweep gas (He) was introduced into the reactor through a side port where samples were inserted to facilitate sample introduction.

A sample (1-10 mg) contained in a quartz holder, or "boat", was inserted into flowing, preheated helium carrier gas. The carrier gas was introduced through the ends of inner and outer tubes and vapors exiting from the pyrolysis reactor (inner tube) were diluted with neat carrier gas in the outer tube. The hot gases exiting the reactor are expanded through an orifice on the apex of a sampling cone into the stage one vacuum at 40 mtorr. The pressure difference is sufficient for free-jet expansion, which quenches the products and allows the full range of products, including light gases, high-molecular-weight compounds, and reactive products, to be simultaneously sampled and analyzed. A molecular beam, collimated through a second expansion, enters an ion source, where approximately 17 eV electron impact ionization is used to form ions. The ionization voltage was adjusted to minimize fragmentation of the lignin model compounds while maintaining good sensitivity. The gas phase residence time is defined as the time in the pyrolysis (inner) tube and in the mixing region of the outer tube. The flow rate of carrier gas in the inner tube was varied from 500 mL/min to 2000 mL/min, keeping total flow rate (inner and outer flow) constant at 10,000 mL/min. This varied the residence time from 0.3 s to 0.6 s.

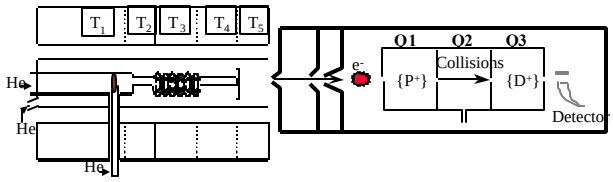

Figure 1. Tubular gas phase pyrolysis reactor coupled to a molecular beam mass spectrometer sampling system.

Results and Discussion

The liquid and gas phase pyrolysis of PPE has been studied at low temperatures (330 – 425 °C).[3] Decomposition proceeds by a free radical chain pathway to produce two sets of products: styrene plus phenol and benzaldehyde plus toluene, in a ratio of 3:1, respectively, at 375 °C. In the FVP of PPE at 500 °C (ca. 0.3 s residence time, 0.9% conversion), the dominant reaction was C-O homolysis, which produced styrene and phenol (which accounted for 97% of the products).[5] Homolysis of the C-C bond, to produce toluene and benzaldehyde, was a minor reaction.

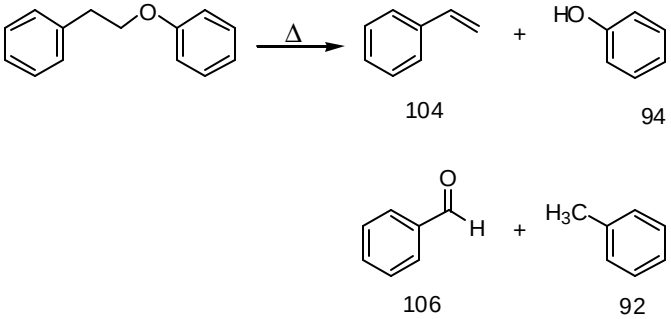

The pyrolysis MBMS of PPE was run at 500, 550, 600 and 650 °C with residence times of 0.3 and 0.6 s. As the temperature and residence time increased, the dominant products that appeared in the mass spectrum were styrene (*m/z* 104) and phenol (*m/z* 94) with very small amounts of toluene (*m/z* 92) and benzaldehyde (*m/z* 106). This product slate is very similar to that found in the FVP experiments. The mass spectrum of the reaction mixture at 600 °C and a residence time of 0.6 s is shown in Figure 2. Benzene (*m/z* 78) can arise from the decomposition of benzaldehyde (confirmed by independent pyrolysis) and is observed as a mass spectral fragmentation product. The *m/z* at 105 is from fragmentation of the PPE, which decreases in intensity as the molecular ion (*m/z* 198) decreases. Thus, the pyrolysis MBMS experiment gives primarily unimolecular products and little bimolecular reactions. However, small quantities of additional products are formed with *m/z* 154, 168, and 180 that appear to be coupling products from the radicals formed in the reaction (phenoxy, benzyl, and phenyl, from decomposition of benzaldehyde to form biphenyl, dibenzofuran, and stilbene), but they also could arise from surface catalyzed reactions. Attempts to increase the yield of these products by addition of a free radical

initiator, such as benzyl phenyl ether, were unsuccessful. Thus, the origin of these products is still under investigation.

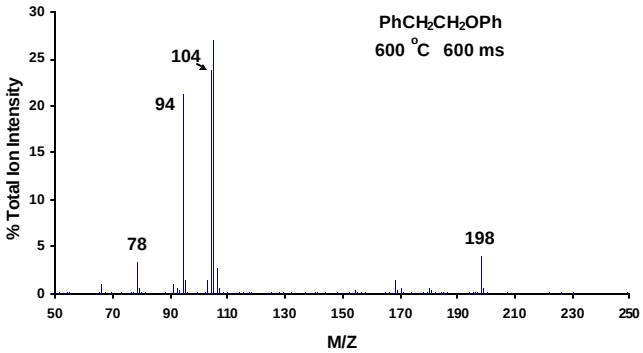

Figure 2. Average spectra of products detected by MBMS from the pyrolysis of PPE at 600 °C and a residence time of 0.6 s.

The pyrolysis MBMS of *o*-CH_3O-PPE was run at 500, 550 and 600 °C at residence times of 0.3 and 0.6 s. The mass spectrum from a run at 500 °C and a residence time of 0.3 s is shown in the Figure 3. The mass at *m/z* 228, 124, and 105 are from mass spectrometer fragmentation of the starting material (see Figure 3), and there is little thermal decomposition of the material. At 600 °C with a residence time of 0.6 s, all the starting material is consumed (see Figure 4) indicating that the *o*-methoxy derivative is more reactive than PPE. The dominant products arise from C-O homolysis and form styrene and hydroxybenzaldehyde (*m/z* 122). Guaiacol (*m/z* 124) was a minor product in the reaction. Independent pyrolysis of guaiacol at 600 °C indicated that it was not stable under these reaction conditions but formed catechol (*m/z* 110) as the major product and small amounts of hydroxybenzaldehyde and phenol. Independent pyrolysis of hydroxybenzaldehyde at 600 °C produced small amounts of phenol (*m/z* 94). Small amounts of toluene and *o*-methoxybenzaldehyde (*m/z* 138) were also found which arise from C-C homolysis.

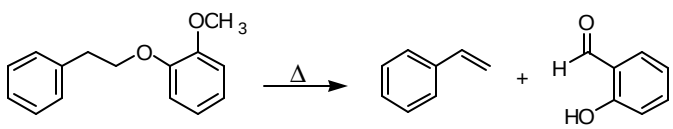

The major products are very similar to those formed in the FVP of *o*-CH_3O-PPE at 500 °C indicating that unimolecular reactions are dominant. *o*-Hydroxybenzaldehyde is formed by C-O homolysis to give the *o*-methoxyphenoxy radical, intramolecular hydrogen abstraction to form *o*-hydroxyphenoxymethyl radical, 1,2-phenyl shift to form *o*-hydroxybenzyloxy radical followed by β–scission of hydrogen. In solution phase at lower temperatures, bimolecular hydrogen abstraction is the dominant reaction and two sets of products are formed: guaiacol plus styrene, and toluene plus *o*-methoxybenzaldehyde, in a 3:1 ratio (at 375 °C).

The FVP of $(o\text{-}CH_3O)_2$-PPE produced a complex set of products.[5] Surprisingly, the dominant product was *o*-cresol (24 mol%), 2,6-dimethoxyphenol (13 mol%), and styrene (22 mol%). These products were formed by C-O homolysis followed by hydrogen abstraction, rearrangement, and β–scission reactions. The mass spectra of the products detected by MBMS from the pyrolysis of $(o\text{-}CH_3O)_2$-PPE at 600 °C and a residence time of 0.6 s is shown in Figure 5. The spectrum is surprisingly simple (compared to the FVP results). The dominant products appear to be styrene (*m/z* 104), cresol (*m/z* 108), *o*-hydroxybenzaldehyde (*m/z* 122), and benzene (*m/z* 78). Independent pyrolysis of 2,6-dimethoxyphenol at 600 °C produced a complex set of products with *m/z*138, 126, 124, 110, 108. This indicates that 2,6-dimethoxyphenol is not a major primary product since its major decomposition products are not observed to a significant extent. More studies are needed to determine the origin of these products. As a consequence of the decomposition and mass spectral fragmentation of the products, it is difficult to determine the primary and secondary products. Thus, the data will be analyzed by multivarariate factor analysis to determine which masses (i.e., products) are correlated.[8] Results from this data analysis will be presented and the mechanisms of the decomposition of these lignin model compounds will be discussed.

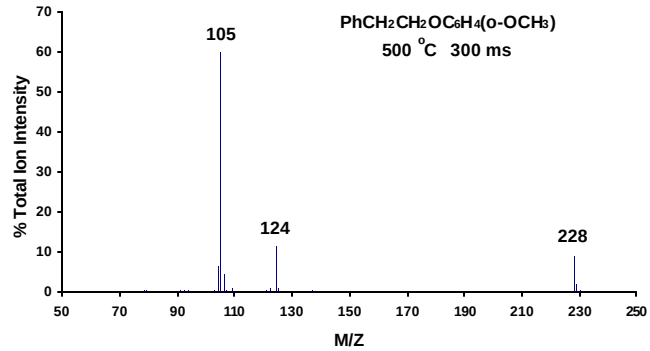

Figure 3. Average spectra of products detected by MBMS from the pyrolysis MBMS of (*o*-CH_3O)-PPE at 500 °C.

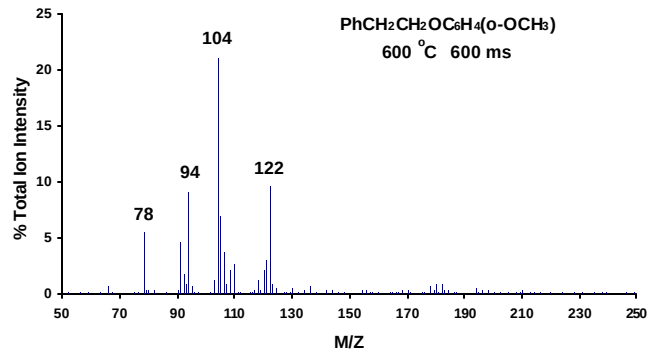

Figure 4. Average spectra of products detected by MBMS from the pyrolysis *o*-CH_3O-PPE at 600 °C and 0.6 s residence time.

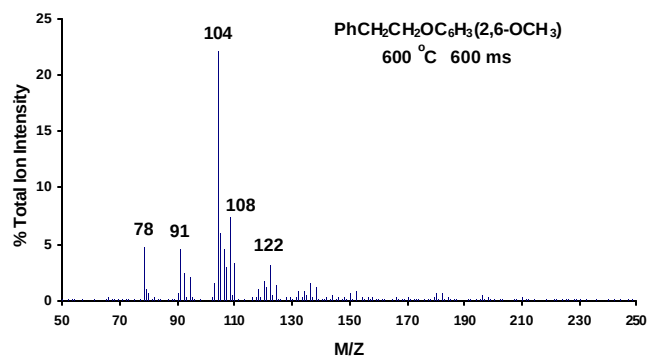

Figure 5. Average spectra of products detected by MBMS from the pyrolysis *o*-CH_3O-PPE at 600 °C and 0.6 s residence time.

Acknowledgement. This research was sponsored by the Division of Chemical Sciences, Geosciences, and Biosciences, Office of Basic Energy Sciences, U.S. Department of Energy under contract

DE-AC05-00OR22725 with Oak Ridge National Laboratory, managed and operated by UT-Battelle, LLC. The authors also acknowledge the financial support from Philip Morris USA.

References

(1) *Developments in Thermochemical Biomass Conversion*; Bridgwater, A. V.; Boocock, D. G. B., Eds; Blackie Academics: London, 1997.
(2) Gargulak, J. D.; Lebo, S. E. Commerical Use of Lignin-Based Materials. In *Lignin: Historical, Biological, and Materials Perspectives;* Glasser, W. G.; Northey, R. A.; Schultz, T. P. Eds.; ACS Symposium Series 742; American Chemical Society: Washington, DC, 2000, pp 304-320.
(3) Britt, P. F.; Buchanan, A. C., III; Malcolm, E. A. *J. Org. Chem.* **1995**, *60*, 6523.
(4) Cooney, M. J.; Britt, P. F.; Buchanan, A. C., III *Prepr. Pap. - Am. Chem. Soc., Div. Fuel Chem.* **1997**, *42*, 89.
(5) Britt, P. F.; Buchanan, A. C., III; Cooney, M. J.; Martineau, D. R. *J. Org. Chem.* **2000**, *65*, 1376.
(6) Evans R.J.; Milne, T.A. *Energy & Fuel* **1987**, 1,123
(7) Shin, E-J.; Nimlos, M. R.; Evans, R. J. Fuel **2001**, 80, 1697.
(8) For an example see: Shin, E.-J.; Nimlos, M. R.; Evans, R. J. *Fuel* **2001**, *80*, 1681.

PYROLYSIS OF α-AMINO ACIDS

Ramesh K. Sharma, W. Geoffrey Chan, Jeffrey I. Seeman[1], and Mohammad R. Hajaligol[*]

Philip Morris USA, Research Center
P. O. Box 26583, Richmond, VA 23261
[1]Saddle Point Frontiers, Richmond, Virginia

Introduction

Amino acids are important constituents of most biomass. Pyrolysis of amino acids produces a complex slate of products [1-5]. Of particular interest among the pyrolysis products are the polycyclic aromatic compounds (PAC) which include polycyclic aromatic hydrocarbons (PAH) and nitrogen containing polycyclic aromatic compounds (N-PAC). Patterson et al.[1] pyrolyzed lysine, leucine and tryptophan and found that the total PAC yield was maximum at 850°C. Higman et al.[2] pyrolyzed proline at 840°C and observed pyrrole, indole, pyridine, isoquinoline, quinoline and picoline as products. Smith et al.[3] pyrolyzed valine, aminobutyric acid, and proline and observed nitriles, quinoline and isoquinoline at 850 °C. Yoshida and Matsumoto[4] observed the formation of amino-β-carbolines from tryptophan at 550 °C. Recently, Chiavari and Galletti[5] reported the main products from pyrolysis of amino acids in a CDS Pyroprobe 100 at 600 °C for 5 s. Despite these studied, there is no detailed study on the effect of temperature and residence time on the product distribution.

In this work, the formation of PAC from pyrolysis of asparagine, proline, and tryptophan was studied under various pyrolysis conditions. The results were analyzed to determine the major product components and the effect of pyrolysis conditions and the structure of amino acid on the PAC yields.

Experimental

Pyrolysis experiments were performed in a quartz reactor in two ways.[6] In the first case, the amino acid was pyrolyzed in a single zone reactor at 300 °C to collect LTT (low temperature tar) and LTC (char). A sample of 200 mg of amino acid was used and pyrolyzed for 60 minutes. The LTT was collected on a Cambridge pad. The pad was extracted with methanol. The LTC was then pyrolyzed further at 625 °C for 60 min to collect HTT (high temperature tar) and HTC (char). In the second case, a two-zone reactor was used and the LTT and HTT leaving the first zone were pyrolyzed further in the second zone at 720-920 °C. The final tars, LTFT (low temperature final tar) and HTFT (high temperature final tar) from LTT and HTT, respectively, were collected similarly. Only the runs with a residence time of 1370 ms in the second zone are discussed in this paper. Helium was used as carrier gas at 120 cm^3/min. The LTT, HTT, LTFT, and HTFT were analyzed by chromatography/ mass spectrometry (GC/MS).

Results and discussion

Asparagine. The overall material balance from pyrolysis of asparagine showed that, at 300 °C, the yield of LTT was negligible but the yield of LTC was 64%. The yields of HTT and HTC were 12% and 23% of initial weight of asparagine. The HTT consisted mainly of maleimide and succinimide with yields of ca. 8 and 48 mg/g of asparagine. Indole and a methylindole were also observed in low yields. Chiavari and Galletti[5] reported maleimide and succinimide from pyrolysis of asparagine at 600 °C.

No LTFT was obtained from asparagine. The yields of a few major PAC in HTFT are shown in **Figure 1**. At 700 °C, succinimide was the major component of HTFT. Both maleimide and succinimide decreased at high temperature. The yield of maleimide passed through a maximum at 770 °C. At 870 °C and above, the yields of two- to four-ring N-PAC, such as a naphthalene carbonitrile, pyrrolcarbazole, a benzoquinoline, and azapyrene, were significant. Most other N-PAC, including fluorenecarbonitrile, and anthracenecarbonitrile, were formed in relatively low yields. Among the PAH, the highest yield was of phenanthrene followed at high temperature by pyrene. The formation of PAH indicates a complete loss of nitrogen from the initial products of pyrolysis.

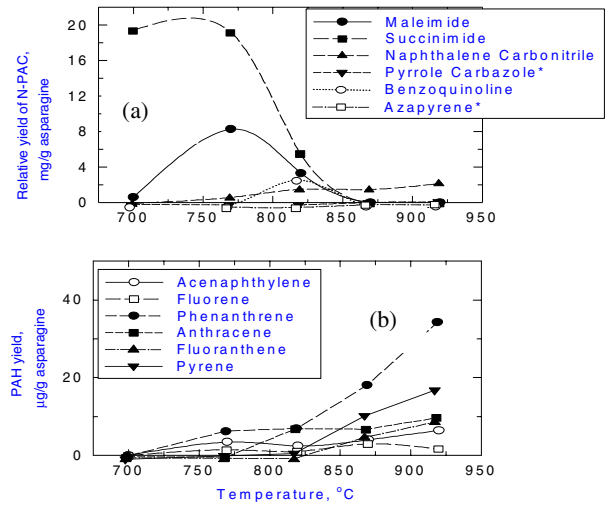

Figure 1. Effect of temperature on the yields of major N-PAC (a) and PAH (b) from the gas phase pyrolysis of HTT from asparagine at 700-920 °C.

Proline. Proline was completely converted into volatile products at 300 °C, with a LTT yield of ca. 80%. The LTT consisted mainly of 2,5-diketopiperazine. No HTT or HTFT was obtained.

The yields of some of the major components of LTFT are presented in **Figure 2**. Above 820 °C, both N-PAC and PAH were observed. Carbonitriles were the main components of the N-PAC fraction. The yield of acridine passed through a maximum at 870 °C. The yields of fluorenecarbonitrile, anthracenecarbonitrile, and azapyrene increased sharply with temperature above 820 °C. At 920 °C, methylbenzonitrile was absent from the products. Indole, quinoline, benzenecarbonitrile, phenylpyridine, naphthalenecarbonitrile, benzoquinoline, fluorenimine, phenanthridine, carbazole, acenaphthopyridine, indenoisoquinoline, pyrrolocarbazole, and cyanopyrene were also observed. Among the PAH, phenanthrene was the major component at all the temperatures. Benzo[a]pyrene was observed only at 920 °C. Other PAH, such as naphthalene, biphenyl, ethenylanthracene, methylanthracene, phenylnaphthalene, benzo[a]fluorene, methylpyrene, benzo(ghi)fluoranthene, and isochrysene were also observed. The yields of acenaphthylene, fluorene, and anthracene either decreased or leveled off at high temperatures. This could be due to their growth into larger PAH. The formation of PAH from proline has also been reported earlier in the literature.[2,3] Smith et al.[3] also reported the formation of butadiene at 650 °C. Thus, the PAH in this study, may have formed via butadiene and related low molecular weight olefins.

Tryptophan. The yields of LTT and LTC from tryptophan were 15% and 56% whereas those of HTT and HTC were ca. 11% and 14%, respectively. The LTT contained indole, a methyl indole, norharman, harman and other indole derivatives, such as indoleethanamine and indoleacetonitrile Ethylindole and dimethylindole were also observed in low yields. The HTT contained similar components but the yields of indole and substituted indoles were lower while those of the harmans were slightly higher. Other two- and three-ring PAC, such as quinoline and carbazole or azafluorene were also observed in small yields in the HTT. Some of tese products have been reported earlier.[5,7]

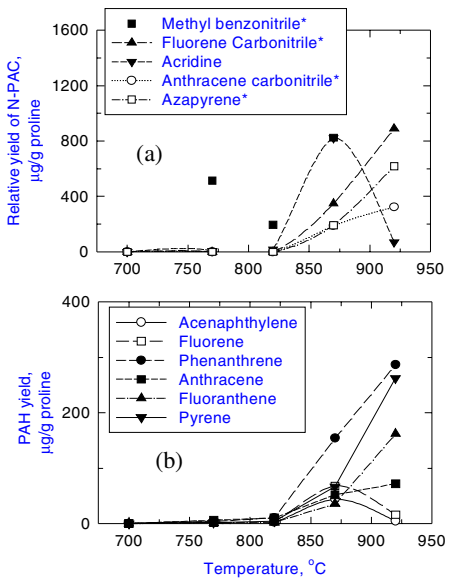

Figure 2. Effect of temperature on the yields of major N-PAC (a) and PAH (b) from the gas phase pyrolysis of LTT from proline at 700-920 °C.

No PAH were observed in the LTFT and HTFT from tryptophan. The constituents of LTFT and HTFT ranged from N-heterocycles to three-ring N-PAC (benzo[a]carbazole and anthracenamine). For both LTFT and HTFT, the yields of indole and skatole decreased as the temperature was increased until they were completely destroyed above 850 °C (**Figure 3**). The temperature had only a small effect on the yields of norharman and harman, although above 820 °C the yields decreased. Whereas harman was completely absent in the product at 920 °C, the yield of norharman remained significantly high even at 920 °C. Essentially similar observations were made by Kleinbauer and Rabache.[7] Harman and norharman were observed in the product even at 250 °C and the yield of norharman decreased slowly at high temperatures whereas the yield of harman decreased sharply. The nearly similar trends in the yields of norharman and harman in this study suggested that the norharman/harman ratio did not vary dramatically with temperature, except at high temperatures. The yield of quinoline remained relatively low at all temperatures. The yields of three-ring N-PAC, benzocarbazole and anthracenamine, became significant only at 920 °C. In the case of HTFT, the yield of carbazole also became significant at high temperatures suggesting that it is one of the end products of the pyrolysis of tryptophan. In addition to the components shown in **Figure 3**, the product also contained cyanocarbazole, indenoisoquinoline, benzo[a]phenanzine, benzo[a]acridine and other products.

Conclusions

The results from the three amino acids showed that the amino acids pyrolyzed differently. The N-PAC from asparagine and proline were mainly aromatic carbonitriles and three- and four-ring aza-arenes. Asparagine and proline also formed PAH, although the yields of PAH were low compared to the yields of N-PAC. In contrast, tryptophan did not form any PAH but it formed β-carbolines and indoles even at low temperatures. The pyrolysis mechanisms may be governed by the structure of the amino acid .

Acknowledgements. The authors are grateful to the Philip Morris USA management for the support of this research.

References

1. Patterson, J.M.; Baedecker, M.L.; Musick, R.; Smith, Jr., W.T. *Tob. Sci.* **1969**, 13, 26.
2. Higman, E.B.; Schmeltz, I.; Schlotzhauer, W.S. *J. Agric. Food Chem.* **1970**, 18, 636.
3. Smith, W.T.; Haidar, N.F.; Patterson, J.M. *Tob. Sci.* **1975**, 19, 142.
4. Yoshida, D.; Matsumoto, T. *J. Agric. Biol. Chem.* **1979**, 43(5), 1155.
5. Chiavari, G.; Galletti, G.C. *J. Anal. Appl. Pyrol.* **1992**, 24, 123.
6. McGrath, T.; Sharma, R.; Hajaligol, M. *Fuel* **2001**, 80, 1787.
7. Kleinbauer S.; Rabache, M. *Sci. Alim.* **1990**, 10, 417.

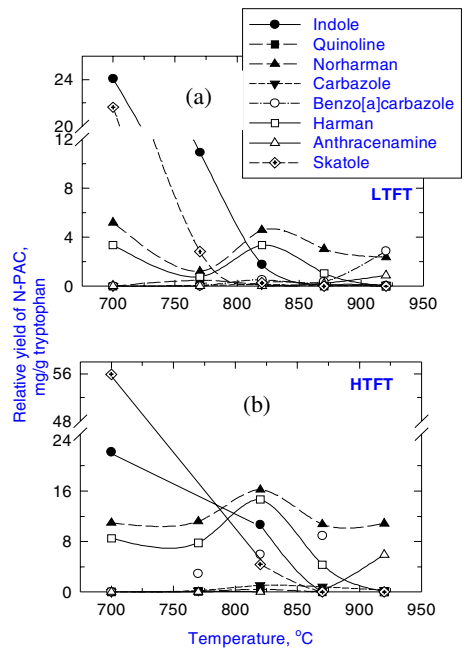

Figure 3. Effect of temperature on the yields of major N-PAC from the gas phase pyrolysis of LTT (a) and HTT (b) from tryptophan at 700-920 °C.

FORMATION OF NITROGEN CONTAINING POLYCYCLIC AROMATIC COMPOUNDS FROM THE CO-PYROLYSIS OF CARBOHYDRATES AND AMINO ACIDS

Phillip F. Britt, A. C. Buchanan, III, Clyde V. Owens, Jr., and J. Todd Skeen

Chemical Sciences Division
Oak Ridge National Laboratory
P.O. Box 2008, Oak Ridge, TN 37831-6197

Introduction

Utilization of biomass for fuel or energy production can reduce our dependence on fossil fuels, and reduce the emissions of CO_2 and other hazardous elements, such as sulfur, lead, and mercury, to the environment. However, pyrolysis, gasification, and combustion of biomass produces polycyclic aromatic hydrocarbons (PAHs),[1] which are environmental pollutants. Nitrogen-containing polycyclic aromatic compounds (N-PACs) can also be formed from pyrolysis of proteinaceous materials found in agriculture and forestry residues (1-25 wt% protein) and in animal waste and sewage (15-30 wt% protein).[2,3] To reduce the formation of PAHs and N-PACs from the thermal processing of biomass, more information is needed on the chemical reactions that lead to these compounds.

In this investigation, the formation of PAHs and N-PACs from the pyrolysis of amino acids and carbohydrates was studied. The low temperature reactions (<350 °C) between amino acids and carbohydrates have been extensively studied.[4] The non-enzymatic browning reaction (i.e., Maillard reaction) leads to a deterioration in the quality of food during storage and cooking (via formation of polymeric brown pigments and volatile compounds).[5] The Maillard reaction is also responsible for the formation of the aroma and flavor of tobacco smoke.[6] However, the high temperature pyrolysis of the intermediates in the Maillard reaction has not been investigated. In this study, the formation of PAHs and N-PACs from the independent pyrolysis of proline and glucose will be compared to pyrolysis of mixtures of proline and glucose and to the pyrolysis of (1-[2'-carboxy)pyrrolidinyl]-1-deoxy-D-fructose), the proline Amadori compound, which is a key intermediate in the Maillard reaction.

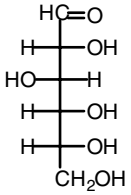

D-Glucose

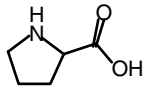

Proline

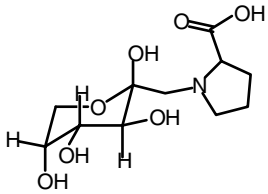

1-[(2'-Carboxy)pyrrolidinyl]-1-deoxy-D-fructose

Experimental

L-Proline (Acros), D-glucose (Acros), acetone (J&W Residue analysis) were used without additional purification. 1-[2'-carboxy)pyrrolidinyl]-1-deoxy-D-fructose was prepared as previously described.[7] Perdeuterated PAHs (phenanthrene-d_{10} and 1,2-benzanthracene-d_{12}) were obtained from Aldrich.

The flow pyrolysis procedure has already been described in detail and will be briefly reviewed.[8] The pyrolysis tube consists of three different sizes of quartz tubing fused together: a 12 in. by 3/4 in. o.d. tube (sublimation chamber) connected to a 19 in. by 0.354 in. o.d. 0.276 in. i.d. tube (the reaction chamber) which tapers to a 1/4 in. o.d. piece of tubing 2 in. long (exit to traps) which terminates with a o-ring sealed ball joint (size 12/5). The pyrolysis tube was connected to two traps by ball joints cooled to 77K. The tip of the entrance tube for the second trap was ca. 1 in. deep into a loosely packed plug of clean glass wool. The glass wool trapped aerosol particles formed at high flow rates (>100 mL min^{-1}). In a typical run, a quartz boat (1 in. x 5/8 in. x 3/8 in.) was charged with a known amount of substrate (typically 200 - 1200 mg) and placed in the 3/4 in. o.d. tube. A glass tube containing a fitting for the introduction of helium and an Ace-Thred adapter was connected to the pyrolysis tube via a 3/4 in. Cajon Ultra-Torr union. Gas flow was controlled by a MKS mass flow controller (either 200 or 1000 mL min^{-1} ± 3% accuracy) and confirmed with a soap bubble meter on the exit of the pyrolysis apparatus (after the cold traps). The residence time in the furnace was calculated from the volume of the reactor (11 mL) in the hot zone (12 in. hot zone with temperature ±2.9 °C at 650 °C), the gas flow rate at room temperature, and a correction for the gas flow rate at the reaction temperature. The sample chamber was heated to 460 °C via an aluminum tube (2.4 in. o.d./2.1 in. i.d. x 6 in long) wrapped with heat tape. The temperature of the reaction chamber was monitored and controlled via two thermocouples next to the sample. The sample was pushed into the sublimation chamber by a glass rod, inserted though the Ace-Thred adapter with an O-ring seal, or by a thermocouple wrapped around the sample boat. The quartz pyrolysis tube was heated by a horizontally mounted three-zone Carbolite tube furnace. The pyrolysis tube was wrapped with a heating tape at the exit of the furnace and heated to ca. 200 °C to prevent condensation of the products. After the pyrolysis, both traps were washed with high purity acetone and the washings were combined (total volume 10-20 mL). Solutions of phenanthrene-d_{10} and 1,2-benzanthracene-d_{12} were added as standards, and the reaction mixtures were analyzed by GC-MS and quantitated by GC-FID (see below) or GC-MS with splitless injection.

Product analysis was performed on a Hewlett-Packard 5890 Series II gas chromatograph equipped with a flame ionization detector, and the identification of products was confirmed by comparison of retention times and mass spectral fragmentation patterns from authentic samples using a Hewlett-Packard 5972A/5890 Series II GC-MS (EI 70 eV). Both instruments were equipped with a J&W DB-5 5% diphenyl-95% dimethylpolysiloxane capillary column (30 m x 0.25 mm i.d. with 0.25 µm film thickness). The injector temperature was 280 ºC, and the detector temperature was 305 ºC. The oven was programmed with an initial temperature of 45 ºC, and the temperature was ramped to 300 ºC at 10 ºC min^{-1} and held for 20 minutes. The carrier gas, helium, was set at a constant flow rate of 1.0 mL min^{-1}. Samples were injected four times onto the GC using a HP 7673 autosampler. Typical shot to shot reproducibility was ±3-5%. The products were quantitated by averaging the GC-FID output relative to the internal standards. Response factors were measured with authentic samples or estimated from measured response factors for structurally related compounds and based on carbon number relative to the internal standards (phenanthrene-d_{10} or 1,2-benzanthracene-d_{12}). The yield of PAHs was also determined by GC-MS analysis from calibration curves of the individual PAHs relative to the deuterated PAH standards in a concentration range of 0.5 to 20 µg mL^{-1}. The limits of detection (LOD) for the PAHs depended upon the complexity of the reaction mixture, but the LOD was typically 20 µg g^{-1} for GC-FID analysis and 0.2 µg g^{-1} for GC-MS analysis with splitless injection.

Results and Discussion

The pyrolysis of proline was initially investigated at 840 °C with a residence time of 10 s (longest possible residence time for the reactor used in this study) to compare the yield of products formed in

previous studies at 850 °C and 840 °C with estimated residence times of 30 s and 10 s, respectively.[9,10] In general, the yield of products agree with those previously reported, except the ratio of isoquinoline to quinoline is low (see Table 1). Isoquinoline has been reported to rearrange to quinoline at 850 °C with a residence time of 13 s, but the conversion was low (2.3%).[11] Thus, it is unlikely that isomerization of isoquinoline is important under these reaction conditions. The 1-[2'-carboxy)pyrrolidinyl] -1-deoxy-D-fructose (i.e., the proline Amadori compound) was pyrolyzed at 840 °C for 10 s, and the yield of phenanthrene and quinoline increased 12 fold and 9-fold, respectively compared to proline. A similar increase in the yield of phenanthrene and quinoline was observed in the pyrolysis of a 1:1 mixture (by wt) of glucose and proline. Clearly, there is a synergistic reaction between the glucose and proline to enhance the formation of PAHs and N-PACs compared to pyrolysis of the individual components.

Table 1. Product Yields from the Pyrolysis of Proline, Glucose, and Proline Amadori Compound

Compound	Proline[9]	Proline[10]	Proline[a]	Glucose[a]	Amadori[a,b]	Proline Glucose[a,c]
Temperature	850 °C	840 °C	840 °C	840 °C	840 °C	840 °C
Time	ca. 30 s	20 s	10 s	10 s	10 s	10 s
Products (mg/g)						
Pyrrole	38.7	27.2	38.9	-	6.7	3.0
Benzene	1.1	1.3	1.6	2.2	8.9	6.2
Benzonitrile	1.0	0.3	1.6	-	1.9	1.7
Quinoline	0.9	0.3	0.3	-	2.6	2.1
Isoquinoline	1.9	1.7	0.09	-	0.6	0.5
Phenanthrene	0.09	NR	0.05	0.10	0.6	0.3
Pyrene	0.09	NR	0.06	0.02	0.2	0.2

[a] This study [b] 1-[2'-carboxy)pyrrolidinyl]-1-deoxy-D-fructose. [c] 1:1 Mixture by weight.

The pyrolysis of the 1-[2'-carboxy)pyrrolidinyl]-1-deoxy-D-fructose, a 1:1 mixture of glucose and proline, glucose, and proline was investigated at 800 °C and 700 °C with a residence time of 1.0 s. For all substrates except proline, char was found in the reactor at 800 °C and in the sublimation boat. The yield of char in the sublimation boat for 1-[2'-carboxy)pyrrolidinyl]-1-deoxy-D-fructose, glucose, and the glucose:proline mixture was 15, 4, and <1 wt%, respectively. The yield (mg product per gram of substrate) of selected products from the pyrolysis of 1-[2'-carboxy)pyrrolidinyl]-1-deoxy-D-fructose is shown in Figure 1. A variety of one to five membered ring PAHs and cyano-substituted PAHs were detected in addition to N-PACs. Molecular ions were also found for products that appeared to be azapyrene (*m/z* 203), azachrysene (*m/z* 229), and azabenzo[a]pyrene (*m/z* 253), but the identity of these products have not been confirmed. A similar slate of products was formed from the pyrolysis a 1:1 mixture of glucose and proline, and PAHs as large as benzo[a]pyrene (0.23 µg/g) and benzo[b,j,k]fluoranthrenes (combined yield 4.6 µg/g) were formed. Pyrolysis of proline or glucose at 800 °C for 1.0 s produced lower yields of PAHs and N-PACs compared to the Amadori compound as shown in Figures 2 and 3. Low yields of benzo[a]pyrene (0.81 and 0.70 µg/g), benzo[b,j,k]fluoranthrenes (0.24 and 2.1 µg/g), and benzo[a]anthracene (0.43 and 3.2 µg/g) were also found in the pyrolysis of proline and glucose, respectively.

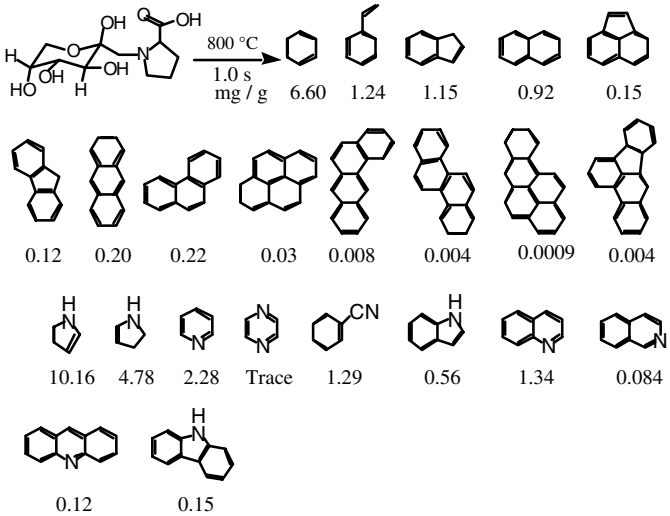

Figure 1. Selected products from the pyrolysis of 1-[2'-carboxy) pyrrolidinyl]-1-deoxy-D-fructose at 800 °C with a residence time of 1.0 s.

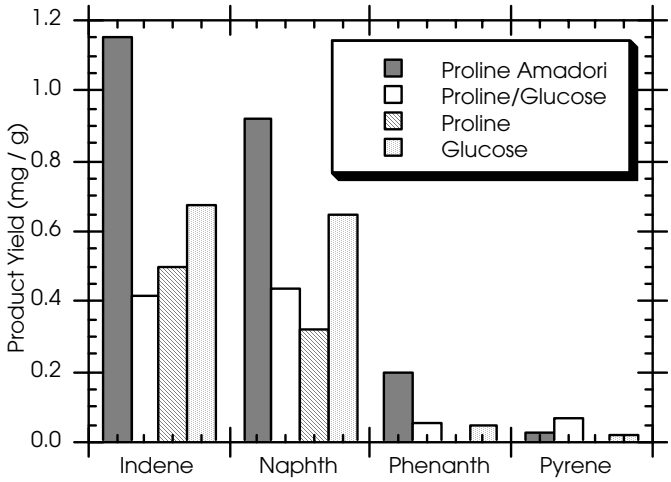

Figure 2. PAH yields from the pyrolysis of 1-[2'-carboxy) pyrrolidinyl]-1-deoxy-D-fructose (Proline Amadori), 1:1 mixture of proline and glucose, proline, and glucose at 800 °C with a residence time of 1.0 s. Naphth and Phenanth is naphthalene and phenanthrene.

Pyrolysis of proline at 700 °C with a 1.0 s residence time only produced single ringed compounds (pyrrole, benzene, styrene, and benzonitrile) and no multi-ringed aromatic compounds. Pyrolysis of 1-[2'-carboxy)pyrrolidinyl]-1-deoxy-D-fructose or a 1:1 mixture of proline and glucose produced significant yields of N-PACs as shown in Figure 4. N-PAC formation was clearly enhanced by the presence of glucose. PAH yields were also enhanced relative proline and glucose as shown in Figure 5.

Conclusions

These experiments clearly showed that glucose increased the formation of N-PACs from the pyrolysis of proline at 700 to 840 °C. PAH yields were also enhanced compared to the independent pyrolysis of proline or glucose. The formation of N-PACs and PAHs from pyrolysis of additional amino acids and carbohydrates is currently under investigation.

Acknowledgment. The authors gratefully acknowledge the financial support from Philip Morris USA. CVO was supported by an appointment to ORNL Postdoctoral Research Associates program administered jointly by Oak Ridge Institute for Science and Education and Oak Ridge National Laboratory.

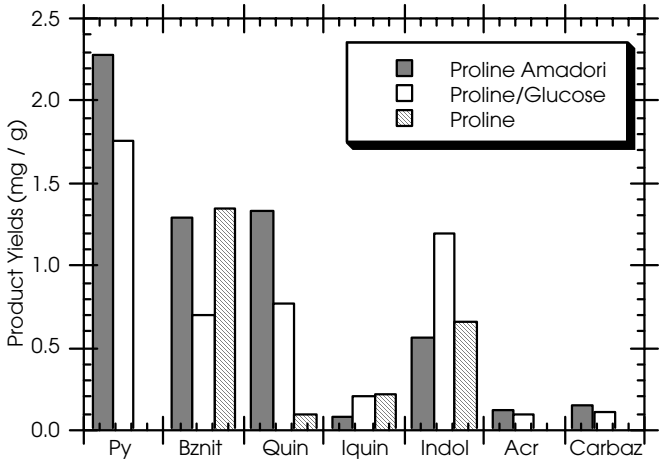

Figure 3. N-PAC yields from the pyrolysis of 1-[2'-carboxy) pyrrolidinyl]-1-deoxy-D-fructose (Proline Amadori), 1:1 mixture of proline and glucose, proline, and glucose at 800 °C with a residence time of 1.0 s. Products include pyridine (Py), benzonitrile (Bznitril), quinoline (Quin), isoquinoline (Isoquin), indole, acridine (Acr), and carbazole (Carbaz).

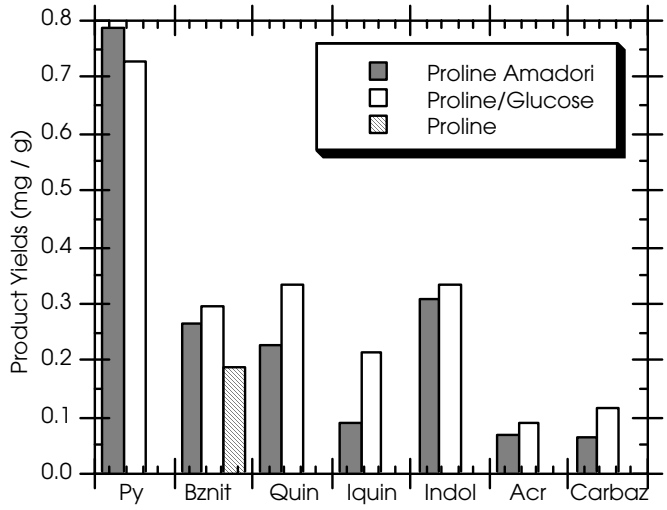

Figure 4. N-PAC yields from the pyrolysis of 1-[2'-carboxy) pyrrolidinyl]-1-deoxy-D-fructose, 1:1 mixture of proline and glucose, proline, and glucose at 700 °C with a residence time of 1.0 s. See Figure 3 for products.

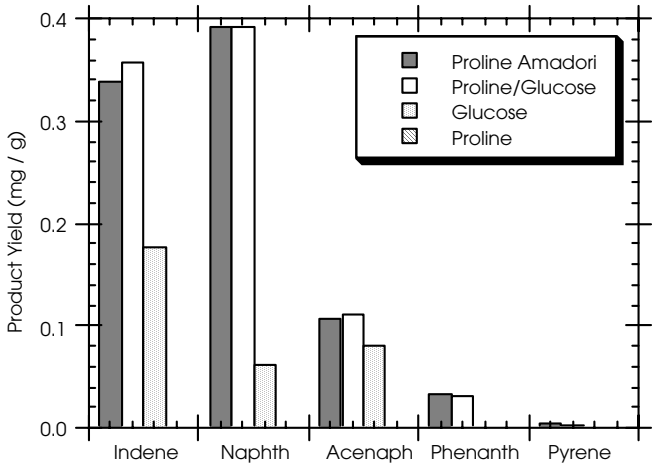

Figure 5. PAH yields from the pyrolysis of 1-[2'-carboxy) pyrrolidinyl]-1-deoxy-D-fructose, 1:1 mixture of proline and glucose, proline, and glucose at 700 °C with a residence time of 1.0 s.

References

(1) (a) *Developments in Thermochemical Biomass Conversion*; Bridgwater, A. V.; Boocock, D. G. B., Eds; Blackie Academics: London, 1997 and references therein. (b) Elliott, D. C. In *Pyrolysis Oils from Biomass: Producing, Analyzing and Upgrading;* Soltes, E. J., Milne, T. A., Eds.; ACS Symposium Series 376; American Chemical Society: Washington, DC, 1988; Chapter 6. (c) *Fundamentals of Thermochemical Biomass Conversion;* Overend, R. P., Milne, T. A., Mudge, L. K., Eds.; Elsevier: Essex, UK, 1985.

(2) (a) Detroy, R. W. In *Organic Chemicals from Biomass;* Goldestein, I. S., Ed.; CRC Press: Boca Raton, Fl, 1981; Chapter 3. (b) Barton, G. M. In *Organic Chemicals from Biomass;* Goldestein, I. S., Ed.; CRC Press: Boca Raton, Fl, 1981; Chapter 11.

(3) For examples see: (a) Patterson, J. M.; Chen, W.-Y.; Smith, W. T., Jr. *Tob. Sci.* **1974,** *18*, 99. (b) Elliott, D. C.; Sealock, L. J., Jr.; Butner, R. S. In *Pyrolysis Oils from Biomass: Producing, Analyzing and Upgrading;* Soltes, E. J., Milne, T. A., Eds.; ACS Symposium Series 376; American Chemical Society: Washington, DC, 1988; Chapter 17.

(4) Huyghues-Despointes, A.; Yaylayan, V. A.; Keyhani, A. *J. Agric. Food Chem.* **1994**, *42*, 2519 and references therein.

(5) (a) *The Maillard Reaction in Foods and Nutrition;* Waller, G. R.; Feather, M. S., Eds.; ACS Symposium Series 215; American Chemical Society: Washington, DC, 1983. (b) *Thermally Generated Flavors: Maillard, Microwave, and Extrusion Processes;* Parliament, T. H., Morello, M. J., McGorrin, R. J., Eds.; ACS Symposium Series 543; American Chemical Society: Washington, DC, 1994.

(6) Leffingwell, J. C. *Rec. Adv. Tob. Sci.* **1976**, *2*, 1.

(7) Yaylayan, V. A.; Huyghues-Despointes, A. *Crit. Rev. Food Sci. Nutr.* **1994**, *34*, 321 and references therein.

(8) (a) Britt, P. F.; Buchanan, A. C., III; Kidder, M. K.; Owens, C. V., Jr.; Ammann, J. R.; Skeen, J. T.; Luo, L. *Fuel* **2001**, *80*, 1727. (b) Owens, C. V., Jr.; Britt, P. F.; Buchanan, A. C., III *Prep. Pap.-Am. Chem. Soc. Div. Fuel Chem.* **2001**, *46*, 264.

(9) Smith, W. T.; Haidar, N. F.; Patterson, J. M. *Tobacco Sci.* **1975**, *19*, 142.

(10) Higman, E. B.; Schmeltz, I.; Schlotzhauer, W. S. *J. Arg. Food Chem.* **1970**, *18*, 636.

(11) Patterson, J. M.; Issidorides, C. H.; Papadopoulos, E. P.; Smith, W. T., Jr. *Tetrahedron Lett.* **1970**, 1247.

BIOMASS PYROLYSIS CHEMISTRY AND GLOBAL KINETICS AT HIGH HEATING RATES

David C. Dayton[a], Alexander L. Brown[a,b], and John W. Daily[b]

[a]National Renewable Energy Laboratory, National Bioenergy Center
1617 Cole Boulevard, Golden, CO 80401 USA
[b]University of Colorado-Boulder,
Department of Mechanical Engineering, Boulder, CO 80309 USA

Introduction

The initial step of biomass thermal conversion involves the primary decomposition of the lignocellulosic matrix that is composed of three interconnected polymeric materials: cellulose, hemicellulose, and lignin. Pyrolysis mechanisms typically include a superposition of the kinetic mechanisms for the individual components of the biomass material. The validity and development of these mechanisms is currently of interest [1-3]. A graphical summary of two global biomass pyrolysis models [1,3] at the experimental conditions of this study is presented in Figure 1.

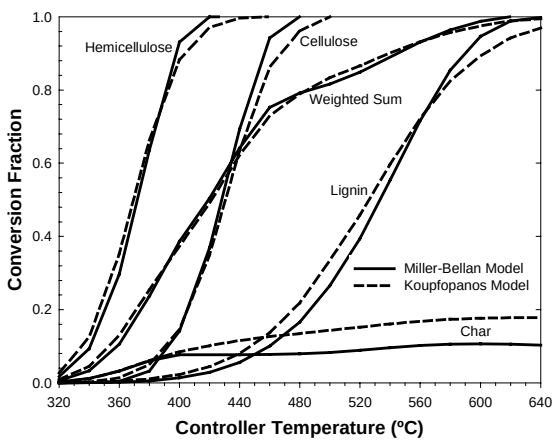

Figure 1. Predictions of the Miller-Bellan (solid) [1] and Koufopanos et al. (dashed) [3] global biomass pyrolysis models at the LEFR reaction conditions.

Experimental Methods

A new continuous feed, laminar entrained flow reactor (LEFR) was recently built and characterized [4] for determining biomass pyrolysis kinetics, gasifier tar production rates, and alkali metal release rates. This reactor is capable of heating rates on the order of 10^3-10^5 K/s, typical of those found in developing gasifiers and in industrial boilers. This reactor is coupled to a molecular beam sampling mass spectrometer (MBMS) system to follow the chemistry of the gas phase products as they evolve during biomass thermochemical conversion processes.

To quantitatively determine biomass pyrolysis kinetics, it is important to understand in detail the many complex physical and chemical processes that a reacting particle undergoes from beginning to end in the reactor. This was the goal of a previous characterization study of the LEFR [4] in which a combination of measurements and theoretical modeling contributed to the detailed understanding of the operating qualities of the reactor. Computational Fluid Dynamics (CFD) simulations were employed to model particle trajectories and residence times and calculate gas temperature profiles. The CFD models included boundary conditions based on measured quantities (e.g. wall temperatures and gas flow rates) so credible time-temperature profiles for particles could be calculated and used in kinetic models to determine global pyrolysis rates. Temperatures are referred to herein by the furnace temperature controller setting at which data were collected, however, it is important to realize that under set reactor conditions the particles actually undergo a specific time-temperature history [4,5].

The results of the LEFR characterization study [4] indicate it is possible to maintain kinetic, rather than heat transport control and to minimize particle velocity lag in the reactor with small (<50 μm) particles. These guidelines were followed during an investigation of global cellulose pyrolysis kinetics [5]. In this paper we build on these initial pyrolysis studies and investigate pine (*pinus radiata*) pyrolysis kinetics, a NIST standard biomass material [6]. The LEFR pyrolysis kinetic measurements for three other NIST standards; sugarcane bagasse, poplar (*populus deltoids*), and wheat straw can be found in the references [7].

Experimental results

The pine pyrolysis mass spectra contained mass peaks commonly associated with cellulose pyrolysis products [5]. Low temperature lignin products were also identified in the pine pyrolysis mass spectra by large peaks that correspond to the lignin precursors (p-coumaryl alcohol, m/z = 150; coniferyl alcohol, m/z = 180; synapyl alcohol, m/z = 210). Higher molecular weight species with m/z = 272, and several species above m/z = 300, were also observed and are associated with lignin decomposition [8].

The pine pyrolysis mass spectra, recorded over a range of temperatures, were analyzed by multivariate analysis to group spectral elements that behave in a similar fashion and to provide a concise and reproducible method for representing a complex and extensive set of mass spectral data. This type of analysis performed on previous batch experimental results suggest that there are three distinct pyrolysis product groups (e.g. Evans and Milne, [8]). Based on the superposition theory for global biomass pyrolysis, distinct pyrolytic product groups should be evident in the primary pyrolysis products as suggested by Figure 1.

Multivariate analysis revealed four principal components that described most of the variance (~95%) in the pine pyrolysis mass spectra. Often, a challenge with multivariate analysis techniques is assigning physical and chemical significance to the statistical relationships that are resolved. Associating the peaks identified in the reconstructed Factor Spectra, shown in Figure 1, from the pine pyrolysis mass spectral data can help to interpret the chemical nature of the four principal components.

The Primary Lignin component spectra includes all the mass peaks above m/z = 150. Most of these masses correspond to the products associated with primary lignin pyrolysis products. However, lower molecular weight species are also included in this component suggesting that pyrolysis products from other lignocellulosic constituents may be grouped in the Primary Lignin factor as well. Peaks at m/z = 73, 85, and 114 are prominent in the Primary Lignin factor spectra and the bulk of the variance of m/z = 144 is attributed to this factor. These lower molecular weight peaks are generally assigned to polysaccharide pyrolysis products. Therefore, while this factor is named "Primary Lignin," the contribution from pyrolysis products of other lignocellulosic components is not completely separated.

The most dominant peak in the Tertiary factor at m/z = 28 is assigned to CO^+ but may have minor contributions from N_2^+ and $C_2H_4^+$. The peak at m/z = 26 is assigned to acetylene ($C_2H_2^+$). Methane is a commonly recognized biomass pyrolysis product and is assigned to the peak at m/z = 16. Benzene and naphthalene are assigned to the peaks at m/z = 78 and m/z = 128, respectively. These aromatic hydrocarbons are thermally stable and tend to evolve from hydrocarbons under high severity pyrolysis. The peak at m/z = 44 is assigned to CO_2^+ but could involve contributions from $C_3H_8^+$, and

$C_2H_4O^+$ as acetaldehyde or ethenol. Minor peaks at m/z = 92 and 94 in all Tertiary factor spectra are assigned to toluene ($C_7H_8^+$) and phenol, $C_6H_6O^+$. The identified products in the Tertiary factor are all considered tertiary biomass pyrolysis products [8]. The factor score plots (see Figure 3) show that scores of the Tertiary factor are low at low reaction temperatures, but increase with increasing pyrolysis severity, as is expected with the tertiary products.

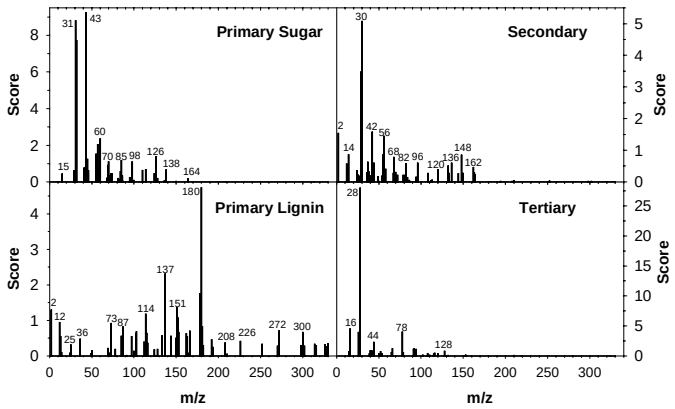

Figure 2. Factor spectra from the pine pyrolysis experiments based on the four-component analysis of the LEFR mass spectral data.

The Primary Sugar factor contains intense peaks at m/z = 32 and 31 assigned to methanol (CH_4O^+ and CH_3O^+). Electron impact or thermal fragments of levoglucosan ($C_6H_{10}O_5$) are assigned to peaks at m/z = 57, 60, 73, and 98. The peak at m/z = 126 is assigned to 5-(hydroxymethyl)-2-furfural, a common polysaccharide pyrolysis product. Other products may also contribute to the signal at m/z = 126. As discussed above, some of the lower molecular weight peaks associated with the Primary Lignin factor are also common to the Primary Sugar factor.

The Secondary factor contains prominent peaks at m/z = 30 (formaldehyde), m/z = 42 (ketene), m/z = 56 (butene or 2-propenal), m/z = 68 (furan), m/z = 82 (2-methylfuran), and m/z = 96 (furfural). A variety of phenolic compounds can be associated with peaks at m/z = 94, 108, 120, 122, and 148. Levoglucosan has a molecular weight of 162 and it is tempting to assign the observed peak to the parent ion, however, it may likely result from a higher molecular weight phenolic compound. These compounds are generally identified as secondary products that form by the gas phase decomposition of larger primary pyrolysis products [8].

Discussion and Conclusions

Factor scores determined from the pyrolysis mass spectra recorded for each of the four NIST biomass samples can be found elsewhere [7]. The variation of the average factor scores as a function of furnace controller temperature for pine pyrolysis is plotted in Figure 3. The Primary Lignin scores are highest at the lowest temperatures (~340ºC), which suggests that the measured relative contribution of lignin is highest at the earliest stages of pyrolysis. The model predictions for lignin pyrolysis indicate that lignin does not start reacting until the controller temperatures are set to 400ºC. At furnace controller temperatures of 500ºC -520ºC, the models predict 50% lignin conversion. Clearly, the models predict that lignin reacts much slower than is suggested by the LEFR data. These discrepancies are not completely surprising, as testing of these models with data at high heating rates has been minimal.

It is more difficult to comment on the model predictions of polysaccharide pyrolysis because the multivariate analysis of the pine mass spectral data does not clearly resolve separate contributions from hemicellulose and cellulose pyrolysis. The pyrolysis models are a good representation of the pyrolysis regime studied in the LEFR experiments if the hemicellulose and cellulose fractions are combined into a single component in the models that gives rise to "primary sugars" as measured in the experiments.

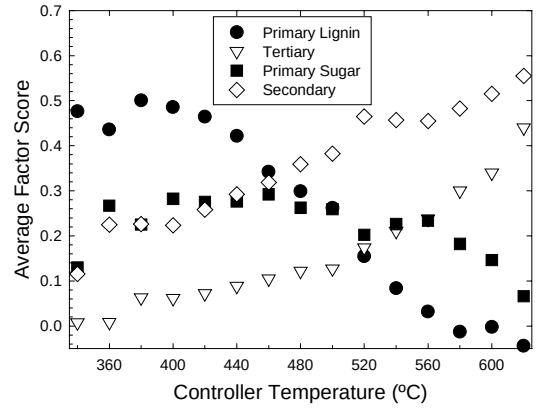

Figure 3. Factor scores from the pine pyrolysis experiments based on the four-component analysis of the LEFR mass spectral data.

If in fact hemicellulose and cellulose react as predicted by the two global biomass pyrolysis models, there should be distinctive pyrolysis regimes where hemicellulose contributes to the polysaccharide signals at the lowest temperatures and the cellulose pyrolysis products begin to form at higher temperatures. The models predict that 50% of the hemicellulose should have reacted as the cellulose begins to react (360ºC -380ºC in the models). The multivariate analysis of the pyrolysis mass spectral data did not clearly suggest a statistically important distinction between these two components. It is not clear from the experiments whether this is because hemicellulose and cellulose do not react in separate regimes, or because the pyrolysis products are so similar there is no mass spectral difference between early and late polysaccharide pyrolysis products. The peaks associated with polysaccharide pyrolysis products that were resolved in the Primary Lignin factor could be indicative of a cellulose/hemicellulose distinction. More detailed information is necessary before this can be confidently determined.

References

1. Miller, R.S.; and Bellan, J. *Combust. Sci. Tech.* **1997** *126,* 97-137.
2. Di Blasi, C.; and Russo, G. In *Advances in Thermochemical Biomass Conversion vol. 2* A.V. Bridgwater, Ed., Blackie Academic and Professional: New York 1994; pp. 906-921.
3. Koufopanos, C.A.; Maschio, G.; and Lucchesi, A. *Can. J. Chem. Eng.* **1989** *67,* 75-84.
4. Brown, A.L.; Dayton, D.C.; Nimlos, M.; and Daily, J.W. *Energy Fuels* **2001** *15,* 1276-1285.
5. Brown, A.L.; Dayton, D.C.; and Daily, J.W. *Energy Fuels* **2001** *15*, 1286-1294.
6. Milne, T.A.; Chum, H.L.; Agblevor, F.; and Johnson, D.K. *Biomass Bioenergy* **1992** *2(1-6)*, 341-366.
7. Brown, A.L. 2001. A Chemical and Kinetic Study of Cellulose and Biomass Pyrolysis at High Heating Rates. Ph.D. Dissertation, University of Colorado at Boulder.
8. Evans, R.J.; and Milne, T.A. *Energy Fuels* **1987** *1*, 123-137.

HEAT TRANSFER CONTROLLED PYROLYSIS OF CELLULOSICS

Eric M. Suuberg and Ivan Milosavljevic

Division of Engineering
Brown University
Providence, RI 02912 USA
Tel. (401) 863-1420, Fax (401) 863-1157
email: eric_suuberg@brown.edu

INTRODUCTION

The thermal decomposition of cellulosic solids has been extensively studied. There have been numerous reviews of various aspects of the problem (e.g., pyrolysis[1-3], modeling of combustion [4, 5]). In recent papers, we have described new results on the global kinetics of cellulose pyrolysis [6-8], suggesting that these are heating-rate dependent because of the role that mass transfer can play in the process [8]. There continues to be considerable debate regarding the kinetics of pure cellulose pyrolysis [e.g., 9,10]. When adding uncertainties regarding the role of transport processes [11] and secondary reactions, the modeling of the processes remains problematic. We have previously presented a number of results from a study in which the behavior of cellulose samples has been examined under simulated fire-level heat fluxes [12]. In this paper, further experimental results are considered,.

The present study is concerned with bulk cellulose pyrolysis under conditions simulating those of a fire, but which are also relevant to any system in which cellulosics undergo pyrolysis. The experiments were carried out in an inert gas environment. The material studied here was "pure" cellulose, selected to produce "realistic", but highly reproducible samples. Samples were pressed to densities typical of those encountered with wood. There have been many other studies of cellulosic pyrolysis of large cellulosic particles [e.g., 12-25]. Some have noted a well-defined pyrolysis front [13-17] and a period of relatively constant mass loss rate [16, 17, 20, 23, 25], particularly with high imposed radiative fluxes. Generally, the data revealed a significant sensitivity to char thermal conductivity [21]. The effects of oxygen [19] and retardants [23] can also be significant in affecting observed behavior.

EXPERIMENTAL

Materials

The cellulose studied in this work was Whatman CF-11 powder, with an ash content of 0.009% and a moisture content of 7.68% (as-received). Powder samples were formed into pellets using an ordinary laboratory press, without any additives. Three different density samples were prepared: 0.965±0.041 g/cm3, 0.691±0.035 g/cm3 and 0.458±0.026 g/cm3. These densities are comparable to those of woods ranging from softwoods to hardwoods. All pellets were 38 mm in diameter and had a thickness of up to about 10 mm.

Radiative Pyrolysis Apparatus

The experimental setup has been described earlier [12]. Briefly, a nitrogen purged pyrolysis chamber houses the sample, whose front surface is heated by quartz lamps. The sample is held inside a ceramic insulator, placed atop an electronic balance. The two tungsten filament heaters supply a constant incident heat flux of 20-60 kW/m^2, and deliver radiation in wavelength range simulating a flame at 1700 K. This is important because the wavelength range of the delivered radiation has a significant impact on the surface reflectivity [11]. Temperature measurements were made within the cellulose using chromel-alumel thermocouples (0.5 mm diameter), positioned at different distances from the sample

RESULTS AND DISCUSSION

Influence of Sample Density on Mass Loss and Temperature Profiles

After turning on the radiant heaters, the sample mass was monitored continuously until a time at which no additional mass loss was observed. Figure 1 shows typical mass loss results for three different density samples, irradiated with a 40 kW/m^2 surface flux. An early heating period (< 500 s) involves little mass loss, except for a small amount of residual moisture. This is followed by active pyrolysis, indicated by the loss of sample mass as, approximately, a linear function of time during much of the period. This indicates a pyrolysis front moving with near-constant propagation velocity into the solid. The result seen here is consistent with those of many above-cited studies, involving constant (high) incident heat flux.

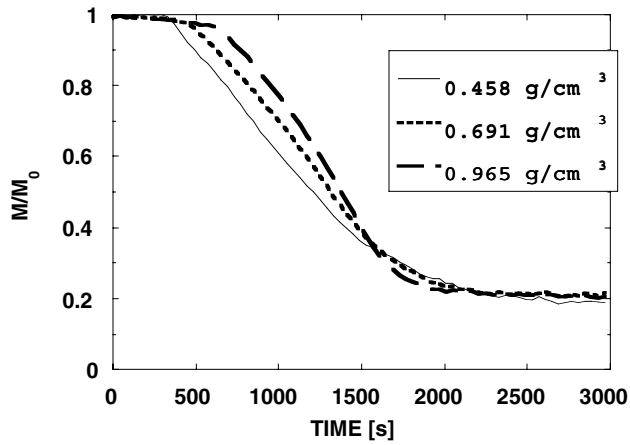

Figure 1. Fractional mass loss from cellulose of 0.458 g/cc (solid line) 0.691 g/cc (dotted line) and 0.965 g/cc (dashed line).

The point of pyrolysis onset depends on sample density. It can be seen from Fig. 1 that the lower the sample density, the earlier pyrolysis starts. The lower density sample behaves as a better "insulator". Its front surface temperature rises faster, which results in an earlier onset of pyrolysis.

The above explanation is made clearer by reference to the sample temperature profiles. Figure 2 shows the temperature history of different thermocouples within the highest density (0.965 g/cm^3) samples, under the conditions as shown in Figure 1. The temperature profiles indicate clearly that the sample loses heat from its back face, and at the time the mass loss reaches near zero rate, a nearly constant temperature profile has been achieved throughout the sample. The final temperature of the back face of the sample is sufficiently low such that some further pyrolysis could be possible, if the temperature were to be raised. This fact should be noted in considering the long-time char yield of Fig. 1. Thus in any such bulk sample experiment, the char yield is operationally defined as the fractional mass left after the mass loss ceases under given conditions. It can, however, be seen from Fig. 1 that the char yield, about 20%, averaged over the entire sample,

is not a very strong function of initial sample density. The particular cellulose used here gives char yields of about 5% or less, when examined in an ordinary thermogravimetric experiment at comparable heating rates [7].

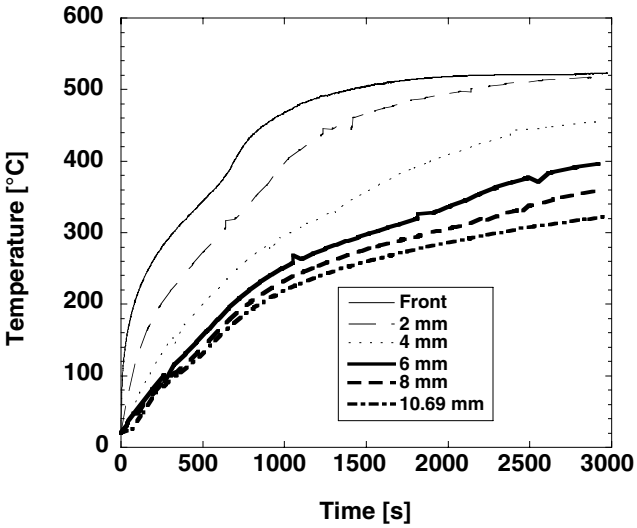

Figure 2. Temperature profiles in a 0.965 g/cc sample subject to a nominal surface flux of 40 kW/m^2.

The effect of sample density on front and back surface temperatures is shown in Figure 3. The better the insulating properties of a sample, the larger the temperature gradient that it will support. These results confirm that sample conductivity increases with density, as has been independently shown [11].

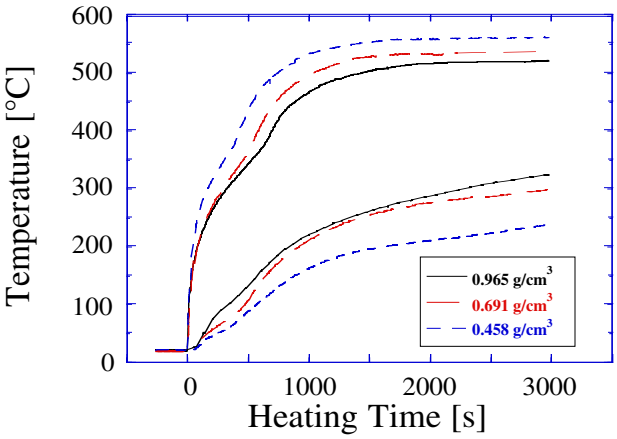

Figure 3. Sample front (top curves) and back face temperatures for nominal 40 kW/m^2 irradiation.

The front surface temperature-time profile always shows an inflection point at around the pyrolysis onset temperature. The reason for this is that as cellulose decomposes, material properties (surface emissivity and thermal conductivity) change [11], and a reaction endotherm occurs [7].

The mathematical modeling of this process has demonstrated that the actual absorbed surface fluxes are much lower than the nominal incident surface fluxes. When taking this into account, it is possible to model the propagation of the thermal wave implied in Figures 2 and 3 quite well. There are large contributions from reflective loss, convective loss, re-radiation and volatiles screening of the incident radiation. The endothermic nature of pyrolysis plays a relatively minor role in determining the thermal behavior.

Experimentally, the observed total mass loss behavior is quite similar in wood and cellulose. This is not particularly surprising, insofar as a conduction-limited pyrolysis process depends only upon the thermal conductivity and thermal diffusivity of the materials, which in this case are quite similar. Where the influence of the starting materials is strongest is in the nature of the volatile products.

The final char yield is a strong function of distance into the char pellet, despite the similarity of average yields at different densities (as noted in Fig. 1). This difference is only partly attributable to the temperature gradient noted above. There is an influence of in-depth cracking of volatiles. The char yield from within 2 mm of the surface was around 10%, whereas the yield near 4 mm was 20% and at 8 mm over 30%.

References

1. Antal, M.J. Jr., in *Advances in Solar Energy,* (K. Boer and J. Duffie, Eds.), American Solar Energy Society, 1982, Vol.1, p. 61.
2. Antal, M.J. Jr., in *Advances in Solar Energy*, (K. Boer and J. Duffie, Eds.), American Solar Energy Society, 1985, Vol.2, p. 175.
3. Antal, M.J., Jr. and Varhegyi, G., *I&EC Res.,* 34:703-717 (1995).
4. Di Blasi, C., *Prog. Energy Comb. Sci*, 19:71-104 (1993).
5. Ohlemiller, T., *Prog. Energy Comb. Sci*, 11:277-310 (1985).
6. Milosavljevic, I.., Suuberg, E.M., *I&EC Res.,* 34:1081 (1995).
7. Milosavljevic, I. , Suuberg, E.M., *I&EC Res.,* 35:653 (1995).
8. Suuberg, E.M., Milosavljevic, I. and Oja, V., *26th Symp. (Int.) on Combustion,* The Combustion Institute, 1996, pp 1515-1521.
9. Reynolds, J.G. , Burnham, A.K. *Energy and Fuels,* 11:88-97 (1997).
10. Gronli M, Antal MJ and Varhegyi G, *I&EC Res.* 38: 2238-2244 (1999).
11. Suuberg, E.M., Aarna, I., and Milosavljevic, I., in *Progress in Thermochemical Biomass Conversion*, A.V. Bridgwater, Ed., Blackwell Science, Oxford, UK, 2001, pp. 1246-1258.
12. Milosavljevic, I. and Suuberg, E.M., *ACS Div. Fuel Chem. Prepr.*, 37(4):1567-1571 (1992).
13. Kanury, M. A. and Blackshear, P.L., *Pyrodynamics* 4:285-298 (1966).
14. Blackshear, P.L., Jr., and Kanury, M.A., *10th Symp. (Int.) on Combustion*, The Combustion Institute, Pittsburgh, 1965, pp. 911-923.
15. Kanury, M.A. , Blackshear, P.L., Jr. *Comb. Sci. Tech.*, 1:339-355 (1970).
16. Lee, C.K., Chaiken, R.F. and Singer, J.M., *16th Symp. (Int.) on Combustion*, The Combustion Institute, Pittsburgh, 1976, pp. 1459-1470.
17. Lee. C.K. and Diehl, J.R., *Comb. Flame*, 42:123-138 (1981).
18. Ohlemiller, T.J., Kashiwagi, T. , Werner, K., *Comb. Flame*, 69:155-170 (1987).
19. Kashiwagi, T., Ohlemiller, T.J., Werner, K., *Comb. Flame*, 69:331-345 (1987).
20. Becker, H.A. and Phillips, A.M., *Comb. Flame*, 58:255-271 (1984).
21. Chan, W.-C., Kelbon, M.,, Krieger, B.B., *Fuel,* 64:1505 (1985).
22. Chan, W.-C., Kelbon, M.,, Krieger, B.B.. *I&EC Res.,* 27:2261 (1988).
23. Chen, Y., Frendi, A., Tewari, S.S., and Sibulkin, M., *Comb. Flame*, 84:121-140 (1991).
24. DiBlasi, C., Gonzalez-Hernandez, E., Santoro, A., *I&EC Res.,* 39:873-882 (2000).
25. DiBlasi, C., Branca, C. and Santoro, A., in *Progress in Thermochemical Biomass Conversion*, A.V. Bridgwater, Ed., Blackwell Science, Oxford, UK, 2001, pp. 1143-1157.
26. Milosavljevic, I., Ph.D. Thesis, Division of Engineering, Brown University, 1994.

ENHANCED WOOD FUELS VIA TORREFACTION

Edward S. Lipinsky, James R. Arcate, and Thomas B. Reed

Innovative Thinking, Inc.
6481 Bellbrook Place
Worthington, OH 43085-2988

Introduction

There is a pressing need for better biomass fuels. Raw biomass has a relatively low energy density, contains too much moisture, is too hygroscopic, can rot during storage, and is difficult to comminute into small particles. This paper presents a technology that has the potential to ameliorate many or all of these deficiencies. It is a form of thermal processing known as "torrefaction".

Torrefaction occurs during the heating of biomass between 200 C and 280 C in thermogravimetric analysis (1). Serious consideration of development of this process as a source of fuels, chemicals, and materials began with the work of Bourgeois in the 1980's (2). Pechiney used torrefied wood as a replacement for charcoal in production of metals from metal oxides (3). Work on related processes that are not directed to fuel and chemical products continues, especially in France and Finland (4,5).

Torrefaction achieves an equilibrium moisture content of 3%, reduction of mass by 20 to 30% (primarily by release of water, carbon oxides, and volatiles) while retaining 80% to 90% of the wood's original energy content as shown in Table 1 and 2. (2)

Table 1. Characteristics of Torrefied Maritime Pine

Species	Maritime Pine
Temperature reached (° C)	280
Yield (on bone dry wood)*	77%
Characteristics of torrefied woods	
High calorific value (bone dry)	
Kcal/kg	5,710
KJ/kg	23,900
Ashes %	0.55
Volatiles %	71.9
Fixed Carbon %	27.7
Elementary Analysis	
C %	59.7
H %	5.6
N %	0.25
O %	32.9

Table 2. Mass & Energy Yields

Species	Maritime Pine
Low calorific value of bone dry wood (kJ/kg)	19,150
Low calorific value of torrefied wood (kJ/kg)	22,600
Yield by weight %	77
Energetic Yield %	90.8

The lignocellulosic biomass feedstock is typically predried to 10% or less moisture content prior to torrefaction. Particle thickness plays an important role in torrefaction in that this parameter determines the duration of the process, given a specific heating rate. We believe that the reaction mechanisms and kinetics are different for thin (wood chips) and thick particles (wood chunks). The chemical reactions that occur when reactive intermediates are trapped in a thick matrix differ from the situations in which products can escape and be swept away in a gas stream. The duration of torrefaction processing is adjusted produce friable, hydrophobic and energy-rich Enhanced Wood Fuels (EWF). The products of both types of reactions are hydrophobic, friable, and energy-rich fuels.

Results and Discussion

Chemistry. The chemistry of torrefaction is influenced by many parameters, including: biomass composition; particle size; processing temperature and time; heating rate; and gas composition, pressure, and flow rate. In the temperature range of 220 C to 280 C, the major decomposition reactions concern hemicellulose. Cellulose also can undergo similar polymer restructuring. Cellulose and lignin also undergo depolymerization reactions, but to a lesser degree.

Commercially available dynamic simulation software (STELLA®, from High Performance Systems, Inc.) was employed to model the reactions of biomass. The model contains modules for hemicellulose, cellulose, lignin, and biomass. Here, we discuss the hemicellulose module of the model (Figure 1).

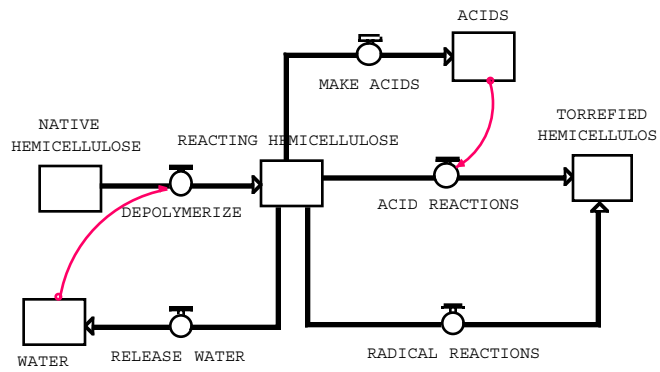

Figure 1. Dynamic simulation model of hemicellulose torrefaction.

The flow sheet shows stocks of hemicellulose, torrefied hemicellulose, water, and acids. The pipes show the flow of materials from starting material to products. The 'wires" show transfer of information.

During thermolysis, native hemicellulose is partly depolymerized by hydrolysis and/or thermal chain scission to provide "reacting hemicellulose". This intermediate is decomposed by acid and radical reactions to yield many substances (e.g., furfural) that recombine to form torrefied hemicellulose. Water and acids are formed during the above reactions and are released into the reaction environment (6). Some of this water may be reused to depolymerize hemicellulose or to release acids from the hemicellulose by hydrolysis of acetate groups. Acids can also be formed by radical reactions.

The water and acids released by hemicellulose become available to depolymerize cellulose and lignin. Wooten (7) and Pastorova (8) have demonstrated that microcrystalline cellulose can form "disordered pyrolytic cellulose" that is a 3-dimensional polymer at about 270 C. If the cellulose is exposed to acids and radicals that originate with hemicellulose, even more degradation of cellulose would be expected. This disordered cellulose is thermostable and contains furan, aliphatic, and keto groups. Evans, et.al. have shown that lignin releases some small phenolic

fragments within the temperature range of torrefaction (9). There also are opportunities for grafting of torrefied hemicellulose onto cellulose and/or lignin. Thus, all of the lignocellulose polymers can participate in torrefaction.

Process description. Because water can play a significant role in torrefaction, the potential effects of added water (in the form of superheated steam or saturated steam) merit investigation. Figure 2 shows a generalized process schematic of such a process.

Raw lignocellulosic biomass is predried to less than 10% moisture using superheated steam (SHS). SHS has a much higher heat capacity than does hot air or nitrogen. Steam also provides an airless drying environment that reduces yield losses from oxidation.

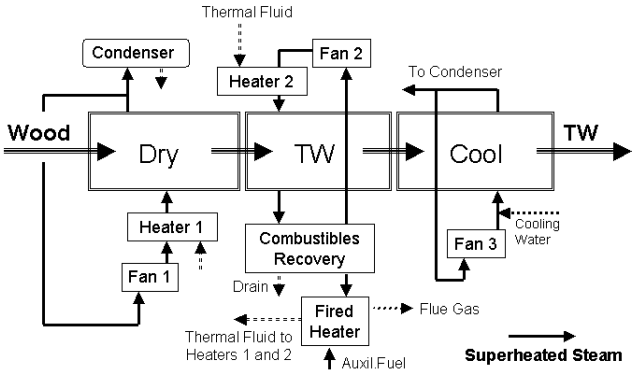

Figure 2. Enhanced Wood Fuels Production Process

Both batch and continuous reactors have been used to produce torrefied wood. We prefer a continuous reactor using superheated steam at atmospheric pressure to dry and torrefy the wood feed. Torrefaction is, on balance, endothermic and releases water, acetic acid, carbon dioxide, carbon monoxide, and other volatiles. This local cooling effect needs to be counteracted. The reaction temperature is closely monitored and controlled. To avoid possible runaway exothermic conditions the torrefaction temperature reaction will not be allowed to exceed 280 C.

Steam containing wood acids and other volatiles is vented from the reactor continuously. This stream is condensed for recovery of acids and combustible volatiles or for waste treatment and disposal purposes.

The EWF is cooled to a safe unloading temperature. The specific properties of the final EWF product may vary depending on the cooling procedure because the hot EWF contains free radicals (10).

EWF can be used in cofiring with coal in electric power plants. Alternatively, EWF can be used in manufacturing fuel pellets and briquettes. Densifying EWF will produce energy-rich, transportable fuels with good properties for outdoor storage.

Cofiring with Coal at Power Plants. Cofiring involves substituting biomass fuels for a portion of coal in an existing power plant furnace. This allows the energy in biomass to be converted to electricity with the high efficiency (in the 33% to 40% range) of a modern coal-fired power plant. Table 3 presents examples of various levels of EWF cofiring.

Table 3. Cofiring TW with Coal in PC Power Plants

EWF tonnes per year	GWh/year	Mwe @ 7000h
30,000	75	12
60,000	150	25
90,000	225	37
120,000	300	49

Compared to the coal it replaces, biomass reduces sulfur dioxide (SO2), nitrogen oxides (NOx), and net greenhouse gas emissions of CO_2.

Cofiring EWF is more attractive than using raw biomass such as wood chips because EWF is friable and can be blended, pulverized and co-fired with coal. The capital and operating costs for separate biomass fuel feed and firing systems are avoided.

Densification. The mass density of EWF pellets is about 23kJ/Kg, compared with 19.3 kJ/Kg for conventional pine wood pellets. Densification of EWF to a volume energy density of about 18 GJ/m^3 can be attained by pelletization. Although this is less than coal (29 GJ/m^3), it is 20% higher than commercial wood pellets. In addition, less than half as much electricity is consumed making EWF pellets. A study for the Pellet Fuel Institute (11) indicated that electricity costs are about $10/ton of wood pellet product. These data are based on old experiments. There are methods for increasing the energy value and reducing further the energy costs of EWF pellets (12).

Densified EWF products have good prospects for use in pellet stoves in residential and commercial heating markets. The size of this market is more than 700,000 tons/year in the United States (13). EWF also could be briquetted or used to make HeatLogs® analogs. This segment of the domestic fuel market is larger than the pellet market. The fireplace log market has special requirements for sustained burning and flame quality because it is frequently a recreational fuel, rather than a utilitarian fuel.

Conclusions

Torrefaction provides fuels that are rich in energy, low in moisture content, resistant to weathering, and easily pulverized or densified. Although these are good features, we must also consider the challenges that confront EWF developers.

The European pioneers in torrefaction have abandoned fuel markets and modified the process so that they can focus on furniture and construction markets. The first major **challenge** in development of EWF is to find and develop viable fuel markets. An example of a potentially viable opportunity is conversion of the wood pellet industry into a torrefied wood pellet industry. This is a matter of inserting torrefaction into an existing enterprise that already has a raw material supply, predrying equipment, and marketing channels. This is much cheaper than a "green field" venture. Another example is the cofiring of EWF with coal to improve environmental performance.

The thermal technology for torrefying biomass uses moderate temperatures in the range of 220 C to 280 C. Traditional torrefaction technology required many minutes for completion of the reactions. However, slowness is not an inherent feature of torrefaction. The major processing **challenge** is to create processes that reduce the processing time to a desirable degree. The superheated steam torrefaction process discussed here may be a successful example.

The chemical reaction mechanisms and kinetics that are at the foundation of torrefaction are complex and not well understood. The problems arise from the interaction of both acids and free radicals with the polymers that comprise lignocellulose. The major **challenges** here are to devise experiments that distinguish acid-catalyzed reactions from radical reactions and to

apply to torrefaction reactions some of the methods used in elucidating radical reaction pathways in hydrocarbon cracking. Modeling can help in thinking about the system, but usable experimental data are essential for progress in this activity.

References

(1) Gaur, S., and Reed, T., Thermal Data for Natural and Synthetic Fuels, Dekker, New York, 1998.

(2) Bourgeois, J., and.Guyonnet,R, in Bioenergy 84, Volume III, edited by H. Egneus, Elesevier, 1985, pp. 153-159.

(3) Girard,P., and Shah, N. , Recent Developments on Torrefied Wood, an Alternative to Charcoal for Reducing Deforestation. FAO/CNRE Workshop, Norway 1989, pp. 101-114.

(4) Dirol, D., and Guyonnet,R, Report to 24th Annual Meeting of The International Research Group on Wood Preservation, Stockholm, 1993.

(5) Viitaniemi,P.; Jamsa , S., Ek; P., Viitanen, H., U.S. Patent 5,678,324, October 21, 1997

(6) Bourgeois, J. and Guyonnet,R., Wood Sci. and Tech., **22**, 143-155, (1988); and **23**, 303-310, (1989).

(7) J. Wooten, et.al., Fuel Chemistry Division Preprints, 46 (1), 191 (2001).

(8) I. Pastorova, et.al., Carbohy. Res., **248**, 151-165 (1993) and, **262**,27-47 (1994).

(9) Evans, R.A., Milne,T.A.,Soltys,M.N., J. Anal.Appl.Pyrolysis **9** (1986) 207-236.

(10) Shafezadeh, F., in Fundamentals of Thermochemical Biomass Conversion, ed. by Overend, Elsevier, New York, 1985, p.183-217.

(11) NEOS Corporation., Wood Pelletization Sourcebook, 1995,available from Pellet Fuel Institute.

(12) Reed, T. B., Trezek, G. and Diaz, L., in "Thermal Conversion of Solid Wastes", J. L. Jones and S. B. Radding, ACS Symposium Series 130, Was D.C. pp 169-177, 1980.).

(13) Pellet Fuel Institute Annual Survey, 2000-2001 (available from Pellet Fuel Institute).

EFFECTS OF RESTRICTED MASS TRANSPORT ON THERMOLYSIS OF LIGNIN MODEL COMPOUNDS

A. C. Buchanan, III, Phillip F. Britt, and Michelle K. Kidder

Chemical Sciences Division
Oak Ridge National Laboratory
Bethel Valley Road
P.O. Box 2008, MS-6130
Oak Ridge, Tennessee 37831-6130

Introduction

Lignin is a renewable resource whose complex structure, chemical and thermal reactivity, and potential for use in a variety of commercial products continues to draw considerable attention.[1,2] Our research has been focusing on the thermolysis mechanisms of model compounds that represent structural elements in native lignins (e.g. β-O-4 and α-O-4 aryl ether linkages)[1a] and in processed lignins (e.g. diphenylmethane linkages from acidic or alkaline treatments in pulping).[1b,c]

We studied in detail the pyrolysis mechanism of phenethyl phenyl ether ($PhCH_2CH_2OPh$, PPE), the simplest model of the β-O-4 aryl ether linkage, in the liquid and vapor phases at 330-445 °C.[3] Two competitive free radical decay pathways were found to be operative, including a significant rearrangement pathway involving an O,C-phenyl shift in the $PhCH_2CH\bullet OPh$ intermediate. Recently, mechanistic studies of methoxy-substituted PPEs, representative of guaiacyl and syringyl units in lignin, have been conducted under high temperature, short contact time conditions (500 °C, < 1 s) using the flash vacuum pyrolysis (FVP) technique.[4] These studies revealed a rich variety of intramolecular transformations for intermediate methoxy-substituted phenoxy radicals. Currently, we are investigating other important PPE structures, such as α-alcohols $PhCH(OH)CH_2OPh$,[5] under FVP conditions.

Another aspect of our research has been investigation of the impact of potential mass transport limitations on thermolysis products, kinetics, and mechanisms through the use of silica-immobilized model compounds for structures in coal and lignin. This has been accomplished through the use of model compounds immobilized on the surface of silica nanoparticles via a Si-O-C_{aryl} linkage. The results of extensive investigations into the pyrolysis mechanisms of hydrocarbon models for structures in coals have been recently reviewed.[6] In this paper, we will summarize our current understanding of the significant role that mass transfer limitations can play in altering reaction pathways for lignin model compounds compared with fluid phase behavior. Initial results from current studies, which focus on the detailed investigations of hydrogen transfer steps under diffusional constraints, will also be presented.

Experimental

Preparation of Surface-Attached Materials. Procedures for the preparation of the surface-attached phenethyl phenyl ether,[7] benzyl phenyl ether,[8] diarylmethane,[9] and 1,3-diphenylpropane[10] models have been described. In general, the precursor phenol was adsorbed onto the dried (200 °C, 4h) surface of a fumed silica (Cabosil M-5, Cabot Corp., 200 $m^2\ g^{-1}$, ca. 4.5 SiOH nm^{-2} or 1.5 mmol SiOH g^{-1}) by solvent evaporation from a benzene slurry. Surface-attachment was performed in a sealed, evacuated (2 x 10^{-6} torr) Pyrex tube at 200-225 °C for 0.5-1.0 h in a fluidized sand bath. Unattached phenol was removed by either sublimation at 225-270 °C for 1 h under dynamic vacuum (5 x 10^{-3} torr), or Soxhlet extraction with dry benzene. Surface coverage analysis was performed on 150-200 mg samples dissolved in 30 mL 1N NaOH overnight. A phenol such as 4-phenylphenol or 4-(2-phenylethyl)phenol in 1N NaOH was added as an internal standard. The solution was acidified with HCl, and extracted with methylene chloride or diethyl ether (3 x 7 mL). The combined organic layer was typically washed with water (1 x 10 mL), dried over $MgSO_4$, filtered, and the solvent removed under reduced pressure. Silylation with *N,O*-bis(trimethylsilyl)-trifluoroacetamide (BSTFA) in pyridine (2.5 M, 0.30 mL) produced the corresponding trimethylsilyl ether. GC analysis was conducted on a Hewlett Packard 5890 Series II gas chromatograph employing a J & W Scientific 30 m x 0.25 mm DB-1 or DB-5 column and flame-ionization detection. Multiple assays provided surface coverages with reproducibility of ± 2 %. Two-component surfaces were prepared by co-attachment of the probe and spacer phenols in an analogous manner.[10]

Pyrolysis Procedure. The pyrolysis apparatus and procedure have been described previously.[6-10] In brief, a weighed amount of sample (0.4-0.6 g) was placed in one end of a T-shaped Pyrex tube, evacuated, and sealed at ca. 2 x 10^{-6} torr. The sample was inserted into a preheated temperature-controlled (± 1.0 °C) tube furnace, and the other end placed in a liquid nitrogen bath. The volatile products collected in the trap were dissolved in acetone (0.1-0.3 mL) containing internal standards and analyzed by GC and GC-MS. Surface-attached pyrolysis products were similarly analyzed after digestion of the silica in aqueous base, addition of internal standards, and silylation of the resulting phenols to the corresponding trimethylsilyl ethers as described above for the surface coverage analysis.

Results and Discussion

Aryl Ethers. Silica-immobilized phenethyl phenyl ether (≈$PhCH_2CH_2OPh$, ≈PPE) and benzyl phenyl ether (≈$PhOCH_2Ph$, ≈BPE) have been studied as models of the corresponding β-O-4 and α-O-4 aryl ether linkages in lignin, where "≈" is used to denote the Si-O-C_{aryl} linkage to the silica surface. Pyrolysis of ≈PPE at 375 °C revealed that the free-radical chain decay mechanism observed earlier for fluid-phase PPE remains operative on the surface.[7] Selectivity in formation of the two sets of products (Figure 1) arises from formation of radicals at the α- and β- carbon sites (Figure 2). This

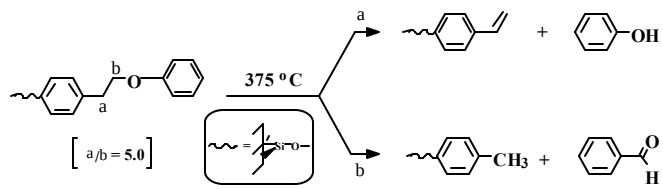

Figure 1. Principal products from pyrolysis of surface-immobilized PPE.

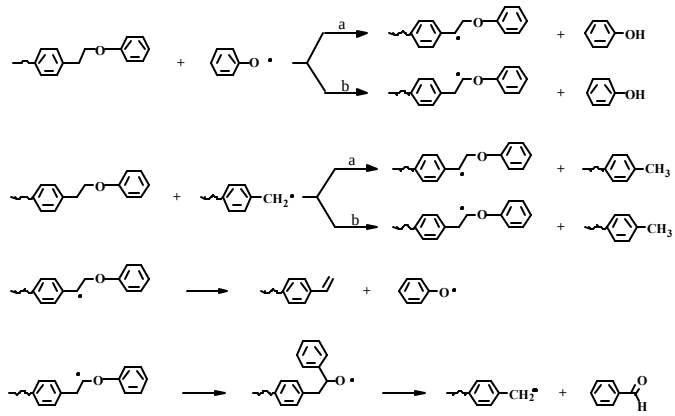

Figure 2. Radical chain propagation steps in pyrolysis of ≈PPE.

α/β-path selectivity was found to vary in a predictable manner with changes in substitution on the PPE framework, and the rearrangement path involving the O,C-phenyl shift remained significant in all cases.

However, in dramatic contrast to solution-phase behavior, where dilution of PPE in biphenyl solvent had no impact on the α/β-

spacer molecules (≈BP) caused a significant change in the product selectivity.[7] For example, the α/β-path selectivity for ≈PPE/≈BP (1:10 mol ratio) increased 4-fold to a value of ca. 20 compared with similar surface coverages of ≈PPE alone. Similar results were found when naphthalene was employed as the surface diluent, and the selectivity change must be attributable to the restrictions on mass transport. Our current hypothesis, depicted in Figure 3, is that the rigid aromatic spacer molecules introduce steric constraints that hinder the O,C-phenyl shift for the β-carbon radical that is the critical step in the rearrangement path. The reduced rate

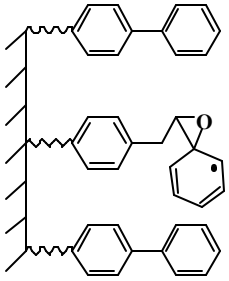

Figure 3. Steric constraints on O,C-phenyl shift on the silica surface in the presence of aromatic spacer molecules.

for this step would permit interconversion of β- and α-radicals via hydrogen transfer and result in larger values for the α/β-path selectivity. Interestingly, if a more flexible spacer molecule is employed, such as diphenylmethane, the steric constraints on the rearrangement path appear to be largely removed. Clearly, an improved understanding of the dynamics of molecular motion and interactions on these dual component surfaces would be beneficial. Studies employing steady-state and transient optical polarization spectroscopy employing surface-immobilized fluorescent probe molecules are currently underway.[11]

Benzyl phenyl ether linkages are much more reactive than PPE linkages, and show significant thermal decomposition at temperatures as low as 275 °C. Our pyrolysis studies on ≈BPE revealed two competitive free radical decay pathways that follow the initial homolysis of the weak O-C bond that produces phenoxy and benzyl radicals.[8] The first is recombination of these radicals at phenoxy ring carbons to form hydroxydiphenylmethane isomers (Figure 4). This path appears to be enhanced compared with BPE pyrolysis in fluid phases as a consequence of the restrictions on diffusion experienced by the phenoxy radical. The second path

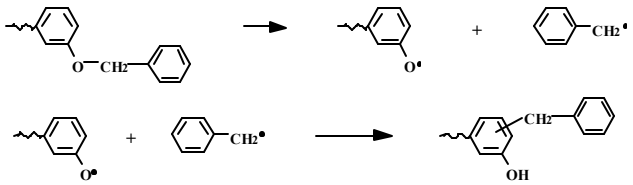

Figure 4. Recombination of surface-bound phenoxy and vapor-phase benzyl radicals to form hydroxydiphenylmethanes.

involves rearrangement of the intermediate ≈PhOCH•Ph radical, formed from radical hydrogen abstraction, by an O,C-phenyl shift. The rearranged radical then undergoes hydrogen abstraction to form silica-immobilized benzhydrol or hydrogen loss to form benzophenone (Figure 5). Interestingly, this rearrangement path had not been previously detected in the pyrolysis of fluid-phase BPE, yet under restricted diffusion conditions the selectivity for this rearrangement path relative to the recombination path was 1.0 at high

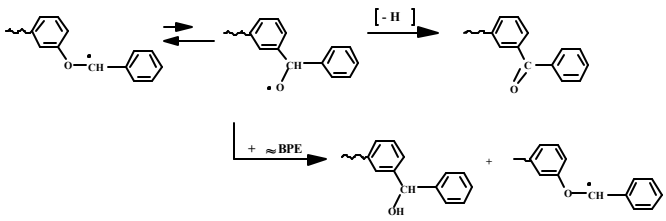

Figure 5. Rearrangement path for ≈BPE involving O,C-phenyl shift.

≈BPE surface coverages (0.24 mmol g^{-1}), and 0.5 at low surface coverages (0.084 mmol g^{-1}). This selectivity depended not only on surface coverage but also on the structure of spacer molecules, which can perturb both the hydrogen transfer step that forms ≈PhOCH•Ph and the O,C-phenyl shift. In the thermal processing of lignin, the aryl ether rearrangement pathway for BPE- and PPE-based structures generates ketone and aldehyde products that have potential commercial value. Increasingly improved knowledge of the fundamental pathways for their formation, and the pyrolysis conditions that increase or decrease their selectivity, could be important in development of advanced processes for recovering these valuable aromatic chemicals.

Diphenylmethanes. We showed above that thermal transformation of a model for the α-O-4 aryl ether in lignin (≈BPE) generates diphenylmethane linkages (Figure 4). Moreover, lignins modified by acidic or basic treatments as in pulping processes generates condensed structures containing diphenylmethane-type

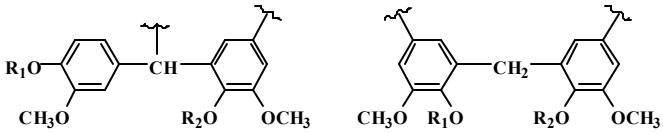

Figure 6. Examples of diphenylmethane-type condensed units in acid or base modified lignins.[1b]

linkages as illustrated in Figure 6.[1b-d] Thermochemical processing of these materials have the potential for PAH formation through cyclodehydrogenation reactions that form fluorene-based structures. We have been studying recently the potential for such PAH formation in the pyrolysis of simple diarylmethanes such as the silica-immobilized diphenylmethane (≈DPM) shown in Figure 7.[9] At 400-425 °C, ≈DPM undergoes slow pyrolysis to form the products shown by a free radical pathway that is accelerated

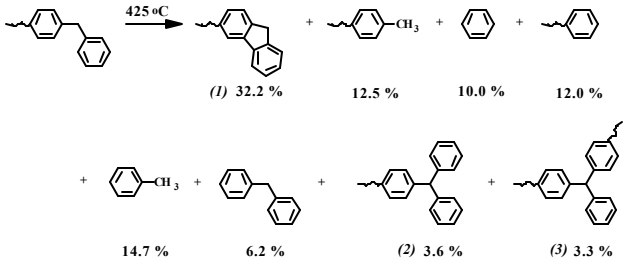

Figure 7. Pyrolysis of silica-immobilized diphenylmethane.

significantly in the presence of free radical sources. The cyclodehydrogenation process to form fluorene (**1**) is indeed observed to be important, and could occur at much lower temperatures for the highly substituted diphenylmethane structures found in lignin (Figure 6). Interestingly, the presence of a co-attached hydrogen donor molecule (tetralin) decreased the cyclodehydrogenation reaction (fluorene yield reduced 2.3-fold) but did not eliminate it. In contrast, fluorene formation has not been reported in fluid phase pyrolysis of DPM in the presence of tetralin or other hydrogen donors. One significant surprise was the formation of the triphenylmethanes, **2** and **3**, which have not been reported in the pyrolysis of DPM in fluid phases. The formation of these products resulted from a radical substitution process (Figure 8) promoted by the restricted mass transport on the surface. Radical substitution reactions resulting in diattached products such as **3** are representative of retrogressive cross-linking reactions that yield more refractory linkages. Similar cyclization and substitution reactions have been observed for other diarylmethanes,[9] although the product selectivity was found to depend on molecular orientation as well as the structure of spacer molecules.

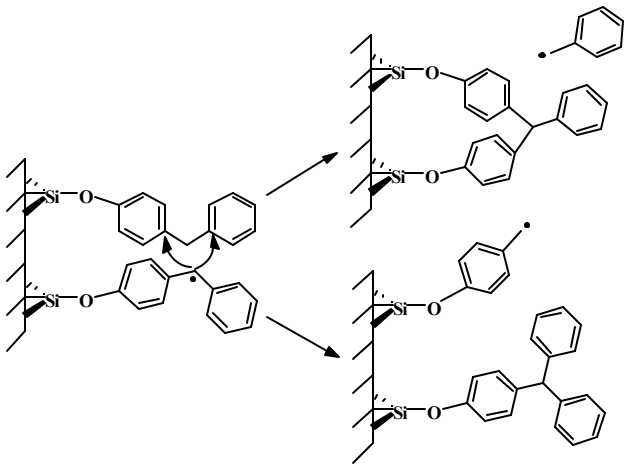

Figure 8. Radical displacement path leading to triphenylmethane formation.

Oriented Hydrogen Transfer. Our current research is addressing the question of whether molecular orientation can play a role in the rates of hydrogen transfer under diffusional constraints during thermochemical processing of fossil and renewable fuels. Efficient utilization of native hydrogen, or added hydrogen from donors, is critical in the thermochemical processing of these hydrogen deficient resources. Our earlier studies employed two component surfaces with 1,3-diphenylpropane (DPP) as a probe molecule,[10] a structural linkage which is also found in processed lignins.[1c] Pyrolysis of DPP in fluid phases occurs at reasonable rates at 375 °C by a free radical chain reaction to cleanly produce toluene and styrene.[12, 13] This decomposition also occurred readily under surface-immobilized conditions, but the overall rate was extremely sensitive to the rate of the key hydrogen transfer propagation step on the surface.[10] The

$$\approx PhCH_2\bullet \;+\; \approx Ph(CH_2)_3Ph \;\rightarrow\; \approx PhCH_3 \;+\; \approx PhCH\bullet CH_2CH_2Ph$$

hydrogen transfer was found to be very sensitive to the spatial separation of these species on the surface. Remarkably, we found that the presence of intervening spacer molecules that possess reactive benzylic C-H bonds can result in significant rate accelerations compared with ≈DPP surfaces containing aromatic spacers such as biphenyl and naphthalene. The rate acceleration was found to results from a novel hydrogen transfer, radical relay process that is illustrated in Figure 9 for a ≈DPM spacer.

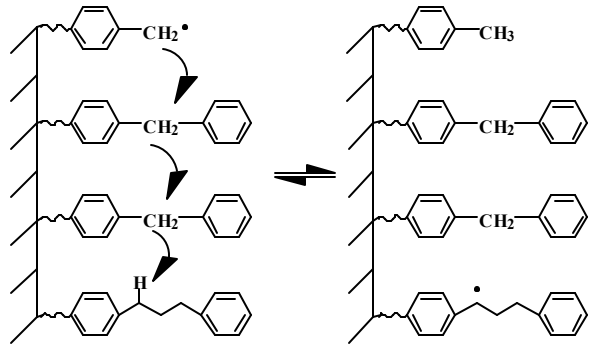

Figure 9. Hydrogen transfer, radical relay pathway.

This pathway was confirmed by deuterium labeling studies, and from correlation of the pyrolysis rate with the reported rates for hydrogen abstraction by benzylic radicals from the hydrogen donating spacer molecules employed.

We are now examining this hydrogen transfer pathway in more detail through the use of spacer molecules that have different orientations with respect to their attachment to the surface as illustrated in Figure 10 for the fluorene spacer.

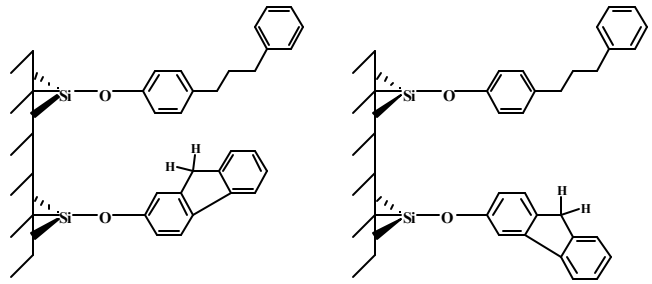

Figure 10. ≈DPP/≈2-FL and ≈DPP/≈3-FL surfaces synthesized to probe orientation effects of spacers on ≈DPP pyrolysis kinetics.

The synthesis of the 2-hydroxyfluorene precursor has been previously described.[10] We have now synthesized the 3-hydroxyfluorene precursor by a multi-step route that will be reported elsewhere. The ≈DPP samples shown in Figure 10 have now been prepared with a ≈DPP surface coverage of ca. 0.08 mmol g^{-1} and the remaining available surface area containing the respective fluorene spacers. Initial pyrolysis results at 375 °C indicate that the ≈DPP/≈3-FL pyrolysis rate is a factor of ca. 2.7 slower than the pyrolysis rate for ≈DPP/≈2-FL. This rate decrease suggests that the fluorene spacer having benzylic hydrogens in a *para*-orientation with respect to the surface linkage is less effective at participating in the hydrogen transfer, radical relay process than the fluorene spacer having a *meta*-orientation. These preliminary findings are now being explored in more detail, and will be extended to other hydroaromatic spacers.

Conclusions

Pyrolysis studies of silica-immobilized model compounds for structures in lignins are providing new molecular level insights into the potential impact of restricted mass transport on reaction pathways. In particular, radical rearrangement, cyclization, and

hydrogen abstraction pathways are sensitive to the structure, orientation, and spatial separation of molecules under diffusional constraints. For aryl ether models, radical rearrangement pathways give rise to new aromatic ketone and aldehyde functional groups that may have commercial value. On the other hand, thermochemical processing of lignins containing diphenylmethane-type linkages can lead to the unwanted formation of PAHs through cyclodehydrogenation reactions. An improved understanding of the role of restricted mass transport, steric effects of neighboring structures, kinetics of hydrogen transfer, etc. will be important for future progress in the thermochemical processing of lignin.

Acknowledgment. This research was sponsored by the Division of Chemical Sciences, Geosciences, and Biosciences, Office of Basic Energy Sciences, U.S. Department of Energy under contract DE-AC05-00OR22725 with Oak Ridge National Laboratory, managed and operated by UT-Battelle, LLC.

References

(1) *Lignin: Historical, Biological, and Materials Perspectives*; Glasser, W. G., Northey, R. A., Schultz, T. P., Eds.; American Chemical Society Symposium Series 742: Washington, DC, 2000. (a) McCarthy, J. L.; Islam, A. Chapter 1. (b) Lai, Y.-Z.; Xy, H.; Yang, R. Chapter 10. (c) Gargulak, J. D.; Lebo, S. E. Chapter 15. (d) Gratzl, J. S.; Chen, C.-L. Chapter 20.
(2) *Developments in the Thermochemical Conversion of Biomass*; Bridgwater, A. V.; Boocock, D. G. B., Eds.; Blackie Academic: London, 1997.
(3) Britt, P. F.; Buchanan, III, A. C.; Malcolm, E. A. *J. Org. Chem.* **1995**, *60*, 6523.
(4) Britt, P. F.; Buchanan, III, A. C.; Cooney, M. J.; Martineau, D. R. *J. Org. Chem.* **2000**, *65*, 1376.
(5) Cooney, M. J.; Britt, P. F.; Buchanan, III, A. C. *Prepr. Pap. – Am. Chem. Soc., Div. Fuel Chem.* **1997**, *42(1)*, 89.
(6) Buchanan, III, A. C.; Britt, P. F. *J. Anal. Appl. Pyrolysis* **2000**, *54,* 127.
(7) Britt, P. F.; Buchanan, III, A. C.; Malcolm, E. A. *Energy Fuels* **2000**, *14*, 1314.
(8) Buchanan, III, A. C.; Britt, P. F.; Skeen, J. T.; Struss, J. A.; Elam, C. L. *J. Org. Chem.* **1998**, *63*, 9895.
(9) Buchanan, III, A. C.; Britt, P. F.; Koran, L. J. *Prepr. Pap. - Am. Chem. Soc., Div. Fuel Chem.* **2001**, *46 (1)*, 225.
(10) Buchanan, III, A. C.; Britt, P. F.; Thomas, K. B.; Biggs, C. A. *J. Am. Chem. Soc.* **1996**, *118*, 2182.
(11) Ivanov, I. N.; Dabestani, R.; Buchanan, III, A. C.; Sigman, M. E. *J. Phys. Chem. B* **2001**, *105*, 10308.
(12) Poutsma, M. L.; Dyer, C. W. *J. Org. Chem.* **1982**, *47*, 4903.
(13) Gilbert, K. E.; Gajewski, J. J. *J. Org. Chem.* **1982**, *47*, 4899.

INFRARED LASER PYROLYSIS OF BIOMASS DERIVED CHARS

Andrew M. Herring, J.Thomas McKinnon, David E. Petrick, Jonathan Filley, Keith W. Gneshin and Bryan McCloskey

Department of Chemical Engineering
Colorado School of Mines
Golden, CO 80401-1887

Introduction

Recent studies have attempted to rationalize a global pyrolysis mechanism for cellulose pyrolysis. [1, 2, 3] However, these mechanisms are based on the observation of stable species many seconds into the pyrolysis event. The observation and validation of the reactive intermediates generated in the first second or less of pyrolysis should enable a better understanding of the kinetics of the processes involved to be developed. The neutral species formed during this short time scale of reaction have been extensively studied by molecular beam mass spectroscopy, MBMS, from tube furnace pyrolysis of volatilized cellulose at increasing temperatures corresponding to primary pyrolysis and to secondary and tertiary cracking products. [4, 5] The subsequent pyrolysis of cellulosic chars formed at different temperatures has also been studied [6] leading to the conclusion that these are predominantly aromatic at temperatures above 310°C.

Infrared laser heating of biomass samples allows very rapid temperature ramps to be achieved. Rapid heating in this way with a carbon dioxide laser has been used to both volatilize organic samples and for the generation of reactive intermediates for subsequent analysis.[7, 8]

In this paper, we describe the identification by MBMS of both radical and molecular reactive intermediates as well as stable end products from the carbon dioxide laser pyrolysis of cellulose and charred cellulose at the site of irradiation. The temperature profiles of the cellulose char surface during laser pyrolysis have been characterized by both experiment and modeling. In general, only the surface of the solid is heated and the assumption is made that the off-gassed volatiles are not further heated. We are, therefore, able to determine the nature of the char from MBMS as well as the important intermediate radicals produced during rapid heating events.

Experimental

All manipulations of char and laser pyrolysis experiments were performed under an inert atmosphere of helium, nitrogen or argon as explained below.

Avicel cellulose (Analtech), propargyl chloride (Aldrich) and 50% 1,5-hexadiyne in pentane (Alfa Aesar) were used as received without further purification. The cellulose was pelletized. Pellets were charred in a quartz tube furnace, the temperature of which was ramped from ambient to 375ºC over 5 min, as measured by a thermocouple at the side of the pellet, in a flow of argon at 1.41cm s^{-1} for times up to 3 h. The pellets were then transferred to a sample post inside the MBMS combustion chamber such that the outside of the sample disc touched the nickel nozzle inlet of the MBMS.

The unpolarized 10.6 µm CO_2 laser radiation (Synrad, 65W Duo-Lase) was directed into the MBMS combustion chamber through an optical train giving a relatively large spot size of *ca.* 2 mm. In a typical experiment, a mass range 0 - 450 amu, was collected in two overlapping 250 amu segments at a scan rate of 0.5 s $scan^{-1}$. 10 background spectra were collected before irradiating the sample, for 3 s with laser radiation fluxes from 3.25 W to 13 W (5% to 20% of full power). The data reported are the average of at least 10 such experiments, the pellet being rotated between each, over at least two pellets. From these experiments, the error in the relative intensities is +/- 10%, data falling outside this range was rejected. Arbitrary intensity scales are presented throughout the paper as many factors, such as vacuum stage pressures, nozzle condition *etc*, independent of the laser pyrolysis experiment influence the absolute intensities obtained. In some experiments, the pellet was rotated continuously while being irradiated; again the data reported are the average from more than one pellet.

Results and Discussion

Figure 1 shows the laser pyrolyzed mass spectra of cellulose and cellulose charred at 375°C for various times, at 0.5s of a low powered laser pulse. All of the major products observed in **Figure 1** for uncharred cellulose fall into the class of primary products of cellulose pyrolysis, that is, no secondary cracking in the gas phase is observed. We can therefore deduce that under these conditions, the products observed in this experiment using cellulose char, discussed below, are volatilized from the surface with no major contributions from gas phase cracking, due to the poor coupling of the infrared radiation with low concentrations of gas phase species.

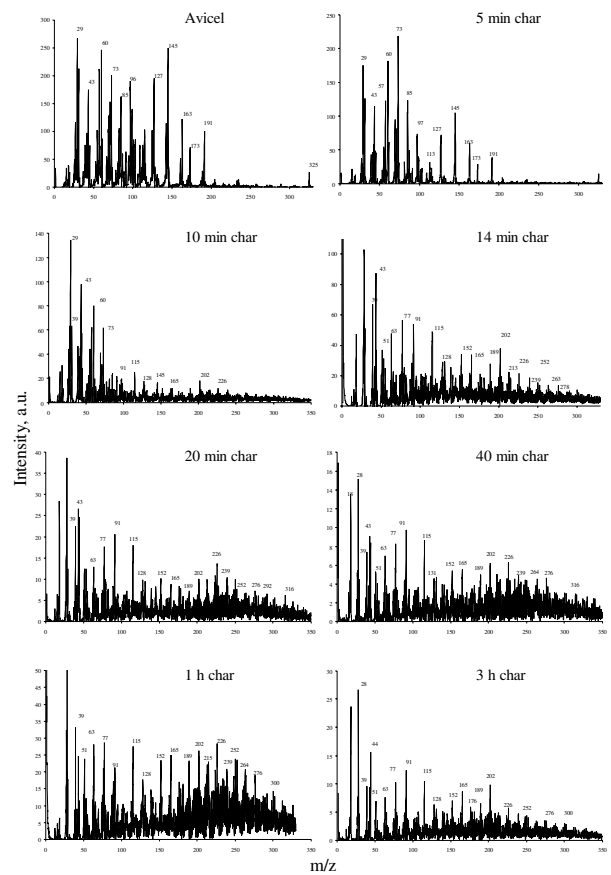

Figure 1. Mass Spectra of Avicel and 375°Ccharred Avicel at 0.5 s of a 3 s 10% laser power pulse..

After 10 min of charring, we begin to see peaks in the mass spectrum that we assign to polyaromatic hydrocarbons or their radicals, M-1.Some carbohydrate is present in this mass

spectrum. This is likely tar that has not yet left the char matrix, as irradiating at 13 W laser power for 0.5 – 1.0 s , an average temperature *ca.* 400ºC higher than at 6.5 W, gives a mass spectrum with no m/z 60 or 73. At the higher laser power, all residual tar is flashed off.

From 14 min to 1 h of charring, the mass spectra obtained from the short time low power laser pyrolysis of char are all similar in that we observe predominantly PAH and little carbohydrate, **Figure 1**. The dominant masses larger than 77 can all be assigned to aromatic, PAH, or PAH radical species. The major trend observed with charring time is the molecular weight growth of the ions assigned to PAH and PAH radicals observed above m/z 202.

The analysis of trends involving the lower molecular weight fragment is a little harder to discern as many of these ions are also present in the mass spectrum of carbohydrate. Nevertheless, it is apparent that at early charring times the lower mass aromatic species, between m/z, 77 and 189 grow in and become constant after the intermittent charring times of 20 min. At this early time, 0.5 –1.0 s, of the laser pulse the low molecular weight region of the spectrum is dominated by masses, m/z 29, 39 and 43. After a further second of irradiating, 1.5- 2.0 s, the dominant low molecular weight peaks are m/z 28, 39 and 44, data not shown. The maximum PAH we have observed in any of these experiments is m/z 376. After 3 h of charring the ions assigned to PAH larger than m/z 202 again diminish, but as stated earlier the smaller aromatic hydrocarbons maintain constant relative intensity, **Figure 1**.

We are observing the fragmentation of PAH moieties from the char surface by laser pyrolysis. These PAH molecules would not form in the gas phase except at very much higher temperatures (because bimolecular reactions will be slow) than we can achieve with our laser under these conditions.

It appears that the depolymerization and decomposition of the cellulose chain first produces smaller PAH up to a molecular weight of 202. These smaller PAH fragments then anneal into larger PAH as the charring process continues. The M-1 species are presumed to be the radicals produced during the laser pyrolysis event.

PAH typically give mass spectra with a dominating molecular ion. However, several of the masses correspond to M-1 ions and we believe that we are observing these PAH as radicals. Laser pyrolysis at 6.5 W, of char produces predominantly phenyl, 77, benzyl, 91, indenyl, 115, $C_{13}H_9$, 165, $C_{17}H_{11}$, 189 and $C_{19}H_{11}$, 239 radicals, M-1 rather than their parents, M, benzene, toluene, indene *etc*. Naphthalene, 128, acenapthylene, 152, pyrene, 202, $C_{18}H_{10}$, 226, $C_{20}H_{12}$, 252 and higher molecular weight species appear as the molecular species. This implies that the larger PAH are rapidly stabilized shortly after the ablation process and that the smaller aromatic and PAH molecules are released as reactive radicals, with the exception of naphthalene, m/z 128.

The conclusion is that we are observing the molecular weight growth of the PAH moieties in the solid bulk with time as the cellulose is charred as has been observed previously. As the cellulose is charred for progressively longer times the PAH anneals into larger and larger PAH moieties that are cleaved from the char surface during the laser pyrolysis event. After 3 h of charring the PAH moieties have begun to anneal into intractable graphite like entities that cannot be cleaved by the laser, so we see a marked cut off of PAH above m/z 202 from the more mature cellulose char.

The largest peaks in the low mass region of the mass spectrum for charring times of 14 minutes to 1 h are m/z 18, 29, 39 and 43. Mass 18 is water and mass 39 corresponds to a common fragment ion, the cyclopropenyl cation, as well as an important PAH precursor, the propargyl radical. The mass spectra of medium to large PAH give a large peak corresponding to a molecular ion with very little fragmentation. This is not true of the smaller aromatic species, e.g. benzene has a m/z fragment 11% the intensity of its molecular ion. In order to begin to assign the peak at m/z 39 to either a fragment ion or as the propargyl radical we created a synthetic mass spectrum. Using the 16 most prominent peaks from mass 77 and above in the MBMS data of cellulose charred for 1 h at 375°C, **Figure 1**, we assigned each to a likely PAH molecule or molecules, using the parent neutral molecule for the PAH that appeared as radicals. The results showed that m/z 39, 51 and 63 are under represented in the synthetic spectrum. These ions are either fragment ions of compounds, whose molecular ions are under the threshold of the experimental data or ions produced by ionization of radicals formed from laser pyrolysis, such as propargyl. It is more plausible that a large proportion of the m/z 39 peak comes from the propargyl radical. Further evidence that the peak at m/z 39 is a radical comes from the fact that it is still present in an experiment in which the ionization potential of the mass spectrometer's ionizer was reduced to 13 eV, a level below the ionization potential of benzene.

Interestingly the peak at m/z 43 is also present in the low ionization potential experiment. The peaks at m/z 29 and 43 are commonly present in mass spectra as fragment ions of carbonyl compounds, such as acetaldehyde and hydroxyacetone. However, the mass spectra of these cellulose chars show little if any evidence of carbonyl compounds. We, therefore, assign the peaks at m/z 43 to the formylmethyl radical and m/z 29 to a fragment ion.

^{13}C NMR analysis reveals a loss in intensity of the aromatic carbons as well as a smaller loss in intensity of the methyl peak upon laser irradiation. Interestingly there is little change in the intensity of the oxygen substituted aromatic carbons. This is either because the oxygenated PAH are intractable or that the irradiated, active char, which has lost its Ar-O moieties, form an equivalent amount of oxygenated PAH on exposure to air. These observations are consistent with our MBMS data where hydrocarbon PAH are the major species detected, with few contributions from oxygen substituted species. Presumably, the oxygenated aromatic species become intractable during the charring. ^{13}C NMR also shows that the number of carbons attached to hydroxyl increases dramatically and there is a slight increase in the number of carbonyl groups in the irradiated char. In keeping with our model of bond cleavage from the char surface, we would expect laser pyrolysis to generate an extremely active char. As these chars were exposed to air for some time before the NMR measurements were performed it is assumed that atmospheric, water and oxygen have quenched the radical ends to form hydroxyl and carboxyl functionalities. It should be noted that a large proportion of the char is probably not molecular and is presumably graphitic in nature.

Conclusions

We propose that charred cellulose has a network of small, up to molecular weight 202, PAH fragments between aliphatic hydroxyl linkages. When such a moiety is irradiated, formylmethyl radical is produced with either a PAH radical, as shown here, or a PAH neutral and a surface radical end. Upon

further charring, water is lost to give PAH moieties separated by olefinic linkages. When these moieties are irradiated, propargyl radical is liberated with again either a PAH radical or a surface radical end. On still more severe charring, the olefinic linkages become incorporated into the PAH. Both the hydroxy methyl and propargyl radical forming pathways postulated to occur during laser heating, probably occur in the maturing char, although more slowly to give the PAH, larger than molecular weight 202, in the solid bulk.

Acknowledgement.

We would like to thank Philip Morris, USA for financial support of this work.

References

1. Brown A.L., Dayton D.C. and Daily J.W., *Energy Fuels*, **2001**, *15*, 1286.
2. Antal, Jr., M.J., Várhegyi G. and Jakab E., *Ind. Eng. Chem. Res.*, **1998**, *37*, 1267.
3. I. Milosavljevic, V. Oja and E.M. Suuberg, *Ind. Eng. Chem. Res.*, **1996**, *35*, 653.
4. Evans R.J. and Milne T.A., *Energy Fuels*, **1987**, *1*, 123.
5. Park, B.-I., Bozzelli J.W., Botty M.R., Bernhard M.J., Mesuere K., Pettigrew C.A., Shi J.-C. and Simonich S.L., *Eniron. Sci. Technol.*, **1999**, *33*, 2584.
6. Pastrorov I., Botto R.E., Arisz P.W. and Boon J.J., *J. Carbohydr. Res.*, **1994**, *262*, 27.
7. Tripathi A., Vaughn C.L., Maswadeh W. and Meuzelaar H.L.C., *Energy Fuels*, **1999**, *13*, 984.
8. Zhan Q., Zenobi R., Buseck P.R. and Teerman S., *Energy Fuels*, **1997**, *11*, 144.

The effect of inorganics on the formation of PAH during low temperature pyrolysis of cellulose

Thomas E. McGrath, Jason A. Hoffman, Jan B. Wooten and Mohammad R. Hajaligol*

Philip Morris USA, Research Center, Richmond, VA 23234
*Current Address: MCV School of Pharmacy, Richmond, VA, USA

Introduction

The effect of inorganic salts on the pyrolysis of cellulose has been extensively studied.[1] It is well known that the presence of inorganic salts can: lower the primary pyrolysis temperature, increase the char yield by accelerating decomposition reactions, increase or decrease the rate of oxidation of the aromatic component of the char, and increase or decrease the heat released from the oxidation of char to CO_2. Although a wealth of information exists, relatively little is known about the effect of inorganic salts on the low temperature formation of polycyclic aromatic hydrocarbons (PAHs).

In an effort to explore the effect of the main indigineous cations found in biomass on the formation of PAHs we have investigated the effect of Na, K, and Ca on the formation of PAHs from cellulose. Cellulose samples loaded with varying weight percentages of sodium, potassium, and calcium were pyrolyzed at temperatures up to 600 ^{o}C. The major components of the cellulose tars were characterized using gas chromatography – mass spectroscopy (GC-MS). The effect of mono- and divalent cations on the aromaticity of chars formed at 300 ^{o}C was studied using nuclear magnetic resonance spectroscopy (NMR). Although the absolute yields of PAHs at temperatures up to 600 ^{o}C may not be significant relative to the higher yields of PAHs formed at elevated temperatures, their formation and yields are deemed important during the smoldering combustion of biomass materials.

Experimental

A schematic of the experimental setup is given in Fig. 1. The experimental apparatus consisted of a quartz tube placed inside a heated zone. The zone had an internal diameter of 2.5 cm and an isothermal length of ca. 7 cm. Helium was used as the carrier gas at a flow rate of 120 cm^3/min. A Cambridge pad placed in a special assembly immediately at the end of the zone was used to collect the product tar condensate. The temperature of the sample in the heated zone was measured using a chromel/alumel (K type) thermocouple. The thermocouple was also used to transport the quartz boat, containing the cellulose samples, to and from the heated zone.

Materials. The cellulose sample was obtained from FMC Corporation, and the inorganic salts were obtained from Acros and Aldrich. The cellulose is a microcrystalline purified and depolymerized α-cellulose derived from fibrous plants (Avicel PH-102). Cellulose samples with 0.1, 1, and 5% w/w of NaCl, KCl, CH_3COOK, and $CaCl_2$, respectively, were prepared by dissolving the desired amount of the salt in water and then adding 2.5 g of cellulose powder to the aqueous salt solution. Samples were stirred for 4 hours and then placed in an oven at 45 ^{o}C for 12 hours. A mortar and pestle was used to grind the samples into a fine powder. A cellulose sample that under went the same procedure was used as the control.

Experimental Procedure. A 500 mg sample was placed in the quartz boat that initially rested in an unheated section of the tube before the heated zone (see Fig. 1). The Cambridge pad assembly was placed on the exit side of the furnace and the exit line was maintained at ~250 ^{o}C to minimize any condensation of the product tar prior to reaching the pad. After the furnace had reached the respective set temperature, the sample was pushed to a pre-determined location in the furnace and pyrolyzed for 10 minutes. The Cambridge pad was removed, placed in an amber screw capped vial, and the washings from the cambridge pad assembly walls added to the vial. A total solvent level of 5 ml of methanol was used and the vial was left to stir overnight. The residence time of gas phase pyrolysis products in the isothermal section of the reactor was calculated to be approximately 4 s at a furnace temperature of 600 ^{o}C.

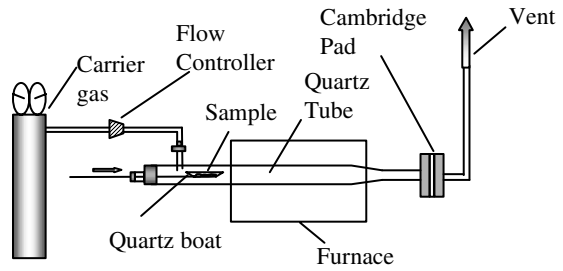

Figure 1. Schematic diagram of apparatus setup

The product condensates were analyzed by GC-MS using a HP 6890 GC equipped with a HP 5973 quadrupole MSD analyzer in the scanning mode. 14 PAH were studied that consisted of two to six condensed aromatic rings. The experimental error in PAH yield measurements varied between 10 to 30%. It should be realized that PAH constituted only a small fraction of the product which was a complex mixture of mostly oxygenated organic compounds. Besides the PAH mentioned above, the tar also contained other PAH, mainly methyl substituted PAH that were not considered in the analysis of this study.

Cross-polarized magic angle spinning (CPMAS) ^{13}C nuclear magnetic resonance (NMR) was used to characterize cellulose chars formed at 300 ^{o}C. Elemental analysis (EA) of cellulose chars was carried out by Galbraith Laboratories, Inc., Knoxville, TN, USA. The NMR and EA data are not reported here.

Results and Discussion

Varying the cation loading from 0.1 to 5% w/w increased the amount of char formed and decreased the overall weight loss of cellulose samples. The weight loss data for cellulose samples loaded with 5% w/w of NaCl, KCl, CH_3COOK, and $CaCl_2$ is given in Table 1. Char yields are expressed on an ash free basis. All cation loaded cellulose samples gave higher char yields and lower tar yields with respect to the control. The Na loaded cellulose sample experienced the highest weight loss of the cation loaded samples. The KCl and CH_3COOK cellulose samples experienced very similar weight losses, while the Ca loaded cellulose sample experienced the lowest weight loss.

The constituents of the product tar condensate derived from the control and cation loaded samples were characterized using GC-MS. The yield of levoglucosan was significantly affected by the presence of cations on the cellulose matrix, decreasing as the cation concentration increased. The above weight loss and levoglucosan yield data is consistent with what has been reported in the literature.[1]

PAH yields were higher from the cation loaded samples compared to the control. PAH yields were calculated on a µg/g of sample and on a µg/g of char basis. The yields of PAH formed from the cation loaded cellulose samples were found to increase with an increase in cation loading. Na and K loaded cellulose samples gave similar PAH yields. When PAH yields were expressed on a µg/g of

char basis the control and the cation loaded samples gave very similar yields of PAHs.

Table 1. Weight Loss of Cation Loaded Cellulose Samples

Zone I Temperature at 600 °C			
[a]Material	[b]Char (mg)	[c]Tar (mg)	[d]Total Wgt. Loss
Cellulose	36	252	93%
Cell. + NaCl	59	210	84%
Cell. + KCl	69	210	81%
Cell. + CH_3COOK	71	191	81%
Cell. + $CaCl_2$	94	183	76%

a = 500 mg sample pyrolyzed
b = Amount of char formed after 10 min at 600 °C in zone I calculated on an ash free basis
c = Amount of tar collected after 10 min at 600 °C in zone I
d = Percent weight lost from sample after 10 min at 600°C in zone I

A comparison of PAH yields formed from the pyrolysis of Na, K, and Ca loaded cellulose samples is given in Fig. 2(a). PAH yields are expressed on a µg/g of sample basis. All three cation loaded samples gave higher PAH yields compared to the cellulose control. The yields of most 2 to 3 ring PAH are very similar for all three cation loaded samples. The yields of 4 ring PAH are lower for the Ca loaded cellulose sample with respect to the other samples. PAH yields were also calculated on a µg/g of char basis as shown in Fig. 2(b). The yields of PAHs from the control and Na and K loaded samples are very similar while the yields of 3 and 4 ring PAH are lower for the Ca loaded sample.

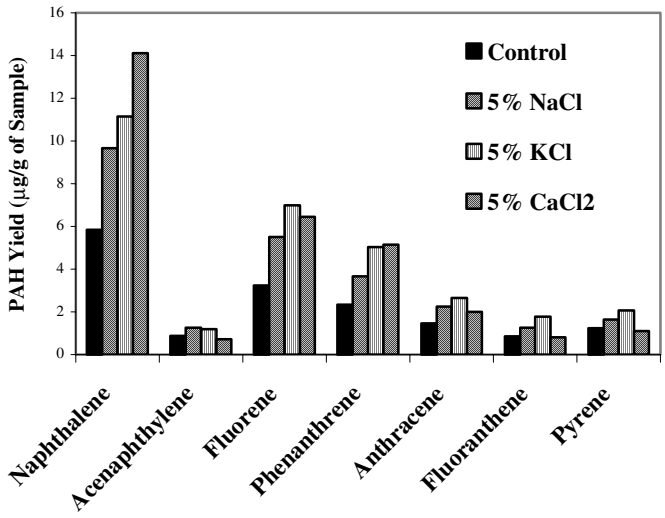

Figure 2(a). PAH yields for the pyrolysis of cation loaded cellulose samples at 600 °C. PAH yields expressed on a µg/g of sample basis.

It is well known that the presence of inorganic salts can increase the char yield. If PAH formation at low temperatures is attributable to precursors formed in the solid char matrix over the 400 to 600 °C temperature range,[2,3] then one might expect an increase in PAH yields as the char yield increases. This assumption appears to hold true for the Na and K loaded samples. Although the Ca loaded samples gave the highest char yields, the lower yields of 3 and 4 ring PAH may indicate a higher degree of cross-linking in this char relative to the other samples.

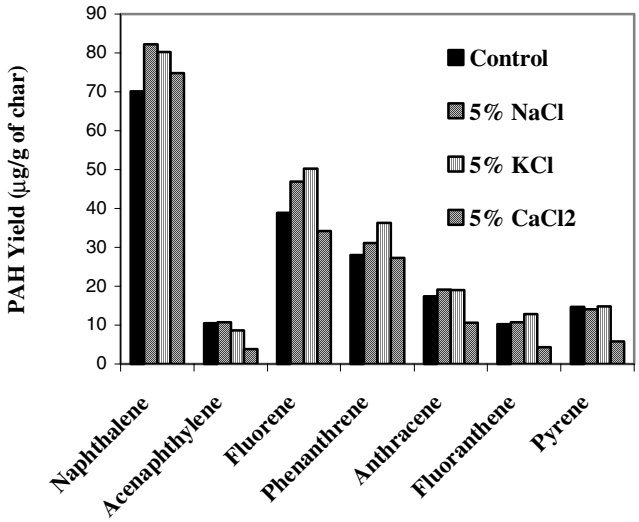

Figure 2(b). PAH yields for the pyrolysis of cation loaded cellulose samples at 600 °C. PAH yields expressed on a µg/g of char basis.

Conclusions

The addition of Na, K, and Ca inorganic salts to cellulose increases char yields and decreases tars yields. The yields of primary decomposition products were *significantly* affected. Increasing the cation loading decreases the yields of levoglucosan and increases the yield of char formed. PAH yields increased with an increase in cation concentration when yields were expressed on a µg/g of sample basis. The yields of PAHs formed were generally very similar when the yields were normalized on a µg/g of char basis. PAH yields from the control and from the Na and K loaded cellulose samples were very similar while lower yields of 3 to 4 ring PAH were formed from Ca loaded samples and this may be attributable to a more highly cross-linked char. Anion effects were also observed: changing the anion from Cl^- to CH_3COO^- for K loaded samples significantly lowers levoglucosan yields and increases the amount of naphthalene and fluorene formed.

Acknowledgement. The authors are grateful to the Philip Morris U.S.A. management for the support of this research. The assistance of B. Miller and K. Patel is also gratefully acknowledged.

References

(1) Shafizadeh, F., *The Chemistry of Solid Wood*, Edt. Roger Rowell, Amercian Chemical Society, Washington, DC, **1984**
Sekiguchi, S., Shafizadeh, F., *Journal of Applied Polymer Science*, **1984**, 29, 1267-1286, Pan, W-P., Richards, G.N., *J. Anal. Appl. Pyrolysis* ,**1989**, 16, 117-126, Liodakis, S.E. et al., *Thermochim. Acta* , 1996, 278, 99-108. Soares, S., et al., *European Polymer Journal*, **2001**, 37, 737-745
(2) E.W. Robb, W.R. Johnson, J.J. Westbrook, and R.B. Seligman, Beitrage zur Tabakforschung, **1966**, 3, 597. B.E. Waymack and D.S. Kellogg, Fuel Chemistry Division Preprints, **2001**, 46, 198.
(3) T. McGrath, G. Chan, M. Hajaligol, "*Low Temperature Mechanism for the Formation of Polycyclic Aromatic Hydrocarbons from the Pyrolysis of Cellulose*", submitted to J. Anal. Appl. Pyrol., **2001**.

DIRECT FORMATION OF AROMATICS FROM BIOPOLYMERS DURING LATE-STAGE, HIGH-SEVERITY PYROLYSIS

Robert J. Evans, Mike J. Looker, and Mark N. Nimlos

National Bioenergy Center
National Renewable Energy Laboratory
1617 Cole Blvd.
Golden, CO 80401

Introduction

The formation of aromatics from biomass pyrolysis by gas phase cracking of the primary products has been well documented.[1-3] Since biopolymers may undergo solid-phase chemical transformations during devolatilization, minor amounts of aromatics may be formed directly from this altered solid phase. Recently, Hajaligol et al[4] reported the direct formation of aromatics from preformed, biopolymer chars heated to 400 - 600 °C. Even if minor compared to the bulk volatile product slate, these aromatics may be significant when compared to the gas phase sources of aromatics under biomass conversion systems such as a fluid bed gasifier.

We report here methodology and results showing this effect directly from biopolymers. Two-stage pyrolysis was used to show the effect of composition and thermal history on the products evolving from the solid phase. Cellulose and pectin were used as model biopolymers and as a matrix to which other model compounds were added. The samples were heated in two stages: T_1 = 350 °C, for 7 minutes, T_2 = 700 °C, for an additional 5 minutes. Molecular Beam Mass Spectrometry (MBMS) was used to observe the evolution of volatile products.

Experimental

The reactor shown in **Figure 1** was used to first expose the sample to low-temperature (T_1) pyrolysis conditions in flowing Helium for seven minutes where some of the sample weight was lost as volatile products. The remaining material is then slid into a hotter region of the furnace (T_2) where a second devolatilization event is observed.

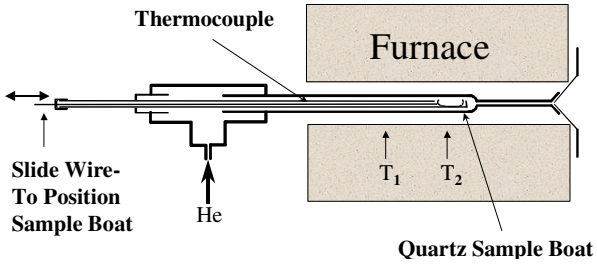

Figure 1. The pyrolysis reactor for variable-temperature pyrolysis studies. The sample is slid to a position and held at the low target temperature (T_1) then slid further into the reactor to expose the sample to a subsequent high reaction temperature (T_2).

A 50:50 mixture of pectin and cellulose was used as the base-case starting material, or matrix. The pectin was from Acros Organics Inc. and the cellulose was from Sigma Chemical Inc. We selected a sample of cellulose that gave a full range of pyrolysis products, including levoglucosan and hydroxyacetaldehyde, which is more representative of the product distribution found in biomass than a highly purified sample, such as Avicel[1]. A higher char yield is also obtained from this cellulose, which means that a reasonable sample of char persists for further evaluation at a higher temperature. A 250 mg sample of the matrix was used resulting in a solid phase after the T_1 treatment of ~50 mg. To study the condensed-phase reactions of other materials, mixtures with the matrix were made at a 10% level of additive and the resulting products compared to those derived from the matrix alone. This approach is necessary since some materials of interest will simply evaporate when studied as a neat sample in this fashion. However, when in the presence of the matrix, these volatile materials may undergo solid-forming reactions as the vapors or thermal reaction products interact with the charring matrix material and hence approximate what happens in biomaterials with complex cell wall structures.

Molecular Beam Mass Spectrometry. The study of pyrolysis by MBMS has been fully described previously.[1] The hot gases exiting the reactor are expanded through an orifice on the apex of a sampling cone into the stage one vacuum at 40 mtorr. The pressure difference is sufficient for free-jet expansion, which quenches the products and allows the full range of products, including light gases, high-molecular-weight compounds, and reactive products, to be simultaneously sampled and analyzed. A molecular beam, collimated through a second expansion, enters an ion source, where approximately 25 eV electron impact ionization is used to form ions that are analyzed by a quadrupole mass filter.

Multivariate Data Analysis. Factor analysis was used to identify subspectra of the time-resolved mass spectra collected during T_2. Two subspectra were identified using the methods of Windig et al.[5] and fractional concentrations were calculated for each spectra.

Results and Discussion

During exposure of the sample to low-temperature (T_1) pyrolysis conditions for seven minutes some of the sample weight was lost as volatile products. The remaining material is then quickly ramped up to high temperature (T_2) where a second devolatilization event is observed typically resulting in a total of 75% weight loss from both stages. Volatiles continued to evolve from the remaining 25% char during a maturation phase with no clearly defined end point. A typical experiment is shown in **Figure 2**.

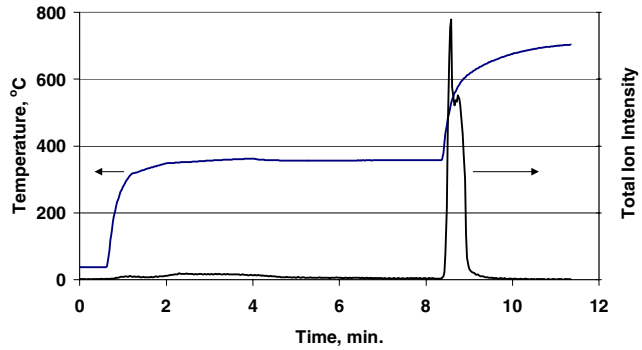

Figure 2. Time-resolved behavior of pectin/cellulose in a two-temperature pyrolysis experiment. The sample is slid to the position for T_1 (350 °C) and held for 7 minutes. Product evolution occurs at this low temperature but is not of interest for this experiment. The remaning solid is then slid to the position for T_2 (700 °C) and held until product evolution stops.

Experiments were performed to evaluate the yield of char from neat pectin and cellulose at typical settings of T_1 and T_2. The char yields for the pectin were higher that for the cellulose sample. The residue yield at T_1=350 °C is 30% for both pectin and cellulose with no significant effect of time at T_1 (5 vs 10 minutes). There is no

evidence that these residues have been converted to a thermally stable form. The point of this experiment is to put the material through a treatment of appropriate severity to make an assessment of potential impact of short thermal pretreatments on aromatic hydrocarbon formation. This timeframe and solid matrix also permits an assessment of potential reactions between the evolving solid structure and other substances of interest that are added and compared to the matrix alone. The residue yields at T_2 from 700 to 800 ^oC were independent of both the T_1 and T_2 temperatures that were studied and consistently around 20% for pectin and 10% for cellulose. We conclude that the low temperature treatment is insufficient to influence the amount of fixed carbon that will result from the high temperature treatment, but the chemical nature of that material may still be influenced by this treatment. We conclude that the parameters of this experiment are not critical to the observations of product formation from char and therefore are more likely to be relevant to a wide range of conditions where chars form. The main purpose of the low temperature treatment is to allow prompt chemical modifications of the material and reactions between co-reactants prior to higher severity pyrolysis

The devolatilization product composition at T_2 is predominantly primary products like what is observed at T_1. To separate the primary products evolving from the remaining unaltered starting material and that which is evolving from the thermally altered matrix material, time-resolved factor analysis of the T_2 mass spectra was performed. This series of mass spectra were subjected to self-modeling factor analysis and resulted in two distinct subspectra. The resolution of the T_2 curve into these two profiles is shown in **Figure 3.**

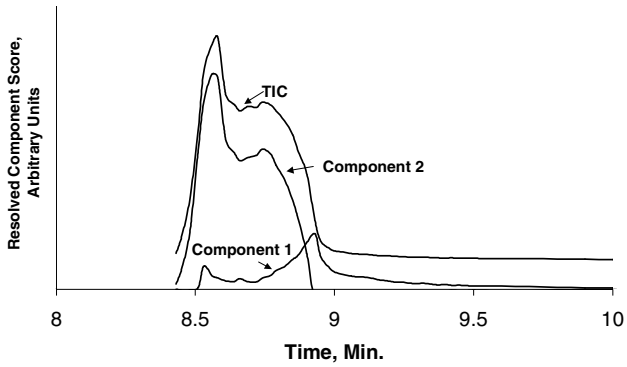

Figure 3. Time-resolved factor analysis of the T_2 evolution profile (TIC) showing evolution curves for the two subspectra shown in Figures 4 and 5.

Component Spectrum 1, shown in **Figure 4**, is a mixture of monoaromatics (m/z 78, benzene; m/z 92, toluene; m/z 106 xylenes), phenols (m/z 94, phenol; m/z 108, cresol; m/z 122, methylcresol), furans (m/z 67, 82 methyl furan), along with CO (m/z 28) and CO_2 (m/z 44). Polynuclear aromatic hydrocarbons were not detected in this experiment, but higher aromatics, such as naphthalene, were seen in other experiments, especially after the major evolution of T_2 products is finished.

Component spectrum 2, shown in **Figure 5**, is a typical carbohydrate primary pyrolysis product. The evolution profiles (**Figure 3**) of the two component spectra over the T_2 event are different with the primary products(component 2) reaching a maximum earlier. The aromatic/phenols continue to evolve and reach a maximum after the primaries are finished.

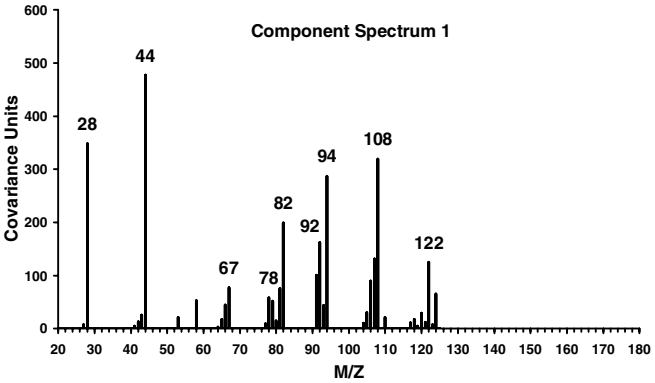

Figure 4. Component spectrum 1 in the time-resolved factor analysis of data in Figure 3.

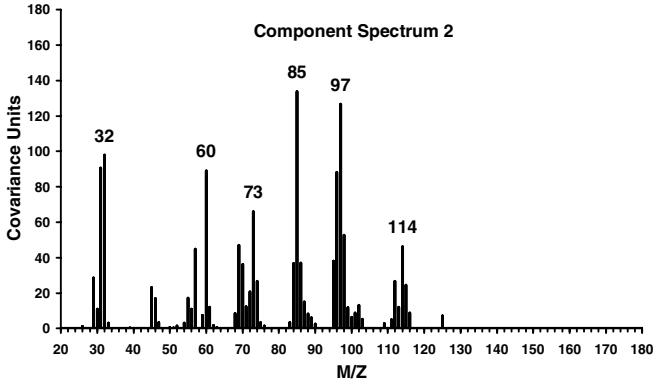

Figure 5. Component spectrum 2 in the time-resolved factor analysis of data in Figure 3.

Effect of Additives. Other biomaterials were tested by adding to the pectin/cellulose matrix and subjected to the same two temperature heating sequence. The following showed an enhancement of the yield of the aromatic/phenolic group: lignin, chlorogenic acid, rutin, proline and linolenic acid. It was surprising that lignin did not show a more significant enhancement. A possible explanation is the lignin addition leads to a more thermally stable residue that does not release low molecular weight volatiles.

Conclusions

In summary, two sub-spectra were evident during high severity pyrolysis of biopolymer samples that had been thermally pretreated: the primary pyrolysis products that also evolved at T_1 and a later evolving group of products that includes phenols and aromatics.

Acknowledgement. The authors gratefully acknowledge the financial support from Philip Morris USA, Inc. and discussions with Mohammad Hajaligol that initiated this work.

References

1. Evans R.J.; Milne, T.A. *Energy & Fuel* **1987,** 1,123.
2. McGrath T,; Sharma R.; Hajaligol, M. *Fuel* **2001**, *80*, 1787.
3. Shin, E-J.; Nimlos, M. R.; Evans, R. J. *Fuel* **2001**, *80*, 1697.
4. Hajaligol, M.; Waymack, B.; Kellogg, D. *Fuel* **2001**, *80*, 1787.
5. Windig W.; Lippert J.L.; Robbins, M.J.; Kresinske, K.R.; Twist, J.P.; Snyder, A.P. *Chemometrics and Intell. Lab.* **1990**, 9, 7.